NCHRP Web Document 60 (Project 20-50[7/12]): Contractor's Final Report

LTPP Data Analysis: Daily and Seasonal Variations in Insitu Material Properties

Prepared for:

National Cooperative Highway Research Program

TRANSPORTATION RESEARCH BOARD
OF THE NATIONAL ACADEMIES

Submitted by:

Eric C. Drumm
Roger Meier
The University of Tennessee, Knoxville
Knoxville, Tennessee

November 2003

ACKNOWLEDGMENT

This work was sponsored by the American Association of State Highway and Transportation Officials (AASHTO), in cooperation with the Federal Highway Administration, and was conducted in the National Cooperative Highway Research Program (NCHRP), which is administered by the Transportation Research Board (TRB) of the National Academies.

THE NATIONAL ACADEMIES

Advisers to the Nation on Science, Engineering, and Medicine

The **National Academy of Sciences** is a private, nonprofit, self-perpetuating society of distinguished scholars engaged in scientific and engineering research, dedicated to the furtherance of science and technology and to their use for the general welfare. On the authority of the charter granted to it by the Congress in 1863, the Academy has a mandate that requires it to advise the federal government on scientific and technical matters. Dr. Bruce M. Alberts is president of the National Academy of Sciences.

The **National Academy of Engineering** was established in 1964, under the charter of the National Academy of Sciences, as a parallel organization of outstanding engineers. It is autonomous in its administration and in the selection of its members, sharing with the National Academy of Sciences the responsibility for advising the federal government. The National Academy of Engineering also sponsors engineering programs aimed at meeting national needs, encourages education and research, and recognizes the superior achievements of engineers. Dr. William A. Wulf is president of the National Academy of Engineering.

The **Institute of Medicine** was established in 1970 by the National Academy of Sciences to secure the services of eminent members of appropriate professions in the examination of policy matters pertaining to the health of the public. The Institute acts under the responsibility given to the National Academy of Sciences by its congressional charter to be an adviser to the federal government and, on its own initiative, to identify issues of medical care, research, and education. Dr. Harvey V. Fineberg is president of the Institute of Medicine.

The **National Research Council** was organized by the National Academy of Sciences in 1916 to associate the broad community of science and technology with the Academy's purposes of furthering knowledge and advising the federal government. Functioning in accordance with general policies determined by the Academy, the Council has become the principal operating agency of both the National Academy of Sciences and the National Academy of Engineering in providing services to the government, the public, and the scientific and engineering communities. The Council is administered jointly by both the Academies and the Institute of Medicine. Dr. Bruce M. Alberts and Dr. William A. Wulf are chair and vice chair, respectively, of the National Research Council.

The **Transportation Research Board** is a division of the National Research Council, which serves the National Academy of Sciences and the National Academy of Engineering. The Board's mission is to promote innovation and progress in transportation through research. In an objective and interdisciplinary setting, the Board facilitates the sharing of information on transportation practice and policy by researchers and practitioners; stimulates research and offers research management services that promote technical excellence; provides expert advice on transportation policy and programs; and disseminates research results broadly and encourages their implementation. The Board's varied activities annually engage more than 4,000 engineers, scientists, and other transportation researchers and practitioners from the public and private sectors and academia, all of whom contribute their expertise in the public interest. The program is supported by state transportation departments, federal agencies including the component administrations of the U.S. Department of Transportation, and other organizations and individuals interested in the development of transportation.
www.TRB.org

www.national-academies.org

CONTENTS

ACKNOWLEDGMENTS

This report was prepared for NCHRP Project 20-50(07/12), under contract with the University of Tennessee. The project investigators were Dr. Eric C. Drumm, University of Tennessee, and Dr. Roger W. Meier, University of Memphis. Assistance was provided by the project team's independent consultants, Dr. Vincent C. Janoo and Dr. Raymond S. Rollings, both of the U.S. Army ERDC-CRREL, Hanover New Hampshire. Other team members contributing to this work were Daner Truss, Lori McDowell, and Gang Zuo, graduate research assistants at the University of Tennessee, and Narwa Laxmikanth, Veeravenkata Koppisetti, and Daniel Yusie, graduate research assistants at the University of Memphis.

SUMMARY

A pavement's ability to withstand traffic loading depends on the stiffness of its component layers and is heavily influenced by the temperature and moisture conditions inside the pavement. These conditions change continuously due to daily and seasonal fluctuations in environmental factors such as air temperature, solar radiation, precipitation, and water table depth.

The most pronounced environmental effects on a pavement's ability to withstand traffic loading occur in situations where ice accumulates beneath the pavement during the winter. The ice binds the soil and aggregate particles together and greatly increases the strength and stiffness of the unbound pavement materials. During the subsequent spring thaw, the surfeit of moisture can weaken those same pavement materials to the point where load restrictions must be emplaced to prevent pavement failure. These load restrictions are a severe burden on the trucking industry and the economic vitality of the affected regions.

As part of the Long Term Pavement Performance (LTPP) Seasonal Monitoring Program (SMP), pavement sites across North America were instrumented to periodically measure the temperature and moisture conditions inside the pavement and some of the environmental factors that affect those conditions. Coupled with periodic FWD tests to determine the stiffness of the pavement layers, this program has produced a data set that can be used to investigate daily and seasonal changes in pavement material properties and relate those changes to the changes in structural capacity that would necessitate load restrictions.

From the flexible pavement sites in the LTPP SMP, site-specific models of asphalt modulus as a function of internal temperature, surface temperature, and air temperature were developed. The

internal temperature produced the best correlation, but the surface temperature produced a model that was almost as good. The air temperature produced the worst correlation because it fails to capture the significant heating affects of solar radiation. Ideally, the solar radiation would be incorporated into the model as an additional variable, but solar radiation was not included in the SMP instrumentation plan.

At most of the pavement sites, seasonal changes in the base and subgrade moduli were lost in the scatter of the data. Even where seasonal changes in moisture content could be discerned, there was no statistically significant correlation between the moisture content and the layer moduli. The only exception to this is at sites with significant wintertime freezing. The TDR probes used to measure moisture content cannot detect soil water when it is frozen, so the moisture content drops to nearly zero during the winter freeze. At the same time, the backcalculated layer moduli increase substantially.

Of the 65 pavement sites in the SMP, 35 were located in wet-freeze or dry-freeze climatic zones and instrumented with electrical resistivity probes to determine the freeze state of the soil during the freeze/thaw period. At some of the wet-freeze sites, the winters were too mild to produce any appreciable freezing and at some of the dry-freeze sites, low moisture contents resulted in cold but unfrozen pavements. Of the 35 freezing sites, 21 sites registered frozen base or subgrade materials during the three years of data collection included in the LTPP database used for this study.

Site-specific models were developed to relate the depth of freezing to the freezing index. Traditionally, the freezing index is defined as the total number of freezing degree-days accumulated during the winter. Here, the freezing index is defined as the number of freezing degree-days accumulated at any point in time. Of the 21 sites that registered freezing, 10 had sufficient data to

develop site-specific freeze depth models. In addition, a general model of freeze depth as a function of the square root of freezing index was developed using data from all of the frozen sites.

A few site-specific models were developed to relate the depth of thawing to the thawing index, which is defined as the number of thawing degree-days accumulated at any point in time. To account for the effects of solar radiation, the thawing index is modified by a term that changes as the days get longer and the sun gets higher in the sky. Because the spring thaw is much shorter than the winter freeze, there was much less data available to model thaw depths. By grouping sites with similar subgrade types together, reasonable models of thaw depth as a function of thawing index were obtained for three different subgrade types: silty sand, silty clay, and sand with silt.

Efforts to model changes in pavement moduli during the winter freeze and spring thaw were hampered by a lack of backcalculated modulus data during that period. In many cases, FWD tests were not performed during the winter months because of the extreme cold. During the spring thaw, FWD tests were performed but the results did not produce any usable layer moduli. During the spring thaw, the soft subgrade material closest to the surface is sandwiched between the stiff granular base layer and the still-frozen subgrade below it. This is not properly modeled by the layered elastic system used to backcalculate the pavement moduli, in which case the backcalculated moduli may not be reliable.

Instead of using back-calculated moduli as an indicator of the seasonal variation in pavement response, the FWD deflections were used directly. In this context, it is useful to reduce each deflection basin to a single index that can be related to a specific type of behavior. Several candidate indices were identified that appear to reflect changes in structural capacity during freezing and thawing periods. While the indices at most sites reflected the change in response during freezing, only a few sites demonstrated what would be considered an obvious thaw weakening response. In some cases, the monthly FWD test schedule substantially missed the brief spring thaw. In other cases, the pavement sites had been designed so as to minimize thaw weakening. To ascertain that the selected indices could detect thaw weakening and recovery, several datasets from outside the LTPP SMP were investigated. These data indicated what would be expected had the LTPP SMP experiment collected more complete FWD response during freezing and thaw periods.

Layered elastic models of the freezing pavement sites were developed. The asphalt modulus was varied throughout the year using the site-specific temperature models developed from the LTPP data. The nominal moduli for the base and subgrade were taken based on backcalculated values from the LTPP database, and then systematically varied to reflect changes with freeze and thaw depth over time. FWD indices from the model were computed weekly throughout the freeze/thaw/recovery period along with the critical strains in the asphalt and subgrade. From this, a methodology was developed and recommendations made for using FWD deflection basin indices to detect the onset of spring thaw and the end of the thaw-weakening period.

CHAPTER 1
INTRODUCTION

1.1 PROJECT OBJECTIVES

Because of the effects of temperature and moisture on pavement materials, knowledge of the variation in insitu material properties of pavement layers is essential for evaluating the effective structural capacity of the pavement. However, the relationships between temperature and moisture conditions and pavement material properties are not well documented. Without this information, selecting appropriate designs for new pavements, choosing rehabilitation strategies for existing pavements, and decision making regarding seasonal load restrictions are difficult tasks. The data available from the Long-Term Pavement Performance (LTPP) studies are expected to provide such information.

Research is needed to identify the relationships between daily and seasonal temperature and moisture conditions and the insitu material properties of pavement layers and to develop methodologies for estimating the pavement's daily and seasonal structural capacity. The findings of this research will provide guidance for the design of new and rehabilitated pavement structures and for decisions regarding seasonal load restrictions.

The objectives of this research are to:

1. Document, based on the data available from the LTPP studies, patterns of change in daily and seasonal insitu pavement material properties;

2. Determine, based on the data available from the LTPP studies, relationships between daily and seasonal *in situ* pavement material properties and temperature, moisture, and other related factors; and

3. Investigate the relationships between these properties and the daily and seasonal structural capacity of flexible and rigid pavements, with the intent of developing guidelines for imposing seasonal load restrictions and issuing seasonal overload permits.

1.2 RESEARCH TASKS

The project was broken into two phases. Phase I comprised three major tasks and produced a working plan to be implemented in Phase II. The working plan enumerated two major tasks for Phase II: Task 4, the performance of the work, and Task 5, the preparation of the final project report. Conceptually, Phase II can be thought of as comprising three subtasks:

Task 4a: Document daily and seasonal patterns of change in pavement material properties such as asphalt and subgrade modulus and modulus of subgrade reaction.

Task 4b: Develop relationships that describe the changes in material properties and structural capacity that result from daily and seasonal changes in temperature, moisture, and other related factors.

Task 4c: Use the relationships developed in Task 4b to develop guidelines for imposing and lifting seasonal load restrictions and issuing seasonal overload permits

1.3 DATA IDENTIFICATION AND AVAILABILITY

The original SMP experimental design comprised 64 LTPP test sections (48 flexible sections and 16 rigid sections) arranged in a factorial design covering different pavement types, subgrade types, and environments (Table 1.1). To fill the design, states were asked to nominate sites for inclusion on the experiment. Some of the nominated sites were never built or never instrumented. Others turned out to lie in a cell other than that originally intended. Table 1.2 shows the actual number of SMP sites in each cell of the experimental design.

Table 1.2 shows that there are half as many flexible pavement sites with fine-grained subgrade soil as originally planned. Part of this stems from an understandable absence of dry-no freeze sites with fine-grained soils. This will impact the research little because dry-no freeze sites are among the least interesting from the standpoint of moisture effects. The same holds true for the absence of dry-freeze and dry-no freeze sites with jointed reinforced concrete pavements. In fact, these absences are compensated by a plethora of wet-freeze and wet-no freeze sites (for flexible and

rigid pavements) that should contain considerable fluctuations in base and subgrade moisture content.

Table 1.3 provides a summary of the SMP sites, including climate zone, pavement type, and subgrade type.

Table 1.1 Original Experimental Design for SMP (LTPP 2000)

Pavement Type	Subgrade Soil	No Freeze		Freeze	
		Dry	Wet	Dry	Wet
Flexible Thin (<125 mm or 5") AC	Fine	3	3	3	3
	Coarse	3	3	3	3
Flexible Thick (>125 mm or 5") AC	Fine	3	3	3	3
	Coarse	3	3	3	3
Rigid Jointed Plain Concrete	Fine	1	1	1	1
	Coarse	1	1	1	1
Rigid Jointed Reinforced Conc.	Fine	1	1	1	1
	Coarse	1	1	1	1

Table 1.2 Realized Experimental Design for SMP

Pavement Type	Subgrade Soil	No Freeze		Freeze	
		Dry	Wet	Dry	Wet
Flexible Thin (<125 mm or 5") AC	Fine	0	2	2	1
	Coarse	1	4	3	3
Flexible Thick (>125 mm or 5") AC	Fine	0	4	1	2
	Coarse	3	3	4	7
Rigid Jointed Plain Concrete	Fine	1	5	1	3
	Coarse	1	1	1	2
Rigid Jointed Reinforced Conc.	Fine	0	1	0	3
	Coarse	0	1	0	1

Table 1.3 Summary of SMP site climate zones and subgrade types

Site Number	State	Climate Zone	AC / PC	Subgrade
01-0101	Alabama	No Freeze / Wet	AC	Subgrade (untreated); Fine-Grained Soils: Sandy Silt
01-0102	Alabama	No Freeze / Wet	AC	Subgrade (untreated); Fine-Grained Soils: Lean Clay with Sand
04-0113	Arizona	No Freeze / Dry	AC	Subgrade (untreated); Coarse-grained Soils: Well-Graded Sand with Silt and Gravel
04-0114	Arizona	No Freeze / Dry	AC	Subgrade (untreated); Coarse-Grained Soil: Silty Sand with Gravel
04-0215	Arizona	No Freeze / Dry	PC	Subgrade (untreated); Coarse-Grained Soil: Silty Sand with gravel
04-1024	Arizona	No Freeze / Dry	AC	Subgrade (untreated) Layer; Coarse-grained Soil: Clayey Sand with Gravel
006-3042	California	No Freeze / Dry	PC	Subgrade (untreated) Layer; Fine-Grained Soils: Sandy Lean Clay
08-1053	Colorado	Freeze / Dry	AC	Subgrade (untreated) Layer; Fine-Grained Soils: Lean Inorganic Clay
09-1803	Connecticut	Freeze / Wet	AC	Subgrade (untreated) Layer; Coarse-Grained Sois: Well-Graded Sand with Silt and Gravel
10-0102	Delaware	Freeze / Wet	AC	Subgrade (untreated) Layer; Coarse-Grained Soils: Poorly Graded Sand
13-1005	Georgia	No Freeze / Wet	AC	Subgrade (untreated) Layer; Coarse-Grained Soil: Clayey Sand
13-1031	Georgia	No Freeze / Wet	AC	Subgrade (untreated) Layer; Coarse-Grained Soil: Silty Sand
13-3019	Georgia	No Freeze / Wet	PC	Subgrade (untreated) Layer; Fine-Grained Soils: Sandy Lean Clay
16-1010	Idaho	Freeze / Dry	AC	Coarse-Grained Soil:Silty Sand ; Subgrade (Untreated)
16-3023	Idaho	Freeze / Dry	PC	Subgrade (untreated) Layer; Coarse-Grained Soils: Silty Sand
18-3002	Indiana	Freeze / Wet	PC	Subgrade (untreated) Layer; Fine-Grained Soils: Sandy Lean Clay
20-4054	Kansas	Freeze / Wet	PC	Subgrade (untreated) Layer; Fine-Grained Solis: Lean Inorganic Clay
23-1026	Maine	Freeze / Wet	AC	Coarse Grained Soil: Silty Sand with gravel ; Subgrade (Untreated)
24-1634	Maryland	Freeze / Wet	AC	Subgrade (untreated) Layer; Fine-Grained Soils: Silt
25-1002	Massachusetts	Freeze / Wet	AC	Coarse-Grained Soils: Poorly Graded Sand with Silt) ; Subgrade (Untreated)
27-1018	Minnesota	Freeze / Wet	AC	Coarse-Grained Soils: Poorly Graded Sand with Silt) ; Subgrade (Untreated)
27-1028	Minnesota	Freeze / Wet	AC	Coarse-Grained Soils: Poorly Graded Sand with Silt) ; Subgrade (untreated)
27-4040	Minnesota	Freeze / Wet	PC	Fine-Grained Soils: Lean Clay with Sand) ; Subgrade (Untreated)
27-6251	Minnesota	Freeze / Wet	AC	Coarse-Grained Soils: Poorly Graded Sand with Silt)
28-1016	Mississippi	No Freeze / Wet	AC	Subgrade (untreated) Layer; Coarse-Grained Soil: Silty Sand
28-1802	Mississippi	No Freeze / Wet	AC	Subgrade (untreated) Layer; Coarse-Grained Soils: Poorly Graded Sand
30-0114	Montana	Freeze / Dry	AC	Subgrade (untreated) Layer; Coarse-Grained Soils: Poorly Graded Sand with Silt
30-8129	Montana	Freeze / Dry	AC	Fined-Grained Soils:Gravely Lean Clay With Sand; Subgrade (Untreated)
31-0114	Nebraska	Freeze / Wet	AC	Fined-Grained Soil: Silty Clay; Subgrade(Untreated)
31-3018	Nebraska	Freeze / Wet	PC	Coarse-Grained Soils: Poorly Graded Sand; Subgrade (Untreated)
32-0101	Nevada	Freeze / Dry	AC	Subgrade (untreated) Layer; Coarse-Grained Soil: Silty Sand
32-0204	Nevada	Freeze / Dry	PC	Subgrade (untreated); Fine-Grained Soils: Sandy Silt
33-1001	New Hampshire	Freeze / Wet	AC	Subgrade (untreated); Coarse-Grained Soils: Poorly Graded Sand with Silt
35-1112	New Mexico	No Freeze / Dry	AC	Subgrade (untreated); Coarse-Grained Soils: Poorly Graded Sand

Table 1.3 Summary of SMP site climate zones and subgrade types (continued)

Site Number	State	Climate Zone	AC / PC	Subgrade
36-0801	New York	Freeze / Wet	AC	Coarse-Grained Soil:Silty Sand; Subgrade (untreated)
36-4018	New York	Freeze / Wet	PC	Coarse-Grained Soils: Silty Gravel with Sand; Subgrade (Untreated)
37-0201	North Carolina	No Freeze / Wet	PC	Fine-Grained Soils: Clay
37-0205	North Carolina	No Freeze / Wet	PC	Subgrade (untreated); Fine-Grained Soils: Clay
37-0208	North Carolina	No Freeze / Wet	PC	Subgrade (untreated); Fine-Grained Soils: Sandy Silt
37-0212	North Carolina	No Freeze / Wet	PC	Subgrade (untreated): Fine-Grained Soils: Sandy Silt
37-1028	North Carolina	No Freeze / Wet	AC	Subgrade (untreated); Coarse-Grained Soils: Poorly Graded Sand with Silt
39-0204	Ohio	Freeze / Wet	PC	Fined-Grained Soil: Silty Clay
40-4165	Oklahoma	Freeze / Wet	AC	Subgrade (untreated); Coarse-Grained Soil: Silty Sand
42-1606	Pennsylvania	Freeze / Wet	PC	Subgrade (untreated); Fine-Grained Soils: Gravelly Lean Clay with Sand
46-0804	South Dakota	Freeze / Dry	AC	Fined-Grained Soil: Silty Clay; Subgrade (untreated)
46-9187	South Dakota	Freeze / Dry	PC	Fine-Grained Soils: Lean Inorganic Clay; Subgrade (Untreated)
48-1060	Texas	No Freeze / Wet	AC	Subgrade (untreated); Coarse-Grained Soil: Silty Sand
48-1068	Texas	No Freeze / Wet	AC	Subgrade (untreated); Fine-Grained Soils: Sandy Lean Clay
48-1077	Texas	No Freeze / Wet	AC	Subgrade (untreated); Fine-Grained Soils: Sandy Silt
48-1122	Texas	No Freeze / Wet	AC	Subgrade (untreated); Coarse-Grained Soil: Clayey Sand
48-3739	Texas	No Freeze / Wet	AC	Subgrade (untreated); Coarse-Grained Soils: Poorly Graded Sand
48-4142	Texas	No Freeze / Wet	PC	Subgrade (untreated); Coarse-Grained Soil: Clayey Sand
48-4143	Texas	No Freeze / Wet	PC	Subgrade (untreated); Fine-Grained Soils: Lean Inorganic Clay
49-1001	Utah	Freeze / Dry	AC	Subgrade (untreated); Coarse-Grained Soil: Silty Sand
49-3011	Utah	Freeze / Dry	PC	Subgrade (untreated); Coarse-Grained Soil: Clayey Gravel With Sand
50-1002	Vermont	Freeze / Wet	AC	Coarse-Grained Soils: Poorly Graded Gravel With Silt and Sand; Subgrade (untreated)
51-0113	Virginia	No Freeze / Wet	AC	Subgrade (untreated); Fine-Grained Soils: Silt
51-0114	Virginia	No Freeze / Wet	AC	Subgrade (untreated); Fine-Grained Soils: Sandy Silty Clay With Gravel
53-3813	Washington	No Freeze / Wet	PC	Subgrade (untreated); Coarse-Grained Soil: Silty Sand
56-1007	Wyoming	Freeze / Dry	AC	Coarse Grained Soil: Silty Sand with gravel; Subgrade (untreated)
83-1801	Manitoba	Freeze / Dry	AC	Coarse-Grained Soil:Silty Sand;Subgrade (untreated)
83-3802	Manitoba	Freeze / Dry	PC	Fine-Grained Soils: Fat Inorganic Clay;Subgrade (untreated)
87-1622	Ontario	Freeze / Wet	AC	Fine-Grained Soils: Sandy Silt; Subgrade (Untreated)
89-3015	Quebec	Freeze / Wet	PC	Coarse-Grained Soils: Poorly Graded Sand; Subgrade (Untreated)
90-6405	Saskatchewan	Freeze / Dry	AC	Coarse-Grained Soil:Silty Sand; Subgrade (Untreated)

To clarify the types of relationships that were produced, it helps to understand that there are three distinct types of data represented in the SMP database:

1. **Environmental Factors** are those external to the pavement system such as air temperature, water table depth, and precipitation, which are the root cause of daily and seasonal changes in pavement performance. In addition, there are internal or "state" variables, such as asphalt mid-depth temperature and subgrade moisture content that describe the internal state of the pavement system. Changes in the environmental factors affect these internal state variables, which in turn affect the pavement material properties.
2. **Material Properties** such as asphalt modulus and modulus of subgrade reaction that cause the pavement to behave differently as it's internal state changes,
3. **Measures of Structural Capacity or Pavement Response** related to the timing of seasonal load restrictions and overload permitting.

Each of these data types is discussed below.

1.3.1 Relevant Environmental Data Elements

Environmental factors are those external to the pavement system such as air temperature, water table depth, and precipitation, which are the root cause of daily and seasonal changes in pavement performance. In addition, there are internal or "state" variables, such as asphalt mid-depth temperature and subgrade moisture content that describe the internal state of the pavement system. Changes in the environmental factors affect these internal state variables, which in turn affect the pavement material properties.

1.3.1.1 Asphalt Concrete Temperature

The seasonal and diurnal variation of asphalt pavement temperature has been related to environmental factors such as air temperature and surface temperature by Lukanen, Stubstad, and Briggs (FHWA Report RD-98-085) using data from the first two rounds of FWD testing at the SMP flexible pavement sites. They used data from the first round of testing (1994-1995) to develop their models, validated the models with data from the second round of testing (1995-1996), then combined the data from both rounds to produce their final model, called BELLS2. The BELLS2 model predicts the mid-depth pavement temperature as a function of the previous day's high and low air temperature, the current surface temperature, and the current time. Such models are useful to predict the change in pavement modulus due to fluctuation of the mid-depth temperature.

1.3.1.2 Portland Cement Concrete Temperature Gradient

For rigid pavements, the actual temperature of the concrete is not as important as the temperature gradient. At each rigid pavement site, there are three thermistors buried in the concrete slab. The uppermost is nominally one inch below the top of the slab, the next is near the slab mid-depth, and the lowest is nominally one inch above the bottom of the slab. The temperature gradient is traditionally assumed to be constant throughout the slab, which implicitly assumes that the temperature distribution is linear.

While the temperature distribution may not be linear at some times of the day, such as when the surface temperature first starts rising at midday or falling after dark, it approaches linearity during the late afternoon, when the temperature gradient achieves its highest positive value, and during the early morning, when it reaches its highest negative value. Since the highest positive and negative gradients are of most interest (because they maximize the curling stresses), the temperature

gradient can be simply be calculated using the temperature difference between the highest and lowest thermistors in the slab. However, for this approach to work, the highest temperature must be near the edges, or the temperatures must be adjusted based on the solar radiation.

1.3.1.3 Temperature Variations in the Subgrade, Subbase, and Unbound Base

While the properties of most unbound materials do not vary with temperature, some of the most significant variations in water content (especially at wet-freeze sites) take place during the winter. Thus, an investigation of the soil temperature variation is appropriate.

Since the dielectric constant for ice is significantly different than that for water, the water contents measured by the TDR probes during the frozen periods may not be representative of actual conditions, and may reflect the presence of ice. This should be considered as relationships between the water content and material properties are investigated. The seasonal changes in subgrade temperature and freeze/thaw depth can also be used to identify the spring thaw time. Used in conjunction with the FWD tests, load restriction periods can be identified.

1.3.1.4 Moisture Content Variations in the Subgrade, Subbase, and Unbound Base

The variation of soil moisture is complicated, because of the influence of a number of factors, such as soil type, precipitation, location of the groundwater table, solar radiation, and the topography. Different models have been developed to simulate the process of wetting and drying of soil. Several researchers have tried to find the correlation between rainfall and variation of subgrade moisture content by observing the precipitation data and moisture data (Cuberledge et al. 1974), or calculating the correlation coefficient directly (Valdez 1991; Hossain et al. 1997). Almost all these researchers ended up with the same conclusion that there is no relationship between rainfall and subgrade moisture variation. This is discussed in more detail in Appendix A.

The variation of soil moisture in the subgrade soil is important to the pavement design process, because change in the soil stiffness or modulus due to moisture variation is the direct cause of the distress in pavements. For most cases, it is not appropriate to predict the variation of soil moisture with an analytical model, which can include all the processes like infiltration, drainage, evaporation and heat transfer. Instead, the variation of soil moisture is obtained from in situ measurements, and then regression methods are used to find the correlation between the soil moisture variation and environmental factors.

1.3.1.5 Freezing Index, Thaw Index and Depth of Freeze Measurements

The freezing index, thaw index and depth of freezing are internal state variables that can have significant effect on the pavement behavior. These factors are discussed in detail in Section 1.3.4.

1.3.2 Environmental Factors Affecting Pavement Material Properties

Changes in the environmental factors often lead to changes in the pavement material properties, such as the modulus of asphalt concrete or modulus of the base and subgrade.

1.3.2.1 Temperature Effects on Asphalt-Bound Materials

It is well known that the stiffness of asphalt concrete is directly related to its temperature, the practical result being that the structural performance of asphalt pavements changes diurnally and seasonally as the internal temperature of the pavement changes. These changes are brought about by fluctuations in air temperature and solar radiation and vary somewhat depending on the binder properties (which change over time due to age hardening and microcracking) and, to a lesser extent, the asphalt mix design.

Most published models of in situ asphalt temperature dependence are based on data from limited geographic areas (typically a single state) where binder properties and mix designs are

relatively constant. As a result, they have limited applicability to a nationwide study such as this. Recently however, Lukanen et al. (2000) modeled in situ temperature dependence using nationwide FWD data from Rounds 1 and 2 of the LTPP SMP. By including geographic latitude as a predictor variable, their model captures at least broad differences in binder properties and mix designs between cold northern states, where low-temperature behavior is the biggest concern, and hot southern states where high-temperature behavior is more important.

When Lukanen et al. did their analysis, a year's worth of monthly FWD data was available for most of the flexible pavement sections in the SMP, but they had not yet been analyzed to determine the pavement layer moduli. Lukanen et al. calculated their own pavement layer moduli using ELMOD, MODULUS, and WESDEF. The LTPP IMS database now contains backcalculated moduli obtained from the same FWD deflection basins using yet another program, MODCOMP. This provides an opportunity to validate their work using a separate (though not independent) set of modulus data. Beyond that, there is little more that can be done to improve on that earlier work. Moduli from later rounds of testing have not yet been released, so the amount of data available is the same as when Lukanen, et al. developed their models. Given the inevitable differences in the thermal response of the binders due to age hardening and microcracking and the absence of any data in the LTPP IMS with which to account for those differences, their relationships are remarkably accurate.

Beyond the question of how asphalt stiffness changes with changing internal temperature is the need to define a characteristic pavement temperature and correlate it to environmental factors such as air temperature and solar radiation. The temperature in an asphalt pavement varies with both depth and time. Below a certain depth, the temperature changes little during the day and is best

predicted by recent levels of the mean air temperature. Above that depth, the temperature varies diurnally due to the absorption of solar radiation during the day and the radiation of stored heat to the atmosphere at night. The amount of variation exhibited on a given day depends on the amount of cloud cover, the wind speed, and the time of year (which influences the angle of the sun's rays). This makes it difficult to determine a single characteristic pavement temperature. Some have suggested that the temperature one-third of the way into the layer correlates best with layer modulus, while others have suggested that the temperature at the layer mid-height is good enough. Van Gurp (1994) recommends using Nijboer's equivalency concept of equal curvatures of bending beams to find the uniform layer temperature that produces the same curvature as the actual nonuniform temperature distribution.

Stubstad, et al. (1994; 1998), building on the work of Southgate and Deen (1969) developed a regression model to predict temperature at the asphalt third-depth or mid-depth using the 5-day mean air temperatures and measured surface temperatures. Lukanen, et al. (2000) developed a slightly less-accurate regression model based on the 1-day mean air temperature, which is easier to obtain than the 5-day mean. Both models are based on data from the LTPP SMP. Since we are constrained to use the same data that was available to those researchers, there is little that can be done to improve on this work.

1.3.2.2 Moisture Effects on Unbound Materials

Unbound materials in the pavement base, subbase, and subgrade are typically characterized by the resilient modulus. The resilient modulus is a function of the material density, the amount of water present and the level of applied stress, and is generally assumed to be independent of temperature. While the density of the unbound materials may change over time (especially in

association with rutting), in pavement design it is usually assumed that the density remains constant. The effects of moisture changes and stress level are of primary interest with respect to the variation of resilient modulus.

For fine-grained subgrades, it is reasonable to assume that the daily variation in moisture content is minimal because of the low permeability of the soil, so daily changes in resilient modulus can be neglected. For the coarse-grained subgrades and unbound base materials, some daily changes in moisture content may be observed in response to significant precipitation events. However, it is not likely that FWD tests were conducted in the rain, but monthly variations in in backcalculated moduli may be slightly affected by preciptation events.

Seasonal variations of moisture content, on the other hand, must be investigated because of the strong relationships that exist between moisture content and resilient modulus for most unbound materials. Seasonal fluctuations in moisture content can be investigated using TDR measurements of volumetric water content, but variations in moisture content should be broken down by climate zone (wet/dry and freeze/no freeze) and material type (fine-grained/coarse-grained). The moisture source (rainfall infiltration or water table capillary rise) may also have an effect on moisture variations. Russam (1970) proposed a classification system for subgrades based on the water table depth and annual rainfall that may be useful for categorizing the various sites. Yoder and Witczak (1975) adopted a similar classification system which is summarized in Table 1.4.

Table 1.4 Subgrade classification for moisture susceptibility (Yoder and Witczak 1975)

Category	Description
1	Subgrades where the water table is close to the surface (defined as a depth less than 20 ft in clays, 10 ft in sandy clays or silts, and 3 ft in sands). The water table is assumed to be the main source of subgrade moisture. Under a relatively impermeable surface, the soil water will tend toward equilibrium with the water table. The subgrade moisture content is governed by fluctuations in the water table depth.
2	Subgrades where the water table is deeper than in Category 1 and the rainfall is more than 10 in. per year. The subgrade moisture content in this category will be governed by seasonal changes in the rainfall.
3	Subgrades where the water table is deep as in Category 2 and the rainfall is less than 10 in. per year. In this category, the moisture content of the subgrade will differ little from that of uncovered soil at the same depth.

To account for differences in the dry resilient moduli of the unbound materials, it will probably be necessary to normalize the data into modular ratios by dividing all the layer moduli at a given site by some baseline value. A common baseline value is the highest value recorded during the year, which yields modular ratios less than or equal to unity. With this approach, a different month would have to be identified for each layer. A more appropriate way might be to pick a month during which the pavement system may be considered “nominal” (such as early summer or late fall when the pavement is not in a deep freeze, a spring thaw, or a drought).

It is usually assumed that the behavior of unbound geo-materials is not dependent upon temperature. While this is true in a cause-and-effect sense, if the resilient moduli of the unbound materials are stress dependent, temperature-dependent changes in the stiffness of the surface layer will change the traffic-induced stresses in the base, subbase, and subgrade. The resilient modulus of many unbound materials varies with stress. In general, coarse-grained materials stiffen with increasing bulk stress and fine-grained materials soften with increasing deviator stress. Before investigating the effects of changing moisture content on base, subbase, and subgrade stiffness, we may have to correct for changes in stiffness arising from this indirect dependence on temperature. Matter and Farouki (1994) indicated that the moisture content effects and temperature effects might reach their peak impacts at different times or seasons. The increase in one factor may be accompanied by a decrease in the other factor. The combined effects of these opposite variations make it hard to separate the effect of each factor.

Temperature may also have an impact on the accuracy of the TDR measurements. A preliminary evaluation of the SHRP-TPP data revealed that in cold seasons, moisture content in the subgrade was lower than in warm seasons (Zhou and Elkins, 1994). Data collected at the Minnesota Road Research Project (Mn/ROAD) showed that seasonal temperature fluctuations were directly related to the seasonal distribution of the unfrozen volumetric moisture content (Ovik et al., 1998). These observations are contrary to the theory that the movement of moisture should be opposite to the direction of the temperature gradient. A similar phenomenon was observed at instrumented pavement sites in Tennessee, some of which had more than three years of TDR data. It was determined however, that the TDR probes were temperature dependent leading to the erroneous conclusion that the subgrade moisture variation was related to soil temperature. Subsequent

calibration for temperaure effects eliminated much of the seasonal water content variation, and the backcalculated subgrade moduli were found to be nearly contant throughout the year (Zuo et al. 2000).

1.3.2.3 Environmental Effects on Rigid Pavement Properties

Environmental effects on rigid pavements, both jointed plain concrete (JPC) and jointed reinforced (JRC) concrete, can be divided into those that affect the concrete slab and those that affect the underlying layers. This section will focus primarily on environmental effects on the concrete slab since effects on the underlying layers have been discussed previously and are equally applicable to flexible and rigid pavements. The one exception to this is joint faulting, which typically develops because of volume changes in the underlying materials. These volume changes can arise due to loss of material (pumping), frost heave, or heave due to expansive soils, all of which are directly related to soil moisture. Faulting problems may or may not appear depending on pavement details such as joint design and slab length. The joint faulting data would reveal whether seasonal changes in moisture can be correlated with faulting and which design details exacerbate or mitigate the problem.

Environmental factors affect concrete pavement slabs in two ways. They can cause deterioration of the concrete itself (which is generally a construction or mix design issue and is beyond the scope of this research) or they can cause volume changes that make the slab change size in the horizontal direction or curl in the vertical direction. (Rather than differentiate between *curl* and *warp* based on the underlying causes of deformation, this report will use the term *curl* as a generic descriptor for all out of plane displacements due to volume changes.)

Curling develops due to differential volume change across the thickness of the slab. This can arise when the concrete tries to undergo a uniform change in volume but friction or some similar mechanism resists the concrete expansion or contraction on one face (usually the underside) or it can arise when temperature or moisture gradients exist across the slab height, causing differential volume change between the top and bottom of the slab. Curling can cause loss of contact between the slab and its underlying support or, if it is resisted by the self-weight of the slab, can cause stresses that shorten the fatigue life of the pavement.

There are many different sources of curling. Some, such as early-age effects (which occur soon after placement due to adverse thermal gradients at the time of setting and tend to curl the pavement upwards), autogenous shrinkage (shrinkage associated with cement hydration that promote upward curling because of base frictional restraint), and carbonation (shrinkage that results from chemical reactions between carbon dioxide and cement hydration products and promotes upward curl) are beyond the scope of this research. Others, such as thermal and moisture effects, are the focus of this research.

Thermal effects result from the fact that concrete increases in volume upon heating. For pavements, there are two thermal considerations. One is associated with diurnal variations in temperature and the other with seasonal variations.

Diurnal variations in ambient temperature cause temperature gradients to develop between the surface and underside of the slab. These promote curling directly, causing the upward curl at night when the surface is cooler than the underside, and downward curl during the day, when the opposite is true. The typical and maximum magnitudes of the temperature gradient in rigid pavements should be determined as a function of climatic zone, season, and time of day (relative to maximum day vs.

maximum night). This would provide the designer a localized and seasonal “rule-of-thumb” (e.g., 1.5ºF per inch of pavement thickness) for anticipated ranges of daytime and nighttime temperature gradients.

Seasonal variations in temperature cause the slabs to lengthen in warm weather and shorten in cool weather. This can be manifested as opening and closing of the joints between slabs or, if resisted by friction on the underside of the slab, upward curling of the slab in cool weather and downward curling in hot weather. As the dimensions of the slab change, the joints between slabs open and close. As the joints open, load transfer efficiency between slabs can drop off, which affects the structural capacity of the pavement. This is discussed further later.

Moisture effects result from the tendency of concrete to shrink and expand in response to changes in moisture. As absorbed water and moisture in small capillary pores is lost from concrete, it undergoes a reduction in volume. Some of this shrinkage is reversible (Neville 1981) but the original length before the first drying will never be reached again (Mehta 1994). After first drying, precipitation, snow melt, and freeze/thaw can cause episodic cycles of wetting and drying. These moisture effects may cause upward or downward curling of the slab and are superimposed on the other curling sources mentioned above. Pavement slabs tend to dry readily from the surface and remain moist on the underside so the general trend will be upward curling.FWD measurements obtained from the corners and edges of concrete slabs can be used to investigate daily and seasonal curling. The FWD deflections can be plotted as a function of applied load (response from three different drop heights) for the center of the slab, edge of the slab, and corner positions. A slab in intimate contact with the underlying medium will have an approximately linear relationship between

drop height and response. In the absence of other site-specific conditions that could produce a nonlinear relationship, any deviations from a linear relation are suggestive of curling.

1.3.3 Effect of Pavement Material Properties on Structural Capacity/Response

Material properties such as asphalt modulus and modulus of subgrade reaction, which change in response to environmental effects, subsequently affect the pavement capacity or response. In rigid pavement, the load transfer efficiency between slabs varies with diurnal and seasonal temperature changes. In the LTTP database, seasonal pavement response was quantified by FWD Testing.

1.3.3.1 Effects of Changes in Modulus on Pavement Response

As discussed previously, seasonal changes in the moisture content of the unbound layers will affect the material response. To account for the seasonal variation in moisture content, the AASHTO *Guide for Design of Pavement Structures* describes a procedure for the identification of a single subgrade resilient modulus value for flexible pavement design. The year is divided into intervals or seasons, with each interval assigned a resilient modulus. Based on the anticipated pavement damage for that modulus value, a single value of M_R known as the "effective roadbed soil resilient modulus," is obtained for design. This approach is a rational method for the incorporation of seasonal variations of subgrade moisture content into the flexible pavement design process. However, a knowledge of the seasonal variation of modulus or a procedure for the determination of the seasonally adjusted resilient modulus is not described.

1.3.3.2 Load Transfer Effeciency in Rigid Pavements

As the dimensions of the slab change, the joints between slabs open and close. As the joints open, load transfer efficiency between slabs can drop off, which affects the structural capacity of the

pavement. FWD measurements across the joints can be used to investigate relationships between joint opening and load transfer efficiency. The load transfer efficiencies could then be related to the AASHTO joint transfer coefficient, J, which is used to account for the ability of the joint to transfer load across a discontinuity such as a crack or joint. The type of load transfer device, the degree of aggregate interlock, and the existence of tied concrete shoulders all affect the value of J. The 1993 *AASHTO Design Guide* suggests that the J values can be increased or decreased for the effects of high thermal coefficients or low heavy truck volume. Consequently, the adjustment of the J-value to account for environmental effects appears to be a rational means to incorporate these effects in the pavement design process.

1.3.4 Changes in Structural Capacity or Response during Freeze - Thaw

The investigation of the change in pavement structural capacity or response during freeze thaw period and the associated timing of seasonal load restrictions and overload permitting is an important factor in this study. These changes occur due to environmentally induced changes in the material properties, specifically changes in the base and subgrade moduli during freezing and thawing. The temperature dependent behavior of the AC layers also plays a role in the response during these periods.

While the change in pavement response during freeze and thaw is important, the estimation of the starting and ending times for spring load restrictions is of great interest to agencies responsible for roadways subject to these effects. Janoo and Shephard (2000) found that the moisture content in the base tended to increase sharply when the temperature in the base reached –2ºC. By the time the temperature reached 0ºC, the moisture content had already peaked and returned to its frost-free value. If, in fact, the strength of the thawing base course is primarily a function of the

moisture content, then instituting load restrictions when the temperature warms up to 0ºC may be too late for averting pavement damage during spring thaw.

1.3.4.1 Freeze/Thaw Effects on Unbound Materials

Pavements in seasonal frost regions are subjected to annual freeze/thaw cycles. During the winter, ice crystals bond soil particles together, increasing the bearing capacity of the pavement system beyond its frost-free levels. The increase in bearing capacity is primarily a function of the type of material and its unfrozen water content. At the same time, ice lenses can form in the subgrade and cause the pavement to heave. Differential frost heave arising from spatially varying subsurface conditions can lead to an increase in pavement roughness.

During the spring, melting ice lenses, coupled with surface water infiltration, can cause the subgrade to become saturated. This can reduce the bearing capacity of the pavement system to the point that load restrictions must be implemented to keep the pavement from failing. The length of the load restrictions, which can have harsh economic consequences, depends on the subsurface materials, frost penetration depth, and drainage conditions.

Finally, in freeze thaw areas, the location of the water table has a significant effect on the amount of water that reaches the freezing front. However, FWD data has shown that there is a reduction in resilient modulus of as much as 50% in closed systems where the water table is too deep to feed the freezing front. It is thought that this could be the result of the redistribution of unfrozen water to the freezing front. This should be considered when examining sites with a deep water table.

It is a common fallacy that there is no thaw weakening of granular materials in the pavement base. To design a base course for strength requires that a significant amount of fines be present. In

cold regions, these fines can reduce the permeability of the layer to the point that water is trapped in the base for long periods during spring thaw, creating an undrained condition under traffic loads.

Another common oversimplification is that all of the water in the subgrade freezes during the winter. In truth, the amount that freezes is a function of the soil type and salt content. It has been observed that the amount of unfrozen water increases with depth. It is not clear what effect this has on the resilient modulus of the subgrade material. The TDR probes installed at the SMP sites could shed valuable light on the actual amount of unfrozen soil water because they only measure the volumetric moisture content of the unfrozen water.

As a rule of thumb, keeping the fines content less than 3% passing the #200 sieve will keep the material non-frost susceptible. Table 1.5 provides a summary of the freezing sites, details of the subgrade soils, and some associated data related to frost susceptibility as available in the LTPP database. The other factor that is critical for frost action is the depth of the water table. Water tables located about 10 feet or below from the surface have negligible impact on migration of water to the freezing front. However, the in-situ moisture can freeze and draw the in-situ moisture from deeper depths to the freezing front. This can also create desiccated layers which in turn drives the frost depth deeper. Therefore, in addition to freezing temperatures, the frost susceptibility of the base and subgrade soils and the location of the water table are critical factors affecting freeze thaw.

Table 1.5 Summary of freezing sites and their characteristics

Site #	State Name	Subgrade Description	Particle Size Range (1)	(2)	AASHTO Classification	Frost Susceptibilty Determined
08-1053	Colorado	Subgrade: Fine-Grained Soils - Lean Inorganic Clay	3% F-C GRAV, 8% F-C SAND		A-7-6	
09-1803	Connecticut	Subgrade: Coarse-Grained Soils - Well-Graded Sand with Silt and Gravel				
10-0102	Delaware	Subgrade: Coarse-Grained Soils - Poorly Graded Sand	trace fn. gravel 73% fn. to crs. sand	NO.10....NO. 200		
16-1010	Idaho	Subgrade: Coarse-Grained Soils - Silty Sand	22% F-C GRAV, 70% F-C SAND	12% F-C GRAV, 75% F-C SAND	A-4	
16-3023	Idaho	Subgrade: Coarse-Grained Soils - Silty Sand	2% F-C GRAV, 58% F-C SAND	8% F-C GRAV, 72% F-C SAND		
18-3002	Indiana	Subgrade: Fine-Grained Soils - Sandy Lean Clay	FINE SAND-COARSE GRAVEL	FINE SAND-FINE GRAVEL		
20-4054	Kansas	Subgrade: Fine-Grained Soils - Lean Inorganic Clay	FINE SAND-FINE GRAVEL	FINE SAND-FINE GRAVEL		
23-1026	Maine	Subgrade: Coarse-Grained Soils - Silty Sand with Gravel	40.8% GRAVEL,42.4% SAND,11.2% FINES	16.1% GRAVEL,71.3% SAND,12.6% FINES	A-4	High
24-1634	Maryland	Subgrade: Fine-Grained Soils - Silt	1.9% GRAVEL,0.2% SAND,97.9% FINES	0.3% GRAVEL,0.2% SAND,99.5% FINES	A-4	
25-1002	Massachusetts	Subgrade: Coarse-Grained Soils - Poorly Graded Sand with Silt	13.5% GRAVEL,79.4% SAND, 7.1% FINES	1.9% GRAVEL,90.9% SAND,7.2% FINES	A-2-4	
27-1018	Minnesota	Subgrade: Coarse-Grained Soils - Poorly Graded Sand with Silt	FINE SAND-COARSE GRAVEL	FINE SAND-FINE GRAVEL		
27-1028	Minnesota	Subgrade: Coarse-Grained Soils - Poorly Graded Sand with Silt	FINE SAND-FINE GRAVEL	FINE SAND-COARSE GRAVEL	A-3	
27-4040	Minnesota	Subgrade: Fine-Grained Soils - Lean Clay with Sand	FINE SAND-FINE GRAVEL	FINE SAND-FINE GRAVEL		
27-6251	Minnesota	Subgrade: Coarse-Grained Soils - Silty Sand	FINE SAND-FINE GRAVEL	FINE SAND-FINE GRAVEL	A-1-b	Low
30-0114	Montana	Subgrade: Coarse-Grained Soils - Poorly Graded Sand with Silt				
30-8129	Montana	Subgrade: Fine-Grained Soils - Gravely Lean Clay with Sand	23% F-C GRAV, 22% F-C SAND	21% F-C GRAV, 19% F-C SAND	A-6	
31-0114	Nebraska	Subgrade: Fine-Grained Soils - Silty Clay				
31-3018	Nebraska	Subgrade: Coarse-Grained Soils - Poorly Graded Sand	FINE SAND-FINE GRAVEL	FINE SAND-FINE GRAVEL	A-3	
32-0101	Nevada	Subgrade: Coarse-Grained Soils - Silty Sand	2%GVL-73%SND			
32-0204	Nevada	Subgrade: Fine-Grained Soils - Sandy Silt				
33-1001	New Hamsphire	Subgrade: Coarse-Grained Soils - Poorly Graded Sand with Silt	7.3% GRAVEL,77.8% SAND,14.9% FINES	4.5% GRAVEL,87.6% SAND,7.9% FINES	A-4	
36-4018	New York	Subgrade: Coarse-Grained Soils - Silty Gravel with Sand	46.1% GRAVEL,32.5% SAND,21.4% FINES	51.3% GRAVEL,32.9% SAND,15.8% FINES	A-4	
39-0204	Ohio	Subgrade: Fine-Grained Soils - Silty Clay				
40-4165	Oklahoma	Subgrade: Coarse-Grained Soils - Silty Sand	0.0% GRAVEL, 72.0% SAND, 28.0% FINES	0.0% GRAVEL, 70.0% SAND, 30.0% FINES	A-2-4	
42-1606	Pennsylvania	Subgrade: Fine-Grained Soils - Silty Clay	26.7% GRAVEL,29.5% SAND,43.8% FINES	27.3% GRAVEL,21.9% SAND,50.8% FINES	A-4	
46-9187	South Dakota	Subgrade: Fine-Grained Soils - Lean Inorganic Clay	FINE SAND-MEDIUM SAND	FINE SAND-FINE GRAVEL	A-7-5	High
49-1001	Utah	Subgrade: Coarse-Grained Soils - Silty Sand	3% F-C GRAV, 83% F-C SAND	0% F-C GRAV, 73% F-C SAND	A-3	
49-3011	Utah	Subgrade: Coarse-Grained Soils - Clayey Gravel with Sand	28% f-c grav, 36% f-c sand	30% F-C GRAV, 35% F-C SAND	A-7-6	
50-1002	Vermont	Subgrade: Coarse-Grained Soils - Poorly Graded Gravel with Silt and Sand	56.4%GRAVEL,31.1%SAND,6.9%FINES,5.6%+3"		A-7-6	Very High
56-1007	Wyoming	Subgrade: Coarse-Grained Soils - Silty Sand with Gravel	16% F-C GRAV, 60% F-C SAND	26% F-C GRAV, 51% F-C SAND	A-2-4	Negligible
83-1801	Manitoba	Subgrade: Coarse-Grained Soils - Silty Sand	MEDIUM-FINE SAND	FINE GRAVEL - FINE SAND		
83-3802	Manitoba	Subgrade: Fine-Grained Soils - Fat Inorganic Clay	MEDIUM GRAVEL - FINE SAND	COARSE - FINE SAND	A-7-5	
89-3015	Quebec	Subgrade: Coarse-Grained Soils - Poorly Graded Sand	11.5% GRAVEL,86.5% SAND,2% FINES	9.6% GRAVEL,86.6% SAND,3.8% FINES	A-4	High
90-6405	Saskatchewan	Subgrade: Coarse-Grained Soils - Silty Sand	MED. GRAVEL - FINE SAND	MED. GRAVEL - FINE SAND	A-2-7	Medium

1.3.4.2 Timing of Load Restrictions

A review of the literature shows that several state Departments of Transportation have developed algorithms for predicting the onset for placement of load restrictions. For example Washington DOT found that the onset of the critical period can be estimated from the thawing Index (TI), based on theoretical studies and field observations (Rutherford, et al. 1985; Mahoney, 1985). There are several definitions of the critical period. One definition is that the onset of the critical period is at the beginning of thaw. The Corps of Engineers assumes that the critical period begins when the stiffness of the critical layer drops below the non-frost stiffness.

Washington and Minnesota define the critical period to begin when the TI is greater than 15 °C days, where the Thawing Index (TI) calculated as follows,

$$TI = T_{mean} - T_{ref}$$

where T_{mean} is the average daily temperature (°C) and T_{ref} is the reference temperature (°C). In Washington, the reference temperature is taken as a constant of –1.7 °C. In Minnesota, it is a variable that ranges from –1.5 °C to 10 °C and is a function of the increase in sunshine in the spring. The load restriction is enacted 3 days after the TI exceeds 15 °C days.

In the COE evaluation procedure, the beginning of spring thaw is based on the freezing index. The air-freezing index (FI) is the peak difference in the cumulative daily mean temperature. The air-freezing index can be used to estimate the frost penetration at a given site. These relationships can be established as a function of soil type and in-situ moisture content using 1-D heat and moisture flow computer programs such as FROST.

The number of thaw cycles during the winter will significantly affect the bearing capacity of pavement structures. There are several methods available today that can account for the strength loss

during these thaw cycles. One is the State of Wisconsin model, UWFROST; the other is the COE Seasonal Layered Elastic Design (SLED) model. The FHWA Integrated Climatic Model can also be used to predict seasonal changes in temperature and moisture content as a function of depth.

UWFROST and SLED are similar to one another; they both have theoretical and empirical sub-models. In general, both require air temperatures, layer thicknesses, thermal and hydraulic material properties, and depth. However, UWFROST is regionally based and will require some modification for use nationally. A nice feature of UWFROST is its modulus prediction model. Based on field FWD tests in Wisconsin, Jong et al. (1998) found that there were two critical periods for a pavement structure. These periods are depicted in Figure 1.1, where the variation in modulus in terms of the normalized modulus or modular ratio:

$$R_m = \frac{M_r(t)}{M_r(t_s)}$$

where, $M_r(t)$ is the resilient modulus at any time t, and $M_r(t_s)$ is the resilient modulus in late summer. The first critical period started when the thaw reached the top of the base course. They found that there was a sharp decrease in modulus (the weakening period) and for their test sites, this period lasted about one month. The second critical period in a pavement structure is the recovery period. They found that this period could last up to four months.

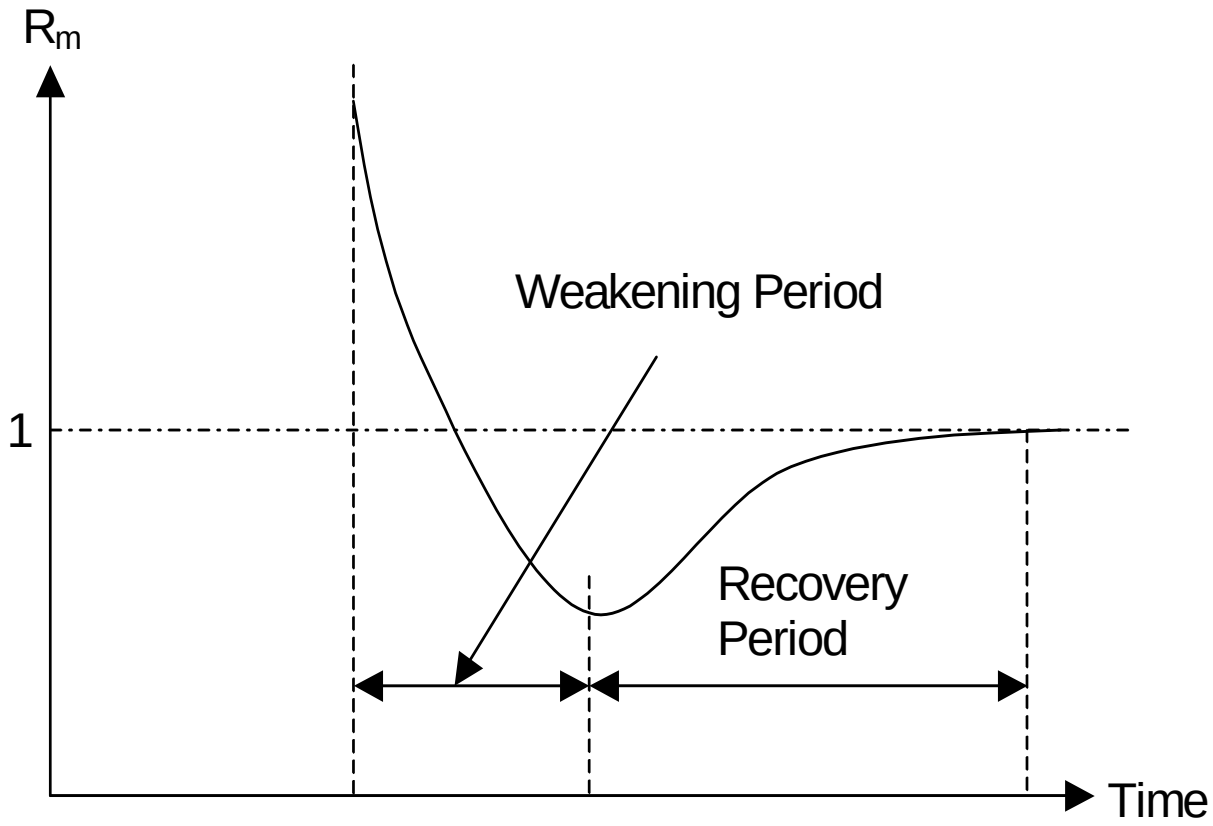

Figure 1.1 Critical periods during thaw (after Jong et al. (1998))

Alternatively, several empirical procedures are available for determining the duration for load restriction. In the Washington DOT method, the length of the thaw period (D) can be estimated from

$$D = 0.018FI + 25$$

where D is the length of the thaw period (days) and FI is the air freezing index (°C-days). Using a similar approach, Minnesota DOT extended the Washington DOT method based on results from MnRoad. The thaw duration was determined from:

$$D = 0.15+0.010FI+1.91P-(1290*P/FI)$$

where D is the length of the thaw period (days), FI is the air freezing index (°C-days), and P is the frost depth (m), which is estimated as

$$P = -0.\ 328 + 0.0578\sqrt{FI}$$

Clearly, using models developed for regional sites can lead to poor results in other locations. To date, Minnesota DOT tends to leave the load restriction on for 8 weeks after placement of the load restriction.

In the COE evaluation method, the length of load restriction is based on frost susceptibility of the base course and subgrade and the number of freeze thaw cycles expected during the winter period. The frost susceptibility of a soil can be determined from Table 1.6. The frost susceptibility of a soil is used to determine the length of the load restriction at the end of thaw. Table 1.7 gives guideline for the time period for load restriction as a function of the frost susceptibility of the soil. For example, the subgrade at SMP site is classified as an SM with 20% passing the #200 sieve. The soil can be is classified a F-3 category frost susceptible soil. Using Table 1.7, a load restriction for a period of 30 days is required. In the COE evaluation process, when the highway undergoes significant freeze thaw cycles, load restrictions are placed approximately one month prior to end of

winter. When the frost is deep and the number of winter thaw cycles is minimal, the load restriction is placed two weeks prior to the beginning of thaw. The estimated beginning of thaw is obtained from a worldwide database, WORLDINDEX. WORLDINDEX is available through the COE PCASE program (http://www.pcase.com). The dividing Air Freezing Index is about 600 degree C-days. The period of load reduction is then estimated from the mean dates found in WORLD INDEX for the site.

In summary, the empirical methods developed on a regional basis, do not appear to work well in general. However, with some modification, similar types of equations can be established as a function of frost depth, soil type, etc. The COE load reduction method takes into account the frost susceptibility of the soil and the number of freeze-thaw cycles.

Table 1.6 Frost susceptibility classification (Yoder and Witczak, 1975)

Frost susceptibility[a]	Frost group	Kind of soil	Amount finer than 0.02 mm (wt %)	Typical soil type under USCS[b]
Negligible to low	NFS[c]	a. Gravels	0–1.5	GW, GP
		b. Sands	0–3	SW, SP
Possibly	PFS[d]	a. Gravels	1.5–3	GW, GP
		b. Sands	3–10	SW, SP
Low to medium	S1	Gravels	3–6	GW, GP, GW-GM, GP-GM
Very low to high	S2	Sands	3–6	SW, SP, SW-SM, SP-SM
Very low to high	F1	Gravels	6–10	GM, GW-GM, GP-GM
Medium to high	F2	a. Gravels	10–20	GM, GM-GC, GW-GM, GP-GM
Very low to very high		b. Sands	6–15	SM, SW-SM, SP-SM
Medium to high	F3	a. Gravels	> 20	GM, GC
Low to high		b. Sands except very fine silty sands	> 15	SM, SC
Very low to very high		c. Clays, $I_p > 12$	—	CL, CH
Low to very high	F4	a. All silts	—	ML, MH
Very low to high		b. Very fine silty sands	> 15	SM
Low to very high		c. Clays, $I_p < 12$	—	CL, CL-ML
Very low to very high		d. Varved clays and other fine-grained banded sediments	—	CL and ML; CL, ML and SM; CL, CH, and ML; CL, CH, ML, and SM

Table 1.7 Length of load restriction at the end of complete thaw for highways

Soil Classification	Load Restriction Period (days)
F1/F2	14
F3	30
F4	45

1.3.4.3 LTPP Databse of FWD Backcalculated Moduli

In order to evaluate the effects of freezing and thawing on base and subgrade moduli, backcalculated moduli must be available during times at which the soil was frozen at some depth (either because it was freezing from the top down or thawing from the top down). Table 1.8 lists the number of FWD testing days for which linear elastic moduli were backcalculated while the site was frozen at some depth along with the number of those days for which backcalculated moduli are available. It is important to note that backcalculated moduli are only available for approximately half of the FWD testing days. This suggests that it may be more effective to use the FWD deflections directly to infer the change pavement response during freezing and thawing.

Table 1.8. Data Availability When Site is Partially Frozen

Site	FWD Testing Days	Backcalculated Days
16-1010	7	4
23-1026	9	3
25-1002	1	1
27-1018	16	11
27-1028	15	9
27-4040	21	11
27-6251	12	6
30-8129	20	8
31-0114	5	0
31-3018	1	0
36-0801	2	0
36-4018	4	3
46-0804	5	2
46-9187	7	2
50-1002	3	2
56-1007	9	7
83-1801	14	1
83-3802	17	11
87-1622	12	6
89-3015	7	1
90-6405	22	11
TOTALS	209	99

1.3.4.4 Review of Field Data outside LTTP Database

To assist in the development of guidelines for the imposition of seasonal load restrictions and overload permitting, this section summarizes the results from a review of field data not in the LTTP database, focusing on determining the beginning of the critical period and the length of the thaw weakening period. Field data from Wisconsin, Vermont and Montana were examined for thaw weakening. In addition, some results from controlled experiment in the FERF are discussed. In general, it was very difficult to find a clear trend on thaw weakening. In some instances, moisture data was available and it clearly showed a significant increase during the early thaw. This infers that the bearing capacity of that layer is reduced during the high moisture content periods.

Wisconsin CRREL conducted an extensive field study on thaw weakening at an airport in Wisconsin. One of the runways had a pavement structure of 7.5 to 12 inches of AC, with 6 to 8 inches of granular base which is a range of thickness similar to many highway pavement structures. Falling weight deflection (FWD) tests were conducted every third day starting at the beginning of thaw during the spring (1986) for a total of approximately 41 days. The frost depth at the site was about 4 feet. The subgrade was classified as a low plastic silty soil (ML). The impact of thawing on the backcalculated base and subgrade moduli is clearly shown in Figure 1.2. However, data during the critical period during significant thaw weakening is absent. The authors suggested that the testing missed the critical period due to a breakdown of the FWD reported between days 12 and 21. Other sites on the airfield were found to provide the same general trend. The water table was quite deep at this site (> 60 feet), and the RMS error of the fit was low (between 0.7 and 1.2%). The largest error was 2.9% and that was on the first day of thaw (day zero in Figure 1.2). The base modulus at the beginning of thaw was about 116 ksi (not shown).

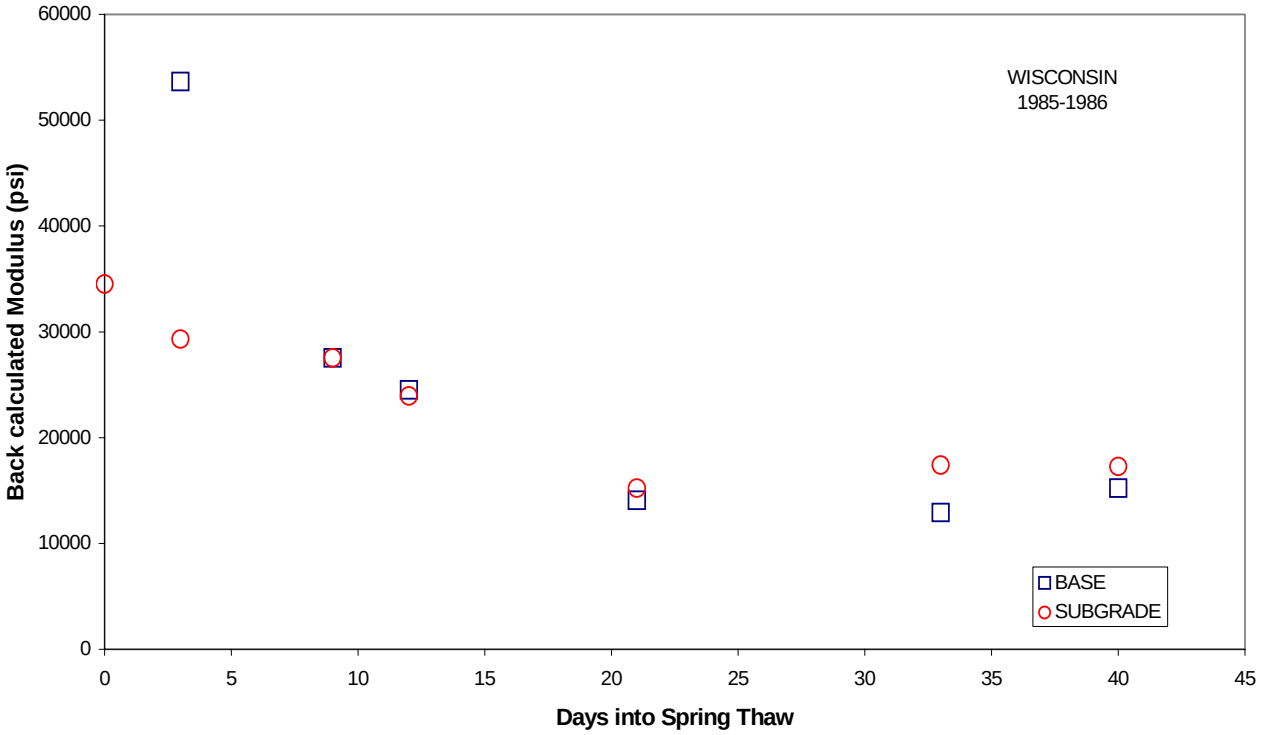

Figure 1.2 Backcalculated base and subgrade moduli during spring thaw (Wisconsin)

Vermont The Vermont Agency of Transportation (VAOT) in the midi-nineties was interested in characterizing the effect of spring thaw on their pavements. They used the SHRP protocol and instrumented several pavements around the state. FWD data was collected periodically during the thaw period using the SHRP protocol of twice a month.

VAOT has a test site in Barre, Vermont where FWD measurements were taken on nearly a daily basis. The pavement structure consisted of 2.5" of AC over a 18" SM base. The subgrade was a sandy silt (ML). The change in the center FWD deflection with time is shown in Figure 1.3. The change in the volumetric moisture content in the subgrade with time is shown in Figure 1.4. The deflection did not return to its pre-frozen value even when the moisture content has returned to its pre-freeze state. This suggests a possible structural change in the sub-surface layer.

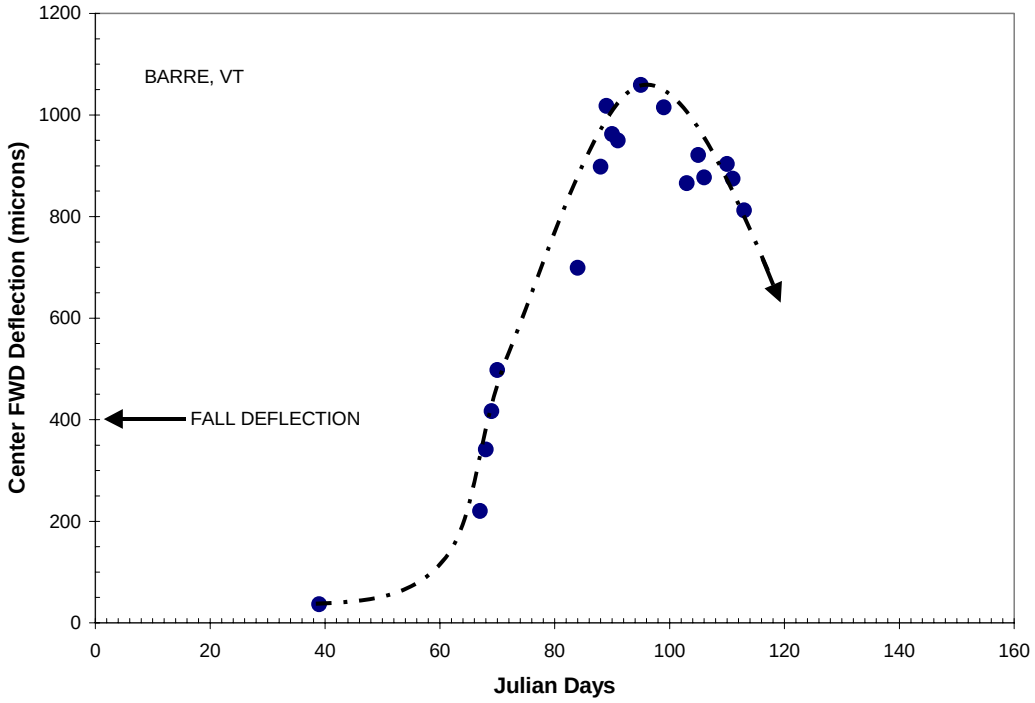

Figure 1.3 Change in FWD center deflection during thaw (Vermont)

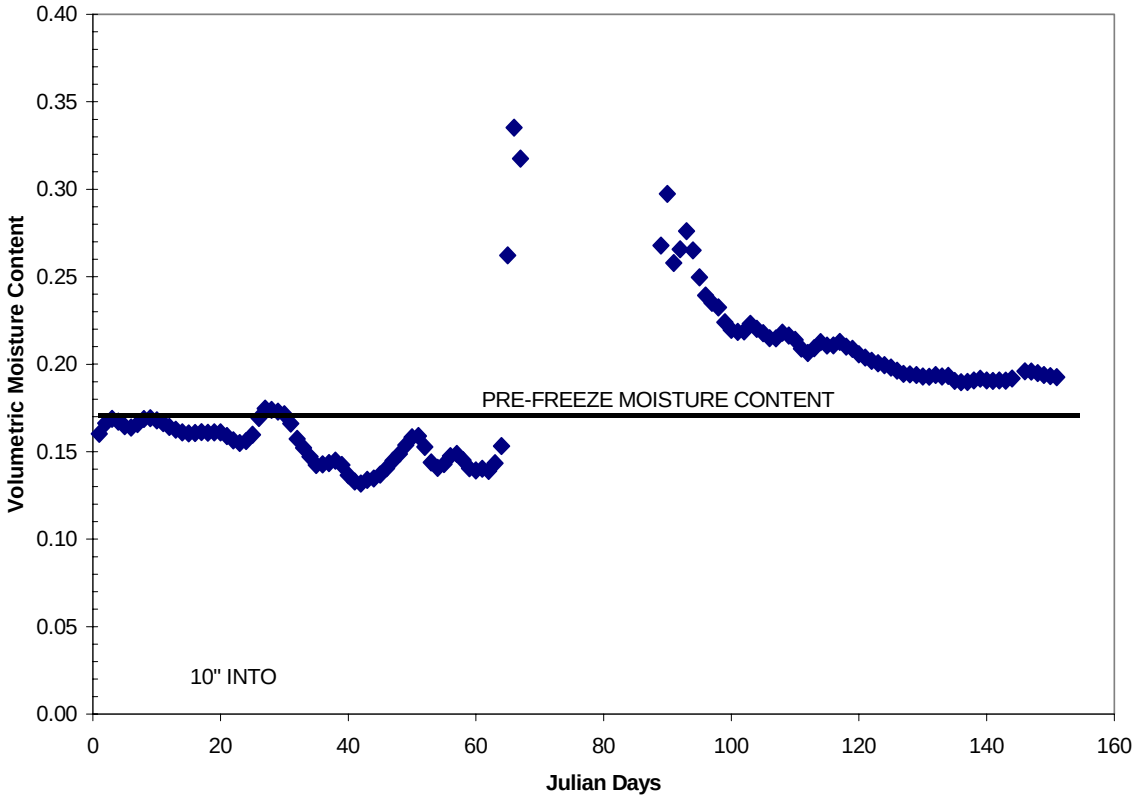

Figure 1.4 Change in subgrade volumetric moisture content during thaw (Vermont)

Montana Montana has an ongoing study on the influence of seasonal variation on pavement performance. The study included instrumentation of several sites with moisture and temperature sensors and falling weight deflection measurements during the year. The data set includes some excellent moisture data that shows changes in the moisture content in the base and subgrade. Examples are shown in Figures 1.5 and 1.6. Although the FWD data was inconclusive, it is of interest to note that the base was classified as an A-1-a base and it showed a significant change in moisture content during the thaw.

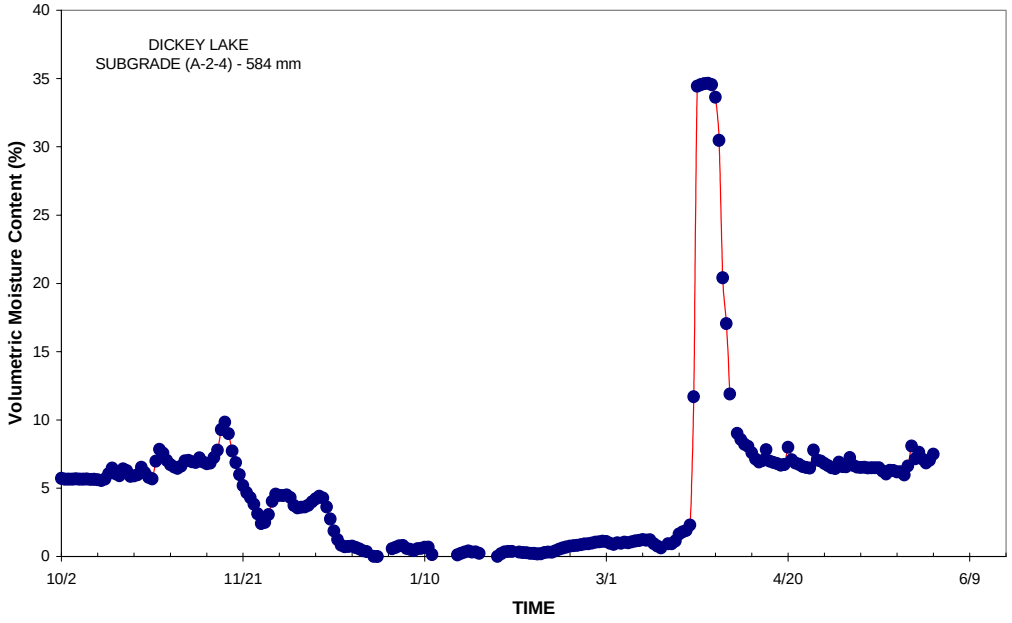

Figure 1.5 Change in volumetric moisture content in subgrade during thaw (Montana)

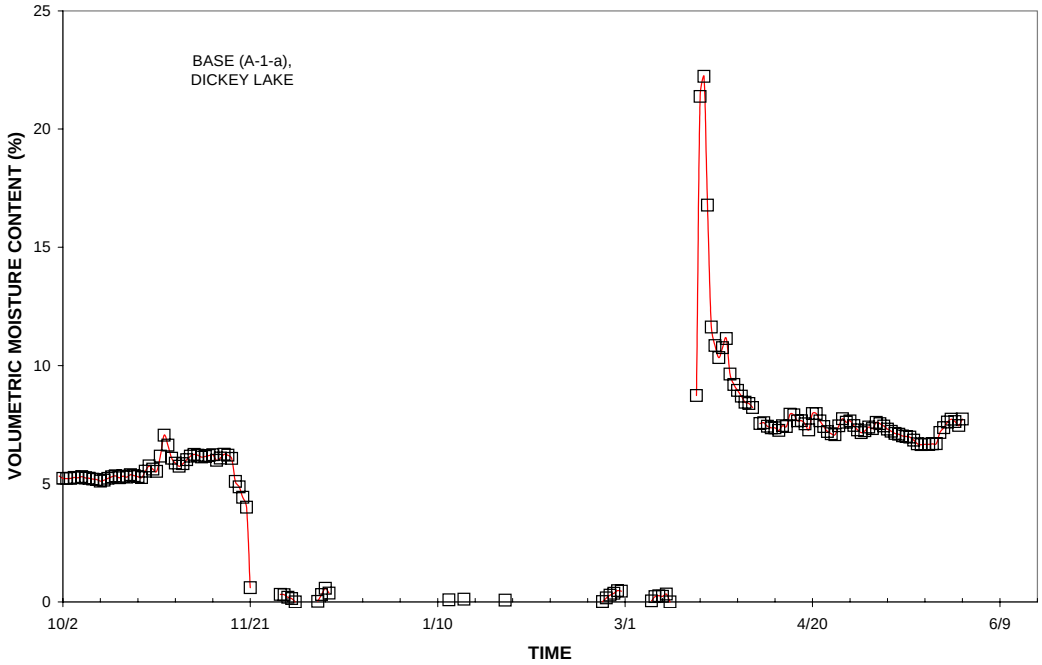

Figure 1.6 Change in volumetric moisture content in base course during thaw (Montana)

Controlled experiments at the Frost Effects Research Facility Studies have been conducted in the Frost Effects Research Facility (FERF) to quantify the influence of freeze thaw on the subsurface properties of pavement structures. An earlier study (Janoo & Berg, 1990) reported that under controlled thawing conditions, FWD deflections reflected the changes in the base and subgrade moduli. It was reported that the modulus of the clay (CH) decreased by a factor of 2.5. The data also indicated that the modulus of the subgrade did not return to its pre-freeze value at the end of thaw.

In another study, FWD tests were conducted on two thawing test sections in the FERF. The cross sections were identical, 3" AC over 9" crushed base over subgrade. The subgrades were different, one was a SM (A-2-4), and the other was a CL (A-4). The sections were frozen and the FWD measurements were obtained during the thaw process. There was no water table in these sections. Any freezing was from the in-situ moisture content. The change in the back-calculated modulus, expressed in terms of the modular ratio with respect to its unfrozen value, are presented in Figures 1.7 through 1.10 for the base and subgrade for both the silty sand (A-2-4) and clay (A-4) subgrade sections.

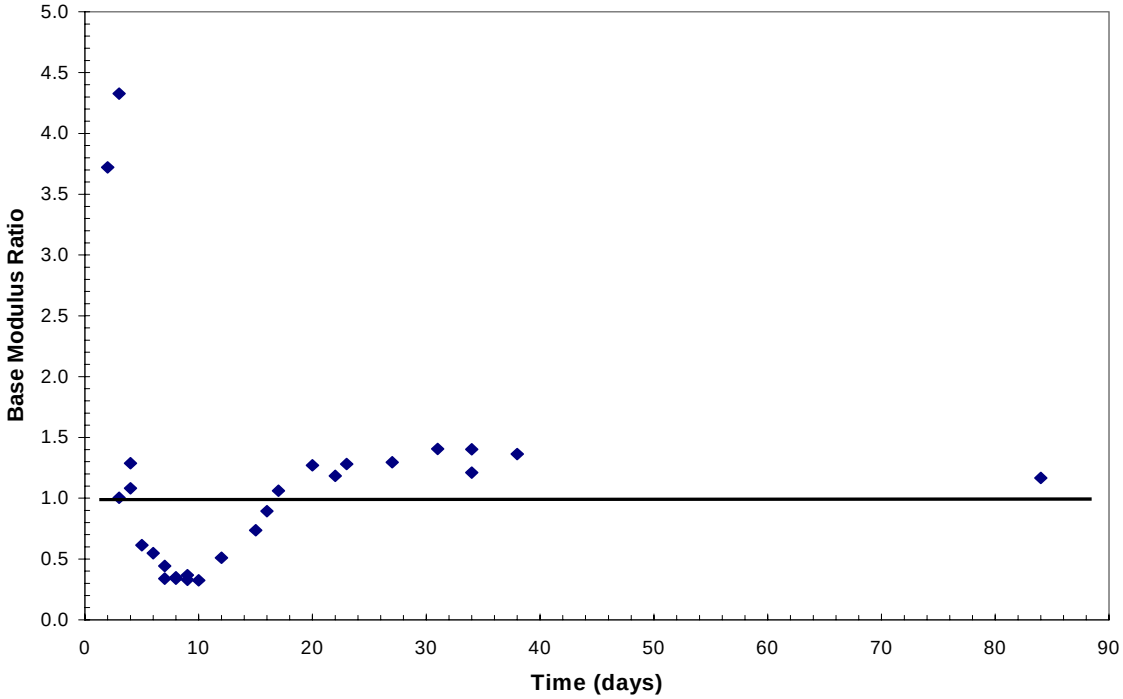

Figure 1.7 Change in base course modulus during thaw (FERF A-2-4 subgrade)

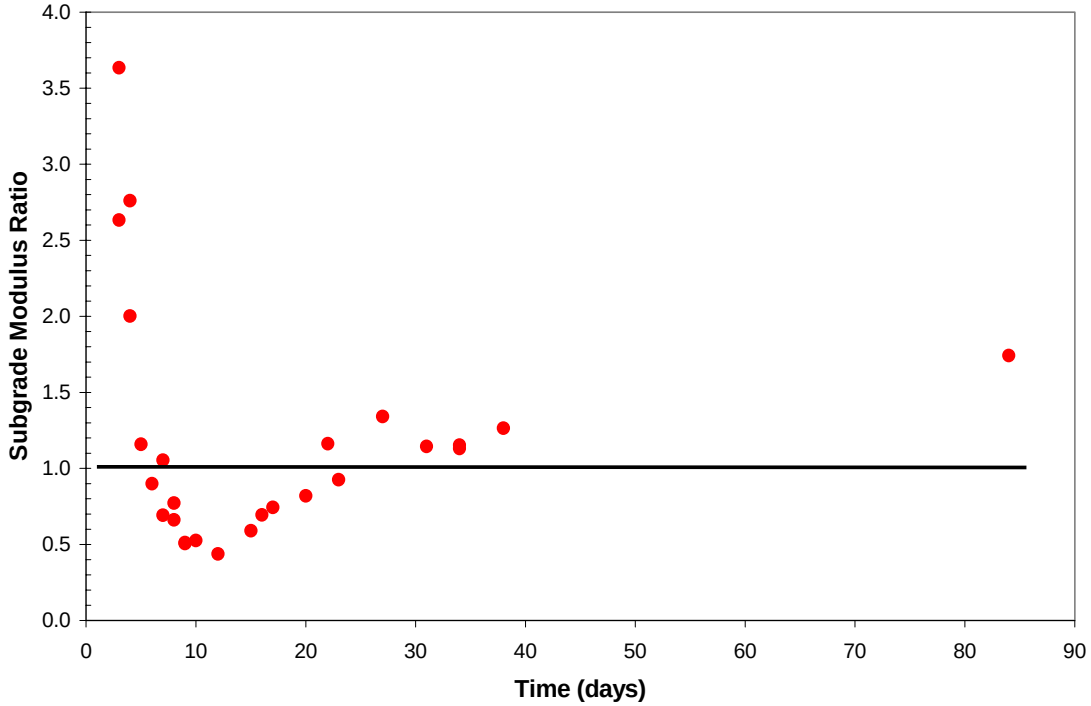

Figure 1.8 Change in subgrade modulus during spring thaw (FERF A-2-4 subgrade)

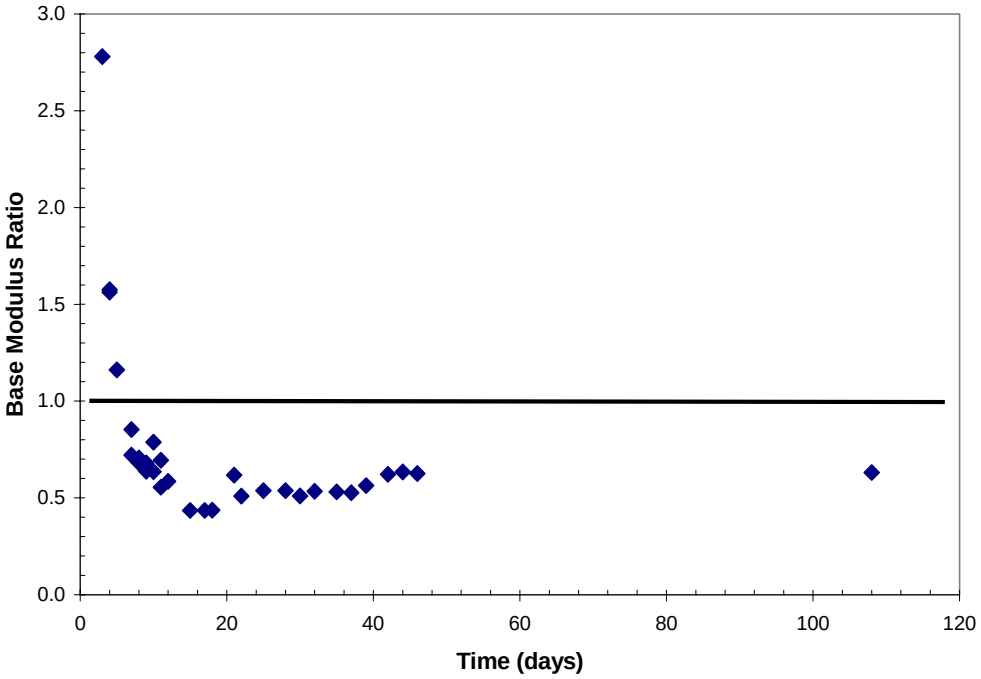

Figure 1.9 Change in base course modulus during thaw (FERF A-4 subgrade)

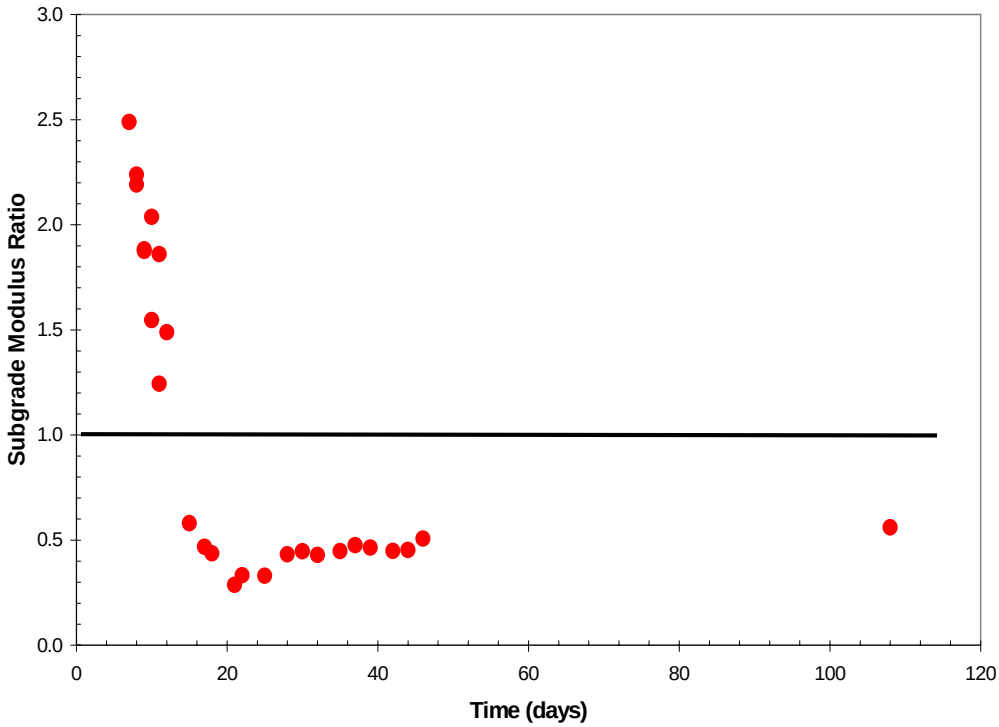

Figure 1.10 Change in subgrade modulus during thaw (FERF A-4 subgrade)

1.4 SUMMARY OF LTPP DATA AVAILABILITY

All of the data used in this study was obtained from Release 11.5 (Version NT3.0) of the LTPP IMS database and is classified as "Level E." Table 1.9 lists the relevant data tables in the LTPP database, and Table 1.10 shows the amount of data presently contained in those tables for the flexible and rigid SMP sites, respectively. With a few exceptions, the number in the table can be read as the number of testing days for which data is available.

Table 1.9 List of relevant LTPP IMS tables

General			
Abbr.	*Table name*	*Unit*	*Description*
EXP	Experiment_section	No.	Includes experiment number and assign date.
T_Layer	TST_L05B	Layers	Table containing layer descriptions for all constructions.
SP_Layer	SPS(1-9)_Layer	Layers	Layer descriptions
SP_Thick	SPS(1-9)_Layer_Thickness	Points	Layer thickness measurements
S9_Mix	SPS9_PMA_Mix_Des_Prop	No.	Plant-mixed asphalt bound layers
INV_Gen	INV_General	No.	Geometric, drainage, and general information.
INV_PCCST	INV_PCC_Strength	No.	Portland cement concrete layers strength data
DEFL	MON_Defl_Master	Days	Master table for FWD data.
PROF	MON_Profile_Master	Days	Profilometer master record.
PROF_T	MON_T_Prof_Index_Section	Days	Transverse Profile.
TRF_Mon	TRF_Monitor_Basic_Info	Years	Summary information concerning data collection and site
TRF_Est	TRF_Est_Anl_Tot_LTPP_Ln	Years	Traffic data - Estimate of annual totals in study
AWS	AWS_Temp_Month	Months	Automatic Weather Station (AWS) monthly air temperature statistics.
CLM	CLM_VWS_Temp_Annual	Year	Climatic Data from Weather Stations
SMP			
Abbr.	*Table name*	*Unit*	*Description*
SMP	SMP_LAYOUT_INFO		Includes SMP install date.
S_Temp	SMP_ATEMP_Rain_Day	Month	Contains daily air temperature and rainfall statistics.
S_Moist	SMP_TDR_AUTO_Moisture	Days	Contains pavement subsurface gravimetric moisture content of material surrounding each TDR probe at the time of installation.
S_Elev	SMP_Elev_AC_Data SMP_Elev_PCC_Data	Days	Contains surface elevation measurement.
S_Fault	SMP_Joint_Fault_Data	Days	Contains PCC faulting measurement.
S_WaterD	SMP_Watertab_Depth_Man	Days	Contains manually collected data on the depth to ground water table.
S_Freeze	SMP_Freeze_State	Days	Contains the soil freeze state(frozen or non-frozen), based on electrical resistivity and soil temperature data.
S_Frost	SMP_Frost_Penetration	Days	Contains the frost penetration depth, based on electrical resistivity and soil temperature data.
Distress			
Abbr.	*Table name*	*Unit*	*Description*
D_AC	MON_DIS_AC_REV	Days	Revised Distress survey information for pavements with AC surfaces.
D_AC_P	MON_DIS_Padias_AC MON_DIS_Padias2_AC	Days	Distress survey information for pavements with AC surfaces.
D_Rut	MON_Rut_Depth_Point	Days	Rutting info for AC surfaces.
D_JPCC	MON_DIS_JPCC_REV	Days	Distress identification for jointed PCC surfaces.
D_JPCC_P	MON_DIS_Padias_JC MON_DIS_Padias42_JPCC	Days	Distress identification for JPCC surfaces.
D_Fault	MON_DIS_JPCC_Fault	Days	Joint faulting for JPCC pavement surfaces.
D_CRCP	MON_DIS_CRCP_Rev	Days	Distress identification for reinforced PCC pavement surfaces.
D_CRCP_P	MON_DIS_Padias2_CRCP MON_DIS_Padias_CRC	Days	Distress identification for reinforced CRC pavement
D_Manual	MON_DIS_AC_REV MON_DIS_JPCC_REV MON_DIS_CRCP_REV	No.	Manual distress identification for AC, reinforced PCC and CRC pavement surfaces.
D_Padias	MON_DIS_Padias_AC MON_DIS_Padias42_AC MON_DIS_Padias_JC MON_DIS_Padias42_JPCC MON_DIS_Padias_CRC MON_DIS_Padias42_CRCP	No.	Distress identification for reinforced AC, JPCC and CRC pavements

Table 1.9 List of relevant LTPP IMS tables (continued)

Testing, Granular			
Abbr.	*Table name*	*Unit*	*Description*
T_AG05	TST_AG05	No.	NAA test for fine aggregate particle shape.
T_SS01	TST_SS01_UG01_UG02	No.	Gradation of coarse, fine, and combined agg.
T_SS02	TST_SS02_UG03	No.	Hydrometric analysis of combined aggregates determined during lab testing.
T_SS03	TST_UG04_SS03	No.	Atterberg limit test results for unbound base/subbase layers or subgrade.
T_SS04	TST_SS04_UG08	No.	Type and class of unbound granular base /subbase and subgrade materials.
T_SS05	TST_UG05_SS05	No.	Moisture density relationship test results for unbound base/subbase or subgrade.
T_SS07A	TST_UG07_SS07_A	No.	Unbound granular base/subbase layer - Subgrade soils
T_SS07B	TST_UG07_SS07_B	No.	Unbound granular base/subbase layer - Subgrade soils.
T_SS08	TST_SS08	No.	Density of Subgrade Soil.
T_SS09	TST_UG10_SS09	No.	Natural moisture content results for unbound base/subbase layers or subgrade.

Material Testing			
Abbr.	*Table name*	*Unit*	*Description*
T_AC02	TST_AC02	No.	Bulk Specific Gravity test results for asphalt bound layers.
T_AC03	TST_AC03	No.	Maximum specific gravity test results for asphalt bound layers.
T_AC04	TST_AC04	No.	Quantitative extraction test results for asphalt bound layers.
T_AC05	TST_AC05	No.	Moisture Susceptibility of Asphaltic Concrete.
T_AC07	TST_AC07_A** TST_AC07_A_WK TST_AC07_A_SUM TST_AC07_B	No.	Asphalt Concrete Layer Resilient modulus test.
T_PC01	TST_PC01	No.	Compressive strength of in-place concrete test results for PCC layers.
T_PC02	TST_PC02	No.	Splitting tensile strength test results for PCC layers.
T_PC04	TST_PC04	No.	Static modulus of in-place concrete test results for PCC layers.
T_Log	TST_Sample_Log	No.	Information about the samples taken from holes, pits, and probes.
T_Hole	TST_Hole_Log	No.	Information about the location and size for holes, pits, and probes.
T_ISD	TST_ISD_Moist	No.	In situ density and moisture test information taken from test pits.

FWD Backcalculation			
Abbr.	*Table name*	*Unit*	*Description*
FWD_DAYS		Days	Number of testing days which have backcalculated layer moduli
FWD_MODS		No.	Number of sets of backcalculated layer moduli
FWD_KVAL		No.	Number of sets of backcalculated k-values

Table 1.10 LTPP data availability report for flexible pavements

ID	FWD_DAYS	FWD_DMOD	TLAYER	SPLAYER	SPTHICK	INV_GEN	TRF_MON	TRF_EST	AWS	CLM	S_TEMP	S_MOIST	S_FROST	S_FREEZE	S_WATER	S_ELEV	DEF_DL	PROF_T	PROF_T
010101-1	25	2117	1	4	55	.	.	.	36	.	24	.	.	.	28	11	32	11	4
010102-1	14	1276	1	4	55	.	.	.	.	.	27	.	.	.	28	10	31	12	5
040113-1	.	.	3	3	55	.	.	.	.	.	21	9	.	.	23	10	31	12	12
040114-1	.	.	3	3	55	.	3	.	.	.	22	6	.	.	22	10	28	12	11
041024-1	.	.	4	.	.	1	4	19	.	20	22	6	8	8	19	8	26	11	14
081053-1	27	2697	4	.	.	1	3	10	.	17	29	33	26	26	37	15	40	16	15
091803-1	10	722	4	.	.	1	3	.	.	17	26	33	36	36	38	17	32	21	11
100102-1	28	2111	6	6	55	.	.	.	.	.	22	.	.	.	21	9	18	9	6
131005-1	.	.	5	.	.	1	.	.	.	17	26	14	.	.	26	11	29	16	7
131031-1	14	2264	5	.	.	1	4	.	.	17	11	10	.	.	10	6	15	10	5
131031-2	27	3683	6	.	.	1	4	.	.	17	10	.	.	.	12	5	12	6	1
161010-1	15	2544	4	.	.	1	5	.	.	28	24	31	28	28	36	14	37	17	17
231026-1	18	1752	4	.	.	1	.	.	.	24	18	22	22	22	24	11	22	13	9
231026-2	15	1806	6	.	.	1	.	.	.	24	11	.	.	.	14	7	11	7	4
241634-1	14	1549	4	.	.	1	.	.	.	21	27	19	19	19	24	12	23	15	10
251002-1	15	1846	5	.	.	1	4	.	.	17	28	31	35	35	37	15	36	21	12
271018-1	29	3398	3	.	.	1	5	.	.	18	9	14	15	15	15	6	16	.	4
271018-2	4	4239	4	.	.	1	5	.	.	18	29	10	.	.	23	13	21	7	7
271028-1	10	1620	.	.	.	1	7	.	.	25	43	32	34	34	35	18	35	13	10
276251-1	10	2706	3	.	.	1	4	.	.	17	40	35	38	.	37	27	41	15	10
281016-1	26	3170	5	.	.	1	2	.	.	17	15	12	.	.	14	6	18	13	5
281802-1	30	4039	5	.	.	1	6	.	.	17	26	18	.	.	27	11	34	17	7
308129-1	12	1028	3	.	.	1	6	.	.	17	30	33	28	.	34	12	45	17	15
310114-1	.	.	4	.	.	.	2	.	.	.	20	.	.	.	9	5	17	10	5
320101-1	26	2587	5	5	55	.	.	.	.	.	9	.	.	.	4	4	18	7	8
331001-1	.	.	5	.	.	1	1	.	.	17	30	30	32	32	34	15	30	18	10
351112-1	26	3288	4	.	.	1	2	.	.	17	18	26	.	.	25	11	26	12	7
360801-1	20	2874	2	4	55	.	.	.	.	.	26	.	.	.	27	12	28	12	7
371028-1	18	5048	.	.	.	1	2	.	.	17	29	13	.	.	27	14	27	14	9
404165-1	3	248	3	.	.	1	2	.	.	17	25	24	.	.	21	10	26	13	7
460804-1	24	2792	3	3	7	.	5	.	.	.	22	22	19	19	23	10	23	9	6
469187-2	26	2643	6	.	.	1	.	.	.	17	20	13	.	.	22	13	17	9	8
481060-1	22	2751	5	.	.	1	6	.	.	17	27	33	.	.	30	13	34	15	6
481068-1	.	.	5	.	.	1	8	.	.	17	28	18	.	.	30	12	33	14	5
481077-1	22	2167	4	.	.	1	7	.	.	17	28	33	.	.	31	13	35	14	5
481122-1	13	1679	6	.	.	1	5	.	.	23	22	30	.	.	31	13	37	16	5
483739-1	13	1934	5	.	.	1	6	.	.	17	9	8	.	.	10	4	14	7	4
483739-2	21	2765	6	.	.	1	6	.	.	17	4	.	.	.	4	2	4	2	.
483739-3	15	1912	7	.	.	1	6	.	.	17	14	.	.	.	8	4	15	6	4
491001-1	13	3554	2	.	.	1	.	.	.	17	26	28	26	26	23	14	31	17	9
510113-1	28	3746	5	5	55	.	.	.	.	.	23	.	.	.	26	12	26	8	7
510114-1	20	174	3	5	55	.	.	.	.	.	21	.	.	.	30	14	24	8	6
561007-1	22	2232	3	.	.	1	4	.	.	17	25	.	.	.	28	13	36	19	19
831801-1	.	.	5	.	.	1	4	.	.	17	49	33	35	33	57	20	40	16	6
871622-1	21	2118	6	.	.	1	4	.	.	21	29	33	37	35	37	13	27	20	13
906405-1	26	2685	2	.	.	1	2	.	.	28	26	35	35	.	32	22	39	17	12
501002-1	.	.	4	.	.	1	4	.	.	17	28	35	36	36	36	15	32	19	12

Table 1.10 LTPP data availability report for flexible pavements (continued)

ID	EXP	D_AC	D_AC_P	D_RUT	T_SS01	T_SS03	T_SS04	T_SS05	T_SS07A	T_SS08	T_SS09	T_AC02	T_AC03	T_AC04	T_LOG	T_HOLE	T_ISD
010101-1	S1	8	.	1	1	1	1	1	1	.	1	12	.	.	5	16	.
010102-1	S1	8	.	1	1	1	1	1	1	.	1	4	.	.	11	18	.
040113-1	S1	12	.	.	1	1	1	1	.	.	1	6	.	.	12	20	11
040114-1	S1	12	.	.	1	1	1	1	.	.	1	6	.	.	5	19	8
041024-1	G1	11	4	.	2	2	2	2	2	.	8	16	2	2	12	39	2
081053-1	G1	13	4	.	1	1	1	1	1	.	1	16	2	2	5	32	3
091803-1	G1	7	4	.	.	.	.	.	.	.	.	12	4	4	9	30	1
100102-1	S1	6	.	.	.	.	2	.	2	.	.	7	.	.	21	19	8
131005-1	G1	10	4	1	2	2	2	2	2	.	4	16	6	4	15	31	2
131031-1	G1	6	4	1	2	2	2	2	2	.	4	12	4	4	13	31	1
131031-2	G6S	3	.	.	.	.	.	.	.	.	.	.	.	.	.	8	.
161010-1	G1	14	5	.	2	2	2	2	2	.	8	16	4	4	14	23	2
231026-1	G1	4	4	.	2	2	2	2	.	.	2	12	4	4	4	20	2
231026-2	G6B	4	.	.	.	.	.	.	.	.	.	.	.	.	.	24	.
241634-1	G2	7	5	2	2	2	2	2	1	.	4	6	2	2	16	28	2
251002-1	G1	6	4	.	2	2	2	2	1	.	4	12	4	4	11	29	.
271018-1	G1	5	3	.	2	2	2	2	2	.	4	4	4	4	12	21	2
271018-2	G1	6	.	.	.	.	.	.	.	.	.	.	.	.	.	.	.
271028-1	G1	9	5	2	2	2	2	2	2	.	4	4	4	4	9	21	1
276251-1	G1	10	4	3	2	2	2	2	2	.	4	2	2	2	12	21	1
281016-1	G2	7	4	1	2	2	2	2	.	.	4	6	2	2	12	29	2
281802-1	G2	8	6	5	2	2	2	2	1	.	4	12	4	4	14	32	2
308129-1	G1	12	4	.	2	2	2	2	1	.	8	16	2	2	13	29	2
310114-1	S1	4	.	.	.	.	.	.	.	.	.	4	4	1	1	6	.
320101-1	S1	9	.	.	1	1	1	1	1	.	1	2	.	.	9	22	12
331001-1	G1	6	4	.	2	2	2	2	.	.	4	8	4	4	9	28	.
351112-1	G1	8	4	.	2	2	2	2	2	.	4	6	2	2	15	29	2
360801-1	S8	7	.	.	1	3	3	1	1	.	1	8	2	2	11	26	7
371028-1	G1	6	4	.	2	2	2	2	1	.	5	12	4	4	11	38	1
404165-1	G2	9	4	.	2	2	2	2	.	.	5	18	13	14	17	30	.
460804-1	S8	6	.	1	.	2	.	2	.	.	2	.	.	.	11	15	.
469187-2	G1	7	.	.	.	.	.	.	.	.	.	.	.	.	.	.	.
481060-1	G1	10	4	2	2	2	2	2	.	.	4	12	4	4	13	29	2
481068-1	G1	9	4	1	2	2	2	2	2	.	4	12	4	4	13	28	2
481077-1	G1	11	3	1	2	2	2	2	1	.	3	9	3	3	11	30	2
481122-1	G1	11	4	4	2	2	2	2	1	.	4	15	4	4	20	29	3
483739-1	G1	4	4	3	2	2	1	2	2	.	4	3	1	1	12	20	2
483739-2	G1	.	.	.	.	.	.	.	.	.	.	.	.	.	.	.	.
483739-3	G1	7	.	.	.	.	.	.	.	.	.	.	.	.	.	8	.
491001-1	G1	13	.	.	2	2	2	2	1	.	8	16	2	2	15	29	2
510113-1	S1	8	.	.	.	.	.	.	.	.	.	2	.	.	4	14	6
510114-1	S1	7	.	.	.	.	3	.	.	1	.	8	.	.	16	14	6
561007-1	G1	16	4	.	2	2	2	2	2	.	8	16	2	2	14	33	2
831801-1	G1	10	5	.	1	2	2	2	.	.	2	.	.	.	10	19	.
871622-1	G1	8	5	.	2	2	2	2	2	.	3	10	6	6	9	20	3
906405-1	G1	11	5	1	2	2	2	2	.	.	2	6	.	.	8	18	2
501002-1	G1	7	4	.	1	1	1	1	.	.	1	12	4	4	11	30	2

Table 1.10 LTPP data availability report for flexible pavements (continued)

ID	DEFL	PROF_T	D_JPCC	D_JPCC_P	D_FAULT	T_SS01	T_SS03	T_SS04	T_SS05	T_SS07A	T_SS08	T_SS09	T_PC01	T_PC02	T_PC04	T_LOG	T_HOLE	T_ISD
040215-1	28	12	1	12	.	11	.	.	.	.	.	.	.	6	6	2	3	28	6
063042-1	26	14	3	10	3	10	2	2	2	2	.	.	6	2	2	2	19	21	.
133019-1	27	16	5	9	4	8	2	2	2	2	2	.	4	2	2	2	13	22	.
183002-1	12	16	2	6	3	5	2	2	2	2	.	.	4	2	2	2	12	19	2
313018-1	18	15	3	6	3	5	2	2	2	2	2	.	4	.	.	.	10	19	.
320204-1	15	8	1	8	.	8	.	.	.	.	.	.	.	6	6	2	10	21	9
370201-1	25	10	1	9	.	9	1	1	4	1	.	3	1	3	6	.	4	13	6
370205-1	3	8	1	1	.	2	.	.	.	.	.	.	.	1	.	.	.	5	3
370208-1	3	7	1	1	.	1	1	1	4	1	.	3	1	6	.	.	8	14	4
370212-1	3	8	1	1	.	1	.	1	4	2	1	3	.	3	6	.	7	17	7
390204-1	15	8	1	1	.	1	.	.	.	.	.	1	.	1	2	2	8	22	7
493011-1	31	17	4	12	4	11	2	2	2	2	2	.	10	.	2	2	16	21	.
533813-1	22	14	4	10	4	19	2	2	2	2	2	.	8	2	2	2	10	21	.
833802-1	30	20	3	9	4	7	2	2	2	2	.	.	2	1	2	2	13	17	6
893015-1	31	19	4	7	3	9	2	2	2	2	2	.	4	2	2	2	10	18	.
204054-1	17	21	4	4	5	12	2	2	2	1	1	.	6	2	2	2	13	21	.
274040-1	36	18	4	8	4	7	2	2	2	1	.	.	4	1	1	2	9	20	2
364018-1	31	3	3	.	3	1	2	2	2	2	1	.	4	2	2	2	2	21	.
421606-1	21	16	5	7	4	14	2	2	2	2	2	.	4	2	2	2	15	20	.
484142-1	34	14	5	9	5	9	2	2	2	2	.	.	5	2	2	2	23	21	.
484143-1	33	14	5	9	5	9	2	2	2	2	.	.	4	2	2	2	14	17	.

Table 1.10 LTPP data availability report for flexible pavements (continued)

ID	EXP	FWD_MODS	FWD_KVAL	T_LAYER	SP_LAYER	SP_THICK	INV_GEN	TRF_MON	TRF_EST	AWS	CLM	S_TEMP	S_MOIST	S_FROST	S_FREEZE	S_WATERD	S_ELEV	S_FAULT
040215-1	S2	320	891	3	3	30	.	3	.	.	.	21	8	.	.	23	10	21
063042-1	G3	239	381	4	.	.	1	7	10	.	18	21	10	.	.	24	6	23
133019-1	G3	619	699	3	.	.	1	5	.	.	17	18	12	.	.	18	9	18
183002-1	G3	273	561	3	.	.	1	7	.	.	21	16	8	8	8	5	4	5
313018-1	G3	388	462	3	.	.	1	7	.	.	17	19	8	8	.	12	4	10
320204-1	S2	.	.	5	5	.	.	.	.	.	.	10	.	.	.	2	.	2
370201-1	S2	153	264	4	4	55	.	1	.	.	.	.	15	.	.	27	12	22
370205-1	S2	533	915	4	4	55	.	1	.	.	.	.	7	.	.	.	.	.
370208-1	S2	.	.	4	4	55	.	1	.	.	.	.	7	.	.	.	.	.
370212-1	S2	349	552	5	5	55	.	1	.	.	.	.	7	.	.	.	.	.
390204-1	S2	688	690	4	4	55	.	.	.	.	.	7	.	.	.	6	3	3
493011-1	G3	343	498	4	.	.	1	.	.	.	17	29	32	29	29	26	10	30
533813-1	G3	56	90	3	.	.	1	7	.	.	31	24	9	.	.	17	7	14
833802-1	G3	81	120	2	.	.	1	4	.	.	17	30	33	31	.	56	24	23
893015-1	G3	83	87	3	.	.	1	.	.	.	17	35	29	31	14	36	14	28
204054-1	G4	522	702	3	.	.	1	3	.	.	17	19	9	8	.	12	6	9
274040-1	G4	809	1185	3	.	.	1	6	.	.	18	31	34	34	.	30	22	28
364018-1	G4	327	375	2	.	.	1	.	.	.	23	30	31	33	.	36	17	32
421606-1	G4	835	1002	3	.	.	1	.	.	.	20	26	12	12	12	26	9	19
484142-1	G4	184	300	4	.	.	1	8	.	.	25	28	30	.	.	30	12	29
484143-1	G4	.	933	4	.	.	1	6	.	.	27	23	27	.	.	28	12	28

CHAPTER 2
FREEZE/THAW PHENOMENA

One of the central objectives of this research is to quantify the changes in pavement properties that occur during the winter freeze and spring thaw. As freezing air temperatures cool the pavement system, the moisture in the unbound pavement layers freezes into ice that binds the aggregate particles together. With prolonged freezing, the same thing happens in the subgrade. The result is an increase in the strength and stiffness of the unbound pavement layers and the soil subgrade. As the water turns to ice, the moisture content drops and the matric suction increases, attracting additional moisture from deeper in the pavement system. If the subgrade soil contains enough silt-sized particles, substantial amounts of moisture can migrate toward the frozen zone, producing a surfeit of ice as the freezing temperatures penetrate the pavement system.

In the spring, sunshine and rising air temperatures start to thaw the pavement system. The water released by the melting ice can be trapped by deeper, still-frozen material, creating saturated or supersaturated conditions. For several weeks, until the excess moisture dissipates, the saturated pavement materials are very soft and weak and provide little structural support. As the moisture content slowly returns to normal, the original strength and stiffness of the pavement materials are recovered. This process can take from several weeks to several months depending on the type of soil and the ease with which the excess water can drain back to the water table.

2.1 DETERMINING FREEZE/THAW DEPTHS

In order to model the effects of freezing and thawing on pavement material properties, it is necessary to know the depth of freezing and thawing at any given time. In the original SMP experimental design, half of the 64 sites were to be located in climate zones characterized by wintertime freezing. Those sites were instrumented to measure, among other things, the moisture

content, temperature, and freeze state in the unbound pavement layers and the upper meter or two of the subgrade (Rada, et. al., 1995). The instruments are typically read once a month in conjunction with routine FWD testing of the pavements and so provide discrete snapshots of the moisture-temperature state of each site. Because the thaw-weakening period usually lasts just a few weeks, one extra site visit is scheduled each year during the spring thaw to better capture the rapidly-changing environmental conditions.

Moisture contents are measured using time-domain reflectometry (TDR) probes. These probes make use of the fact that the travel time of an electromagnetic wave through soil depends on the dielectric constant of the soil which, in turn, depends on the moisture content of the soil. Ten TDR probes are installed at each SMP site. The probe closest to the pavement surface is installed at the mid-height of the highest unbound layer unless that layer is more than 300 mm (12 in) thick, in which case the probe is installed 150 mm (6 in) below the top of the layer regardless of thickness. The next seven probes are installed at 150-mm (6-in) depth intervals and the two deepest probes are installed at 300-mm (12-in) depth intervals. This places the deepest probe approximately 1.8 m (6 ft) below the top of the highest unbound pavement layer.

The temperature profile in the pavement system is measured using thermistors. Thermistors are solid state resistors whose resistance is highly temperature dependent. The temperature can be determined by measuring the voltage drop across the thermistor. To measure temperatures in the unbound pavement layers and subgrade, 15 thermistors are encased in a 25-mm (1-in) diameter by 1.8-m (6-ft) long PVC pipe. The five thermistors closest to the pavement surface are spaced 75 mm (3 in) apart. The rest are spaced 150 mm (6 in) apart. The top of the thermistor probe is installed approximately 50 mm (2 in) below the bottom of the lowest bound pavement layer.

The freeze state in the unbound pavement layers and the near-surface subgrade is determined using electrical resistivity probes. Electricity is conducted exclusively by the water phase of soils because the soil minerals and air voids are nonconductive. Because the electrical resistivity of frozen water is much higher than that of liquid water, it can be used to differentiate frozen and unfrozen soil. Each resistivity probe consists of 36 metal wire electrodes spaced 51 mm (2 in) apart on a solid PVC rod 1.9 m (73 in) long. In theory, this means that freeze/thaw depths can be determined to within 51 mm (2 in). The top of the resistivity probe is installed approximately 50 mm (2 in) below the bottom of the lowest bound pavement layer.

By the time the SMP test matrix was fully populated, there were 65 sites, 35 of which were identified as being in “wet-freeze” or “dry-freeze” climate zones and instrumented as described above (Table 2.1). Data from only 33 of those sites appears in the SMP_FREEZE_STATE table, so frost penetration data must not have been collected at two of the sites. Among the 33 sites at which freeze state data was collected, frozen ground was detected at 21 sites. The other 14 sites included wet-freeze sites with very mild winters and little or no ground freezing, and dry-freeze sites with freezing temperatures but very little soil moisture. If there is little water present, or the water phase is discontinuous, the difference in electrical resistivity between the frozen and unfrozen soil may not be enough to detect reliably. Of course, if there is little soil moisture, the soil does not really freeze, it just gets cold, so those sites shed no light on freeze/thaw behavior anyway.

Figure 2.1 (from site 23-1026 in Maine) exemplifies the temperature and freeze state data collected at the LTPP SMP sites. The solid vertical lines indicate the extent of ground freezing registered by the electrical resistivity probe during each monthly site visit, and the dashed vertical lines denote the extent of below-zero temperatures measured by the thermistor probe.

Table 2.1 Summary of LTPP SMP sites instrumented for freeze/thaw detection

Site ID	State	Climate Zone	Freezing Index (^{o}C-days)	Annual Precip. (mm)	Probes Installed	Data Collected	Freezing Detected	Models Developed
08-1053	CO	D/F	234	224	×	×		
09-1803	CT	W/F	236	1254	×	×		
16-1010	ID	D/F	665	303	×	×	×	×
18-3002	IN	W/F	451	950	×	×		
20-4054	KS	W/F	258	819	×	×		
23-1026	ME	W/F	828	1142	×	×	×	×
24-1634	MD	W/F	94	1159	×	×		
25-1002	MA	W/F	438	1213	×	×	×	
27-1018	MN	W/F	1108	680	×	×	×	×
27-1028	MN	W/F	1388	654	×	×	×	×
27-4040	MN	W/F	1348	714	×	×	×	×
27-6251	MN	W/F	1485	642	×	×	×	×
30-0114	MT	D/F	688	365	×			
30-8129	MT	D/F	580	337	×	×	×	×
31-0114	NE	W/F	410	785	×	×	×	
31-3018	NE	W/F	479	640	×	×	×	
32-0101	NV	D/F	281	223	×	×		
32-0204	NV	D/F	276	222	×	×		
33-1001	NH	W/F	576	966	×	×		
36-0801	NY	W/F	437	891	×	×	×	
36-4018	NY	W/F	584	1099	×	×	×	
39-0204	OH	W/F	375	972	×	×		
39-0901	OH	W/F	306	980	×			
42-1606	PA	W/F	354	994	×	×		
46-0804	SD	D/F	978	423	×	×	×	×
46-9187	SD	D/F	757	442	×	×	×	
49-1001	UT	D/F	124	209	×	×		
49-3011	UT	D/F	260	422	×	×		
50-1002	VT	D/F	786	1010	×	×	×	×
56-1007	WY	D/F	546	255	×	×	×	
83-1801	MB	D/F	1733	478	×	×	×	×
83-3802	MB	W/F	1863	530	×	×	×	
87-1622	ON	W/F	1081	1159	×	×	×	×
89-3015	PQ	W/F	1228	1052	×	×	×	
90-6405	SK	D/F	1863	396	×	×	×	

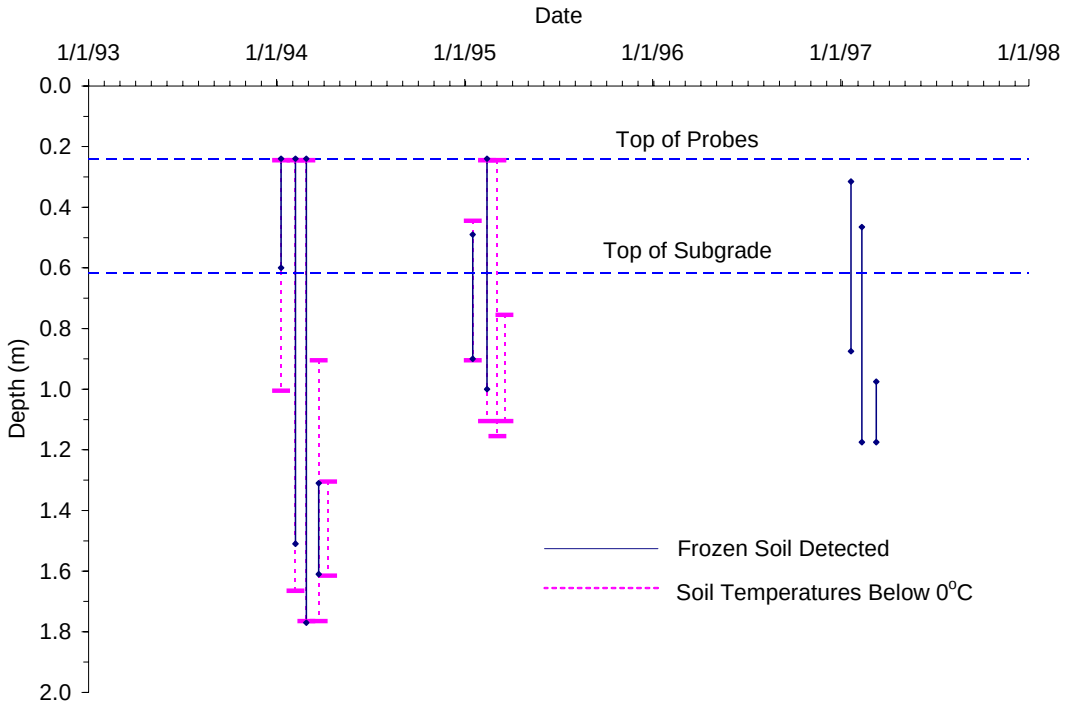

Figure 2.1 Ground freezing measured at site 23-1026

(Similar plots for the other frozen sites appear in Appendix B.) The thermistor probe data seems to correlate fairly well with the electrical resistivity probe measurements during the winter freeze, but not at all during the spring thaw. The thermistor probe records soil temperatures below 0°C for several weeks after the resistivity probe shows the subgrade is frost-free.

The TDR data can help resolve the discrepancies between the thermistor and resistivity data because TDR probes can detect the phase change of the soil water from liquid to solid (Benson, Bosscher, and Jong, 1998). In the TDR technique, the travel time of an electromagnetic pulse is used to determine the apparent dielectric constant of the soil. A polynomial regression model called Topp's equation (Topp, et.al., 1980) is then used to convert the apparent dielectric constant of the soil into an apparent moisture content. Because the dielectric constant of water changes from 80 to 3 when it freezes (Spaans and Baker, 1995), freezing is accompanied by a

dramatic drop in the apparent dielectric constant of the soil. Topp's equation translates that drop into a similarly dramatic drop in the apparent moisture content of the soil. Thawing is likewise accompanied by a sudden increase in the apparent moisture content of the soil.

Figure 2.2 shows the moisture contents recorded in the unbound base at Site 23-1026 during the first two winters of data collection. To help orient the reader, the ground freezing data is duplicated from Figure 2.1. The TDR probes were installed 150 mm (6 in) below the top of the 450-mm (18-in) thick unbound base, 150 mm (6 in) above the bottom of the unbound base, and just above the base/subgrade interface. During both winters, the TDR probes register a sudden drop in moisture content at the onset of freezing, followed by a dramatic increase at the onset of the spring thaw, and culminating in a gradual return to some nominal summertime level. The fact that the post-thaw moisture content was higher than the pre-freeze moisture content suggests that additional moisture was drawn to the freezing soil.

Closer examination of Figure 2.2 shows that both the freeze state and moisture content data suggest a partial thaw in January 1995 that extends to just below Probe 2. The data also shows that the base course re-freezes before the next site visit in February 1995. Just three weeks later, in early March, the resistivity probe indicates the pavement is completely thawed even though the soil temperatures still hover below 0°C and the moisture contents have not changed from their February values. Two weeks later, near the end of March, some portions of the subgrade are still below 0°C, but the moisture contents have increased from roughly half the nominal summertime values to nearly twice the nominal values. This suggests that the ground was still frozen during the early-March site visit, which refutes the electrical resistivity data but supports the thermistor data.

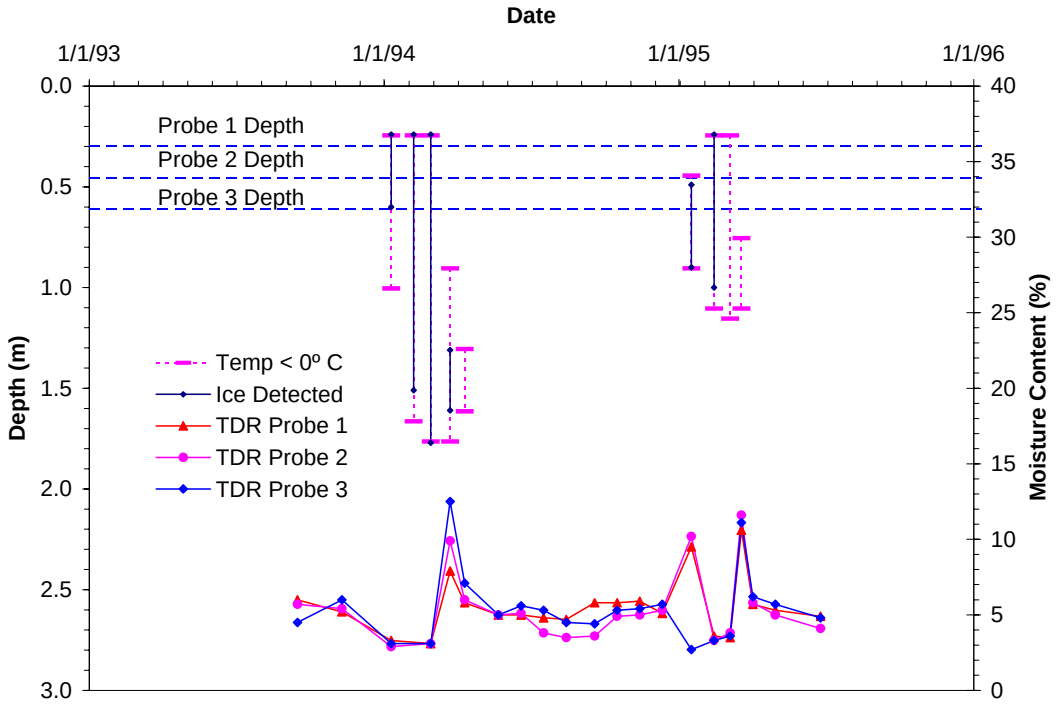

Figure 2.2. Ground freezing and base moisture contents at site 23-1026

Figure 2.3 shows the moisture contents recorded deeper in the pavement system during the same two winters. Probe 4 is 150 mm (6 in) below the top of the subgrade and each subsequent probe is 150 mm (6 in) deeper than the previous one. During the January 1994 site visit, Probe 4 shows a significant drop in the apparent moisture content, Probe 5 shows a moderate drop, and Probe 6 shows a negligible drop. Jong, Bosscher, and Benson (1998) showed that the change in the apparent dielectric constant of the soil that accompanies the transition from frozen to unfrozen, and vice versa, actually occurs over a range of soil temperatures between +0.5°C and −0.5°C . The partial drop in the apparent moisture content at Probe 5 suggests that the actual frost penetration line is somewhere nearby. This, too, corroborates the thermistor data and refutes the resistivity data.

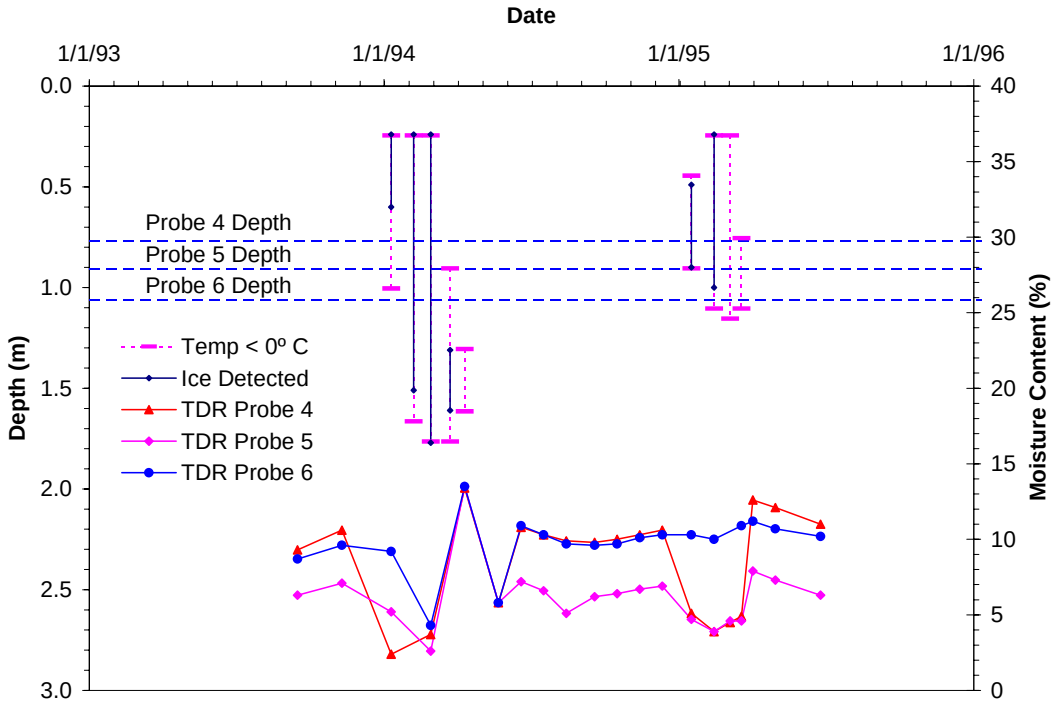

Figure 2.3. Ground freezing and subgrade moisture contents at site 23-1026

During the winter of 1994-95, Probes 4 and 5 show a sharp drop in the apparent moisture content between December 1994 and January 1995 that suggests the site was frozen at least to the depth of Probe 5. Those same probes show a sharp rise in the apparent moisture content between late March and early April that suggests the site didn't completely thaw until approximately April 1. These observations are consistent with the thermistor probe data. The electrical resistivity data, on the other hand, suggests that the site was frost-free nearly a month earlier.

Based on these findings, the freeze/thaw depths on any given day could only be determined by analyzing the data from all three environmental probes simultaneously. This was done for each of the 21 sites that exhibited at least some freezing according to the electrical resistivity probes (which appear to be fairly reliable indicators of freezing but not thawing). The

resulting database was used to develop models of freeze depth and thaw depth as a function of air temperature and to correlate with seasonal changes in measured pavement properties.

2.2 FREEZING AND THAWING INDICES

Many researchers have related the maximum depth of frost penetration during the winter to the freezing index, which is the total area under a plot of daily mean air temperatures (Figure 2.4) during the winter season. Having units of degree-days, the freezing index is a measure of the length and severity of a winter. Both of those factors help to determine the depth of ground freezing during the course of the winter.

If the maximum depth of frost penetration in a given year is related the to number of freezing degree-days accumulated over the winter, then the depth of frost penetration on any given day during the winter should be related to the number of freezing degree-days accumulated up to that point. This assumes, of course, that the annual freezing and thawing events are more-or-less uninterrupted. If there are several cycles of freezing and thawing during the winter, the task becomes much harder because the ground both freezes and thaws from the top down. After each thawing cycle, the thawed ground must re-freeze before the freeze line can penetrate any further into the soil. This cannot be modeled empirically. Finite-difference or finite-element heat flow models must be used instead.

For the sake of simplicity, the term “freezing index” will be used here to denote the accumulated number of freezing degree days at any point during the winter, even though it traditionally refers to the total for the entire season. For temperatures in degrees Celsius, the freezing index is calculated as

$$FI = \sum_{i=1}^{n} \max\left(-T_i, 0\right)$$

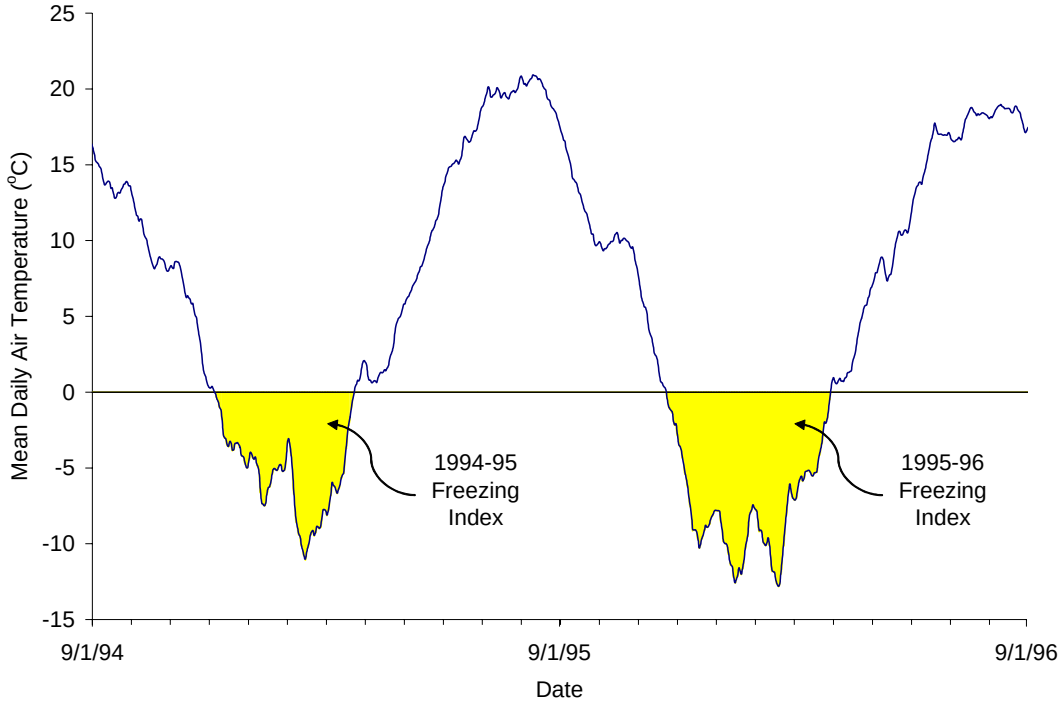

Figure 2.4 Traditional definition of freezing index

where T_i is the daily mean air temperature. Using this definition, the freezing index increases whenever the daily mean air temperature is below zero, otherwise it remains constant. This is essential for modeling daily changes in frost penetration depth. When the air temperature rises above freezing, the ground begins to thaw from the top down. If the freezing index was allowed to decrease during the winter, the frost depth model would predict that the subgrade thaws from the bottom up!

The spring thaw can be modeled using the concept of a thawing index. At its simplest, thawing index is just the opposite of freezing index. It is a running total of positive degree-days instead of negative degree days. For the purpose of this study, the definition was modified slightly so it was equal to zero until the first freeze and could return to zero if the ground were to re-freeze after a brief early-winter thaw (a fairly common occurrence):

$$TI = \begin{cases} 0 & if \;\; FI = 0 \\ \max\left(\sum_{i=1}^{n} T_i \;, 0 \right) & if \;\; FI > 0 \end{cases}$$

To complicate matters, many researchers have noted that thawing begins while the mean daily air temperature is still below zero. This happens because the ground surface is heated both by conduction and radiation. A thawing index based on air temperatures alone accommodates only heating due to conduction. In the middle of the winter, when the sun is low in the sky and the days are short, this is not a bad approximation. When the spring thaw occurs, the sun is halfway towards its zenith and the days and nights are approximately the same length, so the added effects of solar radiation cannot be ignored.

To accumulate thawing degree-days even when the air temperature is below zero, the Minnesota DOT computes thawing degree-days relative to a reference temperature that changes throughout the thawing season (Van Deusen, et. al., 1998). During the first week of February, the reference temperature is −1.5°C (29°F). For the next six weeks, the reference temperature is lowered by 1.5°C (0.9°F) each week until it reaches a minimum of −4.5°C (24°F) in mid-March. Another way to implement this algorithm would be to keep the reference temperature at 0°C (32°F) and add 1.5−4.5°C (3−8°F) to the daily mean air temperature to account for the additional pavement heating that results from solar radiation.

The Minnesota DOT uses the thawing index to determine when to post spring load restrictions. In Minnesota, the spring thaw seldom starts earlier than February 1 nor later than mid-March. To use this same adjustment outside of Minnesota, it needs to be extended beyond the 6-week range from February 1 to mid-March. At its simplest, the contribution of solar radiation can be thought of as a cyclical variable that is at a minimum at the Winter Solstice (December 21) and reaches a maximum at the Summer Solstice (June 21).

Least-squares regression was used to define a sinusoid with a period of 365 days that replicates the MnDOT algorithm during the period from February 1 to March 15. That sinusoid is given by the equation

$$\Delta T(^\circ \mathrm{F}) = 9.81 - 9.27\cos\left(2\pi\frac{A}{365}\right)$$

$$\Delta T\,(^\circ \mathrm{C}) = 5.45 - 5.15\cos\left(2\pi\frac{A}{365}\right)$$

where *A* is the number of days since December 21 of the previous year. Figure 2.5 compares this equation to the MnDOT algorithm. Note that the regression equation provides a negligible solar radiation contribution on the shortest day of the year and a contribution approaching 20°F on the longest day of the year. This is good approximation of the difference between the mean internal pavement temperature and the mean air temperature in the middle of the summer. The final equation for thawing index is therefore

$$TI = \begin{cases} 0 & if\ \ FI = 0 \\ \max\left(\sum_{i=1}^{n} T_i + \Delta T_i\ ,\ 0\right) & if\ \ FI > 0 \end{cases}$$

The freezing and thawing indices can only be calculated if the air temperature data is continuous over the study interval. The first gap in the data immediately stops the summation. Gaps of one or two days can usually be filled in using nonlinear interpolation, but air temperature is much too erratic to successfully interpolate within gaps lasting several days or weeks. Figure 2.6 shows, for each of the 21 sites, the number of temperature entries in table SMP_ATEMP_RAIN_DAY as a percentage of the total length of the data collection period at each site. With the exception of site 31-0114, which does not appear in the table at all, the coverage ranges from 75% to 100%.

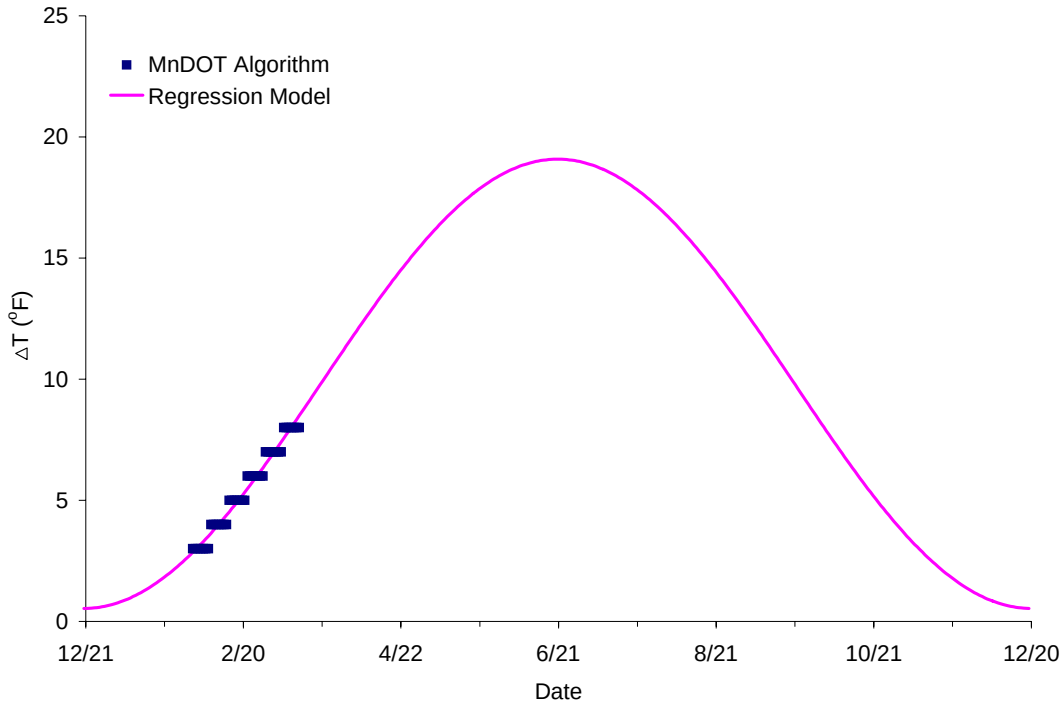

Figure 2.5 Comparison of MnRoad algorithm and regression model

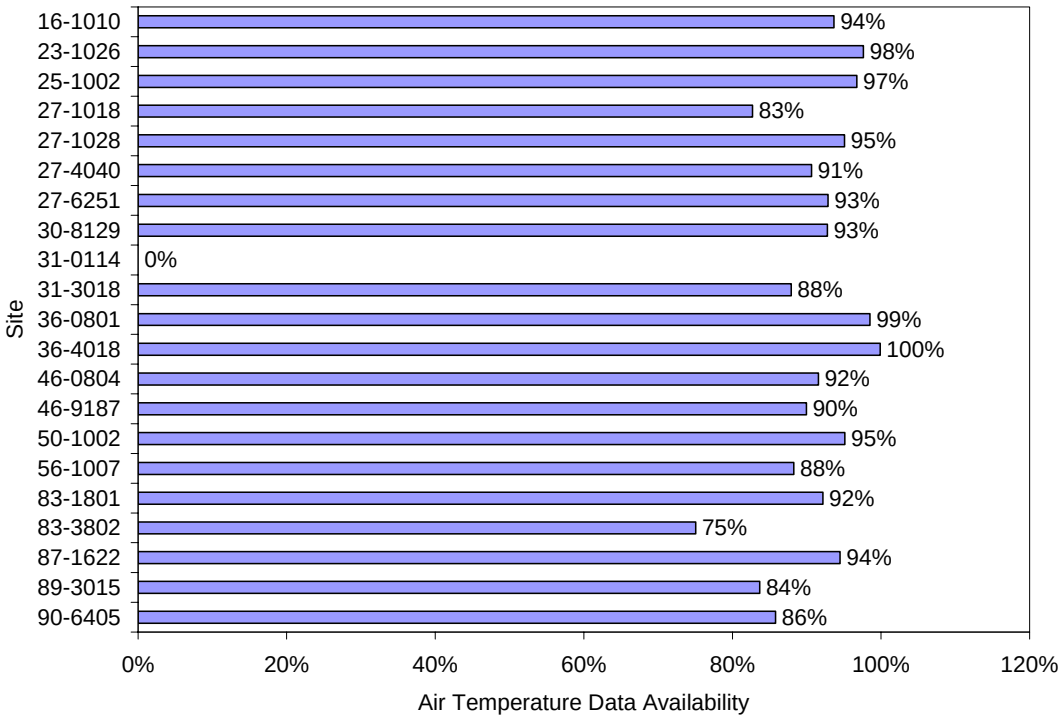

Figure 2.6 Air temperature data availability at freezing sites

Table 2.2 Surrogate air temperature sources for freezing sites

LTPP Pavement Site				Separation	NOAA Weather Station			
Site ID	Lat. (deg)	Long. (deg)	Elev. (ft)	Distance (miles)	COOP ID	Lat. (deg)	Long. (deg)	Elev. (ft)
16-1010	43.68	112.12	4775	11.7	103964	43.52	112.07	4526
23-1026	44.57	70.29	486	10.4	172765	44.68	70.15	397
27-1018	46.03	94.42	1118	3.9	214793	46.00	94.35	1058
27-1028	46.68	95.67	1384	31.3	218579	46.40	95.15	1276
27-4040	47.31	93.72	1305	11	213303	47.25	93.50	1238
27-6251	47.46	94.91	1364	14.8	211374	47.38	94.62	1225
30-8129	46.31	109.14	4440	17.1	247263	46.52	109.35	4195
46-0804	45.93	100.42	1680	6.9	396712	45.90	100.28	1544
50-1002	44.12	73.18	283	24	431081	44.47	73.15	312
56-1007	44.50	108.92	5204	6	481850	44.42	108.90	4960
83-1801	49.77	100.54	1400	65	320941	48.83	100.45	1550

The gaps in the temperature data were filled in using data available from the National Climatic Data Center (NCDC) of the National Oceanographic and Atmospheric Administration (NOAA) through their Climate Data Online website (http://cdo.ncdc.noaa.gov). This website provides internet access to historical surface weather data from more than 19,000 weather stations across the United States. The latitude, longitude, and elevation of every weather station in the CDO database was downloaded to a spreadsheet and an algorithm was developed to identify the weather stations closest to a given LTPP site and with a similar elevation. Table 2.1 lists the 11 sites that had enough data to do freeze/thaw modeling and Table 2.2 lists the 11 weather stations used to fill in the gaps in the air temperature data. Six of the 21 sites had too little data to create any freeze/thaw models and four of the five Canadian sites were too far from any U.S. weather stations to find a reliable surrogate.

Figure 2.7 compares the daily mean air temperatures recorded at site 23-1026 with the same data recorded at the National Weather Service Cooperative Weather Station 172765.

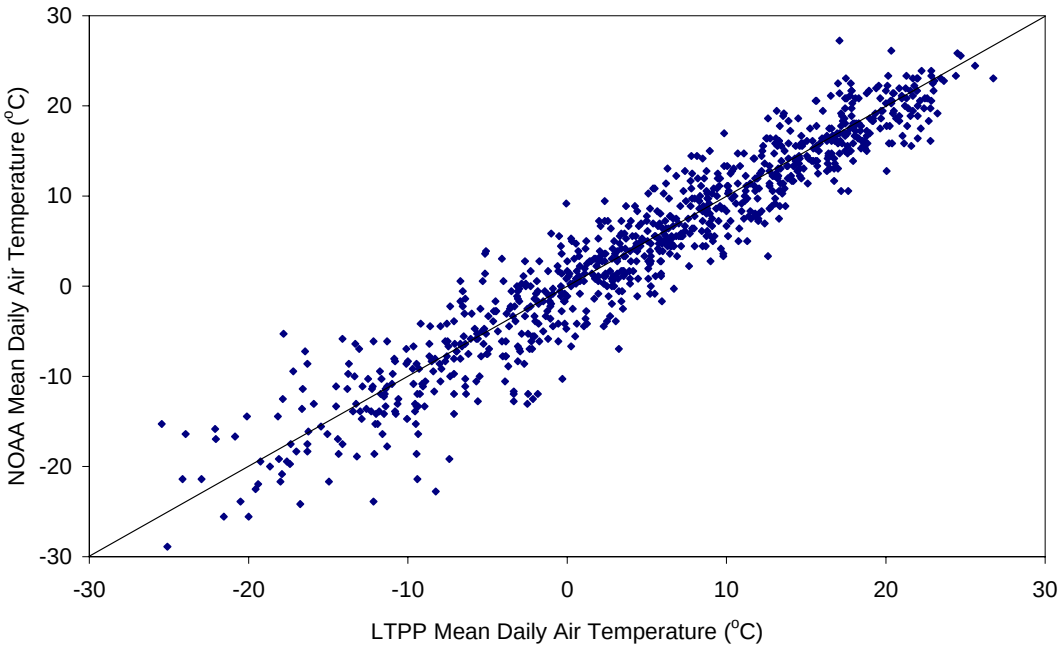

Figure 2.7 Comparison of LTPP and NOAA air temperatures at site 23-1026

(Similar plots for the other ten sites appear in Appendix C.) The two data sets have a correlation coefficient of 0.954 and a mean absolute error of 2.5°C. The errors show a very slight bias (0.4°C) toward overestimation, but are distributed symmetrically about their mean, so the positive and negative errors will cancel each other over time as the surrogate temperatures are added into the freezing and thawing summations.

Figure 2.8 shows the daily mean air temperatures recorded during two winters at site 23-1026. Overlaid on the air temperature plot is a plot of the freezing and thawing indices calculated using the formulas above. Both indices are reset to zero every September 1st; otherwise, they would continue to increase *ad infinitum*.

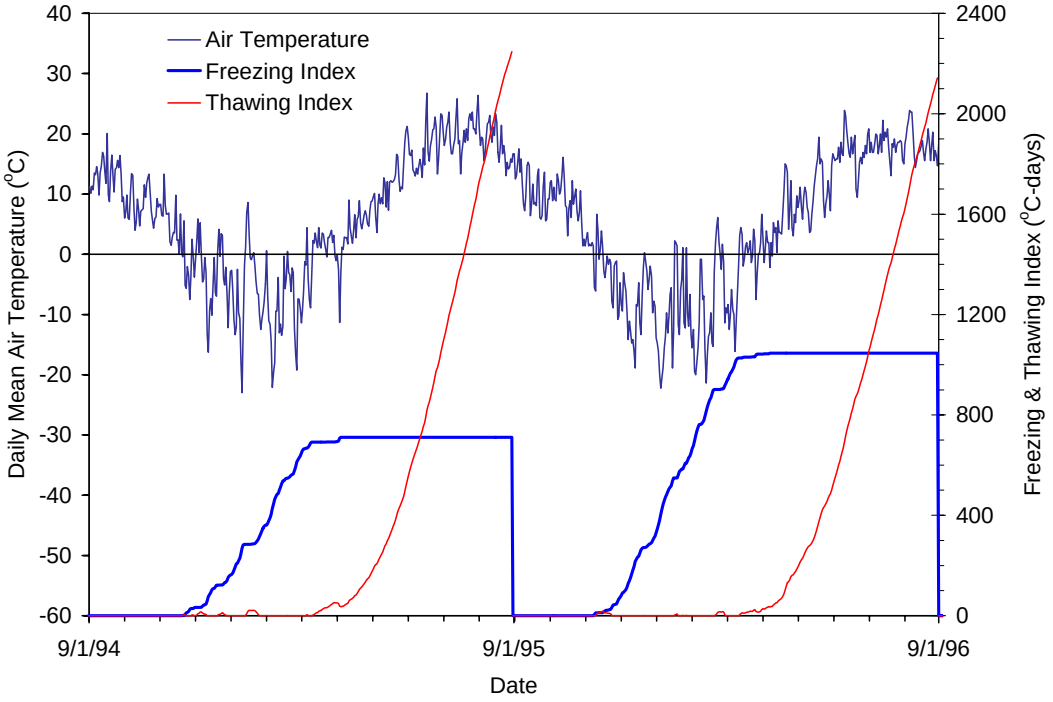

Figure 2.8 Air temperature, freezing index, and thawing index at site 23-1026

2.3 MODELING FREEZE DEPTH

The most common functional form for modeling seasonal freeze depths as a function of freezing index is the square root. This originated with a simple theoretical analysis of heat flow and heat storage in a homogeneous halfspace known as the Stefan equation:

$$D_f = \sqrt{\frac{48\,k\,\mathrm{FI}}{L}}$$

Here, D_f is the freeze depth, k is the thermal conductivity of the mass, L is the volumetric heat of latent fusion of the soil moisture, and FI is the freezing index. Following in this tradition, the monthly measured freeze depths will be modeled as linear functions of the square root of the freezing index.

Figure 2.9 relates the monthly freeze depths at site 23-1026 to the square root of the freezing index calculated for that site. For the most part, the freeze depths identified by the electrical resistivity probe were no more or less plausible than those identified by the thermistor probe, so both sets of data were included in the regression model. In two instances, the moisture content data refuted the resistivity probe results and those data were eliminated. The freeze depth data nonetheless span all three years of data collection.

The data were initially fit by a linear regression model of the form

$$D_f = a + b\sqrt{\mathrm{FI}}$$

A hypothesis test on the intercept *a* showed that it could not be statistically distinguished from zero, so the data was fit a second time by a linear regression model of the form

$$D_f = b\sqrt{\mathrm{FI}}$$

which is consistent with the Stefan equation. The regression model shown in Figure 2.9 has a coefficient of determination (r^2) of 0.8237, which is very reasonable.

Similar freeze depth models for all of the other sites appear in Appendix D. They were all fit in the manner just described. Almost all of the models have coefficients of determination of 0.85 or better. The one exception is site 56-1007 in Wyoming (Figure 2.10). The three environmental probes provide a very ambiguous picture of the freeze state, especially during the winters of 1993-94 and 1996-7 (Figure 2.11). This is the result of relatively mild winters with soil temperatures less than 1°C below freezing and frequent cycling of the air temperatures between freezing and thawing (Figure 2.12). Every time the air temperature rises above freezing and the ground starts to thaw, the relationship between freeze depth and freezing index is obliterated. This accounts for the data scatter in Figure 2.10.

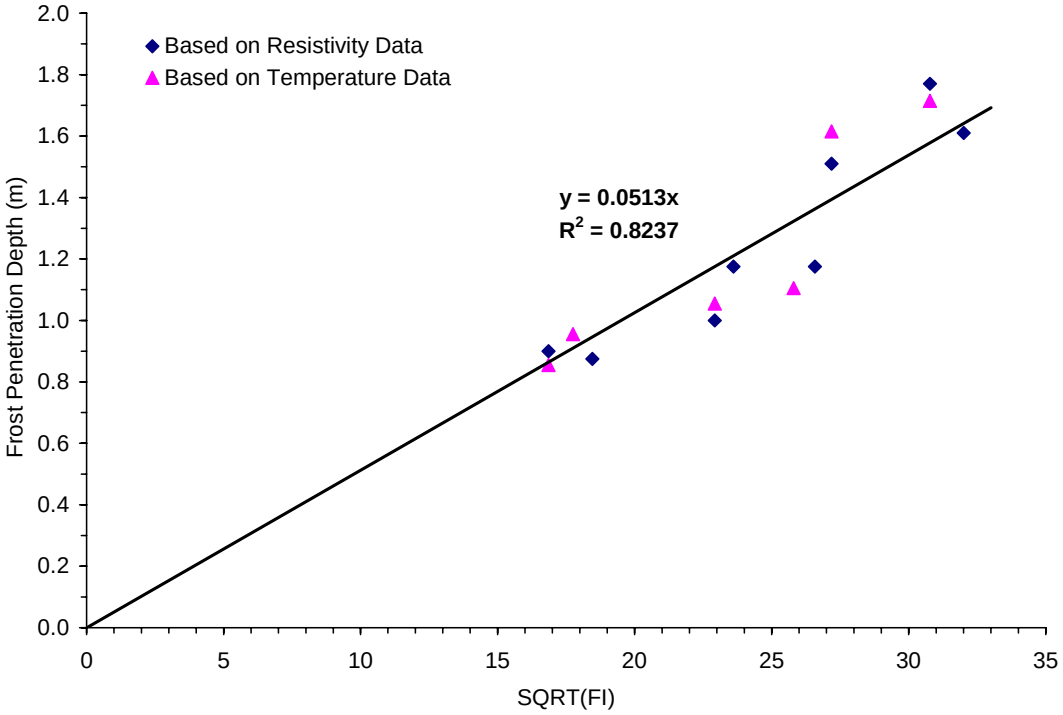

Figure 2.9 Frost depth model developed for site 23-1026

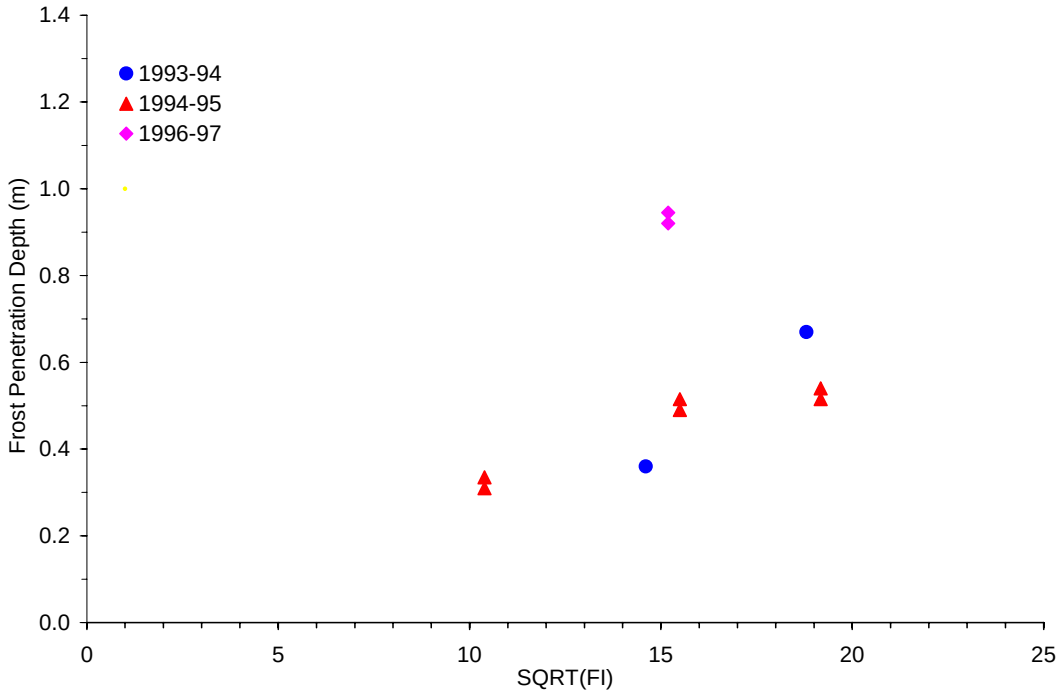

Figure 2.10 Ambiguous freeze depth data for site 56-1007

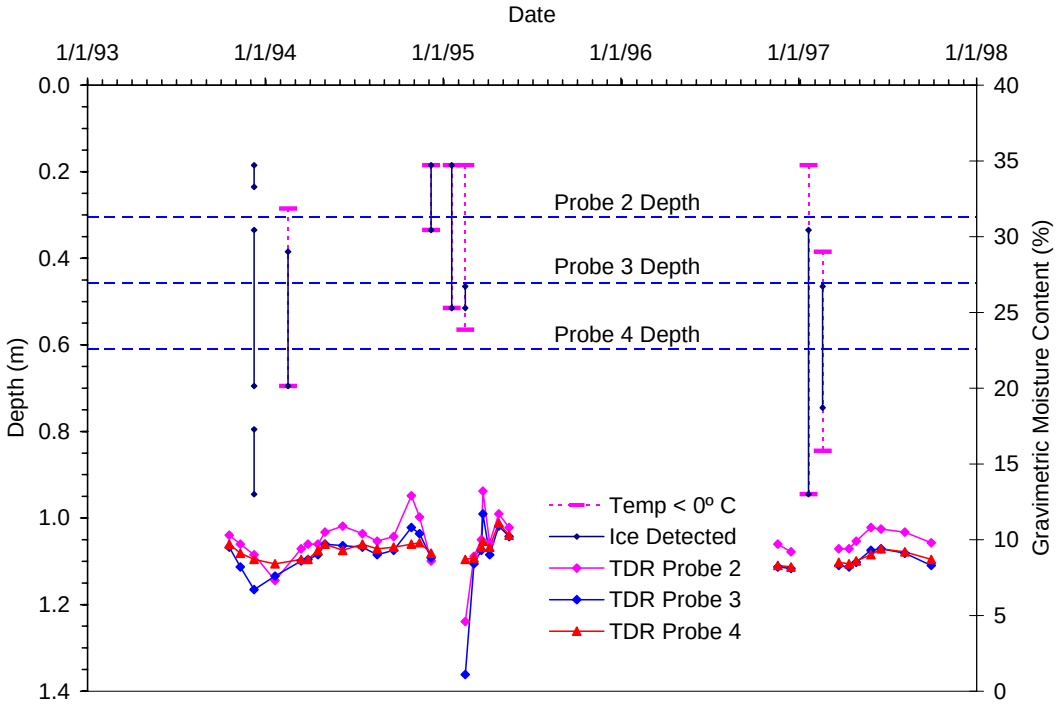

Figure 2.11 Environmental probe data for site 56-1007

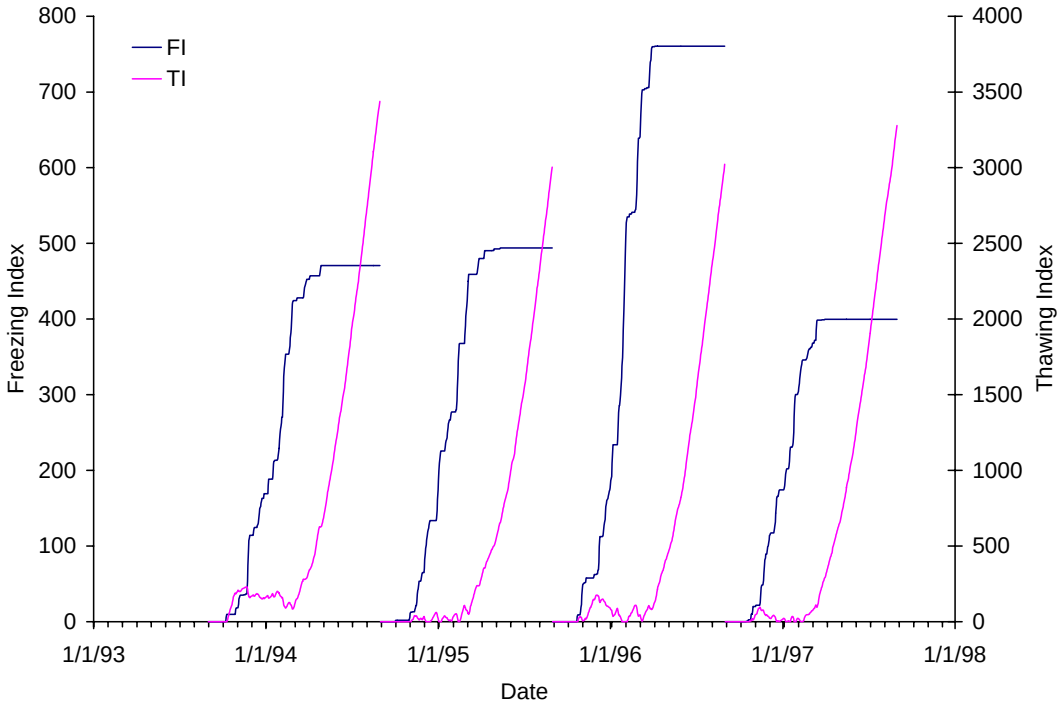

Figure 2.12 Freezing index and thawing index for site 56-1007

The relationship between freezing index and frost penetration depth changes from one site to another based on the type of soil, its moisture content, the thickness of the pavement, and many other parameters that affect the rate at which heat is conducted through the pavement system. Nonetheless, the heat conducting properties of most pavement materials vary within a relatively narrow range, so it may be possible to develop a rudimentary universal model.

Figure 2.13 combines all of the frost depth data from all of the sites that froze (including those that had too little data for site-specific modeling). A simple linear regression on the square root of the freezing index produces a model with a coefficient of determination of 0.722. Hypothesis testing on the intercept showed that the intercept was statistically indistinguishable from zero. Fitting a new regression model with a zero intercept, the relationship between freeze depth and freezing index was found to be

$$D_f = 0.057\sqrt{\mathrm{FI}}$$

where D_f is the freeze depth in meters and FI is the freezing index in Celsius degree-days. In U.S. Customary Units, the relationship is

$$D_f = 0.250\sqrt{\mathrm{FI}}$$

where D_f is in feet and FI is in Fahrenheit degree-days.

2.4 MODELING THAW DEPTH

While the winter freeze usually spans several months, the spring thaw is typically over in just a few weeks. With data being collected no more often than biweekly, there is generally only one or two site visits per year during which the ground is partially thawed. During all of the other site visits, the pavement system is either frozen all the way to the surface or fully thawed. At four of the 11 sites used to develop the freeze depth models, there was one site visit or less with partial thawing during the three years of monitoring.

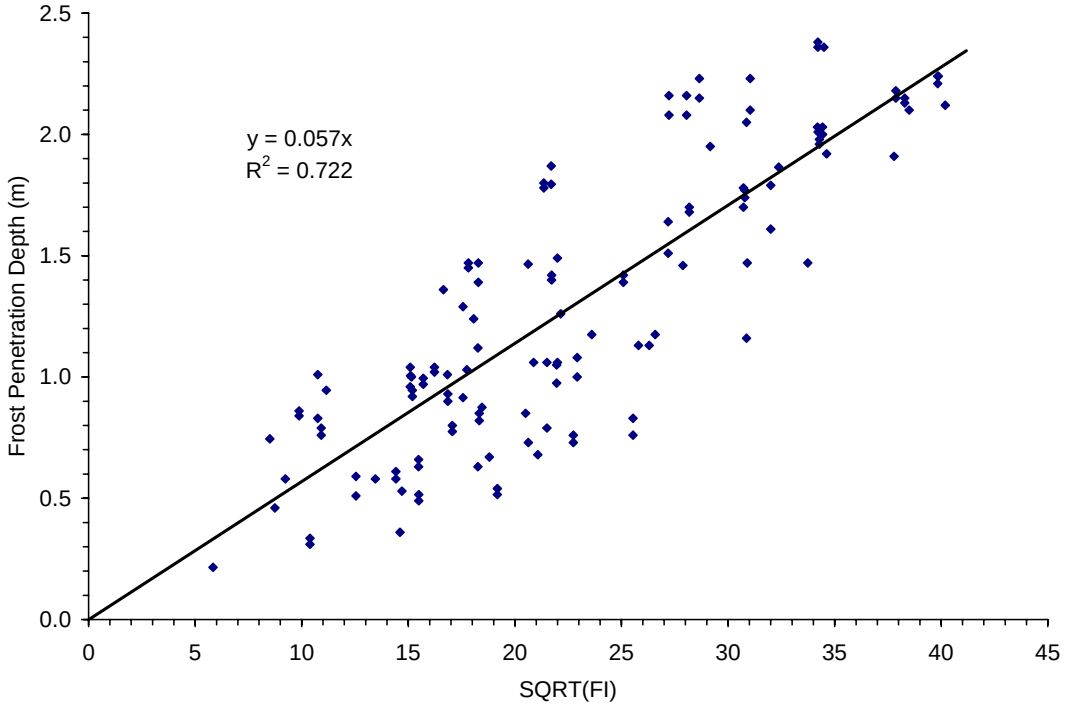

Figure 2.13 Freeze depth model using data from all frozen sites

With so few usable observations, site-specific models of thawing depth could only be developed for a handful of sites. Figure 2.14 shows the model developed for Site 23-1026. The models for the other sites are given in Appendix E.

To obtain thaw depth models for the remaining sites, all the available data was grouped by subgrade type as shown in Table 2.3 and a model was developed for each subgrade type. Figures 2.15 through 2-17 show those models. Figure 2.18 shows all three models together. This figure clearly shows that there is no universal model of thaw depth as a function of thawing index.

Table 2.3 Site grouping used for thaw depth modeling

Group	Site	State	Subgrade Type	Experiment	Pavement
1	27-4040	MN	Lean Clay w/ Silt	GPS-4	JRCP
	30-8129	MT	Lean Clay w/ Sand	GPS-1	AC
	46-0804	SD	Silty Clay	SPS-8	AC
2	27-1028	MN	Sand	GPS-1	AC
	27-1018	MN	Sand w/ Silt	GPS-1	AC
	27-6251	MN	Sand w/ Silt	GPS-1	AC
	50-1002	VT	Gravel w/ Silt & Sand	GPS-1	AC
3	16-1010	ID	Silty Sand	GPS-1	AC
	23-1026	ME	Silty Sand w/ Gravel	GPS-1	AC
	56-1007	WY	Silty Sand w/ Gravel	GPS-1	AC
	83-1801	MB	Silty Sand	GPS-1	AC
	87-1622	OT	Silty Sand	GPS-1	AC

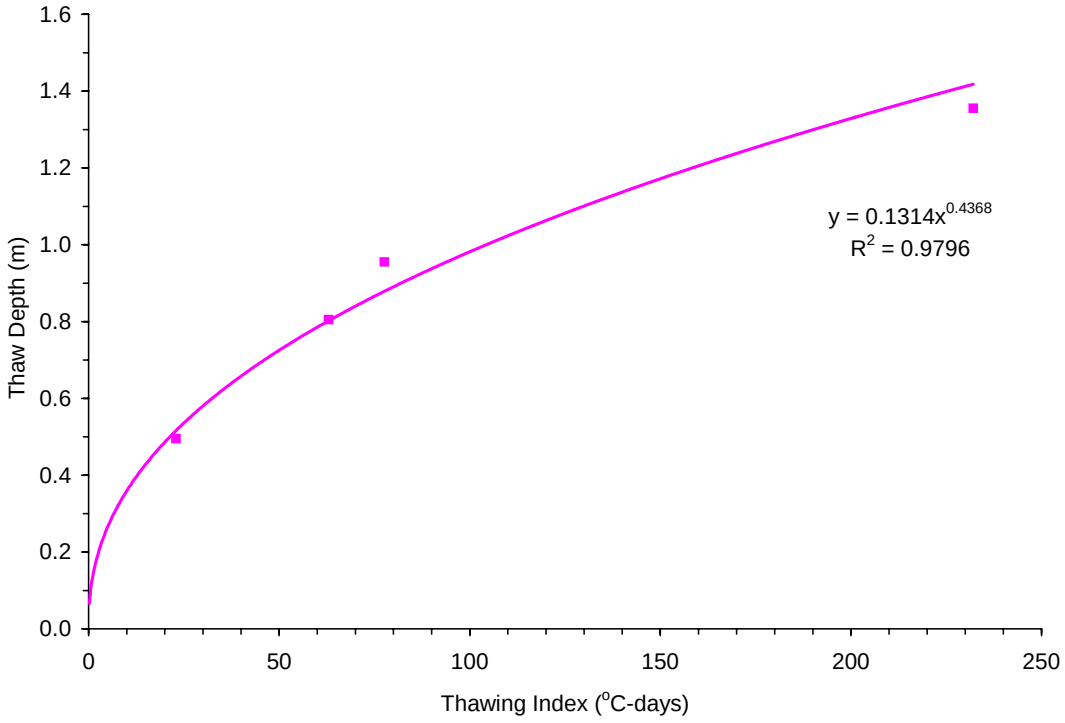

Figure 2.14 Thaw depth model for Site 23-1026

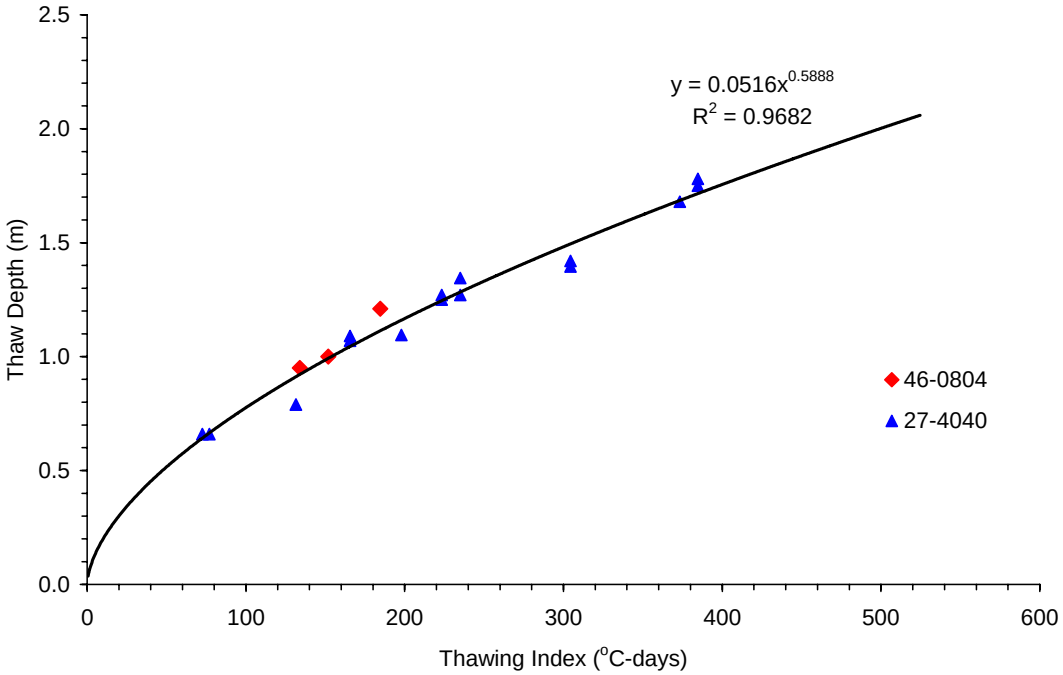

Figure 2.15 Thaw depth model for sites with a silty-clay subgrade

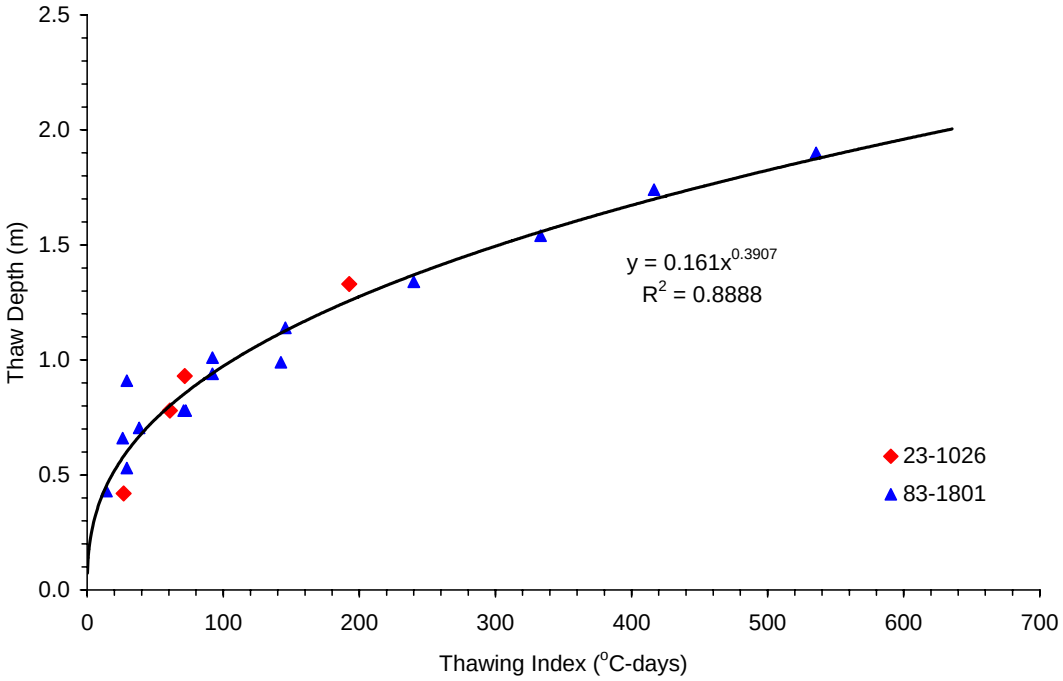

Figure 2.16 Thaw depth model for sites with a silty sand subgrade

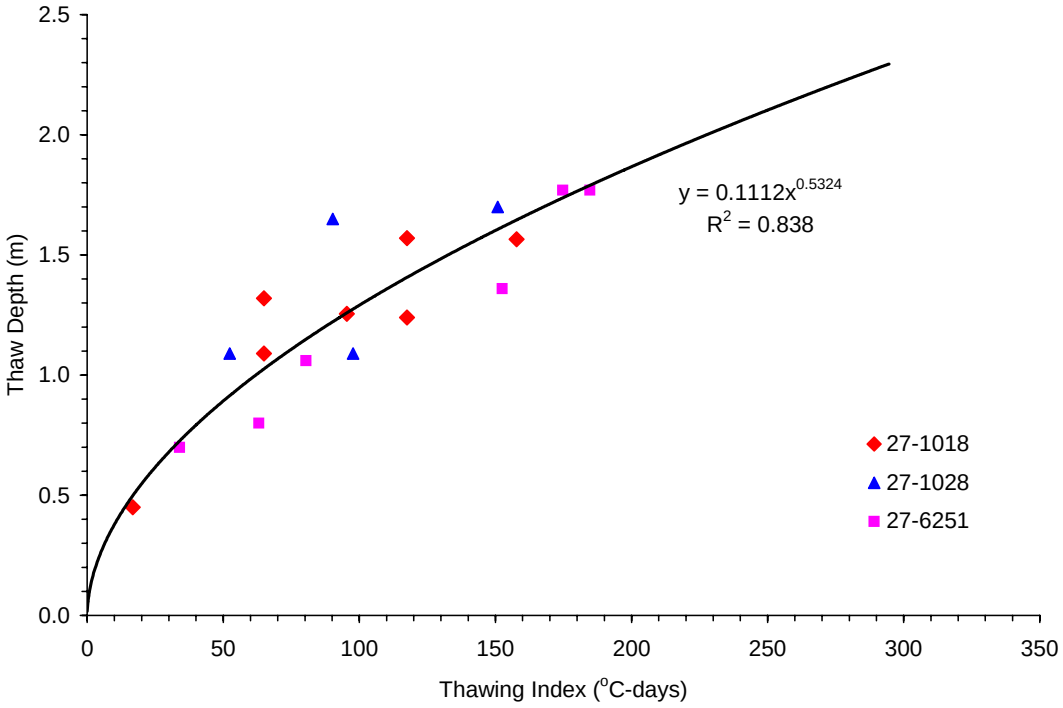

Figure 2.17 Thaw depth model for sites with a sandy subgrade

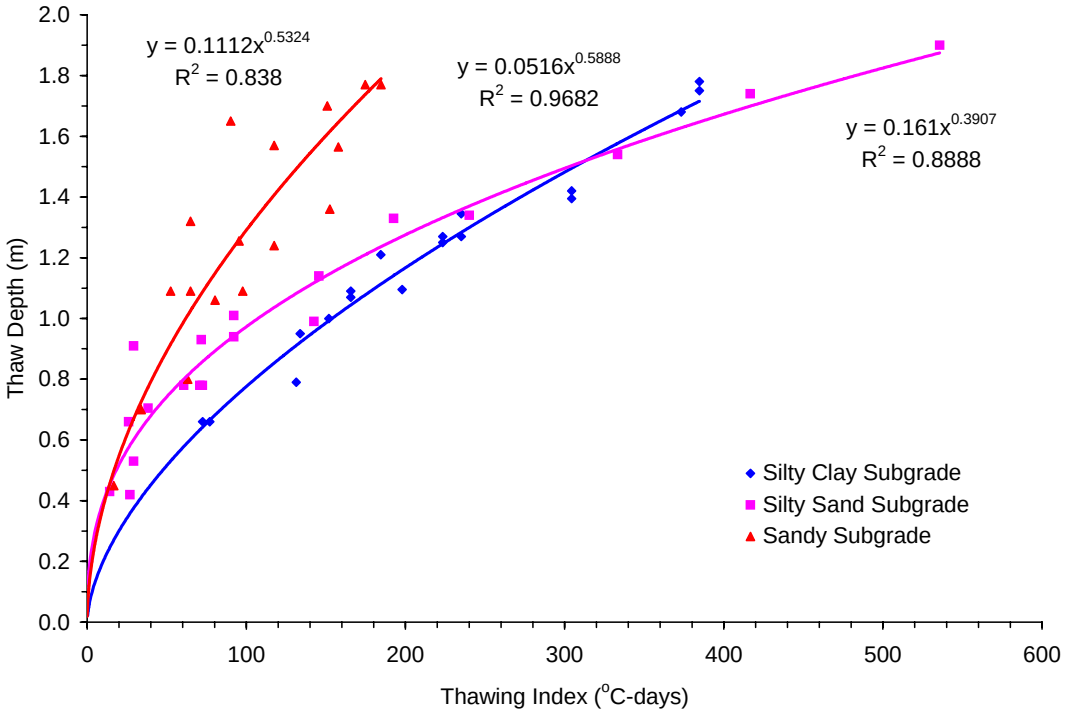

Figure 2.18 Comparison of thaw depth models for the different subgrade types

2.5 ESTIMATING THAW DURATION

Central to this research is the timing of the seasonal load restrictions that are enacted during the spring thaw. The start of spring thaw is fairly easy to determine because it occurs very shortly after the thawing index becomes nonzero. In Washington, for example, experimental data suggested that the critical thaw period began when the thawing index (with a 1.7°C adjustment for solar radiation) reaches 15°C-days (27°F-days) (Rutherford, et. al., 1985). In Minnesota, the critical thaw period is assumed to start when the thawing index (calculated as described earlier) reaches 14°C-days (25°F-days) (Van Deusen, et. al., 1998). Among the 11 sites studied here, these levels were typically reached on the second or third day of above-freezing air temperatures.

The end of the spring thaw is much harder to determine, but just as critical. Rutherford, et. al. (1985) suggested that the duration of the spring thaw could be estimated from the maximum seasonal freezing index as

$$d = 0.018\,\mathrm{FI} + 25$$

where d is in days and FI is in °C-days. As an alternative, the same researchers suggested that the end of spring thaw could be estimated as the date on which the thawing index reaches 30% of the maximum seasonal freezing index.

For each of the sites studied here, four milestones were identified:

1. Date of first freeze
2. Date of full freeze
3. Date of first thaw
4. Date of full thaw

The date of first freeze is just the date on which the freezing index first becomes nonzero (or the first day each year with an average air temperature below zero). The date of full freeze is just the date on which the freezing index reaches its maximum value (which is the FI referenced

in the equation above). The date of first thaw has been taken as the first date on which the thawing index becomes nonzero *and stays nonzero*. Thus, brief thawing periods that are followed by more freezing are ignored. For the sites studied, those brief early-spring thaws generally last less than a week and the thawing index either doesn't reach the critical level or only exceeds the critical value for a day or two before the ground refreezes.

Unfortunately, the date of full thaw cannot be determined with any accuracy because data is only collected on a monthly basis. The last date with at least some measured frost is known, as is the first date with no measured frost. The actual end of the spring thaw occurs somewhere between those two dates. At best, the first date with no measured frost can be used to define an upper bound for the thaw duration.

The freezing and thawing models can also be used to estimate the date of full thaw. If the maximum depth of freezing is known, the thawing model can be inverted to determine the thawing index needed to thaw the pavement system to that depth. For example, the thaw depth model for Site 23-1026 (Figure 2.14) is given by

$$D_t = 0.1314\ \mathrm{TI}^{0.4368}$$

where D_t is the thaw depth in meters and TI is the thawing index in °C-days. The thawing index at which the ground should be thawed to the maximum freeze depth D_{max} can be calculated by setting D_t in the equation above equal to D_{max} and solving for TI.

Table 2.4 shows the freeze milestones established at Site 23-1026 for each of the four winters spanning the data collection period. Also shown are the dates of the last site visit for which frost was recorded and the first site visit for which no frost was recorded. In every case, these bracket the date estimated using the thaw depth model. Similar tables are presented in Appendix F for the other ten sites studied.

Table 2.4 Freeze/thaw milestones for Site 23-1026

Winter	Date of First Freeze	Date of Full Freeze	Date of First Thaw	Estimated Date of Full Thaw	Earliest Possible Thaw Date	Latest Possible Thaw Date
1993-94	10/14/93	4/2/94	3/7/94	4/14/94	4/12/94	5/2/94
1994-95	11/23/94	4/6/95	3/6/95	3/29/95	3/21/95	4/3/95
1995-96	11/10/95	4/9/96	3/13/96	4/15/96	*No Data Collected*	
1996-97	10/30/96	4/10/97	3/20/97	4/8/97	3/25/97	4/8/97

The first three columns in Table 2.5 show, for the same four winters, the maximum freezing index, the maximum freeze depth, and the thawing index required to thaw the ground to the maximum freeze depth. The latter was found by setting the thaw depth model equal to the maximum freeze depth and solving for the thawing index. During the winter of 1995-96, freeze/thaw data was not collected, so the maximum freeze depth had to be estimated from the maximum freezing index; otherwise, it was determined based on the data obtained from the three environmental probes. The fourth column in Table 2.5 shows the ratio of the required thawing index to the maximum freezing index. In all cases, the ratio is substantially less than the 30% value determined by Rutherford, et. al. (1985).

The last two columns in Table 2.5 show estimated thawing durations. One is calculated as the difference between the first thaw date and the date on which the required thawing index was first reached (which was called the “Estimated Date of Full Thaw” in Table 2.4). The other duration is based on the formula presented earlier from Rutherford, et. al. (1985) and significantly overestimates the thaw duration. Similar tables are presented in Appendix G for the other ten sites studied.

Table 2.5 Thaw Duration Estimates for Site 23-1026

Winter	Maximum Freezing Index (^{o}C-days)	Maximum Freeze Depth (m)	Required Thawing Index* (^{o}C-days)	TI:FI Ratio	Estimated Thaw Duration† (days)	Calculated Thaw Duration‡ (days)
1993-94	1030	1.765	271	0.26	38	44
1994-95	711	1.155	130	0.18	23	38
1995-96	1046	1.658	243	0.23	33	44
1996-97	805	1.175	134	0.17	19	39

* Calculated by setting the thaw depth model equal to the maximum freeze depth

† Calculated from the estimated date of full thaw and the data of first thaw

‡ Calculated from the formula $d = 0.018\ FI + 25$

CHAPTER 3
PATTERNS OF CHANGE IN *IN SITU* PAVEMENT MATERIAL PROPERTIES

In the context of structural capacity, the pavement material properties of greatest interest are the pavement layer moduli. During each monthly site visit, a suite of FWD tests was conducted to assess the structural response of the pavement to vehicle loading. The same tests were conducted several times throughout the day to provide some measure of the changes that occur due to daytime heating.

At the flexible pavement sites, FWD tests were performed in the middle of the traffic lane at regular intervals. Pavement layer moduli were backcalculated from the test results using a layered elastic analysis program. Due to software constraints, the pavement analysis was limited to four finite pavement layers overlying an elastic halfspace. As a result, all of the asphalt-bound layers were analyzed as a single surface layer and all of the unbound base and subbase layers were analyzed as a single base layer. Depending on the site, the third layer in the model was typically either the upper 3 ft (0.9 m) of the subgrade or a lime- or cement-treated soil layer. For sites with deep bedrock, the fourth layer represented the rest of the subgrade to a depth of 25 ft (0.75 m) and the underlying halfspace was assumed to be an infinite extension of the subgrade. At sites with shallow bedrock, the fourth layer represented the rest of the subgrade above the bedrock and the underlying halfspace was given elastic properties typical of bedrock.

At the rigid pavement sites, FWD tests were performed at the center of selected slabs to assess the properties of the pavement layers and at selected joints to assess load transfer efficiency from one slab to the next. The pavement layer moduli were backcalculated from the slab-centered test results using two different analytical models. The first, called the elastic solid (ES) model, is similar to that used for the flexible pavement sites. Elastic layers are used to

model the concrete slab, base (if present) and subgrade. In the other model, called the dense liquid (DL) model, the elastic solid subgrade model was replaced by a Winkler spring model. The spring model is characterized by a modulus of subgrade reaction *k* rather than an elastic modulus. It has units of pressure per unit deflection.

3.1 SELECTION OF REPRESENTATIVE PAVEMENT PROPERTIES

The layered elastic pavement models described above contain an implicit assumption that the material properties and layer thicknesses do not vary within the site boundaries. This is never the case. First, the materials themselves change from one location to the next due to differences in composition or even compaction. On top of that, the moisture and temperature change from one location to the next, causing even greater variability in the material properties. Finally, any deviations from the assumed pavement layer thicknesses can cause the backcalculation program to either overestimate or underestimate the layer moduli, causing still more variability in the test results from one test location to the next. The first task is therefore to select a set of layer moduli that best represents the pavement site at a given point in time. The next two sections detail the procedure used for the flexible and rigid pavements, respectively.

3.1.1 Flexible Pavement Moduli

The FWD deflection test results for flexible pavements are found in table MON_DEFL_DROP_DATA of the LTPP Information Management System (IMS). Each FWD test actually consists of four replicate tests at each of three different drop heights. The data from the replicate tests is averaged together to reduce the amount of experimental noise. The averaged load and deflection data for each drop height is found in table MON_DEFL_FLX_BAKCAL_BASIN.

Ideally, each record in MON_DEFL_FLX_BAKCAL_BASIN has a corresponding entry in table MON_DEFL_FLX_BAKCAL_POINT that provides the pavement layer moduli backcalculated from that averaged basin. The backcalculation program, MODCOMP 4.2, iteratively adjusts a set of trial layer moduli until an analytical deflection basin calculated using the trial moduli matches the measured basin. If the root mean squared relative error between the analytical deflections and the measured deflections exceeds 2 percent, the backcalculated moduli are flagged. The moduli are also flagged if they fall outside a 95-percent confidence interval on the mean modulus for the entire site. Only unflagged layer moduli were extracted for this study.

At most flexible pavement sites, the same ten or twelve test locations are used during almost every site visit. Occasionally, FWD tests are performed at other locations and those extraneous tests had to be removed from the data set. For each pavement site, the various test locations were analyzed to determine those most frequently used. For example, Figure 3.1 shows that the vast majority of the FWD testing at site 23-1026 was performed at just nine test locations, so the data from all the other site locations was removed from the extracted data set.

Next, a set of daily average moduli was calculated for each test location to determine which were most in agreement. For example, Figures 3.2 through 3.5 show the average daily asphalt, base, upper subgrade, and lower subgrade moduli, respectively, for site 23-1026. Months with frozen ground are not shown because the high frozen moduli obscure the differences from one test location to another during the rest of the year. Table 3.1 shows the results of a correlation analysis on the moduli. All of the correlation coefficients in roughly the upper quartile are highlighted. From this analysis, four test locations stand out as having the best correlation: 30.5, 38.1, 53.3, and 61. Those locations were chosen to represent this site. Figures 3.6 through 3.9 show how well correlated are the daily moduli for these four locations.

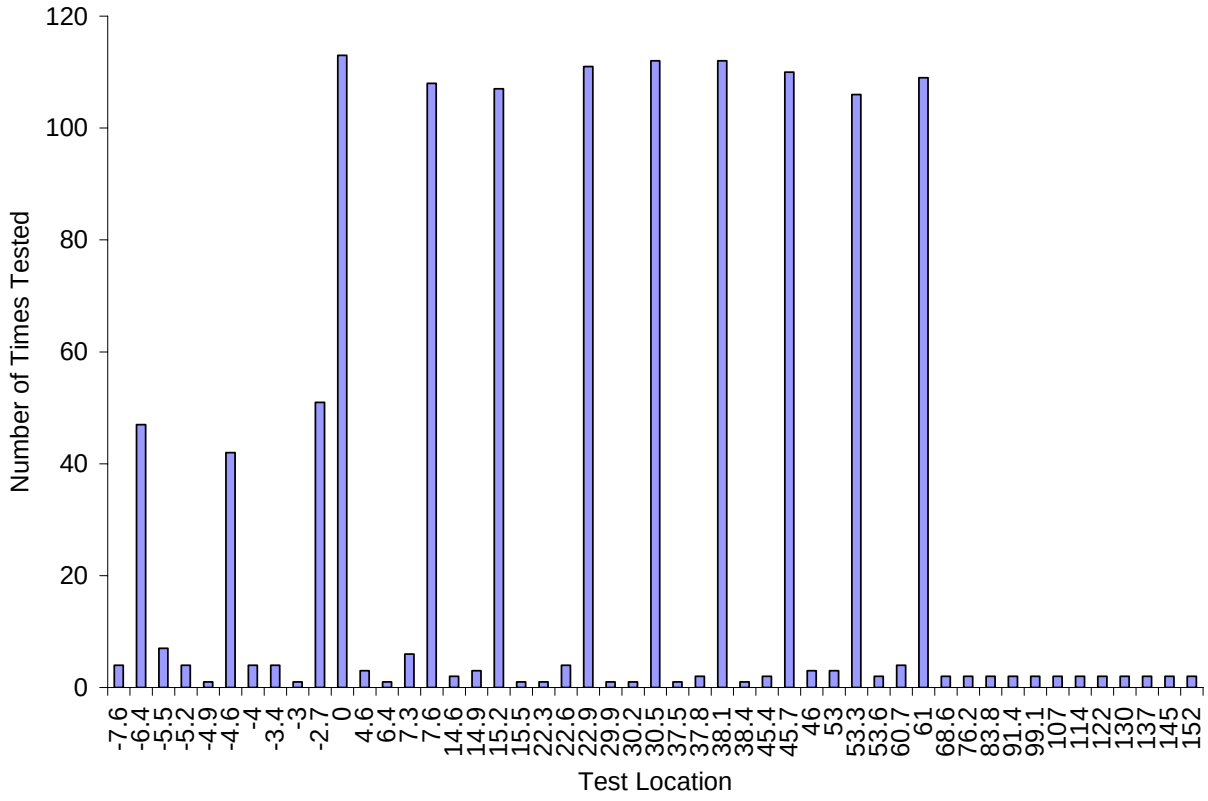

Figure 3.1 Testing frequency at site 23-1025

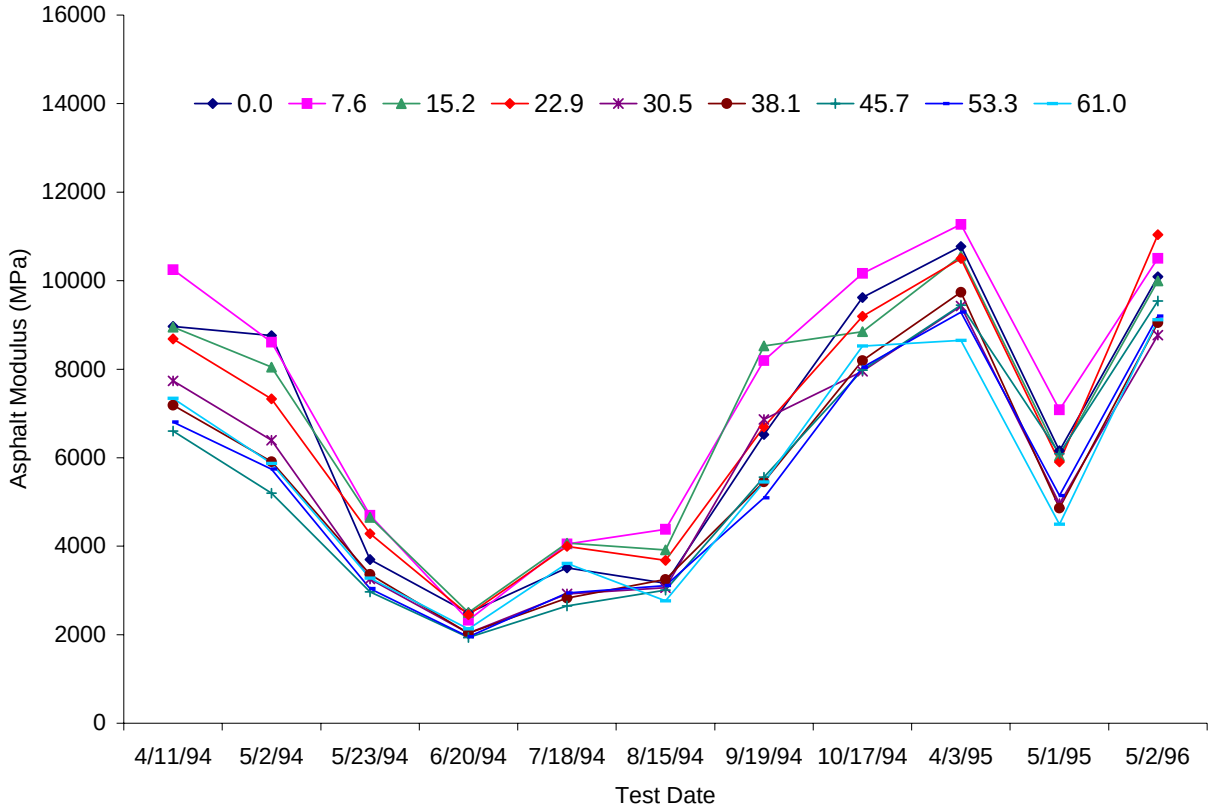

Figure 3.2 Backcalculated asphalt moduli at site 23-1026

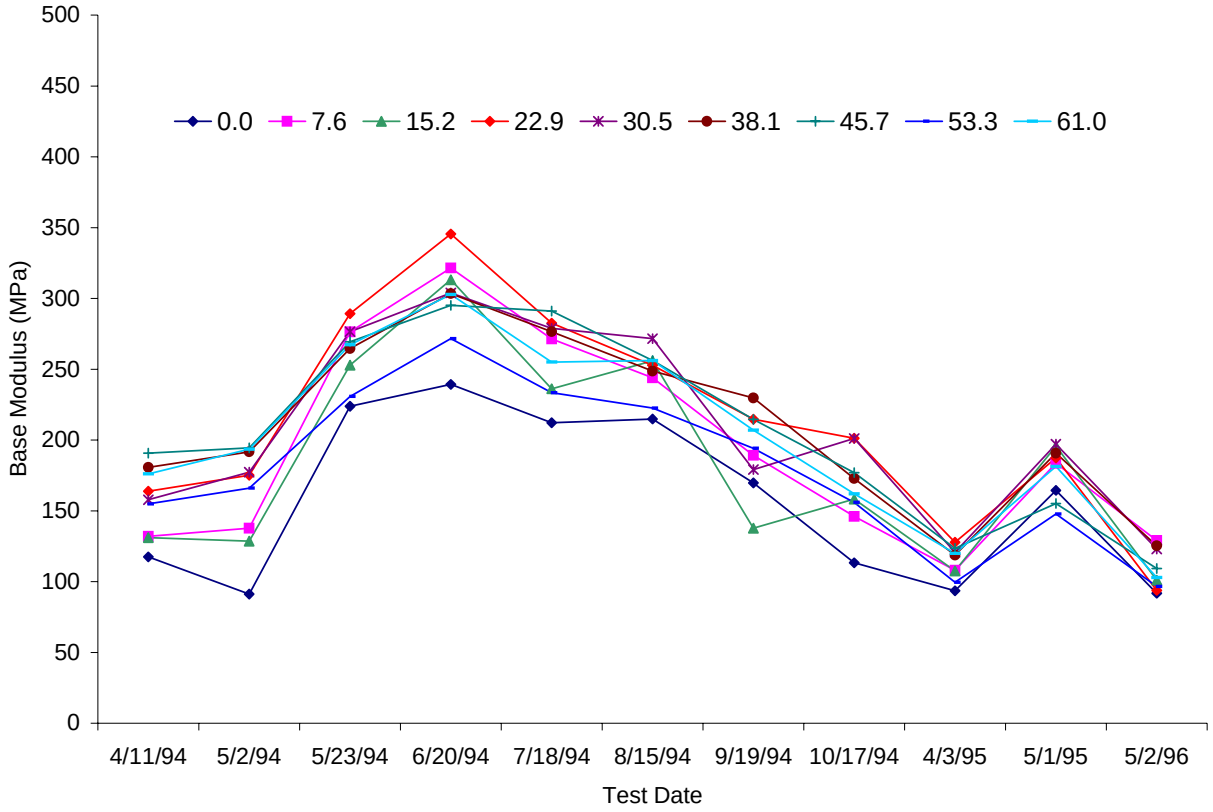

Figure 3.3 Backcalculated base moduli at site 23-1026

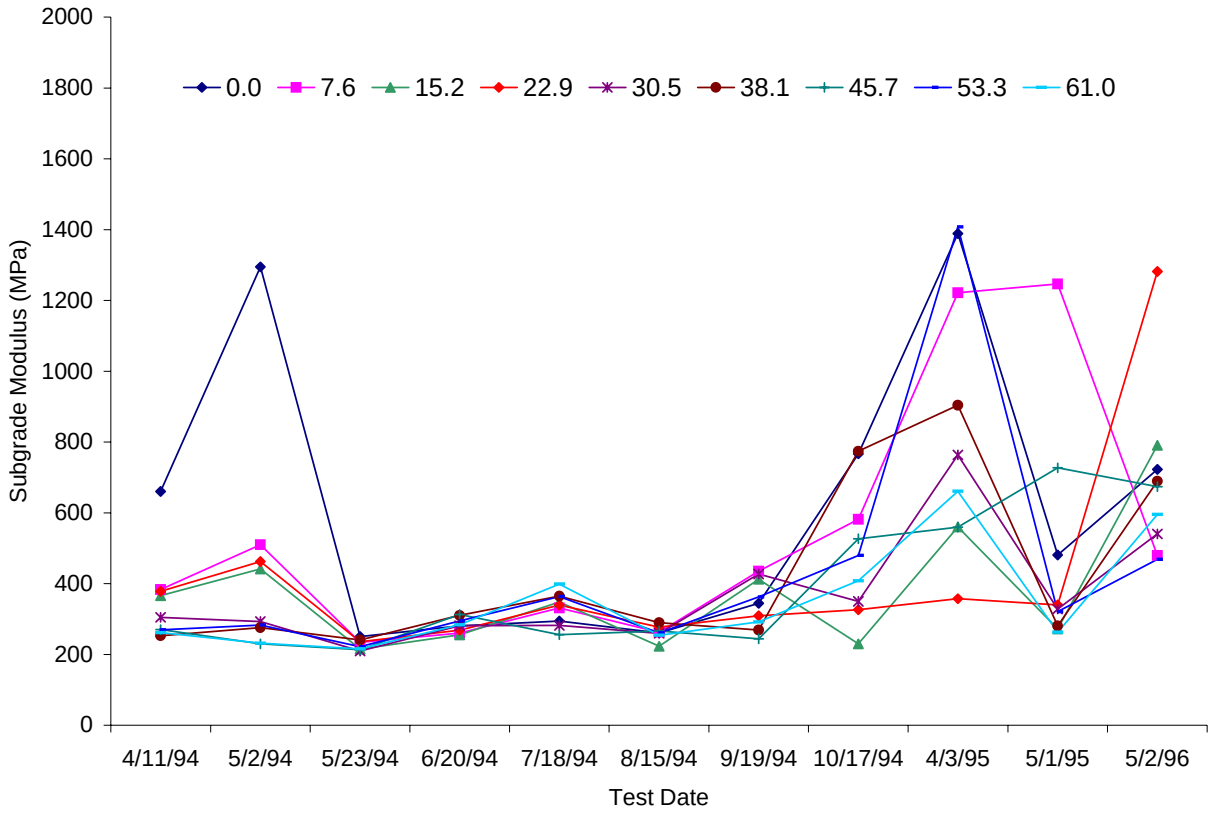

Figure 3.4 Backcalculated upper subgrade moduli at site 23-1026

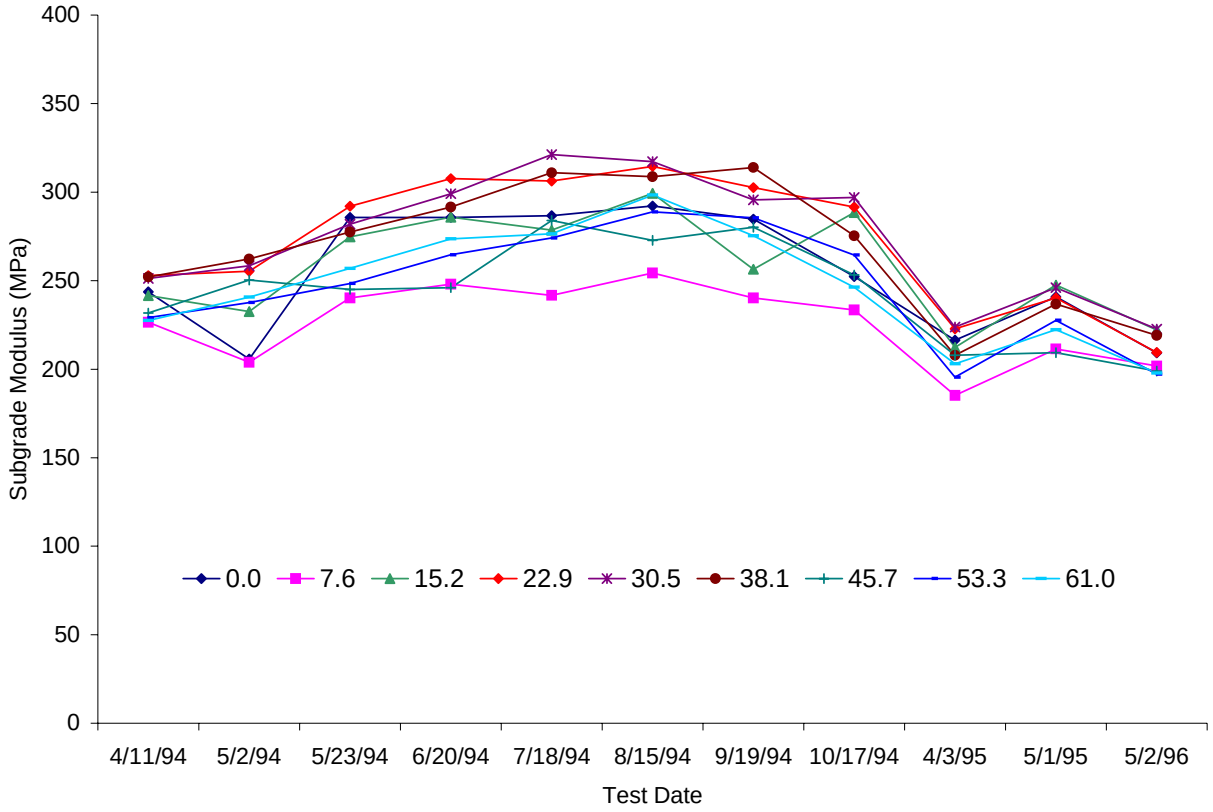

Figure 3.5 Backcalculated lower subgrade moduli at site 23-1026

Table 3.1 Correlation analysis of moduli at site 23-1026

Lower Subgrade Moduli									
	0	*7.6*	*15.2*	*22.9*	*30.5*	*38.1*	*45.7*	*53.3*	*61*
0	1								
7.6	0.9334	1							
15.2	0.8510	0.9226	1						
22.9	0.9064	0.9312	0.9078	1					
30.5	0.8686	0.9087	0.9167	**0.9759**	1				
38.1	0.8561	0.9031	0.8156	**0.9581**	**0.9580**	1			
45.7	0.7310	0.7702	0.7005	0.8969	0.9156	**0.9557**	1		
53.3	0.8463	0.8997	0.8615	**0.9621**	**0.9619**	**0.9777**	0.9299	1	
61	0.8770	0.9044	0.8547	**0.9662**	**0.9536**	**0.9667**	0.9073	**0.9629**	1
Upper Subgrade Moduli									
	0	*7.6*	*15.2*	*22.9*	*30.5*	*38.1*	*45.7*	*53.3*	*61*
0	1								
7.6	0.5473	1							
15.2	0.5240	0.2339	1						
22.9	0.2442	0.0162	**0.8523**	1					
30.5	0.6326	0.6228	**0.7300**	0.3989	1				
38.1	0.5838	0.4689	0.5027	0.3799	**0.7938**	1			
45.7	0.3039	**0.7456**	0.4121	0.4962	0.5542	0.6162	1		
53.3	0.6571	0.6541	0.4545	0.0736	**0.9075**	**0.8051**	0.4273	1	
61	0.5022	0.4371	**0.7321**	0.5504	**0.8841**	**0.9064**	0.5936	**0.8162**	1
Base Moduli									
	0	*7.6*	*15.2*	*22.9*	*30.5*	*38.1*	*45.7*	*53.3*	*61*
0	1								
7.6	**0.9698**	1							
15.2	0.9364	0.9567	1						
22.9	0.9210	0.9523	0.9354	1					
30.5	0.9243	0.9542	**0.9671**	0.9648	1				
38.1	0.9287	0.9497	0.8932	**0.9673**	0.9418	1			
45.7	0.8790	0.9077	0.8566	0.9517	0.9324	**0.9741**	1		
53.3	0.9086	0.9364	0.8950	**0.9764**	0.9471	**0.9917**	**0.9833**	1	
61	0.9184	0.9374	0.9162	**0.9699**	0.9506	**0.9849**	**0.9715**	**0.9896**	1
Asphalt Moduli									
	0	*7.6*	*15.2*	*22.9*	*30.5*	*38.1*	*45.7*	*53.3*	*61*
0	1								
7.6	**0.9827**	1							
15.2	0.9682	**0.9871**	1						
22.9	0.9784	0.9757	0.9711	1					
30.5	0.9768	**0.9890**	**0.9932**	**0.9825**	1				
38.1	0.9742	0.9701	0.9606	**0.9907**	**0.9812**	1			
45.7	0.9450	0.9466	0.9348	0.9746	0.9587	0.9799	1		
53.3	0.9713	0.9623	0.9489	**0.9914**	0.9715	**0.9960**	**0.9891**	1	
61	0.9706	0.9628	0.9535	**0.9904**	0.9718	**0.9839**	0.9601	**0.9845**	1

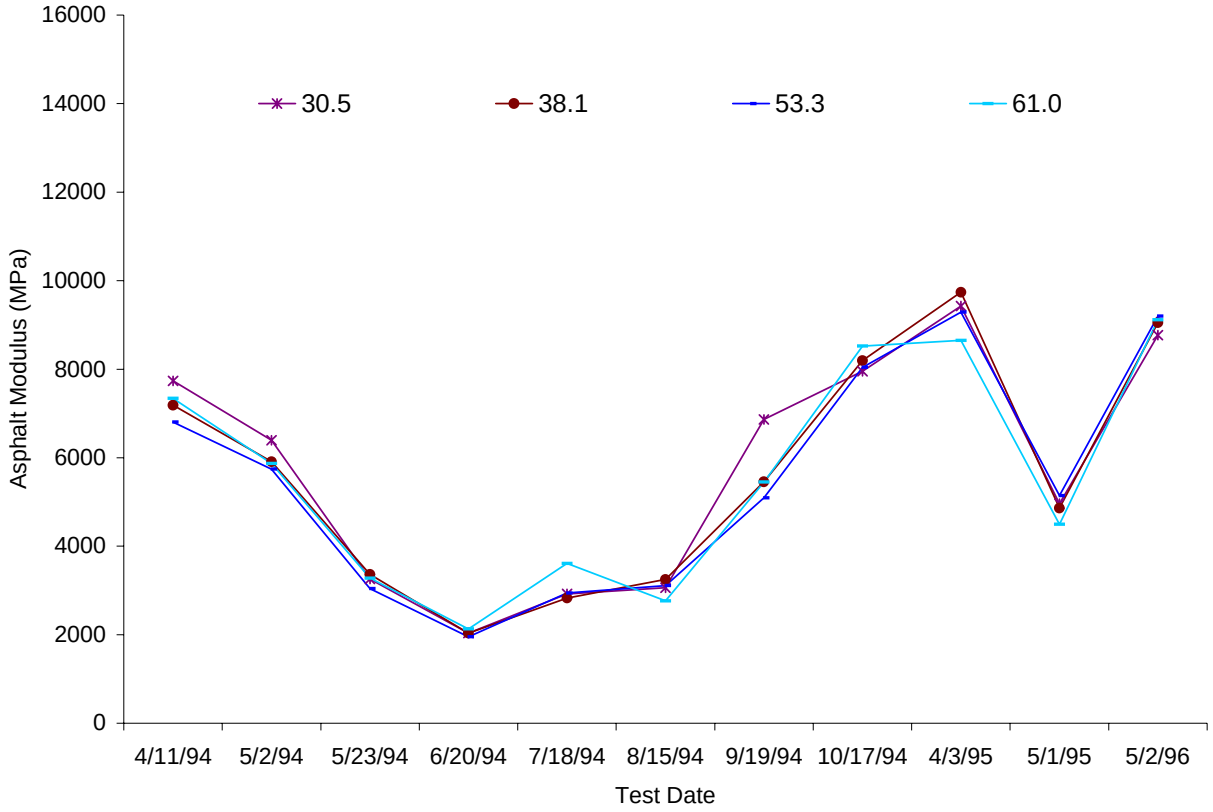

Figure 3.6 Representative asphalt moduli for site 23-1026

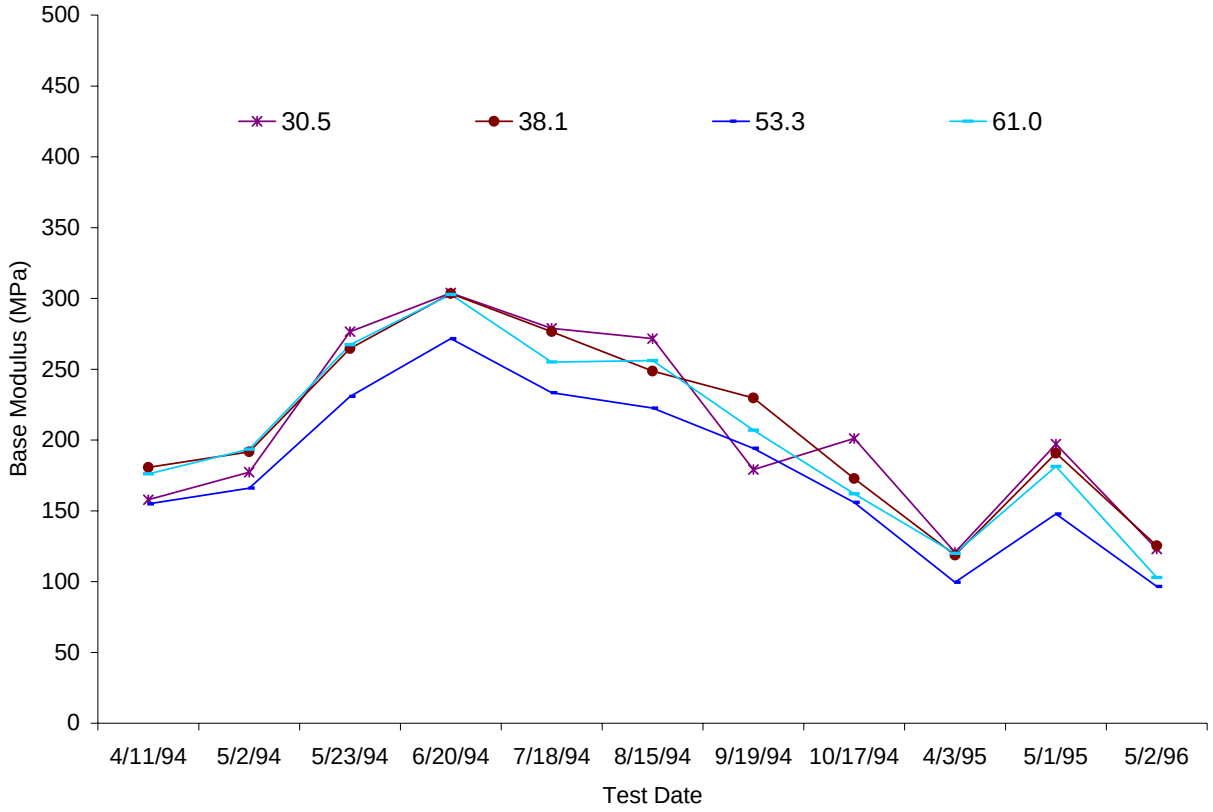

Figure 3.7 Representative base moduli at site 23-1026

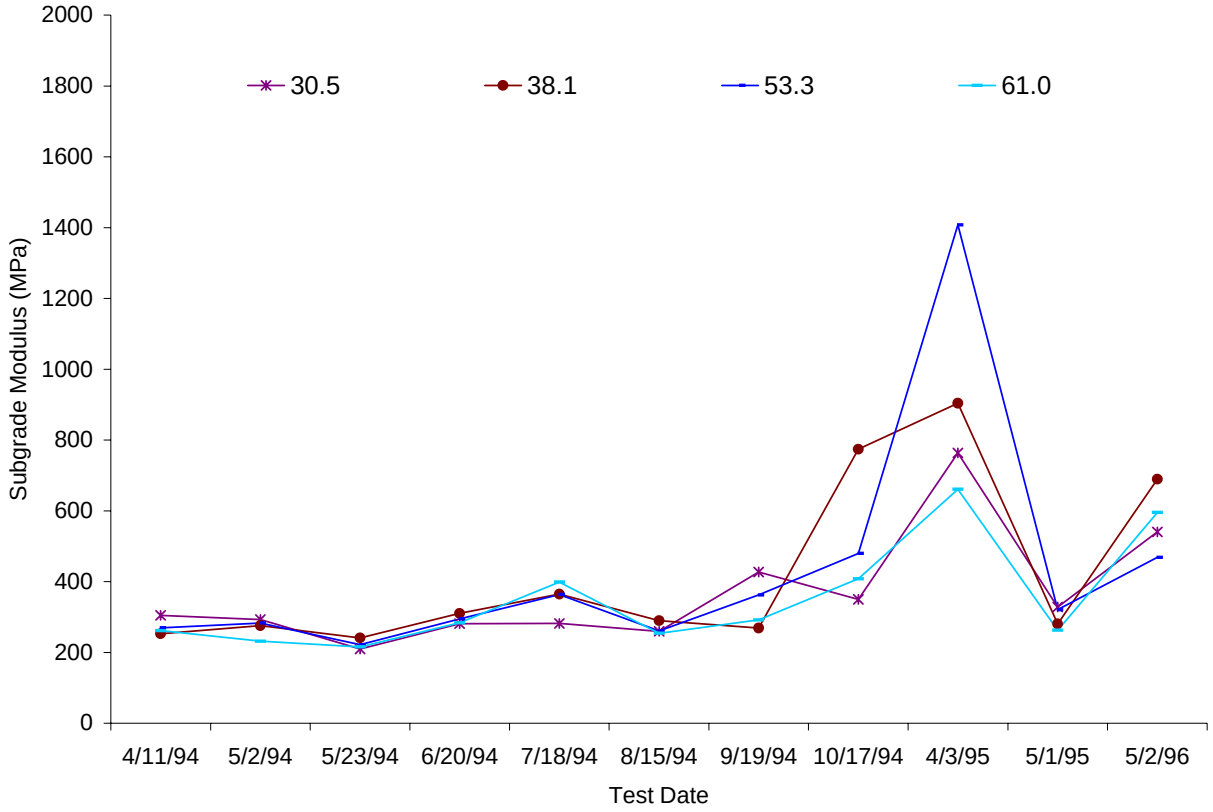

Figure 3.8 Representative upper subgrade moduli at site 23-1026

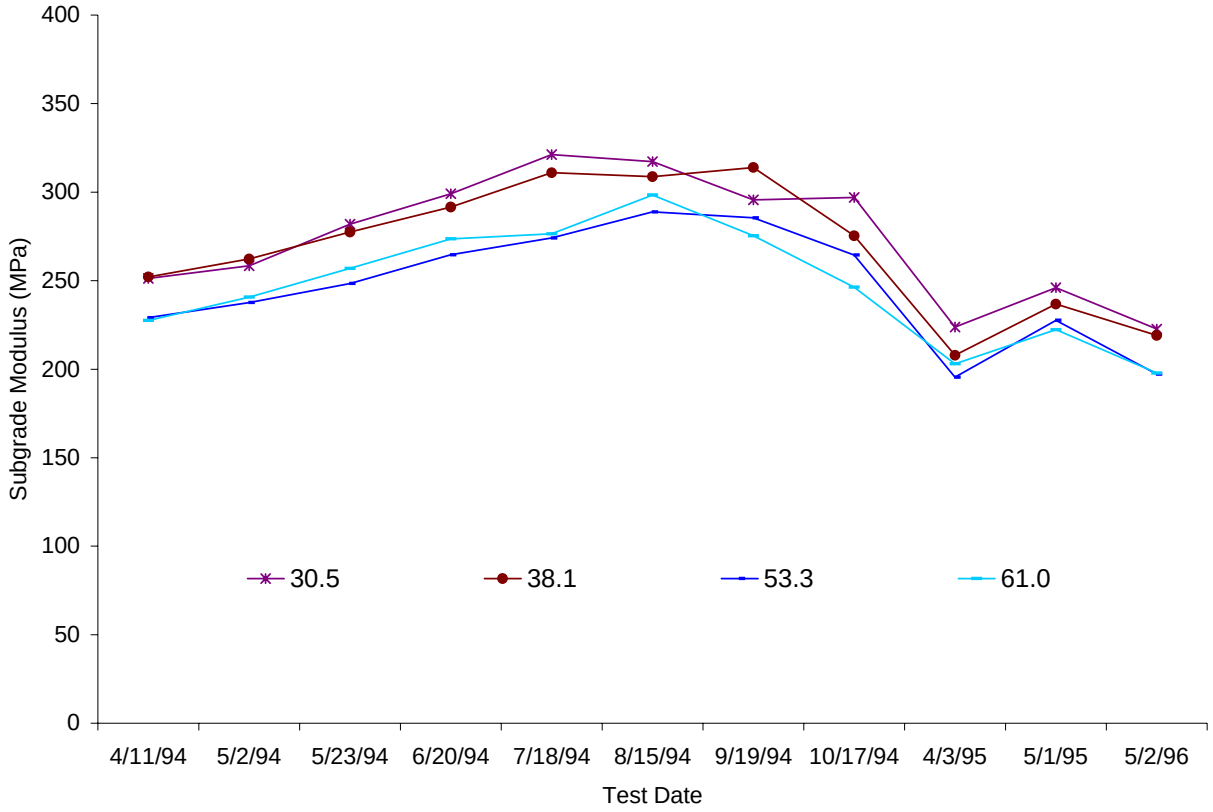

Figure 3.9 Representative lower subgrade moduli at site 23-1026

Looking more closely at Figures 3.6 through 3.9, one observes some interesting parallels between the various layer moduli. For example, the daily average asphalt and base moduli seem to be inversely correlated. This is more clearly shown in Figure 3.10, which compares the average of the daily average asphalt and base moduli from the four selected test locations. A correlation analysis of the two curves shown produces a correlation coefficient of −0.959, which is remarkably high. Similarly, the upper and lower subgrade moduli are inversely correlated with a correlation coefficient of −0.598. Figure 3.11 shows that the subgrade modulus correlation is just as compelling, even though the relationship between the two sets of moduli is not quite as linear as for the asphalt and base moduli.

Correlations between backcalculated layer moduli usually result when the pavement system deviates from the linear elastic assumptions inherent in the backcalculation program. In such cases, the shape of the measured basin is incompatible with the shape of the idealized analytical basin. Say, for example, that the measured basin doesn't exhibit as much curvature as the analytical basin at the end farthest from the point of impact. One way to flatten the curve is to simultaneously underestimate the lower subgrade modulus and overestimate the upper subgrade modulus. Likewise, if the measured basin exhibits more curvature near the point of impact, the curvature of the analytical basin can be increased by simultaneously overestimating the asphalt modulus and underestimating the base modulus. These offsetting errors alter the curvature of the analytical basin without appreciably changing the overall magnitude of the calculated deflections.

In anticipation of just such a problem, the SMP data analysis protocol provided for a nonlinear elastic analysis of the deflection data where needed. The backcalculated pavement layer moduli are found in the table MON_DEFL_FLX_NMODEL_POINT. For the nonlinear

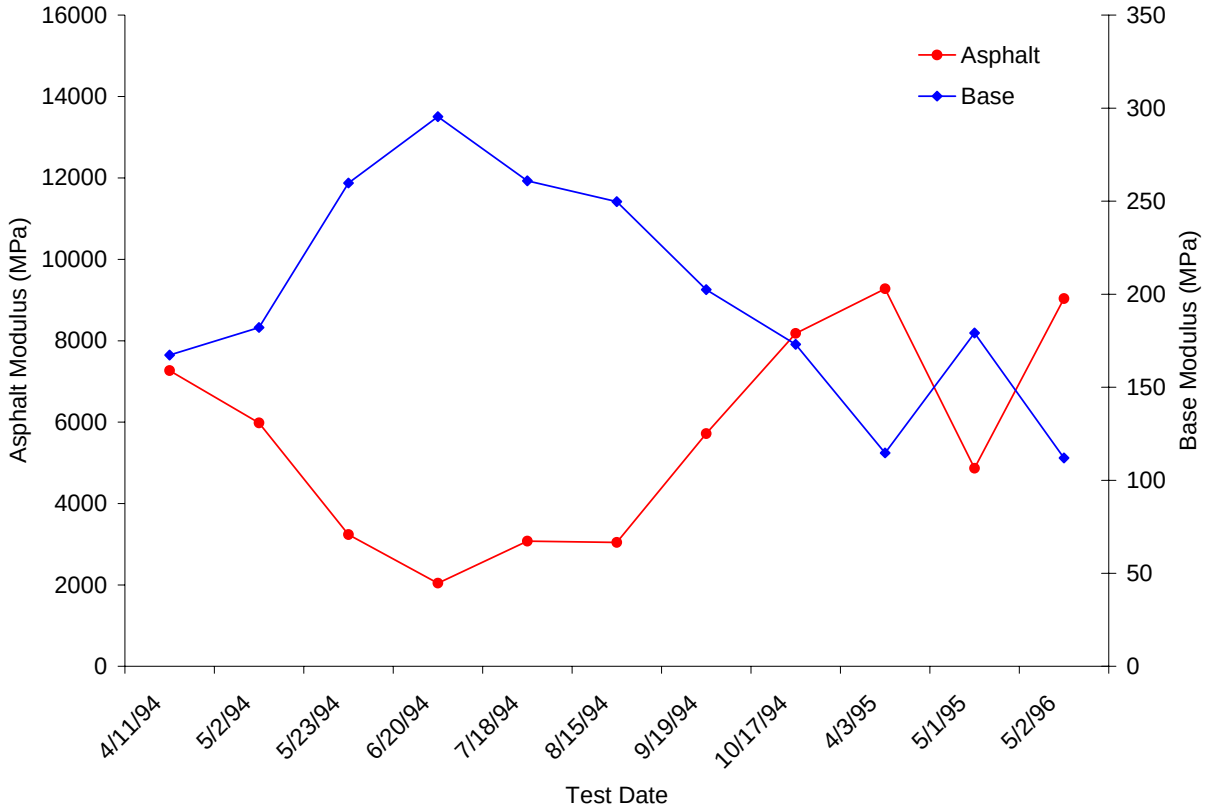

Figure 3.10 Correlation between asphalt and base moduli at site 23-1026

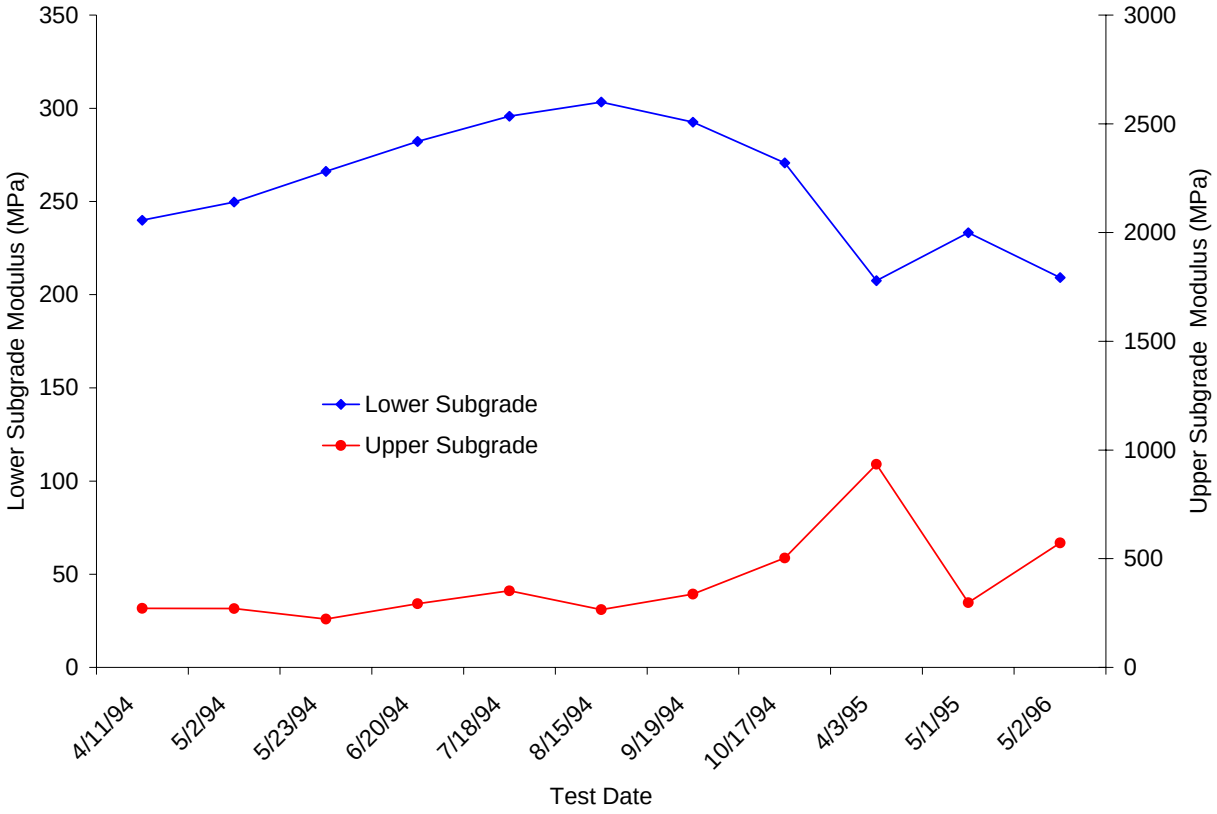

Figure 3.11 Correlation between upper and lower subgrade moduli at site 23-1026

analysis of site 23-1026, the moduli of the base and subgrade layers were assumed to increase as a function of the bulk stress. This is known as the “k-theta” model:

$$M = k_1\theta^{k_2}$$

where M is the elastic (resilient) modulus, θ is the bulk stress and k_1 and k_2 are model fitting constants. This is a common model for granular materials.

Because the nonlinear elastic moduli are stress-dependent, there is no single modulus for each layer. The modulus of each layer varies with depth, due to increasing overburden stress, and with distance from the applied load. Table MON_DEFL_FLX_NMODEL_POINT includes estimated moduli in the middle of each layer for an assumed wheel load equal to the maximum FWD drop load. Figures 3.12 through 3.15 show those moduli for the asphalt, base, upper subgrade, and lower subgrade, respectively. Comparing these figures to the equivalent figures from the linear elastic analysis, one can see that the data scatter is much higher. Table 3.2 shows the results of a correlation analysis on the nonlinear moduli. Clearly, there is far less consistency among the test locations, but a reasonable correlation exists between test locations 22.9, 30.5, and 61.0, as shown in Figures 3.16 through 3.19.

Figure 3.20 shows that even the nonlinear backcalculation produces a correlation between the asphalt and base moduli. The correlation coefficient for the two curves shown is −0.824. This correlation, which is an artifice of the backcalculation process, makes it nearly impossible to study environmental effects on the base modulus. Likewise, there still seems to be a negative correlation between the upper and lower subgrade moduli during certain parts of the year, as shown in Figure 3.21. This also makes it difficult to study changes in the subgrade moduli.

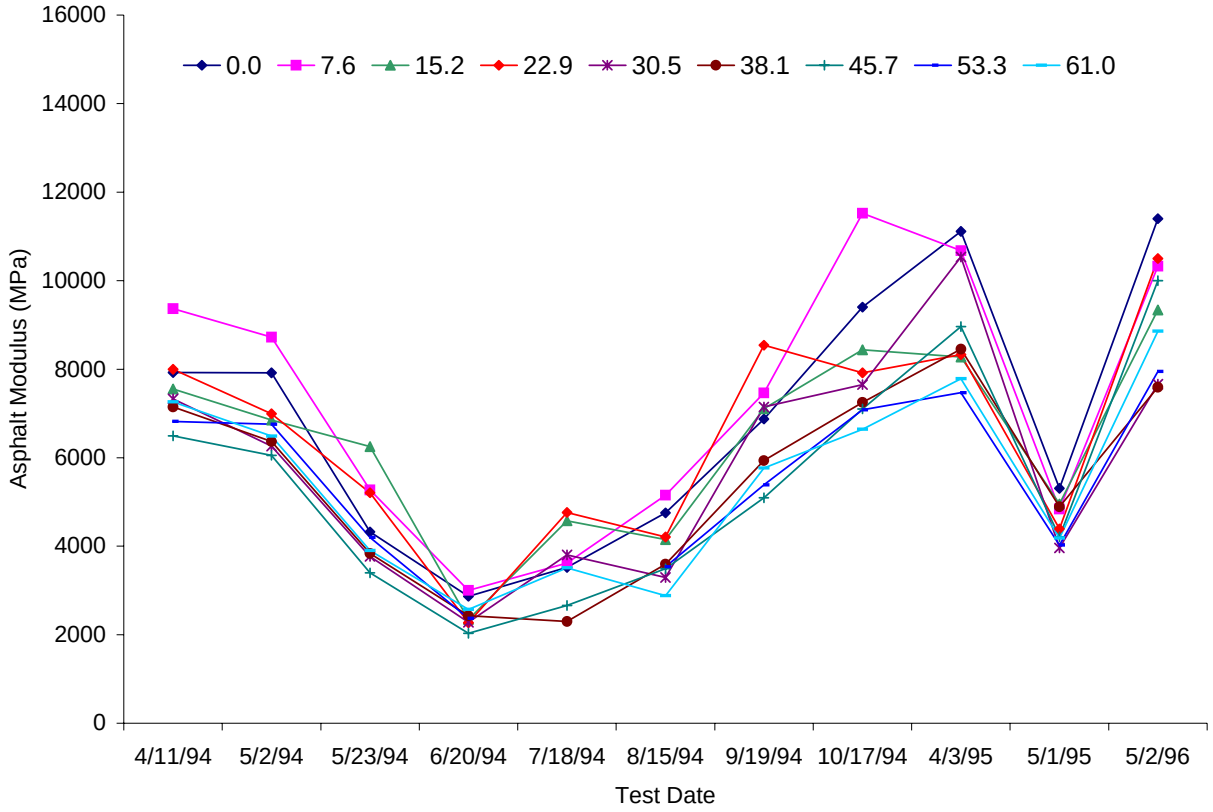

Figure 3.12 Backcalculated nonlinear asphalt moduli at site 23-1026

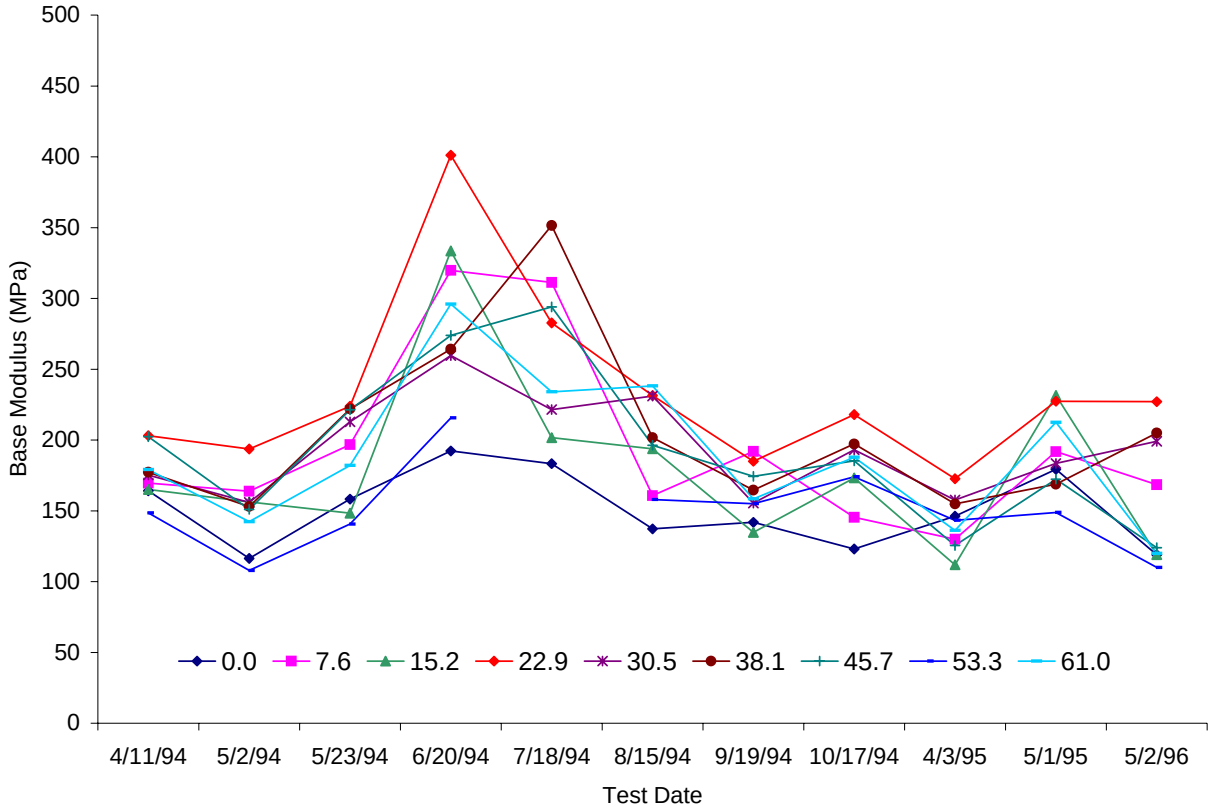

Figure 3.13 Backcalculated nonlinear base moduli at site 23-1026

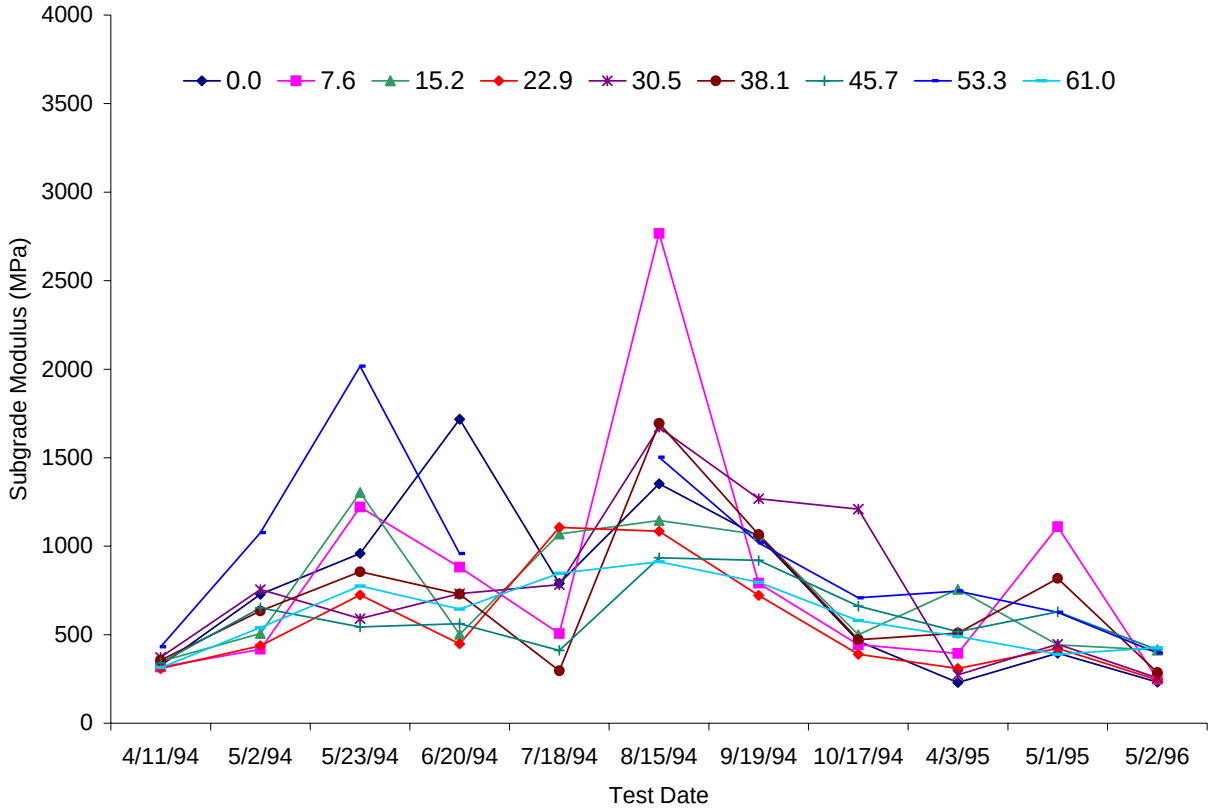

Figure 3.14 Backcalculated nonlinear upper subgrade moduli for site 23-1026

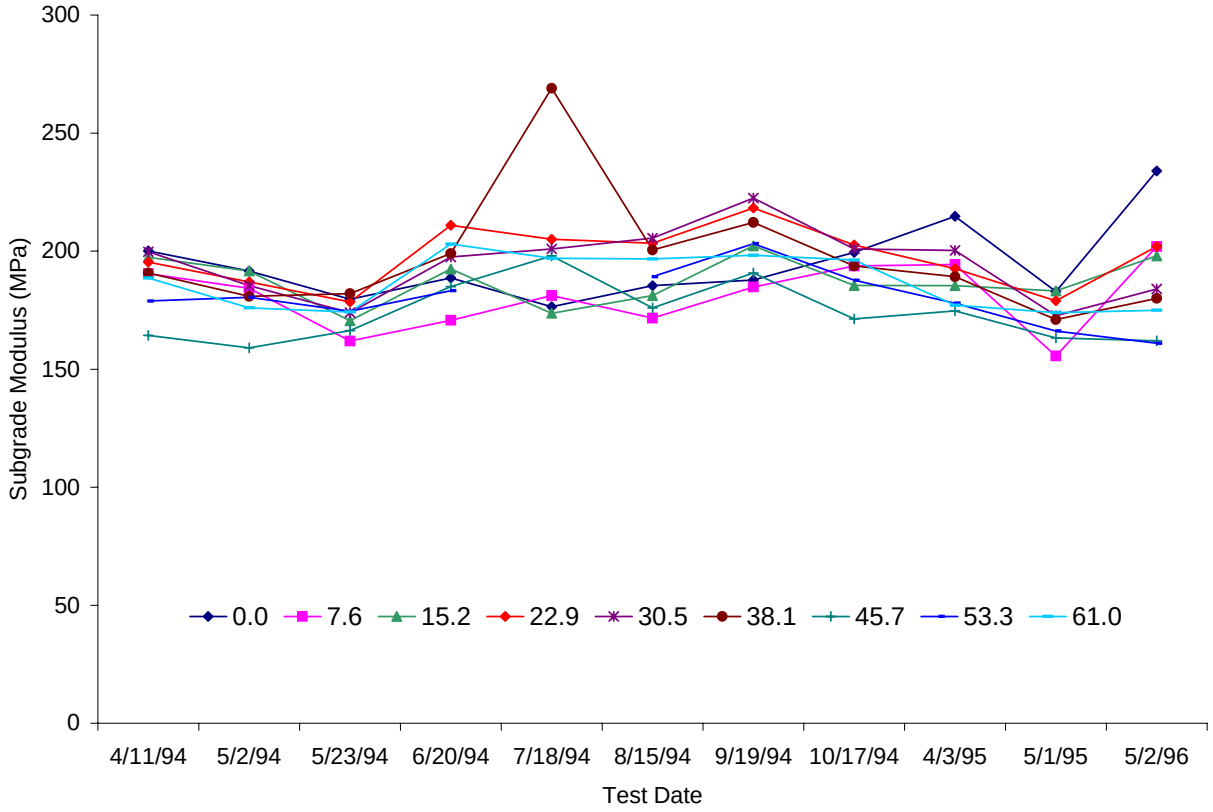

Figure 3.15 Backcalculated nonlinear lower subgrade moduli at site 23-1026

Table 3.2 Correlation analysis of nonlinear moduli at site 23-1026

Lower Subgrade Moduli									
	0	*7.6*	*15.2*	*22.9*	*30.5*	*38.1*	*45.7*	*53.3*	*61*
0	1.0000								
7.6	**0.7743**	1.0000							
15.2	0.5190	0.5268	1.0000						
22.9	0.1000	0.4159	0.4882	1.0000					
30.5	-0.0288	0.4141	0.4009	**0.8494**	1.0000				
38.1	-0.3902	0.0923	-0.2628	0.5381	0.5257	1.0000			
45.7	-0.4026	-0.0325	-0.1132	**0.7086**	0.6812	**0.8646**	1.0000		
53.3	-0.4354	0.0525	0.2267	0.6435	**0.8536**	**0.8989**	**0.7606**	1.0000	
61	-0.3459	0.0451	0.1419	**0.8284**	**0.7720**	0.6179	**0.7551**	**0.7651**	1.0000
Upper Subgrade Moduli									
	0	*7.6*	*15.2*	*22.9*	*30.5*	*38.1*	*45.7*	*53.3*	*61*
0	1.0000								
7.6	0.5815	1.0000							
15.2	0.4427	0.5422	1.0000						
22.9	0.5499	0.6329	**0.8219**	1.0000					
30.5	0.5905	0.6459	0.4738	0.6458	1.0000				
38.1	0.6173	**0.9237**	0.5362	0.5380	0.7206	1.0000			
45.7	0.4957	0.6588	0.4192	0.4148	**0.8323**	**0.8609**	1.0000		
53.3	0.5985	0.6248	**0.8641**	0.7737	0.4323	0.6465	0.4451	1.0000	
61	0.7059	0.5934	**0.8732**	**0.8984**	0.7358	0.5870	0.5571	**0.8079**	1.0000
Base Moduli									
	0	*7.6*	*15.2*	*22.9*	*30.5*	*38.1*	*45.7*	*53.3*	*61*
0	1.0000								
7.6	0.7559	1.0000							
15.2	0.6952	0.7305	1.0000						
22.9	0.6360	**0.8576**	**0.8906**	1.0000					
30.5	0.4856	0.6699	0.7148	**0.8587**	1.0000				
38.1	0.5504	**0.8387**	0.4580	0.6862	0.7233	1.0000			
45.7	0.7374	**0.8677**	0.6838	0.7417	0.7164	**0.8462**	1.0000		
53.3	0.6390	0.6630	0.7722	0.7280	0.6182	0.6213	0.7872	1.0000	
61	0.7243	0.7317	**0.9181**	**0.8320**	**0.8136**	0.6017	**0.8267**	**0.8481**	1.0000
Asphalt Moduli									
	0	*7.6*	*15.2*	*22.9*	*30.5*	*38.1*	*45.7*	*53.3*	*61*
0	1.0000								
7.6	**0.9536**	1.0000							
15.2	0.9178	0.9292	1.0000						
22.9	0.9041	0.8846	**0.9606**	1.0000					
30.5	0.9275	0.9155	0.8847	0.8802	1.0000				
38.1	**0.9624**	**0.9584**	0.9080	0.8785	0.9406	1.0000			
45.7	**0.9924**	0.9227	0.9118	0.9035	0.8988	0.9419	1.0000		
53.3	**0.9638**	**0.9696**	**0.9526**	0.9293	0.9098	**0.9682**	**0.9509**	1.0000	
61	**0.9600**	0.9254	0.9388	0.9455	0.9119	0.9457	**0.9653**	**0.9784**	1.0000

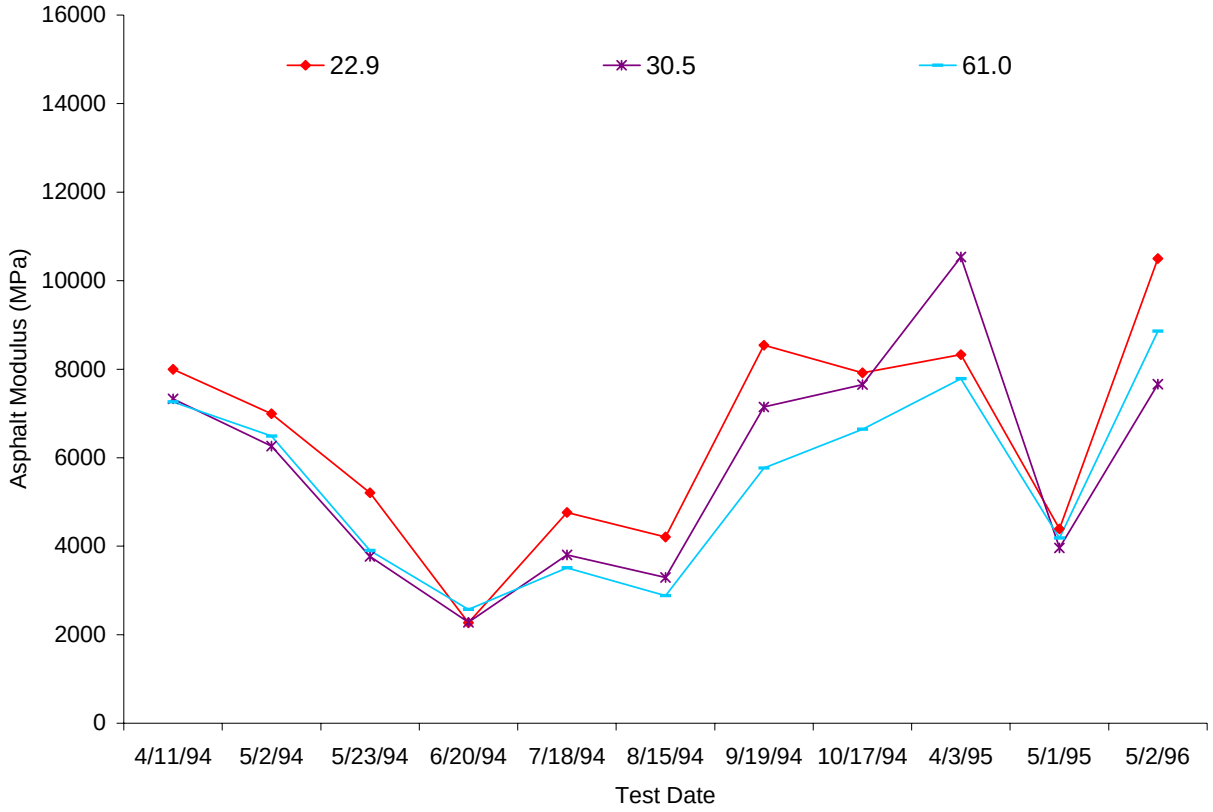

Figure 3.16 Representative asphalt moduli from nonlinear analysis of site 23-1026

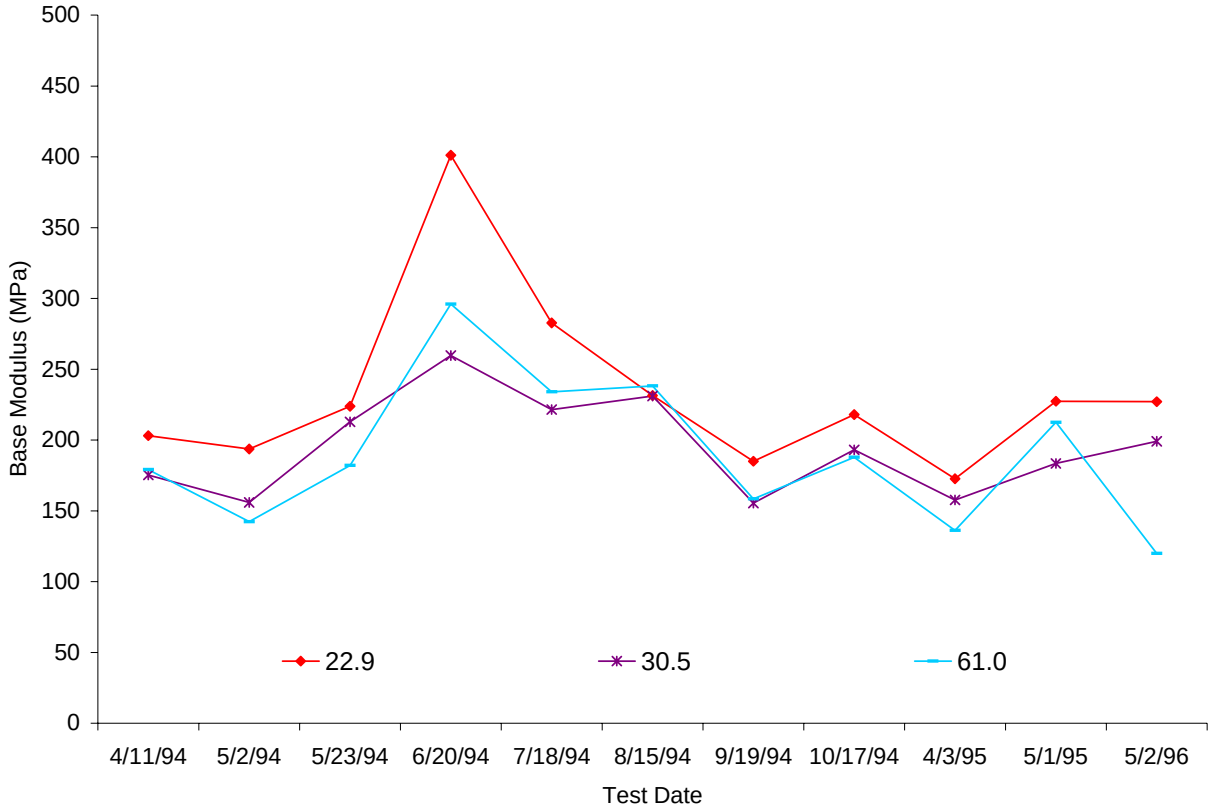

Figure 3.17 Representative base moduli from nonlinear analysis of site 23-1026

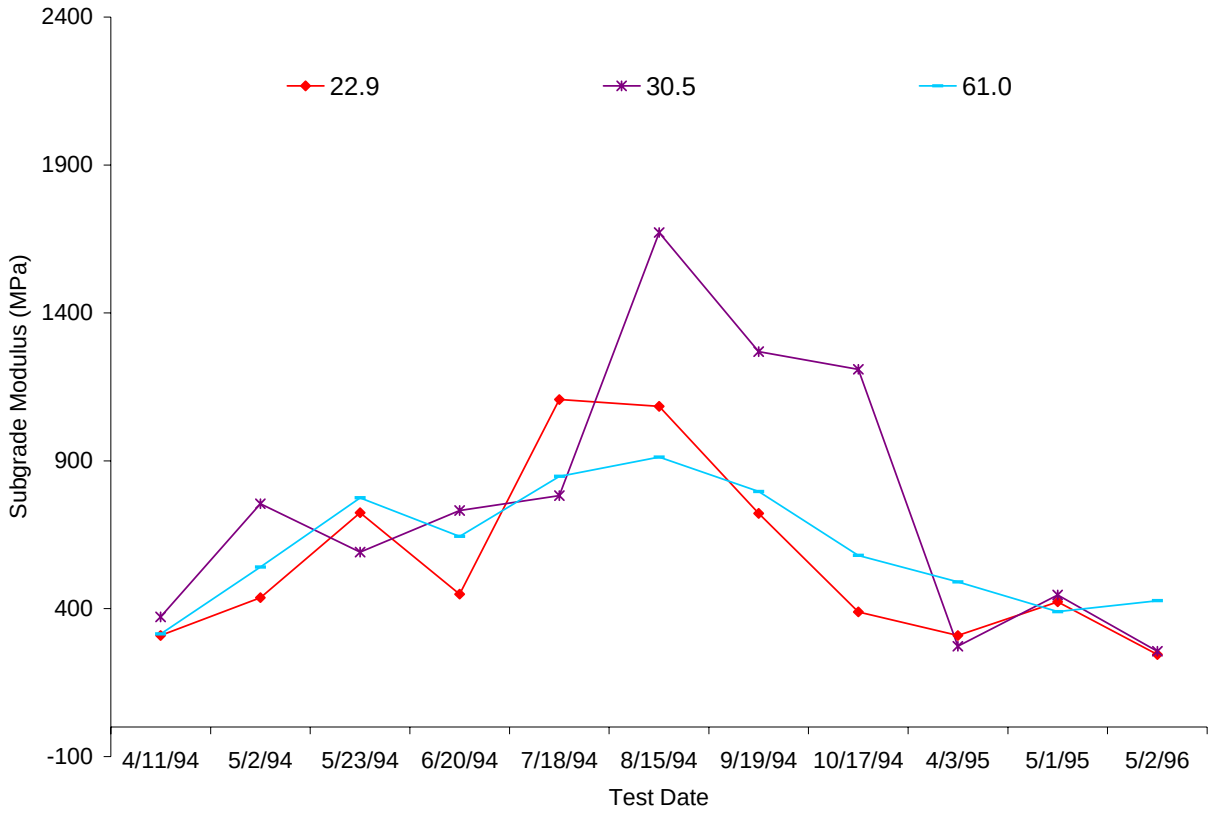

Figure 3.18 Representative upper subgrade moduli from nonlinear analysis of site 23-1026

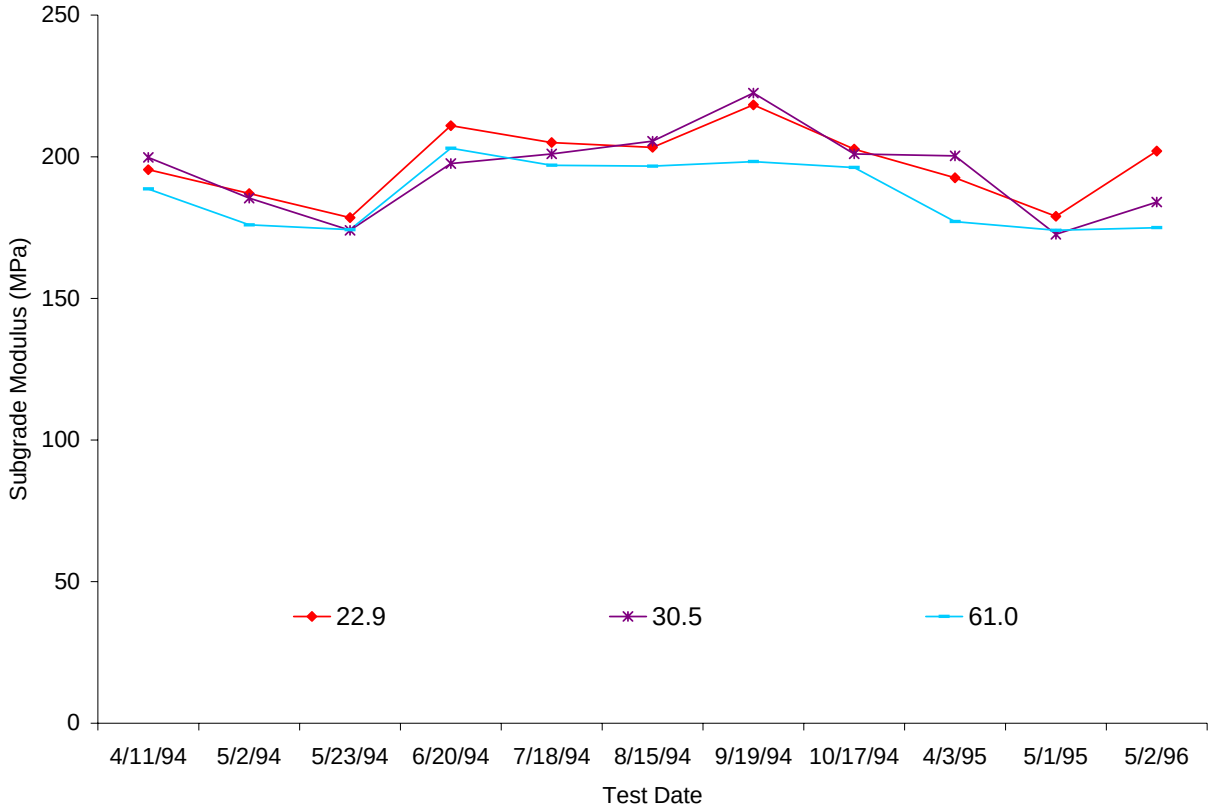

Figure 3.19 Representative lower subgrade moduli from nonlinear analysis of site 23-1026

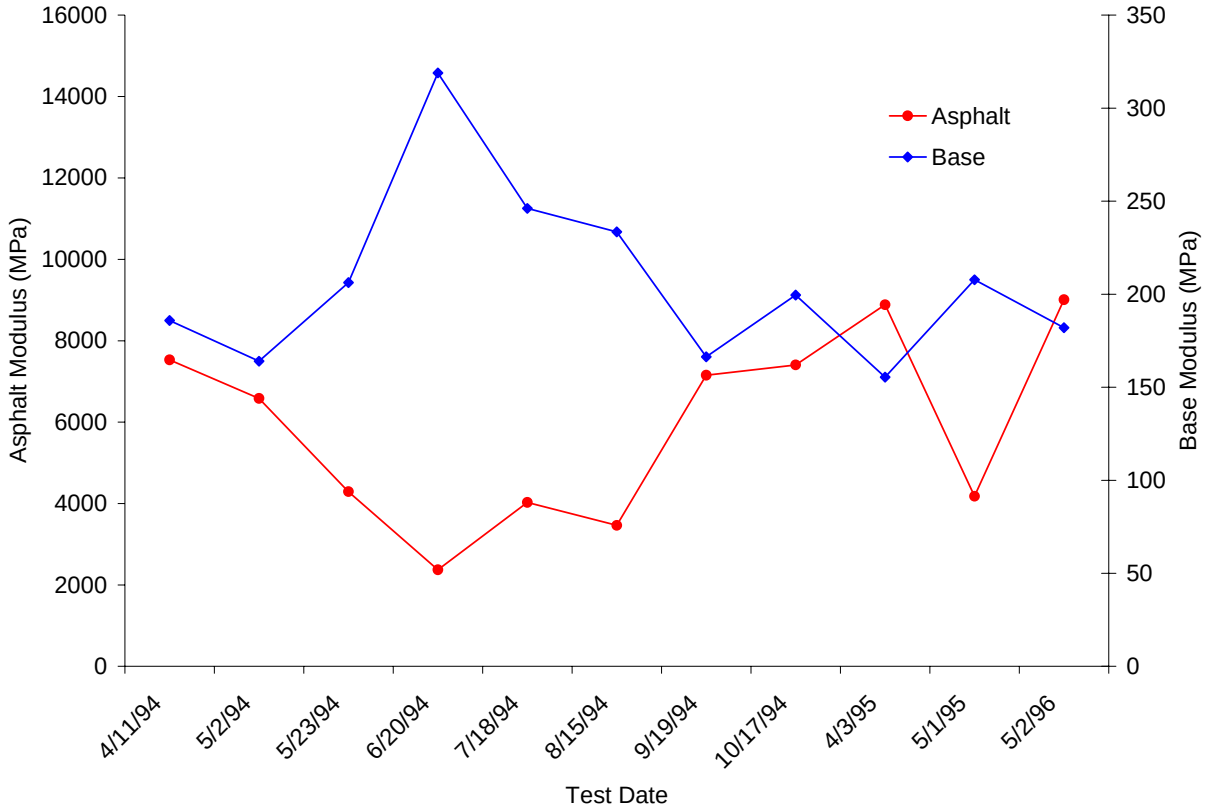

Figure 3.20 Correlation between asphalt and nonlinear base moduli at site 23-1026

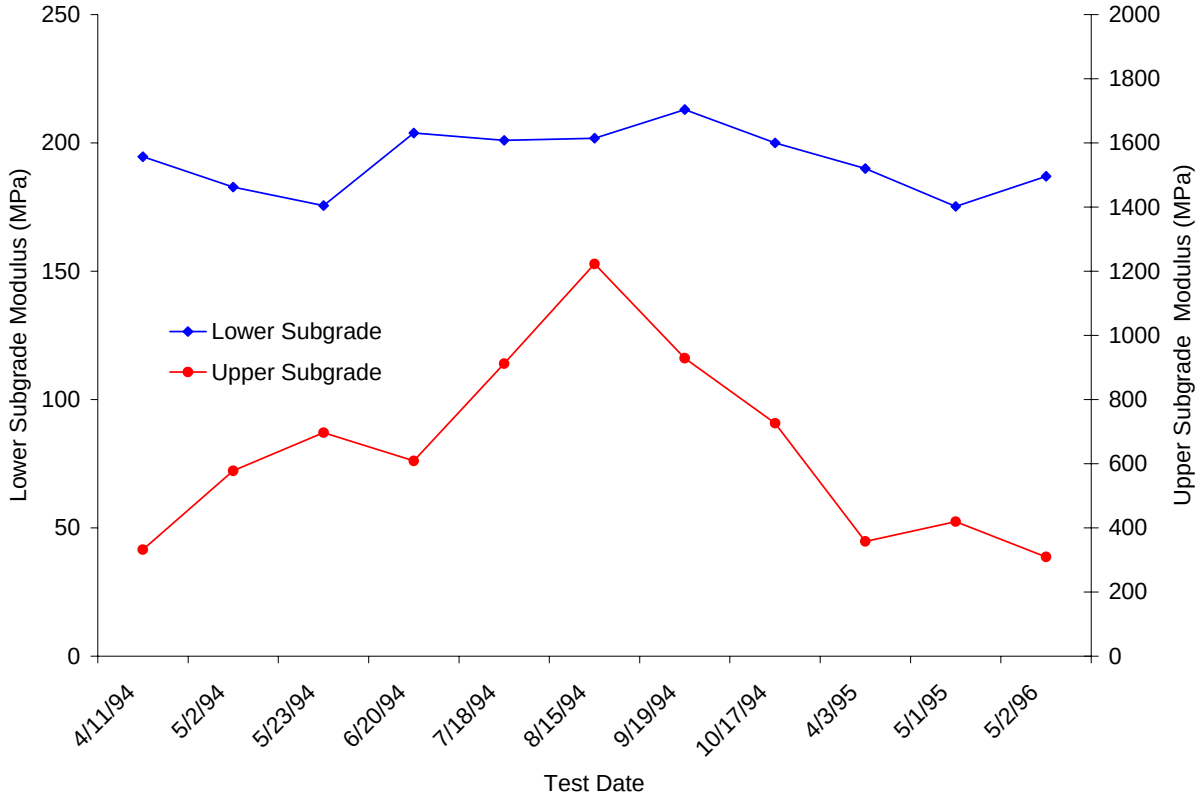

Figure 3.21 Correlation between nonlinear upper and lower subgrade moduli at site 23-1026

3.1.2 Rigid Pavement Moduli

The same procedure outlined above was used to get representative layer moduli for the rigid pavement sites. The averaged FWD load and deflection data for rigid pavements is found in the LTPP IMS table MON_DEFL_RGD_BAKCAL_BASIN and the backcalculated pavement layer moduli are found in the table MON_DEFL_RGD_BAKCAL_POINT.

Recall that two different types of analytical model were used to backcalculate moduli at the rigid pavement sites. One, called the Elastic Solid (ES) model, treats the subgrade as an elastic solid characterized by an elastic (resilient) modulus E_{subgr}. The other, called the Dense Liquid (DL) model, uses a Winkler spring foundation characterized by a modulus of subgrade reaction *k*. Figure 3.22 shows the daily representative k and E_{subgr} values for visits made to site 53-3813. The correlation coefficient between the two plots is 0.9914. This is typical of the results at all 19 rigid pavement sites and shows that, for the purpose of studying seasonal effects, it is not necessary to use both moduli. Only the moduli of subgrade reaction were used in this study.

It is nearly impossible to reliably backcalculate the modulus of a base course beneath a concrete slab, so the modulus of the concrete slab and the base course were coupled for backcalculation purposes. For example, in Figure 3.23, which shows the concrete and base course moduli extracted from the LTPP IMS for seven of the rigid pavement sites, the concrete modulus is either 150, 175, 200, or 250 times as large as the base modulus, depending on the site. This makes it impossible to quantify the environmental effects on the base course independent of the concrete slab. If the modulus of the base course changes due to changing moisture contents, the modulus of the concrete slab must change by a proportional amount. Because of this, only the subgrade properties of the rigid pavement systems were analyzed for environmental effects.

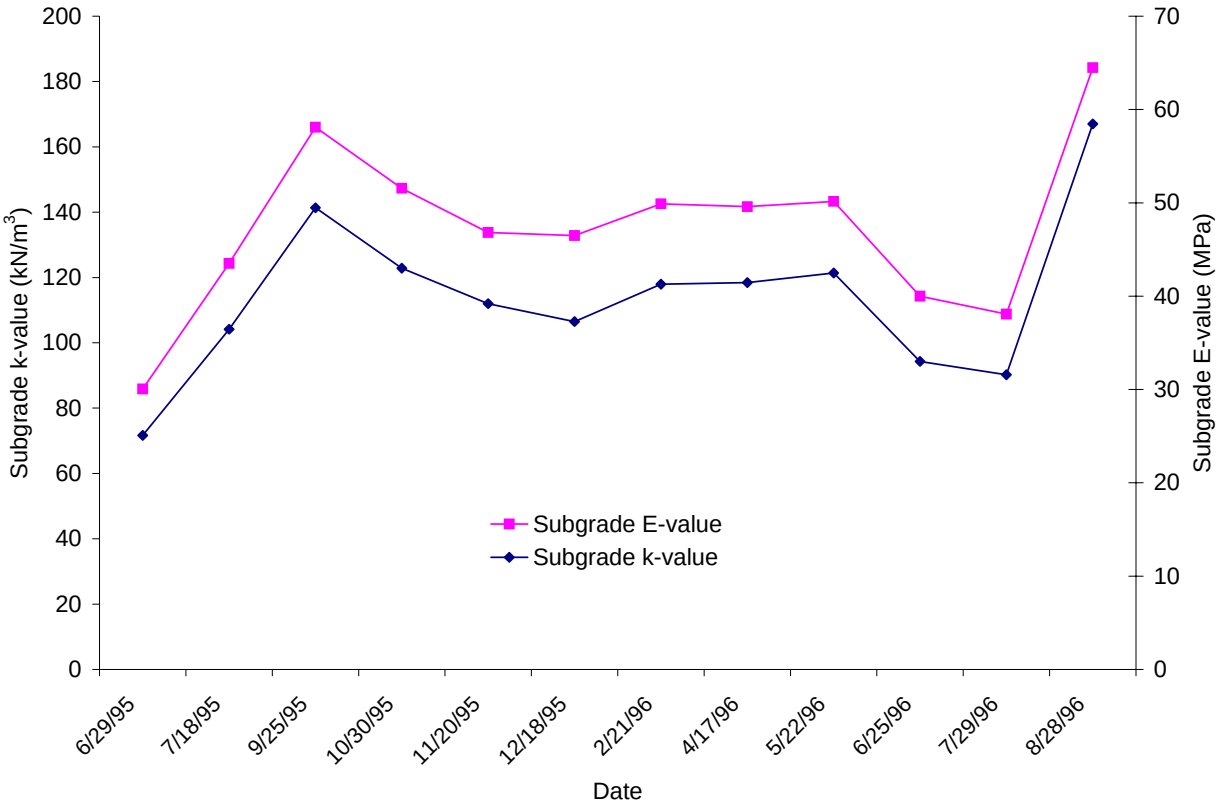

Figure 3.22 Correlation of subgrade k- and E-values at site 53-3813

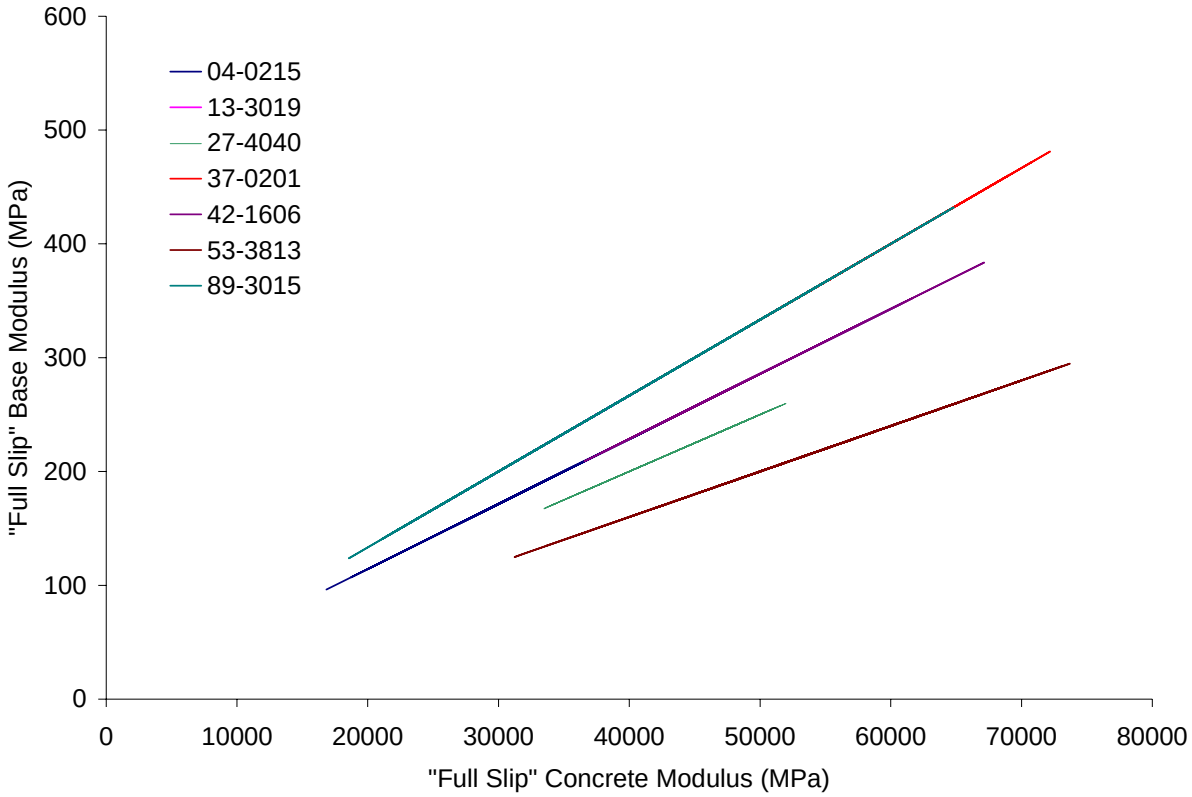

Figure 3.23 Correlation between “full slip” concrete and base moduli

3.2 TEMPERATURE EFFECTS ON RIGID PAVEMENT PROPERTIES

Strictly speaking, the mechanical properties of rigid pavement materials are not temperature dependent. The stiffness of portland cement concrete is certainly unaffected by temperature. The same is generally true of the base and subgrade materials. Nonetheless, consistent daily changes in backcalculated subgrade moduli were observed at several of the rigid pavement sites. These changes are not real; they are an artifact of the backcalculation process. Specifically, they are the result of slab curl.

In the early morning, the top of the concrete slab is cooler than the bottom, so the slab has a tendency to curl upwards. As the slab curls, its weight is transferred to the center of the slab where it is still in firm contact with the ground. During the day, the slab surface heats up and the curvature reverses. The weight of the slab is now transferred to the edges, reducing the contact stress beneath the center. Because the slab is no longer supported by the subgrade, it deflects more when loaded by the FWD. The backcalculation program interprets this increased deflection as a softening of the modulus of subgrade reaction. This phenomena is perfectly exemplified by the backcalculated moduli for site 04-0215 in Arizona.

Figures 3.24 and 3.25 show backcalculated subgrade moduli from four days of testing during the spring and summer months, respectively. The regression models shown in those plots suggest the trend of the data, which is to start at a maximum value of about 80 MPa/m early in the morning and drop to approximately half that value by mid-afternoon. Figures 3.26 and 3.27 typify the temperature profiles in the pavement during the spring and summer, respectively. The maximum negative temperature gradient occurs between 8:00 am and 9:00 am on 3/11/96 and between 7:00 and 8:00 am on 7/22/96. The maximum positive gradient occurs between 2:00 pm and 3:00 pm both days. These limits correspond very closely to the respective times at which the maximum and minimum backcalculated moduli occur in Figures 3.24 and 3.25.

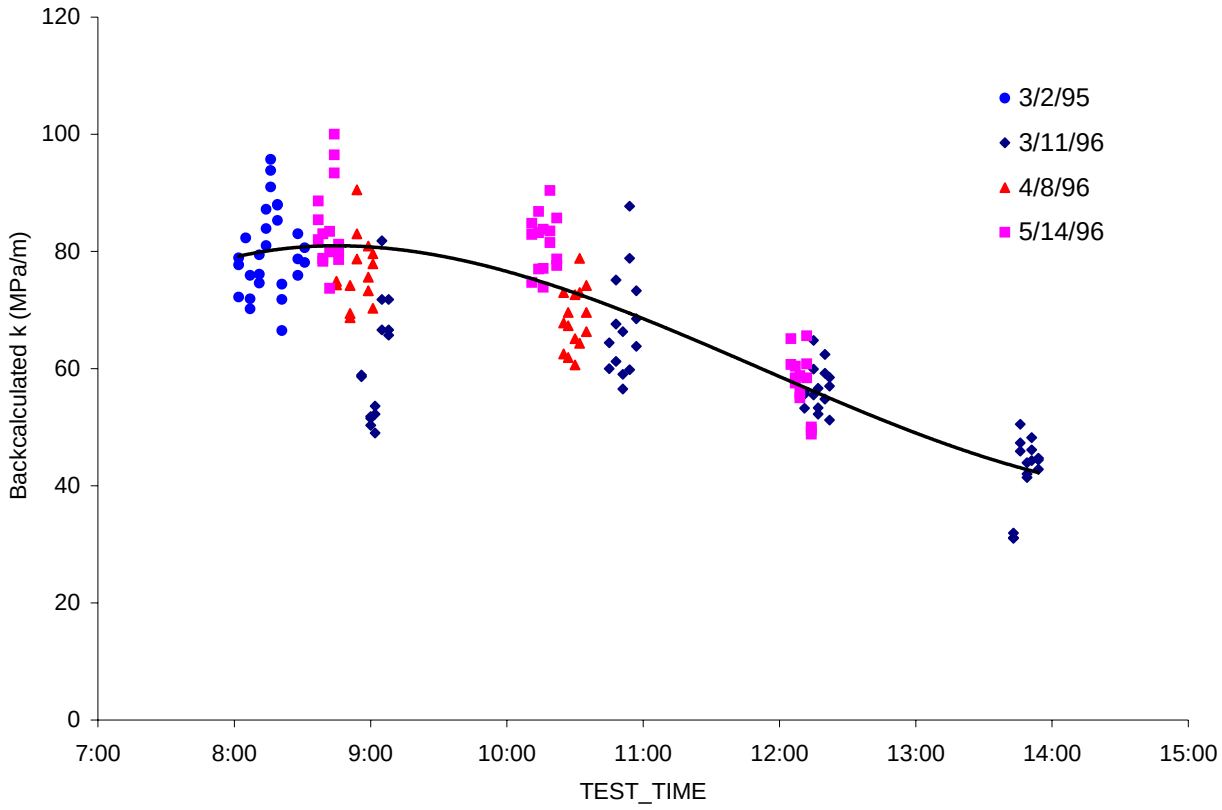

Figure 3.24 Change in backcalculated modulus on spring days at site 04-0215

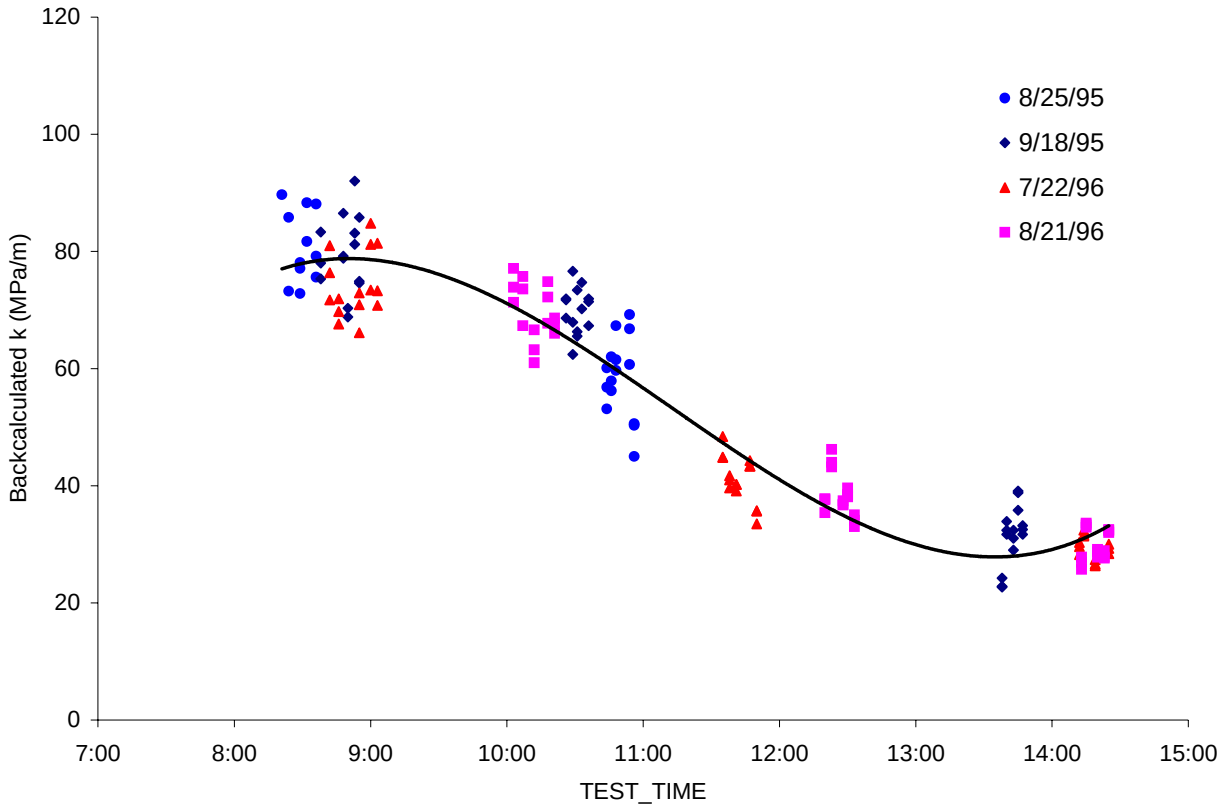

Figure 3.25 Change in backcalculated modulus on summer days at site 04-0215

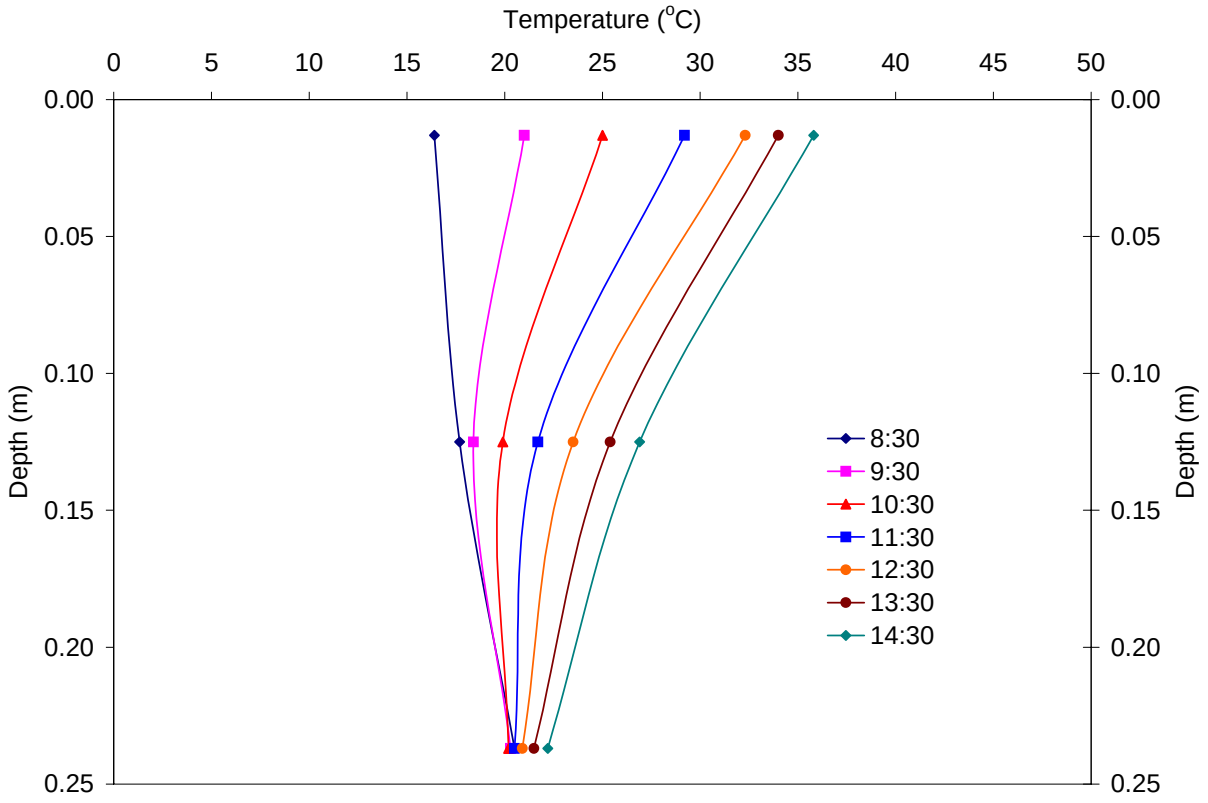

Figure 3.26 Temperature profiles on 3/11/96 at site 04-0215

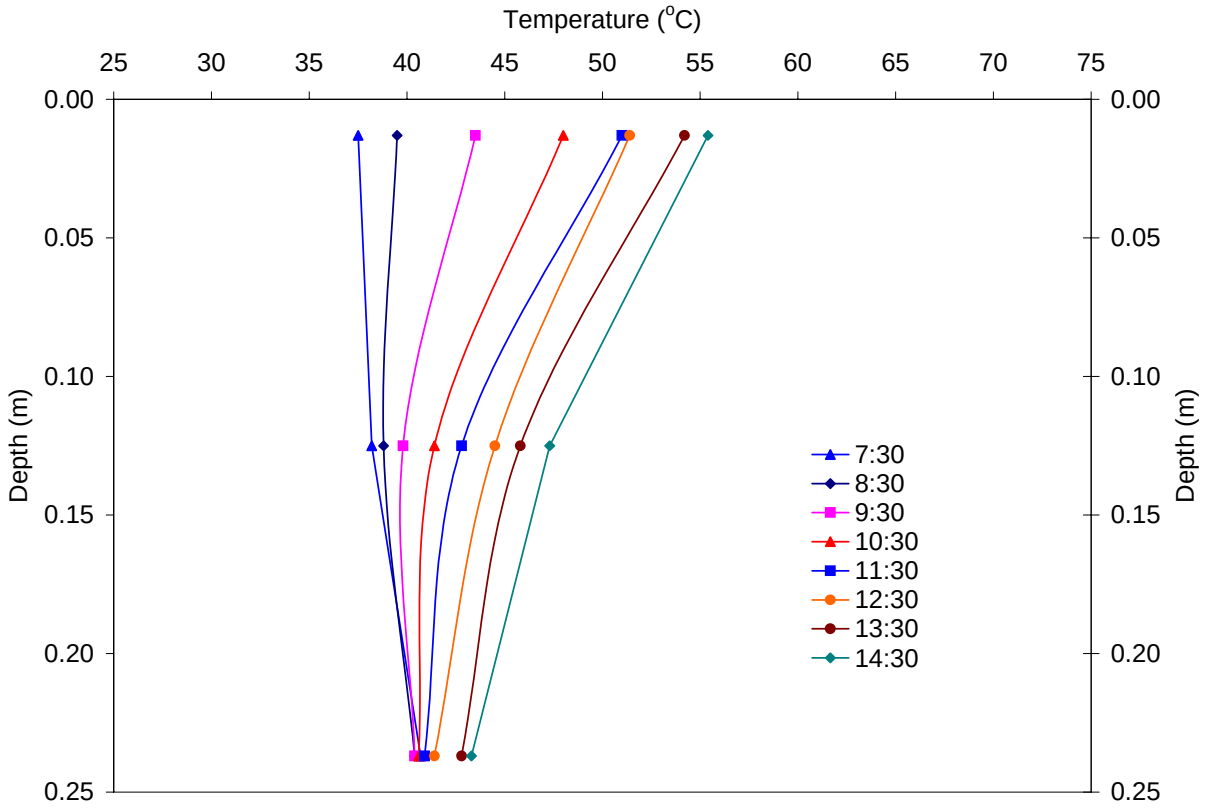

Figure 3.27 Temperature profiles on 7/22/96 at site 04-0215

In Figure 3.28, the backcalculated moduli from the all 12 FWD visits to site 04-0215 are plotted as a function of the temperature gradients in the concrete slab (which were calculated from temperature measurements stored in table MON_DEFL_TEMP_VALUES). As expected, the backcalculated k-value drops as the temperature gradient becomes increasingly positive, but it also drops as the gradient becomes increasingly negative. This was the only site to exhibit this non-monotonic behavior and it is not clear what mechanism could cause this.

Figure 3.29, from site 49-3011 in Utah, better exemplifies the expected monotonic relationship between backcalculated moduli and temperature gradients. The regression model shown in the figure can be used to correct the backcalculated moduli to a temperature gradient of 0°C/m (which should nominally correspond to a flat slab):

$$k_{corr} = k_{calc} + 0.5578 \times Gradient$$

For example, Figure 3.30 shows the k-values backcalculated from FWD tests conducted on March 23, 1994. Spring days such as this exhibit the greatest change in temperature gradient because the nights are still cool but the afternoons are warm and sunny. As shown in Figure 3.31, the temperature gradient was close to zero during the first testing pass at 9:40 am, reached its maximum during the second testing pass just before 2:00 pm and was significantly lower two hours later when the third testing pass of the day was conducted. Because of the associated slab curl, the backcalculated modulus was half as much during the second pass as it was on the first pass and one-fifth higher on the third pass than it was on the second pass. After correcting the backcalculated k-values for the differences in temperature gradient, however, the same average value is obtained throughout the day (Figure 3.32). This keeps the diurnal differences in temperature gradient from obscuring any seasonal changes in the subgrade moduli.

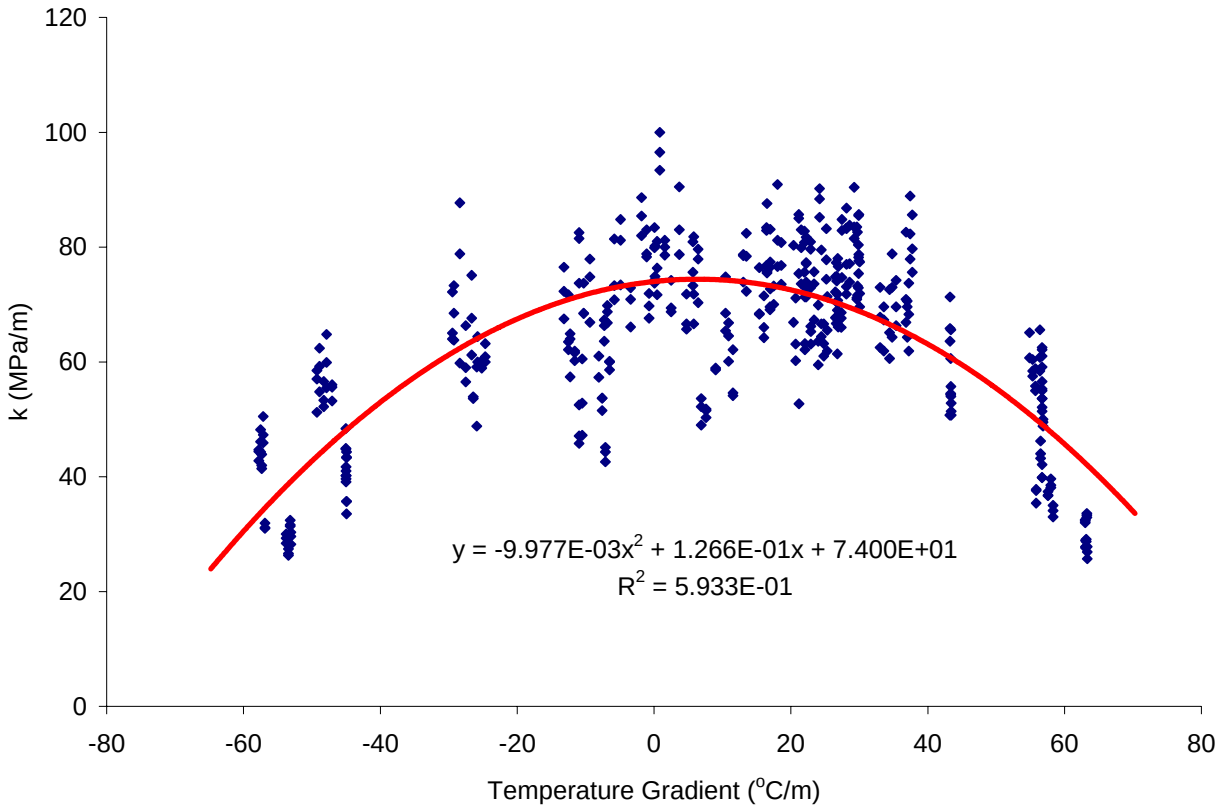

Figure 3.28 Variation of subgrade modulus with temperature gradient at site 04-0215

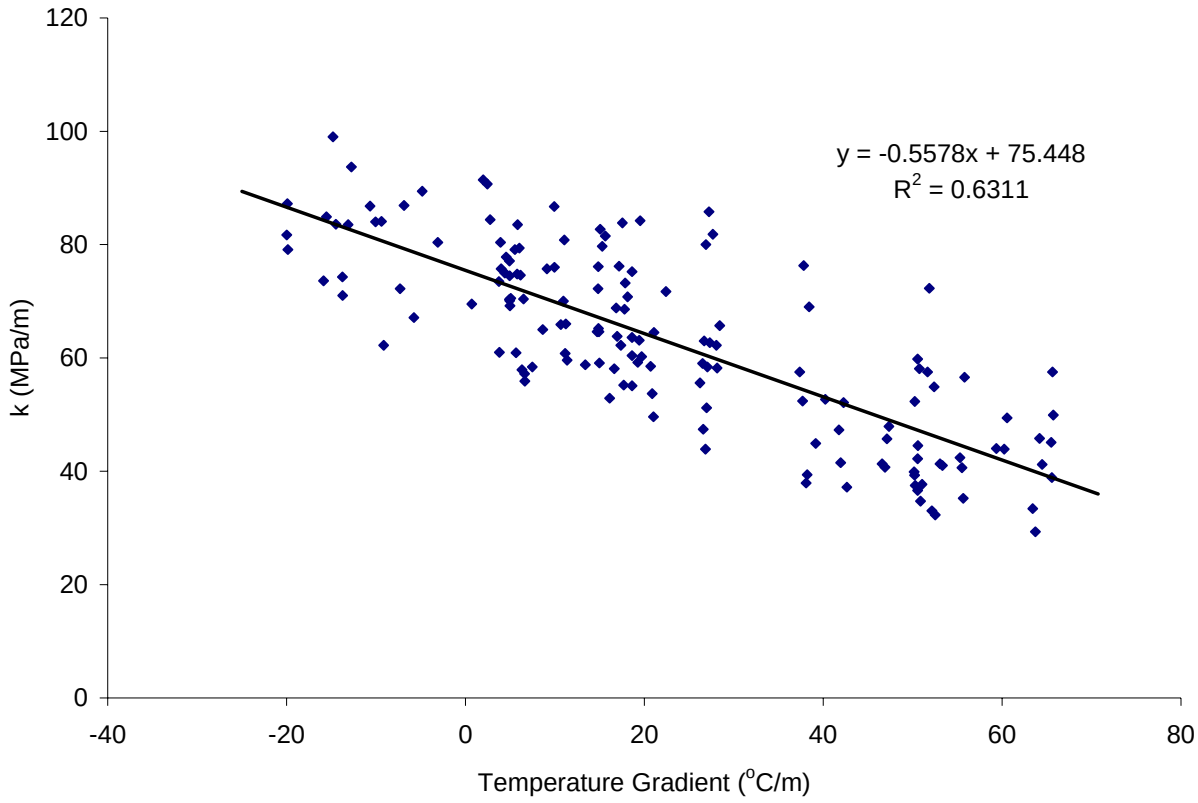

Figure 3.29 Variation of subgrade modulus with temperature gradient at site 49-3011

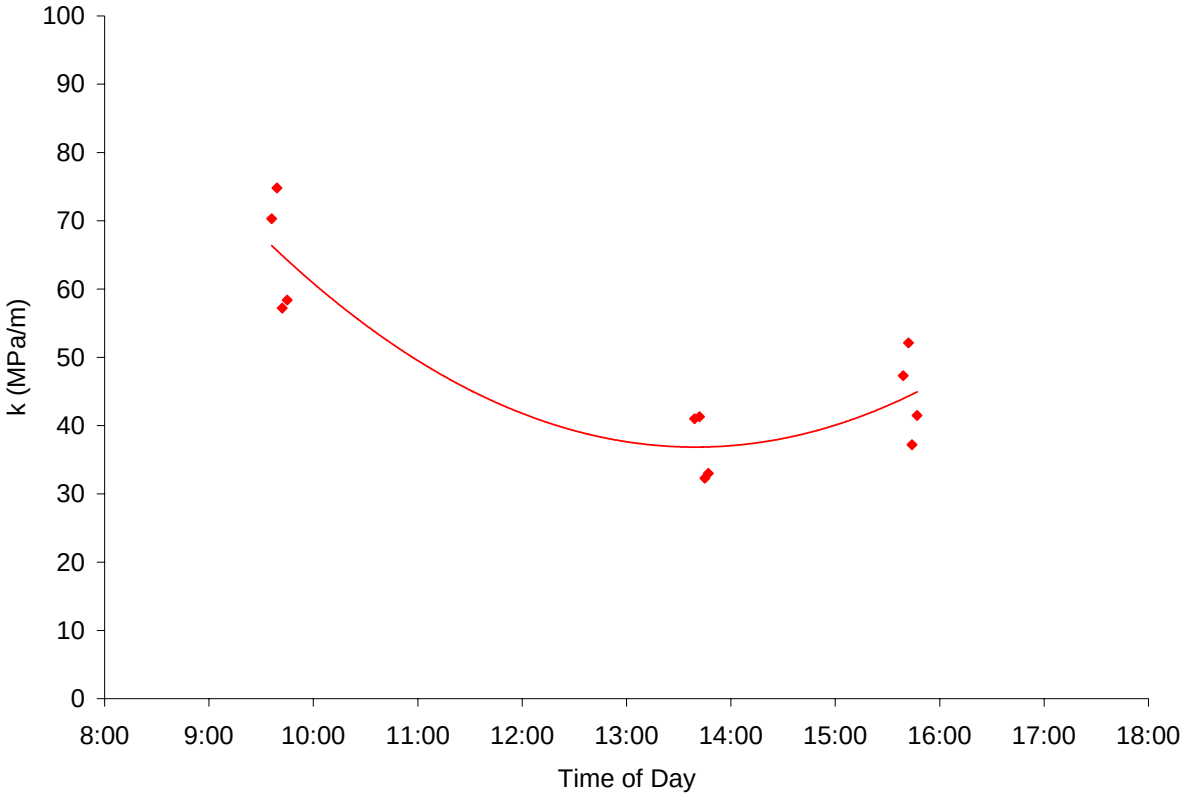

Figure 3.30 Variation in backcalculated moduli on 3/23/94 at site 49-3011

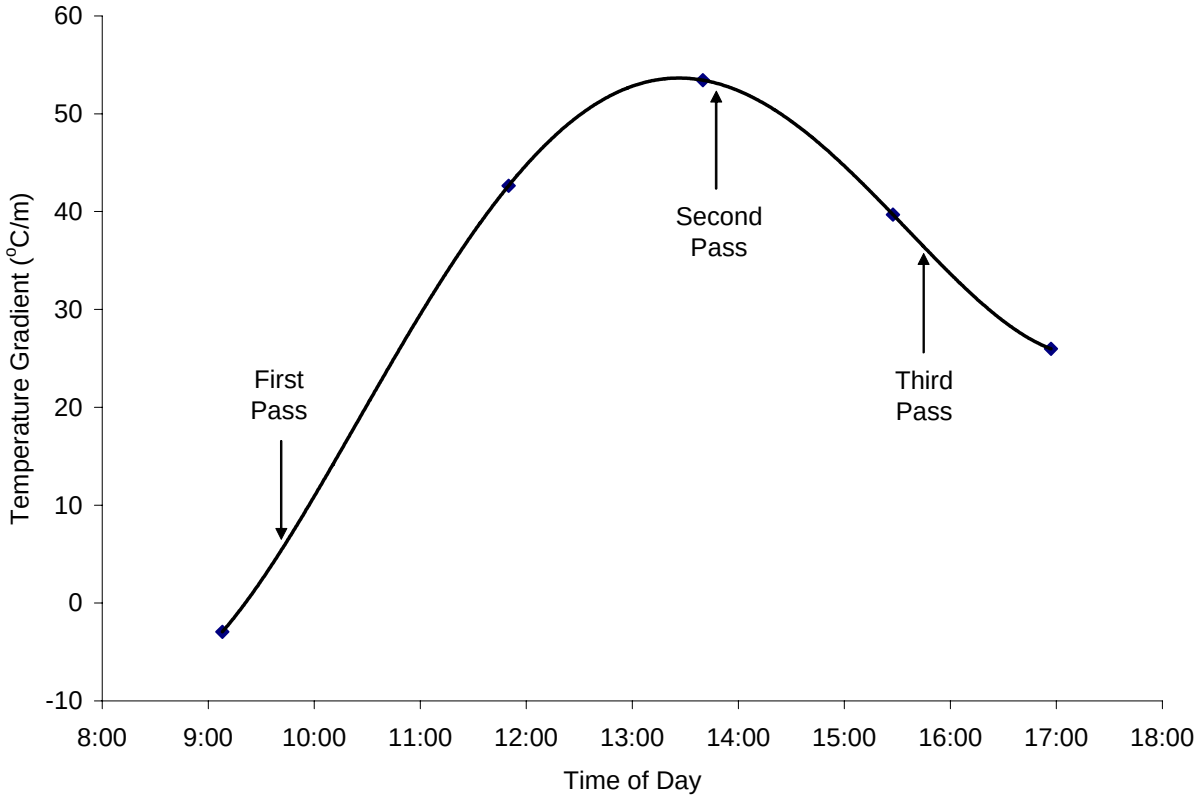

Figure 3.31 Temperature gradient history on 3/23/94 at site 49-3011

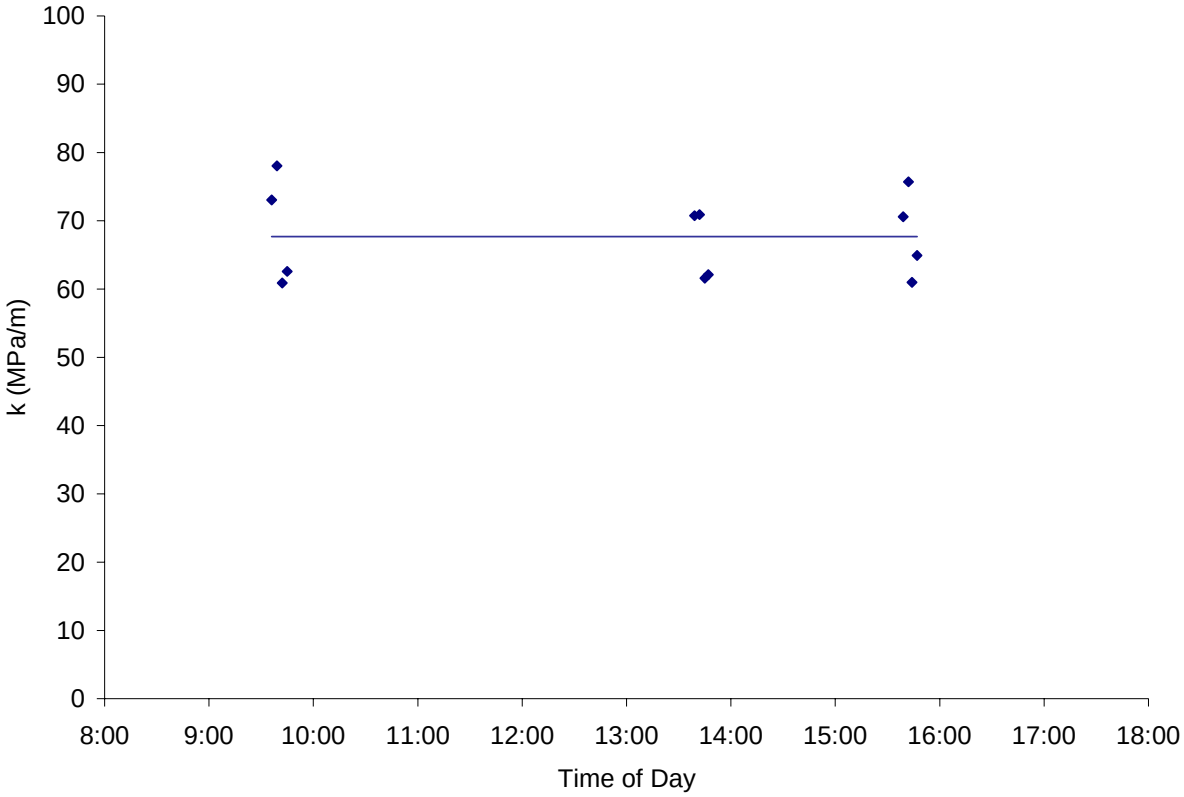

Figure 3.32 Variation in corrected moduli on 3/23/94 at site 49-3011

At the majority of the rigid pavement sites, there was no discernable relationship between the backcalculated subgrade moduli and the temperature gradient. In some cases, such as at site 89-3015 in Quebec (Figure 3.33) the scatter in the data makes it impossible to determine a statistically significant relationship. In others, such as at site 48-4143 in Texas (Figure 3.34) it is clear that the backcalculated moduli are unaffected by changes in the temperature gradient.

3.3 TEMPERATURE EFFECTS ON FLEXIBLE PAVEMENT PROPERTIES

No environmental effect is more pronounced than that of temperature on asphalt layer moduli. The LTPP instrumentation guidelines called for internal temperature measurements to be made 25 mm (1 in) below the top of the asphalt-bound layers, 25 mm (1 in) above the bottom of the asphalt-bound layers, and at the mid-height of the asphalt-bound layers. These temperatures can be used to model the temperature dependence of the asphalt layer moduli.

As was mentioned in Chapter 1, there is some disagreement in the pavements community as to what temperature should be used to model temperature dependence in asphalt pavements. The temperature distribution in the asphalt layer is never actually uniform, so there is no single value that characterizes the temperature of the asphalt. Researchers, for a variety of different reasons, have proposed using temperature measurements at various locations between the third-point and mid-point of the layer. Given the inherent scatter in backcalculated layer moduli, the distinction is largely irrelevant, so the temperature at the layer mid-height has been used for convenience.

It is easy to develop an asphalt modulus model from the LTPP data because the temperature in the asphalt is readily available. Once the model is developed, however, it can only be used if the internal asphalt temperatures are known. In practice, this is seldom the case, so models will be developed based on the surface temperature as well. These will not be quite as accurate, but they will be immensely more useful.

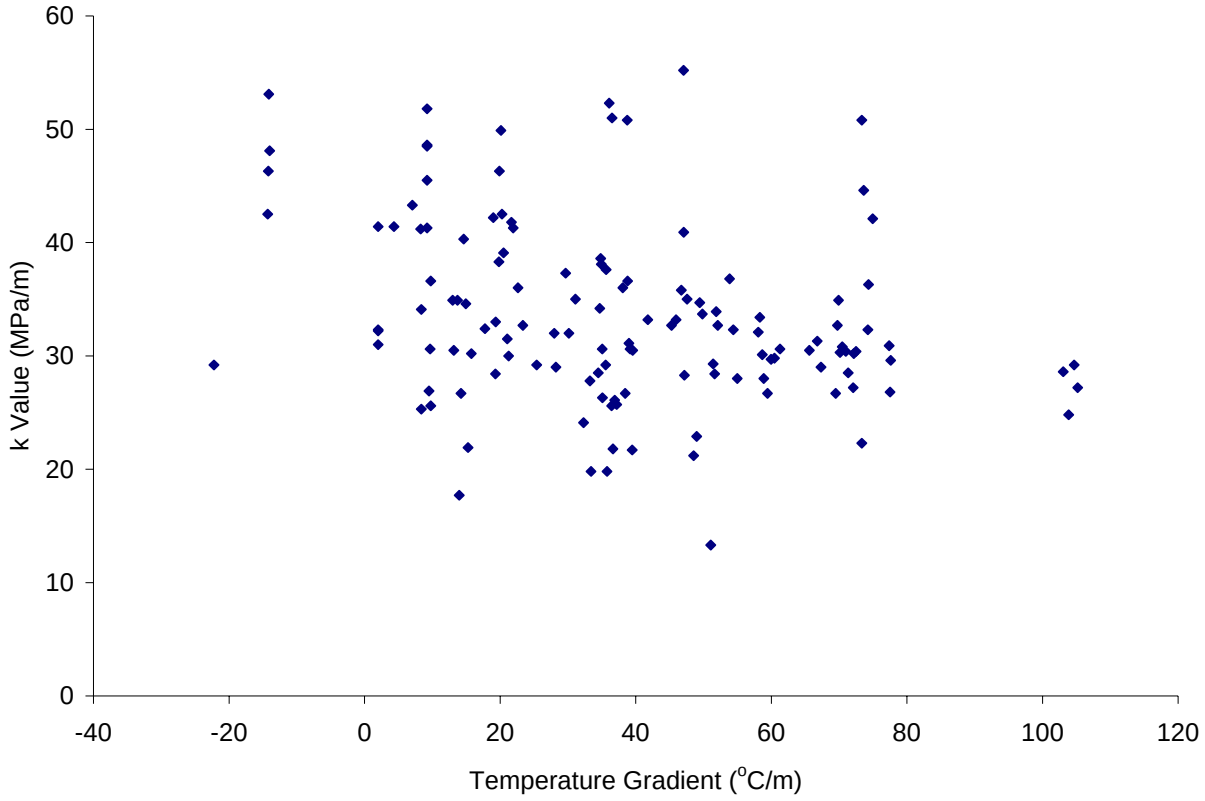

Figure 3.33 Variation of subgrade modulus with temperature gradient at site 89-3015

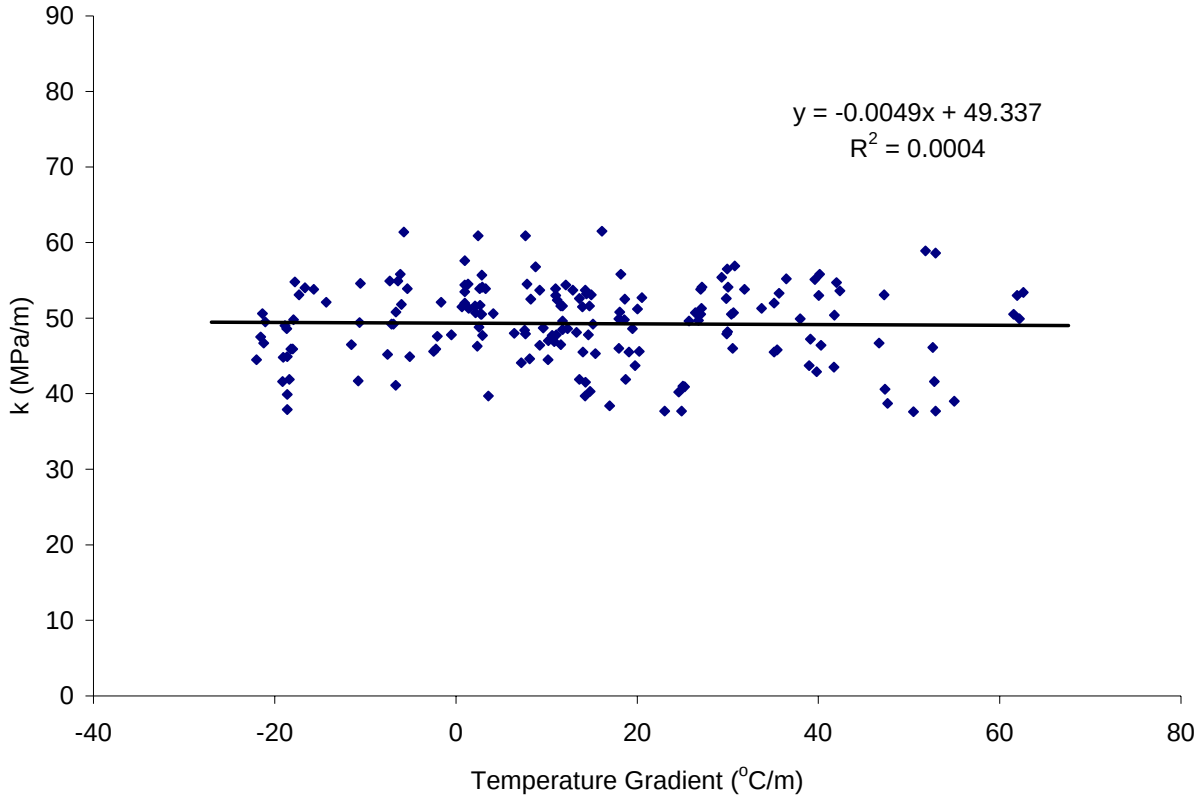

Figure 3.34 Variation of subgrade modulus with temperature gradient at site 48-4143

Figures 3.35 and 3.36 show the asphalt modulus models developed for site 23-1026 using the mid-height and surface temperatures, respectively. Similar plots are presented for all the other flexible pavement SMP sites in Appendices H and I.

An attempt was made at generating more generic models by grouping sites according to the grade of asphalt cement used in the pavement. The reasoning is that different grades are used in different parts of the country because they have differing amounts of temperature dependence. Figure 3.37 shows the group that includes site 23-1026. All of the sites shown in that figure used a binder grade of AC-10. With the exception of site 49-1001, which has been omitted from the regression analysis, there is quite good correlation among the different sites. Binder grade alone does not determine the temperature dependence of an asphalt layer in the field. Mix volumetrics, binder age, and accumulated traffic loadings all affect the stiffness of the asphalt layer. So it is not surprising that some sites behave differently. Appendix J contains similar grouped plots for all the other asphalt binder grades represented in the SMP database.

3.4 RELATIONSHIPS INVOLVING FREEZE/THAW PHENOMENA

Moisture content changes can have a significant effect on the properties of the unbound materials, resulting in measurable changes in the pavement response. When the moisture in the unbound layers freezes, the layer modulus can increase significantly due to the formation of ice. Under the proper conditions, substantial additional moisture can be drawn into the unbound layers as they freeze. This can lead to saturated conditions and significantly reduced layer moduli during the spring thaw. Typical summertime moduli are eventually restored as the excess moisture dissipates. This section will investigate the seasonal changes in subgrade modulus and modulus of subgrade reaction that occur as a result of freezing and thawing.

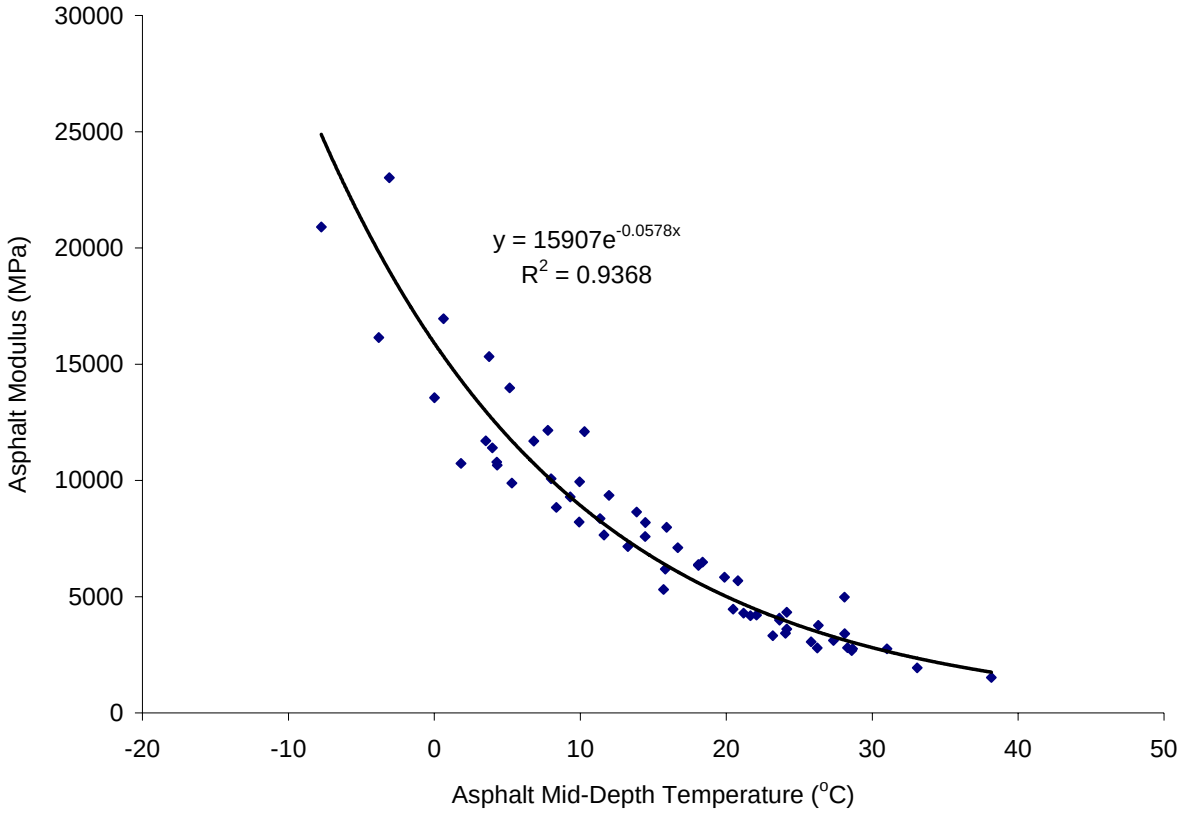

Figure 3.35 Asphalt modulus dependence on mid-depth temperature at site 23-1026

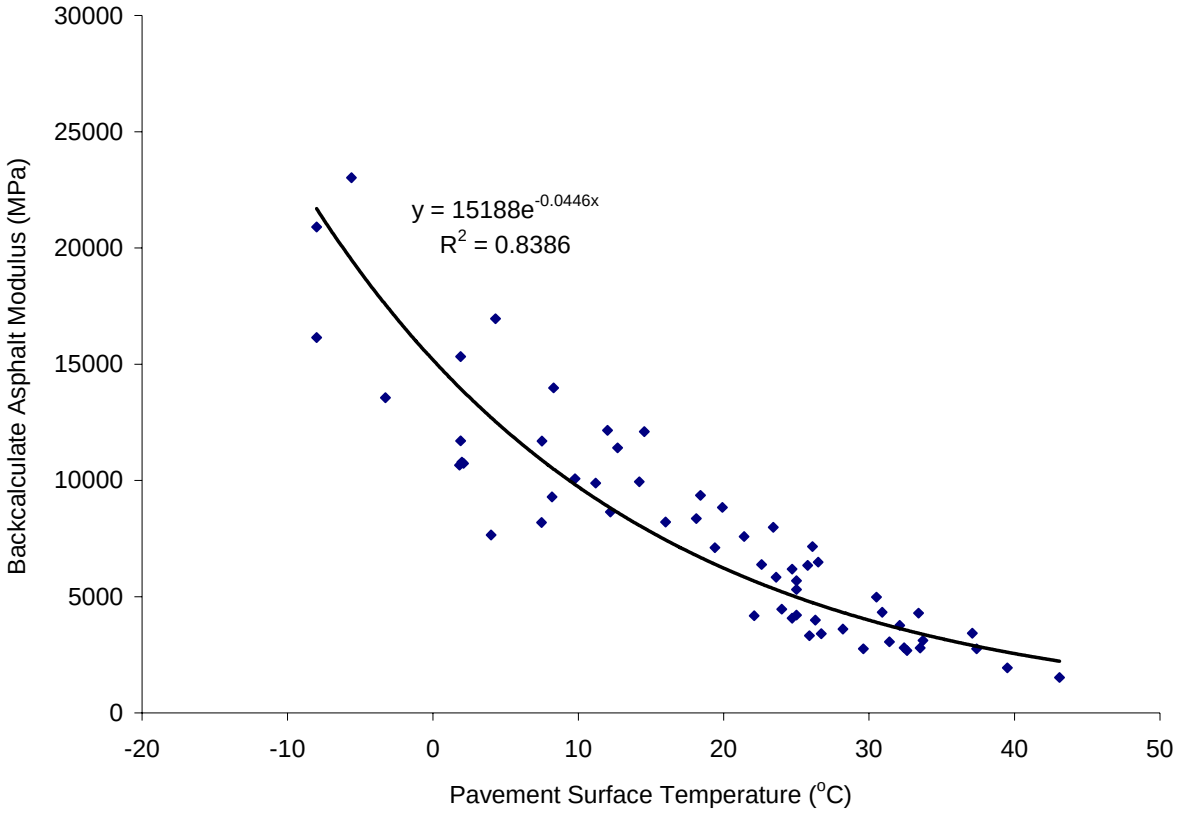

Figure 3.36 Asphalt modulus dependence on surface temperature at site 23-1026

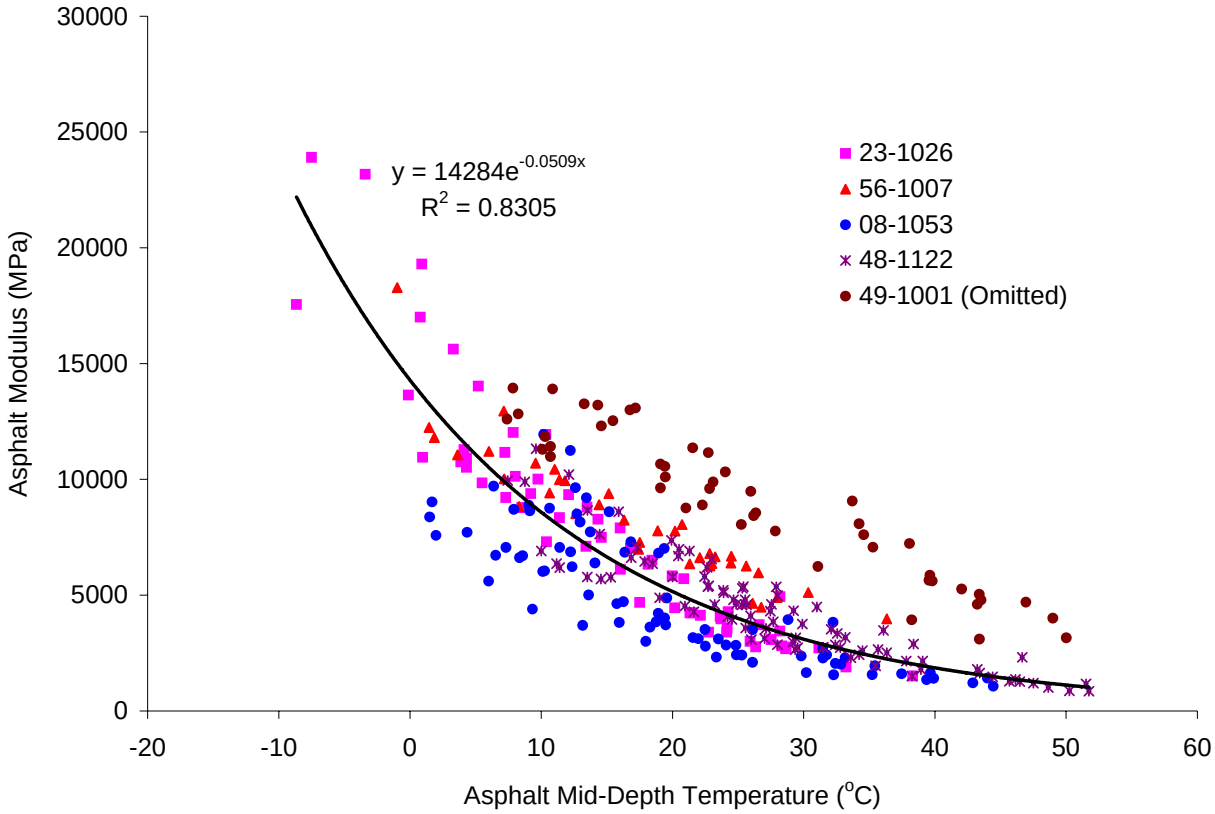

Figure 3.37 Asphalt modulus model for sites using asphalt binder grade AC-10

3.4.1 Seasonal Changes in Subgrade Modulus and k-value in Freezing Sites

Figure 3.38 shows the seasonal variations in the backcalculated subgrade modulus at site 27-1028, a wet-freeze site with a subgrade consisting of poorly graded sand with silt. At this site, the subgrade modulus is fairly constant throughout the year, except during the winter freeze period. Although the amount of data collected in the winter was limited, the modulus is clearly higher than in the summer when not frozen. While frozen, the backcalculated moduli are highly variable and therefore unreliable for modeling purposes.

A similar seasonal variation is shown in Figure 3.39 for site 50-1002, which is a also wet freeze site. The subgrade is poorly graded gravel with silt and sand. At this site, only a single winter modulus value was obtained, but it clearly reflects the frozen state. As at site 27-1028, the modulus seems to be fairly constant when the subgrade is not frozen.

The modulus of subgrade reaction, or k-value, for rigid pavements is observed to vary throughout the year in the same manner. Figure 3.40 shows the seasonal variations in the backcalculated k-value at site 27-4040. During the three years for which backcalculated moduli are available in the LTPP IMS, only a couple of data points with elevated k-values were obtained during the freezing period. Similar results are shown for other sites in Appendix K.

Figure 3.41 shows changes in the subgrade moisture content and water table depth throughout the year at site 23-1026. All of the data has been normalized with respect to the October 1 values (which are listed in the legend), so the vertical axis shows relative rather than absolute magnitudes. The data suggests a sudden drop in moisture content during the winter freeze followed by a significant increase during the spring thaw and a gradual return to the nominal levels in the last spring and summer. As discussed previously, the moisture content at

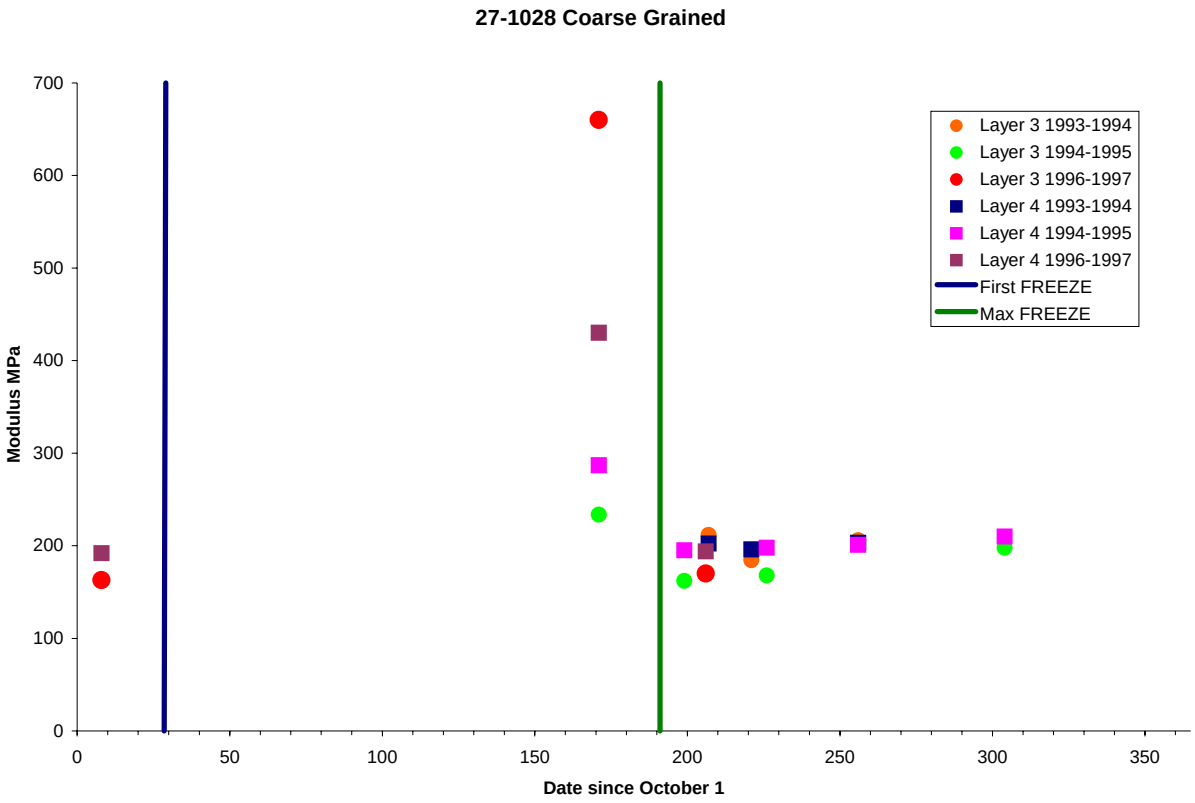

Figure 3.38 Seasonal Changes in Subgrade Modulus, Site 27-1028

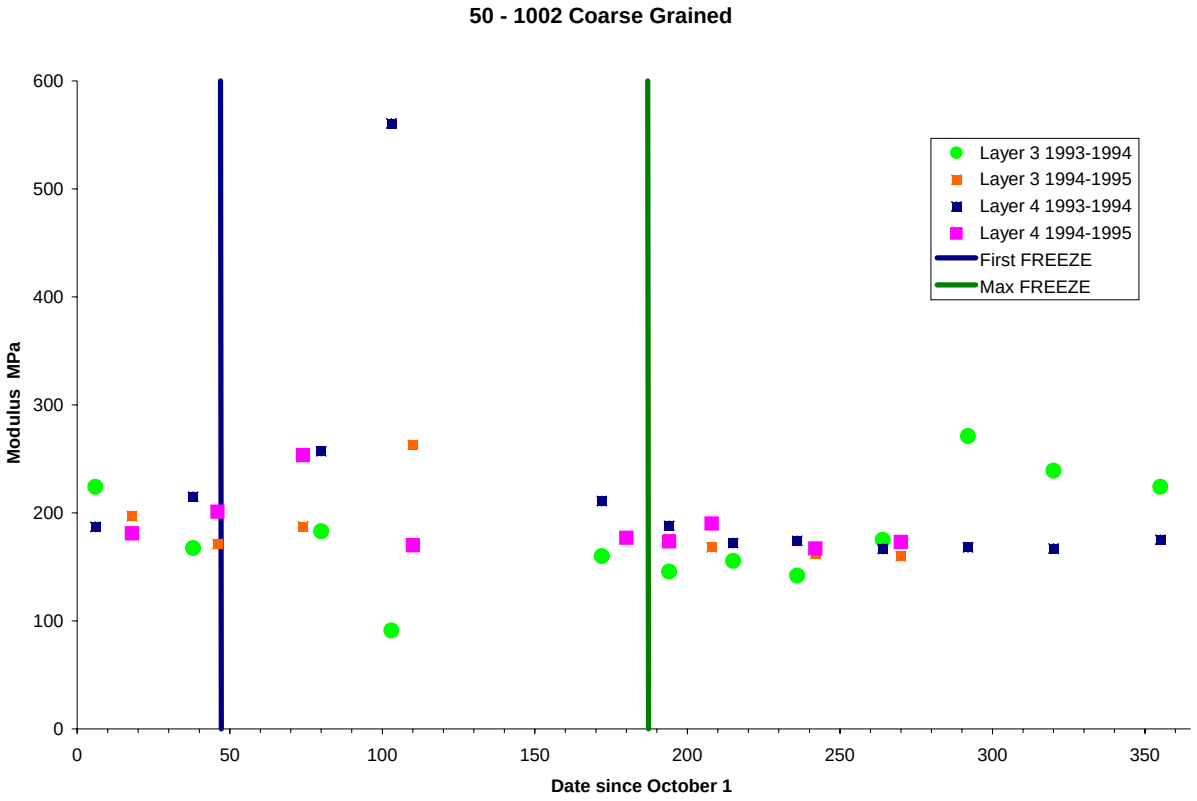

Figure 3.39 Seasonal Changes in Subgrade Modulus, Site 50 - 1002

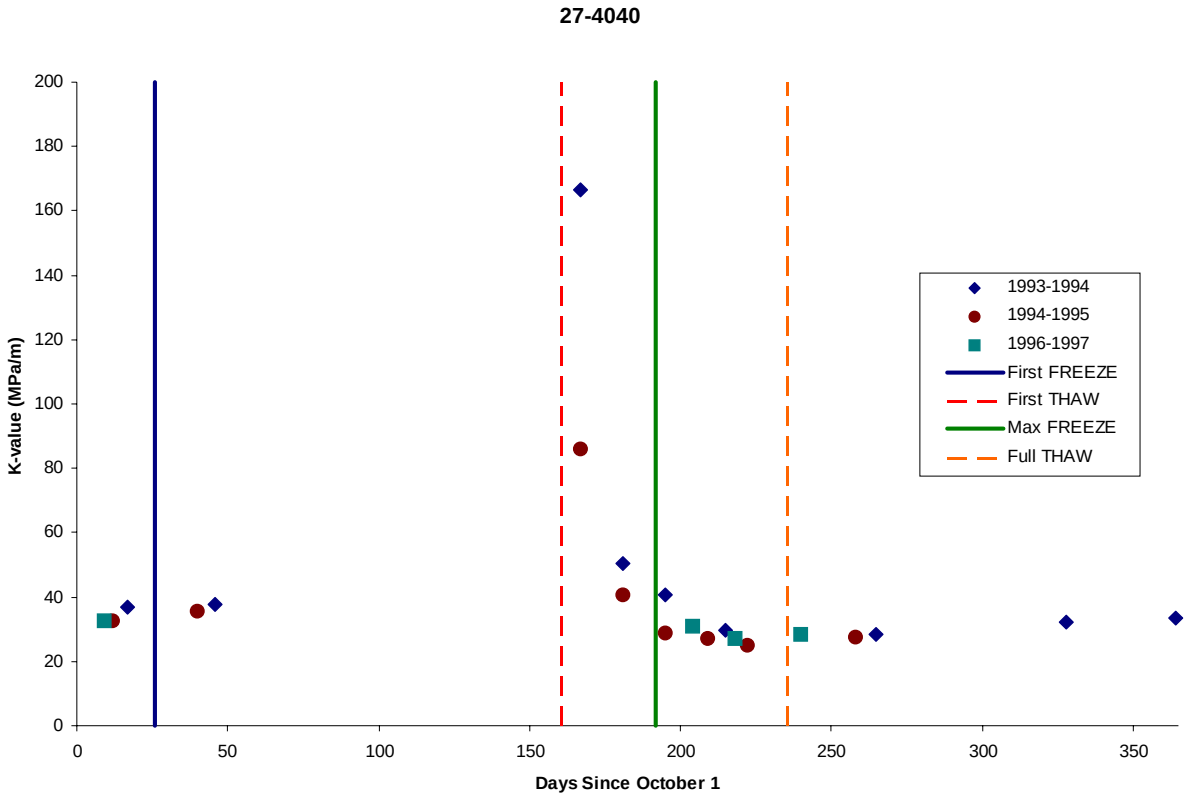

Figure 3.40 Seasonal Variation of Modulus of Subgrade Reaction (Fine-Grained Subgrade: Lean Clay with Sand)

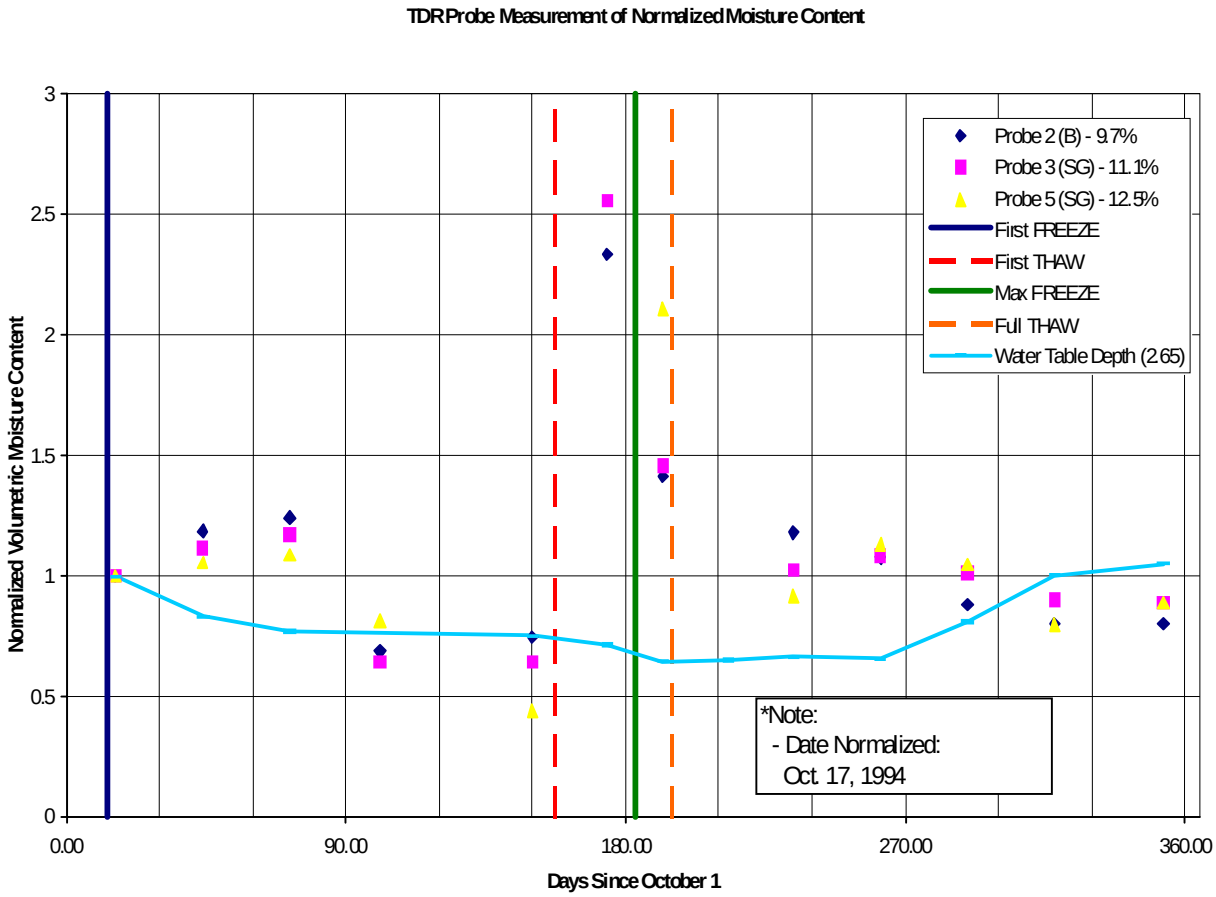

Figure 3.41 Seasonal Variation of Moisture Content (apparent) during Freeze, Site 23-1026 (Coarse-Grained Subgrade: Silty Sand with Gravel)

the LTPP SMP sites is obtained using time domain reflectometry (TDR) probes, which measure changes in the dielectric constant of the soil. When the soil water freezes, the dielectric constant of the soil drops precipitously. This is interpreted by the software as a drop in the water content, but the actual amount of water in the soil is unknown. When the soil water thaws, the TDR measurements once again become reliable, so the significant water content increase shown during the thaw period is real.

3.4.2 Subgrade Modulus and k-value as a Function of Freeze State by Soil Type

Figure 3.42 compares the mean "summer" and "winter" subgrade k-values at three wet-freeze sites with different subgrade soil types. The summer values were calculated using data from April through October, while the winter values were calculated using data from November through March. Of the three rigid pavement sites, the two with sand subgrades experienced a doubling of the subgrade modulus during freezing. The clayey gravel with sand, which might not be expected to be frost susceptible, experienced little change from summer to winter.

3.5 RELATIONSHIPS INVOLVING MOISTURE RELATED PHENOMENON IN THE ABSENCE OF FREEZING

3.5.1 Seasonal Changes in Subgrade Modulus and k-value in No-Freeze Sites

The seasonal variation in subgrade modulus for two sites with coarse-grained subgrades are shown in Figure 3.43 and 3.44. Results are shown for two different subgrade layers based on artificial divisions made during the backcalculation process. While slightly different values were obtained for the two layers, neither site demonstrated consistent variations throughout the year. Similar seasonal variations are shown in Figures 3.45 and 3.46 for sites with fine-grained subgrades.

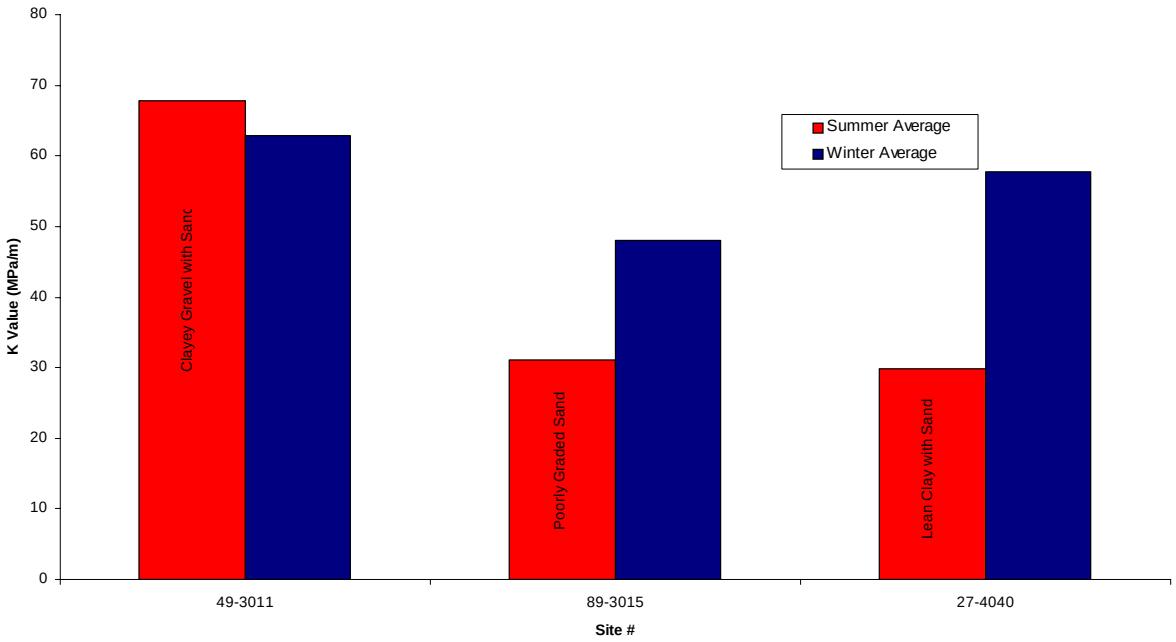

Figure 3.42 Effect of Freeze State and Soil Type on k-value

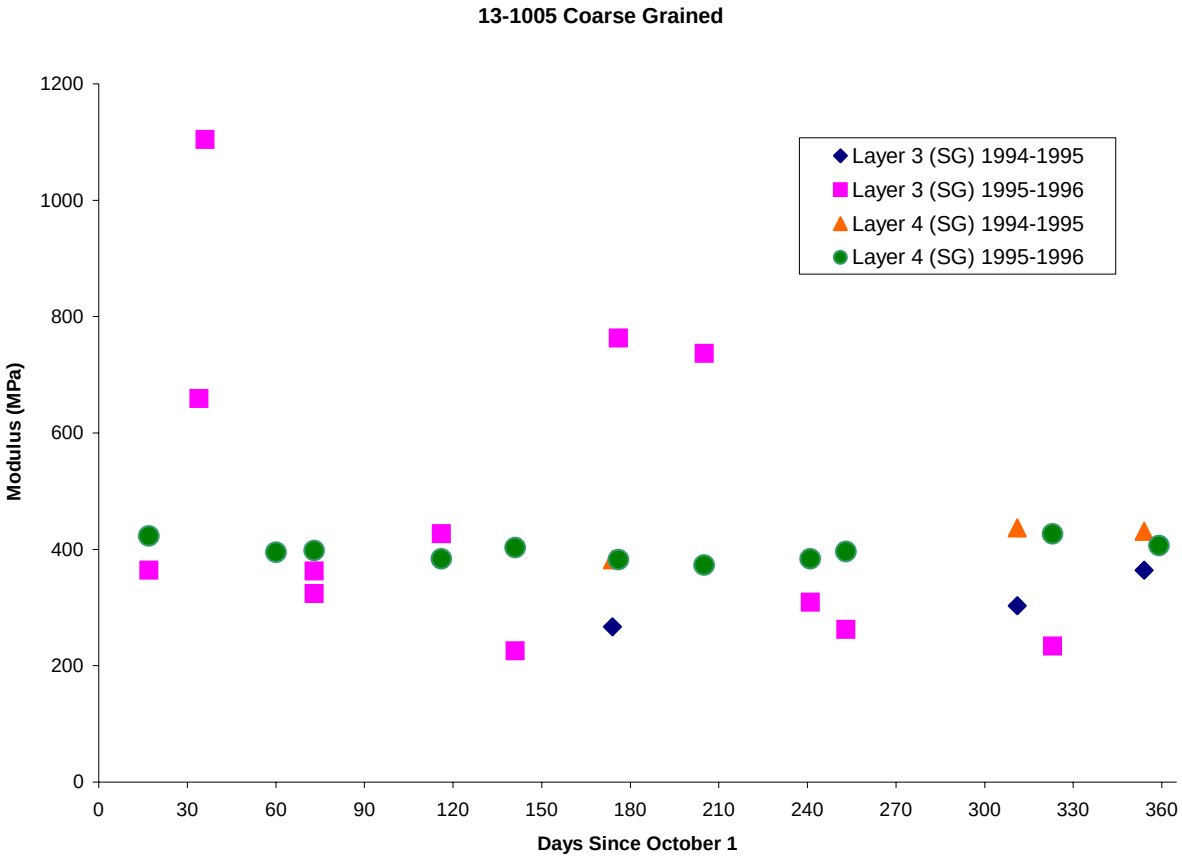

Figure 3.43 Seasonal Variation of Subgrade Modulus, Site 13-1005 (Coarse-Grained Subgrade)

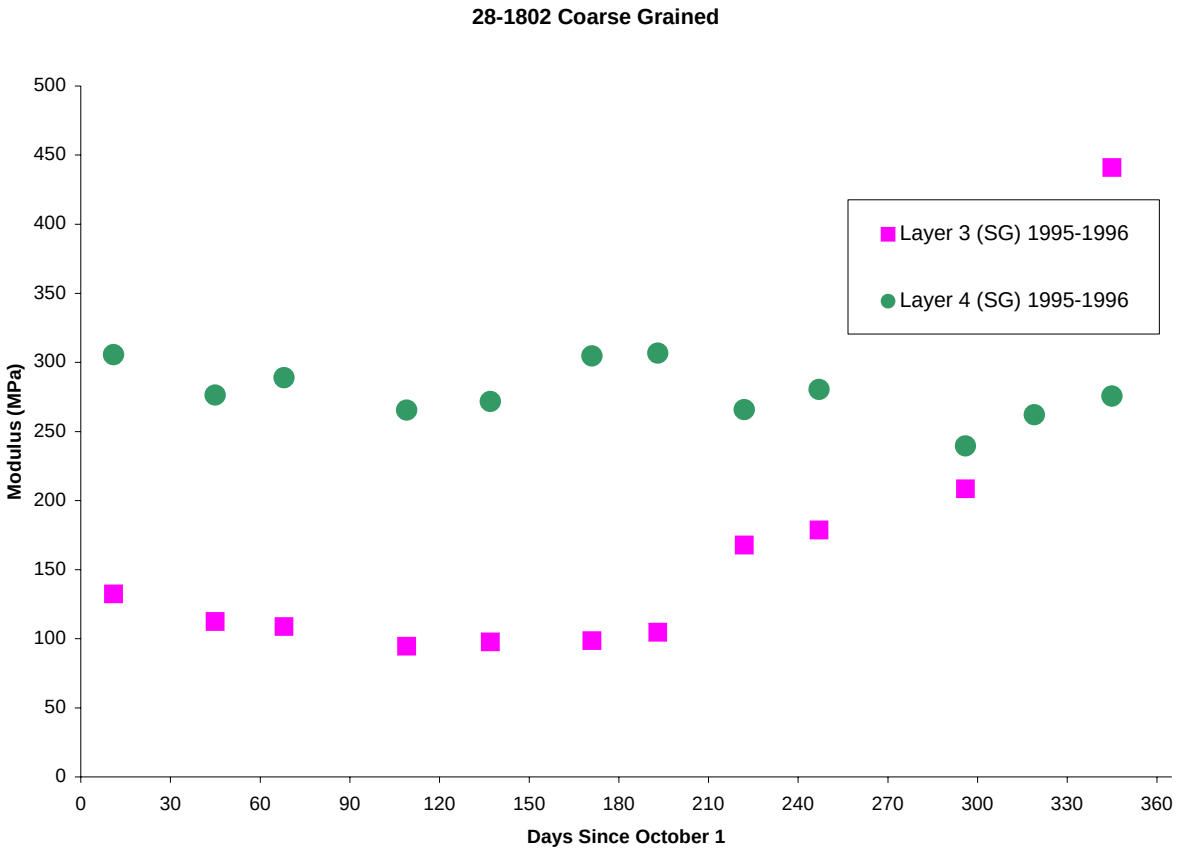

Figure 3.44 Seasonal Variation of Subgrade Modulus, Site 28-1082 (Coarse-Grained Subgrade)

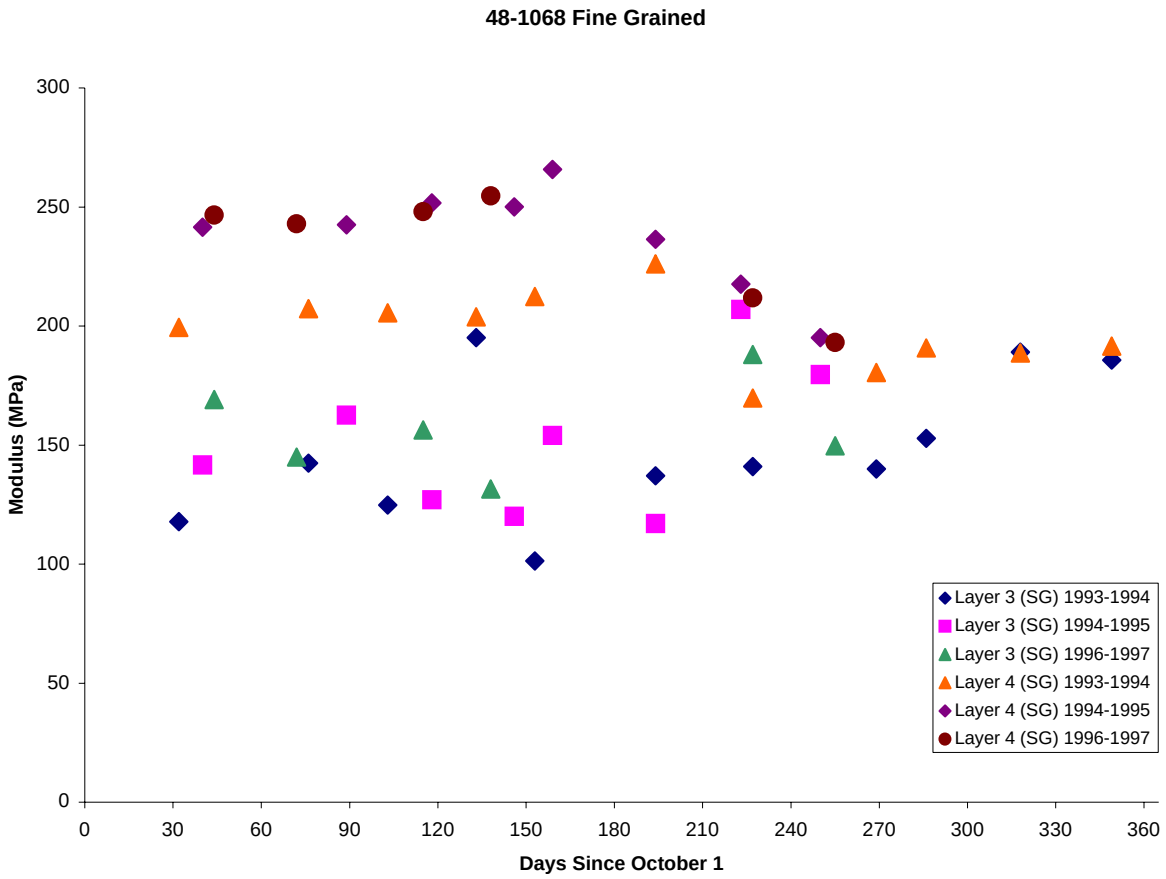

Figure 3.45 Seasonal Variation of Subgrade Modulus, Site 48-1068 (Coarse-Grained Subgrade)

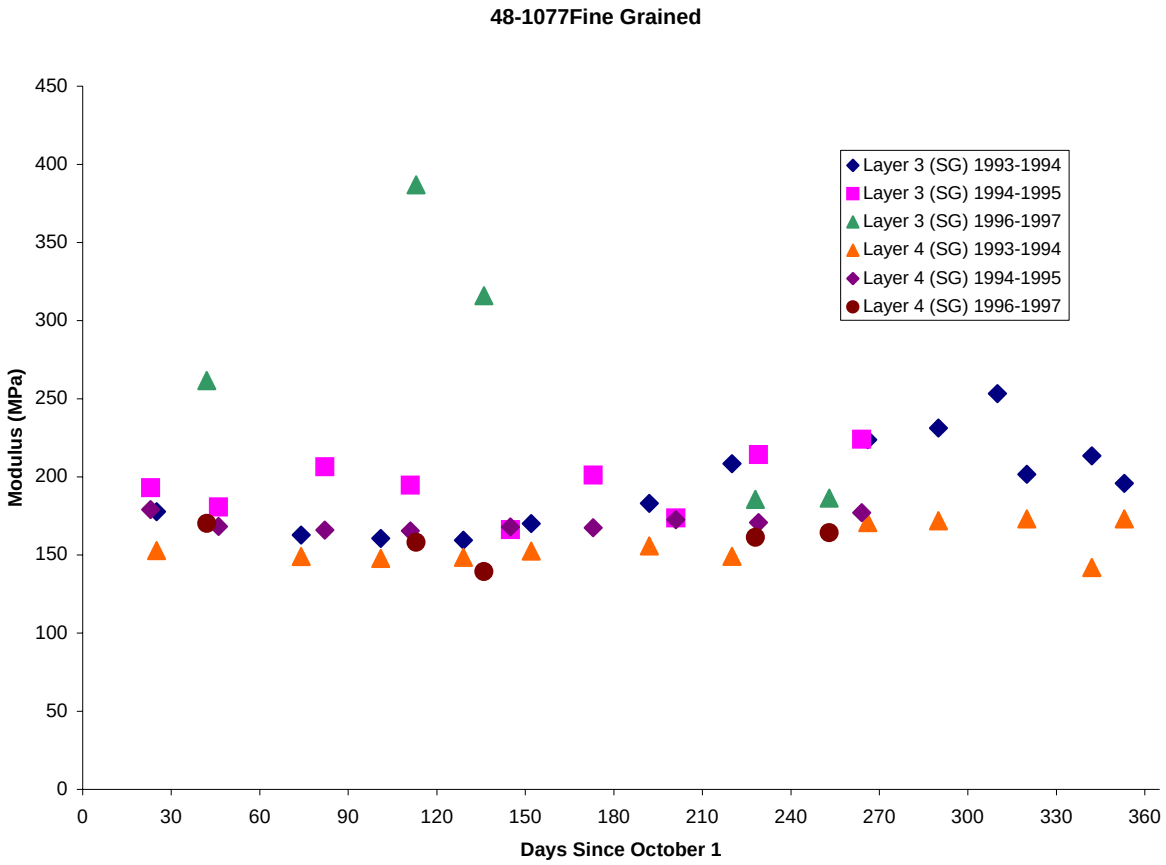

Figure 3.46 Seasonal Variation of Subgrade Modulus, Site 48-1077 (Fine-Grained Subgrade)

Figures 3.47 and 3.48 show seasonal variations in backcalculated k-values for fine- and coarse-grained subgrades, respectively. Figure 3.49 compares the backcalculated k-values from several different sites with different subgrade soil types. As discussed in the previous section, the results are shown in terms of “summer” and “winter” averages. In the absense of freezing, very little seasonal variation in the backcalculated k-values was observed for the sites in the SMP database. Appendix L includes similar results from additional sites.

3.5.2 Relationship Between Moisture Content and Water Table Depth

The relationship between moisture content and water table elevation was investigated for all of the sites. Typical results are shown in Figure 3.50. No meaningful correlation was found for either fine-grained and coarse-grained subgrades, even for TDR probes close to the water table. Appendix M includes more results.

3.5.3 Subgrade Modulus and k-value as a Function of Moisture Content by Soil Type

The backcalculated subgrade moduli were also compared with the water contents at each of the measurement depths. Very little correlation between measured moisture contents and backcalculated layer moduli (either subgrade modulus or k-values), was found, even in fine-grained subgrade soils. Although some changes in the moisture content and the depth to the water table were observed, the backcalculated moduli vary little from one season to the next. Since the seasonal variations are so small, meaningful correlations cannot be found. Appendix N includes some of the results.

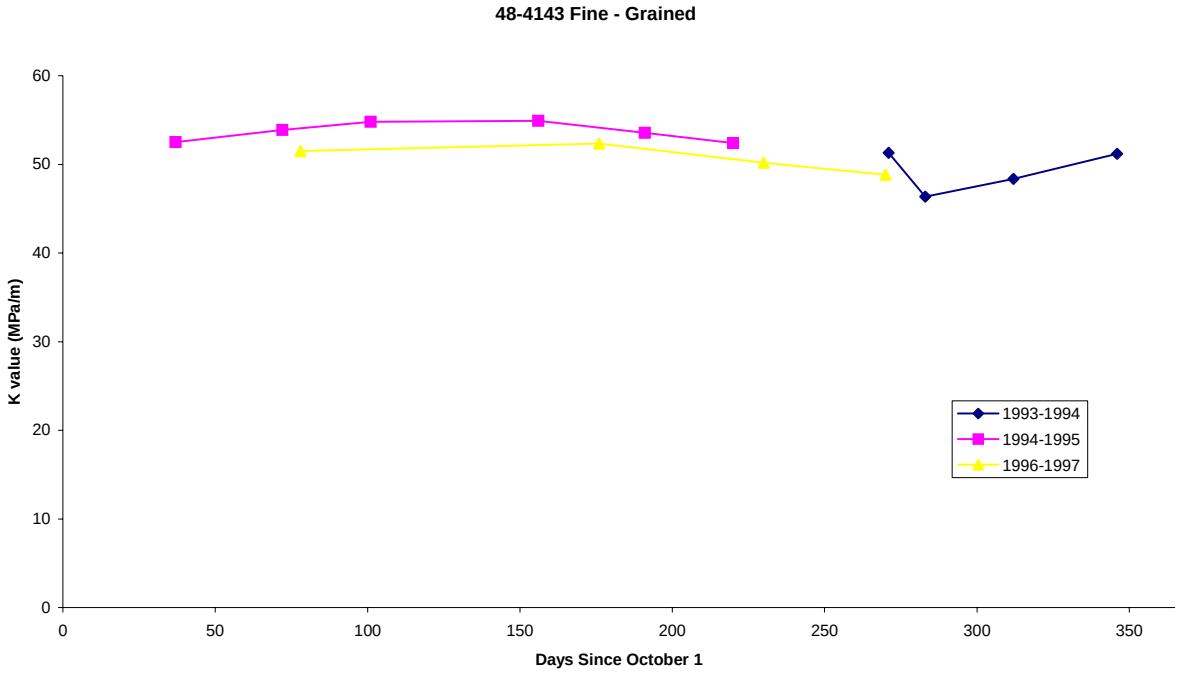

Figure 3.47 Seasonal Variation of k-value, Site 48-4143 (Fine-Grained Subgrade)

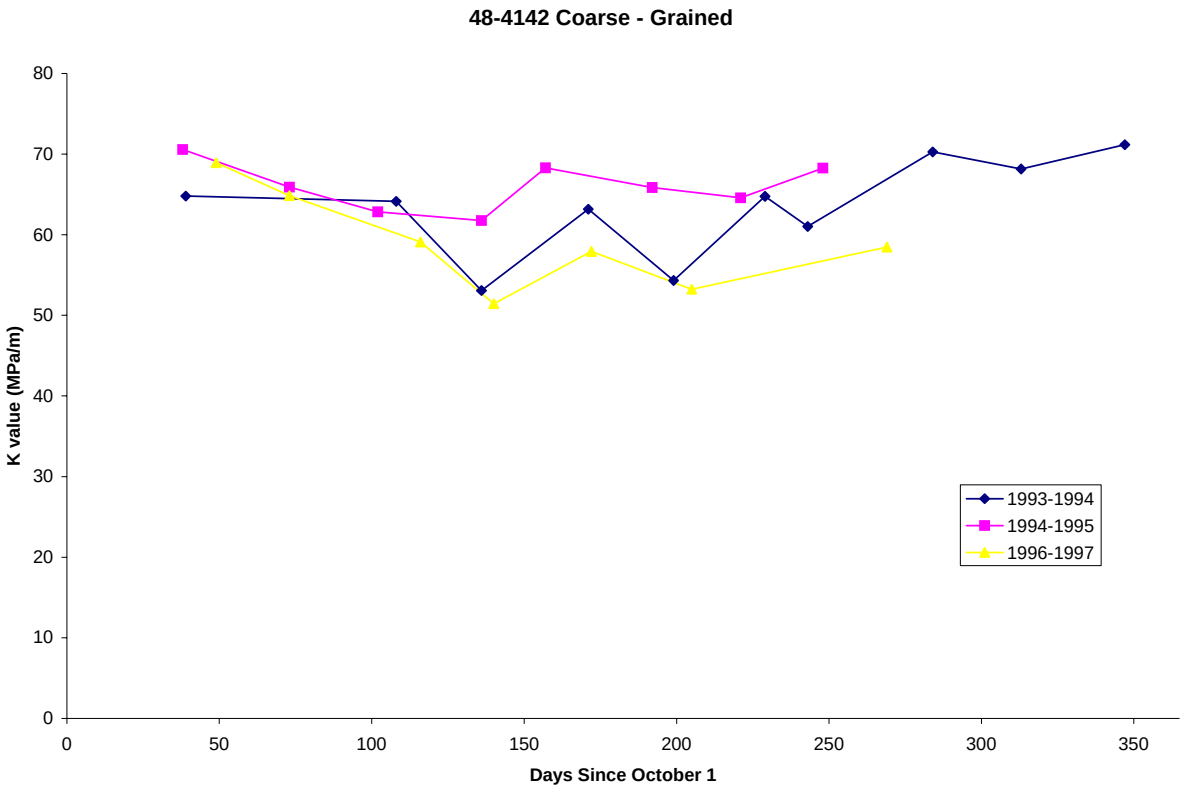

Figure 3.48 Seasonal Variation of k-value, Site # 48-4142 (Coarse-Grained Subgrade)

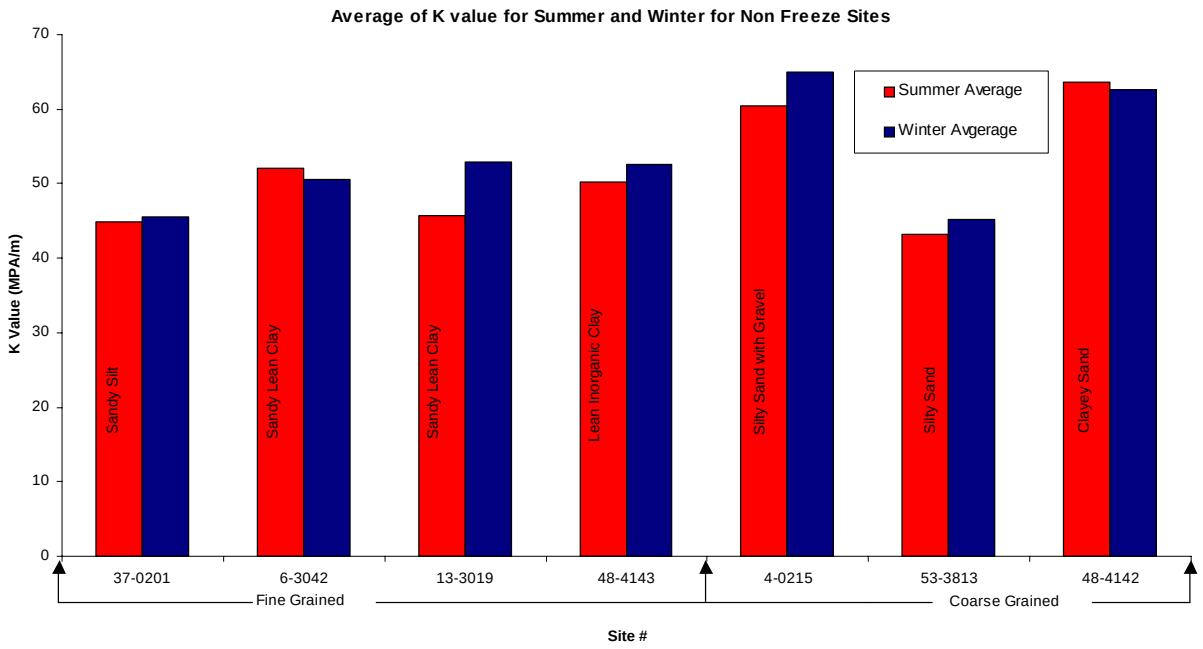

Figure 3.49 Seasonal Differences in k-value for Various Soil Types

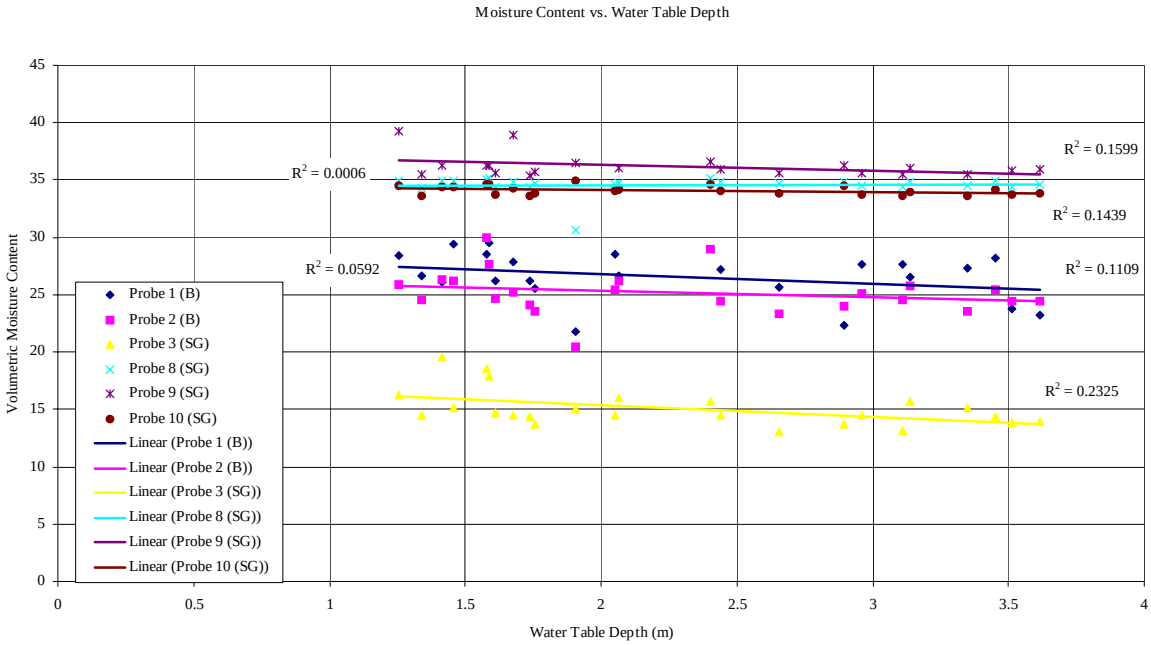

Figure 3.50 Moisture Content vs Water Table Depth, site 24-1634 (fine-grained subgrade)

CHAPTER 4
RELATIONSHIPS BETWEEN PAVEMENT MATERIAL PROPERTIES AND STRUCTURAL RESPONSE

In seasonal frost areas, pavements are subjected to freeze-thaw cycles. During the freezing process, the existing moisture in the subsurface layers freezes and bonds the soil particles together. Under the right conditions, water from below is drawn to the freezing front and creates enriched ice lenses. The bearing capacity of the frozen soil is increased and the pavement structure can withstand loads greater than those for which it was designed. During these periods of hard freezing, overloading of the pavement structure may occur with very little damage, and overload permits may be appropriate.

During thawing periods, the ice lenses formed during the freezing period start to melt. Depending on the drainage characteristics of the pavement structure and the layer materials, an undrained loading condition can be created from traffic on the surface. Under these conditions, the bearing capacity of the pavement structure is severely reduced. To minimize the damage to the pavements during spring thaw, some form of load restriction may need to be applied. However, prolonged load restrictions can have a severe impact on the economy of the region. Therefore, the ability to predict the onset of thaw weakening and the length of the load restriction period is critical to state highway agencies.

4.1 NOMINAL PAVEMENT MATERIAL PROPERTIES

Seasonal variations in pavement response, particularly the response during the winter freeze and spring thaw, can be most effectively investigated by comparison with the "nominal" or more typical response that exists during late summer and early fall. During the nominal period, the water

content of the base and subgrade is relatively low and constant, leaving only temperature-induced changes in asphalt modulus to be considered.

The nominal base, subbase, and subgrade moduli for each of the freeze sites are summarized in Table 4.1. The nominal values were computed as the median of the daily average moduli for all site visits between June and November. Table 4.1 shows which months were used at each site and the number of site visits included in the calculation. An entry of N/A in the column heading "layer number" is for those sites lacking modulus data during the June to November period. In cases where a base layer is indicated but no value is shown, the median backcalculated modulus was either higher than the surface modulus or lower than the subgrade modulus and was discarded as being unrealistic. This often happens when the pavement layer moduli are highly stress dependent (as discussed in the previous chapter). Figure 4.1 illustrates the range of nominal backcalculated modulus values for various base and subgrade types.

Table 4.1 Median nominal values of backcalculated modulus (freeze sites)

Site #	State Name	Back Calc. Layer #	Layer Type	Median of Moduli (MPa)	Months used to deter. Nominal value	# of data pt.
16-1010	Idaho	2	Base: Crushed Gravel	N/A	-	-
		3	Subgrade: Silty Sand	71	6,9,10,11	7
		4	Subgrade: Silty Sand	180	6,9,10,11	7
23-1026	Maine	2	Base: Gravel (uncrushed)	N/A	-	-
		3	Subgrade: Silty Sand with Gravel	214	6,7,8,9,10,11	9
		4	Subgrade: Silty Sand with Gravel	295	6,7,8,9,10,11	9
25-1002	Massachusetts	2	Base: Crushed Gravel	N/A	-	-
		3	Subbase: Soil-Aggregate mixture (predom. Coarse-Grained)	74	6,7,8,9,11	7
		4	Subgrade: Poorly graded Sand with Silt	258	6,7,8,9,11	7
27-1018	Minnesota	2	Base: Gravel (uncrushed)	N/A	-	-
		3	Subgrade: Poorly graded Sand with Silt	261	6	1
		4	Subgrade: Poorly graded Sand with Silt	52	6	1
27-1028	Minnesota	3	Subgrade: Poorly graded Sand with Silt	200	6,8,10	4
		4	Subgrade: Poorly graded Sand with Silt	202	6,8,10	4
27-4040	Minnesota	2	Base: Gravel (uncrushed)	N/A	-	-
		3	Subgrade: Lean clay with Sand	45	6,10	2
		4	Subgrade: Lean clay with Sand	101	6,10	2
27-6251	Minnesota	2	Base: Gravel (uncrushed)	N/A	-	-
		3	Subgrade: Poorly graded Sand with Silt	626	8,10	3
		4	Subgrade: Poorly graded Sand with Silt	64	6,8,10	4
30-8129	Montana	2	Base: Crushed Gravel	N/A	-	-
		3	Subgrade: Poorly graded Sand with Silt	179	6,7,8,9,10,11	9
		4	Subgrade: Poorly graded Sand with Silt	50	6,7,8,9,10,11	9
31-0114	Nebraska			N/A	-	-
31-3018	Nebraska	3	Subgrade: Poorly graded Sand	44	8,9,10,11	4
		4	Subgrade: Poorly graded Sand	158	8,9,10,11	4
36-0801	New York			N/A	-	-
36-4018	New York	2	Subgrade: Silty Gravel with Sand	161	6,7,8,9,10	9
46-0804	South Dakota	2	Base: Crushed Stone	396	10	1
		3	Subgrade: Silty Clay	99	10	1
46-9187	South Dakota	2	Base: Gravel (uncrushed)	N/A	-	-
		3	Subbase: Gravel (uncrushed)	247	6,10,11	3
		4	Subgrade: Lean Inorganic Clay	96	6,10,11	4
50-1002	Vermont	2	Base: Crushed Gravel	N/A	-	-
		3	Subgrade: Poorly Graded Gravel With Silt and Sand	197	6,7,8,9,10,11	9
		4	Subgrade: Poorly Graded Gravel With Silt and Sand	175	6,7,8,9,10,11	9
56-1007	Wyoming	2	Base: Crushed Gravel	N/A	-	-
		3	Subgrade: Silty Sand with Gravel	194	6,8,9,10,11	8
		4	Subgrade: Silty Sand with Gravel	153	6,8,9,10,11	8
83-1801	Manitoba	2	Base: Crushed Gravel	N/A	-	-
		3	Subbase: Gravel (uncrushed)	N/A	-	-
		4	Subgrade: Silty Sand	238	11	1
83-3802	Manitoba	2	Subbase: Bound (treated)	554	6,10	2
		3	Subgrade: Fat Inorganic Clay	97	6,10	2
87-1622	Ontario	2	Base: Crushed Gravel	N/A	-	-
		3	Subbase: Sand	158	6,7,9,10	8
		4	Subgrade: Sandy Silt	251	6,7,9,10	8
89-3015	Quebec	2	Base: Crushed Stone	157	6,7,8,9,10,11	11
		3	Subgrade: Poorly Graded Sand	98	6,7,8,9,10,11	10
90-6405	Saskatchewan	2	Base: Crushed Gravel	N/A	-	-
		3	Subbase: Sand Asphalt	160	6,9	2
		4	Subgrade: Silty Sand	179	6,9	2

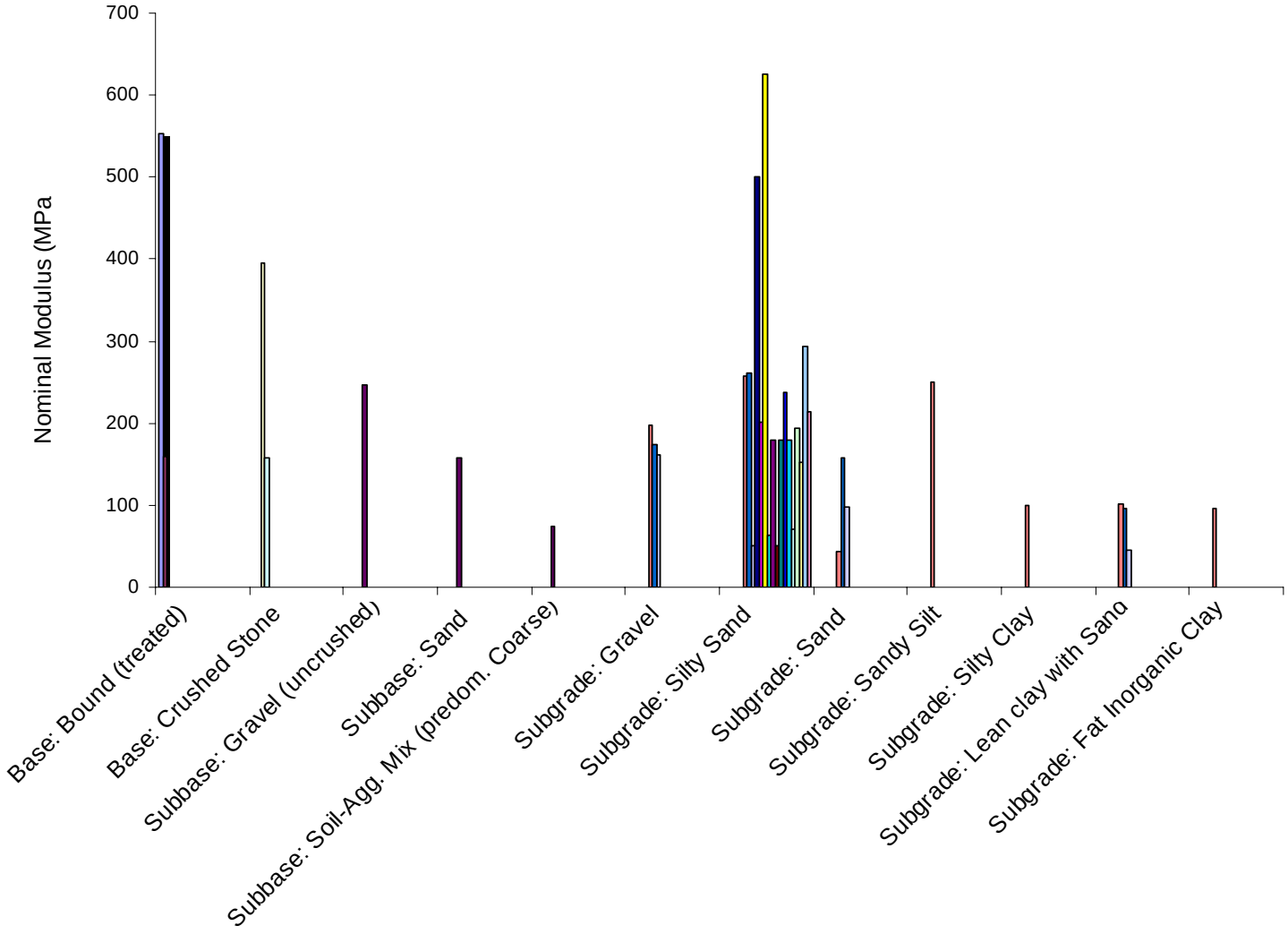

Figure 4.1 Nominal modulus for various base and subgrade types

4.2 FWD BASINS AS AN INDICATOR OF STRUCTURAL CAPACITY

Even under the best of circumstances, FWD backcalculation is as much an art as it is a science. It is especially difficult to backcalculate reliable layer moduli during the spring thaw and recovery because the pavement system is poorly modeled by elastic layer theory. During the winter freeze, low deflections make it difficult to obtain any consistent values and the backcalculated moduli often vary over an enormous range. As a result, for the 21 sites that exhibited freezing, just half of all the FWD tests produced usable subgrade moduli.

In light of the difficulty of backcalculation during the freeze/thaw period, a more rational approach is to use the FWD deflection basins directly. Deflection basin indices can be computed and compared over time to assess the condition of the pavement.

A falling weight deflectometer (FWD) test is performed by dropping a buffered mass onto a 12-in-diameter plate resting on the pavement surface, then measuring the resulting surface deflections at several different offsets. The LTPP data collection protocol (LTPP 2000) calls for deflection measurements 0, 203, 305, 457, 610, 914, and 1524 mm from the center of the loading plate in the direction of vehicle travel. In some testing applications, additional sensors are placed 1219 mm from the loading plate in the direction of travel and 305 mm behind the loading plate. In this report, the sensors are designated by their offset distance. Thus, D_{305} is the deflection measured by the sensor 305 mm from the load plate.

4.2.1 Literature Review of Basin Indices and Their Past Uses

Various pavement deflection indices or shape factors have been proposed for observing changes in pavement behavior over time. These include AREA (several different definitions exist),

Base Curvature Index (BCI), Base Damage Index (BDI), Maximum Deflection, and Surface Curvature Index (SCI) as defined in Table 4.2.

Table 4.2 Deflection Basin Indices

Parameter	Formula
AREA	$6 * [(D_0/D_0) + (2*D_{305}/D_0) + (2*D_{610}/D_0) + (D_{914}/D_0)]$
Deflection at Load Plate (D_0)	D_0
Deflection at 1524 mm (D_{1524})	D_{1524}
Base Curvature Index (BCI)	$D_{610} - D_{914}$
Surface Curvature Index (SCI)	$D_0 - D_{305}$
Basin Damage Index (BDI)	$D_{305} - D_{610}$
Partial Area (PA), m^2	$[(D_{457}+D_{610})/2*0.153] + [(D_{610}+D_{914})/2*0.304] + [(D_{914}+D_{1524})/2*0.610]$
Subgrade Damage Index (SDI)	$D_{610} - D_{1524}$
Subsurface Index (SI)	$D_{305} - D_{1524}$
D_x is the surface deflection measured *x* mm from the loading plate. Typical distances are 0, 203, 305, 457, 610, 914, and 1524 mm from the loading plate (LTPP, 2000).	

The AREA parameter describes the normalized cross-sectional area of the deflection basin, and may be calculated using the deflections at all seven sensors or certain combinations as defined above (VanDeusen et al.1998; Lukanen et al. 1999). The deflection at the outermost sensor, D_{1524}, is assumed to represent the subgrade condition (DeBruin et al., 2002). The SCI is supposed to represent the upper base and subbase, whereas the BDI represents the upper subgrade.

The SCI, BDI, and D_0 were used to evaluate spring thaw conditions for Mn/ROAD test sections (VanDeusen et al.1998). A partial deflection basin area (based on D_{457}, D_{610}, D_{914}, and D_{1524})

was shown by Kestler et al. (1999) to be a good indicator of thaw weakening and recovery for low volume roads, and seemed to correlate well with the subgrade moisture content.

Two additional indices, similar to BCI and BDI, were defined specifically for this study. The first is the Subgrade Damage Index (SDI), which is defined as $D_{610} - D_{1524}$. It is another interpretation of the subgrade condition. The second index, the Subsurface Index (SI), is defined as $D_{305} - D_{1524}$. It is thought to represent the entire subsurface state from the base through the subgrade. However, since the sensor spacing is standardized, the relationship between any two sensors and a particular layer in the pavement system varies some with pavement layer thickness. Thus, the portion of the pavement system that a particular index is said to represent is somewhat approximate. For purposes of investigating the change in response of the base and subgrade during freezing and thaw, indices based on D_0 would not be expected to be as sensitive as those at greater spacings.

When expressed relative to their values under nominal pavement conditions, each of these deflection indices would be expected to decrease during freezing, when the pavement capacity is greatest, then increase during the spring thaw to a value greater than nominal, and finally recover to the nominal value during the summer. This generic response is depicted in Figure 4.2.

Deflection indices were computed for the SMP sites, based on the deflection data from the middle of the traffic lane and from the FWD test performed closest to the instrumentation core hole. For each test, the drop height producing a contact pressure closest to 550 kPa was used. Thus, all of the indices were computed for a stress level corresponding to that often considered in pavement design.

To accentuate seasonal trends, FWD index data from several years were superimposed. Because the timing of the freeze and thaw changes from one year to the next, it can be difficult to

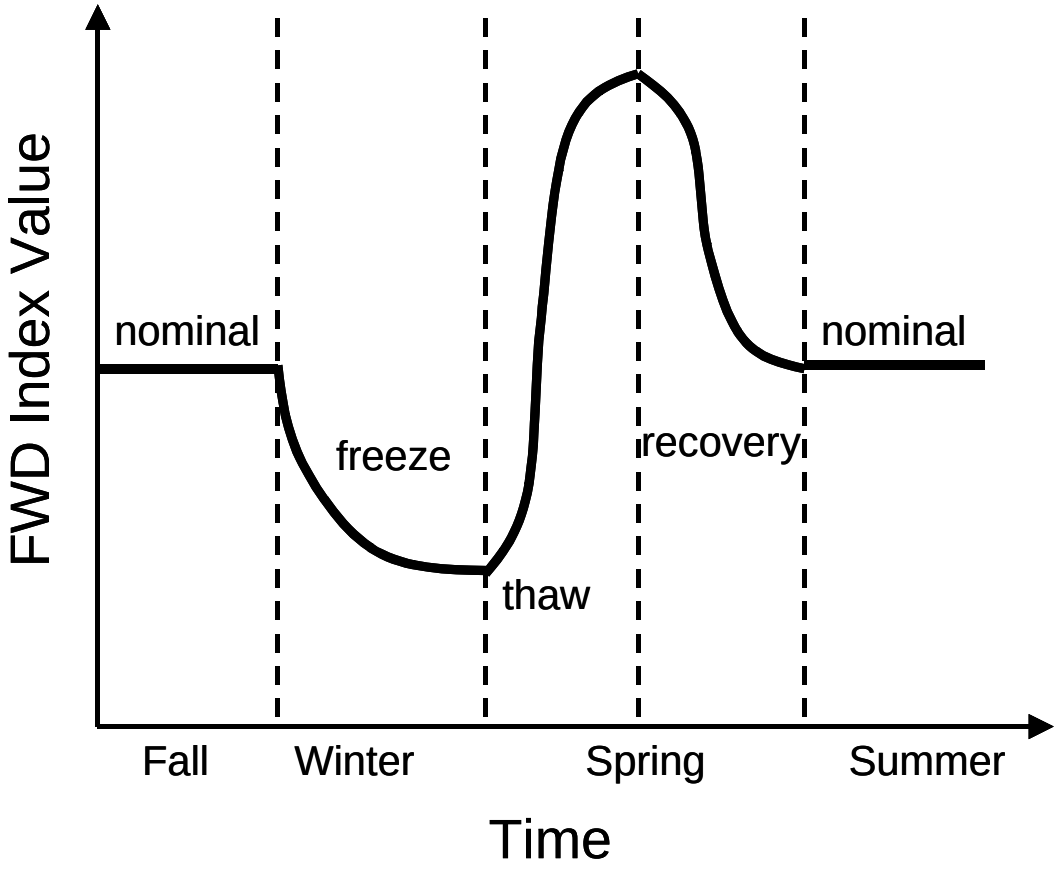

Figure 4.2 Typical seasonal variation of FWD indices

directly compare data from different years. Therefore, the test dates in any given year were expressed relative to the year's four freeze milestones: first freeze, full freeze, first thaw, and full thaw (Section 2.4). Then the FWD test dates were normalized relative to the mean milestone dates for each site. For example, assume that for a given year the period between First Freeze and First Thaw is 37 days, and FWD tests were conducted 20 days after the First Freeze. The deflection indices computed from those tests would be plotted 20/37^{ths} of the time between the mean First Freeze date and the mean First Thaw date for that site. If, the next year, the FWD tests are conducted 15 days after the First Freeze and 42 days elapse between First Freeze and First Thaw, then the basin indices computed from the new FWD tests are plotted 15/42^{nds} of the way between the mean First Freeze and First Thaw dates. This way, all of the index data for a given site can be superimposed on a single graph. Specific cases are discussed below. The seasonal variation of indices D_{1524}, BCI, SDI, SI, and PA are provided in Appendices O, P, Q, R, and S, respectively.

4.2.2 Seasonal Changes in Basin Indices at No-freeze Sites

Figures 4.3 through 4.5 show the Base Curvature Index (BCI), Subgrade Damage Index (SDI), and Subsurface Index (SI), respectively, for Alabama site 01-0101. A time scale originating with October 1 was selected so the critical winter freeze and spring thaw periods would be centered on the time scale. A trend line has been drawn through the data. This site, which has a 190-mm (7.5-in.) asphalt layer and a 200-mm (7.9-in.) base layer over a sandy silt subgrade, demonstrates behavior typical of many no-freeze sites. The seasonal variation of BCI and SDI is minimal. The plot of SI (the difference between D_{305} and D_{1524}) has a value about twice that of SDI (the difference between D_{610} and D_{1524}), and displays a somewhat greater decrease during winter than does the SDI. The explanation is that an index including sensor D_{305} reflects a greater contribution of the stiffer AC

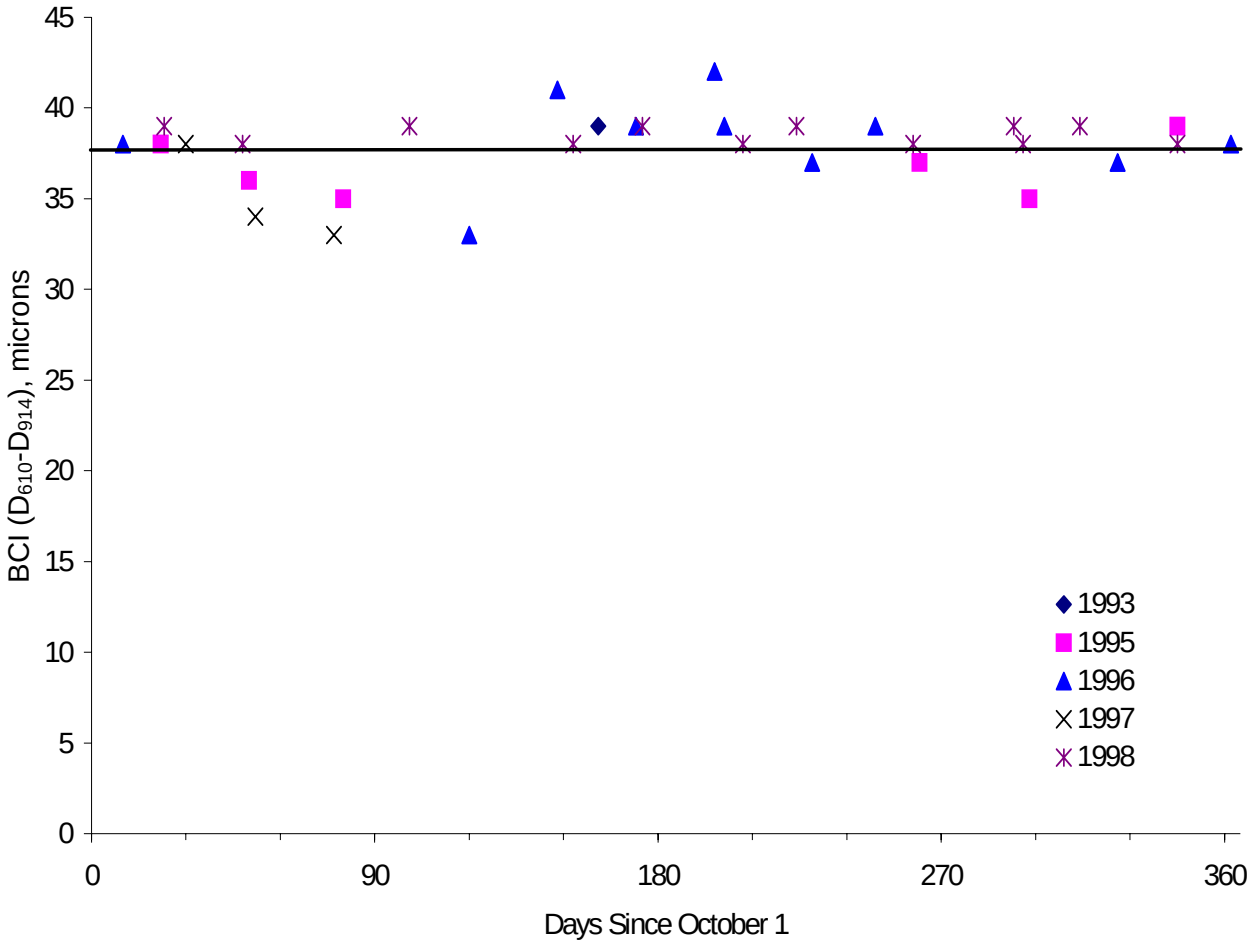

Figure 4.3 Base Curvature Index (BCI) at Site 1-0101-1 (Sandy Silt Subgrade)

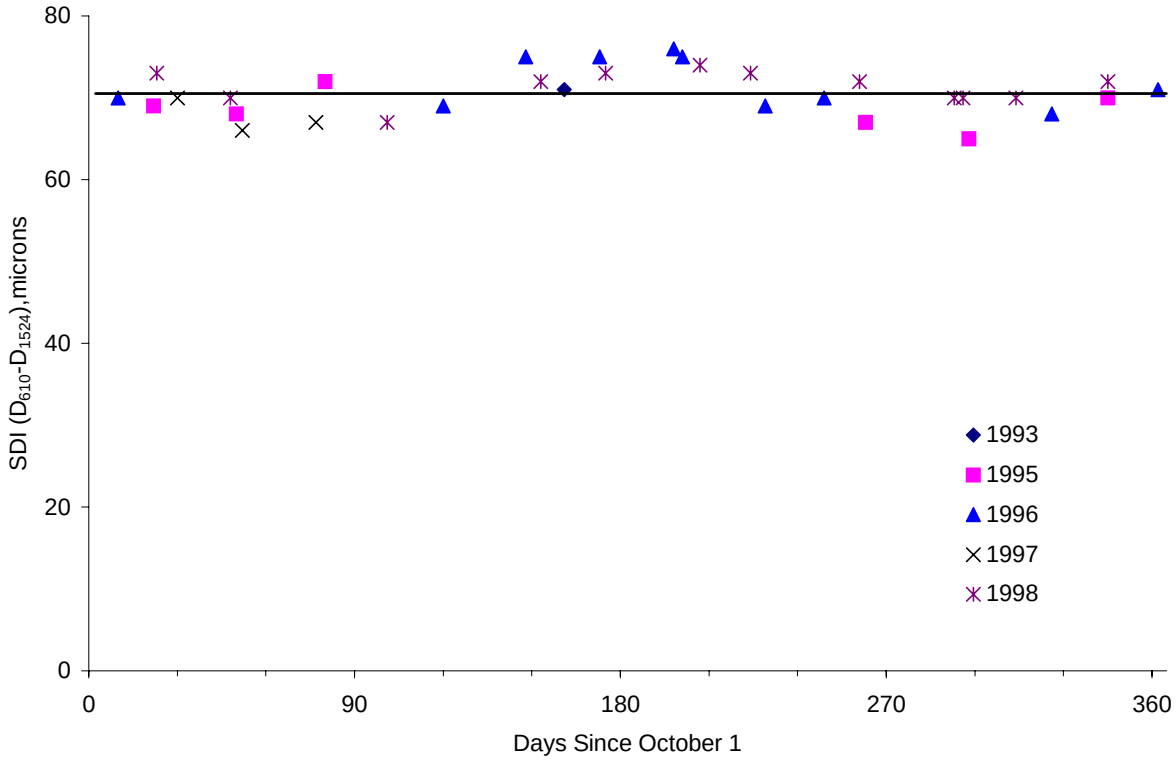

Figure 4.4 Subgrade Damage Index (SDI) at Site 1-0101-1 (Sandy Silt Subgrade)

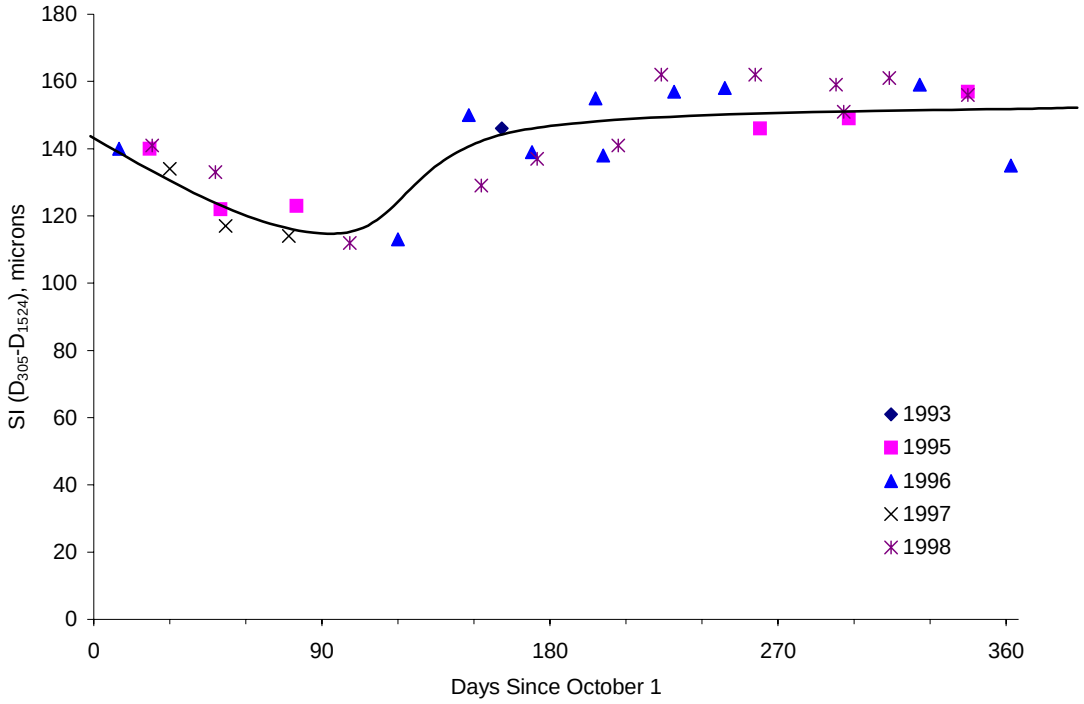

Figure 4.5 Subsurface Index (SI) at Site 1-0101-1 (Sandy Silt Subgrade**)**

response during low temperature periods than does an index based on D_{610}, which reflects the condition of materials at a greater depth. This suggests that the choice of basin index to detect the start and end of the spring thaw may change from site to site depending on the thickness of the pavement layers. Regardless, neither index demonstrates the significant seasonal response expected at the freeze sites.

4.2.3 Seasonal Changes in Basin Indices at Freezing Sites

The pavement response as a function of freeze state was investigated by comparing the computed deflection indices over time (normalized to the mean freeze/thaw milestones). Periods of interest are those where pavement capacity is greater due to freezing or lower due to base/subgrade thawing. Based on the defined freeze milestones, it is anticipated that the pavement capacity will be greatest between First Freeze and Full Freeze, and least between First Thaw and Full Thaw. As the pavement recovers from the thaw, the capacity should gradually return to near that which existed prior to freezing. Since it is desirable to predict the timing of the increased pavement capacity during freezing and the onset of the thaw weakening, an effective FWD deflection basin index should be capable of reflecting these changes in pavement response throughout the year.

4.2.3.1 Typical deflection indices during freeze/thaw at wet sites

The FWD indices D_{1524}, BCI, SDI, SI, and PA were calculated for all the flexible pavement SMP sites in freeze zones (Appendices O-S). Typical data are shown here for Minnesota site 27-6251, which is listed as a wet-freeze site. Wet regions are defined as those areas where the average annual rainfall is more than 500 mm (20 in.), and freeze regions are those areas with an average freezing index of over 85 ^{o}C days (150 ^{o} F days) (LTPP 2000).

Figures 4.6 through 4.11 compare the deflection indices D_{1524}, BCI, SDI, SI, AREA, and PA for Minnesota site 27-6251. Site 27-6251 is a wet-freeze site, with 190 mm (7.4 in.) of asphalt and 250 mm (10 inches) of granular base. The subgrade is a poorly graded sand with silt. The response from several years is superimposed on the mean milestone dates, and is reasonably consistent from year to year. The indices D_{1524}, BCI, SDI, SI and PA, all decrease to a low value after the First Freeze milestone, corresponding to increased pavement capacity. The Base Curvature Index (BCI) in Figure 4.7 has some negative values when the pavement is frozen and deflections are lower. This may be due to the proximity of sensors used in the determination BCI, and the fact that the deflections are very small when the site is frozen. After First Freeze, the values of the indices begin to increase during the thaw period (which may occur before the time of maximum freeze depth), corresponding to a decrease in pavement capacity. If the results from individual years are considered, the indices may be slightly elevated immediately after thaw prior to returning to the nominal value. In Figure 4.10, the index AREA, which is a traditional deflection index, does not appear to reflect seasonal changes in the pavement response and does not seem to be a good indicator of changes in subgrade response due to freezing and thawing.

Figures 4.6 through 4.11, suggest that the indices D_{1524}, BCI, SDI, SI and PA may be useful as predictors of increased pavement capacity when frozen. Changes in these indices may be used to determine the best dates to allow winter overload permits. Index D_{1524} is somewhat more variable than the others, which are functions of several sensors. None of the indices indicate a significant period of thaw weakening, which would be reflected by index values significantly greater than the nominal value. This is investigated further below.

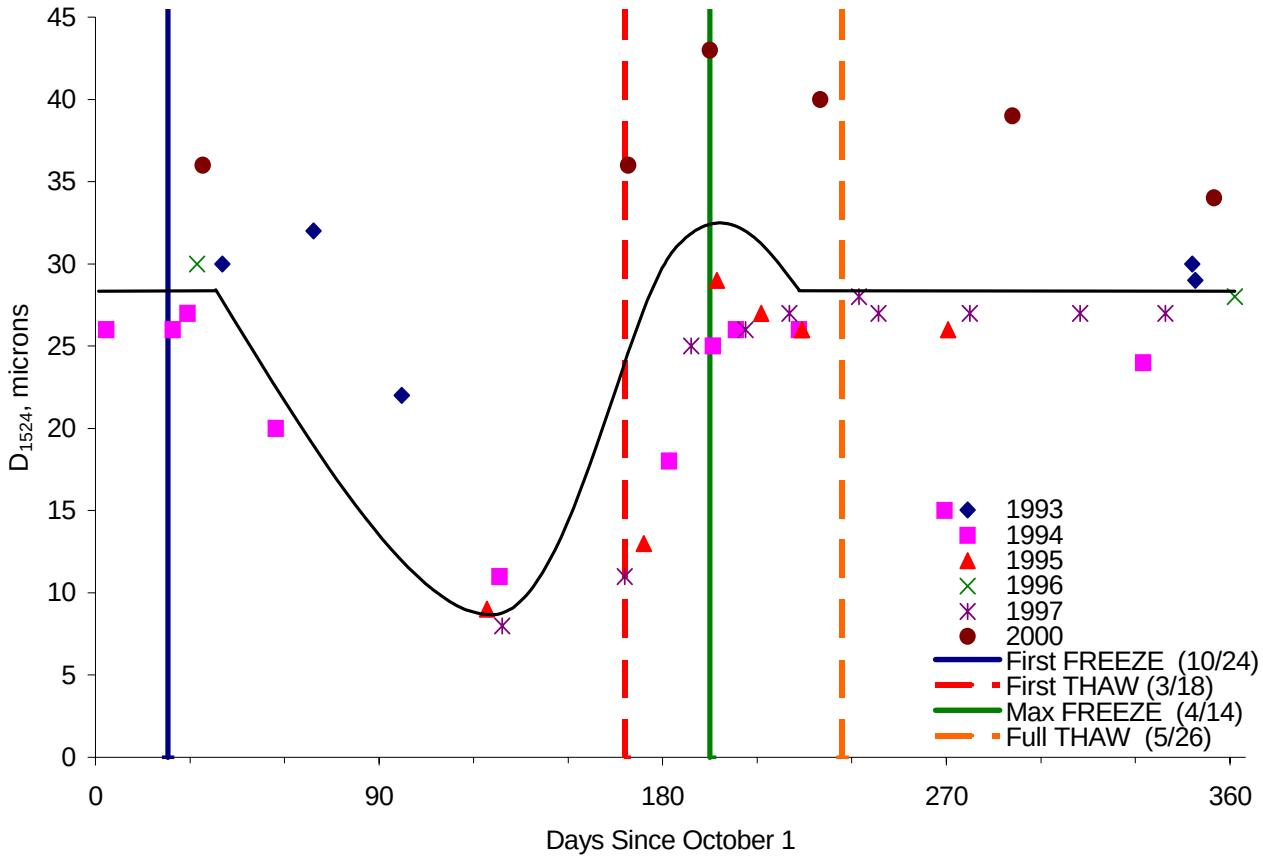

Figure 4.6 Deflection D_{1524} at site 27-6251 (poorly graded sand with silt subgrade)

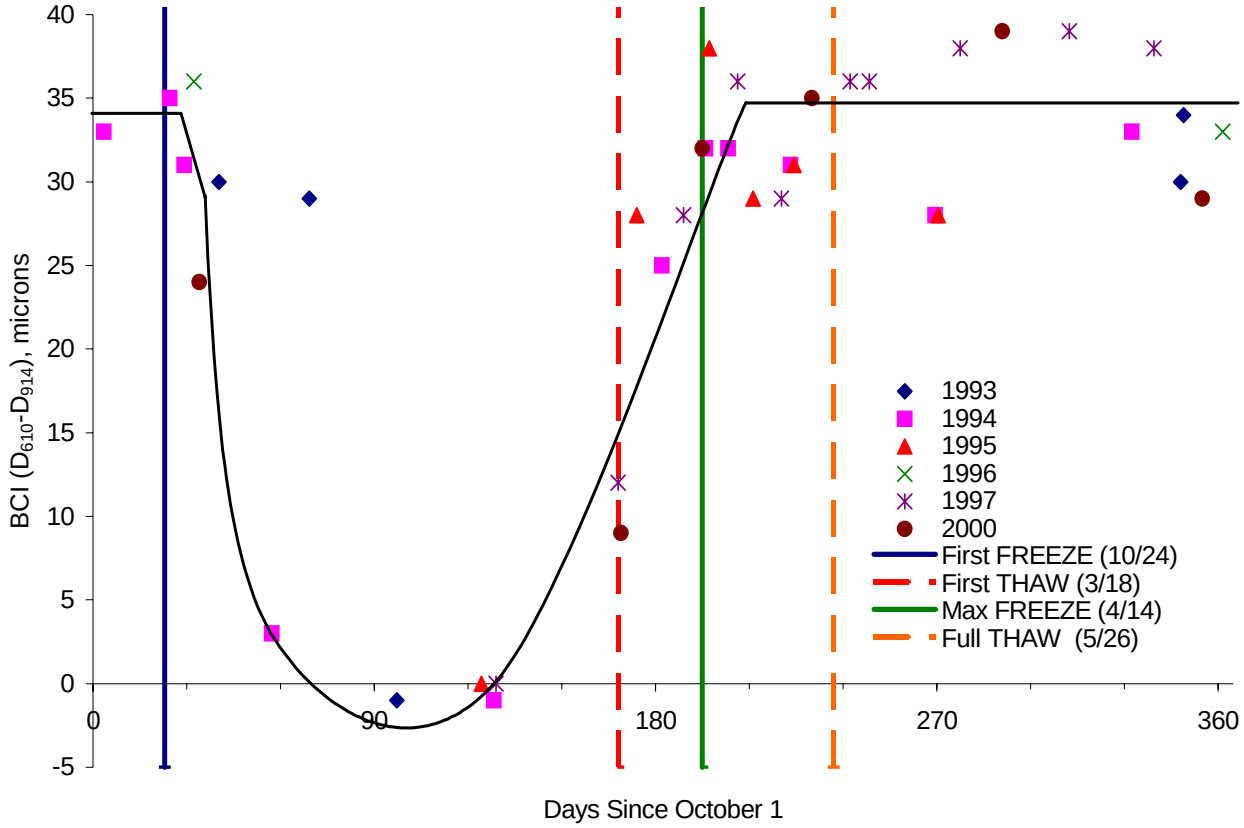

Figure 4.7 Base Curvature Index (BCI) at site 27-6251 (poorly graded sand with silt subgrade)

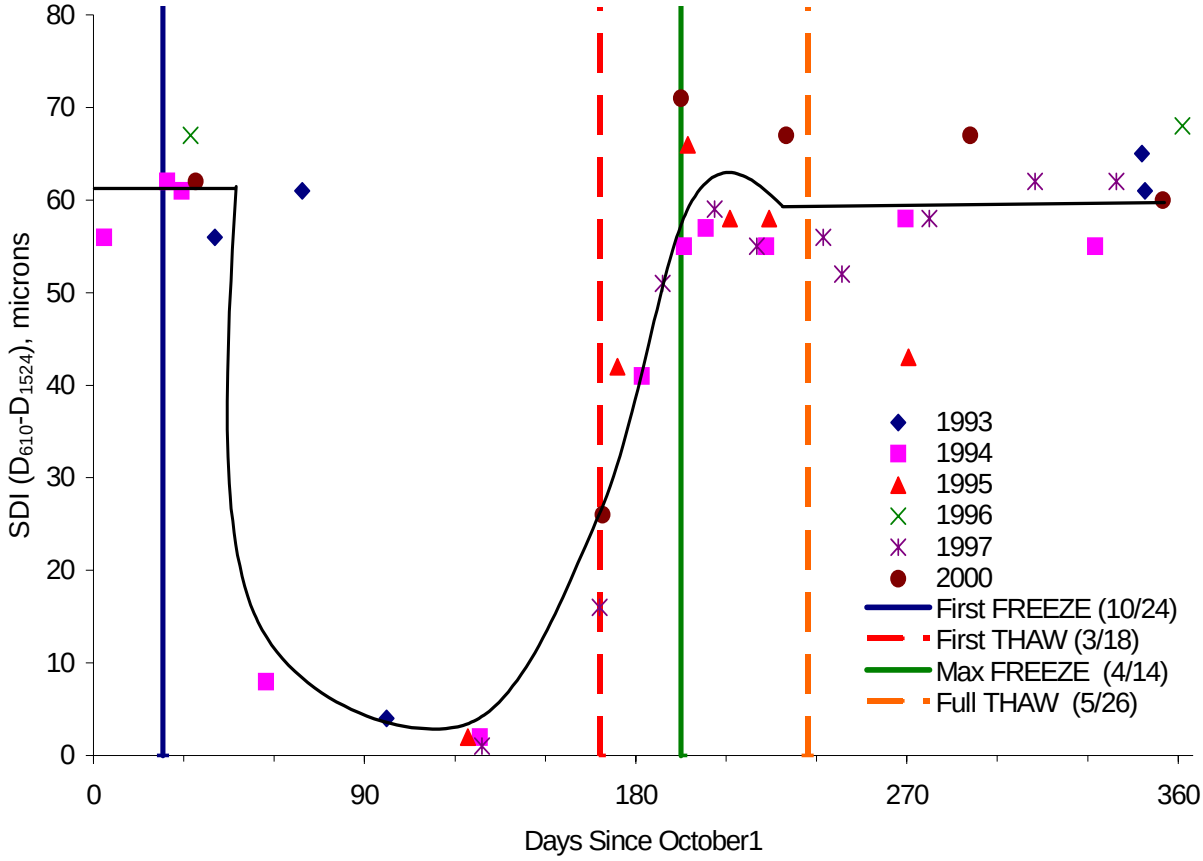

Figure 4.8 Subgrade Damage Index (SDI) at site 27-6251 (poorly graded sand with siltsubgrade)

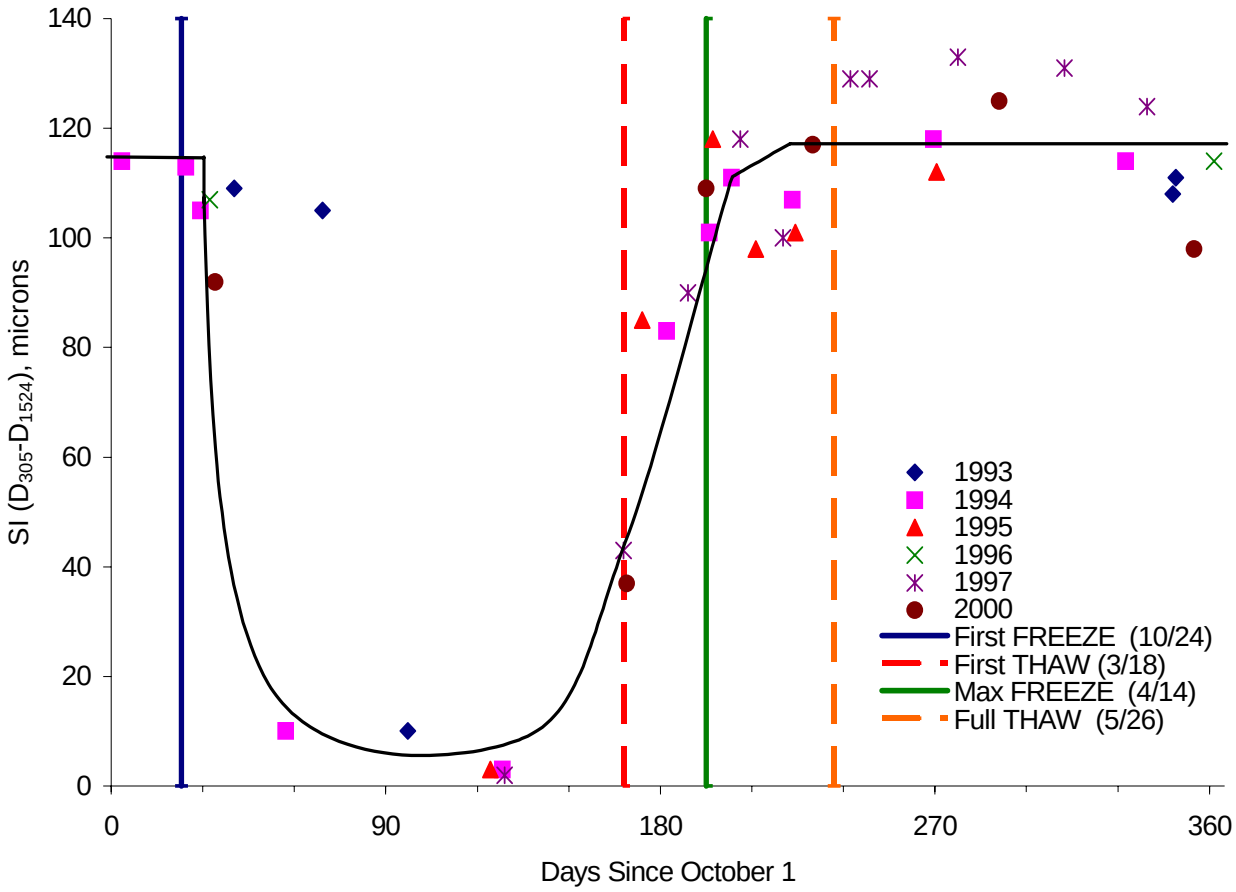

Figure 4.9 Subsurface Index (SI) at site 27-6251 (poorly graded sand with silt subgrade)

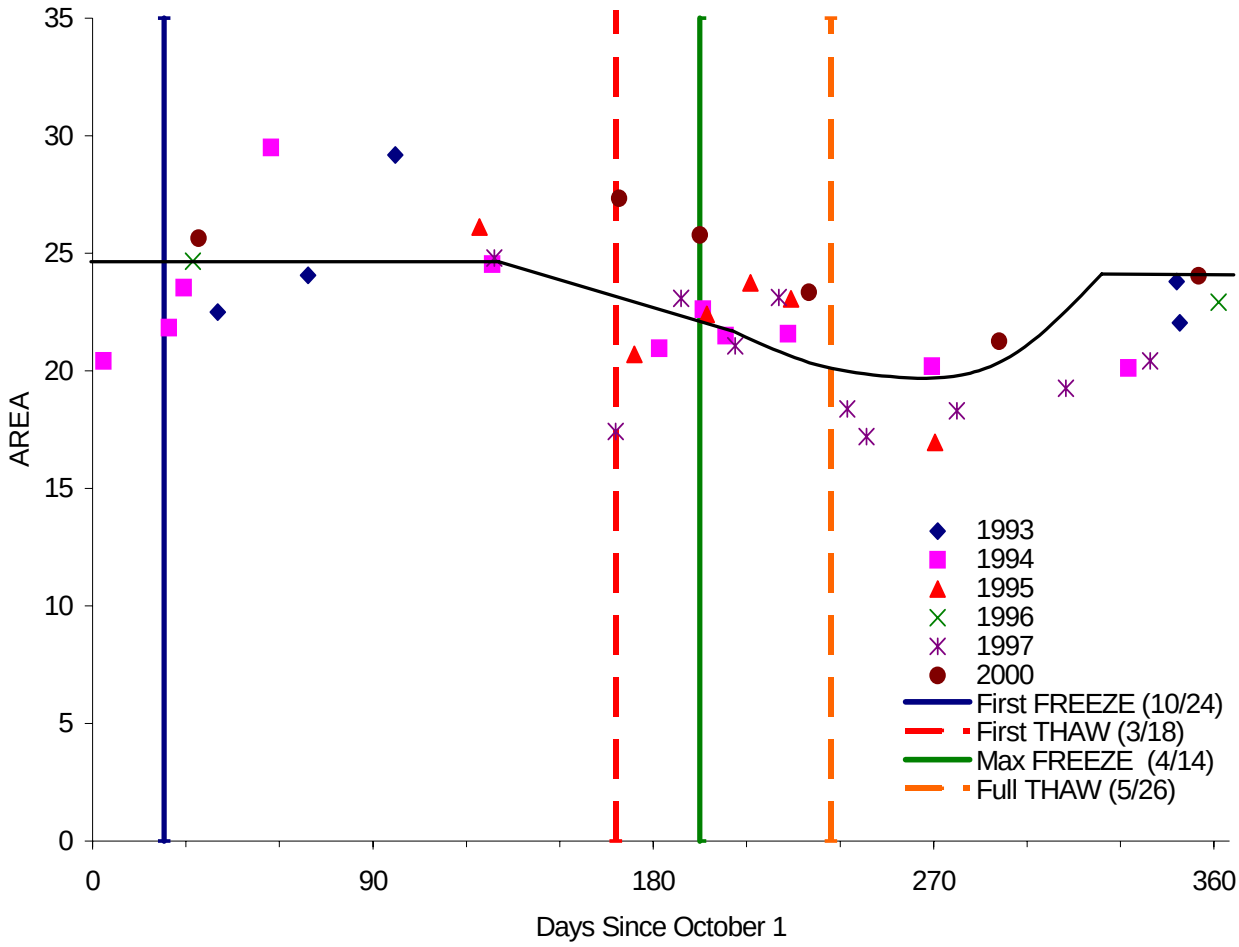

Figure 4.10 Index AREA at site 27-6251 (poorly graded sand with silt subgrade)

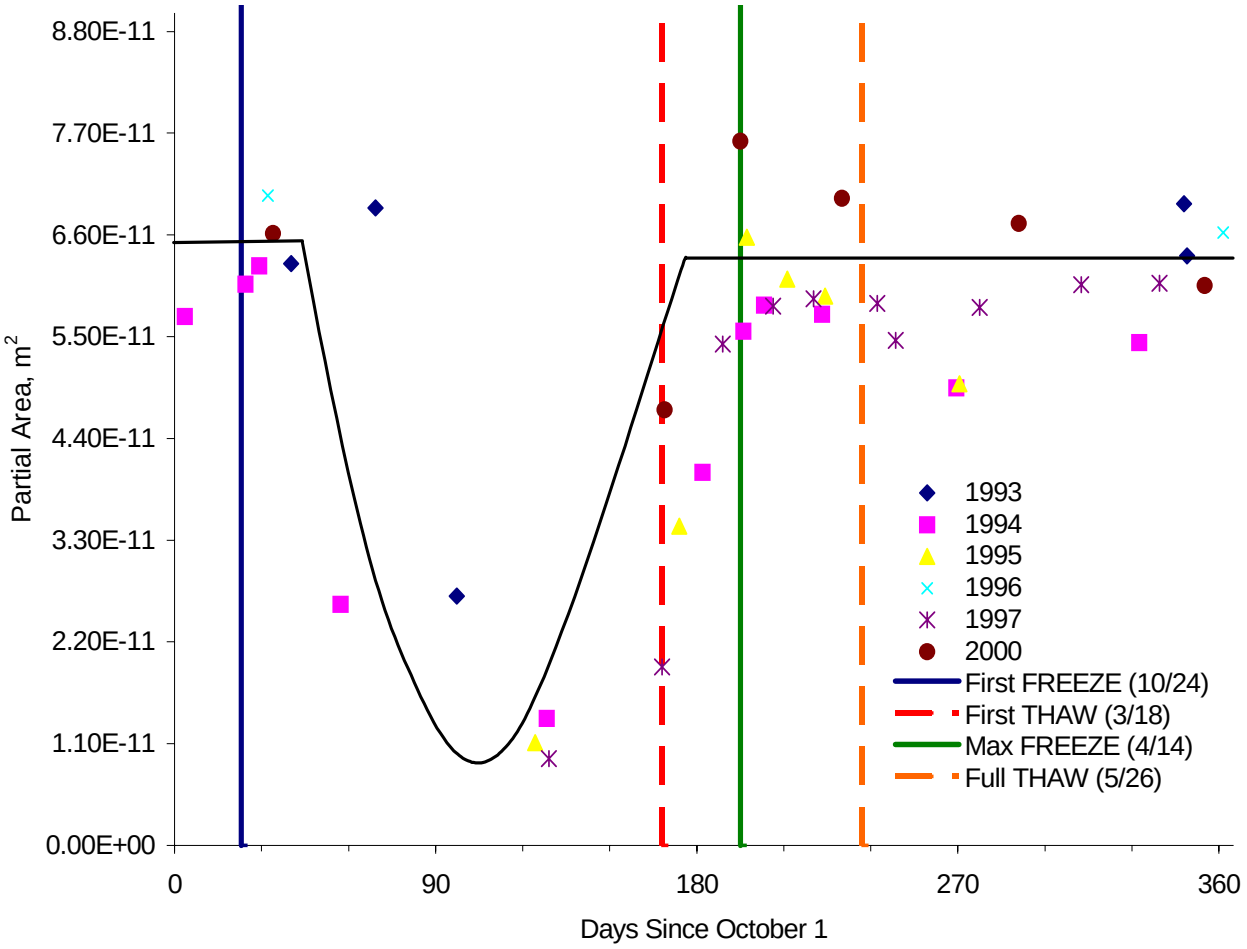

Figure 4.11 Index PA at site 27-6251 (poorly graded sand with silt)

4.2.3.2 Typical deflection indices during freeze thaw at dry sites

For comparison purposes, Figures 4.12 and 4.13 show the Subsurface Index (SI) and the Subgrade Damage Index (SDI) for the Saskatchewan site 90-6405, a dry-freeze site. The response during the freeze period of the year is similar to the wet-freeze sites shown previously, with a significant decrease in index during the freeze period. This further suggests that these indices may be useful in distinguishing periods for overload permits. As in the wet-freeze sites above, a post- freeze increase in the indices during thaw weakening is not strongly exhibited.

4.2.3.3 Comparison of index SI at all freeze thaw sites

Several of the defection indices identified above seem to detect the changes in pavement response that occur during the freeze and thaw periods. Most of the SMP sites (both wet and dry sites) that experienced freezing demonstrated an obvious decrease in index value during the freeze period, yet few showed significant thaw weakening. Figure 4.14 is a schematic of the typical seasonal variation of SI (the difference between the deflection at 305 mm and the deflection at 1524 mm) and depicts two different responses: the solid line corresponds to a pavement that freezes in the winter but does not suffer from thaw weakening in the spring, and the dotted line corresponds to a pavement that suffers considerable thaw weakening. The typical seasonal variation of indices BCI, SDI, and PA is similar.

The seasonal variation of SI for all the frozen SMP sites was qualitatively evaluated with respect to how well the response agreed with the generic freeze response (solid line) in Figure 4.14, and the results are summarized in Table 4.3. The sites with strong or moderate agreement with the freeze response were further evaluated with respect to how well the response agreed with the thaw response (dotted line). While this type of qualitative analysis is very subjective, it can be useful to

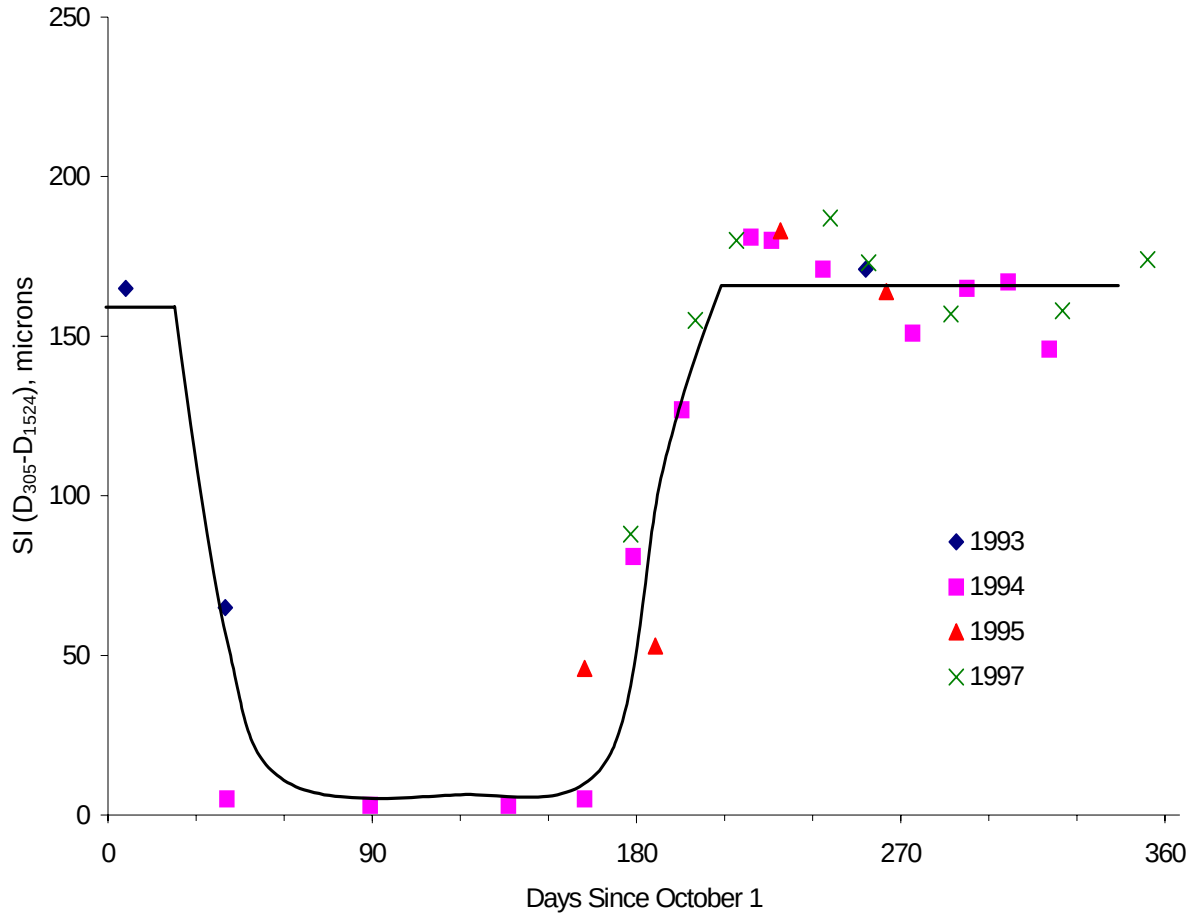

Figure 4.12 Subsurface Index (SI) at site 90-6405 (silty sand subgrade)

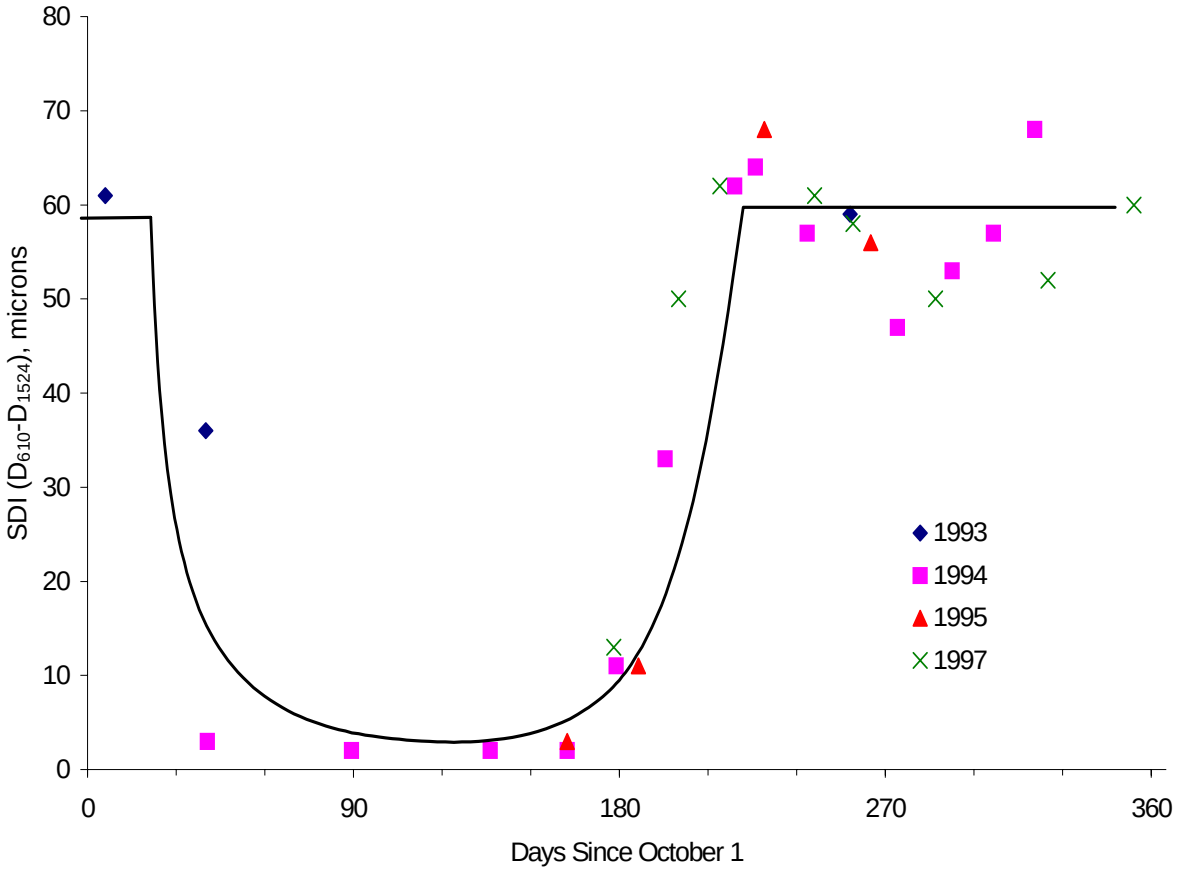

Figure 4.13 Subgrade Damage Index (SDI) at site 90-6405 (Silty sand subgrade)

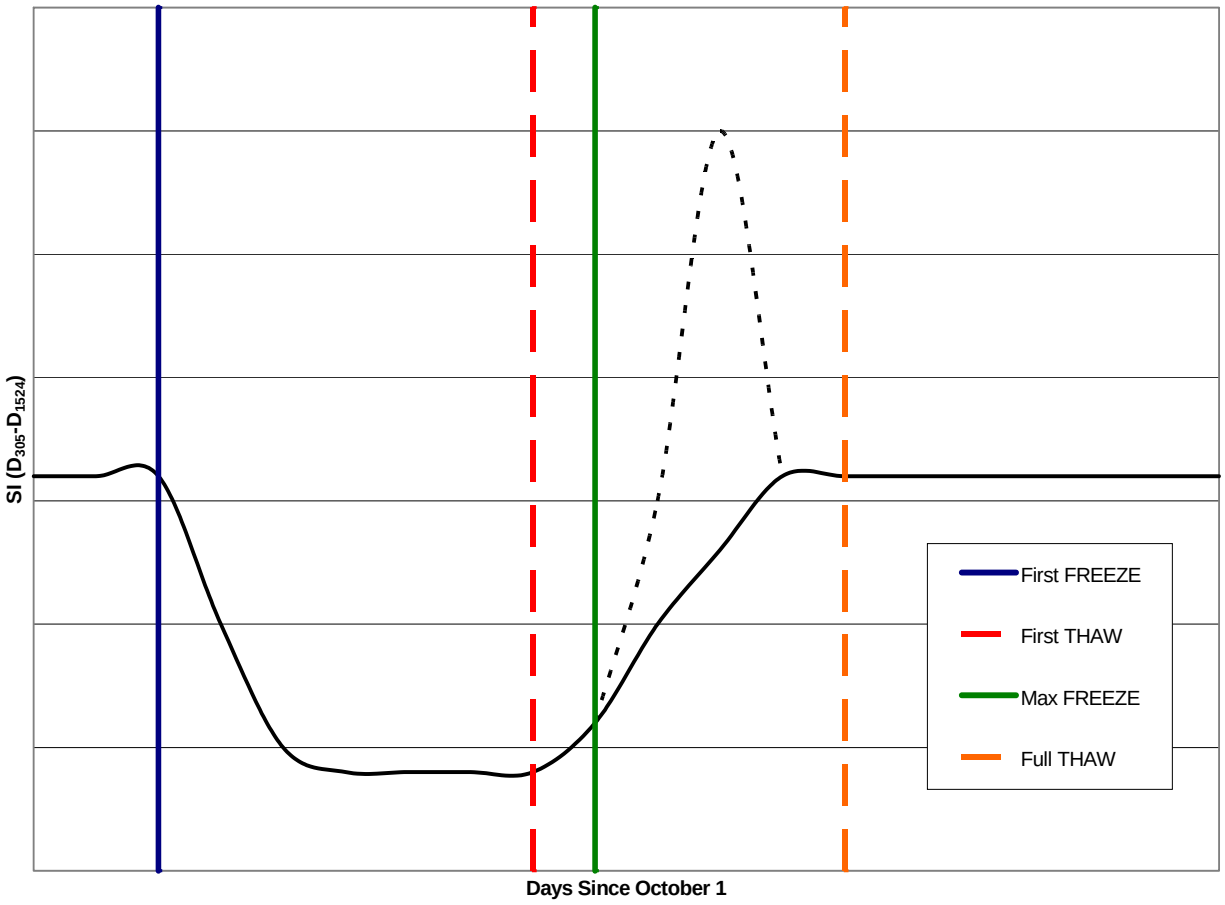

Figure 4.14 Generic FWD deflection index response
(Solid line without thaw weakening; dotted line with thaw weakening)

summarize the observed response. Of the 16 flexible pavement sites with recorded freezing (nine wet and seven dry), all but two wet sites (one moderate and one weak) demonstrated strong agreement with the typical freeze response. This suggests that even the dry-freeze sites may have sufficient soil moisture to show an increase in capacity during the winter freeze.

The thaw weakening response was not consistently observed in the indices from the SMP sites, and when it was observed it was very weak. In fact, there was little difference between the thaw response in the wet and dry sites. Of the 16 flexible pavement sites with recorded freezing, none demonstrated the increase in measured deflections that would be expected during a thaw weakening period. There are several possible reasons that a thaw-weakening response was not observed:

- the thaw period occurred between the site visits for FWD testing;
- the subgrade soils are not particularly frost-susceptible;
- the pavements were designed to minimize thaw weakening.

The response during thaw-weakening periods will be investigated further in the next section.

Table 4.3 Comparison SMP freeze sites with "typical" SI behavior in Figure 4.14

State	Site ID	Climatic Region	Subgrade Type	Years with FWD Data Collection (No Freeze Data in 2000)	Agreement with Generic Response (S=Strong, M=Moderate, W=Weak)	
					Freeze	Thaw Weakening
ME	23-1026	Wet-freeze	Coarse Grained Soil: Silty Sand with gravel; Subgrade (Untreated)	1993 1994 1995 1996 1997	S	M
MA	25-1002	Wet-freeze	Coarse-Grained Soils: Poorly Graded Sand with Silt); Subgrade (Untreated)	1993 1994 1995 1996 1997 (Only freeze in 1994)	M	W
MN	27-1018	Wet-freeze	Coarse-Grained Soils: Poorly Graded Sand with Silt); Subgrade (Untreated)	1993 1994 1995 1996 1997	S	M
MN	27-1028	Wet-freeze	Coarse-Grained Soils: Poorly Graded Sand with Silt); Subgrade (untreated)	1993 1994 1995 1996 1997	S	W
MN	27-6251	Wet-freeze	Coarse-Grained Soils: Poorly Graded Sand with Silt)	1993 1994 1995 1996 1997 2000	S	W
NE	31-0114	Wet-freeze	Fined-Grained Soil: Silty Clay; Subgrade (Untreated)	1995 1996 1998 2000	W	-
NY	36-0801	Wet-freeze	Coarse-Grained Soil: Silty Sand; Subgrade (untreated)	1995 1996 1997 1998 2000 (Only froze in 1996)	S	M
VT	50-1002	Wet-freeze	Coarse-Grained Soils: Poorly Graded Gravel With Silt and Sand; Subgrade (untreated)	1993 1994 1995 1996 1997 2000 (Only Froze 1994 & 1995)	S	W
ON	87-1622	Wet-freeze	Fine-Grained Soils: Sandy Silt; Subgrade (Untreated)	1993 1994 1995 1997	S	M
MT	30-8129	Dry-freeze	Fined-Grained Soils: Gravely Lean Clay With Sand; Subgrade (Untreated)	1992 1993 1994 1995 1997	S	M
MB	83-1801	Dry-freeze	Coarse-Grained Soil: Silty Sand; Subgrade (untreated)	1993 1994 1995 1997 2000	S	W
SK	90-6405	Dry-freeze	Coarse-Grained Soil: Silty Sand; Subgrade (Untreated)	1993 1994 1995 1997	S	M
SD	46-9187	Dry-freeze	Fine-Grained Soils: Lean Inorganic Clay; Subgrade (Untreated)	1990 1991 1992 1994 1995 1996 1997	S	W
WY	56-1007	Dry-freeze	Coarse Grained Soil: Silty Sand with gravel; Subgrade (untreated)	1993 1994 1995	S	M
SD	46-0804	Dry-freeze	Fined-Grained Soil: Silty Clay; Subgrade (untreated)	1994 1995 1997 2000	S	W
ID	16-1010	Dry-freeze	Coarse-Grained Soil: Silty Sand; Subgrade (Untreated)	1993 1994 1995 1996 1997	S	W

4.3 INVESTIGATION OF FREEZE/THAW/RECOVERY USING FWD DATA FROM OUTSIDE THE LTPP

Three data sets from outside the LTPP SMP database were studied to supplement the investigation discussed above. These data sets, which contain much more FWD data during the critical thaw period, can be used to help validate the conclusions drawn from the LTTP data by filling in some of the gaps mentioned above. The data were obtained from the U.S. Army Frost Effects Research Facility (FERF) in Hanover, New Hampshire; from a test site in Barre, Vermont; and from the Mn/ROAD low-volume road test site. Below, FWD index data is reviewed for comparison with the response observed in the LTPP sites above.

4.3.1 FERF Tests

A series of controlled experiments was performed at the U.S. Army Frost Effects Research Facility (FERF) to investigate freeze/thaw effects on general aviation airport pavements (Janoo and Berg, 1990). The test sections consisted of 75 mm (3 in.) of asphalt over a 230-mm (9-in) crushed stone base. One test section had a silty sand (A–2–4 or SM) subgrade and one had a silty clay (A–4 or CL) subgrade. The test sections were artificially frozen to an approximate depth of 1.25 m (48 in.) and allowed to thaw naturally. FWD tests were conducted prior to freezing then daily during the thaw period.

Several candidate FWD indices were computed from the FERF data, including AREA, D_0, D_{1524}, BCI, BDI, SDI, SI. The indices SI and SDI , which were among the best predictors based on the LTPP SMP data above, are shown in Figures 4.15 through 4.18 for the SM and CL subgrades. The data is plotted relative to the first day of thaw, which was controlled in the FERF experiments. Both indices clearly depict the thaw weakening and recovery periods, with peak thaw values

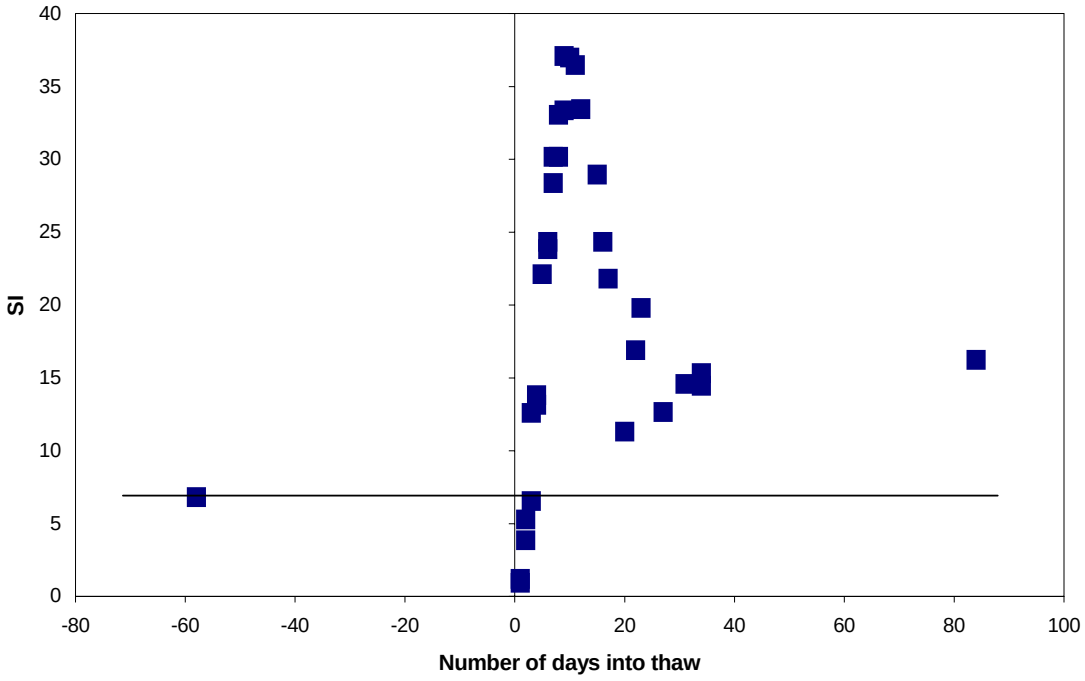

Figure 4.15 Subsurface Index (SI) from the FERF data (SM subgrade)

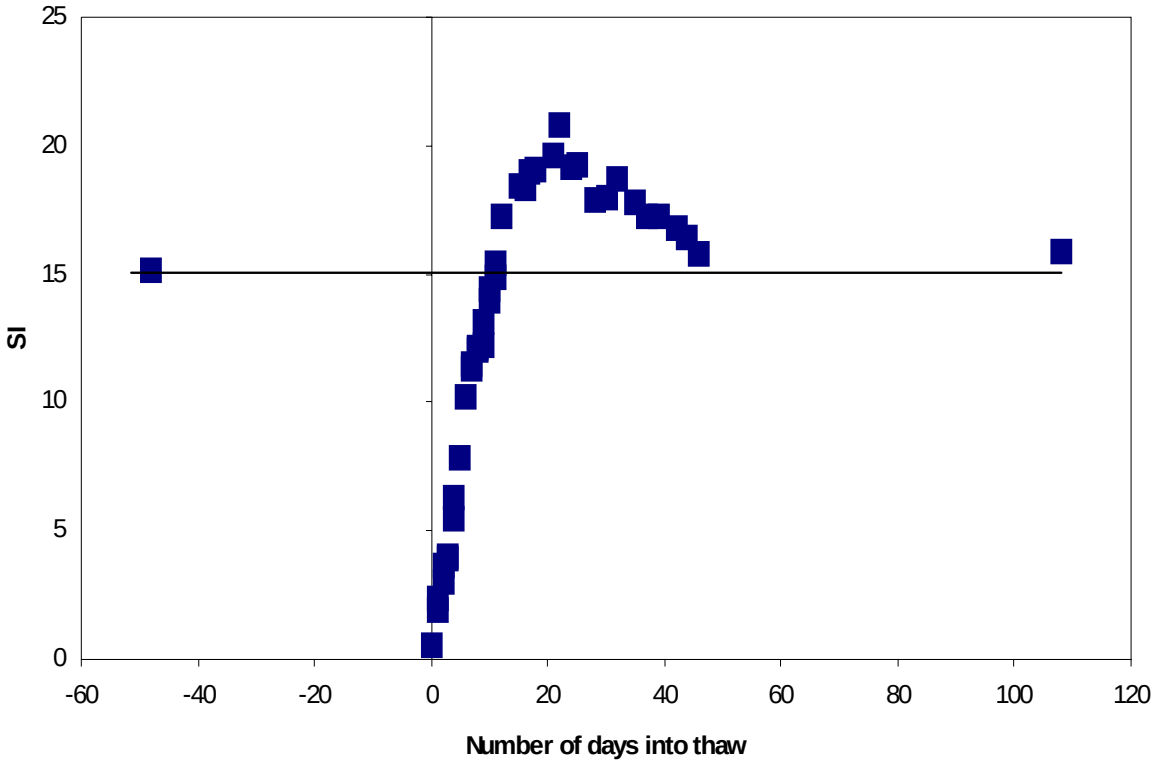

Figure 4.16 Subsurface Index (SI) from the FERF data (CL subgrade)

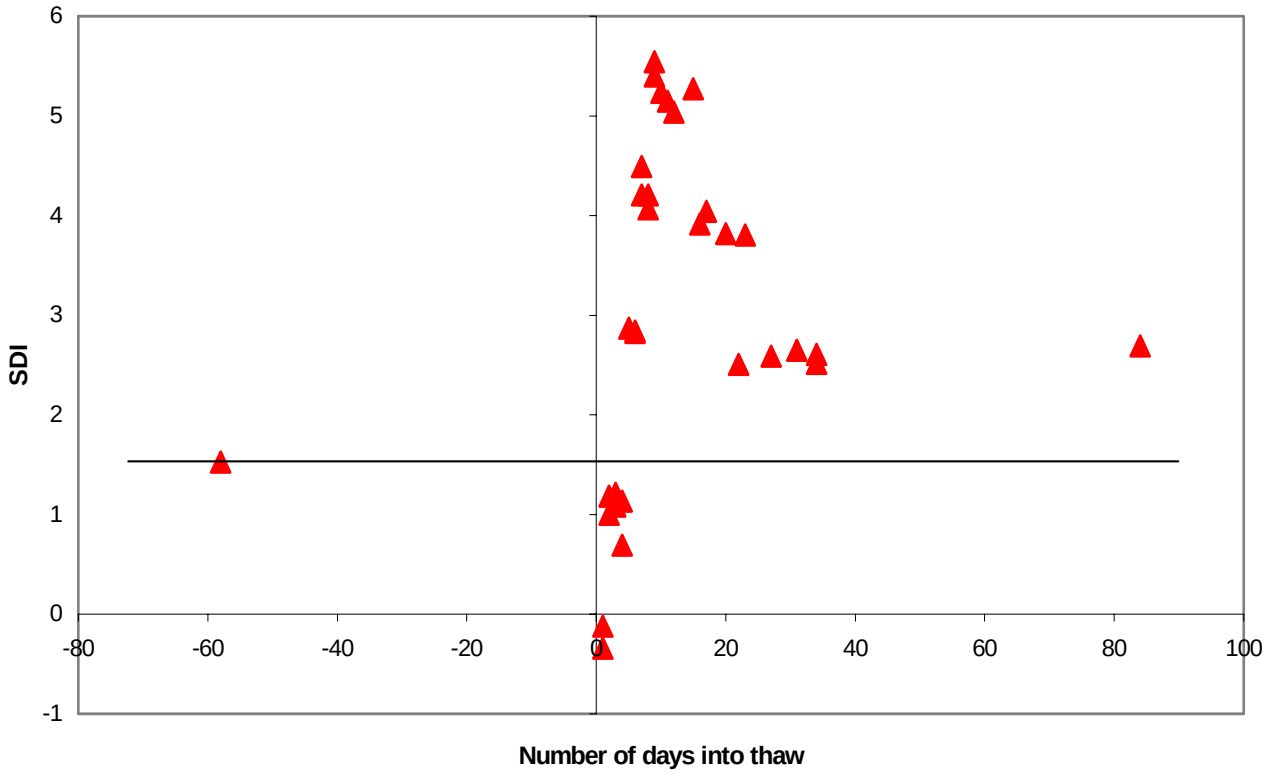

Figure 4.17 Subgrade Damage Index (SDI) from the FERF data (SM subgrade)

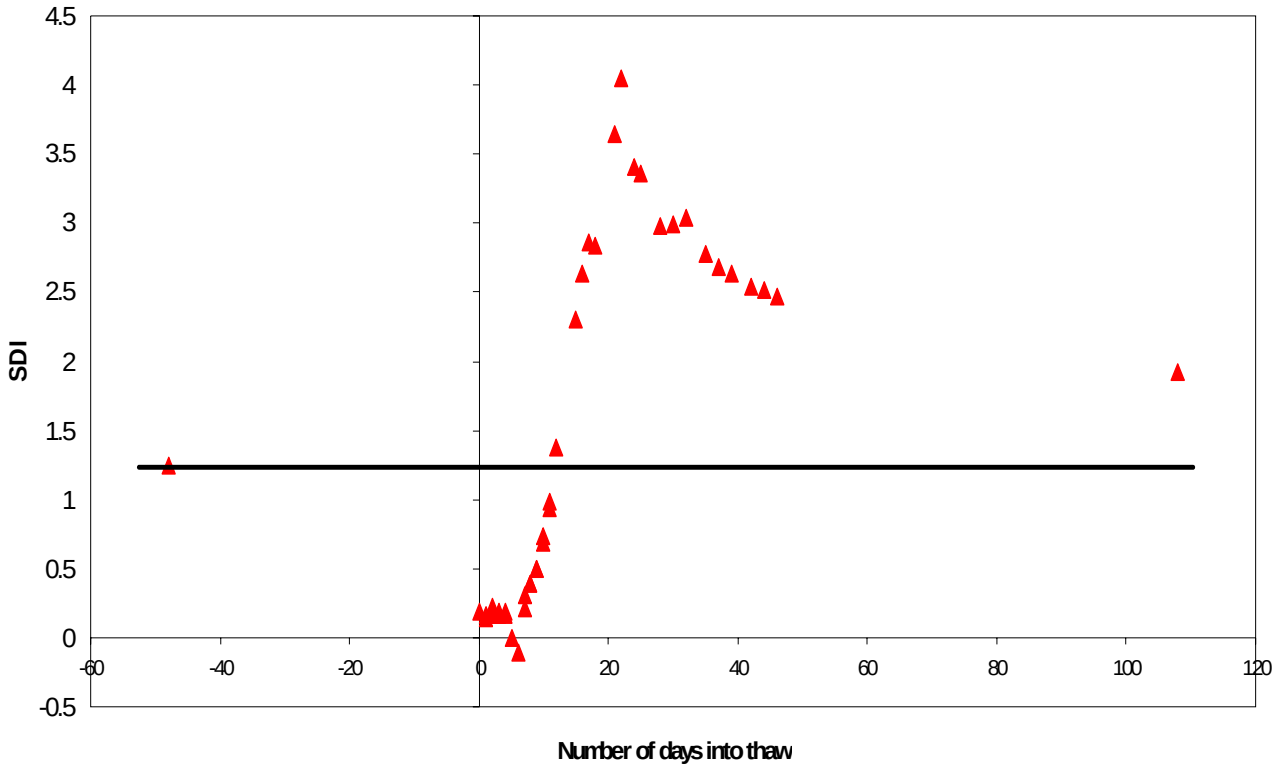

Figure 4.18 Subgrade Damage Index (SDI) from the FERF data (CL subgrade)

significantly greater than the nominal values. Although the pavement layers are identical, the indices during thaw are about 4 times the nominal values for the SM subgrade, and about 1.5 times the nominal values for the CL subgrade..

4.3.2 Vermont Test

The Vermont Agency of Transportation (VAOT) conducted FWD tests at a field test section in Barre, Vermont to investigate spring thaw behavior. The pavement section consisted of 65 mm (2.5 in.) of asphalt over 450 mm (18 in.) of silty sand base. The subgrade was a sandy silt (ML). FWD data were collected nearly every day during the freeze/thaw period of 1993-94. Freezing started around December 5, 1993 and thawing began on or about March 25, 1994. Moisture data from that site suggests that the recovery period began around April 21.

Figures 4.19 and 4.20 show the variation of SI and SDI during the freeze/thaw period. The thaw weakening is clearly depicted by both indices, with the thaw values about 1.3 times the nominal values, although the recovery does not appear to be complete when testing was stopped.

4.3.3 Mn/ROAD Test

A set of daily FWD measurements during the freeze/thaw period was obtained from the Mn/ROAD project (Worel 2003). The data was from the low-volume test section, and has a relatively thin 90-mm (3.5-in) asphalt layer and a relatively thick 460-mm (18-in.) base. The test section is founded on a silty clay (CL) subgrade. Figures 4.21 and 4.22 show the variation in SI and SDI at this site, and indicate that the indices during the thaw weakening period are about twice the nominal values.

The deflection indices calculated from each of these three external data sets show trends similar to those observed in the LTPP data, but include more data during the critical thaw and

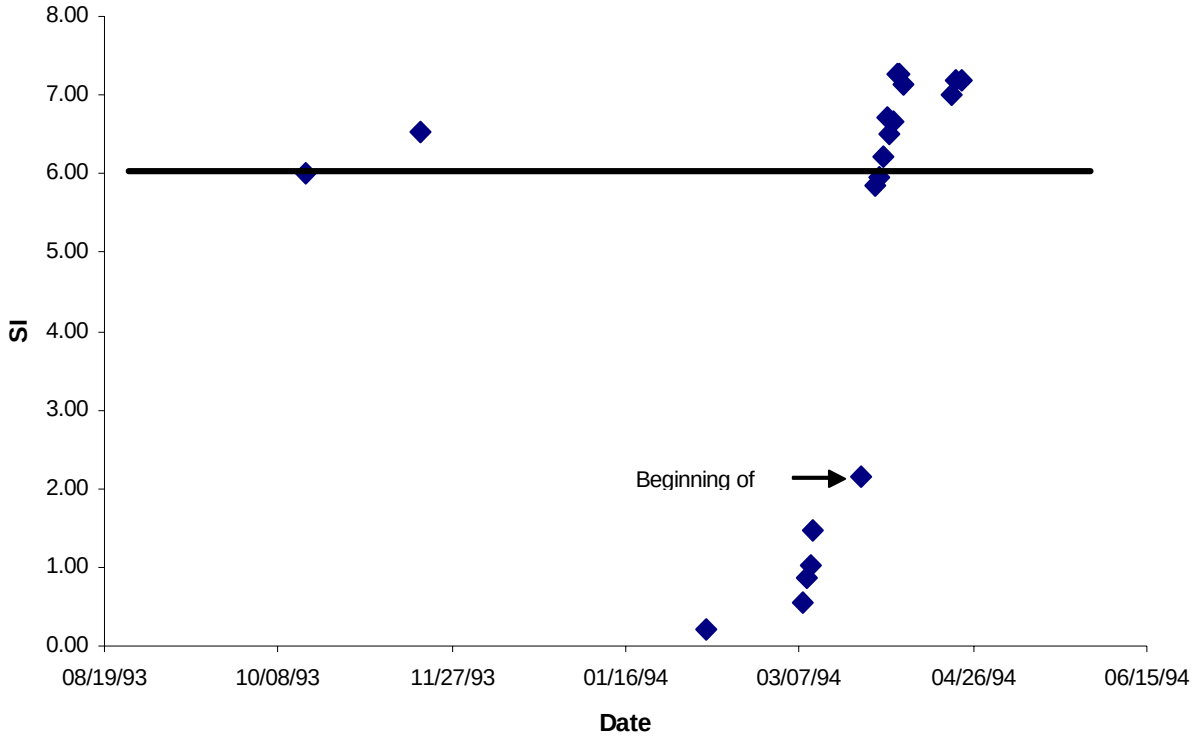

Figure 4.19 Subsurface Index (SI) at the Vermont site (ML subgrade)

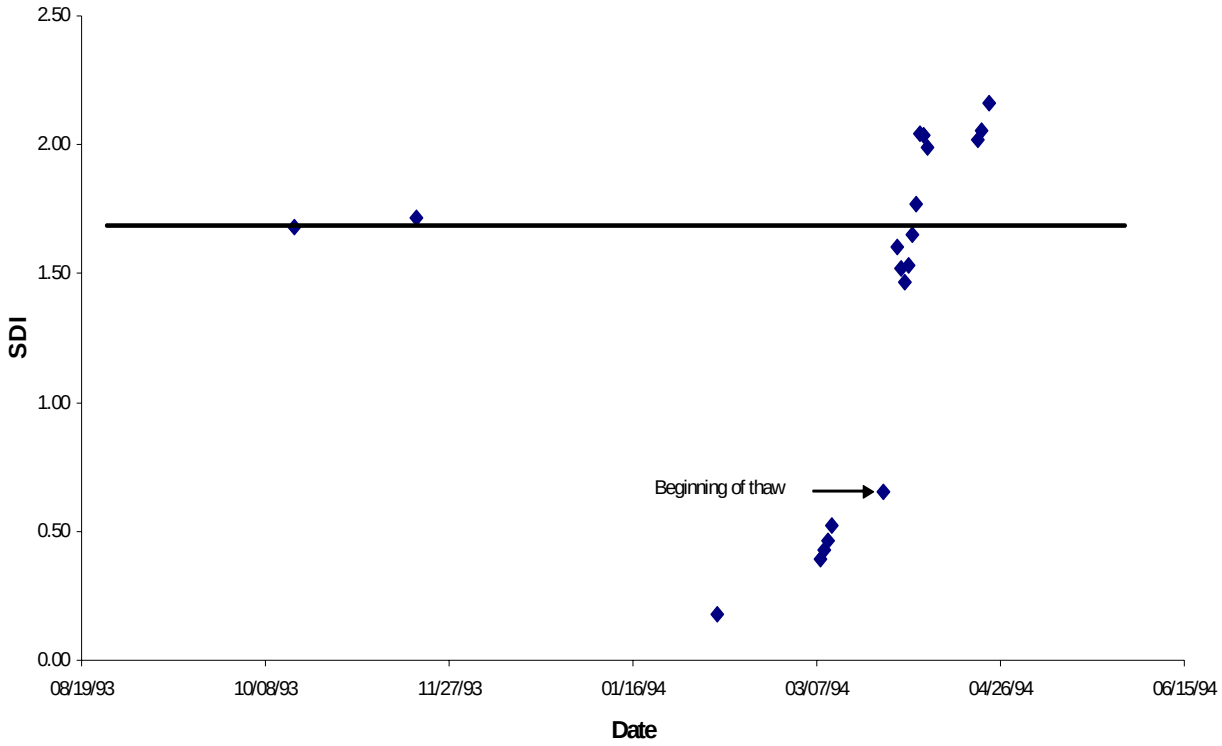

Figure 4.20 Subgrade Damage Index (SDI) at the Vermont site (ML subgrade)

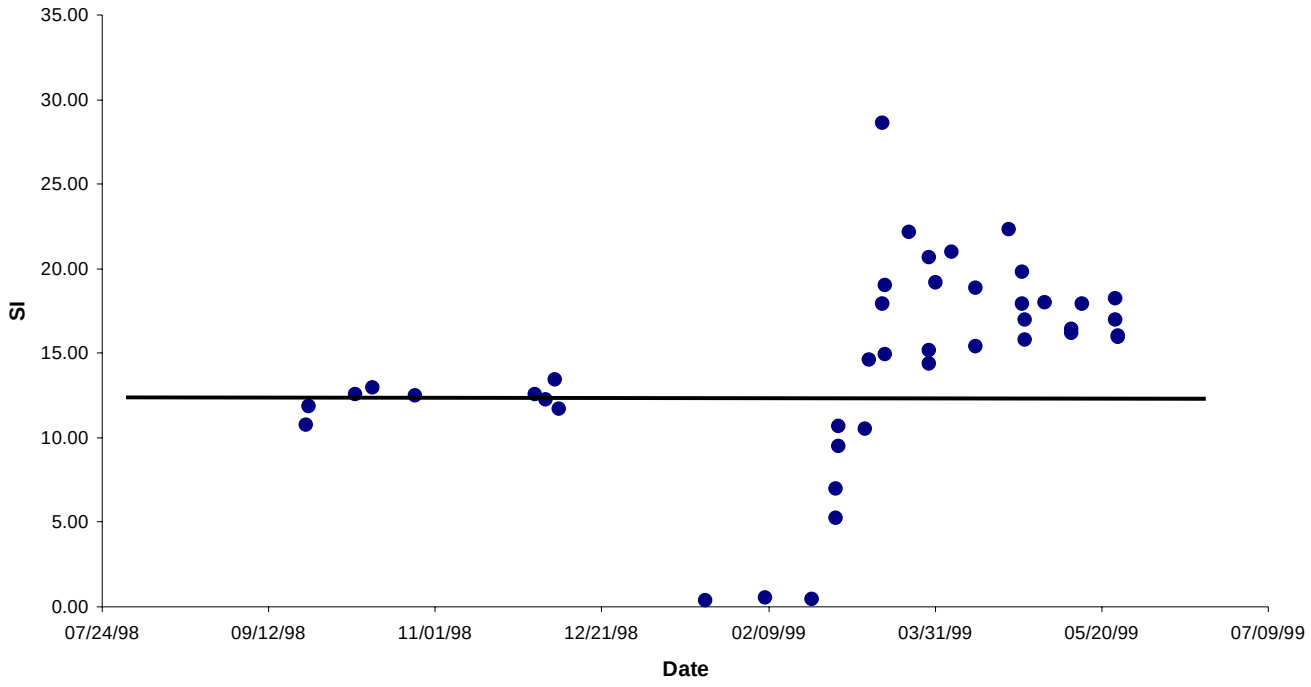

Figure 4.21 Subsurface Index (SI) at the Mn/ROAD site (CL subgrade)

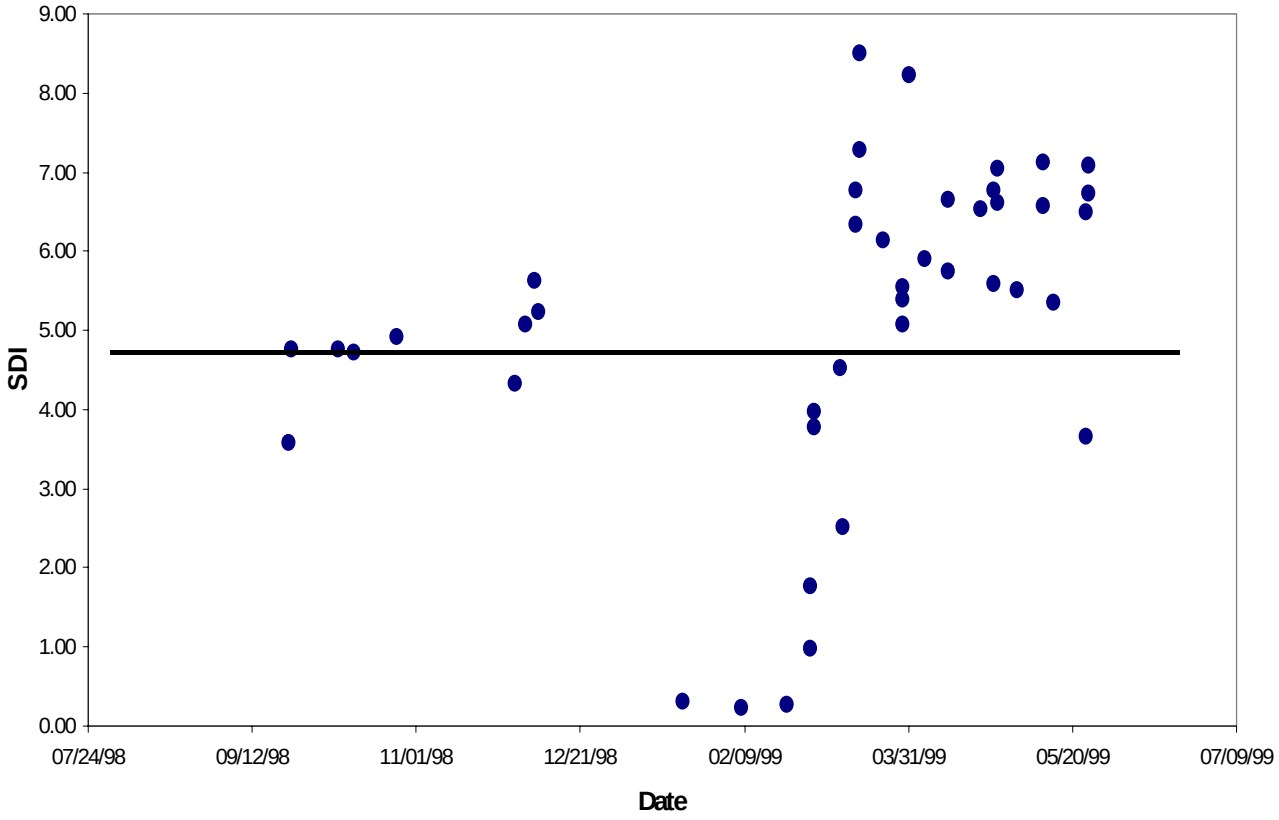

Figure 4.22 Subgrade Damage Index (SDI) at the Mn/ROAD site (CL subgrade)

recovery periods. These data clearly depict the periods of freezing and thaw weakening and, in general, the recovery period. During the thaw weakening period, the indices are 1.3 to 4 times their nominal values, depending on the pavement design and the subgrade type. These data, like the data from the LTPP SMP data set, support the concept of using FWD indices to detect changes in pavement capacity during freeze and thaw.

Based on the review of FWD indices determined from both the LTPP database and the above studies from outside the LTPP database, indices BCI, SDI, SI, and PA were selected as the most sensitive to the freeze/thaw response. What remains is to develop a methodology by which these indices can be correlated to specific levels of structural capacity that would allow them to be used for posting and removing load restrictions and issuing overload permits. This is addressed in the next sections.

4.4 DEVELOPMENT OF A LAYERED ELASTIC MODEL TO INVESTIGATE SEASONAL EFFECTS

The use of deflection basin indices to identify periods of freeze, thaw weakening, and thaw recovery has been demonstrated using data from the LTPP SMP sites as well as several more complete data sets from elsewhere. These indices appear to be useful for identifying seasonal pavement response during the freeze and thaw period, and the detection of the end of freeze and start of thaw appears to be relatively straightforward. However, the end of the thaw-weakening period, at which time load restrictions can be lifted, is not obvious from the LTPP data. This is due, in part, to the absence of a well-defined thaw recovery in most of the data.

To further investigate the use of deflection basin indices for ending load restrictions, a series of computer analyses were performed to relate the observed FWD deflections to the stresses and

strains in the pavement system. A similar layered elastic approach was utilized by Rutherford et al. (1985) and Rutherford (1989), to compute the critical strains and allowable loads during the spring thaw. The critical mode of distress, either horizontal strain at the bottom of the asphalt layer or vertical strain at the top of the subgrade, was found to depend on pavement thickness.

4.4.1 Layered Elastic Model of LTPP Pavement Sites

A number of layered elastic pavement analysis programs exist. In this study the Bitumen Structure Analysis in Roads (BISAR) computer program (De Jong et al. 1973) was used to model the LTPP FWD test sites. BISAR is a layered elastic modeling program that can predict the deflections, strains, and stresses in asphalt concrete pavements. The FWD test was represented by a vertical load of 40 kN applied to a circular area with a 300-mm diameter. A typical year was divided into 52 weeks or steps, each with different pavement properties at different depths. By varying the pavement properties throughout the entire year, the analyses can be used to obtain the seasonal response, and to assist in the interpretation of the response during gaps in the actual field data. In addition, the BISAR analysis allows the computation of strains in the pavement system.

To represent the gradual onset of freezing and thawing in the pavement, the subgrade above the maximum freeze depth was divided into 6 layers as depicted in Figure 4.23, which represents site 27-6251 (Minnesota). The top half of the frozen subgrade was divided into 4 layers of equal thickness, and the bottom half was divided into 2 layers of equal thickness. The maximum freeze depth was estimated from the freeze depth model described in Section 2.3. The subgrade below the

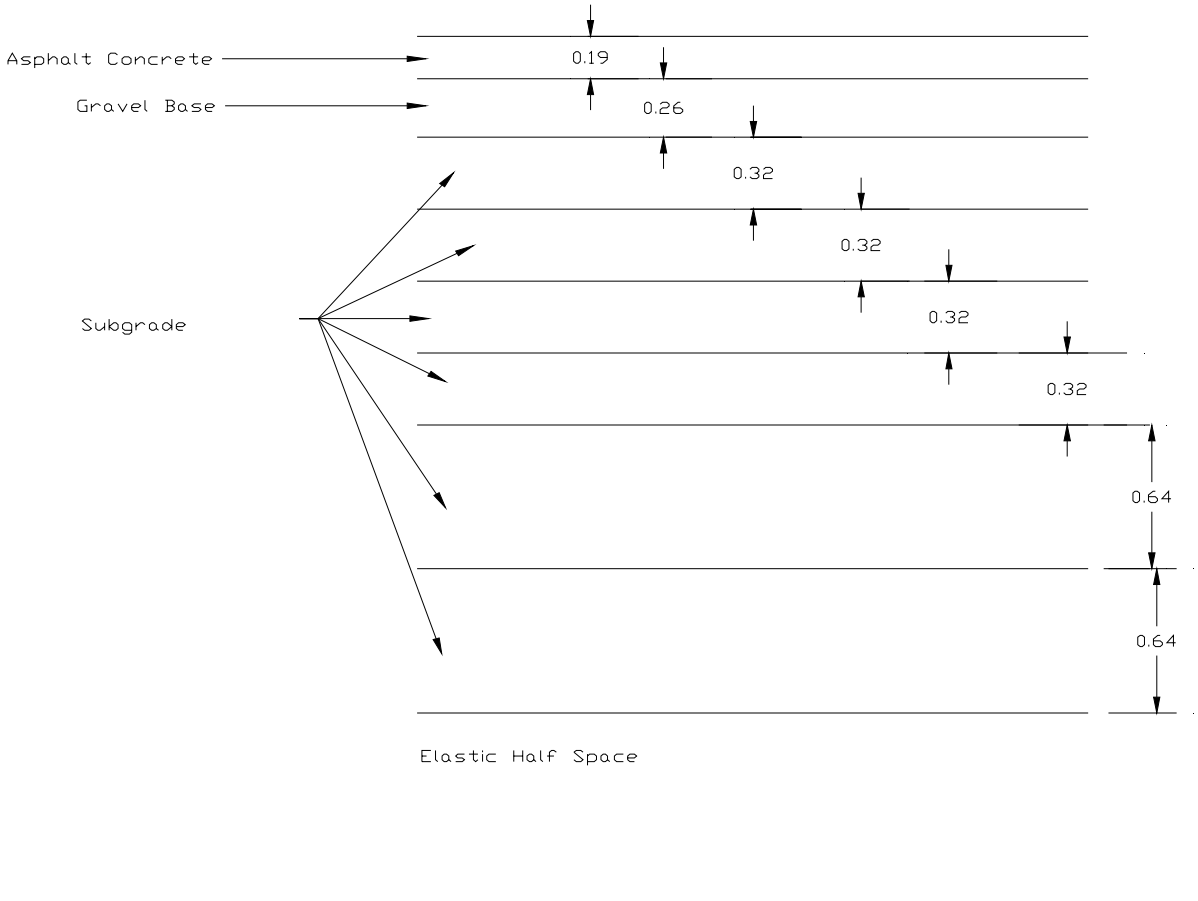

Figure 4.23 Layered elastic model for Minnesota site 27-6251

freeze depth was represented by an elastic half space with the unfrozen or nominal modulus. The properties of the subgrade layers were sequentially changed to reflect the progression of freezing or thawing, and the effect on the computed FWD deflection indices observed.

Layered elastic models were developed for the wet-freeze and dry-freeze sites for which a site-specific freeze depth model, an AC temperature model, and AC surface temperature data were available. The sites analyzed are summarized in Table 4.4.

Table 4.4 Sites analyzed with BISAR based on available models from LTPP database

Site		Freeze - Thaw Data		AC Temp Data		BISAR Model
Number	State	Milestones	Frost Penetration	Model	Surface Temperature Data During Fwd Test	
16-1010	ID	x	x	x	x	x
23-1026	ME	x	x	x	x	x
25-1002	MA				x	
27-1018	MN	x	x	x	x	x
27-1028	MN	x	x	x	x	x
27-6251	MN	x	x	x	x	x
30-8129	MT	x	x	x	x	x
31-0114	NE				x	
36-0801	NY				x	
46-0804	SD	x	x		x	
46-9187	SD				x	
50-1002	VT	x	x	x	x	x
56-1007	WY			x	x	
83-1801	MB	x	x		x	
87-1622	ON		x	x	x	x
90-6405	SK				x	

4.4.2 Asphalt Modulus Model

The modulus of the asphalt layer was varied with temperature based on a site-specific asphalt modulus model developed from the LTPP data (Section 3.3). The relationship between asphalt modulus and pavement surface temperature was modeled by the equation:

$$E_{AC} = Ae^{BT}$$

where E_{AC} is the asphalt modulus (MPa), T is the pavement surface temperature (°C), and A and B are site-specific model parameters. The model parameters used for each freezing AC site are summarized in Table 4.5.

Table 4.5 Site–specific asphalt modulus model parameters

Site	A	B
16-1010	16528	-0.033
23-1026	16010	-0.0467
27-1018	8450.9	-0.0186
27-1028	21002	-0.0016
27-6251	12457	-0.0405
30-8129	20096	-0.0454
50-1002	12971	-0.0549
87-1622	10638	-0.0283

The annual variation of surface temperature at each site was simplified to follow a sinusoidal function approximating the surface temperatures measured during the FWD testing. Thus, for each week or analysis step, the AC modulus was varied based on the asphalt surface temperatures taken during the LTPP SMP FWD testing.

4.4.3 Base and Subgrade Modulus Models

The pavement subgrade moduli were assumed to have nominal values during the late summer and fall (Section 4.1). Changes in the base and subgrade moduli during freezing and thawing were taken relative to these nominal values. Frozen layers were assumed to have a modulus twice the nominal value, and thawing layers were assumed to have a modulus one half the nominal value. Thus, the behavior of the layered elastic model could be investigated in 52 steps over the entire year, which was taken to start on October 1 and progress from nominal to freezing to thawing and back to nominal again. Backcalculated FWD values were used for the nominal subgrade moduli. The base moduli were all set to 500 MPa since only limited backcalculated data was available. Table 4.6 summarizes the moduli used for the base, subgrade and when applicable, sub-base layers.

Table 4.6 Nominal Base and Subgrade Moduli for LTPP Model Sites

Site	Base		Subgrade/Subbase	
	Modulus (MPa)	Poisson's Ratio	Modulus (MPa)	Poisson's Ratio
16-1010	500	0.35	71	0.30
23-1026	500	0.35	214	0.30
27-1018	500	0.35	260	0.30
27-1028	500	0.35	200	0.30
27-6251	500	0.35	600	0.30
30-8129	500	0.35	179	0.40
50-1002	500	0.35	197	0.35
87-1622	500	0.35	250/350	0.40/0.35
Note: Frozen modulus values were assumed to be twice the nominal, while thawed modulus values were assumed to be one half the nominal				

4.4.4 Modeling the Annual Variation of Freeze/Thaw Depth

The moduli of the base and subgrade were varied from nominal, to freezing, to thawing according to the time of year. To represent the progression of freezing and thawing over time, the pavement year was divided into the following periods: fall, winter, spring thaw, base recovery, subgrade recovery, and summer. Each period was further subdivided such that the depth at which a given state occurred changed with time, yielding a total 52 steps or analysis periods. The progression of these states with time and depth is shown in Table 4.7, which suggests the manner in which the subgrade layers freeze and thaw from the top down. Two different scenarios were modeled as indicated in Table 4.7: one with spring thaw and one without spring thaw. The second scenario is identical to the first except that the base and subgrade models skip the weakening stage and return directly to the nominal values. This second scenario was investigated to represent the LTPP SMP sites which did not display a strong thaw weakening stage, either due to thick base layers or gaps in the data collection.

Table 4.7 Assumed Annual Variation of Freeze and Thaw depths in Asphalt Concrete Pavement Systems

a) With Spring Thaw

Seasonal Behavior		Fall	Winter							Spring Thaw					Base Recovery		Subgrade Recovery						Summer
Step Number	# Layers	1-15	16	17	18	19	20	21	22	23	24	25	26	27	28	29	30	31	32	33	34	35	36-52
AC	1	N	N	N	N	N	N	N	N	N	N	N	N	N	N	N	N	N	N	N	N	N	N
Base	1 (opt)	N	F	F	F	F	F	F	F	T	T	T	T	T	N	N	N	N	N	N	N	N	N
Subbase	2 (opt)	N	N	F	F	F	F	F	F	F	T	T	T	T	T	T	N	N	N	N	N	N	N
		N	N	N	F	F	F	F	F	F	F	T	T	T	T	T	T	N	N	N	N	N	N
and/or		N	N	N	N	F	F	F	F	F	F	F	T	T	T	T	T	T	N	N	N	N	N
Subgrade	6	N	N	N	N	N	F	F	F	F	F	F	F	T	T	T	T	T	T	N	N	N	N
	(4, if	N	N	N	N	N	N	F	F	F	F	F	F	F	T	T	T	T	T	T	N	N	N
	Subbase)	N	N	N	N	N	N	N	F	F	F	F	F	F	F	T	T	T	T	T	T	N	N
Elastic HS	1	N	N	N	N	N	N	N	N	N	N	N	N	N	N	N	N	N	N	N	N	N	N

(N = Nominal Properties, F = Frozen Properties, T = Thawed Properties)

Table 4.7 Assumed Annual Variation of Freeze and Thaw depths in Asphalt Concrete Pavement Systems

b) Without Spring Thaw

Seasonal Behavior		Fall	Winter							Subgrade Recovery							Summer
Step Number	# Layers	1-15	16	17	18	19	20	21	22	23	24	25	26	27	28	29	30-52
AC	1	N	N	N	N	N	N	N	N	N	N	N	N	N	N	N	N
Base	1 (opt)	N	F	F	F	F	F	F	F	N	N	N	N	N	N	N	N
Subbase	2 (opt)	N	N	F	F	F	F	F	F	F	N	N	N	N	N	N	N
		N	N	N	F	F	F	F	F	F	F	N	N	N	N	N	N
and/or		N	N	N	N	F	F	F	F	F	F	F	N	N	N	N	N
Subgrade	6	N	N	N	N	N	F	F	F	F	F	F	F	N	N	N	N
	(4, if	N	N	N	N	N	N	F	F	F	F	F	F	F	N	N	N
	Subbase)	N	N	N	N	N	N	N	F	F	F	F	F	F	F	N	N
Elastic HS	1	N	N	N	N	N	N	N	N	N	N	N	N	N	N	N	N

(N = Nominal Properties, F = Frozen Properties, T = Thawed Properties)

4.5 APPLICATION OF MODEL TO PREDICT BASIN INDEX CHANGES

The frozen sites in the SMP database listed in Table 4.4 were analyzed in the manner described above to obtain surface deflections corresponding to the locations of the FWD sensors, the horizontal strain at the bottom of the asphalt layer, and the vertical strain at the top of the subgrade. The results from Minnesota sites 27-6251, with 190 mm (7.4 in.) of asphalt and 250 mm (10 in.) of granular base, and site 27-1018, with 115 mm (4.5 in.) of asphalt and 130 mm (5.2 in.) of granular base, will be discussed here. The subgrade at both sites is a poorly graded sand with silt, and since neither site has a subbase, the subgrade in both was divided into six layers.

Figure 4.24 shows selected FWD deflection basins obtained using the linear elastic model for site 27-6251. The deflection basins are color coded according to season. For comparison, actual FWD deflection basins developed from the LTPP database are shown in Figure 4.25. The model represents the seasonal changes in FWD basin shape very well, although the actual maximum deflections under the load may not always agree. The differences in magnitude can be attributed to assumptions made in the selection of material properties, differences in the timing of the various freeze/thaw events, and the arbitrary selection of the factors applied to the base and subgrade moduli during the freezing and thaw periods. These differences in the magnitude of the deflection will not have a big impact on the investigation of the seasonal variation of the FWD indices, since it is the change in the indices over time which is of interest. A similar comparison is made in Figures 4.26 and 4.27 for site 27-1018. The predicted FWD basins for all the freeze sites are provided in Appendix T.

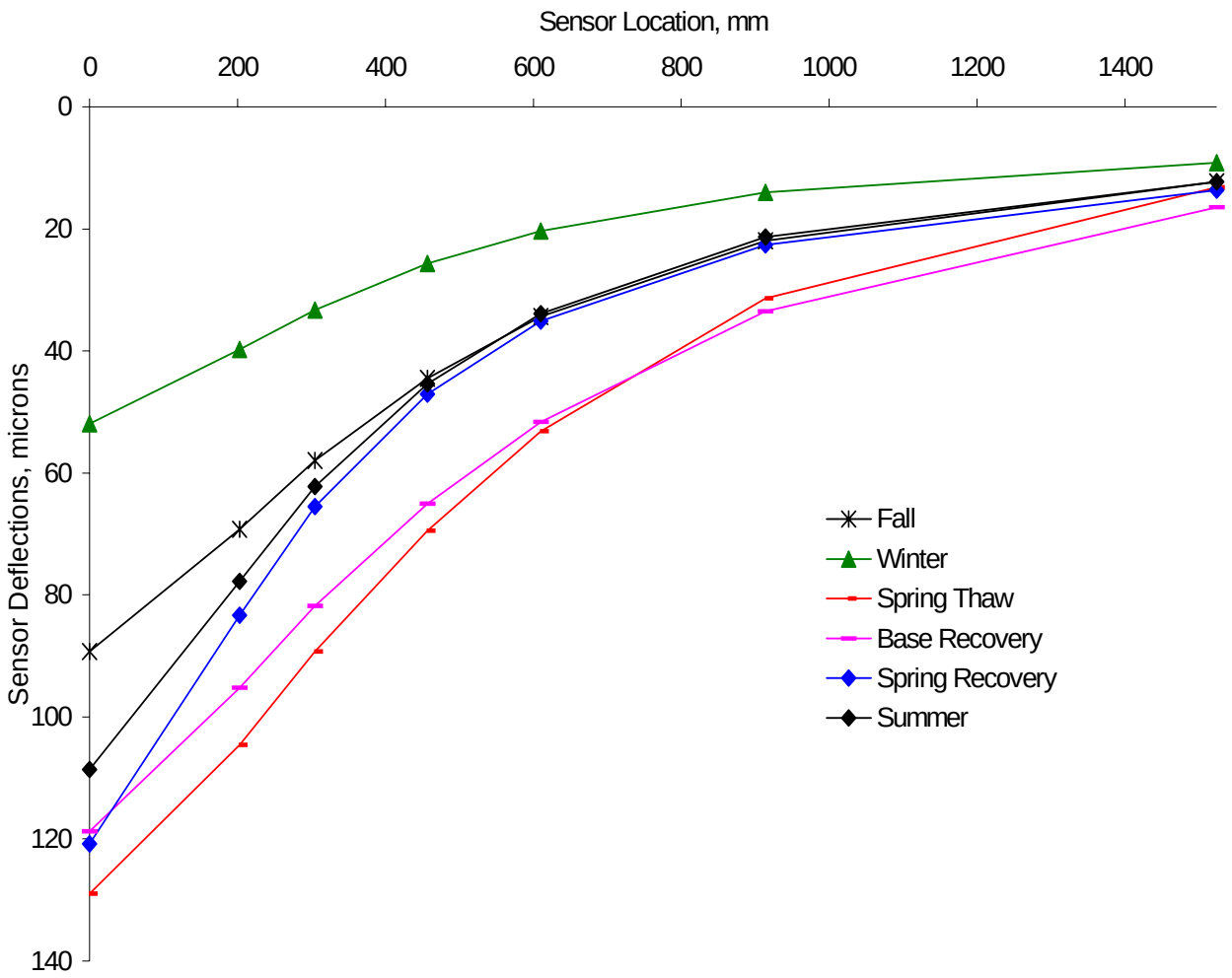

Figure 4.24 Deflection basins at site 27-6251 from layered elastic model

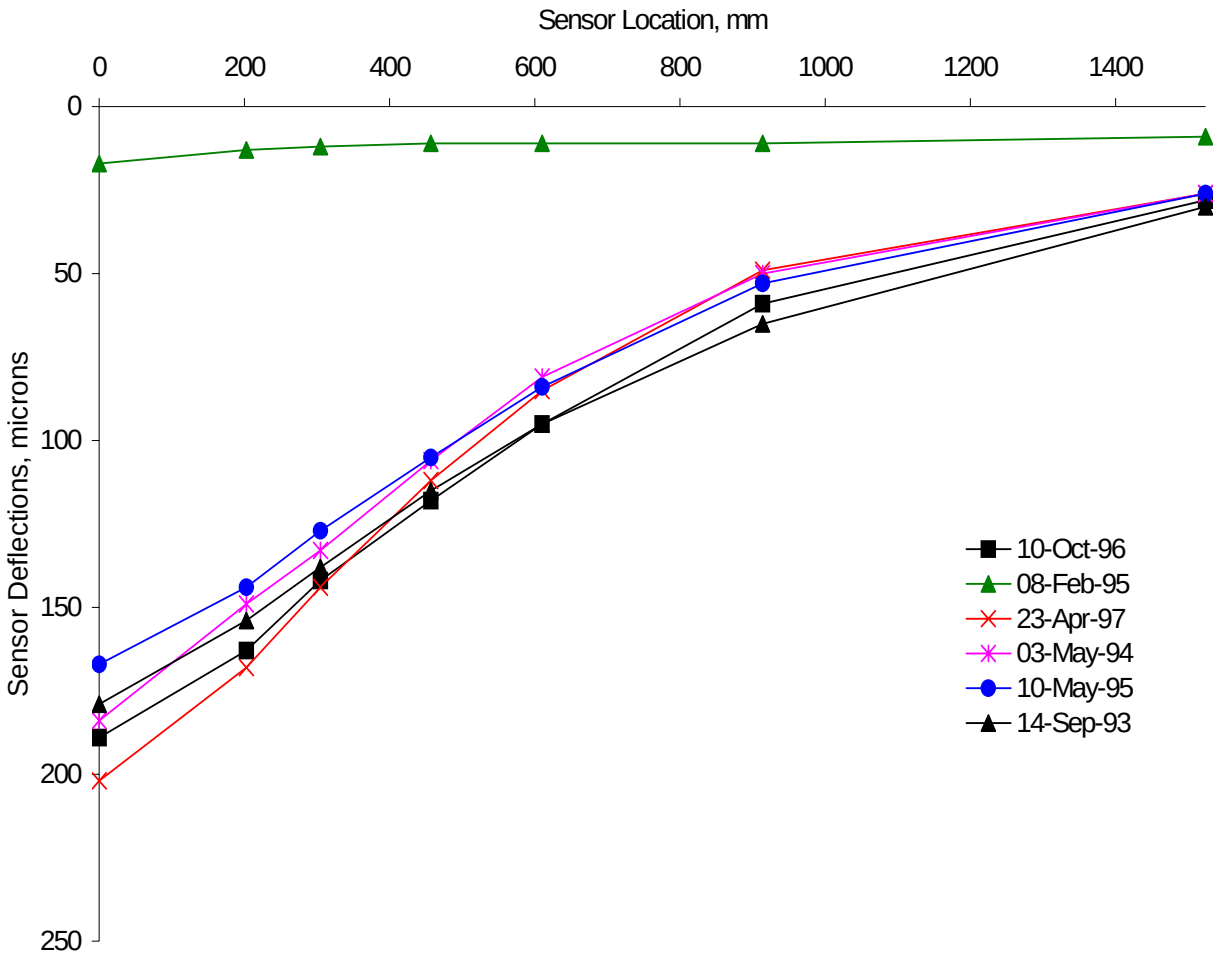

Figure 4.25 Deflection basins at site 27-6251 from LTPP

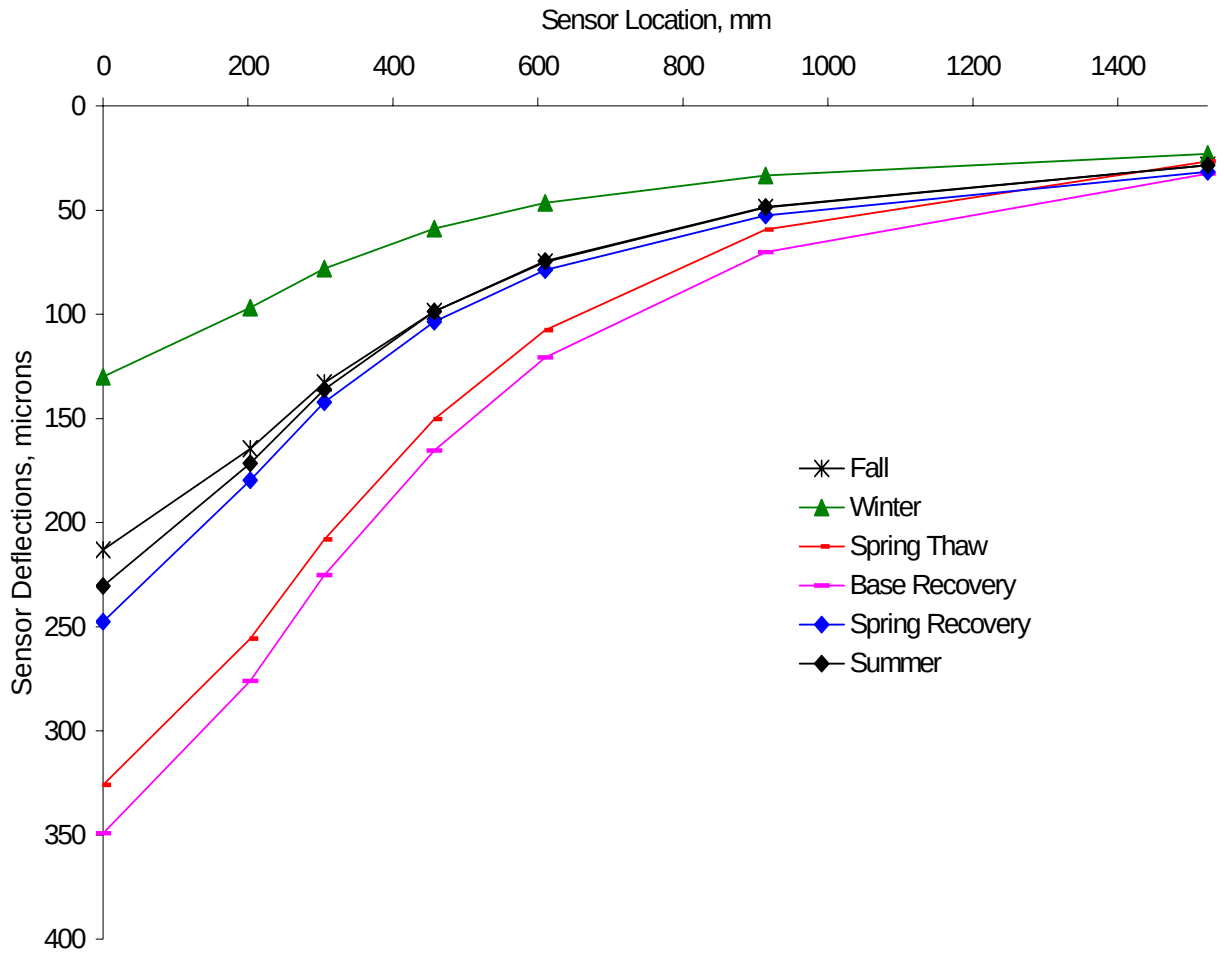

Figure 4.26 Deflection basins at site 27-1018 from layered elastic model

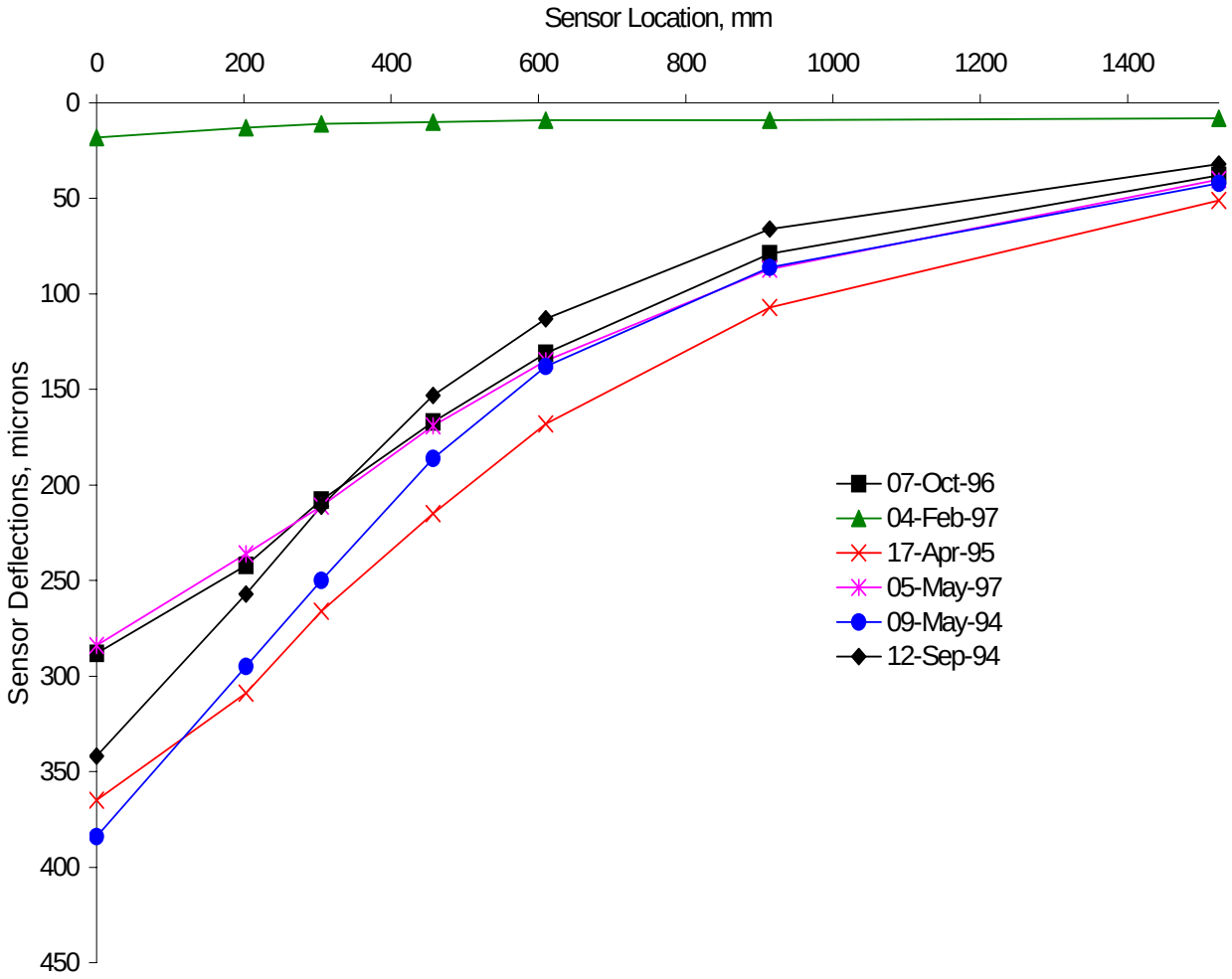

Figure 4.27 Deflection basins at site 27-1018 from LTPP

4.5.1 Seasonal Changes in Basin Indices During Freeze/Thaw/Recovery

From the results of the BISAR layered elastic analysis, the seasonal variation of the FWD indices BCI, SDI, SI, and PA was investigated. These indices were determined with and without thaw weakening, as outlined in Table 4.7. Again, this was done to investigate the suggestion in Section 4.2 that significant thaw weakening was not measured at the LTPP sites.

Figures 4.28 and 4.29 show the seasonal variation of index BCI calculated for sites 27-6251and 27-1018, respectively. The horizontal time scale is the week number starting with the week of October 1. Similar response was obtained for the other freezing sites as shown in Appendix U. The seasonal variation for both sites is similar, except that the BCI for site 27-1018, which is the thinner of the two sites, is about twice that of site 27-6251. In both cases, the model for the spring thaw response produces an index value that is about twice the nominal value occurring in early October. This is consistent with the observations from the data with complete thaw measurements obtained from outside the LTPP data set.

Similar pairs of graphs are provided for the SDI (Figures 4.30 and 4.31), the SI (Figures 4.32 and 4.33) and the PA (Figures 4.34 and 4.35). Appendices V, W, and X contain the seasonal variation of indices SDI, SI, and PA, respectively, for the remaining freeze sites. In each case the index accurately reflects the increased capacity (lower index) during freeze, and a significant loss of capacity (greater index) during the thaw weakening period. These results tend to support the premise that the LTPP sites did not experience significant thaw weakening, since most of the data (as summarized in Table 4.3) returned to the nominal values with very little evidence of decreased capacity during thaw.

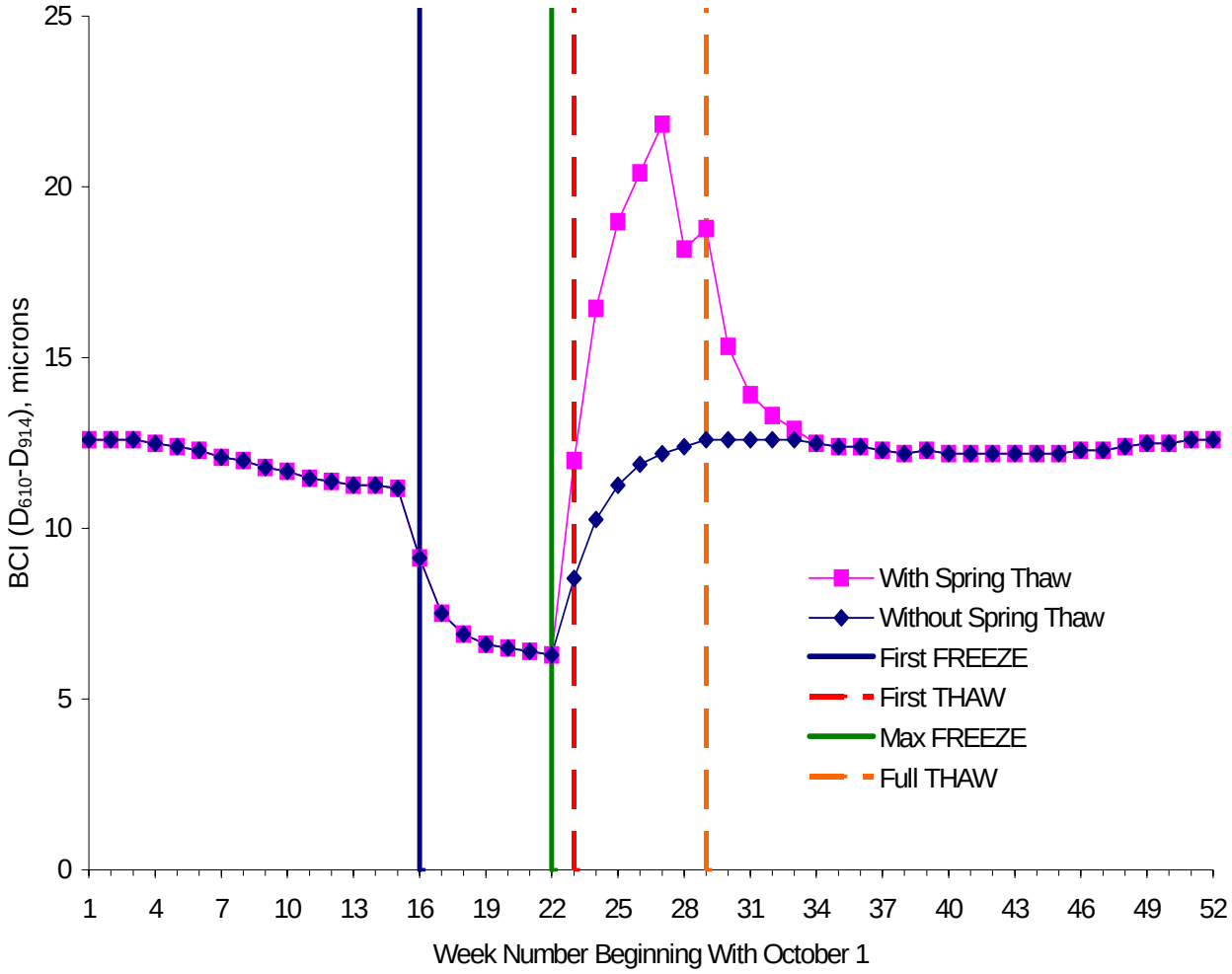

Figure 4.28 Base Curvature Index (BCI) from site 27-6251 model

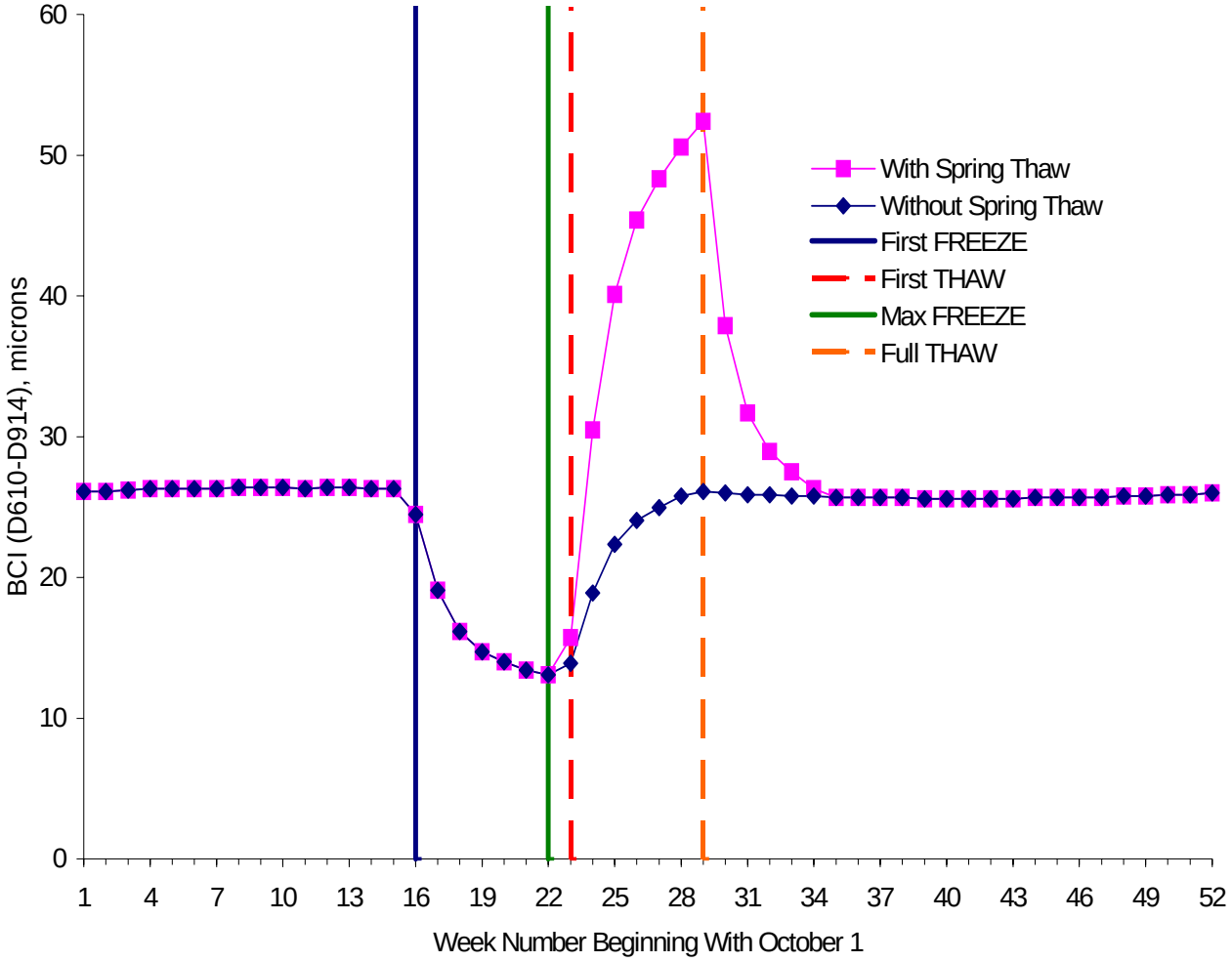

Figure 4.29 Base Curvature Index (BCI) from site 27-1018 model

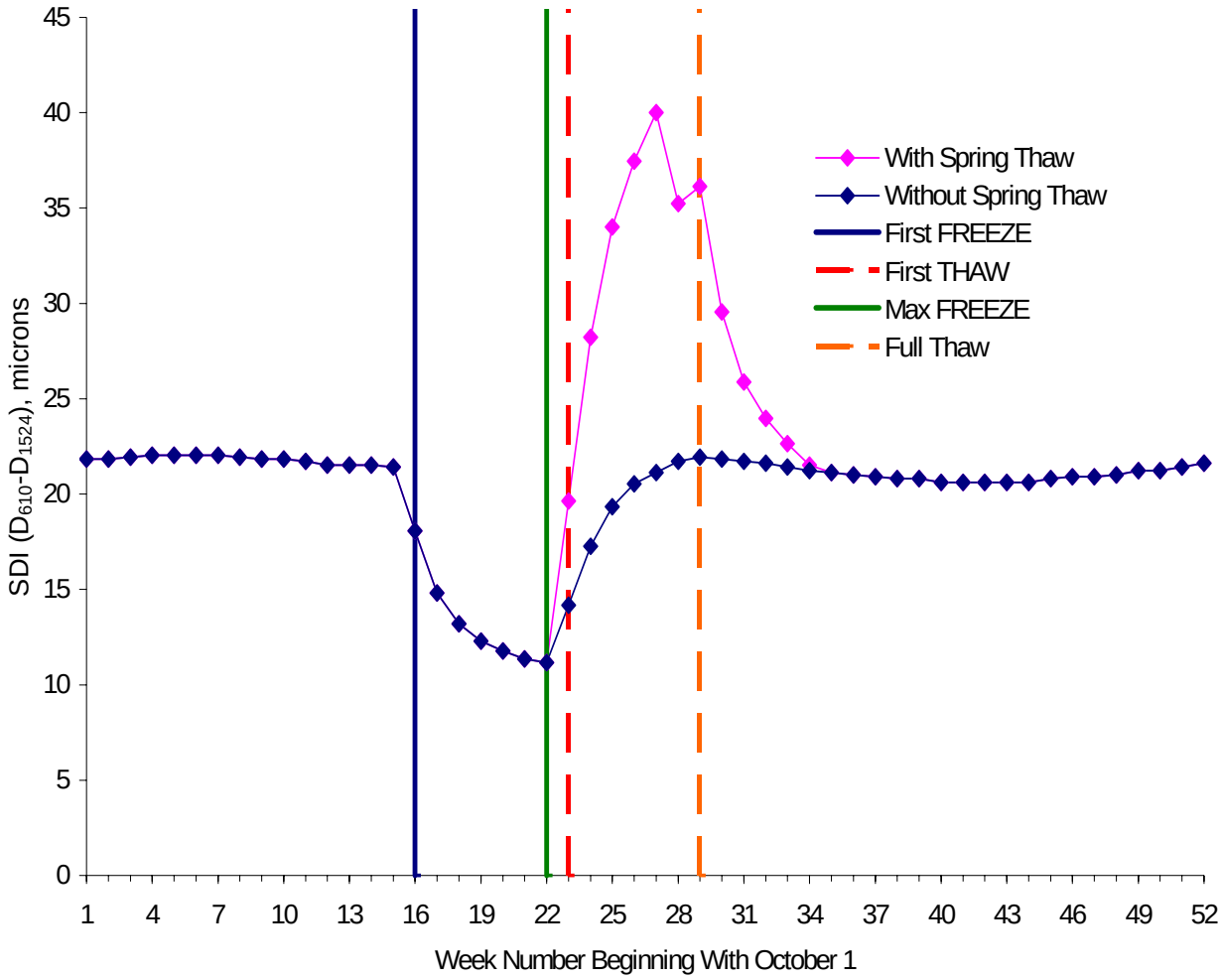

Figure 4.30 Subgrade Damage Index (SDI) from site 27-6251 model

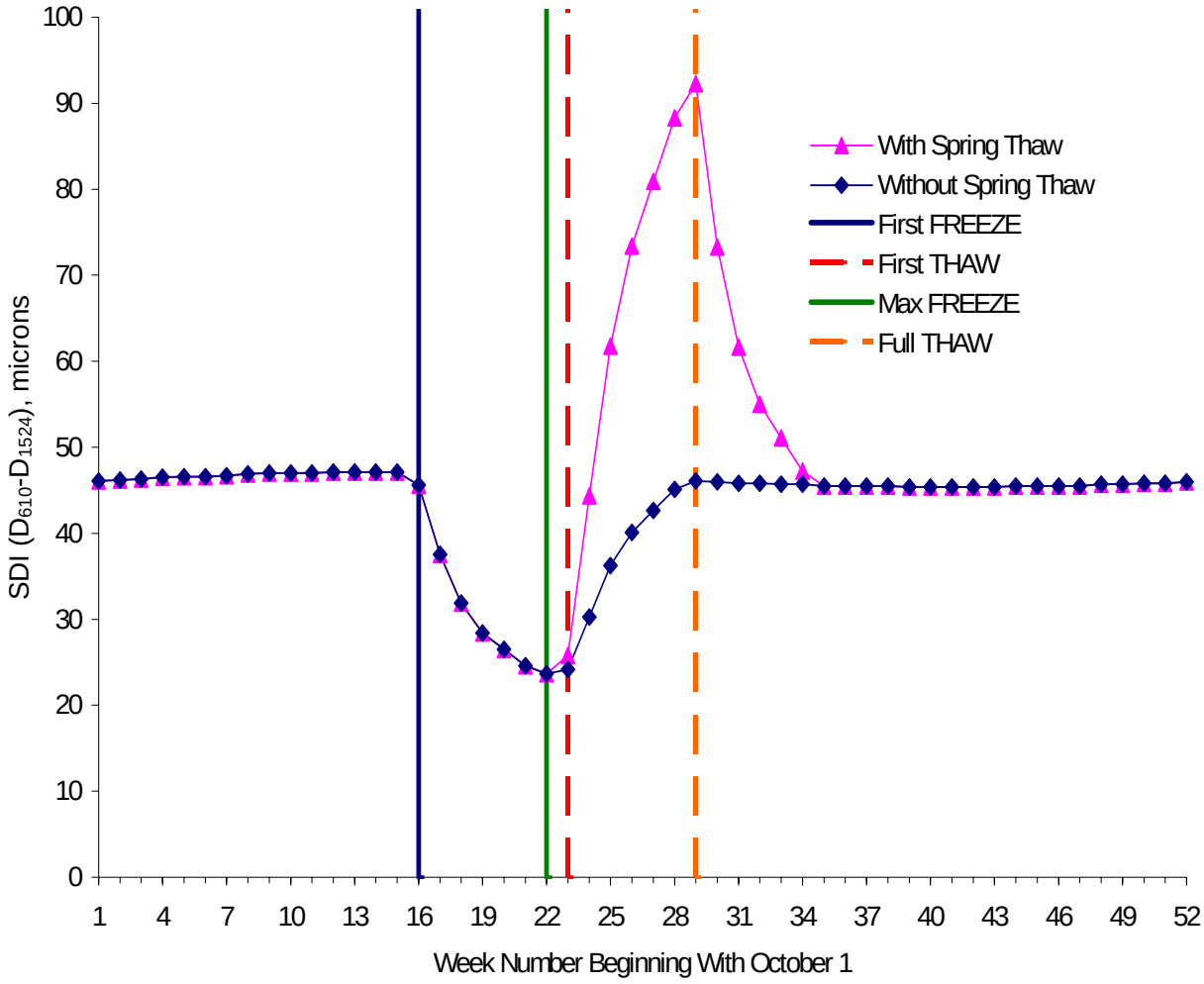

Figure 4.31 Subgrade Damage Index (SDI) from site 27-1018 model

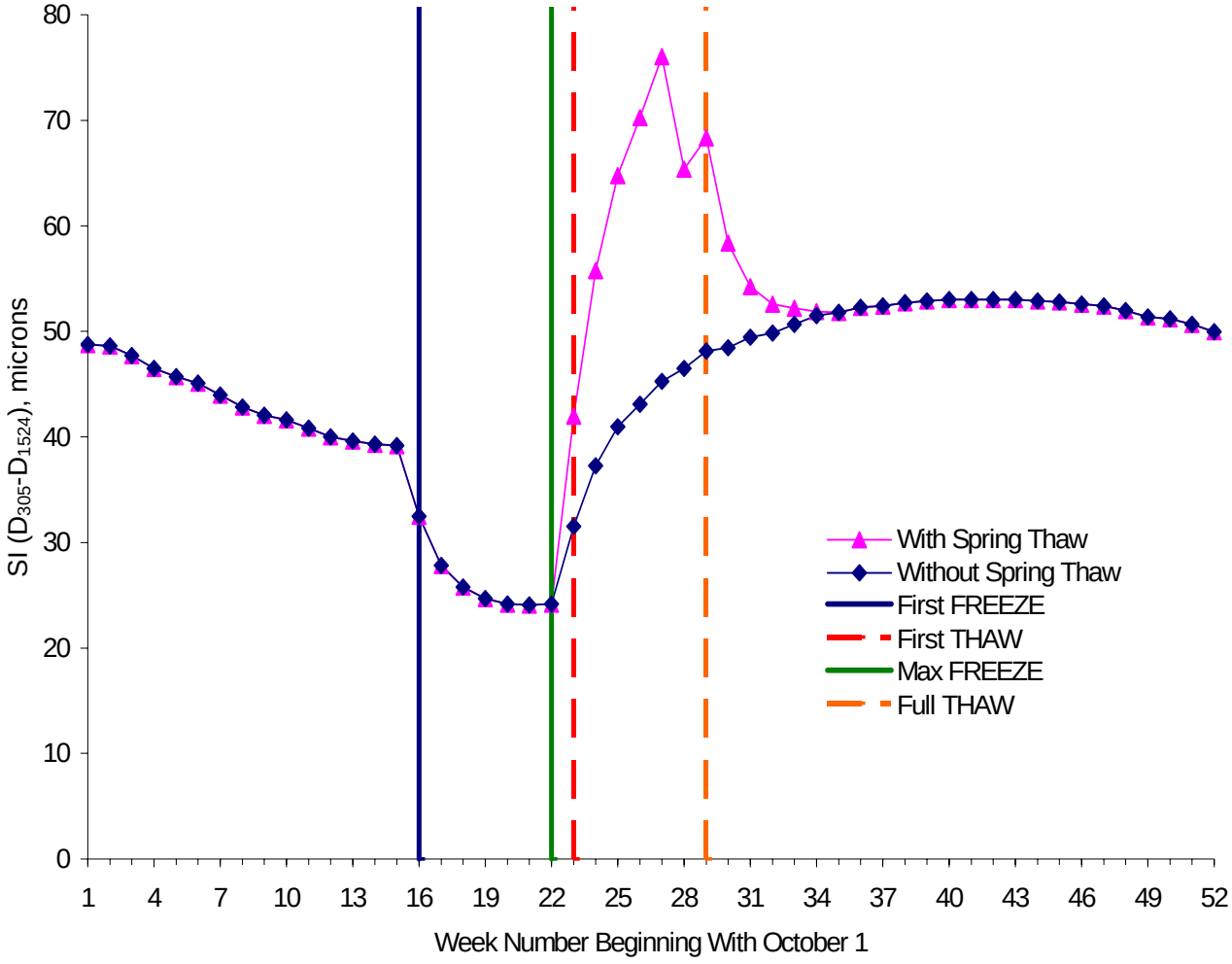

Figure 4.32 Subsurface Index Site (SI) from site 27-6251 model

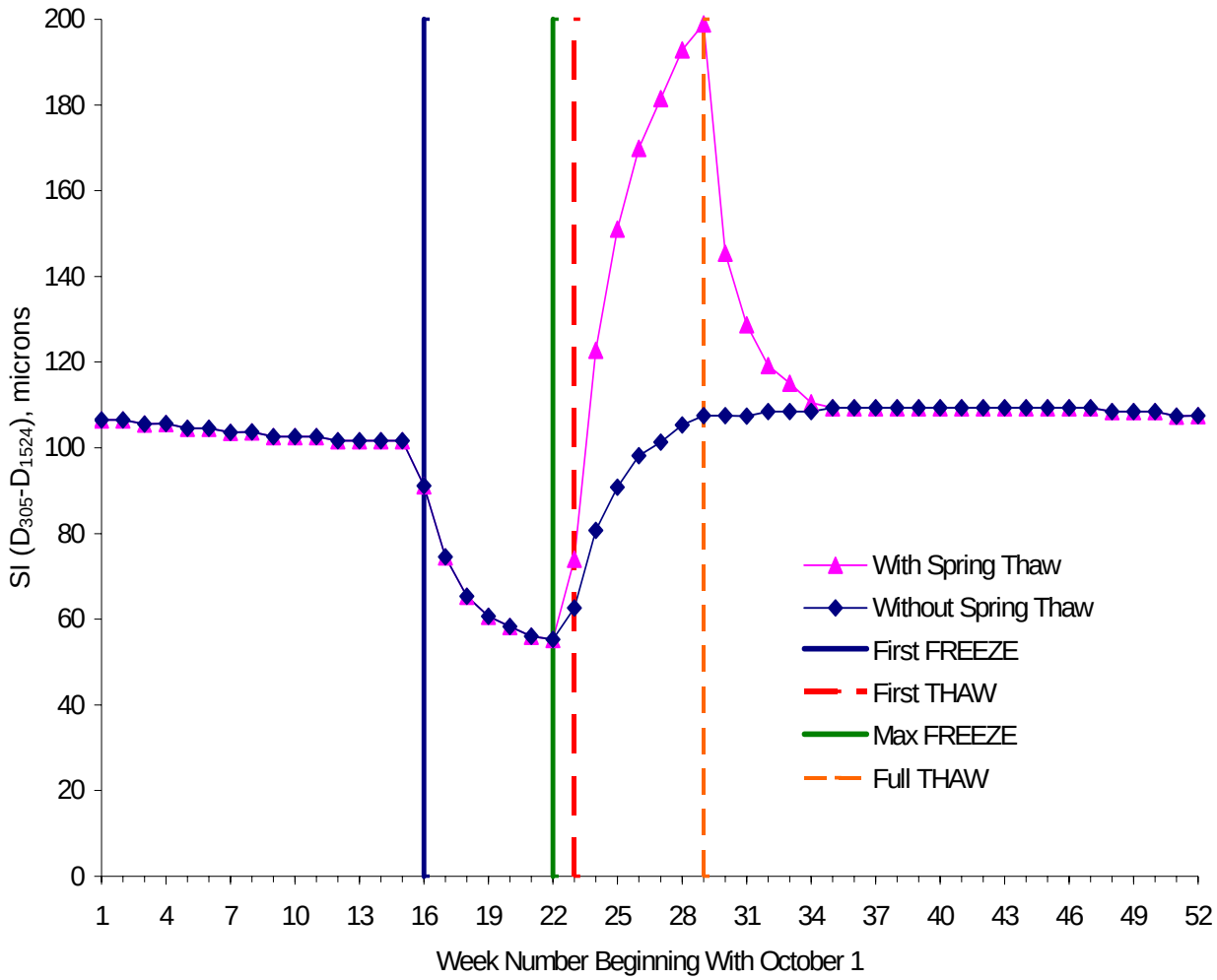

Figure 4.33 Subsurface Index (SI) from site 27-1018 model

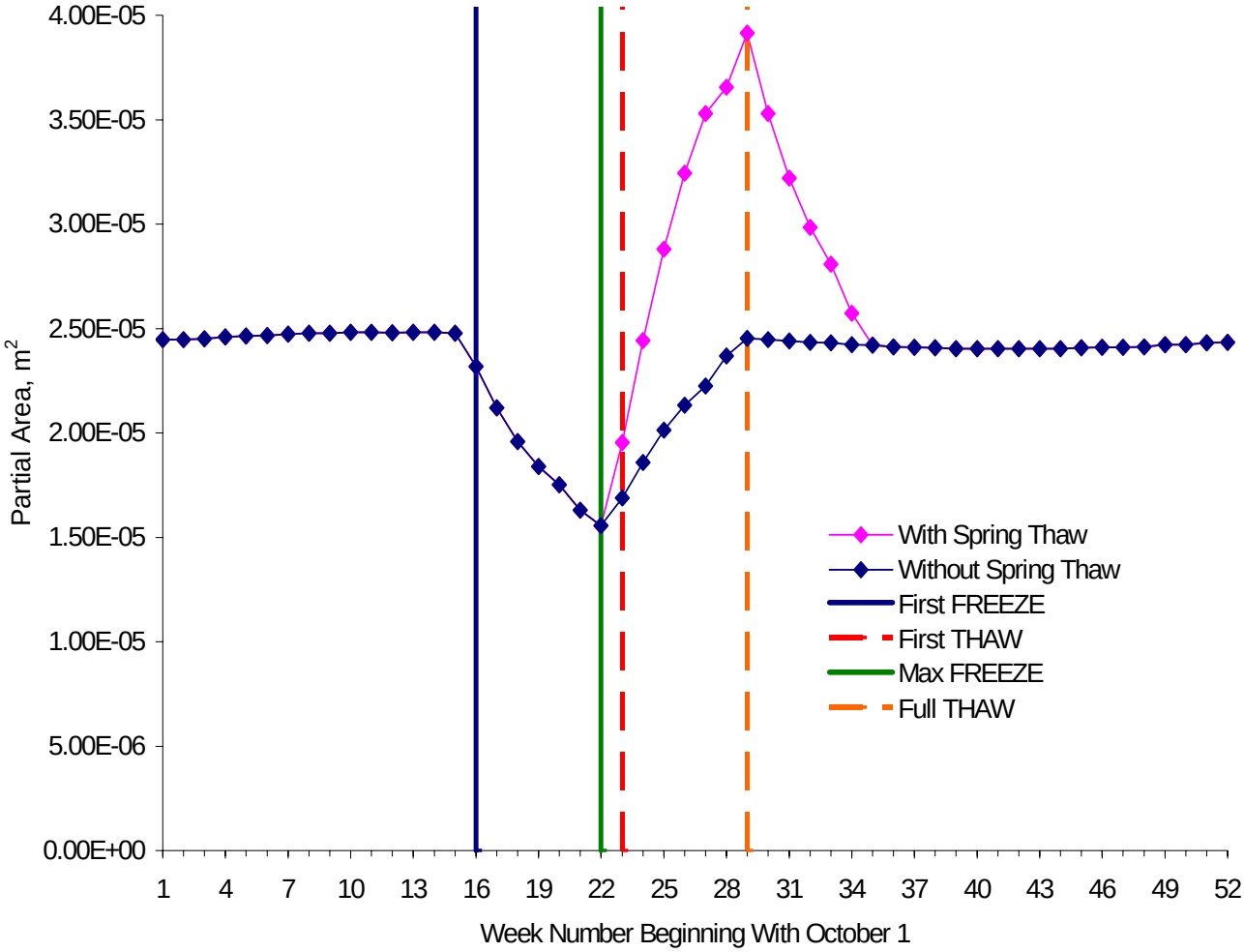

Figure 4.34 Partial Area (PA) from site 27-6251 model

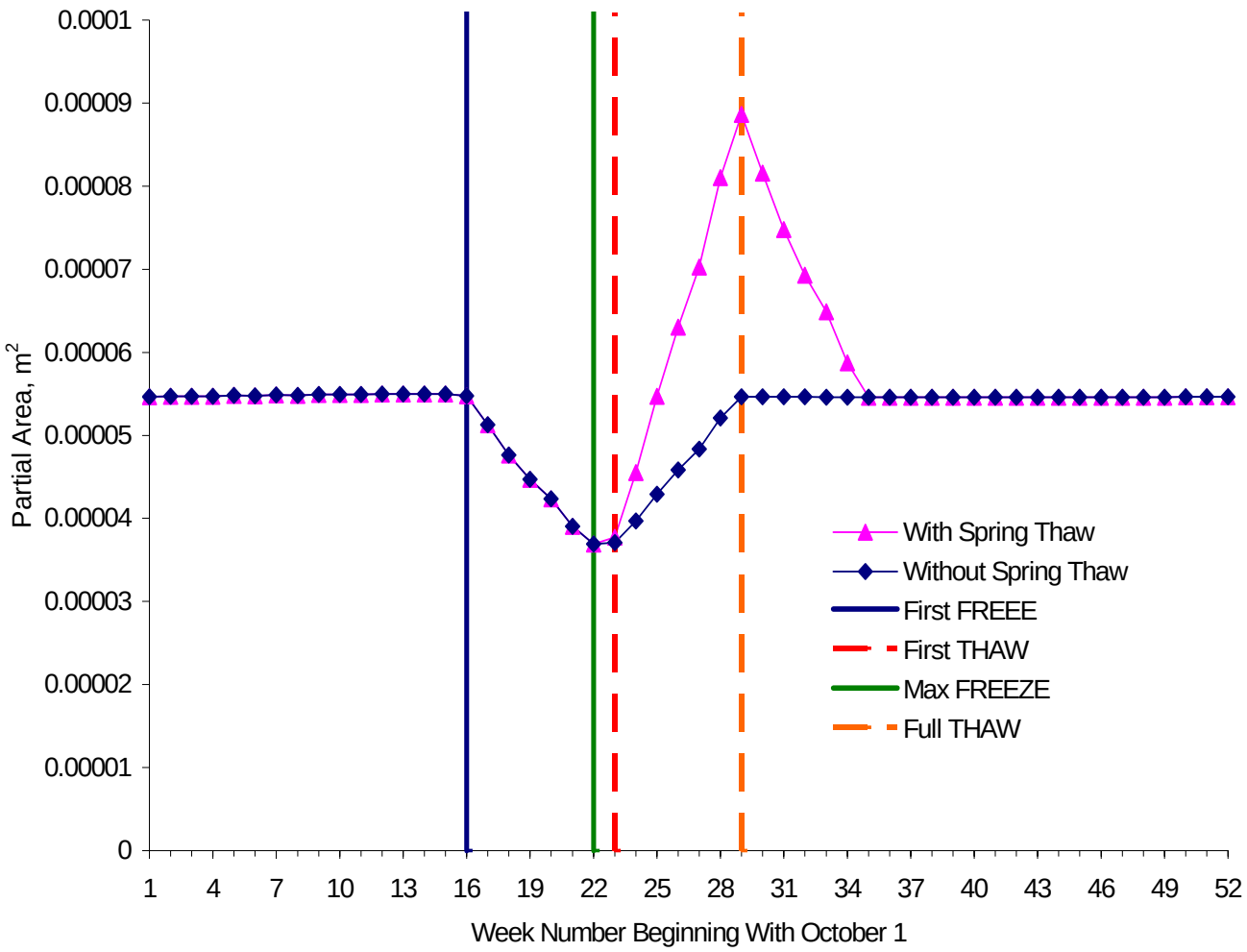

Figure 4.35 Partial Area (PA) from site 27-1018 model

The idealized seasonal variation obtained from the layered elastic model is similar for the four selected indices (BCI, SDI, SI, and PA). The similarity is evident in Figures 4.36 and 4.37, where the seasonal variation of the indices for site 27-6251 27-1018 have been normalized with respect to the nominal value, and superimposed. This suggests that a ratio of the indices may be useful for the detection of freeze and thaw induced changes in pavement capacity.

4.5.2 Seasonal Changes in Strain at the Bottom of the AC Layer and Top of the Subgrade

One of the primary goals of this study was to develop guidelines for the lifting of load restrictions after the pavement capacity has recovered following spring thaw. Since pavement damage is usually assumed to be related to the magnitude of horizontal strain at the bottom of the AC layer, ϵ_{AC}, or the vertical strain at the top of the soil subgrade, ϵ_{SG}, the application of load restrictions should be such that these strains are limited during spring thaw. The layered elastic models developed for the LTPP sites can be used to simulate the conditions during spring thaw, and to identify the periods when the strains are excessive. If it is assumed that the strains generated in the pavement system during the middle of the summer represent the worst non-thaw conditions, yet are acceptable from a pavement damage perspective, then these summer strains can be taken as the limiting or critical strains above which loading should be restricted during the spring thaw. An investigation of the FWD basin indices from the layered elastic model can be used to determine how the change in indices correspond to changes in these critical strains, leading to guidance for the removal of load restrictions.

Figures 4.38 and 4.39 show the seasonal variation of horizontal strain at the bottom of the asphalt layer, normalized with respect to the value obtained for the week of October 1, for sites 27-6251 and 27-1018, respectively. For the thicker pavement system, site 27-6251, the ϵ_{AC} during

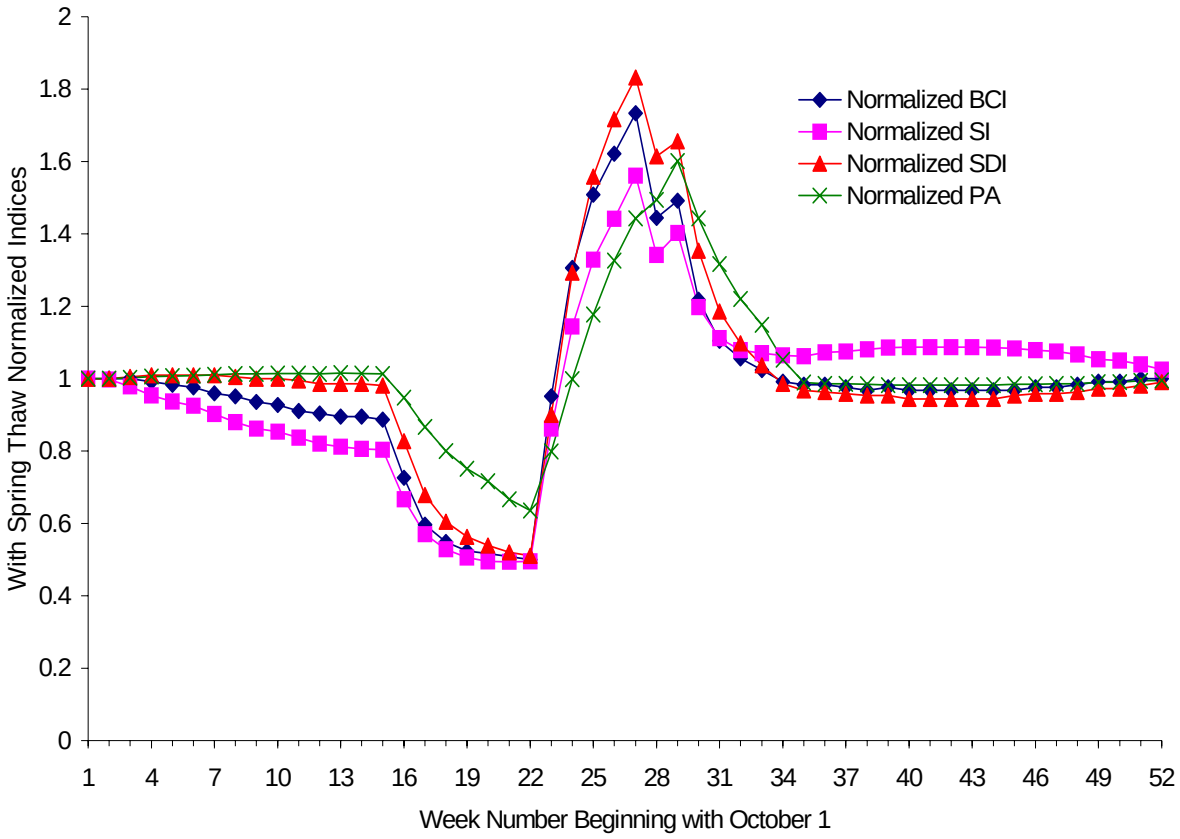

Figure 4.36 Normalized FWD indices from site 27-6251 model

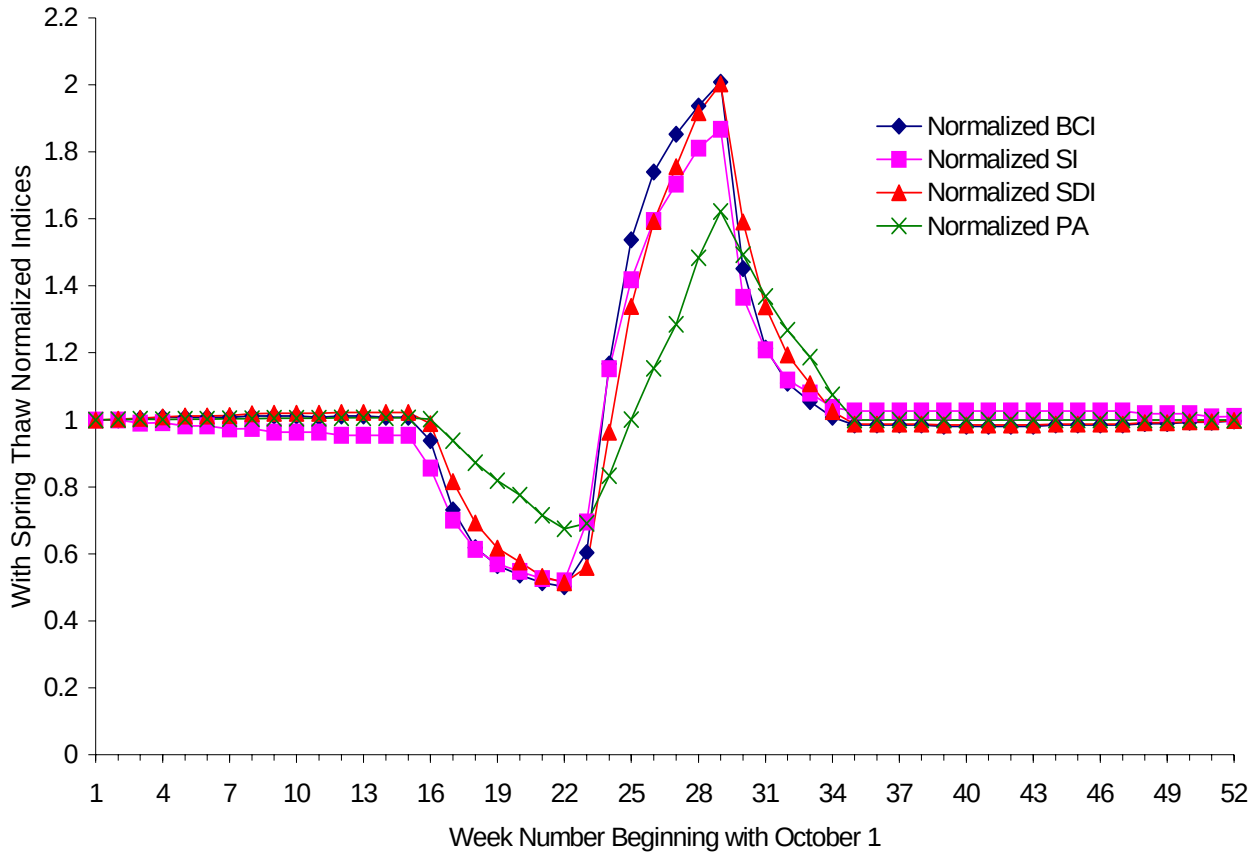

Figure 4.37 Normalized FWD indices from site 27-1018 model

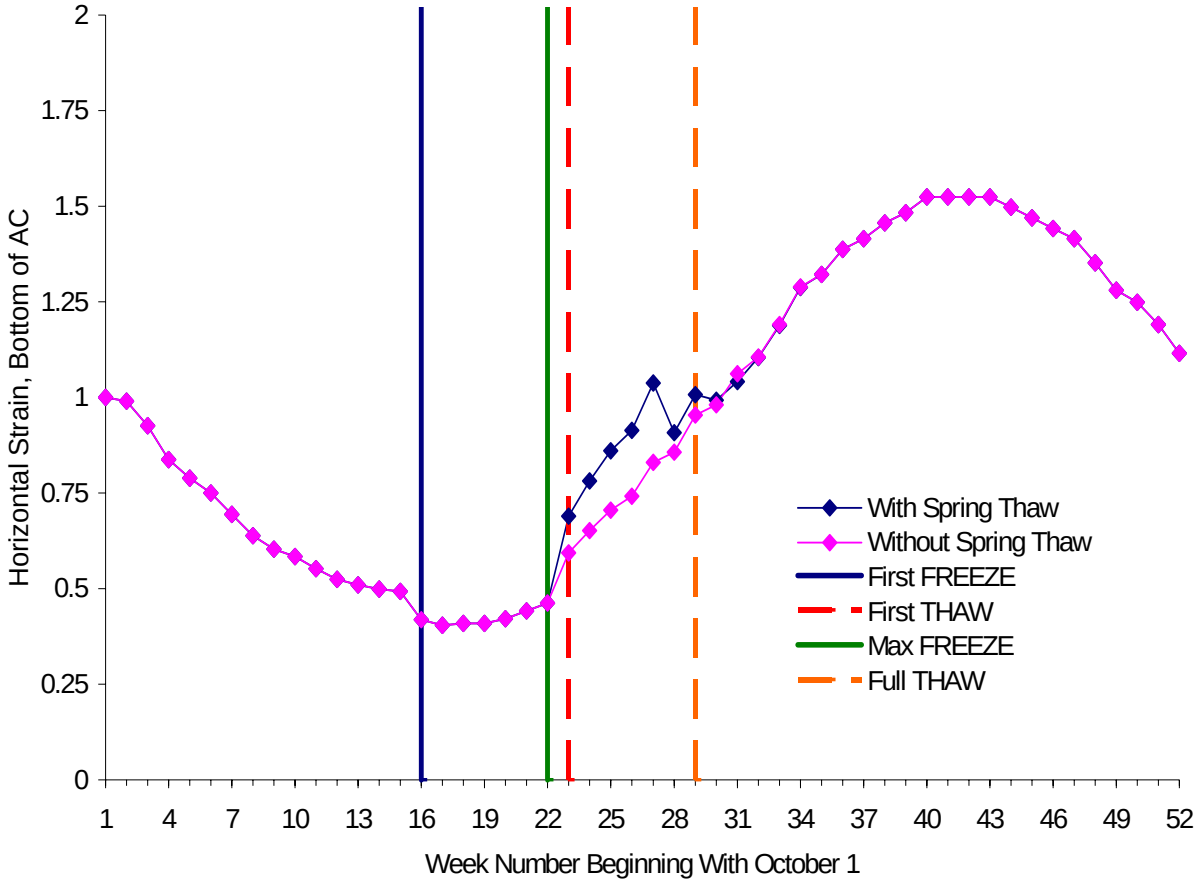

Figure 4.38 Normalized horizontal strain, bottom of AC, at site 27-6251

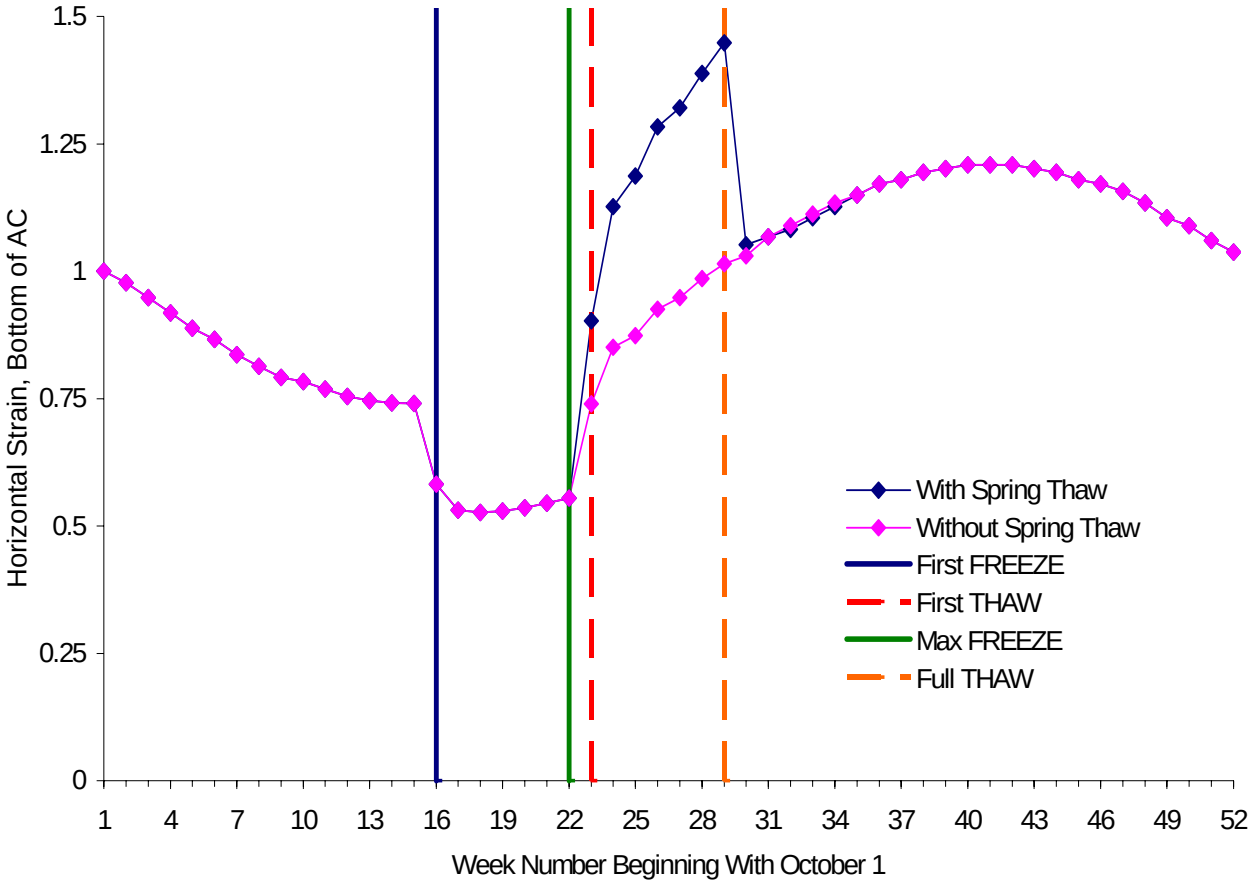

Figure 4.39 Normalized horizontal strain, bottom of AC, site 27-1018

the idealized thaw weakening is not much greater than for the case without thaw weakening, and the summer strains are clearly the most critical. For the thinner pavement at site 27-1018, the ϵ_{AC} during thaw weakening is significantly greater than for the case without thaw weakening, and during the period from about week 25 to 29 greater than the maximum strains occurring during the summer (Week 41). It is therefore concluded that the asphalt tensile strain is not critical for the thicker pavement at site 27-6251, but is critical at site 27-1018. The predicted seasonal variation of normalized asphalt tensile strain for the other freeze sites is provided in Appendix Y.

The seasonal variation of the vertical strain in the soil subgrade, ϵ_{SG}, is shown in Figures 4.40 and 4.41 for sites 27-6251 and 27-1018, respectively. The values have been normalized with respect to the value obtained for the week of October 1. In both cases, the ϵ_{SG} is much greater for the case with the thaw weakening than for the case without thaw weakening, and exceed the maximum computed during the summer months. This suggests that thaw weakening during the period from weeks 24 to 29 would be a concern at both sites based on a subgrade strain criteria . The seasonal variation of the predicted normalized subgrade strain is provided for the other freeze sites in Appendix Z.

4.5.3 Procedure for Determination of Site Specific Critical Indices

By comparing the time history of the computed FWD indices with the history of the computed strains, the FWD index values corresponding to the beginning and end of the thaw weakening period can be determined. Since a number of assumptions were made in the development of the layered elastic model, the magnitude of the computed FWD indices may not closely agree with the magnitude measured from field FWD testing. However, if the index values are expressed in terms of index ratios, where the index at any time is divided by the nominal index value on October 1, the relative

changes in behavior in the model and field can be compared.. Thus, when the pavement is freezing and the index values are decreasing, the index ratio has a value less than unity. Upon thaw, the index ratio begins to increase, and if the pavement experiences thaw weakening, the index ratio will exceed one..

Two specific limit values of the index ratio are important, and are defined as the Thaw Index Ratio, R_t and the Recovery Index Ratio, R_r :

$$R_t = \frac{I_{thaw}}{I_{nominal}} \qquad R_r = \frac{I_{recovery}}{I_{nominal}}$$

where I_{thaw} = the index value corresponding to the time when the strain first exceeds the summer maximum strain

$I_{recovery}$ = the index value corresponding to the time when the strain first recovers to a value less than the summer maximum strain

$I_{nominal}$ = the nominal index value from the fall or October

The index value I_{thaw} corresponds to periods of increasing index value, while the index $I_{nominal}$ corresponds to periods of decreasing index values.

A third index is useful, the Maximum Index Ratio, R_{max} :

$$R_{\max} = \frac{I_{maximum}}{I_{nominal}}$$

where $I_{maximum}$ = the index value corresponding to the time when the strain is maximum.

If the Thaw Index Ratio, R_t and the Recovery Index Ratio, R_r can be estimated for a given pavement system under specific climactic conditions, field FWD testing during the critical thaw weakening period can be used to make decisions relative to the timing of load restrictions. Load restrictions can be placed when increasing index ratios reach the limiting value, R_t . Likewise, when the index ratios are falling, the load restrictions can be lifted when the ratio falls below the other limiting value, R_r.

Rather than normalizing the index values with respect to the nominal values, an alternative approach would be to normalize the FWD indices with respect to the values obtained in the summer when the strains are maximum. However, there are two reasons why this was not done. First, most of the selected index values (selected to emphasize base and subgrade changes) are not significantly different in the summer than in the fall, even though the strains may be significantly different. Secondly, it is much more difficult in practice to conduct FWD tests at several locations during the hottest period of the summer. It is more practical to obtain the nominal defection basin at the identified sites during a longer fall period.

The time histories of ϵ_{AC} and ϵ_{SG} , such as those shown in Figures 4.38 through 4.41, for the freeze sites were examined to identify the times (or steps, Table 4.7) at which the strains became critical. Determination of the magnitude of the index values at these times yielded the Thaw Index Ratio, R_t and the Recovery Index Ratio, R_r for each of the freeze sites which experienced thaw weakening. The Maximum Index Ratio, R_{max} was also determined, to for comparison with the sites for which thaw weakening did not occur under the idealized model conditions. The results of this investigation are summarized in Table 4.8 for the AC tensile strain criterion, and in Table 4.9 for the subgrade strain criterion.

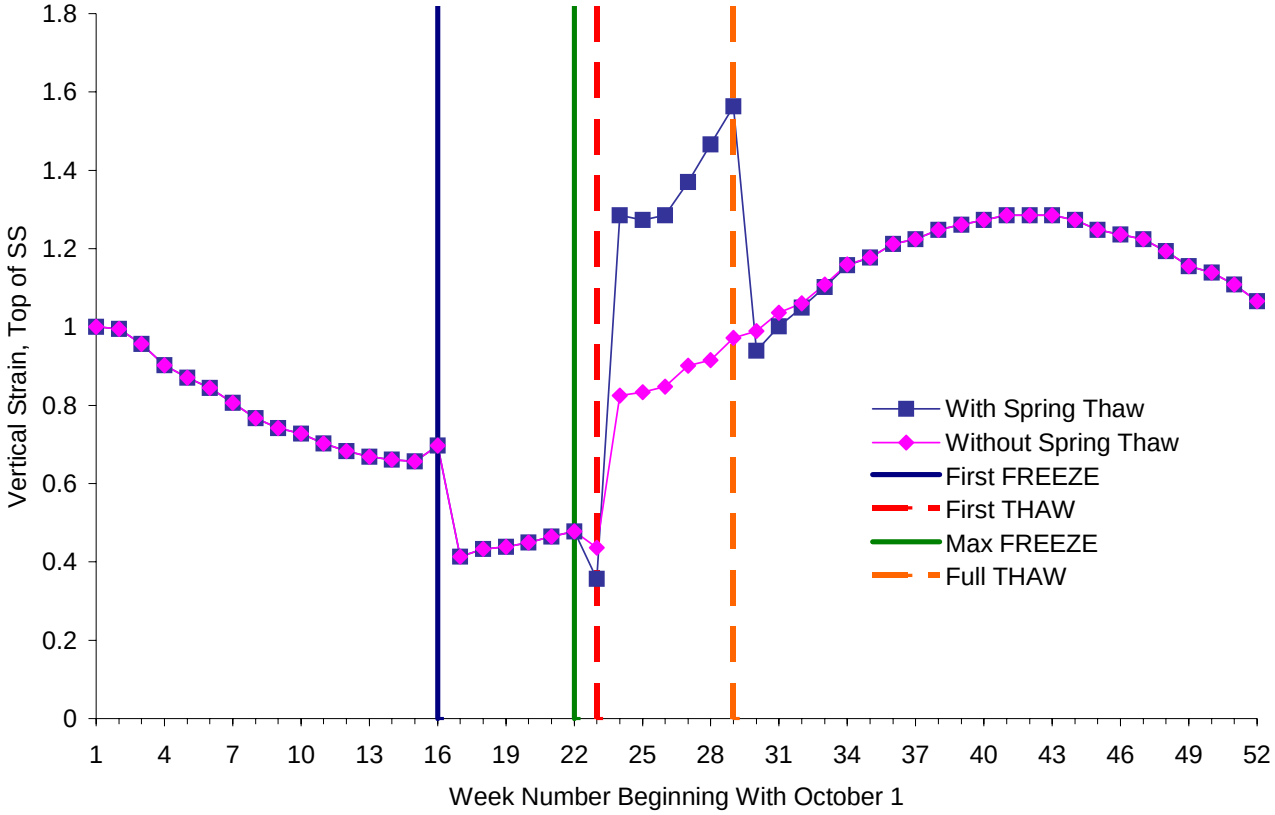

Figure 4.40 Normalized vertical strain, top of subgrade, site 27-6251

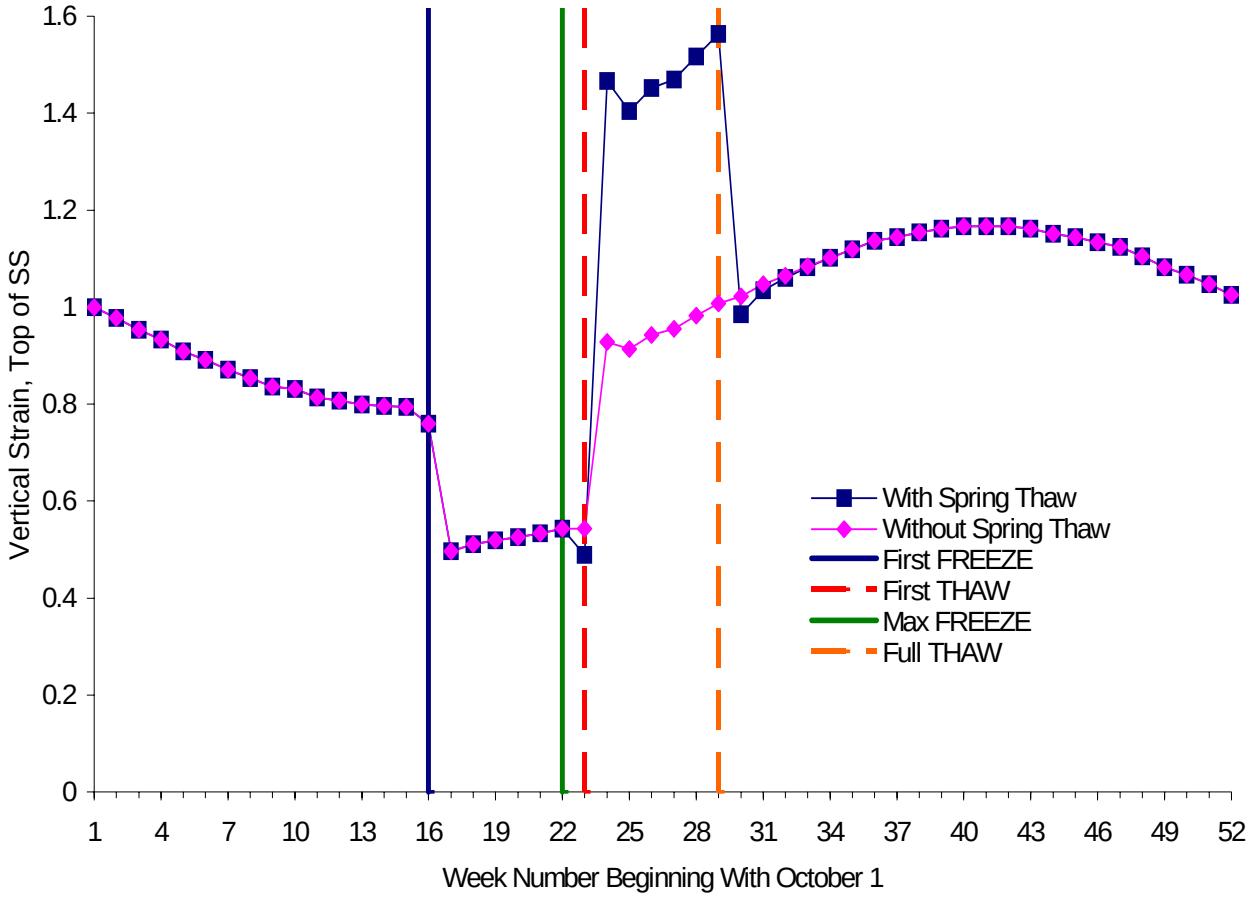

Figure 4.41 Normalized vertical strain, top of subgrade, site 27-1018

Table 4.8 Critical FWD index ratios relative to maximum summer conditions- AC strain criterion

Site	Basin Index	Nominal (Oct 1) Index	Initial Thaw Threshold			Maximum Strain			End of Recovery			notes
			Week strain first exceeds summer max AC strain	Index value	Thaw Index Ratio, R_t	Week of maximum thaw strain	Index value	Max Thaw Index Ratio, R_{max}	Week strain first recovers	Index value	Recovery Index Ratio, R_r	
16-1010	BCI	26	NA			NA			NA			no thaw effect
	SDI	70										
	SI	97										
	PA	16										
23-1026	BCI	21	NA			27	32	1.52	NA			
	SDI	42					65	1.55				
	SI	78					115	1.47				
	PA	6					7.4	1.23				
27-1018	BCI	26	26	45	1.15	29	52	2.00	30	38	1.46	
	SDI	46		73	1.59		92	2.00		73	1.59	
	SI	107		170	1.59		199	1.86		145	1.36	
	PA	5.5		6.3	1.15		8.9	1.62		8.2	1.49	
27-1028	BCI	24	NA			29	36	1.50	NA			
	SDI	51					84	1.65				
	SI	82					125	1.52				
	PA	7.1					12	1.69				

Site	Basin Index	Nominal (Oct 1) Index	Initial Thaw Threshold			Maximum Strain			End of Recovery			notes
			Week strain first exceeds summer max AC strain	Index value	Thaw Index Ratio, R_t	Week of maximum thaw strain	Index value	Max Thaw Index Ratio, R_{max}	Week strain first recovers	Index value	Recovery Index Ratio, R_r	
27-6251	BCI	13	NA			27	22	1.69	NA			
	SDI	22					40	1.82				
	SI	49					76	1.55				
	PA	2.5					3.5	1.40				
30-8129	BCI	21	27	37	1.76	27	37	1.76	28	25	1.19	
	SDI	44		67	1.52		67	1.52		53	1.20	
	SI	96		158	1.65		158	1.65		108	1.13	
	PA	6.8		7.9	1.16		7.9	1.16		7.7	1.13	
50-1002	BCI	18	NA			27	27	1.50	NA			
	SDI	36					56	1.56				
	SI	66					97	1.47				
	PA	6					7.3	1.22				
87-1622	BCI	21	NA			27	36	1.71	NA			
	SDI	39					67	1.72				
	SI	81					128	1.58				
	PA	5.2					6.8	1.31				

Note: Values for index PA are in units of m^2 $x10^{-5}$

Table 4.9 Critical FWD index ratios relative to maximum summer conditions- subgrade strain criterion

Site	Basin Index	Nominal (Oct 1) Index	Initial Thaw Threshold			Maximum Strain			End of Recovery			notes
			Week strain first exceeds summer max SG strain	Index value	Thaw Index Ratio, R_t	Week of maximum thaw strain	Index value	Max Thaw Index Ratio, R_{max}	Week strain first recovers	Index value	Recovery Index Ratio, R_r	
16-1010	BCI	26	24	21	0.81	24	21	0.81	30	31	1.19	
	SDI	70		57	0.81		57	0.81		83	1.19	
	SI	97		78	0.80		78	0.80		115	1.19	
	PA	16		15	0.94		15	0.94		18	1.13	
23-1026	BCI	21	24	25	1.19	27	32	1.52	30	25	1.19	
	SDI	42		40	0.95		65	1.55		54	1.29	
	SI	78		85	1.09		115	1.47		95	1.22	
	PA	6		6	1.00		7.4	1.23		7.6	1.27	
27-1018	BCI	26	24	30	1.15	29	52	2.00	30	38	1.46	
	SDI	46		44	0.96		92	2.00		73	1.59	
	SI	107		123	1.15		199	1.86		145	1.36	
	PA	5.5		4.6	0.84		8.9	1.62		8.2	1.49	
27-1028	BCI	24	NA			29	36	1.50	NA			
	SDI	51					84	1.65				
	SI	82					125	1.52				
	PA	7.1					12	1.69				

Site	Basin Index	Nominal (Oct 1) Index	Initial Thaw Threshold			Maximum Strain			End of Recovery			notes
			Week strain first exceeds summer max SG strain	Index value	Thaw Index Ratio, R_t	Week of maximum thaw strain	Index value	Max Thaw Index Ratio, R_{max}	Week strain first recovers	Index value	Recovery Index Ratio, R_r	
27-6251	BCI	13	24	16	1.23	29	19	1.46	30	15	1.15	
	SDI	22		28	1.27		36	1.64		30	1.36	
	SI	49		56	1.14		68	1.39		58	1.18	
	PA	2.5		2.4	0.96		3.9	1.56		3.5	1.40	
30-8129	BCI	21	24	32	1.52	27	37	1.76	30	25	1.19	
	SDI	44		55	1.25		67	1.52		53	1.20	
	SI	96		135	1.41		158	1.65		108	1.13	
	PA	6.8		7	1.03		7.9	1.16		7.7	1.13	
50-1002	BCI	18	24	22	1.22	27	27	1.50	30	20	1.11	
	SDI	36		45	1.25		56	1.56		42	1.17	
	SI	66		76	1.15		97	1.47		75	1.14	
	PA	6		6.4	1.07		7.3	1.22		6.9	1.15	
87-1622	BCI	21	24	27	1.29	29	34	1.62	30	26	1.24	
	SDI	39		46	1.18		67	1.72		53	1.36	
	SI	81		96	1.19		122	1.51		99	1.22	
	PA	5.2		5.1	0.98		7.3	1.40		6.6	1.27	

Note: Values for index PA are in units of m^2 $x10^{-5}$

Of the eight sites that were modeled, only 2 (sites 27-1018 and 30-8129) experienced thaw weakening based on the AC criterion, whereas 7 experienced thaw weakening based on the subgrade strain criterion. With the exception of site 16-1010 which experienced minimal effect from the idealized thaw, the maximum index ratio R_{max} was between 1.15 and 2.0.

Each of the deflection basin indices investigated above (BCI, SDI, SI and PA) appear capable of detecting the loss of capacity during thaw weakening. The Thaw Index Ratio, R_t and the Recovery Index Ratio, R_r are site-specific limiting values, and should be dependent upon the layer properties, the imposed conditions during thaw, and the pavement thickness. Likewise, the FWD index that is the best indicator of changing pavement capacity is likely to depend upon the layer thicknesses and the extent to which the moduli change during thaw.

An approach has been described by which site-specific index ratios could be determined for any site. Required are estimates of the nominal material properties, typical variation of surface or air temperature, and assumptions relative to the magnitude of frozen and thawed layer moduli. The next chapter describes how this methodology could be implemented.

CHAPTER 5
IMPLEMENTATION OF RESEARCH FINDINGS

It was shown in Chapter 4 that FWD measurements can be used directly to evaluate the changes in pavement response during to freezing and thawing. A combination of field measured FWD response and the results from a layered elastic model were used to estimate the timing for the placement and lifting of load restrictions.

5.1 FWD INDICES TO DETECT THAW WEAKENING

The methodology described in the previous chapter can be implemented on a site-by-site basis in accordance with the following steps:

I. Identification of pavement monitoring locations and preliminary data collection.
   - A. Identify the monitoring stations for which the subgrade and moisture conditions are representative of the area of concern and are likely to serve as good indicators of thaw weakening for the pavement. These may be areas that have been subject to thaw weakening distress in the past.
   - B. Estimate the pavement layer thickness or obtain representative pavement cores
   - C. Determine the typical maximum freeze depth at the site from a freeze depth model such as that developed in Chapter 2:

$$D_f = 0.250\sqrt{FI}$$

     where D_f = the freeze depth in feet and
     FI = the typical freezing index in ^oF Days
   - D. For each station, mark or paint a specific "spot" on the pavement such that all subsequent FWD test drops can strike the same location on the pavement. Choose a drop spot free of significant cracking or distress and away from any repaired pavement core holes.

II. Development of layered elastic model of pavement system
   - A. Identify a layered elastic computer code such as BISAR, and create a model for the pavement based on the layer thickness determined in the field.
   - B. Divide the subgrade into several sublayers with a total depth equal to the typical depth of freeze determined for the site. These layers will be above an elastic half-space.
   - C. Identify nominal properties for each of the pavement layers, either based on values from the literature or if available, backcalculated from FWD testing. The actual values chosen may not be critical since the relative change in response is what is of

interest.

D. Choose freeze and thaw factors to apply to the nominal material properties. In this study, a factor of 2 was applied during freeze and a factor of 0.5 was applied during thaw.

E. Identify AC modulus values corresponding to the nominal conditions, freeze conditions, and at the maximum anticipated summer temperature.

F. Conduct a series of analysis cases, similar to that in Table 4.6, to represent the conditions throughout the year. There need not be as many steps as indicated in the table, but at a minimum the following 9 steps or analyses are recommended:
   1. Nominal or fall conditions (1 step)
   2. Full Freeze for full depth of subgrade (1 step)
   3. Spring thaw, considering several steps as the base and subgrade thaw progressively from the top down (at least 3 steps)
   4. Recovery, considering several steps as the base and subgrade recover to nominal conditions (at least 3 steps)
   5. Summer corresponding to the highest temperature and greatest critical strains (1 step)

   Obtain analysis output for the horizontal tensile strain at the bottom of the AC layer, the vertical strain at the top of the soil subgrade, and the pavement surface deflections corresponding to the locations of the FWD sensors

III. Analysis of results from layered elastic model of pavement system

A. Create graphs similar to that shown schematically in Figure 5.1 for the variation of the computed tensile strain at the bottom of the AC layer and compressive strain at the top of the subgrade. Normalize the strains relative to the nominal values.

B. From the analysis results or the graphs, determine the threshold value of strain corresponding to the highest anticipated temperature that may exist in the summer. Thaw strains below this threshold value are assumed not to be detrimental to the pavement.

C. If the analysis produces strains greater than the threshold strains, identify the analysis steps corresponding to the greatest thaw strain below the threshold value, and the greatest recovery strain below the threshold value as depicted in Figure 5.1. Alternatively, identify the analysis step at which the threshold strain is first exceeded. If all the computed strains are below the threshold value, identify the analysis steps for which the strains are maximum.

D. From the surface deflections computed in the model, determine the value of the FWD indices for the nominal conditions, and the indices for the thaw and recovery threshold analysis steps or maximum strain step identified above. Normalize the index values with respect to the nominal values to determine the Thaw Index Ratio, R_t and the Recovery Index Ratio, R_r, or if the threshold strains were not exceeded in the analysis, the Maximum Index Ratio, R_{maxr}. It may be helpful to create graphs similar to that shown schematically in Figure 5.2 for the variation of the normalized indices over time.

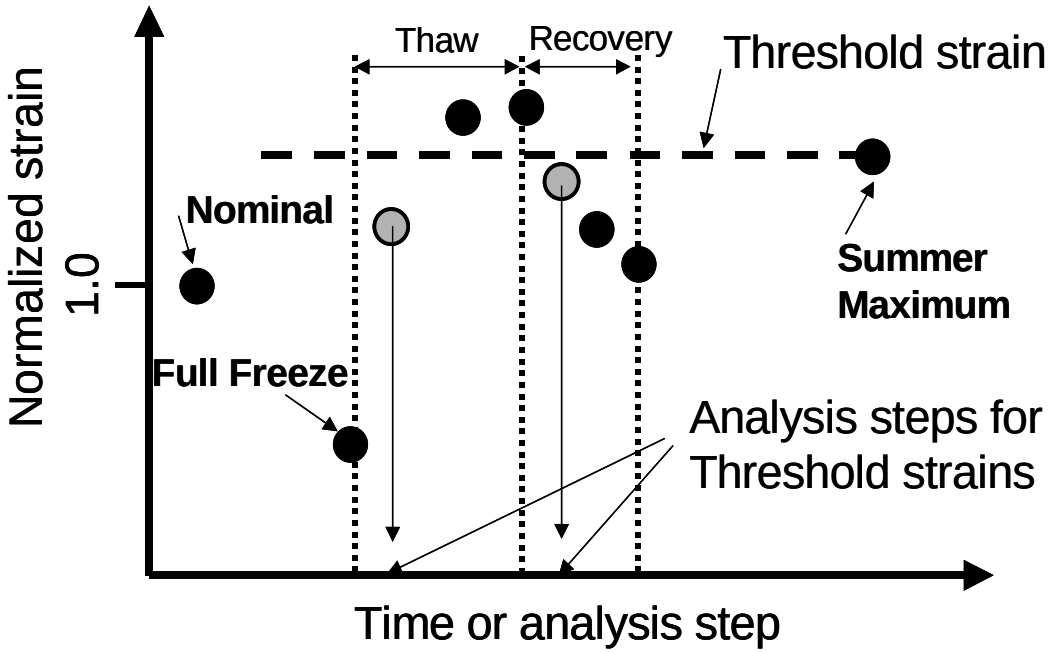

Figure 5.1 Variation of computed normalized strain versus time or analysis step

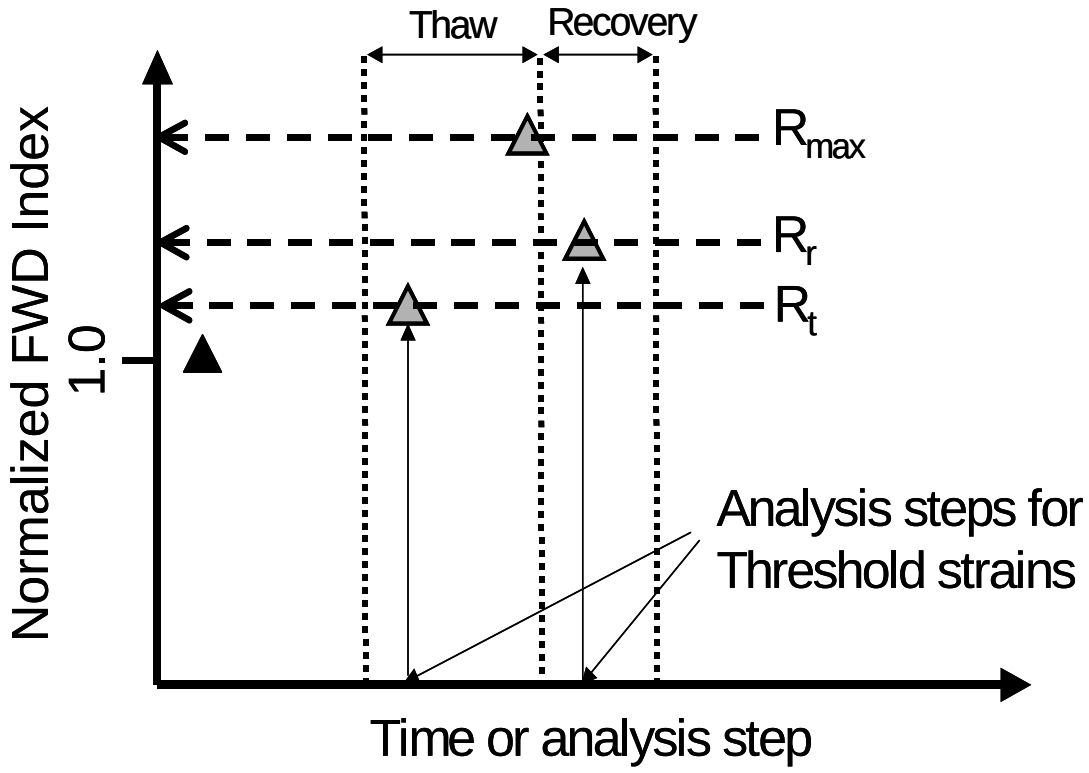

Figure 5.2 Normalized FWD indices at analysis steps corresponding to the threshold strains

IV. Measurement of pavement response with FWD during nominal or fall conditions

A. Conduct FWD testing during the fall at the "marked" location. Obtain results at multiple drop heights, and use data at the drop heights that produce contact pressures closest to 80 psi (550 kPa).

B. Determine nominal values for the FWD deflection indices BCI, SDI, SI and PA.

V. Measurement of pavement response with FWD during freeze

A. As the freeze index, FI, approaches the anticipated annual maximum value, perform FWD testing. Test at the "marked" location and at multiple drop heights, and use data at the drop heights that produce contact pressures closest to 80 psi (550 kPa). This testing is important only in that it will establish the lower bound of the FWD indices and assure that the values obtained during thaw reflect decreased capacity.

B. Obtain the minimum values of the FWD indices, which should have values less than 1.0, as depicted by Point A in the schematic shown in Figure 5.3.

VI. Measurement of pavement response with FWD during the anticipated thaw period

A. Supported by calculation of the Thaw Index, TI, conduct FWD testing as soon as possible after measurable thaw has occurred. Test at the "marked" location and at multiple drop heights, and use data at the drop heights that produce contact pressures closest to 80 psi (550 kPa).

B. Immediately compute the normalized FWD indices to detect any increase from that measured during the known freeze period.

C. Compare the normalized FWD indices with the Thaw Index Ratio, R_t.

1. Provided normalized FWD index is less than Thaw Index Ratio for all indices, the pavement should still have adequate capacity. This condition is depicted by Point B in Figure 5.3

2. If the value of the normalized FWD index approaches R_t, such as Point C in Figure 5.3, institute load restrictions

D. If the threshold strains were not exceeded in the analysis (a Thaw Index Ratio was not determined for the site), compare the normalized FWD indices with the Maximum Index Ratio

1. Provided normalized FWD index is less than Maximum Index Ratio for all indices, the pavement should still have adequate capacity. This case is depicted by Point D in Figure 5.3

2. If the value of the normalized FWD index exceeds R_{maxr}, such as Point E, monitor the site closely to make sure the pavement does not have a significant loss of capacity. Notable distress would indicate that the pavement model used for the site did not reflect the actual field conditions, since the observed deflection indices were larger than those obtained with the model.

VII. Measurement of pavement response with FWD during the anticipated recovery period

A. Repeat the FWD testing during the load restriction period until the normalized deflection indices begin to show a decrease indicating that recovery has begun.

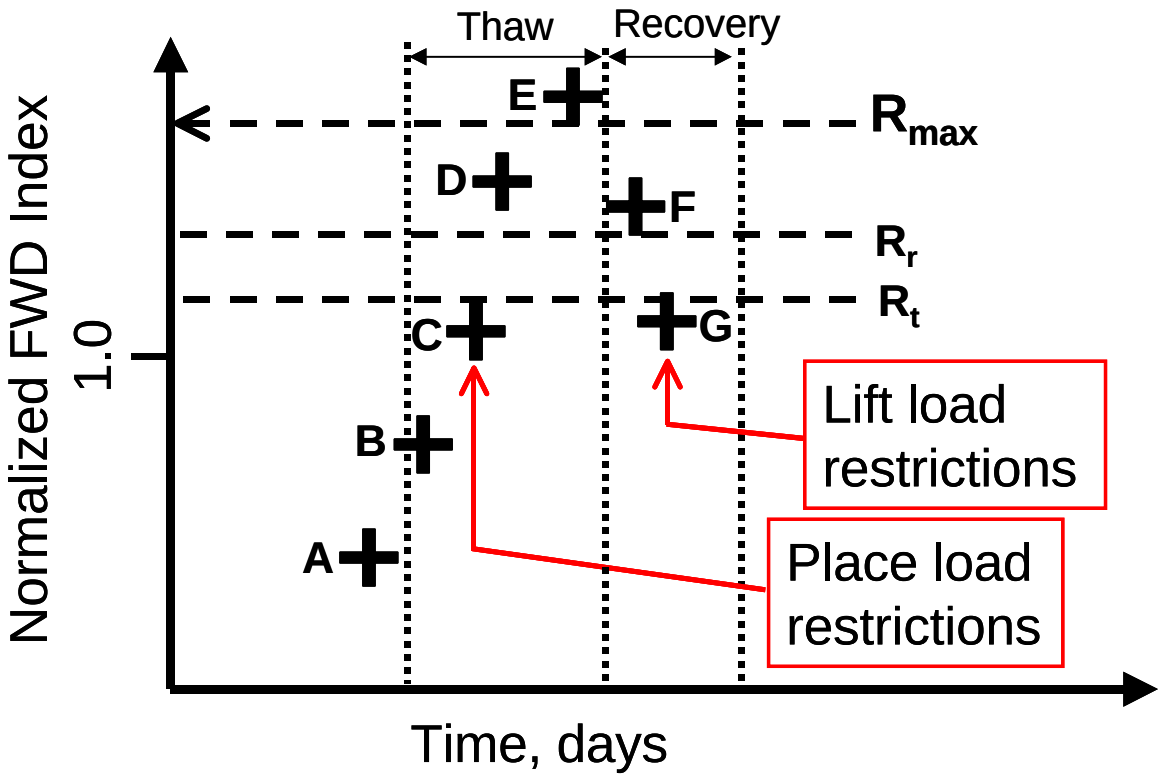

Figure 5.3 FWD indices from field testing to determine the timing of load restrictions

B. Compare the normalized FWD indices with the Recovery Index Ratio, R_r.
   1. If the normalized FWD index is greater than the Recovery Index Ratio for all indices, such as that depicted by Point F, the load restrictions should remain in place.
   2. If the value of the normalized FWD index drops below R_r as reflected by Point G, lift the load restrictions.

An advantage of using the FWD deflections directly is that the indices and/or index ratios can be determined in the field during the course of the FWD testing. Sophisticated backcalculation computer programs are not required to obtain moduli. Knowledge of the threshold index ratios and the nominal values for the site can be used with a spreadsheet program to compare the measured pavement response with the index ratios. Agencies will likely find that local experience may provide insight into when to best test for threshold values, and further simplifications may be developed.

CHAPTER 6
FINDINGS AND SUGGESTED RESEARCH

The findings of this investigation will be discussed, and suggestions for future research offered, in terms of the project objectives:

1. Document, based on the data available from the LTPP studies, patterns of change in daily and seasonal insitu pavement material properties;
2. Determine, based on the data available from the LTPP studies, relationships between daily and seasonal *in situ* pavement material properties and temperature, moisture, and other related factors; and
3. Investigate the relationships between these properties and the daily and seasonal structural capacity of flexible and rigid pavements with the intent of developing guidelines for imposing seasonal load restrictions and issuing seasonal overload permits.

6.1 Patterns of Change in Daily and Seasonal *In Situ* Pavement Material Properties

At most of the pavement sites that did not experience wintertime freezing, seasonal changes in the backcalculated subgrade moduli were lost in the scatter of the data. This can be attributed, in part, to the lack of any consistent changes in water content throughout the year (as will be discussed in the next section). One explanation for this finding may be that the most significant moisture effects are episodic rather than seasonal. For example, the base and subgrade may become saturated during a week of heavy rain and take a week or two to dry out afterwards. Because the SMP sites are only visited once a month or less, the entire episode could be missed entirely. Future research into environmental effects should include continuous (or at least daily) monitoring of the environmental factors in order to get a better picture of the frequency and duration of these episodes and their potential impact on the pavement layer moduli.

At sites with significant wintertime freezing, the backcalculated layer moduli were found to increase substantially during the frozen periods, as expected, but the relative magnitude of the increase was erratic and hard to model. In most cases, there was little or no modulus data available during the spring thaw, so it was impossible to document thaw weakening. In part, this is attributed to the testing frequency. The SMP experimental design called for monthly FWD testing with one additional testing day during the estimated thaw period. As documented in Appendix B, the spring thaw was entirely missed in some cases and captured by just one testing date in many others. The only way to ensure that the thaw weakening period is fully captured is to monitor the instrumentation continuously and conduct FWD tests on a daily or weekly basis during the thaw.

Even when FWD testing was conducted, there was seldom any modulus data available during the thaw period. This is most likely because the backcalculation attempts were unsuccessful. It is extremely hard, with the layered elastic programs used in the LTPP, to accurately model a soft, saturated soil layer trapped between a much-stiffer base layer and the still-frozen subgrade beneath it. Advanced modeling techniques are needed to handle such a pavement profile. One approach would be to model the thawed soil as a separate layer. In the LTPP IMS, the same site layering was used throughout the year, regardless of the freeze depth or thaw depth. A parametric study should be undertaken to see if more consistent results are obtained by modeling the frozen soil and the thawed soil as layers separate from the underlying subgrade. Going further, it might help to give the thawed soil layer frictionless interfaces to better simulate saturated conditions.

Another reason for the lack of documented thaw weakening is that many of the pavements seem not to be particularly frost-susceptible. As explained in the next section, only a couple of sites exhibited a significant increase in the subgrade moisture content during the spring thaw. The

"typical" thaw-weakening response only occurs when a significant amount of water migrates to the freezing soil as the result of capillary rise. Absent this increase in moisture content, the thawed soil is little different than it was before freezing, so the modulus is unchanged. This appears to be the case at most of the SMP sites that froze.

At the flexible pavement sites, the backcalculated base moduli were found to be significantly negatively correlated with the backcalculated asphalt moduli. As a result, the backcalculated base moduli exhibit the inverse temperature dependence of the asphalt layers, even though the base materials themselves should be temperature independent. This phenomenon is an artifact of the backcalculation process. When the behavior of the pavement system deviates from the assumptions of layered elasticity, the backcalculation program introduces compensating errors in alternating layer moduli as it tries to match the deflection basin. The same negative correlation was seen between the upper and lower subgrade moduli. This suggests that much of the month-to-month changes in the backcalculate moduli are not directly the result of environmental changes but are, instead, tied more to month-to-month changes in the degree to which layered elasticity is a valid model for the pavement system. The effects are lessened, but not totally eliminated, by using nonlinear material models. Unfortunately, only a small percentage of the FWD basins were analyzed using nonlinear models. Future research should concentrate on more and better nonlinear analyses of the FWD data collected for the SMP.

At the rigid pavement sites, the base moduli were found to be perfectly linearly correlated with the backcalculated concrete moduli by design. This was done because it is so difficult to "see" the base layer beneath the concrete slab. If the base moduli were backcalculated independently, the

data scatter would likely be significant and the accuracy of the results would be questionable. Any environmental effects would be lost in the data scatter.

At some of the rigid pavement sites, it was also found that slab curl significantly affected the backcalculated subgrade moduli. Of the 14 rigid pavement sites with a reasonable quantity of backcalculated moduli, half exhibited a strong or moderate relationship between the backcalculated subgrade modulus and the temperature gradient in the concrete slab. In most cases, the temperature gradient dependence was captured by a linear relationship that could be used to correct the backcalculated k-values to a zero-gradient (uncurled) condition. This is an area that needs further study. In particular, it would be helpful to know how the distribution of the contact stresses between the slab and the foundation changes throughout the day due to slab curl. It would also be useful to be able to predict the temperature gradient in the concrete slab at any point during the day so backcalculated moduli could be corrected. Despite a significant effort, no such model could be developed from the data in the LTPP IMS. The temperature gradient is extremely sensitive to the amount of solar radiation striking the pavement. The midday temperature gradients on sunny days were found to be as much as ten times greater than on cloudy or rainy days, making it impossible to predict the temperature gradient without some measure of the solar radiation. Unfortunately, solar radiation was not one of the environmental factors included in the SMP design and cloud cover was only recorded during site visits and so yielded too little data for modeling purposes. It is essential to include solar radiation measurements in any future experiments on environmental effects.

6.2 Relationships Between Daily and Seasonal *In Situ* Pavement Material Properties and Temperature, Moisture, and Other Related Factors

From the flexible pavement sites in the LTPP SMP, site-specific models of asphalt modulus as a function of internal temperature, surface temperature, and air temperature were developed. The internal temperature produced the best correlation, but the surface temperature produced a model that was almost as good. The air temperature produced the worst correlation because it fails to capture the significant heating affects of solar radiation. Ideally, the solar radiation would be incorporated into the model as an additional variable, but solar radiation was not included in the SMP instrumentation plan.

Of the 65 pavement sites in the SMP, 35 were located in wet-freeze or dry-freeze climatic zones and instrumented with electrical resistivity probes to determine the freeze state of the soil during the freeze/thaw period. At some of the wet-freeze sites, the winters were too mild to produce any appreciable freezing and at some of the dry-freeze sites, low moisture contents resulted in cold but unfrozen pavements. Of the 35 freezing sites, 21 sites registered at least some frozen base or subgrade materials during the three years of data collection included in the IMS.

Site-specific models were developed to relate the depth of freezing to the freezing index, which is defined in this study as the number of freezing degree-days accumulated at any point in time. Of the 21 sites that registered freezing, 10 had sufficient data to develop site-specific freeze depth models. In addition, a general model of freeze depth as a function of the square root of freezing index was developed using data from all of the frozen sites.

A few site-specific models were developed to relate the depth of thawing to the thawing index, which is defined as the number of thawing degree-days accumulated at any point in time. To account for the effects of solar radiation, the thawing index is modified by a term that changes as the days get longer and the sun gets higher in the sky. Because the spring thaw is much shorter than

the winter freeze, there was much less data available to model thaw depths. By grouping sites with similar subgrade types, reasonable power law models of thaw depth as a function of thawing index were obtained for three different subgrade types: silty sand, silty clay, and sand with silt.

The freeze-depth and thaw-depth models were used, in conjunction with the thawing index, to estimate the date of full thaw each year at each site. As summarized in Appendix D, this effort was very successful in some cases but not others. It was most successful when site-specific models were available for both the freeze depth and the thaw depth and neither model had to be extrapolated beyond its data range. At many of the coldest sites, the depth of frost penetration far exceeded the depth of the frost detection probes, so the actual depth of frost penetration had to be extrapolated from the freeze depth model. An extrapolated thaw depth model was then used to estimate the number of thawing degree-days needed to completely thaw the pavement system to that depth. This introduced significant errors in the calculation of thaw duration. So, too, did the use of generic thaw depth models based on subgrade type.

This is a fruitful area for future research. In areas where there was not a lot of freeze/thaw cycling in the early spring, the simple models developed here worked reasonably well. Much better models could have been developed had the thermistors and frost probes been monitored daily instead of monthly. In many cases, the discrepancies between the frost probes and the soil temperatures could have been resolved had significantly more data been available. With only monthly snapshots, it is impossible to distinguish bad readings from meaningful changes. Also, at the coldest sites, 8-foot or 9-foot probes would have eliminated the need to estimate the maximum freeze depth.

6.3 Relationships Between Properties and the Daily and Seasonal Structural Capacity of Flexible and Rigid Pavements, with the Intent of Developing Guidelines for Imposing Seasonal Load Restrictions and Issuing Seasonal Overload Permits

Efforts to model changes in pavement moduli during the winter freeze and spring thaw were hampered by a lack of backcalculated modulus data during these periods. In many cases, FWD tests were not performed during the winter months because of the extreme cold. During the spring thaw, FWD tests were performed but the results did not produce any usable layer moduli. During the spring thaw, the soft subgrade material closest to the surface is sandwiched between the stiff granular base layer and the still-frozen subgrade below it. This is not properly modeled by the layered elastic system used to backcalculate the pavement moduli, so it is hard to obtain reliable moduli.

Instead of using back-calculated moduli as an indicator of the seasonal variation in pavement response, the direct use of the FWD deflections was investigated. In this context, it is useful to reduce each deflection basin to a single index that can be related to a specific type of behavior. FWD deflection data from the LTPP SMP database were used to compute various basin indices and to identify changes in pavement response during periods of freezing and thaw. Several candidate indices were identified that appeared to reflect changes in structural capacity during freezing and thawing periods. While the indices at most sites reflected the change in response during freezing, only a few sites demonstrated what would be considered an obvious thaw weakening response.

To ascertain that the selected indices could detect thaw weakening and recovery, several datasets from outside the LTPP SMP were investigated. These datasets were from studies specifically designed to investigate the freeze-thaw response, and contained much more frequent deflection measurements during the thaw and recovery periods than did the LTPP SMP experiments.

Data from these studies were found to be helpful in the interpretation of the LTPP data, and supported the conclusion that the FWD data could be used as an indicator of changing response during the transition from nominal behavior through freeze, thaw, and recovery. The data from outside the LTPP SMP database also suggests that the SMP experimental design, which only provided a single additional series of FWD deflections during the estimated thaw period, likely did not capture the peak thaw response. In some cases, the monthly FWD test schedule substantially missed the brief spring thaw. In other cases, the pavements had been designed so as to minimize thaw weakening, or the sites were comprised of subgrade types that do not experience significant thaw weakening.

To fill in the gaps in the database, the pavements were modeled as layered elastic systems using the BISAR computer code. The moduli for the base and subgrade were systematically varied to reflect changes in response as the pavement goes from the nominal (or summer/fall conditions) to freeze, thaw and finally recovery back to the nominal conditions. The layered elastic models for each site were developed from data in the LTPP SMP database. For example, the nominal layer moduli were obtained from the back-calculated FWD response reported in the database. The asphalt modulus was varied with temperature throughout the year using the site-specific models developed from the LTPP data. The site-specific freeze depth models were used to define the freezing depth for each site model, and actual temperature data taken at the time of the FWD testing was used in the analysis. The site-specific layered elastic models were used to compute, for each week of the year, the FWD indices from the surface deflections and the critical strains in the asphalt and subgrade. Thus, the layered elastic models were based directly on the LTTP database and were used to supplement the gaps in the recorded response during the critical thaw weakening period.

The results from the site-specific layered elastic analyses were used to develop a methodology (summarized in Chapter 5) for predicting the time of post-thaw recovery. Equating the critical strains during thaw and recovery with the largest strains predicted during the heat of the summer (when the critical strains are assumed to be acceptable), the timing of the end of the recovery period can be defined and the corresponding FWD indices used to trigger the removal of load restrictions. Even if the LTPP database contained more complete FWD data during the thaw period, layered elastic analyses would be needed to determine the acceptable values of these strains. Almost all backcalculation programs can output stresses and strains at selected points in the pavement system along with the backcalculated layer moduli. In the future, critical stresses and strains should be included in the LTPP IMS in order to facilitate this type of analysis. This is especially true when nonlinear material models are used in the backcalculation because the analysis of the pavement system is not as straightforward as it is with linear elastic models.

REFERENCES

Benson, Craig H., Bosscher, Peter J., and Jong, Da-Tong (1998) "Predicting the Effects of Freezing and Thawing on Pavement Support," Report WI/SPR-02-98, Wisconsin Department of Transportation, Madison, WI.

Byrum, C. R. (2000) "Analysis of LTPP JCP Slab Curvatures Using High Speed Profiles." Transportation Research Board.

Cumberledge, G. L., Hoffman, Bhajandas, A. C., and Cominsky, R. J. (1974) Moisture Variation in Highway Subgrades and the Associated Change in Surface Deflections. Transportation Research Record 497, pp. 40 - 49.

DeBruin, P. W., Visser, Alex T., and Jordan, Gerrit J. (2002) "Modeling the Changes in Pavement Layers During Rehabilitation and the Effect of These Changes on the Structural Capacity". 15th ASCE Engineering Mechanics Conference. New York, NY: June.

De Jong, D. L., Peatz, M. G. F., And Korswagen, A. R. (1973) *Computer Program BISAR Layered Systems Under Normal and Tangential Loads*. Konin Klijke Shell-Laboratoium, Amsterdam, External Report AMSR.0006.73.

Hinshaw, R. F. and Northrup, J. L.(1991) "Predicting Subgrade Moisture Under Aggregate Surfacing." Transportation Research Record 1291, pp. 193-203.

Hossain, M.., Kotdwala, S. J., Long, B., and Gisi, A. J. (1997) Subgrade Moisture Monitoring Using Time Domain Reflectometry. [Paper No. 970370]. Washington, D.C. Transportation Research Board 76th Annual Meeting.

Ioannides, A.(1991) "Theoretical Implications of the AASHTO 1986 Nondestructive Testing Method 2 for Pavement Evaluation." Transportation Research Record 1307 , pp. 211–220.

Janoo, V. C. (1999) "Evaluating Pavement Performance in Cold Regions".

Janoo, V. C. and Berg, R. L. (1990) "Predicting the behavior of asphalt concrete pavements in seasonal frost areas using nondestructive techniques." CRREL Report 90-10.

Janoo, V. C., Berg, R. L., Bigl, S. R., and Tomita, H. (1992) "Use of falling weight deflectometer (FWD) to characterize seasonal variation in pavement response" Road Engineering Association of Asia and Australasia, 7th Conference, Singapore, June 22-26. Vol.2, pp.395-404. (CRREL Report No: MP 3220)

Janoo, V., and Cortez, E. (2002) "Pavement Evaluation in Cold Regions", Proceedings, 11th International Conference, Cold Regions Engineering, Cold Regions Impacts on Transportation and Infrastructure, American Society of Civil Engineers, Ed. K.S. Merrill, pp. 360-371.

Janoo, Vincent and Shephard, Kent. (2000) “Seasonal Variation of Moisture and Subsurface Layer Moduli.” TRB Pre-Print. Transportation Research Board 79th Annual Meeting.

Jong, Da-Tong, Boscher, P. J., and Benson, C. H. (1998) “Field Assessment of Changes in Pavement Moduli Caused by Freezing & Thawing.” Transportation Research Record No. 1615, Transportation Research Board, pp. 41-48.

Kestler, M. A, Hanek, G., Truebe, M., and Bolander, P. (1999) “Removing Spring Tahw Load Restrictions from Low-Volume Roads” Transportation Research Record No.1652, Vol. 2, pp 188-197.

Khogali, W. E. and Anderson, K. O. (1996) “Evaluation of Seasonal Variability in Cohesive Subgrades Using Backcalculation.” Transportation Research Record 1546, TRB, National Research Council, pp. 140–150.

Linsley, R. K., Franzini, J. B., Freyberg, D. L., and Tchobanoglous, G. (1992) Water Resources Engineering. New York, McGraw-Hill.

LTPP Manual for Falling Weight Deflectometer Measurements Operational Field Guidelines Version 3.1. August 2000.

Lukanen, E. O., Stubstad, R., and Briggs, R. C. (2000) “Temperature Predictions and Adjustment Factors for Asphalt Pavements.” FHWA Report RD-98-085, Federal Highway Administration, McLean, VA.

Matter, N. S. and Farouki, O. T. (1994) “Detailed Study on the Climatic and Seasonal Variation Effects on Pavements in Northern Ireland.” 4th Int. Conf. on the Bearing Capacity of Roads and Airfields, *Proceedings*, pp. 721–737.

Rada, G. R., Elkins, G. E., Henderson, B, Van Sambeek, R. J., and Lopez, Jr. A. (2000) “LTPP Seasonal Monitoring Program Instrumentation Installation and Data Collection Guidelines.” FHWA Report RD-94-110, Federal Highway Administration, McLean, VA

Richter, C. A. (1991) “Seasonal Monitoring of Pavements—A Whole Lot More.” Road and Airport Pavement Response Monitoring Systems, American Society of Civil Engineers, New York, NY. pp. 182–195.

Rohde, G. T. (1994) “Determining Pavement Structural Number from FWD Testing.” Transportation Research Record 1448, TRB, National Research Council, pp. 61–68.

Russam, K. (1970) “Subgrade Moisture Studies by the British Road Research Laboratory.” Highway Research Record 301, pp. 5–17.

Rutherford, M. S., Mahoney, J. P., Hicks, R. G., and Rwebingira, T. (1985) Guidelines for Spring Highway Use Restrictions, Report No. FHWA-RD-86-501, Washington State Department of Transportation.

Rutherford, M. S. (1989) "Pavement Response and Load Restrictions on Spring Thaw-Weakened Flexible Pavements." Transportation Research Record 1252, pp. 1-11.

Southgate, H. F. and Deen, R. C. (1969) "Temperature Distribution Within Asphalt Pavements and Its Relationship to Pavement Deflection." HRB, National Research Council, Highway Research Record 291 . pp. 116–131.

Spaans, E. and Baker, J. (1995) "Examining the Use of Time Domain Reflectometry for Measuring Liquid Water Content in Frozen Soil," Water Resources Research, v. 31, n. 12, pp. 2917–2925.

Stubstad, R. N., Baltzer, S., Lukanen, E. O., and Ertman-Larsen, H. J. (1994) "Prediction of AC Mat Temperatures for Routine Load/Deflection Measurements." 4th Int. Conf. on the Bearing Capacity of Roads and Airfields, Proceedings, pp. 401–412.

Stubstad, R. N., Lukanen, E. O., Richter, C. A., and Baltzer, S. (1998)"Calculation of AC Layer Temperatures From FWD Field Data." 5th Int. Conf. on the Bearing Capacity of Roads and Airfields, Proceedings, pp. 919–928.

Topp, G., Davis, J., and Annan, A. (1980) "Electromagnetic Determination of Soil Water Content: Measurements in Coaxial Transmission Lines," Water Resources Research, v. 16, n. 3, pp. 574–582.

Valdez, F. (1991) Subgrade Resilient Modulus Evaluation. FHWA-GA-91-8801.

VanDeusen, D., Schrader, C., Bullock, D., and Worel, B. (1998) "Springtime Thaw Weakening and Load Restrictions in Minnesota" Transportation Research Record No.1615, pp 21 - 31.

VanDeusen, D., Schrader, C., Bullock, D., and Worel, B. (1998) "Recent Research on Springtime Thaw Weakening and Load Restrictions in the State of Minnesota", Transportation Research Record No. 1615, Transportation Research Board, pp. 41-48.

Van Gurp, C. (1994) "Effect of Temperature Gradients and Season on Deflection Data." 4th Int. Conf. on the Bearing Capacity of Roads and Airfields, Proceedings, pp.199–214.

Worel,. Ben (2003) Personal communication, February.

Yoder, R. E. and Witczak, M.W. (1975) Principles of Pavement Design. New York, Wiley.

APPENDIX A

LITERATURE REVIEW OF ENVIRONMENTAL FACTORS AFFECTING PAVEMENT PROPERTIES

APPENDIX A: TABLE OF CONTENTS

INTRODUCTION

Temporal changes in environmental factors such as temperature and moisture content can cause significant variations in the properties of pavement materials, thus affecting the response and performance of the pavement system. In many areas, freezing and thawing of the pavement layers can result in abrupt changes in the properties of the pavement layers, and the loss of capacity during spring thaw often leads to premature pavement failure. The back-calculated layer moduli determined from Falling Weight Deflectometer testing of flexible pavements can be highly dependent upon the temperature and/or temperature gradient at the time of the test. Likewise, variations in pavement temperature and subgrade moisture content affect the performance and back calculated properties of rigid pavements. The following review summarizes recent research findings relative to the daily and seasonal variations in temperature and moisture conditions and their effects on material properties and pavement structural capacity. The review first discusses the effects of moisture content variations on unbound materials, followed by freeze thaw effects on pavement systems, temperature effects on the back-calculated moduli of flexible pavements and concludes with a review of climatic effects on concrete pavements.

EFFECTS OF MOISTURE CONTENT VARIATION ON UNBOUND MATERIALS

The pavement design procedures presented in the American Association of State Highway Officials (AASHTO) *Guide for Design of Pavement Structures* [*1*] require the use of mechanical properties for the asphalt concrete, base course, and soil subgrade. The stiffness of the soil subgrade and base materials are represented by the resilient modulus, M_R which replaces the empirical "soil support value" used in the earlier design guides. A sensitivity analysis of the AASHTO's design equation showed that the resilient modulus of the unbound materials has the most pronounced effect on the structural number (SN) of flexible pavements [*2*]. Since the behavior of unbound base materials is similar to that of coarse-grained subgrade materials, the effects of moisture content changes are similar. Typically, the resilient modulus of unbound materials is determined in the laboratory in accordance with AASHTO T294 [*3*] under conditions of maximum dry density and optimum water content.

Although pavement subgrades are usually compacted close to optimum water content and maximum dry density during construction, seasonal variations in water content or degree of saturation occur. Most fine-grained soils exhibit a decrease in modulus as the water content is increased, leading to increased deflections in the pavement subgrade. Coarse-grained materials may experience this change, depending upon the amount of fine grained particles present. In general, an increased deflection in the subgrade leads to a decrease in pavement design life ([*4*]; [*5*]; [*6*]).

Seasonal variations in soil moisture content

The variation of soil moisture is complicated, because of the influenced of a number of factors, such as soil type, precipitation, location of the groundwater table, solar radiation, and the topography. Different models have been developed to simulate the process of wetting and drying of soil.

The variation of soil moisture in the subgrade soil is important to the pavement design process, because change in the soil stiffness or modulus due to moisture variation is the direct cause of the distress in pavements. For most cases, it is not appropriate to predict the variation of soil moisture with an analytical model, which can include all the processes like infiltration, drainage, evaporation and heat transfer. Instead, the variation of soil moisture is obtained from in situ measurements, and then regression methods are used to find the correlation between the soil moisture variation and environmental factors.

Subgrade Soil Moisture and Hydrologic cycle

The variation in soil moisture with time is part of the earth's hydrologic cycle. Water reaches the surface of the ground in the forms of condensation and precipitation. It then runs from the slopes in thin sheets into streams and rivers and eventually arriving at the ocean, or infiltrates into the soil and is transmitted to groundwater or is stored in the soil near surface where it comes back to the sky by evaporation or transpiration of plants. A schematic [*7*] of hydrologic cycle is depicted in Figure. 1.

As shown in Figure. 1, soil moisture domain or region can be divided into two major zones, separated by the groundwater table, i.e., unsaturated zone and saturated zone. The boundary of these two zones, the groundwater table, varies seasonally. A localized saturated zone or a perched saturated zone may exist as a result of the underlying semipervious soils. Generally, such zones are much thinner than the two major zones. The unsaturated zone is the part of soil moisture domain most commonly involved with pavement engineering. The interaction of soil moisture changes between the unsaturated zone and the saturated zone, together with precipitation and evaporation, makes the properties of the unsaturated zone very complicated.

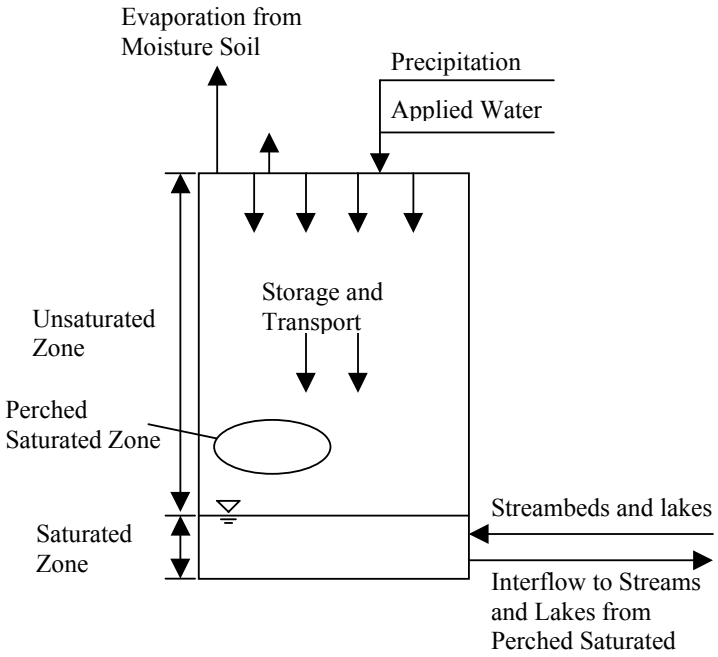

Figure 1 Schematic of the Hydrologic Cycle (after [*7*])

Enhanced Integrated Climatic Model (EICM)

Enhanced Integrated Climatic Model ([*8*]; [*9*]) is a one-dimensional coupled heat and moisture flow program for the analysis of pavement systems due to climatic factors such as temperature, rainfall, wind speed and solar radiation. A schematic of the entire model ([*10*]) is shown in Figure 2. It consists of four independently developed models which have been integrated into the EICM:

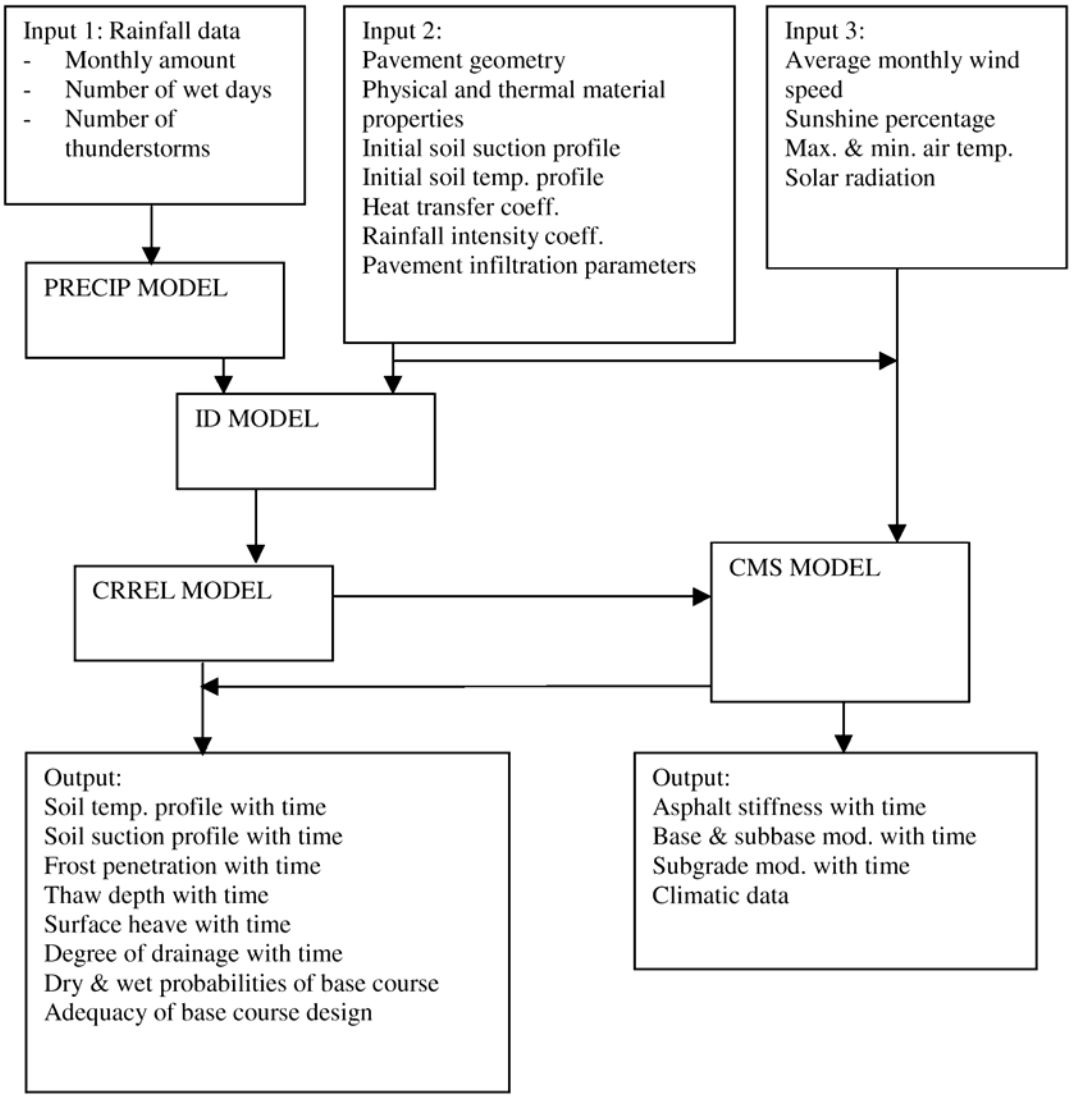

Figure 2 Schematic of the Enhanced Integrated Climatic Model ([*10*])

1. **Precipitation model** ([*11*]) is used to generate precipitation patterns from historical climatic data available from National Oceanic and Atmospheric Administration (NOAA). Based on the statistical information calculated from 30 years of precipitation data, the number of wet days of each month and the intensity of rainfall can be generated using congruential algebra

and number theory. It is recommended that if an extreme rainfall event is to be modeled, actual rainfall data should be used instead of generated data.

2. **Infiltration-Drainage Model** (ID Model) [*12*] models the water infiltration through the cracks in the pavement surface and subsequent flow in the drainage layer. This model can also perform a pavement design evaluation. The wetting front penetrating into the subgrade at a given time is calculated. The modulus of the base course is assumed to be constant for a degree of saturation lower than 60 percent. For a degree of saturation higher than 60 percent, the reduction of base course modulus is assumed to be proportional to the increase of surface deflection due to the increase in degree of saturation. Subgrade modulus can be determined as a function of the degree of saturation, which is correlated with the wetting front, from a linear regression equation.
3. **The CRREL model** [*13*] developed at the U. S. Army Cold Regions Research and Engineering Laboratory (CRREL), is used to compute the one-dimensional coupled heat and moisture flow in the subgrade soil at temperatures that are above, below, and at the freezing temperature of water. This model provides reasonably accurate predictions of frost and thaw penetration, heave, and settlement. Darcy's law is used in the moisture flow model. The unfrozen unsaturated water content is related to the negative pore water pressure through the Soil-Water Characteristic Curves (SWCC). The SWCC can be expressed by the Gardner function,

$$\theta_u = \frac{n}{1 + A_w |h|^a}$$

where n = porosity of the soil,
A_w, a = constants describing the soil-water characteristic curve,
h = negative pore water pressure (suction).

4. **The Climate-Materials-Structural Model** (CMS Model) [*14*] is used to simulate climatic conditions that control temperature and moisture conditions in the pavement layers and in the subgrade. A one-dimensional, forward finite difference, heat transfer model is used to determine frost penetration and temperature distribution in the pavement system. Base and subbase moduli are calculated from unfrozen and frozen moduli and temperature. Unfrozen subgrade modulus is a regression function of water content, which is obtained from the CRREL model.

A schematic of the EICM calculation procedure of subgrade resilient modulus is depicted in Figure 3.

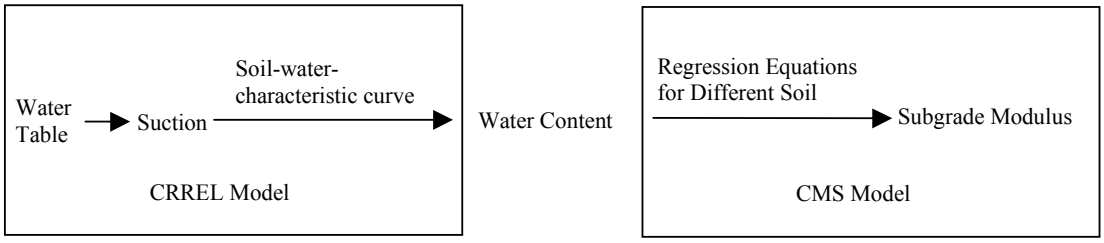

Figure 3 Procedures for the Subgrade Resilient Modulus Calculation in EICM

The ID model, which accounts for the precipitation and infiltration, is not used in the direct calculation of the subgrade modulus. The subgrade modulus is determined only as a function of the distance above the water table. Thus, the ID model only applies to sites with a high water table. For sites with a low water table, this model would result in an unreasonably low and relatively constant moisture content, even if the subgrade is subjected to climatic variations. In addition, for pavement sites with a shallow water table, soil suction may not vary linearly with distance from the water table as calculated from hydrostatic pressure [*15*]. For example, the existence of a coarse gravel layer right above the water table would provide a capillary break. Nevertheless, for many conditions the combination of water table position and SWCC still serve as a reasonable approach to estimate moisture content which can be correlated to the subgrade resilient modulus.

Birgisson and Newcomb [*10*] used the EICM to compare field and model predictions of seasonal variations in flexible pavements at the Minnesota Road Research Project (Mn/ROAD). The results indicated that the EICM can provide reasonable prediction of seasonal variations in temperature, layer modulus, and volumetric moisture content, except during the spring thaw period. Two flexible pavement test sites were studied in this research, both with shallow water tables (<20 ft.). Therefore, the moisture content of the subgrade was mainly influenced by the ground water table location. For sites with a deeper ground water table, the results might not be as good.

Soil Suction and Water Content

Soil-Water Characteristic Curves

Soil suction is the negative pore water pressure that exists in unsaturated soils. The non-linear relationship between suction and moisture content can be represented by Soil-Water Characteristic Curves (SWCC). The SWCC usually simplified with two curves, one for the drying (desorption) path and the other for the wetting (adsorption) path. The actual moisture variation in soil is much more complicated than this. A complete set of drying and wetting paths for a heavy clay soil is shown in Figure 4 [*15*]). The drying (curve A) and wetting (curve B) do not follow the same path, which is a phenomenon called hysteresis. It should be noted that the second drying curve (curve C) does not coincide with the first drying curve (curve A), but is similar to the wetting curve B. Curve D is the same soil drying from an initially slurried condition. Loops E and F are intermediate suction loops. It was suggested that in general, the drying curve alone is sufficient for most civil engineering uses [*16*]. It is unlikely that the variation of subgrade moisture in the field will follow the continuous change as curve A, B, and C. The fluctuation of moisture content in subgrade is actually a series of small hysteresis loops similar to E and F. The complete set of soil-water characteristic curves to represent all the possible variation of soil moisture would be very complex. Thus, for engineering applications, using only one path is probably not much different from using both the drying and wetting paths.

As indicated in Figure 4, the SWCC is highly nonlinear. The curvature of the SWCC depends upon the distribution or presence of a dominant pore size. A sudden drop of moisture content within a certain suction range occurs when there is a large number of pores of certain size, so that moisture keeps decreasing while suction does not change much, until almost all the pores of this size are drained. For a clayey soil with a broad range of particle sizes, Figure 5, there is not a dominant pore size as in the sandy and silty soils.

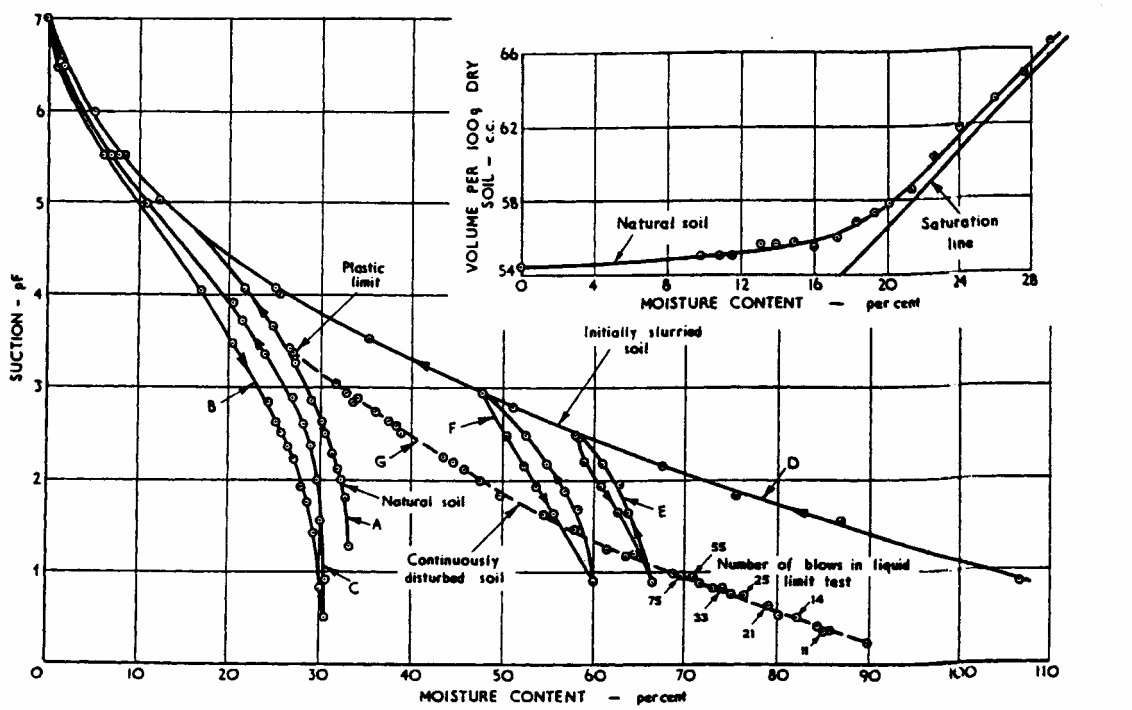

Figure 4. Soil-Moisture Characteristic Curve [*15*]

Numerous relationships have been used to model the SWCC, and a comprehensive literature review on those equations was performed by Fredlund and Xing [*17*]. A general form of the relationship between water content and suction, by which the SWCC can be determined by the pore-size distribution of a soil uniquely, was developed from pore-size distribution of the soil.

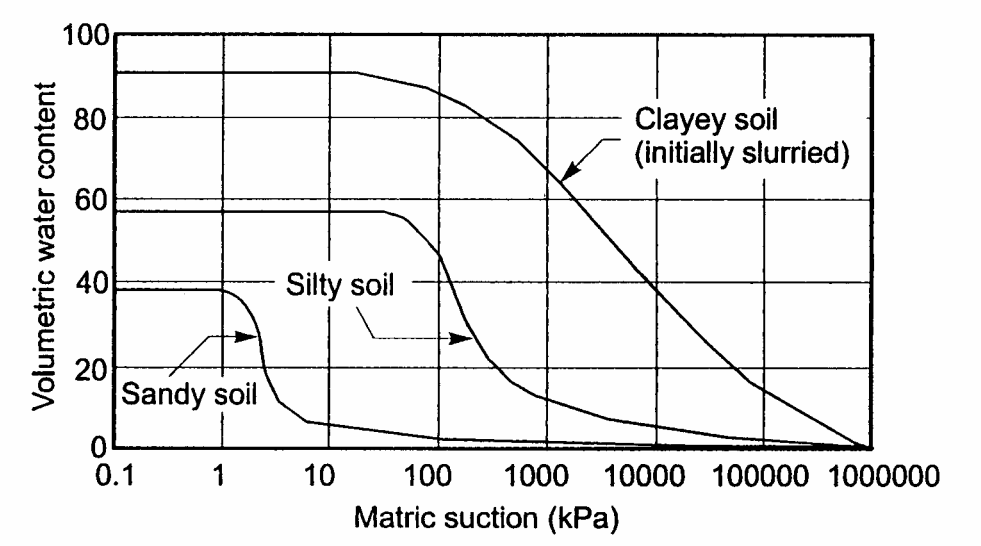

Figure 5 Soil-Water Characteristic Curves for Different Soils [*17*]

Since soil suction has a direct impact on soil properties [*18*], it is preferred over moisture content for the estimation of subgrade modulus. This is because i) small error in moisture content may lead to a very serious error in the mechanical properties when the moisture content approaches saturation [*19*]; ii) different soils have been observed to reach the maximum resilient modulus at the same suction level [*20*].

By definition, soil suction at any location above the water table is the negative hydrostatic pressure calculated by multiplying the unit weight of water by the distance to the water table. With the suction, the moisture content at that location can then be obtained from the SWCC. This provides a straightforward way to estimate the field moisture content of subgrade, provided that water table is known and is at shallow depth. This method was also used in the U. S. Army Cold Regions Research and Engineering Laboratory (CRREL) Model [*13*], which was adopted in the Enhanced Integrated Climate Model (EICM) ([*8*]; [*9*]).

Pressure Plate Test

The soil-water characteristic curve (SWCC) can be obtained by the pressure plate test, which is a test using high air entry plate and axis translation technique. A schematic of the typical apparatus used in the pressure plate tests is shown in Figure 6. The soil specimen is tested in an air pressure chamber with a water compartment on the bottom. Soil specimen is put on a saturated high air entry disk, which is in contact with the water in the water compartment. The disk, generally ceramic, acts as a membrane between air and water. The maximum air entry value should be greater than the maximum anticipated suction during the test. The fine pores in the ceramic disk withstand the flow of air due to the surface tension of water. The contractile skin, which joins the pores, prevents the air from entering the water chamber, as long as the air pressure is below the maximum air entry value. According to Kelvin's equation (2), the air entry value is inversely proportional to the maximum pore radius.

$$(u_a - u_w)_d = \frac{2T_s}{R_s}$$

where $(u_a - u_w)_d$ = air entry value of the high air entry disk,

T_s = surface tension of the contractile skin, a function of temperature,

R_s = radius of the maximum pore size.

In a natural unsaturated soil, the pore-water pressure is usually negative, and can result in water cavitation problems in the measurement system. An axis translation technique is used to overcome the cavitation problems by maintaining the pore-water pressure at zero while increasing the pore-air pressure. Thus, the suction in the soil is equal to the applied air pressure. In the pressure plate drying test, air pressure is increased and, as a result, water is forced out of the soil specimen through the high air entry disk into the water chamber. Thus, the drying path of soil-water characteristic curve can be obtained by recording the volume of water drained from the specimen at different applied air pressure. Similarly, the wetting curve can be obtained in the pressure plate wetting test.

Prediction of Pore-Size-Distribution (PSD) Curve

Laboratory tests to determine the SWCC are always time consuming. Researchers have tried to predict it from pore-size-distribution curve ([*21*]; [*22*]; [*23*]), because of the similarity between these two curves.

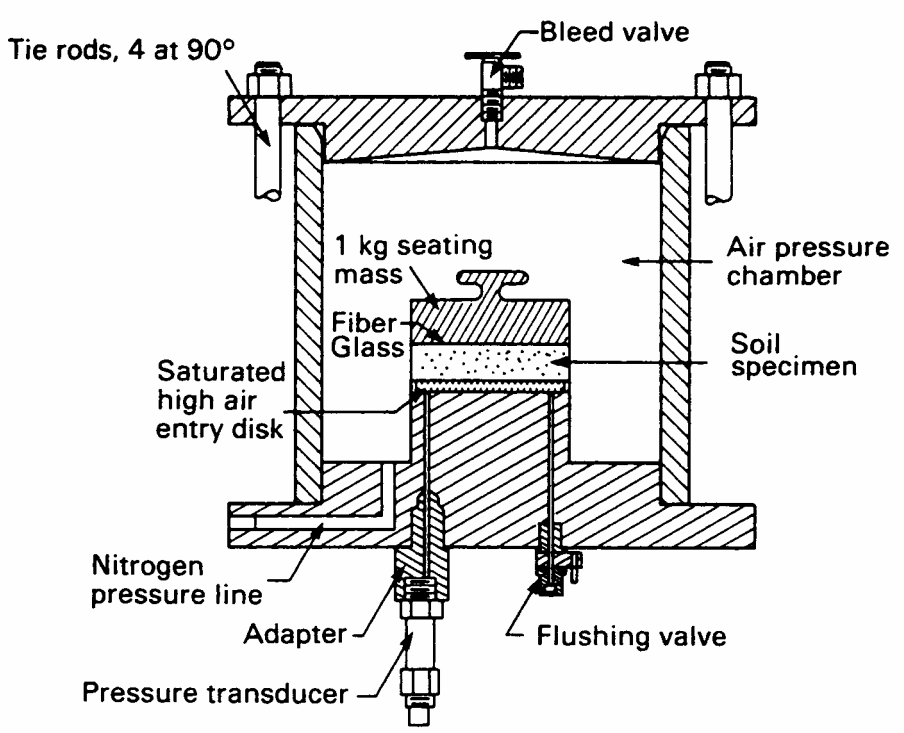

Figure 6 Pressure Plate Apparatus for Measuring Negative Pore-Water Pressures Using the Axis-Translation Technique (from Olson and Langfelder, 1965) [*18*]

Stochastic Model

Aberg [*24*] proposed a simple stochastic model to describe void characteristics of noncohesive soils and similar granular materials. The concept of grain chord, the intersection between a straight line and a soil particle, was introduced to describe the one-dimensional grain-void relationship, as shown in Figure 7. The soil mass is regarded as a group of parallel infinitely thin tubes. In this way, voids and grains can be represented in the form of total number of void chords and grain chords. It is assumed that the length of a void chord mainly depends on the size of the smallest adjacent grain, because the void sizes in a graded soil are mainly determined by the fine grains, which successfully fill the space between the large grains. The average length of void chords is assumed to be proportional to the average grain chord. The constant in this relationship, which depends on the shape of the grains, can be determined from a proctor test. Equations that account for grain type, grain shape, degree of densification, and size of compaction container were developed.

Aberg [*22*] further developed this model, so that it can be used to predict pore-size-distribution of granular soils. The cumulative distribution curve for the void volume corresponding to the grain size x_b for a soil at the maximum dry density with no loose particles is given by the following equation:

$$z_b = 1 - \frac{A_b}{A_0}$$

where

$$A_b = \int_{y_b}^{1} \frac{y}{x(y)} dy - y_b \int_{y_b}^{1} \frac{dy}{x(y)}$$

and

$A_0 = A_b$ evaluated at $y_b = 0$

x = the grain size in the GSD curve,

y = the volume fraction of grains with grain size not greater than x.

A similar equation for soils with below the maximum density was also provided.

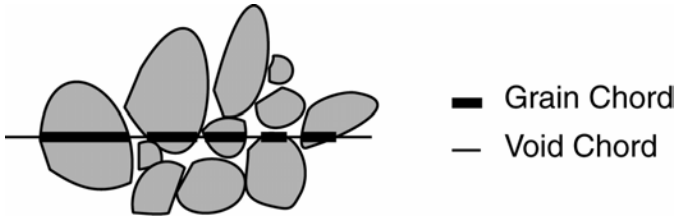

Figure 7 Grain Chords and Void Chords in a Soil Mass

Physicoempirical Model

Arya and Paris [*21*] proposed a physicoempirical model to predict soil moisture characteristic curve from particle-size distribution and bulk density data. The cumulative particle-size distribution curve was first divided into fractions, and then soil particles reassembled into discrete domains. Equations relating volumetric moisture content with pore volume were developed. The relationship between pore size and relevant particle size can be obtained by assuming that i) particles in a discrete domain are uniform-size spheres defined by the mean particle radius of the fraction and ii) pores are uniform-size cylindrical capillary tubes. In this way, suction was calculated from moisture content. A constant, which was used to correct for the fact that natural soil particles are not spheres, can be determined from laboratory tests. Predictions using this model showed close agreement with experiment data on two types of soils: i) river loam; ii) mixtures of a silty clay, a swelling soil and a sandy loam.

Fredlund's Model

Fredlund et al. [*23*] proposed a method of estimating the soil-water characteristic curve from the grain-size distribution curve and volume-mass properties. It was assumed that the SWCC for each uniform particle size is relatively unique. The grain-size distribution curve was first fitted by the same equation as used to fit the SWCC [*17*]. The grain-size distribution curve was then divided up into small divisions of uniform soil particles. A packing porosity could then be estimated for each division and a SWCC also estimated. The SWCC for certain soil can then be obtained by summing up these divisional SWCC. This method has been incorporated in the SoilVision software [*25*]. This prediction model was found to be particularly accurate for sands and reasonably accurate for silts. Reasonable results could also be obtained for clays and tills, but the results were sensitive to the packing porosity.

Soil Moisture in Cuts, fills, and Uncovered/Covered Ground

Soil Moisture in Cuts and Fills

Khogali and Anderson [*26*] reported the significant differences between subgrade stiffness in cut sections and fill sections. Moduli backcalculated from FWD in the cut section experience large seasonal fluctuations than their counterparts in the fill section, and the subgrade moduli of fill areas were 65% greater than their counterparts in cut areas. These differences were believed to be caused by superior compaction and drainage in fill areas.

Soil Moisture in Uncovered Ground

Croney [*15*] pointed out that "to establish moisture equilibrium, water may flow from a granular soil of low moisture content into an adjacent clay soil of initially much higher moisture content. Even in a mass of uniform soil, moisture migration may take place from areas of low moisture content to areas of higher moisture content, depending on the previous moisture history of the soil." It is the potential that controls the movement of moisture. This potential may be mechanical potential, thermal potential, chemical potential and electrical potential. Chemical and electrical potential usually have little effect on soils with low ion content.

The flow of moisture under mechanical potential in saturated or unsaturated soil can both be approximated by Darcy's Law. The difference is that the hydraulic conductivity in saturated flow is a constant while it is a function of moisture content in unsaturated flow [*7*].

Topsoil usually shows a quick response to rainfall and sharp increase of suction during continuously rainless days. Moisture variation occurs in uncovered ground primarily above a soil depth of 2 m, particularly in the upper 100 cm of soil. The rate at which the suction increases has been found to decrease with the elapsed time from the rain cessation [*27*].

The flow of moisture under a thermal gradient is complex. Generally, moisture (both in liquid phase and vapor phase) tends to move opposite the temperature gradient, i.e., towards low temperature zone. However, the phenomenon of moisture in the liquid phase flowing in the opposite direction as the vapor phase was reported by Gurr et al. [*28*]. In the experiment the effect of a temperature gradient on the movement and distribution of the water in soil was examined in closed columns of soil for a wide range of initial water content. Small amounts of salts acting as a tracer served to distinguish between liquid and vapor movement. The result showed higher water content toward the colder end, but a high concentration of salt toward the hot end. This indicates a net transfer of water from hot to cold, in which water evaporating from the hotter end moves to the colder end, where it condenses and returns as a liquid when a favorable gradient of pressure potential has been established.

Freezing and thawing cycles cause drastic change in soil moisture. In winter, the accumulation of water during the formation of ice lenses reduces the soil moisture content away from the lens, and in the early spring, thawing results in a sudden increase in the moisture content. The mechanism of freezing and thawing in soil is quite different from the unfrozen moisture variation. Freeze-thaw variations are discussed in more detailed elsewhere in this report.

Soil Moisture Movement and Distribution in Covered Ground

When the ground surface is covered by pavement, infiltration of water from precipitation is reduced significantly. If the surface shielding of pavement is completely impermeable, on a wet day the moisture content under the center of the pavement will be much lower than that under the edge. On a dry day, the opposite will be true, with the moisture content under the center of the pavement higher than that under the edge. There will be a lag between the moisture change in the soil under the central part and under the edge of the pavement. The length of the lag depends on the hydraulic conductivity of soil. This effect was reported during a study of seasonal variation in soil moisture in Britain [*29*]. A finite element simulation of moisture distribution under surface shielding was also consistent with this phenomenon [*30*].

Roadside vegetation is believed to play an important role in the process of subgrade moisture removal. Plant root systems can remove moisture from the subgrade soil at great depth by transpiration, although a dry soil crust at the soil surface can prevent evaporation from taking place ([*31*]; [*32*]). Moisture removal ability of the roadside vegetation varies with both the type of plant and the season. Week of the year in was recommended as a good indicator of the approximate stage of vegetal development, which reflects typical evapotranspiration conditions [*33*].

The phenomenon of the subgrade moisture accumulation during and after construction has been reported by a number of researchers. Seasonal variation of moisture content was found to be superimposed on a trend of increasing moisture over time [*34*]. Vaswani [*35*] observed that the rate of increase is dependent on soil density, compaction and soil gradation. It was observed that one or two years after construction, the rate of moisture content increase slowed down, and the fluctuation due to temperature gradient became noticeable. After about 10 years, there was practically no change in subgrade moisture and temperature gradient had no effect. Maree et al. [*36*]explained this accumulation of subgrade moisture by the compaction of traffic.

Russam [*29*] proposed a classification of subgrades based on the water table depth and annual rainfall. Similar classifications were adopted by Yoder and Witczak [*37*]. The description of the three main categories of subgrade is as follows:

Category 1 – Subgrades where a water table is close to the surface, at a depth less than 20 ft in clays, 10 ft in sandy clays or silts, and 3 ft in sands. The depth to the water table is the main factor of the variation of moisture content of subgrades. Under a relatively impermeable surface, the soil water will tend toward equilibrium with the water table. The moisture content is governed by the fluctuation of water table.

Category 2 – Subgrades where the water table is deeper than that described in category 1 and the rainfall is more than 10 in. per year. The moisture content in this category will be governed by seasonal changes in the rainfall.

Category 3 – Subgrades where the water table is deep and the rainfall is less than 10 in. per year. In this category the moisture content of subgrade will differ little from the uncovered soil at the same depth.

A reasonably precise estimation can be made for the subgrade moisture content of category 1 from the depth of the water table and SWCC, but the fluctuation of the water table is also related to rainfall. An important assumption in the category 1 subgrades is that the surface of the pavement is impermeable, and the variation of soil moisture is related only to the fluctuation of water table. In fact, the surface layer of most pavements is never completely impermeable.

Longitudinal joints in flexible pavements [*38*] and expansion joints in rigid pavements [*39*] provide paths for infiltration. Cracks that develop as a result of inevitable distress of the pavement will increase the permeability of the surface layer.

The infiltration of precipitation through these joints and cracks will make any theoretical model more complicated. Rahim and Picornell [*31*] proposed a computer program to model the moisture movement under the pavement. In the program, the expansive subsurface soil was simulated by rectangular blocks separated by parallel cracks. When all the cracks in the subgrade are filled with water during a rainfall event, all the remaining rainfall was assigned to run off. Cracks tend to close after the absorption of water and re-open when water is depleted. The volume change of each soil block is assumed to be equal to the volume of water absorbed or lost by the block. The rate of water movement in each block is controlled by master block curves derived by modeling the one-dimensional unsaturated water flow within the soil block subjected to zero suction for the wetting phase or 15 bars suction for the drying phase. The only form of moisture removal was assumed to be the plant transpiration of roadside vegetation. The cross-section of the pavement was divided into three regions, i.e. pavement, edge, and uncovered. In the 'uncovered' region, moisture can be removed by plant transpiration. Roots of the vegetation are assumed to extend under the pavement and form the 'edge' region. In the 'pavement' region, water can only infiltrate through the cracks of the pavement surface, through which no moisture will be removed. This model explains the accumulation of moisture after construction and the phenomenon that subgrade moisture close to the edge exhibits more variation. However, according to this model, water will never be removed from the subgrade soil which is out of reach of the of the roadside vegetation root system. The infiltration of water is through vertical cracks only. Lateral moisture movement never takes place. No theoretical models exist to simulate the moisture movement and distribution properly. Even the Enhanced Integrated Climatic Model ([*8*], and [*9*]) does not account for the infiltration of water from the surface and the lateral movement of moisture from uncovered soil to the subgrade.

Statistical Analysis of Subgrade Moisture Based on Precipitation

Since the theoretical models have a number of limitations, statistical analysis of data from field instrumentation is often used.

Several researchers have tried to find the correlation between rainfall and variation of moisture content by observing the precipitation data and moisture data ([*40*]), or calculating the correlation coefficient directly ([*41*]; [*42*]). Almost all these researchers ended up with the same conclusion that there is no relationship between rainfall and subgrade moisture variation. Some attribute this result to insufficient instrumentation, for instance, rainfall data was not collected at the testing site, but obtained from a nearby weather station, and rainfall at these two different locations could be different [*41*]. Some researchers found a lag between rainfall and subgrade moisture variation by eyeballing the precipitation vs. soil moisture data ([*43*]; [*44*]). The lag of response could vary from 3 weeks to 2 months. A rational statistical method capable of finding the lag between two time series, the Cross-Correlation Method, was first used in this kind of analysis by Bandyopadhyay and Frantzen [*45*]. The lag obtained using Cross-Correlation Method is up to 3 weeks. Several factors could affect this lag, some major factors are listed as following:

1. **Distress of the surface layer**

The Intensity of cracks on the pavement surface, the aperture of the cracks and the permeability of the filling material govern the infiltration rate during rainfall.

2. **Thickness of the HMA layer**

Thickness of the HMA layer will affect the properties of the subgrade. It is found that for HMA layer thickness < 6 in, spring is the most critical season. When the HMA layer thickness > 6 in, summer is the most critical season [*46*].

3. Effective drainage of the base course

Effective drainage of the base course controls how fast the water that infiltrates through the cracks and joints of the surface layer can be drained. An effective drainage layer can prevent the water from perching at the interface between the base course and the subgrade, and consequently reduces the amount of water that reaches the subgrade.

4. Slope of the shoulder

Slope of the shoulder is another important factor of the pavement structure that affects the variation of subgrade moisture content. A properly designed shoulder can remove the runoff caused by rainfall rapidly. For the same rainfall event, a properly designed shoulder will produce less infiltration of water through the pavement surface and more infiltration of water into the soil off the shoulder. This may result in the relatively low moisture content in the subgrade and a longer lag between the rainfall event and the increase in subgrade moisture content.

5. Topography of the site location

Surface runoff always tends to flow to the lower position due to the gravity, so higher moisture content is always found in the low-lying areas.

6. Intensity and duration of the rainfall

Intensity and duration of the rainfall also affect subgrade moisture variation. During a rainfall event, less water infiltrates through the pavement surface layer and base course into the subgrade than infiltrates into the uncovered ground, because of the relatively low permeability of the surface layer. The higher the rainfall intensity, the more significant the differences between the moisture content under the pavement and the nearby uncovered ground. This difference in moisture content will affect the time needed for the moisture to come to equilibrium.

As mentioned before, the hydraulic conductivity of the unsaturated soil is governed by the moisture content. If the intensity of rainfall is low and at the same time the duration is short, not enough water will be able to infiltrate into both the pavement surface and the topsoil of the uncovered ground. Thus the conductivity is not high enough to let the water reach the subgrade or deep into the uncovered ground. The small amount of moisture will soon be evaporated after the rainfall, and will have very little effect on increasing the moisture content of the subgrade. There must be a threshold of rainfall below which the moisture content of the subgrade will not be affected.

Thom [*47*] proposed a correlation between the thresholded rainfall and the variation of subgrade moisture content. Monthly total rainfall less than 0.1 inch was assumed to have no effect on the variation of moisture content. This threshold value seems to be quite arbitrary, but according to Thom [*47*], a somewhat arbitrarily selected threshold may yield good results, because if there is a correlation between the variation of subgrade moisture and a true threshold value, there will also be correlations with thresholds near the true value. Unfortunately, Thom [*47*] only found good correlation between the thresholded rainfall and moisture content in the natural soil. The same correlation for pavement subgrades was very poor. It should be noted that Thom did not notice the lag between rainfall and the change in subgrade moisture content. If cross-correlation method were used, better results would probably have been obtained.

7. Moisture Movement due to Temperature Gradient

Russam [*29*], Vaswani [*35*], and Hall and Rao [*44*] have reported the phenomenon of moisture movement due to temperature gradient in pavement subgrade. This movement of water

in the vapor phase might be significant only where a sharp seasonal fall in temperature occurs, and a zone of wet soil exists not far below the surface of sandy or silty clay soils [*29*].

The relationship between the variation of the subgrade moisture content and precipitation is not simply a time lag. The subgrade moisture content on the n th day is not only influenced by the precipitation which occurred on the $(n-lag)$ th day, but is also affected by the precipitation which occurred before the $(n-lag)$ th day as well. Hinshaw and Northrup [*48*] used the antecedent-precipitation index (API) to predict the degree of saturation of the shallow subgrade soil under aggregate surfacing. When good weather station data close to the site were available, this prediction yielded a R^2 value of 0.78. The antecedent-precipitation index (API) is an index that accounts for the time effect of rainfall using weighting factor, defined by the following equation [*33*],

$$P_{a_N} = bP_{a_{N-1}} + P_N$$

where P_{a_N} is the precipitation index value at the end of the N th day

$P_{a_{N-1}}$ is the precipitation index value on the previous day

P_N is the precipitation recorded on the N th day

b is a coefficient.

It is reasonable to use API directly to predict the subgrade moisture under aggregate surfacing, but if the subgrade moisture under a surface layer with low permeability is to be predicted, the combination of a cross-correlation analysis and API might be more favorable. In short, the use of a threshold rainfall, cross-correlation, and antecedent precipitation index may provide a better way to predict the subgrade moisture content from precipitation.

Models for Resilient Modulus

Fine-grained materials

Generally, the resilient modulus of fine-grained soil is believed to be a function of deviator stress. Different models have been proposed to simulate this function.

1. Bilinear Model [49]

$$M_R = K_1 + K_2\sigma_d \text{ when } \sigma_d < \sigma_{di}$$
$$M_R = K_3 + K_4\sigma_d \text{ when } \sigma_d > \sigma_{di}$$

where M_R = Resilient modulus,

σ_d = Deviator stress,

σ_{di} = Deviator stress at which the slope of M_R changes,

K_1, K_2, K_3, and K_4 = Model parameters.

A breakpoint resilient modulus, M_R at σ_{di} was often used to characterize the resilient properties of subgrade soils.

2. Two-Parameter Power Model [50]

$$M_R = k\sigma_d^n$$

where k, n = Model parameters.

3. Semilog Model [51]

$$\log M_R = c_{1d} - m_{1d}(\sigma_1 - \sigma_3)$$

where c_{1d}, m_{1d} = Model parameters.

4. Hyperbolic Model [52]

$$M_R = \frac{k + n\sigma_d}{\sigma_d}$$

where k, n = Model parameters.

5. Octahedral Model [53]

$$M_R = k\frac{\sigma_{oct}^n}{\tau_{oct}^m}$$

where σ_{oct}, τ_{oct} = Octahedral stresses,
m, n = Model parameters.

Suction plays an important part in the model of resilient modulus. Generally, the lower the moisture content, the higher the suction, and consequently the higher the modulus. However, a critical suction, beyond which resilient modulus will drop with increasing suction, was reported by Edil and Motan [*19*] based on a series of resilient modulus tests on a silty loam and a sandy mix. The critical value is approximately 2% dry of optimum. Similar result was obtained by Gehling et al. [*54*]. Effects of confining pressure on the relation between suction and resilient modulus was reported by Phillip and Cameron [*55*]. For suction < 3.8 pF (620 kPa), confining pressure was found to have little effect on resilient modulus. When suction >3.8 pF (620 kPa), for stiff clay, Resilient modulus was found to increase with confining pressure; for soft clay, resilient modulus was found to decrease with confining pressure.

Coarse-grained materials

The resilient modulus of coarse-grained soil is believed to be a function of bulk stress, given in equation (8), a two-parameter power model in the same form as the one used for fine-grained soil [*56*]. Although this has been questioned by a number of researchers ([*57*]; [*58*]), it is still the most widely used model.

$$M_R = K_1\theta^{K_2}$$

where θ = Bulk stress = Sum of principal stresses = $\sigma_1 + \sigma_2 + \sigma_3$,
K_1, K_2 = Model parameters.

Gradation of granular material and the drainage condition in laboratory cyclic test are both considered to have effect on resilient modulus.

A study conducted by Raad, et al. [*59*] demonstrated the significant effect of gradation on resilient behavior of unbound material. Crushed sedimentary river deposits of igneous origin were tested under saturated undrained loading conditions. The resilient modulus for all aggregate gradations was observed to decrease as a result of the increase in pore water pressure and corresponding decrease in effective stress. Resilient moduli of dense-graded aggregates were high, while open-graded aggregates exhibited low resilient modulus. Open-graded aggregates were more resistant to pore water pressure buildup than the dense-graded aggregates. For aggregates with the same gradation, the increase of fine content can make the material more susceptible to pore water pressure buildup.

Pappin et al. [*60*] performed a series of repeated triaxial tests on well-graded limestone in both saturated and partially saturated conditions to determine the effect of pore water pressure on resilient behavior of the material. It was found that the resilient stress-strain behavior of saturated granular materials is identical to that of dry material, provided that full drainage is allowed. For the undrained tests, both the saturated and partially saturated specimens behave in accordance with the predictions of the dry model provided that an effective stress analysis is performed.

Heydinger et al. [*61*] performed an analysis of resilient modulus for different aggregate materials with different gradations and different moisture content. It was indicated from this test that the effect of gradation is different for different aggregate materials. For limestone aggregate, the open-graded specifications had higher moduli than the dense-graded specifications. For gravel aggregate, no obvious trend in the variation of resilient modulus with respect to gradation could be found. For slag aggregate, the denser gradation tended to have high moduli but there was no consistent trend for the variation of modulus with moisture condition.

The research of Tian et al. [*61*] also concluded that among three different gradations varying from finer to coarser limit, an open-graded aggregate (coarser limit gradation) produces higher resilient modulus, because of faster drainage. A Multiple Linear Regression (MLR) model was developed, in which both gradation and moisture content were taken into account. The regression model is a function of bulk stress, deviator stress, moisture content, c, tan(ϕ), and unconfined compressive strength. The last three variables were considered to be dominated by gradation.

Thom and Brown [*62*] argued that the effect of moisture on resilient behavior of aggregates is not the pore water pressure, but lubrication. The conclusion was drawn after a series of repeated load drained triaxial tests on a crushed-rock aggregate with variations in grading and degree of compaction. During testing, moisture content varied and no noticeable pore pressure were developed, although a trend of decreasing stiffness with increasing moisture content is apparent.

General Model

A general model for the resilient modulus [*63*] is given in equation (9). This equation can be used to model both fine-grained soils and coarse-grained soil. When $K_2 = 0$, this equation is equivalent to the two-parameter model of fine-grained soils; when $K_3 = 0$, this equation is equivalent to the two-parameter model of coarse-grained soils. Both the bulk stress and deviator stress are considered in this model, so it is believed to give more reasonable values of resilient modulus.

$$M_R = (K_1 p_a)\left(\frac{\theta}{p_a}\right)^{K_2}\left(\frac{\tau_{oct}}{p_a}\right)^{K_3}$$

where τ_{oct} = Octahedral shear stress,

p_a = Atmospheric pressure,

K_1, K_2, K_3 = Model parameters.

Micro-mechanics Model

Theoretical models based on micro-mechanics have been used to account for the change in response due to water content variations. Chandra et al. [*64*] and Jin et al. [*65*] proposed a model in which soil particles were simulated by idealized spheres of the same size. The packing configuration of spheres was assumed to be somewhere between face-centered cubic (fcc), which is the densest arrangement, and simple cubic (cs), which is the loosest arrangement. Both temperature and suction variations will result in a change in the bulk stress, and consequently result in a change in the modulus,

$$\Delta M_R = K_1 K_2 \theta^{K_2 - 1} (\Delta\theta_T + \Delta\theta_S)$$

where M_R = Resilient modulus

ΔM_R = Change in resilient modulus,

K_1, K_2 = Constants,

θ = Bulk stress = $\sigma_1 + \sigma_2 + \sigma_3$,

$\Delta\theta_T$ = Change in bulk stress due to the change in temperature, and

$\Delta\theta_S$ = Change in bulk stress due to the change in suction.

The bulk stress change due to the temperature variation $\Delta\theta_T$ for an assembly of randomly packed spherical particles was described as follows:

$$\Delta\theta_T = \left[\frac{X}{\sqrt{2}\omega} + \frac{(1-X)}{4\omega}\right]\left(\frac{1}{3}\alpha_v \Delta T\right)^{3/2}$$

where X = The volumetric fraction of face-centered cubic (fcc) grains,

$\omega = \dfrac{3(1-\nu^2)}{4E}$, a property of the material,

α_v = Cubical thermal coefficient,

ν = Poisson's ratio of the material,

E = Young's modulus of elasticity of the material, and

ΔT = Change in temperature.

The bulk stress change due to the suction variation $\Delta\theta_S$ is

$$\Delta\theta_S = -\Delta(\text{suction})\frac{V_W}{V_T}$$

where $\Delta(\text{suction})$ = Change in suction,

V_W = Volume of water, and

V_T = Total volume.

According to this model, after running the resilient test on the material at certain temperature and suction level, the resilient modulus of a material at any temperature and suction can be

obtained. However, in natural soils, the estimation of volumetric fraction of fcc grains is difficult.

Regression Method

The most common way to correlate moisture content with resilient modulus is through the use of regression method. Factors besides moisture content are also found to affect the resilient modulus. These factors are 1) stress state, which includes the magnitude of deviator stress and confining stress, and the number of repetitive loading and their sequence; 2) soil strength, such as unconfined compressive strength and California Bearing Ratio (CBR); 3) other soil properties, such as plasticity index, liquid index, plastic limit, soil classification, percentage of fine; 4) test condition, such as whether specimen is grouted to the base plate, sample age, etc. A number of regression equations have been developed ([*40*]; [*66*]; [*67*]; [*68*]; [*69, 70*]; [*71*]; [*72*]; [*73*]).

Another interesting study performed by Lee et al. [*74*] found that the relationship between the stress at 1% strain in the unconfined compression test and the moisture content coincides with the relationship between resilient modulus and moisture content. This correlation was observed for both disturbed and undisturbed samples.

Moisture Content and Resilient Modulus

Laboratory Data

Cumberledge et al. [*40*] concluded from a study of pavement surface deflection associated with moisture variation that the percentage change in deflection depends significantly upon the moisture variation in the subgrade. An equation was developed through stepwise multi-linear regression analysis to predict pavement deflection from moisture content, percentage of fine passing #200 sieve, liquid limit, and dry density of the subgrade, and the thickness of the pavement system.

Carmichael and Stuart [*69*] developed a regression model based on extensive literature review. The database contained more than 3,300 records of resilient modulus test results for more than 250 different soils at specific confining pressures and deviator stresses. Two regression equations were given for cohesive soil and granular soil.

For cohesive soil:

$$\begin{aligned} M_R = {} & 37.431 - 0.4566(PI) - 0.6179(\%w) \\ & - 0.1424(S200) + 0.1791(CS) - 0.3248(DS) \\ & + 36.422(CH) + 17.097(MH) \end{aligned}$$

where M_R = resilient modulus (ksi),
PI = plasticity index,
%w = percentage water,
S200 = percentage passing #200 sieve, and
CS = confining stress (psi),
DS = deviator stress (psi),
CH = 1 for CH soil,
= 0 otherwise (for MH, ML, or CL soil)
MH = 1 for MH soil
= 0 otherwise (for CH, ML, or CL soil).

For granular soil:

$$M_R = 0.523 - 0.0225(\%w) + 0.544(\log T) + 0.173(SM) + 0.197(GR)$$

where T = bulk stress (psi) (DS + 3CS),
SM = 1 for SM soil,
= 0 otherwise;
GR = 1 for GR soil
= 0 otherwise.

This model was verified by another 300 resilient modulus testing results. The scatter in the results was attributed to the fact that before AASHTO T274-82, no standard resilient modulus test procedure existed. It was suggested that the relationships was useful as a preliminary estimation of resilient modulus and its seasonal variation, provided that the input variables are within the range from which the equations were developed.

Dividing the subgrade into different types before carrying out the regression analysis seemed to be a fairly efficient procedure. In a similar analysis of the data from North Atlantic and Southern SHRP Regions of the Strategic Highway Research Program Long-Term Pavement Performance (SHRP – LTPP) study [*70*], it was found that $R^2 = 0.56$, when all the data were used to develop a single regression model. After the subgrade was divided into clay, silt and sand, $R^2 = 0.8886$, 0.7809, and 0.8371, respectively. It should be noted that the combination of input variables in this regression model is quite complicated, and moisture content is only considered in the clay model.

Hudson, et al. [*69*] proposed a regression equation to estimate resilient modulus from soil properties including liquid index, degree of saturation, AASHTO soil classification, deviator water content, and plastic limit. A complete design handbook based on the resilient response of Tennessee subgrades was developed. This handbook allows the resilient modulus to be estimated with a minimum of laboratory testing.

Drumm et al. [*73*] proposed a method to correct the resilient modulus for the effect of saturation based on the testing result of 11 soils in Tennessee. The gradient of resilient modulus with respect to saturation, obtained from laboratory resilient moisture test, was used predict resilient modulus wet of optimum water content.

Field Data

The Seasonal Monitoring Program (SMP) sites, which form a part of the Long-Term Pavement Performance Program (LTPP) provide an opportunity to investigate relationship between resilient modulus and environmental effects. Resilient moduli of different layers are determined by back-calculation from the results Nondestructive Testing (NDT), such as FWD. Because the moduli of the surface layers of both flexible pavements and the rigid pavements are affected by temperature, the FWD measurements must be correct for temperature. Although the modulus of asphalt concrete decreases with elevated temperature in the summer and increases in the winter, the behavior of Portland cement concrete layers is opposite, because the shrinkage of concrete increases the width of the cracks [*75*].

Ali and Lopez [*76*] performed a statistical analysis in which different analysis methods, such as multiple linear regression, principal component analysis, and stepwise regression analysis, were used. The resilient modulus was predicted based on the temperature in the base, the

temperature gradient, and the moisture contents measured at different depths. Unfortunately, only about 30 percent of the modulus variation could be explained by the regression model.

It should be noted that the temperature effects more than just the modulus of the surface layers. The stress state of the subgrade is also affected by temperature, both directly and indirectly. The change in the stress state, in turn, affects the subgrade modulus, since subgrade modulus is stress-dependent. Four reasons that can lead to the change in the subgrade stress state with temperature are listed below.

a) **Change in the stiffness of the asphalt surface layers –** The temperature-induced changes in the modulus of the asphalt layers affects the level of stresses transferred to the underlying subgrade. [*32, 77*]; [*78*]; [*79*]).

b) **Measurement induced variation** – The stiffness of the buffers or pads on the FWD deveice are also affected by temperature. At the same drop height, the duration of impact increases with temperature. As a result, the stress state within the subgrade is also changed. ([*32, 77*])

c) **Thermally induced Stress** – According to the previously mentioned micro-mechanics model ([*64*]; and [*65*]), in granular subgrade, a rise in temperature causes an increase in the contact forces between particles, consequently increases the bulk stress. van Gurp [*32*] indicated that the lower the initial bulk stress and the more closely packed the subgrade is, the more the subgrade stiffness is affected by the increase in soil temperature.

d) **Change in the suction** – An increase of temperature will decrease the surface tension in the pore water, decreasing the suction in the subgrade. This will result in a decrease in the effective stresses [*80*] and a decrease in the subgrade resilient modulus.

Although temperature effects on unbound materials are often neglected, the above aspects may be evident in the back-calculated moduli of unbound materials determined from FWD testing. Matter and Farouki [*77*] indicated that the moisture content and temperature effects might reach their peak impacts at different times or seasons. Thus, the effects of one factor may be offset by the effects of the other, making it hard to separate them.

Moisture Content and Constants in the Resilient Modulus Model

A total of 271 test results were evaluated by Rada and Witczak [*81*]. It was found that for crushed, angular materials, when the two-parameter power model is used, an increase in moisture leads to a small to moderate decrease in the K_1 value and relatively minor changes in the K_2 magnitude. But, sand gravels showed a marked decrease in K_1 and increase in K_2 with increasing moisture, and an increase of fine material (percent passing #200 sieve) will make sand gravel material more susceptible to moisture variation.

A regression equation can be used to predict resilient modulus from bulk stress, %200, compactive effort, and degree of saturation. Similar to Killingsworth et al [*70*], in comparison to the general model, higher values were also obtained for all the other aggregates but the slag, when aggregates are divided into slity sands, sand gravels, sand-aggregate blends, crushed stones, limerocks, and slags.

Jin, et al. [*65*] observed that regression coefficient K_1 decreases and K_2 increases, as moisture content increases from the testing of two glacial deposit soils. Tian, et al. [*82*] also reported an increase in moisture content leads to a decrease in K_1 and an insignificant increase in K_2 for aggregate base. Tian, et al. [*82*] considered that K_2 could be assumed to be 0.5.

Mohammad, et al. [*83*] performed a multiple linear regression based on the laboratory repeated load triaxial test on eight subgrade soils commonly found in Louisiana. Soil classifications of these soils vary from sand to clay. The normalized octahedral stress model, which was considered to be more practical and realistic in the material characterization, was used in the multiple linear regression. Multiple linear regression was used to predict resilient modulus constants K_1, K_2 and K_3. The three different sets of input variables studied. The first consisted of basic soil properties such as moisture content, dry density, degree of compaction, liquid limit, plastic limit, percentage of sand and percentage of silt. The second consisted of the same basic properties plus CBR. The third set consisted of the basic properties plus UCS. The best result was obtained using only basic soil properties as input variables.

Simulation of In-Situ Moisture Condition

The objective of laboratory resilient modulus test is to study the resilient behavior of material as close to the in-situ condition as possible. Stress state of a subgrade below a pavement can be reproduced very well by the testing apparatus, but the simulation of soil moisture and density variation is a much tougher task. Of course, tests on undisturbed samples is the most desirable, but undisturbed samples must be obtained from the field at different times of the year, in order to study the effect of moisture variation. In practice, soil samples are prepared at required density and moisture content by different compactive method, such as impact, kneading, or static.

Seed et al. [*84*] performed a comprehensive study on method of compaction. It was found that when compacted dry of optimum, impact and kneading compaction will not result in shear deformation in soil. But when compacted wet to optimum, soil structure will be changed. The change in soil structure will significantly reduce the resilient modulus. Static compaction can maintain the same soil structure, regardless of the compaction water content. Soil samples prepared by kneading possess a structure similar to that produced by rubber tired rollers during construction. The phenomenon that small changes in water content and density have large effects on the resilience of the soil was also attributed to effects of changes in soil structure in this range. Static compaction at a higher water content was recommended to simulate the typical increase of moisture content after the construction of the pavement. This method is superior to the commonly used soaking after compaction method, because soaking can not provide a uniform distribution moisture content in the sample. Although kneading compaction is found to be the best method to represent the soil fabric in the field, other researchers have reported the difficulties experienced in producing a consistent moisture content and dry density curve [*85*].

Jones and Witzak [*67*] indicated that at high saturation levels, the modular ratio of laboratory-molded to field samples is near unity, while, for lower degrees of saturation, unconservative estimates of the field modulus may be obtained with laboratory compacted samples. This conclusion was drawn from the subgrade resilient modulus tests of the San Diego County Experimental Base Project, which was constructed in 1966 and continued until 1973. Subgrade soil for all test sections was A-7-6. This finding increases the confidence in the use of laboratory-compacted samples for the evaluation of in situ subgrade modulus in high degree of saturation.

Elfino and Davidson [*86*] proposed a method to condition the soil sample to in-service moisture content after compaction in the mold. The water content was varied through the natural matric suction developed in the specimen, corresponding to a specified elevation above the water

table. Different soil exhibited different response to the moisture variation. Poorly-graded sand specimens exhibited both a decrease in water content with increasing height above the water table and an increase in resilient modulus due to the matric suction. Clayey sand and silty specimens exhibited both an increase in water content and a decrease in resilient modulus relative to the conditions at optimum water content.

Li and Selig [*87*] indicated that soil physical state, defined by moisture content and dry density, and which is subject to the change of environment, can be represented by a combination of two basic paths in the moisture versus dry density curve, namely, constant dry density and constant compactive effort. The constant dry density causes a greater change in resilient modulus with change in moisture content than constant compact effort. The difference becomes smaller when moisture content is above the optimum. Based on 27 repeated triaxial test results from the literature on 11 fine-grained soils, regression equations were developed for constant dry density and constant compact effort. With the regression equations, resilient modulus can be predicted at any moisture content from soil properties.

Thadkamalla and George [*88*] discussed how different method of moisture conditioning affects the results of resilient modulus tests. Two coarse-grain and two fine grain soils were conditioned using three different methods of wetting, namely, capillary saturation, vacuum saturation, and molding wet of optimum. The resilient modulus of coarse grain soils was not significantly affected by either water content or mode of saturation. In case of fine grain soils, the resilient modulus of vacuum saturated specimens decreased exponentially with increasing degree of saturation, whereas, it decreased linearly with capillary saturation and also with specimens molded wet of optimum. In the case of fine grain soil, the decrease in resilient modulus for both capillary saturated specimens and those molded wet of optimum was nearly identical. The precipitous decrease in resilient modulus with degree of saturation was believed to correspond to the forced water entry phase. The capillary saturation is not considered a satisfactory method, because it is time-consuming when compared to molding wet of optimum (3.5 days compared to 1-3 hours), and the moisture distribution is almost as non-uniform as molding wet of optimum.

Incorporation of Seasonal moisture variations into Pavement Design

To account for the seasonal variation in moisture content, the AASHTO *Guide for Design of Pavement Structures* [*1*] describes a procedure for the identification of a single subgrade resilient modulus value for flexible pavement design. The year is divided into intervals or seasons, with each interval assigned a resilient modulus. Based on the anticipated pavement damage for that modulus value, a single value of M_R known as the "effective roadbed soil resilient modulus," is obtained for design.

The AASHTO procedure [*1*] is a rational means for the incorporation of seasonal variations of subgrade moisture content into the flexible pavement design process. However, a procedure for the determination of the seasonally adjusted resilient modulus is not described.

Guan et al. [*89*] proposed a weighted average method to determine the effective subgrade resilient modulus. Another approach developed by Guan et al. [*89*], follows the seasonal weighting factor approach of Gomez-Achecar and Thompson [*90*]. The seasonal effect of environmental conditions on M_R can be represented using the following equation:

$$WF_i = \frac{nM_{R_i}^{-2.32}}{\sum_{i=1}^{n} M_{R_i}^{-2.32}}$$

where WF_i = Weighting Factor for i-th Month,
M_{R_i} = Resilient Modulus of Subgrade for i-th Month,
n = Number of months used.

The Weighting Factor equation assigns relative damage to the calculated subgrade modulus for each month, and can be used to determine an effective M_R. The weighted mean value of subgrade modulus for any set of values is at a point where WF_i is equal to 1. The effective annual subgrade modulus is determined by solving the Weighting Factor equation for M_{R_i} with WF_i equal to 1. The effective modulus corresponds to a unique value of modulus that results in the same annual pavement damage expected from the seasonal modulus values. Additionally, the Weighting Factor approach can be used to discern the most important seasons for evaluating pavement performance. In both approaches to determining the weighted average of seasonal values, it is important to give careful consideration to selecting the seasons with the most pronounced environmental effect upon M_R.

Before resilient modulus is used as an input variable of pavement design, Bhajandas et al. [*91*] tried to account for seasonal variation by using deflection adjustment factors. Uhlmeyer et al. ([*92*]; [*93*]; [*94*]) tried to provide guidance for the selection of seasonal adjustment factors for layer moduli, based on both lab and NDT results. The adjustment factor is the ratio of measured modulus of a given month to the modulus measured in a dry season (the maximum measured modulus). Aggregate is found to be more susceptible to seasonal variation than subgrade, especially in freezing and thawing environments. Adjustment factors were used as following

(1) Drainage factors (m) are related to these adjustment factors for the design of base.
(2) Adjustment factors when multiplied by the subgrade resilient modulus can be used to calculate equivalent resilient modulus.

Subgrade Moisture Variation in Tennessee

Temperature, moisture content and climatic data from four instrumented sites have been collected for more than three years. The objective of the instrumentation is to study the environmental effects on pavement performance. The data collected from these four sites show that subgrade moisture variation is directly related to temperature (Drumm et al. 1998), which is opposite to the theory that the movement of moisture should be opposite to the direction of temperature gradient. This is not the only finding of such phenomenon. A preliminary evaluation of the SHRP-LTPP data revealed that in cold seasons, moisture content in the subgrade was lower than in warm season [*95*]. Data collected at the Minnesota Road Research Project (Mn/ROAD) also showed that the seasonal temperature fluctuations were directly related to the seasonal distribution of the unfrozen volumetric moisture content[*96*].

One thing in common of all these instrumentation studies is that Time Domain Reflectometery (TDR) probes were used to measure the volumetric moisture content. TDR probes measure the dielectric constant of the subgrade soil, and the result is then converted to volumetric moisture content. Dielectric constant of most minerals composing the soil skeleton does not exceed 10 - 12, whereas the dielectric constant of water is of the order of magnitude of

80. Therefore, any change in the amount of water in a soil has a very marked effect on its overall dielectric constant. A higher water content will result in higher dielectric constant. A study of dielectric properties of soil in [*97*] revealed that dielectric constant of compact samples with low moisture content increased with increasing temperature. This might explain the high moisture content measured by the TDR probes in summer. Further laboratory experiments would help to verify this hypothesis.

FREEZE THAW EFFECTS ON PAVEMENT SYSTEMS

Pavements in seasonal frost regions are subjected to annual freeze thaw cycles. In the winter, when the pavement structure is frozen, the bonding of the ice to the subsurface layer particles increases the bearing capacity of the pavement structure and therefore can handle larger loads than the pavement was designed for. However on the other hand with the formation of ice lenses, the pavement structure can be subjected to frost heave. Differential frost heave due to varying subsurface conditions can lead to an increase in pavement roughness.

During the spring, the melted ice lenses and surface water infiltration can lead to a saturated condition in the subsurface layers. The bearing capacity of the pavement structure is reduced, thus it will be necessary to reduce the allowable load on the pavement structure inadequately designed for thaw weakening. The length of load reduction will depend on the subsurface material, depth of frost penetration and drainage conditions.

In cold regions, frost heave and thaw weakening happens annually, for the life of the pavement structure. The pavement structure can be said to be subjected to form of thermal and moisture fatigue. For lack of a better term, the pavement structure is said to be subjected to 'environmental fatigue'. In addition, if the surface is constructed from asphalt concrete, it may be prone to low temperature cracking.

The Integrated Model (IM) developed for the Federal Highway Administration in 1993 attempts to incorporate the influence of climate on pavement performance [*98*]. Specifically, the IM uses temperature, moisture content, rainfall, wind speed and solar radiation to predict the material properties of the various layers, which in turn can be used to predict the performance of a pavement structure. The model can be used for both flexible and rigid pavements.

The model is made of four components; PRECIPITATION MODEL, INFILTRATION & DRAINAGE MODEL, CLIMATIC-MATERIALS-STRUCTURAL MODEL and the CRREL FROST HEAVE-THAW SETTLEMENT MODEL. A brief description of the various models is presented. Details can be found elsewhere ([*98*]; [*11*]; [*12*]; [*13*]).

The flowchart in Figure 8, describes how the Long Term Pavement Performance (LTPP) data can be used to predict the daily and seasonal variation of the pavement layer properties. The following information from the specific pavement section (SPS) are collected; air temperature, pavement temperature, subsurface layer temperatures, subsurface moisture content, frost penetration, amount of rainfall, short and long wave radiation and wind speed. This information with the back-calculated layer moduli can be used to develop material models for inclusion in the Integrated Model.

The PRECIP model is used to predict the amount of rainfall in the area. This is input to the INFILTRATION/DRAINAGE model. The INFILTRATION model uses the results from the PRECIP model to determine the probability of the wetness of the base. The DRAINAGE model predicts how drainable the base course is.

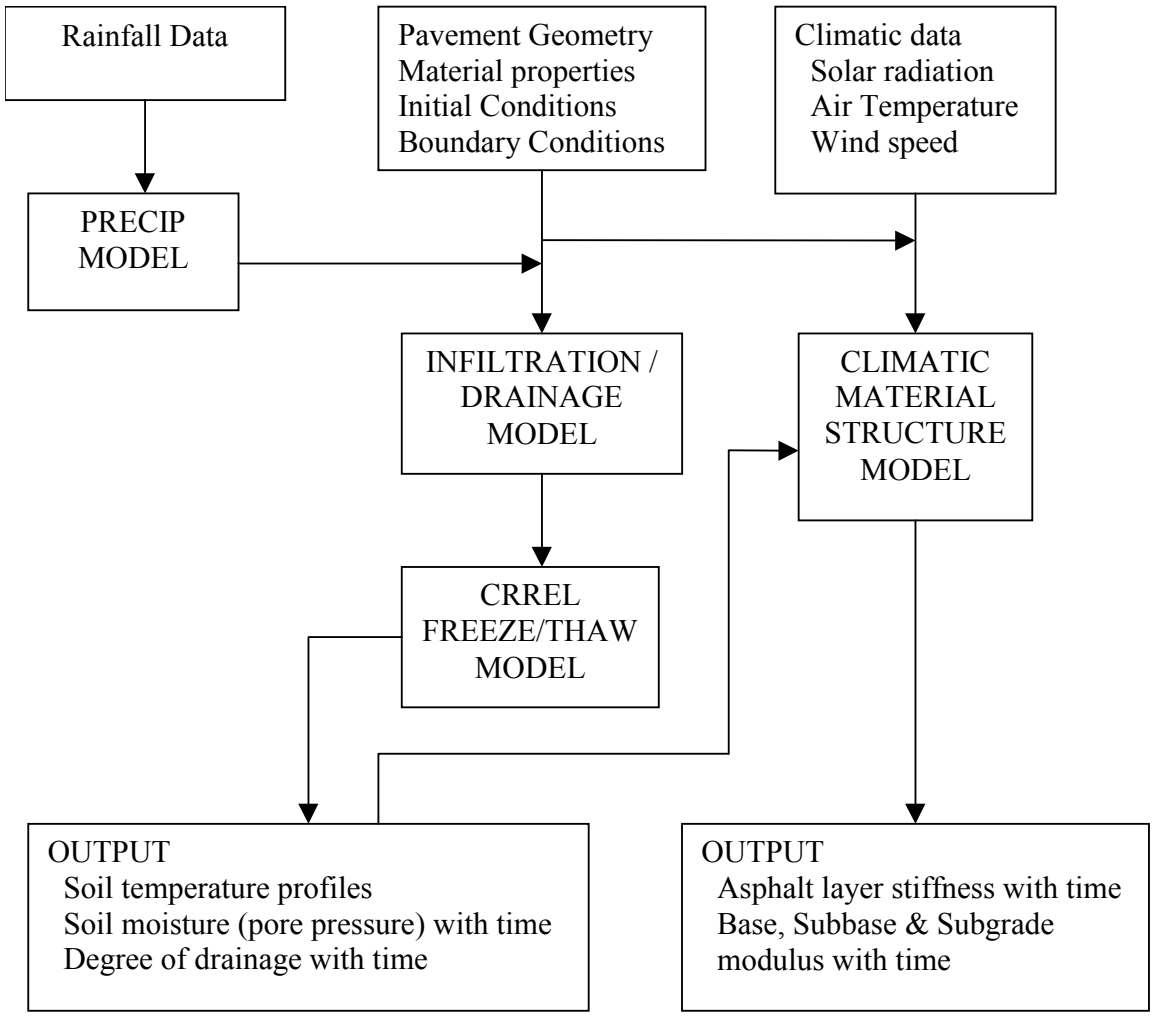

Figure 8. Integrated Climatic Model.

For material characterization, the more relevant models are the CRREL freeze thaw and the Climatic Materials Structural (CMS) models within IM. The CMS model predicts the asphalt layer stiffness as a function of time (temperature), the modulus of the base, subbase and subgrade as a function of time (moisture content). Although, the layer temperatures, densities, ice and moisture contents are predicted by the CRREL model, only the change in the moisture content as a function of time is used.

A review of models for predicting the stiffness (modulus) of asphalt concrete, base/subbase and subgrade in the Integrated Model is presented below. In addition to the models in IM, other models available in the literature are also presented. Note that the focus on the discussion is on material properties during freezing & thawing.

Asphalt concrete

The asphalt concrete stiffness in the CMS model is calculated from

$$S_m = S_b\left[1+\left(\frac{2.5}{n}\right)\left(\frac{C_v}{1-C_v}\right)\right]^n$$

$$n = 0.821\log\left(\frac{400000}{S_b}\right)$$

where, S_m = asphalt concrete stiffness (kg/cm^2)
S_b = bitumen stiffness
C_v = amount of aggregate in mixture (volumetric)

The effect of temperature on stiffness is through the bitumen stiffness (S_b)

There are other models available for predicting the stiffness of the asphalt concrete and should be considered. For example, the Asphalt Institute [*99*] model is a function of pavement temperature, mixture properties and frequency of loading;

$$\log E = 5.553833 + 0.028829\frac{P_{200}}{f^{0.17033}} - 0.03476(V_v) + 0.070377(\eta_{70^\circ F,10^6})$$
$$+ 0.000005\left(t_p{}^{(1.3+0.49825\log f)}P_{ac}^{0.5}\right) - 0.00189\left(t_p{}^{(1.3+0.49825\log f)}\frac{P_{ac}^{0.5}}{f^{1.1}}\right) * 0.931757\left(\frac{1}{f^{0.02774}}\right)$$

where, E = asphalt concrete dynamic modulus
P_{200} = % aggregate passing #200 sieve
f = frequency
V_v = % air voids in mix
$\eta_{70°F,\,10}{}^6$ = absolute viscosity
P_{ac} = % asphalt content by weight
t_p = pavement temperature (°F)

The AI model requires significant knowledge of the AC mix. There are several models based on temperature only. For example, [*100*], based on back-calculated asphalt concrete modulus recommended using the following equation for predicting the stiffness of the asphalt concrete;

$$E_t = 15{,}000 - 7900\log(t)$$

where E_t = asphalt concrete modulus (MPa)
t = pavement temperature (°C)

The range of temperatures that this equation is valid is between 0 °C and 40 °C. The temperature range for the AI equation is –20 °C to 40 °C.

A similar model to Ullidtz [*100*], was proposed by Janoo and Berg [*101*] based on back-calculation of asphalt concrete modulus during a thaw cycle;

$$E_{AC} = 5994 - 242(T)$$

where E_{AC} = asphalt concrete modulus (MPa)
T = pavement temperature (°C)

In the Seasonal Layered Elastic Design (SLED) [*102*], CRREL uses a combination of models to predict the asphalt concrete modulus. At temperatures greater or equal to 1 °C, the

Ullidtz model as described above is used. At temperatures below 1 °C, the model developed by Schmidt [*103*] is used;

$$E = 10^{\left(6.285-1.931E-2(T)-3.280E-4\left(T^2\right)-1.888E-5\left(T^3\right)+1.175E-7\left(T^4\right)+1.502E-8\left(T^5\right)-2.022E-10\left(T^6\right)\right)}$$

where, E = asphalt concrete modulus (psi)
T = pavement temperature (°C)

SLED is a research tool and is not available to the public. Finally, with respect to asphalt concrete, based on laboratory resilient modulus tests using a loading pulse simulating a FWD load, Johnson et al., [*104*] developed a model based on temperature for predicting the resilient modulus of asphalt concrete;

$$M_r = e^{(9.429-7,47E-2(T))}$$

where, M_r = asphalt concrete modulus (MPa)
T = pavement temperature (°C)
E = asphalt concrete modulus (MPa)

Base/subbase modulus

The design of a base course is a compromise between strength and drainability. In the Climatic Materials Structural sub-model, the assumption is made that the modulus of the base/subbase layers is generally insensitive to changes in moisture content. The model expects as input from the user the frozen and unfrozen base/subbase modulus. The Integrated Model covers the issue of the drainability of the base course through its DRAINAGE sub-model. The model predicts the degree of saturation of the base course as a function of time. In the DRAINAGE model, an attempt to relate the base course modulus to the degree of saturation is made. The model assumes a constant modulus if the degree of saturation (S) is below 60%. When S is greater than 60%, the base course dry modulus is decreased by a ratio of deflections between the dry and the current (S) state. However, as mentioned above this relationship is not used in the Integrated Model.

Experience with base course material is that it is not free draining as assumed in the Integrated Model. Commonly, states allow anywhere between 5 to 15% fines (material passing the #200 sieve) in their base course specifications [*105*].. Haynes and Yoder [*106*] found that granular materials subjected to repeated loading became unstable when S was greater than 80%. Thompson [*107*], based on test track results, attributed the failure of the test sections to the base course where S was in the range of 86 to 90%. An analysis conducted on base course materials used in airport construction, [*105*] showed that base courses having more than 3% can create a weakening situation during spring thaw, Figure 9. The analysis used the model developed by Casagrande and Shannon [*108*]. This is very similar to the DRAINAGE sub-model in the Integrated Model. The results indicate that it took approximately 40 days to drain down to 80% degree of saturation when the fine content is 3%. When the fine content was increased to 5%, the number of days to reach 80% degree of saturation was 300 days, a factor of approximately ten.

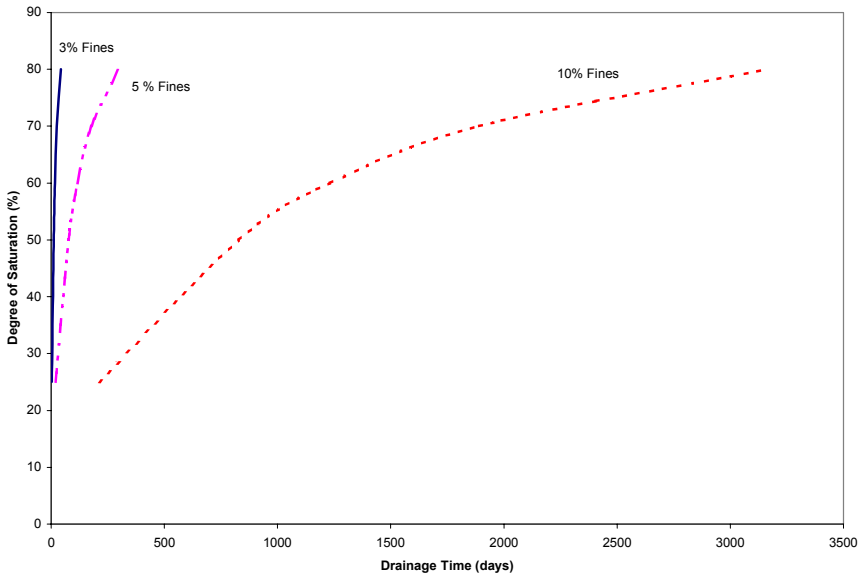

Figure 9. Effect of fines content on base course drainage, (after [*105*])

It is quite clear from the analysis that most base courses are prone to thaw weakening in cold regions. This is indirectly confirmed by field measurements of moisture content in the base layer, Figure 10 [*109*]. In this particular case, the moisture content in the base course increased by a factor of 5 during the spring thaw, Figure 10. The length of thaw weakening was approximately 3 weeks. Besides the gradation and fine contents, the modulus of base course is a function of moisture content and temperature.

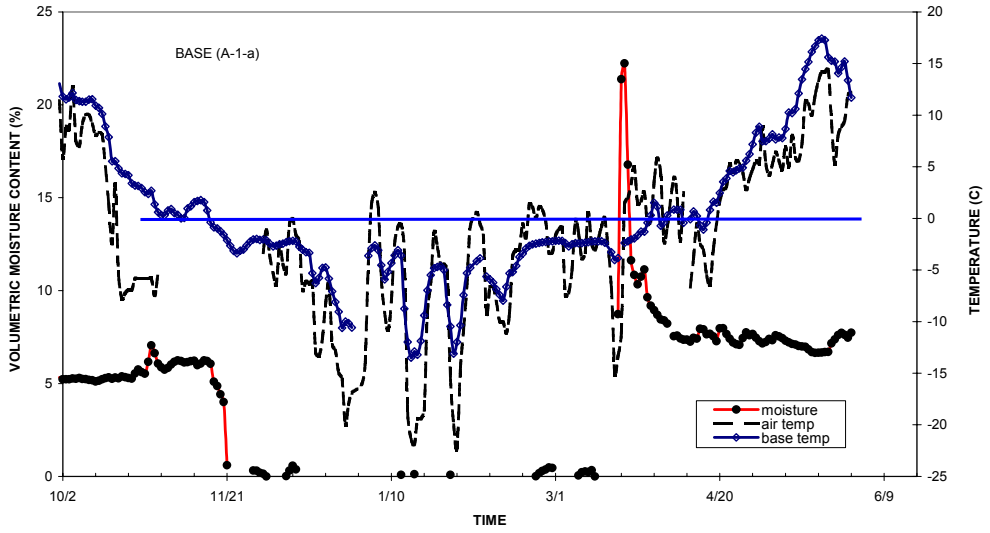

Figure 10. Moisture content change in the base course (after [*109*])

Prediction of base course resilient modulus is limited. Based on laboratory testing, Johnson et al. [*104*] developed models for predicting the frozen and thawed modulus. One of the models for a frozen base is

$$M_r = 18.9\left(\frac{w_u}{0.075}\right)^{-4.82}$$

and one of the models for a frozen subbase is

$$M_r = 81.8\left(\frac{w_u}{0.055}\right)^{-4.02}$$

where $w_u = 0.03(-T)^{-0.25}$

M_r = resilient modulus (MPa)

w_u = unfrozen water content

T = freezing temperature (°C)

Based on the same study, Johnson et al. [*104*], developed models for predicting the base and subbase modulus during thaw. They predicted the resilient modulus as a function of moisture content, stress state and dry density. One of their models for a thawed base is

$$M_r = 2.56\times10^4\left(\frac{101.36-\psi}{\psi}\right)^{-1.99}(J_1)^{0.37}(\gamma_d)^{2.90}$$

and one of their models for a thawed subbase is

$$M_r = 8.00\times10^8\left(\frac{101.36-\psi}{\psi}\right)^{-2.99}(J_1)^{0.37}(\gamma_d)^{-5.55}$$

where M_r = resilient modulus (MPa)

ψ = moisture tension or suction (kPa)

J_1= first stress invariant (kPa)

γ_d = dry density (Mg/m^3)

The above equations for thawed modulus clearly demonstrate the non-linearity of the resilient modulus during thaw. The dry density of the base course as a function of time can be obtained from the CRREL model. The CRREL freeze/thaw model is a 1-D coupled heat moisture flow model. The model can be used to predict temperatures in the asphalt, base, subbase and subgrade layers. With the thermal properties (thermal conductivity, specific heat and latent heat of fusion) and hydraulic properties of the various layers, the depth of frost penetration, thaw penetration and ice content in the base, subbase and subgrade is determined. Thermal and hydraulic properties of different soil types can be found in Guymon et al. [*13*].

Another factor that affects the resilient modulus of the base course is the percentage of rounded material in the mixture. Janoo and Bayer [*110*] found that the resilient modulus was significantly reduced when there was a 50-50 blend of crushed aggregates and natural gravel. The results in Figure 11 are based on laboratory testing of 300mm diameter and 600mm tall samples. Note that at lower bulk stress, the difference is minimal with the exception of the 50-50 blend. At higher stress levels, the resilient modulus increases with increasing crushed materials, with the exception of the 50-50 blend. Additional testing is being conducted to verify this

anomaly. Some state DOTs allow up to 50% of natural gravel in the base course layer and this may become an issue. The effect of freeze thaw may further accentuate the reduction of the resilient modulus of the 50-50 aggregate blend.

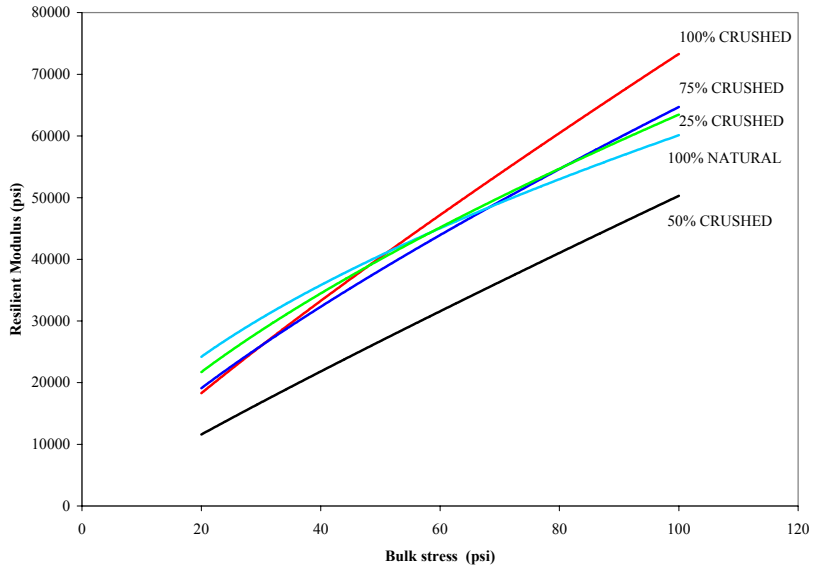

Figure 11. Effect of aggregate angularity on resilient modulus (after [*110*])

Models for subgrade materials discussed below may also be applicable to the base course.

Subgrade

In the Integrated Model (IM), the subgrade modulus for the frozen and unfrozen state can be an input by the user or can be determined by the program for fine grained soils with the following regression equations;

$$E_r = 27.06 - 0.526\theta \quad \text{for } \gamma_d > 100 \text{ pcf}$$
$$E_r = 18.18 - 0404\theta \quad \text{for } \gamma_d < 100 \text{ pcf}$$

where E_r = resilient modulus (ksi)
θ = volumetric water content (%)

For thawing subgrade modulus, the following model is used in the IM;

$$E_r(t) = \left[\frac{E_r(100 - \text{Re}\,duct)}{\text{Re}\,cper} + (E_r * \text{Re}\,duct) \right]$$

where, $E_r(t)$ = resilient modulus as a function of time t
Re*duct* = % of unfrozen resilient modulus
Re*cper* = time period for modulus to regain 80% of its original value

The default value for Re*duct* is 10%. The frozen modulus is assumed to be 100 times the unfrozen modulus.

Johnson et al., [*104*] based on laboratory resilient modulus tests, developed the following for frozen sand subgrades:

$$M_r = 2.59\left(\frac{w_u}{0.29}\right)^{-0.85}\left(J_1\right)^{0.93}$$

$$w_u = 0.0314\left(-T\right)^{-0.29}$$

and for thawed sand subgrades:

$$M_r = 1.35\times10^6\left(101.36-\psi\right)^{-2.36}\left(J_1\right)^{-3.25}\left(\gamma_d\right)^{-3.06}$$

where: M_r = resilient modulus (MPa)
w_u = unfrozen moisture content
ψ = moisture tension or suction (kPa)
J_1= first stress invariant (kPa)
γ_d = dry density (Mg/m^3)
T = freezing temperature (°C)

The model is similar for the base and subbase with the exception that a stress term is added to the subgrade in the frozen condition. For frozen clays, Bigl & Berg *(8)* presented the following model;

$$M_r = 846\left(w_{u-g}\right)^{-2.161}$$

where: w_{u-g} = gravimetric unfrozen water content.

Simonsen et al., [*111*] reviewed the results from resilient modulus testing of various subgrade soils in New Hampshire. The resilient modulus was conducted at freezing and thawing temperatures. For freezing and thawing conditions they recommended the following models as a function of soil type.

For Glacial Till (A-4) and Silty Fine Sand (A-2-4)

$$M_r = k_1 T^{k_2}{\sigma_d}^{k_3}$$

where σ_d is the principal stress difference (σ_1 - σ_3) and

$$k_1 = 3648;\ k_2 = 0.71,\ k_3 = 0.34$$

for the glacial till and

$$k_1 = 3069;\ k_2 = 0.60,\ k_3 = 0.38.$$

for the silty fine sand

For Coarse Gravelly Sand (A-1-b)

$$M_r = e^{\left(k_1+\frac{k_2}{T}\right)}$$

where $k_1 = 8.17$ and $k_2 = 0.90$.

For Fine Sand (A-1-a)

$$M_r = k_1\left|T\right|^{k_2}\left(J_1\right)^{k_3}\left(\sigma_d\right)^{k_4}$$

where $k_1 = 16069$, $k_2 = 0.49$, $k_3 = -3.0$ and $k_4 = 2.6$

For Marine Clay (A-7-5)

$$M_r = k_1 |T|^{k_2} \sigma_3^{k_3}$$

where $k_1 = 363$, $k_2 = 1.42$, $k_3 = 0.46$

These equations can be used for the freezing and thawing process. When completely thawed they found for some of the soils, the thawed modulus was significantly lower than that prior to freezing. This is shown in Figure 12 for the marine clay (after [*112*]). For thawed soils prior to recovery, Simonsen et al. [*111*] were unable to get any reasonable correlations. They recommended using the pre-freeze modulus and then applying a reduction factor.

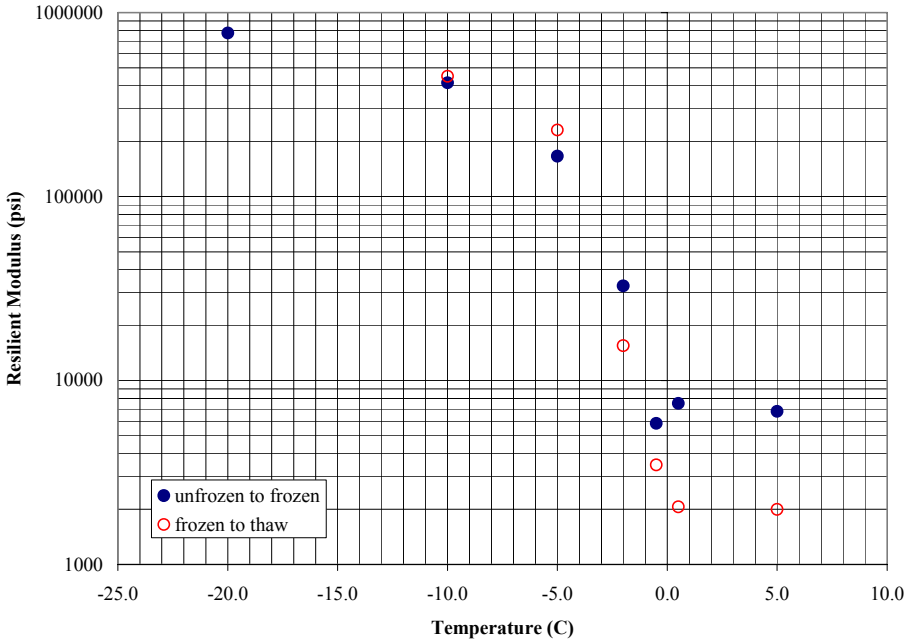

Figure 12. Change in resilient modulus of marine clay subjected to freeze-thaw cycle (after [*112*]).

For Glacial Till (A-4) & Silty Fine Sand (A-2-4)

$$M_r = k_1 J_1^{k_2}$$

where, for the glacial till;

$$k_1 = 238, k_2 = 0.87$$

and for the silty fine sand

$$k_1 = 386, k_2 = 1.14.$$

For the coarse gravelly sand (A-1-b), fine sand (A-1-a) and the marine clay (A-7-5);

$$M_r = k_1 (J_1)^{k_2} (\sigma_d)^{k_3}$$

where, for the Coarse gravelly sand

$$k_1 = 398,\ k_2 = 0.77,\ k_3 = -0.12$$

for the Silty fine sand

$$k_1 = 235,\ k_2 = 0.23,\ k_3 = 0.24$$

and for the Marine clay

$$k_1 = 6.92,\ k_2 = 0.68,\ k_3 = -0.81$$

The appropriate reduction factors are shown in Table 2.

Table 2. Coefficients for pre-frozen subgrade modulus calculations.

Soil Type	Reduction Factor
Glacial Till	0.73
Silty Fine Sand	0.81
Coarse gravelly sand	0.77
Silty fine sand	0.50
Marine clay	0.43

The models discussed so far are non-linear. The modulus is dependent not only on the temperature, moisture content and density, but also on the stress state.

A simpler model relating the subgrade modulus to temperature and moisture content during freezing & thawing was developed using data from Montana field sites [*109*]. The model has the same structure as those developed by Simonsen et al. [*111*];

$$M_r = k_1 (T_{ref} - T)^{k_2} (w_v)^{k_3}$$

where: M_r = resilient modulus (MPa)
T = subgrade temperature (°C)
T_{ref} = reference temp (20 °C)
w_v = volumetric moisture content

For an A-2-4 soil

$$k_1 = 105,\ k_2 = 0.2,\ k_3 = 0.4.$$

For an A-4 soil,

$$k_1 = 200,\ k_2 = 0.7,\ k_3 = 0.7.$$

Summary

A summary of various models for predicting the resilient modulus of asphalt concrete, base/subbase and subgrade during freezing and thawing are presented. Many of these models can

be validated using the LTPP data and incorporated into the Integrated Model. Some of the models, especially those that attempt to predict the thawed material properties are highly non-linear and may require some simplification prior to use with the Integrated Model.

TEMPERATURE EFFECTS ON FLEXIBLE PAVEMENTS

Introduction

The structural capacity of flexible pavements is heavily influenced by the stiffness of the asphalt concrete layer. The asphalt concrete stiffness is a function of temperature and varies throughout the day as well as through the year. Asphalt concrete temperature can affect the structural performance of the pavement in two ways. The stiffness of asphalt concrete is directly related to pavement temperature; the stiffness decreases as the temperature increases. A decrease in asphalt concrete stiffness results in higher stresses being transmitted to the base and subgrade. Most base and subgrade materials are stress-dependent. Typically, granular materials are stiffer at higher stress levels and cohesive soils are weaker at higher stress levels. Therefore, the asphalt concrete temperature indirectly affects the behavior of the base and subgrade. This variation in structural capacity with time and temperature means that pavement damage does not occur uniformly throughout the year. In order for pavement engineers to design flexible pavements efficiently, temperature effects must be considered in the design process. In order to account for temperature effects, relationships between temperature and asphalt concrete stiffness must be developed and the asphalt temperature must be determined. The asphalt temperature can be determined from direct measurement or from correlations with weather data.

Pavement Temperature

The pavement temperature varies daily and seasonally. Asphalt concrete pavement temperatures follow a nearly sinusoidal pattern, both daily and yearly. The pavement surface experiences the greatest temperature fluctuation. The temperature fluctuation decreases with depth. Below 12 in., almost no diurnal variation occurs. The surface normally reaches the highest temperature for the entire pavement in the afternoon and the lowest temperature for the entire pavement during the night. With increasing depth in the pavement, the time at which the maximum temperature is reached is much later than the time when the surface temperature reaches a maximum. Since pavement temperatures vary significantly with time and depth, one temperature cannot adequately describe the pavement [*113*].

Air Temperature

The air temperature is an important factor in determining the pavement temperature. The air temperature history of the site can provide an indication of the previous long-term influences on the pavement temperature. The amount of air-time history data that is required is debatable. The AASHTO design method, adopted from research by Southgate and Deen [*114*], requires air temperature information for the preceding five days. Other methods only require air temperature data from the preceding day ([*115*]; [*116, 117*]).

Solar Radiation

Both air temperature and solar radiation can increase the pavement temperature, but the effects of solar radiation are greater. The maximum possible amount of solar radiation changes

daily as the sun's path changes. Without cloud cover, solar radiation would be at a maximum on June 21 and at a minimum on December 21 [*113*]. The latitude of the site can also have an affect on the amount of solar radiation. Daily radiation amounts in the summer are nearly the same for sites in the northern and southern regions, but the southern regions receive more radiation per hour. The higher hourly radiation levels increase the difference between the air and pavement temperatures [*118*]. Analysis has shown that on days with the same air temperature and total solar radiation, the daily peak solar radiation intensity affects the maximum pavement temperature. In addition, low daily solar radiation and high peak solar radiation intensity has the same effect on the maximum pavement temperature as high daily solar radiation with low peak solar radiation intensity. Therefore, the daily peak solar radiation intensity is as important as the daily solar radiation intensity [*115*].

Cloud cover and shading can significantly affect the surface temperature by limiting the amount of solar radiation that reaches the pavement [*113*]. The surface temperature can drop 10–15°F due to just 10 minutes of local shade [*119*]. The influence of shading is significant enough to warrant the use the use of different temperature prediction methods for research FWD testing, such as collection of LTPP data, and routine FWD testing. The testing location is shaded for approximately 6 minutes during collection of LTPP data, while the pavement is typically shaded for less than a minute during normal testing by state highway departments [*117*]. Although the surface temperature is sensitive to shading, temperatures deeper in the asphalt concrete are not affected by short periods of local shading.

Temperature Gradient

The asphalt concrete temperature is a function of time as well as depth. On a cloudy day, temperatures throughout the pavement may be nearly uniform, whereas temperatures may vary by more than 60°F on a sunny summer day. Therefore, the temperature gradient should not be neglected when considering temperature effects [*113*]. Analyses have shown that the asphalt concrete temperature is nearly uniform at some point every morning. Data collected in Kuwait showed that the temperature is uniform about 2.5 hours after sunrise [*120*]. Field records from North Carolina also showed uniform asphalt temperatures at approximately the same time each morning [*116*]. As the day progresses, the surface temperature of the pavement increases faster than do temperatures deeper in the pavement. The surface temperature typically peaks during the mid-afternoon, at which time the surface temperature begins to decrease while temperatures deeper in the pavement continue to increase.

Temperature Prediction Models

Numerous procedures and relationships have been developed to estimate the pavement temperature from weather data. Although the temperature can be measured directly by drilling a hole in the pavement, this procedure is time consuming and several holes are needed to measure the temperature gradient. Therefore, procedures to estimate the pavement temperature are desirable. The surface temperature is usually measured since this can be done nondestructively. Some of the methods are based heavily on theory, considering heat transfer theory and viscoelastic behavior, while others are based solely on empirical data and regression analyses. Many of the relationships that have been developed are based on regional data and their usefulness in other climates is questionable.

Southgate and Deen [*114*] developed relationships for estimating the pavement temperature from data collected in College Park, Maryland. This procedure predicts the pavement temperature for asphalt thicknesses less than 12 in. using surface temperature, amount of heat

absorption, and the air temperature history from the preceding 5 days. A fourth-order polynomial is used to estimate the temperature-depth relationship for a given hour. A complete set of curves was developed to predict the temperature for different depths at different times of the day. This procedure has been adopted by AASHTO, but the curve included in the AASHTO Guide is based on a temperature gradient typical of 1:00 P.M and may not extend to data obtained at other times.

A more recent procedure, termed BELLS, has been developed using data from the LTPP Seasonal Monitoring Program ([*121*]; [*122*]; [*117*]). The original BELLS model predicts pavement temperature using the asphalt concrete thickness, 5-day mean air temperature, infrared surface temperature reading, and time of day. Due to faulty infrared temperature gauges used during data collection, the original BELLS model [*122*] overpredicts at low asphalt temperatures and underpredicts at high asphalt temperatures. A newer version [*117*], based on corrected infrared temperature data, is much more accurate.

Additional models, named BELLS2 and BELLS3, were developed using only the previous day's high and low temperatures and separate sine functions for pavement warming and cooling. The BELLS2 equation was developed from FWD data collected using the LTPP testing protocol and implicitly includes six minutes of shading by the FWD trailer and tow vehicle. The BELLS3 equation was developed for use during more routine pavement monitoring, when shading is limited to less than a minute. The BELLS2 equation is:

$$T_d = 2.78 + 0.912T_s + (\log d - 1.25)[0.553T_a - 0.428T_s + 2.63f_A] + 0.027T_s f_B$$

and the BELLS3 equation is:

$$T_d = 0.95 + 0.892T_s + (\log d - 1.25)[0.621T_a - 0.448T_s + 1.83f_A] + 0.042T_s f_B$$

where

d = Asphalt layer mid-depth or third-depth, mm
T_d = Pavement temperature at asphalt layer mid-depth or third-depth, °C
T_s = Infrared surface temperature, °C
T_a = Average air temperature the day before testing
f_A = sine function with an 18-hour cycle and a 15.5-hour phase shift
f_B = sine function with an 18-hour cycle and a 13.5-hour phase shift

Because The BELLS equations are empirical models based on daytime temperature data, they may not be accurate during the night. Similarly, they should only be used when the layer thickness is between 45 mm and 305 mm and should not be used when the pavement temperature is below freezing.

Another temperature prediction procedure has been developed using data from North Carolina [*123*]. It was observed that the gradients for different seasons are parallel if the data is plotted on a logarithmic scale. The temperature gradients on a logarithmic scale consisted of two straight lines, one above the shallowest thermocouple, located at 28 or 38 mm (1.0 or 1.5 in.), and one below the shallowest thermocouple. The logarithmic temperature gradients are mostly parallel regardless of season and time of day. The difference in gradients was minimized by shifting the gradients to a reference 38 mm depth. Once the gradients were shifted, equations were derived to represent the gradient shape below 38 mm for each hour of the working day. Since the temperature at a depth of 38 mm cannot be determined nondestructively, the 38 mm depth temperature had to be related to surface temperature. The first step of the procedure is to

calculate the mid-depth temperature in the reference temperature gradient using the following equation:

$$T_d = Ad^B$$

where

Td = pavement temperature at mid-depth (°F),
d = mid-depth of asphalt concrete layer (in.),
A, B = regression constants given for each hour of the working day.

The calculated reference mid-depth temperature from the preceding equation is adjusted to the actual mid-depth temperature by multiplying the calculated reference mid-depth temperature by a shift factor. The shift factor is calculated by dividing the measured surface temperature (°F) by the reference surface temperature for the hour that the FWD test was performed.

A procedure using the surface temperature time history and fundamental principles of heat transfer has also been developed using data from North Carolina [*116*]. During FWD tests, surface temperatures are measured at time intervals to develop an accurate short-term surface temperature history. Before the day's first surface temperature measurement, a modified sine-wave function is used to simulate the surface temperature-time history. The maximum air temperature from the day before and the minimum air temperature for the morning of testing are needed to generate the surface temperature history since the preceding day. These values can easily be obtained (e.g. local newspapers). Field records show that a nearly uniform temperature condition occurs in the pavement at approximately the same time every morning; the time when this condition occurs is called the "crossing time." The crossing time and temperature are used in the prediction procedure as the initial time and initial temperature. The shape of the surface temperature within a day approximates a sine function, except that the rate of temperature change in the heating and cooling cycles are different. Therefore, the surface temperature history is modeled using a sine curve with two different periods, one for the heating cycle and one for the cooling cycle. Inaccurate representation of the morning's surface temperature history has a much greater effect on the prediction accuracy than inaccurate representation of the previous 24-hour temperature-time history.

Another procedure for predicting pavement temperature was suggested by Ovik et al. [*124*]. The temperature in the asphalt layer at various depths and time of year was calculated using a sinusoidal function, called the "whiplash" equation. The whiplash equation is a function of average surface temperature, time, depth, and thermal diffusivity.

$$T(x,t) = T_{mean} + Ae^{-x\sqrt{\frac{2\pi}{P\alpha}}} \sin\left(\frac{2\pi}{P}(t) - x\sqrt{\frac{2\pi}{P\alpha}}\right)$$

where

T(x,t) = soil temperature as a function of depth and time, °C,
x = depth, m,
T_{mean} = average temperature at surface, °C,
A = maximum temperature amplitude, (T_{max} - T_{mean},°C),
P = period or recurrence cycle,
α = thermal diffusivity, area/time,
t = time measured from when the surface temperature passes through T_{mean}, (days).

The Enhanced Integrated Climatic Model (EICM) can also be used to predict pavement temperatures. The EICM predictions match temperatures observed in the field well if the correct material properties and parameters are used. A limitation of the EICM is that extensive material testing is required to determine all of the program inputs, which is not economical for highway engineers [*10*].

SUPERPAVE Models

Several asphalt concrete temperature prediction models have been developed specifically for predicting the low and high pavement temperatures used in the SUPERPAVE binder selection procedure ([*115*]; [*125*]; [*118*]). SHRP considers the low air temperature to be the design low pavement temperature. The SHRP high pavement surface temperature model is:

$$T_{surf} = T_{air} - 0.00618Lat^2 + 0.2289Lat + 24.4$$

where

T_{surf} = High asphalt pavement temperature at the surface, °C
T_{air} = High air temperature, °C
Lat = Latitude of the section, degrees.

The SHRP high temperature model estimates are generally higher than actual SMP high pavement temperatures. The SHRP low temperature estimates were as much as 13°C lower than SMP field measurements at a depth of 25 mm. New models have been developed using LTPP data. The LTPP low temperature model is a function of low air temperature, latitude, and depth to surface. The LTPP low temperature estimates are not nearly as conservative as the SHRP estimates, especially at lower air temperatures; LTPP estimates of low temperature are generally 7°C to 8°C higher than the SHRP model. The LTPP low temperature model is:

$$T_{pav} = -1.56 + 0.72T_{air} - 0.004Lat^2 + 6.26\log_{10}(H + 25)$$

where

T_{pav} = Low asphalt pavement temperature below the surface, °C
T_{air} = Low air temperature, °C
Lat = Latitude of the section, degrees
H = depth to surface, mm.

For the high temperature model, the SHRP and LTPP models are in good agreement for air temperatures below 25°C. SHRP estimates may be as much as 5°C higher than LTPP estimates at higher temperatures. The LTPP high temperature model is:

$$T_{pav} = 54.32 + 0.78T_{air} - 0.0025Lat^2 - 15.14\log_{10}(H + 25)$$

where

T_{pav} = High asphalt pavement temperature below the surface, °C
T_{air} = High air temperature, °C
Lat = Latitude of the section, degrees
H = depth to surface, mm.

New low and high temperature models where developed and compared to the SHRP and LTPP models, using data from Wisconsin [*115*]. The WisDOT low temperature model agreed well with the LTPP model, but not the SHRP model. The recommended WisDOT temperature model for maximum pavement temperature matched actual pavement temperatures better than

the LTPP or SHRP models, which both use latitude as a substitute for solar radiation. This suggests that solar radiation must be considered in predicting maximum pavement temperature.

Temperature Correction Procedures

The methods previously discussed were developed to estimate the asphalt concrete temperature. Once the temperature is known, relationships are required to estimate the asphalt concrete stiffness given a certain temperature. Methods have also been developed to adjust FWD deflections based on temperature. Relationships have been developed based on laboratory testing, empirical relationships from FWD data, viscoelastic theory, and statistical analyses. Once the temperature-modulus or temperature-deflection relationship is known, the measurements are usually adjusted to a standard or reference temperature to be used by pavement engineers for design purposes.

Equivalent Temperature

A topic of great debate has been what temperature should be used in the asphalt concrete stiffness correlation. As mentioned earlier, the asphalt concrete temperature changes with time and depth. Some methods use the temperature at a specified depth, while others calculate an average or equivalent temperature. Although it is typical for the pavement temperature to be measured at a specific depth below the surface, the optimum depth for temperature measurement depends on the thickness of the asphalt concrete layer. Previous research has shown that the single temperature measurement that best describes the general asphalt temperature is located at a depth of 30-60% of the total asphalt concrete thickness. Research by Baltzer and Jansen [*126*] shows that the temperature-asphalt modulus relationship is different depending on whether the asphalt is heating up or cooling down. At approximately the one-third depth, the temperature-asphalt modulus relationship appears to be the same for the heating and cooling cycles. Therefore, it was suggested that the one-third depth temperature be correlated with asphalt modulus. Others have claimed that no improvement is seen by correlating asphalt modulus to the one-third depth temperature instead of the mid-depth temperature [*123*]. AASHTO recommends determining the average temperature by calculating the mean of the temperatures at the surface, mid-depth, and bottom of the asphalt layer. When temperature gradients are present in the pavement, Van Gurp [*32*] recommends calculating a weighted mean asphalt temperature based on the pavement temperatures at different depths. The equation developed to calculate the weighted mean temperature is based on Nijboer's equivalency concept of equal curvatures of bending beams. An equivalent asphalt concrete temperature can also be found by integrating the temperature gradient over depth and dividing by the asphalt concrete thickness. A more elaborate approach for handling the nonuniform temperature distribution is to subdivide the asphalt layer into numerous sublayers for analysis. Analyses have shown that the results are similar when using the equivalent asphalt concrete temperature and when subdividing the asphalt concrete into sublayers [*127*].

Asphalt Modulus Correction Models

Parker [*128*] studied the effect of temperature on asphalt concrete moduli from falling weight deflectometer data collected in Alabama. A power curve model similar to the relationships suggested by Lee et al. [*129*] and Witczak [*130*] was developed to estimate the asphalt concrete modulus:

$$E_1 = \frac{322,000}{T^{1.591}}$$

where

E_1 = asphalt modulus, ksi, and
T = pavement test temperature, °F.

Modulus correction factors were developed from this modulus-temperature relationship by forming ratios of the estimated modulus at 70°F to estimated moduli at other temperatures. The correction factors allow the correction of moduli measured between 30°–120°F to a 70°F design temperature.

Another correction procedure has been derived from asphalt concrete temperature-stiffness relationships and elasticity relations used to calculate composite modulus [*131*]. The method includes an adjustment factor that estimates the change in overall pavement stiffness due to a change in asphalt concrete stiffness and the pavement geometry. The average pavement temperature, the ratio of AC-bound thickness to non-AC-bound thickness, and the modular ratio of AC-bound to non-AC-bound layers are needed to calculate the adjustment factor. The change in asphalt concrete modulus with temperature can be estimated with a simplified version of the Asphalt Institute relationship:

$$\frac{E_{std}}{E_{field}} = 10^{-0.0002175(t_o^{1.886} - t^{1.886})}$$

where

t = test temperature (°F),
t_o = standard temperature (°F),
E_{std} = asphalt concrete modulus at the standard temperature (70°F) and frequency
E_{field} = asphalt concrete modulus at the test temperature.

An alternative relationship for asphalt temperatures above 35°F was developed by Ullidtz [*100*]:

$$\frac{E_{std}}{E_{field}} = \left[3.319 - 1.751 * \log\left(\frac{(t-32)}{1.8} \right) \right]^{-1}$$

The modular ratio of the AC-bound to non-AC-bound layers must be estimated to calculate the adjustment factor; fortunately, the adjustment factor is not affected much by variation in the modular ratio. The composite modulus adjustment factor proposed is shown below.

$$\frac{E_{e,std}}{E_{e,field}} = \left[\frac{1 + \sqrt[3]{z_{std} x^3 \left(\frac{1-\mu_2^2}{1-\mu_1^2} \right)}}{1 + \sqrt[3]{\frac{E_{field}}{E_{std}} z_{std} x^3 \left(\frac{1-\mu_2^2}{1-\mu_1^2} \right)}} \right]^3$$

where

$E_{e,std}$ = composite modulus at the reference temperature,
E_{std} = asphalt concrete modulus at 70°F,
E_{field} = asphalt concrete modulus at the test temperature,
$E_{e,field}$ = composite modulus at the test temperature,

z = ratio of AC-bound layer modulus to non-AC-bound layer moduous,
x = ratio of AC-bound layer thickness to non-AC-bound layer thickness,
μ_1 = Poisson's ratio of AC-bound layer, and
μ_2 = Poisson's ratio of non-AC-bound layer.

Another temperature correction model [*126*], which is valid within the temperature range 5–30°C, is given by:

$$E_{ref} = 10^{-0.018(T_{ref} - T_{AC})} E_{AC}$$

where

T_{ref} = the reference temperature in °C,
E_{ref} = the reference AC E-modulus in MPa,
T_{AC} = the AC temperature during the FWD test, at one third the total AC thickness (°C),
E_{AC} = the AC modulus found from FWD testing and backcalculation (MPa).

A similar relationship has been developed by others ([*119*]; [*132*]):

$$E_{68} = 10^{0.0153(T-68)} E_T$$

where

E_{68} = corrected AC modulus to the reference temperature of 20°C (68°F),
E_T = backcalculated AC modulus from FWD testing at temperature T (°F), and
T = the AC layer mid-depth temperature (°F) at the time of FWD testing.

The slight differences between this model and the previous model could be attributed to several things, among them location-specific factors such as the grade of asphalt cement or even the backcalculation program used. For example, a similar temperature correction equation developed from LTPP data [*121*] uses a variable coefficient:

$$ATAF = 10^{slope*(T_r - T_m)}$$

where:

ATAF = Asphalt temperature adjustment factor
slope = Slope of the log modulus versus temperature relationship
(-0.0195 for the wheelpath and -0.021 for mid-lane are recommended)
T_r = Reference mid-depth hot-mix asphalt (HMA) temperature
T_m = Mid-depth hot-mix asphalt (HMA) temperature

The variable *slope* is correlated with the latitude of the site, which is related to the asphalt cement grading. Studies have shown that asphalt concrete mixtures with stiffer binders have a higher modulus than asphalt mixtures with softer binders, especially in the summer ([*121*]; [*124*]) under stiffness must be implicitly or explicitly included in any relationship between asphalt concrete modulus and temperature.

An exponential model was developed correlating the asphalt concrete modulus with the asphalt layer temperature at a depth of 25 mm below the surface [*76*].

$$E1 = e^{(9.37196 - 0.03608145*T1)}$$

where

E1 = asphalt concrete modulus (MPa), and
T1 = Temperature in °C at a depth of 25 mm in the asphalt concrete layer.

A modulus-temperature correction equation based on data from Texas is [*133*]:

$$E_{Tw} = E_{Tc}\left(\frac{T_w}{T_c}\right)^{2.4462}$$

where

E_{tw} = the adjusted modulus of elasticity at T_w, MPa,
E_{tc} = the measured modulus of elasticity at T_c, MPa,
T_w = the temperature to which the modulus of elasticity is adjusted, °F, and
T_c = mid-depth pavement temperature at the time of FWD data collection, °F.

Badu-Tweneboah et al. [*134*] developed two procedures for estimating asphalt concrete pavement moduli as a function of temperature. The first procedure involves dynamic indirect tension testing of asphalt cores or laboratory-compacted specimens at different temperatures. An equation fit to that data can be used to estimate in situ asphalt moduli obtained during nondestructive testing. The second procedure involves viscosity testing of asphalt cement recovered from the pavement. Regression analysis is used to develop a relationship between viscosity and temperature that can be used to estimate the asphalt modulus in the field.

Park and Kim [*135*] developed a temperature correction procedure that also accounts for the viscoelastic properties of the asphalt concrete. Most existing temperature correction procedures are based on statistical analyses of data from a limited set of asphalt mixture types and pavement structures and do not effectively correct for certain conditions. By using the time-temperature superposition principle, the effects of time and temperature can be accounted for by a single variable called reduced time. New modulus and deflection correction procedures were developed that account for the thermorheological mixture properties. A theoretical modulus correction factor can be defined if the relaxation modulus and the time-temperature shift factor for the asphalt mixture are available (from laboratory tests). The proposed method can handle unusual mixtures because it explicitly accounts for the viscoelastic properties of the mixture. The temperature shift factor does not vary much among mixtures with the same binder. Therefore, a typical function for the shift factor can be established for each state to be used in deflection analysis. Another advantage of the proposed procedure is that it may be applied to pavements with microcracks in the asphalt concrete mixture.

Deflection Correction Models

Determination of deflection correction factors is more complicated than modulus correction factors because the deflections are influenced by all of the pavement layers. Studies have shown that deflections corrected using the AASHTO temperature-deflection correction procedure still exhibit temperature dependency ([*131*]; [*132*]). An alternative method has been developed to correct the maximum deflection to a reference temperature, based on data from North Carolina ([*119*]; [*132*])

$$D_{68} = 10^{\alpha(68-T)} D_T$$

where

D_{68} = adjusted deflection to the reference temperature of 20°C (68°F),
D_T = deflection measured at temperature T (°F),
α = $3.67 \times 10^{-4} * t^{1.4635}$ for wheelpath, or $3.65 \times 10^{-4} * t^{1.4241}$ for lane center,
t = thickness of AC layer (in.), and
T = the AC layer mid-depth temperature (°F) at the time of FWD testing.

A temperature correction method has been developed using data from Texas [*133*]. For this study, it was found that only deflections at the first two sensors (0" and 12" radial offsets) were significantly affected by temperature. Different equations were developed for intact and cracked pavements. The equation to correct the maximum deflection of intact pavements is:

$$W_{Tw}^{1} = W_{Tc}^{1}\left[\frac{1.0823^{-0.0098*t}}{0.8631} T_{w}^{0.8316} T_{c}^{-0.8419}\right]$$

where

W_{Tw}^{1} = the w_1 (0" offset) deflection adjusted to temperature T_w, mm,
W_{Tc}^{1} = the measured w_1 (0" offset) deflection at T_c, mm.
T_w = reference temperature, °C,
T_c = mid-depth pavement temperature at the time of FWD data collection, °C,
t = the thickness of the pavement, mm,

CLIMATIC EFFECTS ON CONCRETE PAVEMENTS

Introduction

A rigid pavement consists of a system of portland cement concrete slabs that provide the primary structural component of the rigid pavement. Below this there is generally a base course, sometimes styled as a subbase course, that can serve a variety of functions including drainage, construction platform, frost protection, structural strengthening or some combination of these. Below this is the subgrade or fill. Environmental effects on rigid pavements can be divided into those that effect the surface concrete slabs and those that effect the underlying layers. This section will consider only the effects on the concrete slabs. Other important effects such as pumping, frost heave, soil weakening due to moisture etc., that occur within the underlying layers are discussed in other sections.

The environment affects the slabs in one of two ways. It may cause deterioration and change in the structural capacity of the material itself or it may cause differential volume changes in the slab that lead to displacements, restraint of which develop stresses in the slab. The first is generally a durability issue while the second has a variety of sources that are primarily temperature and moisture related. The end effect of the volume changes is to cause a tendency for the slab to curl. This report will use the term *curl* as a generic descriptor for all out of plane displacements of the pavement slab due to volumetric changes occurring within the slab. Some writers differentiate between the terms *curl* and *warp* based on causes of the deformations. However, the American Concrete Institute [*136*] does not and uses the terms interchangeably to refer to out of plane deformations typically caused by temperature or moisture. This convention will be followed in this report.

The remaining discussion of environmental effects on rigid pavements will consider durability effects, mechanisms of curling, early-age effects, moisture effects, temperature effects, carbonation effects, and will conclude with a review of their implications for design and analysis of rigid pavements.

Durability Effects

The primary environmentally induced durability problem faced by rigid pavements is exposure to freezing and thawing while in a moist condition. Pavement slabs on ground are exposed to moisture from the atmospheric environment and from subsurface (ground water, vapor movement, capillary rise) and surface sources. Application of deicing salts to the pavement surface exacerbates the problem. Consequently, pavement slabs generally exist, even in arid environments, under moisture conditions that expose them to potential deterioration from freezing and thawing if they are not properly protected.

The literature on freezing and thawing effects in concrete is voluminous. Two relatively recent compilations and analyses are American Concrete Institute 2000b and Klieger and Lamond [*137*], and the topic is extensively covered in texts on concrete technology. Summarizing from these sources, concrete can be protected from the effects of freezing and thawing while critically saturated (91%) by:

(1) gaining adequate maturity before being exposed to freezing. This is generally taken to be a compressive strength of 500 psi (3.45 MPa) which under reasonable curing temperatures is reached by the second day. If concrete freezes prior to gaining adequate strength, it will scale down to the depth of freezing. If the concrete is to be exposed to extended freezing while critically saturated, desirable practice would be to allow it to gain a compressive strength of 4,000 psi (27.6 MPa)and to allow a period of drying following curing.

(2) using sound aggregate resistant to freezing and thawing. D-cracking and popouts are the two primary defects likely to be encountered. Most specifications such as ASTM C 33 contain specific limits on deleterious materials that contribute to popout problems. Durability- or D-cracking develops in certain fine-grained, predominately sedimentary, rocks whose pore structure makes the aggregate vulnerable to cracking when frozen while critically saturated, but there is no completely satisfactory test for identifying such aggregates ([*138*], [*139*]). At present, past history of aggregate performance from specific sources or ASTM C 666 appear to be the best approaches to ascertaining an aggregate=s vulnerability to D-cracking. Popouts are primarily an aesthetic and nuisance problem on highways, but D-cracking causes progressive cracking and deterioration of the concrete slab and is a structural issue.

(3) providing adequate air-entrainment in the concrete matrix. Purposely entrained air bubbles on the order of 0.1 mm in diameter or smaller that are sufficiently closely spaced provide protection to the concrete matrix when exposed to freezing and thawing under moist conditions. It is general practice today to use entrained air for concrte pavements exposed to freezing and thawing.

Today's technology is generally adequate to allow construction of concrete pavements that will not deteriorate from exposure to freezing and thawing. This does not imply that we do not have problems but only that we have not applied our knowledge adequately or their has been a construction problem in the field.

Other potential environmental deterioration problems such as from cyclic wetting and drying are usually indicative of distinctly substandard concrete that should not be used highway pavements. Other durability problems such as from traffic (abrasion) or chemical reactions (alkali-aggregate reaction or sulfate attack) are outside the scope of this report.

Mechanisms of Curling

Curling develops due to differential volume change across the thickness of the slab. Typically this arises when the concrete tries to undergo a uniform change in volume but friction or some similar mechanism resists the concrete expansion or contraction on one face or when some gradient exists across the slab that causes differential volume change between the top and bottom. For example, when concrete undergoes autogenous shrinkage from cement hydration, the surface of the slab is free to shrink or decrease in volume but the shrinkage on the bottom surface is resisted by friction between the slab and the underlying base course. The result is increased shrinkage on the surface relative to the bottom and a tendency to curl upwards. Temperature and moisture gradients commonly develop in pavement slabs and are another source of curling. If a slab=s underside is wet or warm relative to its surface, there will be a differential shrinkage between top (smaller volume) and bottom (larger volume), the slab will tend to curl upwards. If the conditions are reversed, the slab will tend to curl downwards.

Specific mechanisms that can cause this differential shrinkage between top and bottom of the slab will be discussed in subsequent sections.

The amount of curl is a function of the amount of differential shrinkage between the top and bottom of the slab and the slab thickness and length between joints. Consider a unit width cut through the center of a slab that is exposed to some differential shrinkage between top and bottom faces. This unit width approximates a beam and the deflection due to the differential shrinkage can be calculated as [*140*]:

$$a_{sh} = \xi_{sh}\phi_{sh}l^2$$

where

a_{sh} = deflection due to differential shrinkage

ξ_{sh} = deflection coefficient that depends on boundary conditions

ϕ_{sh} = curvature due to differential shrinkage

l = length

If this unit width beam is subjected to an upward deflection by differential shrinkage on its upper and lower faces, it is equivalent to a cantilever beam with a fixed end at the center of the slab where the deflection (w) and slope (dw/dx) are equal to zero. In this case, ξ_{sh} is 2, and l is 2 of the slab length.

The shrinkage curvature (ϕ_{sh}) for an unreinforced member may be expressed as ([*141*], [*142*]):

$$\phi_{sh} = \frac{\Delta_{sh}}{h}$$

where:

Δ_{sh}= differential shrinkage between top and bottom

h = slab thickness

Substituting this into the original equation with ξ_{sh} = 2 and slab length (L) = 2l

$$\Delta_{sh} = \frac{8a_{sh}h}{L^2}$$

Figure 13 shows the amount of differential shrinkage needed to calculate 1/8 in. (3mm) and 1/4 in. (6mm) upward curl for slabs of various length and thickness. As slab length increases, the amount of differential shrinkage needed to cause curl decreases dramatically, and as a slab thickness decreases its vulnerability to curling increases. Field observations and theory both

establish that potential curling problems increase as slab length increases and thickness decreases. Upward curled slabs suffer a large proportion of corner breaks at well below design traffic levels (e.g., [*143*]).

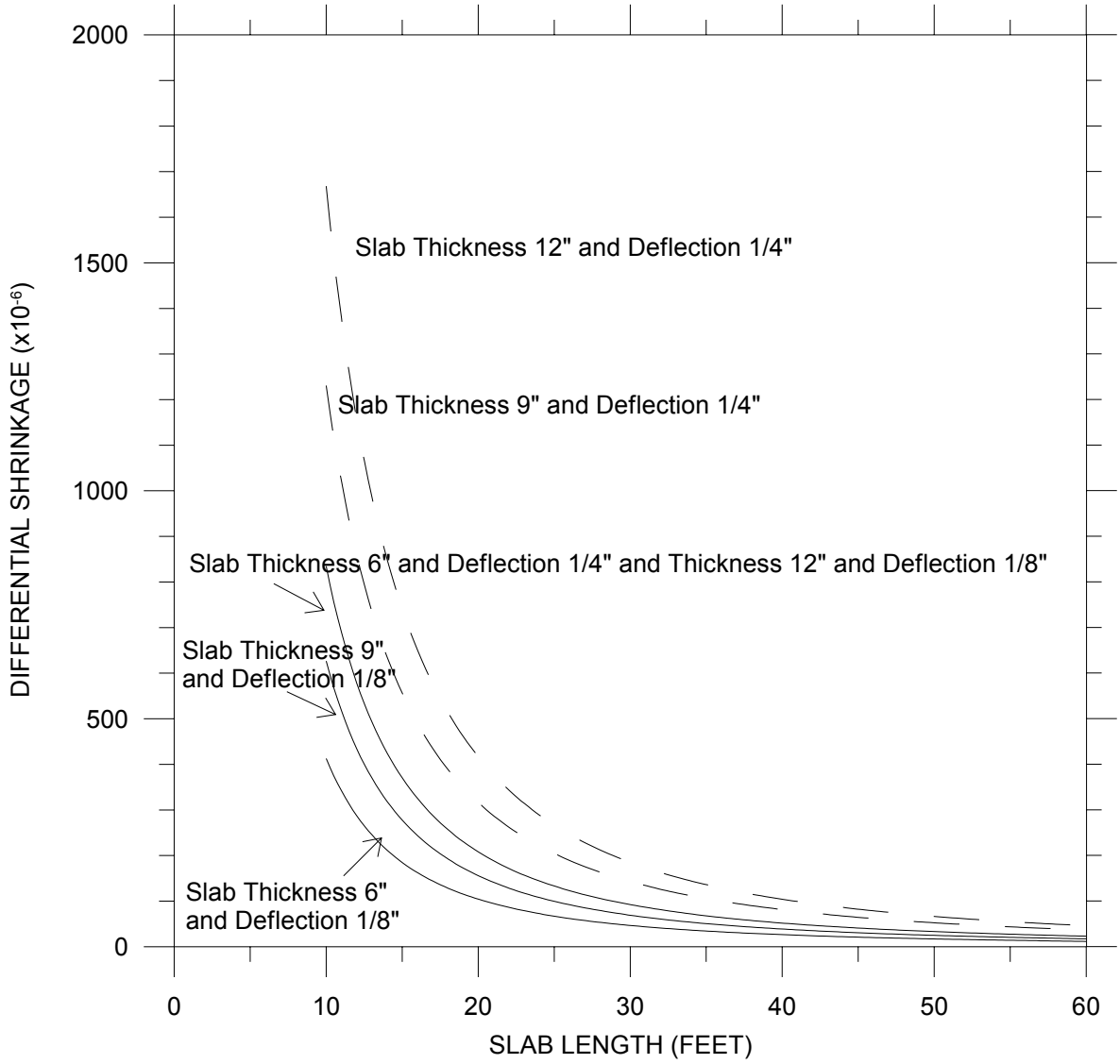

Figure 13. Amount of Differential Shrinkage Required to Cause Curling for Slabs of Various Length and Thickness

Even if the differential shrinkage does not cause curling and physical separation of the slab and base, the forces encouraging curling will cause stresses in the slab if they are restrained. ACI Committee 207 [*144*] provides an analysis method for vertically supported slabs subject to volume change with discontinuous shear restraint along the bottom face. For slabs placed on subgrades of little or no tensile capacity and with less shear strength than the concrete itself , cracking will begin at the approximate center of the slab when a parabolic stress distribution develops through the slab depth with the tensile stress equal to the tensile capacity of the concrete. The cracking moment, M_{cr}, from this stress distribution is equal to $f_t = Bh^2/10$ where f_t

is the tensile strength of the concrete and B is the width of the section. This cracking moment is resisted by an external balancing moment, M_r, dependent on the weight of the concrete alone. M_r can be approximated as $0.075\ W_c BhL^2$ where W_c is the weight of the concrete. Setting the cracking moment, M_{cr}, equal to the restraining moment, M_r, one can solve for the stress at which cracking occurs as a function of L and h

$$\sigma_{cr} = f_t^{'} = 0.75 W_c \frac{L^2}{h}$$

Figure 14 shows that as slab length increases or thickness decreases, the induced tensile stresses in the slab increase dramatically and the stresses easily can exceed the tensile capacity of concrete. If the applied curling stresses exceed the tensile capacity of the concrete, a crack will form in the approximate center of the slab.

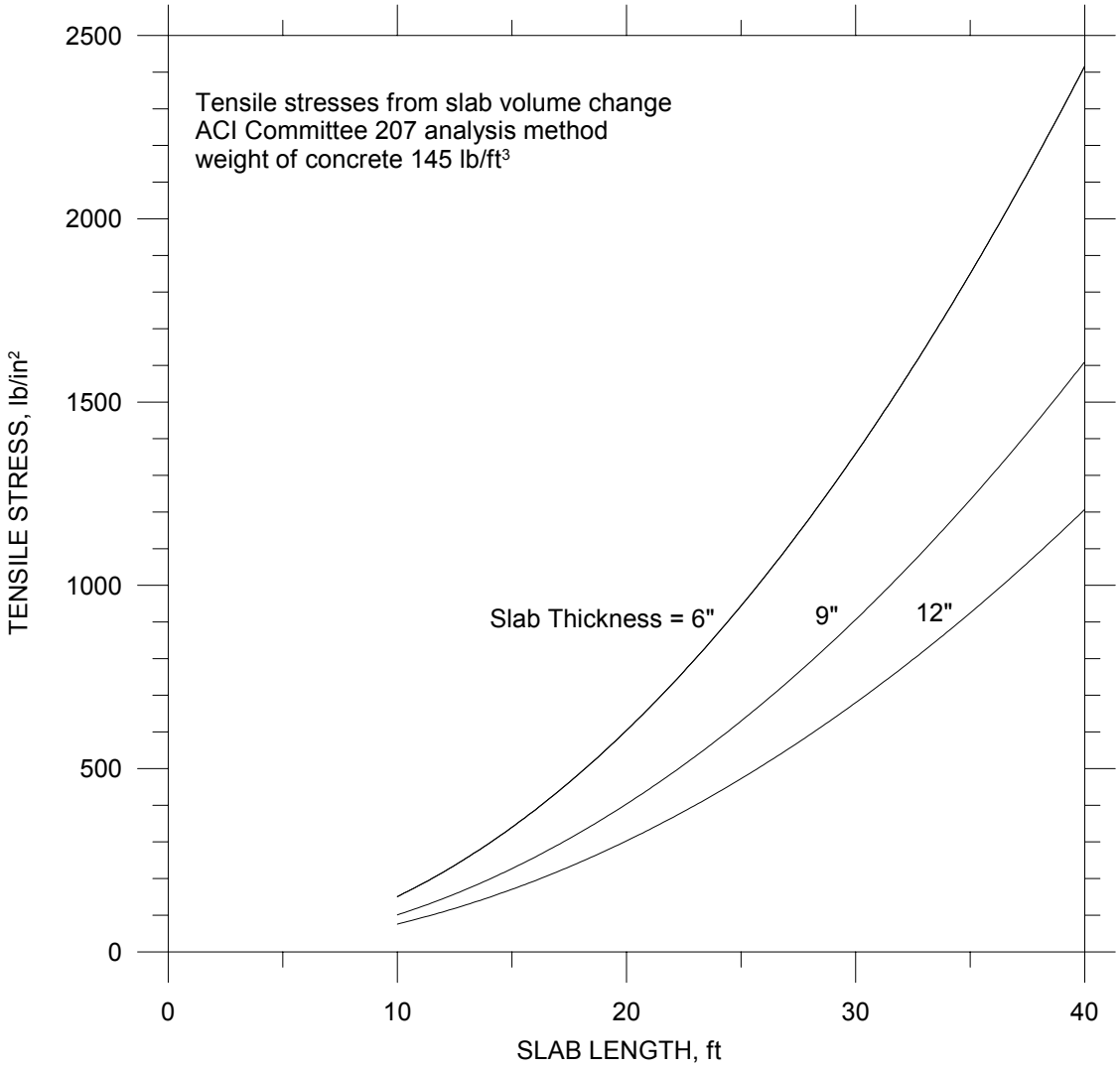

Figure 14. Tensile Stresses from Volume Change for Slabs of Varying Length and Thickness

Sources of Curling

Differential volume change is the driving force behind curling. Sources of this include early-age effects, autogenous shrinkage, moisture effects, thermal effects, and carbonation. In pavement slabs all of these sources may be acting simultaneously, but for clarity, they will be discussed independently.

Early-Age Effects

Rhodes [*145*] conducted an investigation of various curing regimes that included over 1,000 laboratory specimens and a series of beam warping tests. This study, particularly the beam warping tests, revealed that important curling contributions develop very early in the life of a concrete slab. In the warping tests, twelve beams were cast on waterproof, dry sand, and saturated sand subbases and their temperature, moisture, and deformations were monitored from the end of finishing to 7 days. During this period they were exposed to periodic daily radiant surface heat that raised beam surface temperatures up to 130^{o}F. Beams were cured using clear membrane, clear membrane with dry burlap (burlap for insulation and heat retention), and no curing. All beams without exception exhibited a permanent upward curl almost from the moment of final set. At no time after the first 10 hours were any beams except for a few periods of maximum surface temperature under the burlap insulated beams warped concave downwards. A particularly significant observation was

> *Temperature gradients of 15^{o}F or more are established in the 8-inch slabs before final set takes place and produce a differential thermal volume change which occurs initially without appreciable stress because of the plasticity of the concrete in this interval... Thus an elastic structure is being established at a time when a considerable temperature difference exists between the top and bottom of the slab, and the concrete is becoming rigid with the top layer in an expanded condition. Any reduction in the temperature gradient from this time onwards tends to produce uplifting of the beam ends...while in general no significant moisture gradient exists up to the time when final set takes place, a temperature gradient very near the maximum has been built up in the interim.*

This work provides an explanation of observations of permanent, upward curl, particularly at early ages that is sometimes observed in the field and why the Aexpedient@ field solution of soaking a curled slab=s surface is usually unsuccessful. These results also suggest that a slab cast during a warm day will seldom be warped downwards due to this initial tendency for upward warping. This early age behavior is potentially very important but few experiments collect data at such an early age and this contribution to the curling problem is often overlooked.

Autogenous Volume Changes.

These volume changes are associated with cement hydration alone and are independent of environmental effects such as temperature or moisture. Initial expansions during the first several months are on the order of 30 x10^{-6} and ultimate shrinkage after several years usually does not exceed 100 x 10^{-6} in./in. [*146*]. The small magnitude of autogonenous shrinkage usually results in it being ignored in most practical purposes although there has been an increased interest in this topic by researchers as very low water-cement ratios where this phenomena can be significant [*147*].

Moisture Effects.

As moisture in the small capillary pores and adsorbed water is lost from concrete, it undergoes a reduction in volume. Plain, normal-weight concrete that is dried from a saturated condition to equilibrium with air at 50 percent relative humidity will undergo shrinkage on the order of 400 to 800 x 10^{-6} [*147*]. The magnitude of shrinkage is a function of numerous factors including cement composition, cement paste content and quality, aggregate properties, and admixture characteristics. A portion of this shrinkage is reversible and a portion is not [*148*]. After a few cycles of wetting and drying , the shrinkage becomes reversible but the original length before the first drying will never be reached [*147*].

Thermal Effects.

Concrete has a positive coefficient of thermal expansion and increases in volume upon heating. A coefficient of thermal expansion of 5.5 x $10^{-6}/^{o}$F is widely used although the actual value is a function of aggregate type, paste properties, moisture, and specific temperature regime [*149*]. For pavements, there are two thermal considerations. One is associated with seasonal variation in temperature which causes a lengthening of the slab in warm weather and contraction in cool weather that is resisted by friction on the underside of the slab. The second is the temperature gradient that develops between the surface and underlying portions of the slab from ambient environmental heating and cooling of the slab=s surface.

Carbonation Effects

Carbonation shrinkage occurs as a result of chemical reactions between carbon dioxide and cement hydration products to typically produce calcium carbonate and moisture with a resulting decrease in volume [*147*]. Carbonation normally proceeds slowly, and since it occurs simultaneously with drying shrinkage, it is difficult to separate the two effects. The sequence of drying and carbonation affects the total shrinkage markedly [*148*]. Simultaneous drying and carbonation shrinkage produces lower total shrinkage compared with drying followed by carbonation while alternate wetting and drying of concrete in air containing carbon dioxide causes carbonation shrinkage to become increasingly pronounced [*150*].

Summary

Pavement slabs in the field are exposed to a number of adverse volume changes that can generate internal stresses or physical curling of the slab edges and corners. This in turn can lead to cracking in the center of the pavement slabs and corner breaks. If curling stresses are to be analyzed the following sources of curling should be evaluated

(1) Early-age curling from adverse thermal gradients at the time of setting. This is a permanent curl occurring soon after placement and tending to curl the pavement upwards.

(2) Drying shrinkage that begins at the cessation of curing and approaches some asymptotic value dependent on local climatic conditions. Part of this shrinkage is irreversible. Modern concrete mixtures are using ever larger volumes and types of admixtures that often increase shrinkage. Hence current mixture practices may adversely influence curling in the field, but this topic has received little attention to date. Pavement slabs tend to dry readily from the surface and remain moist on the underside so the general trend will be upward curling.

(3) Cyclic temperature and moisture gradients from varying environmental conditions. These fluctuating gradients are caused by moment to moment variations in environmental heating and cooling of the slab that occurs on an hourly and seasonal basis and periodic wetting

followed by drying from rains, snow melt and other environmental sources of moisture. These may cause upward or downward curling of the slab and are superimposed on the previous curling sources.

(4) Autogenous shrinkage is small and can probably be neglected except perhaps for some of the lowest water-cement ratio mixes that are placed using heavy dosages of modern water-reducing admixtures. This source of shrinkage encourages upward curling because of base frictional restraint.

(5) Carbonation shrinkage will probably be a factor only to the degree that it influences drying shrinkage and its effects are probably best lumped in with that source of shrinkage as it is difficult to separate the effects in the field. This effect promotes upward curl.

The aggregate effect of these sources of curling is a general tendency for upward curling, but hot or wet surface concrete relative to conditions at the bottom of the slab could overcome these other effects.

Implications for Design and Analysis of Pavements

Professor Harold Westergaard is generally recognized as the pioneering theoretician who provided the beginnings of a sound analytical basis for analysis of rigid pavements. His work in the 1920's and much of the subsequent work by him and others in the rigid pavement field has been based on the following assumptions:

(1) infinite slab size or free edge with infinite slab in the remaining directions.

(2) full contact between slab and subgrade

(3) dense liquid subgrade (representation of subgrade and base with an equivalent spring constant or modulus of subgrade reaction

(4) linear elasticity

(5) medium thick plate theory (no compressibility within the plate)

The previous discussion of mechanisms and sources of curling pavement slabs illustrates that significant stresses can be induced in the pavement slab by non-load related phenomena, and potential curling challenges the second assumption above directly.

Immediately after formulating his first theoretical solution for calculating load induced stresses in an infinite plate on a Winkler foundation [*151*], Westergaard [*152*] developed additional solutions to consider stresses in the plate from thermal gradients. This work was based on assuming:

(1) infinite slab self-weight (which again assures full slab and subgrade contact).

(2) applicability of the principle of superposition for the combined effect of load and thermal stresses

(3) linear temperature variation through the slab depth

(4) night-time slab condition is the mirror image of the day-time condition

These solutions were adapted by Bradbury [*153*] and continue to be quoted in well-respected texts such as Yoder and Witczak [*37*] and Huang [*154*].

Much of the technical literature on rigid pavements published in the last 75 years is centered on the adequacy, effect, and need for the fundamental assumptions set forth in these two pioneering papers by Westergaard ([*151*] and [*152*]) and continue to have a profound influence on the profession.

The assumptions of full contact between the slab and subgrade and infinite slab can be avoided today with the more powerful analytical tools available through finite element analysis ([*155*], [*156*], [*157*], [*158*], [*159*], [*160*]). Similarly the assumption of linear thermal gradients

has been largely replaced with nonlinear thermal gradients (e.g., [*161*], [*162*]). Ioannides [*162*] has applied the technique of artificial neural networks to the curling problem with some success.

The assumption of simple linear superposition of thermal and load stresses .has also been reexamined by researchers ([*163*], [*164*], [*165*], [*166*]), but no consensus on an alternative has evolved. Other researchers ([*167*], [*168*]) have questioned the fundamental concept of linear superposition for this application. Concrete has an essentially linear fatigue relationship between the ratio of stress to strength and the log of cycles as a function of minimum to maximum stress ratio ([*169*], [*170*]). This stress ratio is the maximum stress to which a specimen is loaded during a fatigue test divided by the stress which is left loaded on the specimen when the maximum load is removed. Most laboratory beam tests, which have been used by many for the basis of rigid pavement design, were run at a ratio of 0.10 to 0.15. Other investigators have included higher ratios (bridges, for example where there are large dead loads), and as this ratio increases the number of cycles to failure increases for any given strength to stress ratio [*169*]. According to a reanalysis of the AASHO Road Test data by Domenichini and Marchionna [*167*], the minimum to maximum stress ratio during the test varied from 0.16 to 0.6 depending on the season and time of day. Minimum or at rest stress was calculated as stresses from thermal gradients and maximum stress was the load plus these thermal stresses. Hence, there is an interesting argument that the effect of thermal and other curling related stresses is to establish an at-rest state of stress which determines the flexural fatigue relationship for the concrete under traffic load.

Today's analytical tools provide powerful methods of calculating the effects of curling and calculating the contributions of thermal gradients in the pavement. Contributions of other sources of curling besides the thermal gradient remain largely ignored and unanalyzed. The technical literature is replete with examples that curling is a real phenomena in the field (e.g., [*171*], [*143*]), but the crucial connection between theoretical calculations and field performance remains undone so that curling analysis techniques still have little impact on design practice [*172*]. The prevalent practice is to limit slab sizes as a function of thickness to try to keep curling stresses to levels where they have not historically caused problems. The following observation by Yoder and Witczak [*37*] remains as valid concerning current practice as it was a quarter century ago:

> *It is important to note that warping stresses are not considered when determining thickness of pavement. The philosophy that governs the design, simply stated, is AJoints and steel are used to relieve and/or take care of warping stresses, and the design, then, is based upon load alone when considering thickness.@*

However, the research community is taking up the issue with more intensity and study, and a few consultants are beginning to include some curling calculations in their design work. At present, the approaches are simplistic and usually only explicitly consider cyclic thermal gradients. Much more work is needed to quantify the contributions from other sources of curling behavior, determine state-of-stress conditions within the pavements from these influences, and determine how these various curling mechanisms effect the pavement's field performance under load.

REFERENCES

1. AASHTO. AASHTO Guide for the Design of Pavement Structures. 403. 1993. Washington, D.C., American Association of State Highway Officials.
2. R. L. Baus and J. A. Fogg, AASHTO Flexible Pavement Design Equation Study. Journal of Transportation Engineering 115, 559-564 (1989).

3. AASHTO. AASHTO Interim Method of Test for Resilient Modulus of Unbound Granular Base/Subbase Materials and Subgrade Soils - SHRP Protocol P46. 1182. 1992. Washington, D.C., American Association of State Highway Officials.
4. M. R. Thompson and R. P. Elliot, ILLI-PAVE - Based Response Algorithms for Design of Conventional Flexible Pavements. Transportation Research Record 1043 50-57 (1985).
5. R. P. Elliot and S. I. Thornton, Resilient Modulus and AASHTO Pavement Design. Transportation Research Record 1196 (1988).
6. C. L. Monismith, Analytically-Based Asphalt Pavement Design and Rehabilitation-Theory to Practice (1962-1992), TRB Distinguished Lecture. Transportation Research Record 1354 5-25 (1992).
7. G. L. Guymon, Unsaturated Zone Hydrology, pp. 210-210, PTR PRENTICE HALL, Englewood Cliffs, New Jersey 1994.
8. R. L. Lytton, D. E. Pufahl, C. H. Michalak, H. S. Liang and B. J. Dempsey. An Integrated Model of the Climatic Effects on Pavements. FHWA-RD-90-033. 1990.
9. G. Larson and B. J. Dempsey. Enhanced Integrated Climatic Model Version 2.0. Contract DTFA MN/DOT 72114. 1997.
10. B. Birgisson, J. Ovik and D. E. Newcomb. Analytical Predictions of Seasonal Variations in Flexible Pavements at the Mn/Road Site. 2000. Washington, D. C. the 79th Annual Meeting in January 2000 of the Transportation Research Board.
11. H. S. Liang and R. L. Lytton, Rainfall Estimation for Pavement Analysis and Design. Transportation Research Record 1252 42-49 (1989).
12. S. J. Liu and R. L. Lytton. Environmental Effects on Pavement-Drainage. FHWA-DTFH-61-87-C-00057. 1985. Washington, D.C., Federal Highway Administration.
13. G. L. Guymon, R. L. Berg and T. C. Johnston. Mathematical Model of Frost Heave and Thaw Settlement in Pavements. 1986. U.S. Army Cold Regions Research and Engineering Laboratory.
14. B. J. Dempsey, W. A. Herlach and A. J. Patel. The Climatic-Material-Structural Pavement Analysis Program. FHWA/RD-84/115. 1985. Washington, D. C., Federal Highway Administration.
15. D. Croney, J. P. Coleman and W. P. Black. Movement and Distribution of Water in Soil in Relation to Highway Design and Performance. 40, 226-252. 1958. Highway Research Board.
16. D. J. Janssen and B. J. Dempsey, Soil-Moisture Properties of Subgrade Soils. Transportation Research Record 790 61-67 (1981).
17. D. G. Fredlund and A. Xing, Equations for the Soil-Water Characteristic Curve. Canadian Geotechnical Journal 31, 521-532 (1994).
18. D. G. Fredlund and H. Rahardjo, Soil Mechanics for Unsaturated Soils, John Wiley & Sons, Inc., 1993.
19. T. B. Edil and S. E. Motan, Soil-Water Potential and Resilient Behavior of Subgrade Soils. Transportation Research Record 705 54-63 (1979).
20. E. S. Motan and T. B. Edil, Repetitive-Load Behavior of Unsaturated Soils. Transportation Research Record 872 41-48 (1982).
21. L. M. Arya and J. F. Paris, A Physicoempirical Model to Predict the Soil Moisture Characteristic from Particle-Size Distribution and Bulk Density Data. Soil Science Society of America Journal 45, 1023-1030 (1981).

22. B. Aberg, Void Size in Granular Soils. Journal of Geotechnical Engineering 112, 236-239 (1996).
23. M. D. Fredlund, D. G. Fredlund and G. W. Wilson. Prediction of the Soil-Water Characteristic Curve from Grain-Size Distribution and Volume-Mass Properties. 1997. Rio de Janeiro, Brazil. Third Brazilian Symposium on Unsaturated Soils.
24. B. Aberg, Void Ratio of Noncohesive Soils and Similar Materials. Journal of Geotechnical Engineering 118, 1315-1334 (1992).
25. M. D. Fredlund, W. S. Sillers, D. G. Fredlund and G. W. Wilson. Design of a knowledge-based system for unsaturated soil properties. 659-677. 1996. Third Canadian Conference on Computing in Civil and Building Engineering.
26. W. E. I. Khogali and K. O. Anderson, Evaluation of Seasonal Variability in Cohesive Subgrades Using Backcalculation. Transportation Research Record 1546 140-150 (1996).
27. K. Musiake, Y. Oka and M. Koike, Unsaturated Zone Soil Moisture Behavior Under Temperate Humid Conditions -- Tensiometric Observations and Numerical Simulations. Journal of Hydrology 179-200 (1988).
28. C. G. Gurr, T. J. Marshall and J. T. Hutton, Movement of Water in Soil due to a Temperature Gradient. Soil Science 74, (1952).
29. K. Russam, Subgrade Moisture Studies by the British Road Research Laboratory. Highway Research Record 301 5-17 (1970).
30. Z. G. Ter-Martirosyan, I. I. Demin and E. A. Demina, Effect of Surface Shielding on Modification of Moisture Regime and Displacements of Swelling Soil. Soil Mechanics and Foundation Engineering 23, 158-161 (1986).
31. M. A. B. A. Rahim and M. Picornell. Moisture Movement Under the Pavement Structure. Research Report 1165-1, Research Study 10-8-88-1165. 1989. The Texas State Department of Highways and Public Transportation with The U.S. Department of Transportation Federal Highway Administration, Center for Geotechnical & Highway Materials Research. 1989.
32. C. van Gurp. Effect of Temperature Gradients and Season on Deflection Data. 1, 199-214. 1994. Minneapolis, Minnesota. The 4th International Conference on the Bearing Capacity of Roads and Airfields.
33. R. K. Linsley, J. B. Franzini, D. L. Freyberg and G. Tchobanoglous, Water-Resources Engineering, McGraw-Hill, Inc., 1992.
34. T. A. Haliburton, Highway Designs to Resist Subgrade Moisture Variations. Highway Research Record No 360 45-56 (1971).
35. N. K. Vaswani, Case Studies of Variations in Subgrade Moisture and Temperature under Road Pavements in Virginia. Transportation Research Record 532 30-42 (1975).
36. J. H. Maree, N. J. W. Van Zyl and C. R. Freeme, Effective Moduli and Stress Dependence of Pavement Materials as Measured in Some Heavy-Vehicle Simulator Tests. Transportation Research Record 852 52-60 (1982).
37. E. J. Yoder and M. W. Witczak, Principles of Pavement Design, pp. 736-736, John Wiley & Sons, 1975.
38. N. R. Rainwater, R. E. Yoder, E. C. Drumm and G. V. Wilson, Comprehensive Monitoring Systems for Measuring Subgrade Moisture Conditions. Journal of Transportation Engineering 125, 439-448 (1999).
39. J. W. Guinnee. Field Studies on Subgrade Moisture Conditions. 40, 253-267. 1958. Highway Research Board.

40. G. Cumberledge, G. L. Hoffman, A. C. Bhajandas and R. J. Cominsky, Moisture Variation in Highway Subgrades and the Associated Change in Surface Deflections. Transportation Research Record 497 40-49 (1974).
41. S. F. Valdez. Subgrade Resilient Modulus Evaluation. FHWA-GA-91-8801. 1991.
42. M. Hossain, S. J. Kotdwala, B. Long and A. J. Gisi. Subgrade Moisture Monitoring Using Time Domain Reflectometry. [Paper No. 970370]. 1997. Washington, D.C. Transportation Research Board 76th Annual Meeting.
43. B. D. Marks and A. Haliburton, Subgrade Moisture Variations Studied with Nuclear Depth Gages. Highway Research Record 276 14-24 (1969).
44. D. K. Hall and S. Rao, Predicting Subgrade Moisture Content for Low-Volume Pavement Design Using In Situ Moisture Content Data. Transportation Research Record 1652 98-107 (1999).
45. S. S. Bandyopadhyay and J. A. Frantzen, Investigation of Moisture-Induced Variation in Subgrade Modulus By Cross-Correlation Method. Transportation Research Record 945 10-15 (1983).
46. R. P. Elliott and M. R. Thompson, ILLI-PAVE Mechanistic Analysis of AASHO Road Test Flexible Pavements. Transportation Research Record 1043 39-49 (1985).
47. H. C. S. Thom, Quantitative Evaluation of climatic Factors in Relation to Soil Moisture Regime. Highway Research Record 301 1-4 (1970).
48. R. F. Hinshaw and J. L. Northrup, Predicting Subgrade Moisture Under Aggregate Surfacing. Transportation Research Record 1291 193-203 (1991).
49. M. R. Thompson and Q. L. Robnett, Resilient Properties of Subgrade Soils. Journal of Transportation Engineering 105, 71-89 (1979).
50. J. Moossazadeh and M. W. Witczak, Prediction of Subgrade Moduli for Soil that Exhibits Nonlinear Behavior. Transportation Research Record No 810 9-17 (1981).
51. D. G. Fredlund, A. T. Bergan and P. K. Wong, Relation Between Resilient Modulus and Stress Conditions for Cohesive Subgrade Soils. Transportation Research Record 642 73-81 (1977).
52. E. C. Drumm, Y. Boateng-Poku and T. Johnson Pierce, Estimation of Subgrade Resilient Modulus from Standard Tests. Journal of the Geotechnical Engineering Division 116, 774-789 (1990).
53. B. Shackel. The Derivation of Complex Stress-strain Relations. 353-359. 1973. Moscow. 8th Int. Conf. on Soil Mech. and Found. Engng.
54. W. Y. Y. Gehling, J. A. Ceratti, W. P. Nunez and M. R. Rodrigues. A Study of the Influence of Suction on the Resilient Behaviour of soils from Southern Brazil. 1, 47-53. 1998. Beijiing, China. Second International Conference on Unsaturated Soils.
55. W. Phillip and D. A. Cameron. The influence of soil suction on the resilient modulus of expansive soil subgrades. Unsaturated Soil . 1995.
56. R. G. Hicks and C. L. Monismith, Factors Influencing the Resilient Response of granular Materials. Highway Research Record 345 15-13 (1971).
57. S. F. Brown and J. W. Pappin, Analysis of Pavements with Granular Bases. Transportation Research Record 810 17-23 (1981).
58. Nataatmadja and A. K. Parkin, Characterization of Granular Materials for Pavements. Canadian Geotechnical Journal 26, 725-730 (1989).
59. L. Raad, G. H. Minassian and S. Gartin, Characterization of Saturated Granular Base Under Repeated Loads. Transportation Research Record 1369 (1992).

60. J. W. Pappin, S. F. Brown and M. P. O'Reilly, Effective Stress Behaviour of Saturated and Partially Saturated Granular Material Subjected to Repeated Loading. Geotechnique 42, 485-497 (1992).
61. G. Heydinger, Q. Xie, B. W. Randolph and J. D. Gupta, Analysis of Resilient Moulus of Dense- and Open-Graded Aggregates. Transportation Research Record 1547 (1996).
62. N. H. Thom and S. F. Brown, Effect of Moisture on the Structural Performance of a Crushed-Limestone Road Base. Transportation Research Record 1121 (1987).
63. J. Uzan, Resilient Characterization of Pavement Materials. International Journal for Numerical and Analytical Methods in Geomechanics 16, 453-459 (1992).
64. D. Chandra, K. M. Chua and R. L. Lytton, Effects of Temperature and Moisture on the Load Response of Granular Base Course Material in Thin Pavements. Transportation Research Record 1252 33-41 (1989).
65. M. S. Jin, K. W. Lee and W. D. Kovacs, Seasonal Variation of Resilient Modulus of Subgrade Soils. Journal of Transportation Engineering 120, 603-616 (1994).
66. M. R. Thompson and Q. L. Robnett. Resilient Properties of Subgrade Soils. 1976. University of Illinois, Urbana-Champaign. Civil Engineering Studies Transportation Engineering Ser. No. 14, Illinois Cooperative Highway and Transportation Ser. No. 160.
67. M. P. Jones and M. W. Witczak, Subgrade Modulus on the San Diego Test Road. Transportation Research Record 641 1-6 (1977).
68. T. Visser, Queiroz C. and W. R. Hudson, Study of Resilient Characteristics of Tropical Soils for Use in Low-Volume Pavement Design. Transportation Research Record 898 133-140 (1983).
69. R. F. Carmichael III and E. Stuart, Predicting Resilient Modulus: A Study to Determine the Mechanical Properties of Subgrade Soils. Transportation Research Record 1043 145-148 (1985).
70. M. Killingsworth, J. F. Daleiden, A. L. Simpson and R. Zamora, Analysis of Procedures for Establishing In-situ Subgrade Moduli. Transportation Research Record 1462 (1994).
71. J. Hudson, E. C. Drumm and M. Madgett. Design Handbook for the Estimation of Resilient Response of Fine-grained Subgrades. 917-931. 1994. Minneapolis. 4th International Conference on the Bearing Capacity of Roads and Airfields.
72. R. Pezo and W. R. Hudson, Prediction Models of Resilient Modulus for Nongranular Materials. Geotechnical Testing Journal 17, 349-355 (1994).
73. E. C. Drumm, J. S. Reeves, M. R. Madgett and W. D. Trolinger, Subgrade Resilient Modulus Correction for Saturation Effects. Journal of Geotechnical Engineering 123, 663-670 (1997).
74. W. Lee, N. Bohra, A. G. Altschaeffl and T. D. White, Resilient Modulus of Cohesive Soils. Journal of Geotechnical and Geoenvironmental Engineering 123, 131-136 (1997).
75. F. McCullough and A. Taute, Use of Deflection Measurements for Determining Pavement Material Properties. Transportation Research Record 852 (1982).
76. H. A. Ali and A. Lopez, Statistical Analysis of Temperature and Moisture Effects on Pavement Structural Properties Based on Seasonal Monitoring Data. Lopez, A 48-55 (1996).
77. N. S. Matter and O. T. Farouki. Detailed Study on the Climatic and Seasonal Variation Effects on Pavements in Northern Ireland. 1, 721-737. 1994. Minneapolis, Minnesota. The 4th International Conference on the Bearing Capacity of Roads and Airfields.

78. Long, M. Hossain and A. J. Gisi, Seasonal Variation of Backcalculated Subgrade Moduli. Transportation Research Record 1577 70-80 (1997).
79. J. W. Andrew, N. M. Jackson and E. C. Drumm. Measurement of Seasonal Variation in Subgrade Properties, Geotechnical Special Publication No. 85, Application of Geotechnical Principles in Pavement Engineering. 13-38. 1998. Boston, Massachusetts. Sessions of Geo-Congress 98. Papagiannakis, A. T. and Schwartz, C. W.
80. S. C. H. Cheung, M. N. Gray, R. N. Yong and A. M. O. Mohamed. The Effects of Moisture Content, Salinity and Temperature on the Load-Bearing Capacity of a Dense Clay-Based Backfill. 212, 491-498. 1991. Material Research Society Symposium.
81. G. Rada and M. W. Witczak, Comprehensive Evaluation of Laboratory Resilient Moduli Results for Granular Material. Transportation Research Record 810 (1981).
82. P. Tian, M. M. Zaman and J. G. Laguros, Gradation and Moisture Effects on Resilient Moduli of Aggregate Bases. Transportation Research Record 1619 75-84 (1998).
83. L. N. Mohammad, B. Huang, A. J. Puppala and A. Allen, Regression Model for Resilient Modulus of Subgrade Soils. Transportation Research Record 1687 47-54 (1999).
84. H. B. Seed, C. K. Chan and C. E. Lee. Resilient Characteristics of Subgrade Soils and Their Relation to Fatigue Failures in Asphalt Pavements. 611-636. 1962. Ann Arbor, Michigan, Univ. of Michigan. International Conference on the Structure Design of Asphalt Pavements.
85. S. Muhanna, M. S. Rahman and P. C. Lambe, Resilient Modulus Measurement of Fine-Grained Subgrade Soils. Transportation Research Record 1687 3-21 (1999).
86. M. K. Elfino and J. L. Davidson. Modeling Field Moisture in Resilient Moduli Testing, Resilient Moduli of Soils: Laboratory Conditions. ASCE Geotechnical Special Publication No.24 , 31-51. 1989.
87. Li and E. T. Selig, Resilient Modulus for Fine-Grained Subgrade Soils. Journal of Geotechnical Engineering 120, 939-957 (1994).
88. G. B. Thadkamalla and K. P. George, Characterization of Subgrade Soils at Simulated Field Moisture. Transportation Research Record 1481 (1995).
89. Y. Guan, E. C. Drumm and N. M. Jackson, Weighting Factors for Seasonal Subgrade Resilient Modulus. Transportation Research Record No 1619 94-100 (1998).
90. M. Gomez-Achezar and M. R. Thompson. Mechanistic Design Concepts for Full-Depth Asphalt Concrete Pavements. 41. 1984. Urbana-Champaign, University of Illinois. Civil Engineering Studies, Transportation Engineering Series.
91. C. Bhajandas, G. Cumberledge and G. L. Hoffman, Flexible Pavement Evaluation and Rehabilitation Transportation Engineering. Journal of ASCE 103, 75-85 (1977).
92. J. S. Uhlmeyer, J. P. Mahoney, G. Hanek, G. Wang, R. L. Copstead and D. J. Jassen. Estimation of Seasonal Effects for Pavement Design and Performance - Volume I. FHWA-FLP-95-006. 1995. San Dimas, California, USDA-Forest Service.
93. J. S. Uhlmeyer, J. P. Mahoney, G. Hanek, G. Wang, R. L. Copstead and D. J. Jassen. Estimation of Seasonal Effects for Pavement Design and Performance - Volume II. FHWA-FLP-95-007. 1995. San Dimas, California, USDA-Forest Service.
94. J. P. Mahoney, L. M. Pierce and R. L. Costead. Estimation of Seasonal Effects for Pavement Design and Performance - Volume III. FHWA-FLP-95-008. 1996. San Dimas, California, USDA-Forest Service.
95. H. Zhou and G. E. Elkins. Pavement Responses to Seasonal Variations. 1994. Minneapolis, Minnesota. The 4th International Conference on the Bearing Capacity of Roads and Airfields.

96. J. Ovik, B. Birgisson and D. E. Newcomb. Relating Climate Factors to Pavement Subsurface Conditions, In: Cold Regions Impact on Civil Works. 1998. Duluth, Minnesota. Ninth International Conference on Cold Regions Engineering.
97. G. Ya. Chernyak. Dielectric Methods for Investigating Moist Soils. 1967. Published for the U.S. Department of the Interior and the National Science Foundationby the Israel By Program for Scientific Translation.
98. R. L. Lytton, D.E.Pufahl, C.H.Michalak, H.S.Liang and B.J.Dempsey. An Integrated Model of the Climatic Effects on Pavements. FHWA-RD-90-033 . 1993.
99. Asphalt Institute. Research and Development of the Asphalt Institute's Thickness Design Manual (MS-1). 82-2. 1982.
100. P. Ullidtz. Pavement Analysis. 1987. Elsevier Science.
101. V. C. Janoo and R.L.Berg. Layer Moduli Determination during Freeze-Thaw Periods. 26-35. 1991. Nondestructive Deflection Testing and Backcalculation for Pavements, Proceedings, Transportation Research Record No. 1377, Transportation Research Board.
102. S. R. Bigl and R.L.Berg. Modeling Mn/Road Test Sections with the CRREL Mechanistic Pavement Design Procedure. CRREL Special Report 96-21. 1996. US Army Corps of Engineers. Cold Regions Research & Engineering Laboratory.
103. R. J. Schmidt, Use of ASTM Tests to Predict Low Temperature Stiffness of Asphalt Mixes. Transportation Research Record 544 35-45 (1975).
104. T. C. Johnson, R.L.Berg, E.J.Chamberlain and D.M.Cole. Frost Action Predictive Techniques for Roads and Airfields, A Comprehensive Survey of Research Findings. CRREL Report 86-18. 1986. US Army Corps of Engineers. Cold Regions Research & Engineering Laboratory.
105. V. C. Janoo, R. Eatan and L. Barna. Evaluation of Airport Subsurface Materials. CRREL Special Report 97-13. 1997. US Army Corps of Engineers, Cold Regions Research & Engineering Laboratory.
106. J. H. Haynes and E.J.Yoder, Effects of Repeated Loading on Gravel and Crushed Stone Base Material used in the AASHTO Road Test. Highway Research Board Record 39, 82-96 (1963).
107. O. O. Thompson. Evaluation of Flexible Pavement Behavior with emphasis on the Behavior of Granular Layers. 1969. University of Illinois.
108. Casagrande and W.L.Shannon. Base Course Drainage for Airport Pavements. 77, 1-23. 1951. American Society of Civil Engineers.
109. Janoo V.C. and K.Shepherd. Seasonal Variation of Moisture and Subsurface Layer Moduli. 2000. Washington D.C. 2000 Transportation Research Board Meeting.
110. V. C. Janoo and J.Bayer Jr. Effect of Angularity on the Resilient Modulus of Base Course Materials. 2000.
111. Simonsen E., V.Janoo and U.Isacsson. Resilient Properties of Unbound Road Materials during Seasonal Frost Condition. TRITA-IP FR 99-50. 1999. Royal Institute of Technology, Division of Highway Engineering. On Thaw Weakening of Pavement Structures.
112. Janoo V.C., J.Bayer Jr., G.Durell and C.Smith Jr. Resilient Modulus for New Hampshire Subgrade Soils for use in Mechanistic AASHTO Design. 99-14. 1999. US Army Corps of Engineers. Cold Regions Research & Engineering Laboratory.

113. L. Straub, H. N. Schenck, Jr. and F. E. Przybycien. Bituminous Pavement Temperature Related to Climate. Highway Research Record 256 , 53-77. 1968. Washington, D. C., HRB, National Research Council.
114. H. F. Southgate and R. C. Deen. Temperature Distribution Within Asphalt Pavements and Its Relationship to Pavement Deflection. Highway Research Record 291 , 116-131. 1969. Washington, D. C., HRB, National Research Council.
115. P. J. Bosscher, H. U. Bahia, S. Thomas and J. S. Russell. Relationship Between Pavement Temperature and Weather Data. Transportation Research Record 1609 , 1-11. 1998. Washington, D. C., TRB, National Research Council.
116. L. Shao, S. W. Park and Y. R. Kim. Simplified Procedure for Prediction of Asphalt Pavement Subsurface Temperature Based on Heat Transfer Theories. Transportation Research Record 1568, 114-123. 1997.
117. R. N. Stubstad, E. O. Lukanen, C. A. Richter and S. Baltzer. Calculation of AC Layer Temperatures From FWD Field Data. Fifth International Conference on the Bearing Capacity of Roads and Airfields , 919-928. 1998. Trondheim, Tapir Publishers.
118. M. Solaimanian and T. W. Kennedy. Predicting Maximum Pavement Surface Temperature Using Maximum Air Temperature and Hourly Solar Radiation. Transportation Research Record 1417 , 1-11. 1993. Washington, D. C., TRB, National Research Council.
119. Y. R. Kim, B. O. Hibbs and Y.-C. Lee. New Temperature Correction Procedure for FWD Deflections of Flexible Pavements. Proceedings, 4th International Conference on the Bearing Capacity of Roads and Airfields , 413-443. 1994.
120. F. Bissada and H. Guirguis. Temperature Dependency of Dynamic Deflection Measurements on Asphalt Pavements. Transportation Research Record 930 , 57-59. 1983. Washington, D. C., TRB, National Research Council.
121. O. Lukanen, R. Stubstad and R. C. Briggs. Temperature Predictions and Adjustment Factors for Asphalt Pavements. FHWA-RD-98-085. 2000. Federal Highway Administration.
122. R. N. Stubstad, S. Baltzer, E. O. Lukanen and H. J. Ertman-Larsen. Prediction of AC Mat Temperatures for Routine Load/Deflection Measurements. Proceedings, 4th International Conference on the Bearing Capacity of Roads and Airfields , 401-412. 1994.
123. H. Inge and Y. R. Kim. Prediction of Effective Asphalt Layer Temperature. Transportation Research Record 1473 , 93-100. 1999. Washington, D. C., TRB, National Research Council.
124. J. Ovik, B. Birgisson and D. E. Newcomb. Characterizing Seasonal Variations in Flexible Pavement Material Properties. Transportation Research Record 1684 , 1-7. 1999. Washington, D. C., TRB, National Research Council.
125. Mohseni. LTPP Seasonal Asphalt Concrete (AC) Pavement Temperature Models. FHWA-RD-97-103. 1998. Federal Highway Adminstration.
126. S. Baltzer and J. M. Jansen. Temperature Correction of Asphalt-Moduli for FWD-Measurements. Proceedings, 4th International Conference on the Bearing Capacity of Roads and Airfields , 754-768. 1994. Trondheim, Norway.
127. J. R. d. Almeida. Back-Calculation of Flexible Pavements with Consideration of Temperature Gradients. Fifth International Conference on the Bearing Capacity of Roads and Airfields , 487-496. 1998. Trondheim, Tapir Publishers.

128. H. A. Ali and N. A. Parker. Using Time Series to Incorporate Seasonal Variations in Pavement Design. Transportation Research Record 1539 , 33-43. 1996. Washington, D. C., TRB, National Research Council.
129. S. W. Lee, J. P. Mahoney and N. C. Jackson. Verification of Backcalculation of Pavement Moduli. Transportation Research Record 1196 , 85-95. 1988. Washington, D. C., TRB, National Research Council.
130. M. W. Witczak. Design of Full Depth Air Field Pavements. Proceedings, Third International Conference on the Structural Design of Asphalt Pavements . 1972.
131. M. Johnson and R. L. Baus. Alternative Method for Temperature Correction of Backcalculated Equivalent Pavement Moduli. Transportation Research Record 1355 , 75-81. 1992. Washington, D. C., TRB, National Research Council.
132. Y. R. Kim, B. O. Hibbs and Y.-C. Lee. Temperature Correction of Deflections and Backcalculated Asphalt Concrete Moduli. Transportation Research Record 1473 , 55-62. 1995. Washington, D. C., TRB, National Research Council.
133. D.-H. Chen, H.-H. Lin, J. Bilyeu and M. Murphy. Temperature Correction on FWD Measurements. TRB Pre-Print. Transportation Research Board 79th Annual Meeting . 2000.
134. K. Badu-Tweneboah, M. Tia and B. E. Ruth. Procedures for Estimation of Asphalt Concrete Pavement Moduli at In Situ Temperatures. Transportation Research Record 1121 , 1-6. 1987. Washington, D. C., TRB, National Research Council.
135. S. W. Park and Y. R. Kim. Temperature Correction of Backcalculated Moduli and Deflections Using Linear Viscoelasticity and Time-Temperature Superposition. Transportation Research Record 1570 , 108-117. 1997. Washington, D. C., TRB, National Research Council.
136. American Concrete Institute. Cement and Concrete Terminology. ACI Committee Report 2116R-90. 2000. Detroit, Michigan. Manual of Concrete Practice.
137. Significance of Tests and Properties of Concrete and Concrete-Making Materials, STP 169C, American Society of Testing and Materials, Philadelphia, Pennsylvania 1994.
138. M. P. Rollings and R.S.Rollings, Geotechnical Materials in Construction, McGraw Hill, New York, New York 1996.
139. R. Schwartz, D-Cracking of Concrete Pavements. Transportation Research Record 134 (1987).
140. American Concrete Institute. Prediction of Creep, Shrinkage, and Temperature Effects in Concrete Structures. ACI Committee Report 209R-92. 2000. Detroit, Michigan. Manual of Concrete Practice.
141. L. Miller, Warping of Reinforced Concrete Due to Shrinkage. American Concrete Institute 54, (1958).
142. R. S. Rollings. Field Performance of Fiber-Reinforced Concrete Airfield Pavements. 1986. Washington D.C., Federal Aviation Administration.
143. R. S. Rollings, Curling Failures of Steel Fiber Reinforced Concrete Slabs. Journal of Performance of Constructed Facilities 7, (1993).
144. American Concrete Institute. Effect of Restraint, Volume Change, and Reinforcement on Cracking of Mass Concrete. ACI Committee Report 207.2R-95. 2000. Detroit, Michigan. Manual of Concrete Practice.

145. C. Rhodes. An Appraisal of the Membrane Method of Curing Concrete Pavements. 1949. Lansing, Michigan, Michigan State Highway Department. Engineering Experiment Station Bulletin 108.
146. W. Washa, Volume Changes, Significance of Tests and Properties of Concrete and Concrete-Making Materials, STP 169B, American Society of Testing and Materials, Philadelphia, Pennsylvania 1966.
147. P. K. Mehta, Volume Change, Significance of Tests and Properties of Concrete and Concrete-Making Materials, STP 169C, American Society of Testing and Materials, Philadelphia, Pennsylvania 1994.
148. M. Neville, Properties of Concrete, Pitman Books Limited, London, United Kingdom 1981.
149. J. M. Scanlon, Thermal Properties. In Significance of Tests and Properties of Concrete and Concrete-Making Materials, STP 169C. (Ed. P. Klieger and J. Lamond) ASTM, Philadelphia, PA, 1994.
150. J. Verbeck, Carbonation of Hydrated Portland Cement Concrete, STP 205, American Society of Testing and Materials, Philadelphia, Pennsylvania 1958.
151. M. Westergaard, Stresses in Concrete Pavements Computed by Theoretical Analysis. Public Roads 7, (1926).
152. M. Westergaard. Analysis of Stresses in Concrete Pavements Due to Variations of Temperature. Highway Research Board. 6. 1927. Washington, D.C.
153. R. D. Bradbury. Reinforced Concrete Pavements. 1938. Washington, D.C., Wire Reinforcement Institute.
154. Y. H. Huang, Pavement Analysis and Design, Prentice-Hall, Englewood Cliffs, New Jersey 1993.
155. Y. H. Huang and S.T.Wang, Finite Element Analysis of Rigid Pavements with Partial Subgrade Support. Transportation Research Record 671 (1974).
156. M. Tabatabie and E.J.Barenberg, Finite Element Analysis of Jointed or Cracked Concrete Pavements. Transportation Research Record 671 (1978).
157. M. Ioannides. Analysis of Slabs-on-grade for a Variety of Loading and Support Conditions. 1984. University of Illinois.
158. G. T. Korovesis. Analysis of Slab-on-Grade Pavement Systems Subjected to Wheel and Temperature Loadings. 1990. University of Illinois.
159. M. I. Hammons and A.M.Ioannides. Developments in Rigid Pavement Response Modeling. TR GL 96-15. 1996. Vicksburg, Mississippi, USAE Waterways Experiment Station.
160. M. I. Hammons. Development of an Analysis System for Discontinuities in Rigid Airfield Pavements. [TR GL 97-3]. 1997. Vicksburg, Mississippi, USAE Waterways Experiment Station.
161. Choubane and M.Tia., Nonlinear Temperature Gradient Effect on Maximum Warping Stresses in Rigid Pavements. Transportation Research Record 1370 (1992).
162. M. Ioannides and L.Khazanovich, Nonlinear Temperature effects on Multilayered Concrete Pavements. Journal of Transportation Engineering 124, (1998).
163. M. I. Darter. Design of Zero-Maintenance Plain Jointed Concrete Pavement. FHWA-RD-77-111. 1977. Washington, D.C., Federal Highway Administration.
164. M. Ioannides and G. T. Korovesis. Discussion of "Effect of Concrete Overlay Debonding on Pavement Performance," by van Dam, T., Blackmon, E., and Shahin, M. Y. Transportation Research Record 1136. 1987.

165. M. Ioannides and R.A.Salsilli-Murua, Temperature Curling in Rigid Pavements: An Application of Dimensionless Analysis. Transportation Research Record 1227 (1989).
166. M. Ioannides. Curling Analysis, Change and Continuity. 1998. Bussaço Portugal. 4th International Workshop on Design Theories and Their Verification of Concrete Slabs for Pavements and railroads.
167. Domenichini and A.Marchionna. Influence of Stress Range on Plain Concrete Pavement Fatigue Design. 1981. West Lafayette, Indiana. 2nd International Conference on Concrete Pavements, Purdue University.
168. R. S. Rollings. Developments in the Corps of Engineers Rigid Airfield Design Procedures. 1989. West Lafayette, Indiana, Purdue University. 4th International Conference on Concrete Pavements.
169. American Concrete Institute. Considerations for Design of Structures Subjected to fatigue Loading. ACI Committee Report 215-74. 2000. Detroit, Michigan. Manual of Concrete Practice.
170. R. S. Rollings. Evolution of the Military's Concrete Airfield Pavement Design Procedures. 1998. Bussaço Portugal. 4th International Workshop on Design Theories and Their Verification of Concrete Slabs for Pavements and railroads.
171. R. Byrum. Analysis of LTPP JCP Slab Curvatures Using High Speed Profiles. presented at the annual meeting, Transportation Research Board . 2000. Washington, D.C.
172. R. S. Rollings and D.P.Pittman, Field Instrumentation and Performance Monitoring of Rigid Pavements. Journal of Transportation Engineering 118, (1992).

APPENDIX B

TEMPERATURE, MOISTURE, AND FREEZE STATE PLOTS

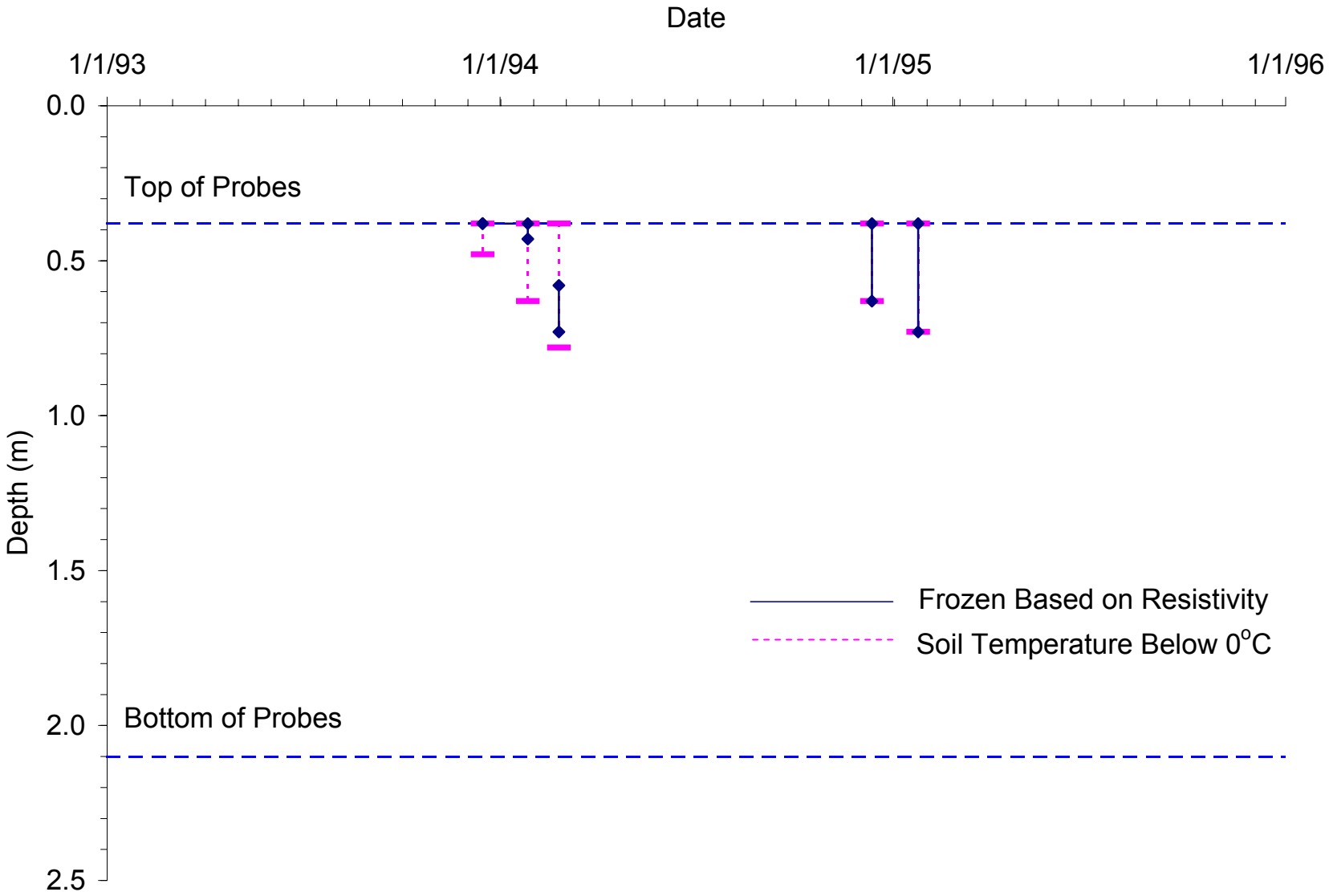

Figure B-1. Freeze State Based on Soil Resistivity and Soil Temperature at Site 16-1010

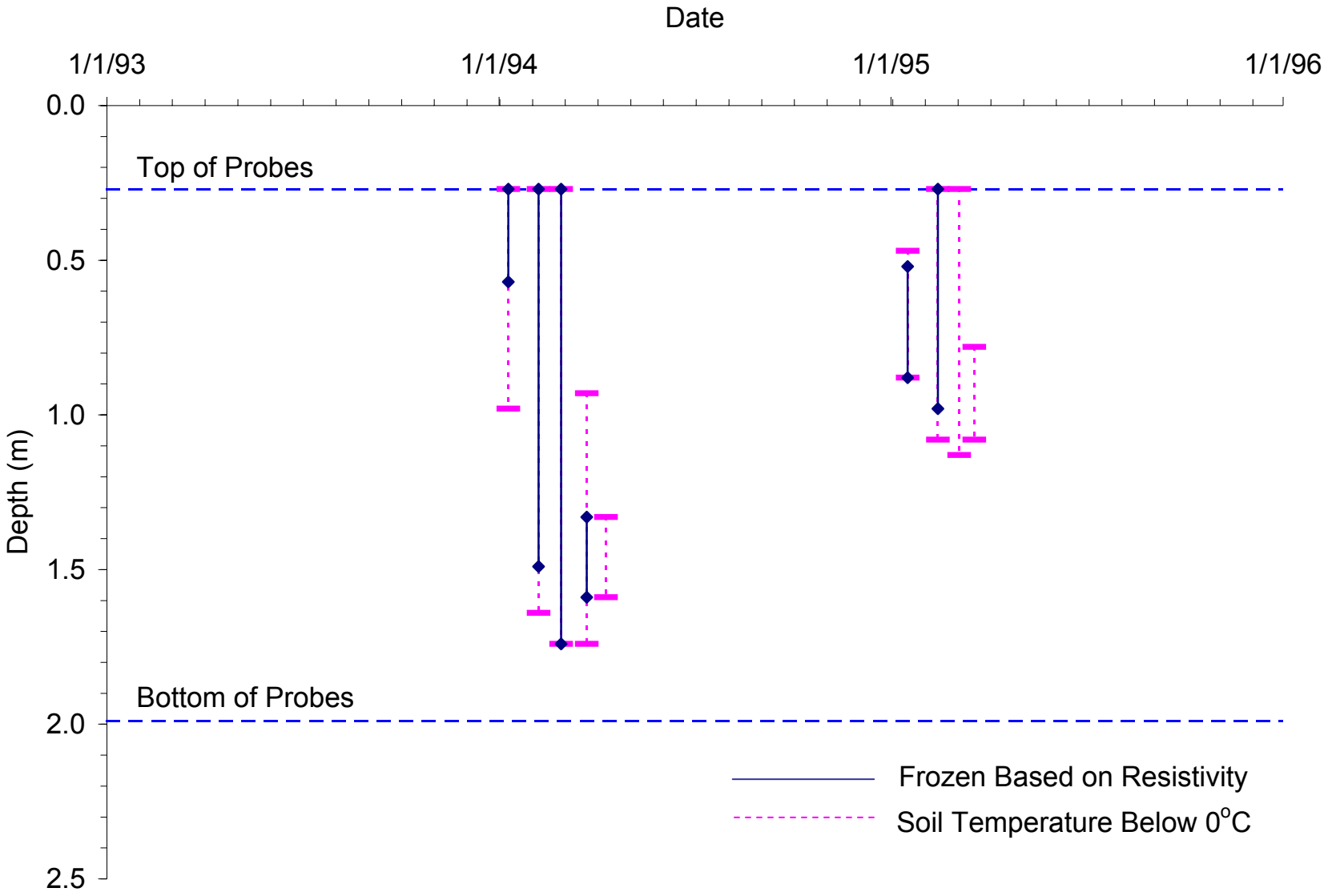

Figure B-2. Freeze State Based on Soil Resistivity and Soil Temperature at Site 23-1026

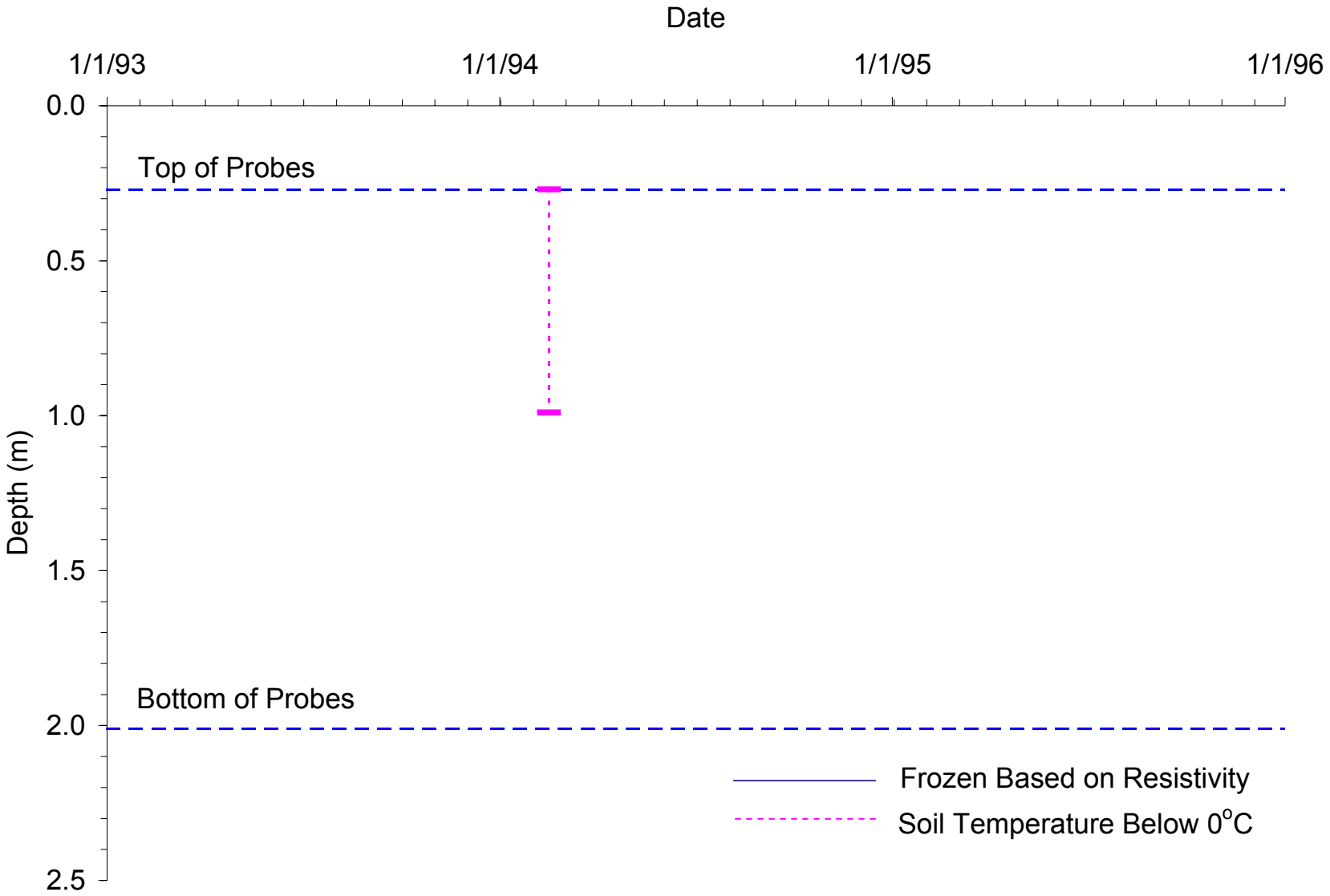

Figure B-3. Freeze State Based on Soil Resistivity and Soil Temperature at Site 25-1002

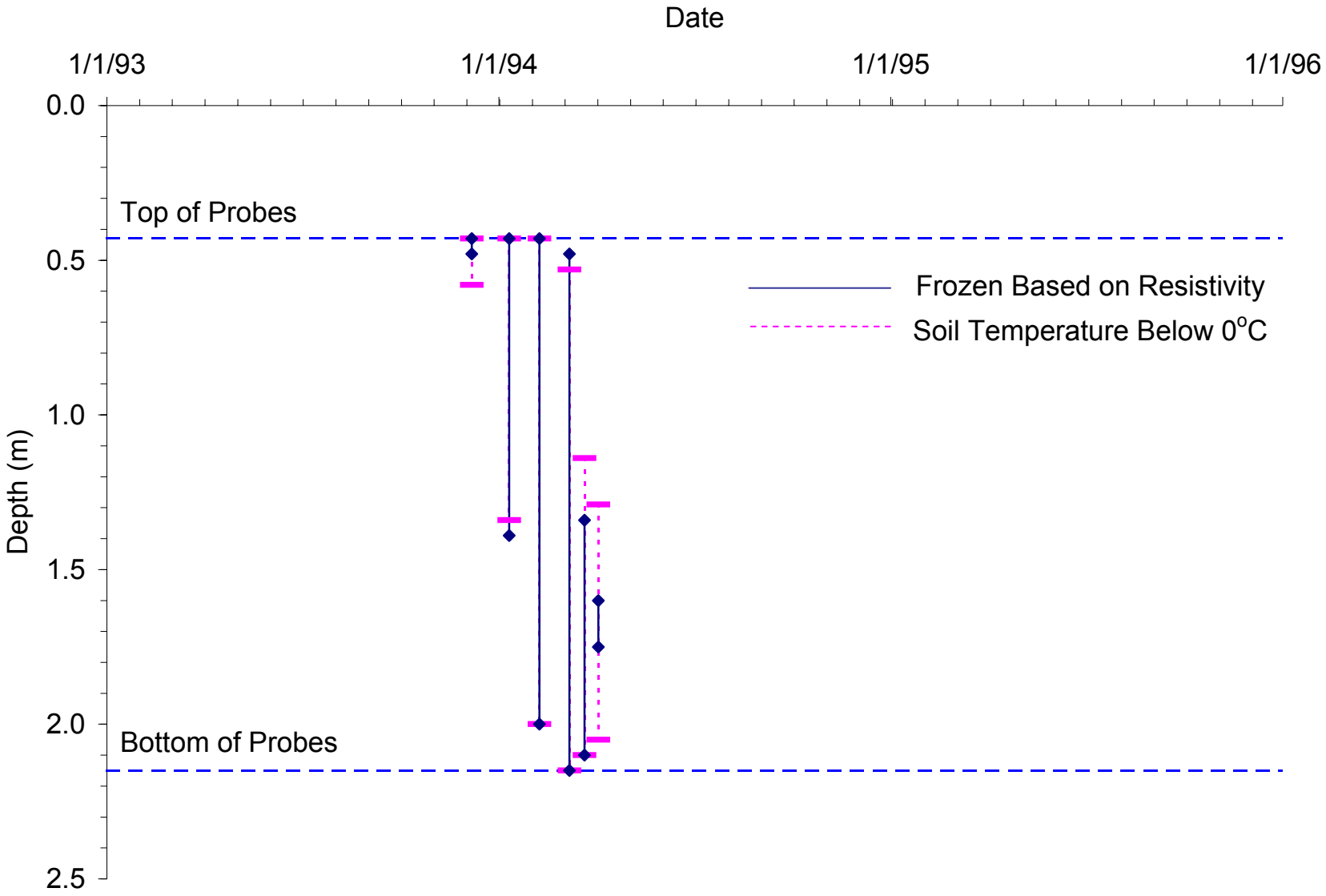

Figure B-4. Freeze State Based on Soil Resistivity and Soil Temperature at Site 27-1018

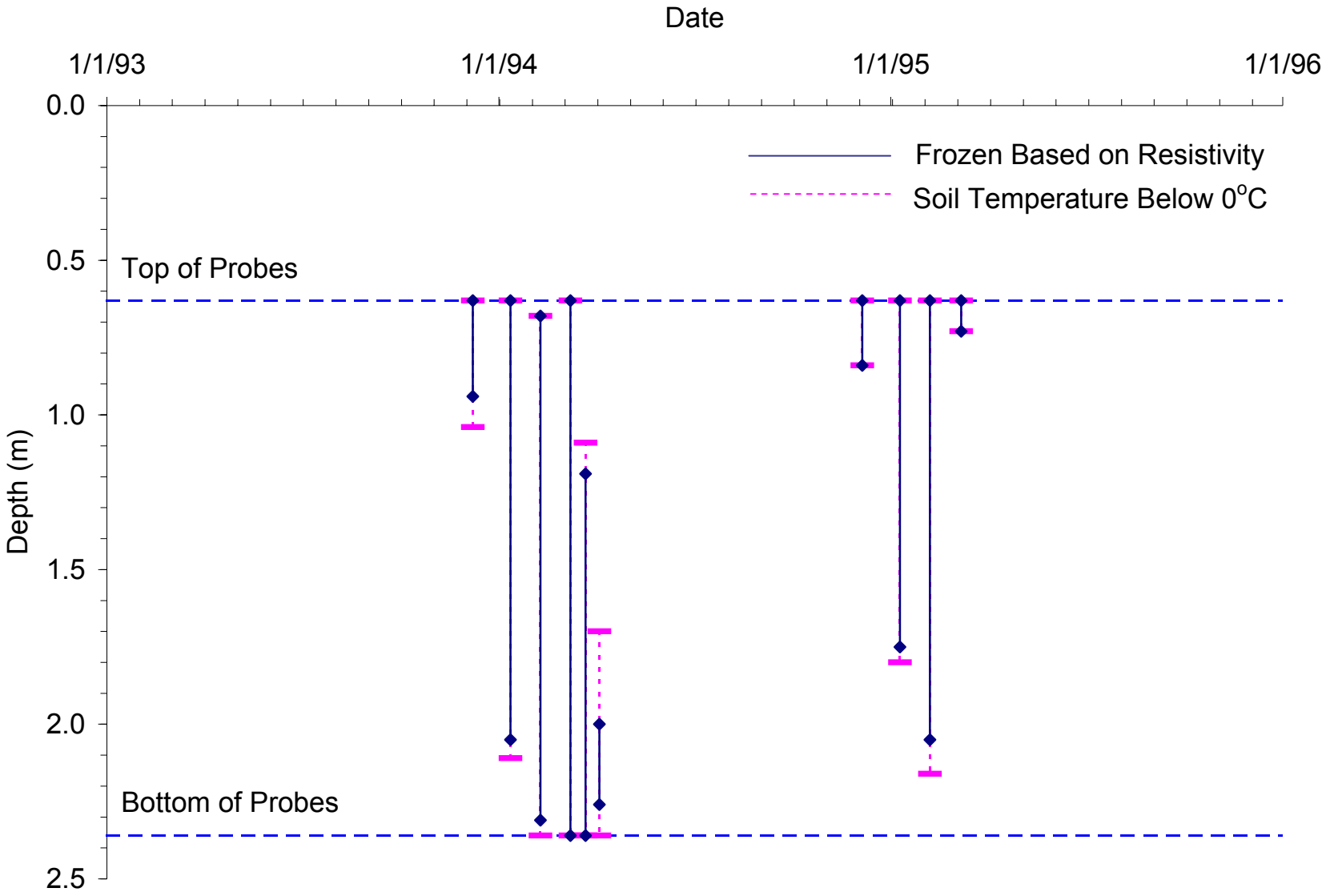

Figure B-5. Freeze State Based on Soil Resistivity and Soil Temperature at Site 27-1028

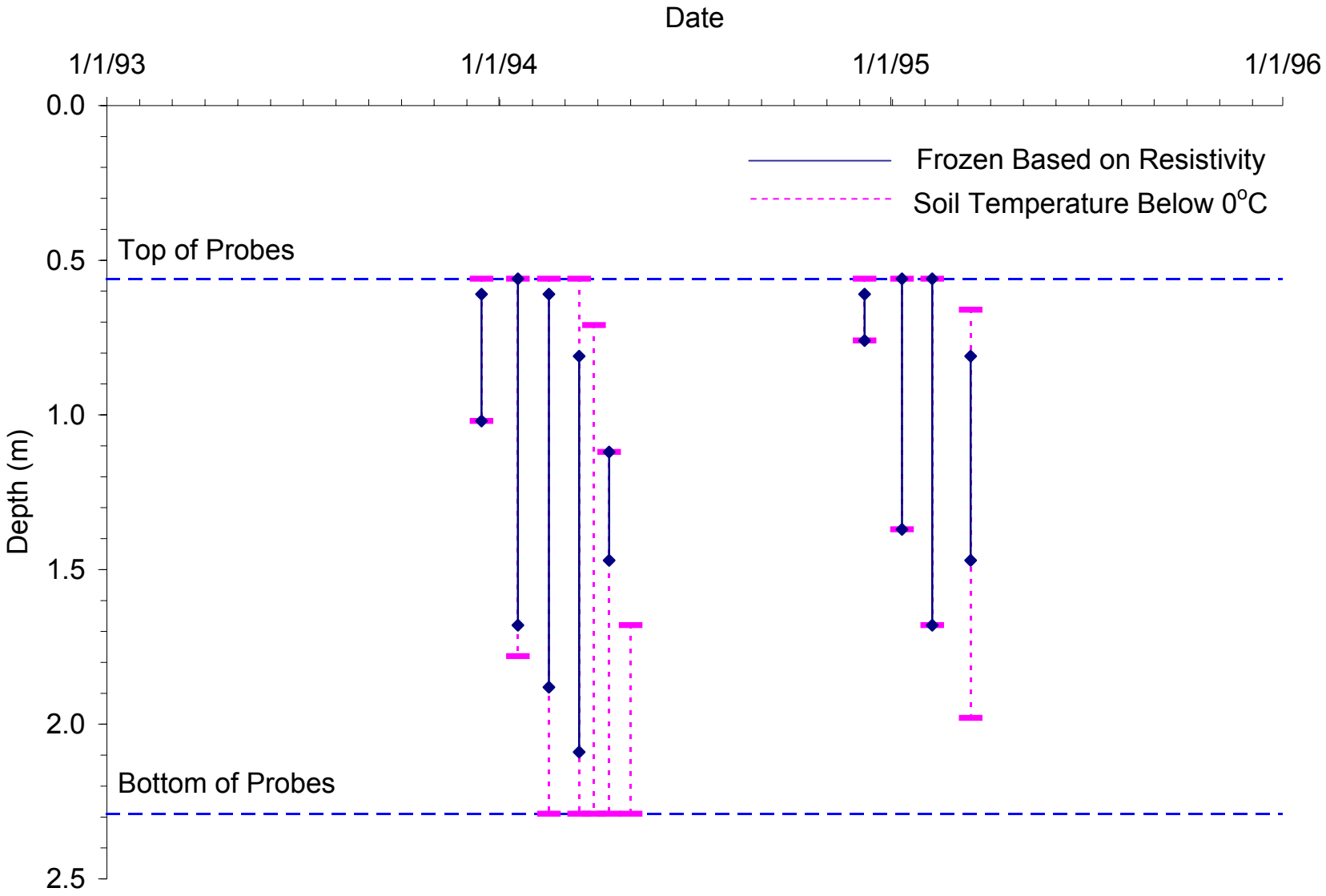

Figure B-6. Freeze State Based on Soil Resistivity and Soil Temperature at Site 27-4040

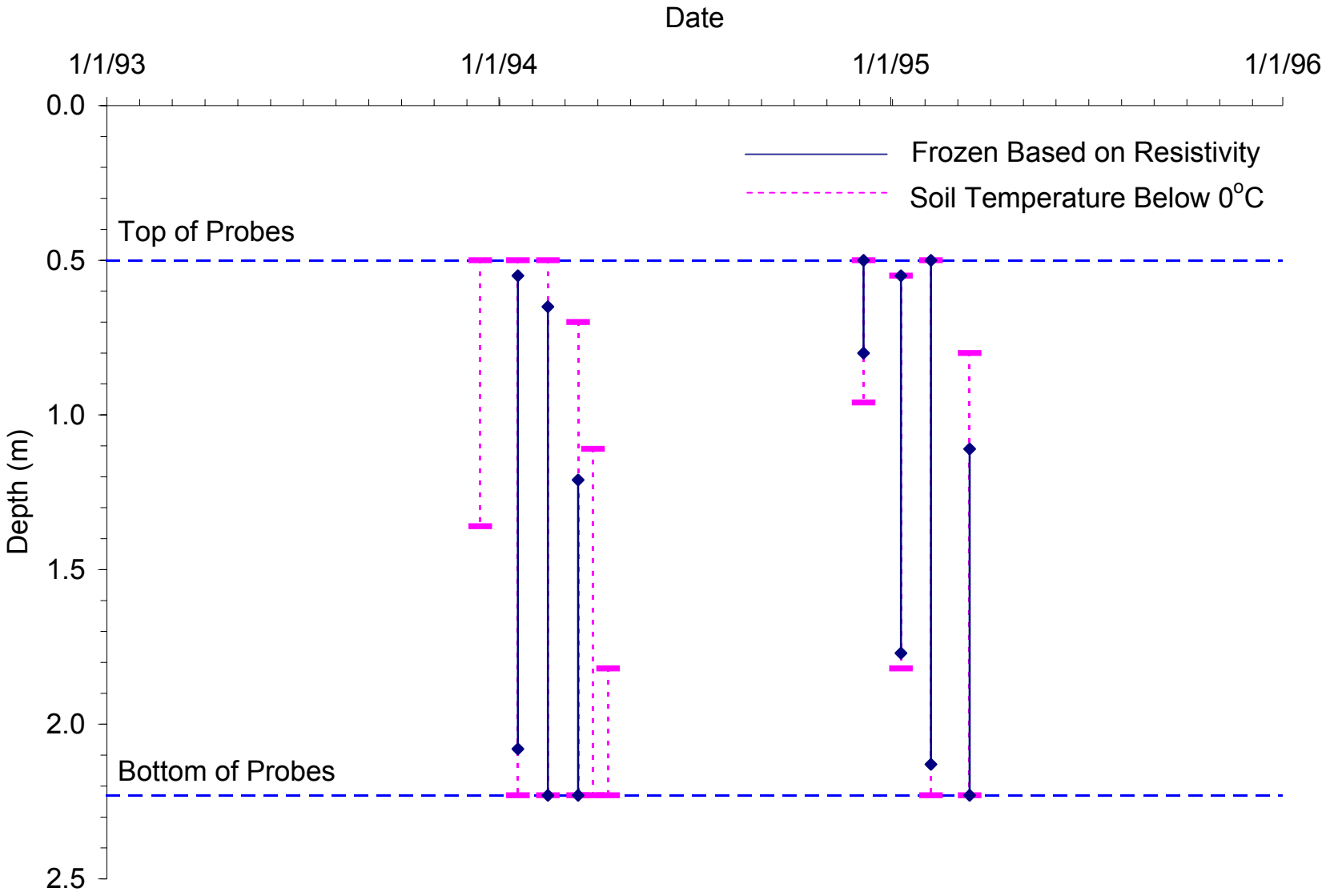

Figure B-7. Freeze State Based on Soil Resistivity and Soil Temperature at Site 27-6251

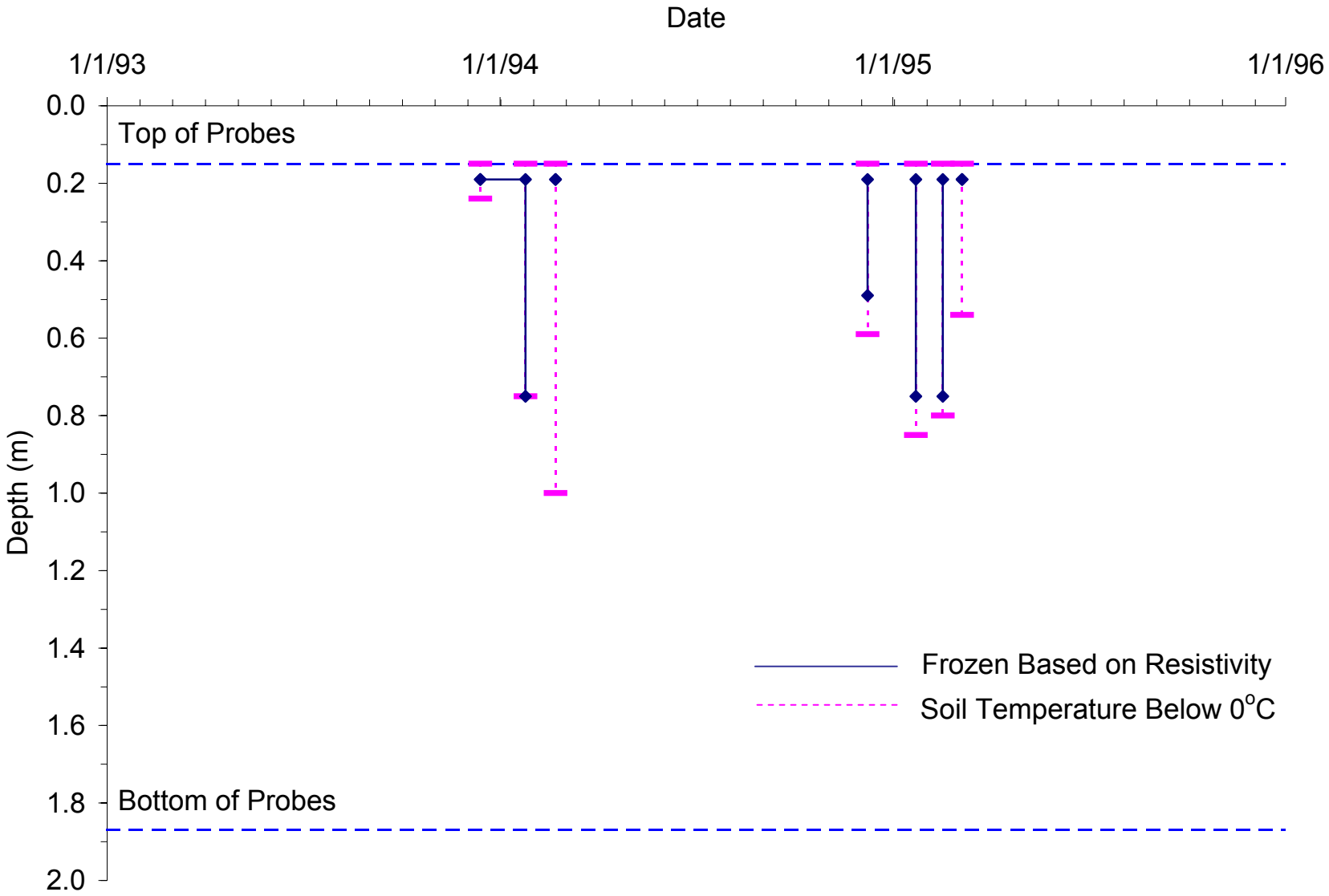

Figure B-8. Freeze State Based on Soil Resistivity and Soil Temperature at Site 30-8129

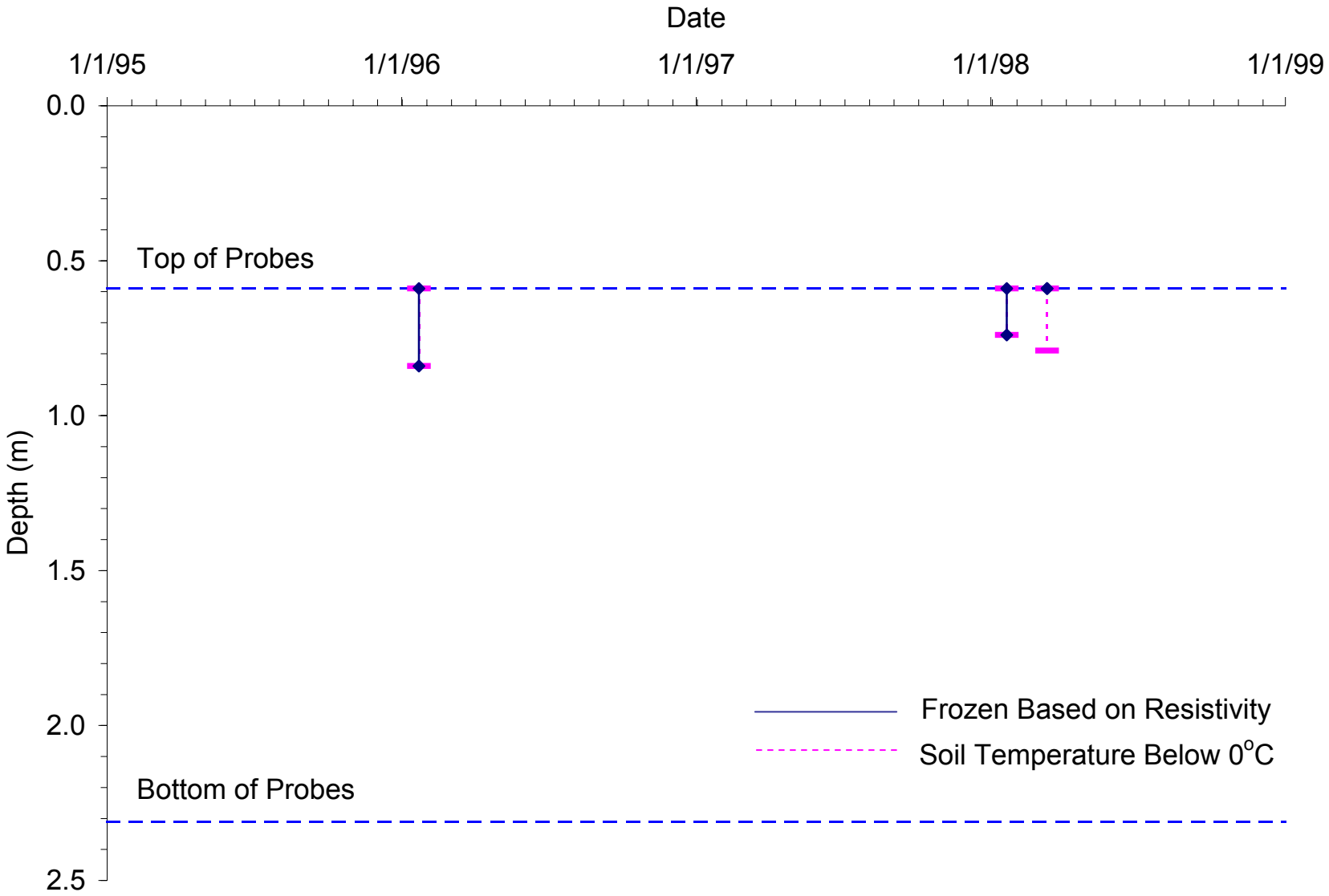

Figure B-9. Freeze State Based on Soil Resistivity and Soil Temperature at Site 31-0114

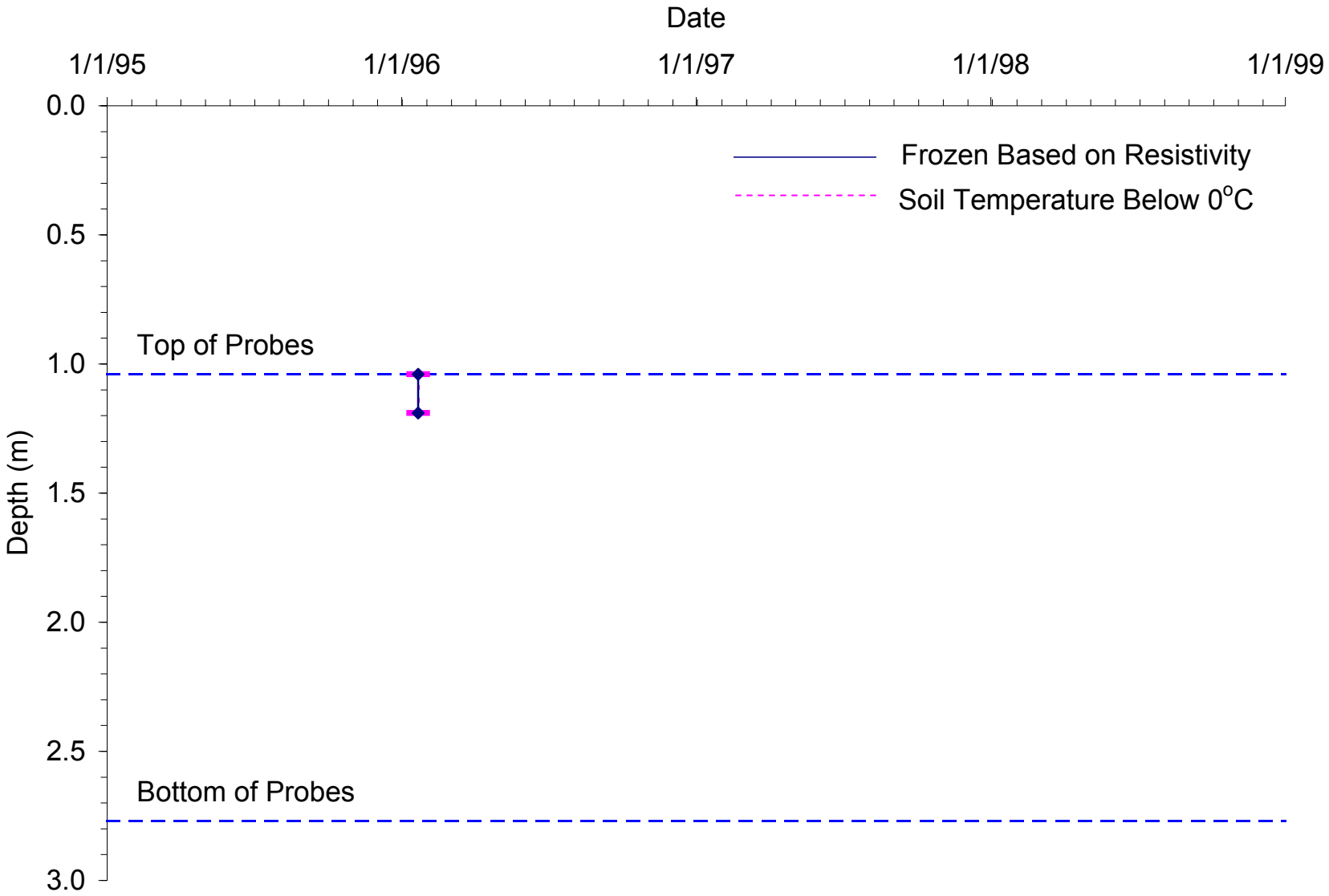

Figure B-10. Freeze State Based on Soil Resistivity and Soil Temperature at Site 31-3018

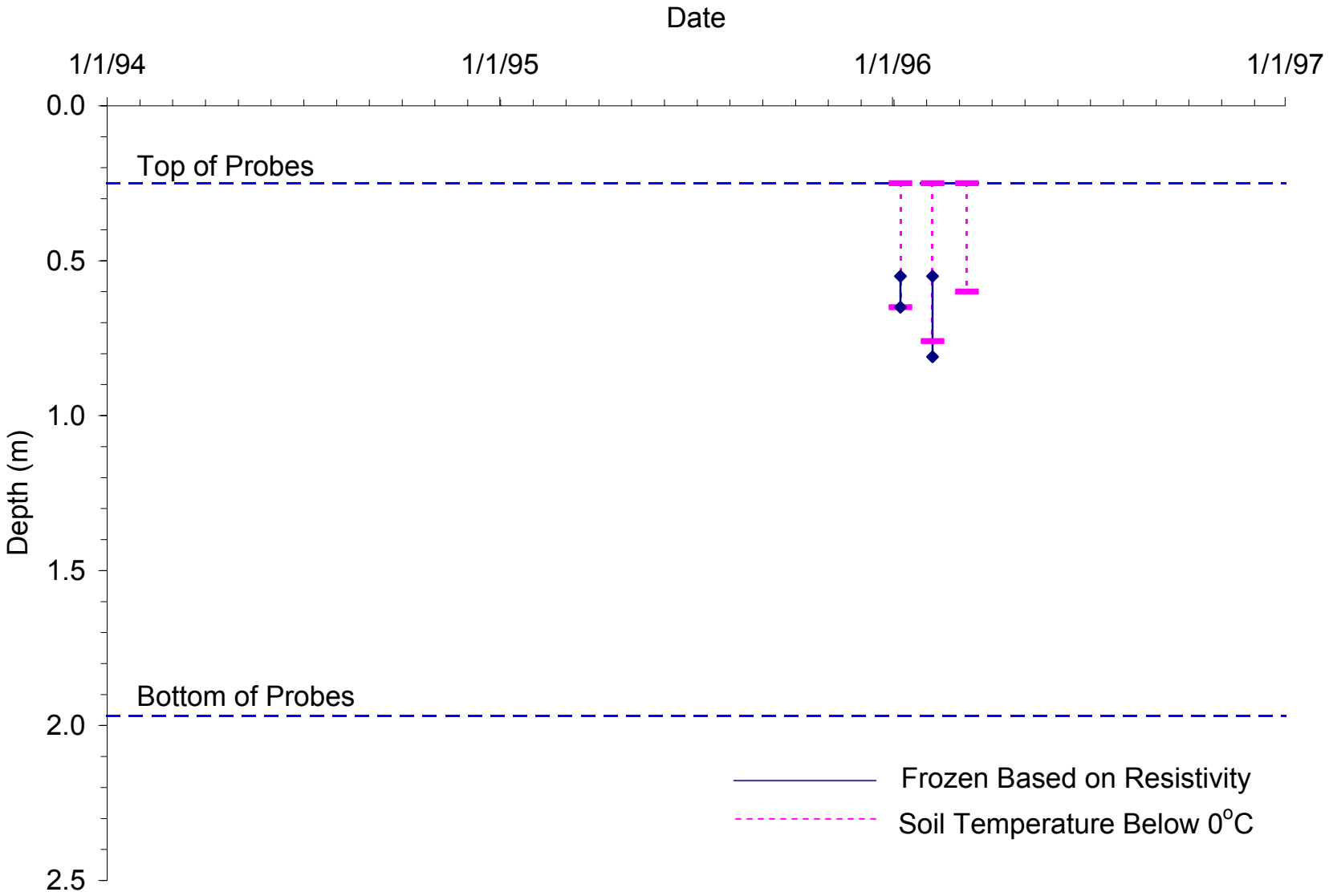

Figure B-11. Freeze State Based on Soil Resistivity and Soil Temperature at Site 36-0801

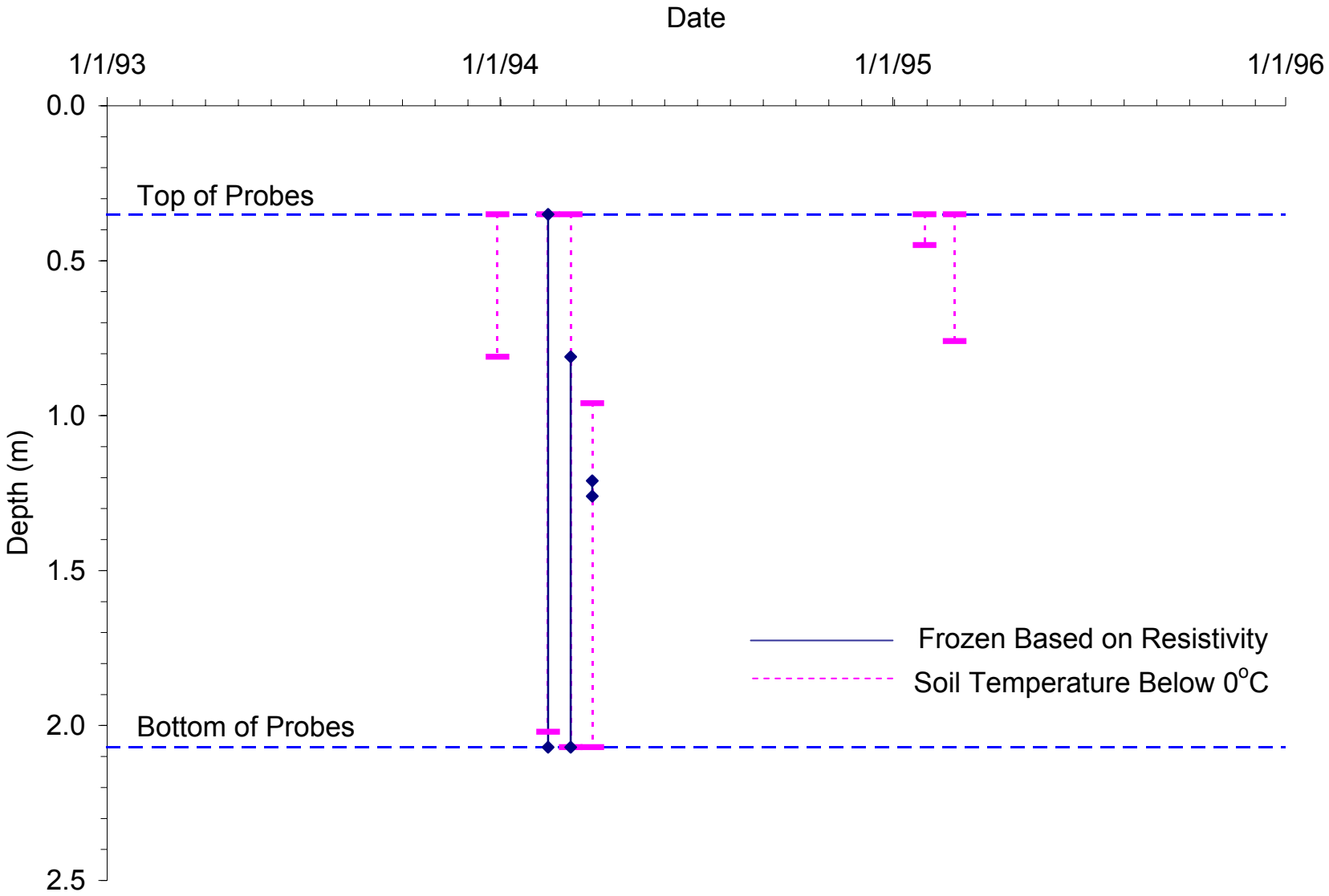

Figure B-12. Freeze State Based on Soil Resistivity and Soil Temperature at Site 36-4018

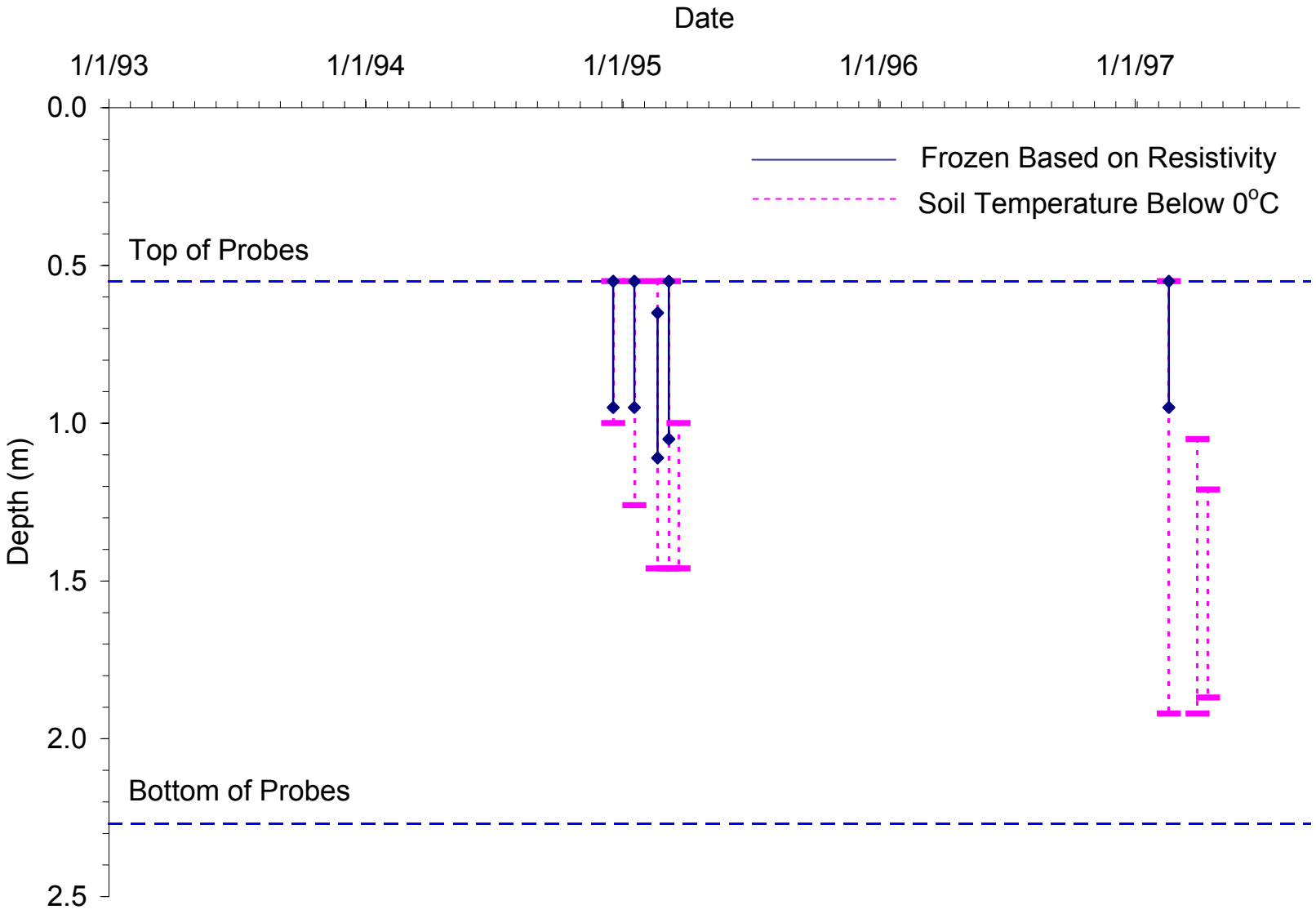

Figure B-13. Freeze State Based on Soil Resistivity and Soil Temperature at Site 46-0804

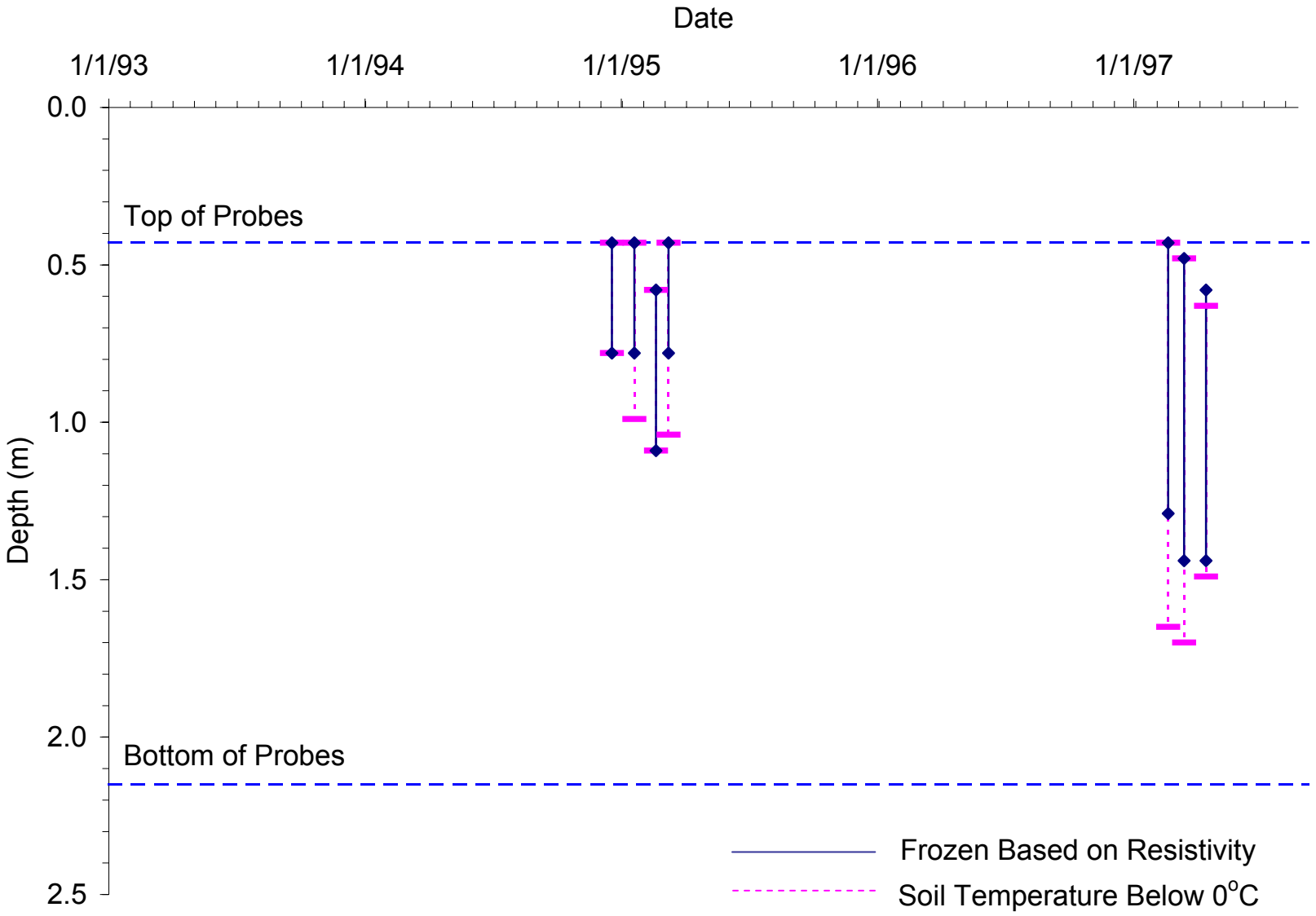

Figure B-14. Freeze State Based on Soil Resistivity and Soil Temperature at Site 46-9187

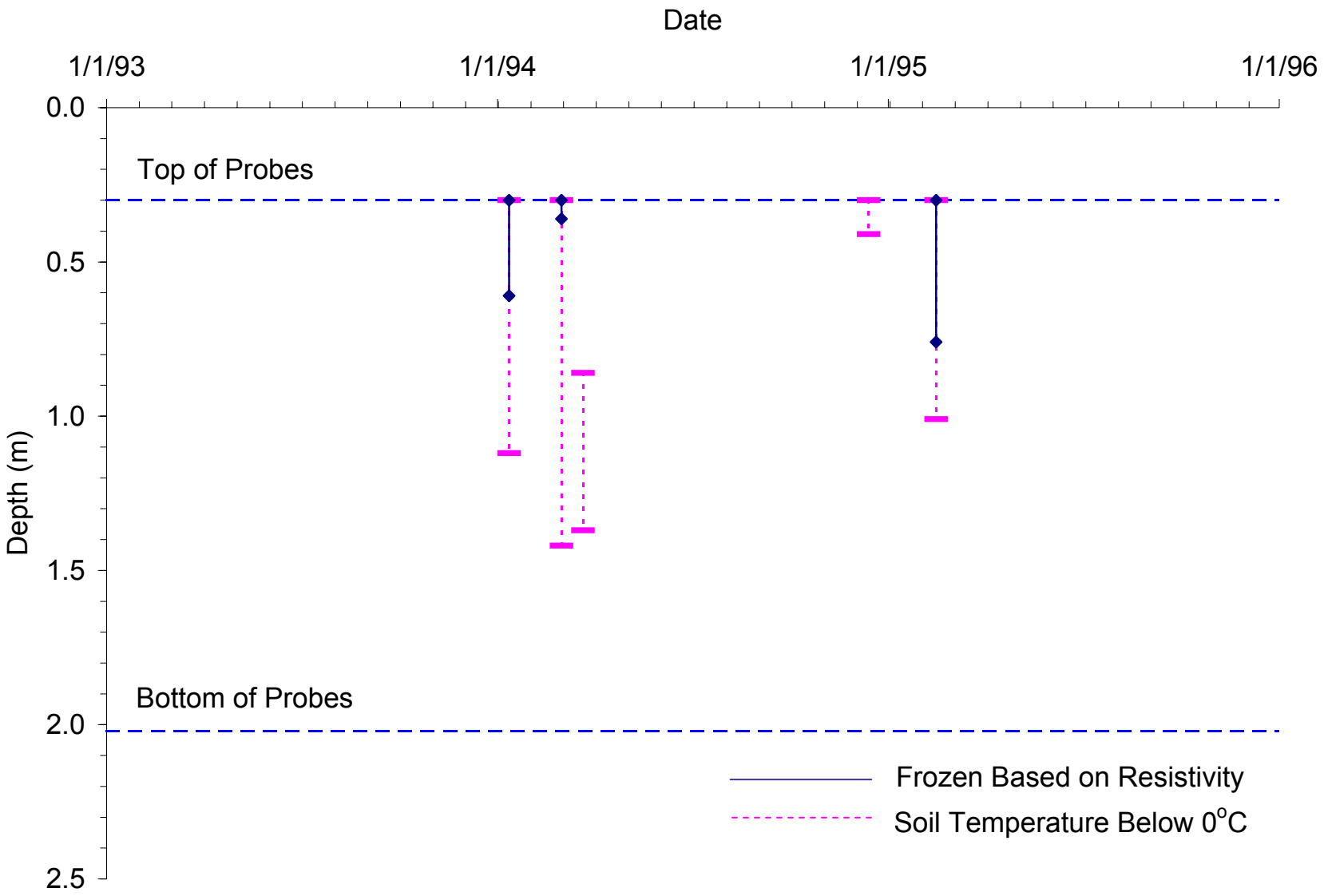

Figure B-15. Freeze State Based on Soil Resistivity and Soil Temperature at Site 50-1002

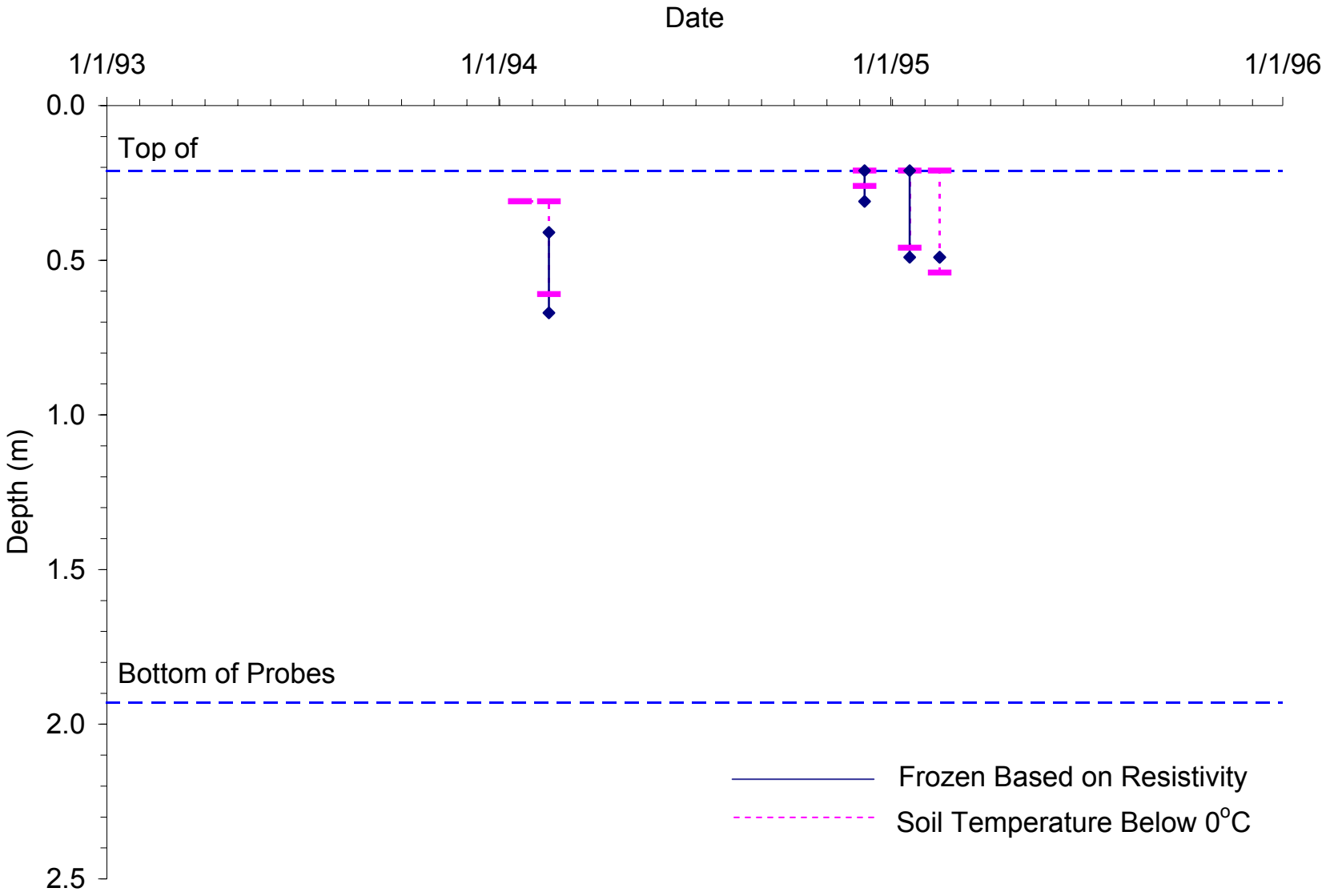

Figure B-16. Freeze State Based on Soil Resistivity and Soil Temperature at Site 56-1007

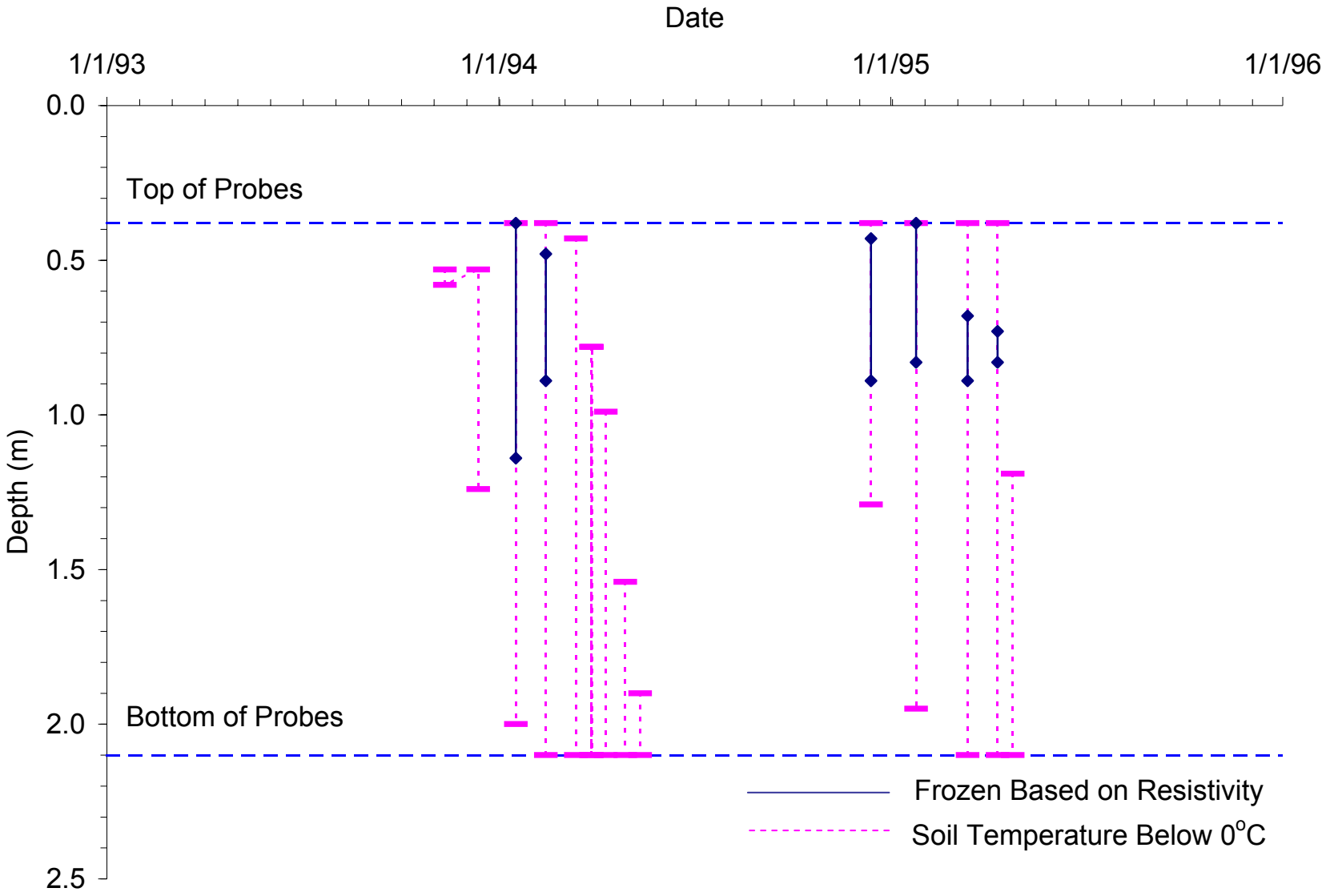

Figure B-17. Freeze State Based on Soil Resistivity and Soil Temperature at Site 83-1801

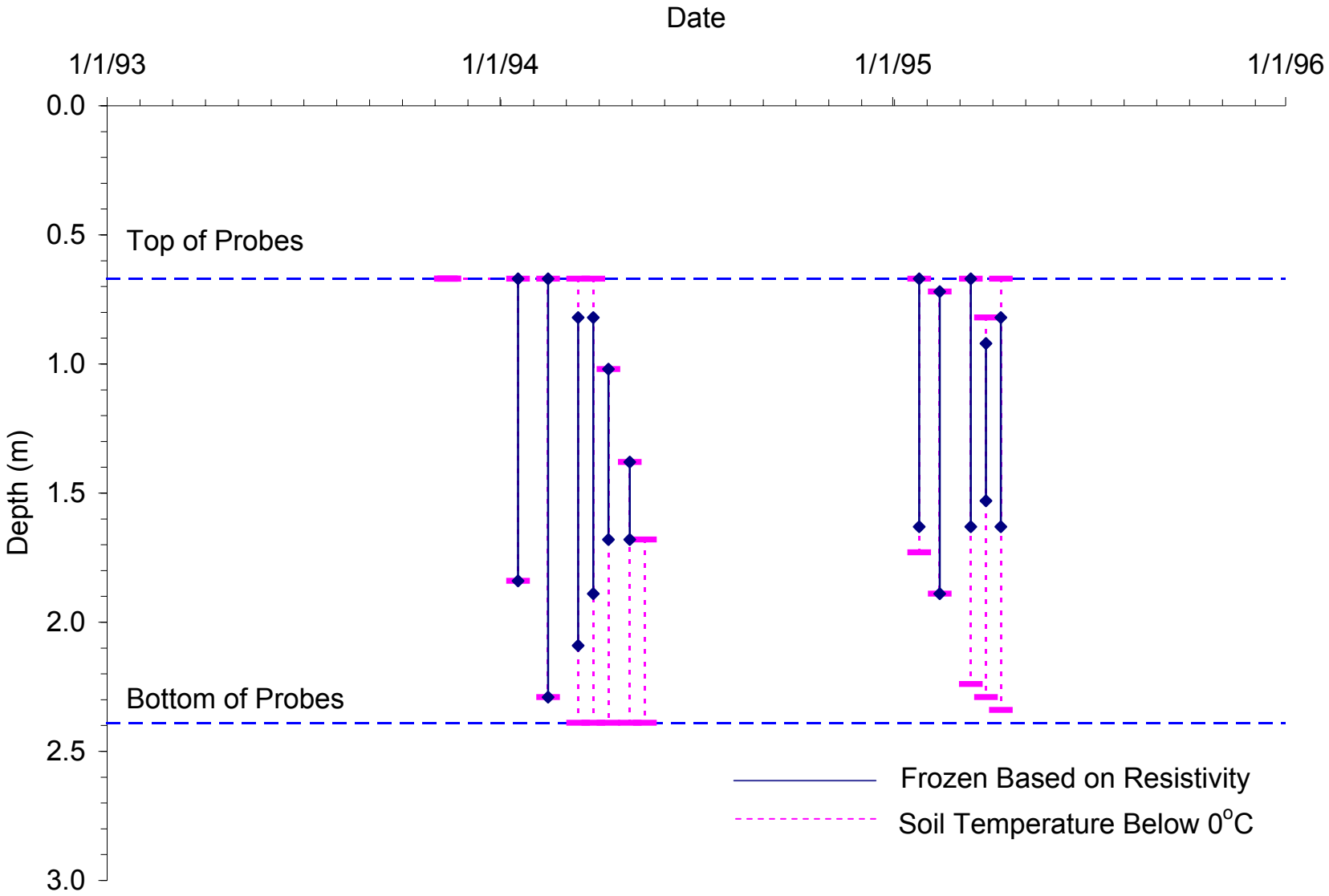

Figure B-18. Freeze State Based on Soil Resistivity and Soil Temperature at Site 83-3802

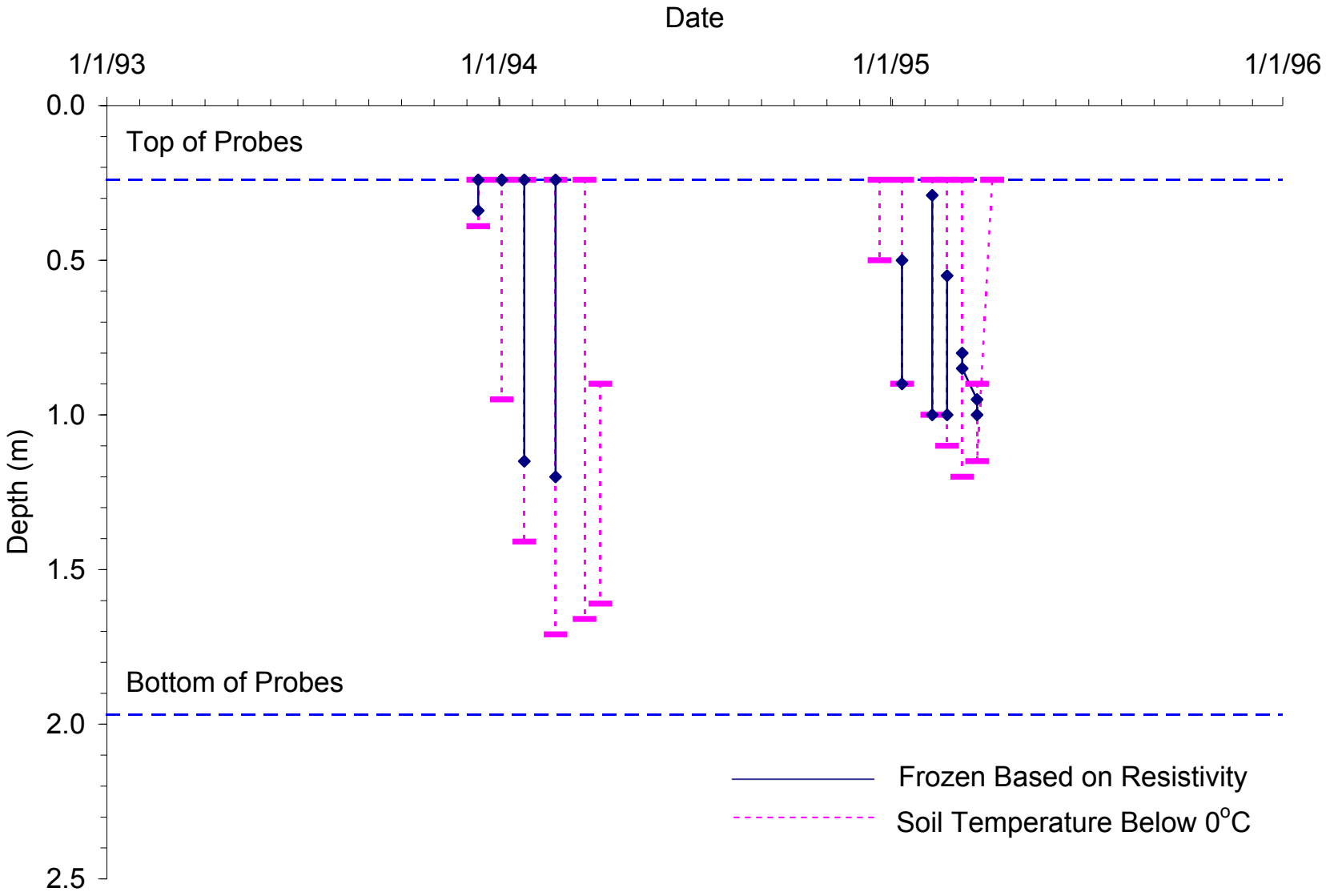

Figure B-19. Freeze State Based on Soil Resistivity and Soil Temperature at Site 87-1622

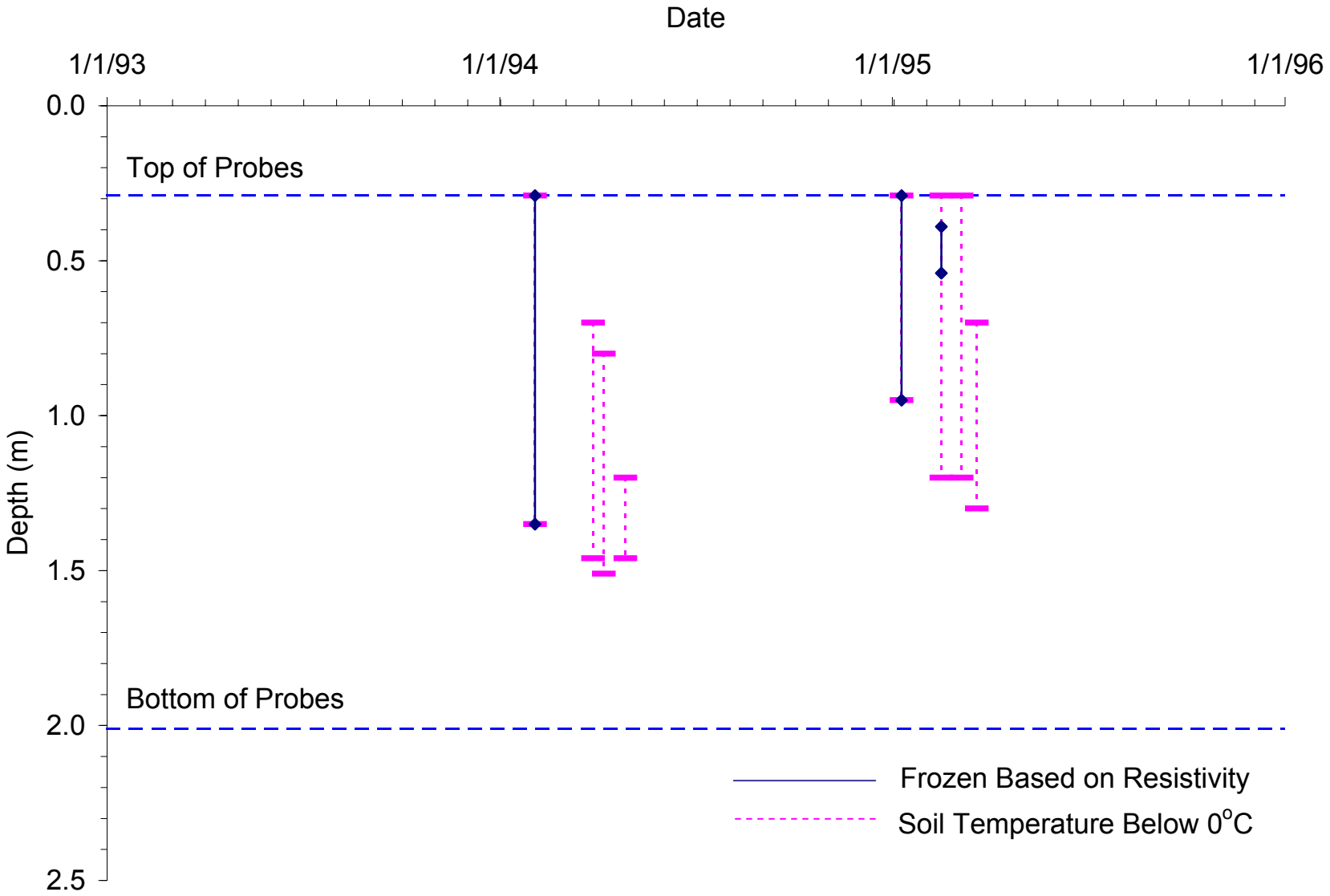

Figure B-20. Freeze State Based on Soil Resistivity and Soil Temperature at Site 89-3015

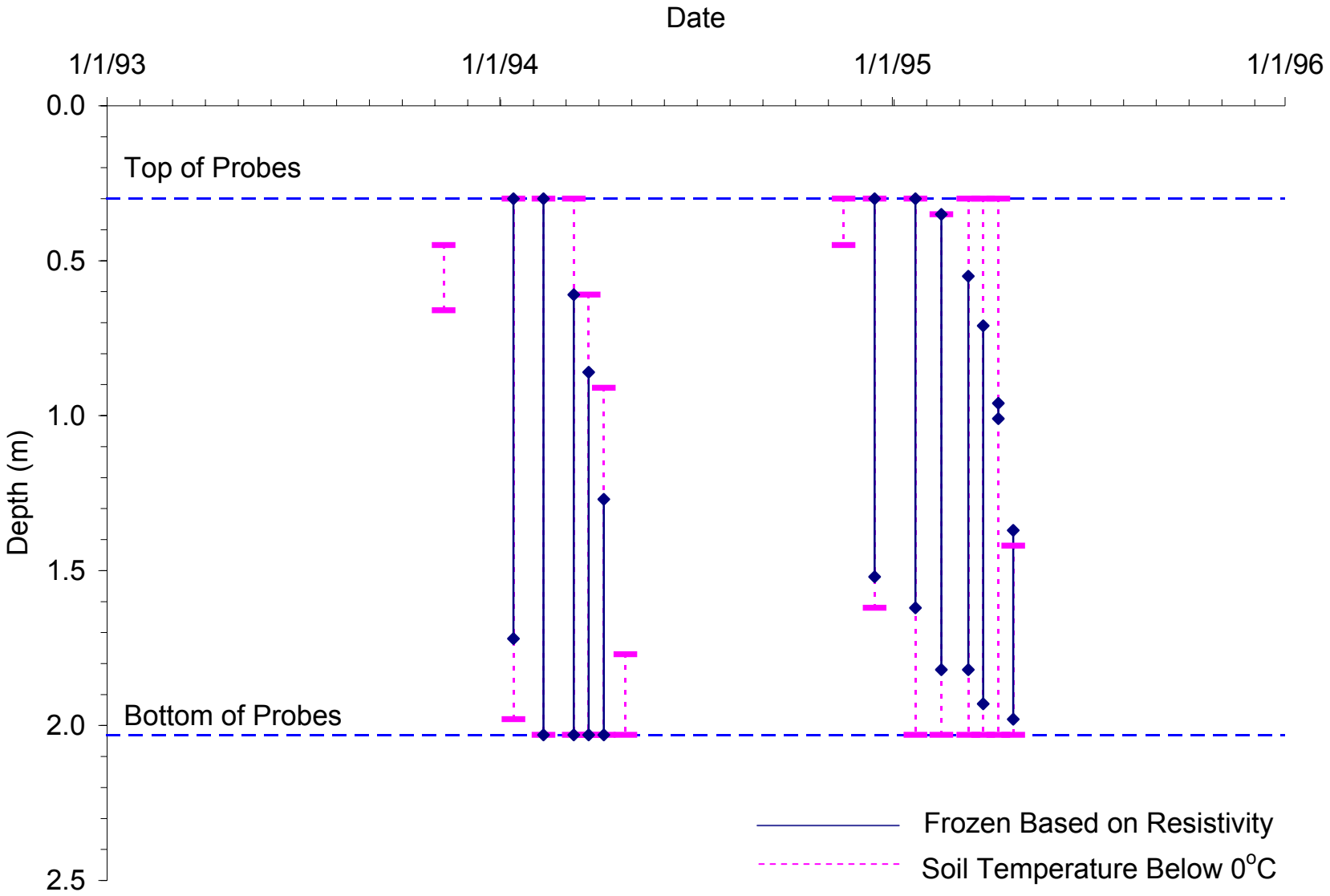

Figure B-21. Freeze State Based on Soil Resistivity and Soil Temperature at Site 90-6405

APPENDIX C

COMPARISONS OF MEASURED AND SURROGATE AIR TEMPERATURES

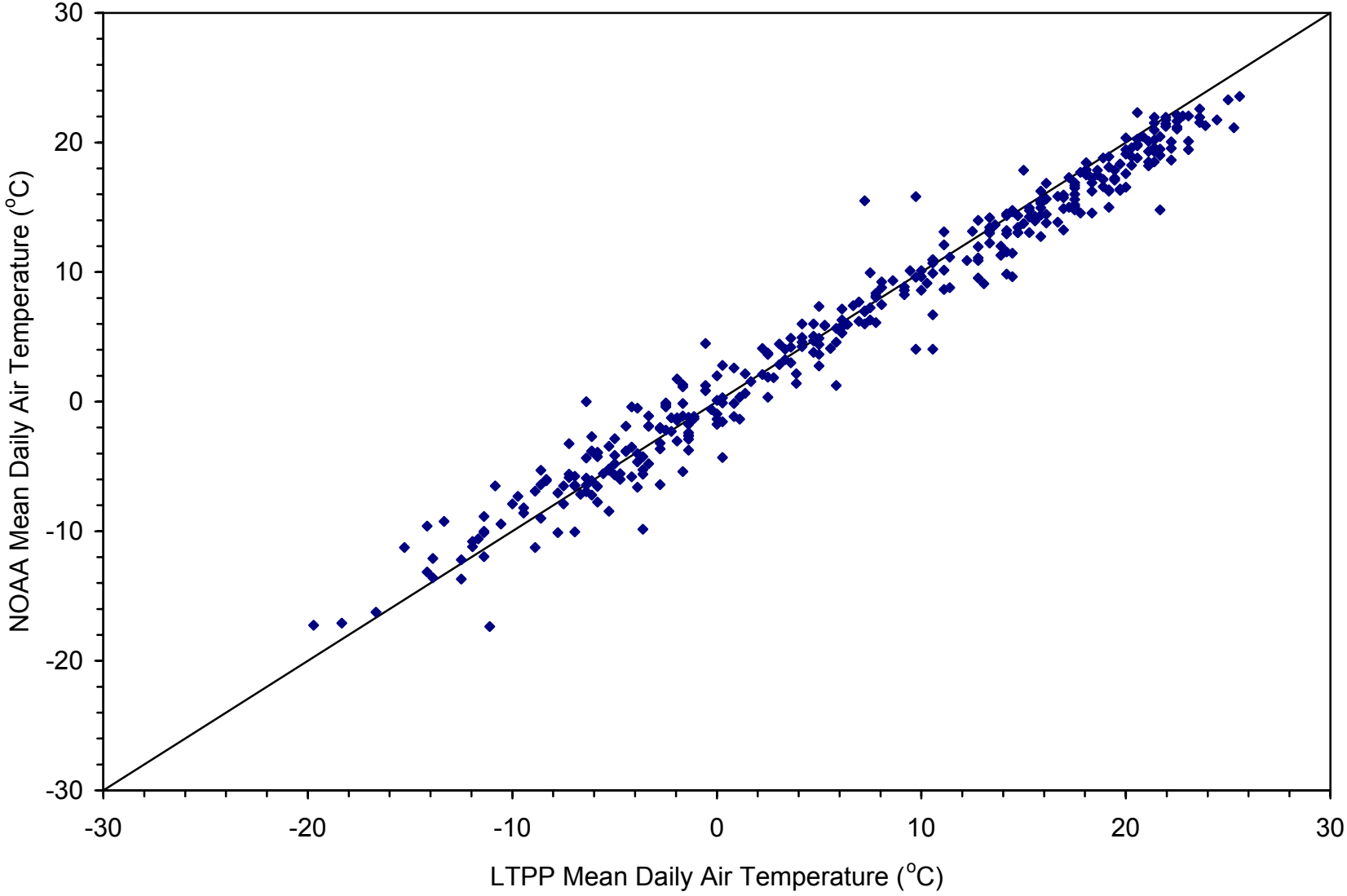

Figure C-1. Comparison of Measured and Surrogate Air Temperatures at Site 16-1010

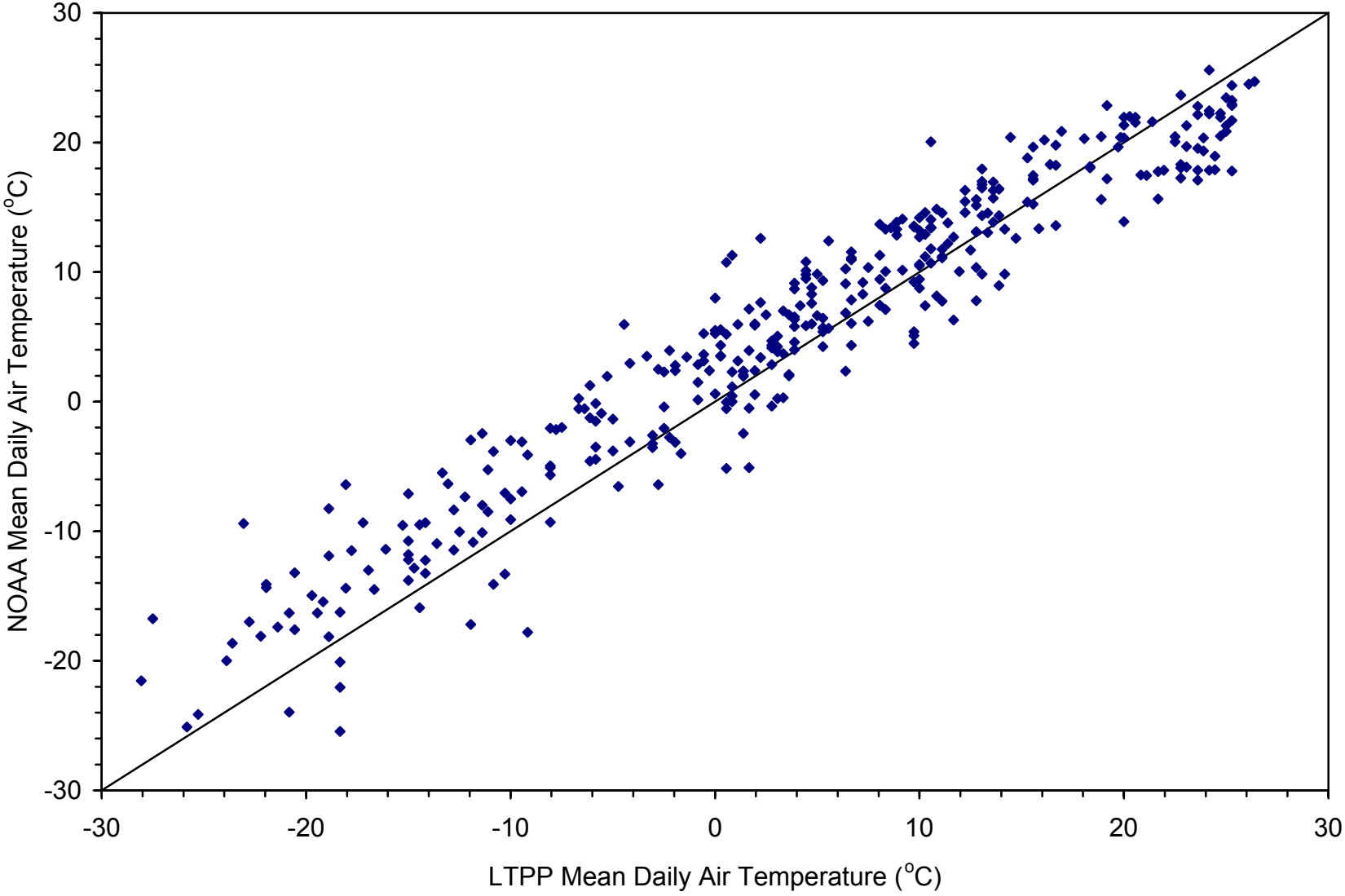

Figure C-2. Comparison of Measured and Surrogate Air Temperatures at Site 23-1026

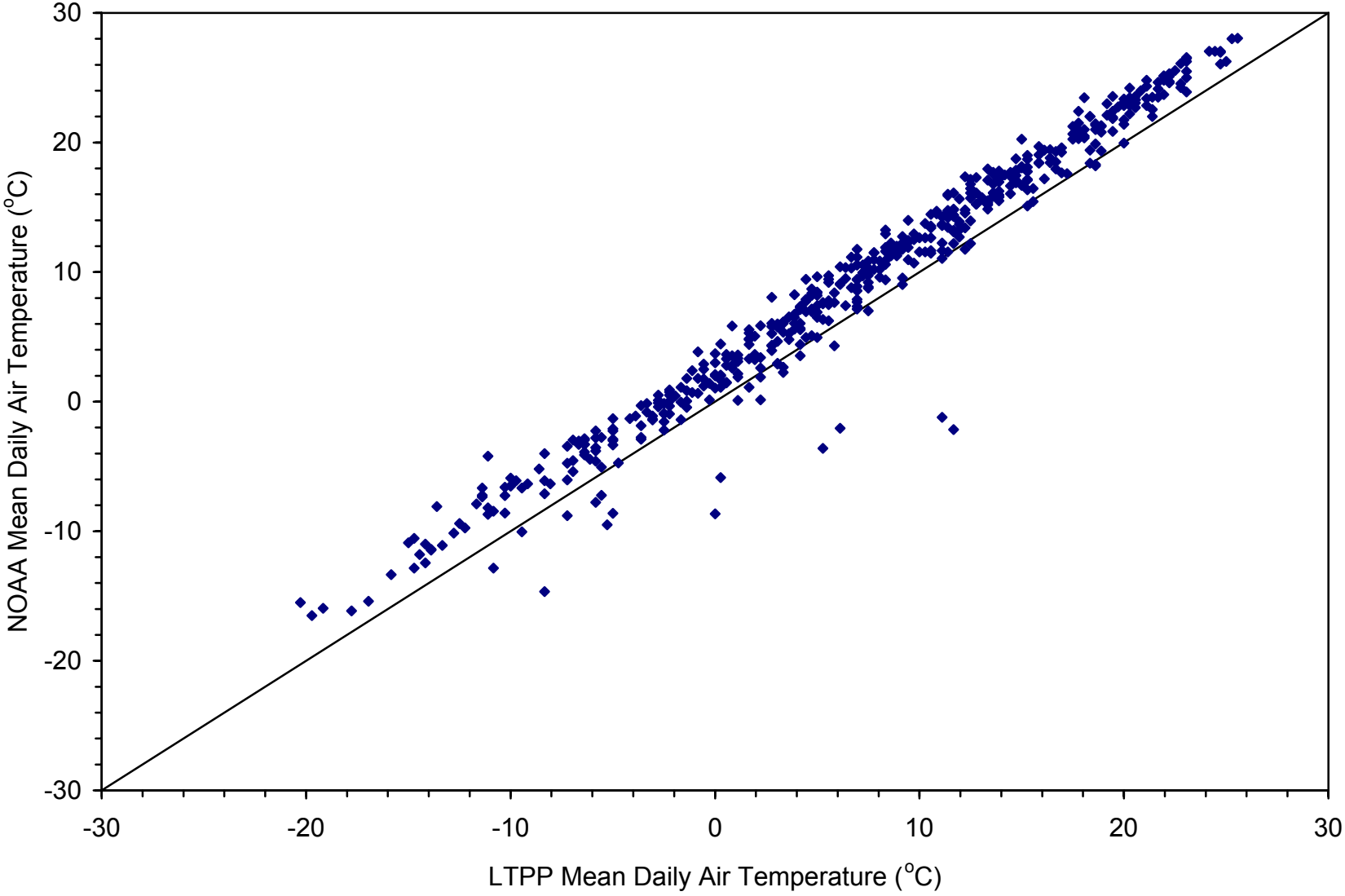

Figure C-3. Comparison of Measured and Surrogate Air Temperatures at Site 25-1002

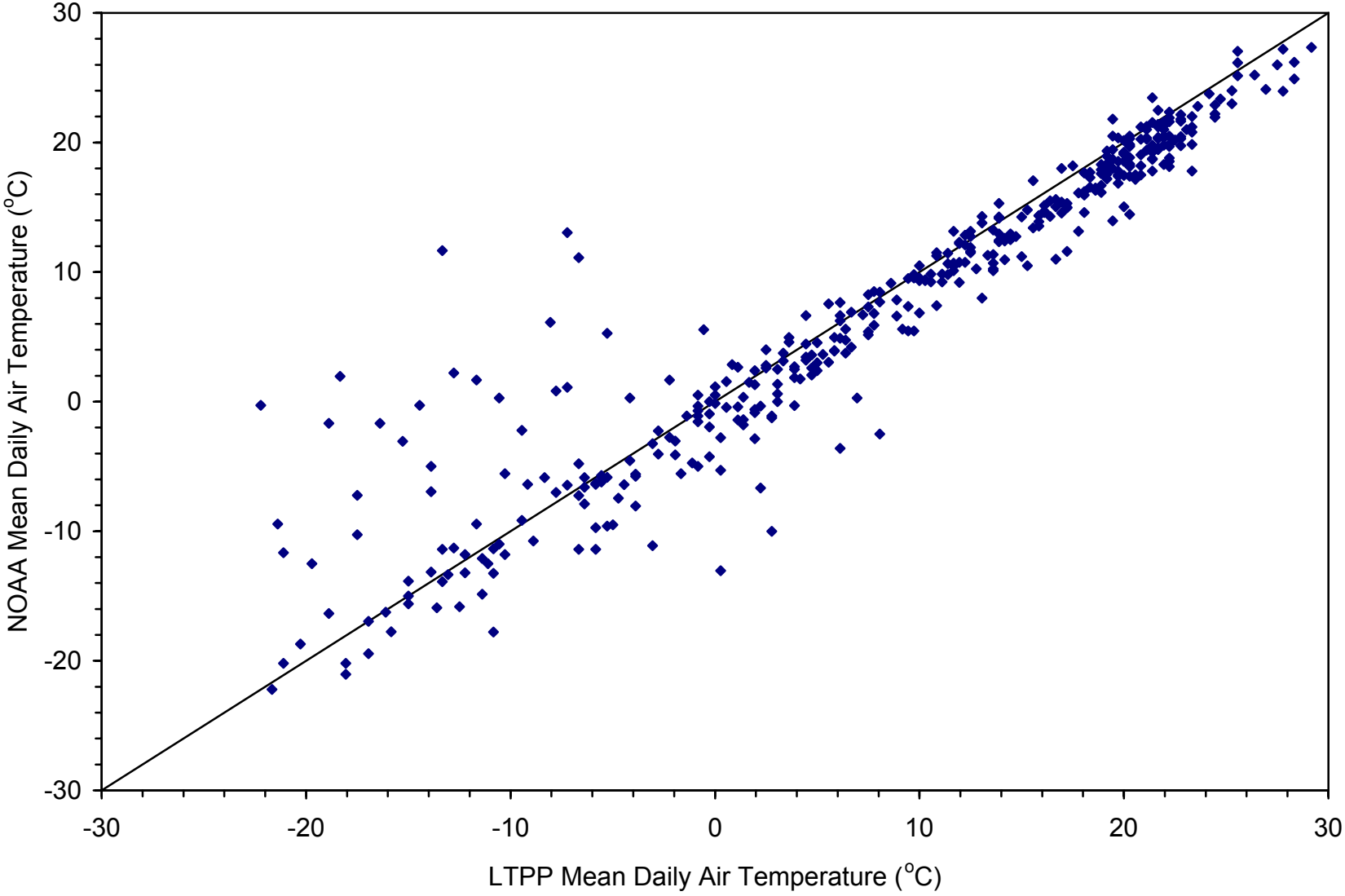

Figure C-4. Comparison of Measured and Surrogate Air Temperatures at Site 27-1018

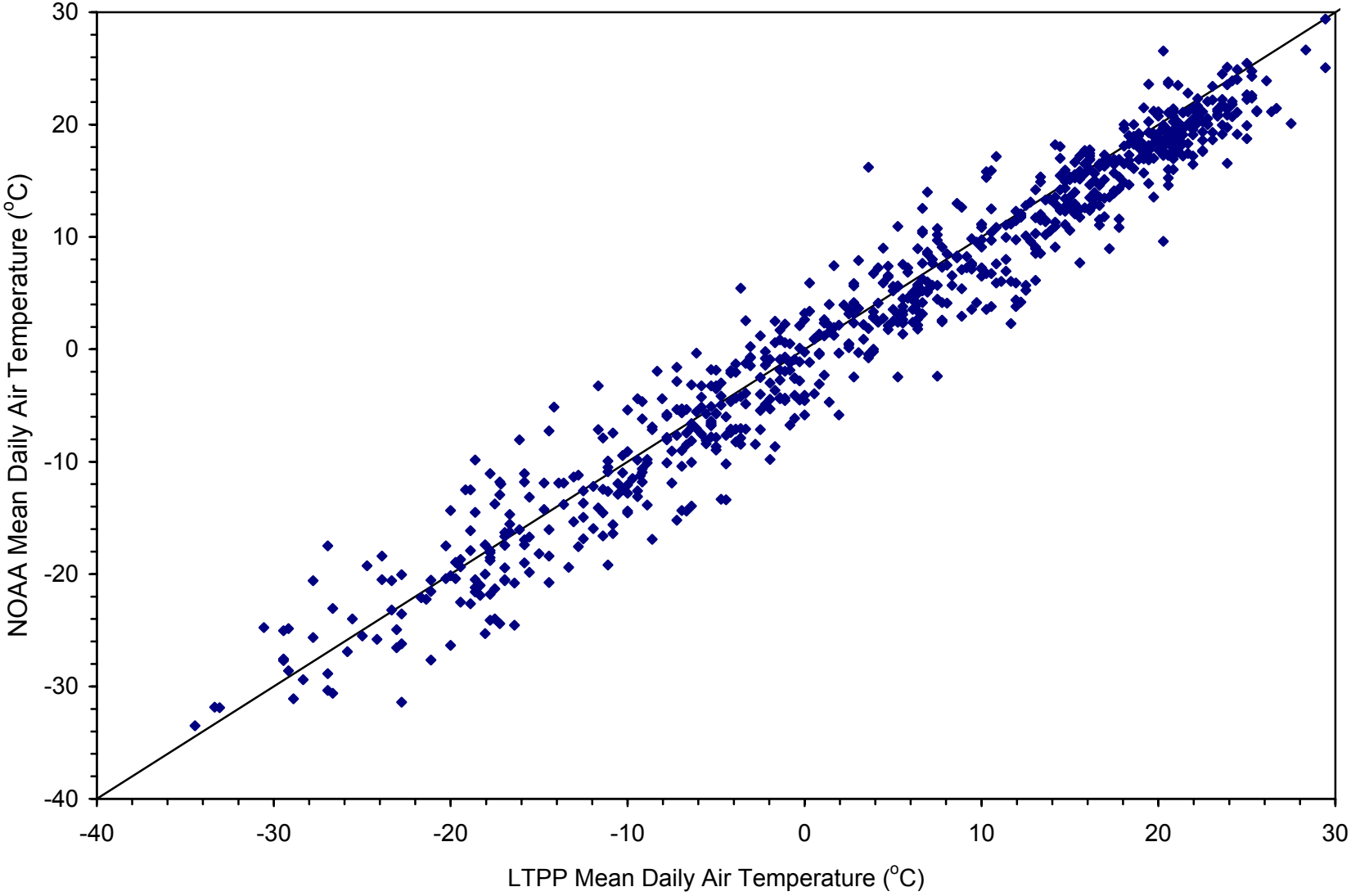

Figure C-5. Comparison of Measured and Surrogate Air Temperatures at Site 27-1028

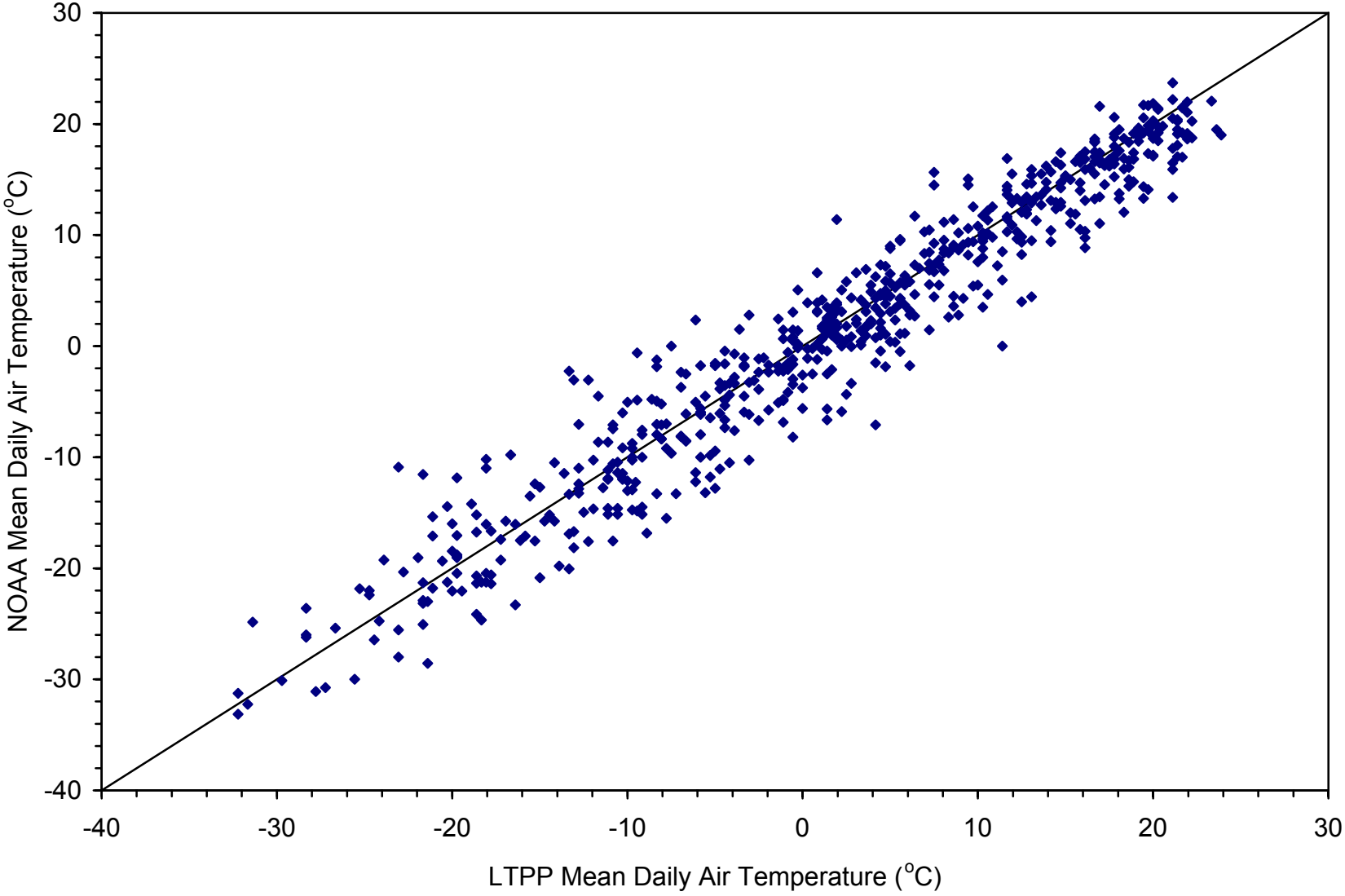

Figure C-6. Comparison of Measured and Surrogate Air Temperatures at Site 27-4040

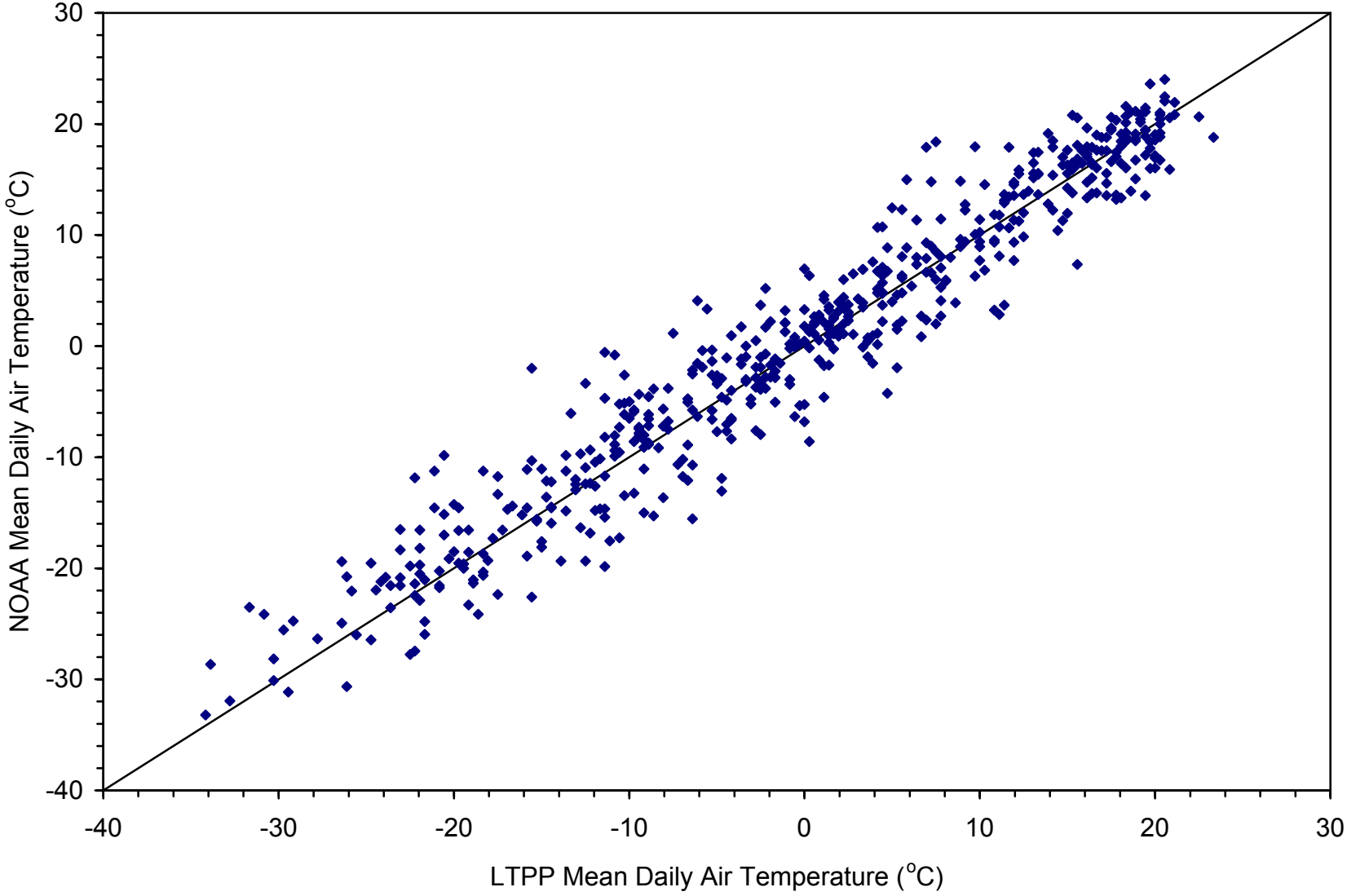

Figure C-7. Comparison of Measured and Surrogate Air Temperatures at Site 27-6251

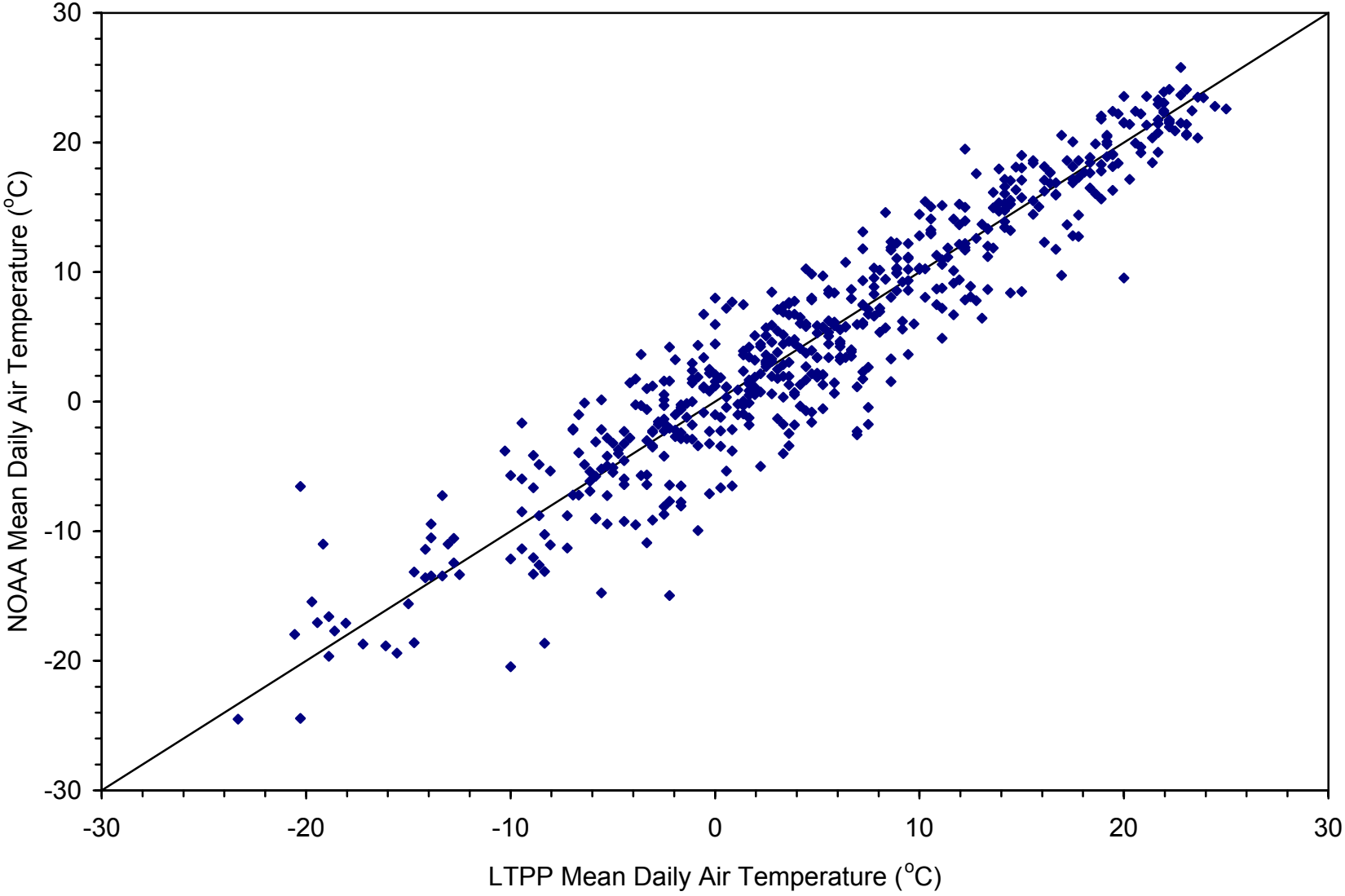

Figure C-8. Comparison of Measured and Surrogate Air Temperatures at Site 30-8129

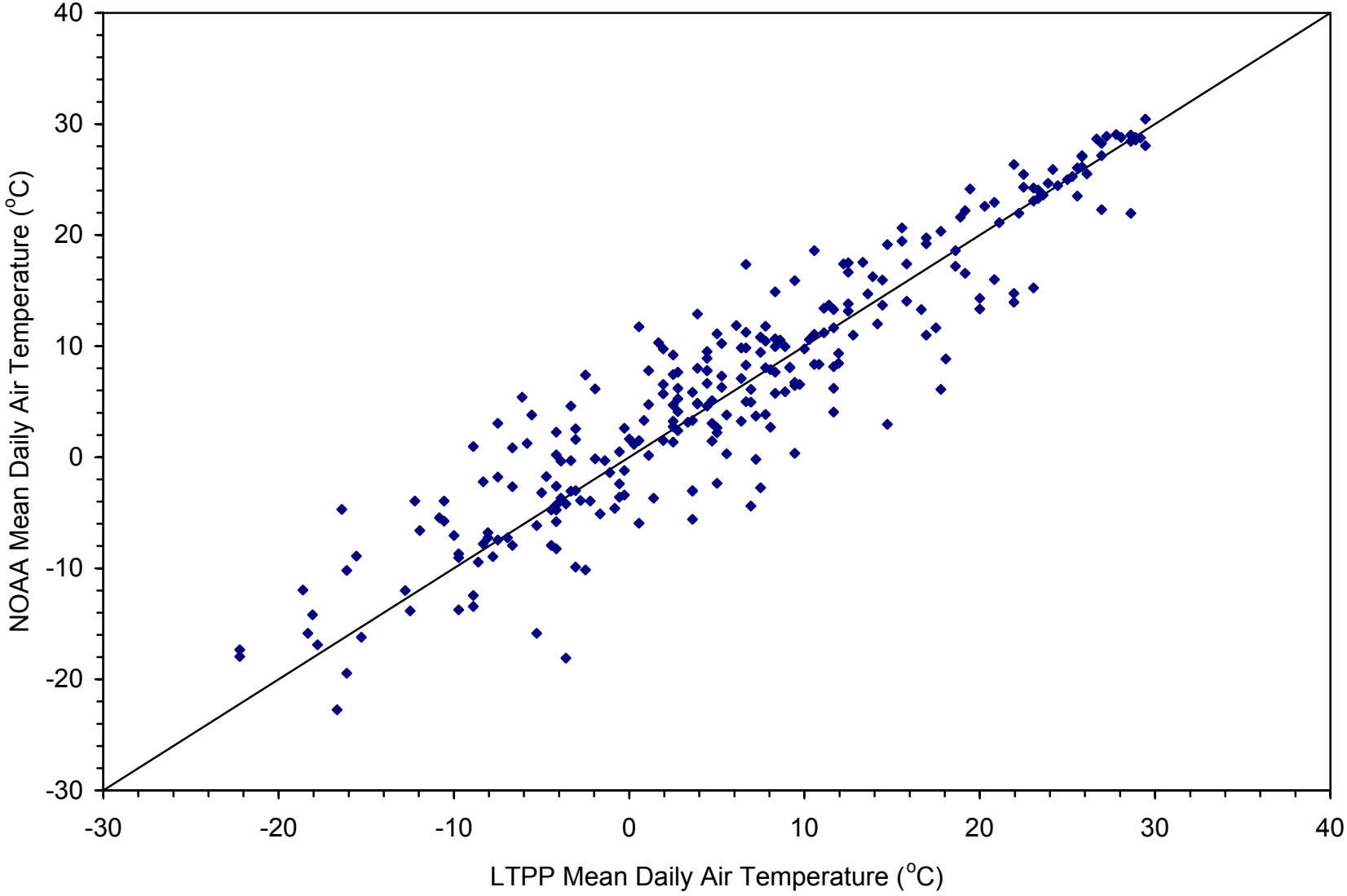

Figure C-9. Comparison of Measured and Surrogate Air Temperatures at Site 31-0114

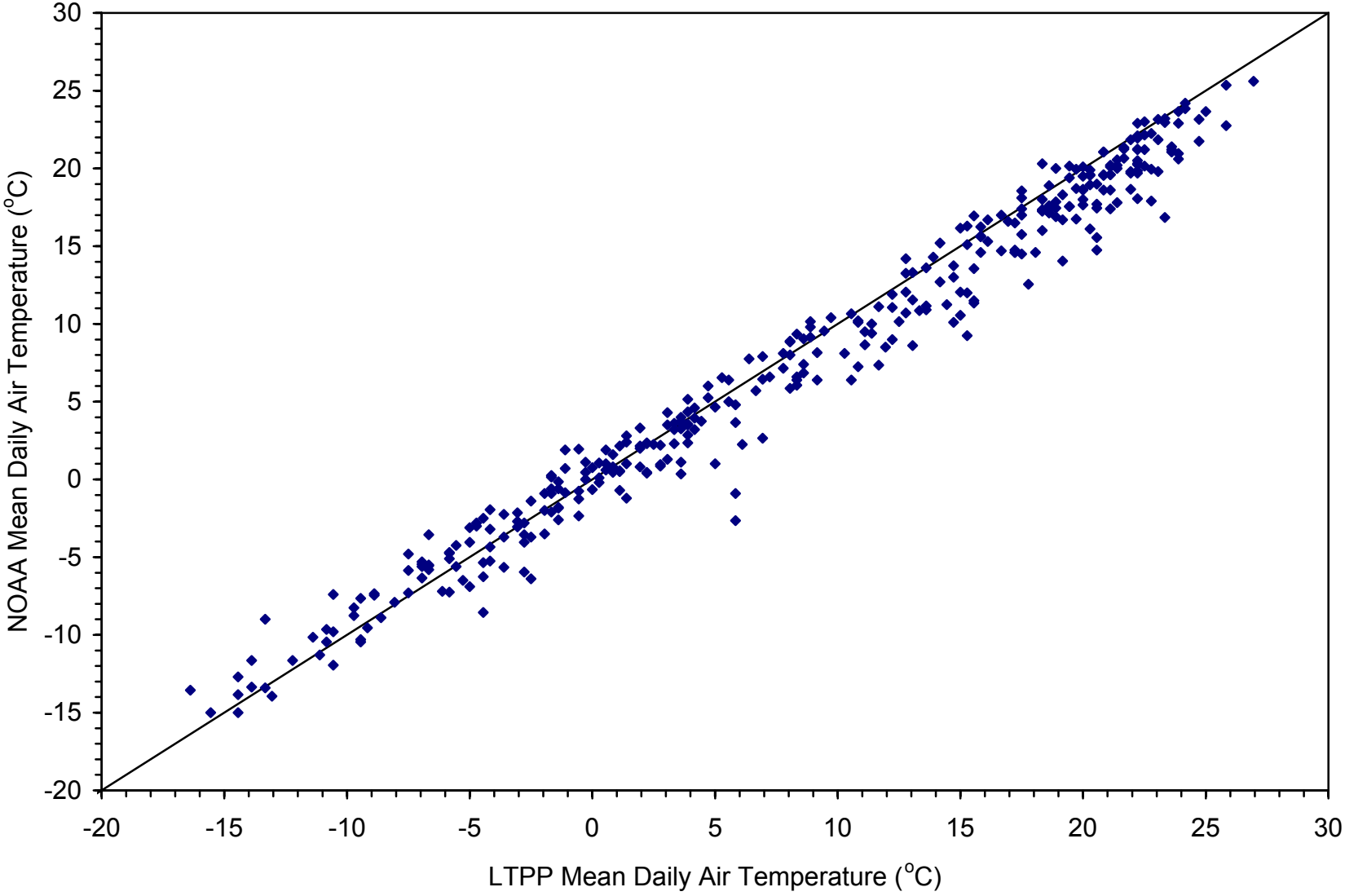

Figure C-10. Comparison of Measured and Surrogate Air Temperatures at Site 36-0801

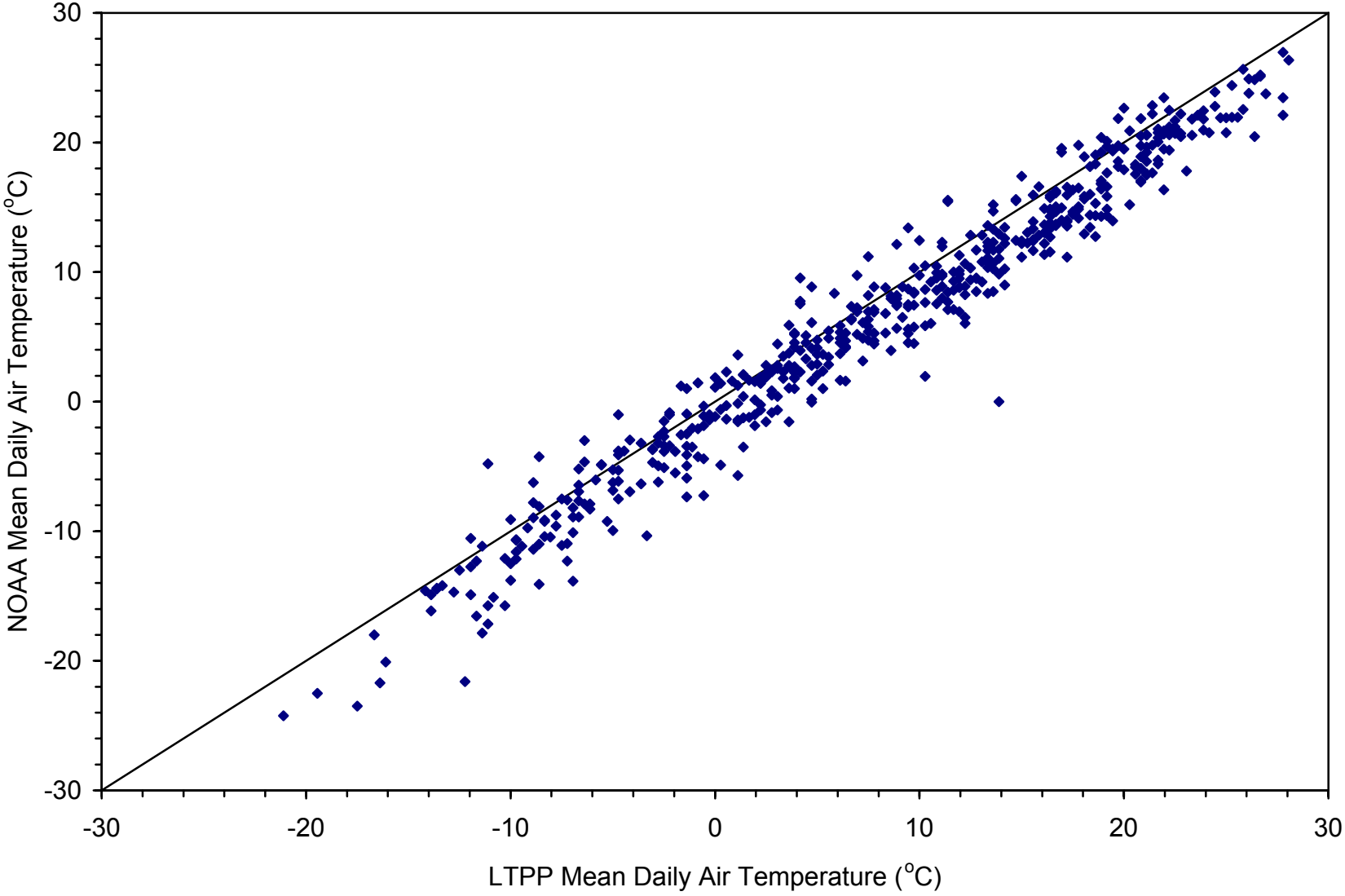

Figure C-11. Comparison of Measured and Surrogate Air Temperatures at Site 36-4018

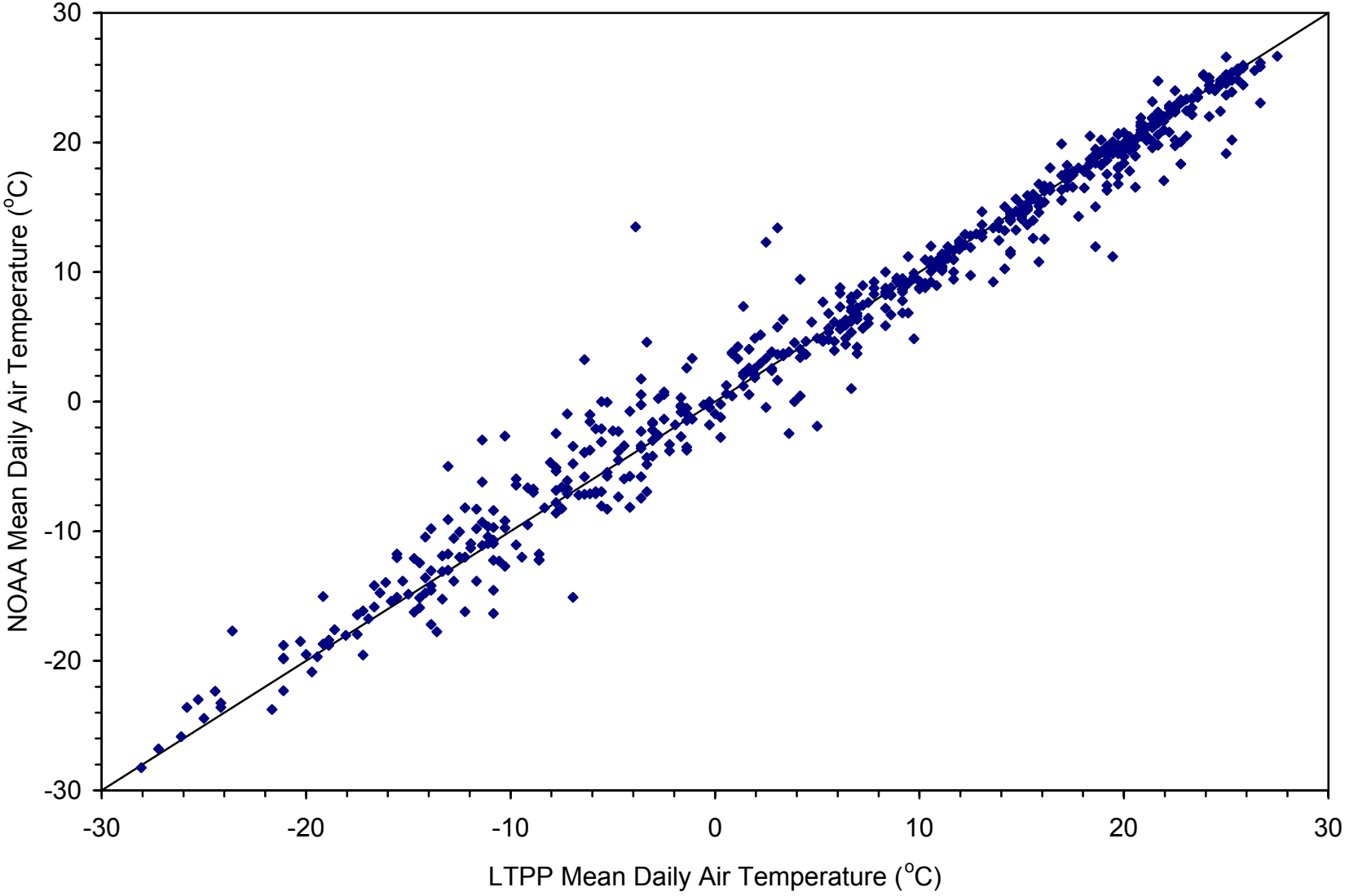

Figure C-12. Comparison of Measured and Surrogate Air Temperatures at Site 46-0804

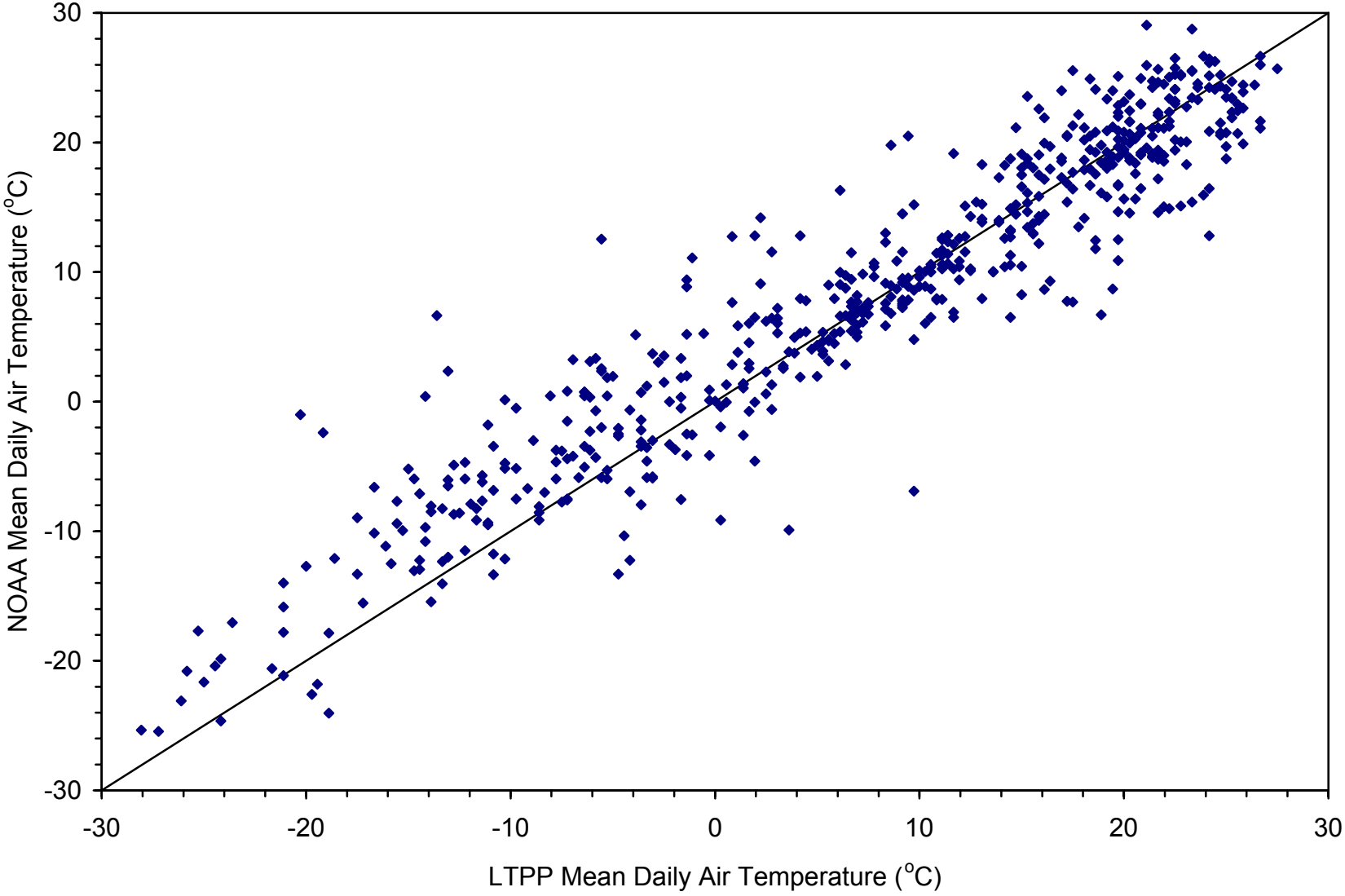

Figure C-13. Comparison of Measured and Surrogate Air Temperatures at Site 46-9187

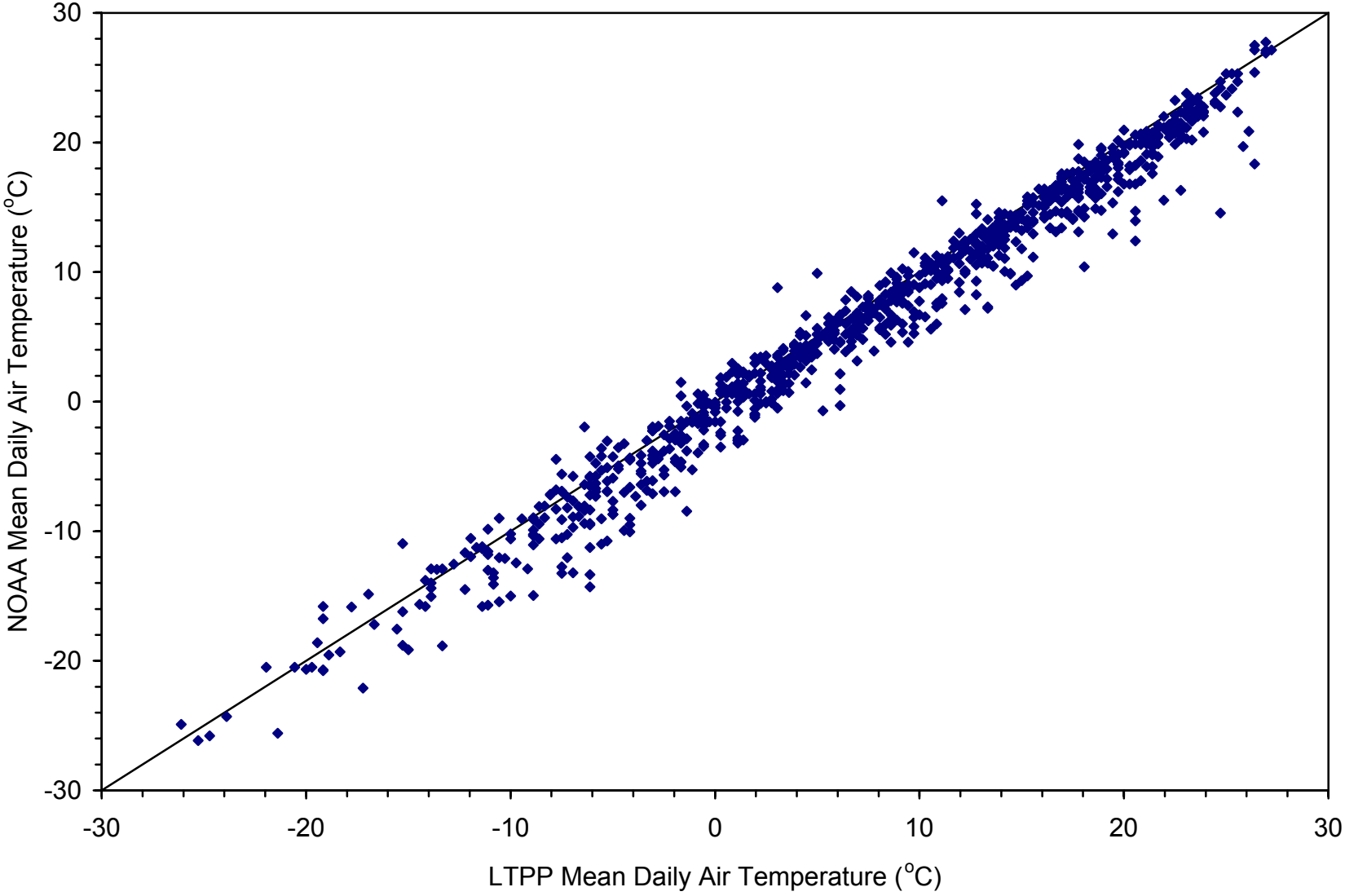

Figure C-14. Comparison of Measured and Surrogate Air Temperatures at Site 50-1002

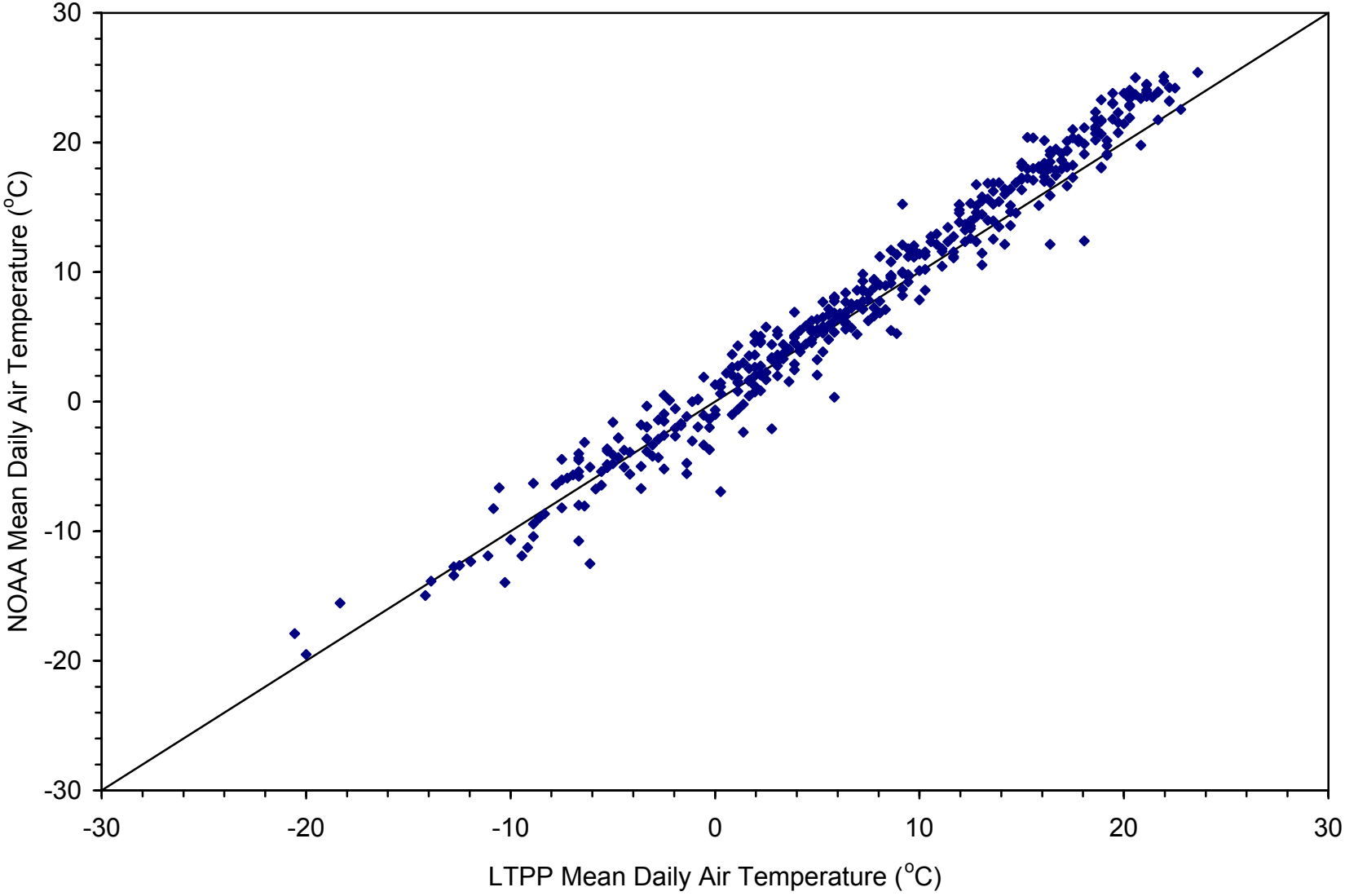

Figure C-15. Comparison of Measured and Surrogate Air Temperatures at Site 56-1007

APPENDIX D

FREEZE DEPTH MODELS

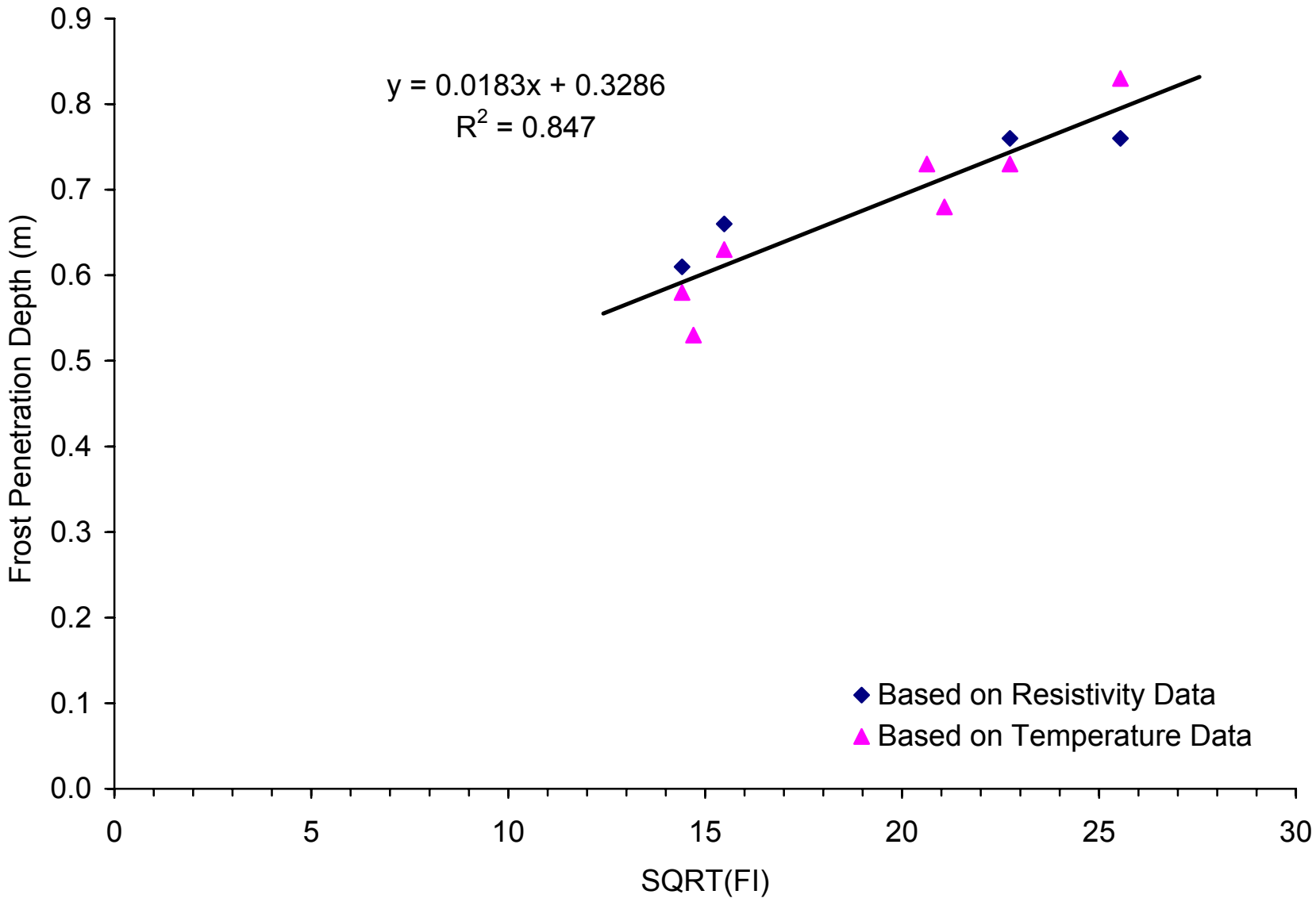

Figure D-1. Freeze Depth Model for Site 16-1010

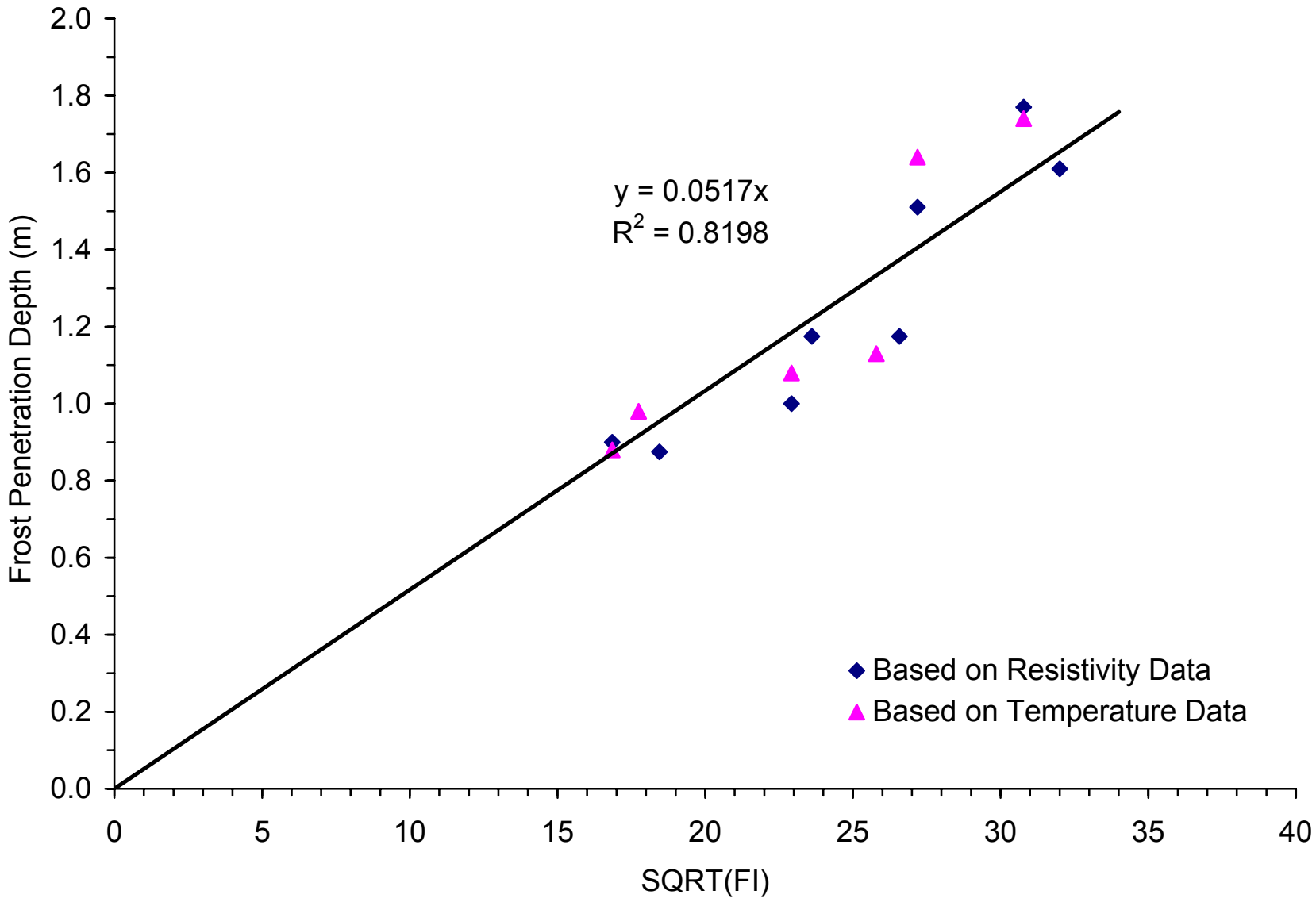

Figure D-2. Freeze Depth Model for Site 23-1026

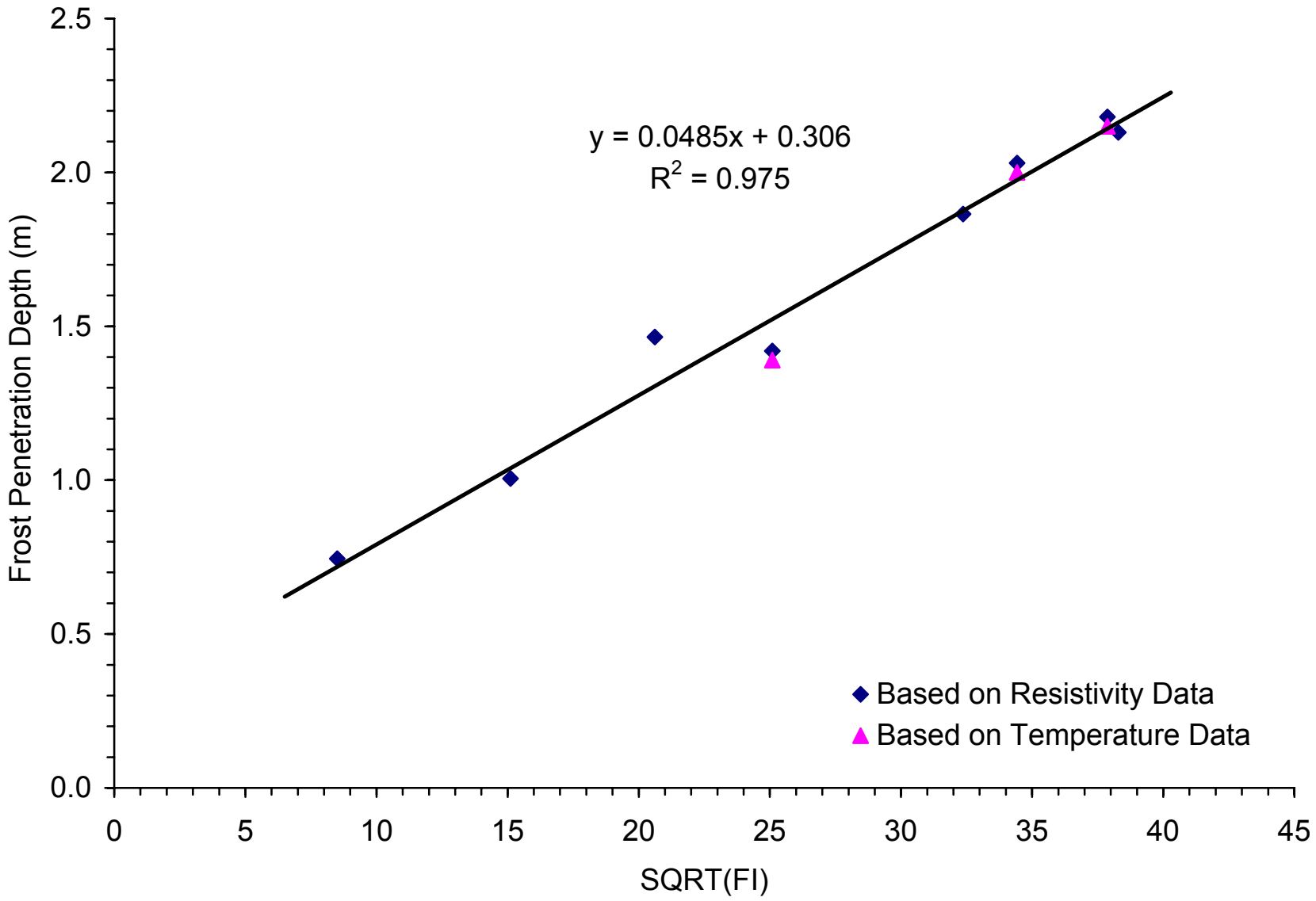

Figure D-3. Freeze Depth Model for Site 27-1018

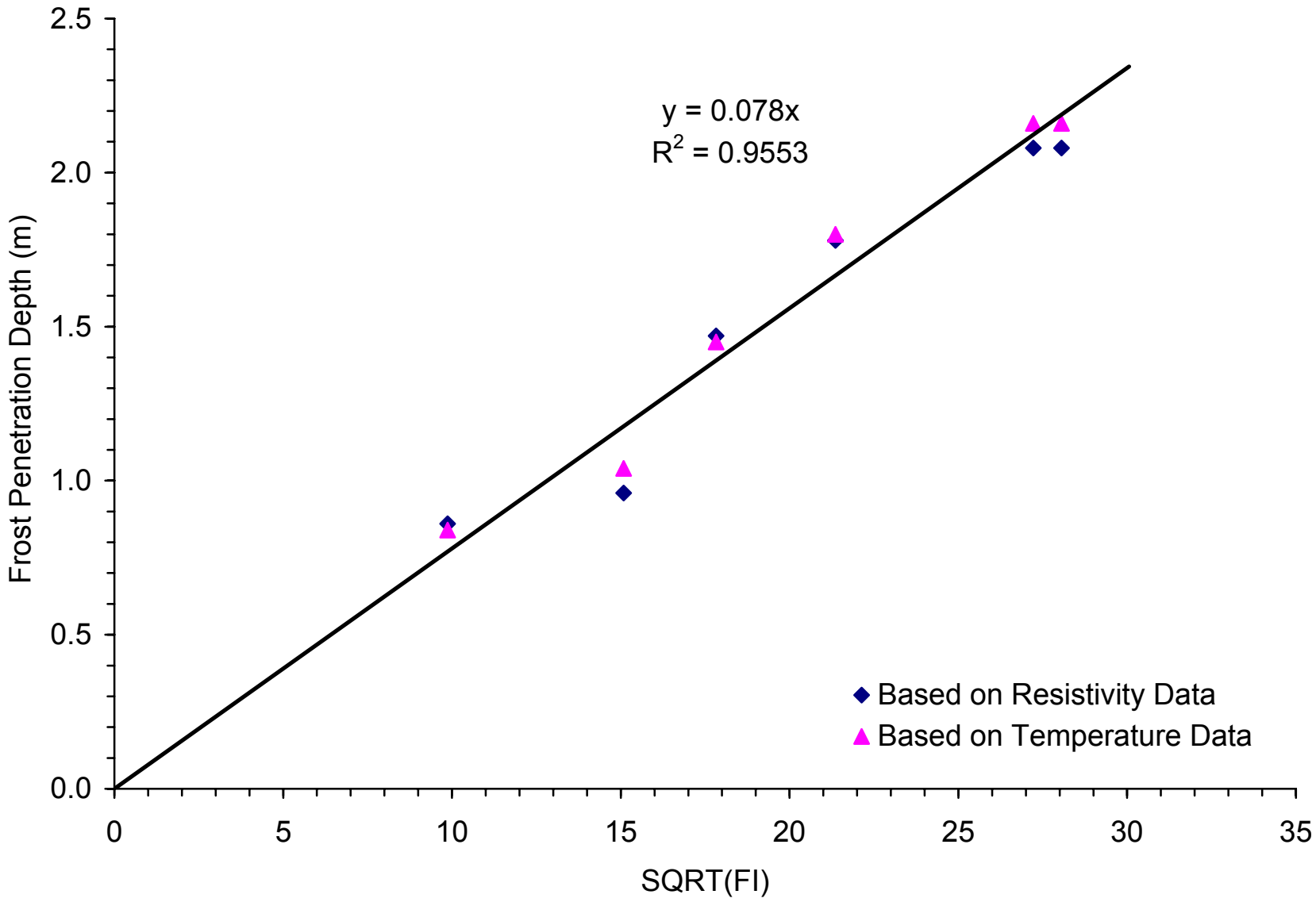

Figure D-4. Freeze Depth Model for Site 27-1028

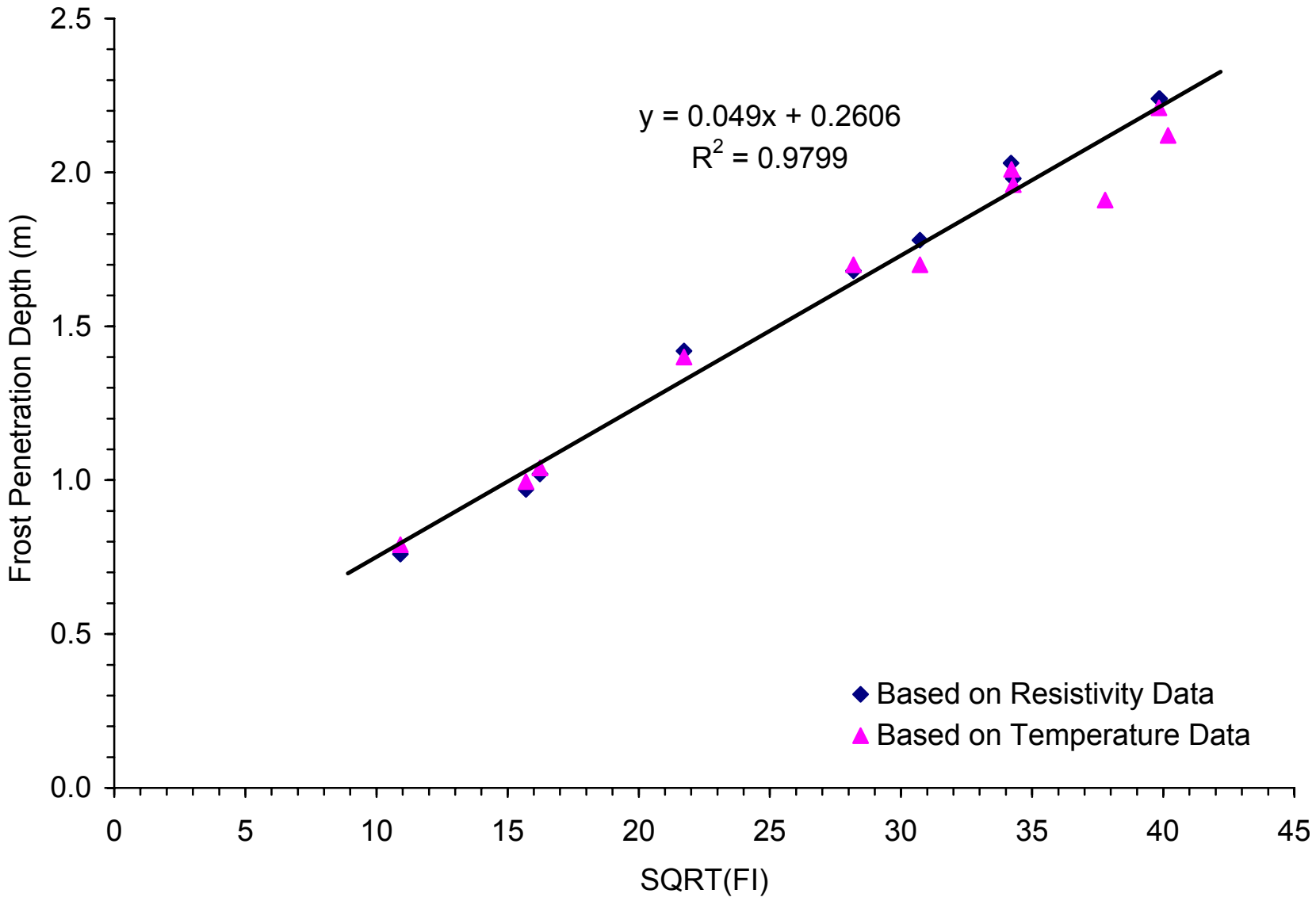

Figure D-5. Freeze Depth Model for Site 27-4040

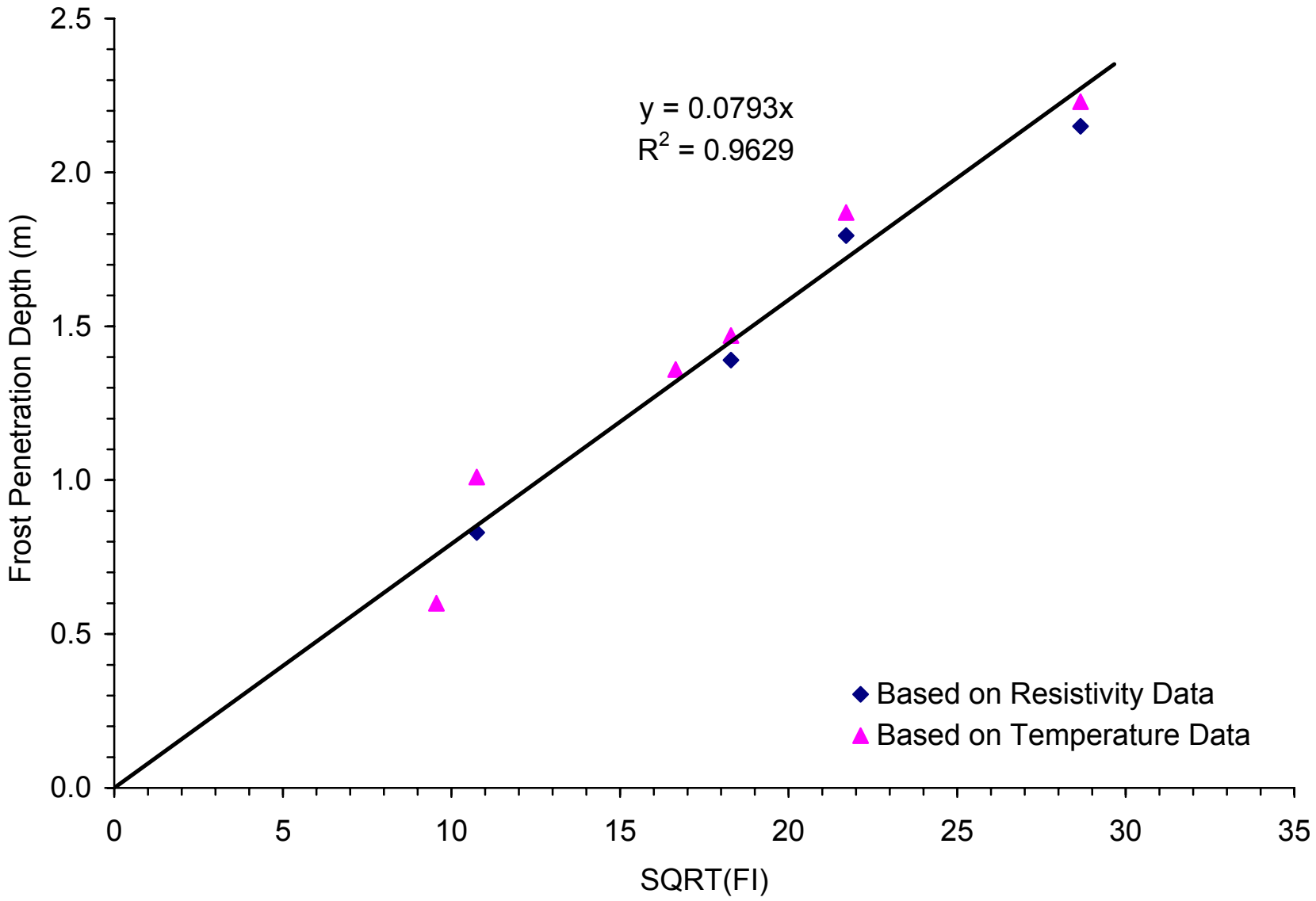

Figure D-6. Freeze Depth Model for Site 27-6251

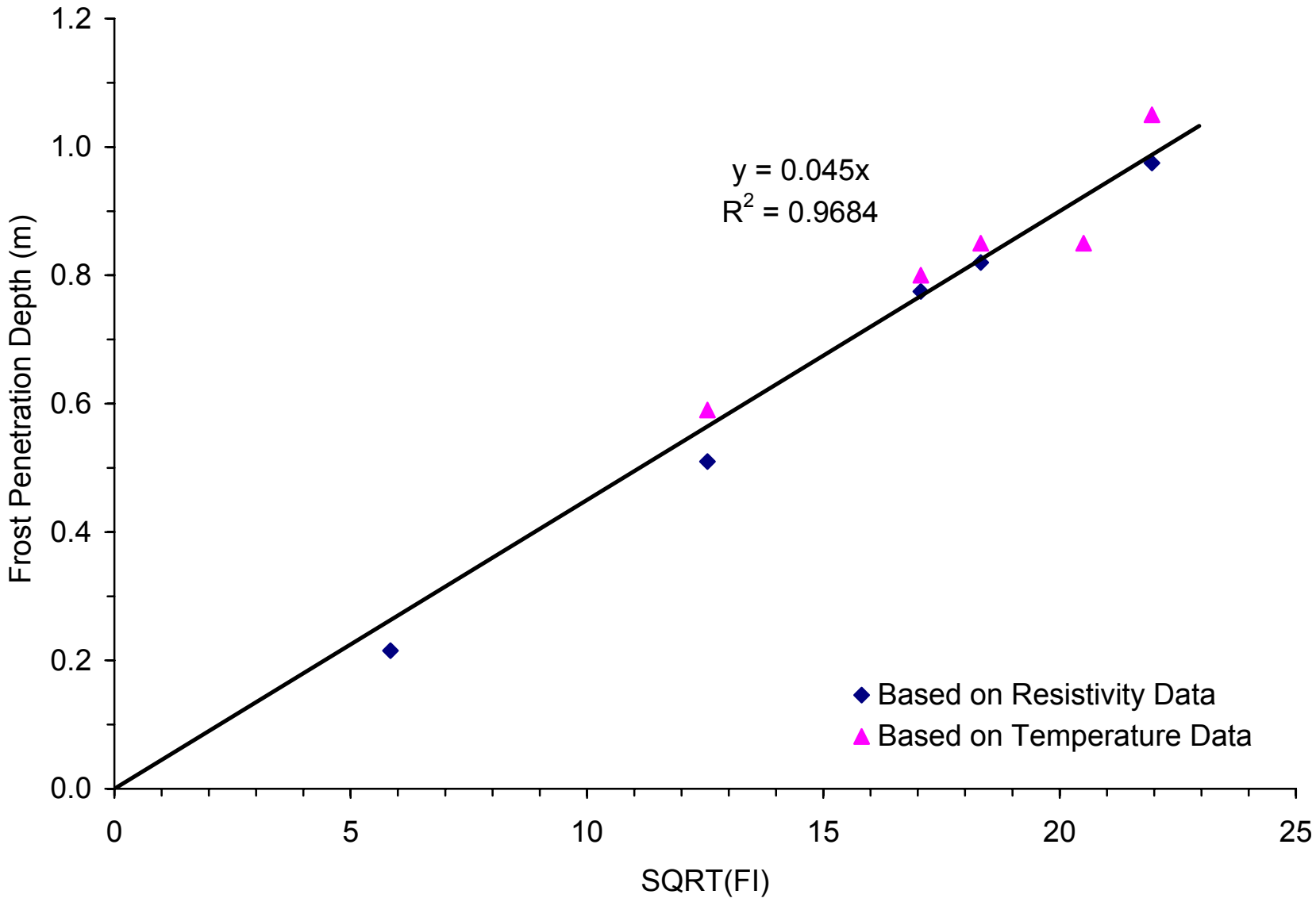

Figure D-7. Freeze Depth Model for Site 30-8129

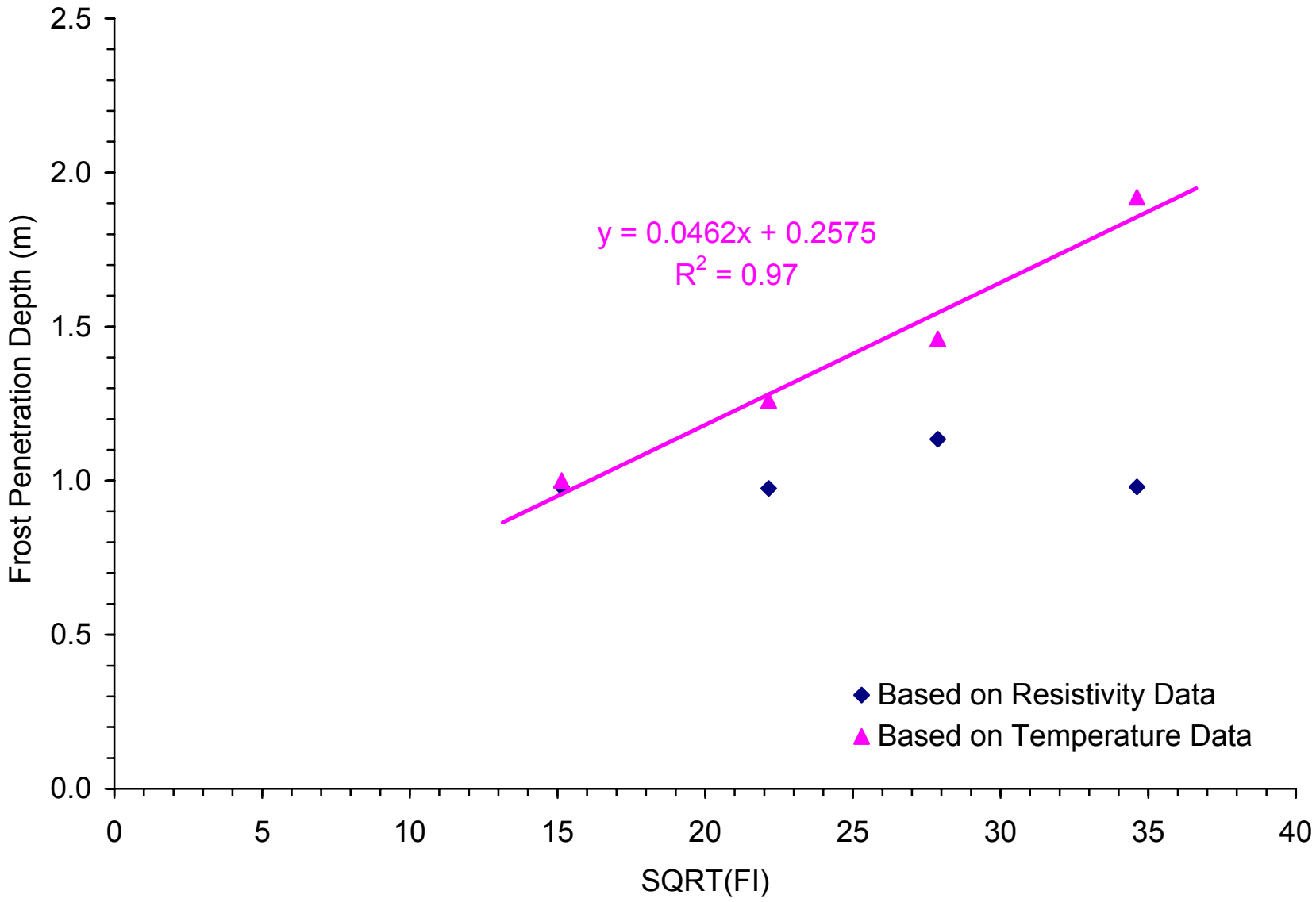

Figure D-8. Freeze Depth Model for Site 46-0804

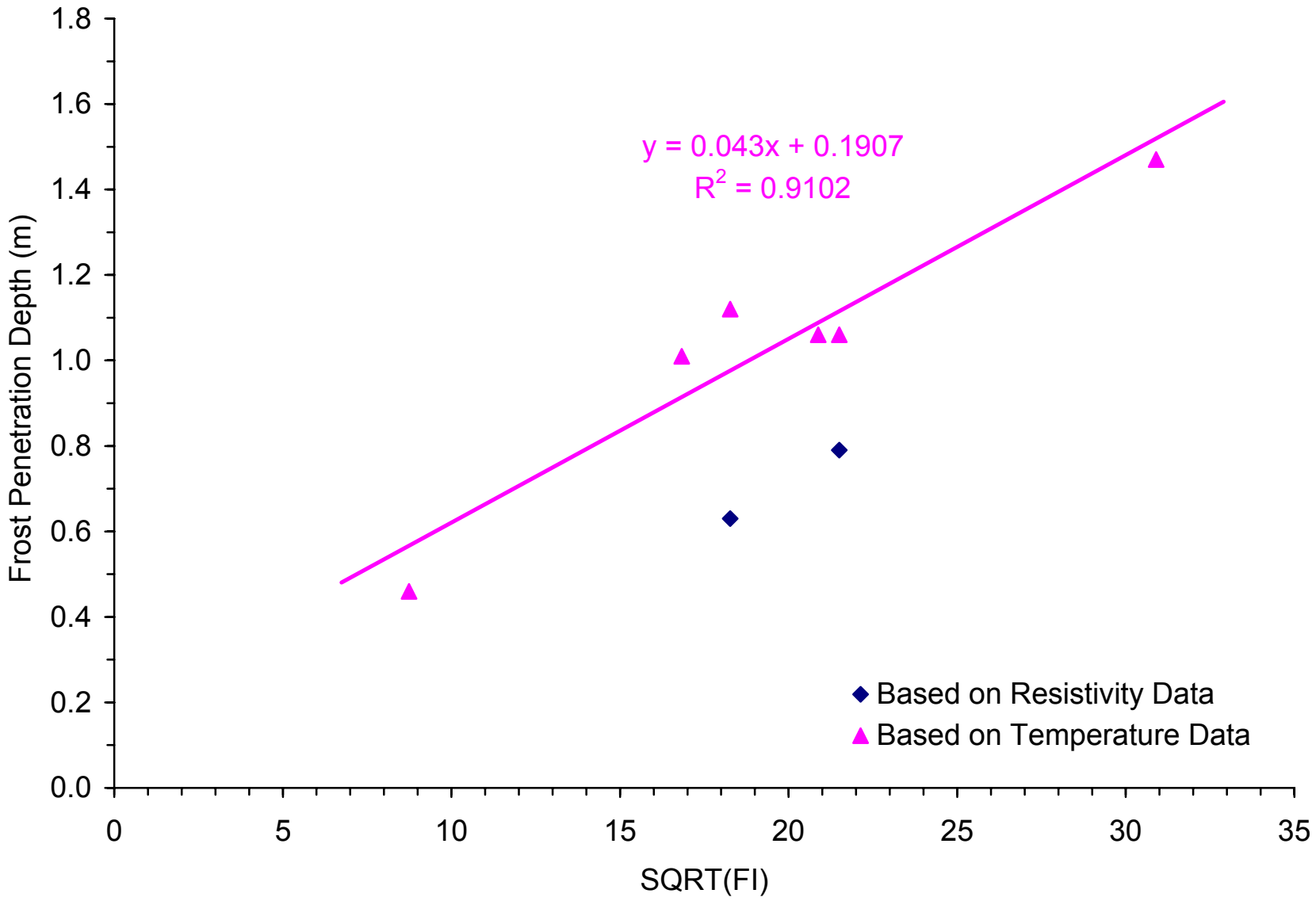

Figure D-9. Freeze Depth Model for Site 50-1002

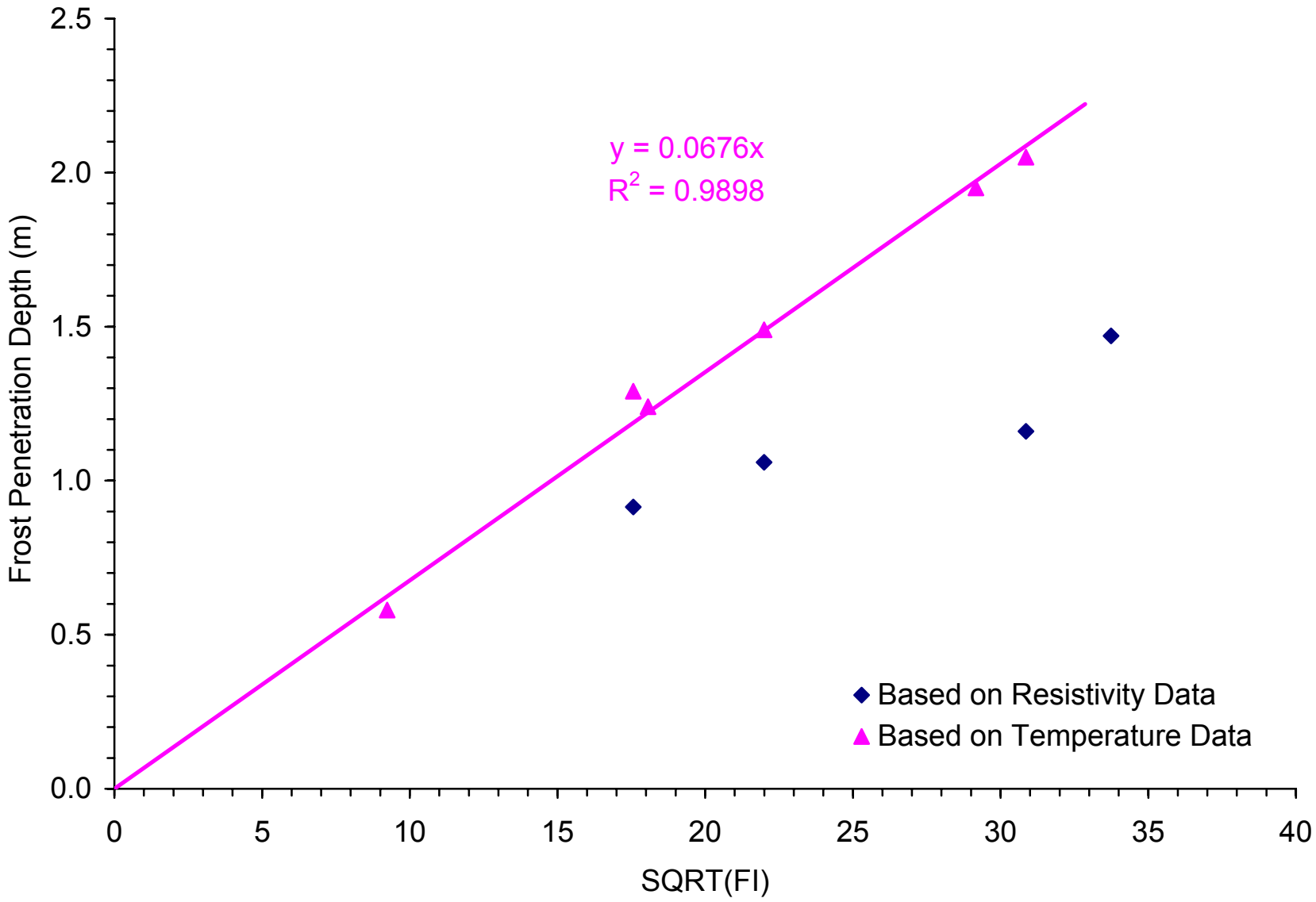

Figure D-10. Freeze Depth Model for Site 83-1801

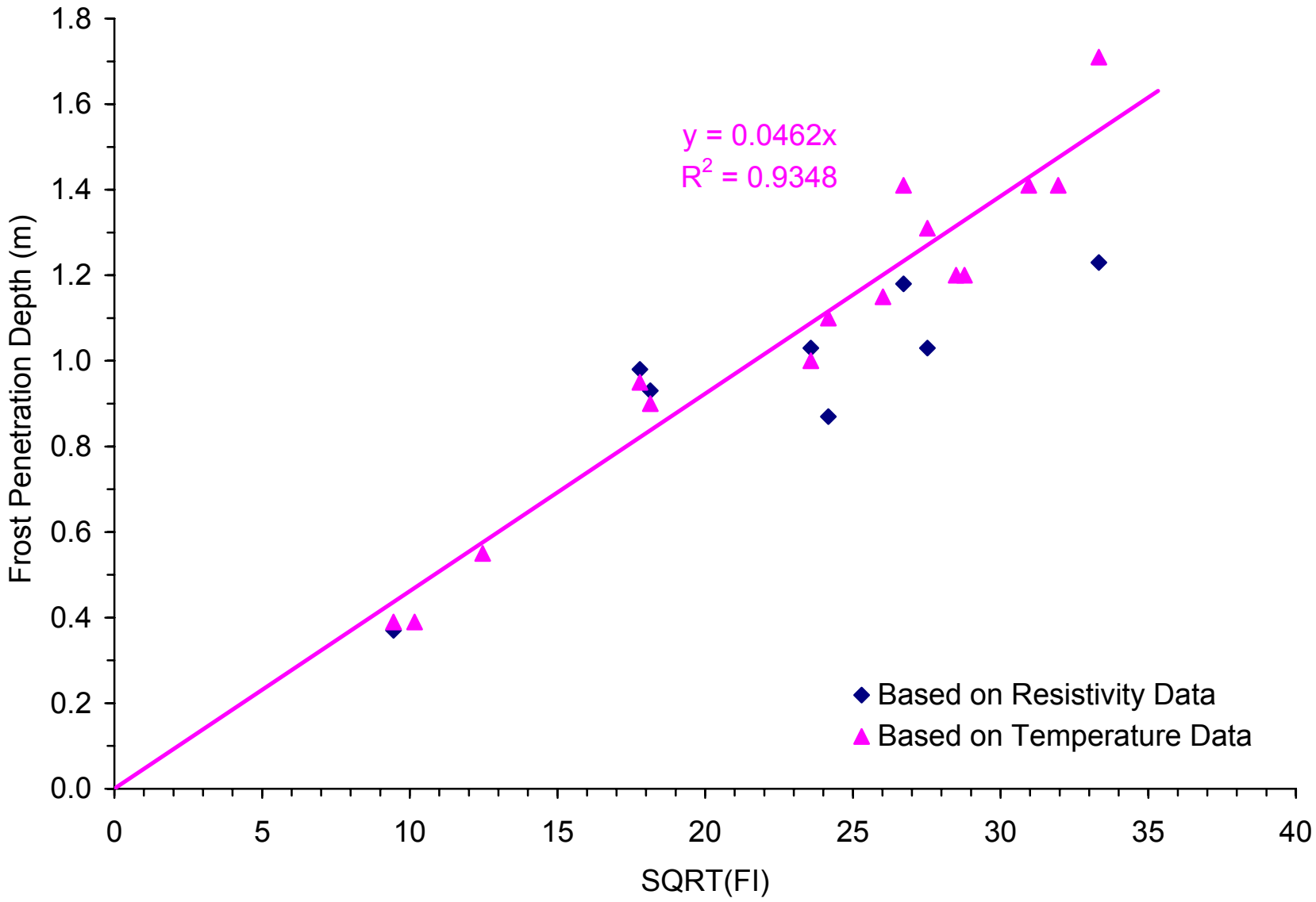

Figure D-11. Freeze Depth Model for Site 87-1622

APPENDIX E

THAW DEPTH MODELS

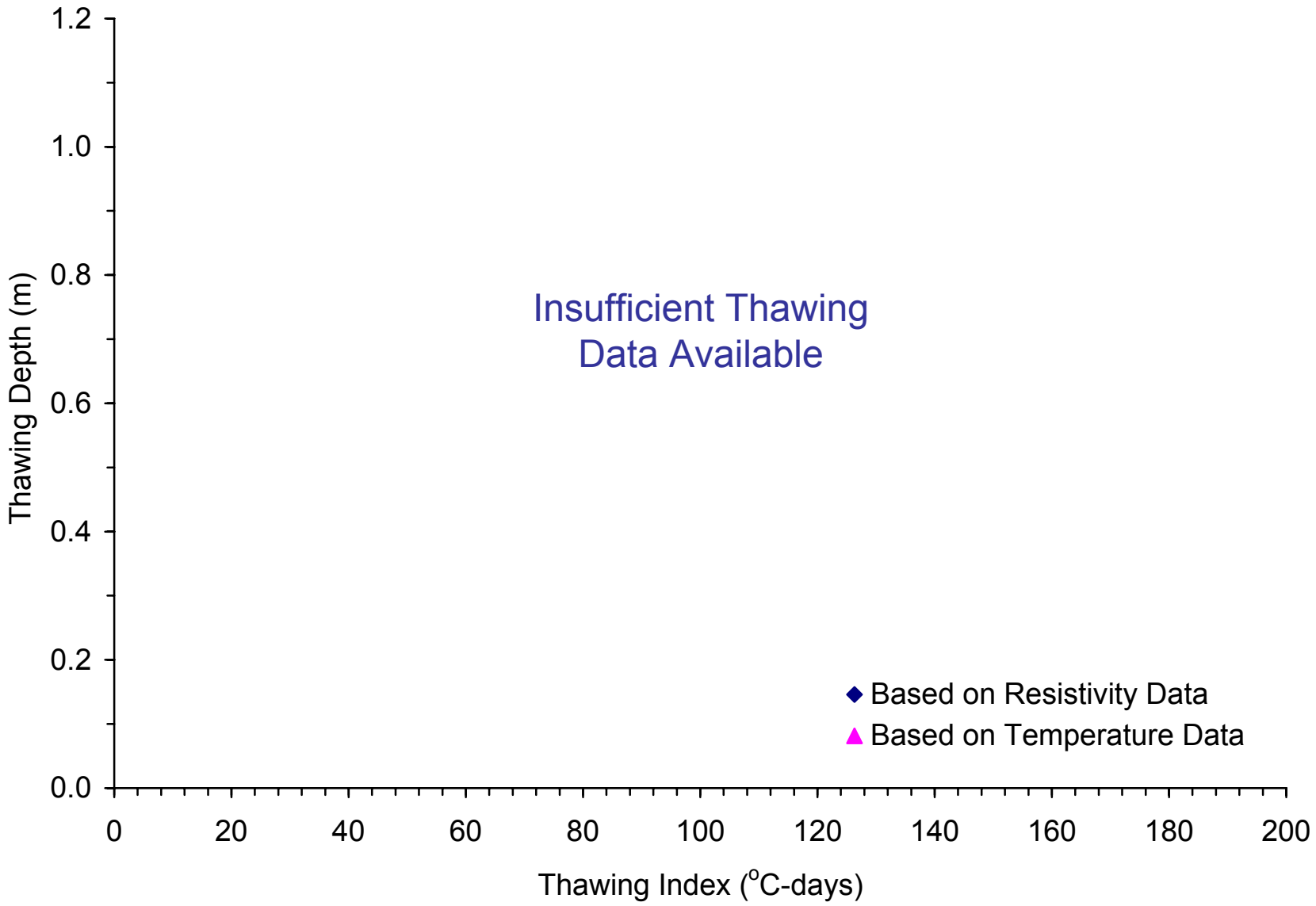

Figure E-1. Thaw Depth Model for Site 16-1010

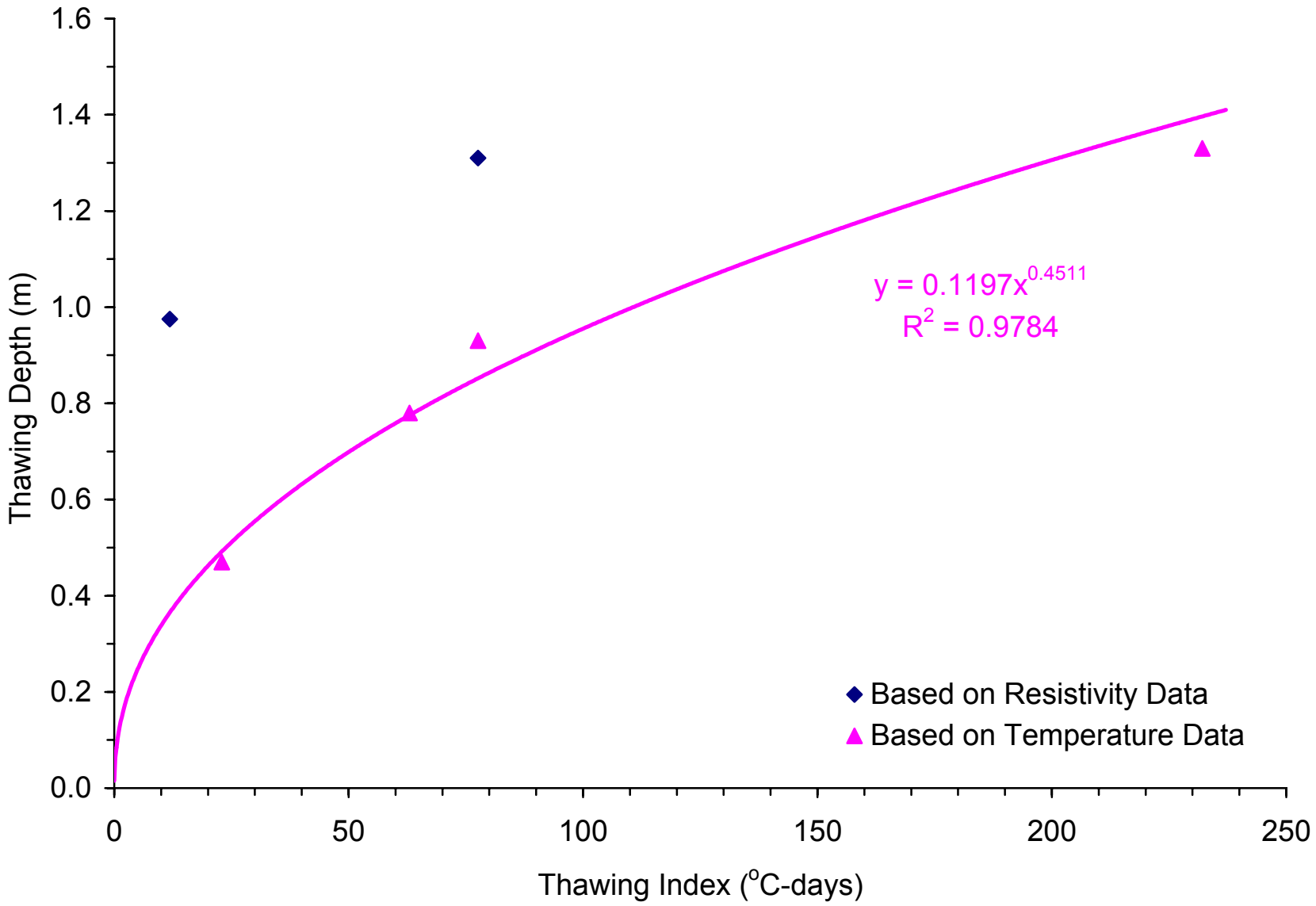

Figure E-2. Thaw Depth Model for Site 23-1026

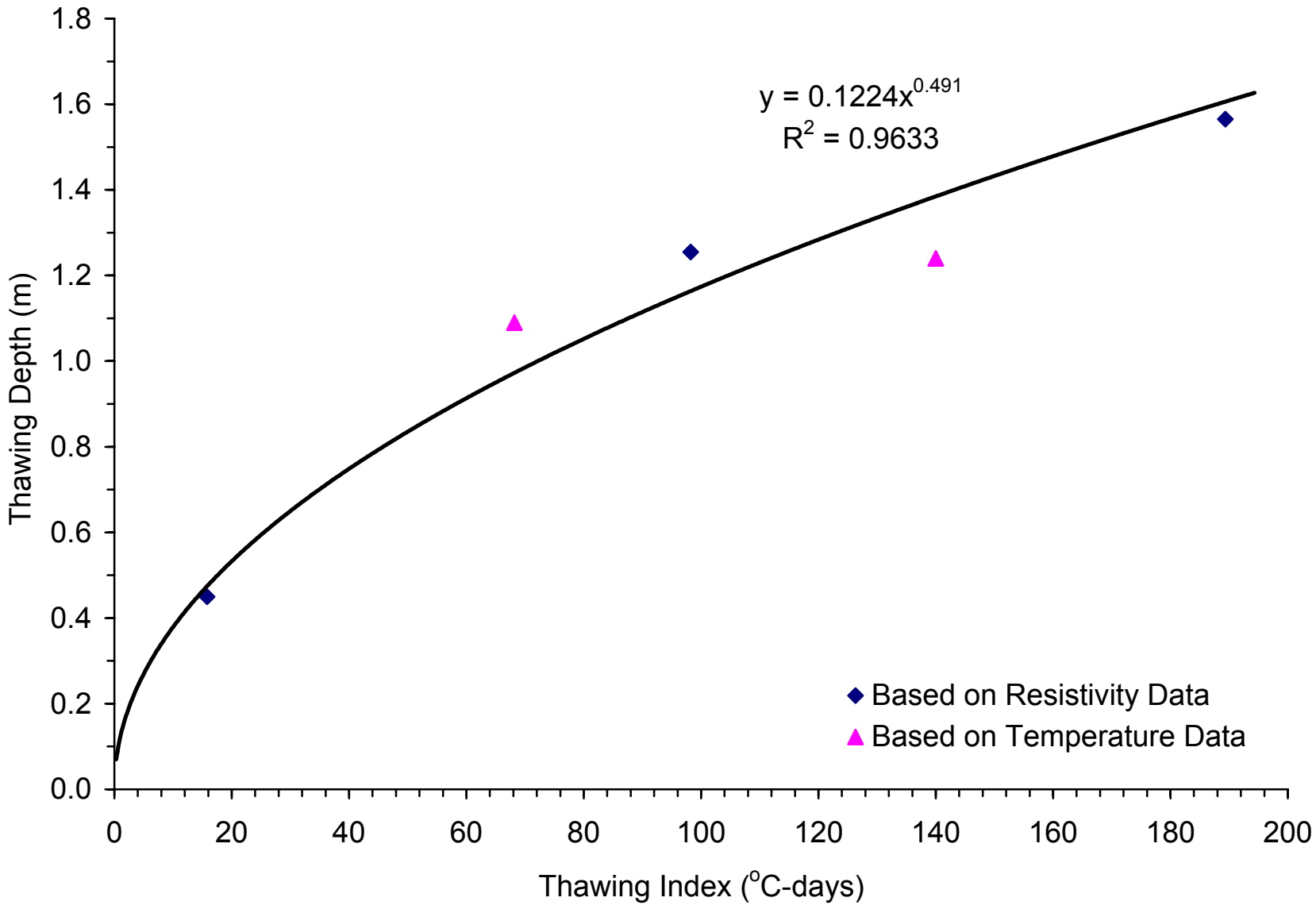

Figure E-3. Thaw Depth Model for Site 27-1018

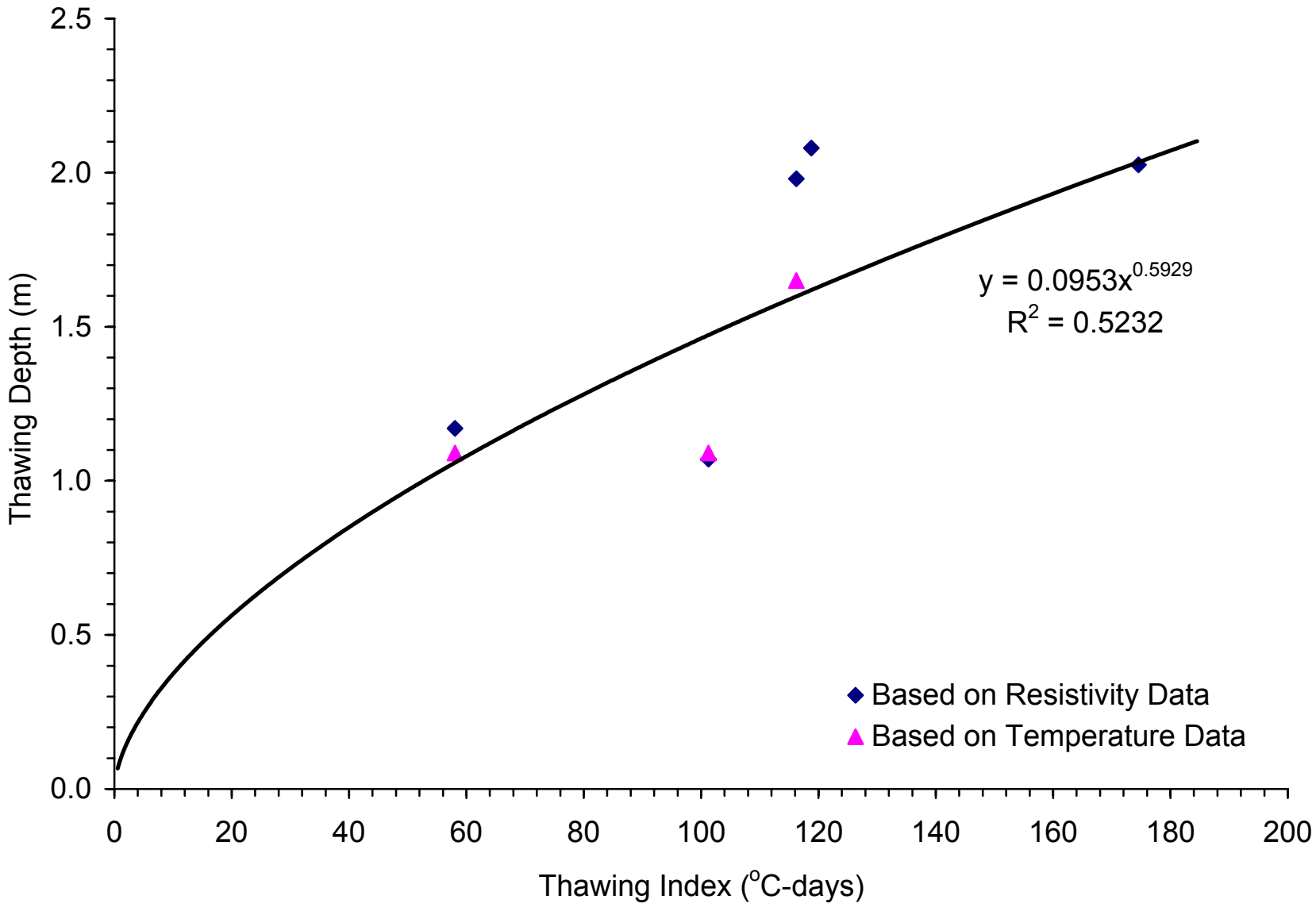

Figure E-4. Thaw Depth Model for Site 27-1028

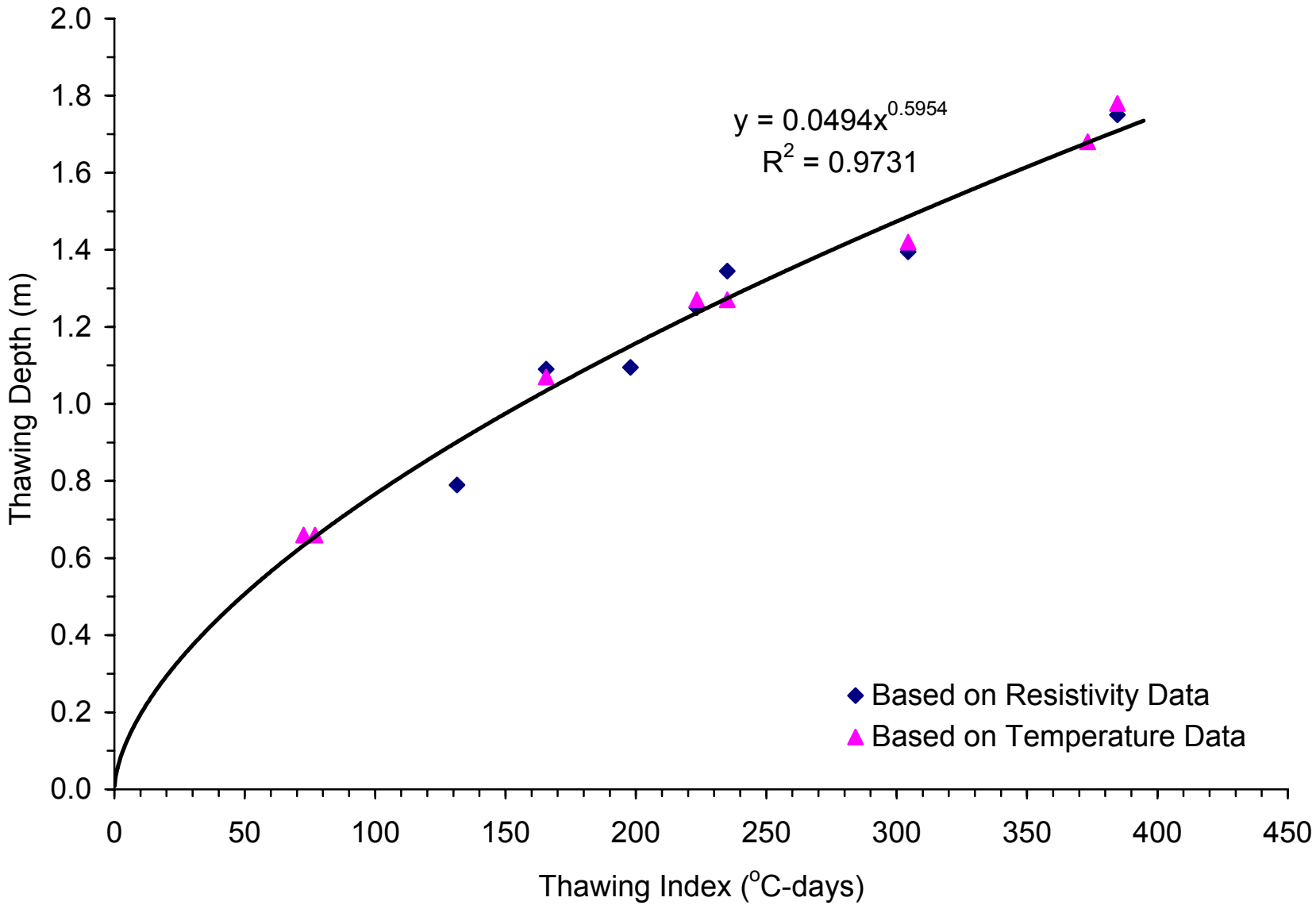

Figure E-5. Thaw Depth Model for Site 27-4040

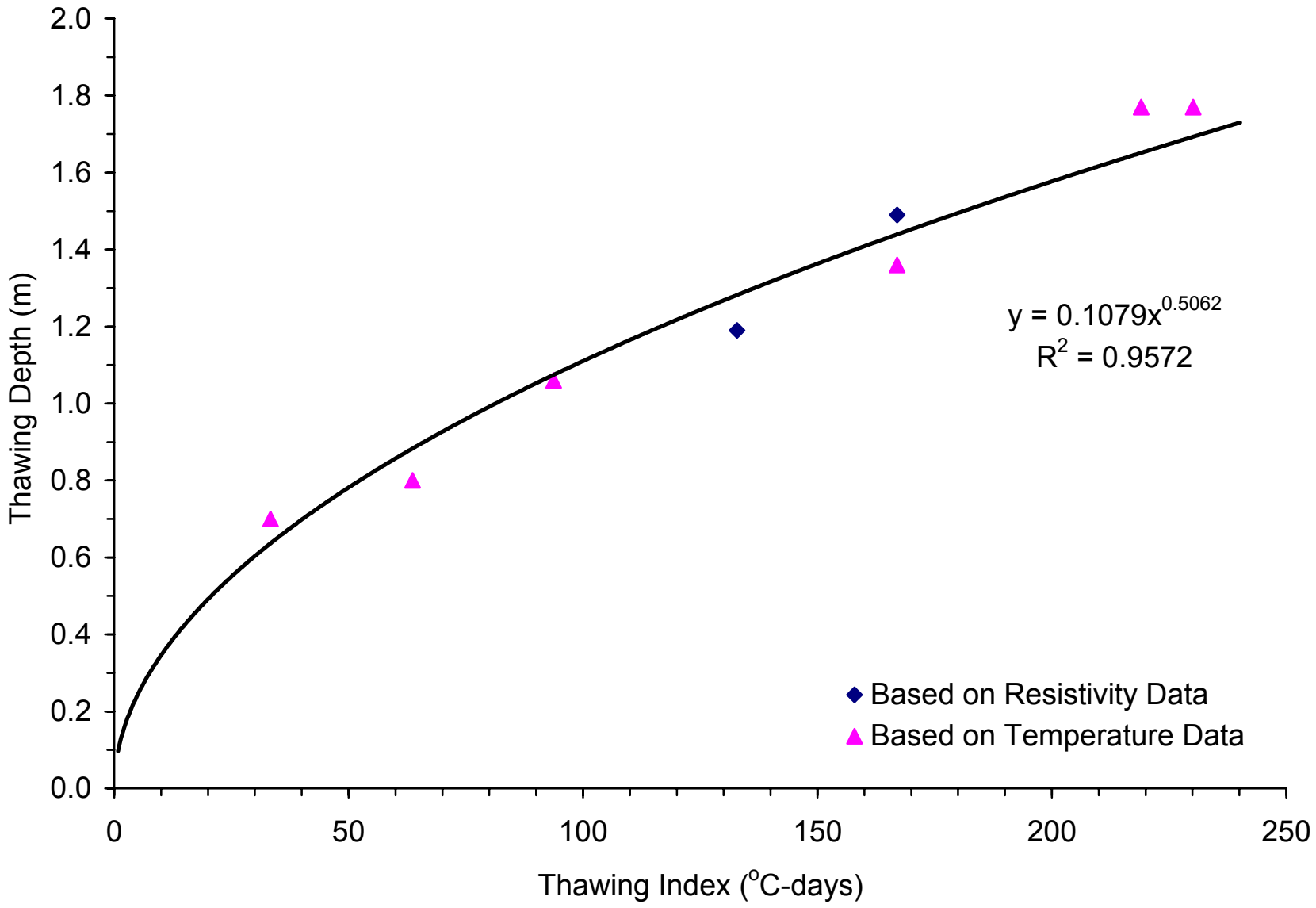

Figure E-6. Thaw Depth Model for Site 27-6251

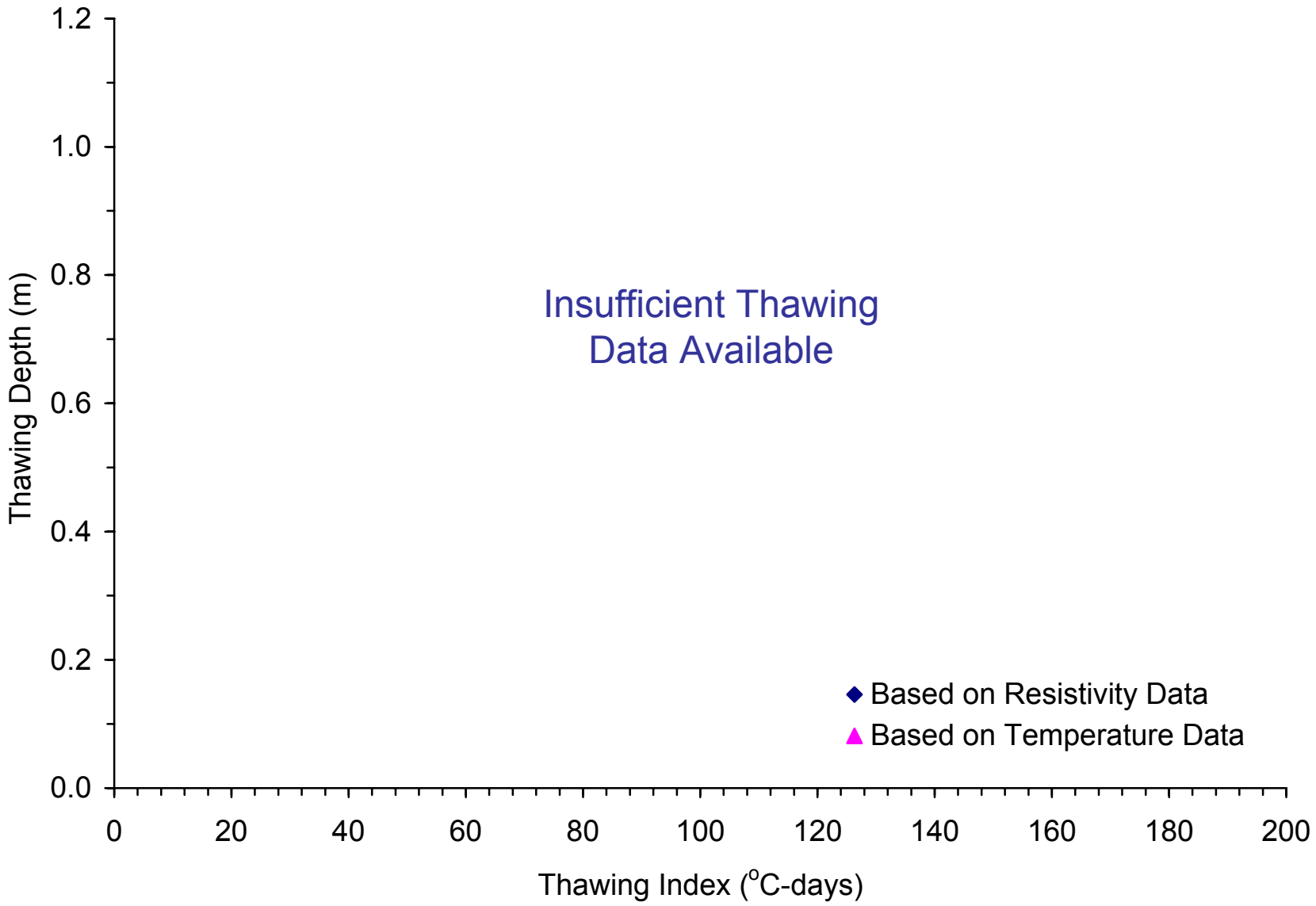

Figure E-7. Thaw Depth Model for Site 30-8129

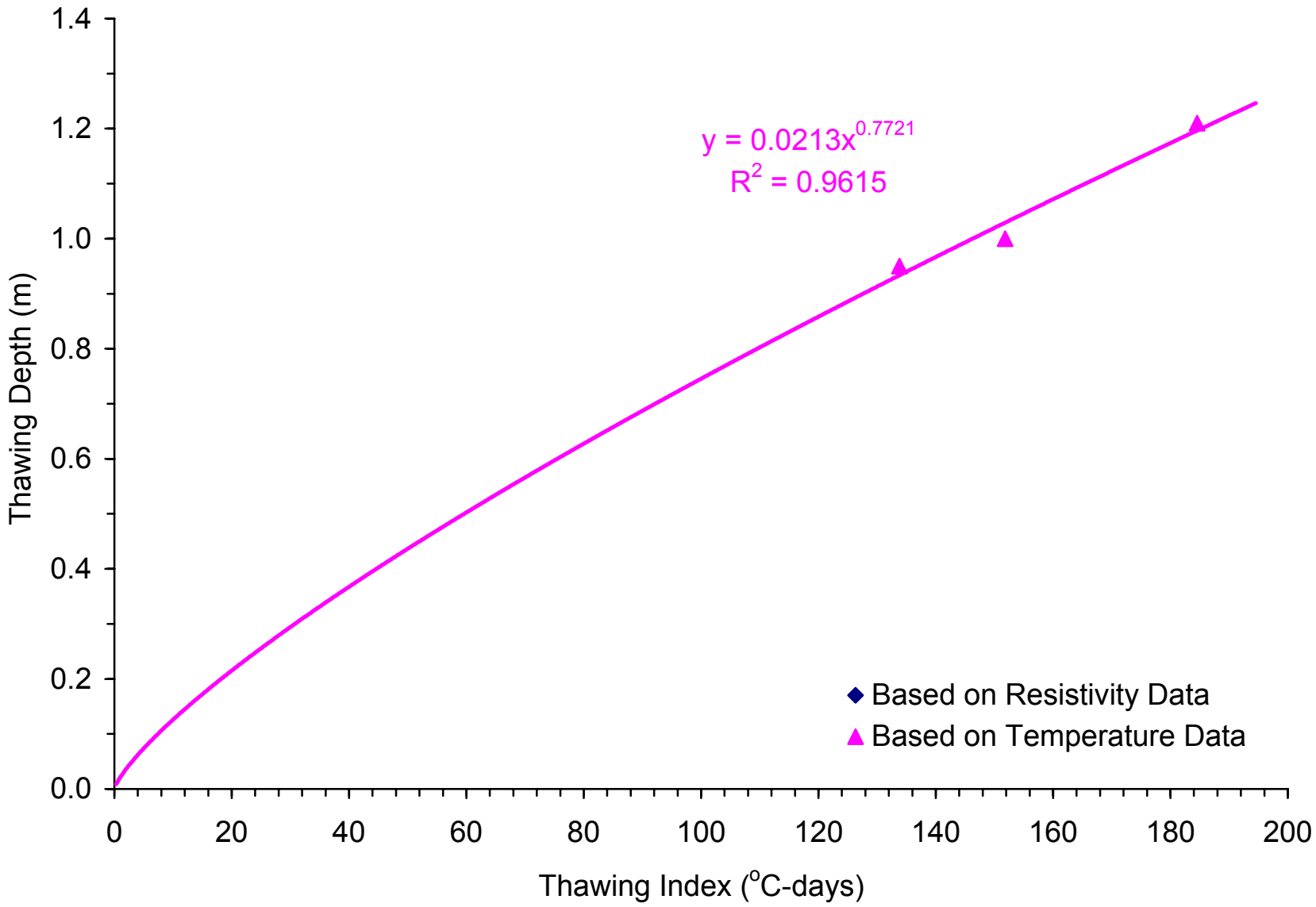

Figure E-8. Thaw Depth Model for Site 46-0804

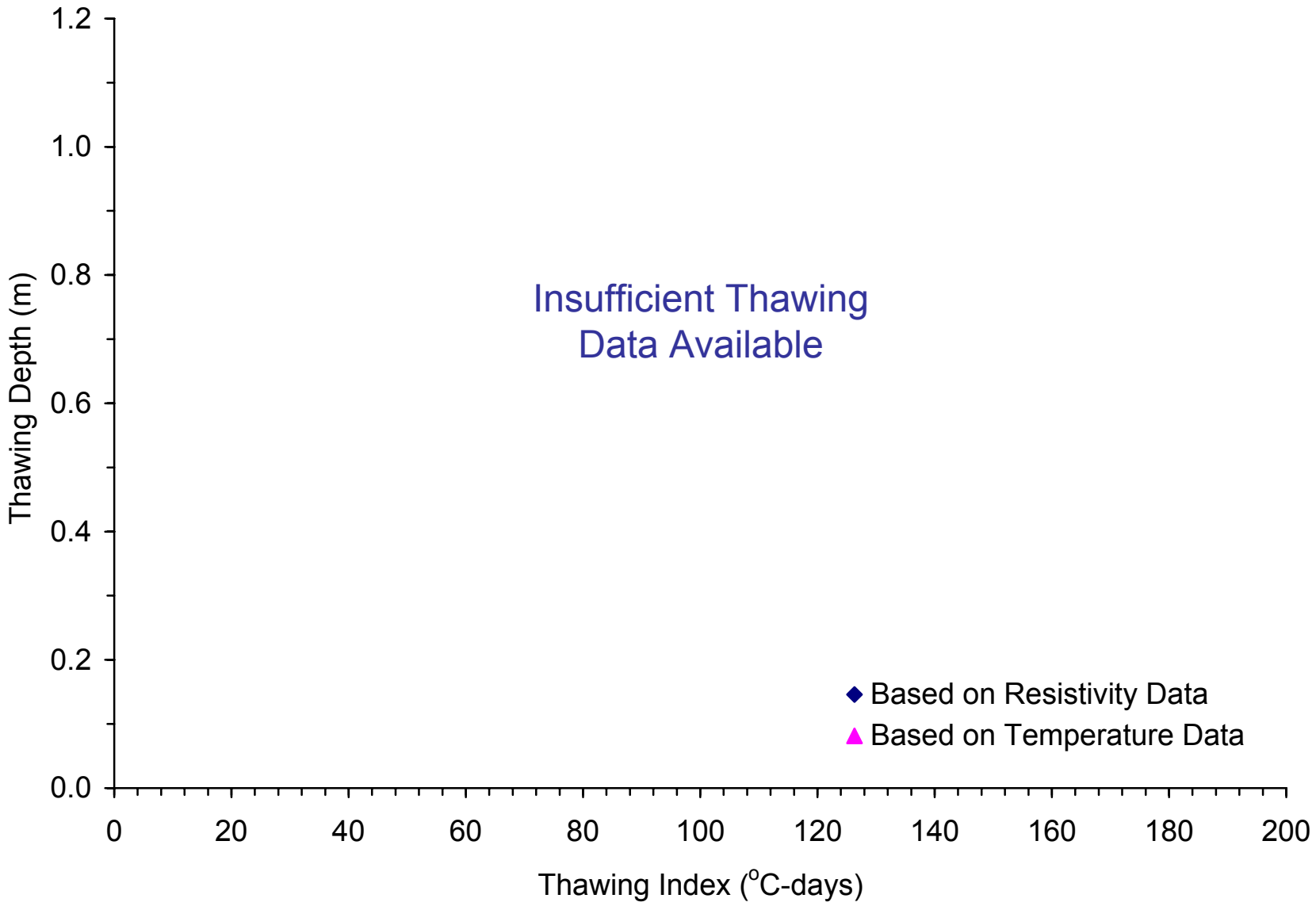

Figure E-9. Thaw Depth Model for Site 50-1002

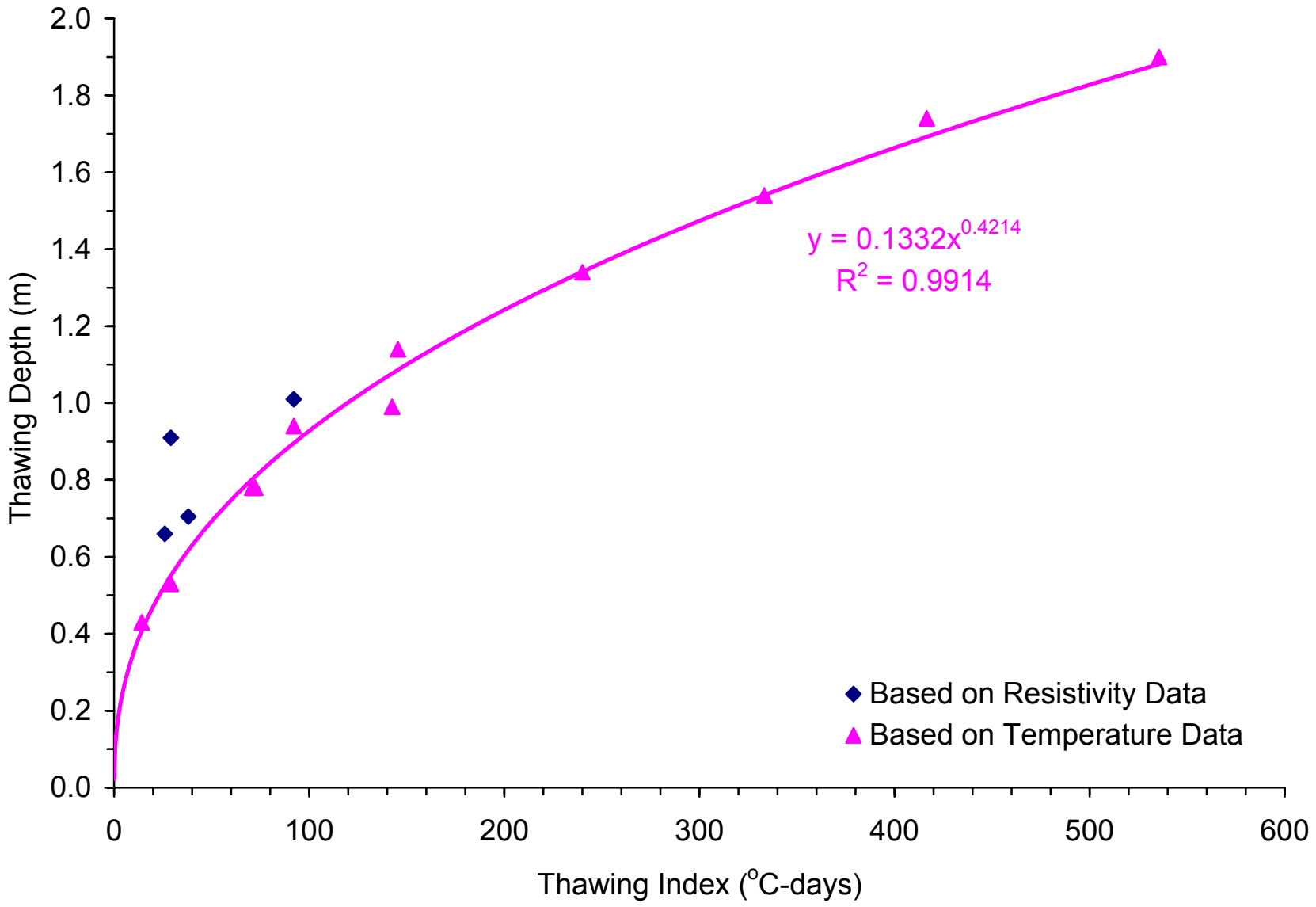

Figure E-10. Thaw Depth Model for Site 83-1801

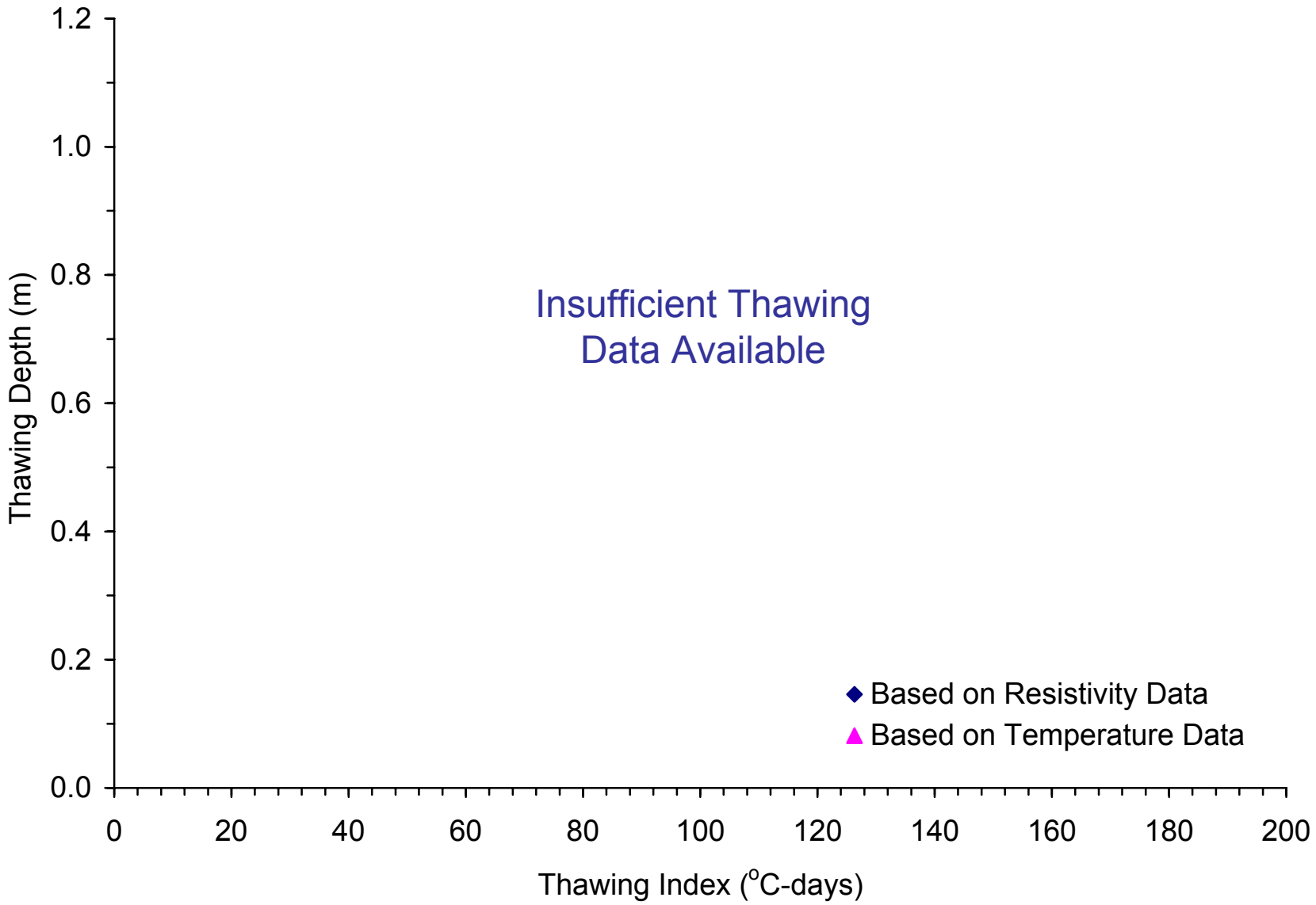

Figure E-11. Thaw Depth Model for Site 87-1622

APPENDIX F

FREEZE/THAW MILESTONES

Table F-1. Freeze/Thaw Milestones for Site 16-1010

Winter	Date of First Freeze	Date of Full Freeze	Date of First Thaw	Estimated Date of Full Thaw*	Earliest Thaw Date†	Latest Thaw Date‡
1993-94	10/29/1993	3/24/1994	2/24/1994	3/7/1994	2/26/1994	3/21/1994
1994-95	10/29/1994	3/29/1995	2/18/1995	2/27/1995	1/26/1995	2/21/1995
1995-96	10/31/1995	3/30/1996	2/6/1996	3/10/1996	*No Data Collected*	
1996-97	10/17/1996	4/12/1997	2/12/1997	3/12/1997	1/28/1997	2/25/1997

* Based on generic thaw model for silty sand subgrades

† Based on last date with some frozen soil measured

‡ Based on first date with no frozen soil measured

Table F-2. Freeze/Thaw Milestones for Site 23-1026

Winter	Date of First Freeze	Date of Full Freeze	Date of First Thaw	Estimated Date of Full Thaw*	Earliest Thaw Date†	Latest Thaw Date‡
1993-94	10/14/1993	4/2/1994	3/7/1994	4/14/1994	4/12/1994	5/2/1994
1994-95	11/23/1994	4/6/1995	3/6/1995	3/29/1995	3/21/1995	4/3/1995
1995-96	11/10/1995	4/9/1996	3/13/1996	4/16/1996	*No Data Collected*	
1996-97	10/30/1996	4/10/1997	3/20/1997	4/8/1997	3/25/1997	4/8/1997

* Based on site-specific thaw model

† Based on last date with some frozen soil measured

‡ Based on first date with no frozen soil measured

Table F-3. Freeze/Thaw Milestones for Site 27-1018

Winter	Date of First Freeze	Date of Full Freeze	Date of First Thaw	Estimated Date of Full Thaw*	Earliest Thaw Date†	Latest Thaw Date‡
1993-94	10/29/1993	4/6/1994	3/2/1994	4/20/1994	4/5/1994	4/25/1994
1994-95	11/19/1994	4/4/1995	3/10/1995	4/10/1995	3/21/1995	3/31/1995
1995-96	11/2/1995	4/13/1996	3/11/1996	4/29/1996	*No Data Collected*	
1996-97	10/30/1996	4/11/1997	3/9/1997	4/17/1997	4/8/1997	4/21/1997

* Based on site-specific thaw model

† Based on last date with some frozen soil measured

‡ Based on first date with no frozen soil measured

Table F-4. Freeze/Thaw Milestones for Site 27-1028

Winter	Date of First Freeze	Date of Full Freeze	Date of First Thaw	Estimated Date of Full Thaw*	Earliest Thaw Date†	Latest Thaw Date‡
1993-94	10/29/1993	4/5/1994	3/12/1994	5/7/1994	4/6/1994	4/25/1994
1994-95	10/25/1994	4/11/1995	3/10/1995	4/28/1995	4/5/1995	4/18/1995
1995-96	11/2/1995	4/7/1996	3/11/1996	5/18/1996	*No Data Collected*	
1996-97	10/30/1996	4/16/1997	3/18/1997	5/14/1997	4/11/1997	4/24/1997

* Based on generic thaw model for sand subgrades

† Based on last date with some frozen soil measured

‡ Based on first date with no frozen soil measured

Table F-5. Freeze/Thaw Milestones for Site 27-4040

Winter	Date of First Freeze	Date of Full Freeze	Date of First Thaw	Estimated Date of Full Thaw*	Earliest Thaw Date†	Latest Thaw Date‡
1993-94	10/21/1993	4/6/1994	3/2/1994	5/13/1994	5/5/1994	5/18/1994
1994-95	11/3/1994	4/11/1995	3/10/1995	5/4/1995	4/29/1995	5/11/1995
1995-96	10/22/1995	4/13/1996	3/11/1996	5/22/1996	*No Data Collected*	
1996-97	10/30/1996	4/12/1997	3/17/1997	5/15/1997	5/7/1997	5/28/1997

* Based on site-specific thaw depth model

† Based on last date with some frozen soil measured

‡ Based on first date with no frozen soil measured

Table F-6. Freeze/Thaw Milestones for Site 27-6251

Winter	Date of First Freeze	Date of Full Freeze	Date of First Thaw	Estimated Date of Full Thaw*	Earliest Thaw Date†	Latest Thaw Date‡
1993-94	10/2/1993	4/5/1994	3/2/1994	5/20/1994	4/14/1994	5/3/1994
1994-95	11/3/1994	4/11/1995	3/10/1995	5/12/1995	4/14/1995	4/28/1995
1995-96	10/30/1995	4/27/1996	4/8/1996	6/7/1996	*No Data Collected*	
1996-97	10/30/1996	4/12/1997	3/19/1997	5/30/1997	4/10/1997	4/23/1997

* Based on site-specific thaw depth model

† Based on last date with some frozen soil measured

‡ Based on first date with no frozen soil measured

Table F-7. Freeze/Thaw Milestones for Site 30-8129

Winter	Date of First Freeze	Date of Full Freeze	Date of First Thaw	Estimated Date of Full Thaw*	Earliest Thaw Date†	Latest Thaw Date‡
1993-94	10/8/1993	4/28/1994	2/27/1994	3/17/1994	2/23/1994	3/17/1994
1994-95	11/2/1994	4/10/1995	2/16/1995	3/30/1995	3/8/1995	3/23/1995
1995-96	10/23/1995	4/1/1996	2/6/1996	4/16/1996	*No Data Collected*	
1996-97	10/15/1996	3/16/1997	1/30/1997	3/28/1997	2/22/1997	3/12/1997

* Based on generic thaw model for clayey subgrades

† Based on last date with some frozen soil measured

‡ Based on first date with no frozen soil measured

Table F-8. Freeze/Thaw Milestones for Site 46-0804

Winter	Date of First Freeze	Date of Full Freeze	Date of First Thaw	Estimated Date of Full Thaw*	Earliest Thaw Date†	Latest Thaw Date‡
1993-94	*No Data Collected At This Site*					
1994-95	11/18/1994	4/11/1995	3/10/1995	4/21/1995	3/24/1995	4/6/1995
1995-96	10/30/1995	4/5/1996	3/10/1996	5/3/1996	*No Data Collected*	
1996-97	10/30/1996	4/13/1997	3/8/1997	5/1/1997	4/15/1997	4/29/1997

* Based on site-specific thaw model

† Based on last date with some frozen soil measured

‡ Based on first date with no frozen soil measured

Table F-9. Freeze/Thaw Milestones for Site 50-1002

Winter	Date of First Freeze	Date of Full Freeze	Date of First Thaw	Estimated Date of Full Thaw*	Earliest Thaw Date†	Latest Thaw Date‡
1993-94	11/24/1993	4/8/1994	3/7/1994	4/6/1994	3/3/1994	3/22/1994
1994-95	11/23/1994	4/8/1995	3/6/1995	3/20/1995	2/16/1995	3/17/1995
1995-96	11/9/1995	3/28/1996	2/20/1996	3/31/1996	*No Data Collected*	
1996-97	11/12/1996	4/10/1997	2/18/1997	4/6/1997	2/14/1997	3/13/1997

* Based on generic thaw model for sand subgrades

† Based on last date with some frozen soil measured

‡ Based on first date with no frozen soil measured

Table F-10. Freeze/Thaw Milestones for Site 83-1801

Winter	Date of First Freeze	Date of Full Freeze	Date of First Thaw	Estimated Date of Full Thaw*	Earliest Thaw Date†	Latest Thaw Date‡
1993-94	10/2/1993	4/6/1994	3/1/1994	7/2/1994	5/13/1994	6/17/1994
1994-95	10/31/1994	4/10/1995	3/11/1995	6/25/1995	5/17/1995	6/21/1995
1995-96	10/29/1995	4/13/1996	4/7/1996	8/2/1996	*No Data Collected*	
1996-97	10/22/1996	4/15/1997	3/19/1997	7/22/1997	5/2/1997	6/2/1997

* Based on site-specific thaw depth model

† Based on last date with some frozen soil measured

‡ Based on first date with no frozen soil measured

Table F-11. Freeze/Thaw Milestones for Site 87-1622

Winter	Date of First Freeze	Date of Full Freeze	Date of First Thaw	Estimated Date of Full Thaw*	Earliest Thaw Date†	Latest Thaw Date‡
1993-94	11/1/1993	4/7/1994	3/20/1994	5/8/1994	4/7/1994	4/25/1995
1994-95	11/10/1994	4/7/1995	3/11/1995	4/17/1995	4/7/1995	4/20/1995
1995-96	11/4/1995	4/11/1996	3/12/1996	5/16/1996	*No Data Collected*	
1996-97	11/1/1996	4/11/1997	3/25/1997	5/6/1997	4/4/1997	5/1/1997

* Based on generic thaw model for silty sand subgrades

† Based on last date with some frozen soil measured

‡ Based on first date with no frozen soil measured

APPENDIX G

THAW DURATION ESTIMATES

Table G-1. Thaw Duration Estimates for Site 16-1010

Winter	Maximum Freezing Index (°C-days)	Maximum Freeze Depth (m)	Required Thawing Index* (°C-days)	TI : FI Ratio	Estimated Thaw Duration† (days)	Calculated Thaw Duration‡ (days)
1993-94	659	0.80	60	0.09	11	37
1994-95	609	0.78	57	0.09	9	36
1995-96	680	0.80	62	0.09	33	37
1996-97	585	0.77	55	0.09	28	36

* Calculated by setting the thaw depth model equal to the maximum freeze depth

† Calculated from the estimated date of full thaw and the date of first thaw

‡ Calculated from the formula $d = 0.018\ FI + 25$

Table G-2. Thaw Duration Estimates for Site 23-1026

Winter	Maximum Freezing Index (°C-days)	Maximum Freeze Depth (m)	Required Thawing Index* (°C-days)	TI : FI Ratio	Estimated Thaw Duration† (days)	Calculated Thaw Duration‡ (days)
1993-94	1030	1.77	271	0.26	38	44
1994-95	711	1.16	130	0.18	23	38
1995-96	1046	1.67	246	0.24	34	44
1996-97	805	1.18	134	0.17	19	39

* Calculated by setting the thaw depth model equal to the maximum freeze depth

† Calculated from the estimated date of full thaw and the date of first thaw

‡ Calculated from the formula $d = 0.018\ FI + 25$

Table G-3. Thaw Duration Estimates for Site 27-1018

Winter	Maximum Freezing Index (°C-days)	Maximum Freeze Depth (m)	Required Thawing Index* (°C-days)	TI : FI Ratio	Estimated Thaw Duration† (days)	Calculated Thaw Duration‡ (days)
1993-94	1487	2.18	351	0.24	49	52
1994-95	997	1.84	249	0.25	31	43
1995-96	1544	2.21	363	0.24	49	53
1996-97	1364	1.87	257	0.19	39	50

* Calculated by setting the thaw depth model equal to the maximum freeze depth

† Calculated from the estimated date of full thaw and the date of first thaw

‡ Calculated from the formula d = 0.018 FI + 25

Table G-4. Thaw Duration Estimates for Site 27-1028

Winter	Maximum Freezing Index (°C-days)	Maximum Freeze Depth (m)	Required Thawing Index* (°C-days)	TI : FI Ratio	Estimated Thaw Duration† (days)	Calculated Thaw Duration‡ (days)
1993-94	1678	3.20	549	0.33	56	55
1994-95	1222	2.73	407	0.33	49	47
1995-96	1839	3.34	598	0.33	68	58
1996-97	1830	3.34	595	0.33	57	58

* Calculated by setting the thaw depth model equal to the maximum freeze depth

† Calculated from the estimated date of full thaw and the date of first thaw

‡ Calculated from the formula $d = 0.018\ FI + 25$

Table G-5. Thaw Duration Estimates for Site 27-4040

Winter	Maximum Freezing Index (^{o}C-days)	Maximum Freeze Depth (m)	Required Thawing Index* (^{o}C-days)	TI : FI Ratio	Estimated Thaw Duration† (days)	Calculated Thaw Duration‡ (days)
1993-94	1661	2.34	651	0.39	72	55
1994-95	1209	1.99	498	0.41	55	47
1995-96	1864	2.48	717	0.38	72	59
1996-97	1635	2.32	642	0.39	59	54

* Calculated by setting the thaw depth model equal to the maximum freeze depth

† Calculated from the estimated date of full thaw and the date of first thaw

‡ Calculated from the formula d = 0.018 FI + 25

Table G-6. Thaw Duration Estimates for Site 27-6251

Winter	Maximum Freezing Index (^{o}C-days)	Maximum Freeze Depth (m)	Required Thawing Index* (^{o}C-days)	TI : FI Ratio	Estimated Thaw Duration† (days)	Calculated Thaw Duration‡ (days)
1993-94	1684	3.25	837	0.50	79	55
1994-95	1270	2.83	633	0.50	63	48
1995-96	1991	3.54	987	0.50	60	61
1996-97	1827	3.39	907	0.50	72	58

* Calculated by setting the thaw depth model equal to the maximum freeze depth

† Calculated from the estimated date of full thaw and the date of first thaw

‡ Calculated from the formula d = 0.018 FI + 25

Table G-7. Thaw Duration Estimates for Site 30-8129

Winter	Maximum Freezing Index (°C-days)	Maximum Freeze Depth (m)	Required Thawing Index* (°C-days)	TI : FI Ratio	Estimated Thaw Duration† (days)	Calculated Thaw Duration‡ (days)
1993-94	554	1.06	169	0.31	18	35
1994-95	581	1.08	177	0.30	42	35
1995-96	861	1.32	247	0.29	70	41
1996-97	854	1.32	245	0.29	57	40

* Calculated by setting the thaw depth model equal to the maximum freeze depth

† Calculated from the estimated date of full thaw and the date of first thaw

‡ Calculated from the formula d = 0.018 FI + 25

Table G-8. Thaw Duration Estimates for Site 46-0804

Winter	Maximum Freezing Index (^{o}C-days)	Maximum Freeze Depth (m)	Required Thawing Index* (^{o}C-days)	TI : FI Ratio	Estimated Thaw Duration† (days)	Calculated Thaw Duration‡ (days)
1993-94	*No Data Collected At This Site*					
1994-95	1009	1.77	306	0.30	42	43
1995-96	1249	1.97	352	0.28	54	47
1996-97	1474	2.14	392	0.27	54	52

* Calculated by setting the thaw depth model equal to the maximum freeze depth

† Calculated from the estimated date of full thaw and the date of first thaw

‡ Calculated from the formula d = 0.018 FI + 25

Table G-9. Thaw Duration Estimates for Site 50-1002

Winter	Maximum Freezing Index (°C-days)	Maximum Freeze Depth (m)	Required Thawing Index* (°C-days)	TI : FI Ratio	Estimated Thaw Duration† (days)	Calculated Thaw Duration‡ (days)
1993-94	1026	1.57	144	0.14	30	43
1994-95	621	1.26	96	0.15	14	36
1995-96	787	1.40	116	0.15	40	39
1996-97	644	1.28	99	0.15	47	37

* Calculated by setting the thaw depth model equal to the maximum freeze depth

† Calculated from the estimated date of full thaw and the date of first thaw

‡ Calculated from the formula d = 0.018 FI + 25

Table G-10. Thaw Duration Estimates for Site 83-1801

Winter	Maximum Freezing Index (°C-days)	Maximum Freeze Depth (m)	Required Thawing Index* (°C-days)	TI : FI Ratio	Estimated Thaw Duration† (days)	Calculated Thaw Duration‡ (days)
1993-94	1866	2.92	1521	0.81	123	59
1994-95	1567	2.68	1236	0.79	106	53
1995-96	2333	3.27	1982	0.85	117	67
1996-97	2224	3.19	1873	0.84	125	65

* Calculated by setting the thaw depth model equal to the maximum freeze depth

† Calculated from the estimated date of full thaw and the date of first thaw

‡ Calculated from the formula $d = 0.018\ FI + 25$

Table G-11. Thaw Duration Estimates for Site 87-1622

Winter	Maximum Freezing Index (°C-days)	Maximum Freeze Depth (m)	Required Thawing Index* (°C-days)	TI : FI Ratio	Estimated Thaw Duration† (days)	Calculated Thaw Duration‡ (days)
1993-94	1313	1.69	409	0.31	49	49
1994-95	858	1.36	234	0.27	37	40
1995-96	1312	1.69	409	0.31	65	49
1996-97	1048	1.50	304	0.29	42	44

* Calculated by setting the thaw depth model equal to the maximum freeze depth

† Calculated from the estimated date of full thaw and the date of first thaw

‡ Calculated from the formula $d = 0.018\ FI + 25$

APPENDIX H

ASPHALT MODULUS MODELS BASED ON SURFACE TEMPERATURE

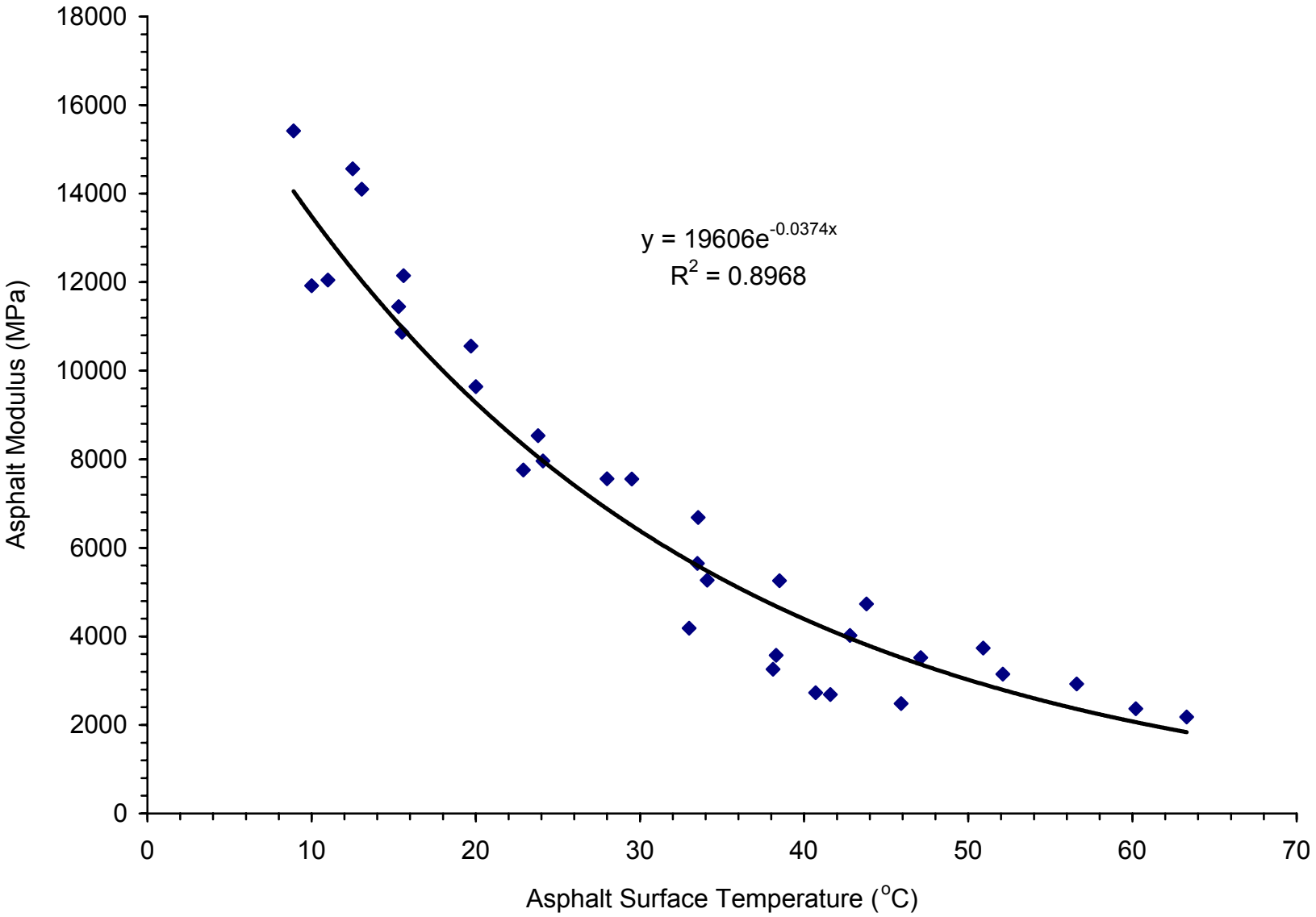

Figure H-1. Asphalt Modulus Model for Site 04-0113

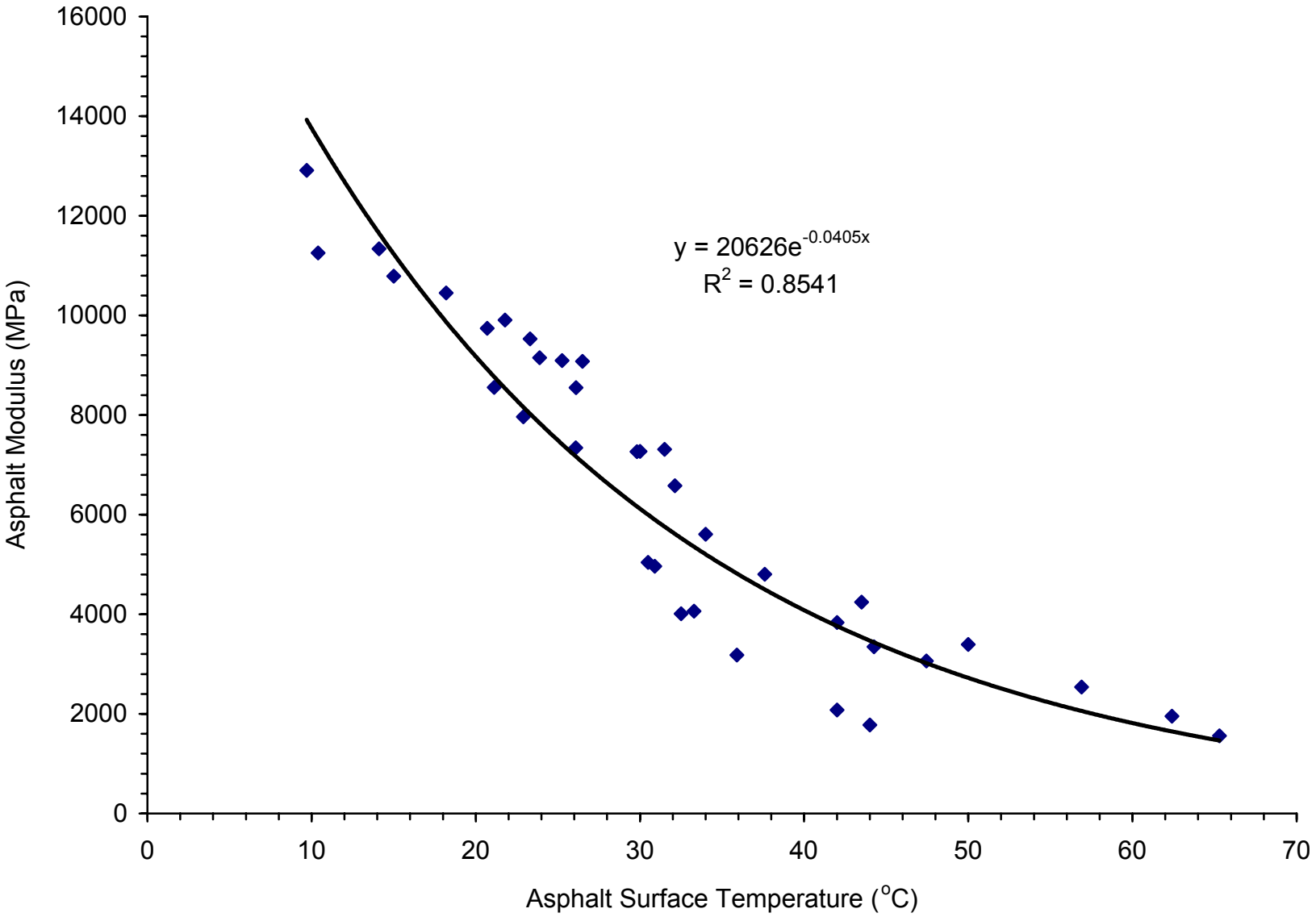

Figure H-2. Asphalt Modulus Model for Site 04-0114

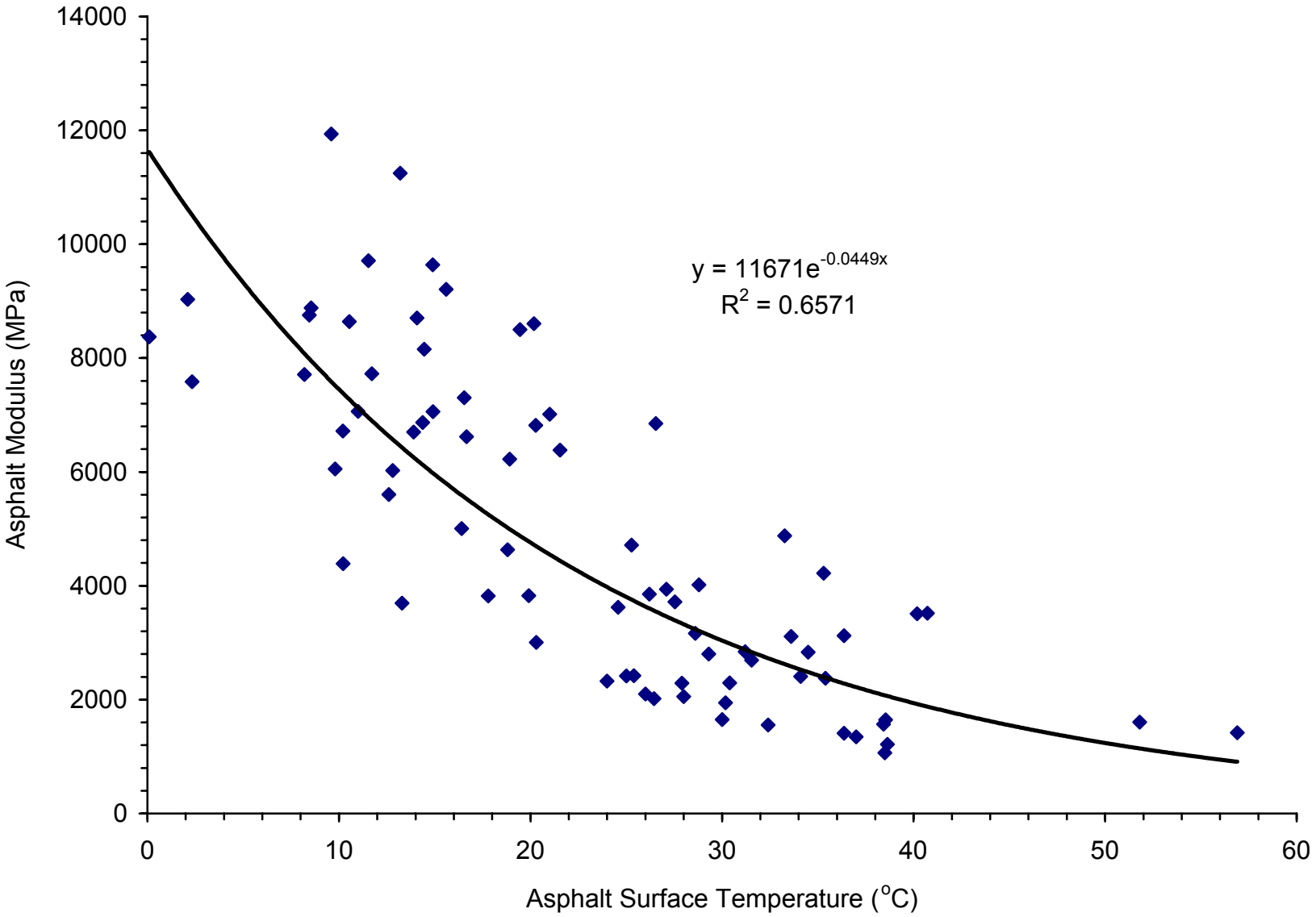

Figure H-3. Asphalt Modulus Model for Site 08-1053

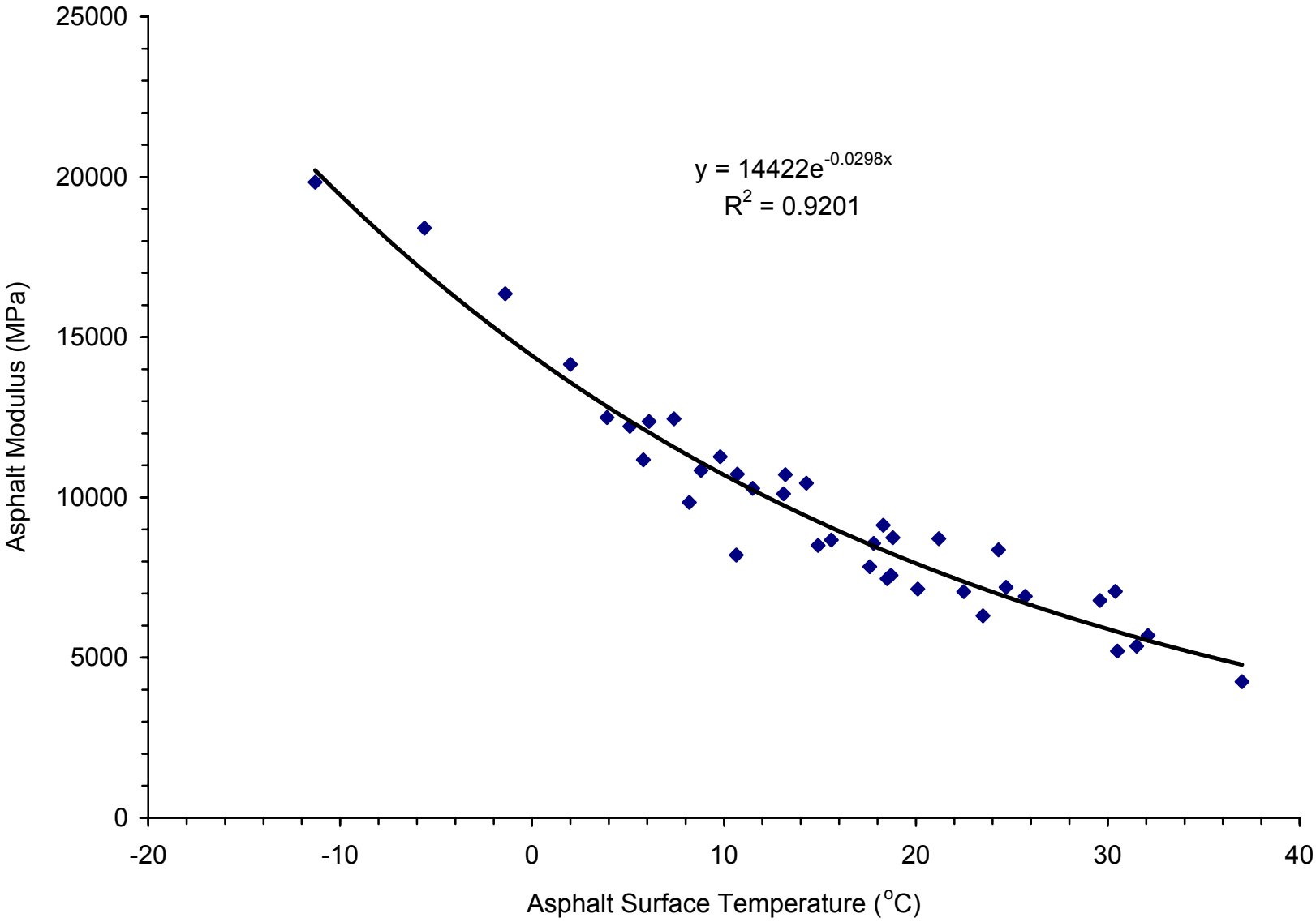

Figure H-4. Asphalt Modulus Model for Site 09-1803

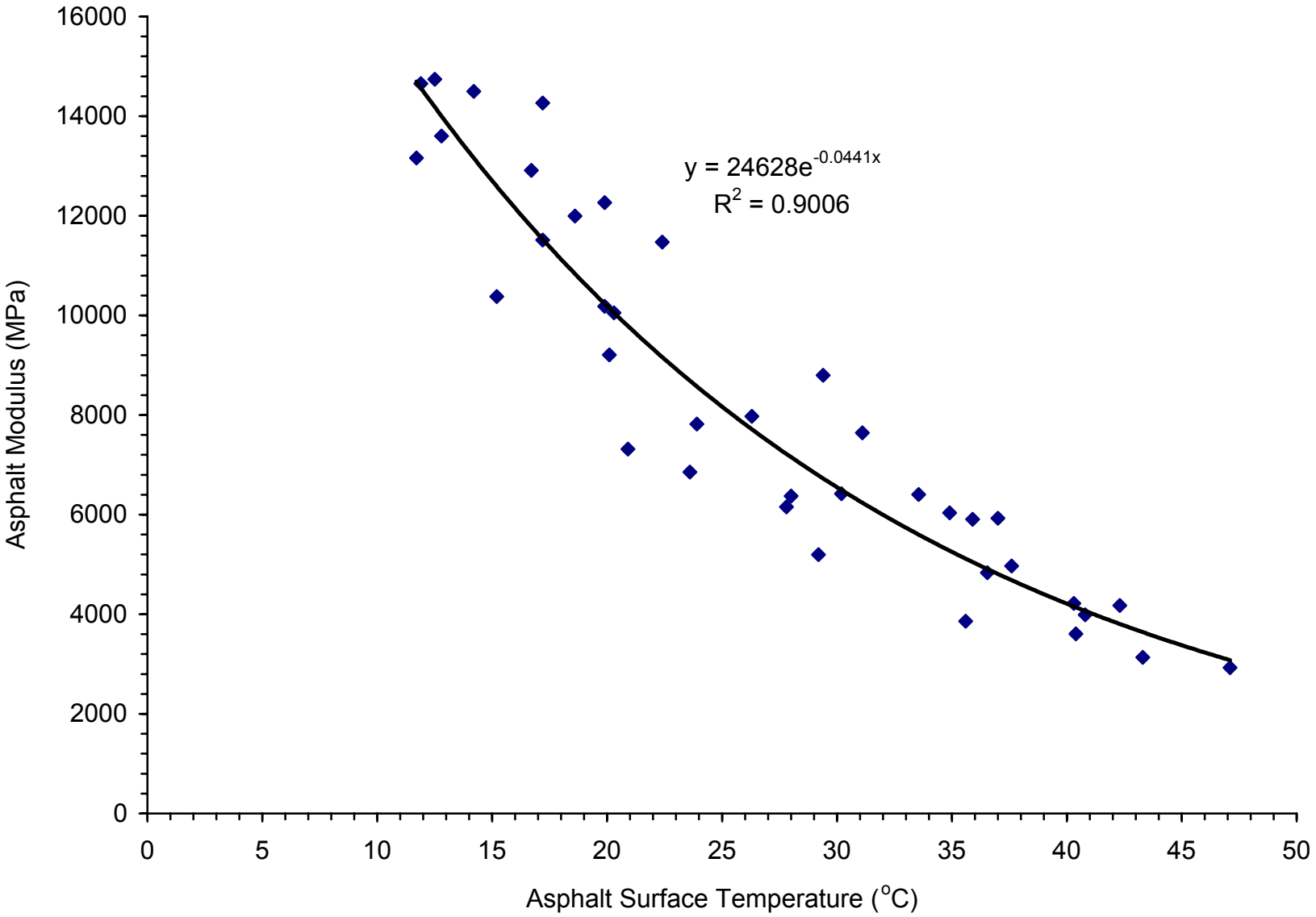

Figure H-5. Asphalt Modulus Model for Site 13-1005

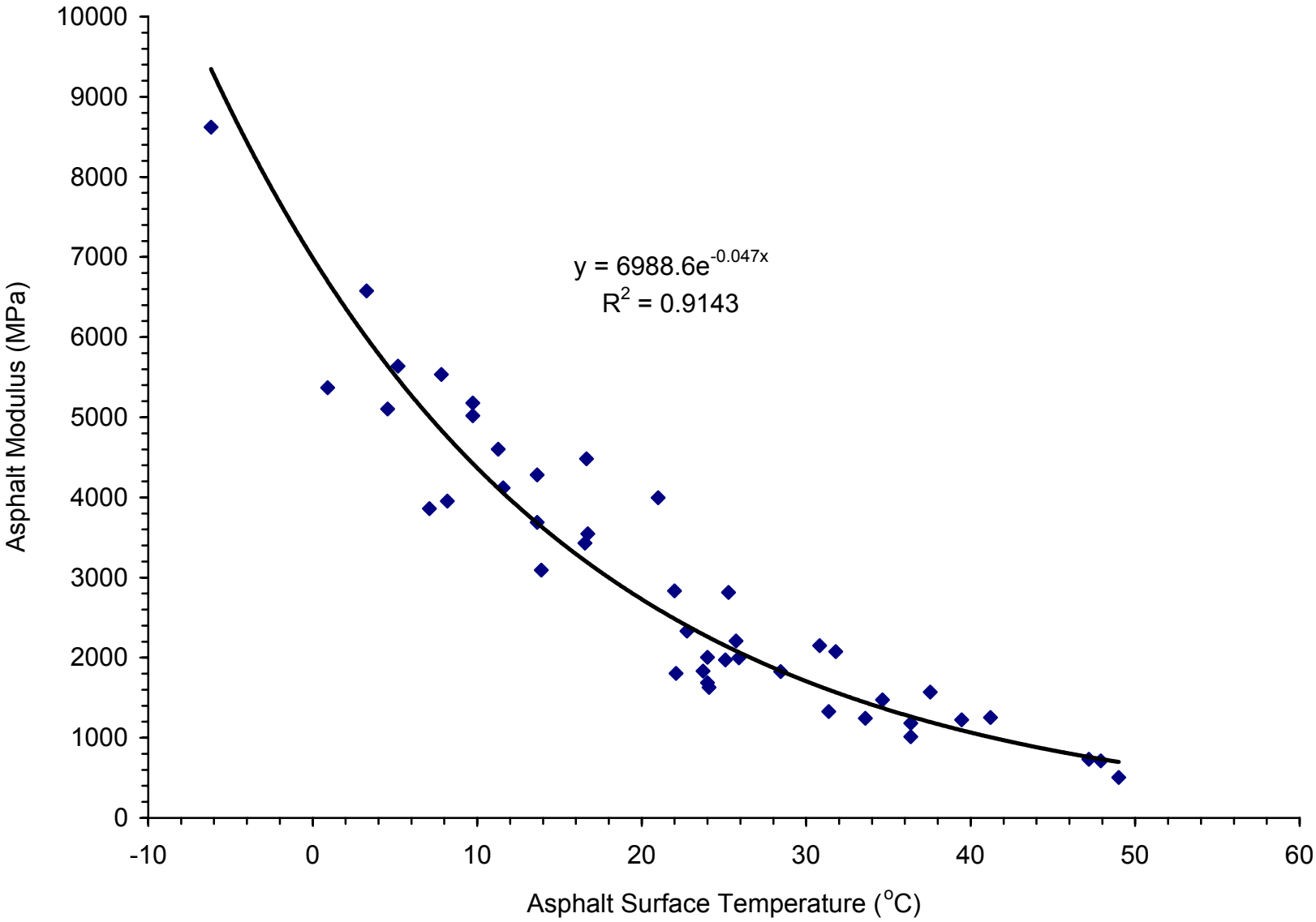

Figure H-6. Asphalt Modulus Model for Site 13-1031

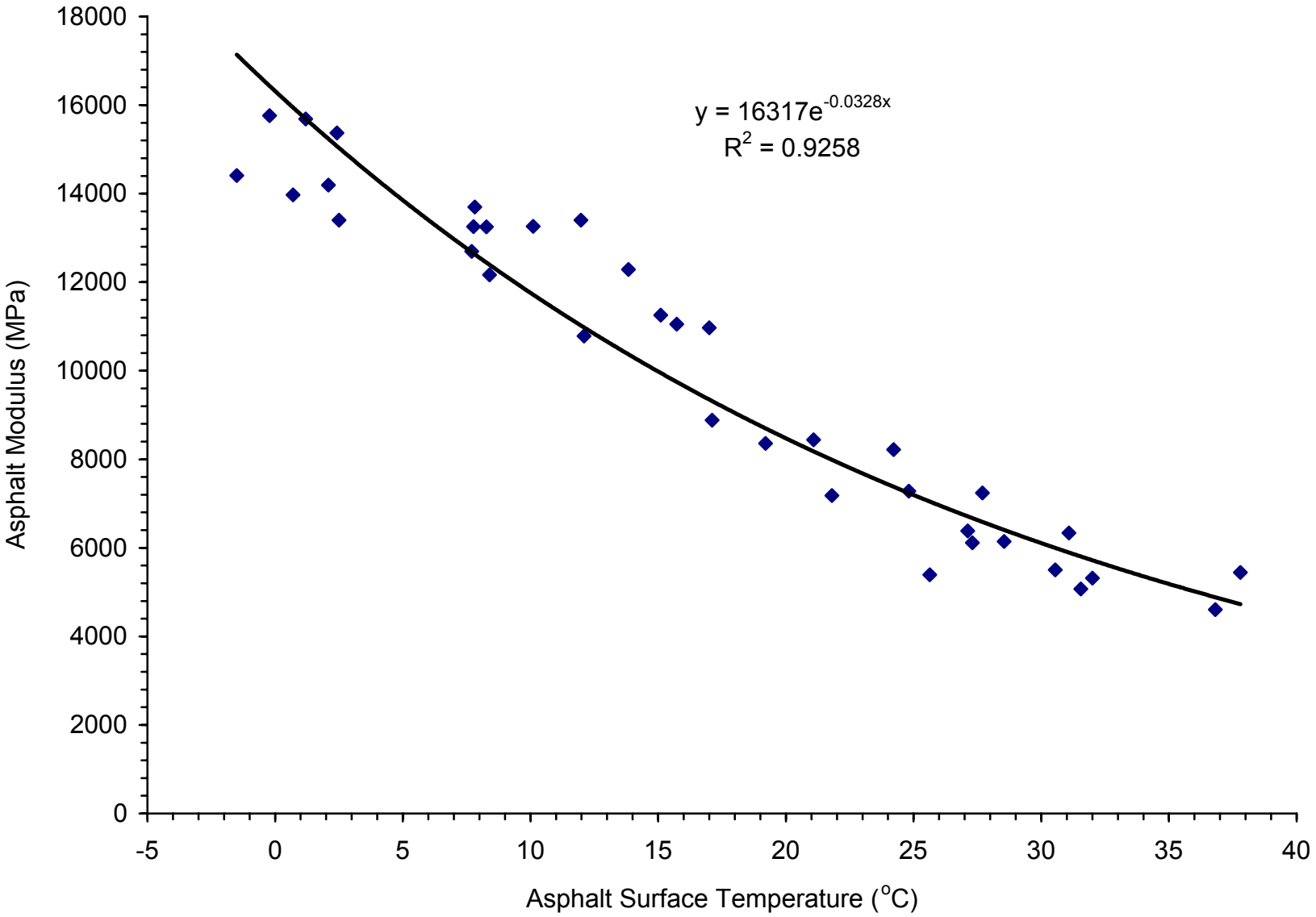

Figure H-7. Asphalt Modulus Model for Site 16-1010

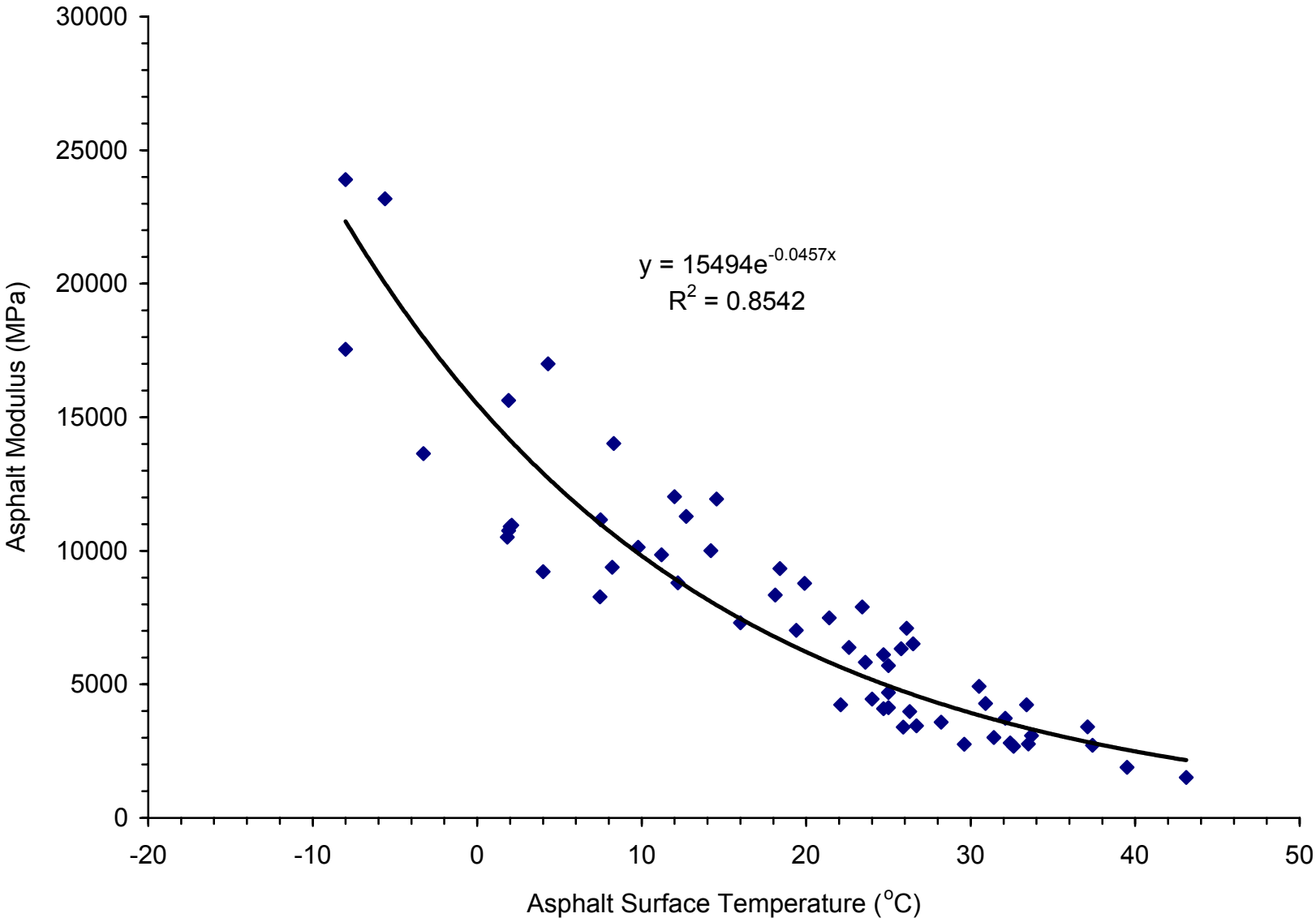

Figure H-8. Asphalt Modulus Model for Site 23-1026

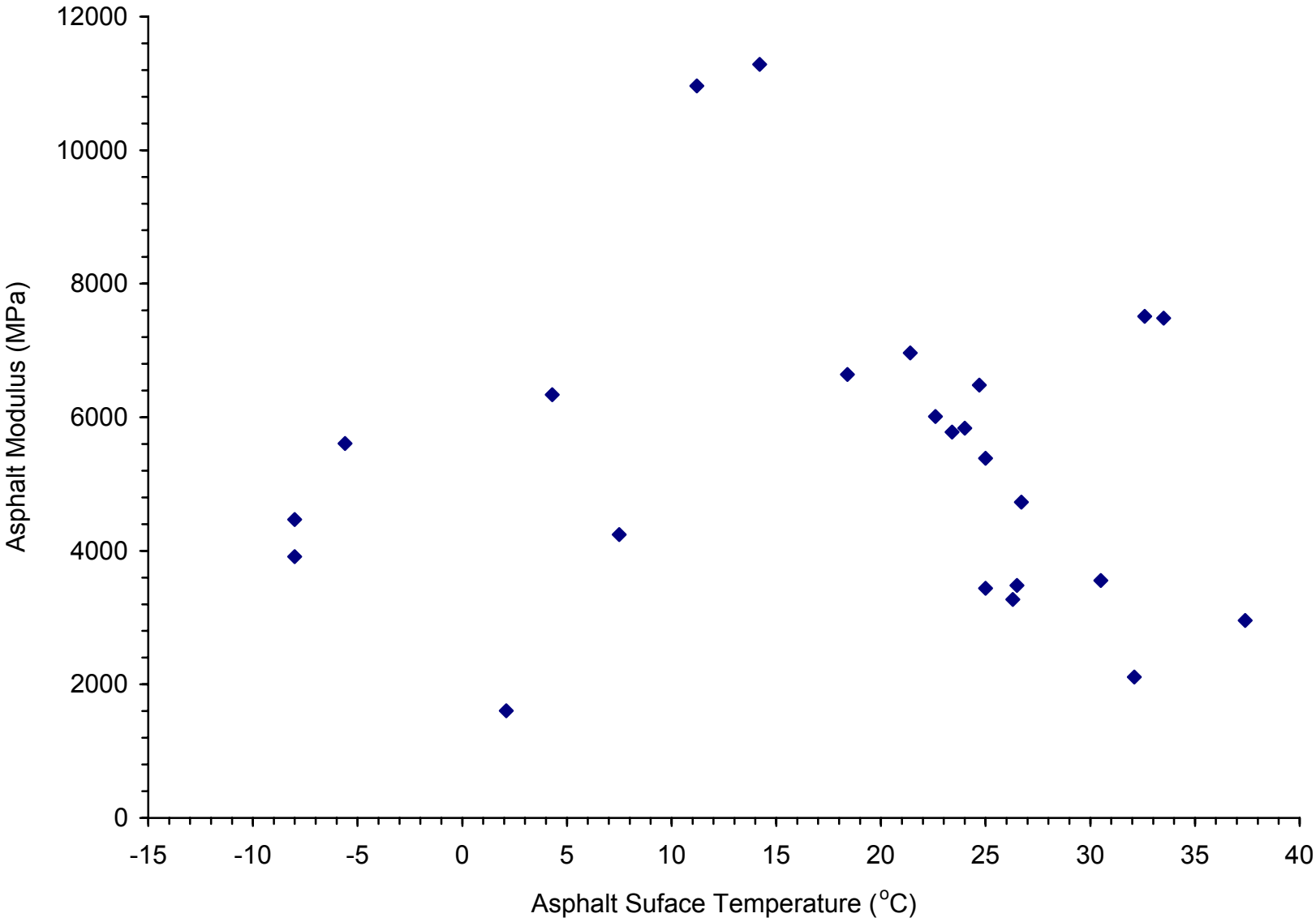

Figure H-9. Asphalt Modulus Model for Site 24-1634

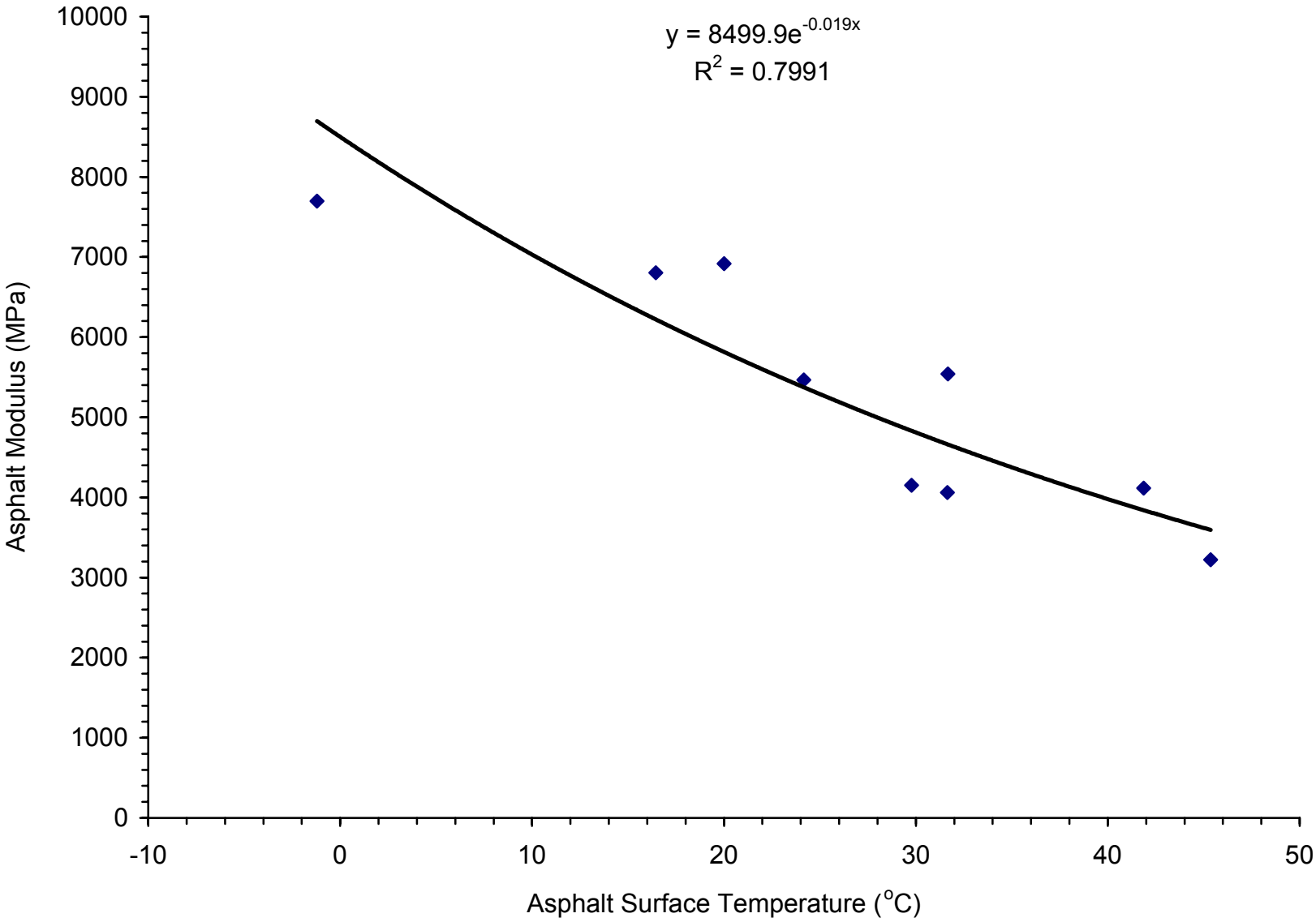

Figure H-10. Asphalt Modulus Model for Site 27-1018

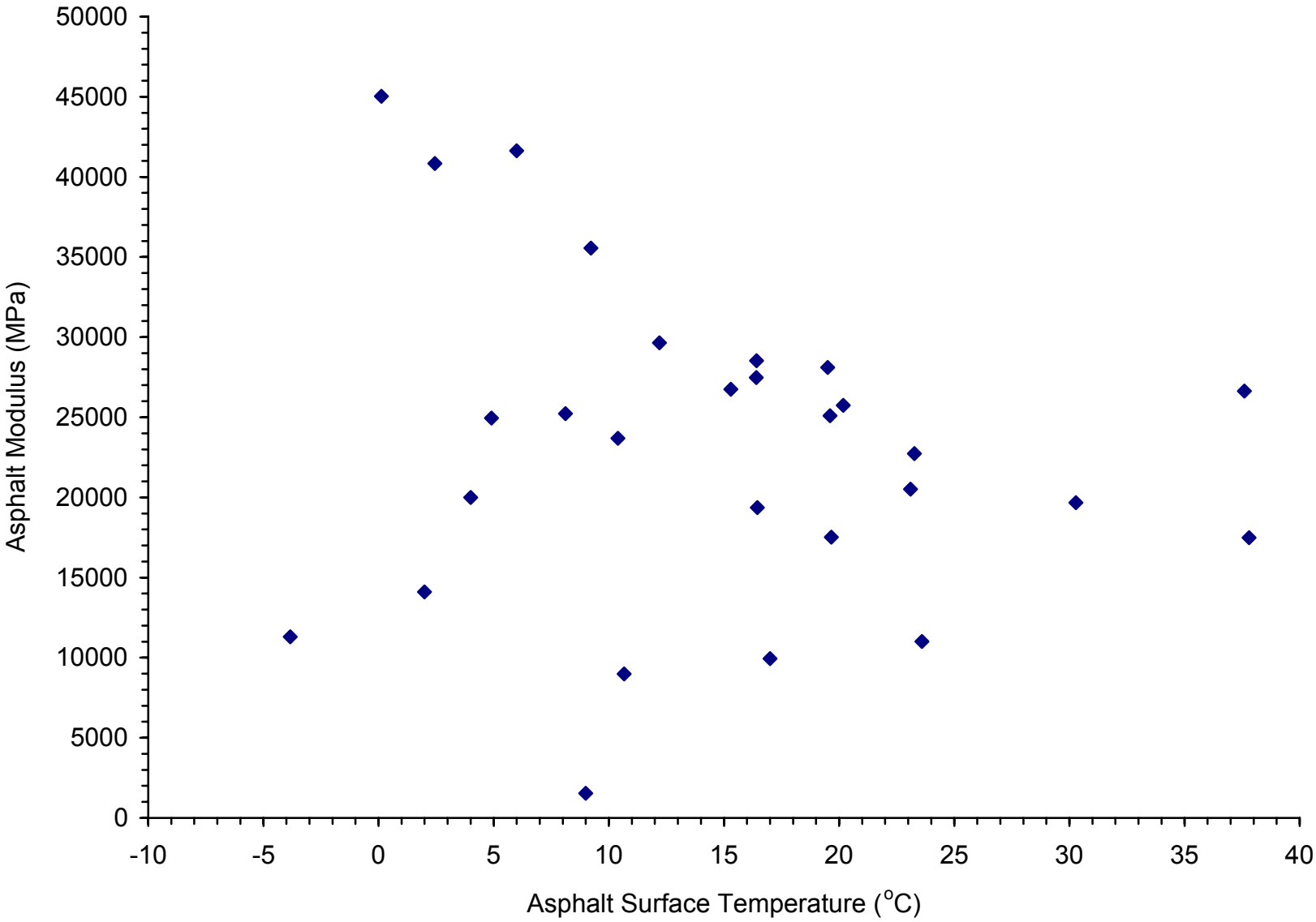

Figure H-11. Asphalt Modulus Model for Site 27-1028

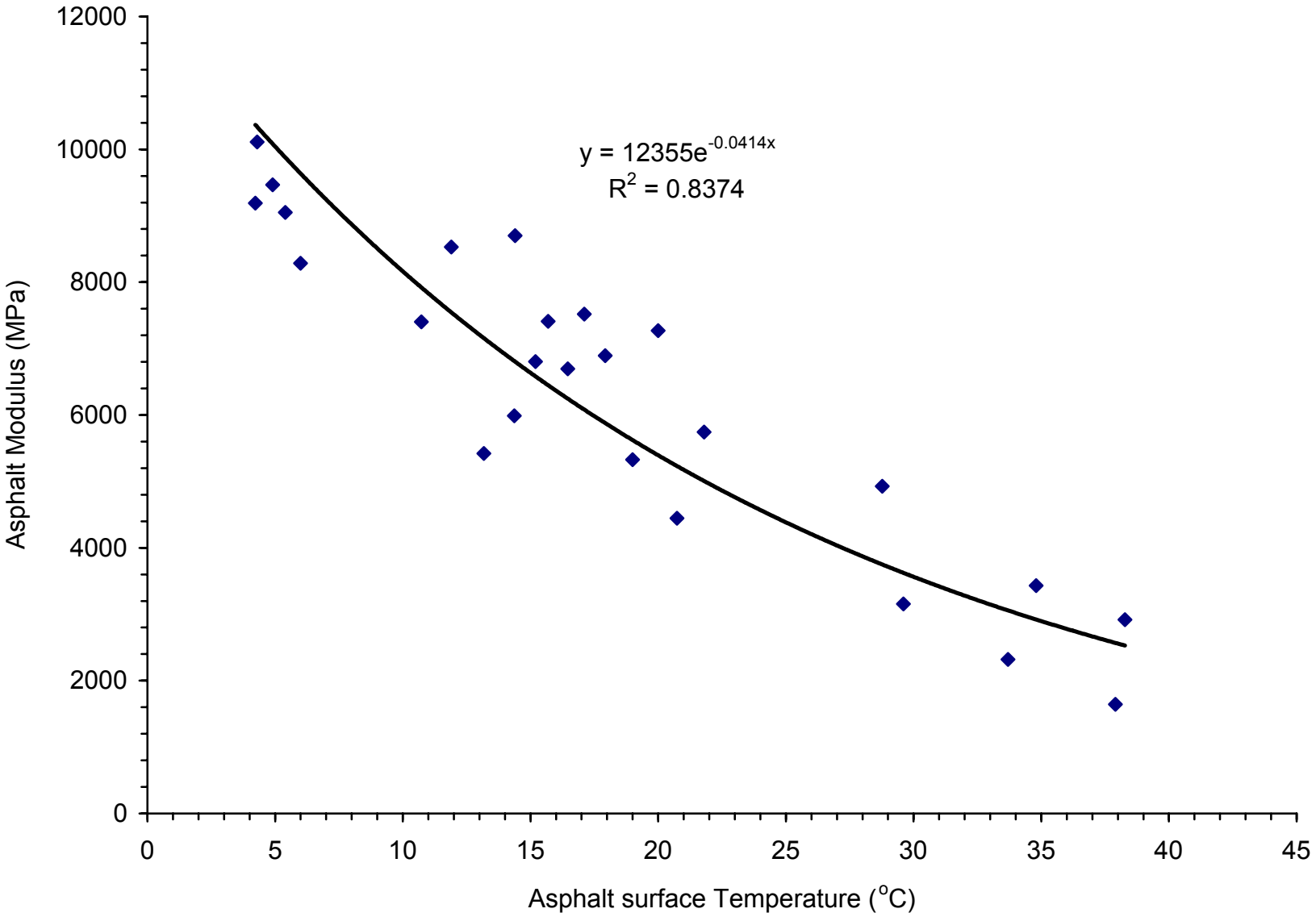

Figure H-12. Asphalt Modulus Model for Site 27-6251

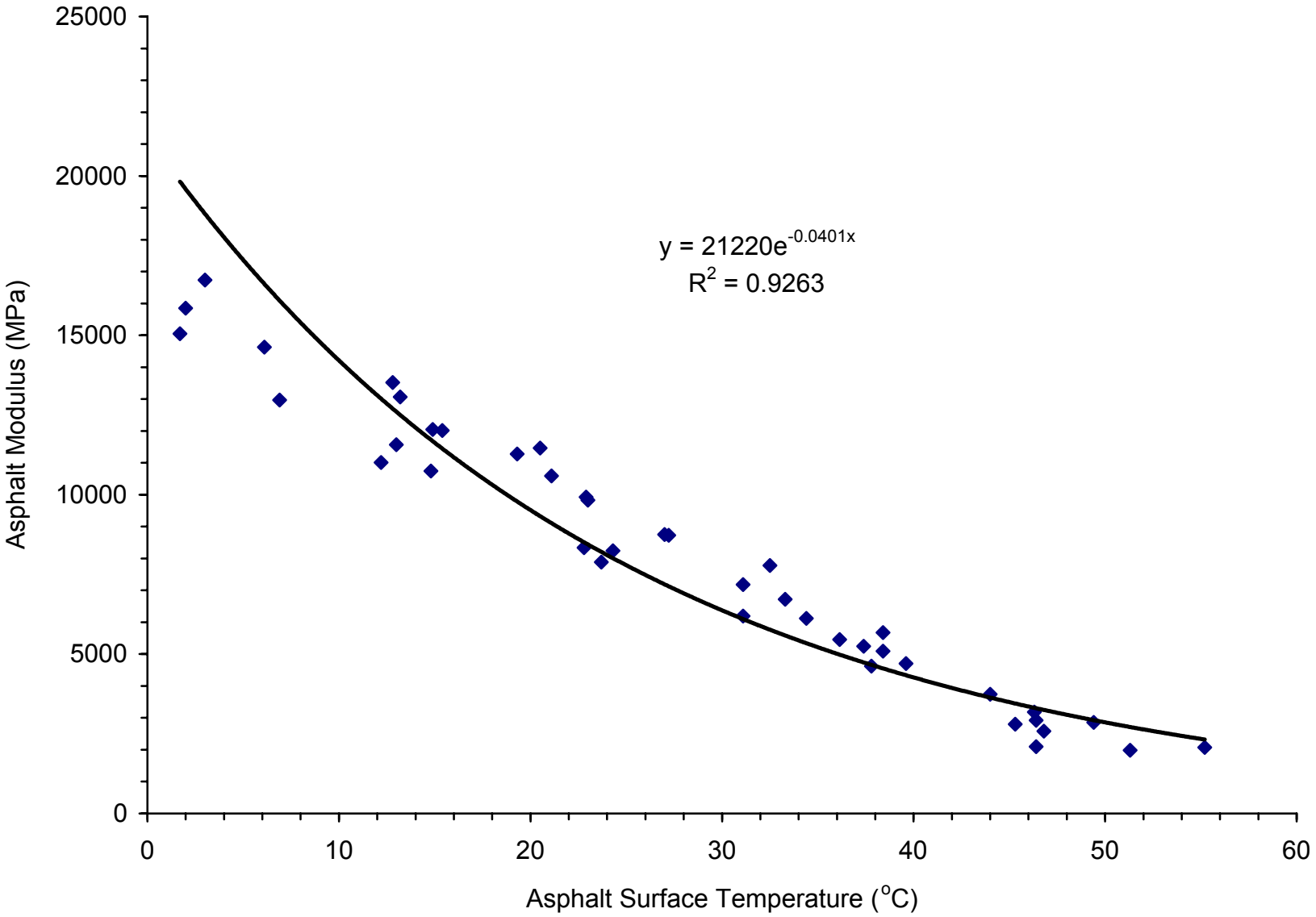

Figure H-13. Asphalt Modulus Model for Site 28-1016

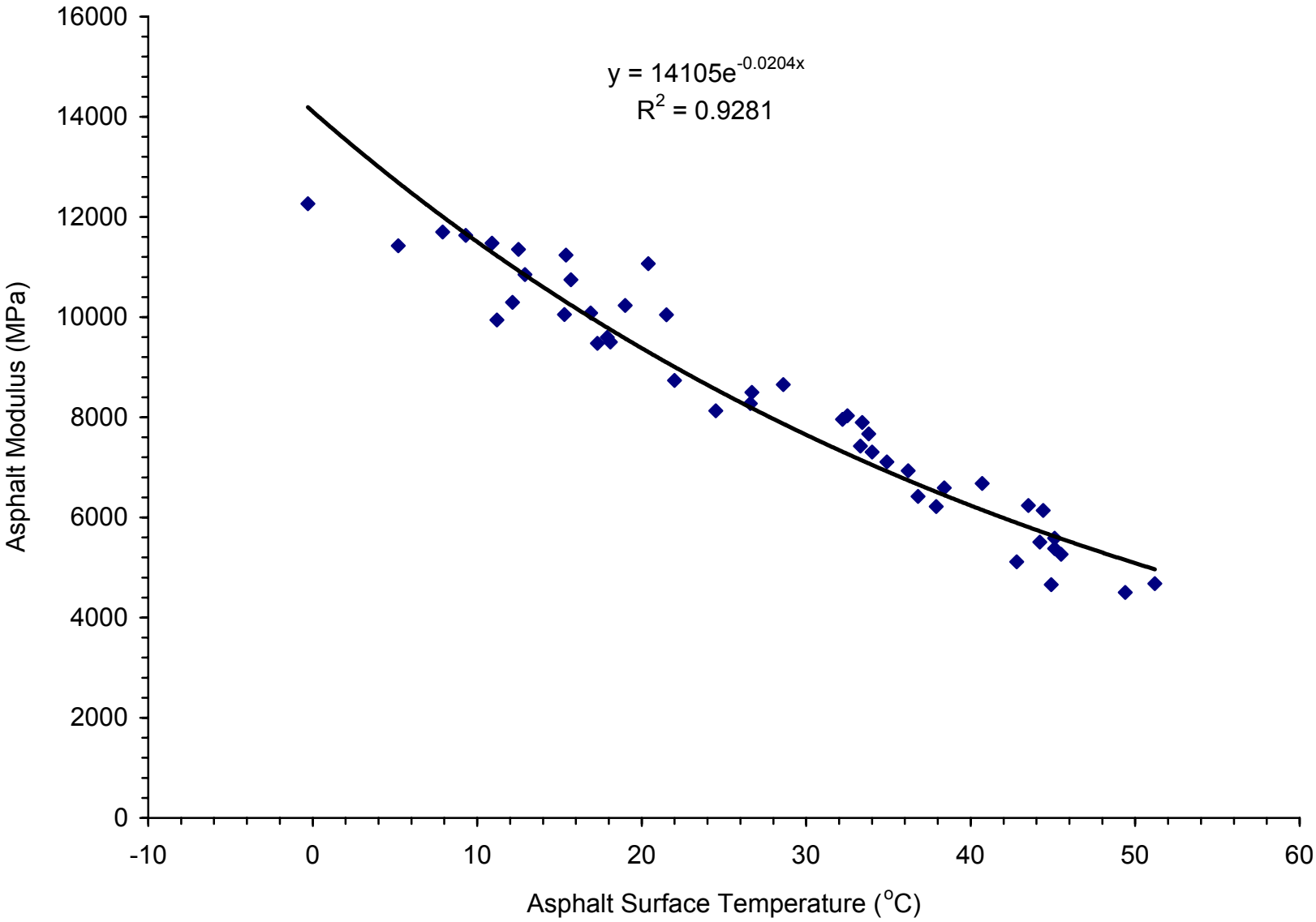

Figure H-14. Asphalt Modulus Model for Site 28-1802

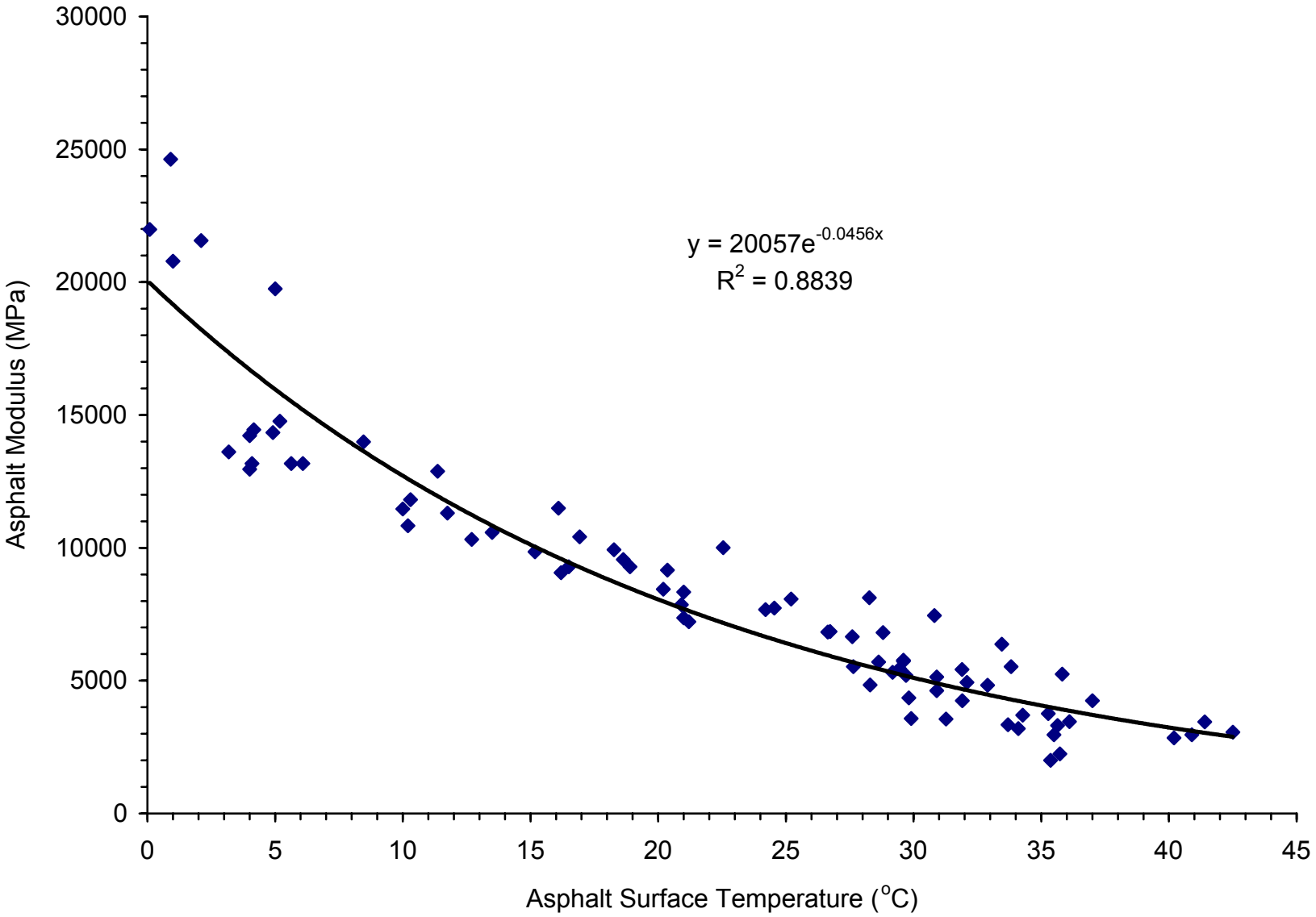

Figure H-15. Asphalt Modulus Model for Site 30-8129

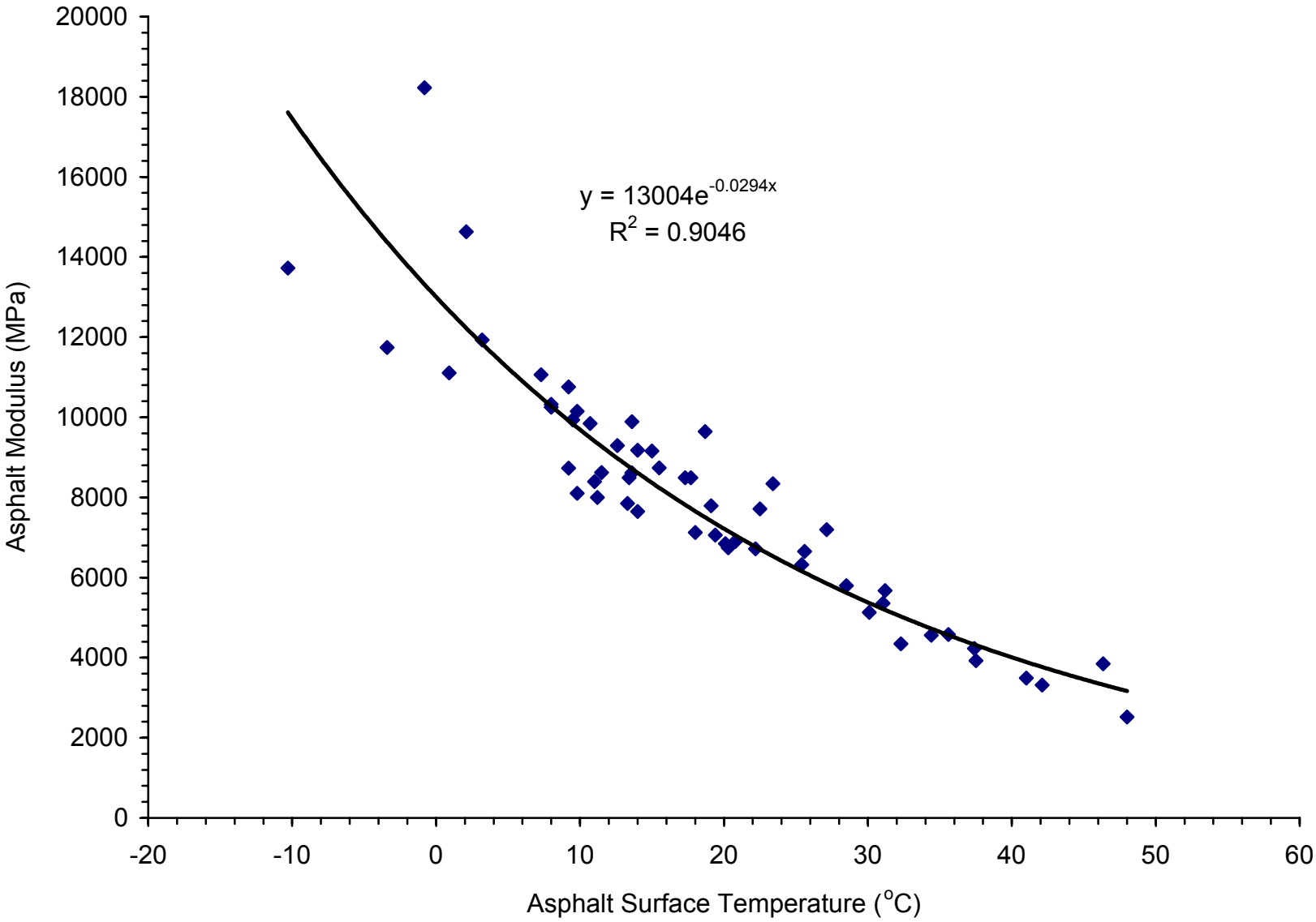

Figure H-16. Asphalt Modulus Model for Site 33-1001

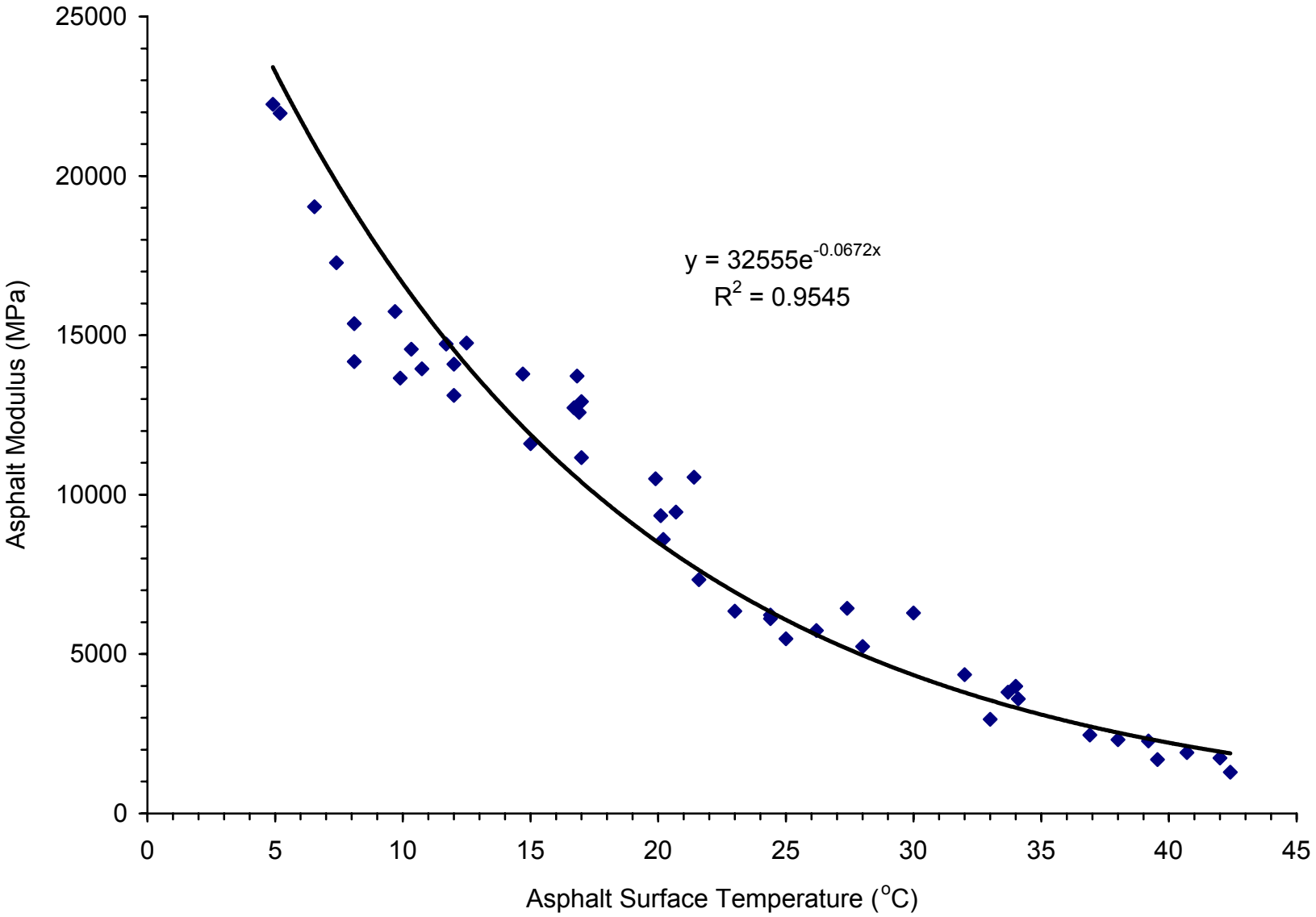

Figure H-17. Asphalt Modulus Model for Site 35-1112

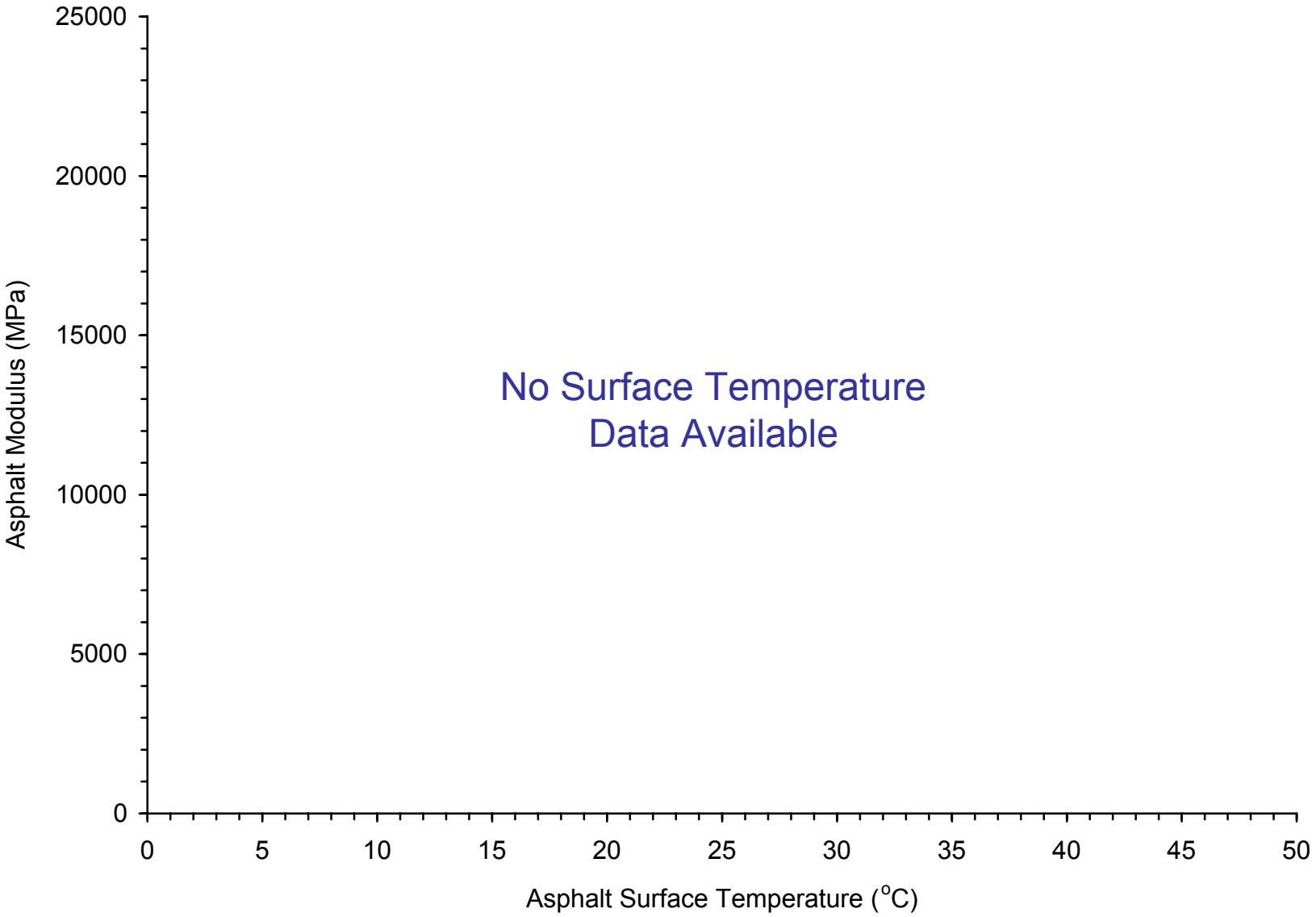

Figure H-18. Asphalt Modulus Model for Site 37-1028

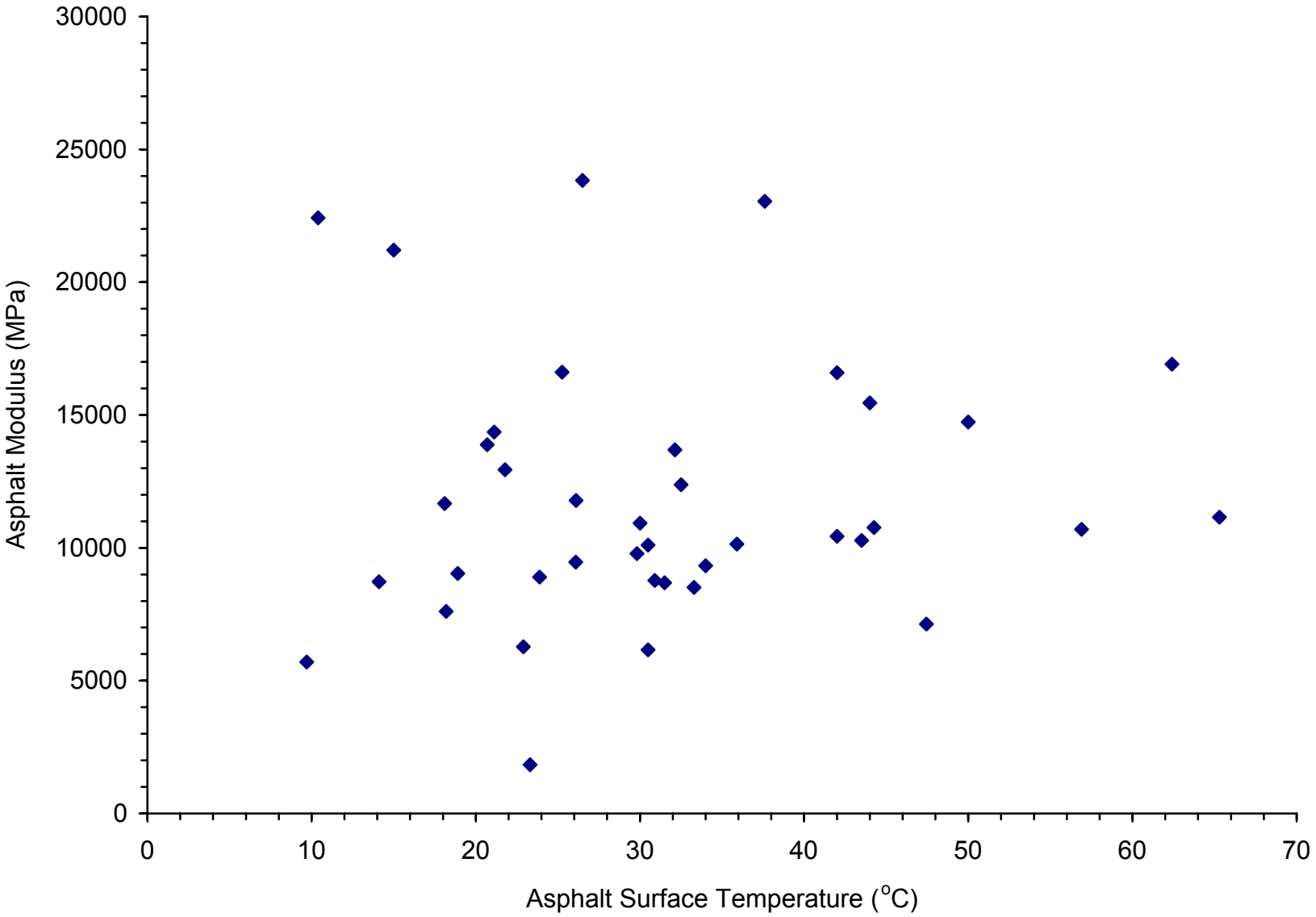

Figure H-19. Asphalt Modulus Model for Site 40-4165

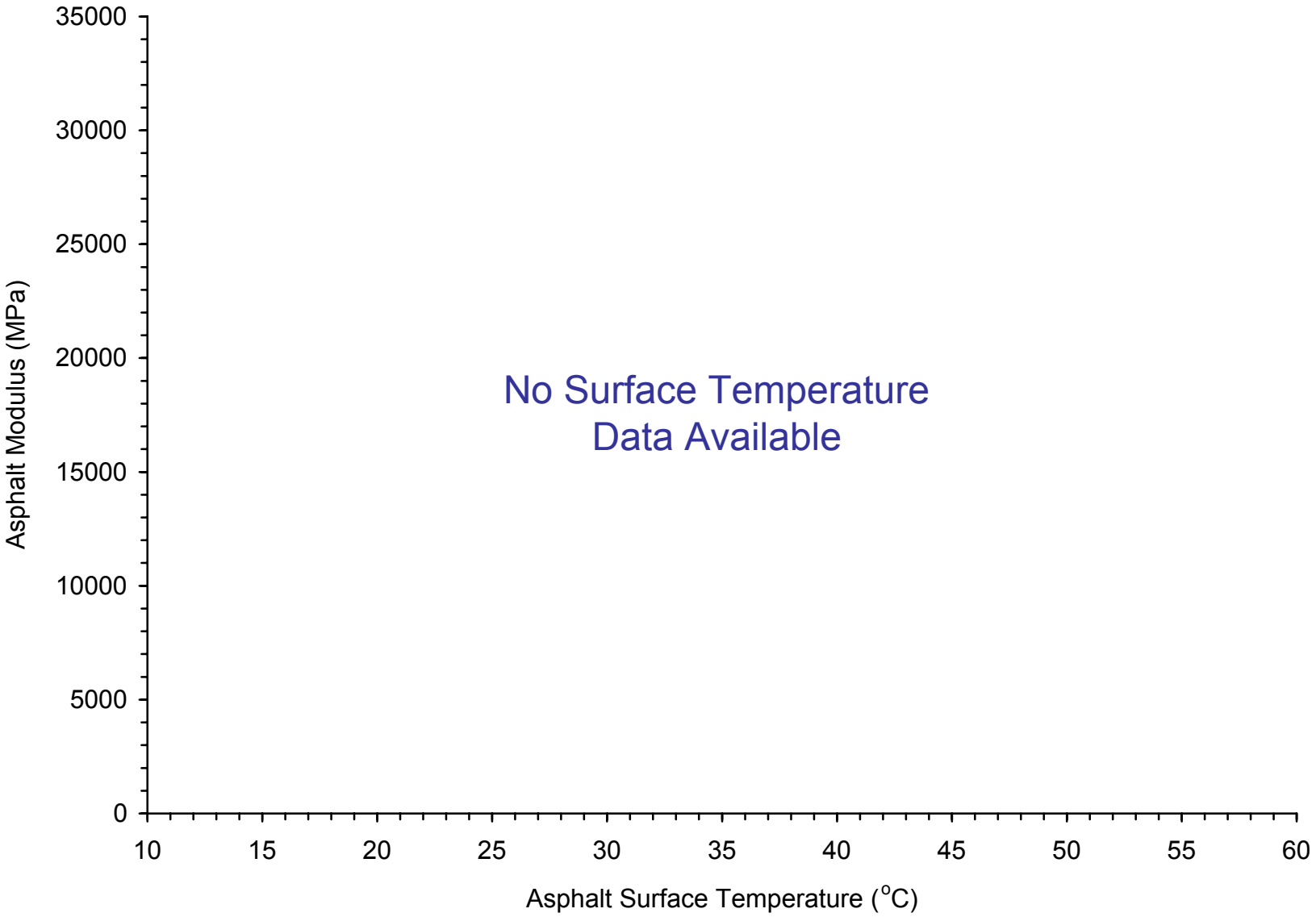

Figure H-20. Asphalt Modulus Model for Site 47-3739

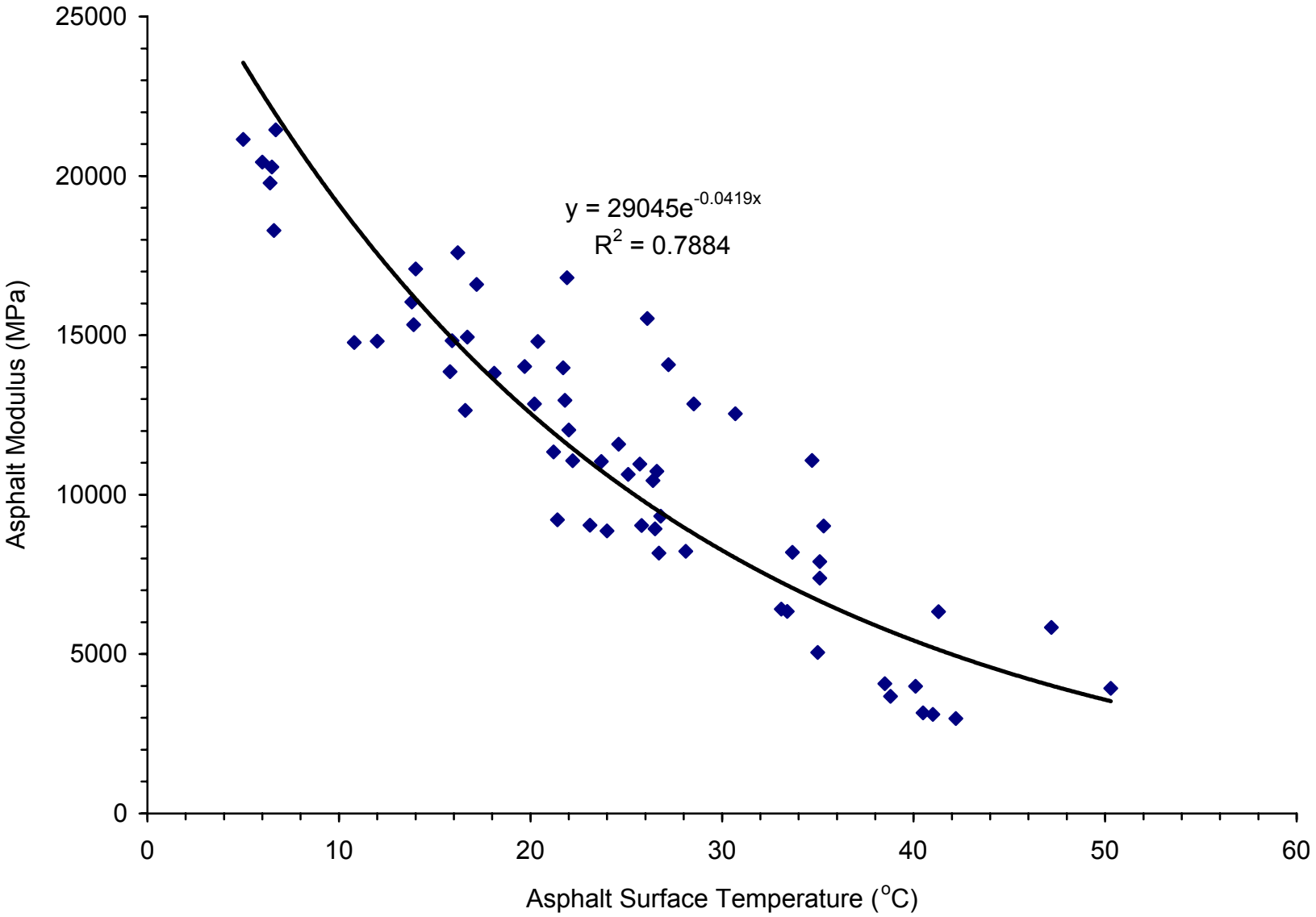

Figure H-21. Asphalt Modulus Model for Site 48-1060

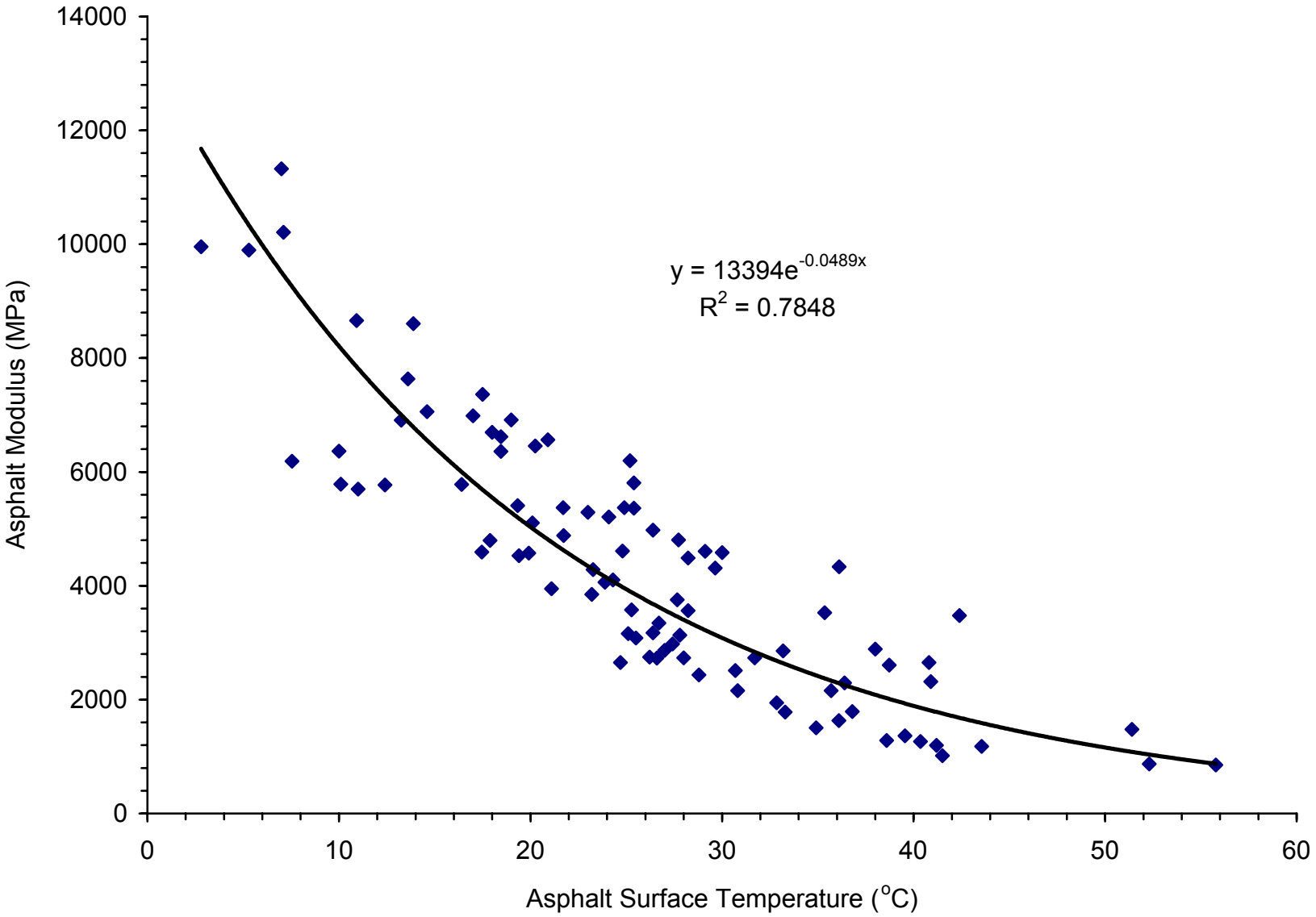

Figure H-22. Asphalt Modulus Model for Site 48-1122

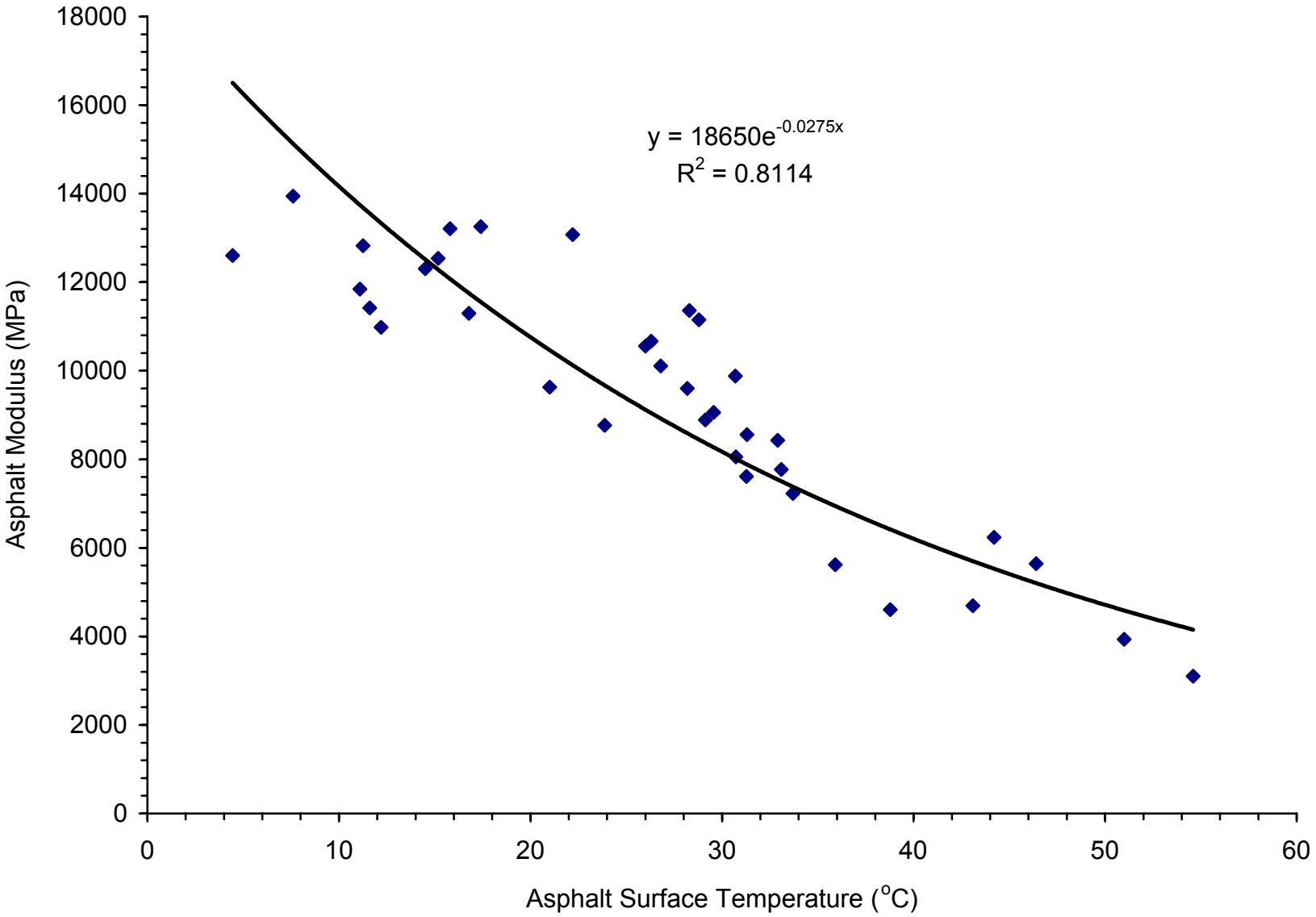

Figure H-23. Asphalt Modulus Model for Site 49-1001

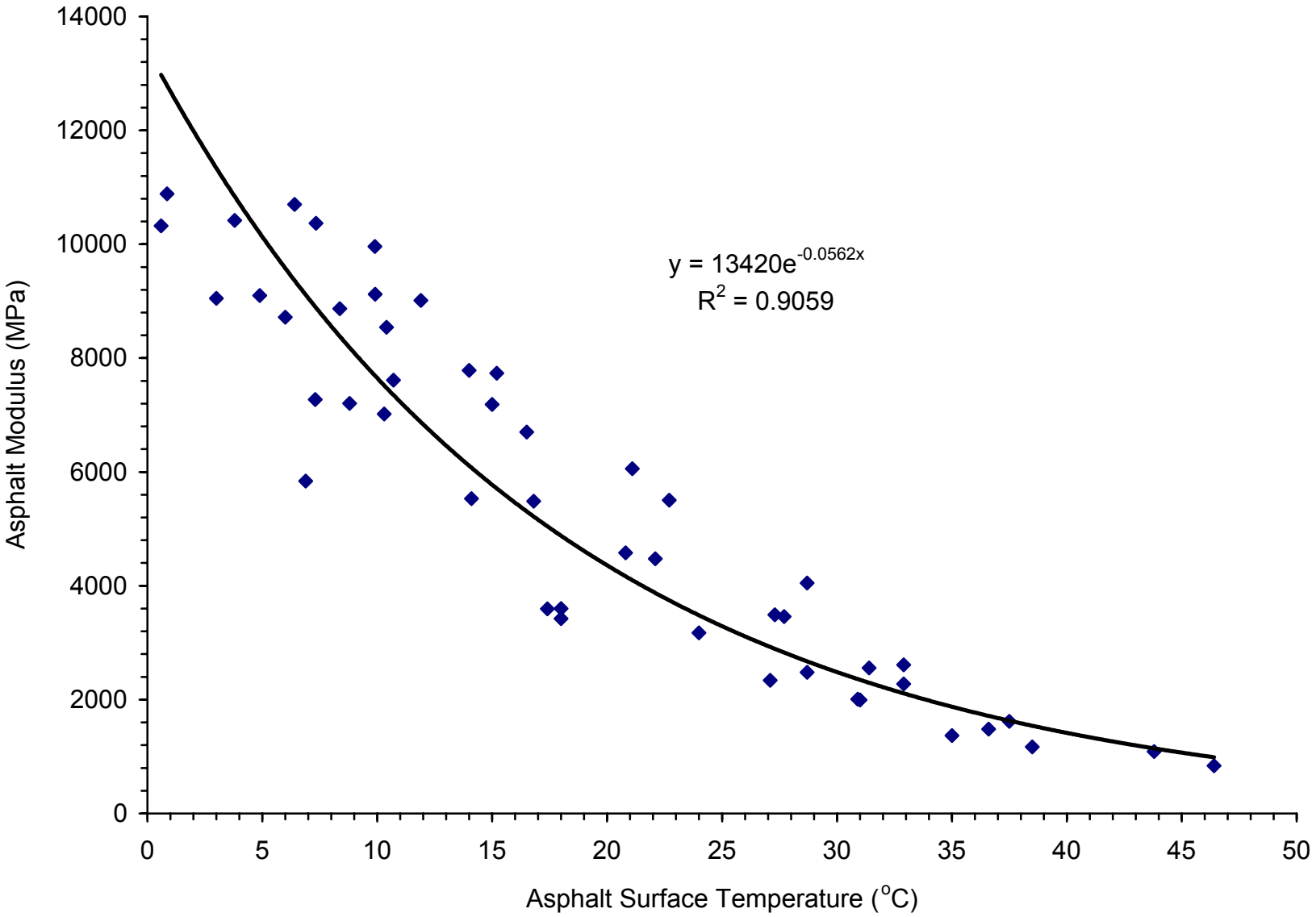

Figure H-24. Asphalt Modulus Model for Site 50-1002

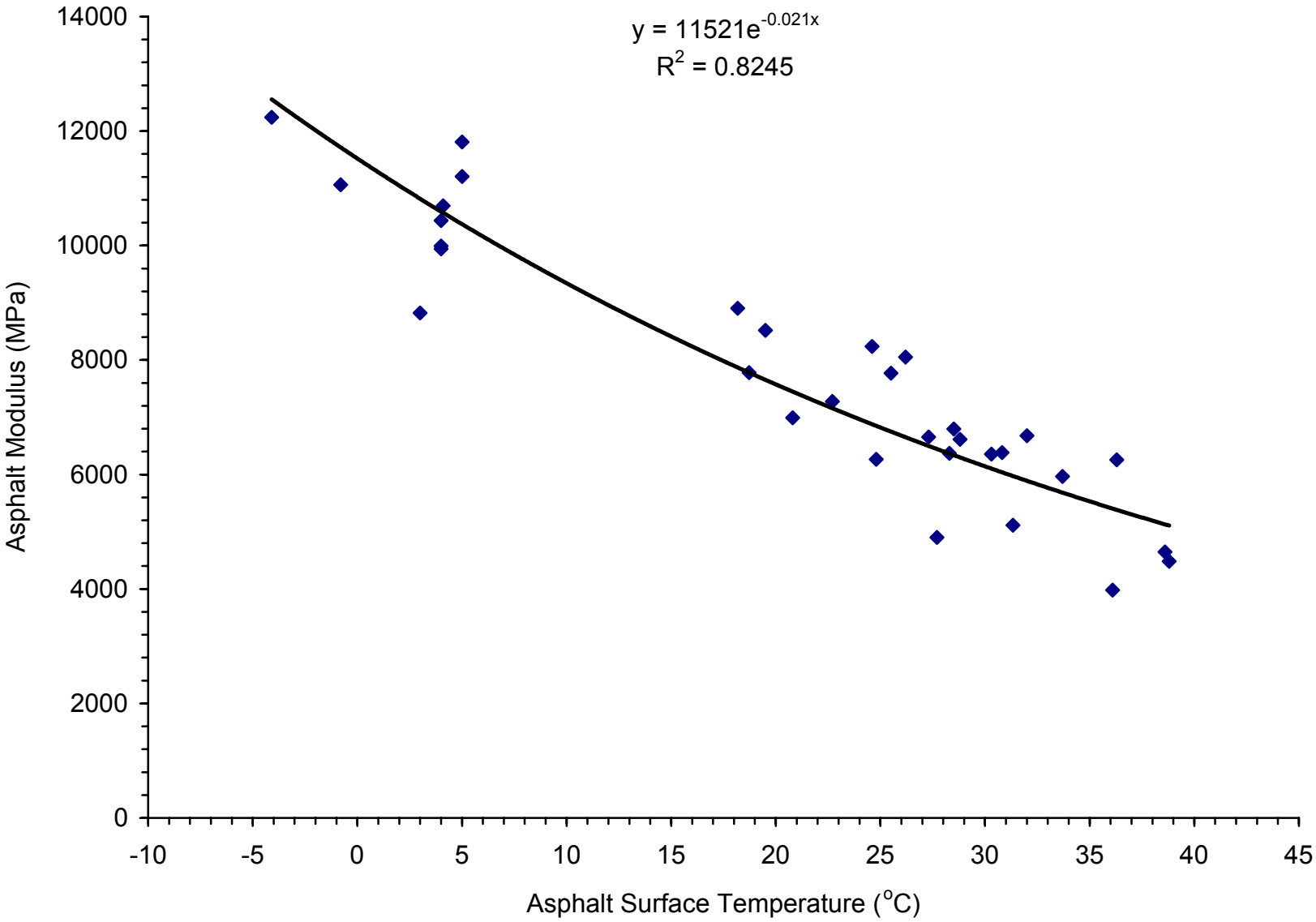

Figure H-25. Asphalt Modulus Model for Site 56-1007

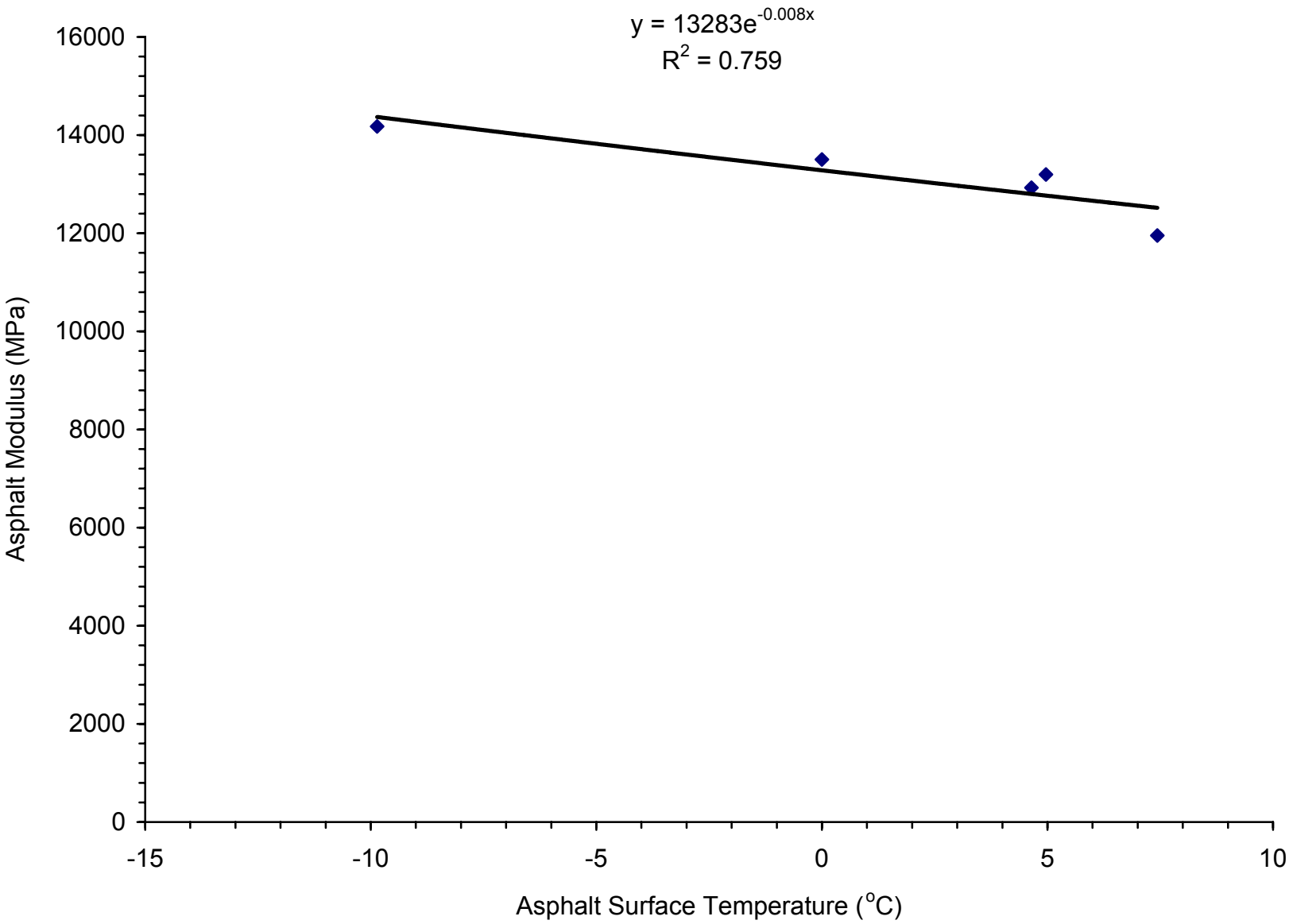

Figure H-26. Asphalt Modulus Model for Site 83-1801

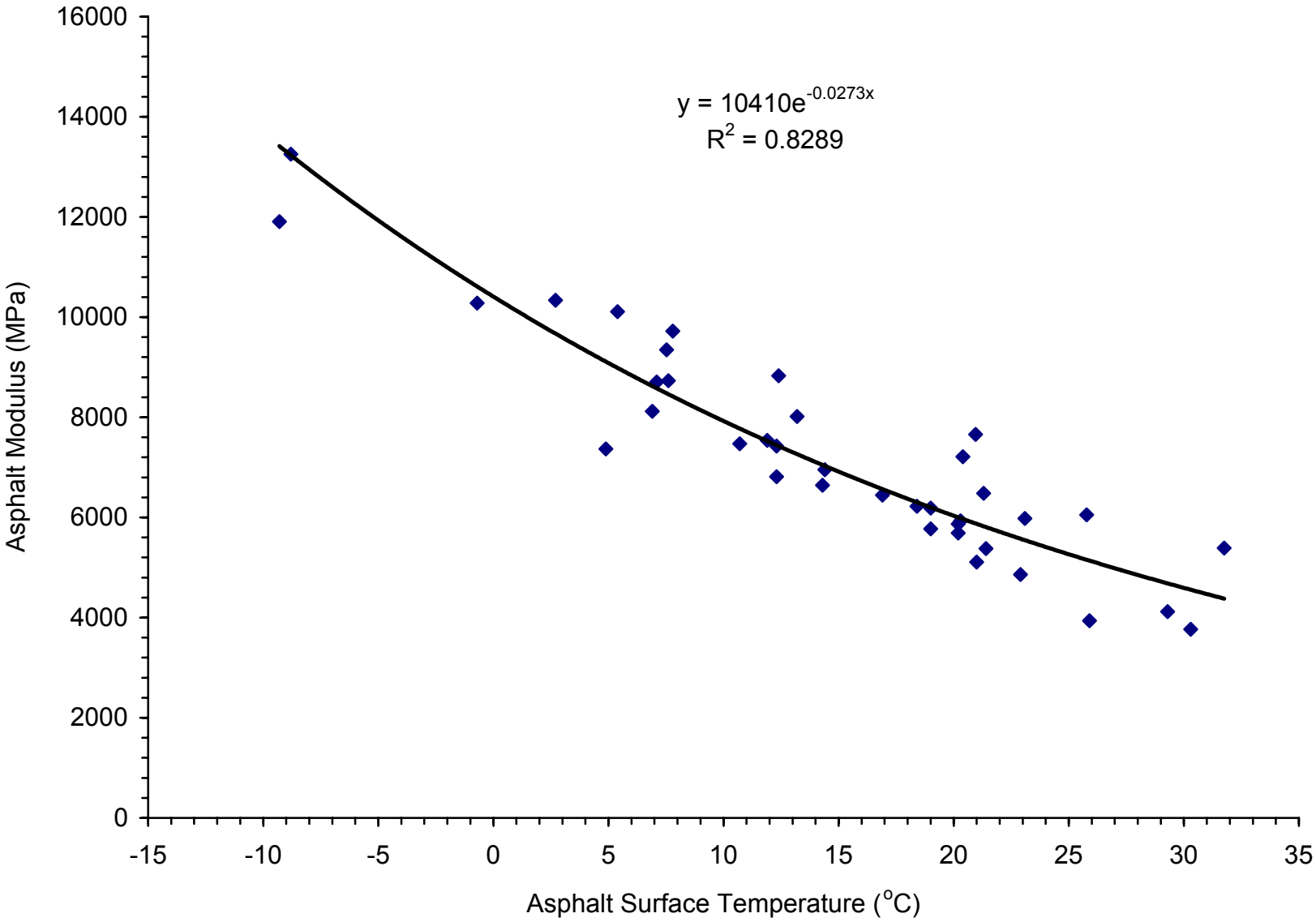

Figure H-27. Asphalt Modulus Model for Site 87-1622

APPENDIX I

ASPHALT MODULUS MODELS BASED ON MID-DEPTH TEMPERATURE

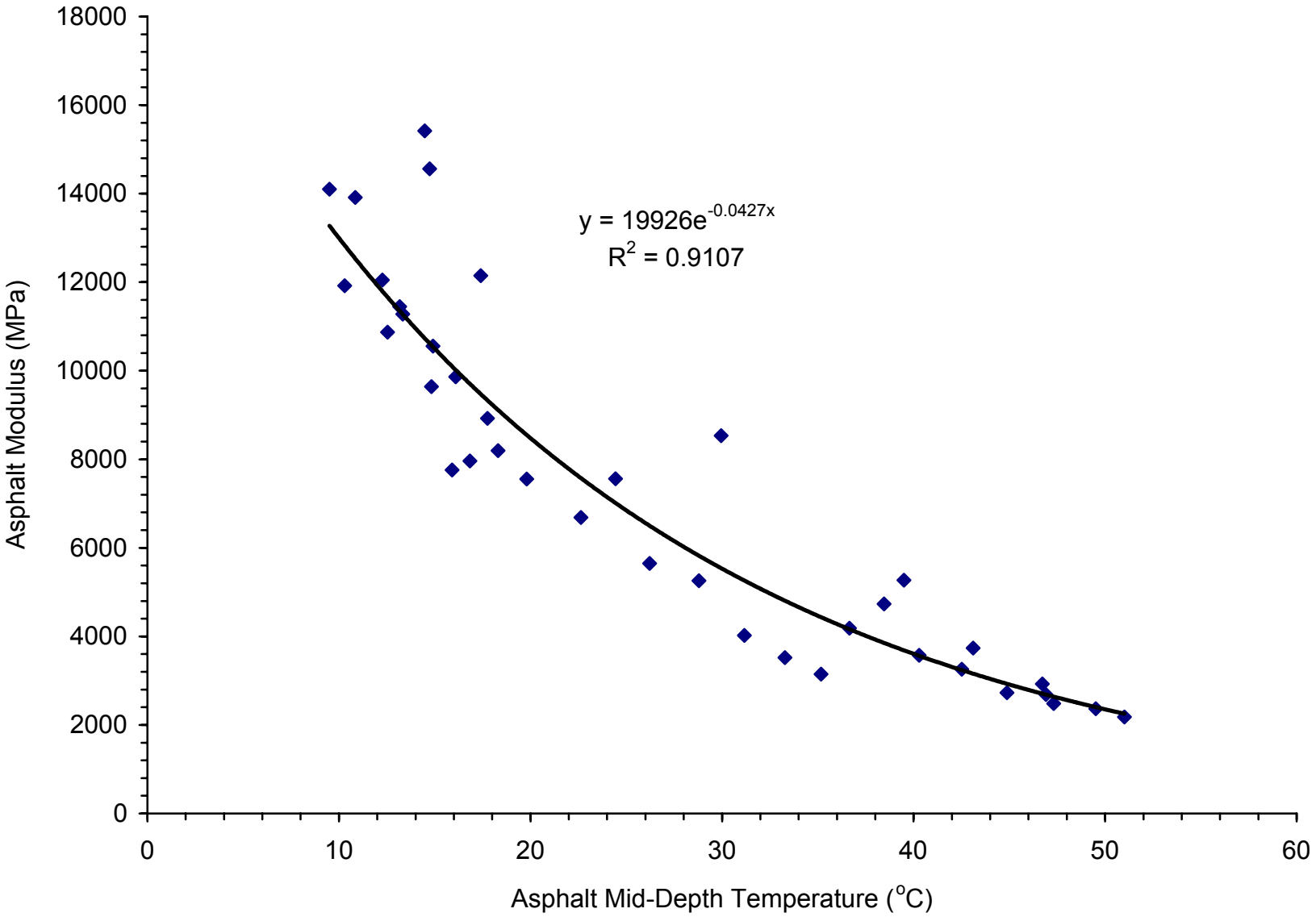

Figure I-1. Asphalt Modulus Model for Site 04-0113

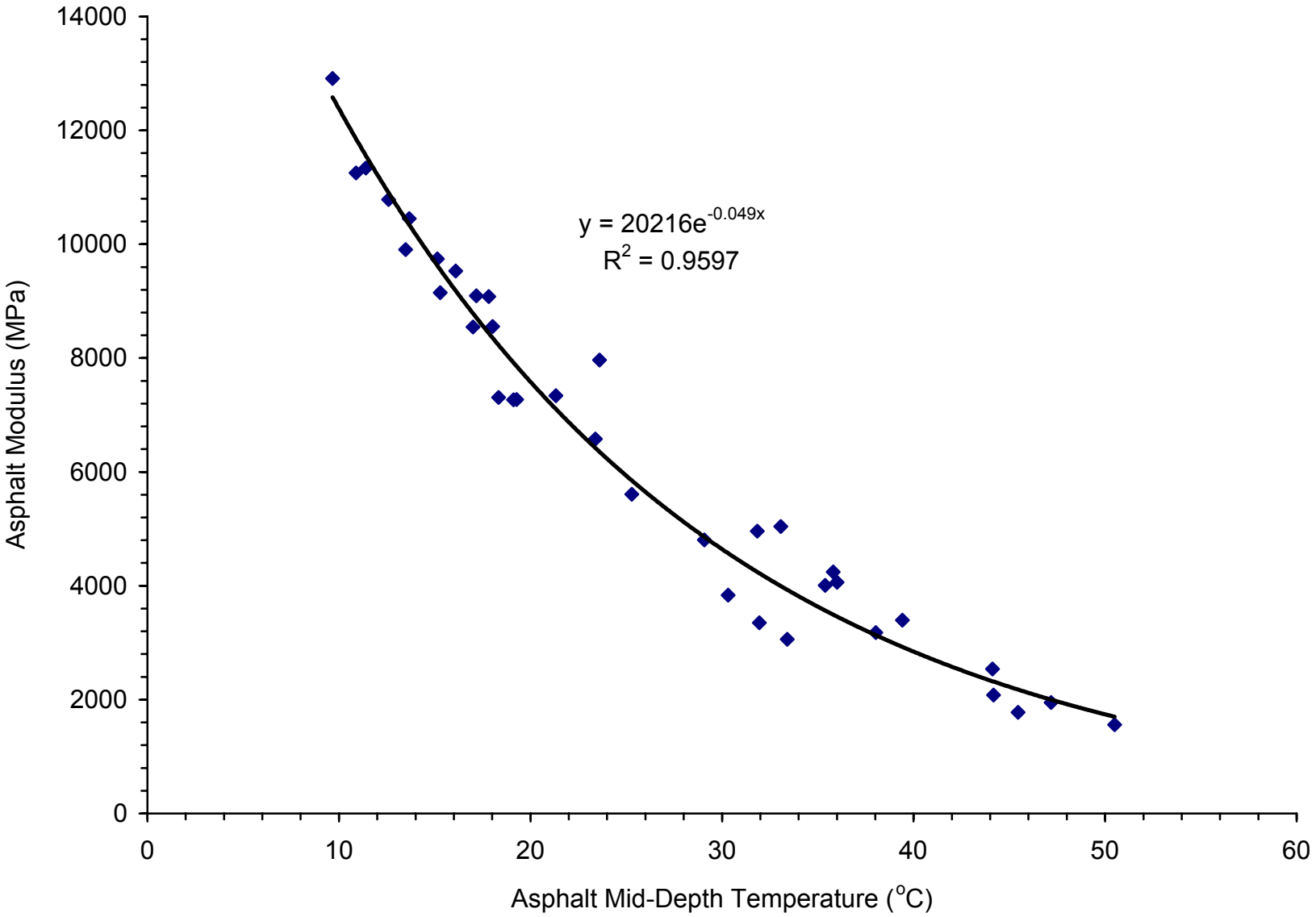

Figure I-2. Asphalt Modulus Model for Site 04-0114

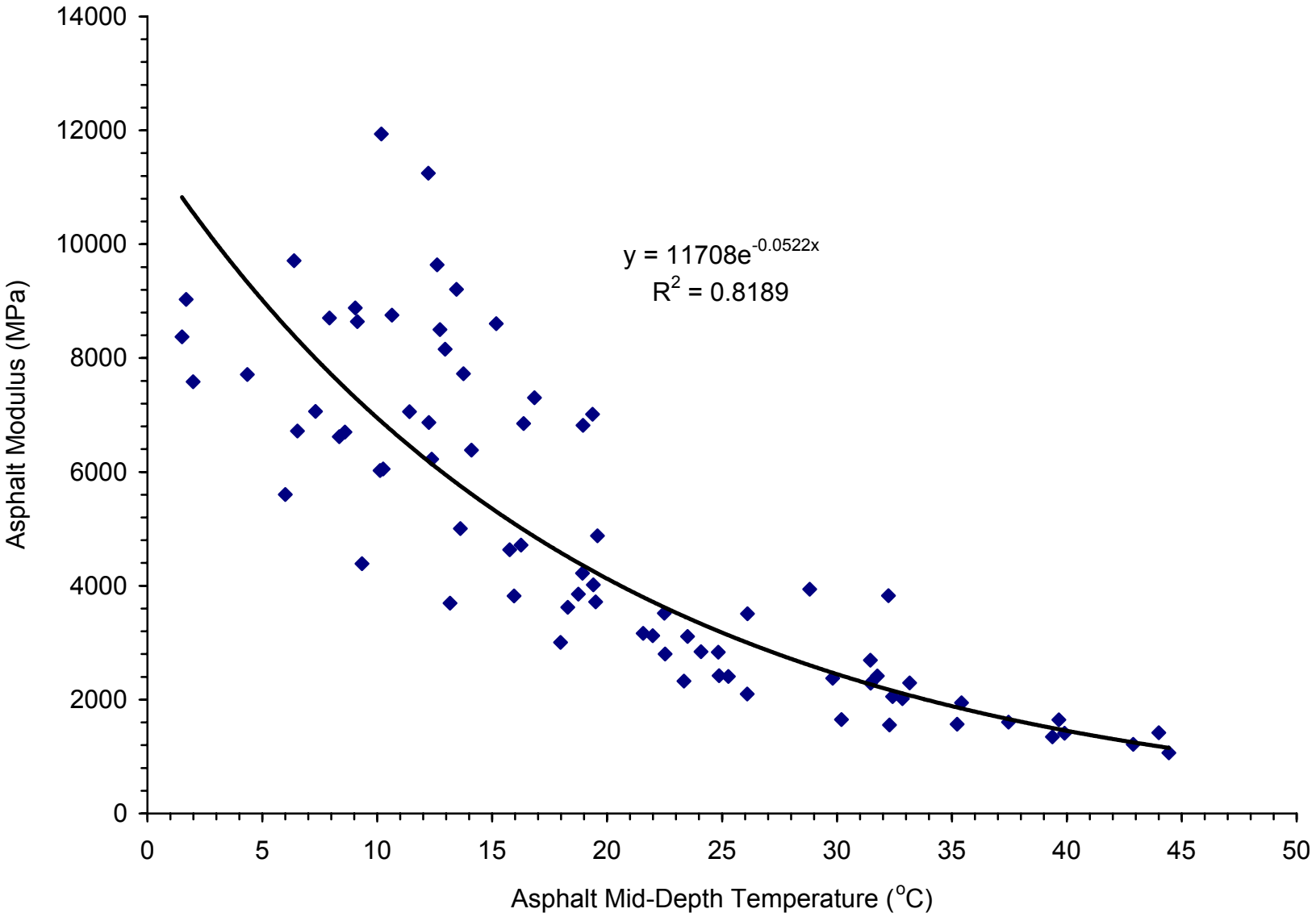

Figure I-3. Asphalt Modulus Model for Site 08-1053

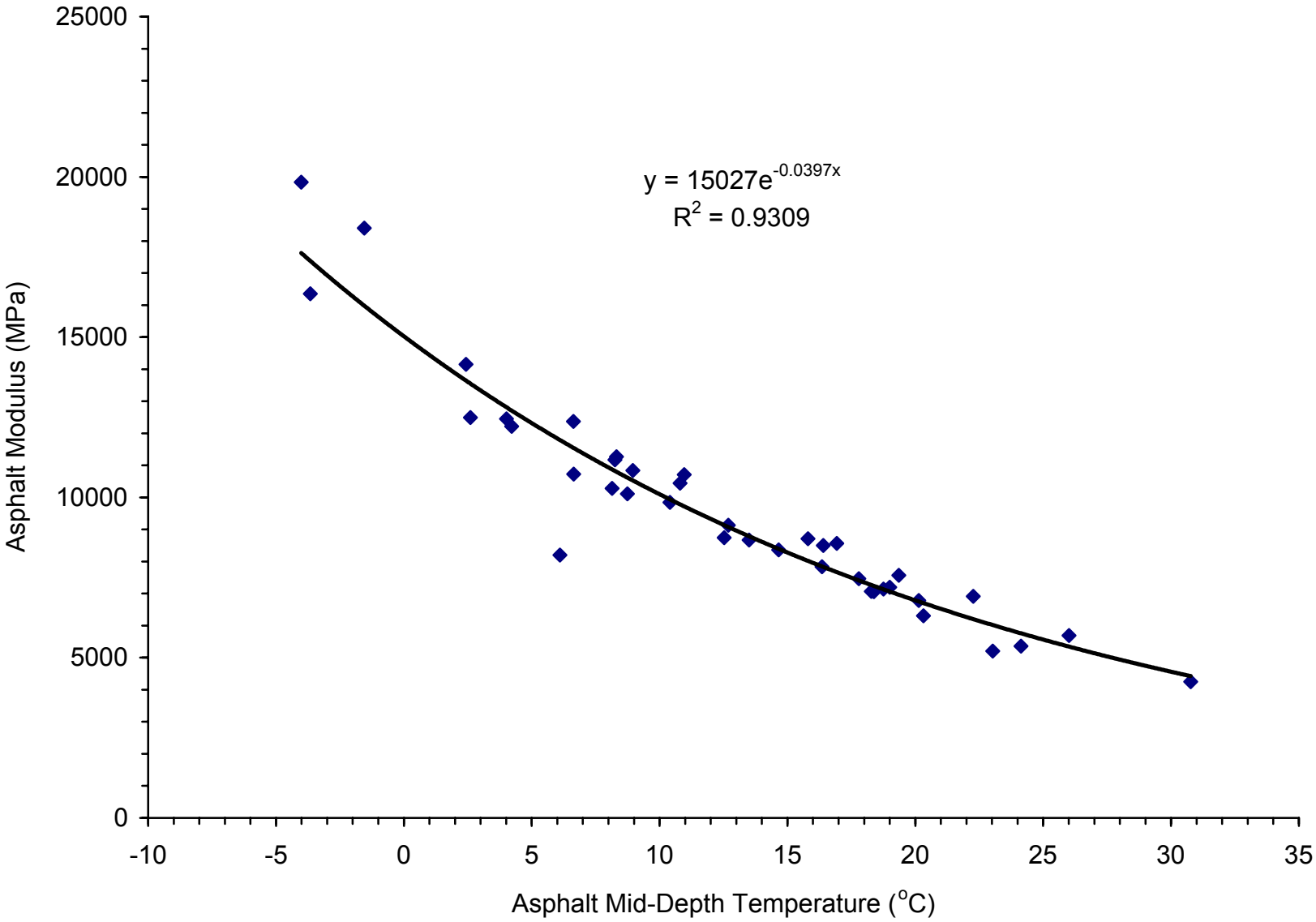

Figure I-4. Asphalt Modulus Model for Site 09-1803

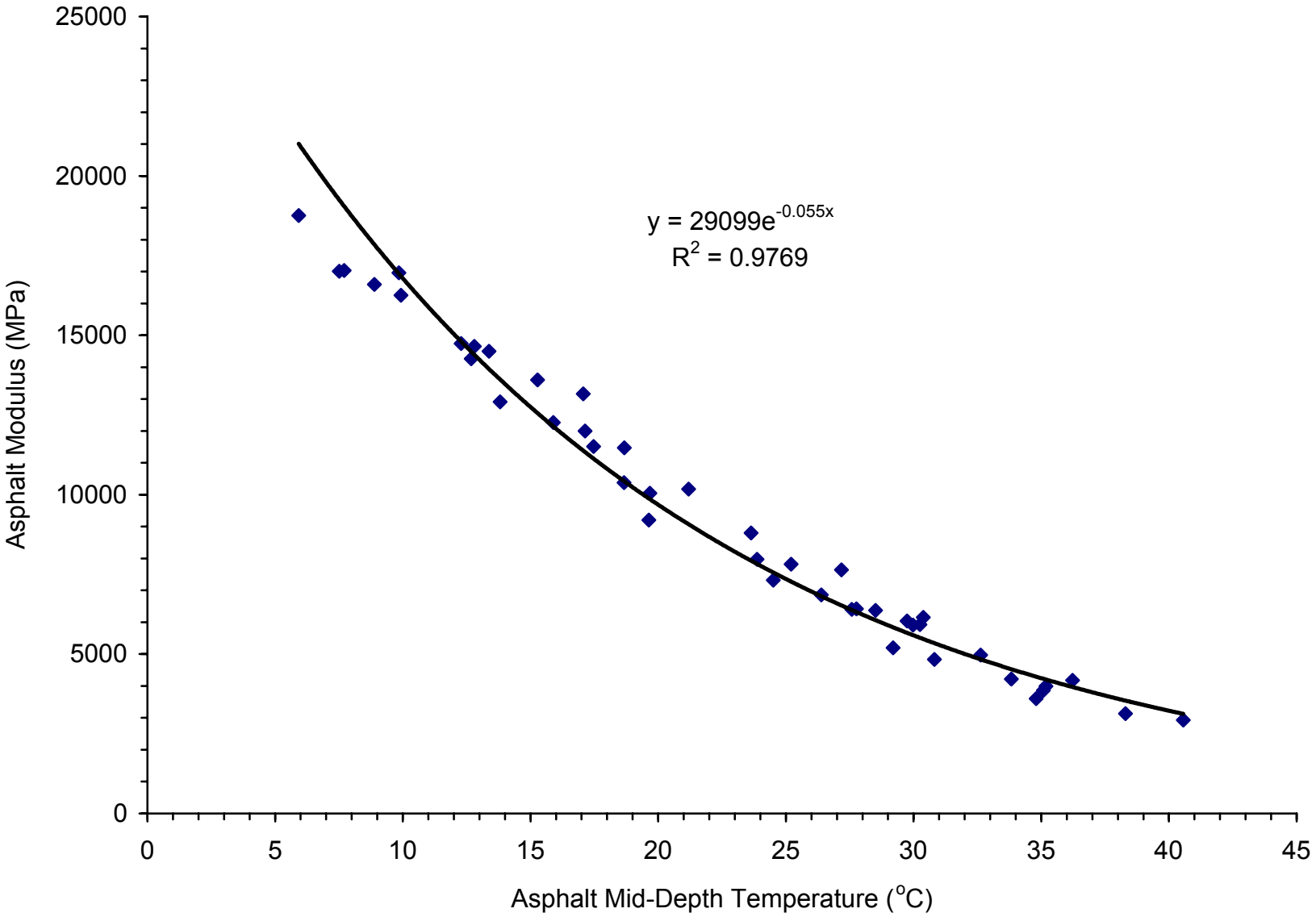

Figure I-5. Asphalt Modulus Model for Site 13-1005

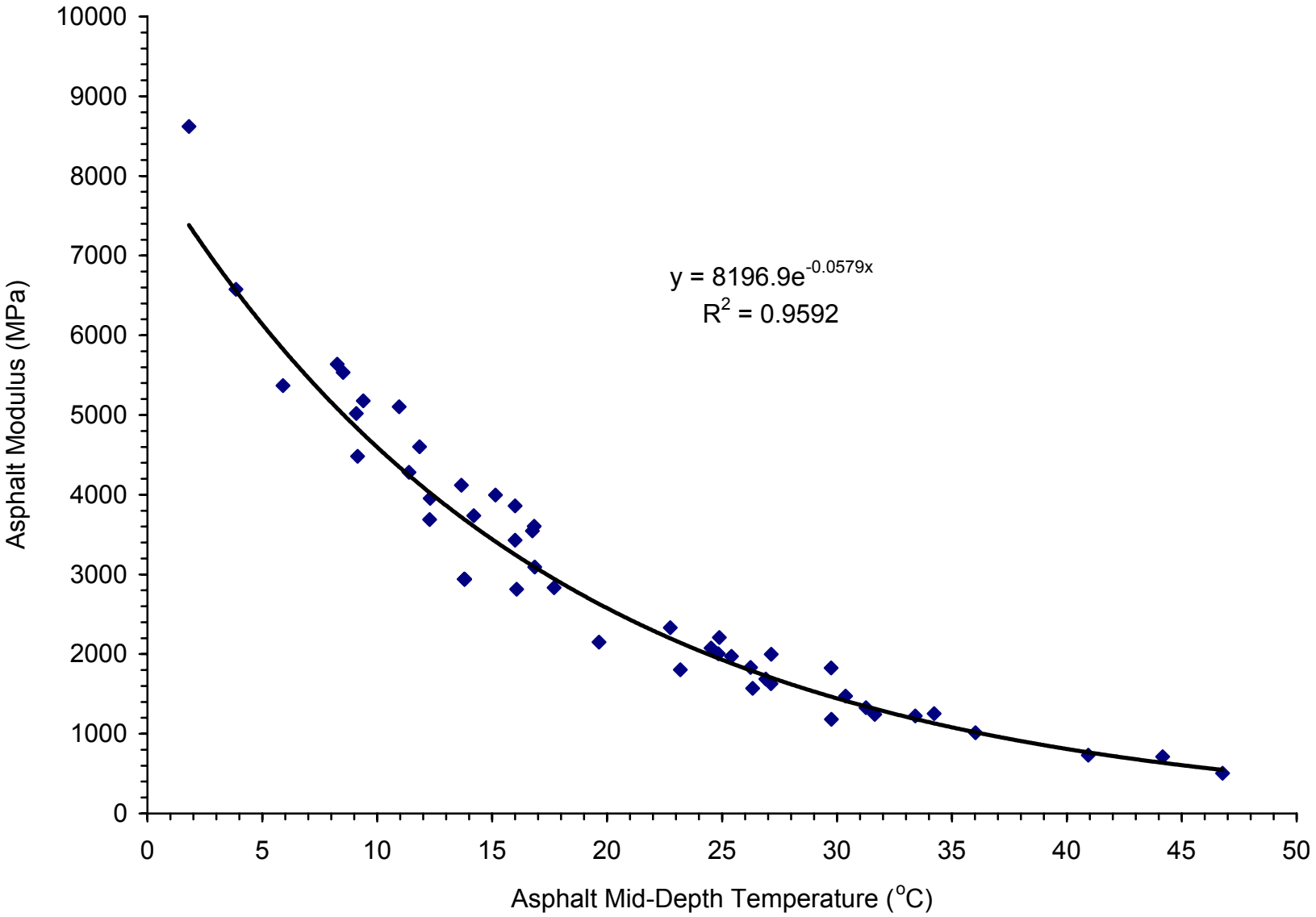

Figure I-6. Asphalt Modulus Model for Site 13-1031

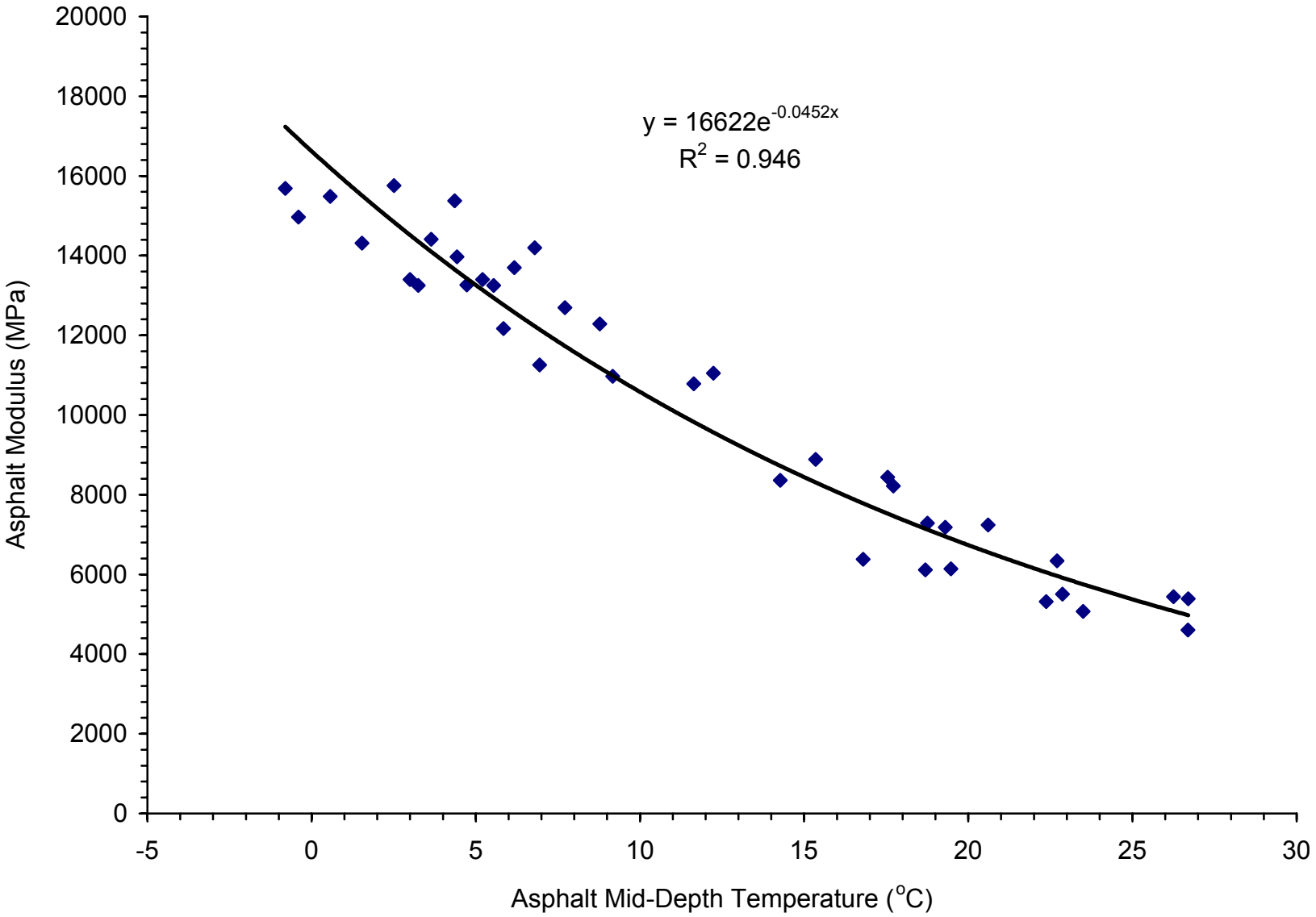

Figure I-7. Asphalt Modulus Model for Site 16-1010

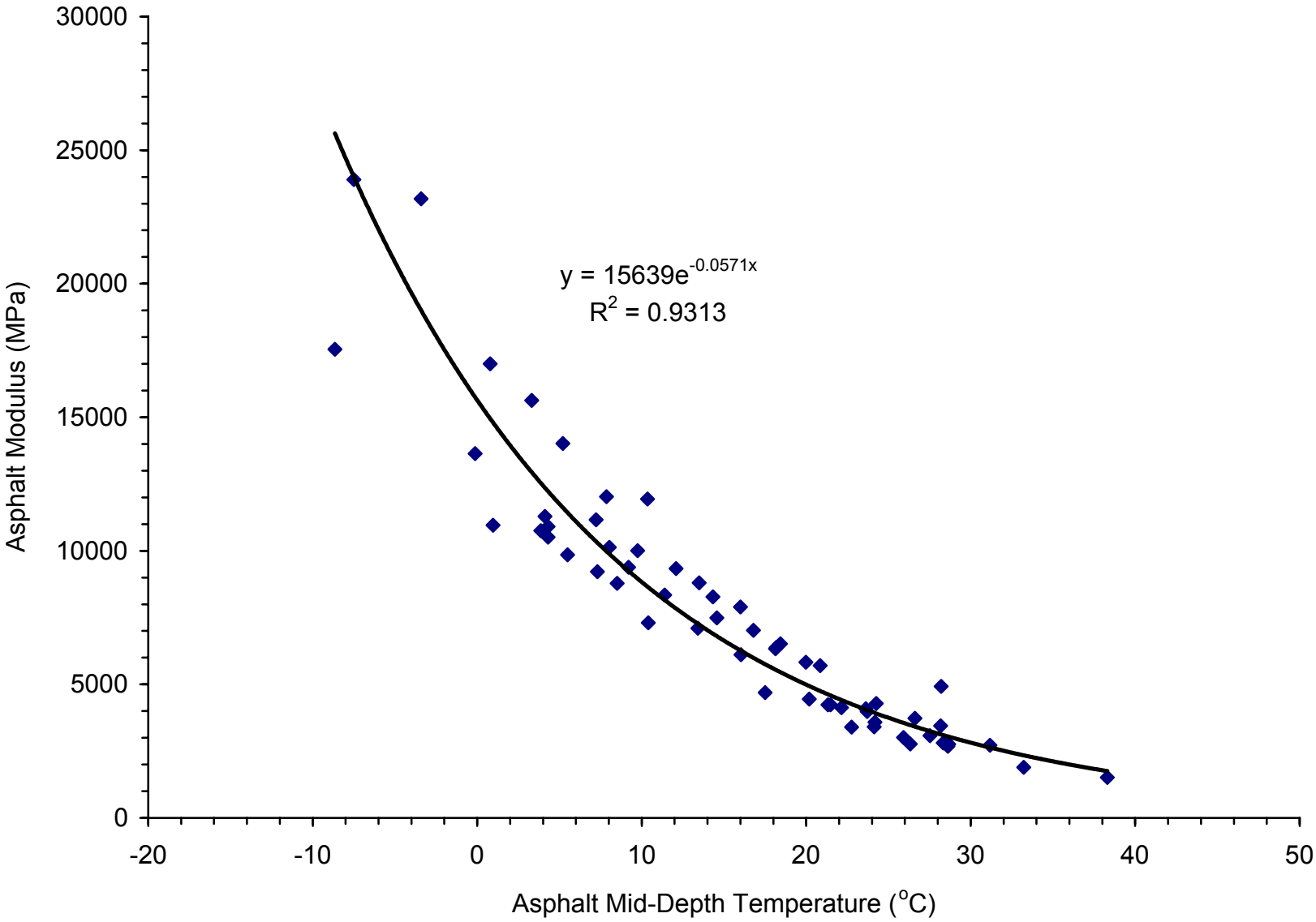

Figure I-8. Asphalt Modulus Model for Site 23-1026

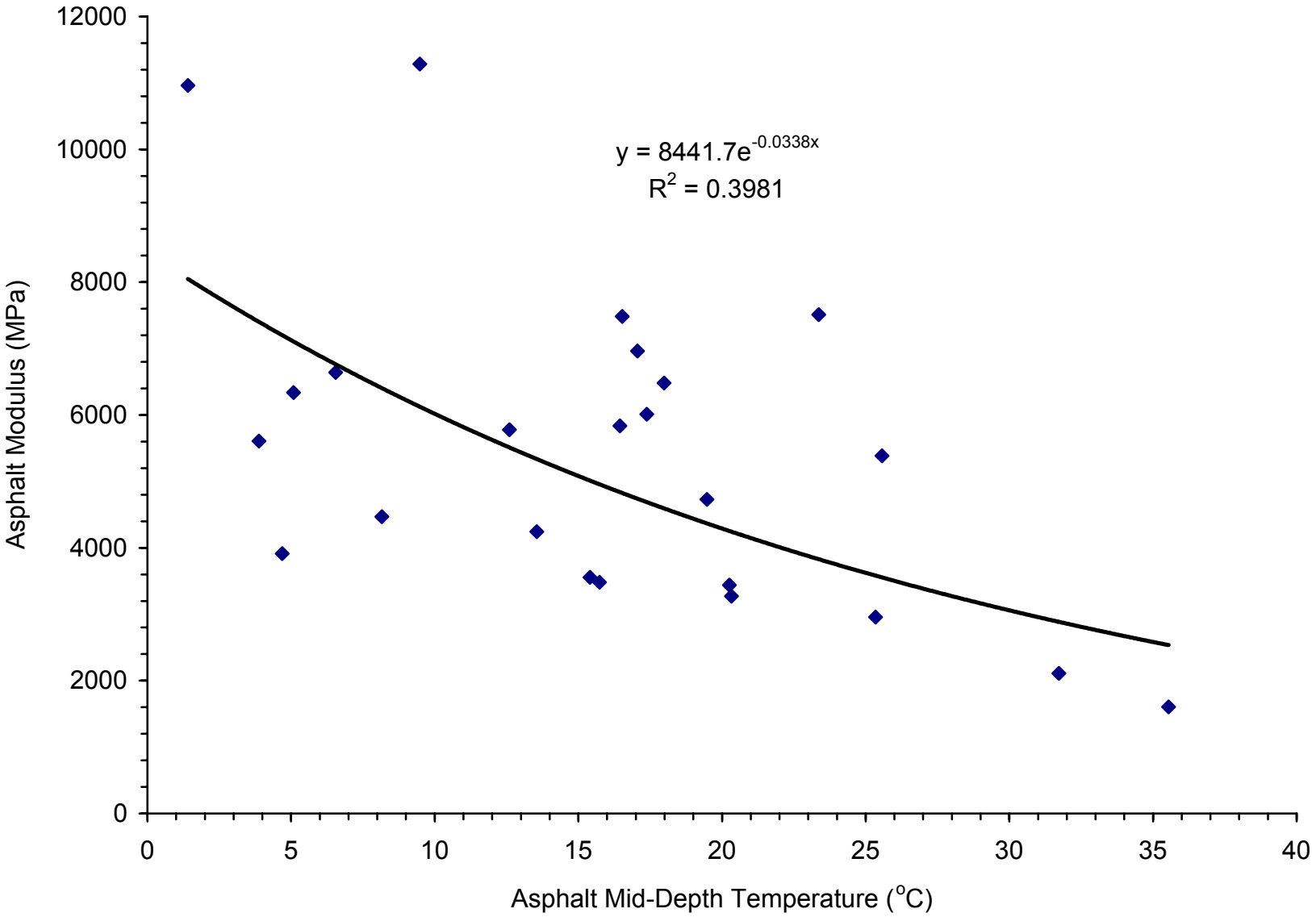

Figure I-9. Asphalt Modulus Model for Site 24-1634

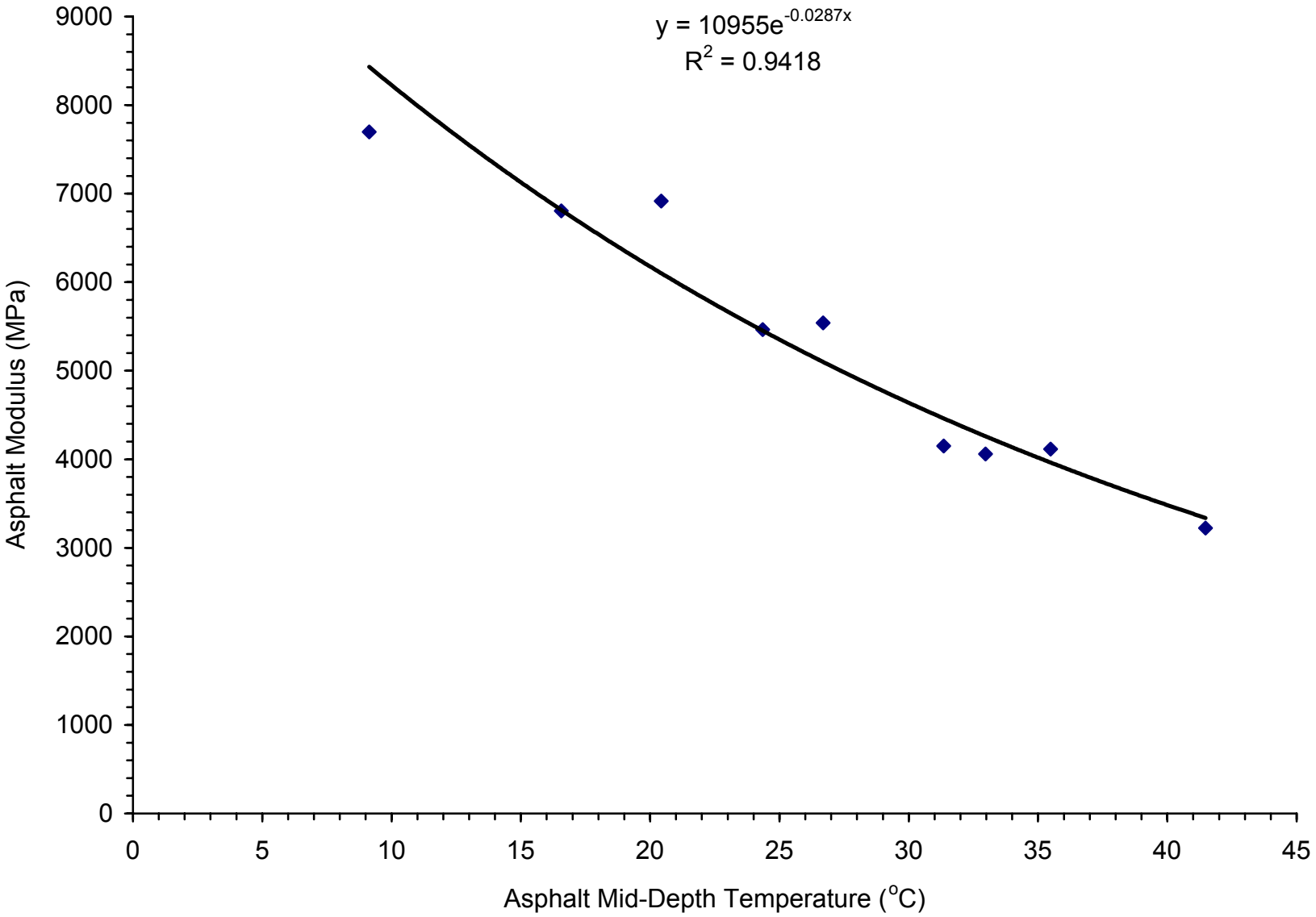

Figure I-10. Asphalt Modulus Model for Site 27-1018

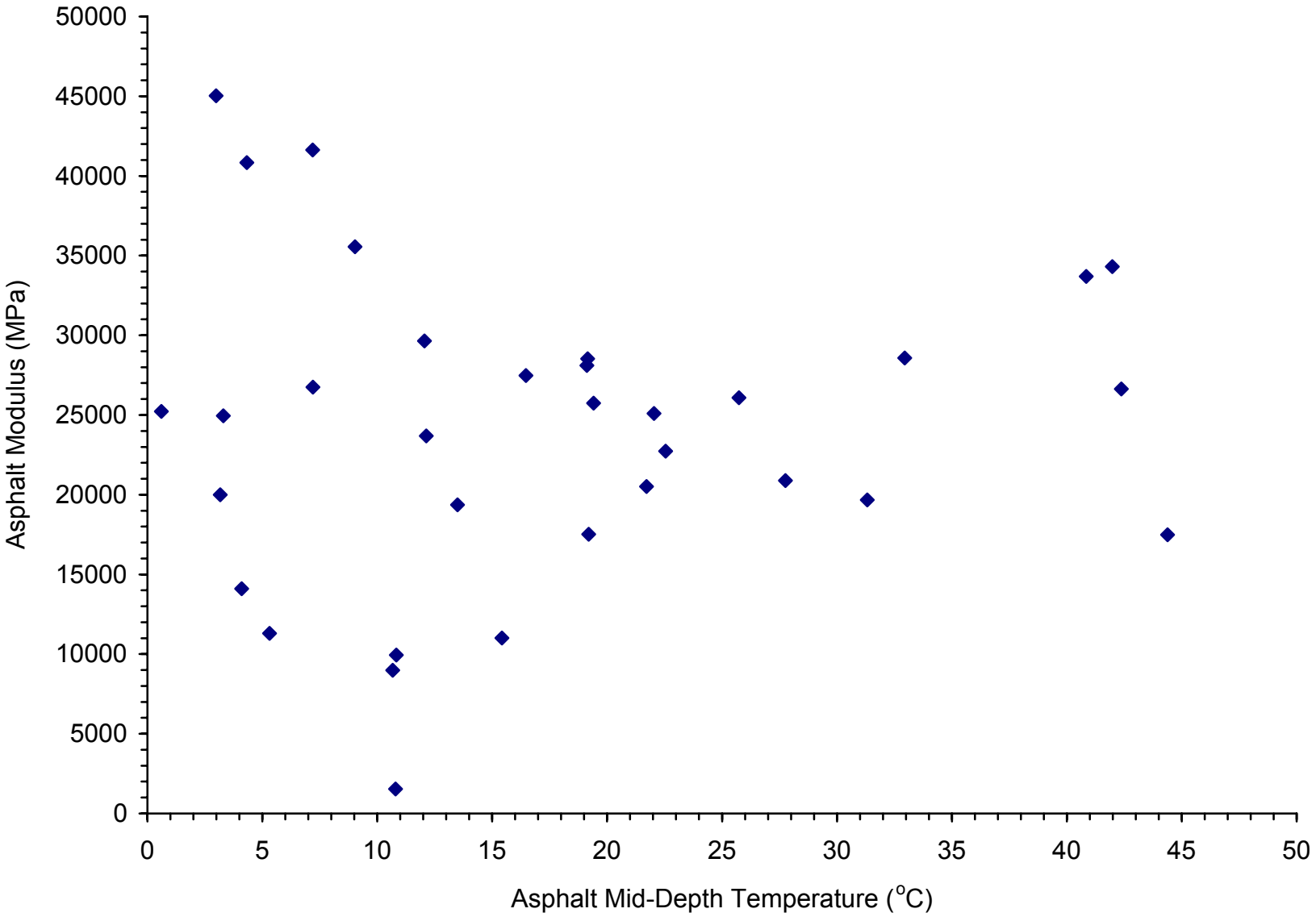

Figure I-11. Asphalt Modulus Model for Site 27-1028

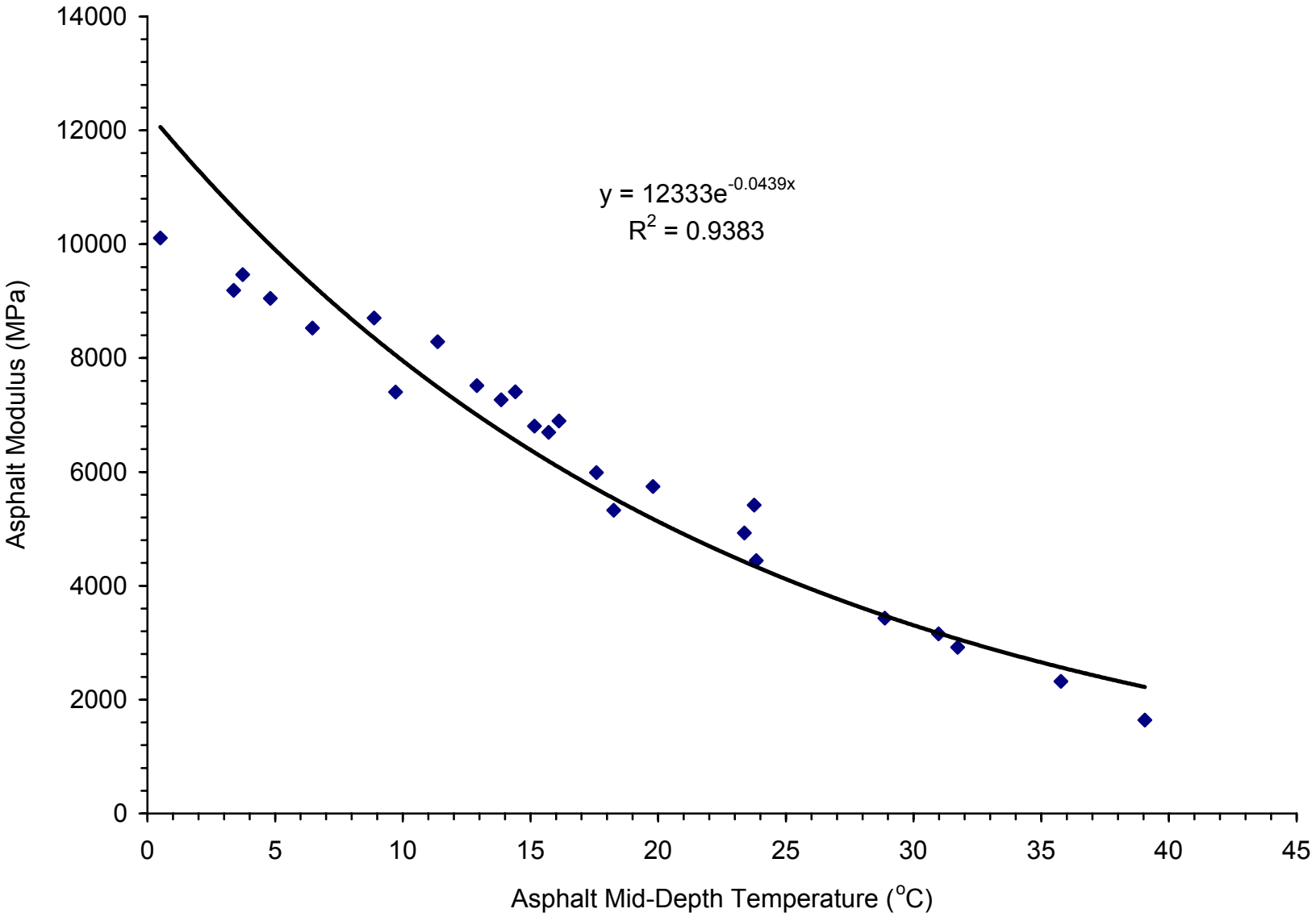

Figure I-12. Asphalt Modulus Model for Site 27-6251

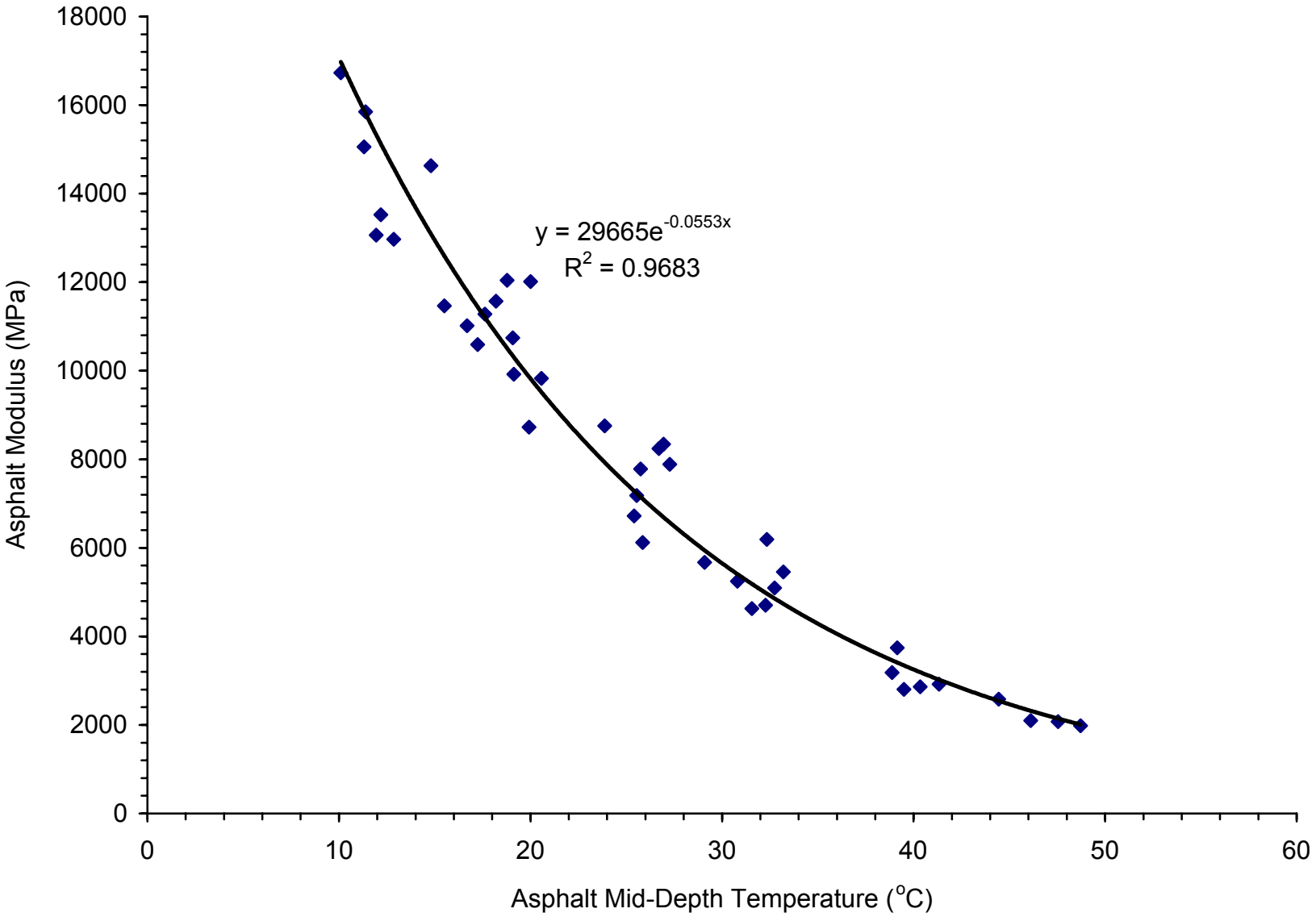

Figure I-13. Asphalt Modulus Model for Site 28-1016

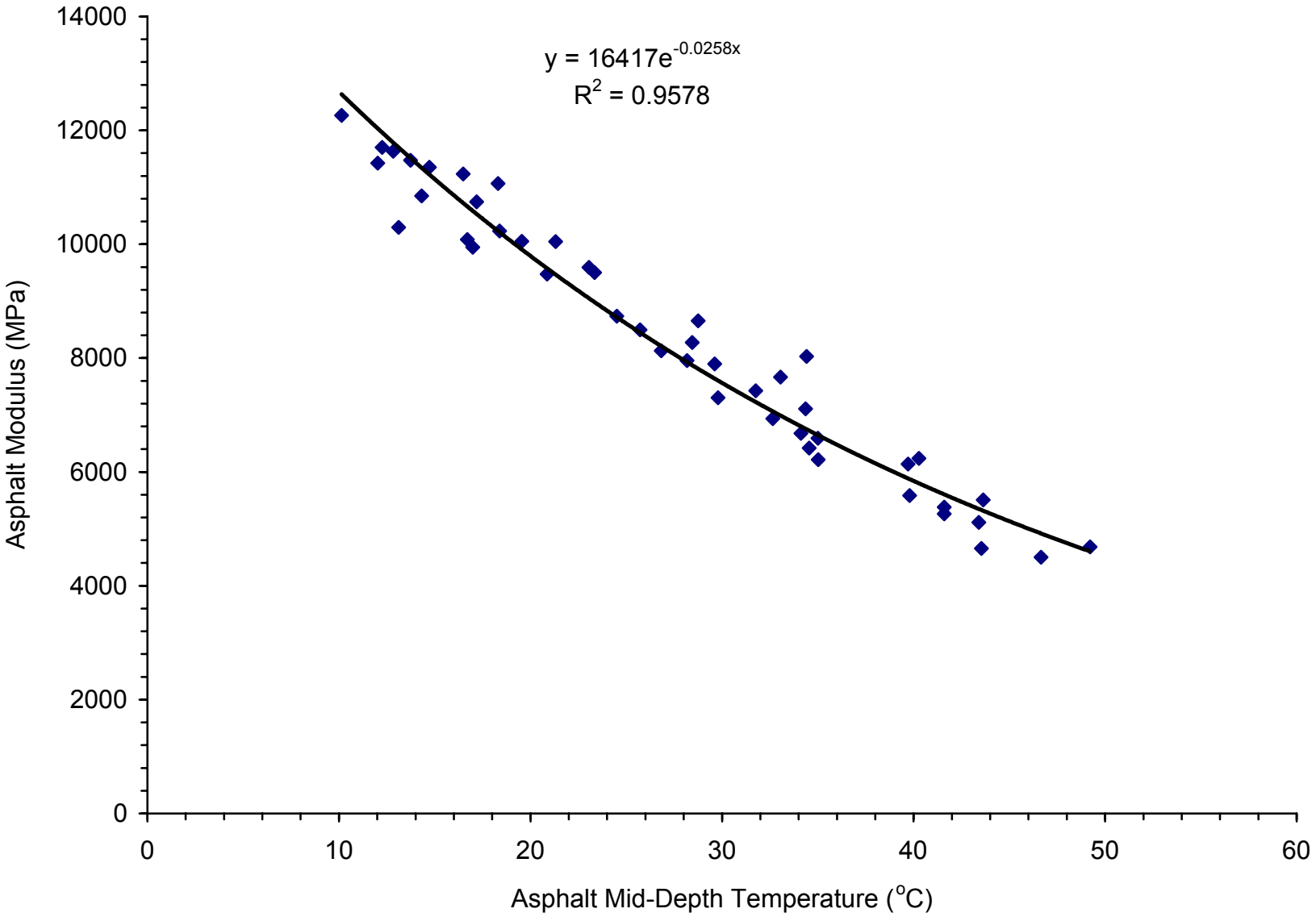

Figure I-14. Asphalt Modulus Model for Site 28-1802

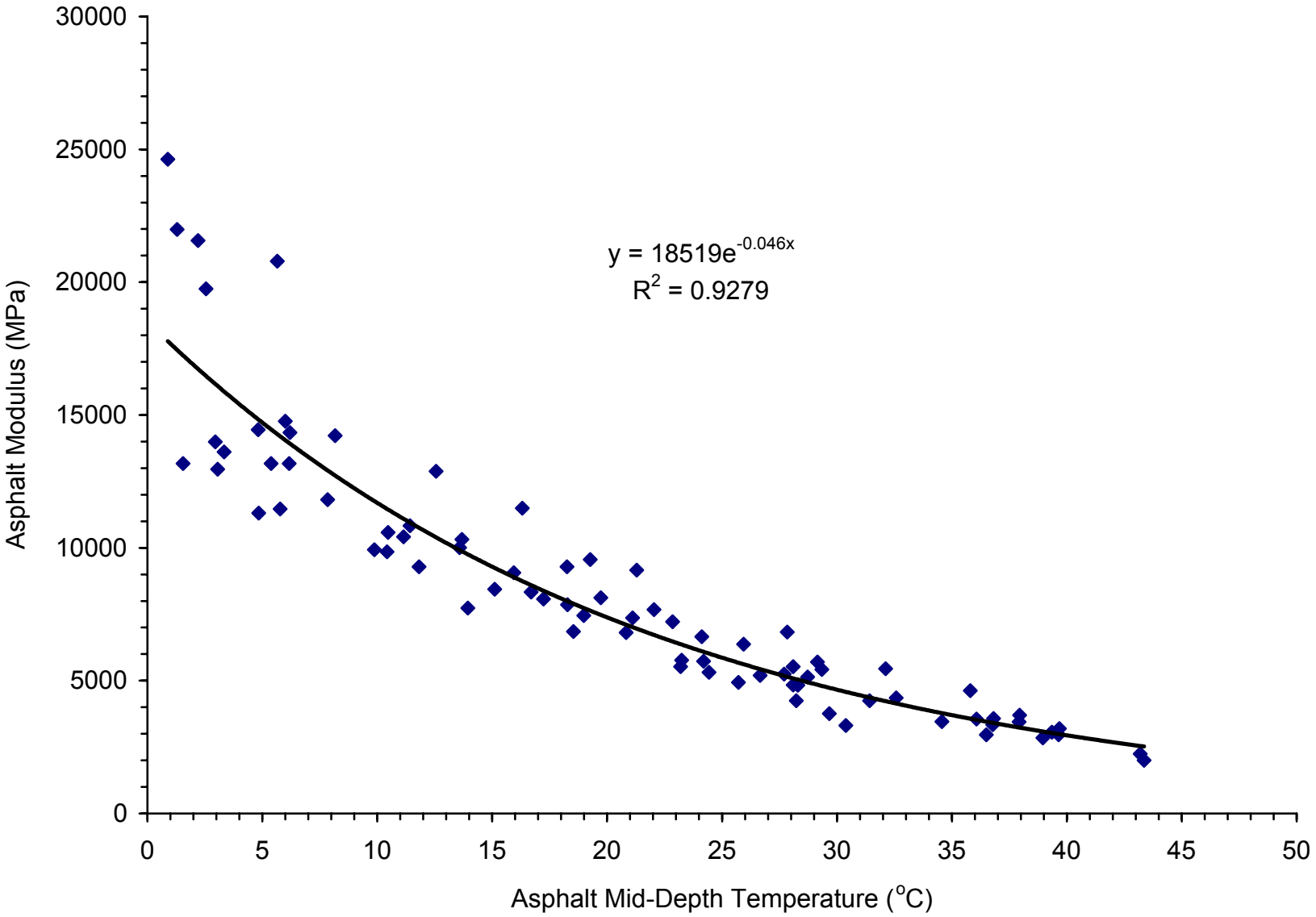

Figure I-15. Asphalt Modulus Model for Site 30-8129

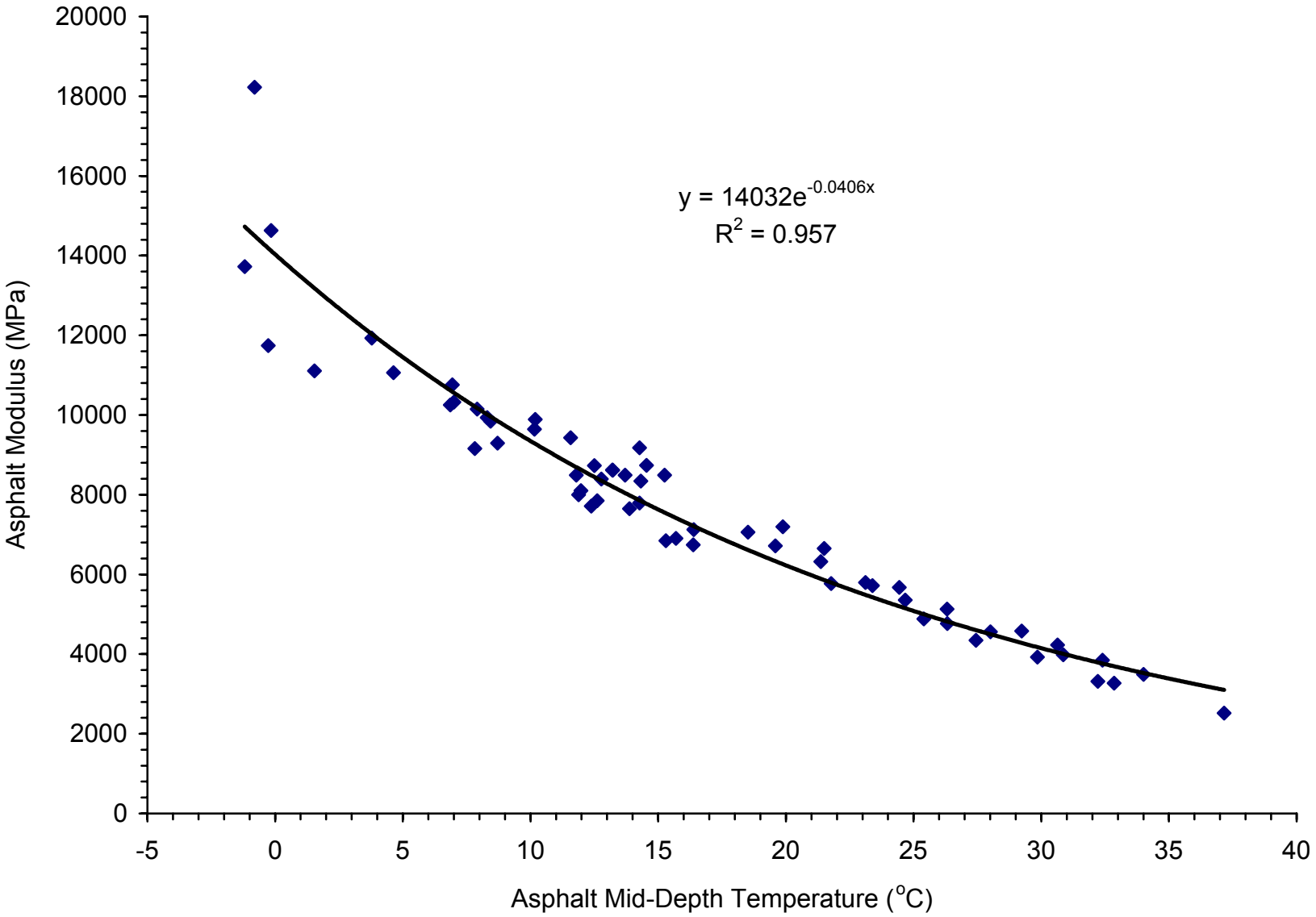

Figure I-16. Asphalt Modulus Model for Site 33-1001

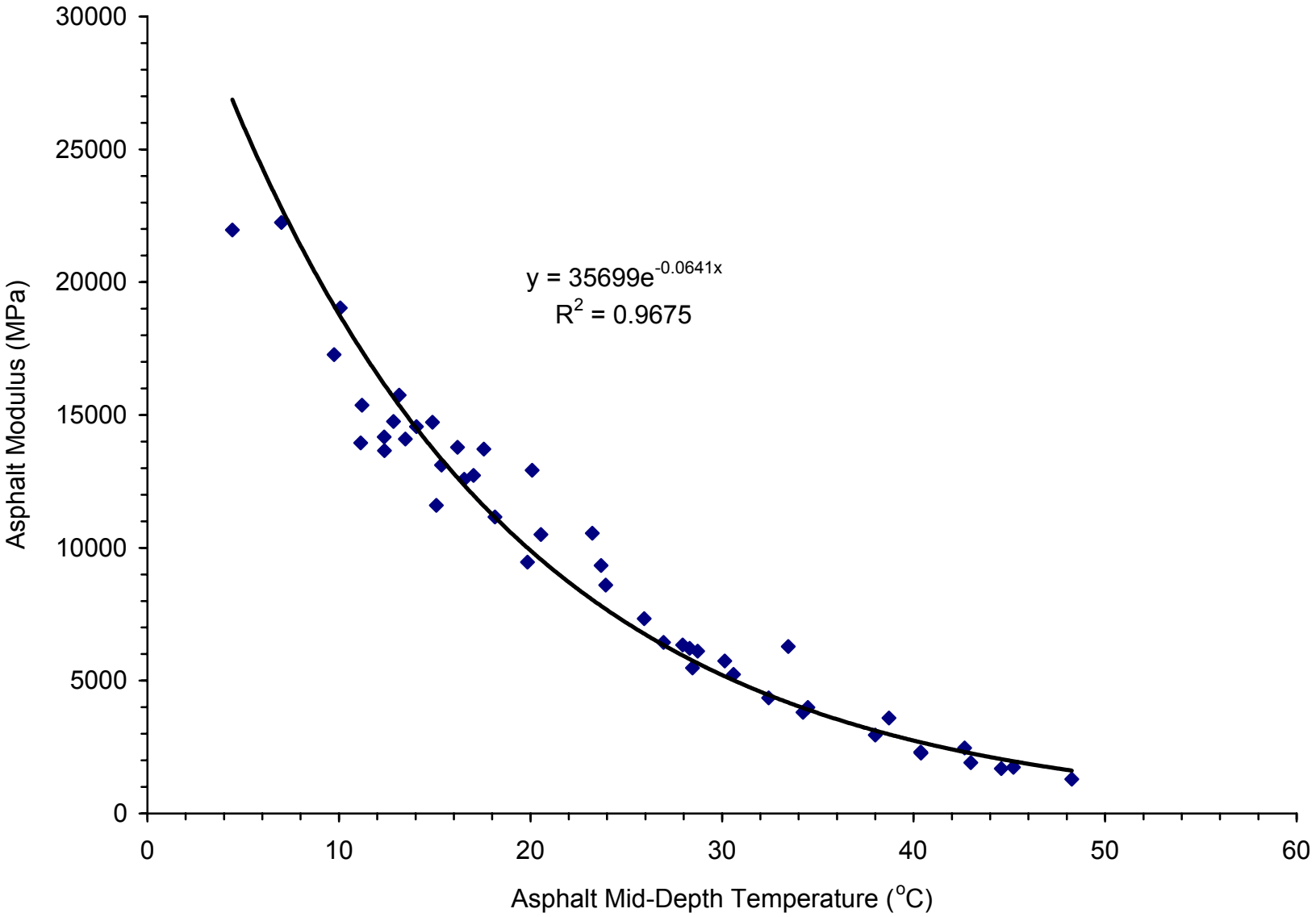

Figure I-17. Asphalt Modulus Model for Site 35-1112

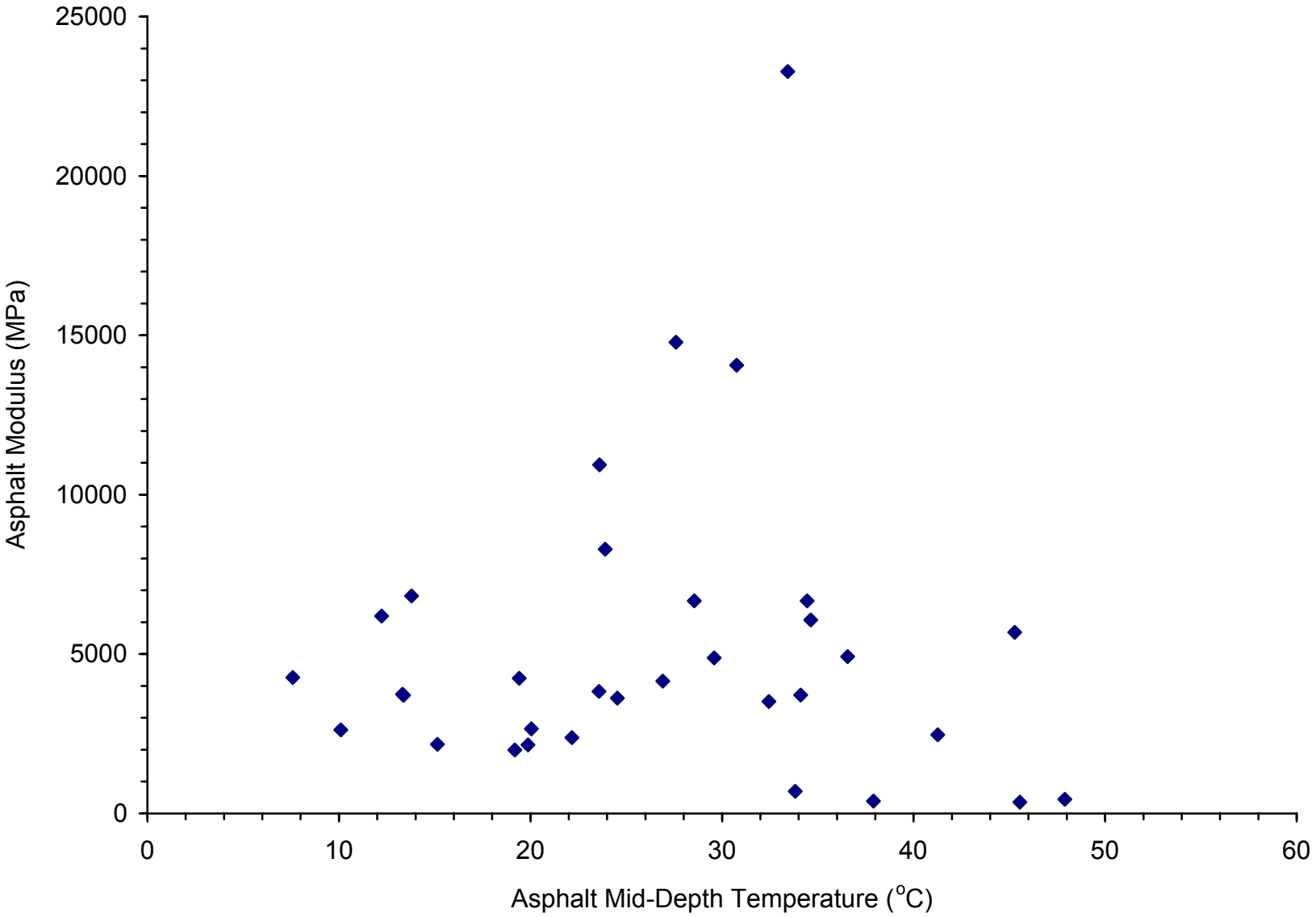

Figure I-18. Asphalt Modulus Model for Site 37-1028

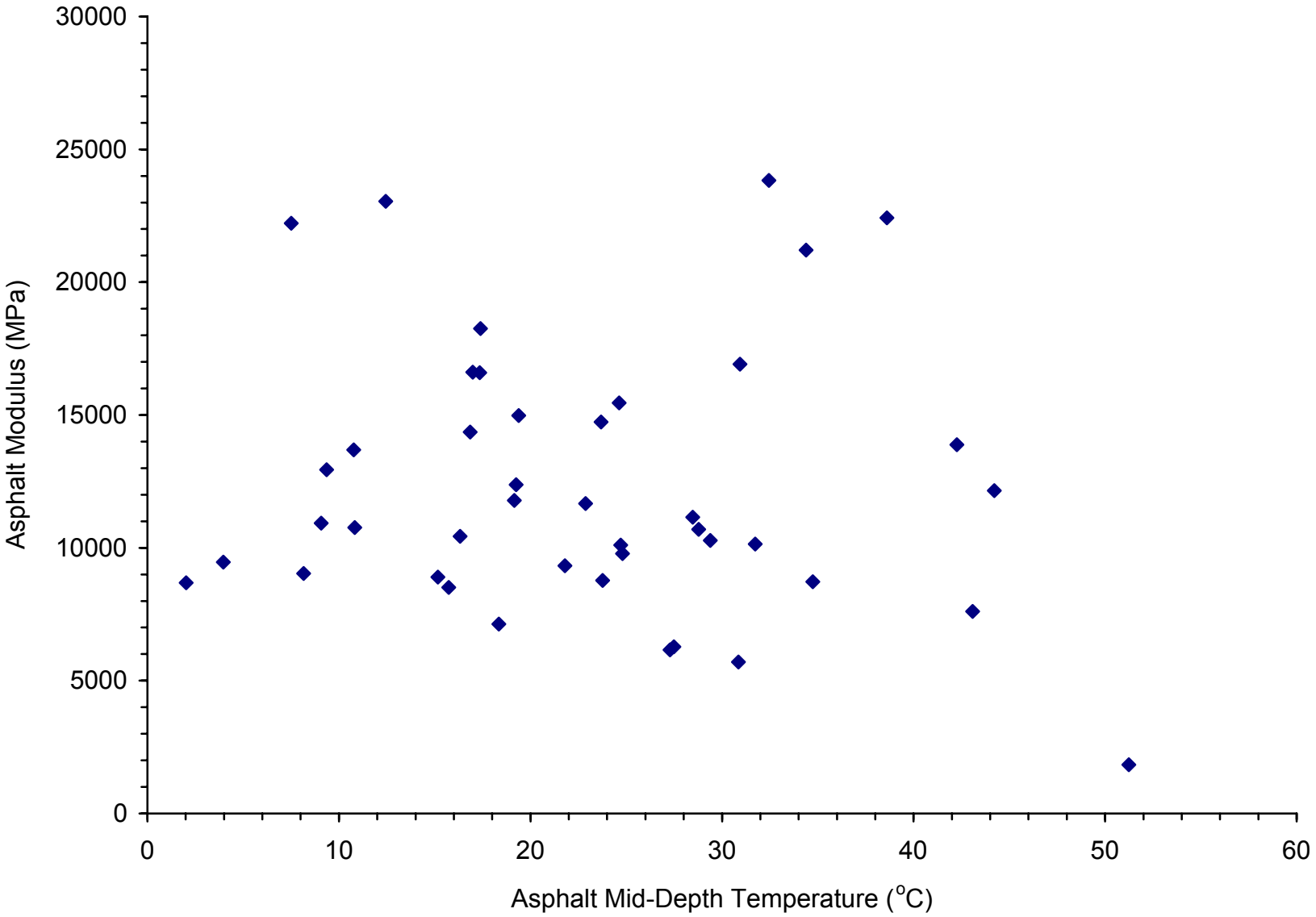

Figure I-19. Asphalt Modulus Model for Site 40-4165

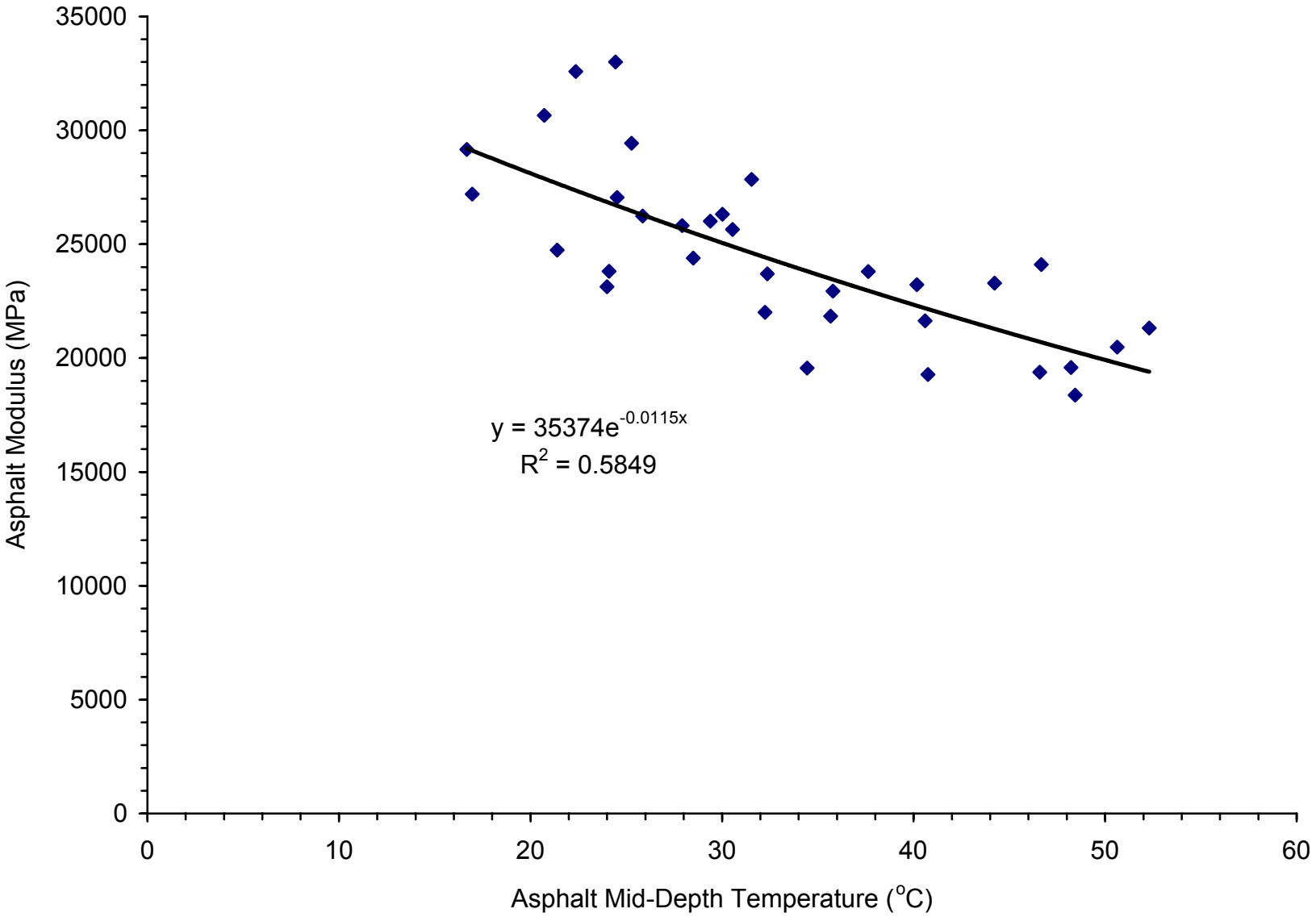

Figure I-20. Asphalt Modulus Model for Site 47-3739

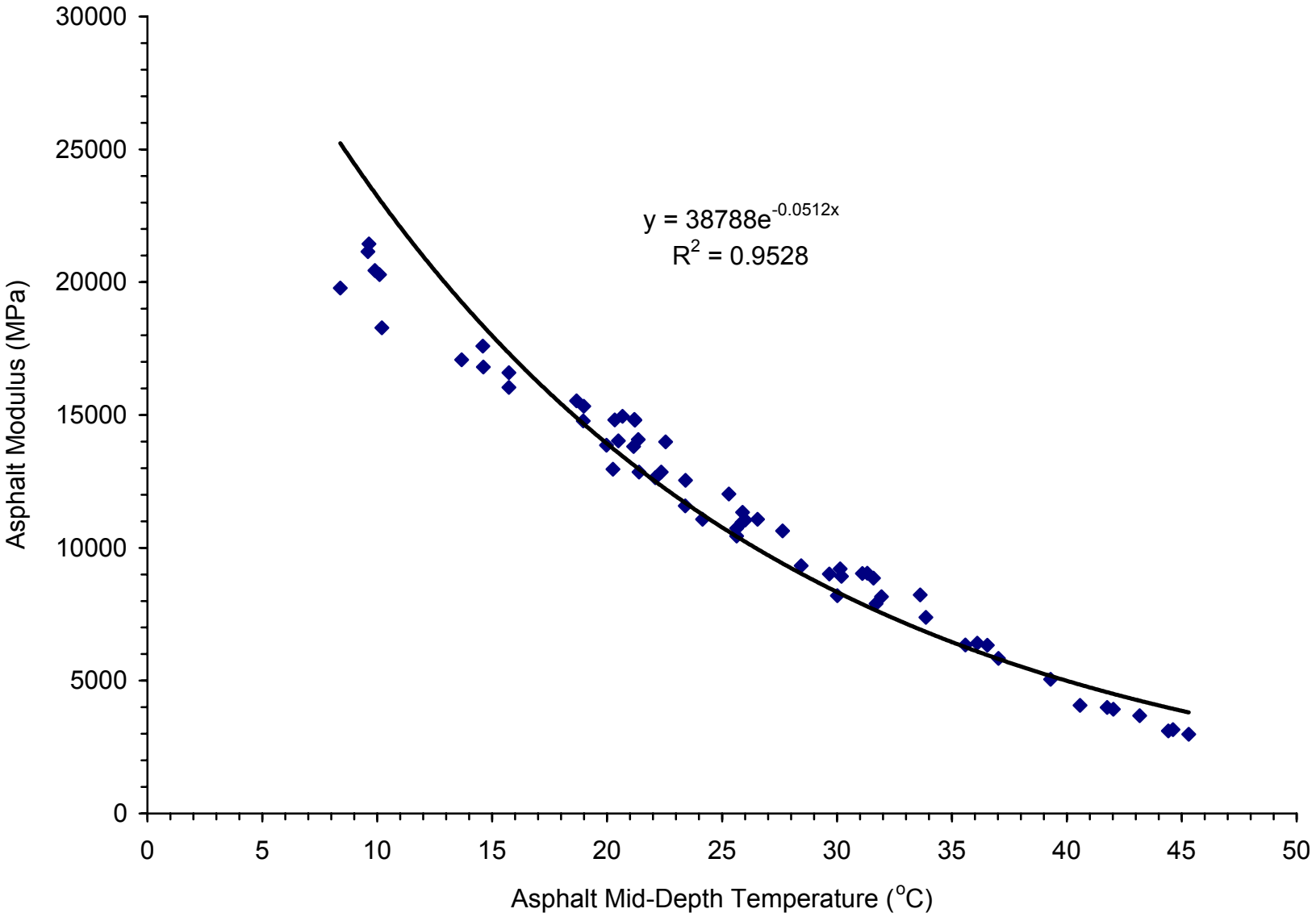

Figure I-21. Asphalt Modulus Model for Site 48-1060

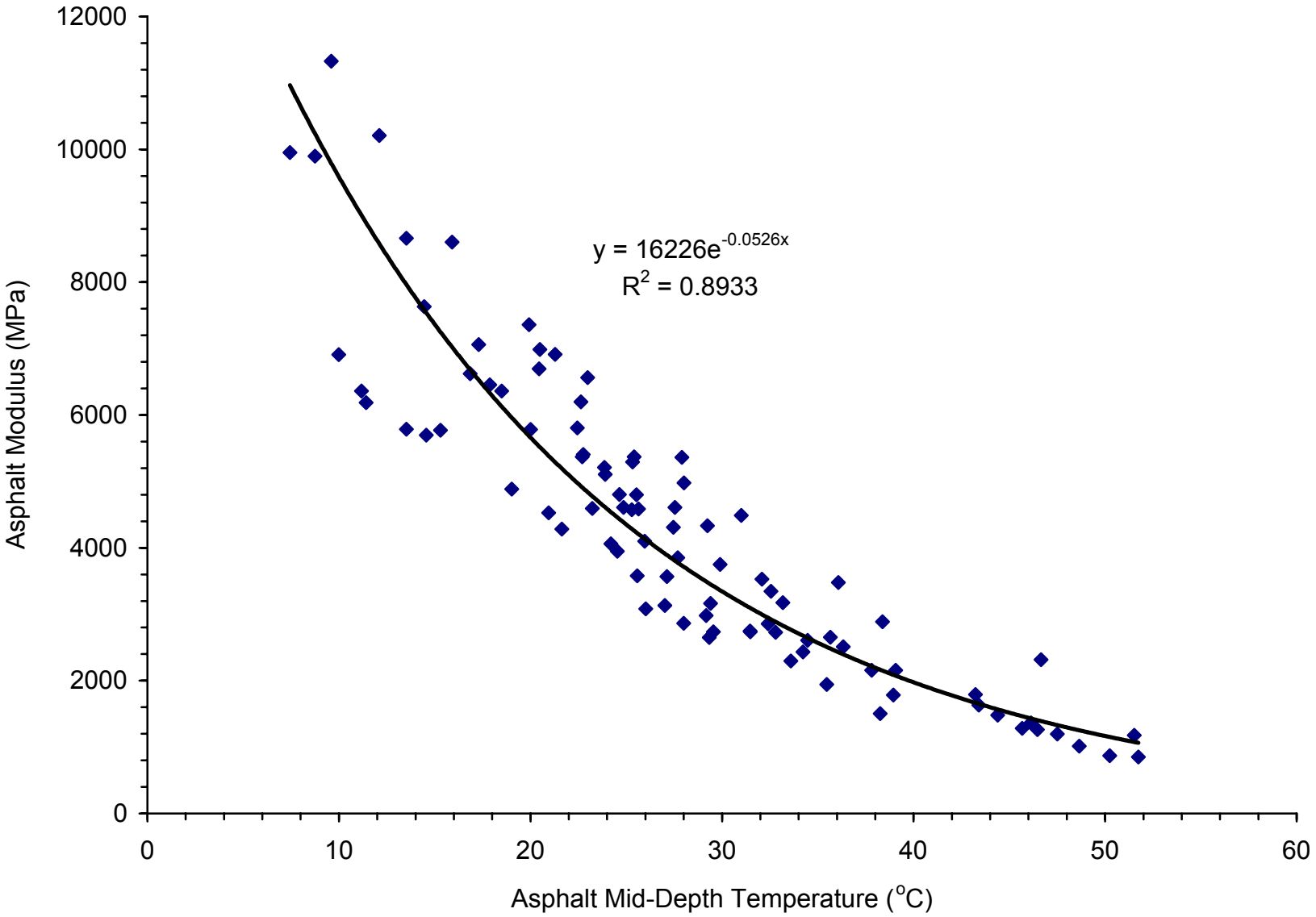

Figure I-22. Asphalt Modulus Model for Site 48-1122

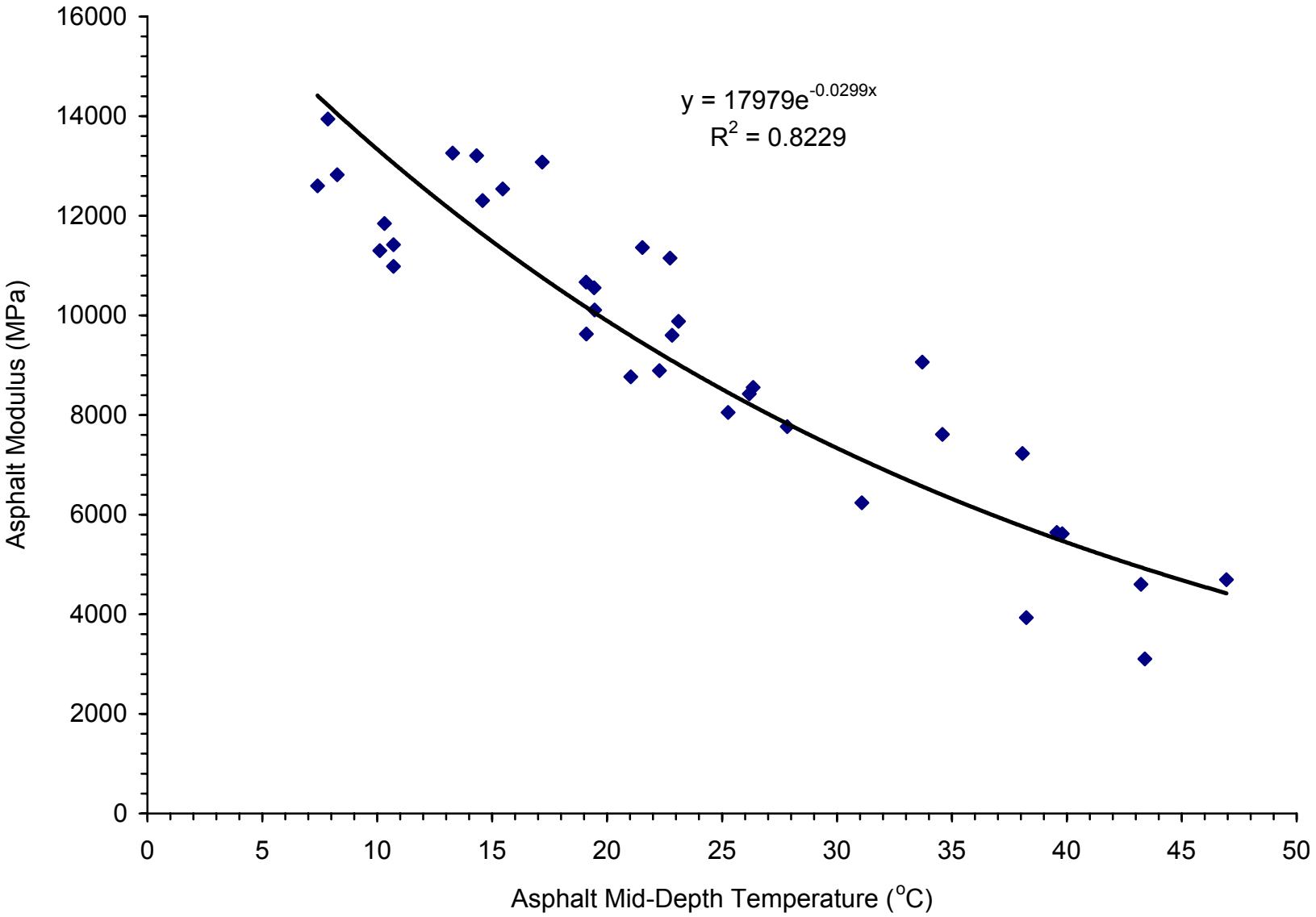

Figure I-23. Asphalt Modulus Model for Site 49-1001

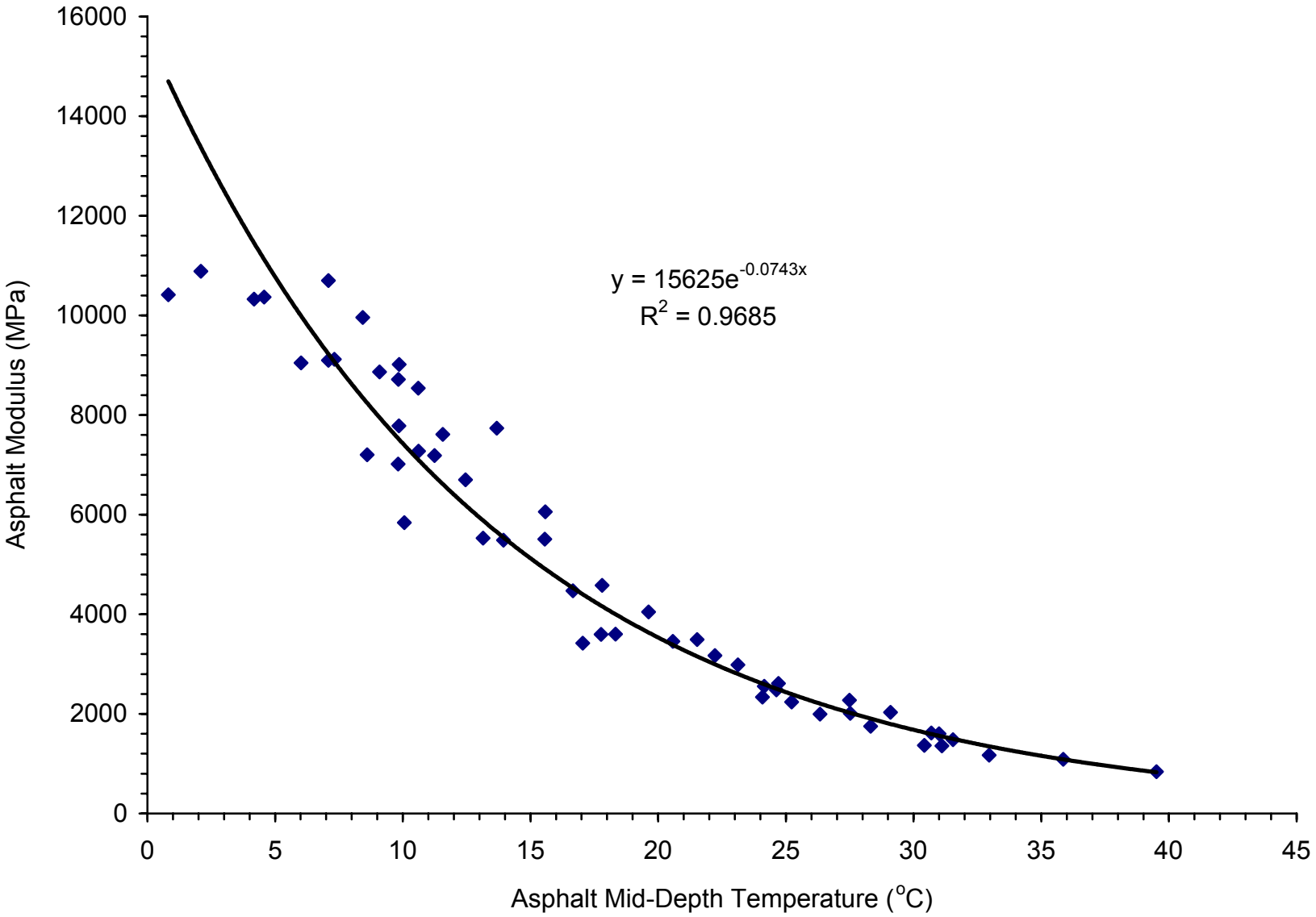

Figure I-24. Asphalt Modulus Model for Site 50-1002

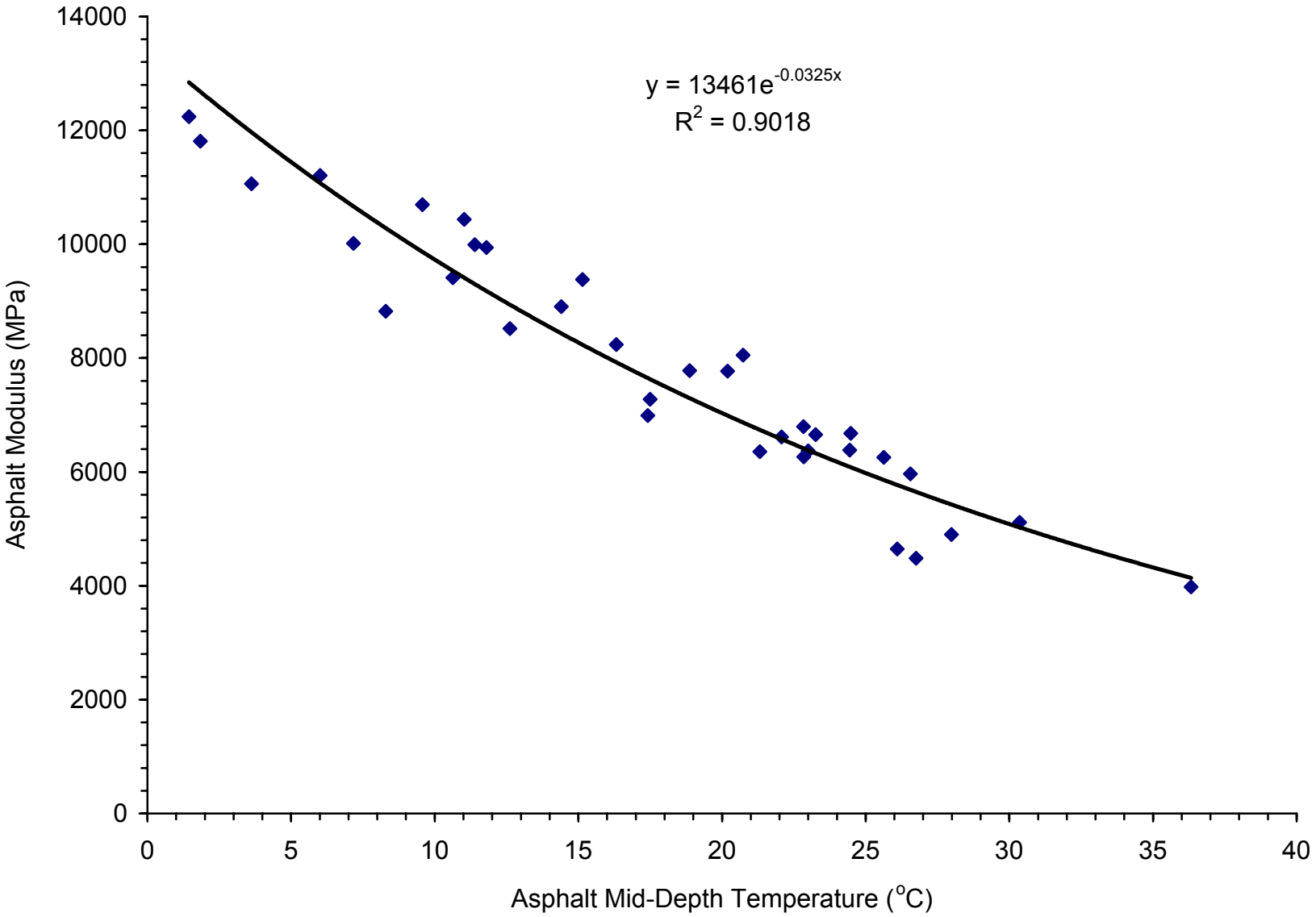

Figure I-25. Asphalt Modulus Model for Site 56-1007

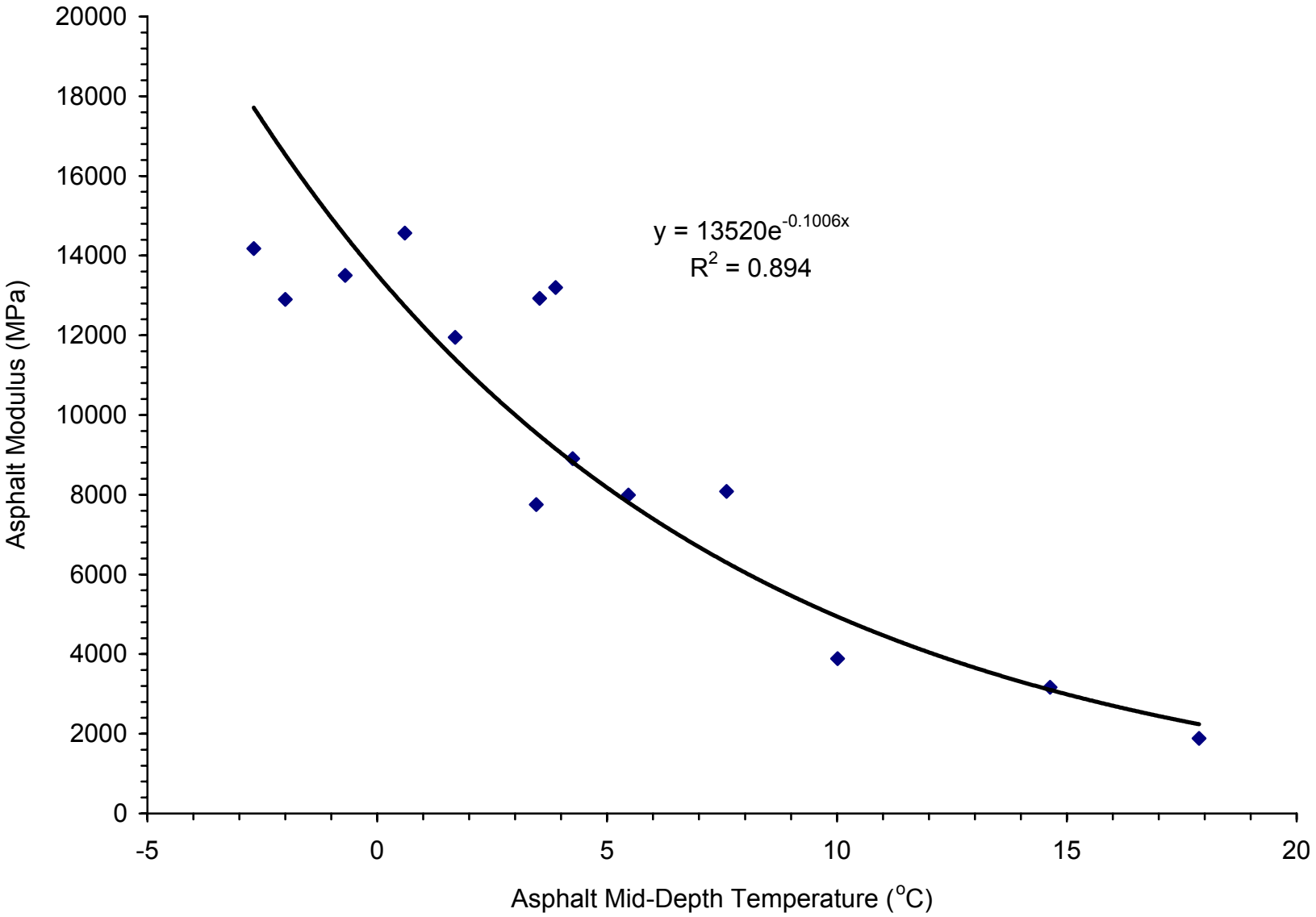

Figure I-26. Asphalt Modulus Model for Site 83-1801

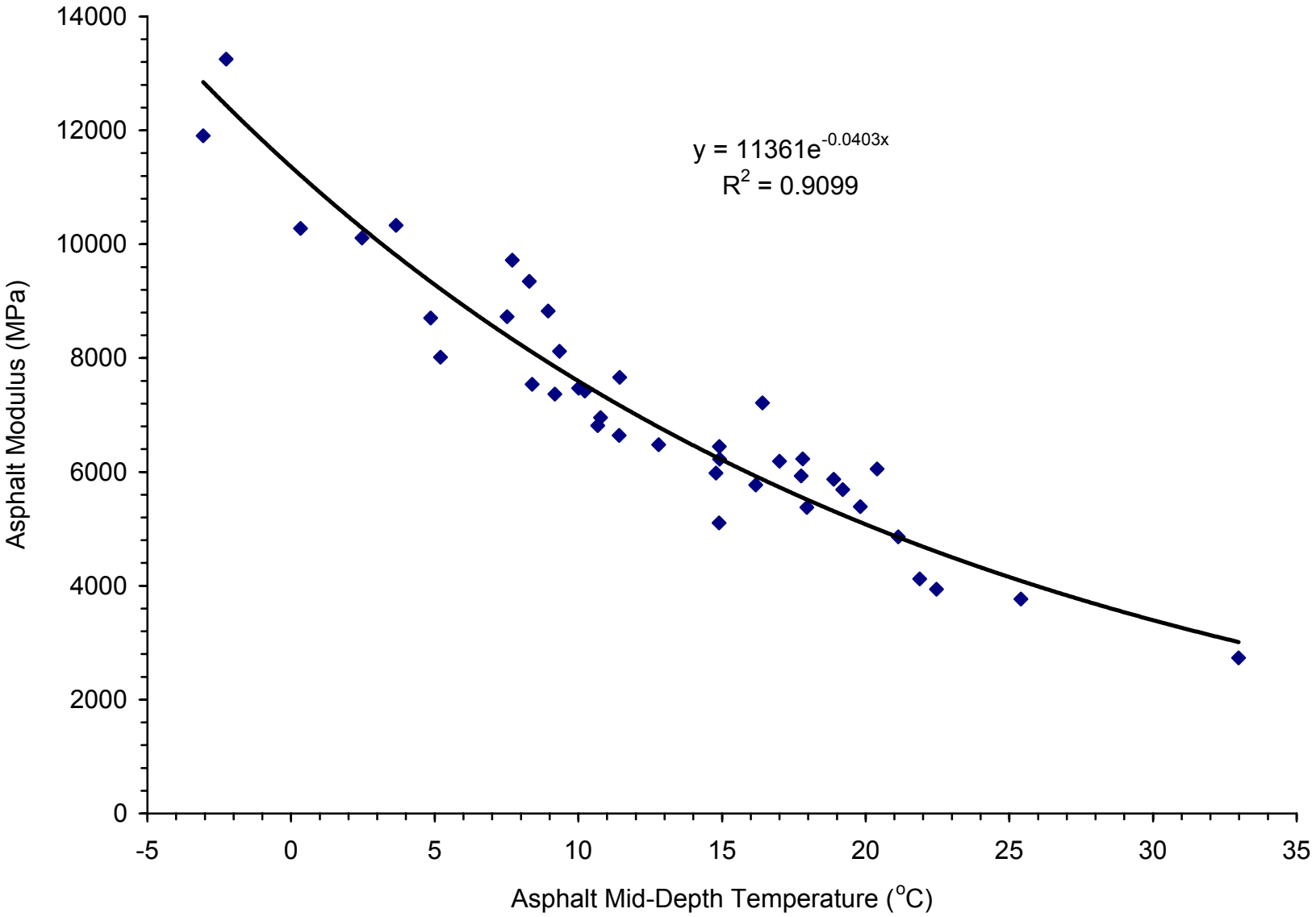

Figure I-27. Asphalt Modulus Model for Site 87-1622

APPENDIX J

ASPHALT MODULUS MODELS FOR DIFFERENT ASPHALT CEMENT GRADES

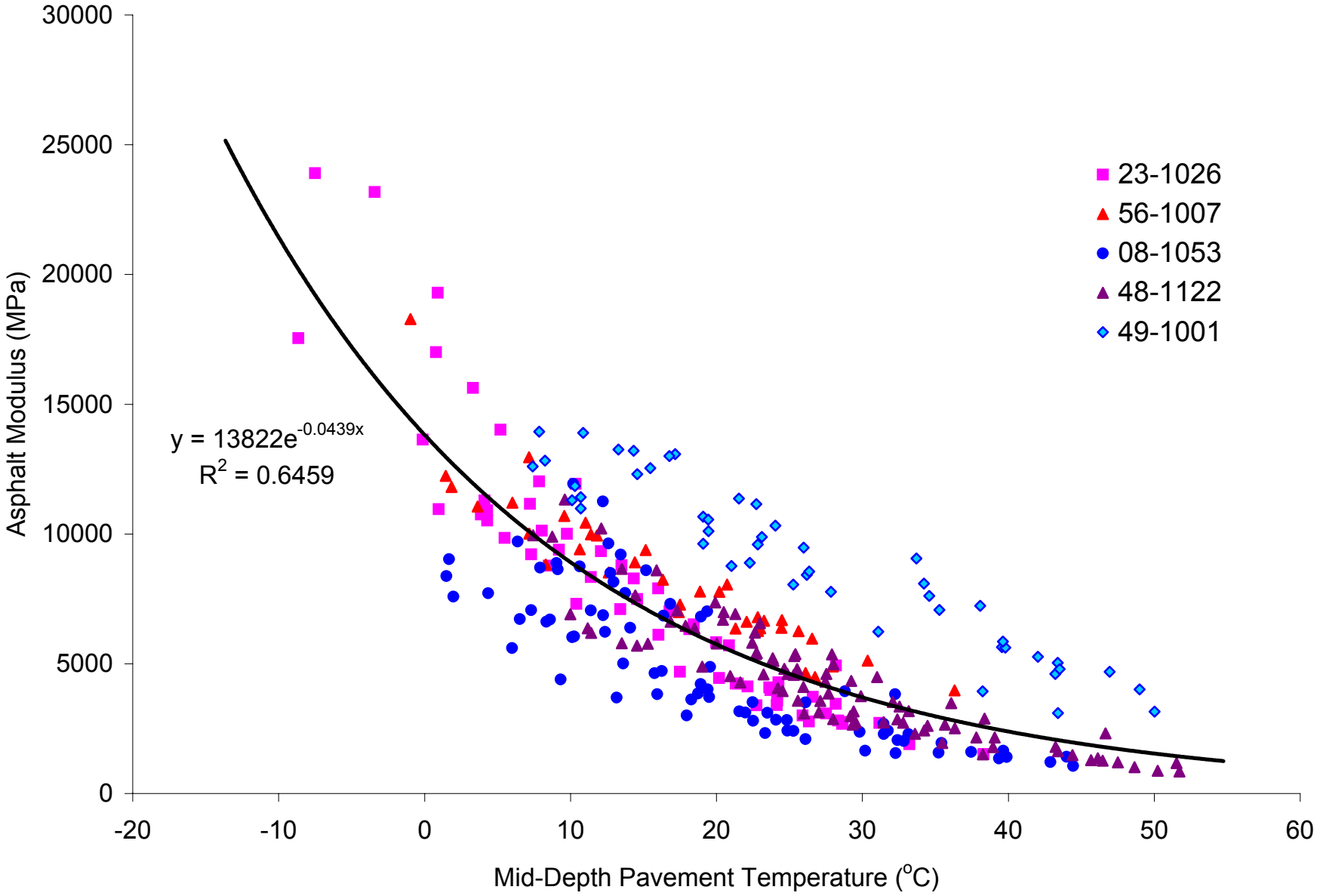

Figure J-1. Asphalt Modulus Models for Sites with Binder Grade AC-10

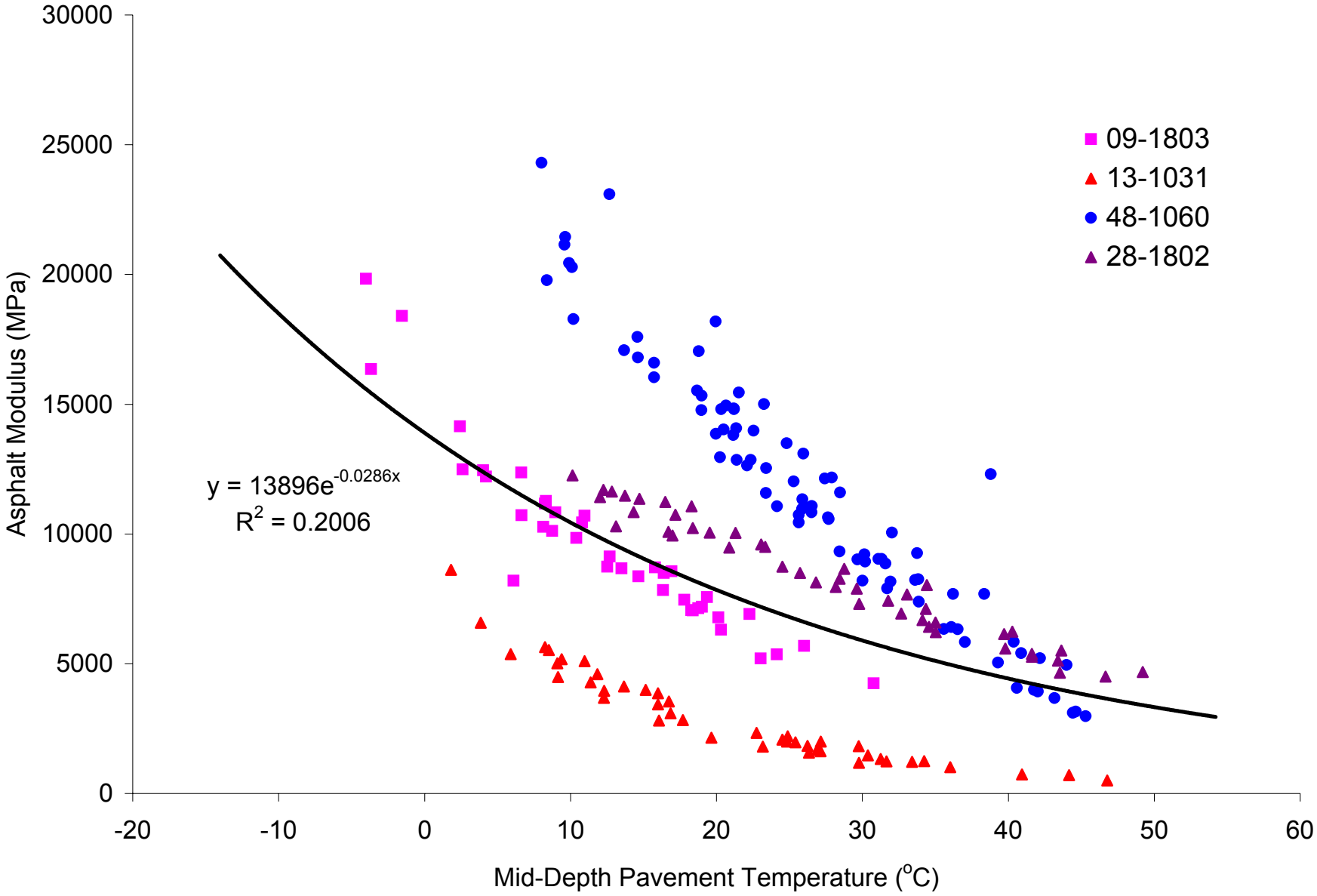

Figure J-2. Asphalt Modulus Models for Sites with Binder Grade AC-20

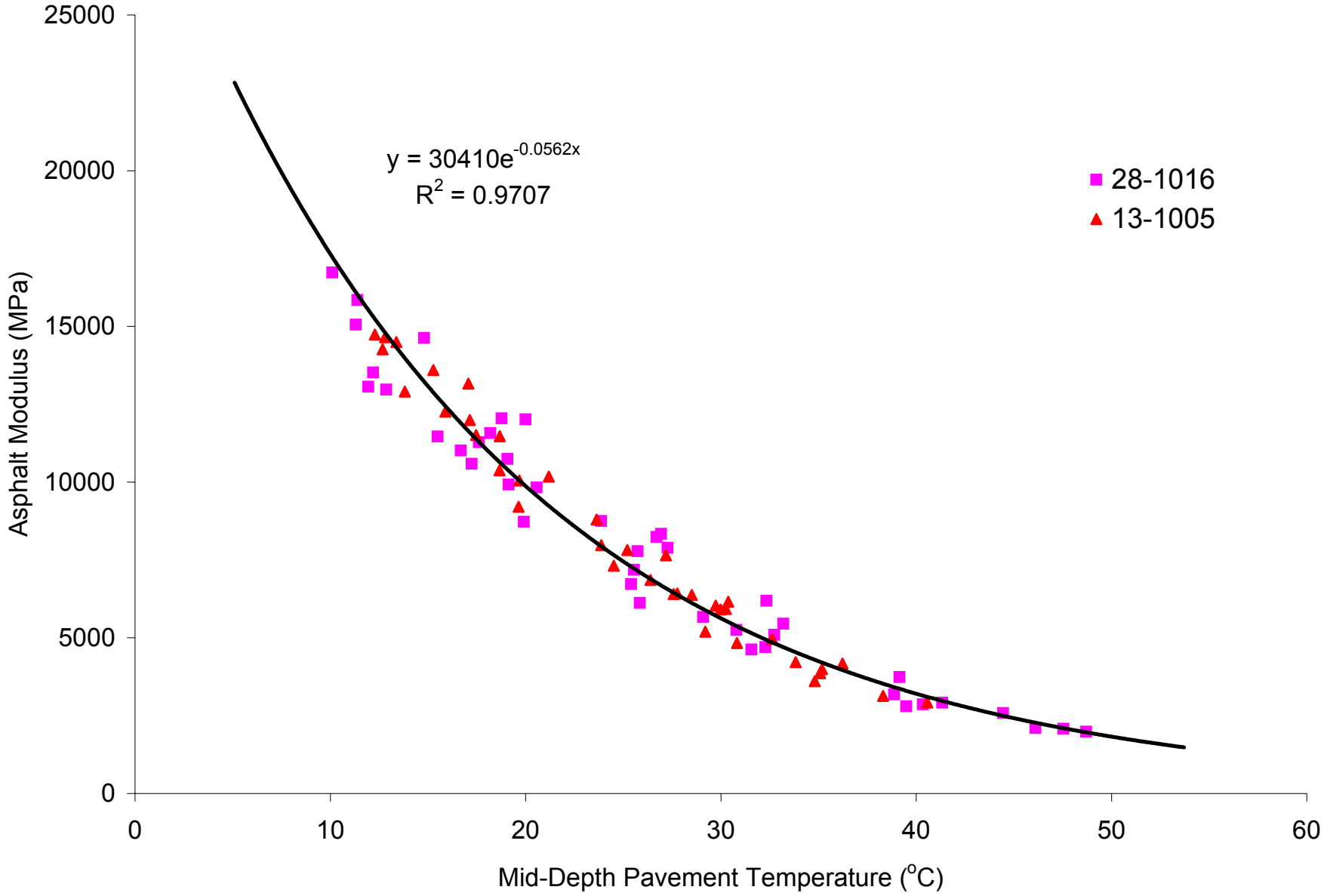

Figure J-3. Asphalt Modulus Models for Sites with Binder Grade AC-30

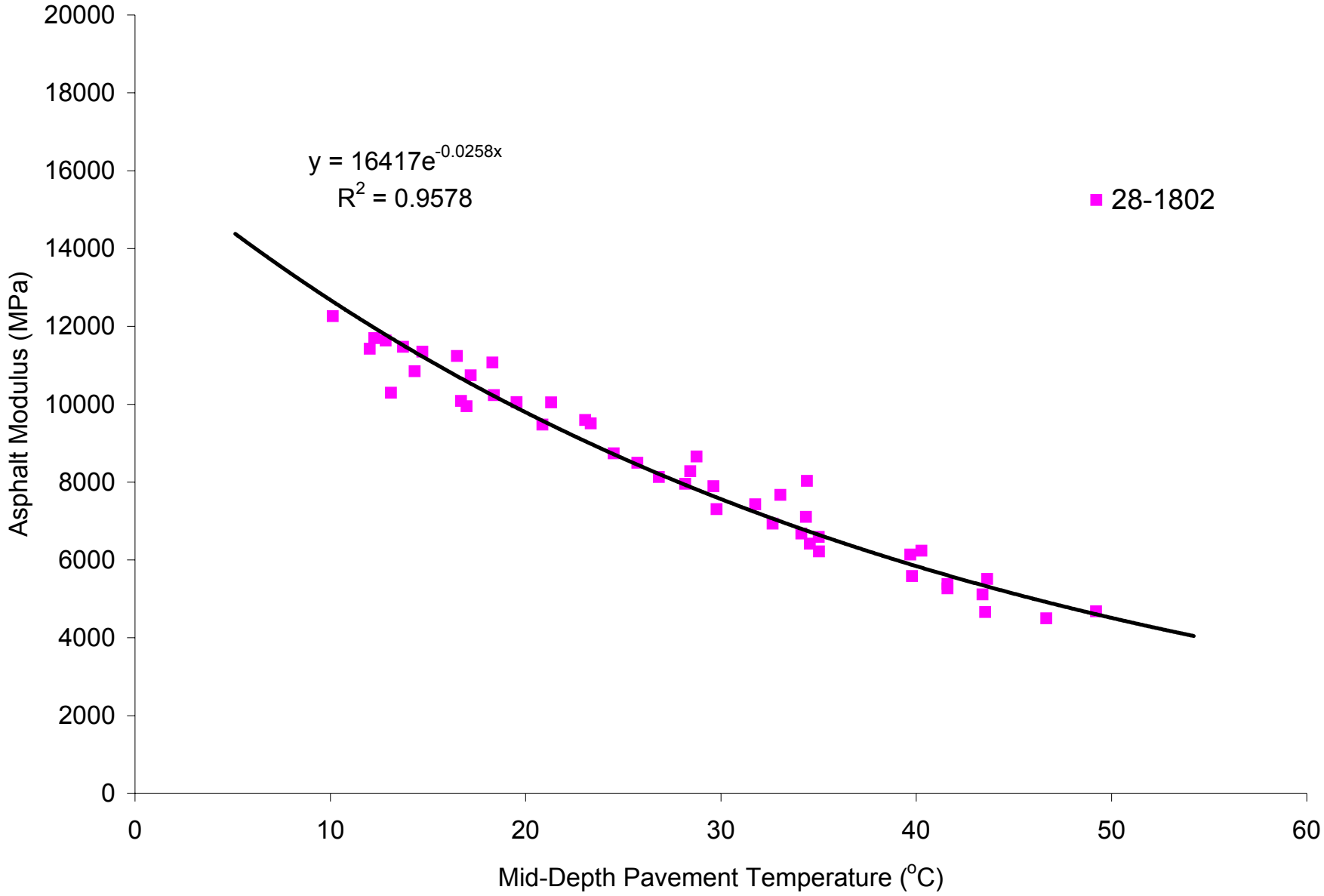

Figure J-4. Asphalt Modulus Models for Sites with Binder Grade AC-40

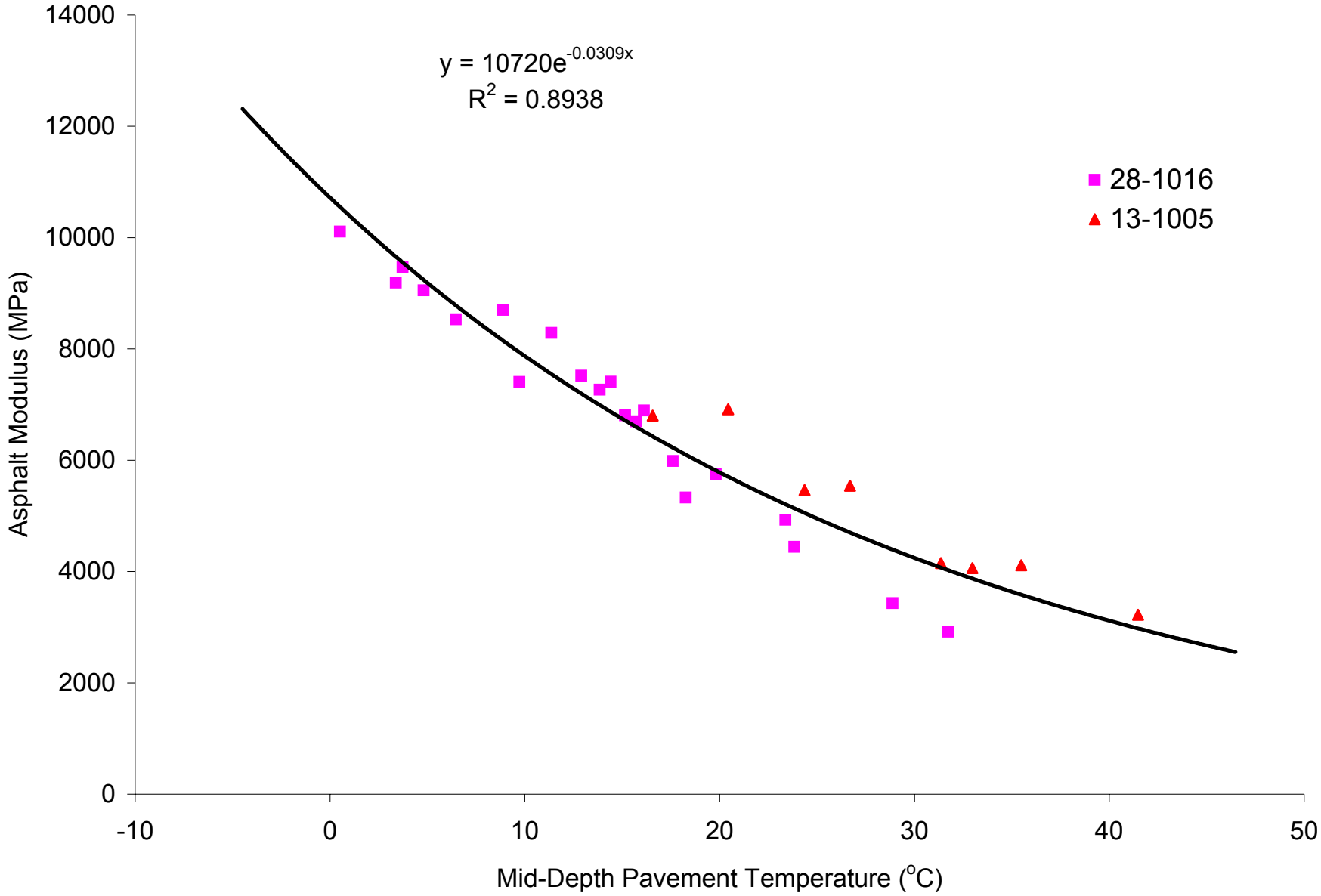

Figure J-5. Asphalt Modulus Models for Sites with Binder Grade 120-150

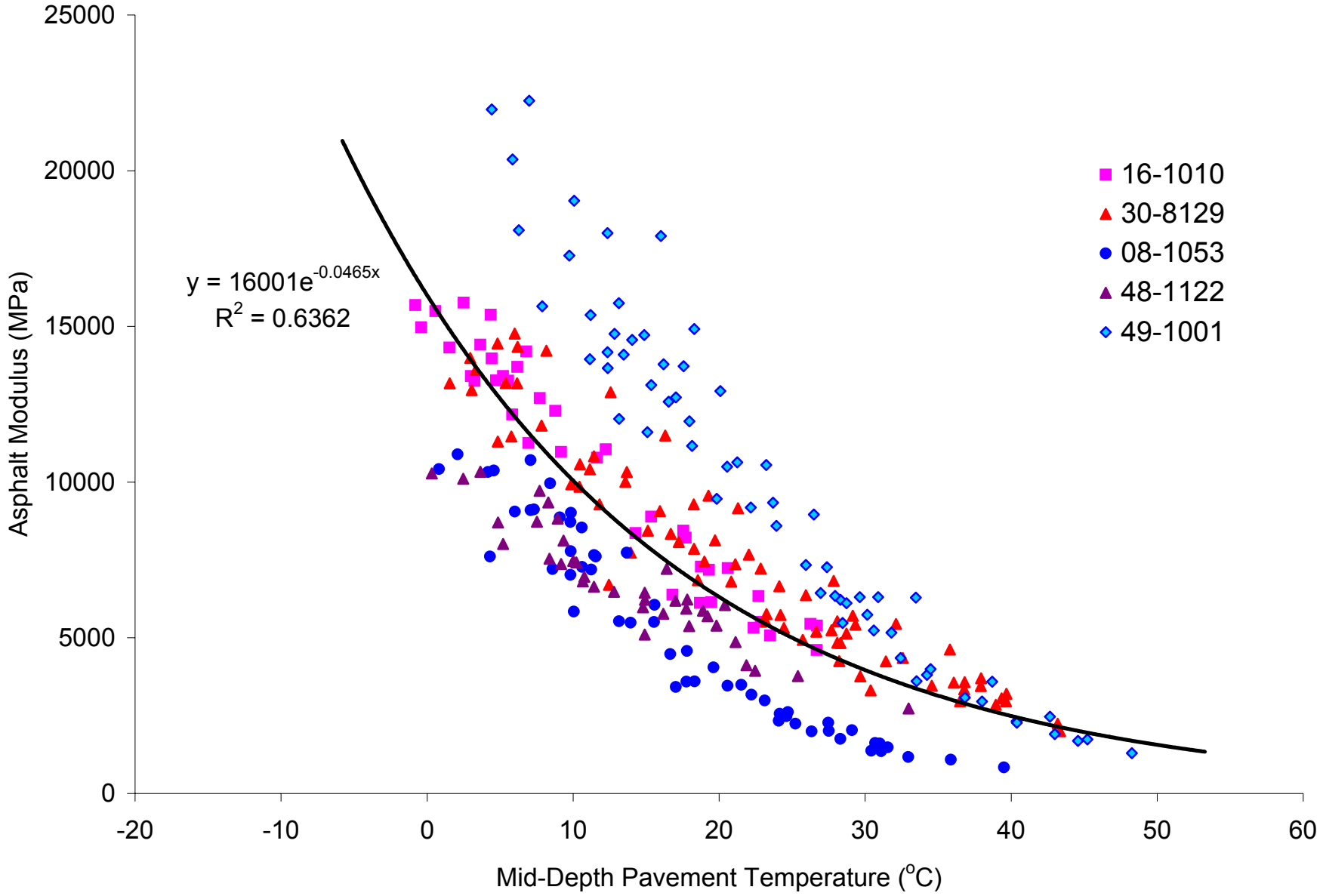

Figure J-6. Asphalt Modulus Models for Sites with Binder Grade 85-100

APPENDIX K

SEASONAL VARIATIONS OF SUBGRADE MODULUS AND k-VALUE AT FREEZING SITES

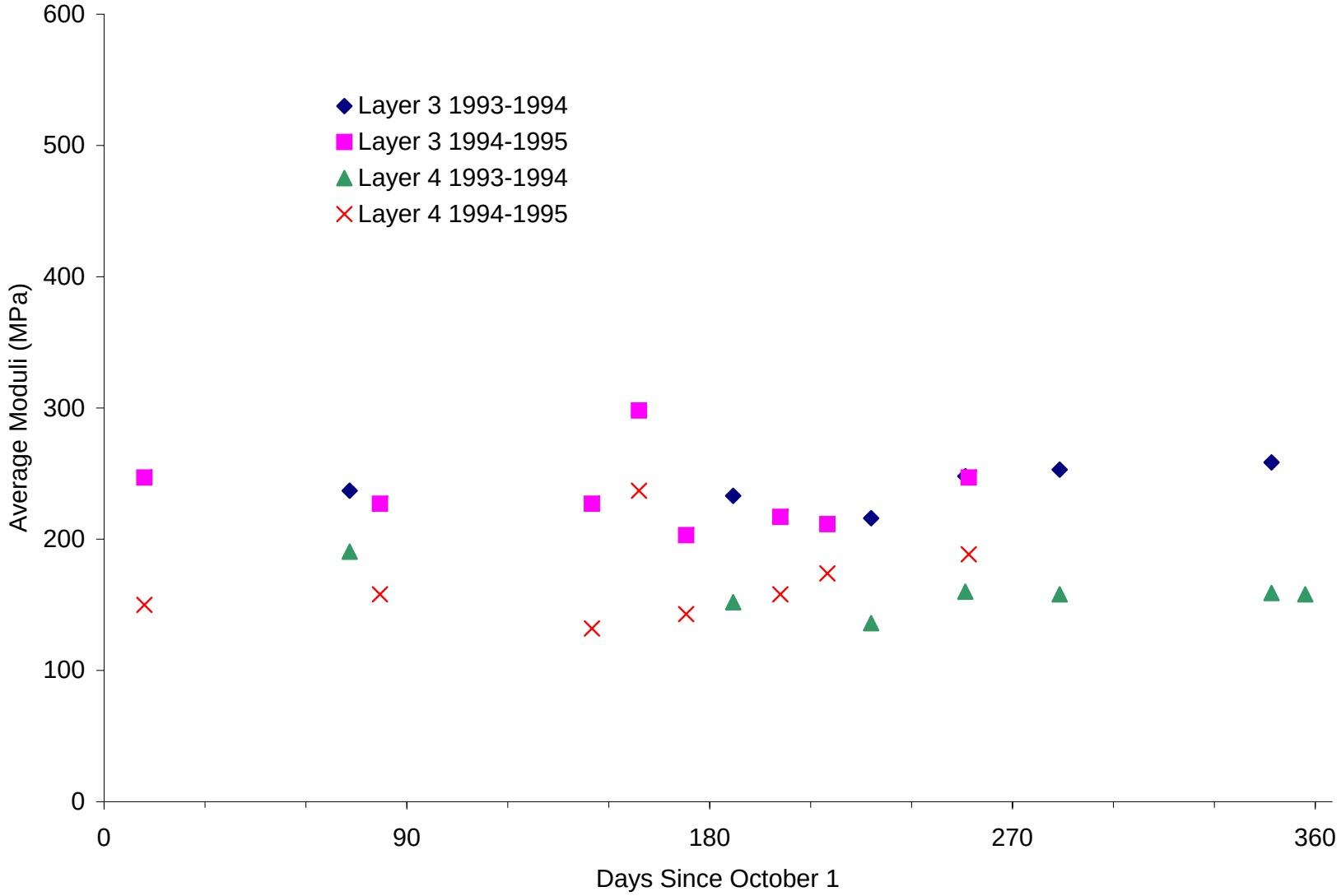

Figure K-1. Seasonal Variation of Subgrade Modulus at Site 87-1622 (Sandy Silt)

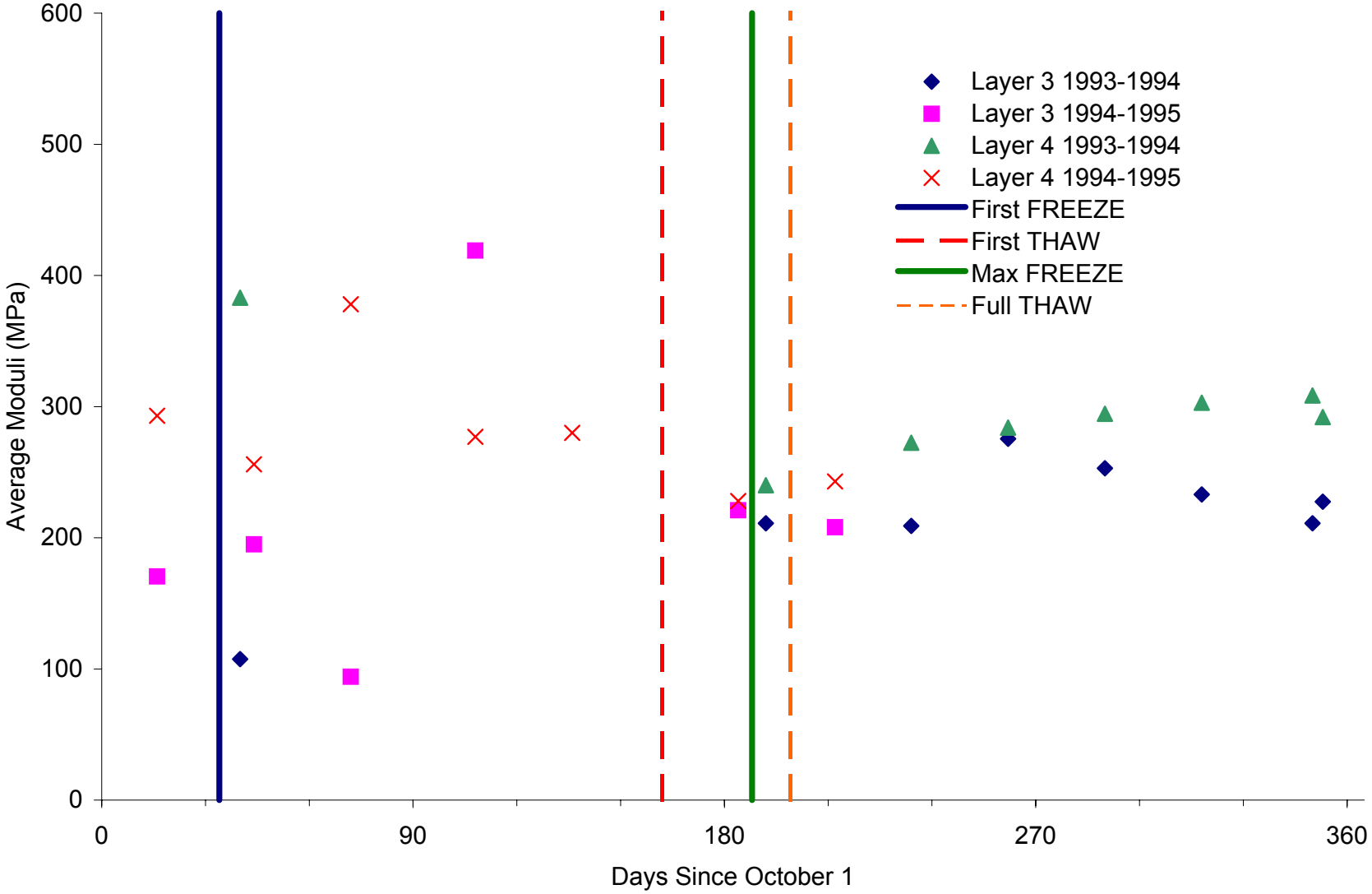

Figure K-2. Seasonal Variation of Subgrade Modulus at Site 23-1026 (Silty Sand with Gravel)

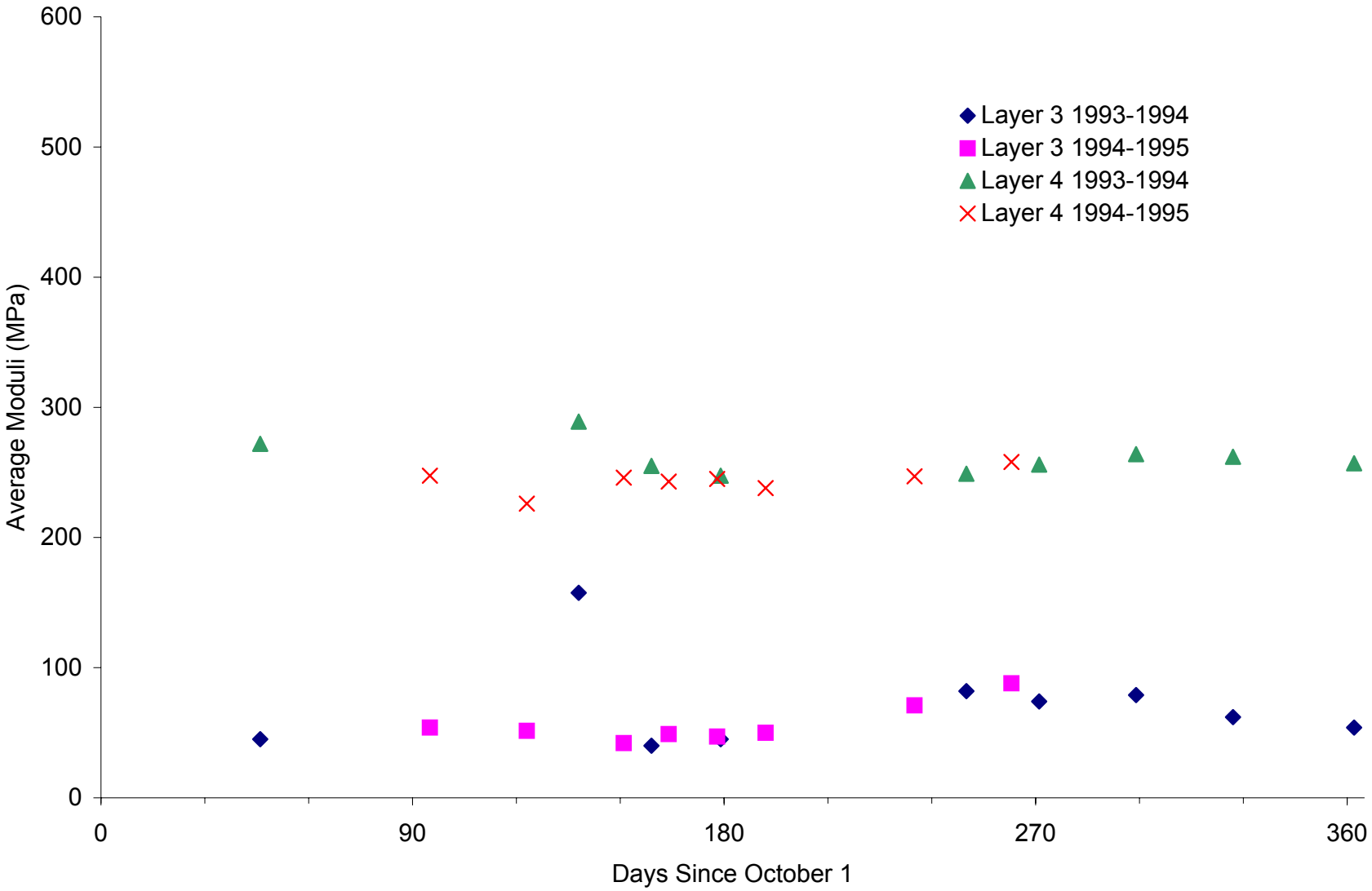

Figure K-3. Seasonal Variation of Subgrade Modulus at Site 25-1002 (Poorly Graded Sand with Silt)

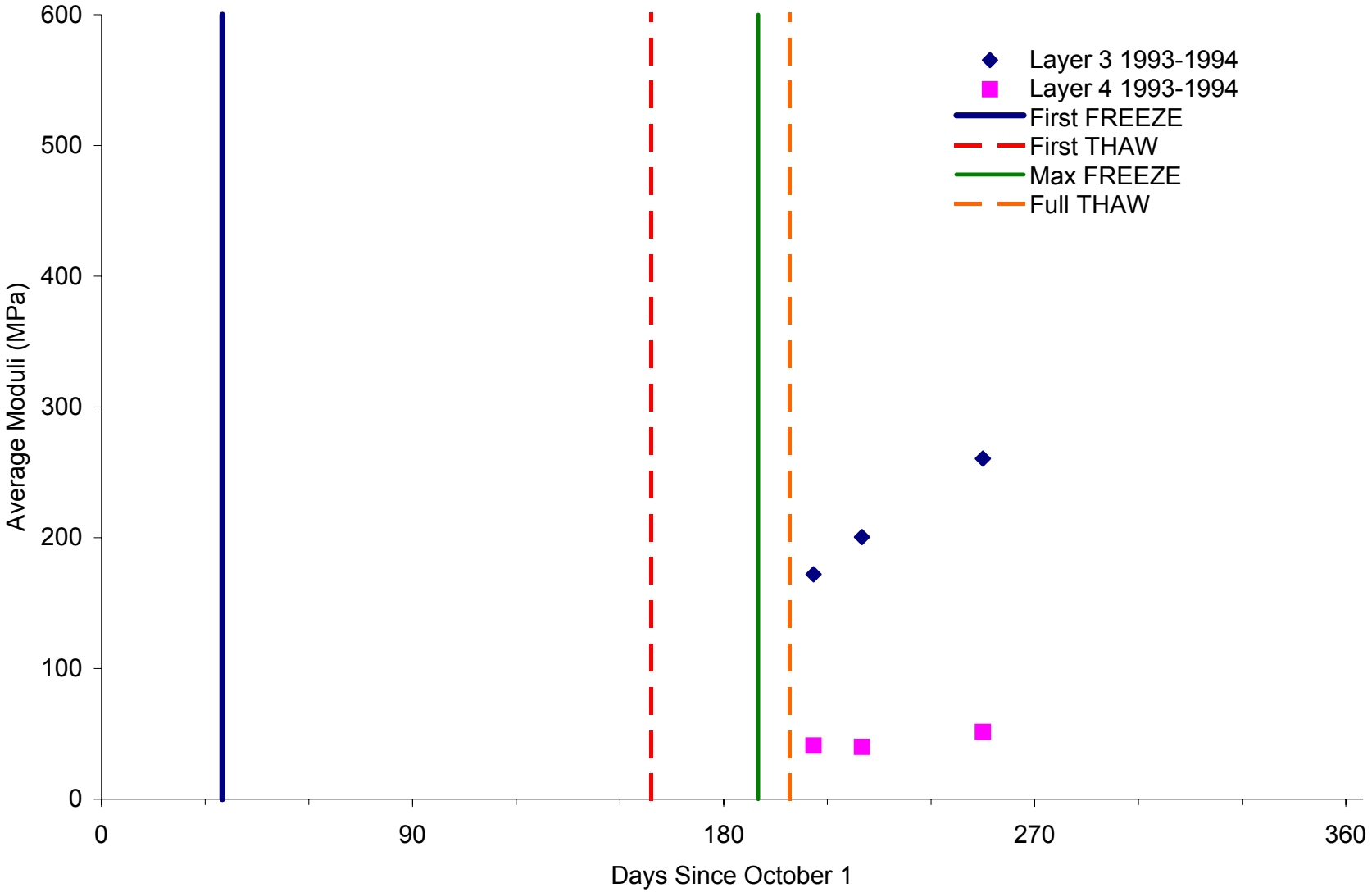

Figure K-4. Seasonal Variation of Subgrade Modulus at Site 27-1018 (Poorly Graded Sand with Silt).

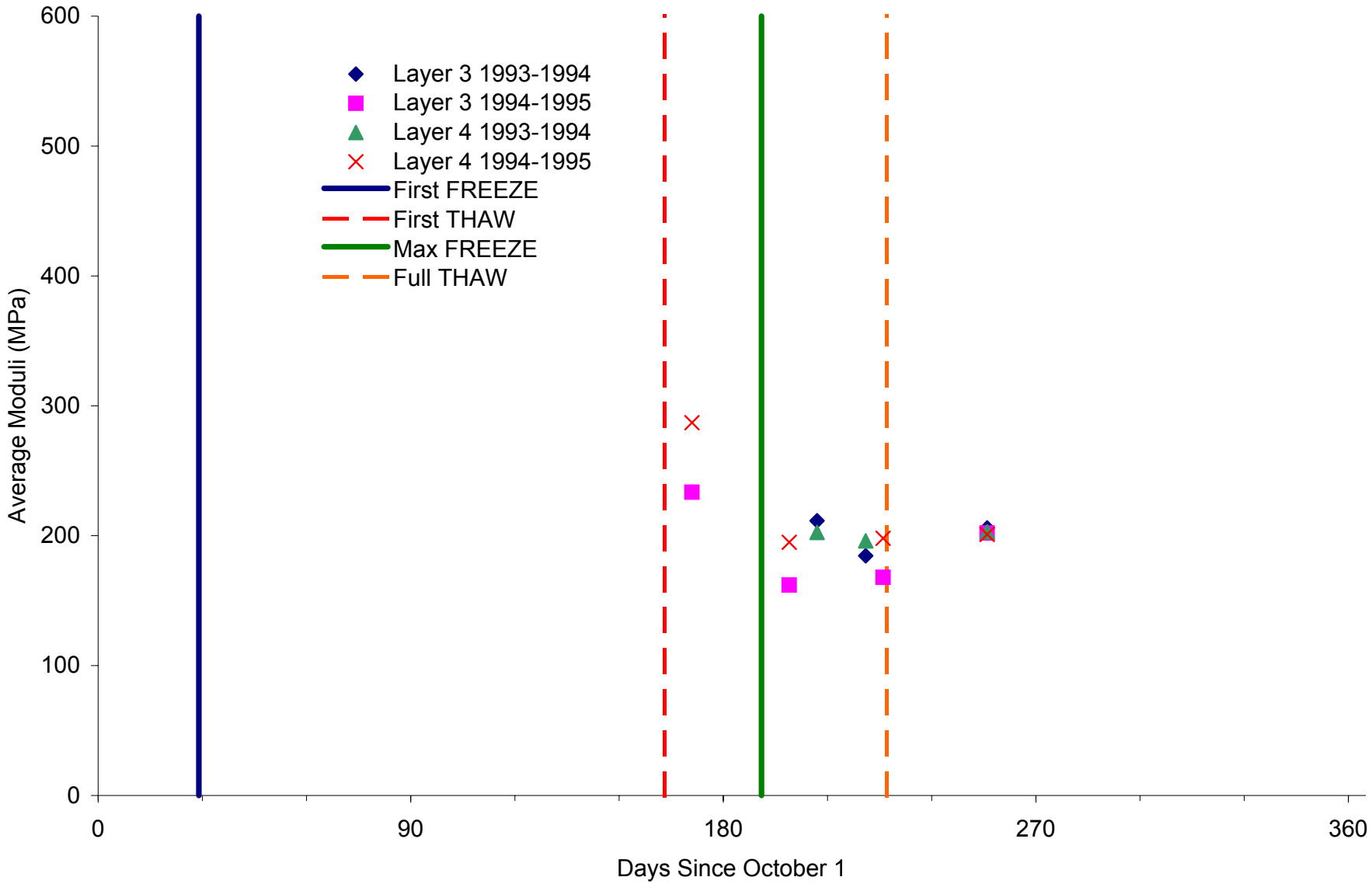

Figure K-5. Seasonal Variation of Subgrade Modulus at Site 27-1028 (Poorly Graded Sand with Silt)

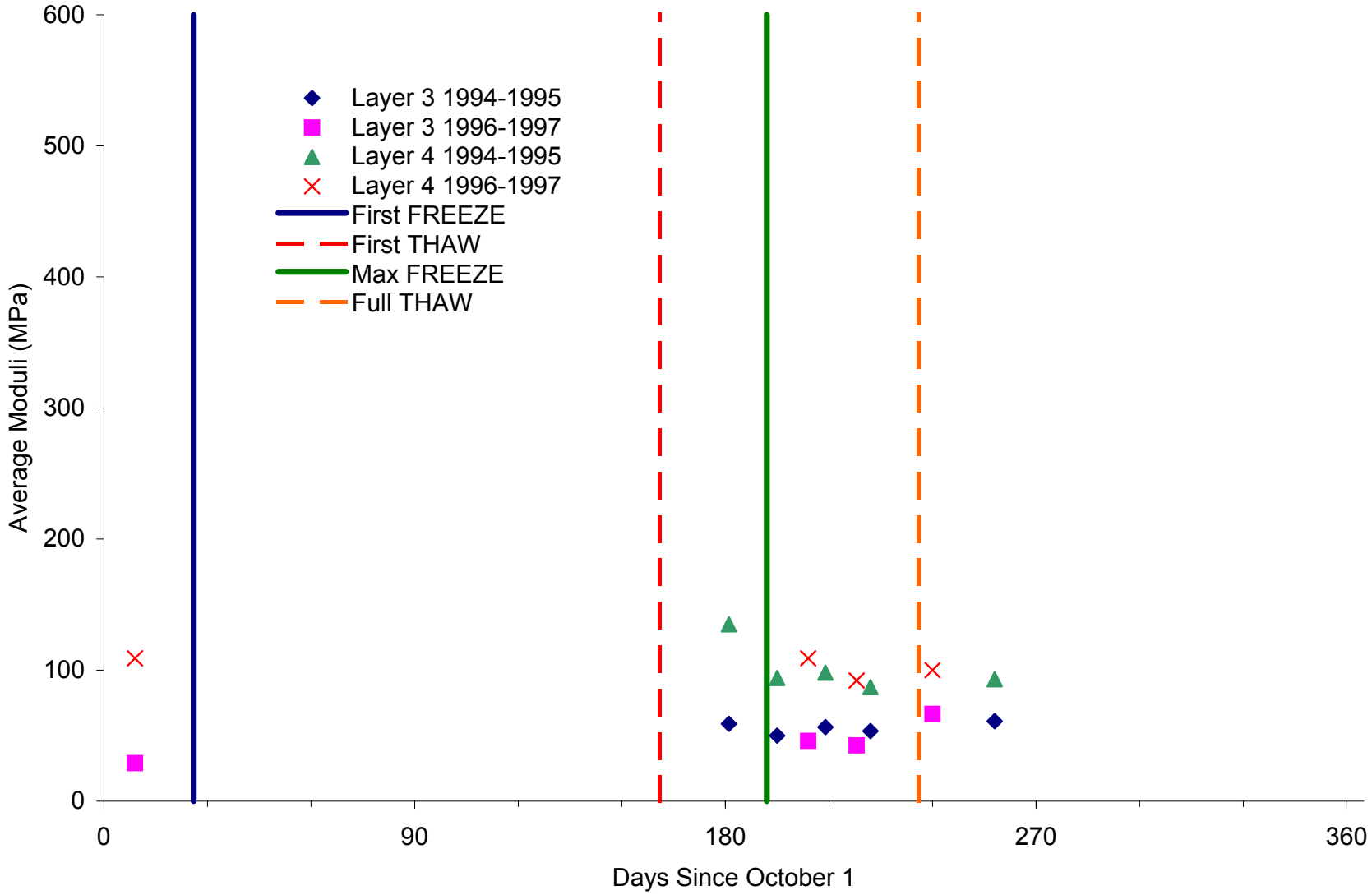

Figure K-6. Seasonal Variation of Subgrade Modulus at Site 27-4040 (Lean Clay with Sand)

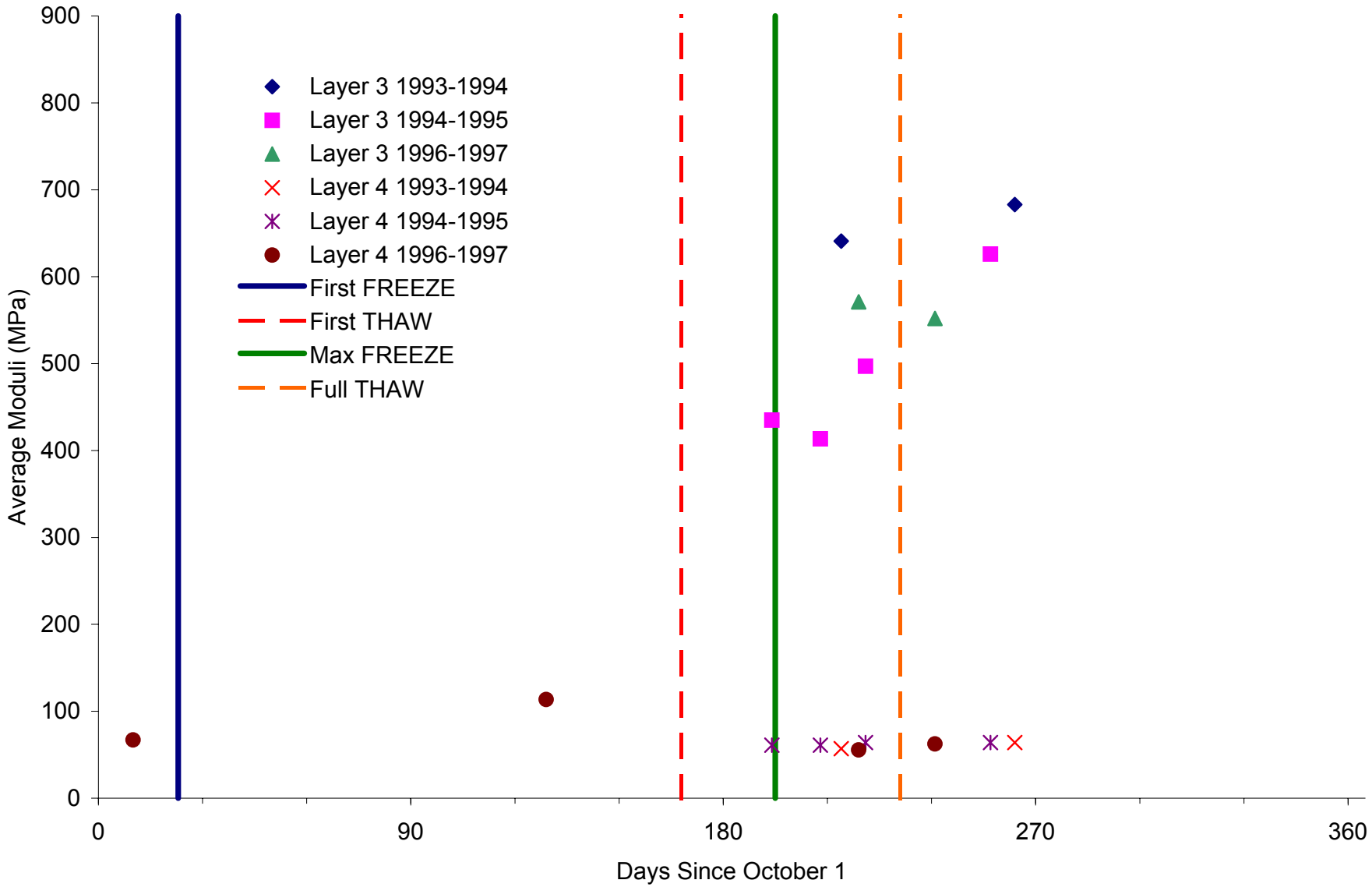

Figure K-7. Seasonal Variation of Subgrade Modulus at Site 27-6251 (Poorly Graded Sand with Silt)

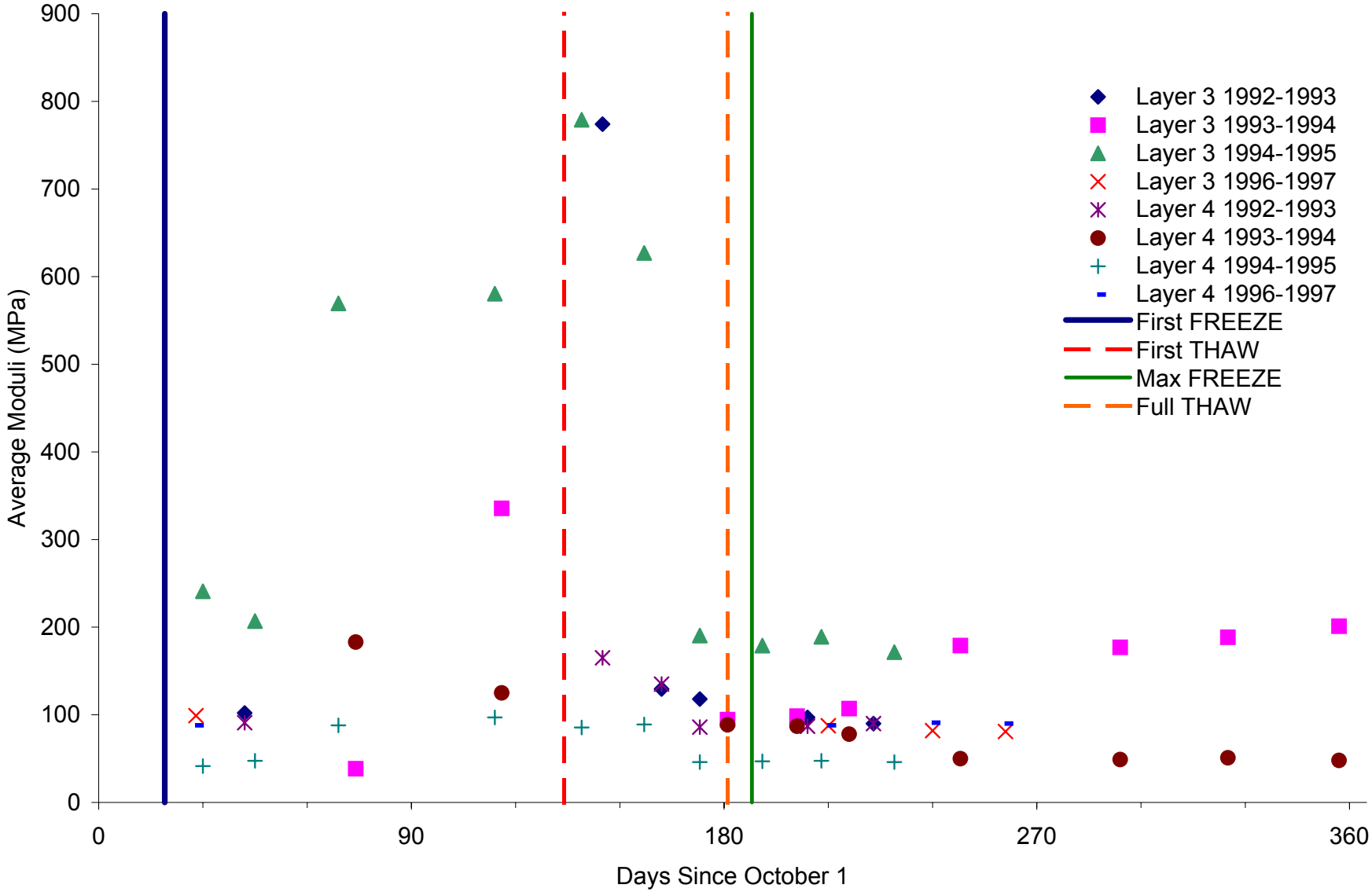

Figure K-8. Seasonal Variation of Subgrade Modulus at Site 30-8129 (Gravely Lean Clay with Sand)

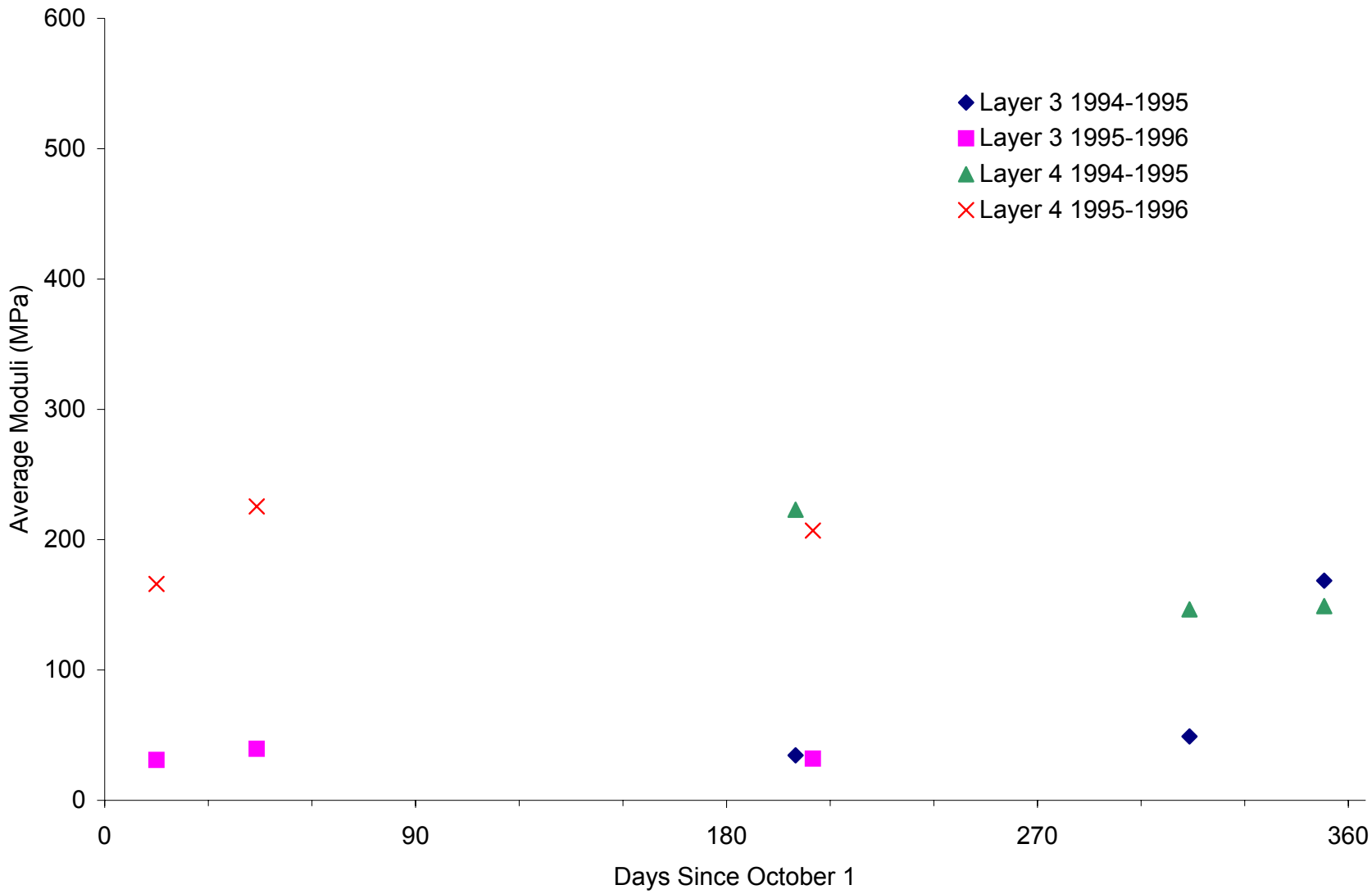

Figure K-9. Seasonal Variation of Subgrade Modulus at Site 31-3018 (Poorly Graded Sand)

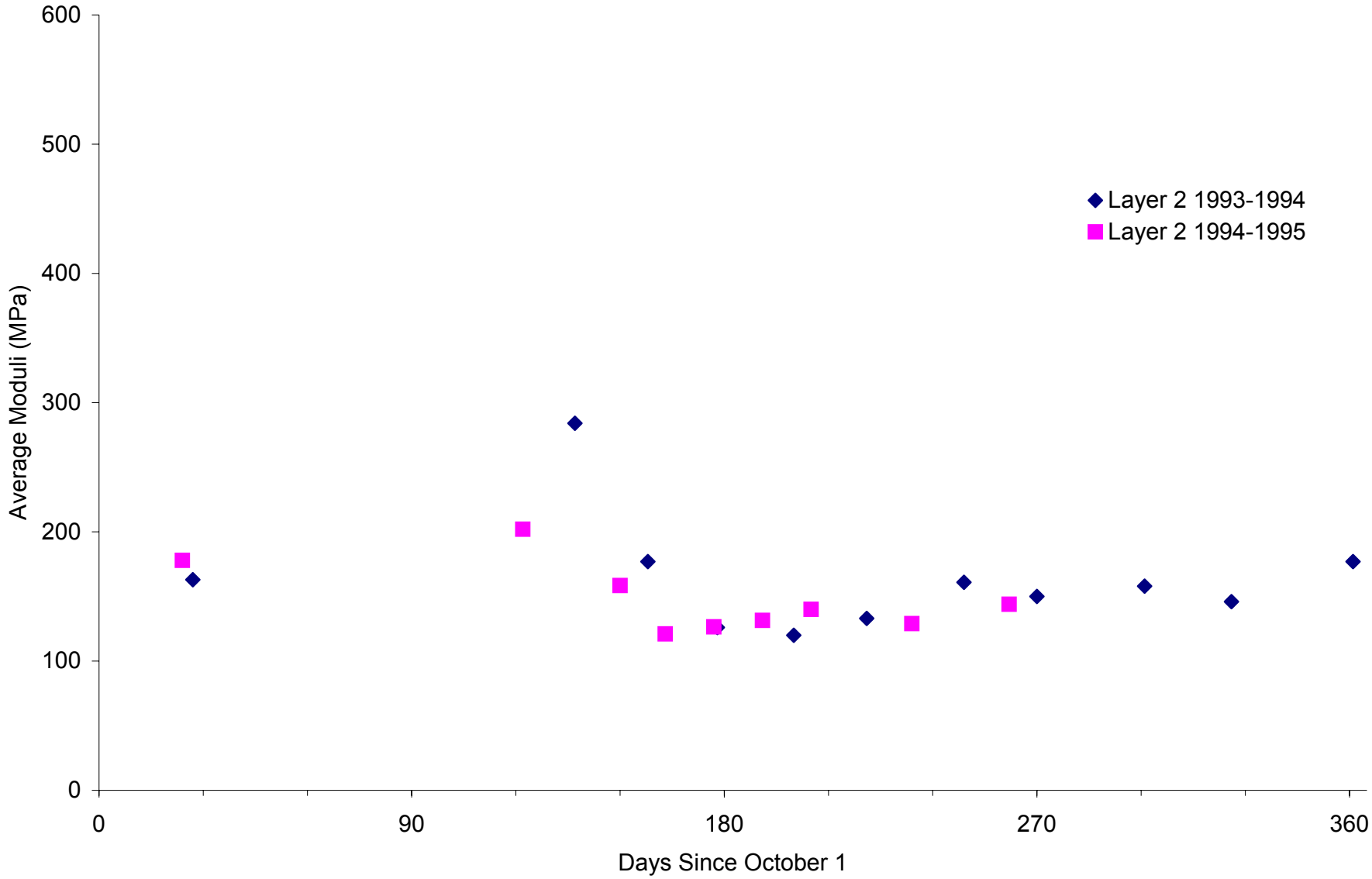

Figure K-10. Seasonal Variation of Subgrade Modulus at Site 36-4018 (Silty Gravel with Sand)

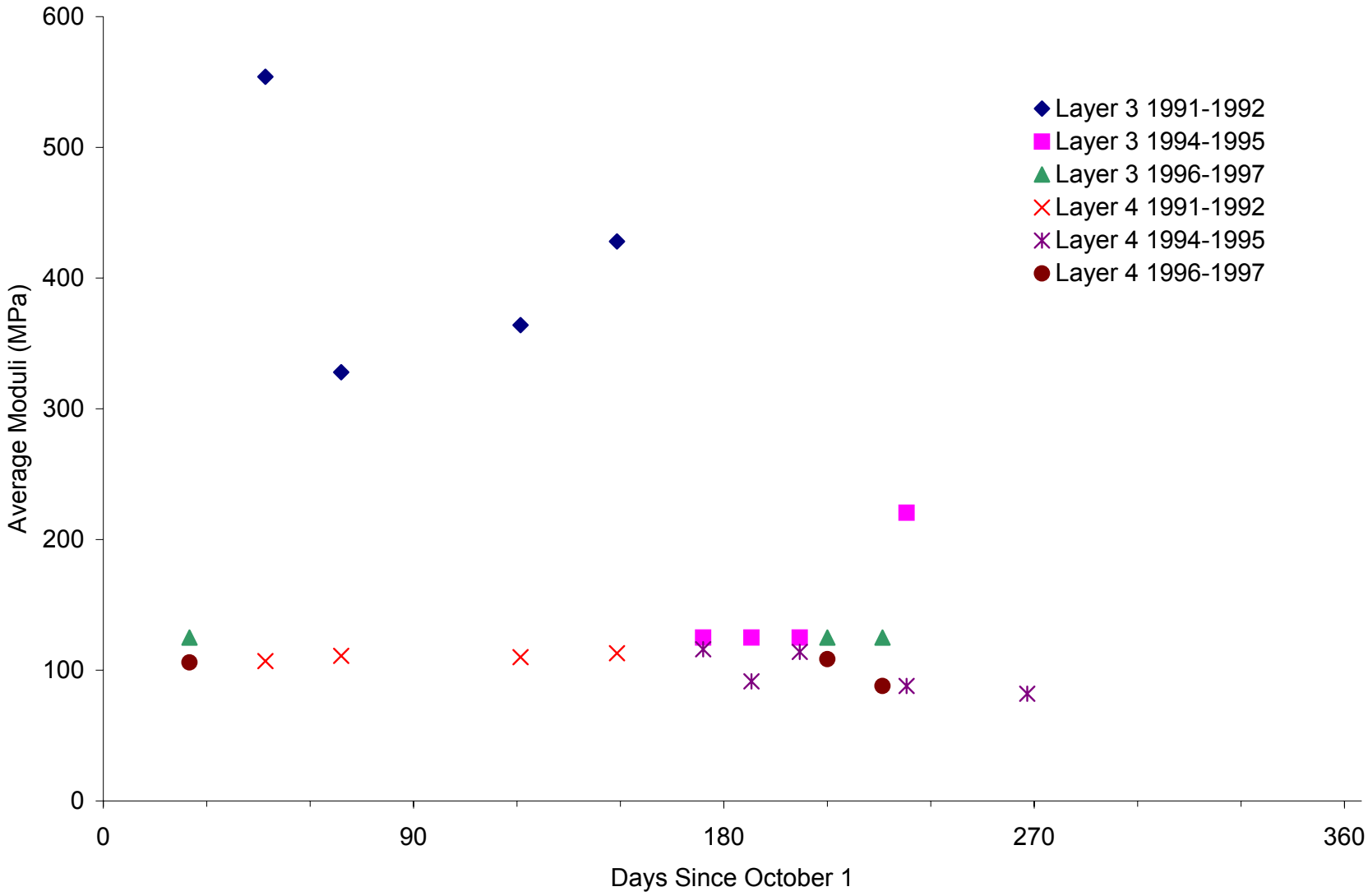

Figure K-11. Seasonal Variation of Subgrade Modulus at Site 46-9187 (Lean Inorganic Clay)

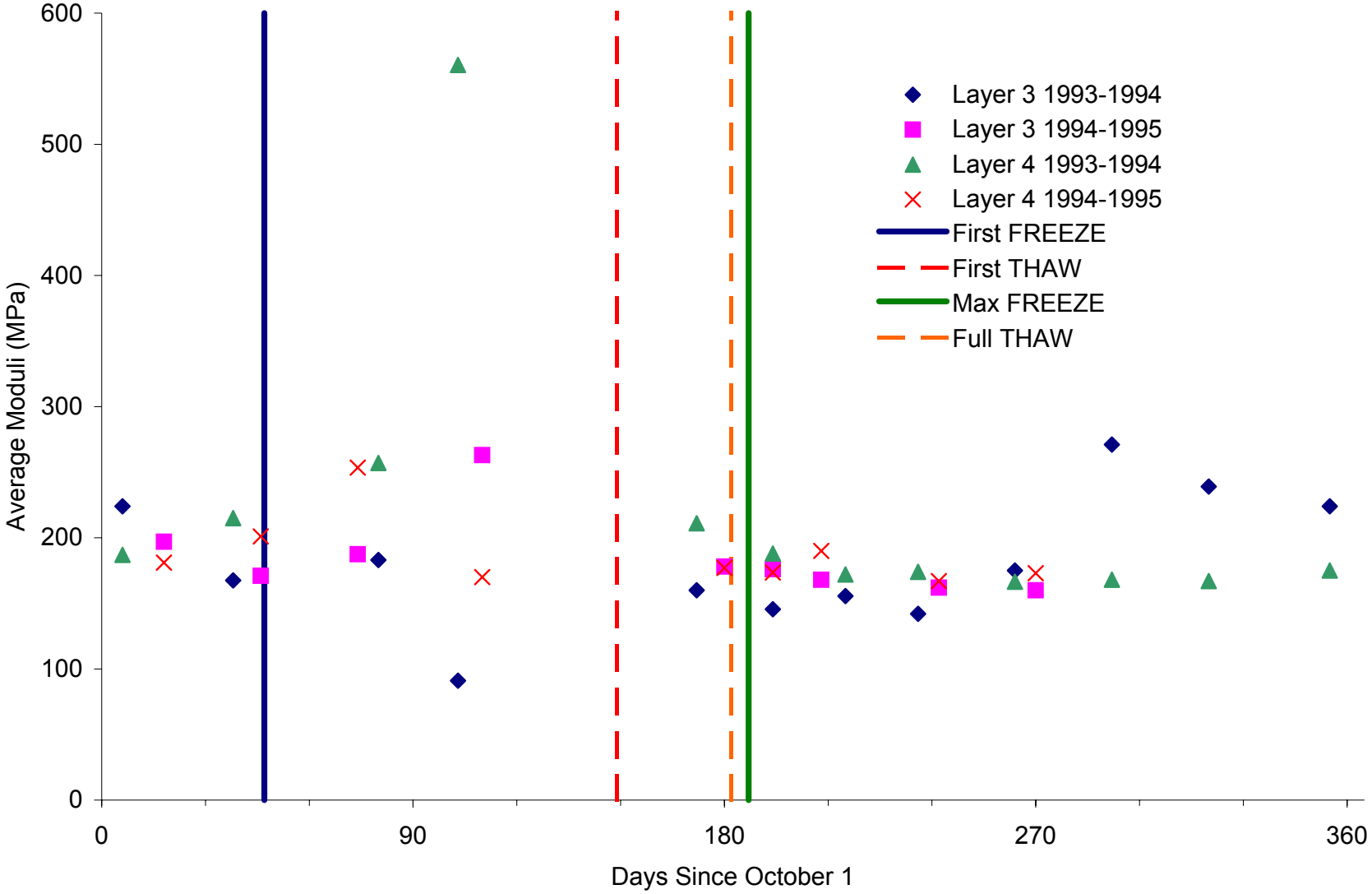

Figure K-12. Seasonal Variation of Subgrade Modulus at Site 50-1002 (Poorly Graded Gravel with Silt and Sand)

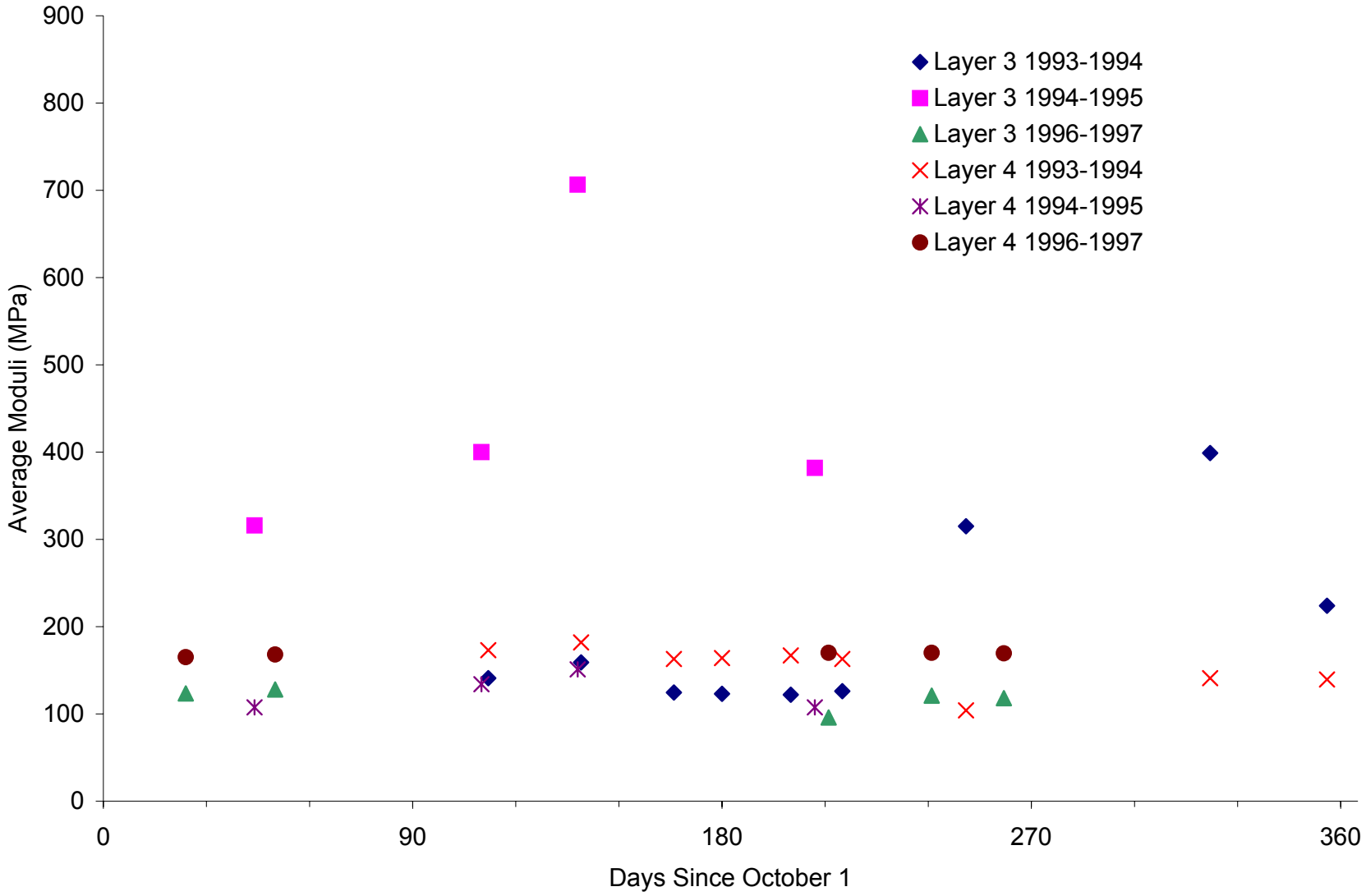

Figure K-13. Seasonal Variation of Subgrade Modulus at Site 56-1007 (Silty Sand with Gravel)

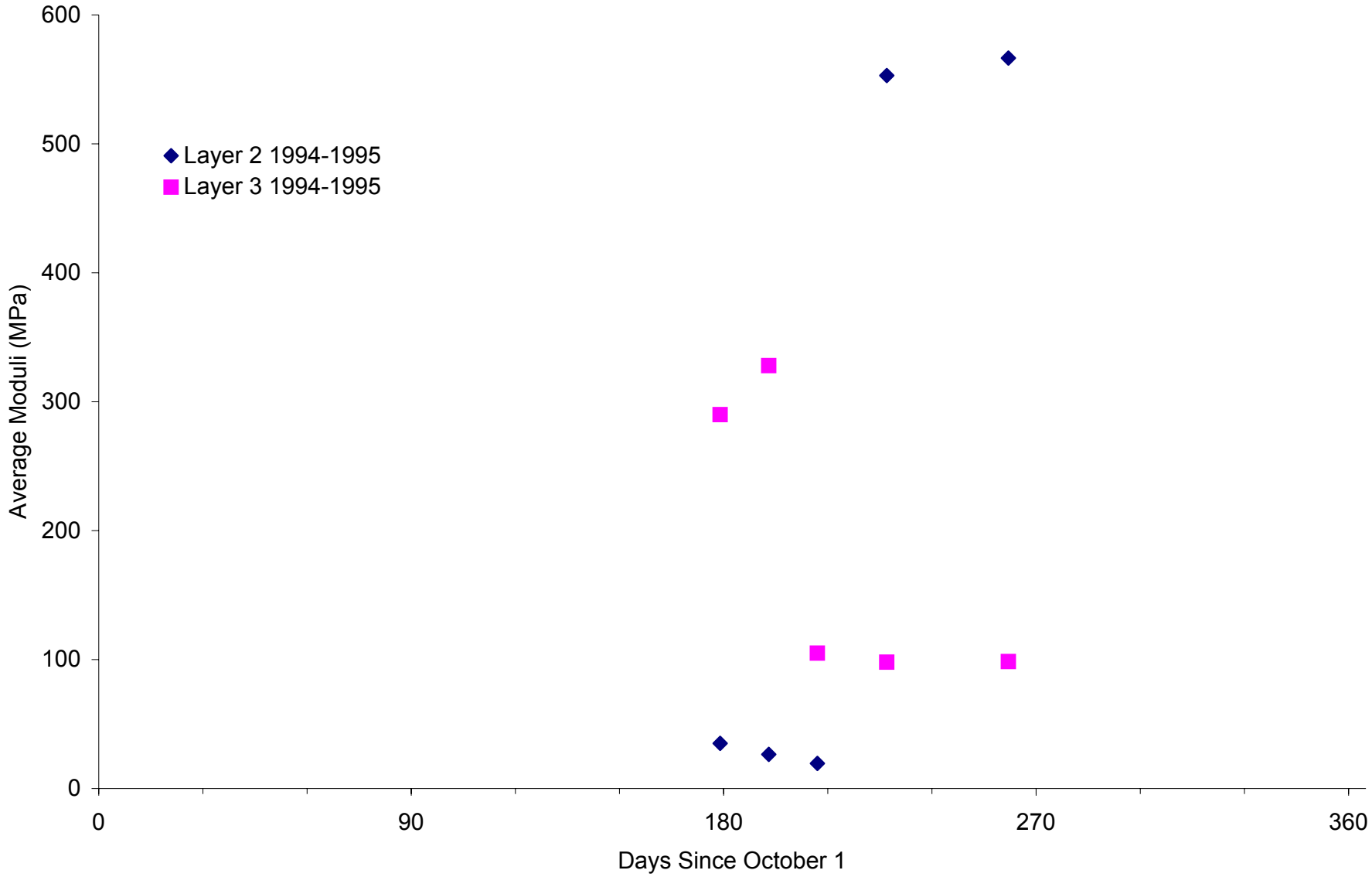

Figure K-14. Seasonal Variation of Subgrade Modulus at Site 83-3802 (Fat Inorganic Clay)

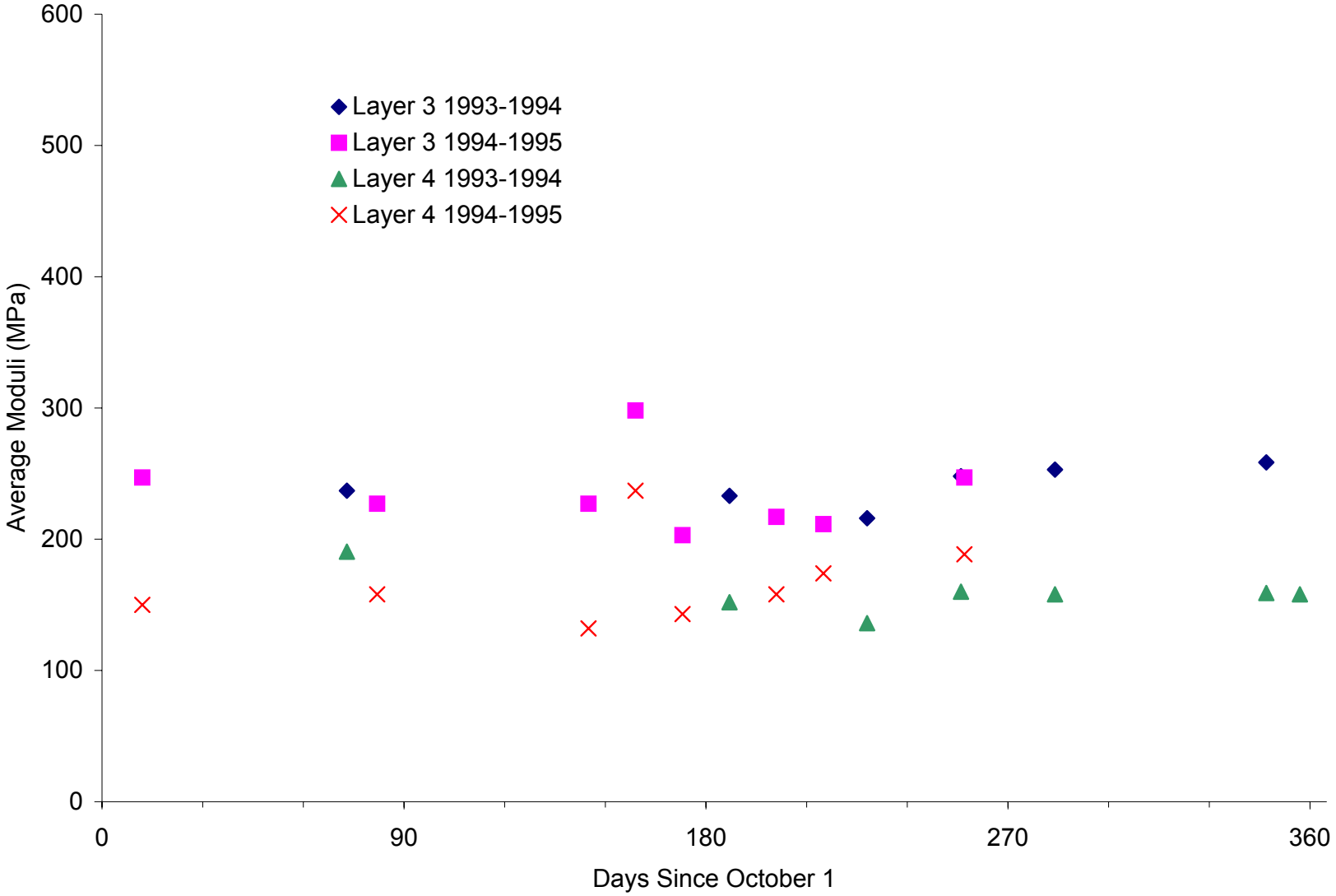

Figure K-15. Seasonal Variation of Subgrade Modulus at Site 87-1622 (Sandy Silt)

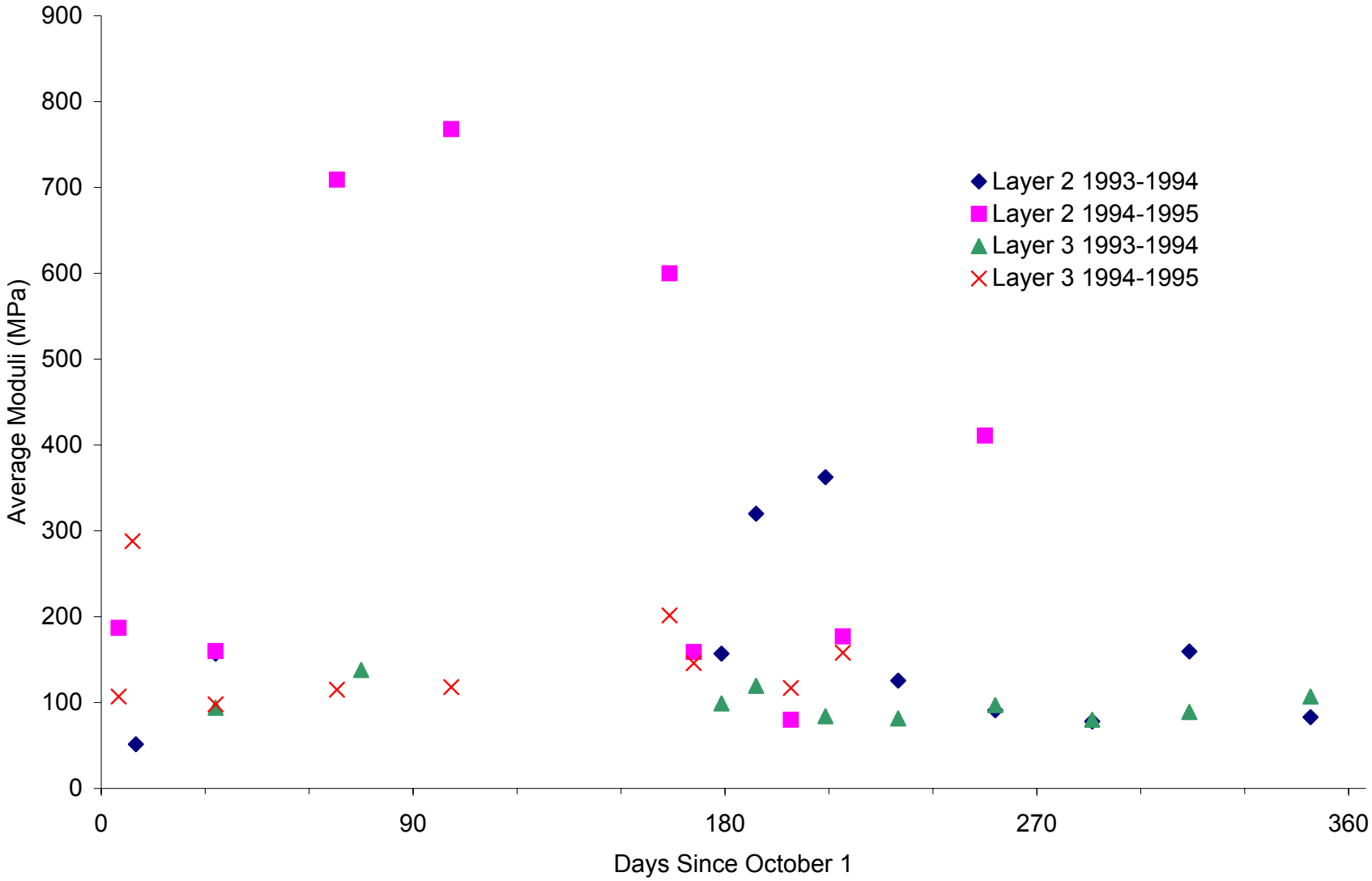

Figure K-16. Seasonal Variation of Subgrade Modulus at Site 89-3015 (Poorly Graded Sand)

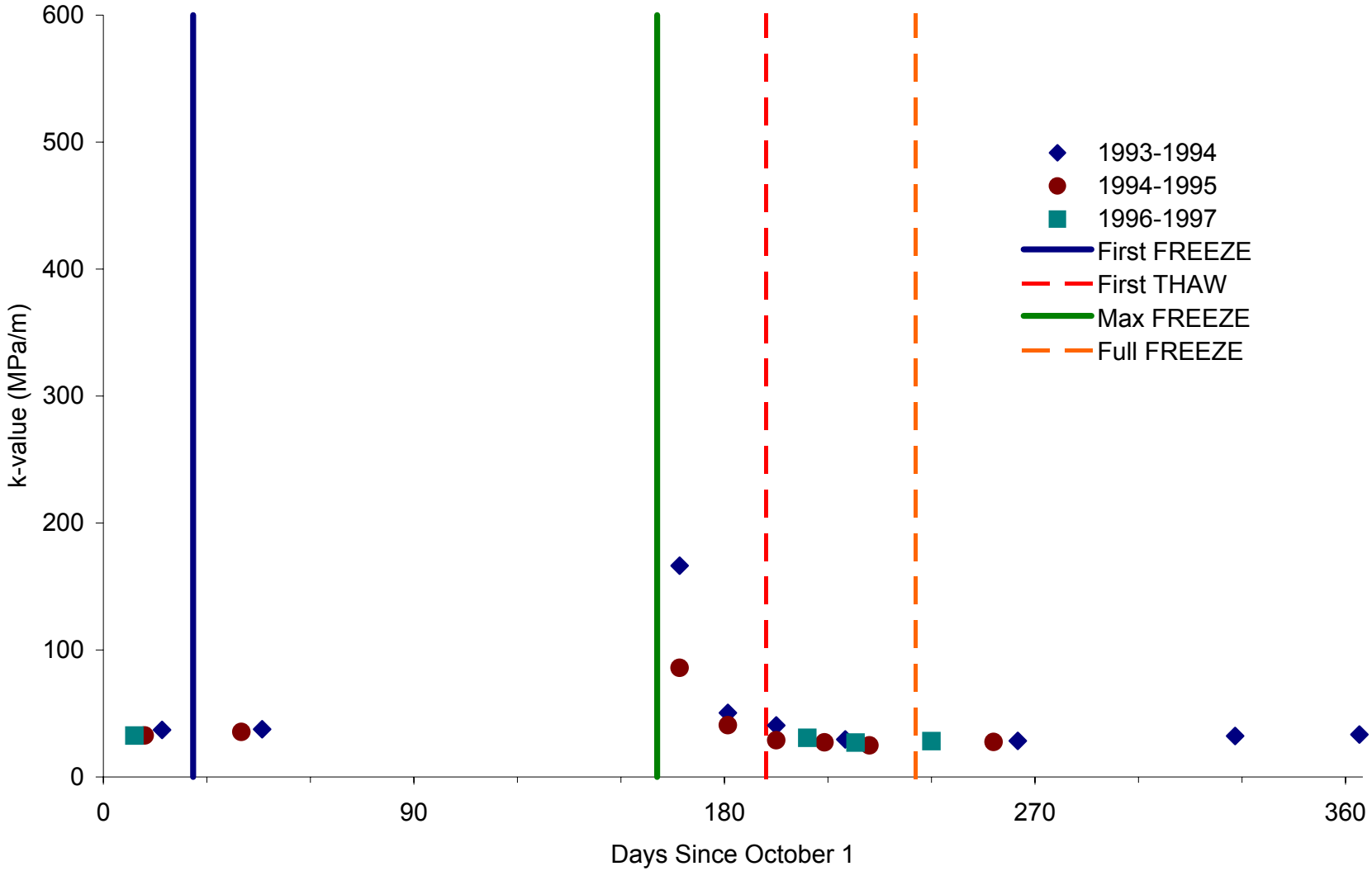

Figure K-17. Seasonal Variation of Subgrade k-value at Site 27-4040 (Lean Clay with Sand)

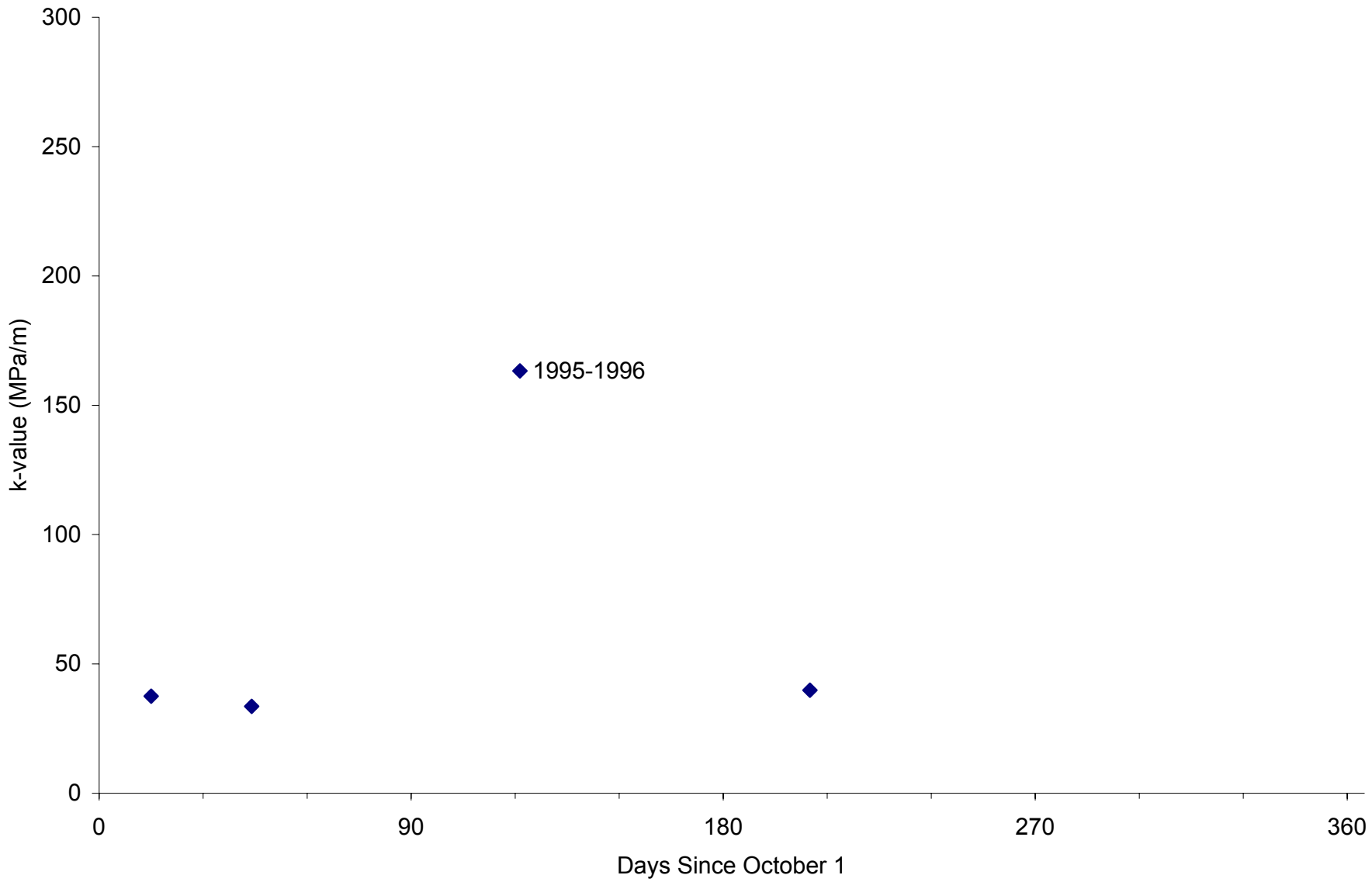

Figure K-18. Seasonal Variation of Subgrade k-value at Site 31-3018 (Poorly Graded Sand)

APPENDIX L

SEASONAL VARIATIONS OF SUBGRADE MODULUS AND k-VALUE AT NO-FREEZE SITES

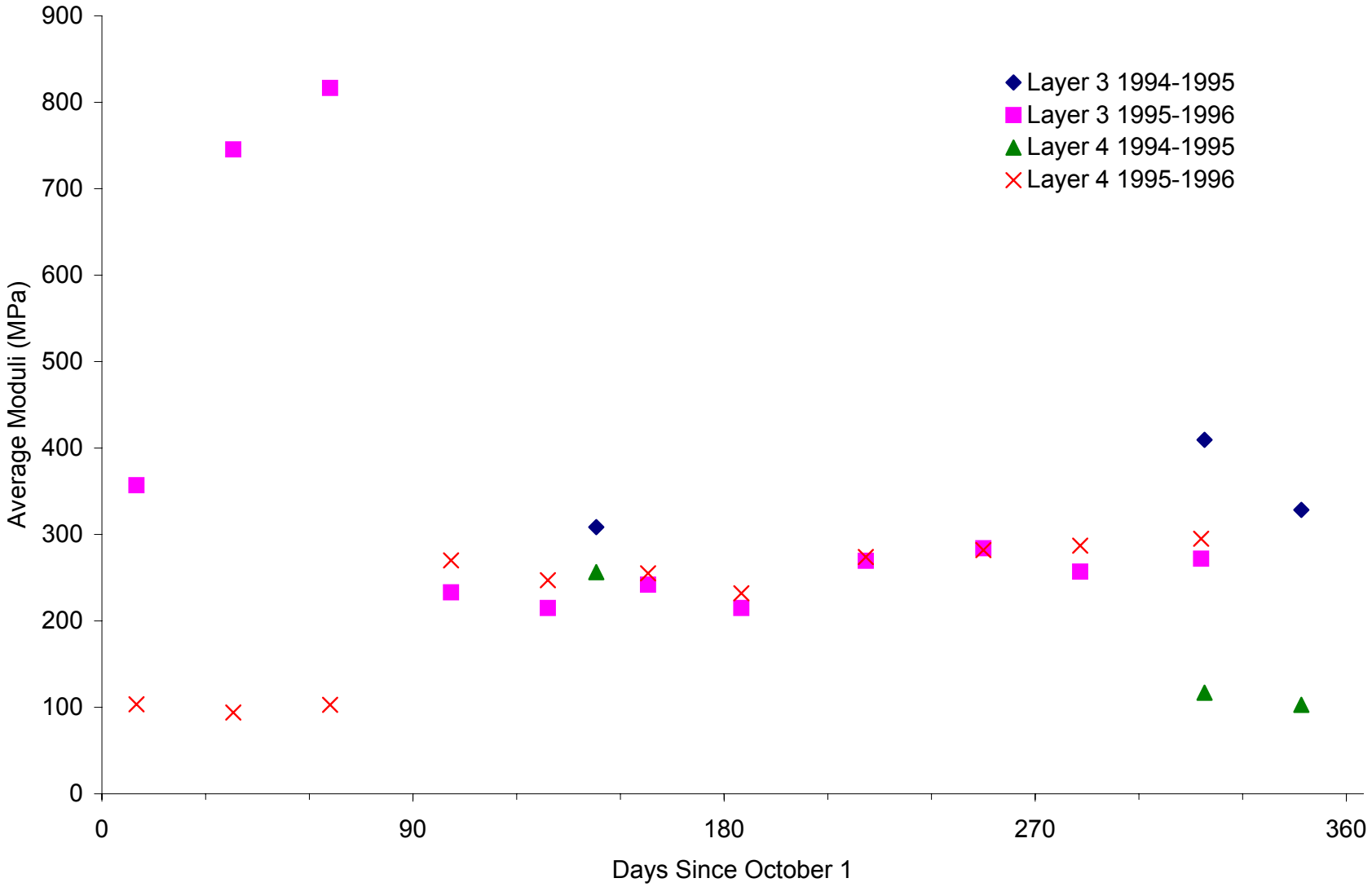

Figure L-1. Seasonal Variation of Subgrade Modulus at Site 04-0113 (Well-Graded Sand with Silt and Gravel)

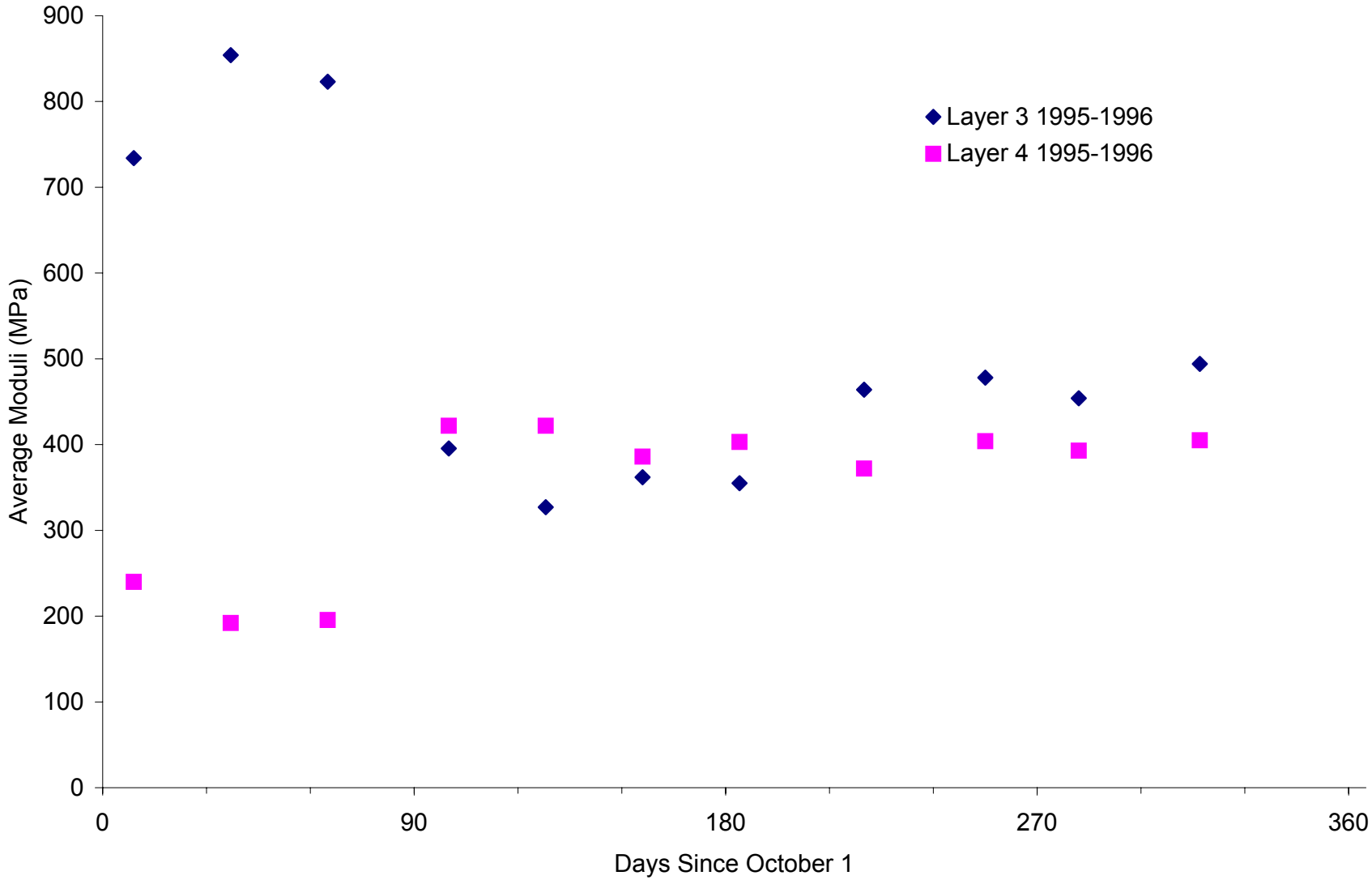

Figure L-2. Seasonal variation of Subgrade Modulus at Site 04-0114 (Silty Sand with Gravel)

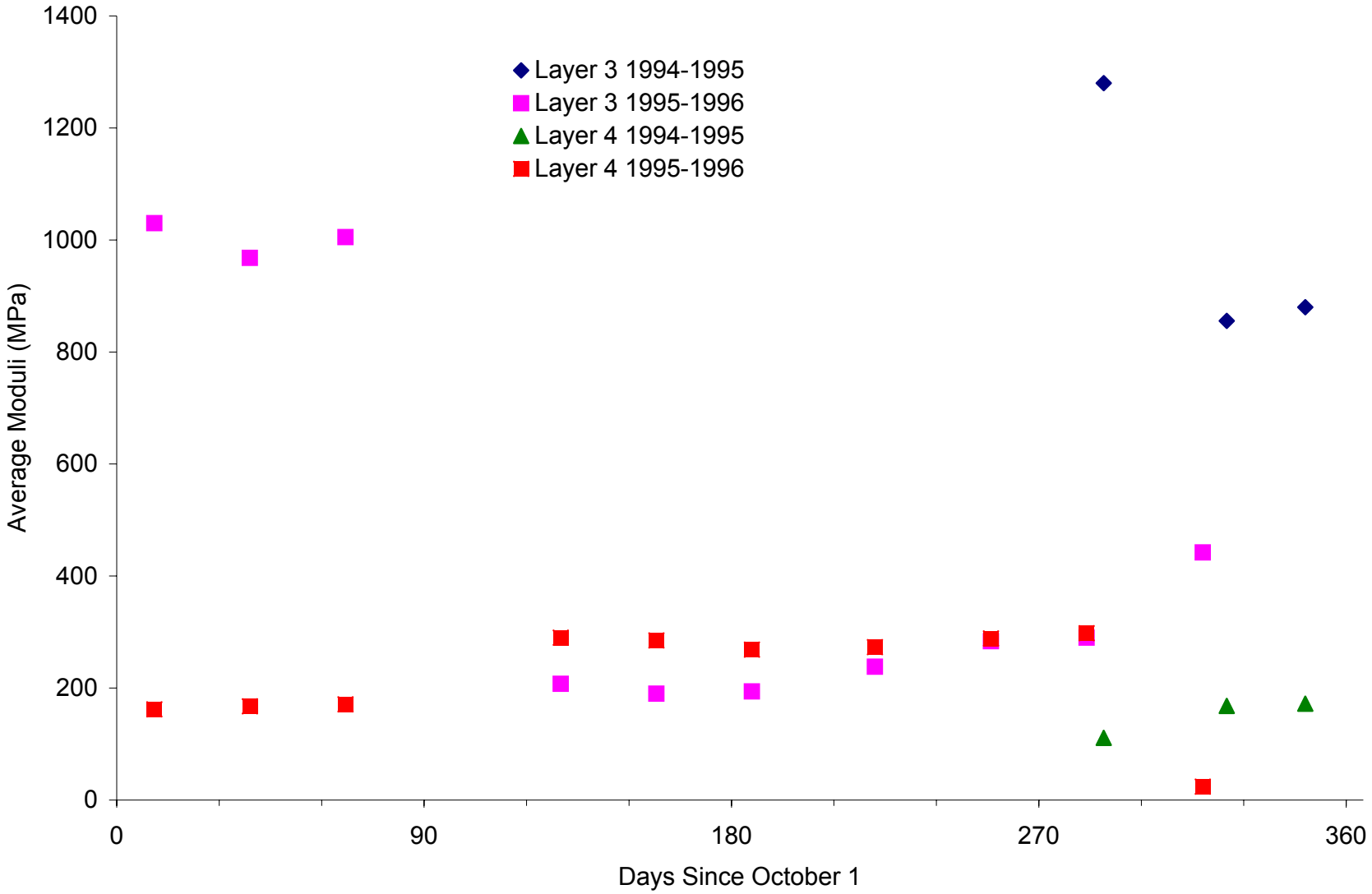

Figure L-3. Seasonal Variation of Subgrade Modulus at Site 04-1024 (Clayey Sand with Gravel)

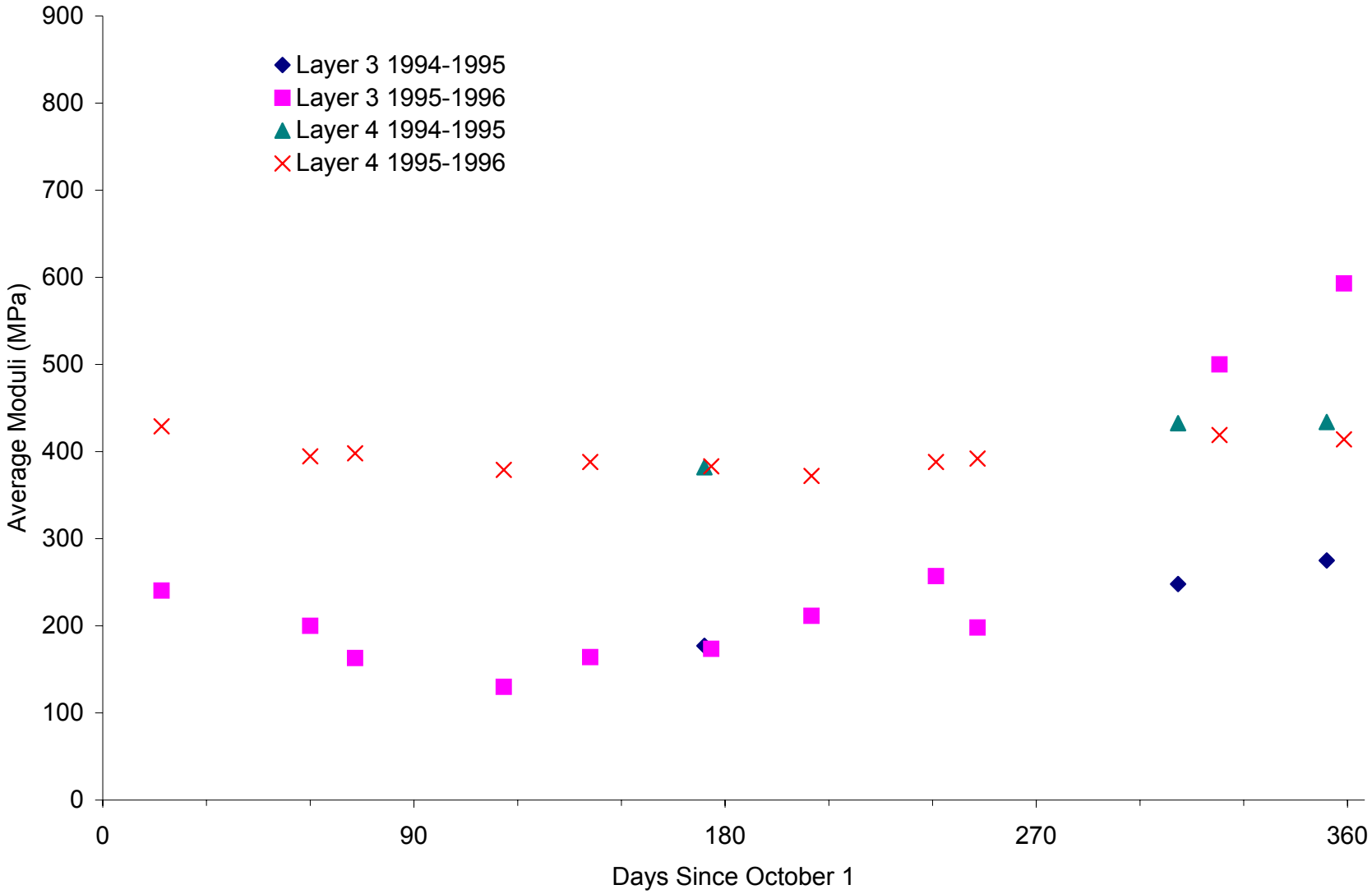

Figure L-4. Seasonal Variation of Subgrade Modulus at Site 13-1005 (Clayey Sand)

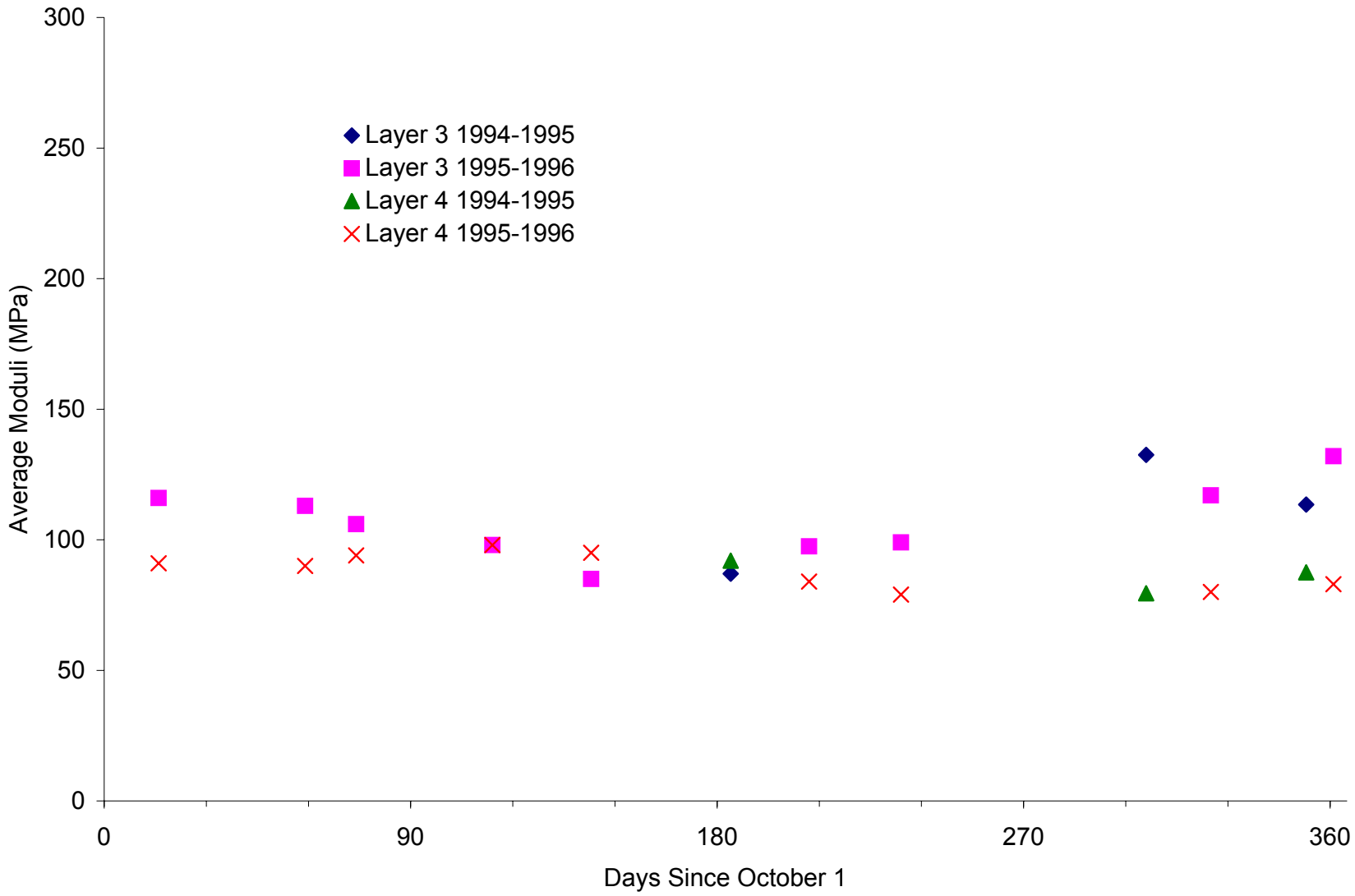

Figure L-5. Seasonal Variation of Subgrade Modulus at Site 13-1031 (Silty Sand)

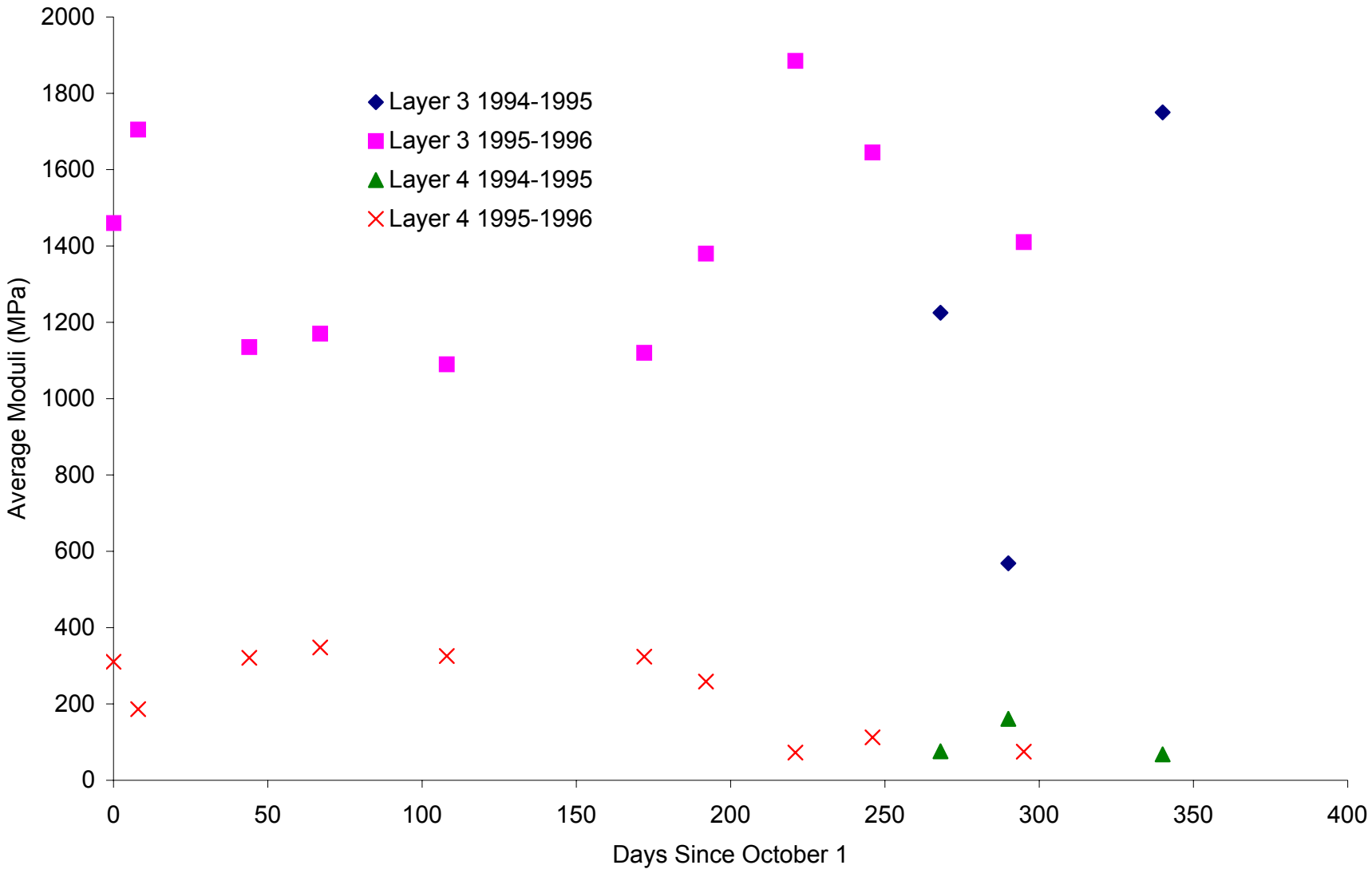

Figure L-6. Seasonal Variation of Subgrade Modulus at Site 28-1016 (Silty Sand)

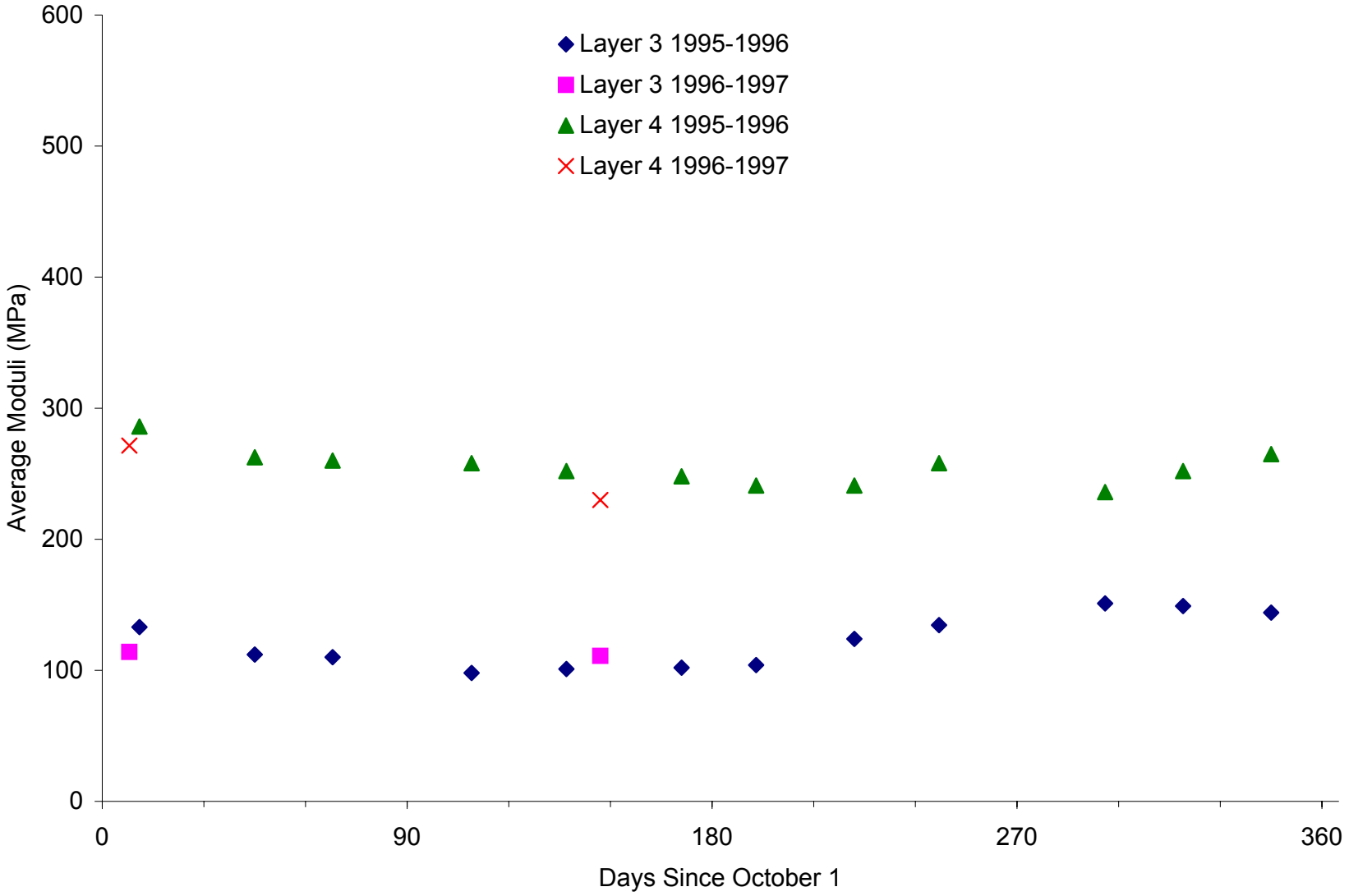

Figure L-7. Seasonal Variation of Subgrade Modulus at Site 28-1802 (Poorly Graded Sand)

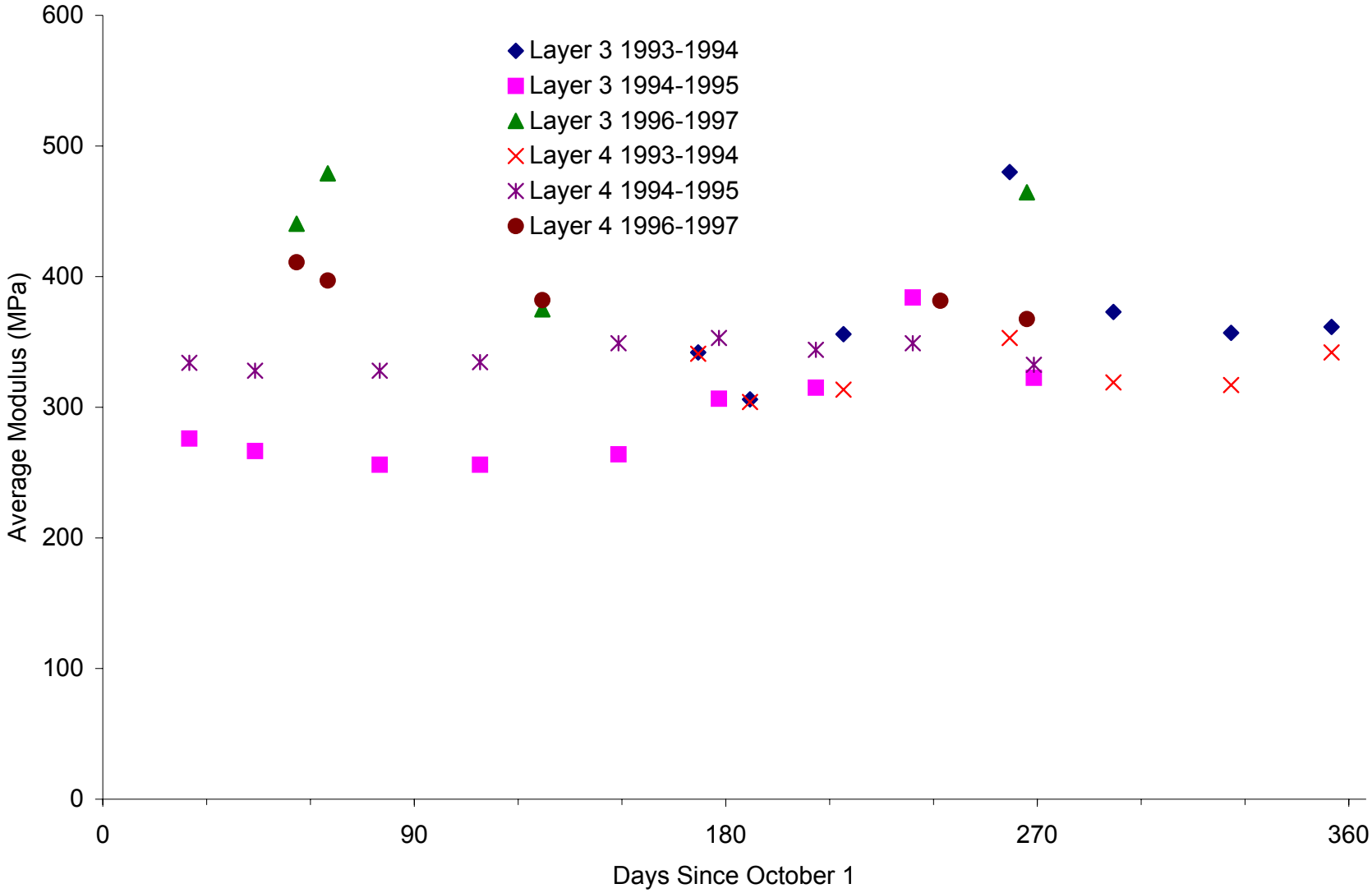

Figure L-8. Seasonal Variation of Subgrade Modulus at Site 35-1112 (Poorly Graded Sand)

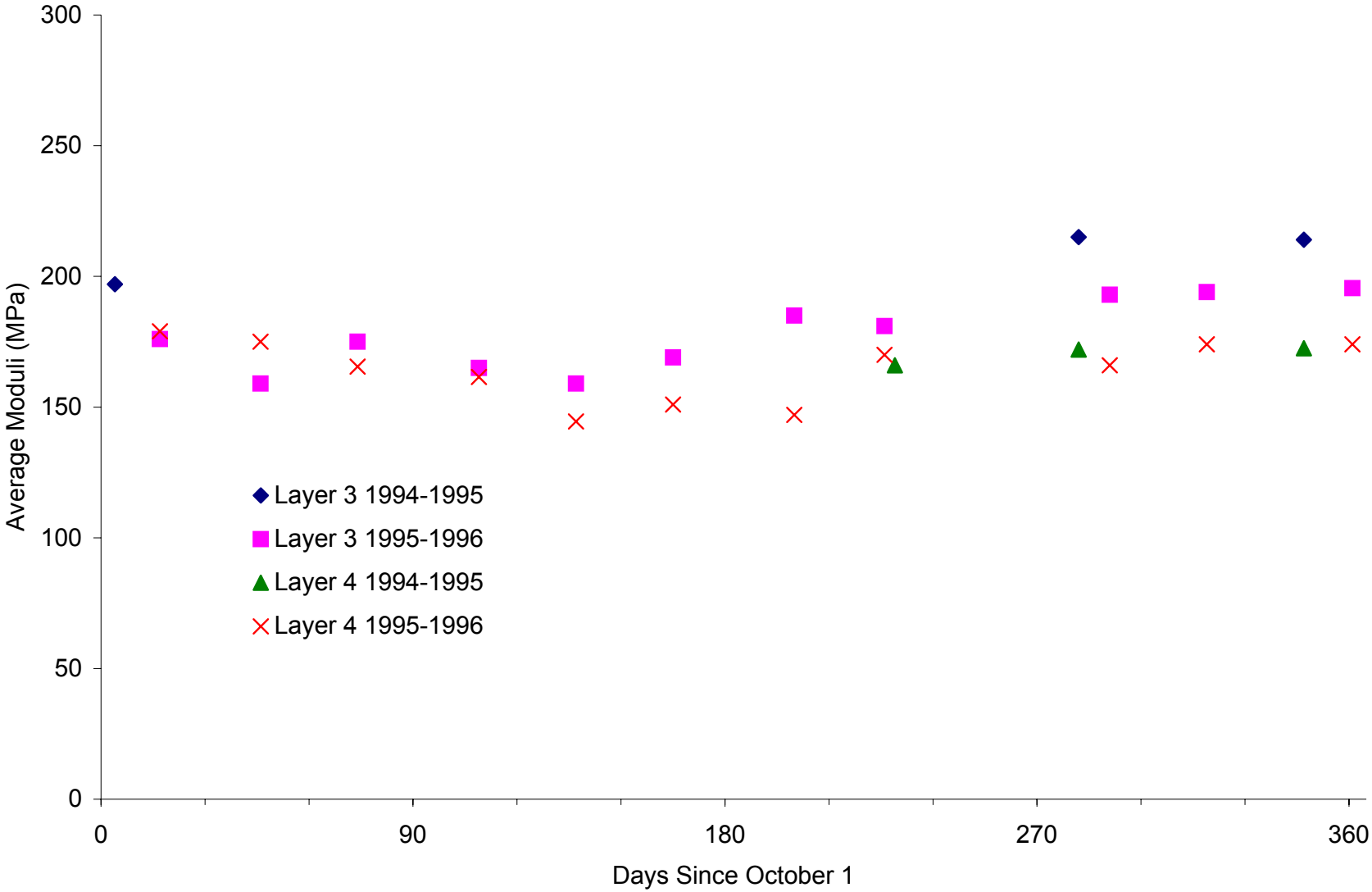

Figure L-9. Seasonal Variation of Subgrade Modulus at Site 37-1028 (Poorly Graded Sand with Silt)

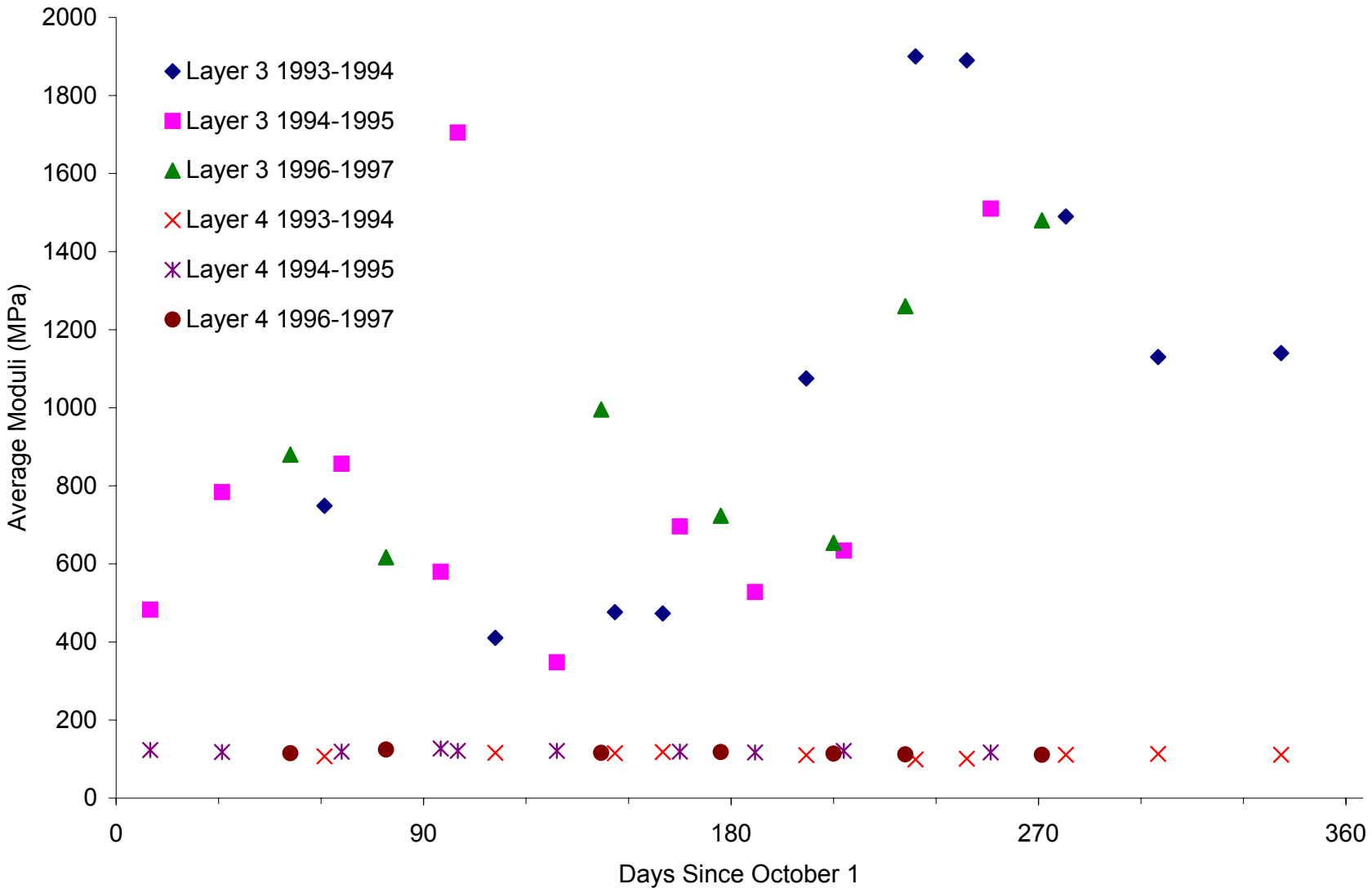

Figure L-10. Seasonal Variation of Subgrade modulus at Site 48-1060 (Silty Clay)

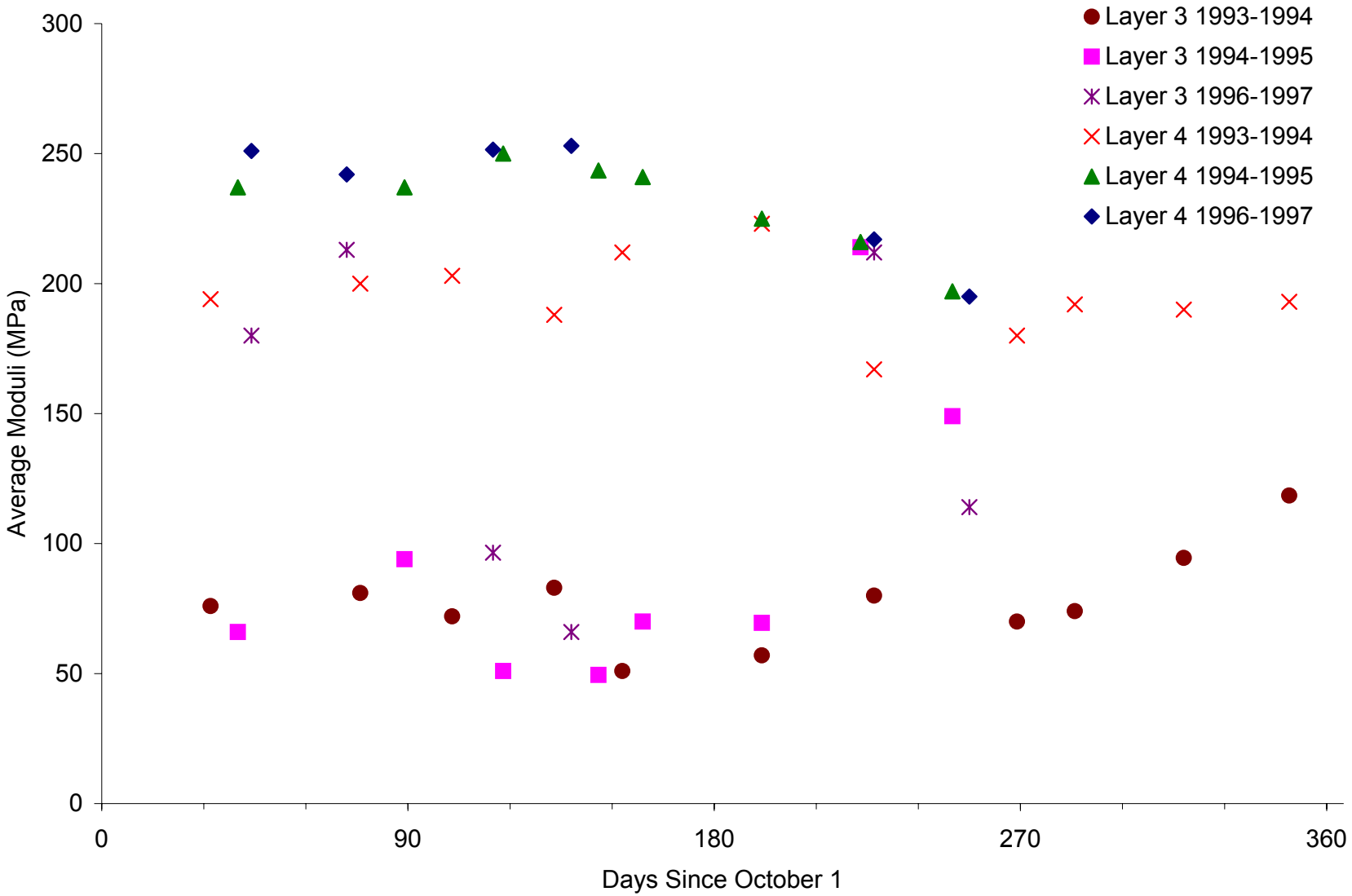

Figure L-11. Seasonal Variation of Subgrade Modulus at Site 48-1068 (Sandy Lean Clay)

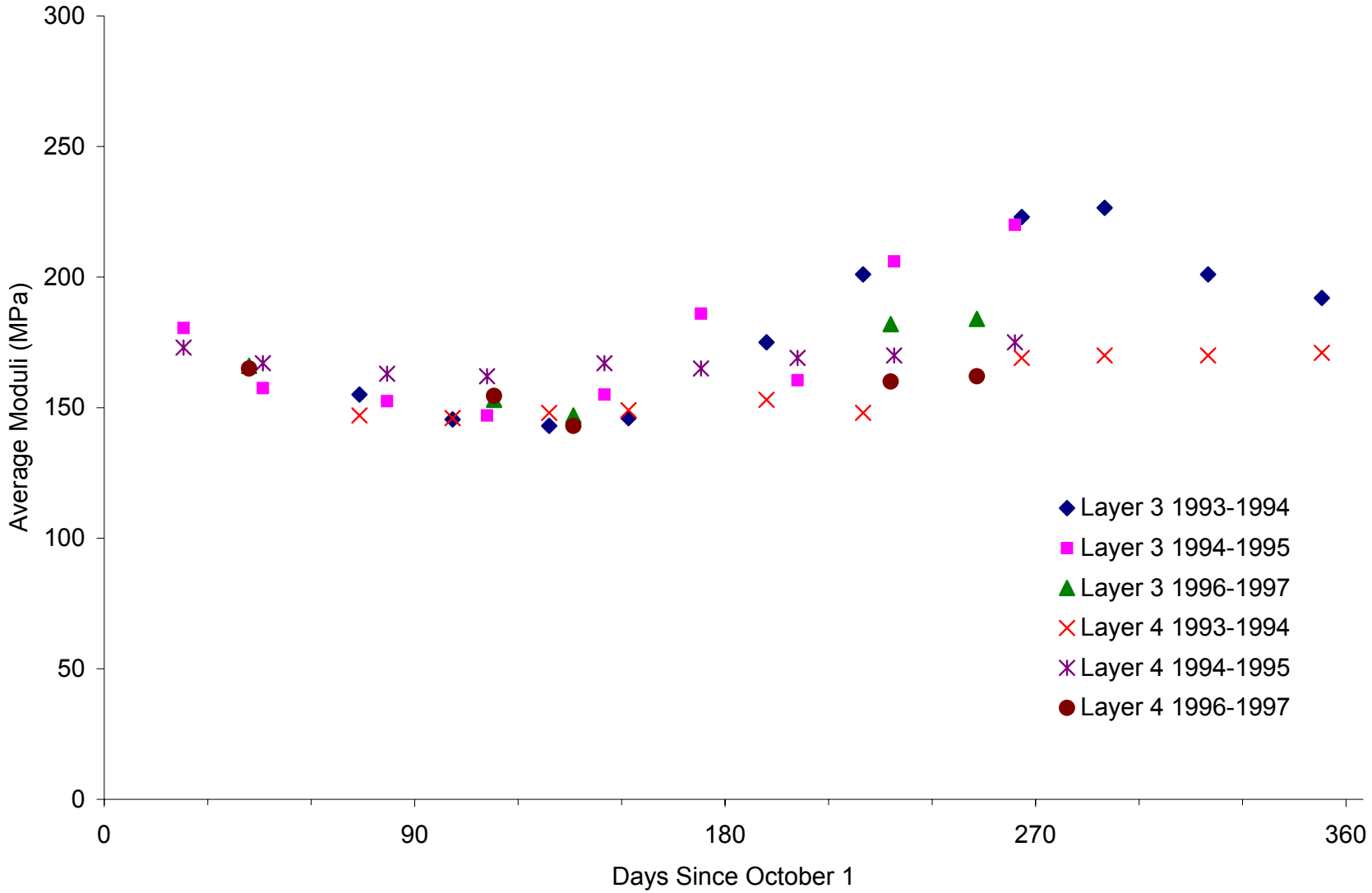

Figure L-12. Seasonal Variation of Subgrade Modulus at Site 48-1077 (Sandy Silt)

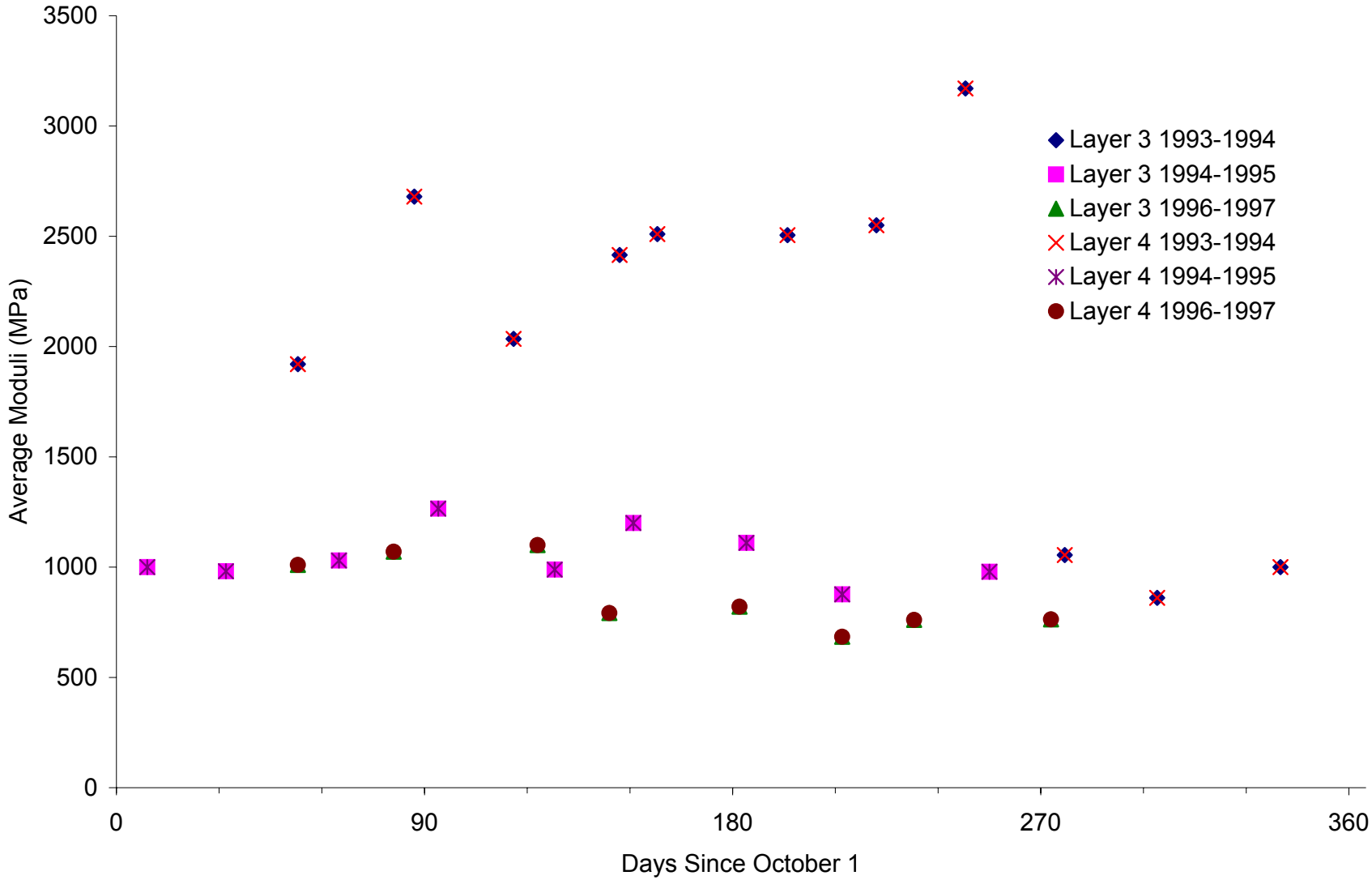

Figure L-13. Seasonal Variation of Subgrade Modulus at Site 48-1122 (Clayey Sand)

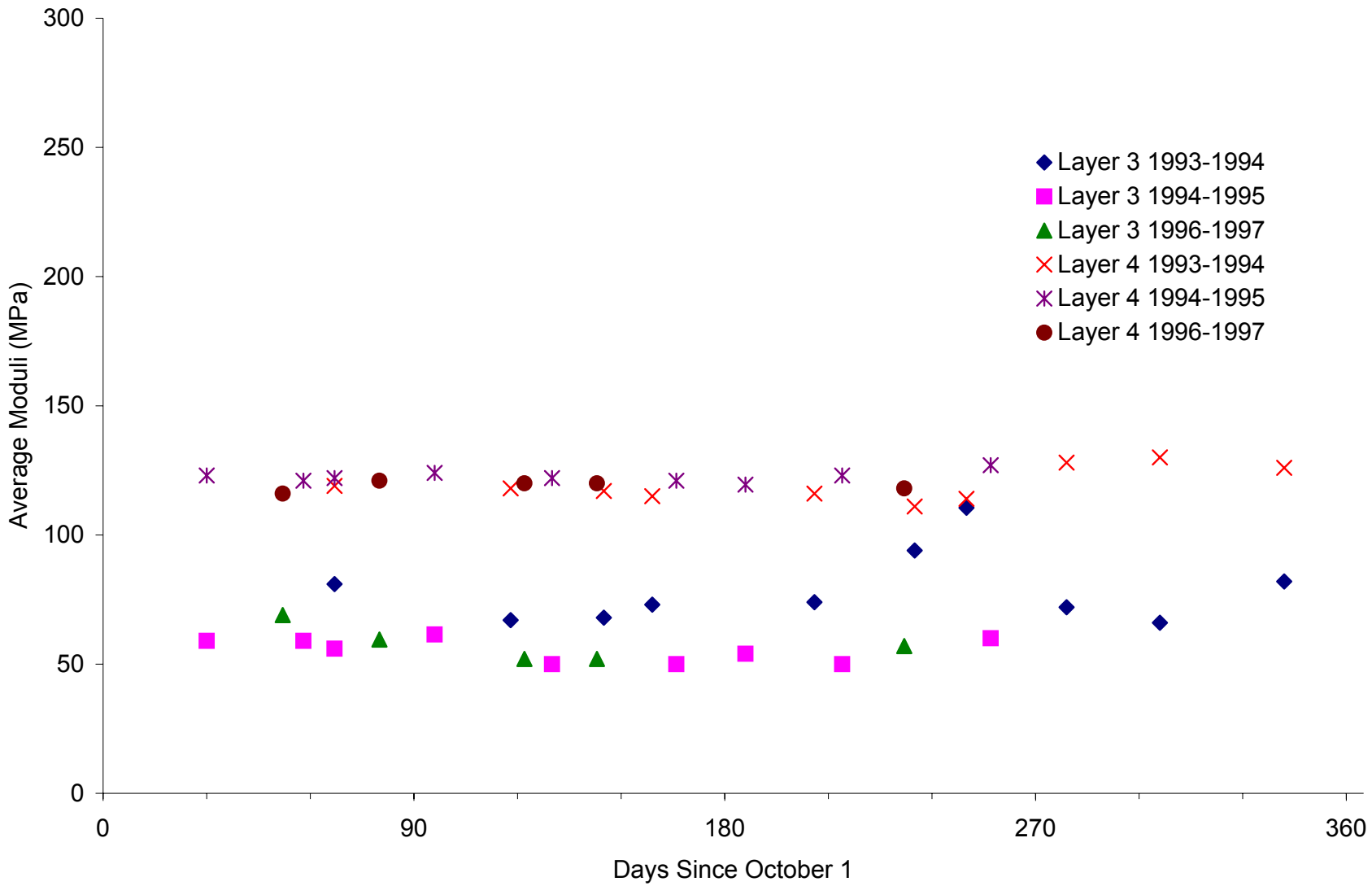

Figure L-14. Seasonal Variation of Subgrade Modulus at Site 48-3739 (Poorly Graded Sand)

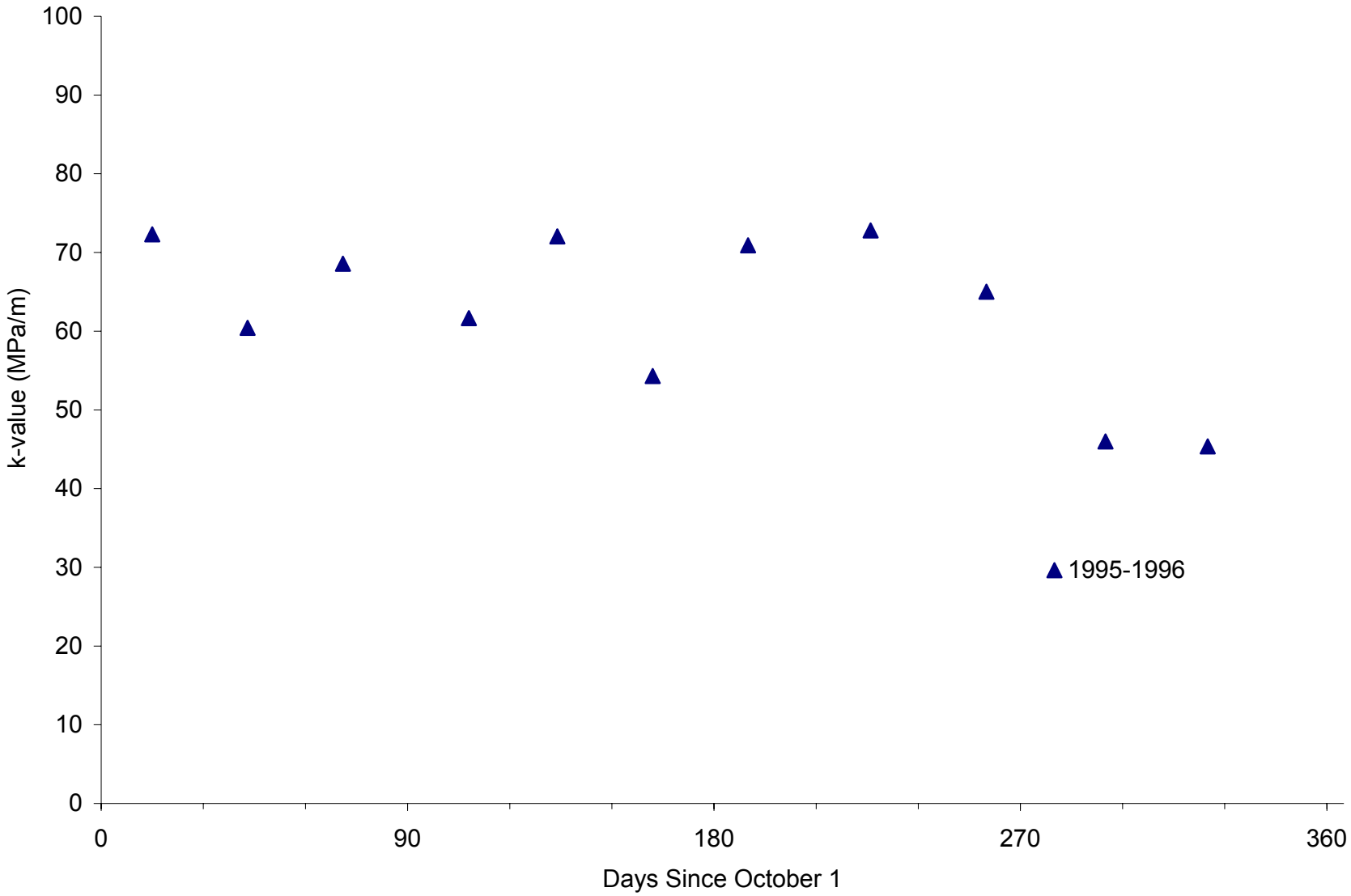

Figure L-15. Seasonal Variation of Subgrade k-value at Site 04-0215 (Silty Sand with Gravel)

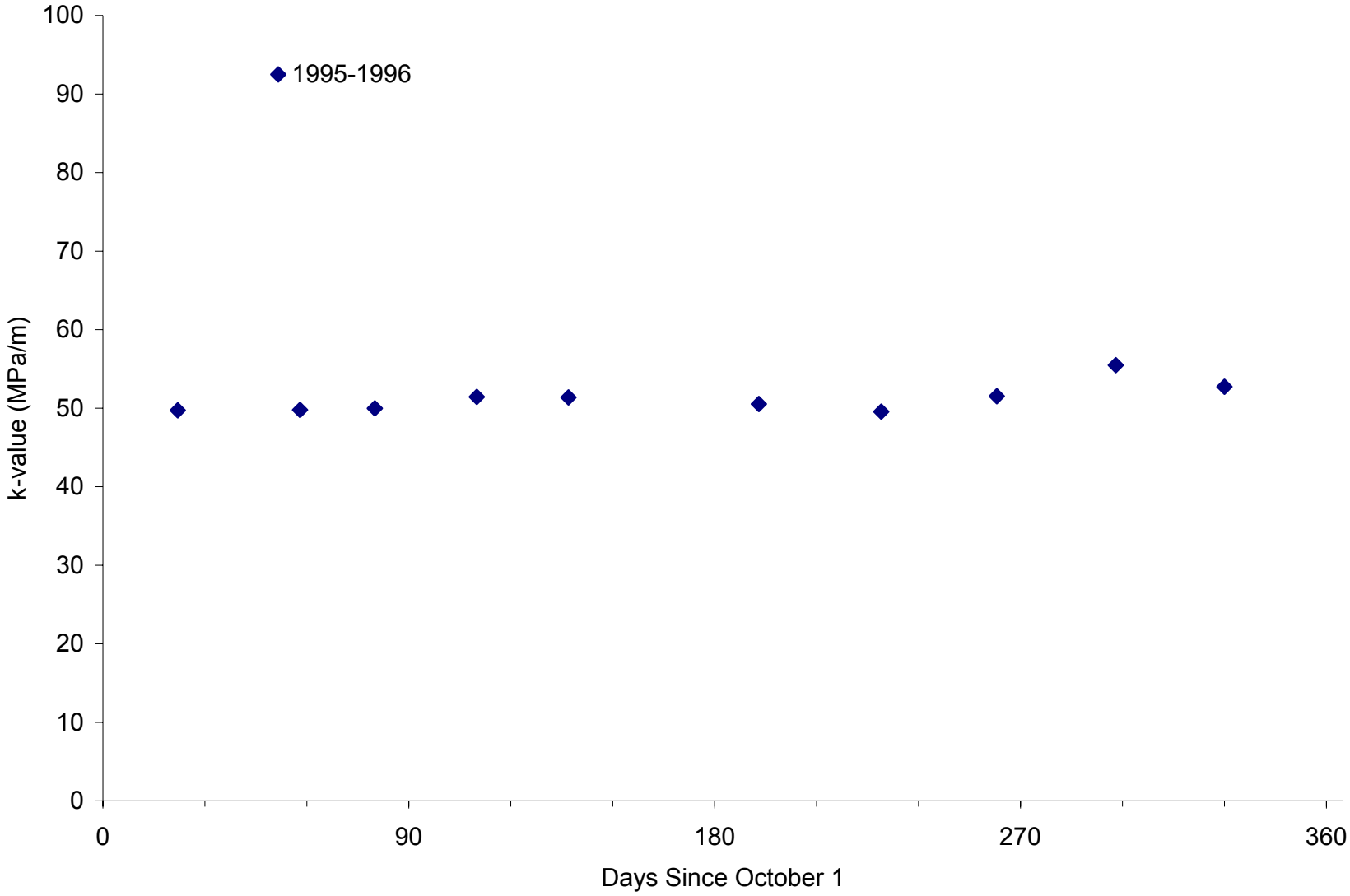

Figure L-16. Seasonal Variation of k-value at Site 06-3042 (Sandy Lean Clay)

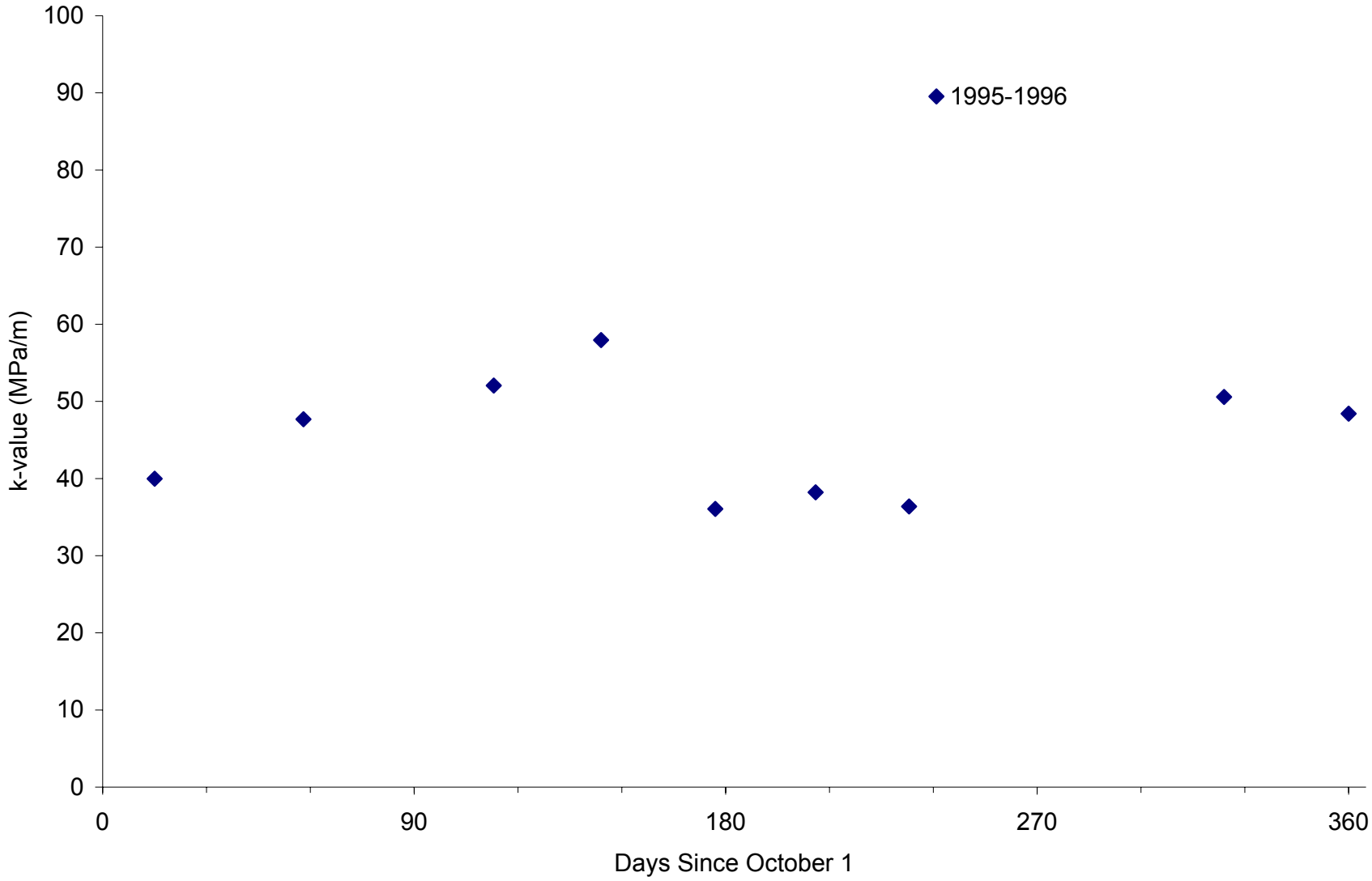

Figure L-17. Seasonal Variation of k-value at Site 13-3019 (Sandy Lean Clay)

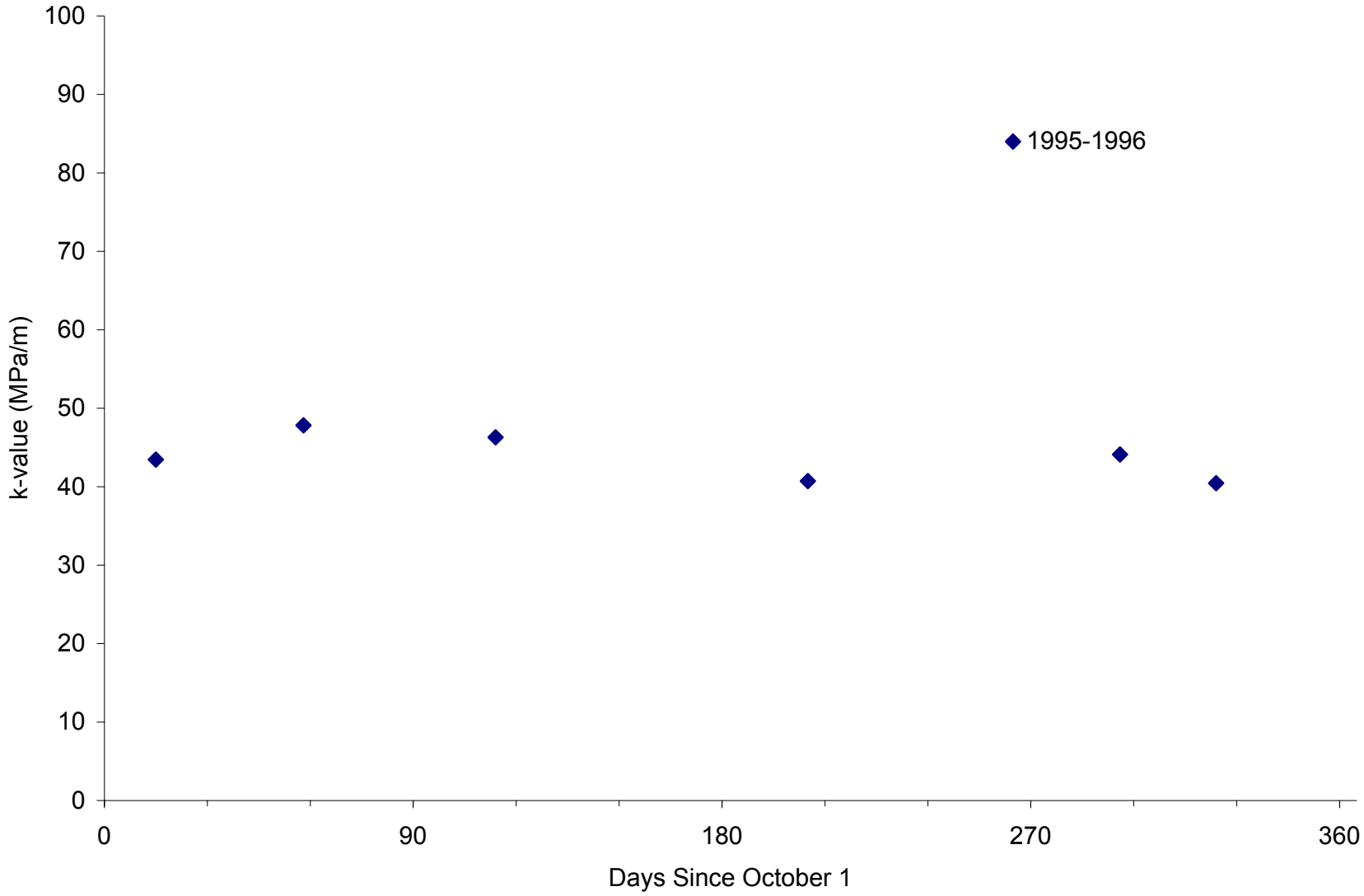

Figure L-18. Seasonal Variation of Subgrade k-value at Site 37-0201 (Clay)

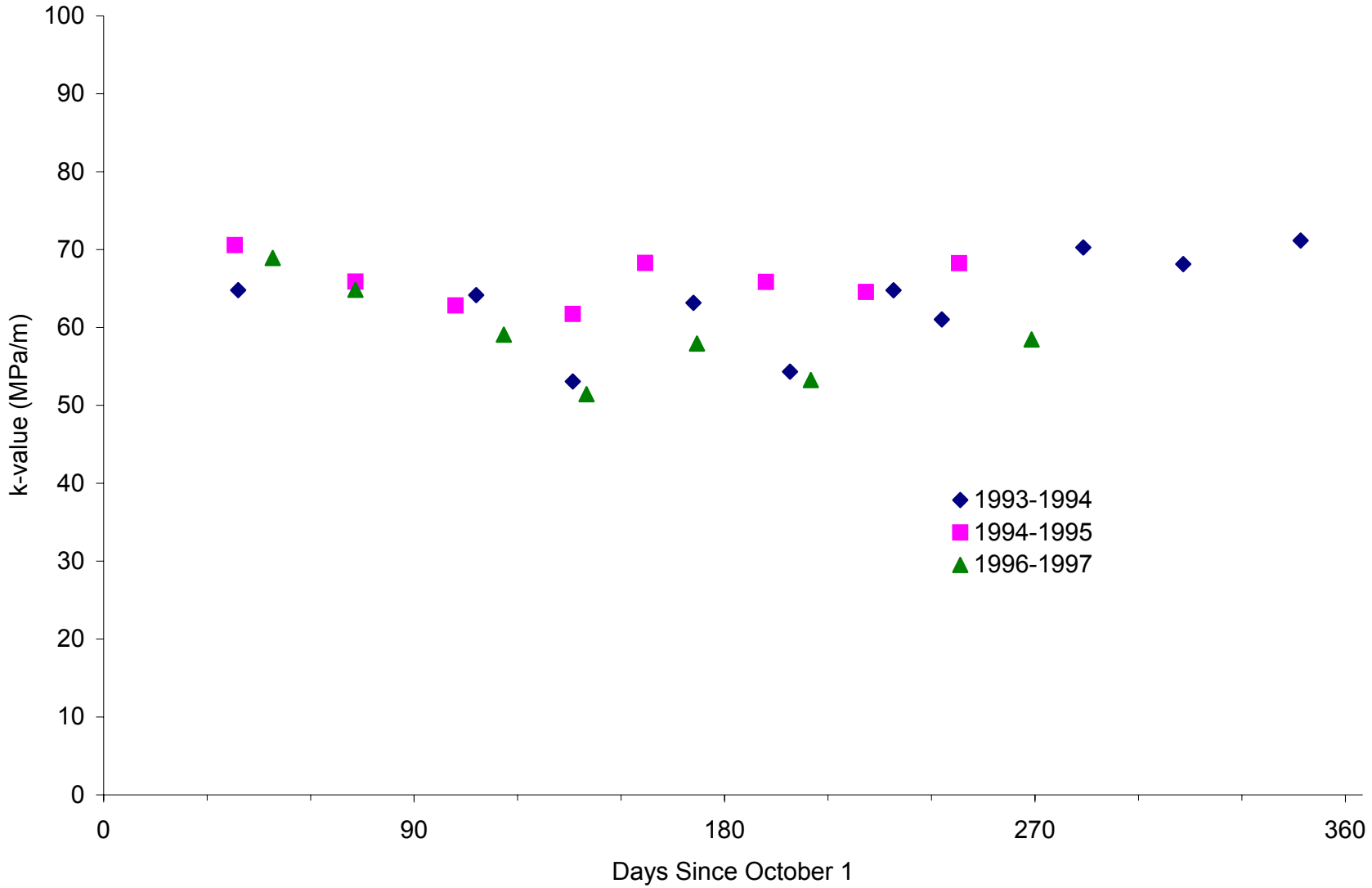

Figure L-19. Seasonal Variation of Subgrade k-value at Site 48-4142 (Clayey Sand)

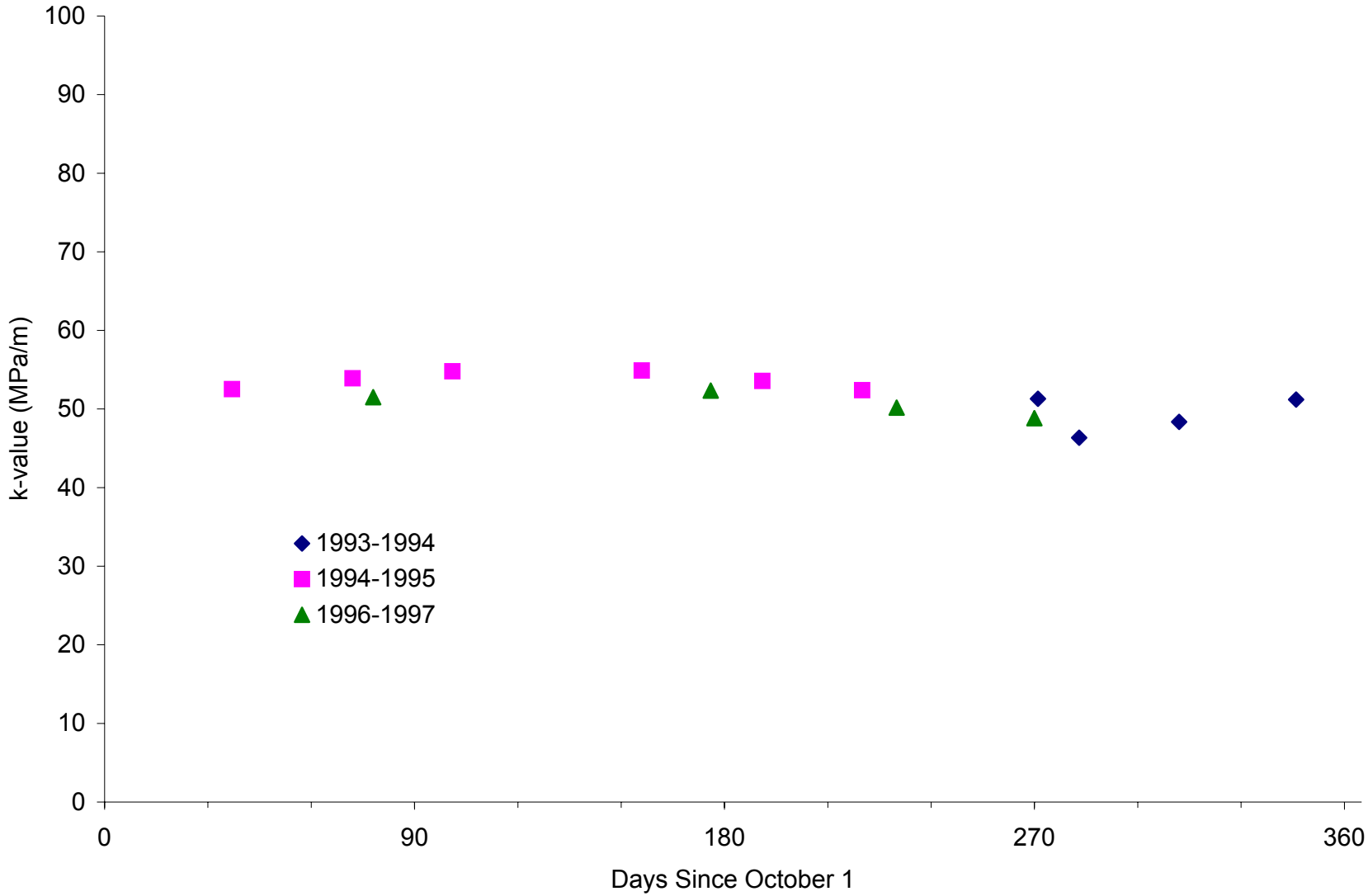

Figure L-20. Seasonal Variation of Subgrade k-value at Site 48-4143 (Lean Inorganic Clay)

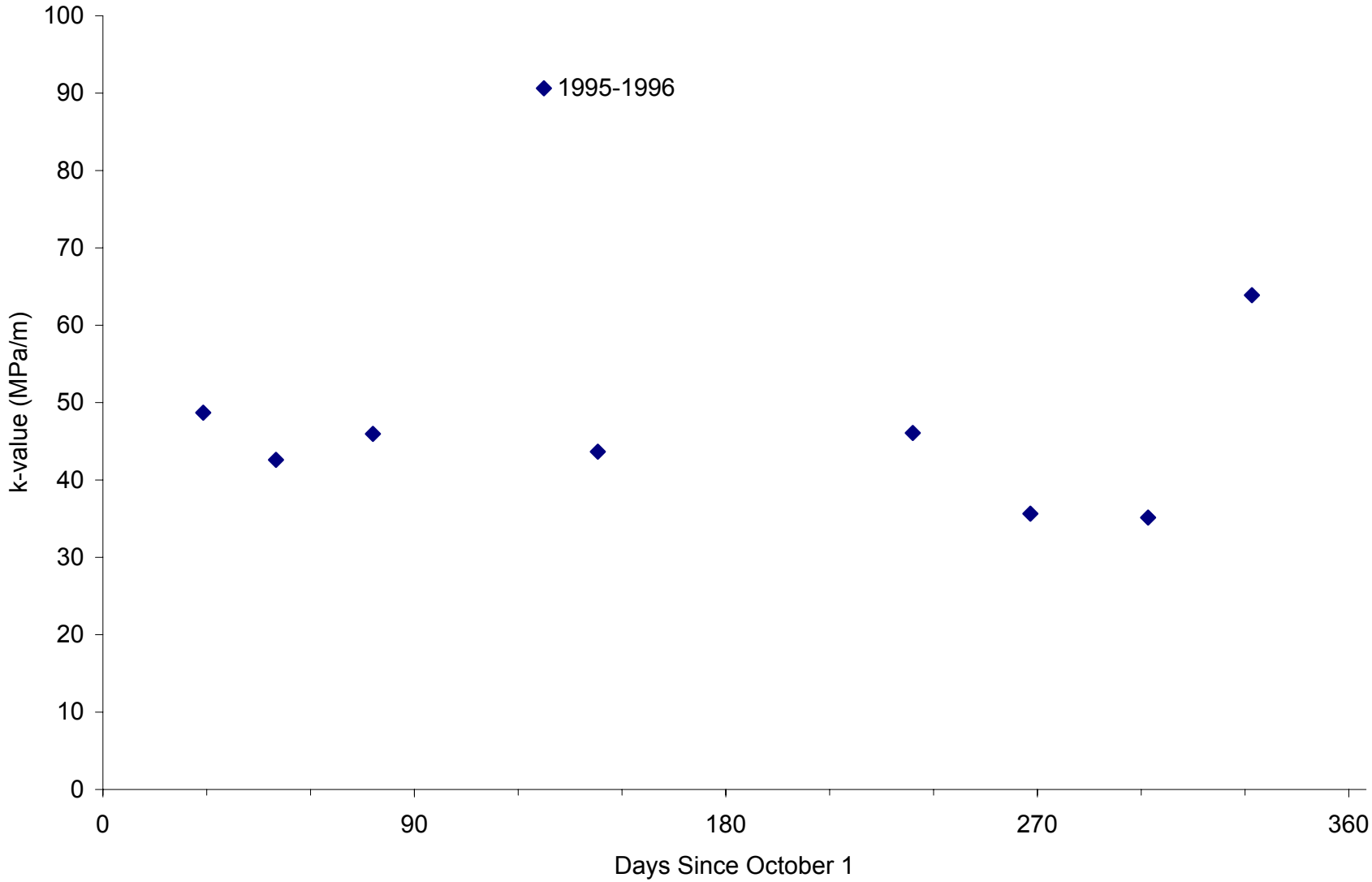

Figure L-21. Seasonal Variation of Subgrade k-value at Site 53-3813 (Silty Sand)

APPENDIX M

MOISTURE CONTENT VARIATIONS WITH WATER TABLE DEPTH AT NO-FREEZE SITES

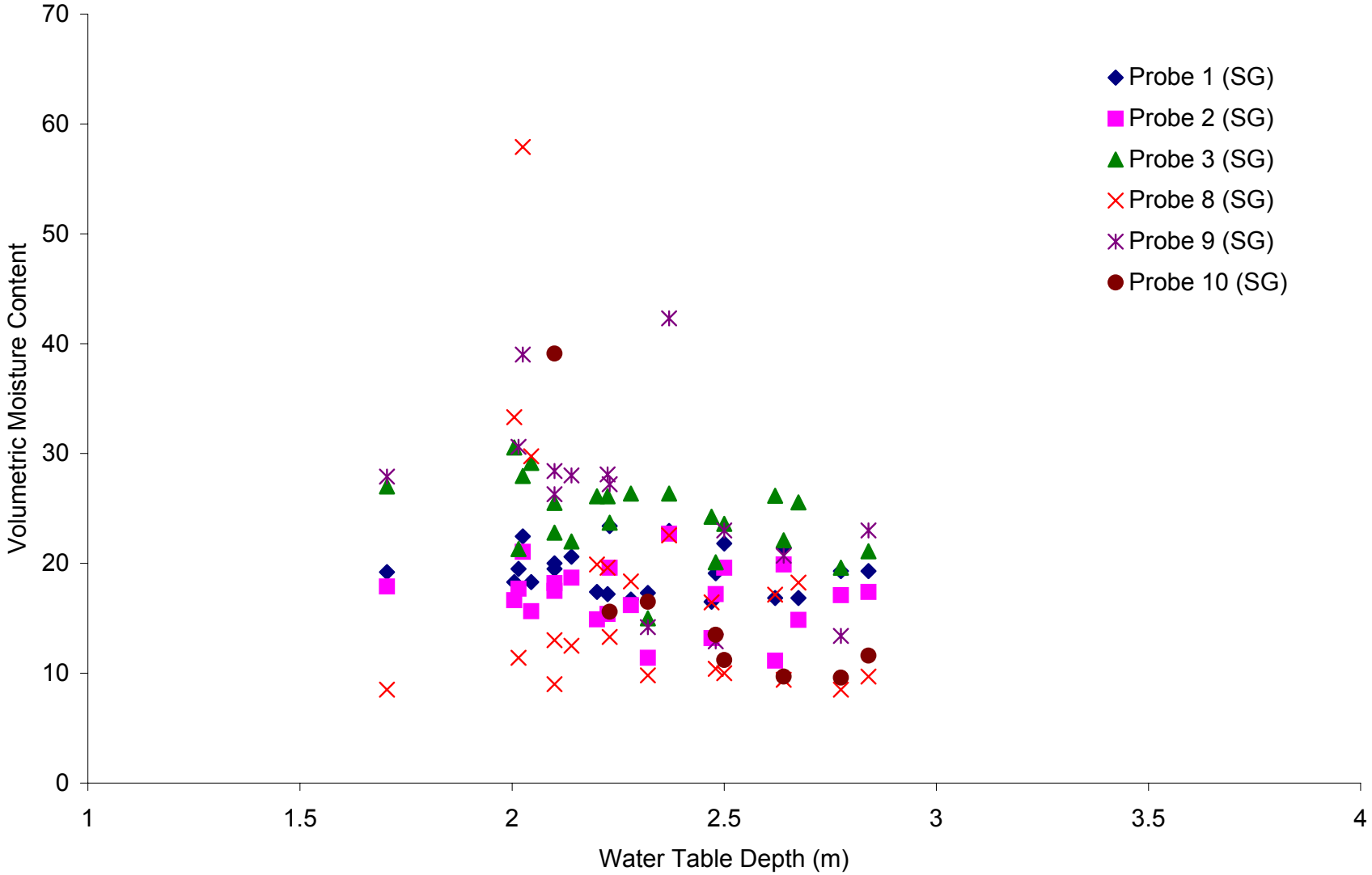

Figure M-1. Comparison of Subgrade Moisture Content and Water Table Depth at Site 37-1028 (Poorly Graded Sand with Silt)

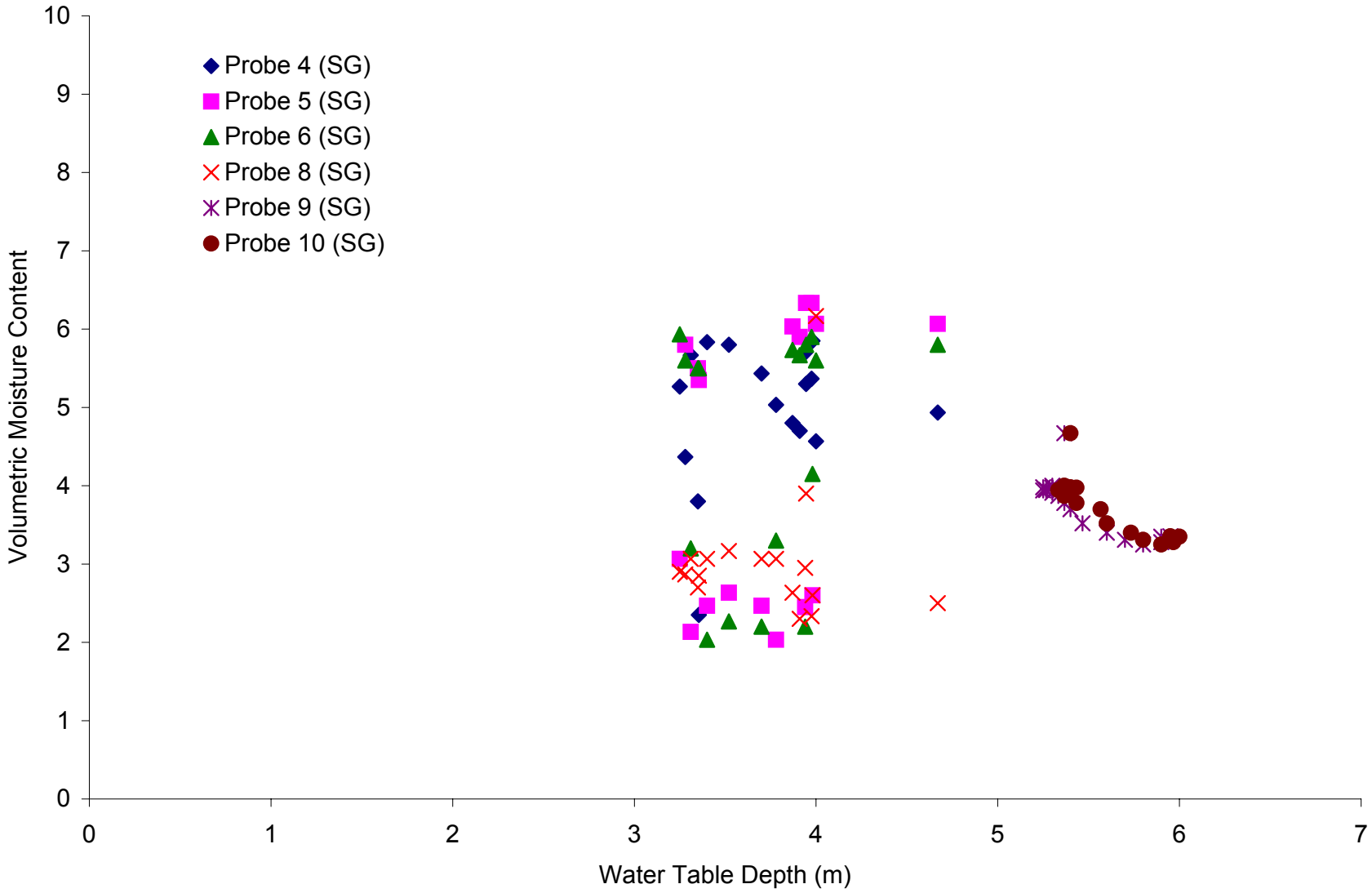

Figure M-2. Comparison of Subgrade Moisture Content and Water Table Depth at Site 48-3739 (Silty Sand)

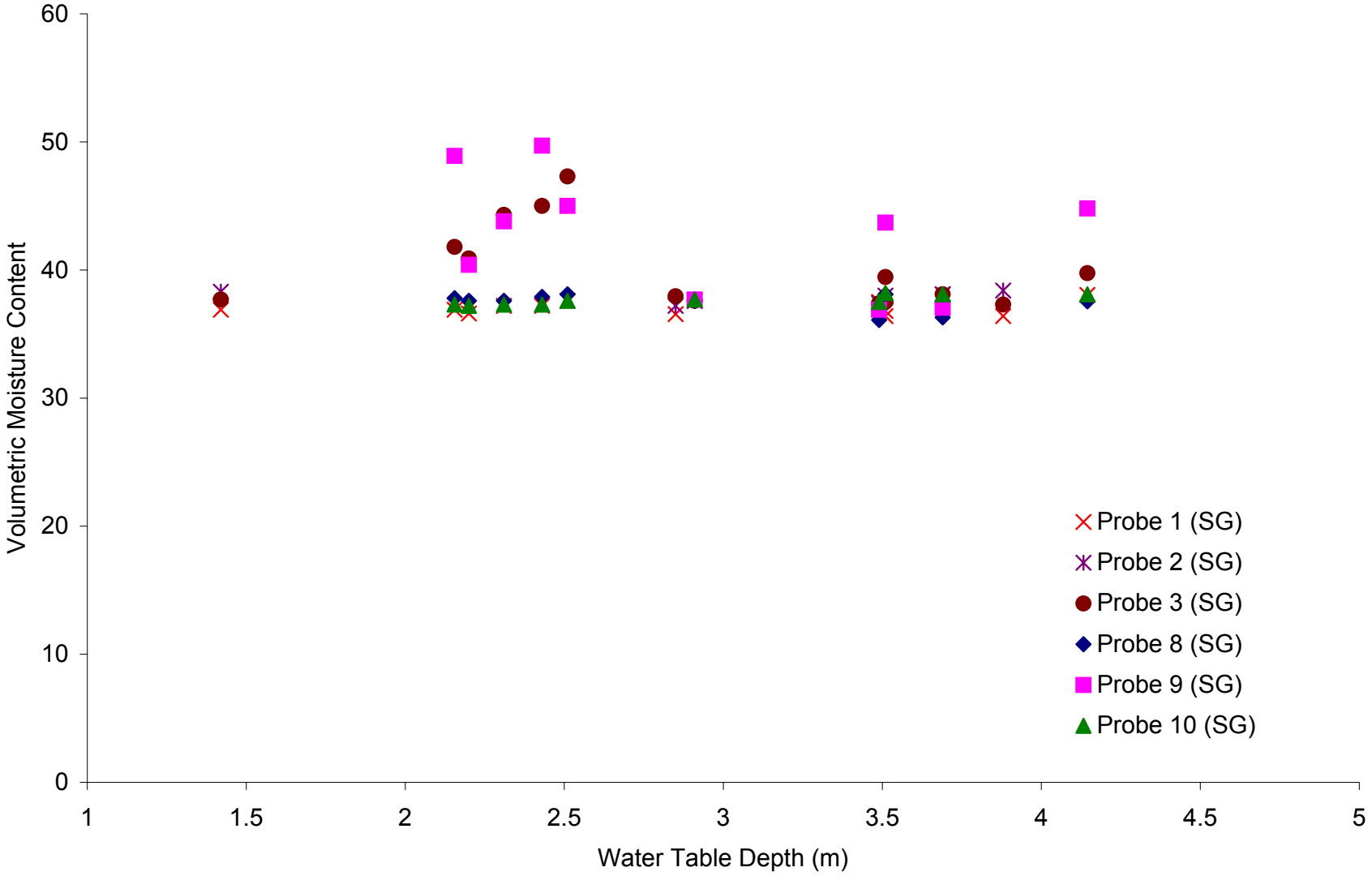

Figure M-3. Comparicon of Subgrade Moisture Content and Water Table Depth at Site 06-3042 (Sandy Lean Clay)

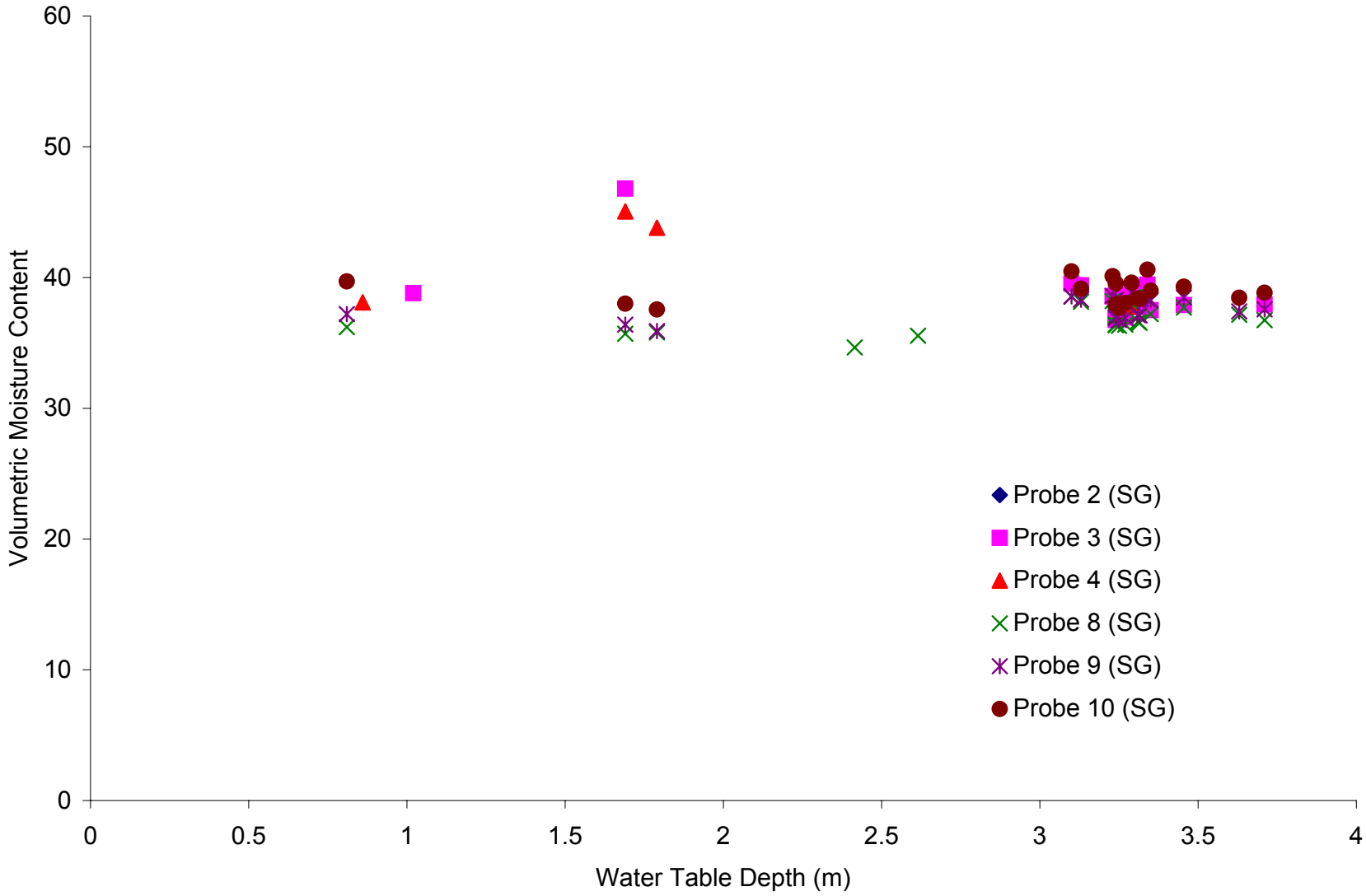

Figure M-4. Comparison of Subgrade Moisture Content and Water Table Depth at Site 48-4143 (Lean Inorganic Clay)

APPENDIX N

SUBGRADE MODULUS AND k-VALUES VERSUS WATER CONTENT

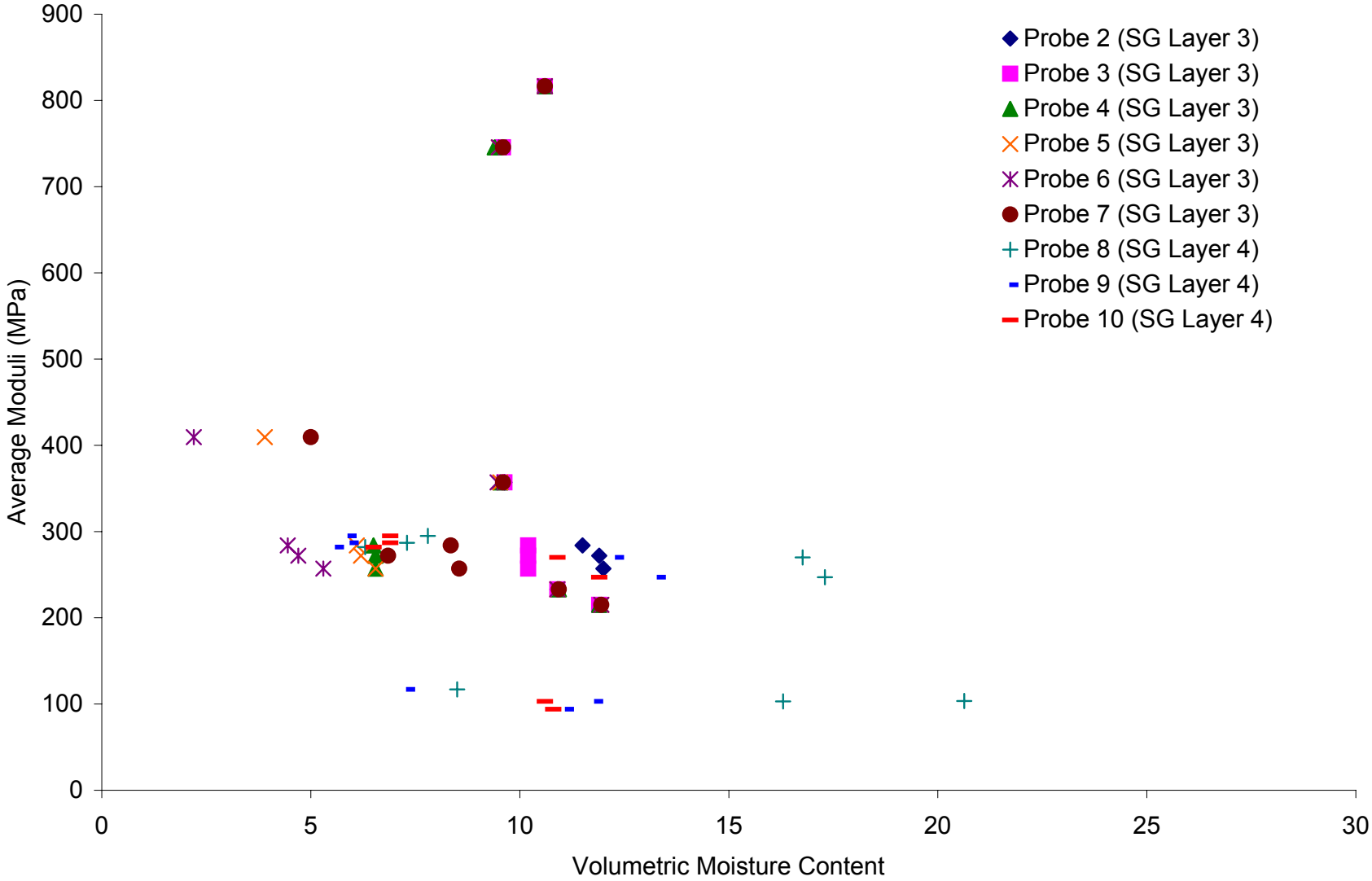

Figure N-1. Variation in Subgrade Modulus as a Function of Moisture Content at Site 04-0113 (Well-Graded Sand with Silt and Gravel)

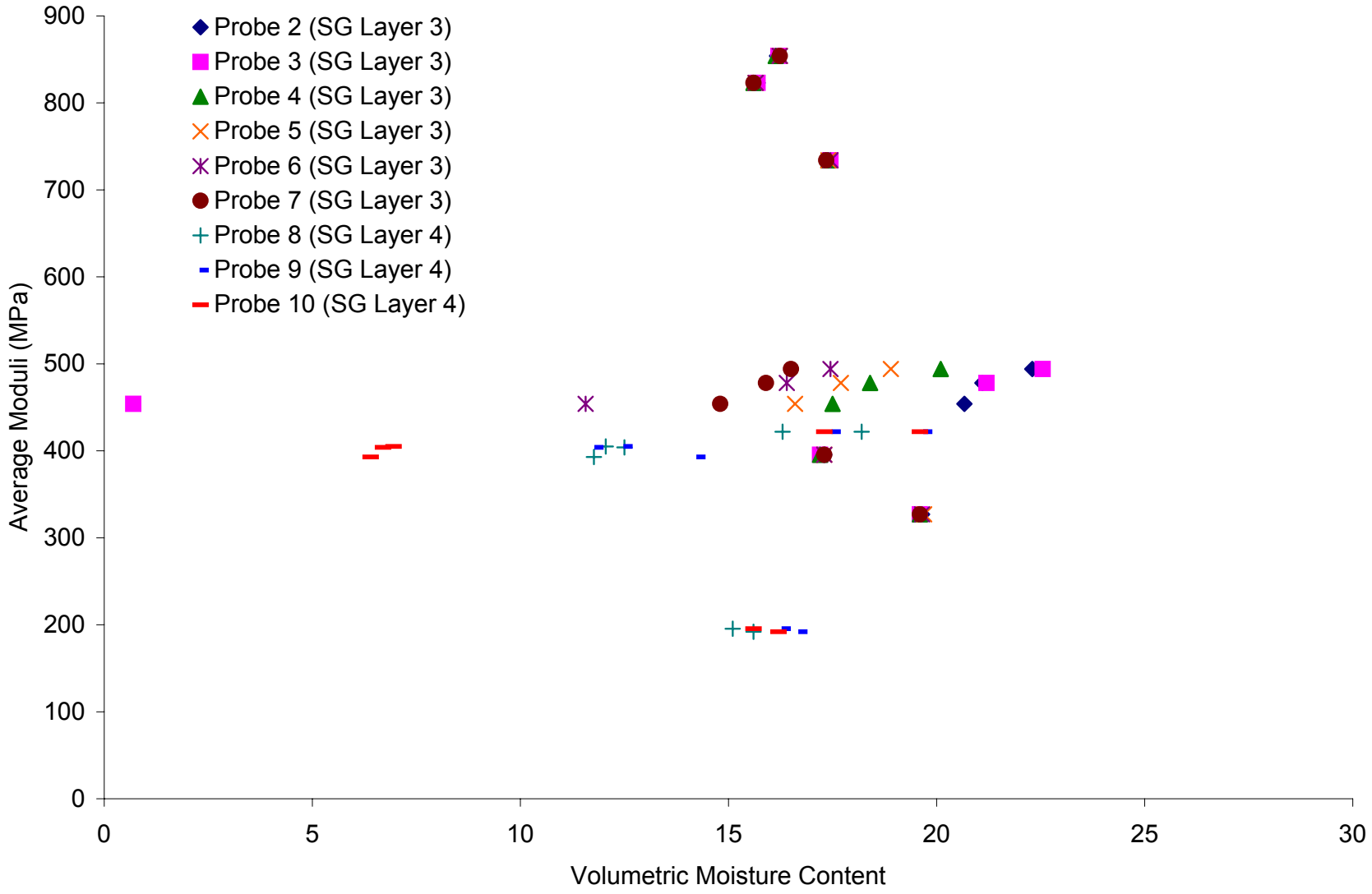

Figure N-2. Variation in Subgrade Modulus as a Funciton of Moisture Content at Site 04-0114 (Silty Sand with Gravel)

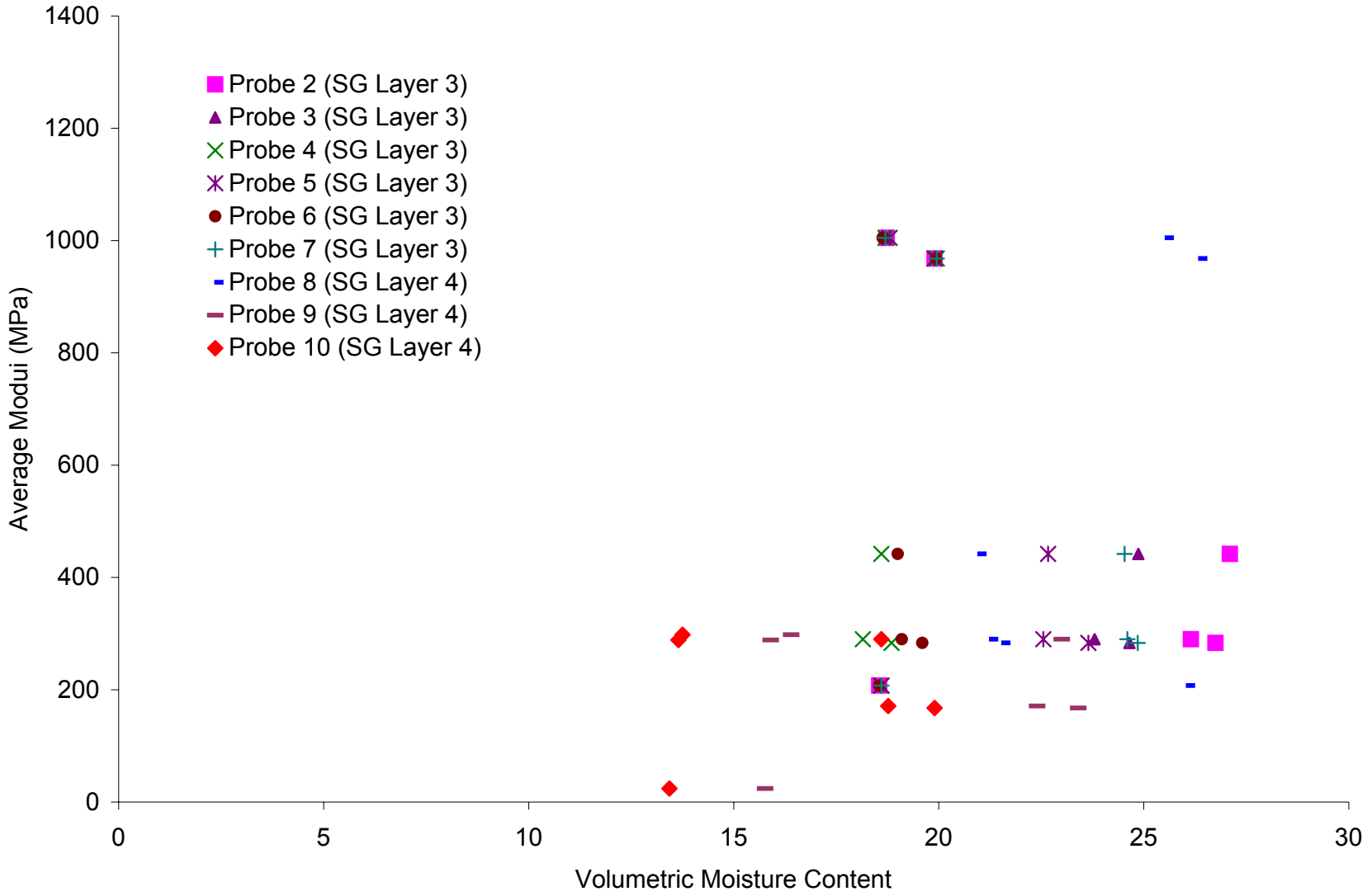

Figure N-3. Variation in Subgrade Modulus as a Function of Moisture Content at Site 04-1024 (Clayey Sand with Gravel)

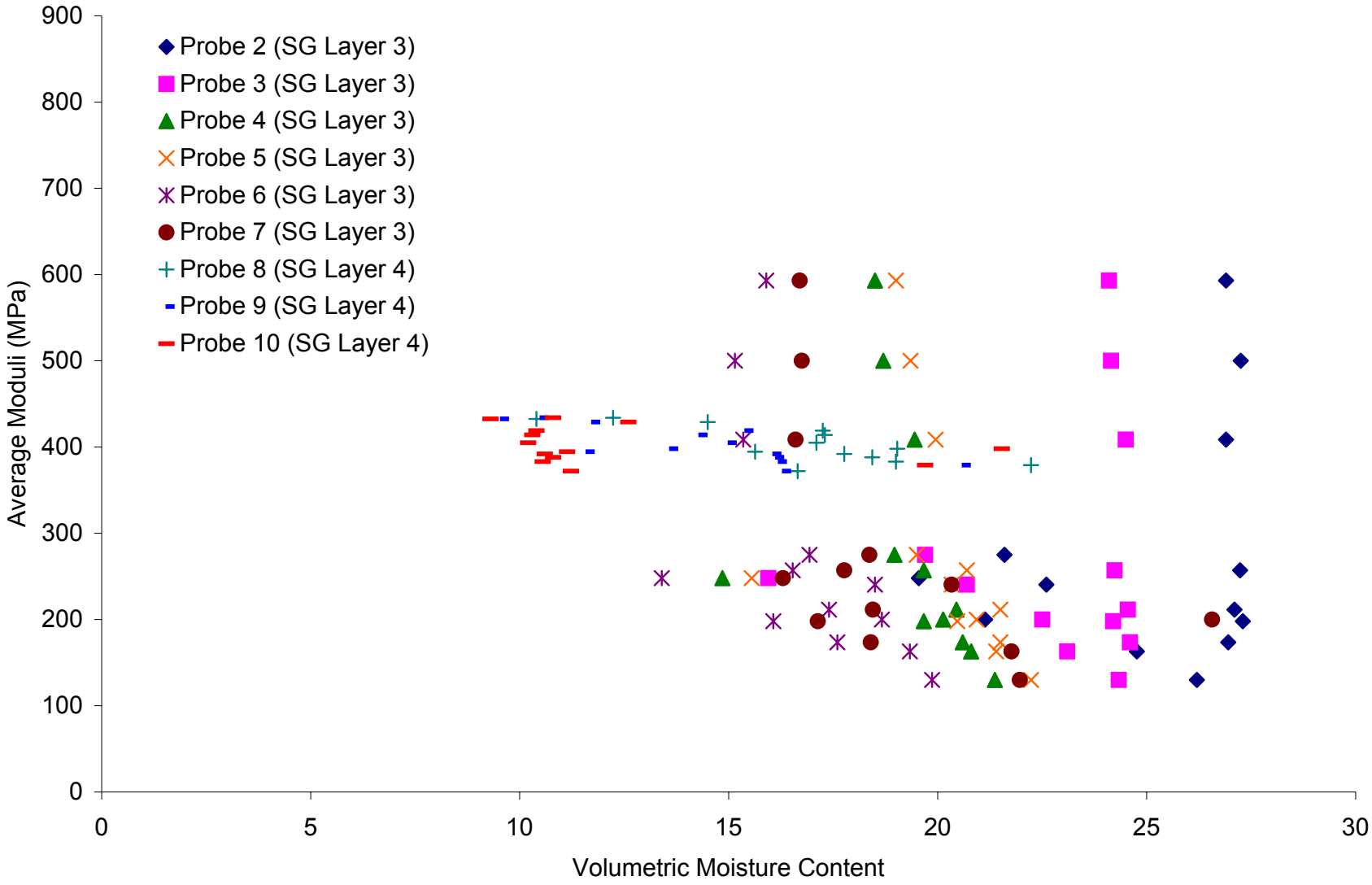

Figure N-4. Variation in Subgrade Modulus as a Function of Moisture Content at Site 13-1005 (Clayey Sand)

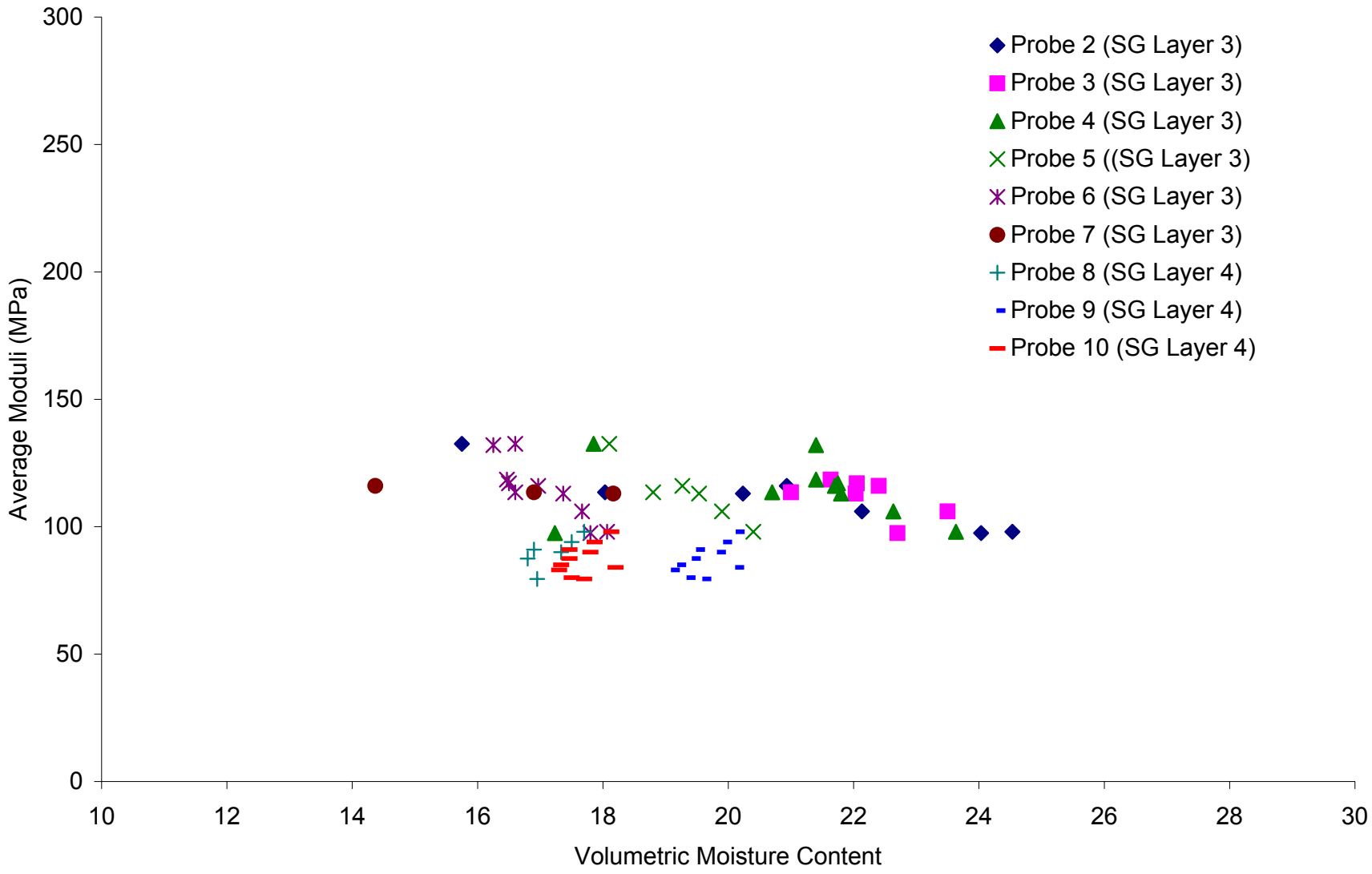

Figure N-5. Variation in Subgrade Modulus as a Function of Moisture Content at Site 13-1031 (Silty Sand)

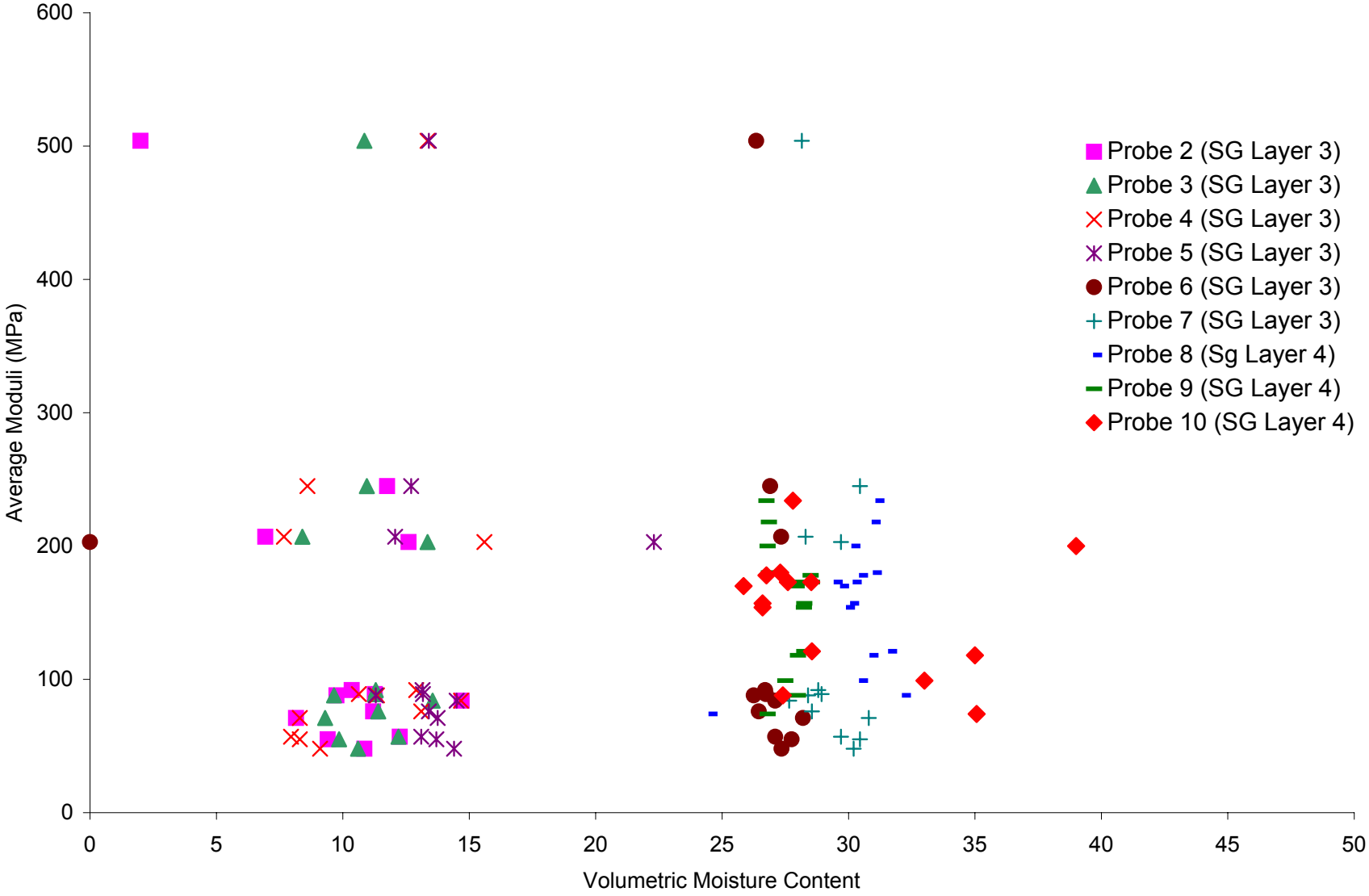

Figure N-6. Variation in Subgrade Modulus as a Function of Moisture Content at Site 16-1010 (Sitly Sand)

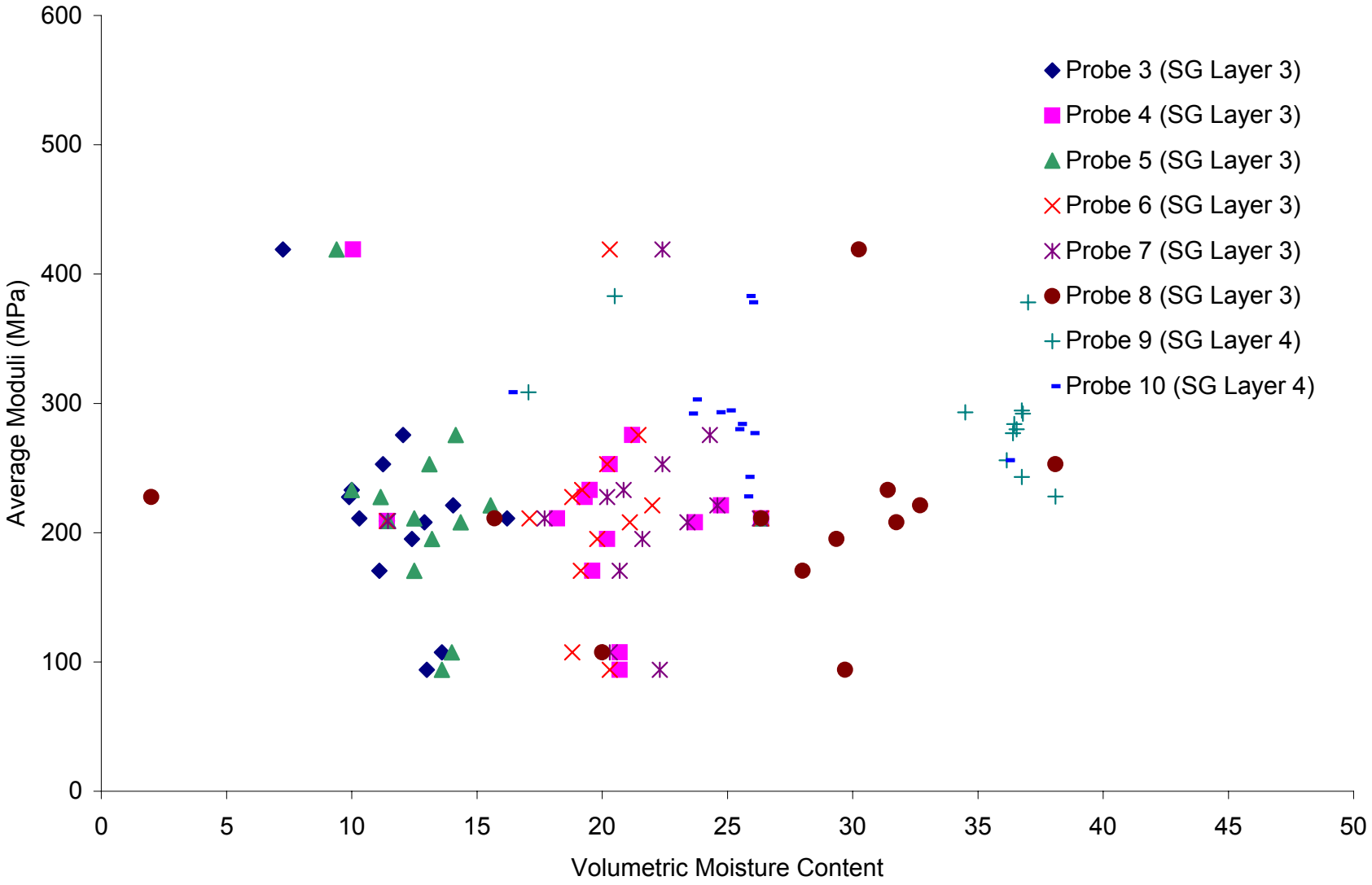

Figure N-7. Variation in Subgrade Modulus as a Function of Moisture Content at Site 23-1026 (Silty Sand with Gravel)

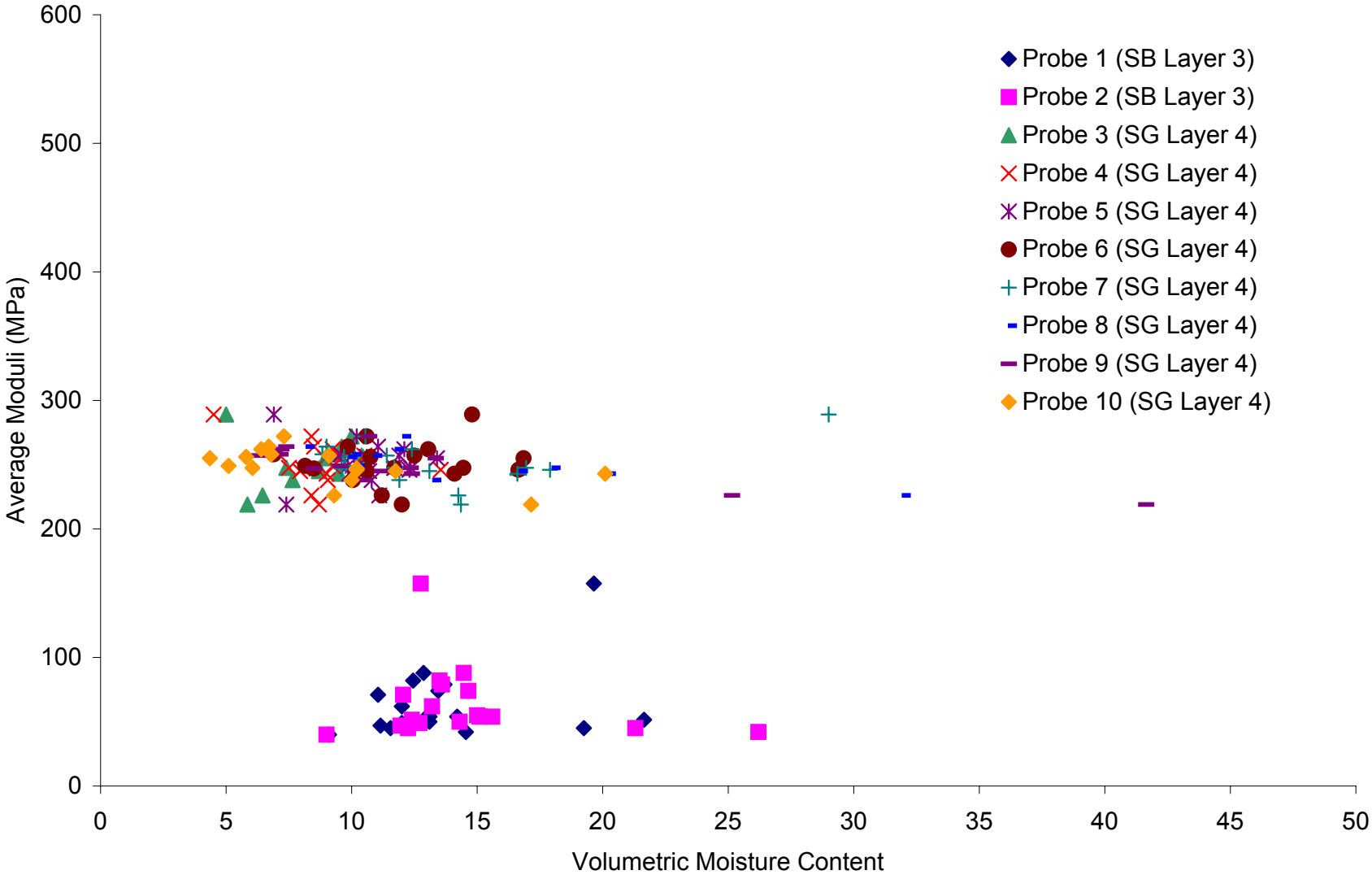

Figure N-8. Variation in Subgrade Modulus as a Function of Moisture Content at Site 25-1002 (Poorly Graded Sand with Silt)

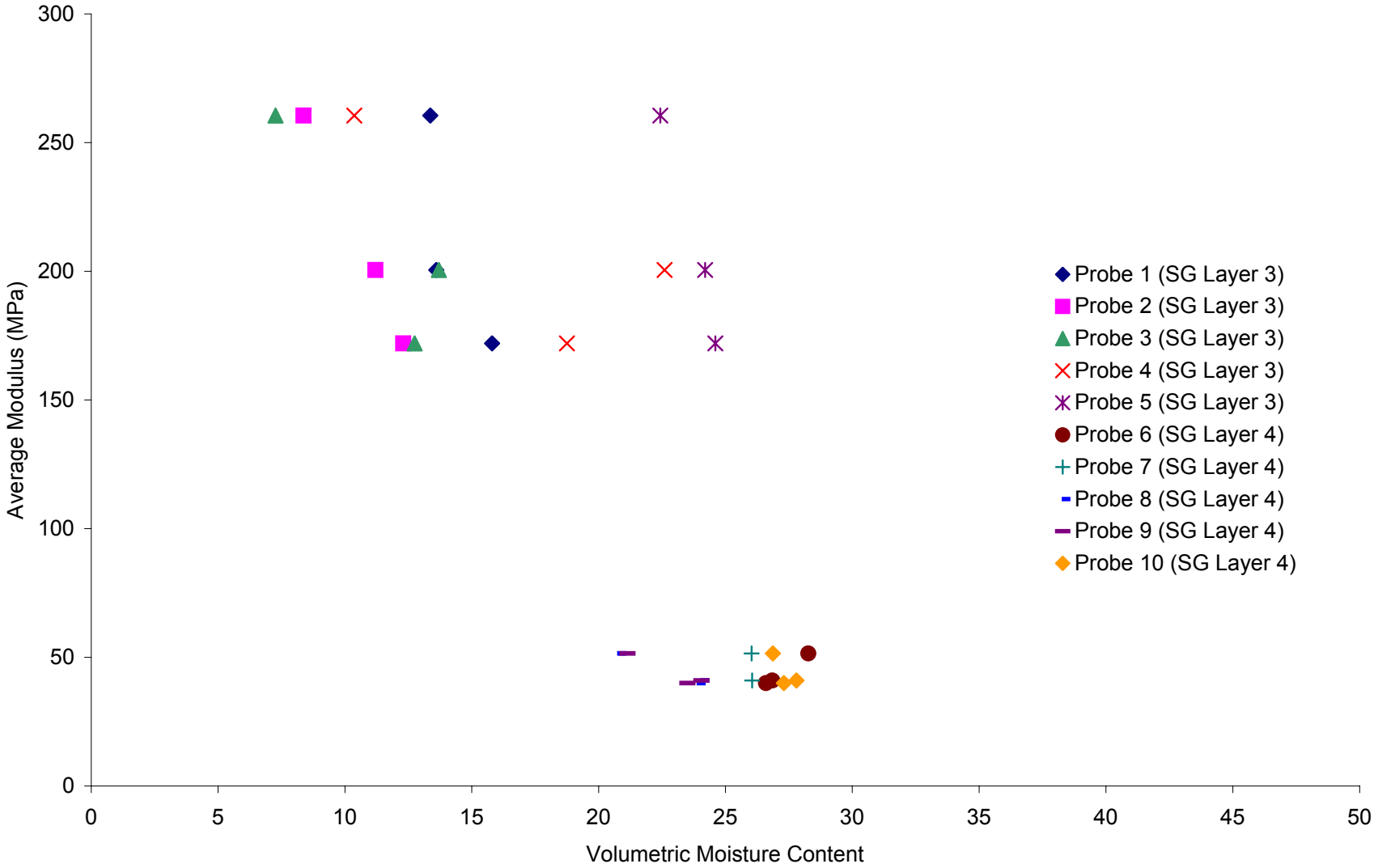

Figure N-9. Variation in Subgrade Modulus as a Function of Moisture Content at Site 27-1018 (Poorly Graded Sand with Silt)

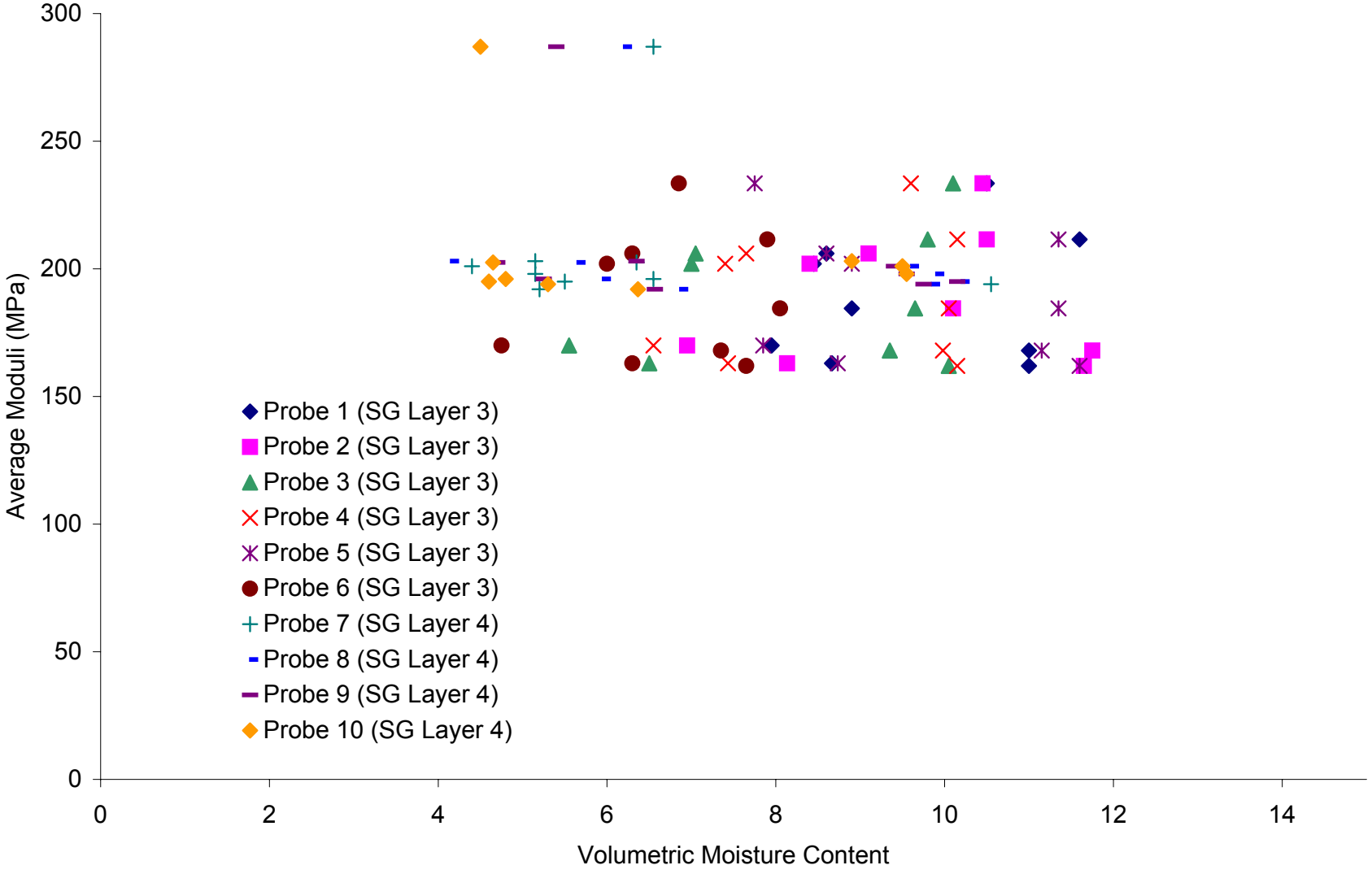

Figure N-10. Variation in Subgrade Modulus as a Function of Moisture Content at Site 27-1028 (Poorly Graded Sand with Silt)

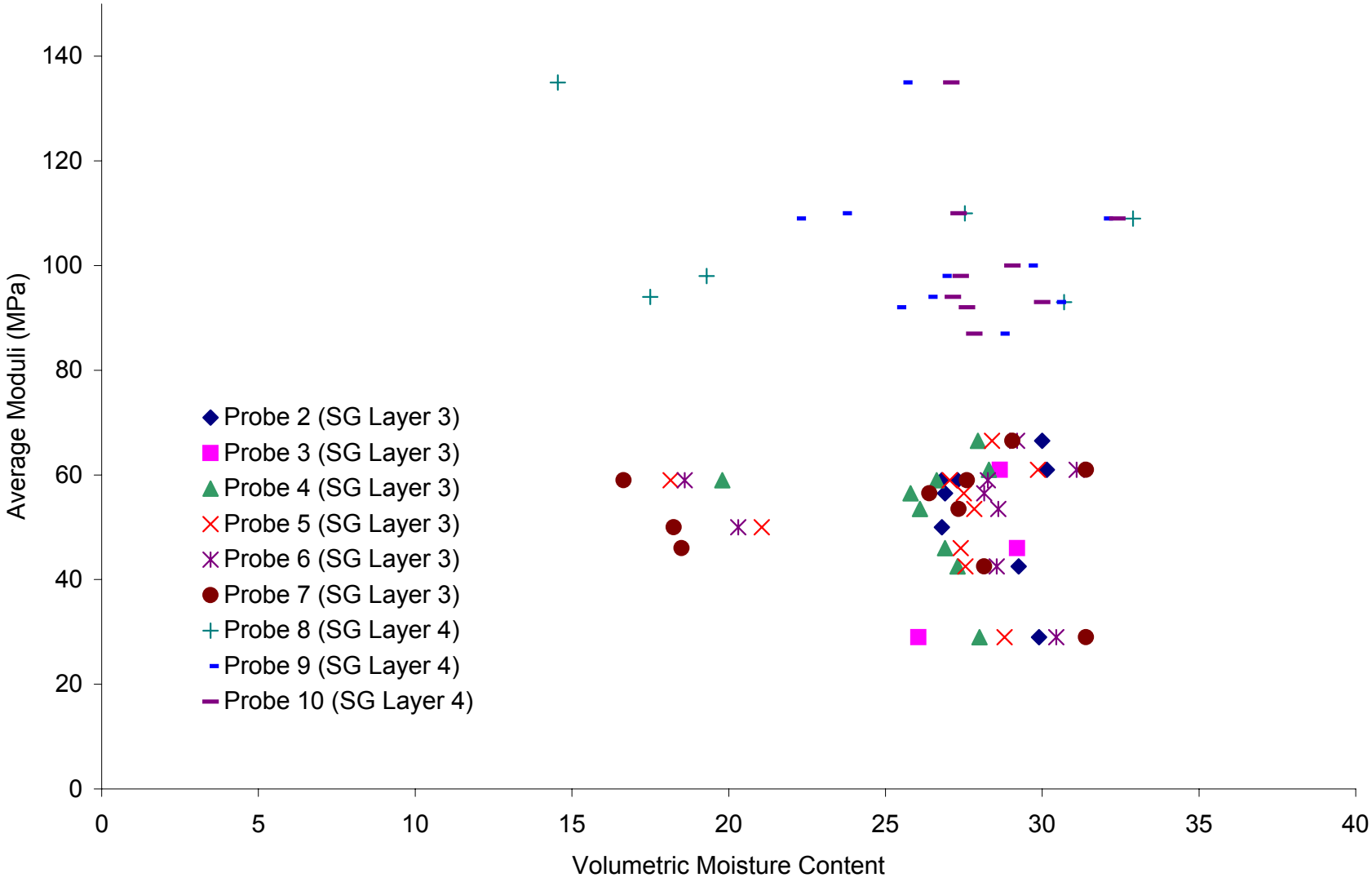

Figure N-11. Variation in Subgrade Modulus as a Function of Moisture Content at Site 27-4040 (Lean Clay with Sand)

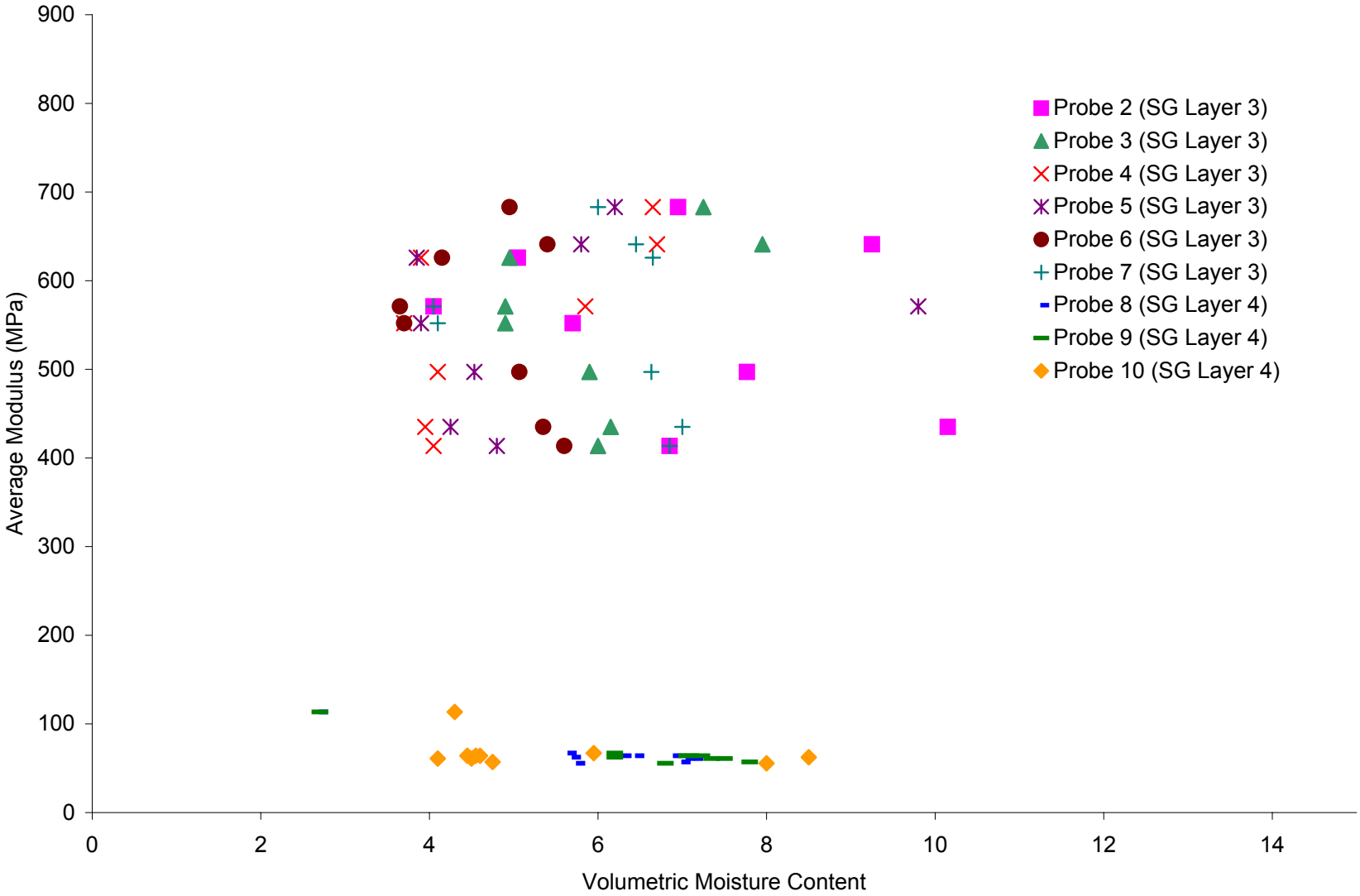

Figure N-12. Variation in Subgrade Modulus as a Function of Moisture Content at Site 27-6251 (Poorly Sand with Silt)

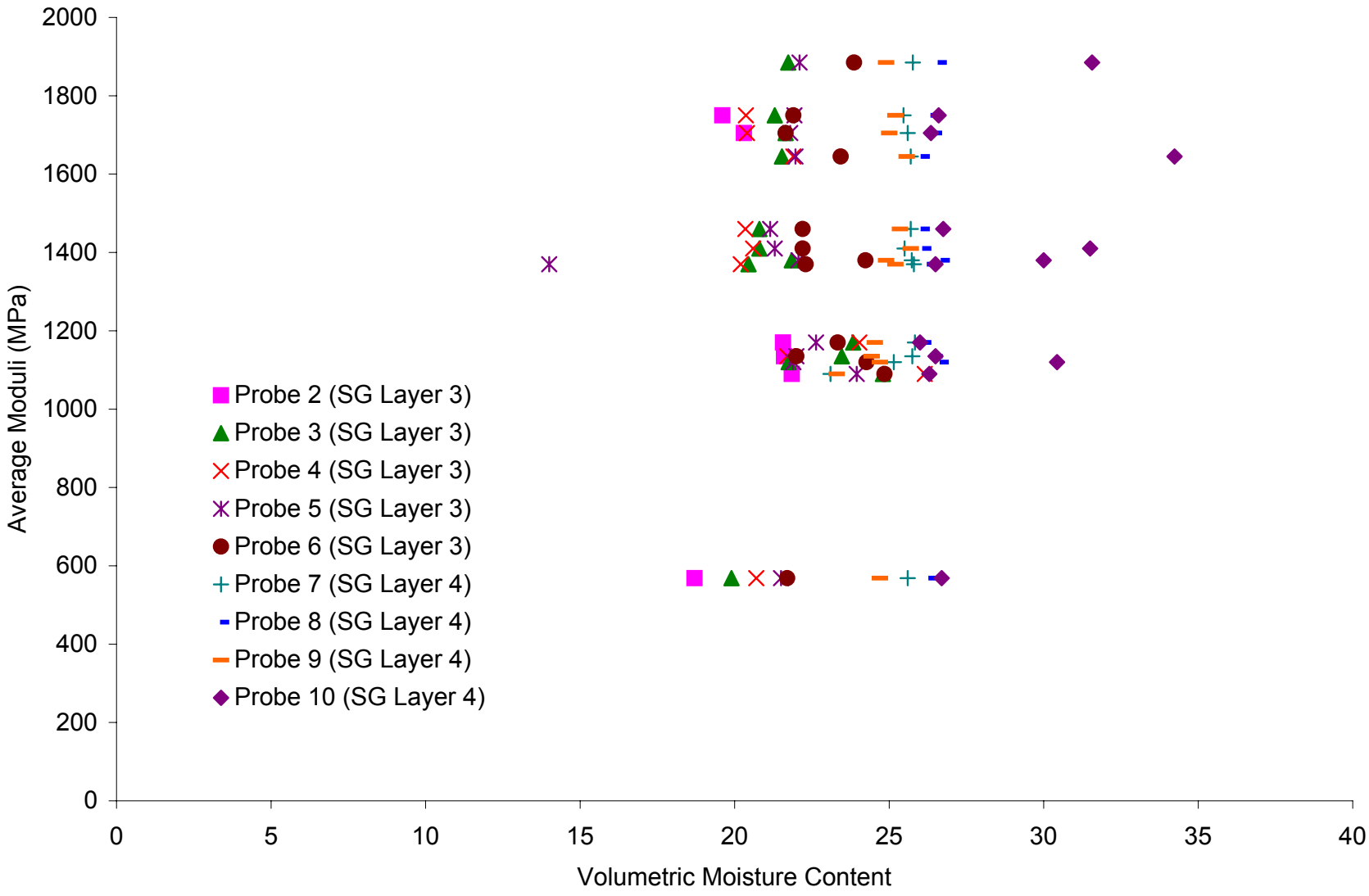

Figure N-13. Variation in Subgrade Modulus as a Function of Moisture Content at Site 28-1016 (Silty Sand)

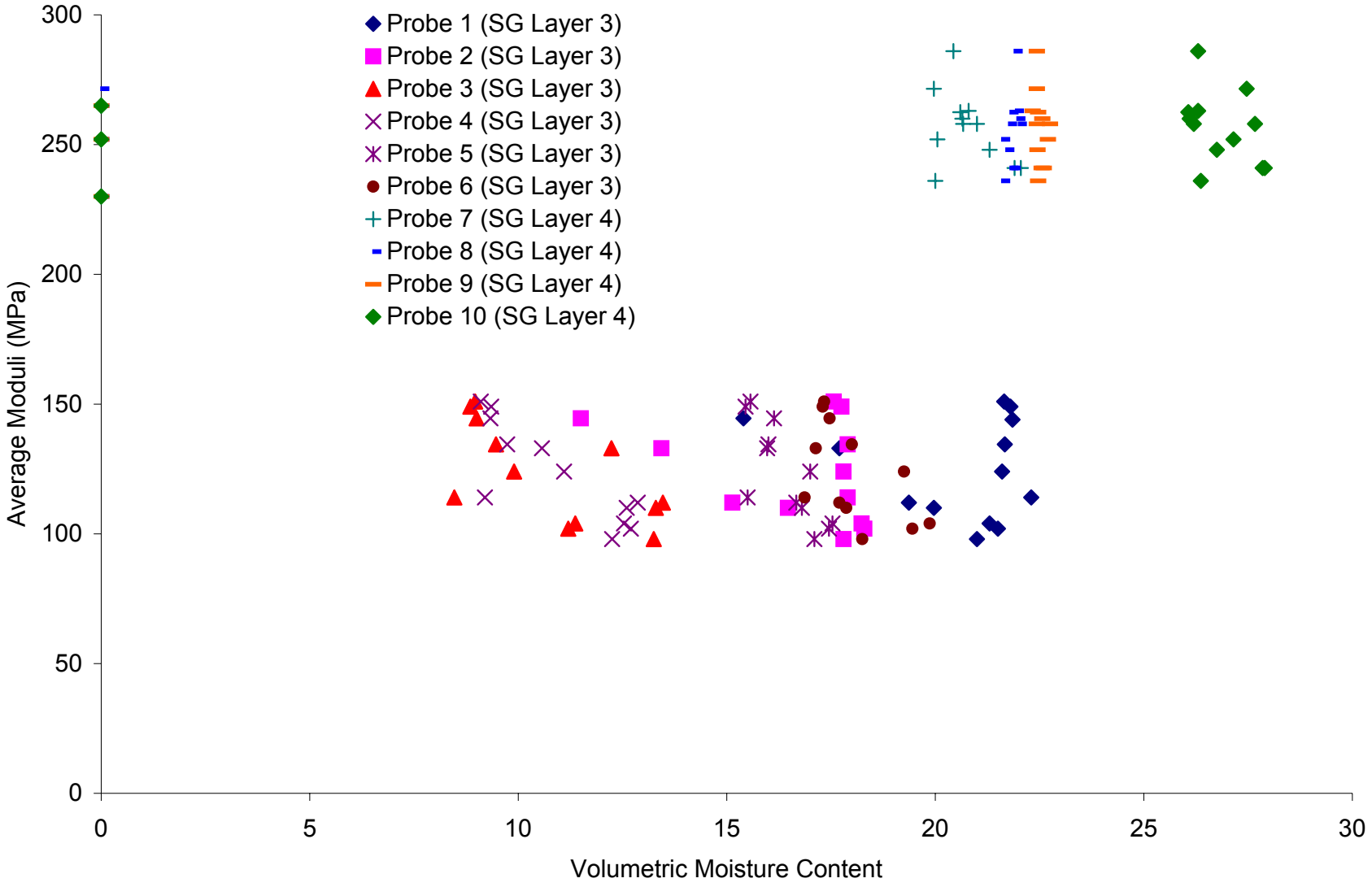

Figure N-14. Variation in Subgard Modulus as a Funciton of Moisture Content at Site 28-1802 (Poorly Graded Sand)

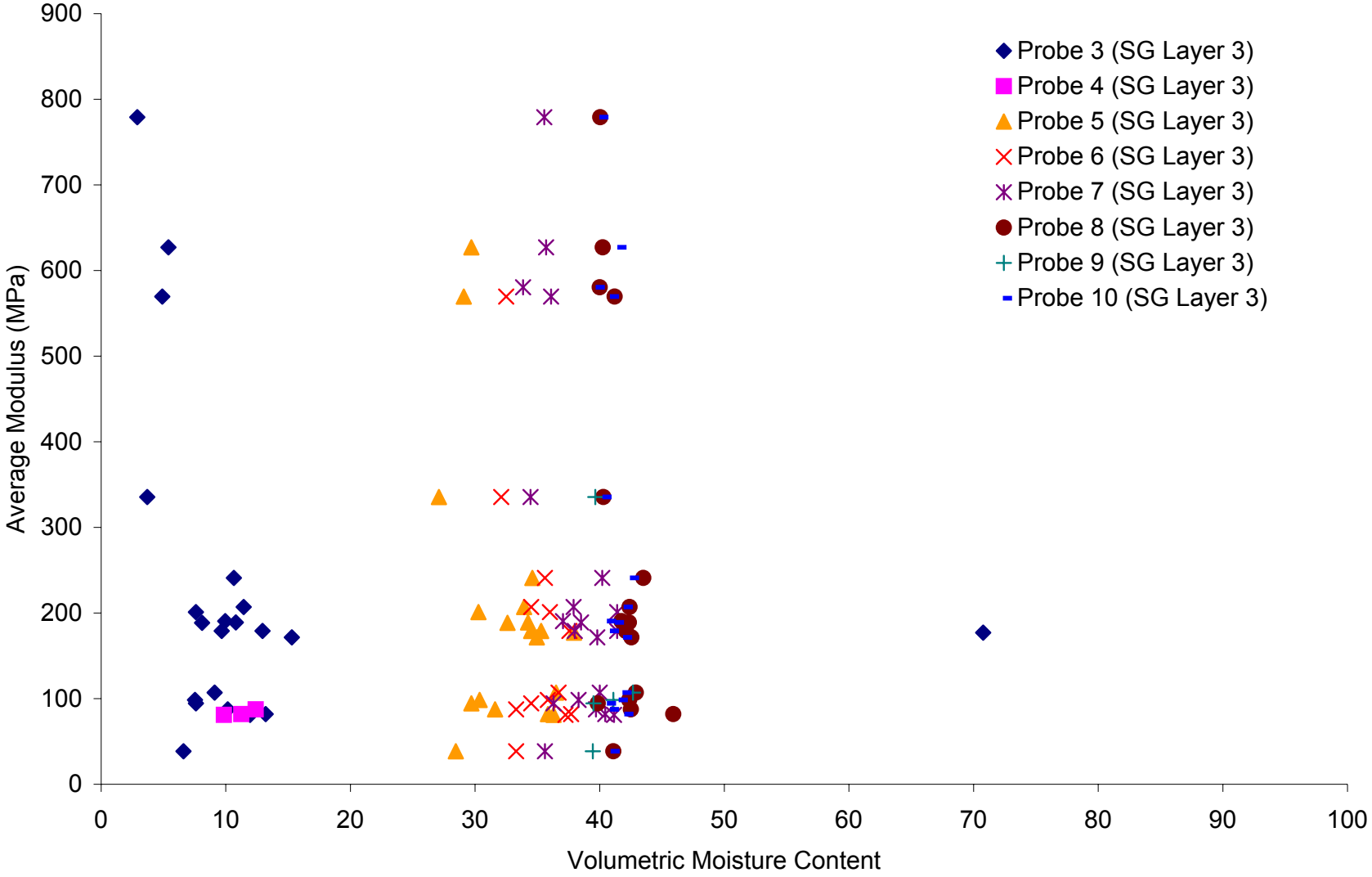

Figure N-15. Variation in Subgrade Modulus as a Function of Moisture Content at Site 30-8129 (Gravely Lean Clay with Sand)

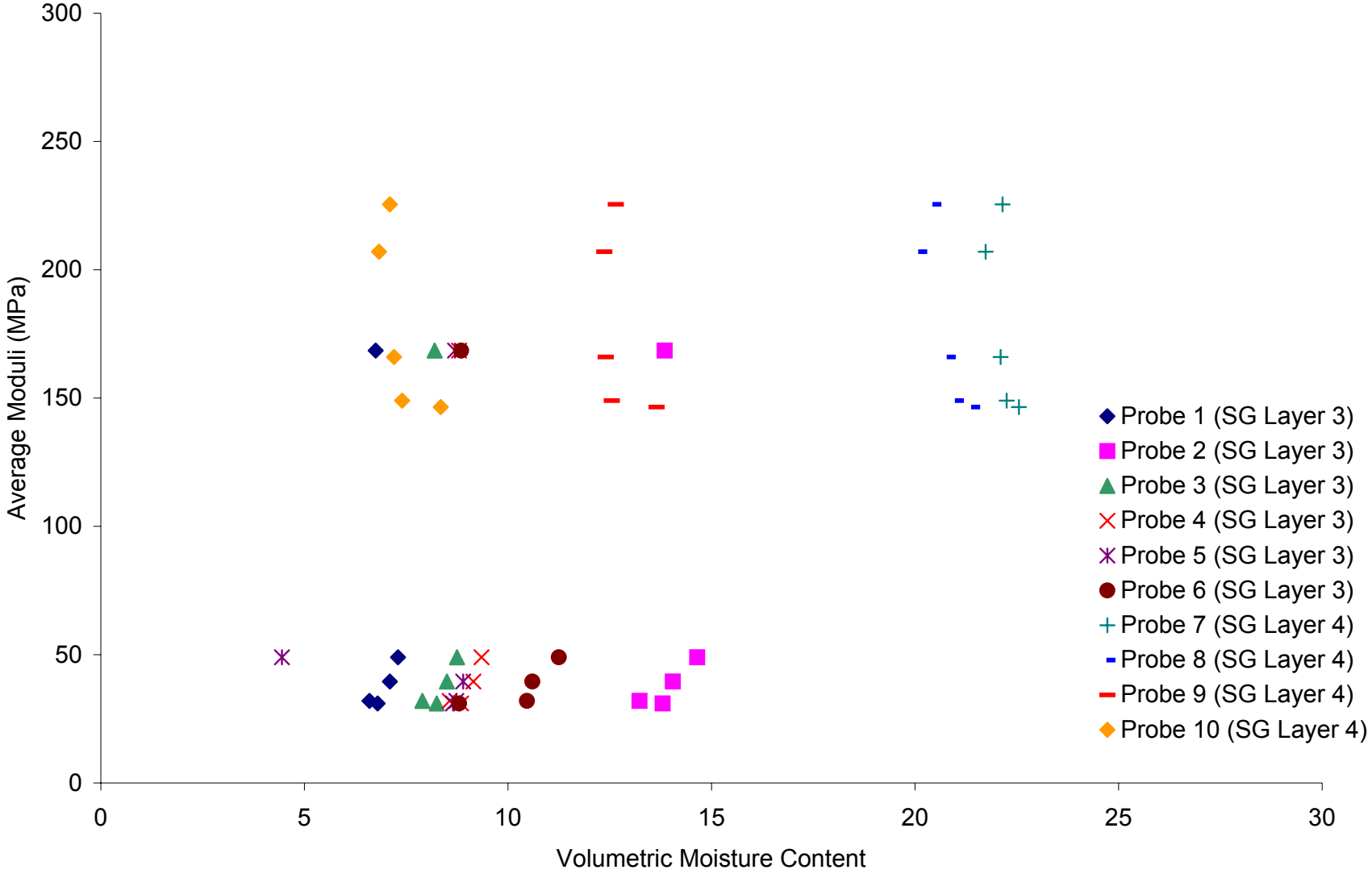

Figure N-16. Variation in Subgrade Modulus as a Function of Moisture Content at Site 31-3018 (Poorly Graded Sand)

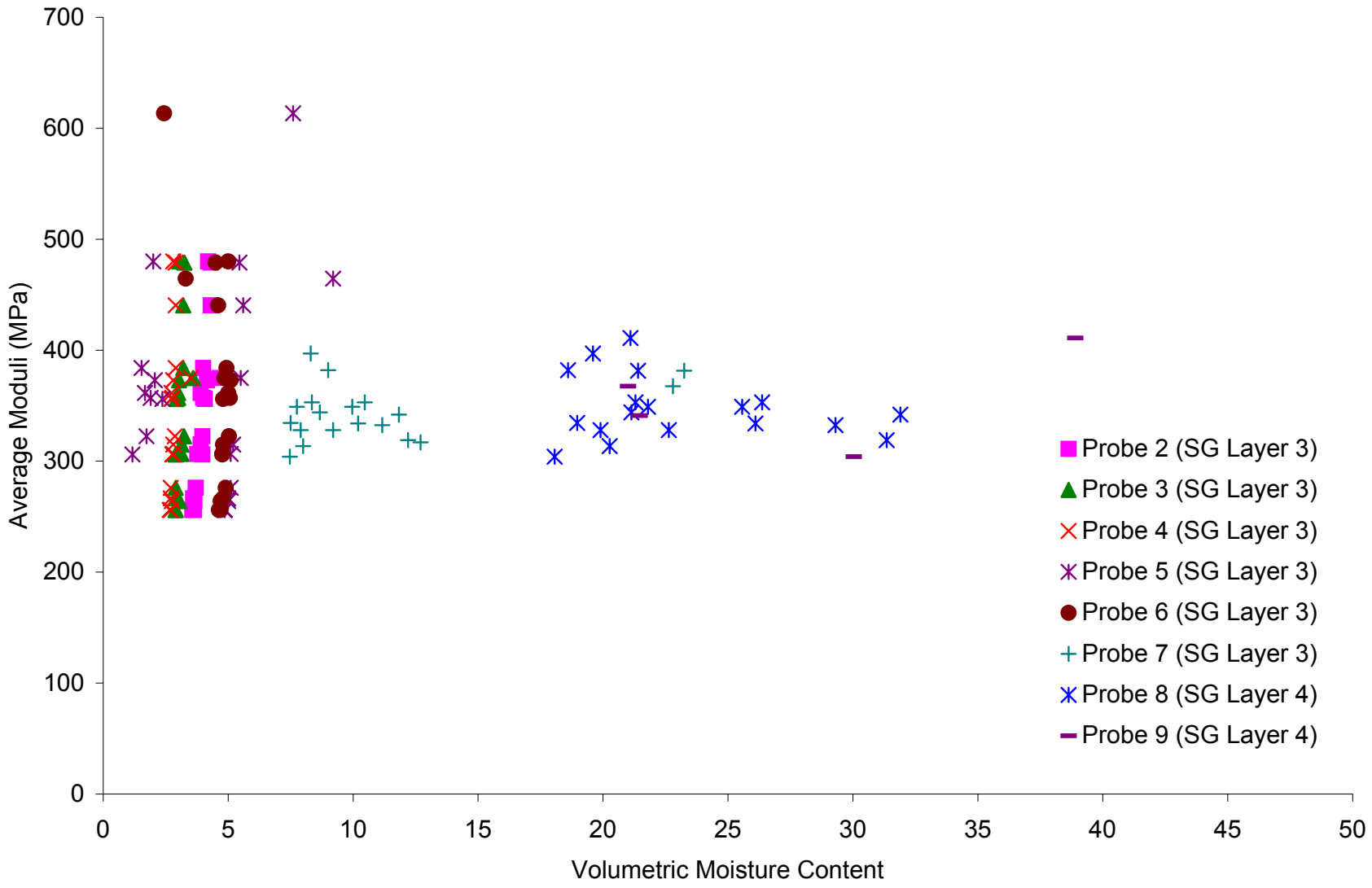

Figure N-17. Variation in Subgrade Modulus as a Function of Moisture Content at Site 35-1112 (Poorly Graded Sand)

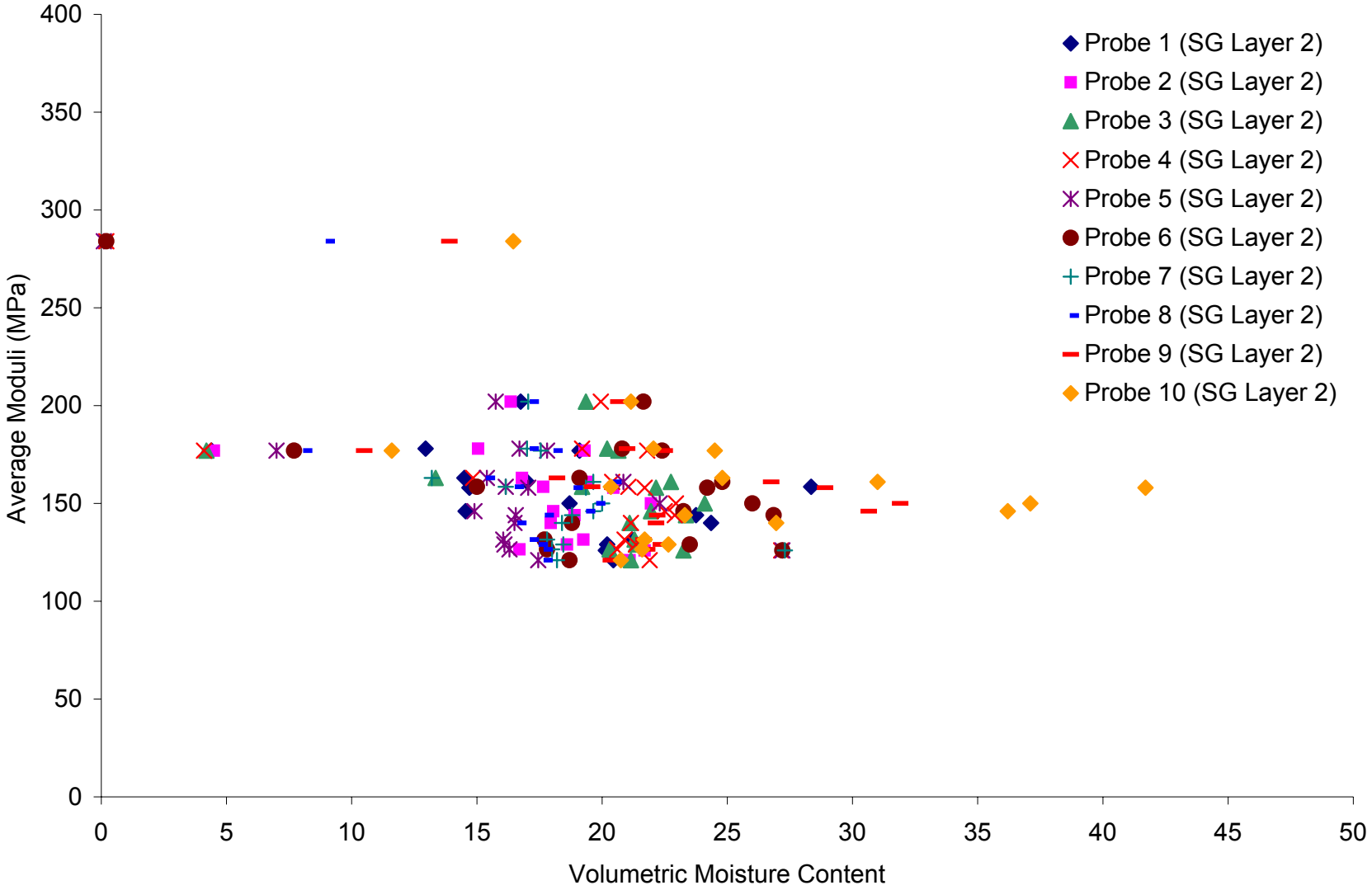

Figure N-18. Variation in Subgrade Modulus as a Function of Moisture Content at Site 36-4018 (Sandy Silt)

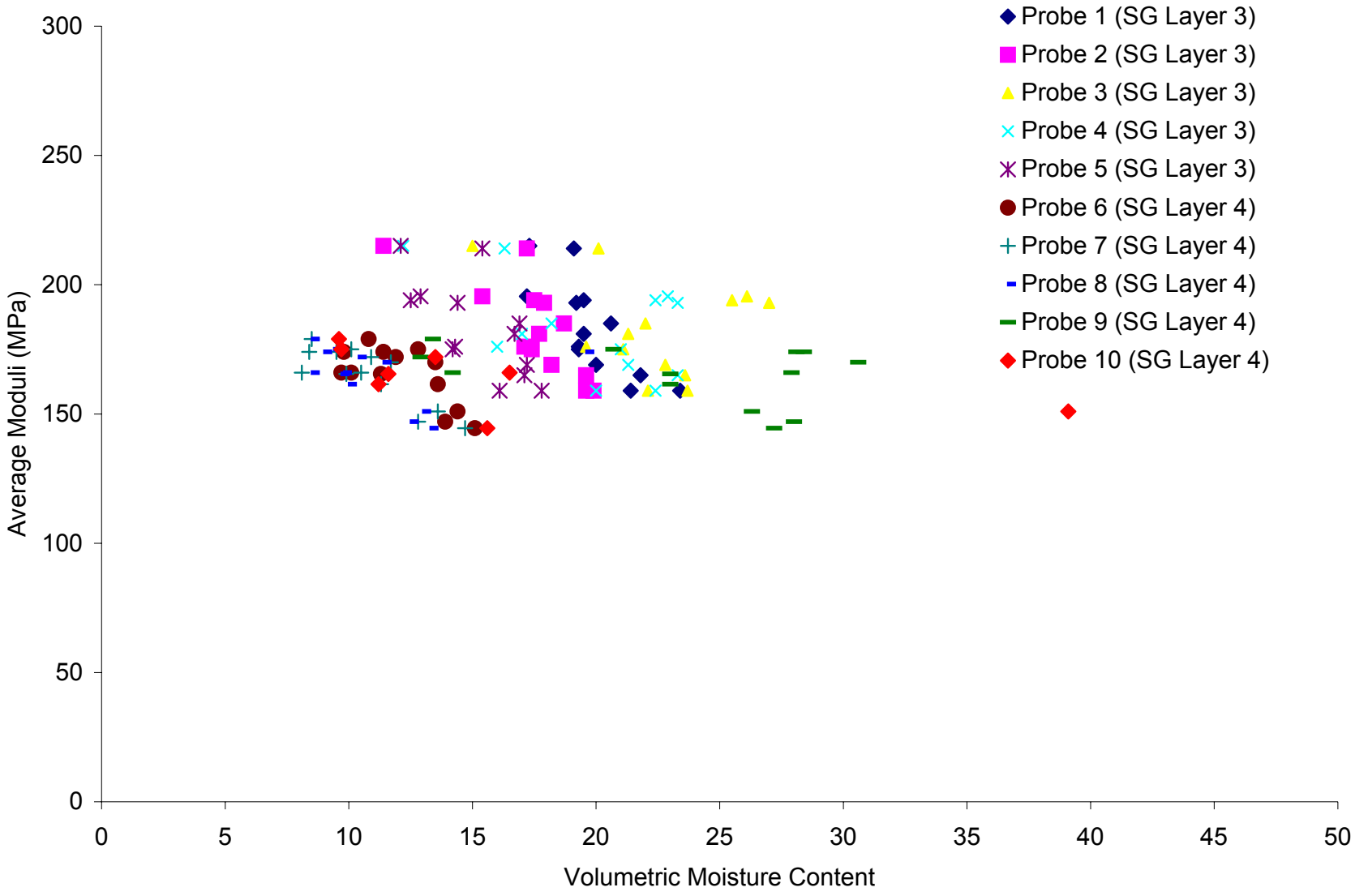

Figure N-19. Variation of Subgrade Modulus as a Function of Moisture Content at Site 37-1028 (Poorly Graded Sand with Silt)

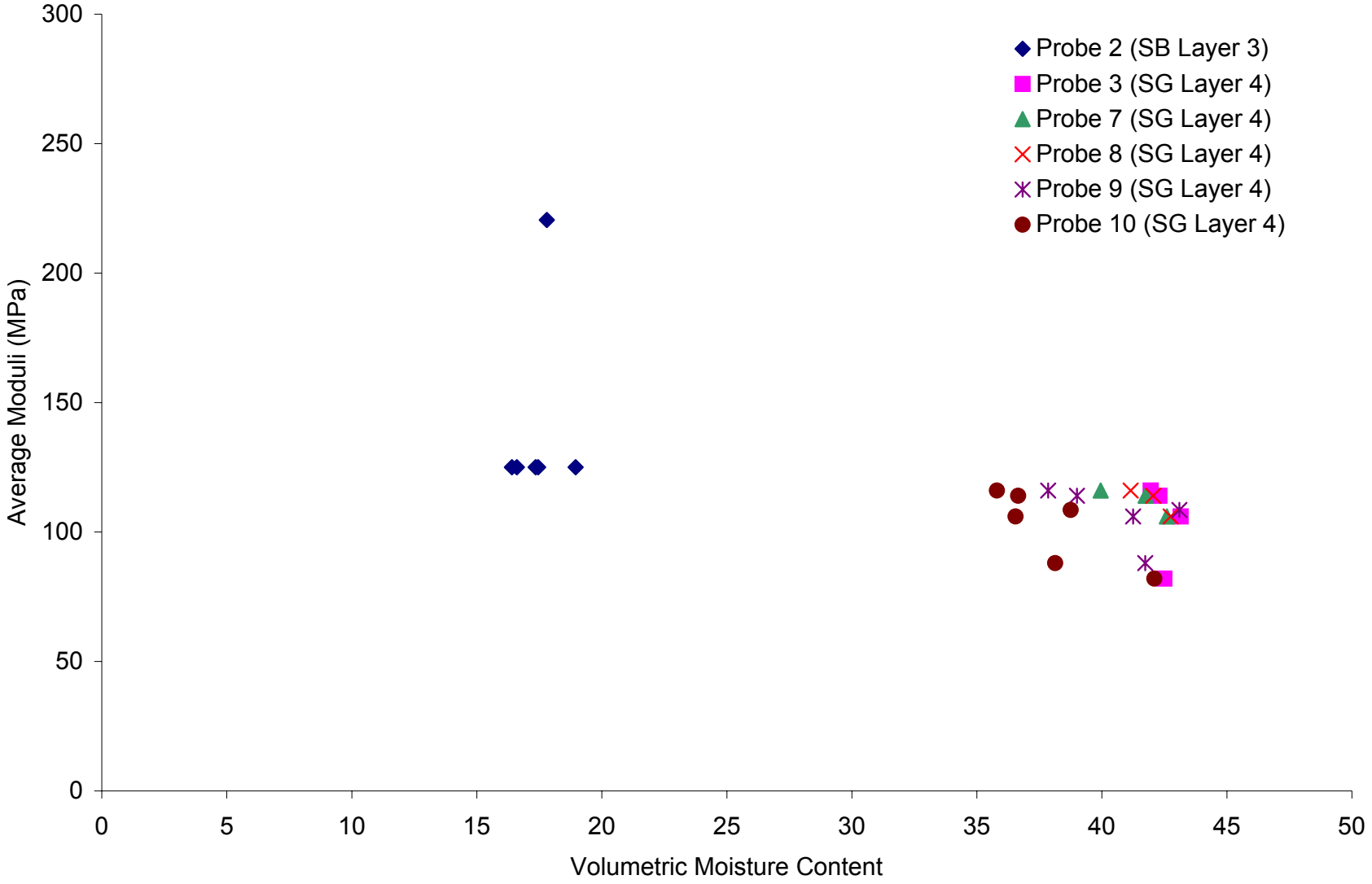

Figure N-20. Variation in Subgrade Modulus as a Function of Moisture Content at Site 46-9187 (Lean Inorganic Clay)

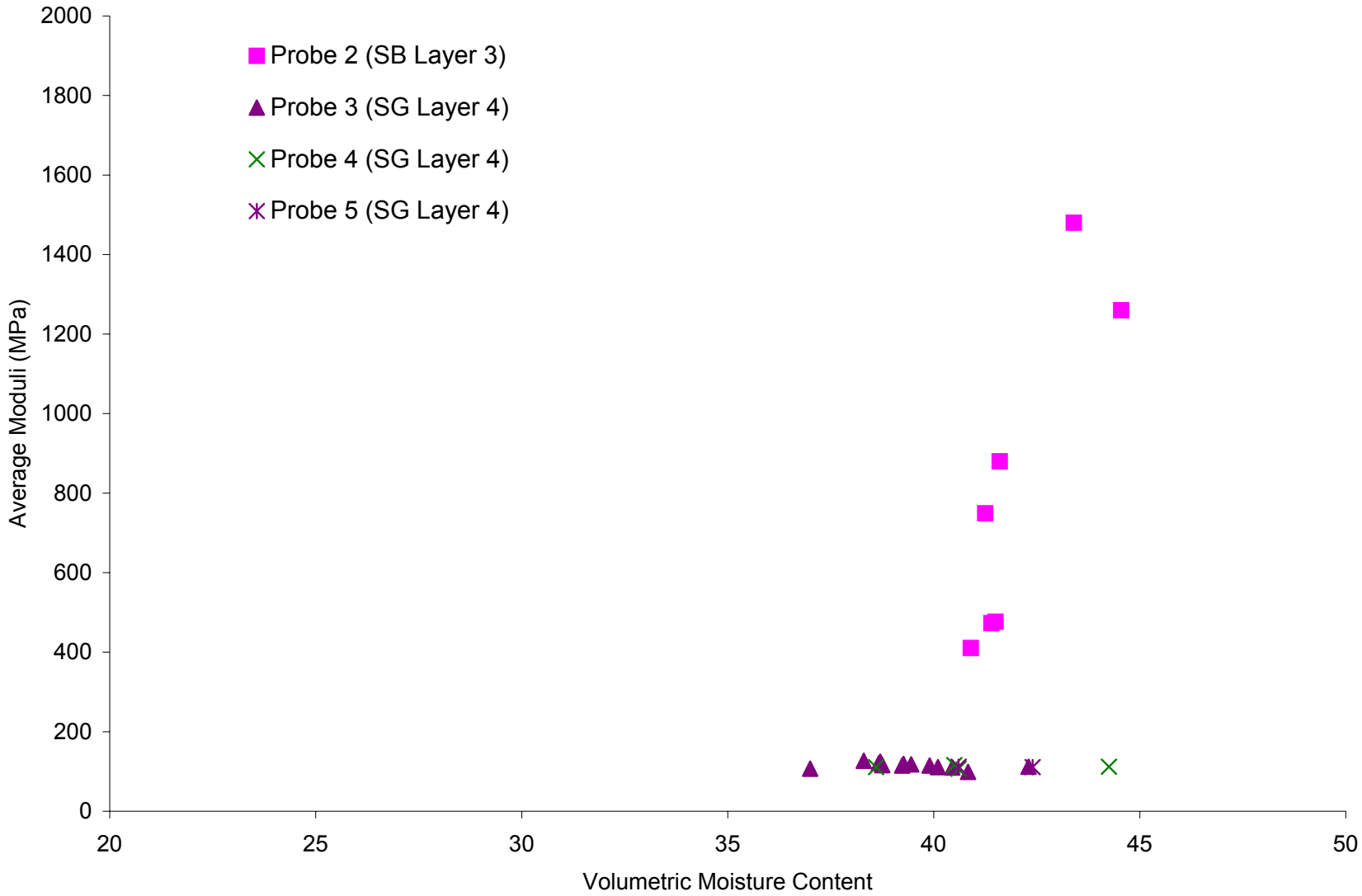

Figure N-21. Variation in Subgrade Modulus as a Function of Moisture Content at Site 48-1060 (Silty Clay)

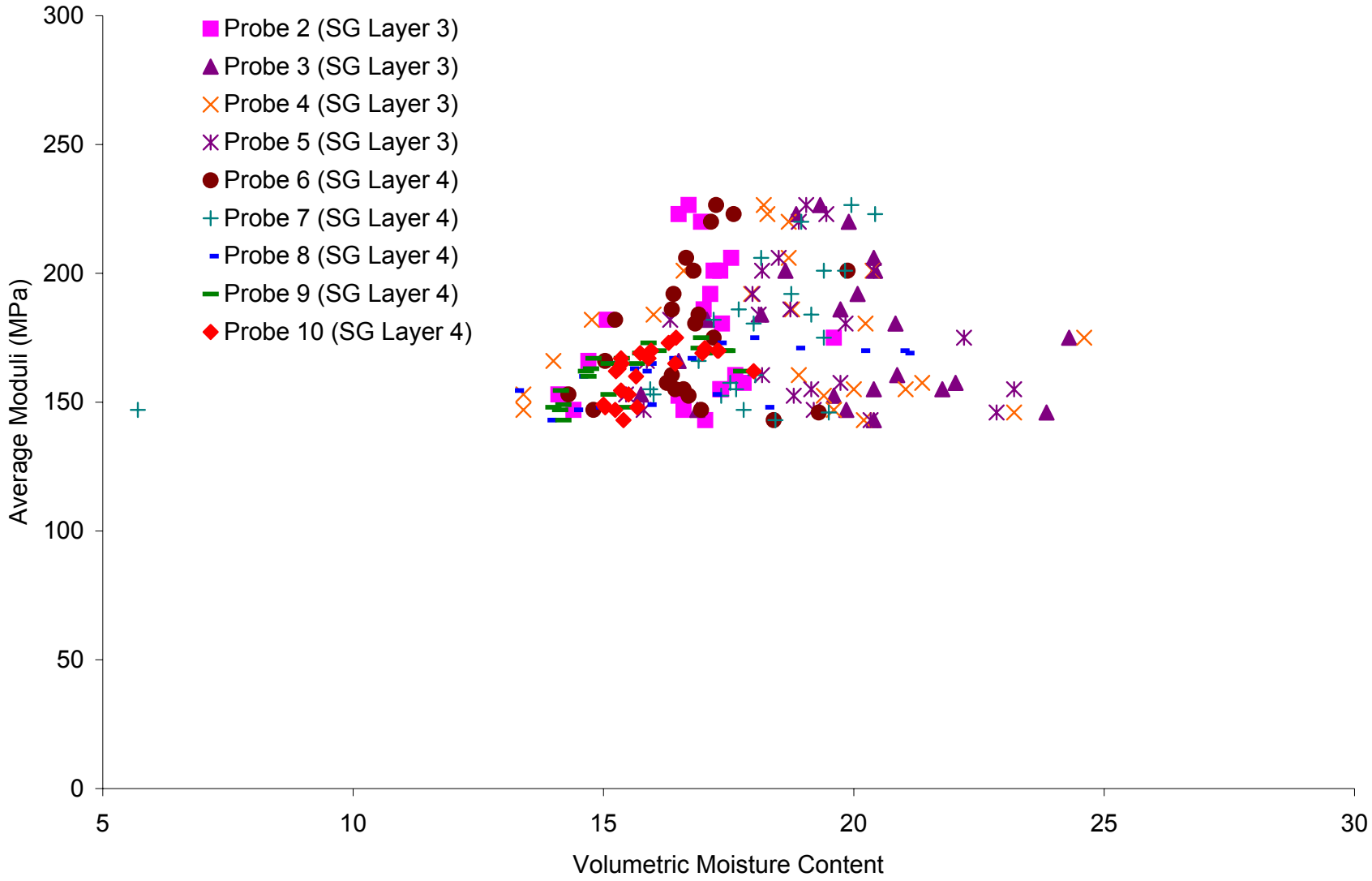

Figure N-22. Variation in Subgrade Modulus as a Function of Moisture Content at Site 48-1077 (Sandy Silt)

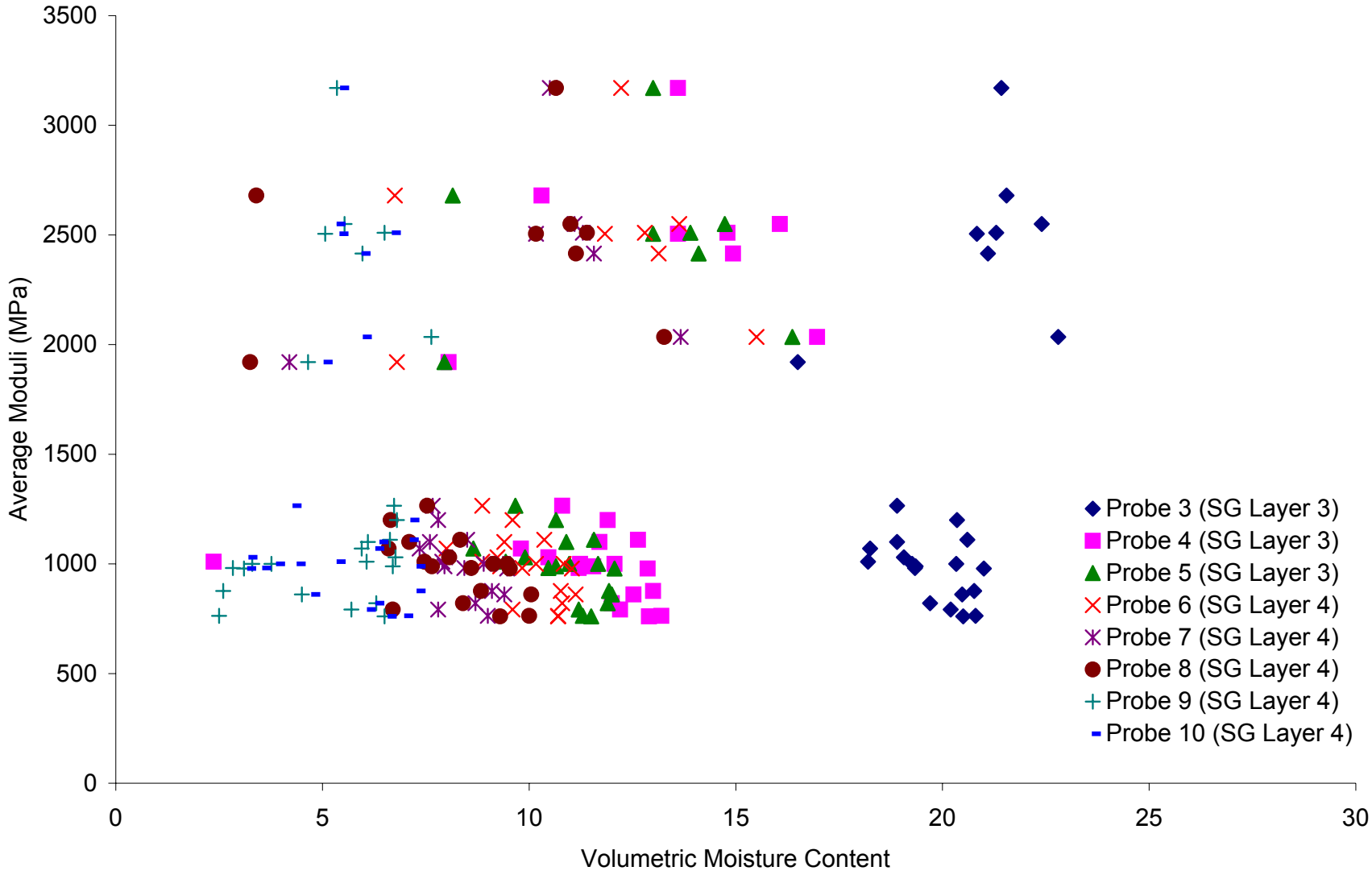

Figure N-23. Variation in Subgrade Modulus as a Function of Moisture Content at Site 48-1122 (Clayey Sand)

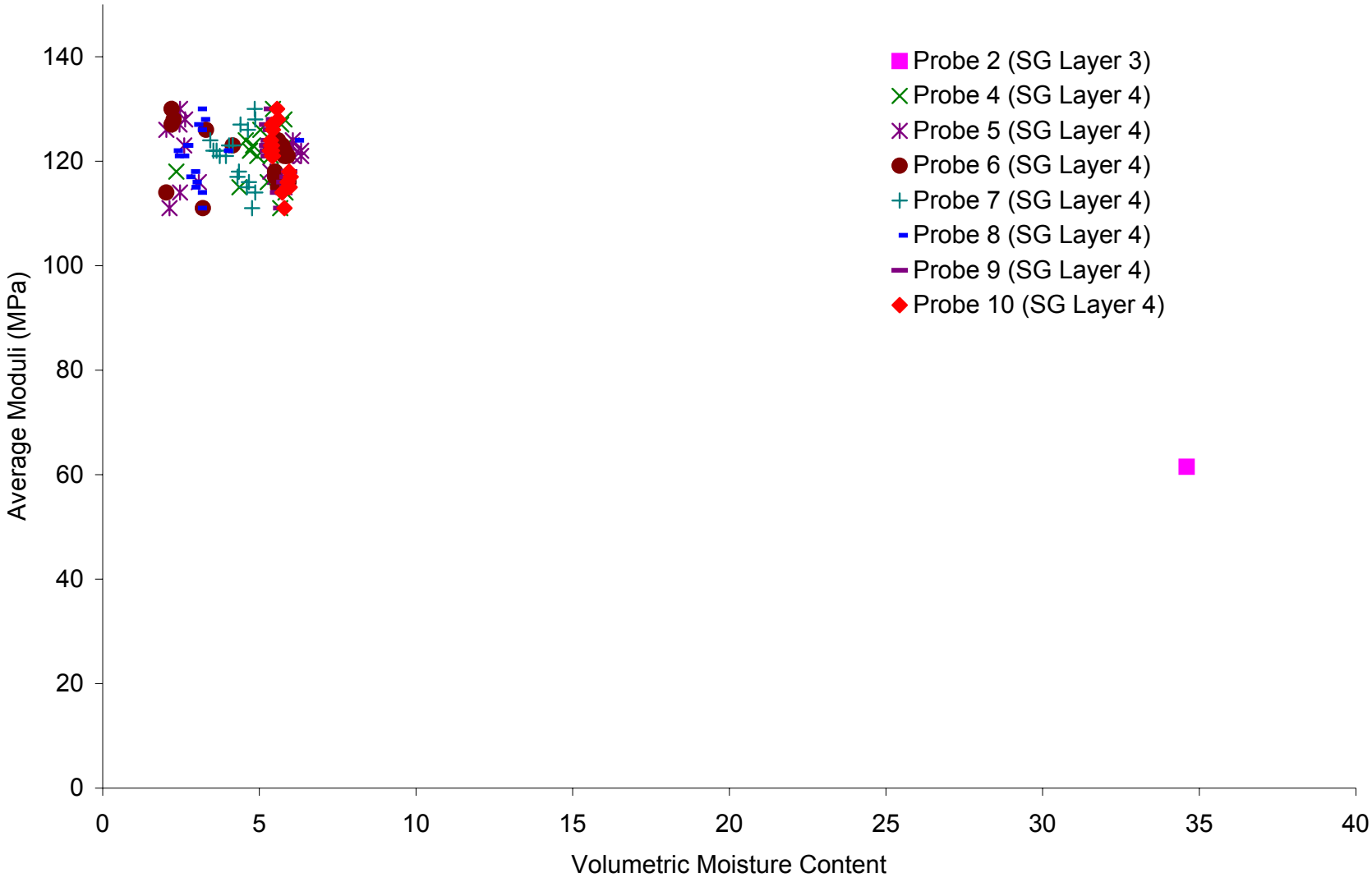

Figure N-24. Variation in Subgrade Modulus as a Function of Moisture Content at Site 48-3739 (Poorly Graded Sand)

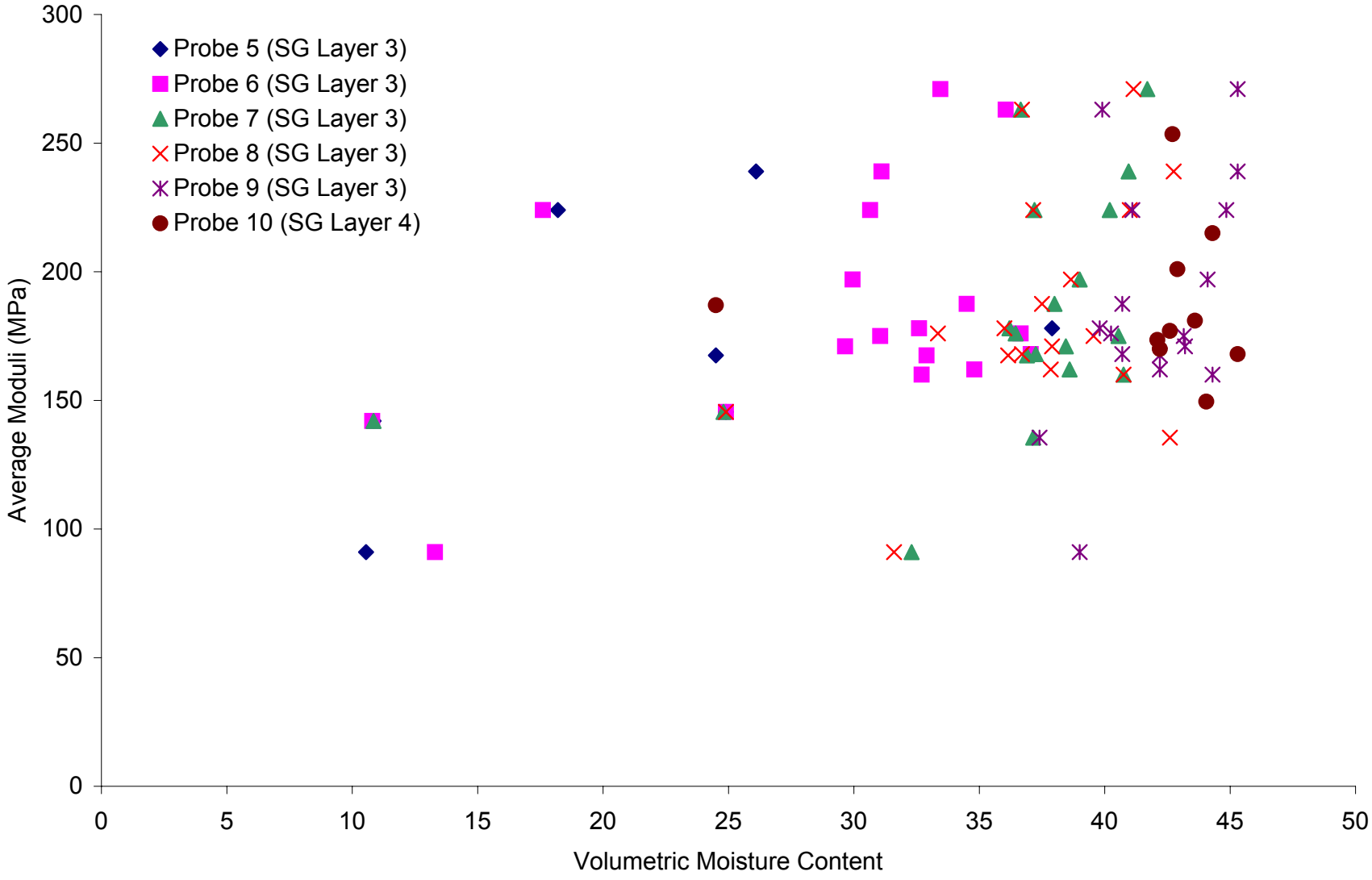

Figure N-25. Variation in Subgrade Modulus as a Function of Moisture Content at Site 50-1002 (Poorly Graded Gravel with Silt and Sand)

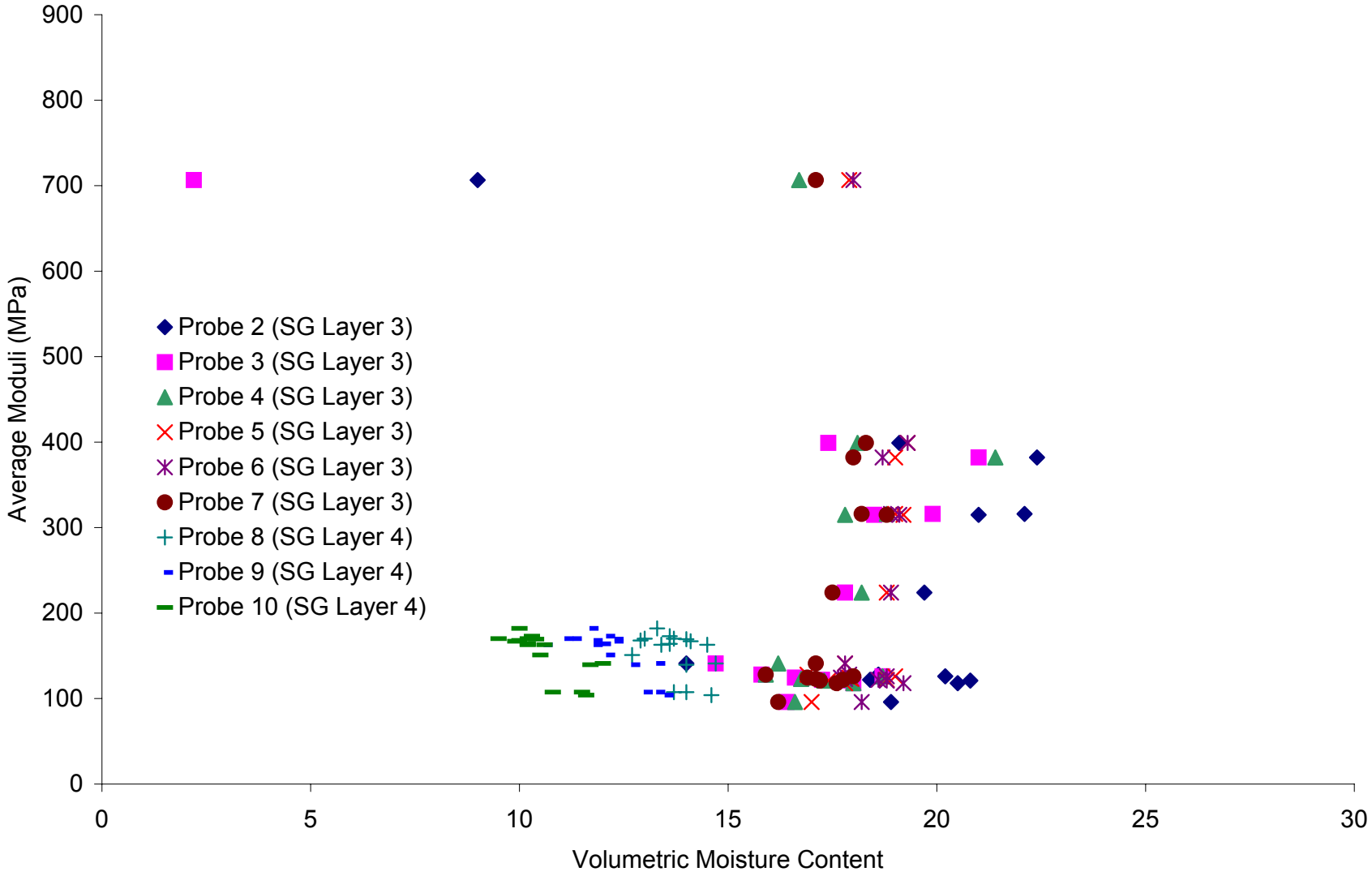

Figure N-26. Variation in Subgrade Modulus as a Function of Moisture Content at Site 56-1007 (Silty Sand with Gravel)

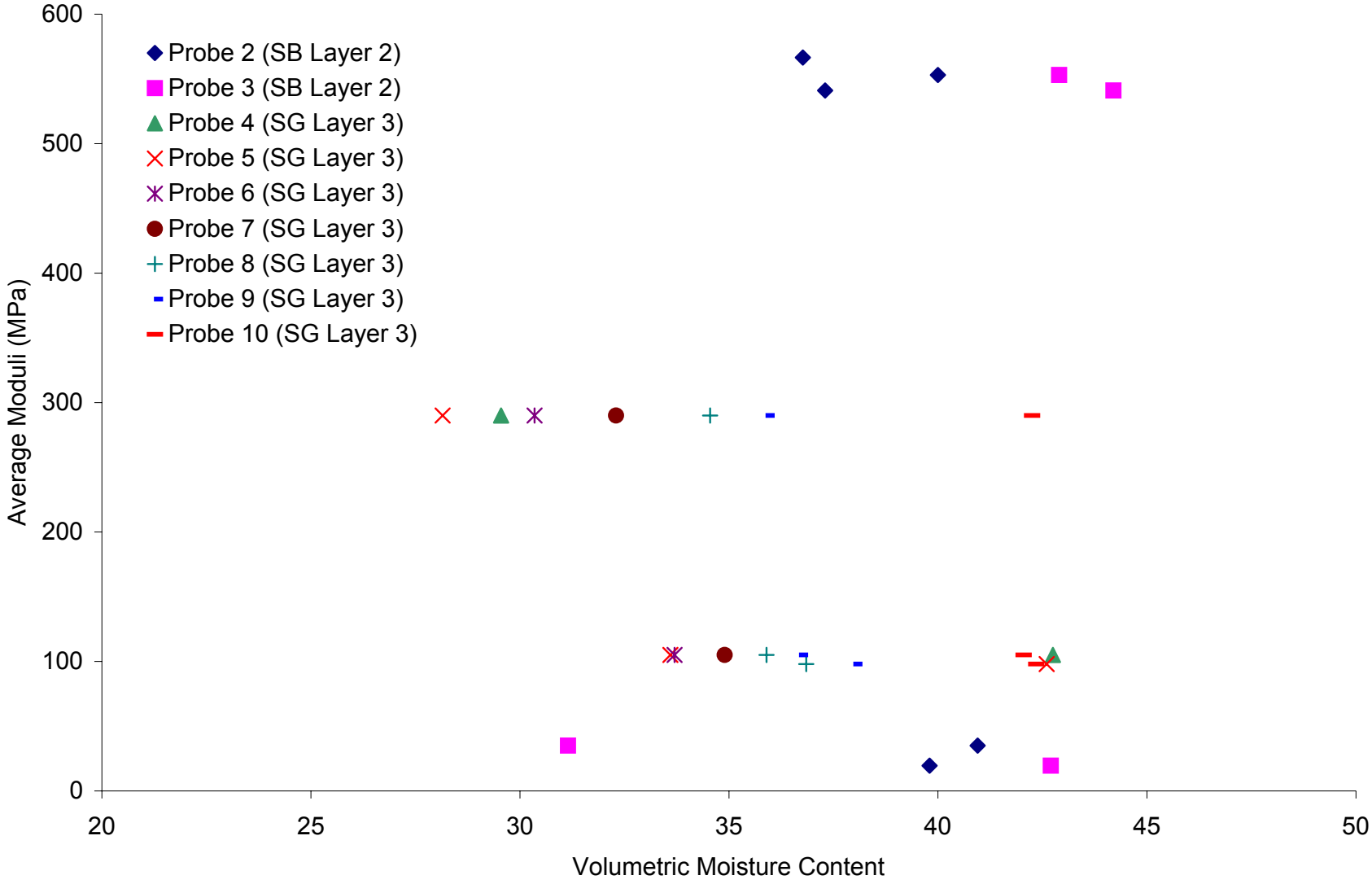

Figure N-27. Variation in Subgrade Modulus as a Function of Moisture Content at Site 83-3802 (Silty Sand)

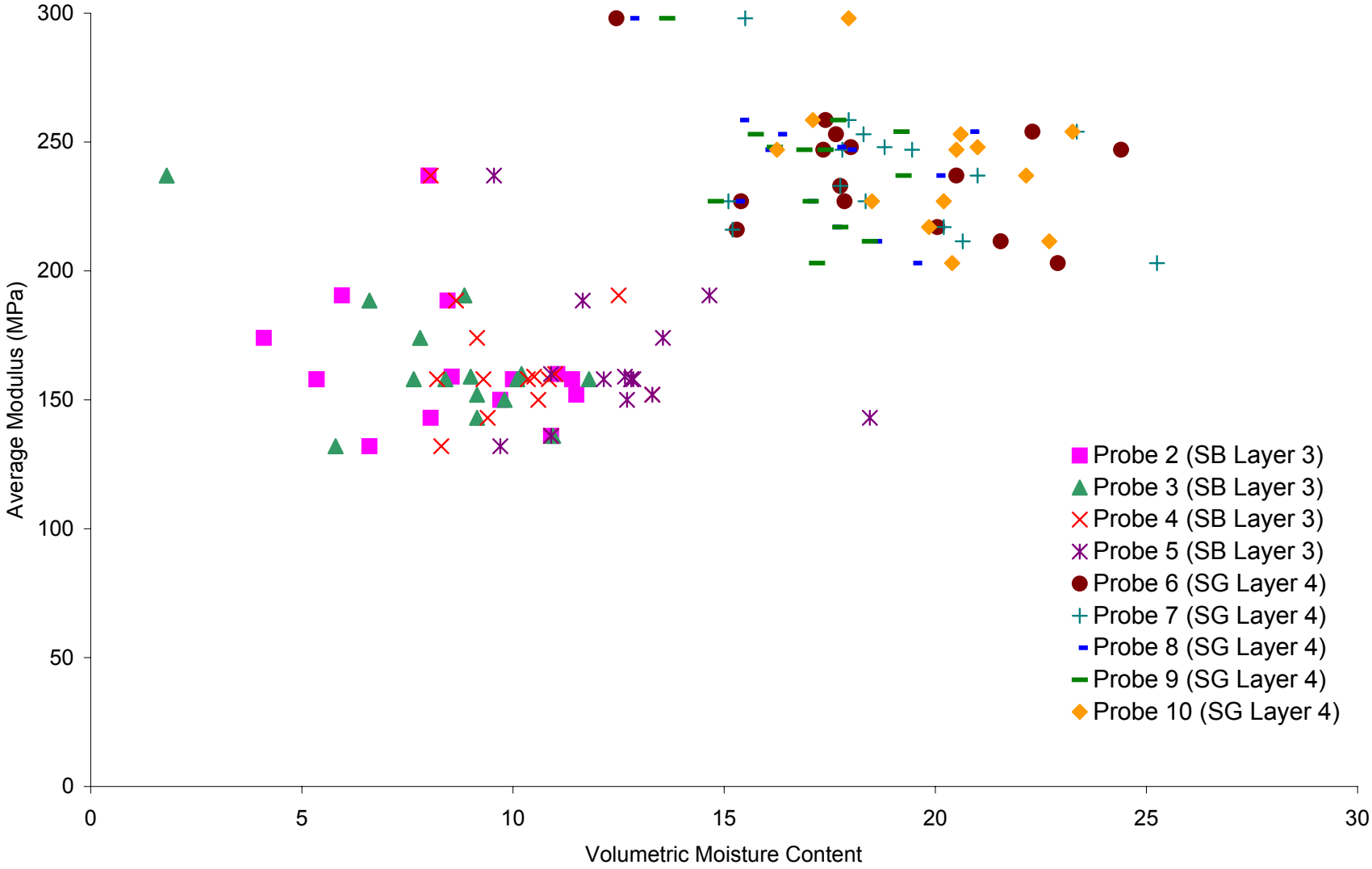

Figure N-28. Variation in Subgrade Modulus as a Function of Moisture Content at Site 87-1622 (Sandy Silt)

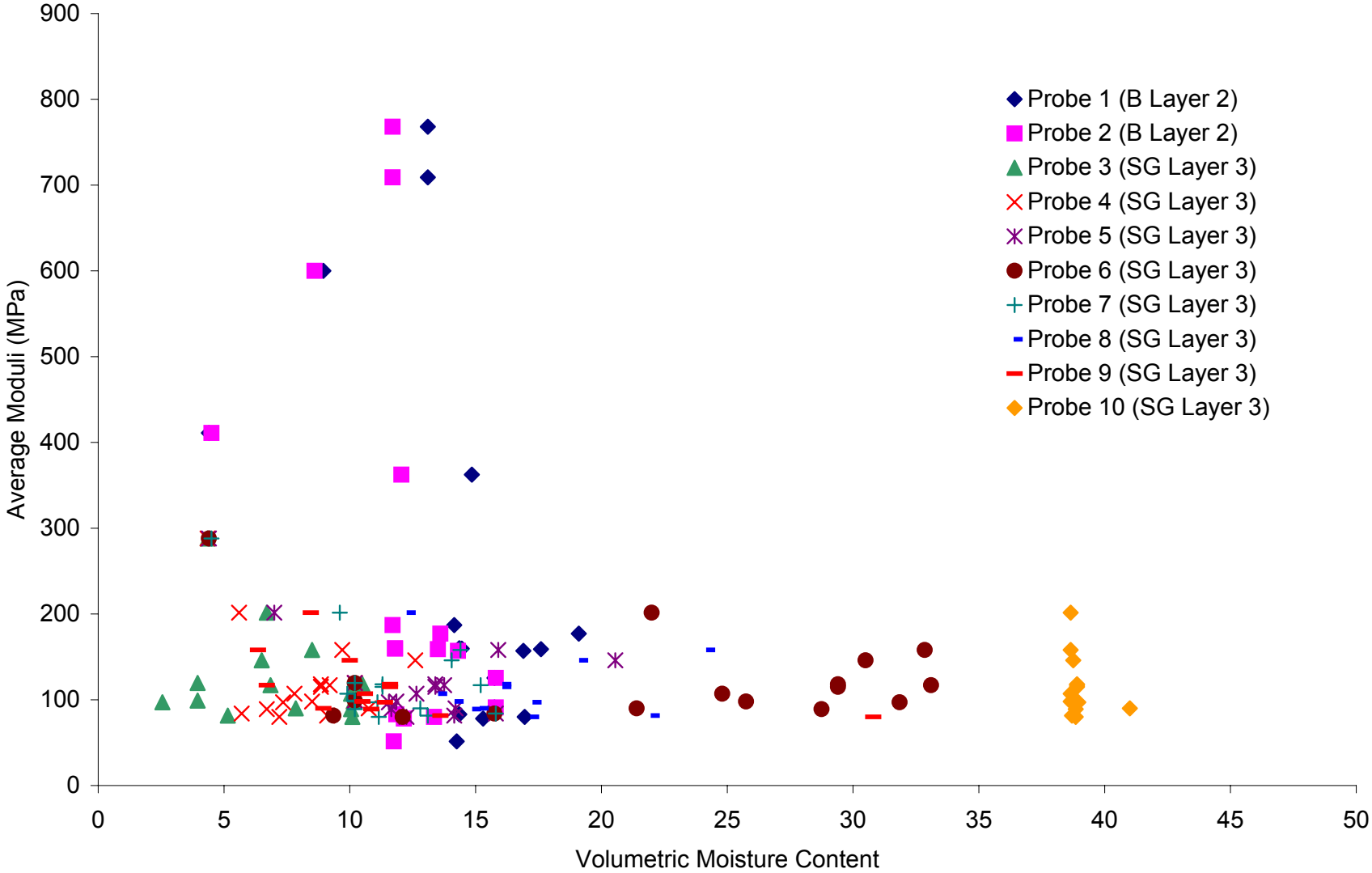

Figure N-29. Variation in Subgrade Modulus as a Function of Moisture Content at Site 89-3015 (Poorly Graded Sand)

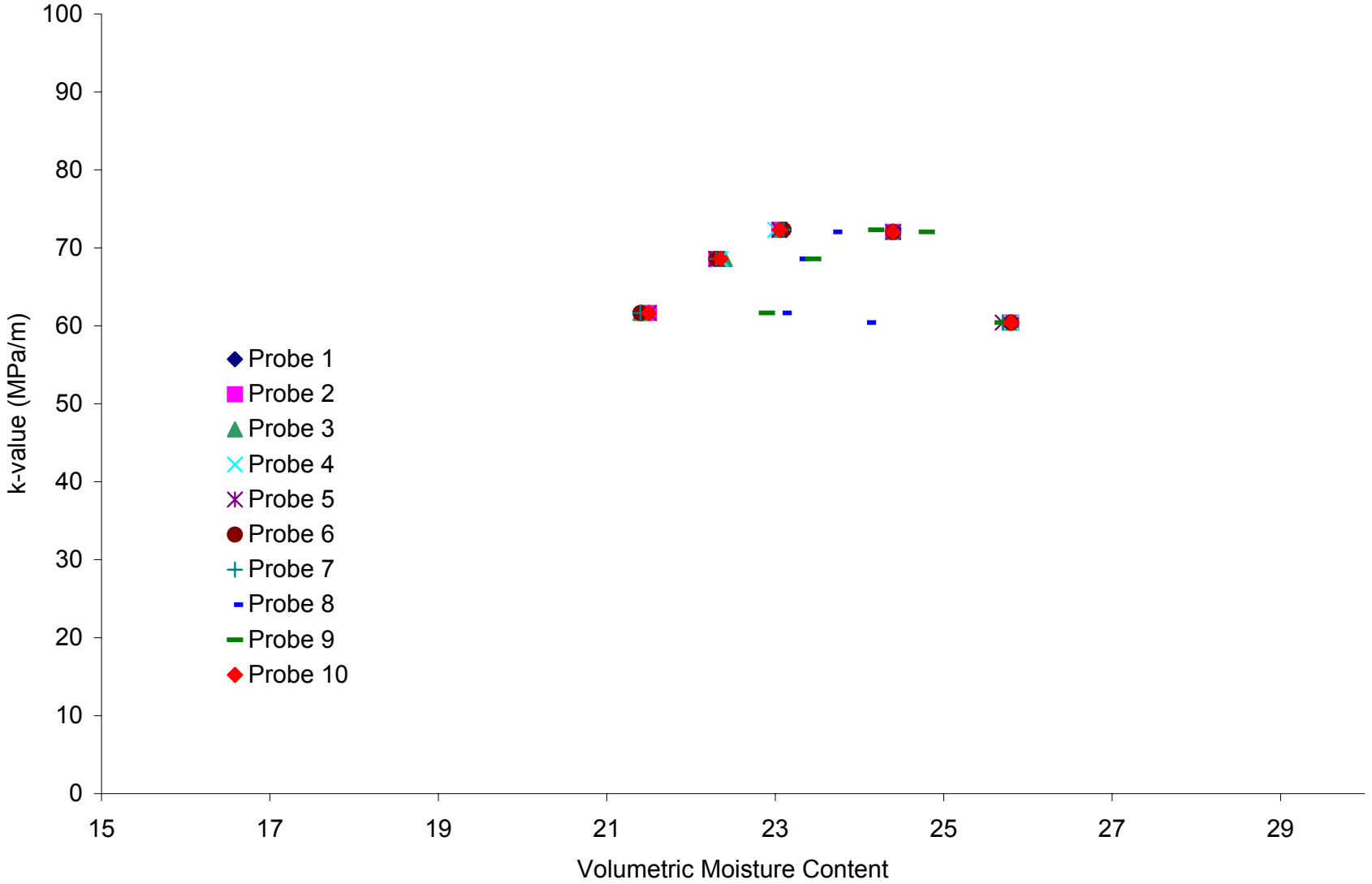

Figure N-30. Variation in Subgrade k-value as a Function of Moisture Content at Site 04-0215 (Silty Sand with Gravel)

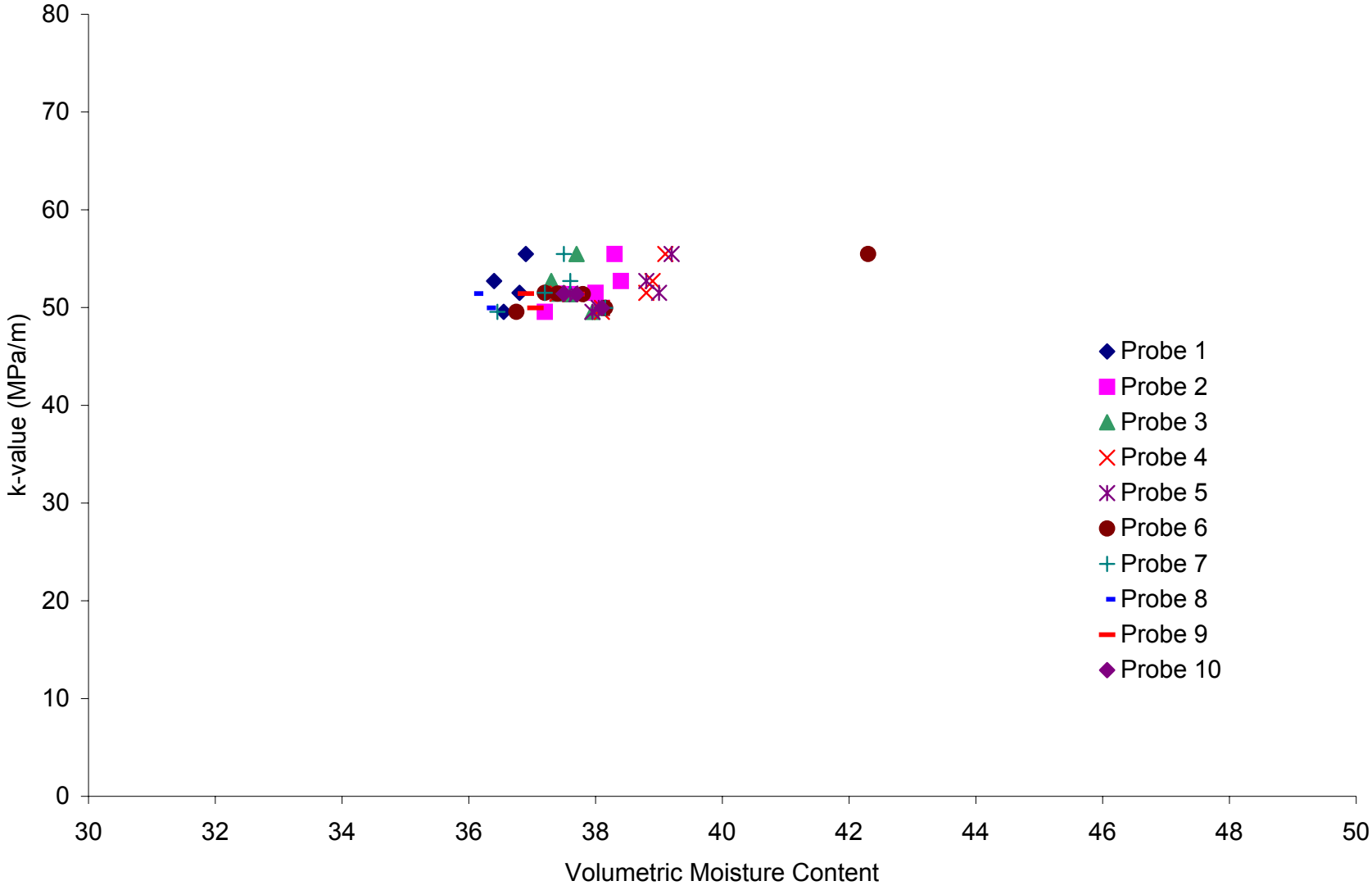

Figure N-31. Variationin Subgrade k-value as a Function of Moisture Content at Site 06-3042 (Sandy Lean Clay)

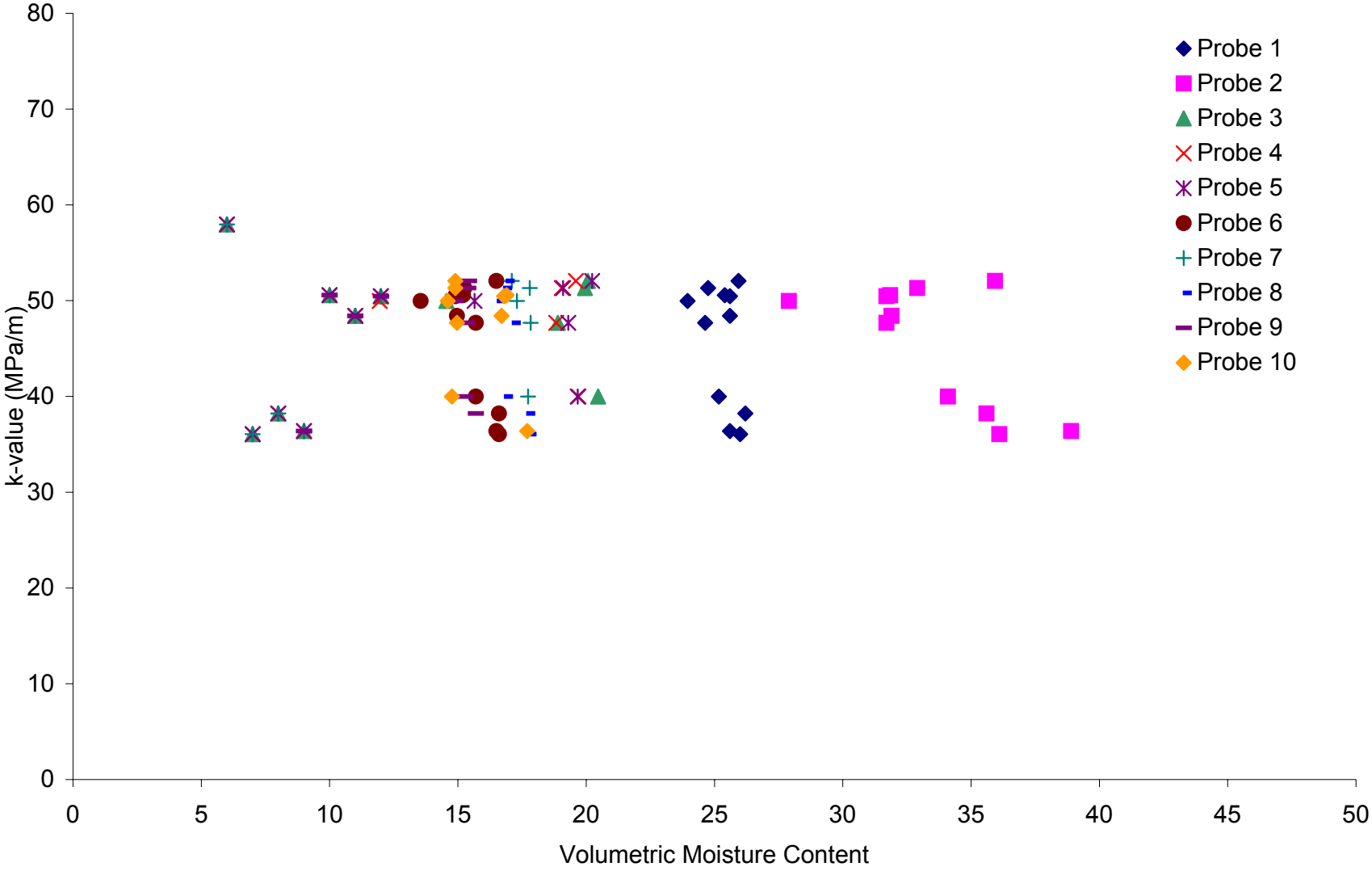

Figure N-32. Variation in Subgrade k-value as a Function of Moisture Content at Site 13-3019 (Sandy Lean Clay)

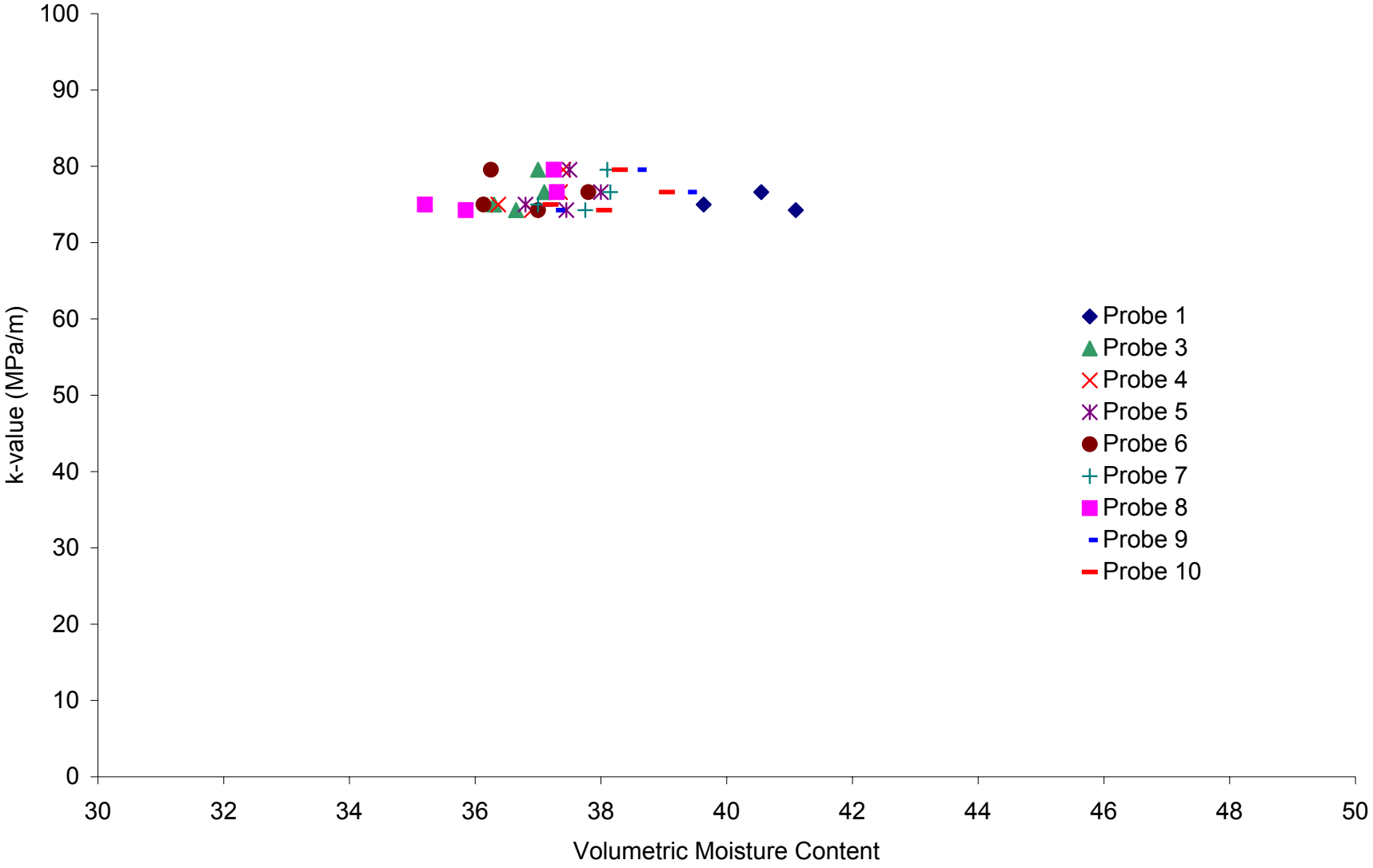

Figure N-33. Variation in Subgrade k-value as a Function of Moisture Content at Site 20-4054 (Lean Inorganic Clay)

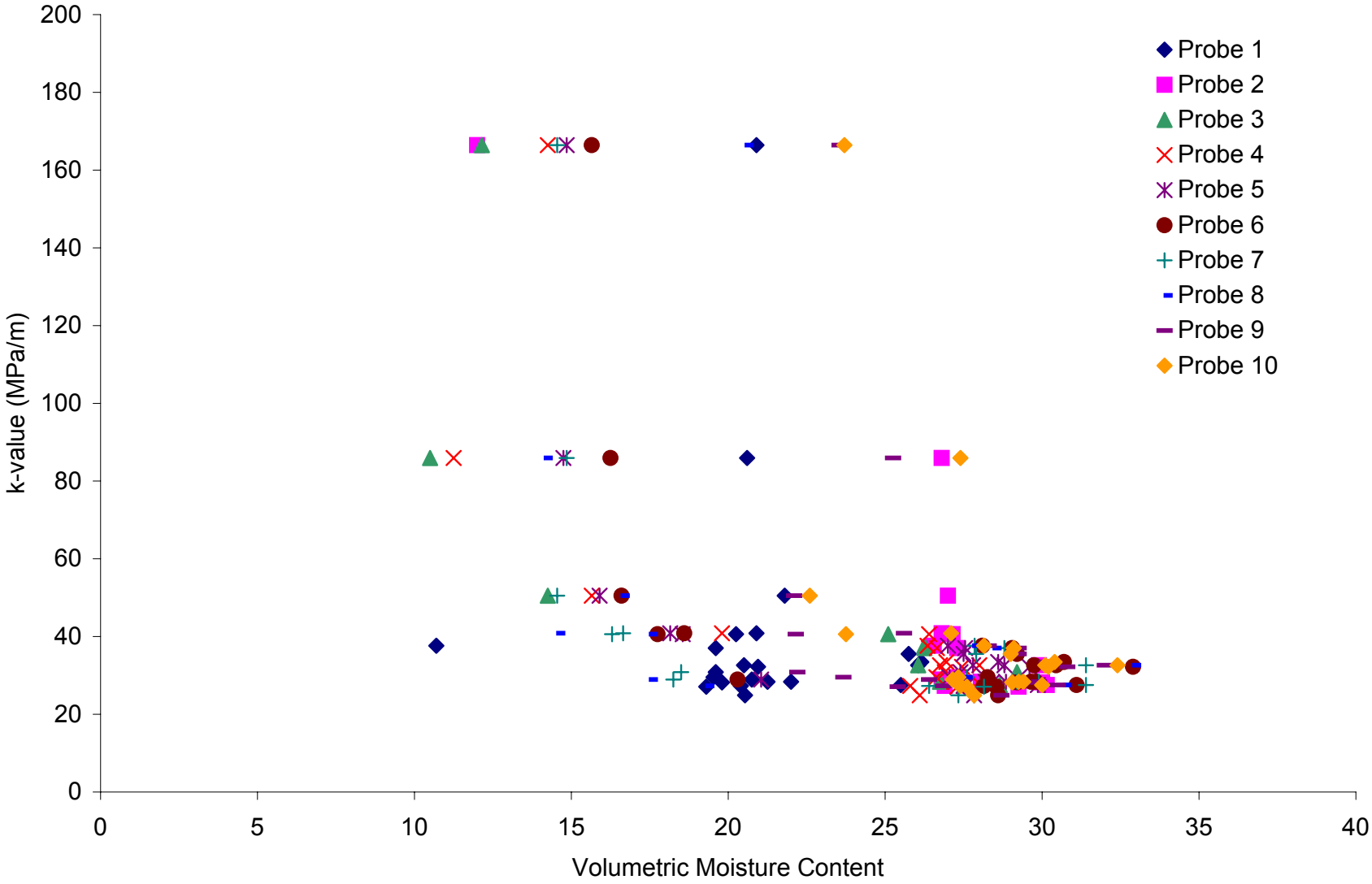

Figure N-34. Variation in Subgrade k-value as a Function of Moisture Content at Site 27-4040 (Lean Clay with Sand)

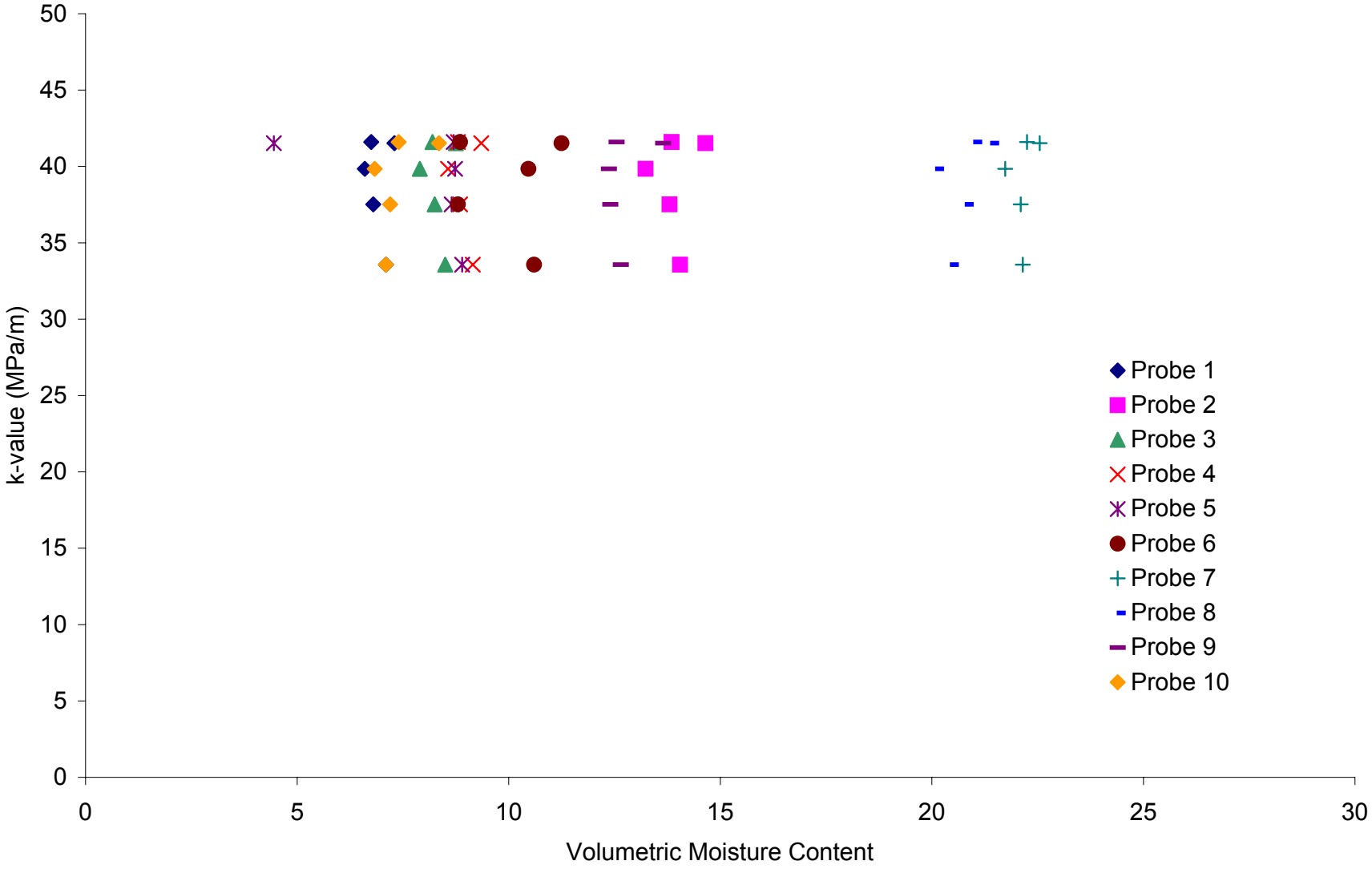

Figure N-35. Variation in Subgrade k-value as a Function of Moisture Content at Site 31-3018 (Poorly Graded Sand)

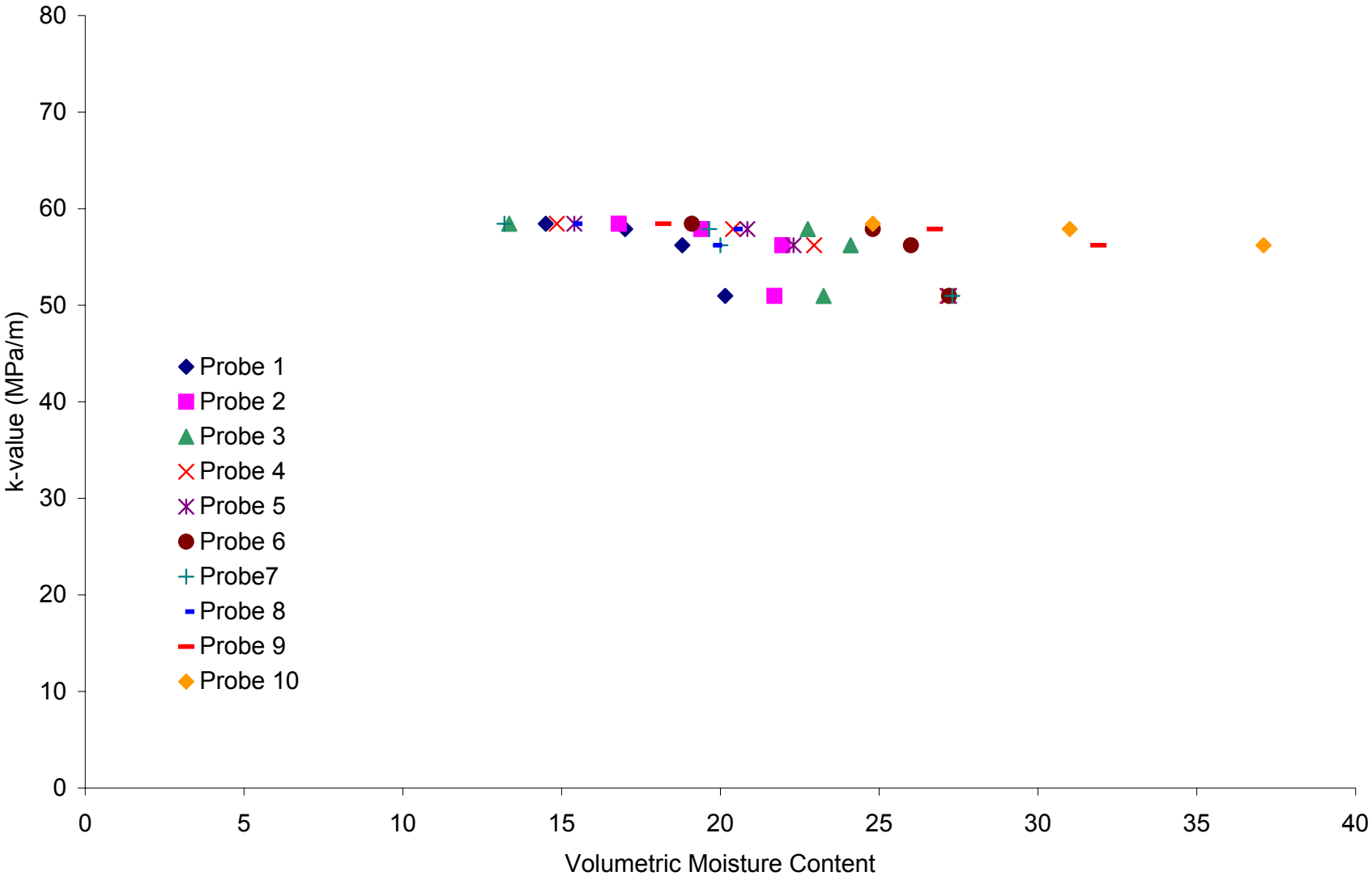

Figure N-36 Variation in Subgrade k-value as a Function of Moisture Content at Site 36-4018 (Sandy Silt)

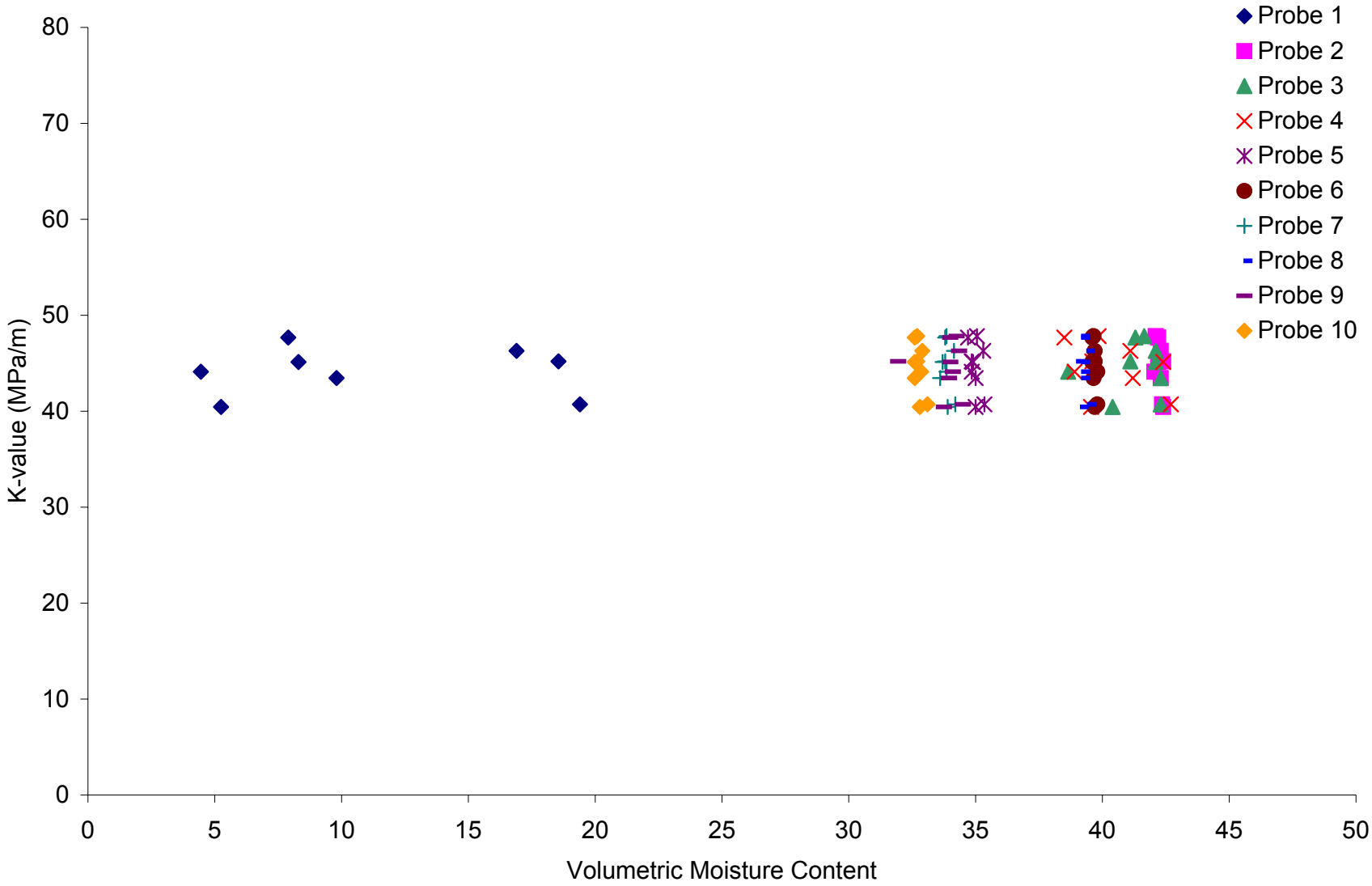

Figure N-37. Variation in Subgrade k-value as a Function of Moisture Content at Site 37-0201 (Clay)

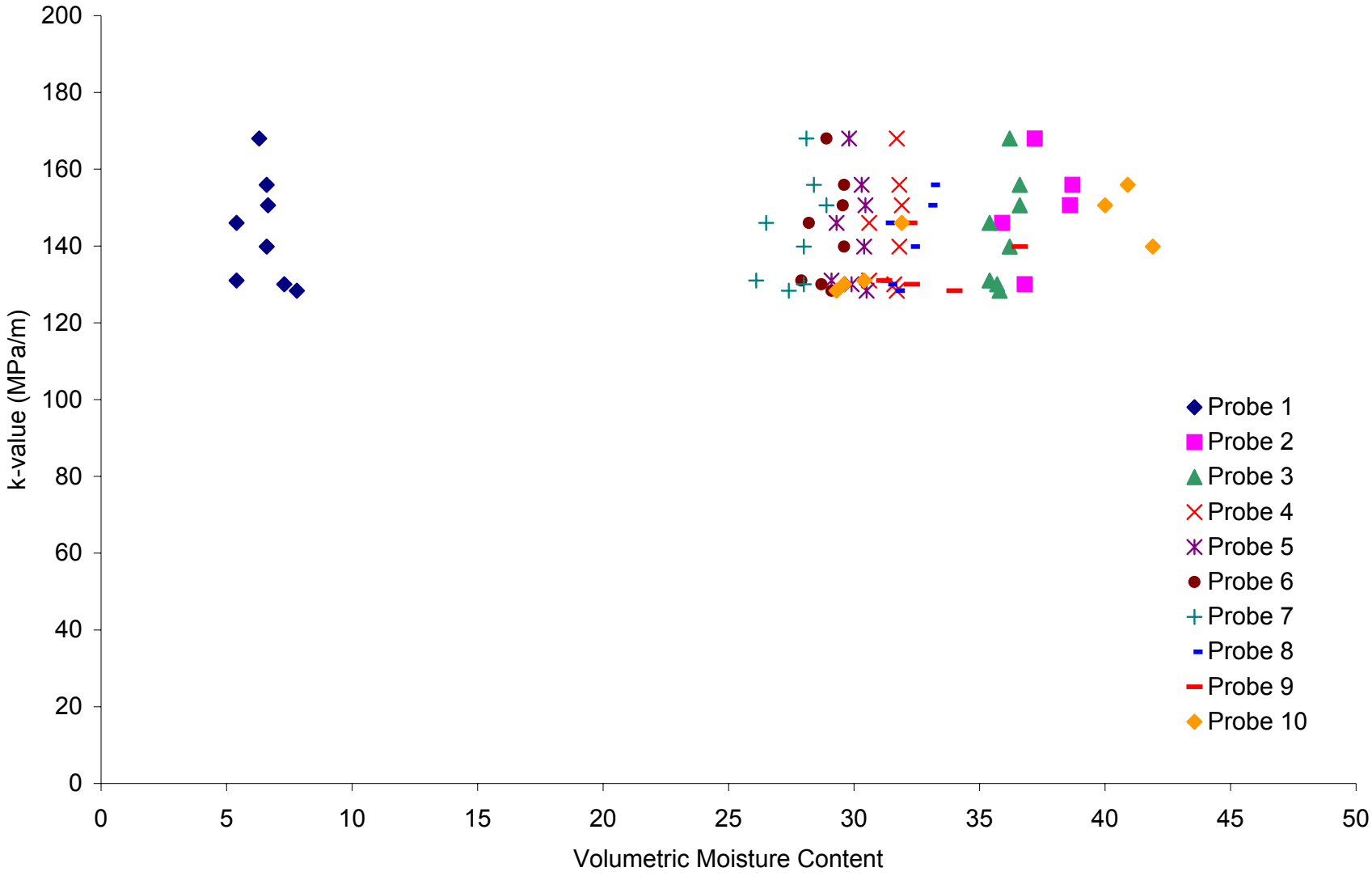

Figure N-38. Variation in Subgrade k-value as a Function of Moisture Content at Site 42-1606 (Gravely Lean Clay with Sand)

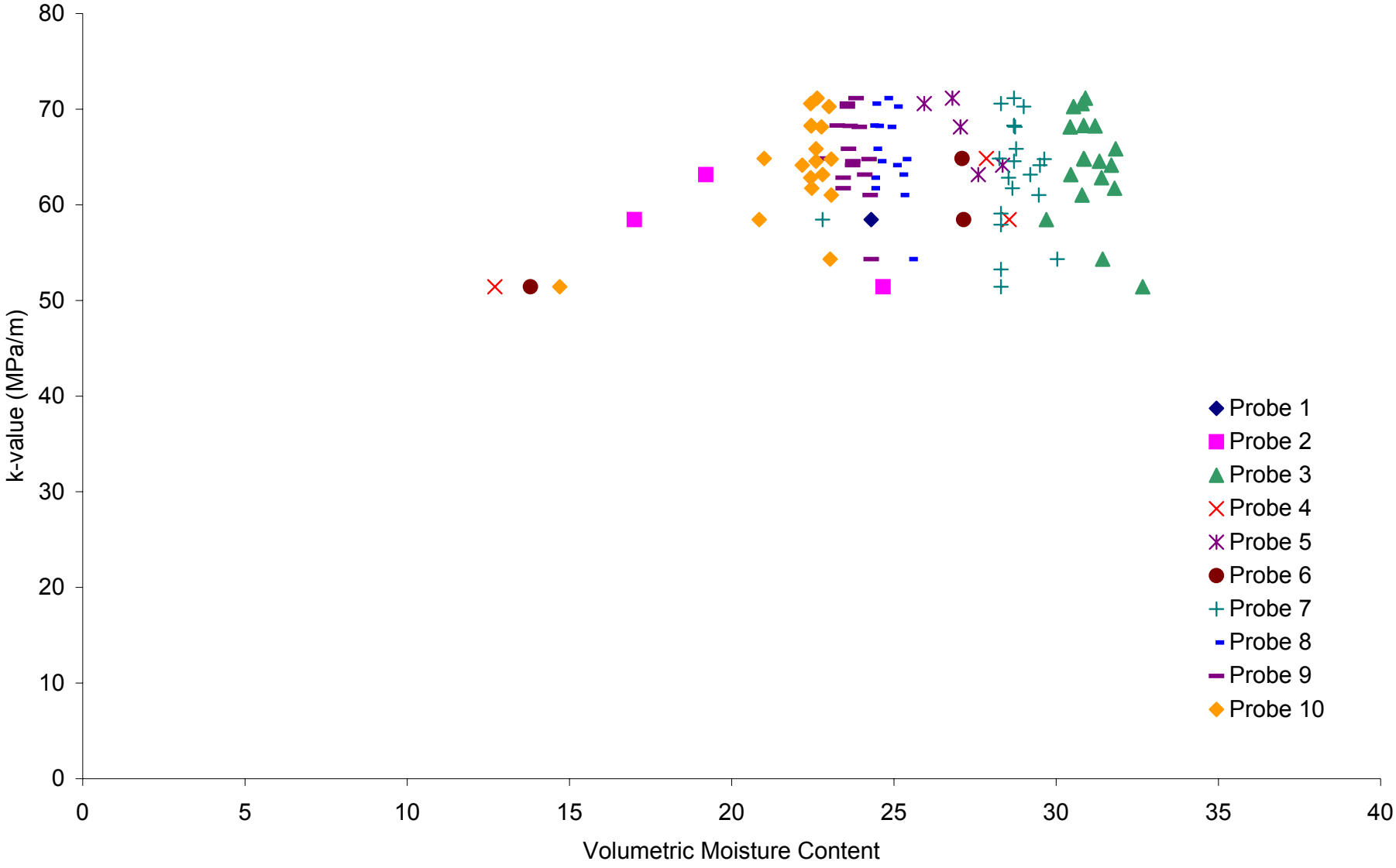

Figure N-39. Variation in Subgrade k-value as a Function of Moisture Content at Site 48-4142 (Clayey Sand)

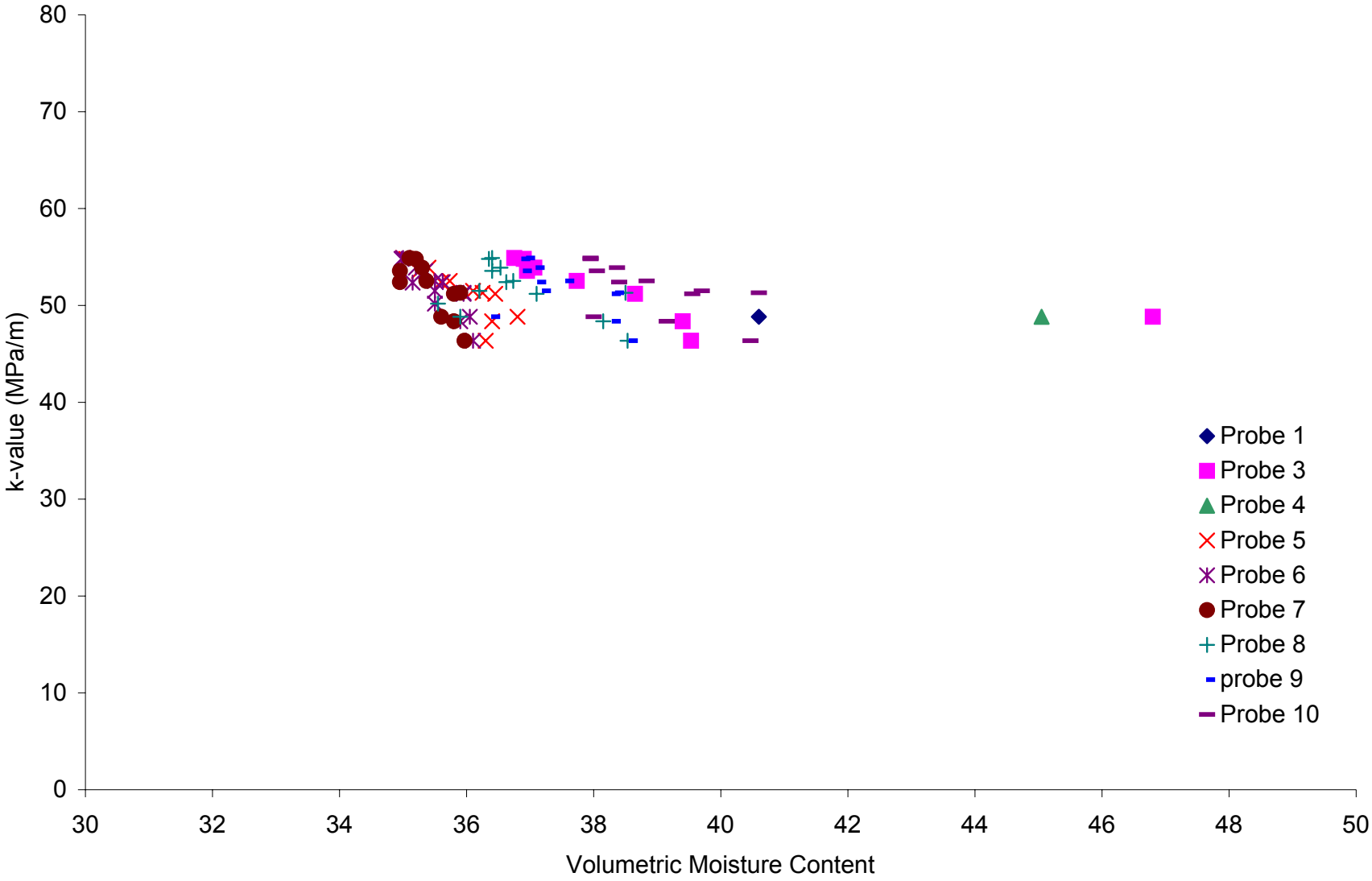

Figure N-40. Variation in Subgrade k-value as a Function of Moisture Content at Site 48-4143 (Lean Inorganic Clay)

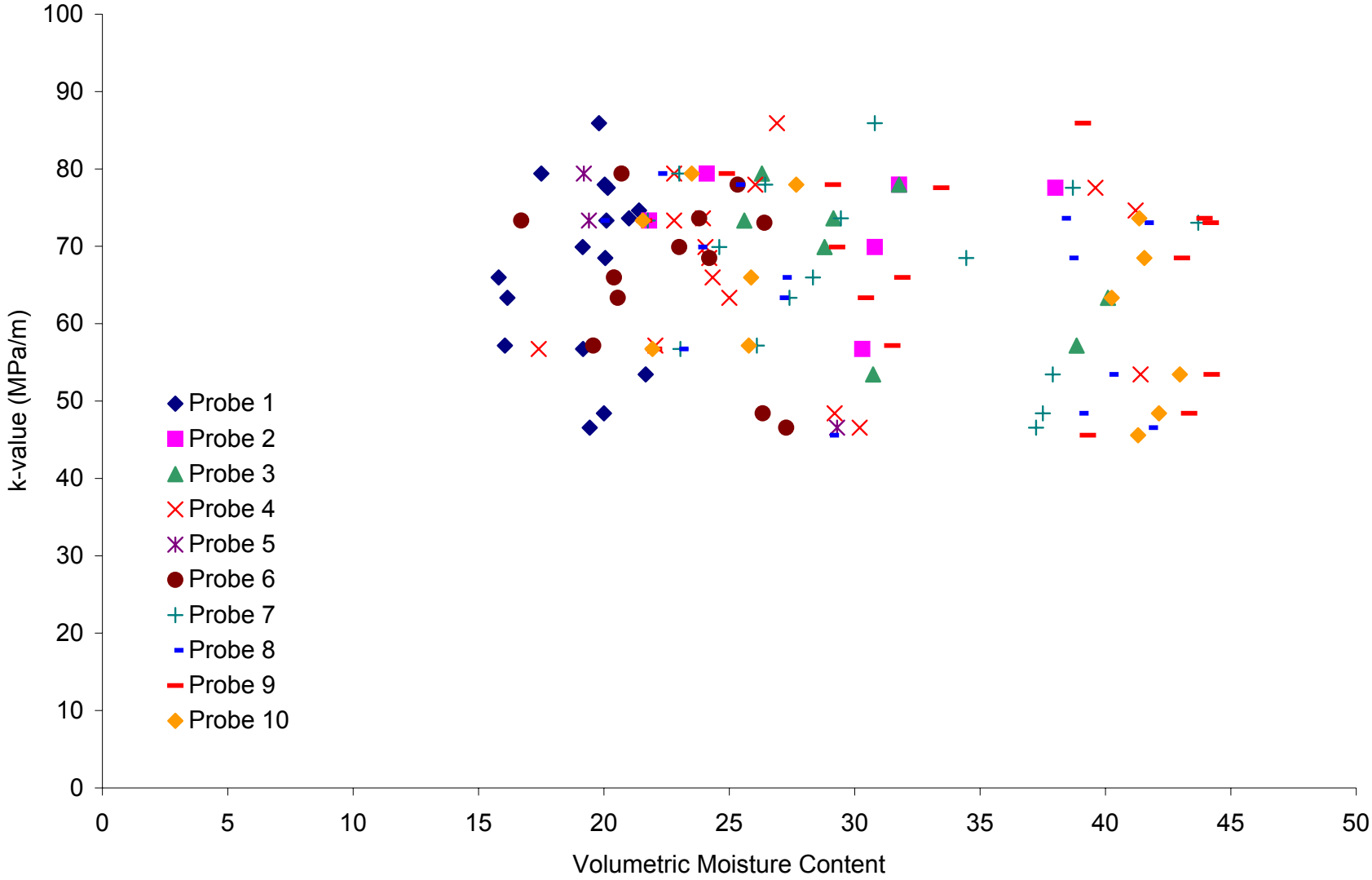

Figure N-41. Variation in Subgrade k-value as a Function of Moisture Content at Site 49-3011 (Clayey Gravel with Sand)

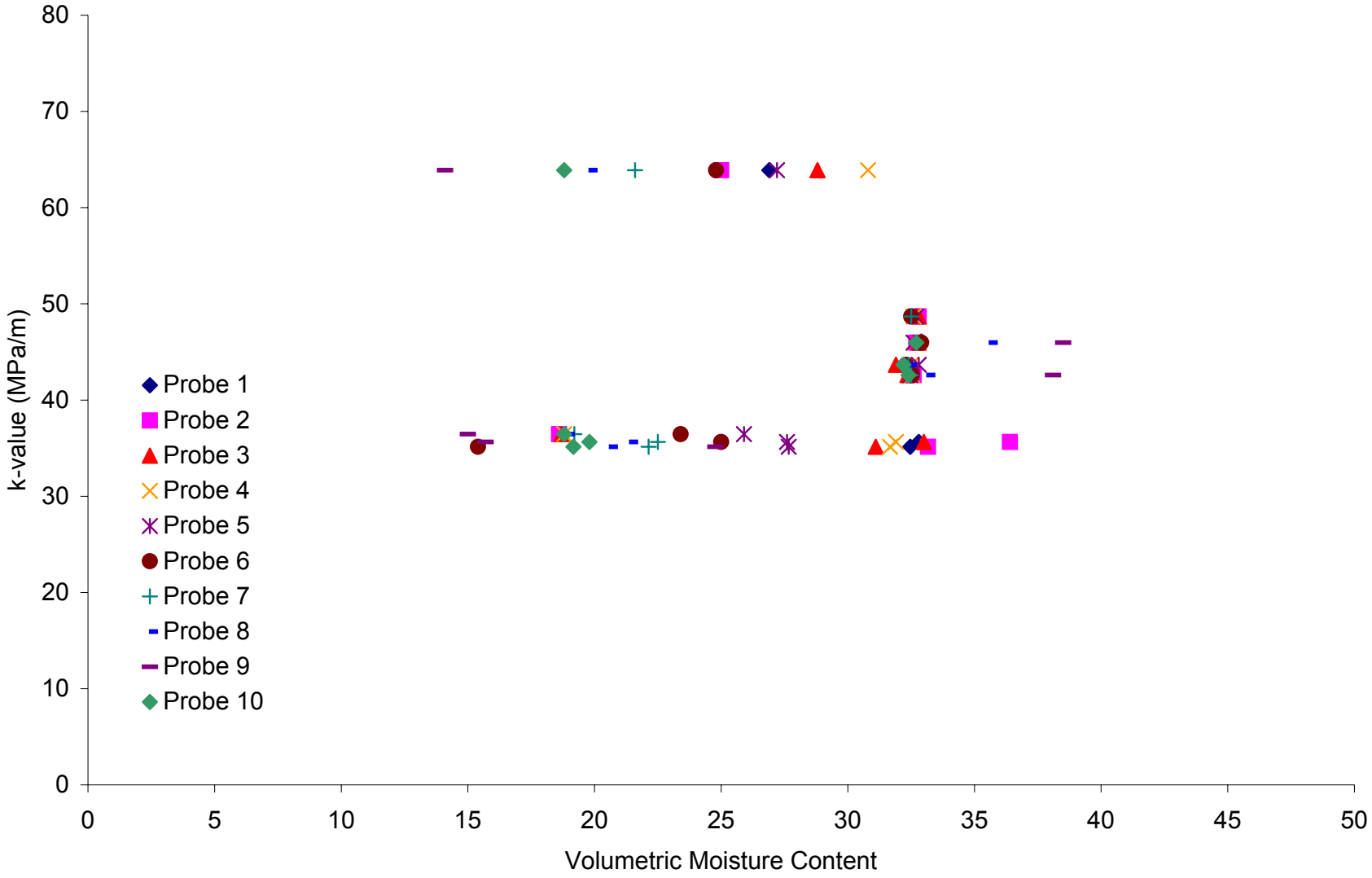

Figure N-42. Variation in Subgrade k-value as a Function of Moisture Content at Site 53-3813 (Silty Sand)

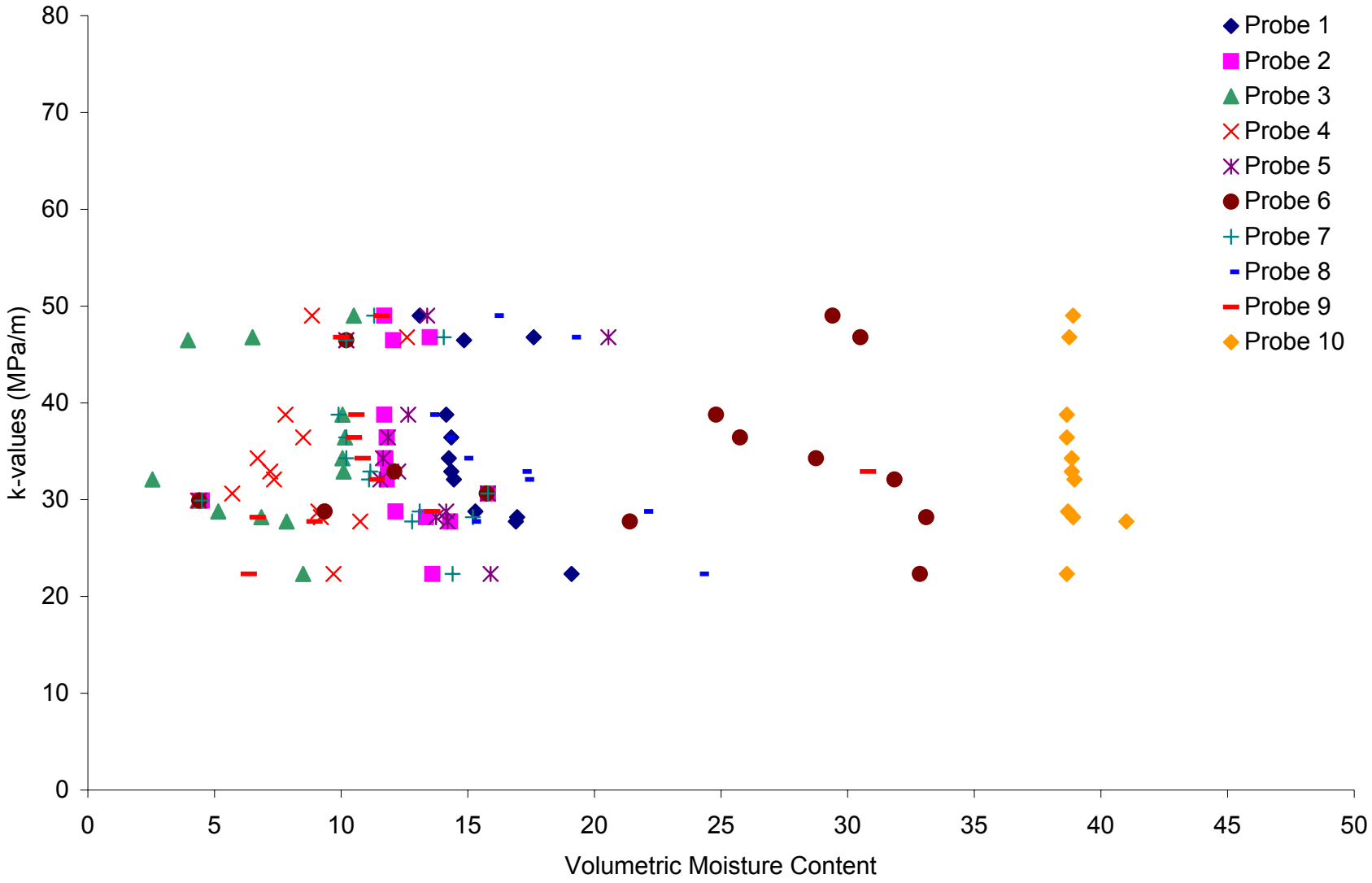

Figure N-43. Variation in Subgrade k-value as a Function of Moisture Content at Site 89-3015 (Poorly Graded Sand)

APPENDIX O

SEASONAL VARIATIONS OF INDEX D_{1524}

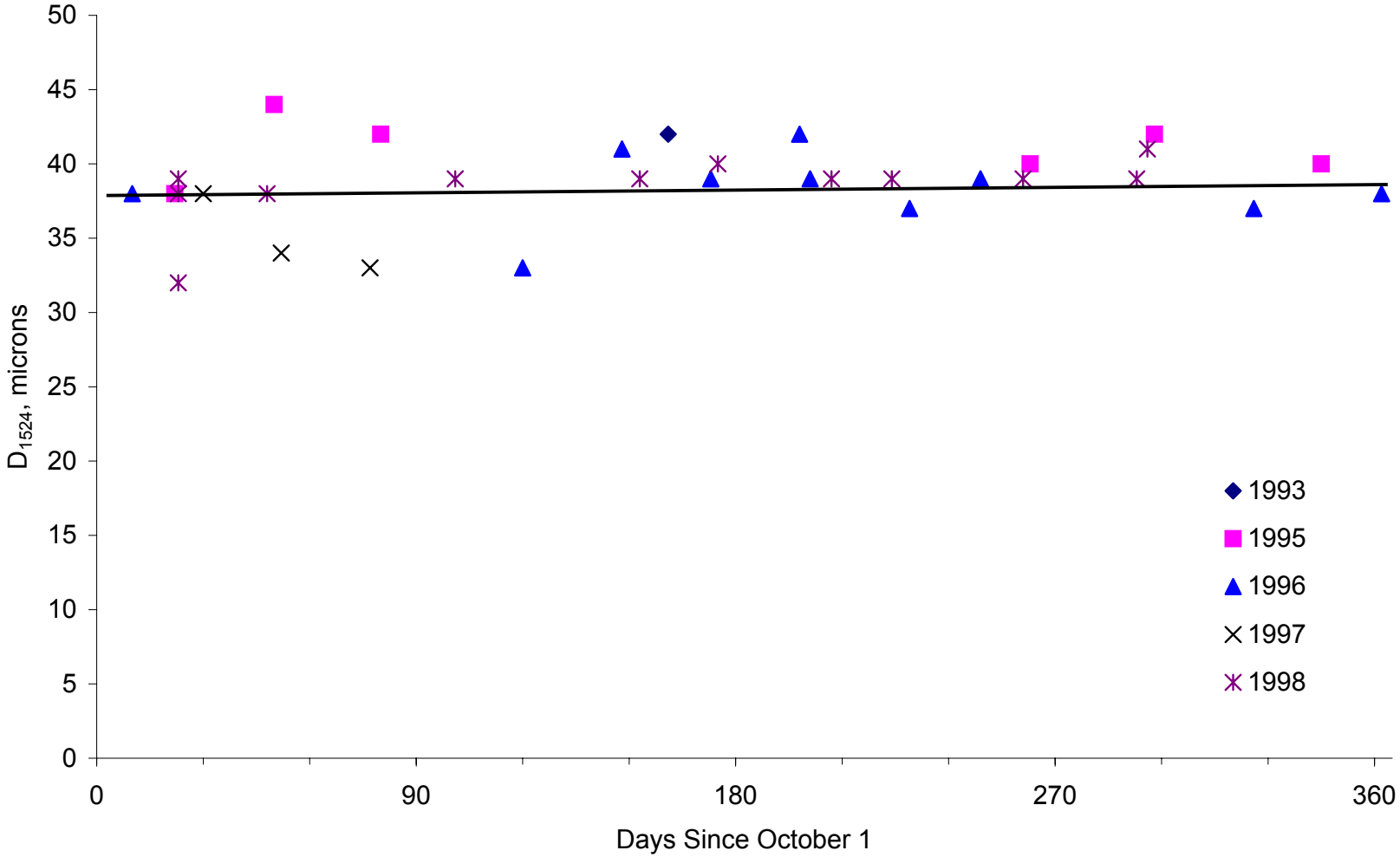

Figure O-1. Index D_{1524} at Site 01-0101 (Sandy Silt)

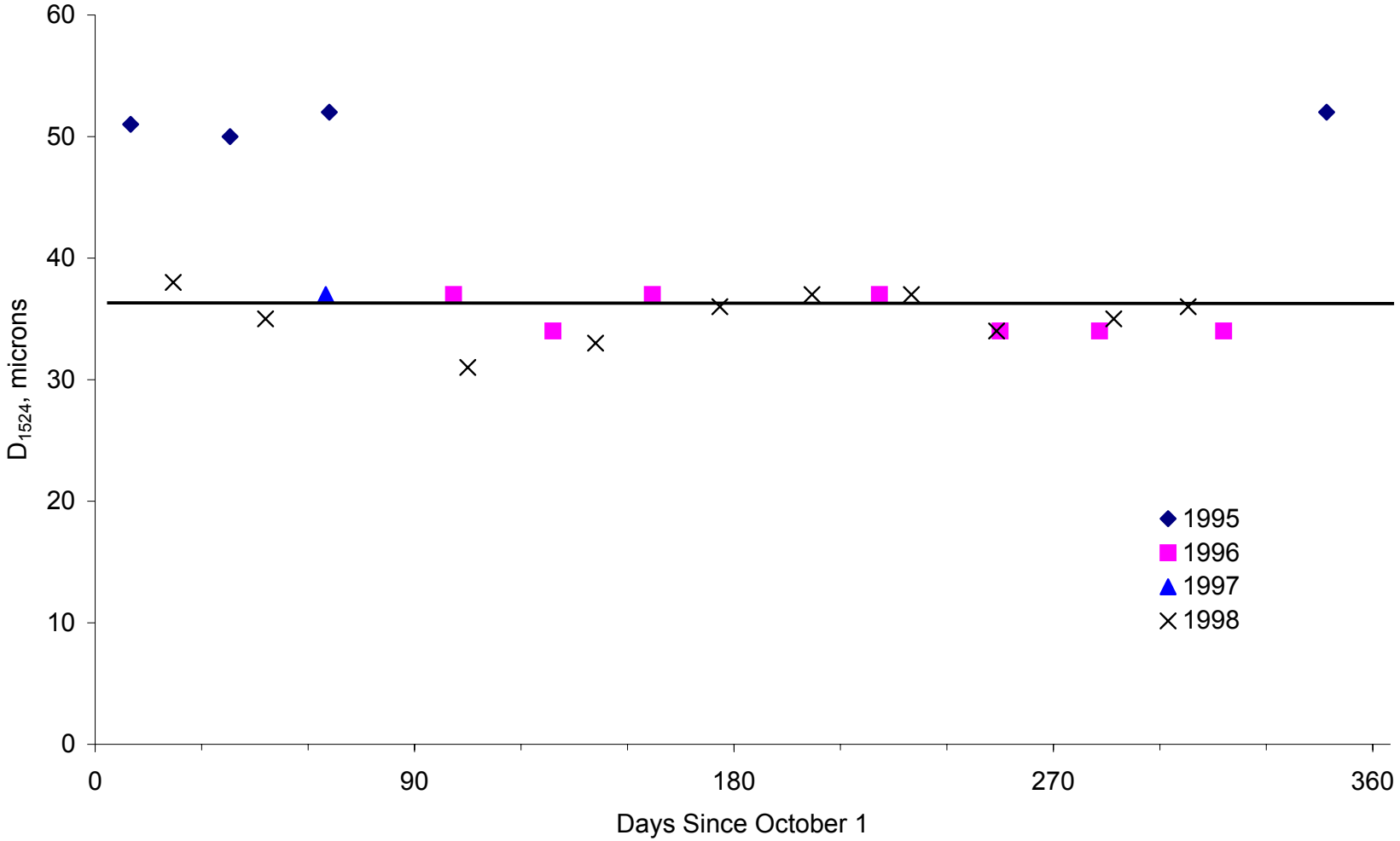

Figure O-2. Index D_{1524} at Site 04-0113 (Well Graded Sand with Silt and Gravel)

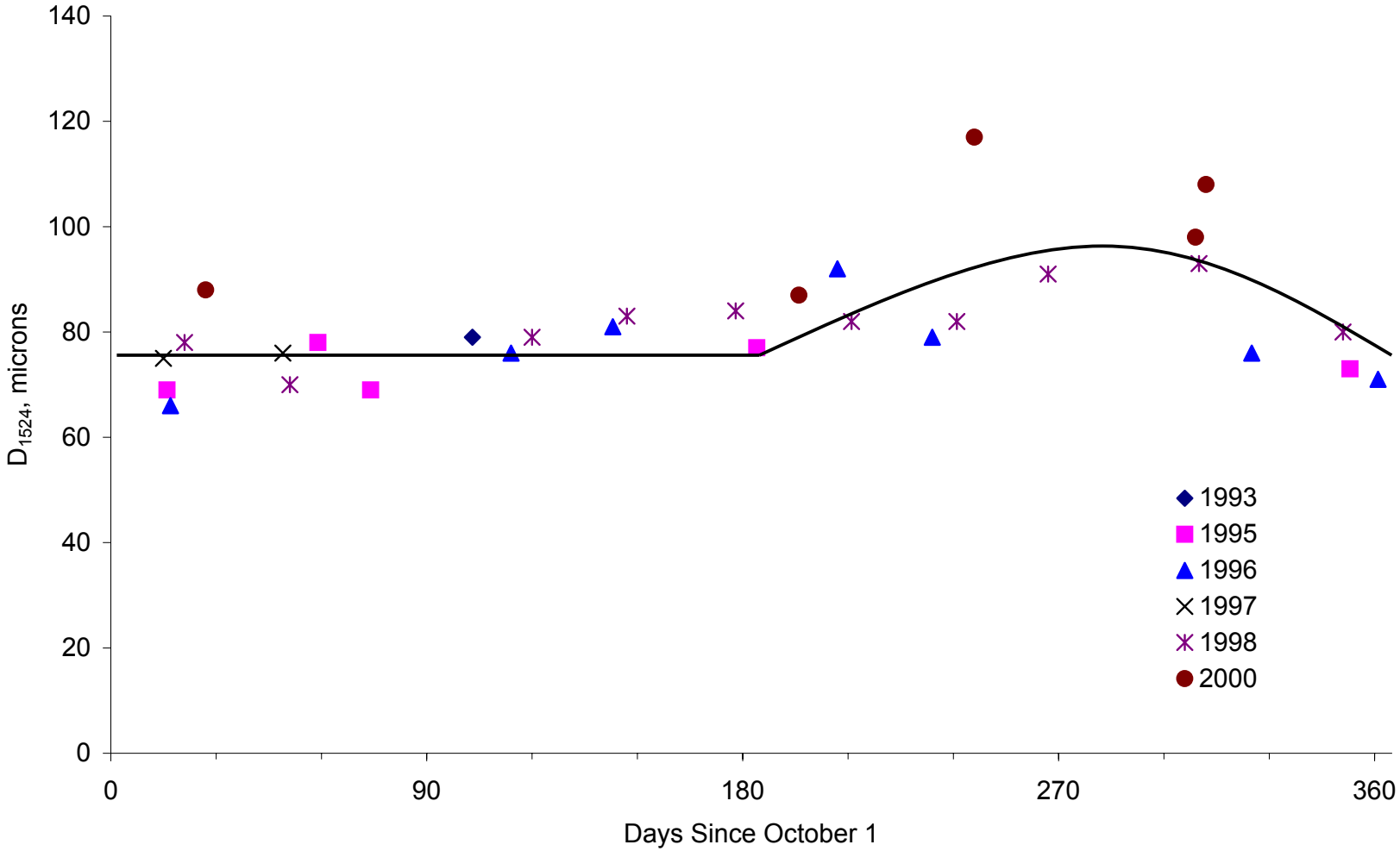

Figure O-3. Index D_{1524} at Site 13-1031 (Silty Sand)

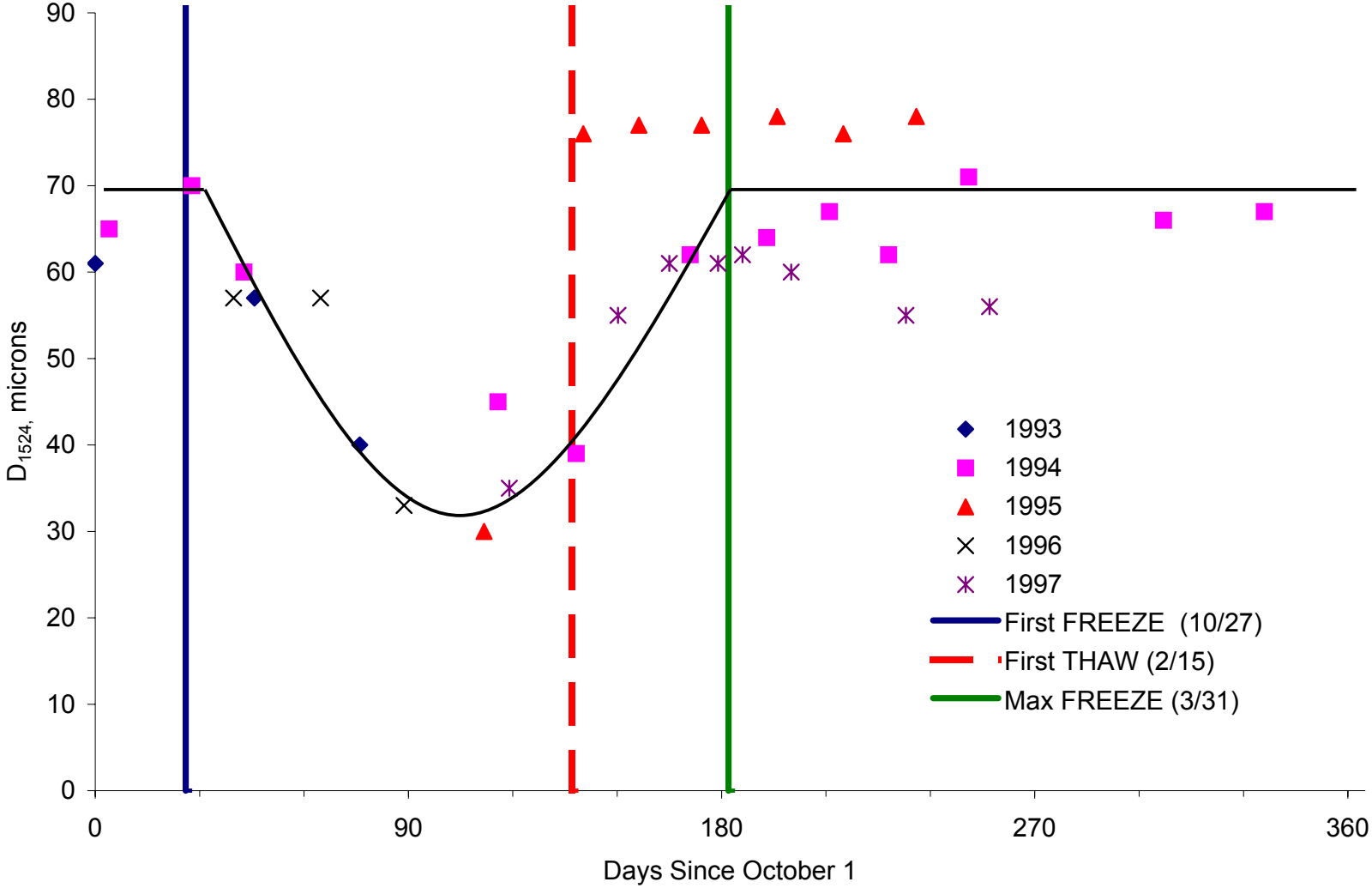

Figure O-4. Index D_{1524} at Site 16-1010 (Silty Sand)

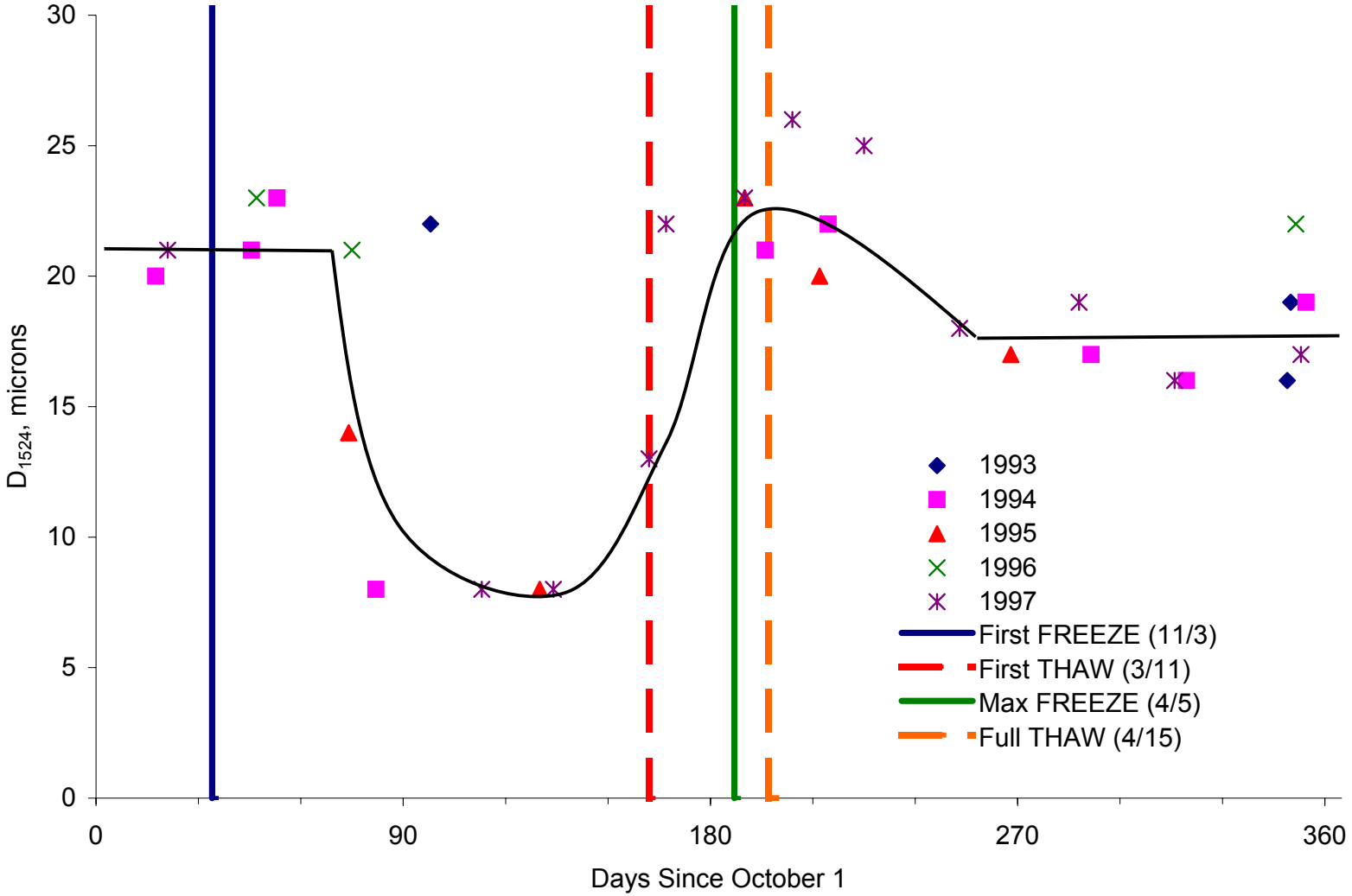

Figure O-5. Index D_{1524} at Site 23-1026 (Silty Sand with Gravel)

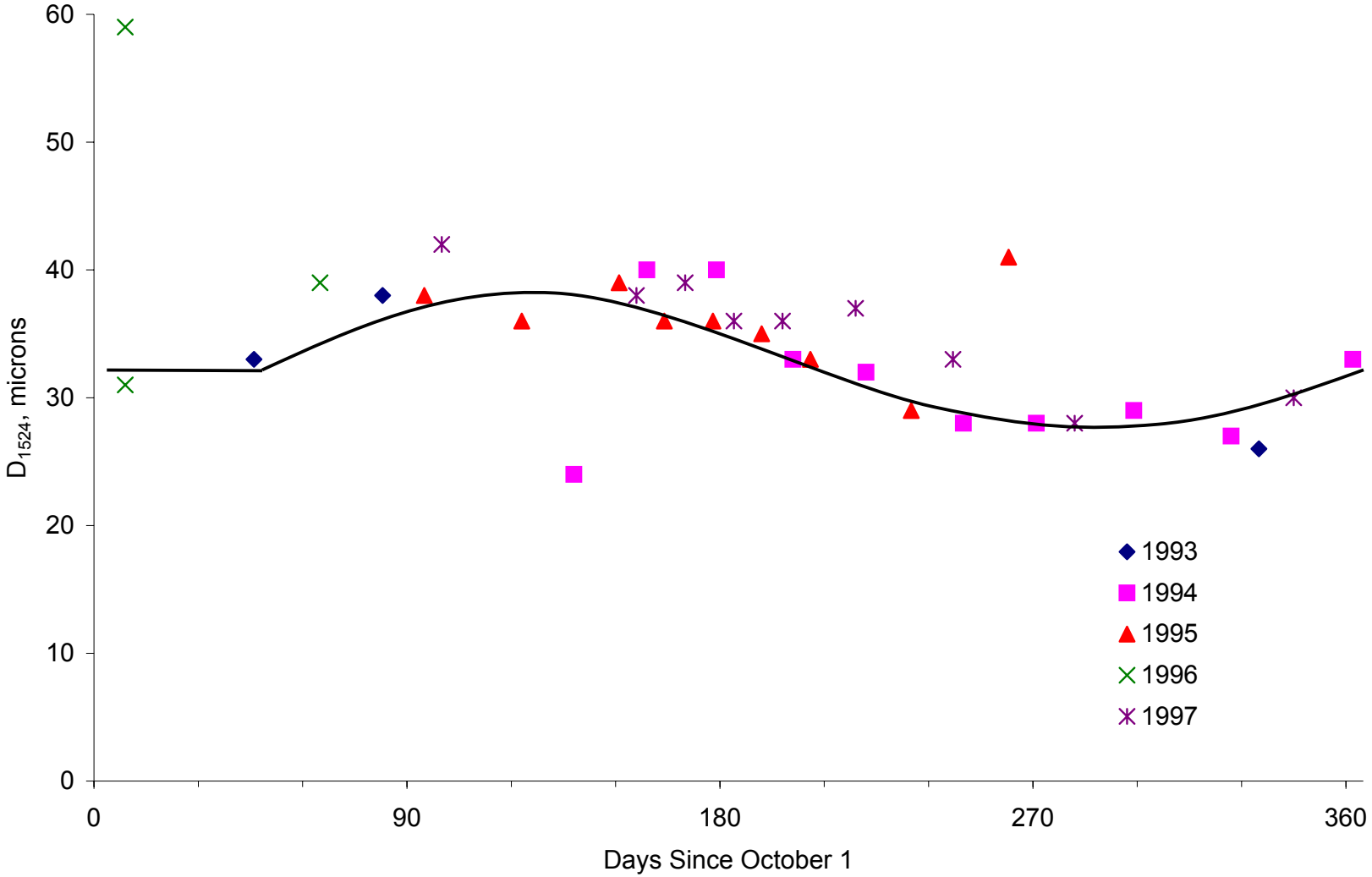

Figure O-6. Index D_{1524} at Site 25-1002 (Poorly Graded Sand with Silt)

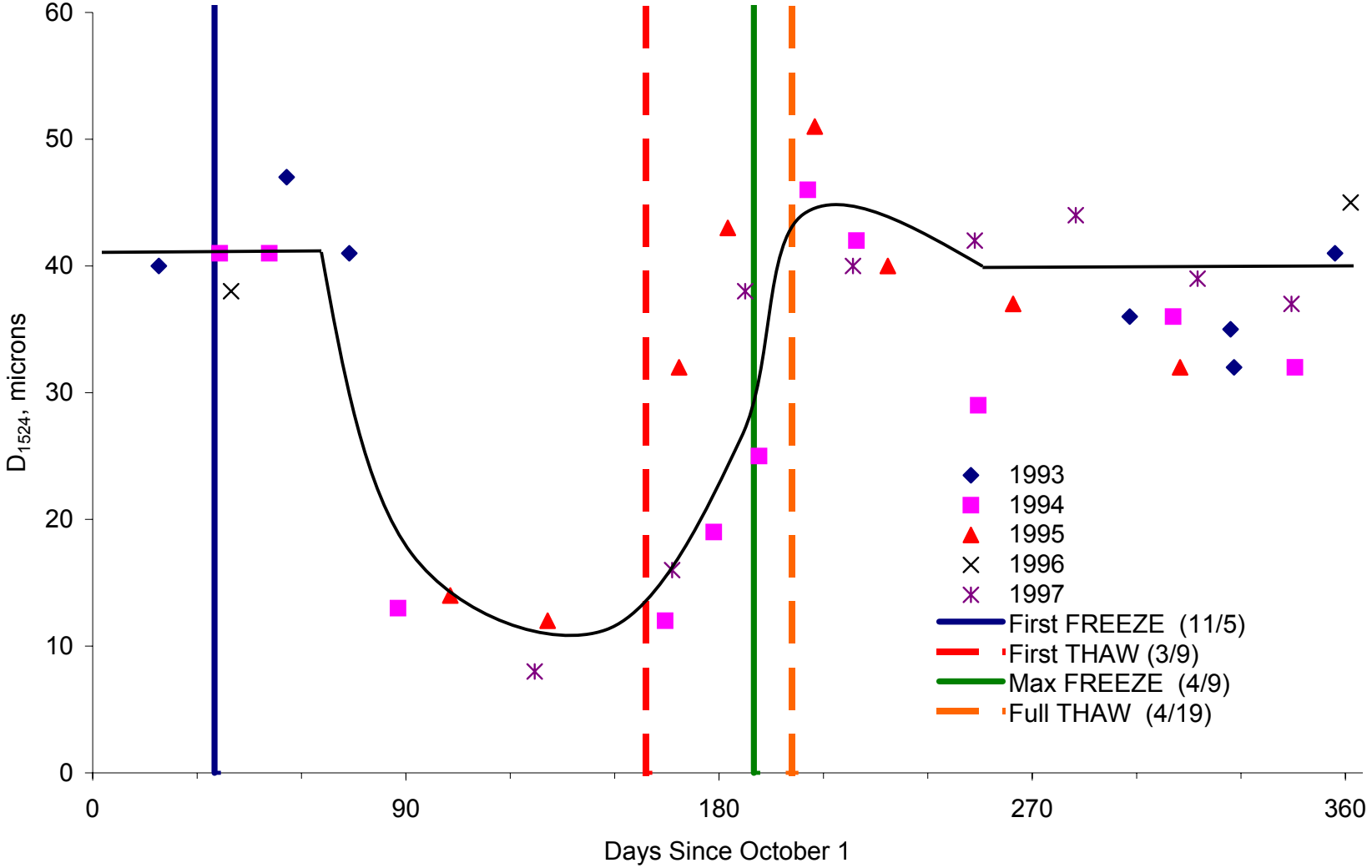

Figure O-7. Index D_{1524} at Site 27-1018 (Poorly Graded Sand with Silt)

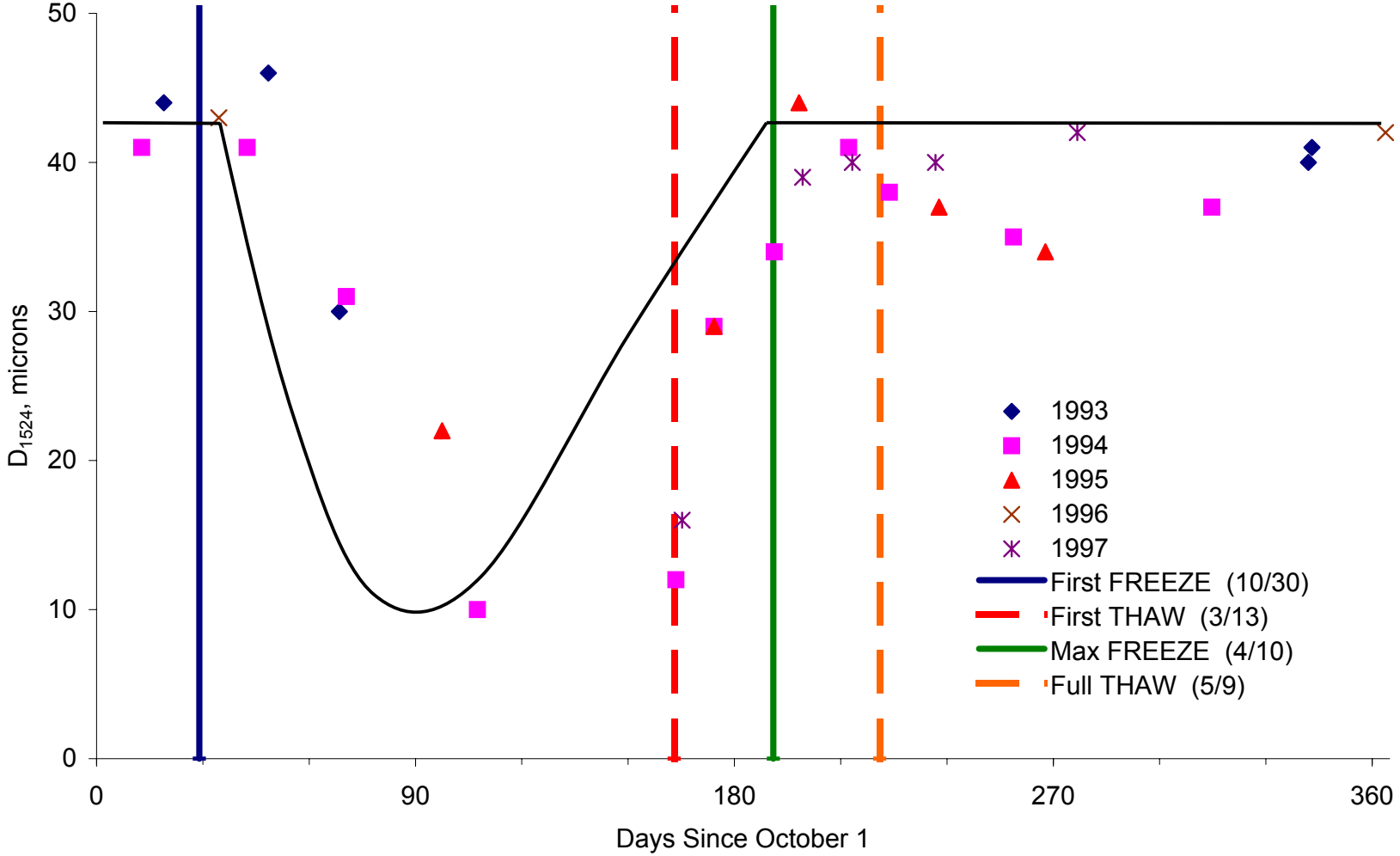

Figure O-8. Index D_{1524} at Site 27-1028 (Poorly Graded Sand with Silt)

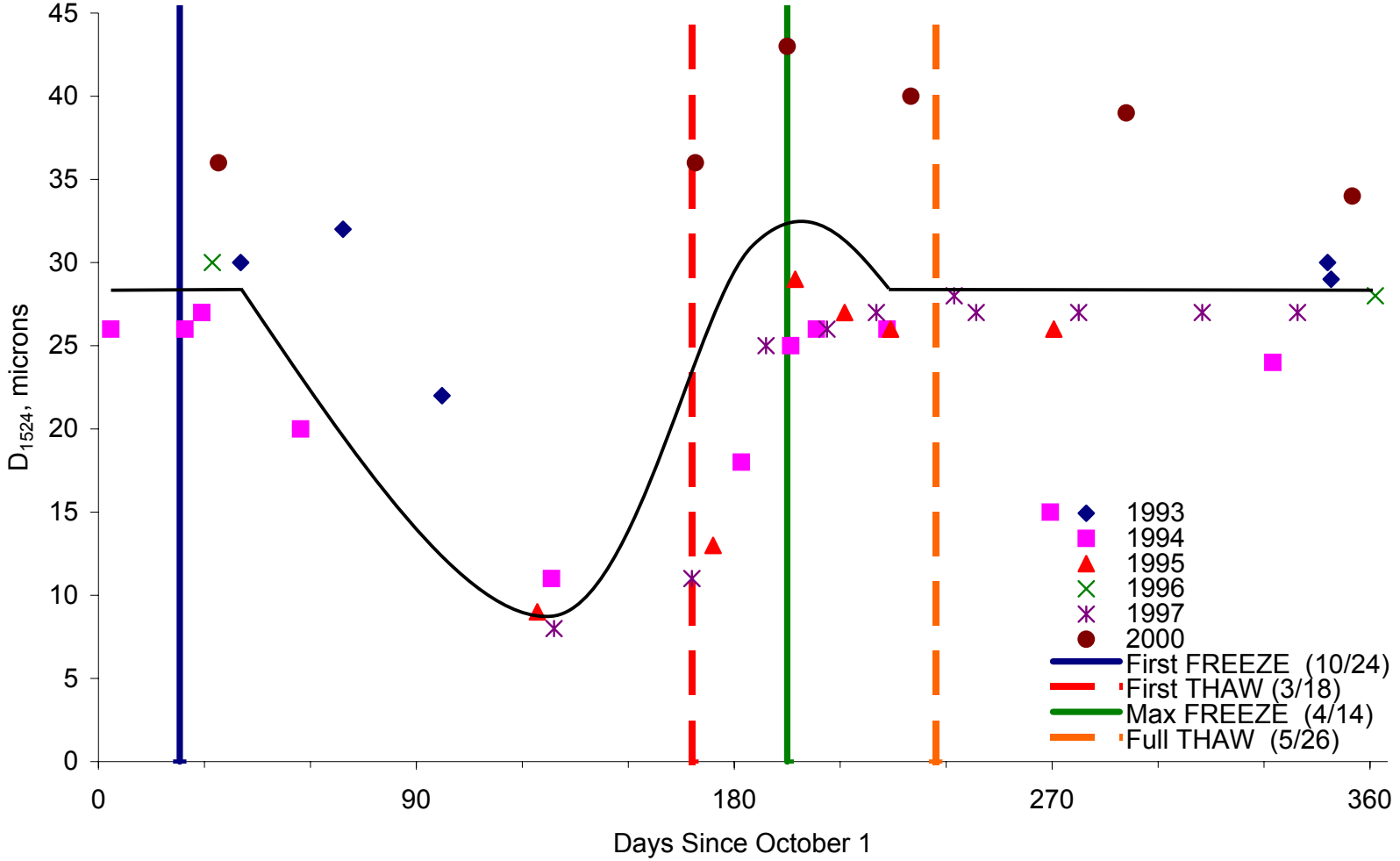

Figure O-9. Index D_{1524} at Site 27-6251 (Poorly Graded Sand with Silt)

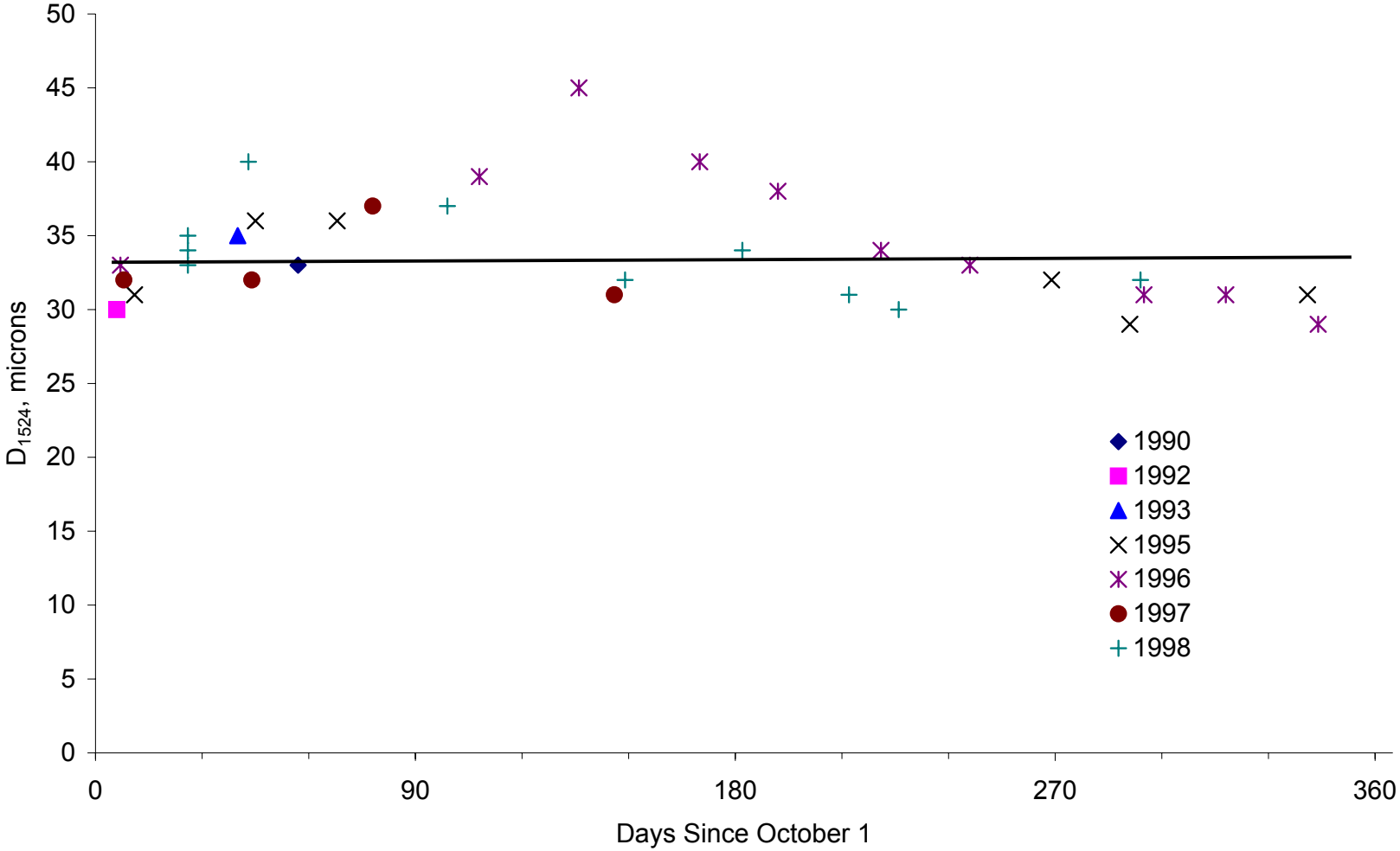

Figure O-10. Index D_{1524} at Site 28-1802 (Poorly Graded Sand)

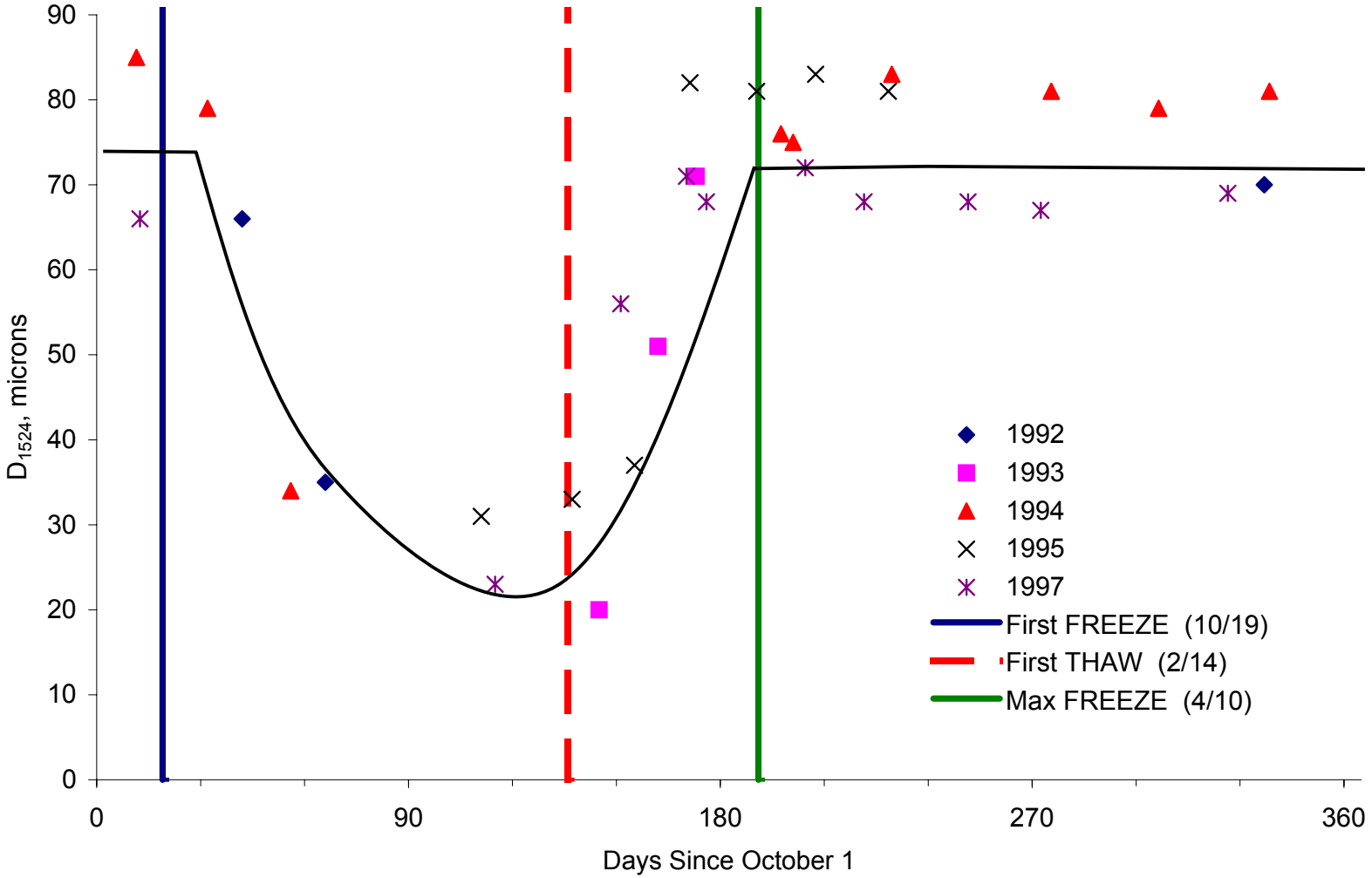

Figure O-11. Index D_{1524} at Site 30-8129 (Poorly Graded Sand with Silt)

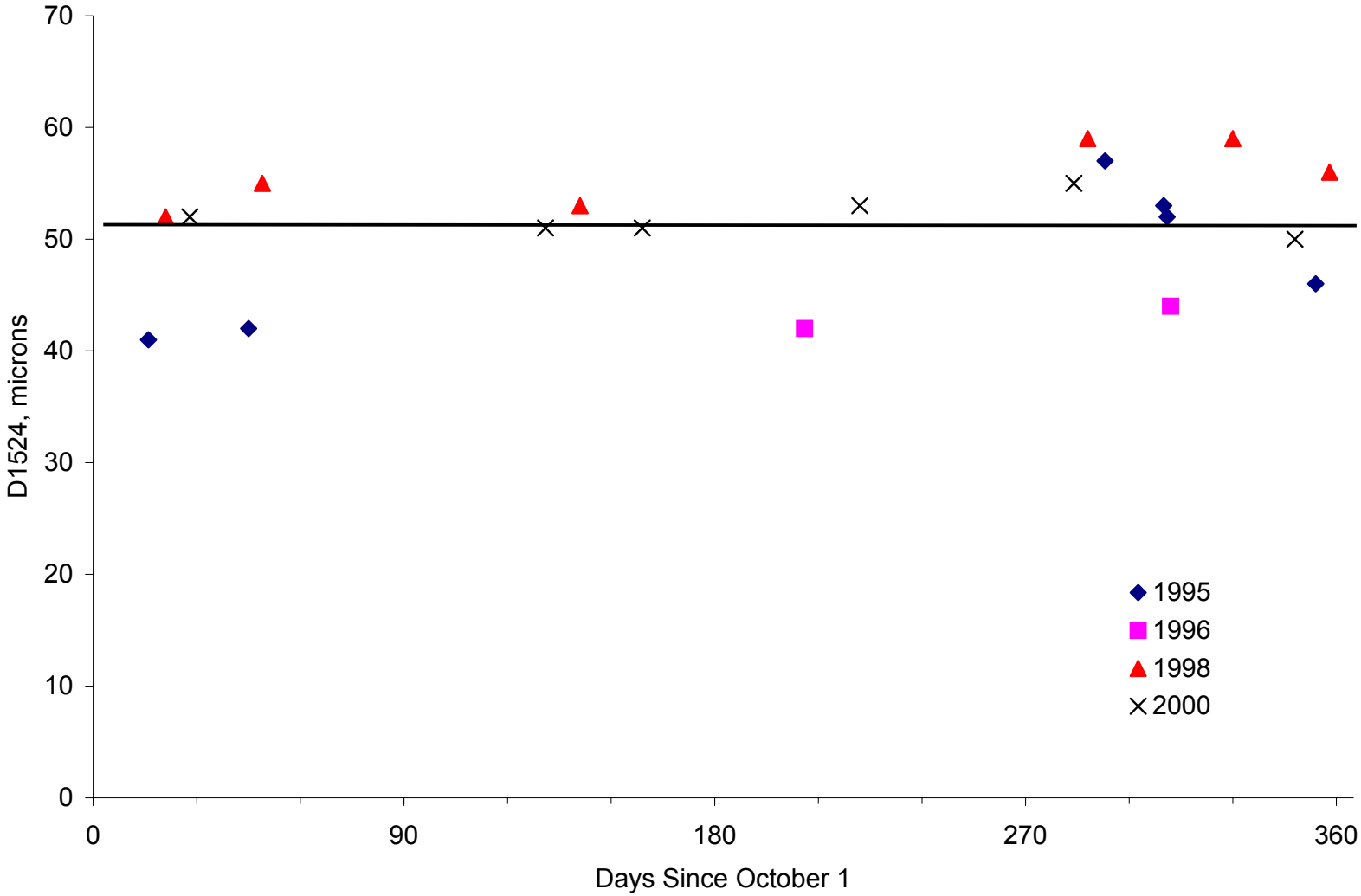

Figure O-12. Index D_{1524} at Site 31-0114 (Silty Clay)

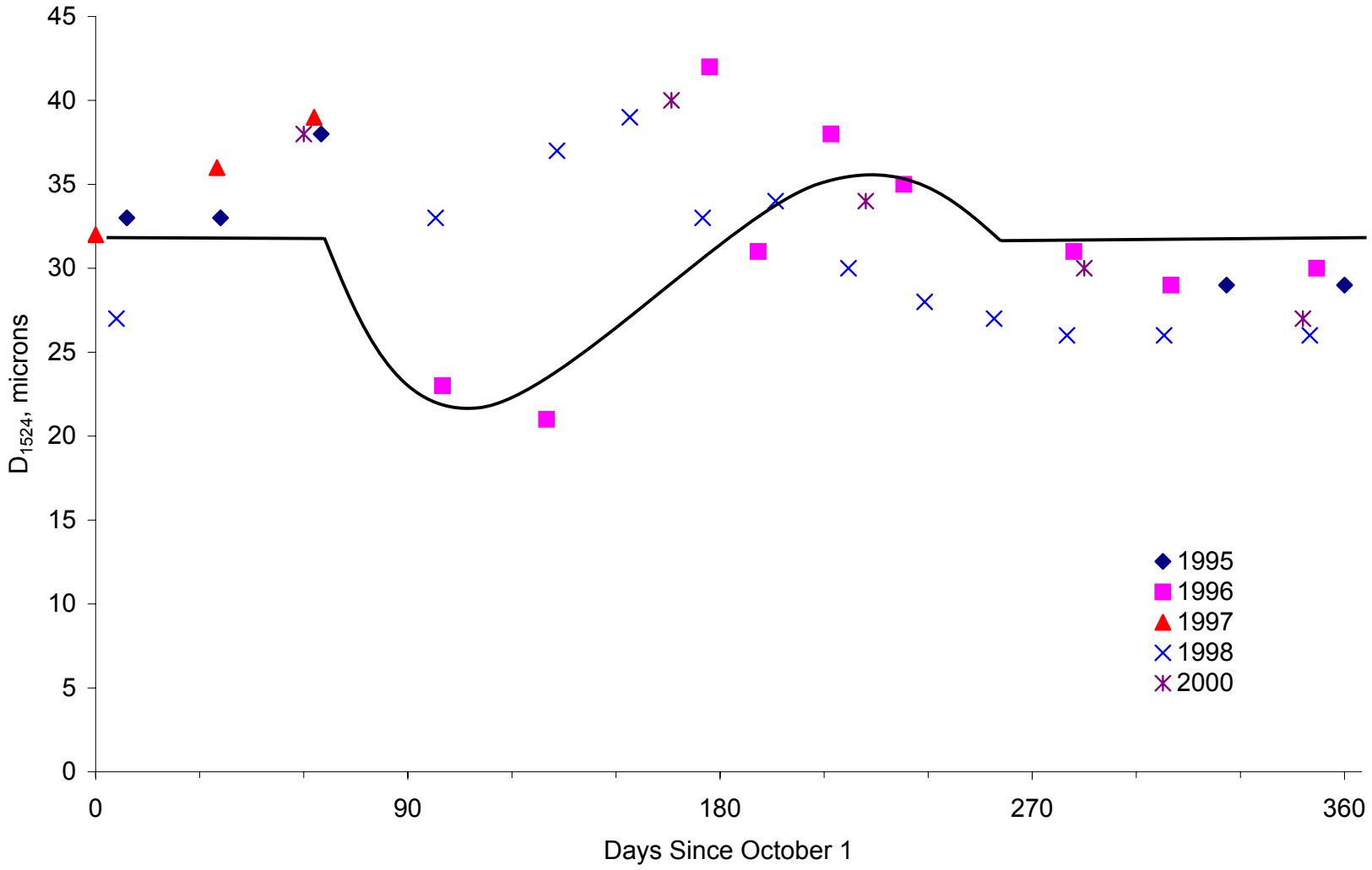

Figure O-13. Index D_{1524} at Site 36-0801 (Silty Sand)

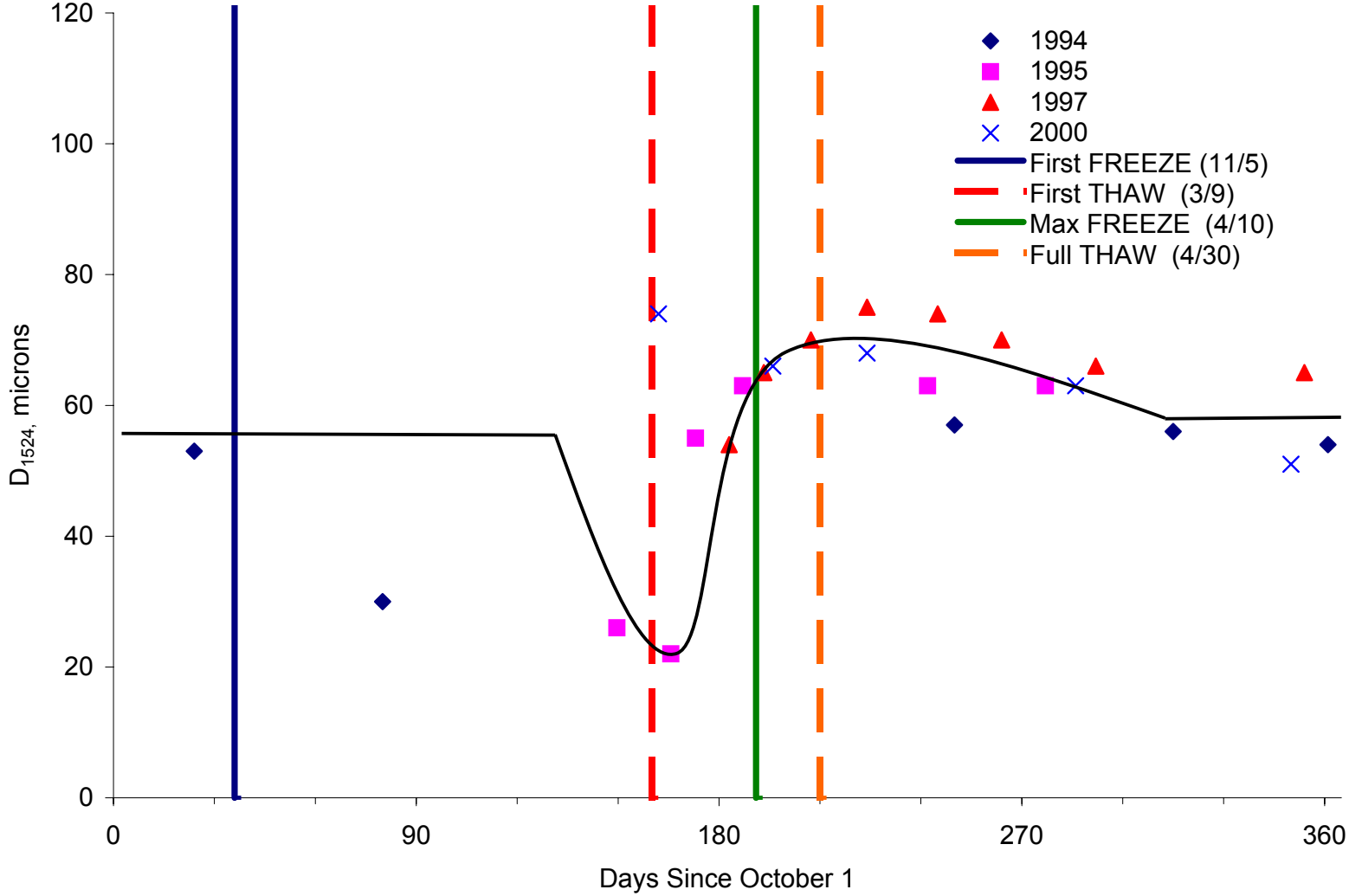

Figure O-14. Index D_{1524} at Site 46-0804 (Silty Clay)

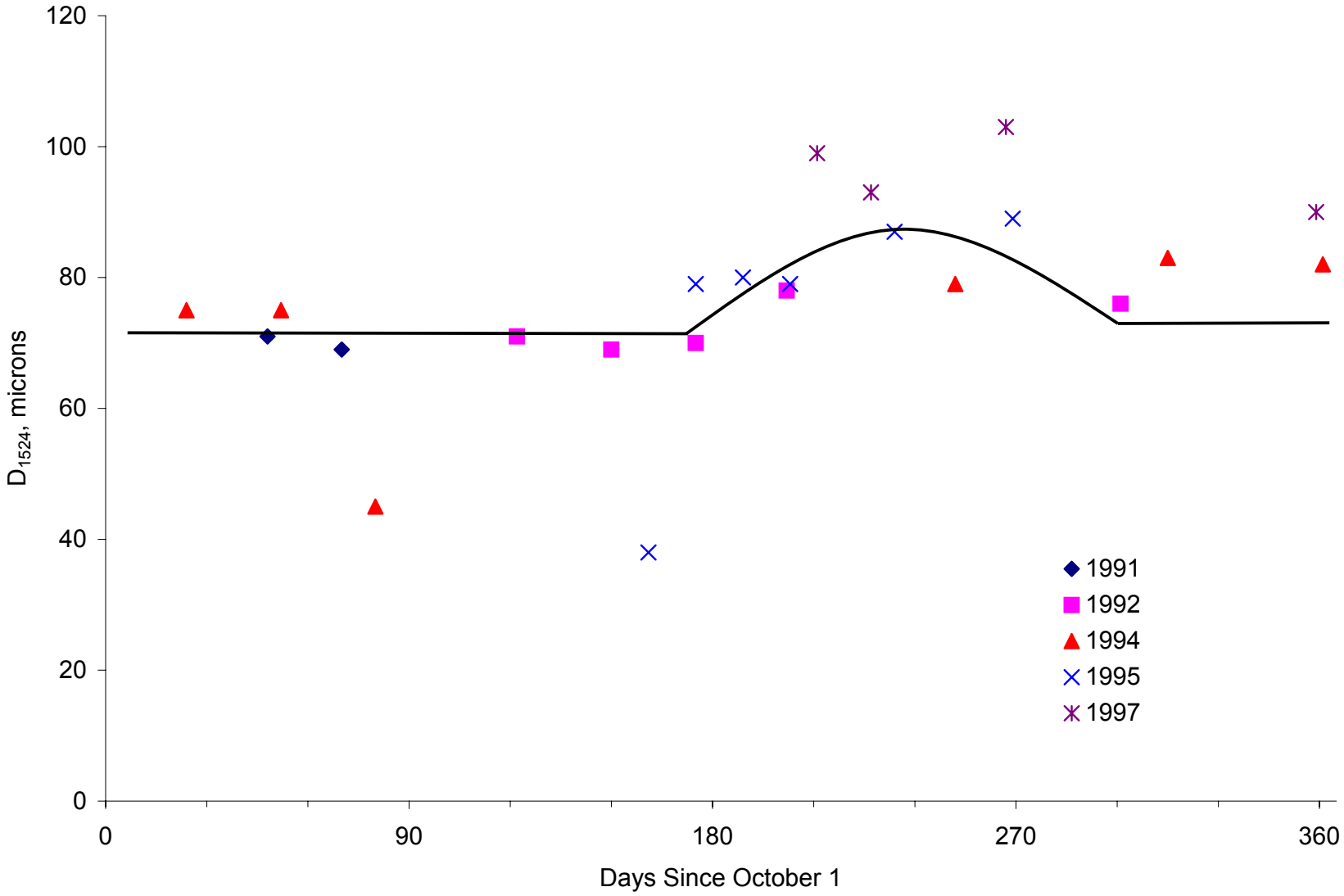

Figure O-15. Index D_{1524} at Site 46-9187 (Lean Inorganic Clay)

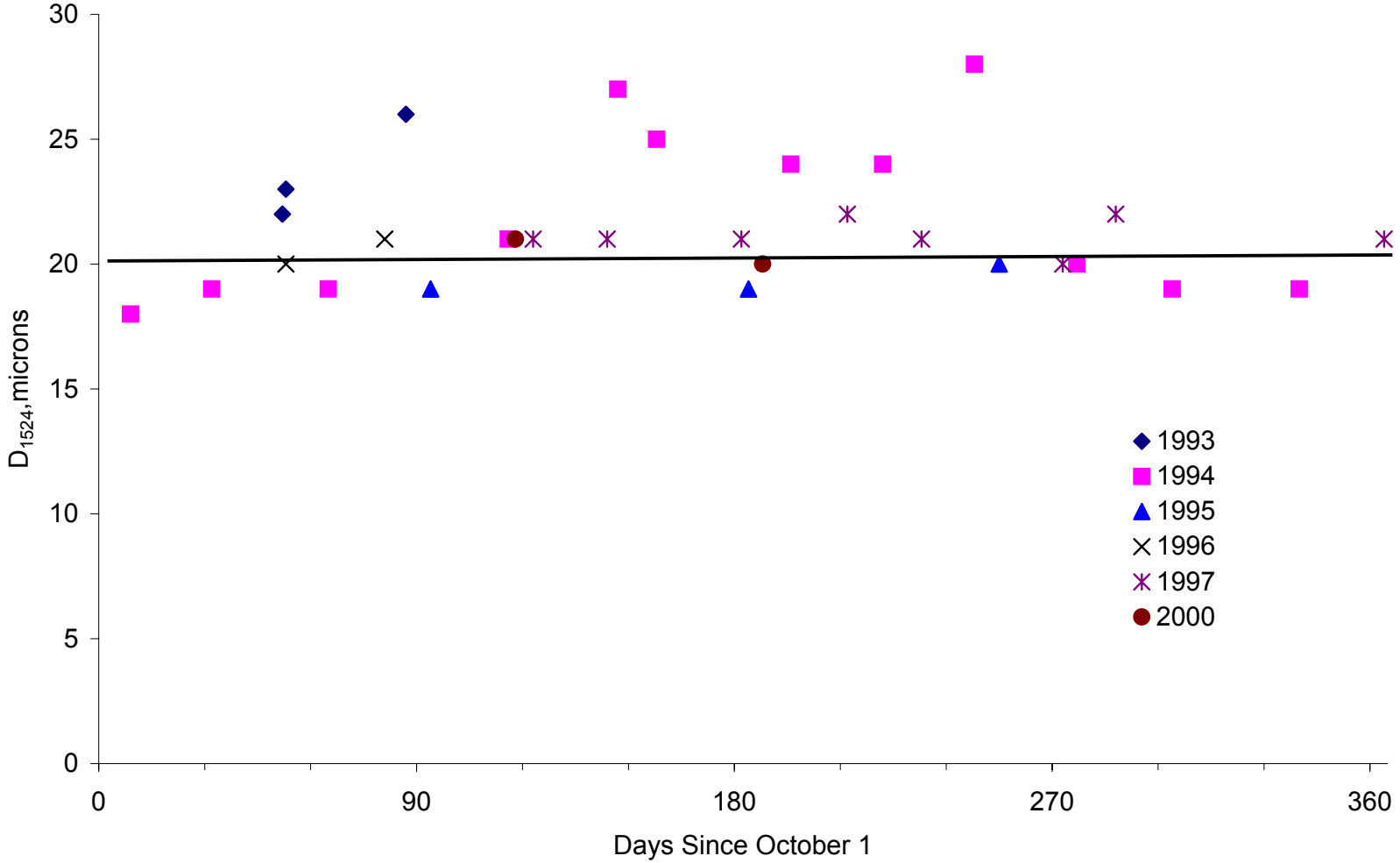

Figure O-16. Index D_{1524} at Site 48-1122 (Clayey Sand)

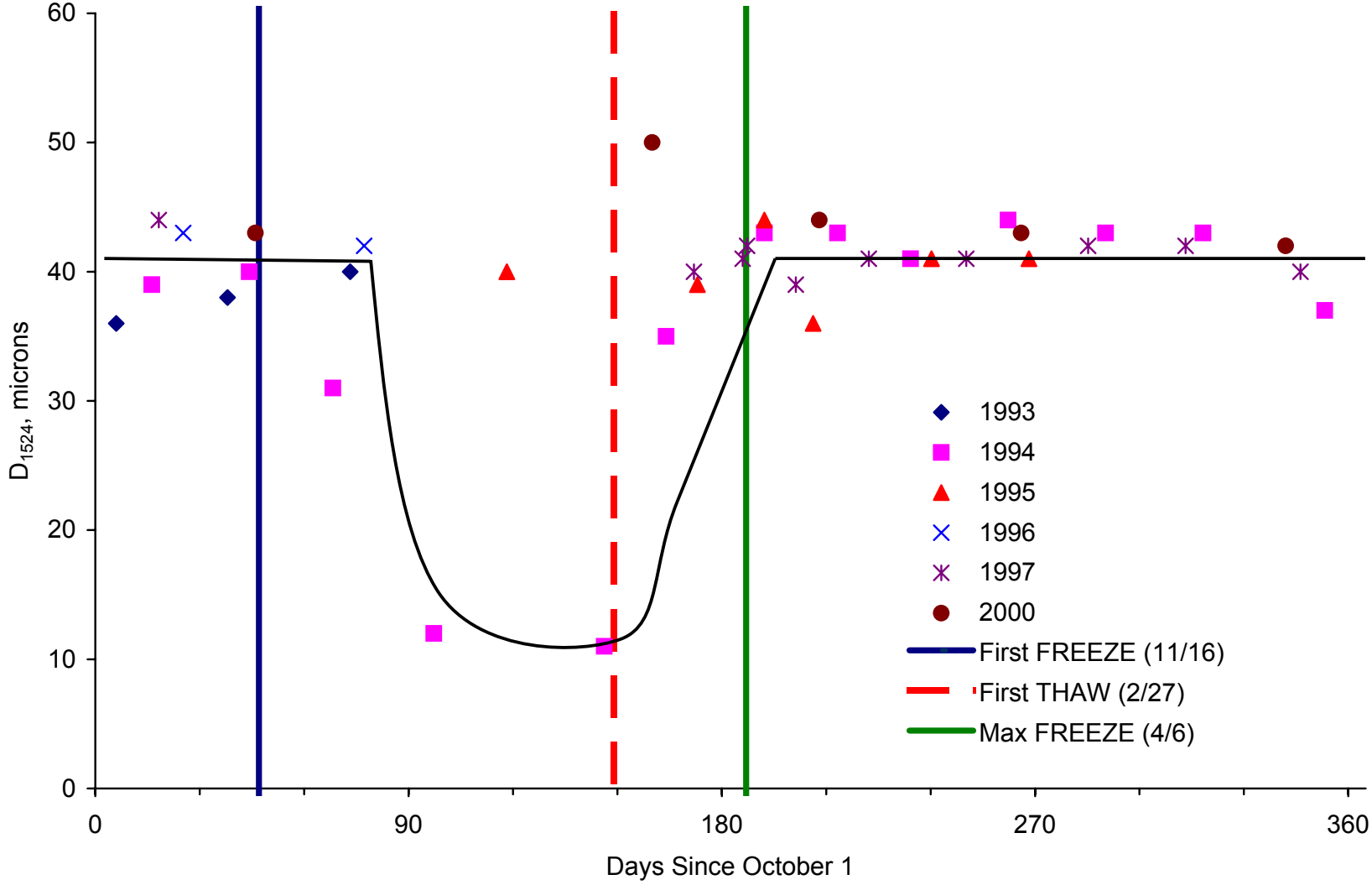

Figure O-17. Index D_{1524} at Site 50-1002 (Poorly Graded Gravel with Silt and Sand)

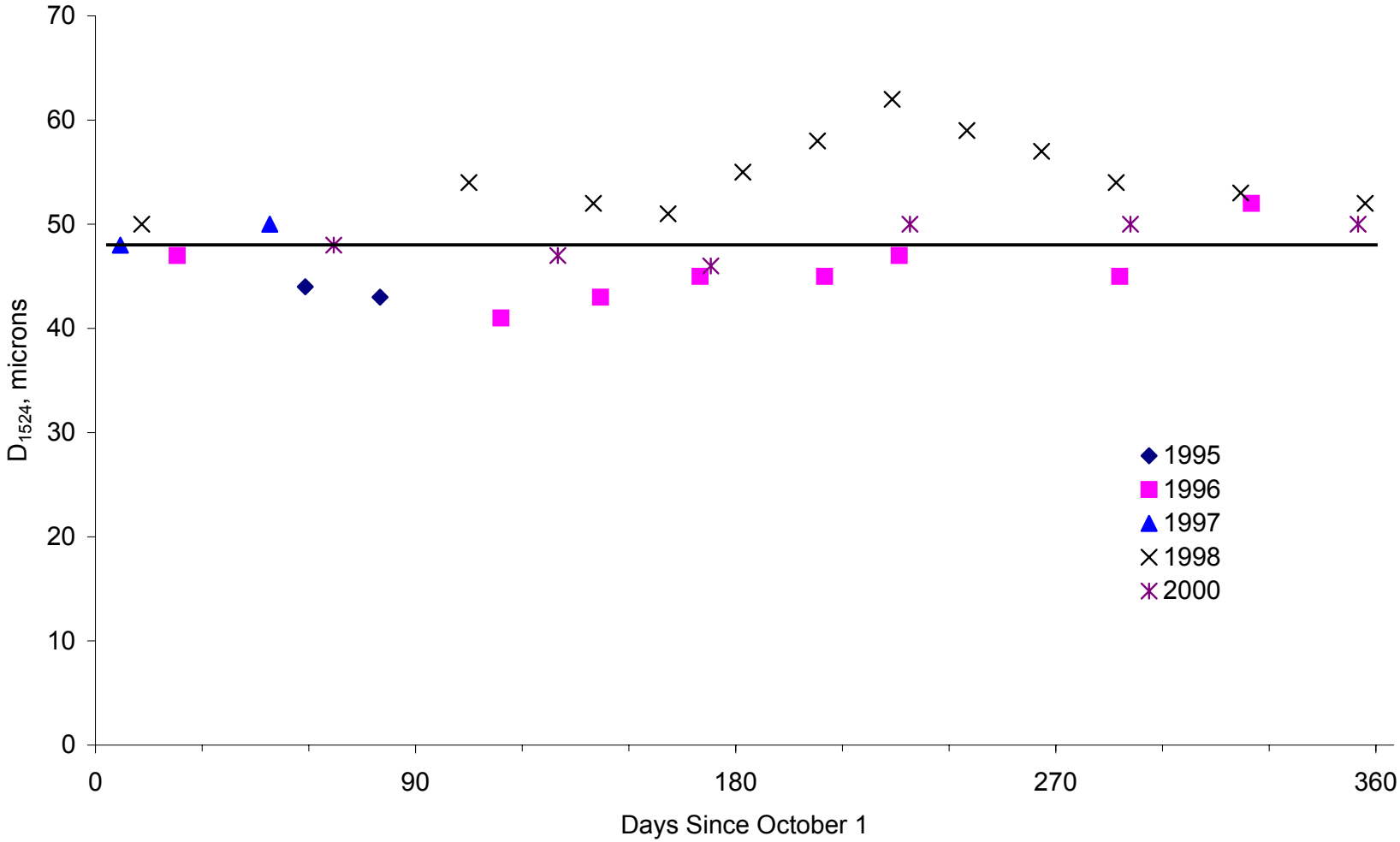

Figure O-18. Index D_{1524} at Site 51-0113 (Silt)

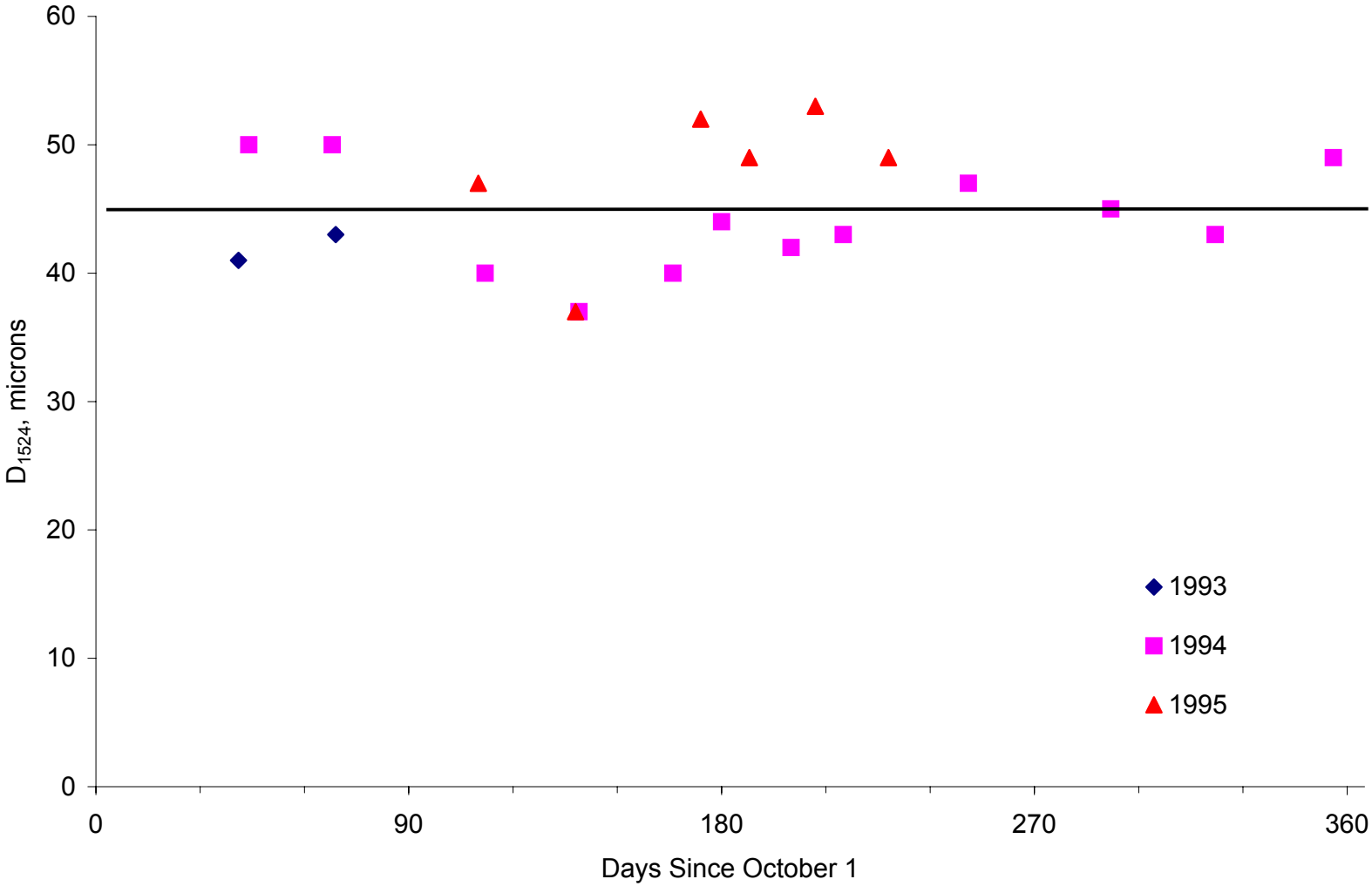

Figure O-19. Index D_{1524} at Site 56-1007 (Silty Sand with Gravel)

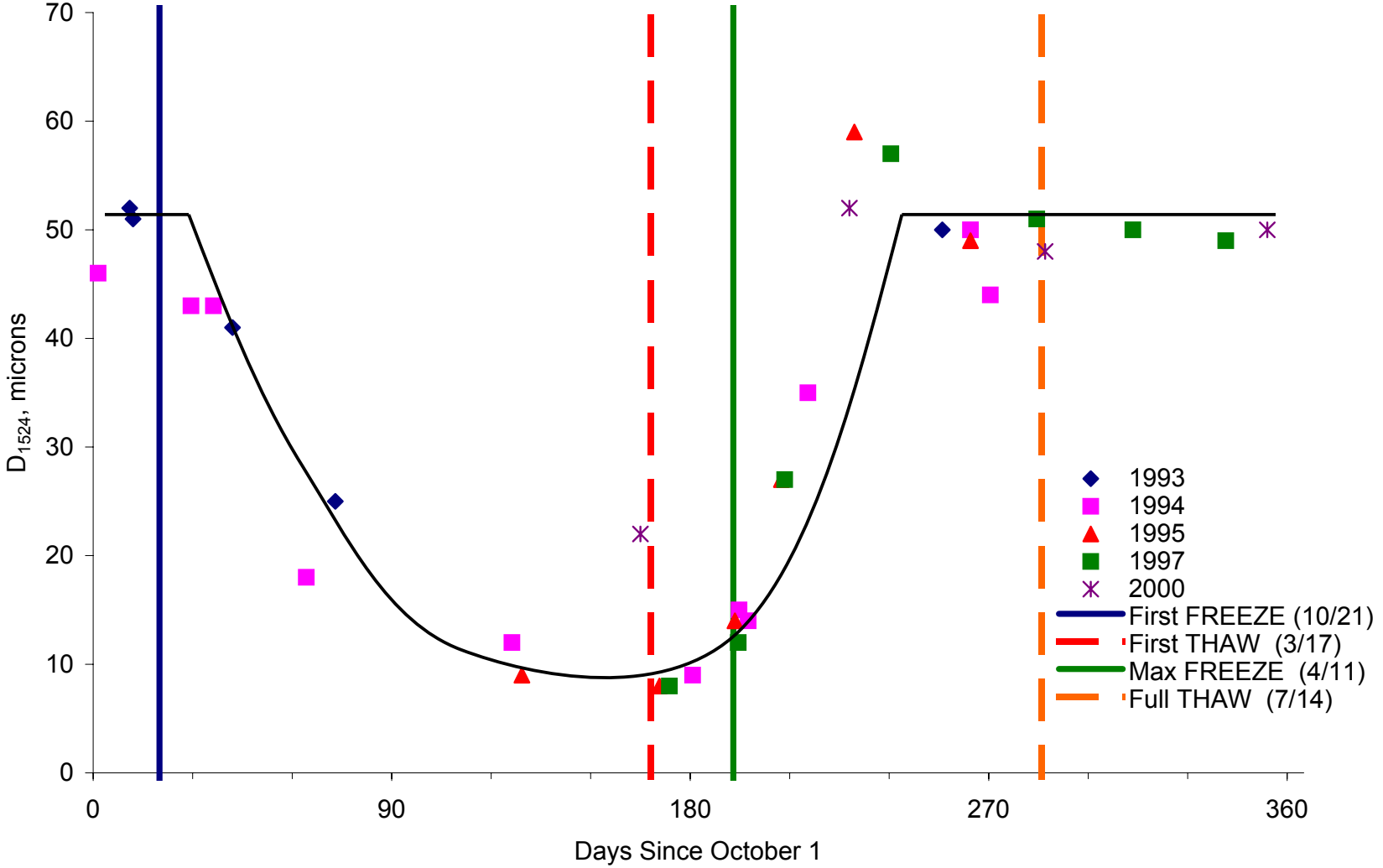

Figure O-20. Index D_{1524} at Site 83-1801 (Silty Sand)

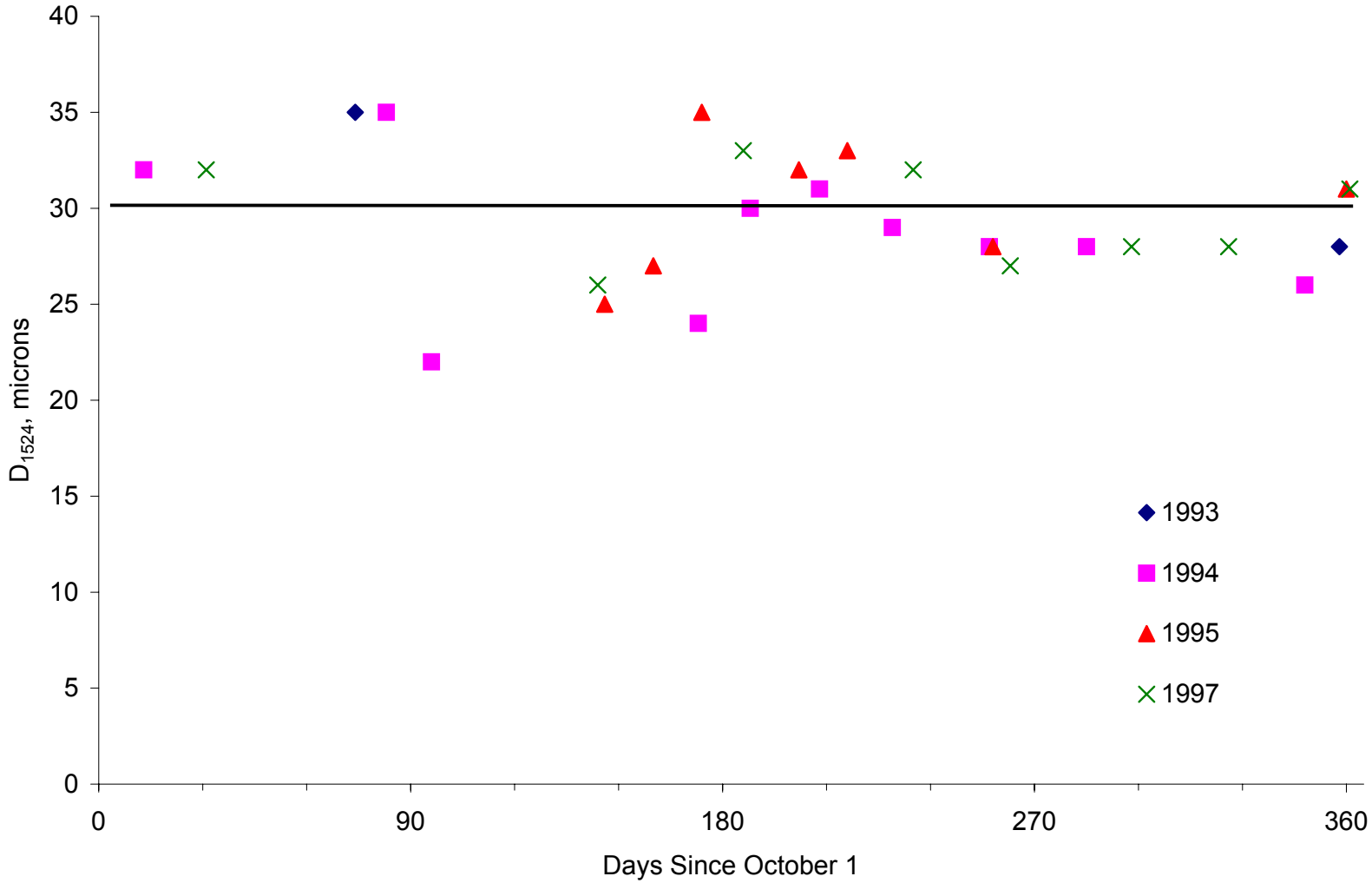

Figure O-21. Index D_{1524} at Site 87-1622 (Sandy Silt)

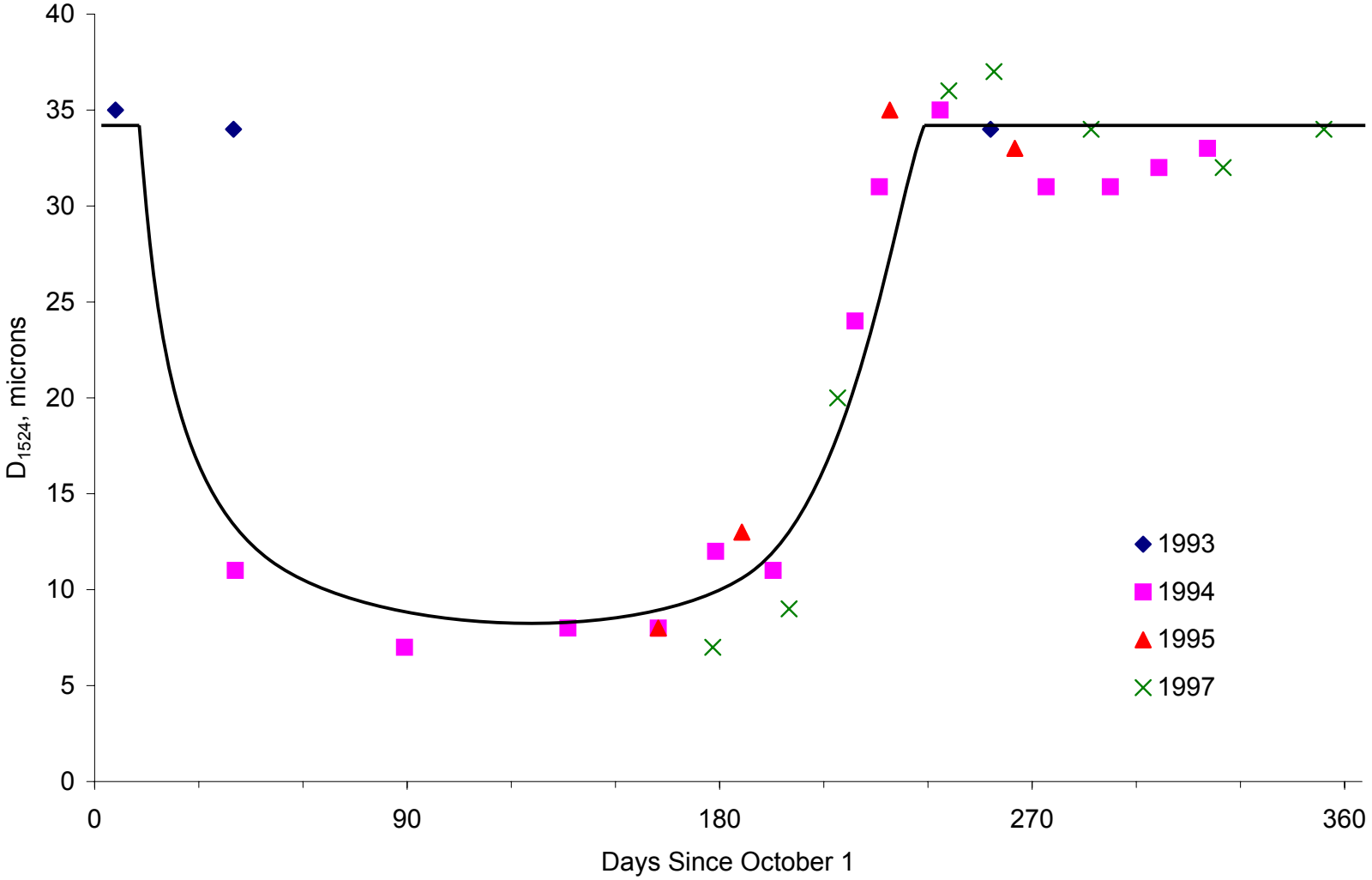

Figure O-22. Index D_{1524} at Site 90-6405 (Silty Sand)

APPENDIX P

SEASONAL VARIATIONS OF INDEX BCI

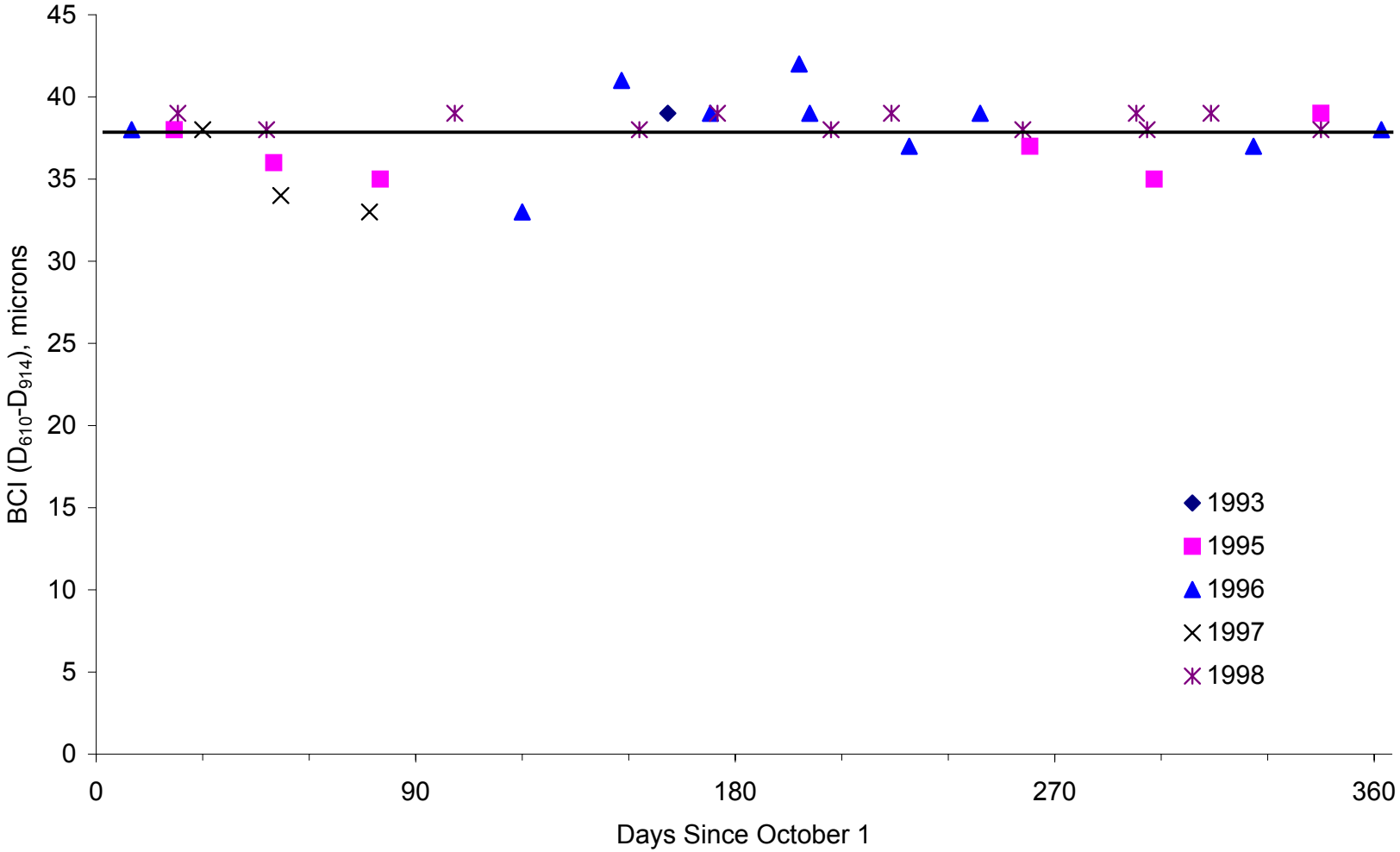

Figure P-1. Index BCI at Site 01-0101 (Sandy Silt)

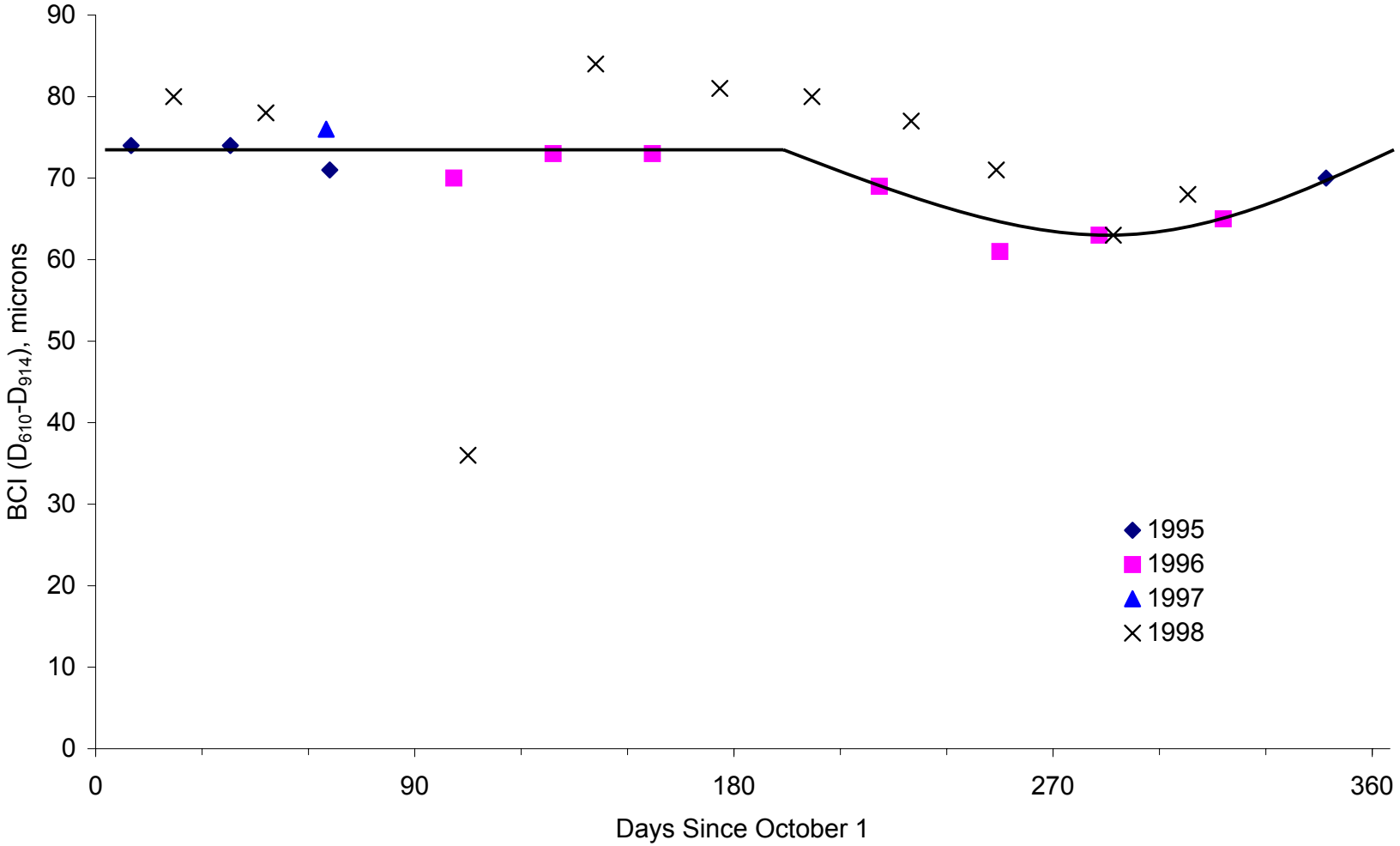

Figure P-2. Index BCI at Site 04-0113 (Well Graded Sand with Silt and Gravel)

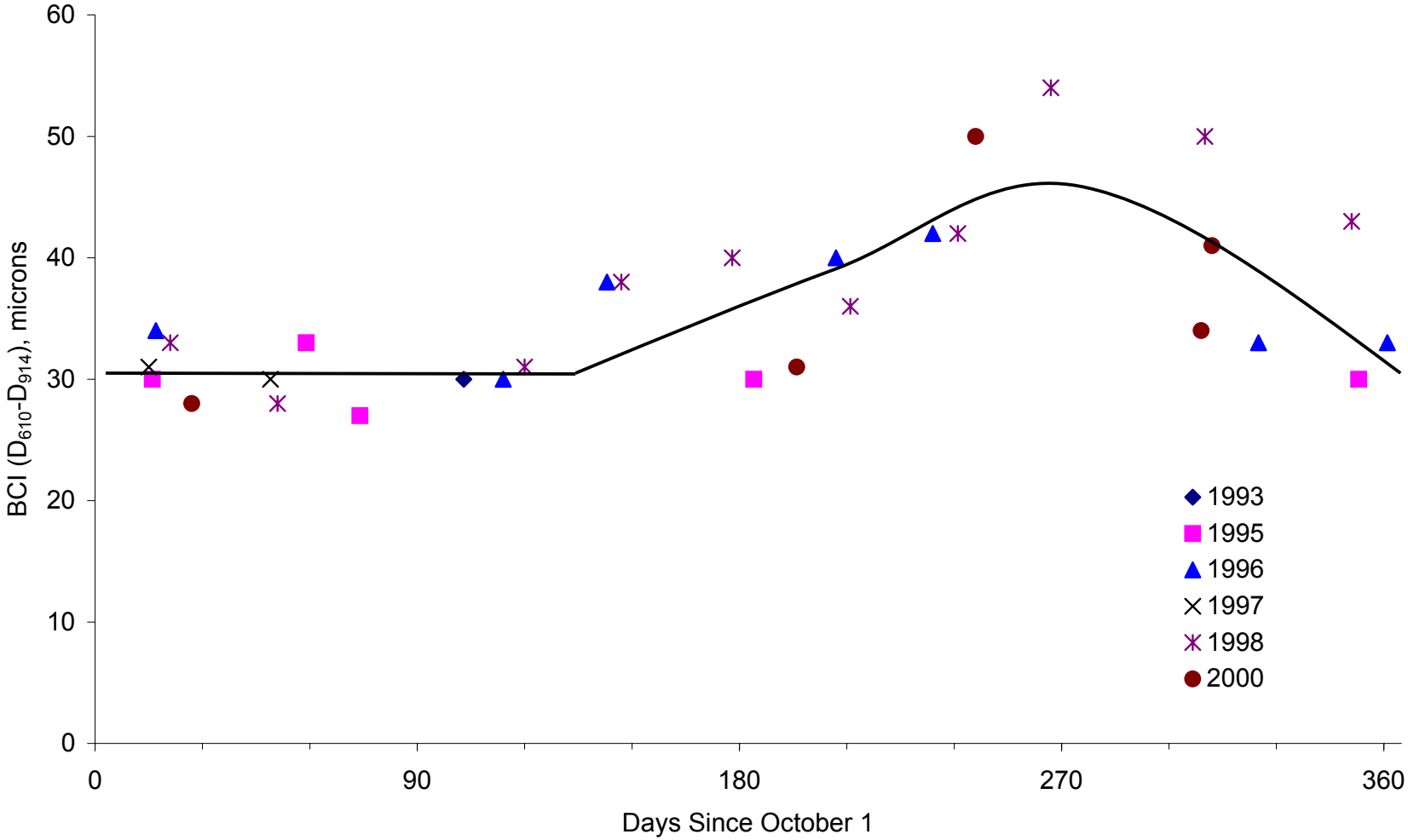

Figure P-3. Index BCI at Site 13-1031 (Silty Sand)

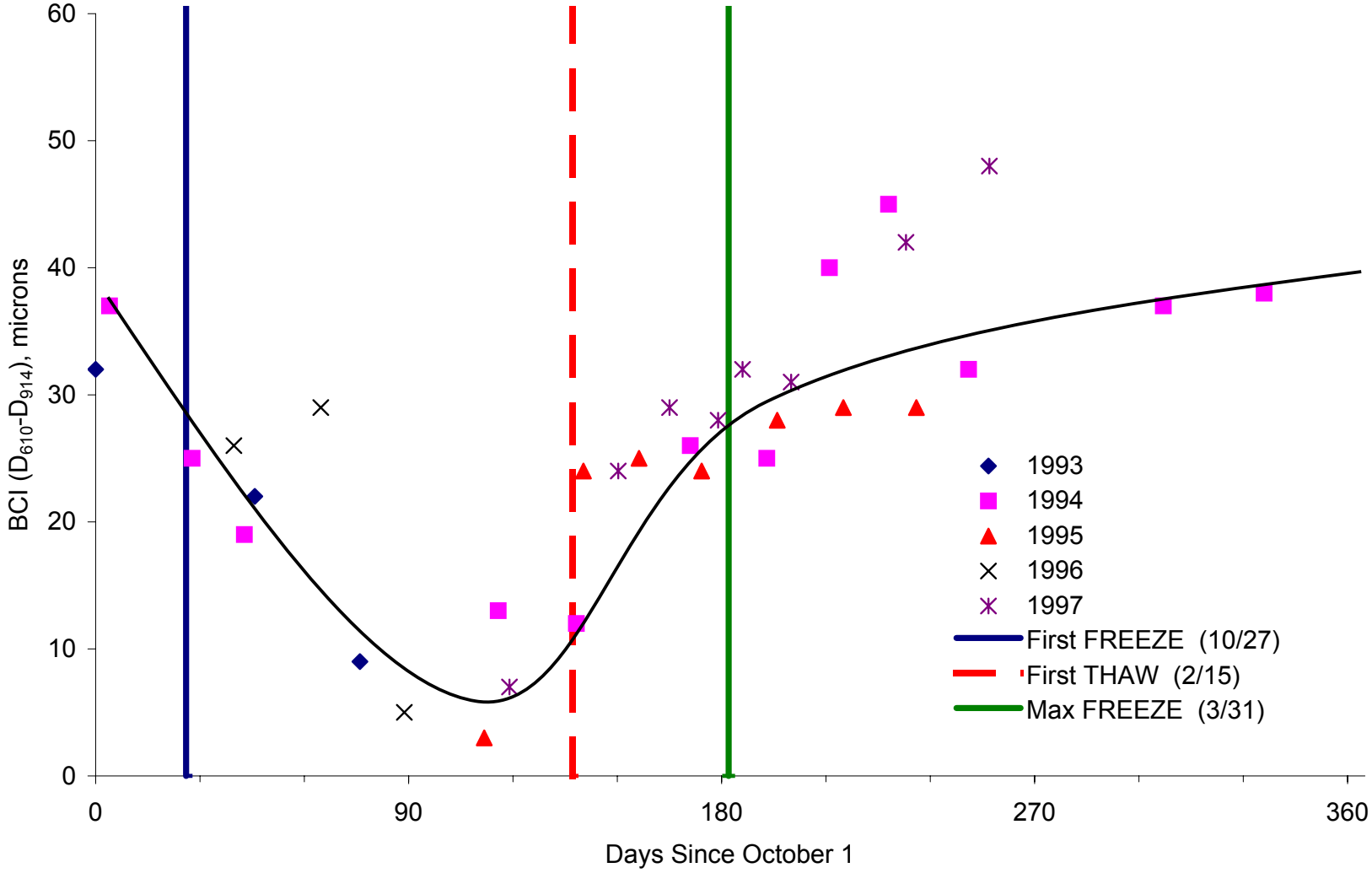

Figure P-4. Index BCI at Site 16-1010 (Silty Sand)

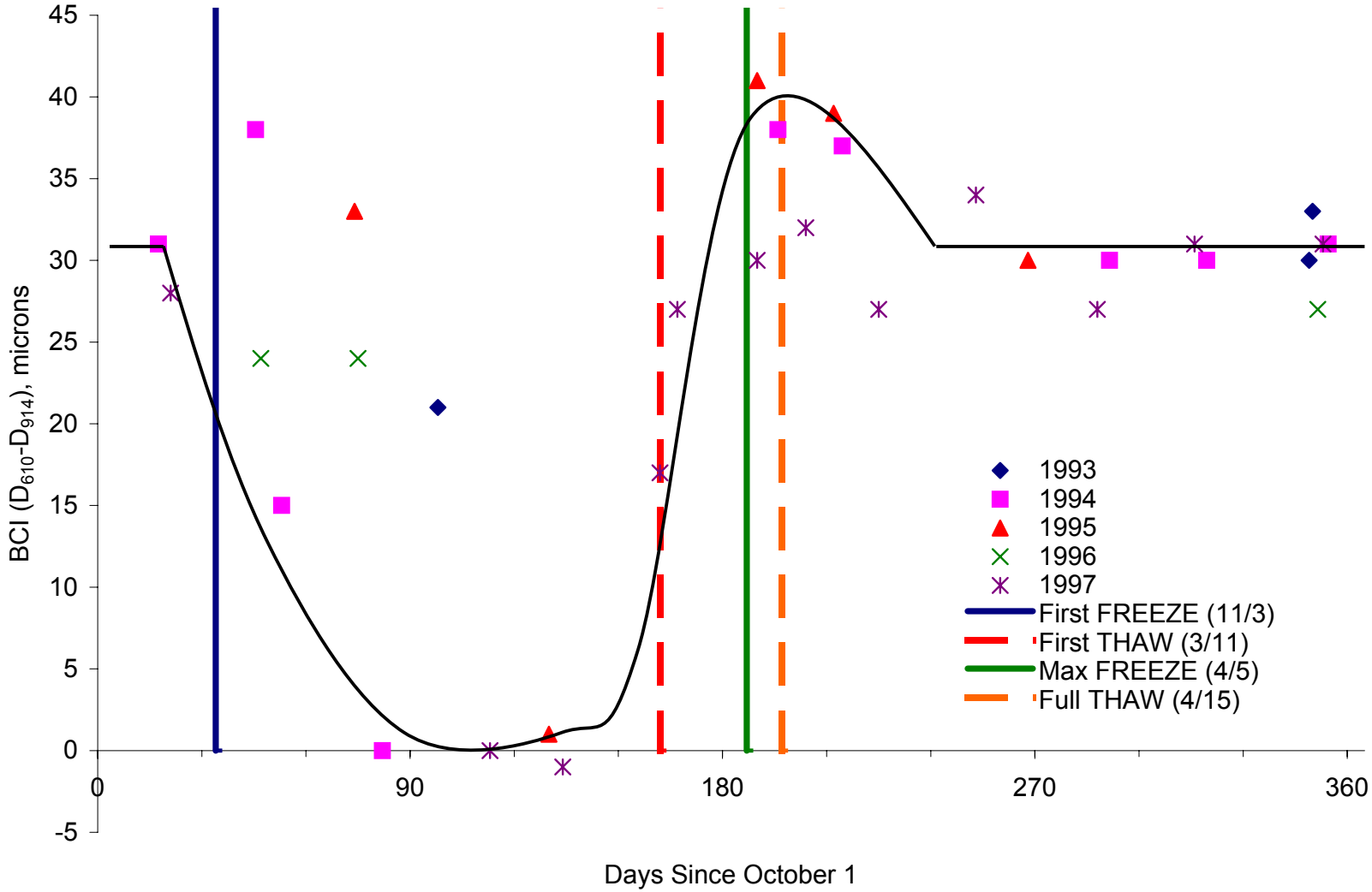

Figure P-5. Index BCI at Site 23-1026 (Silty Sand with Gravel)

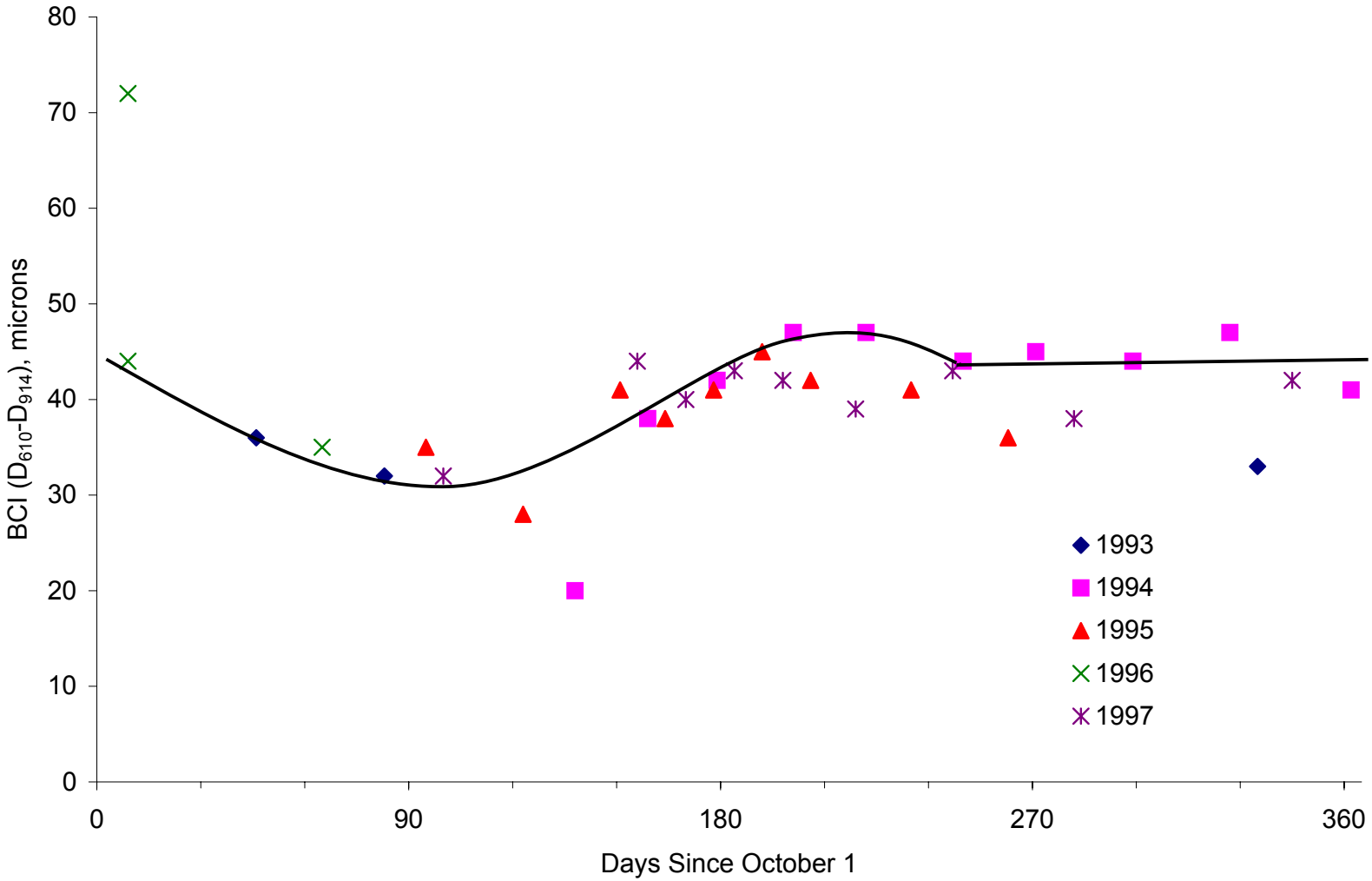

Figure P-6. Index BCI at Site 25-1002 (Poorly Graded Sand with Silt)

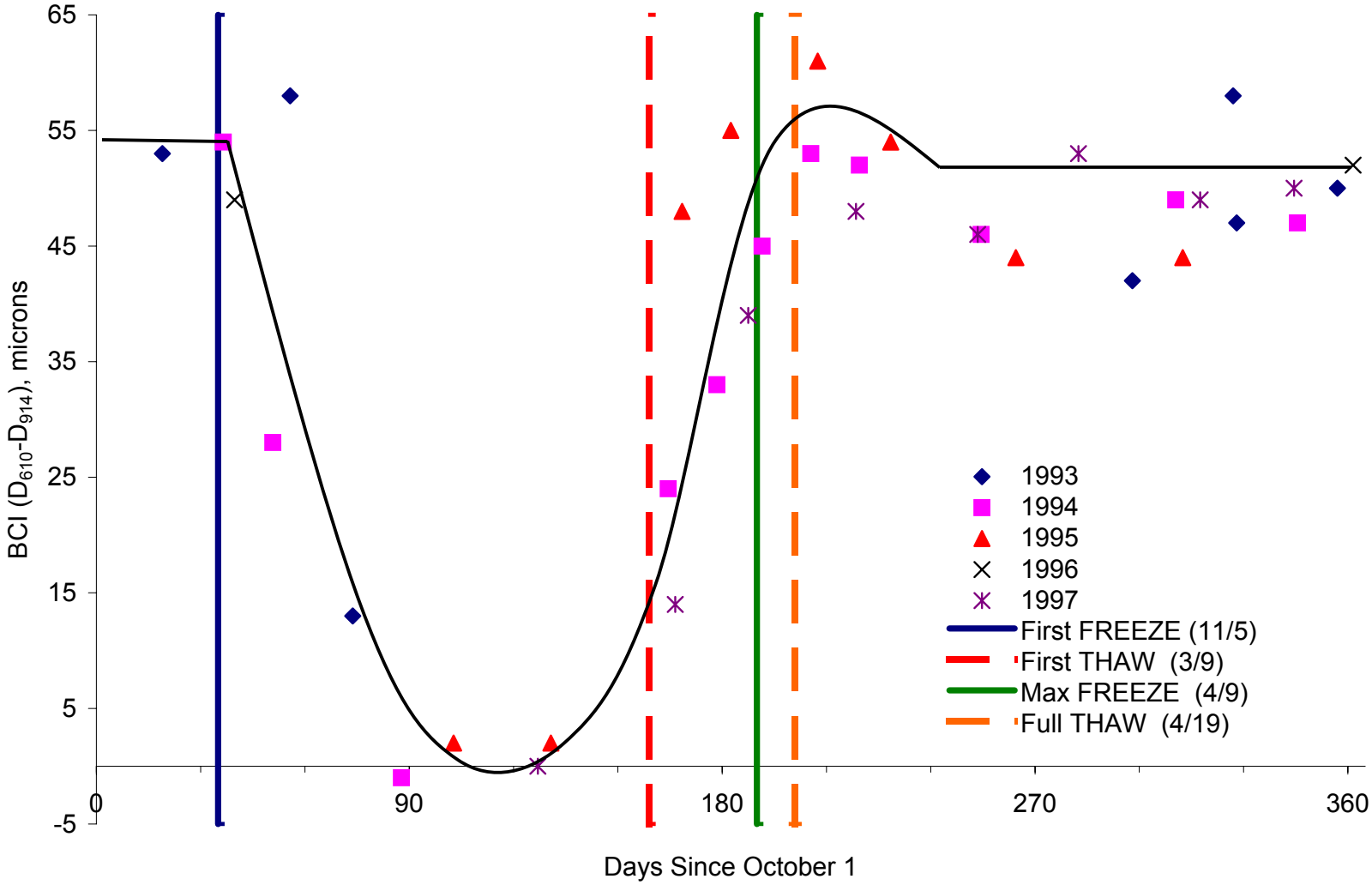

Figure P-7. Index BCI at Site 27-1018 (Poorly Graded Sand with Silt)

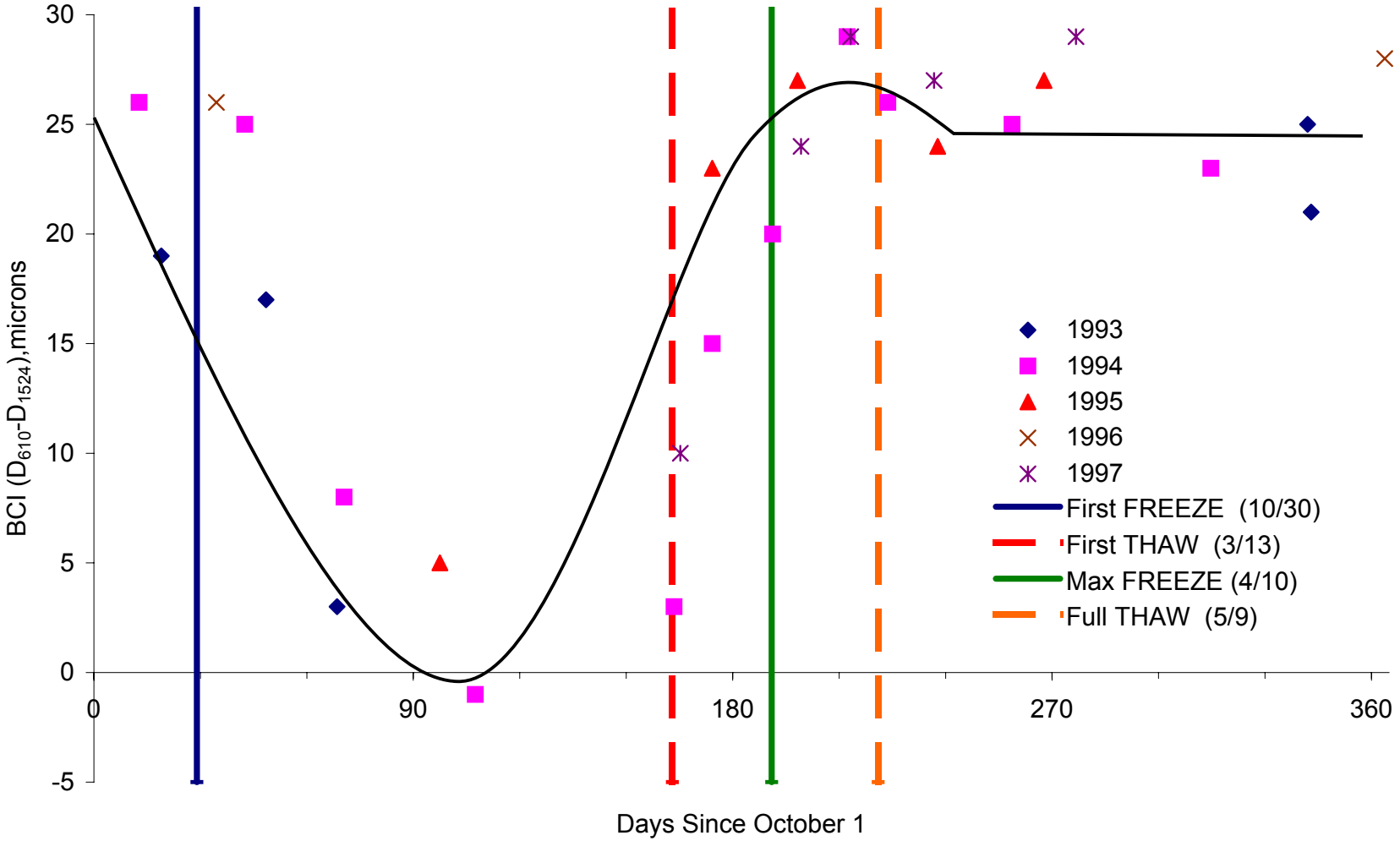

Figure P-8. Index BCI at Site 27-1028 (Poorly Graded Sand with Silt)

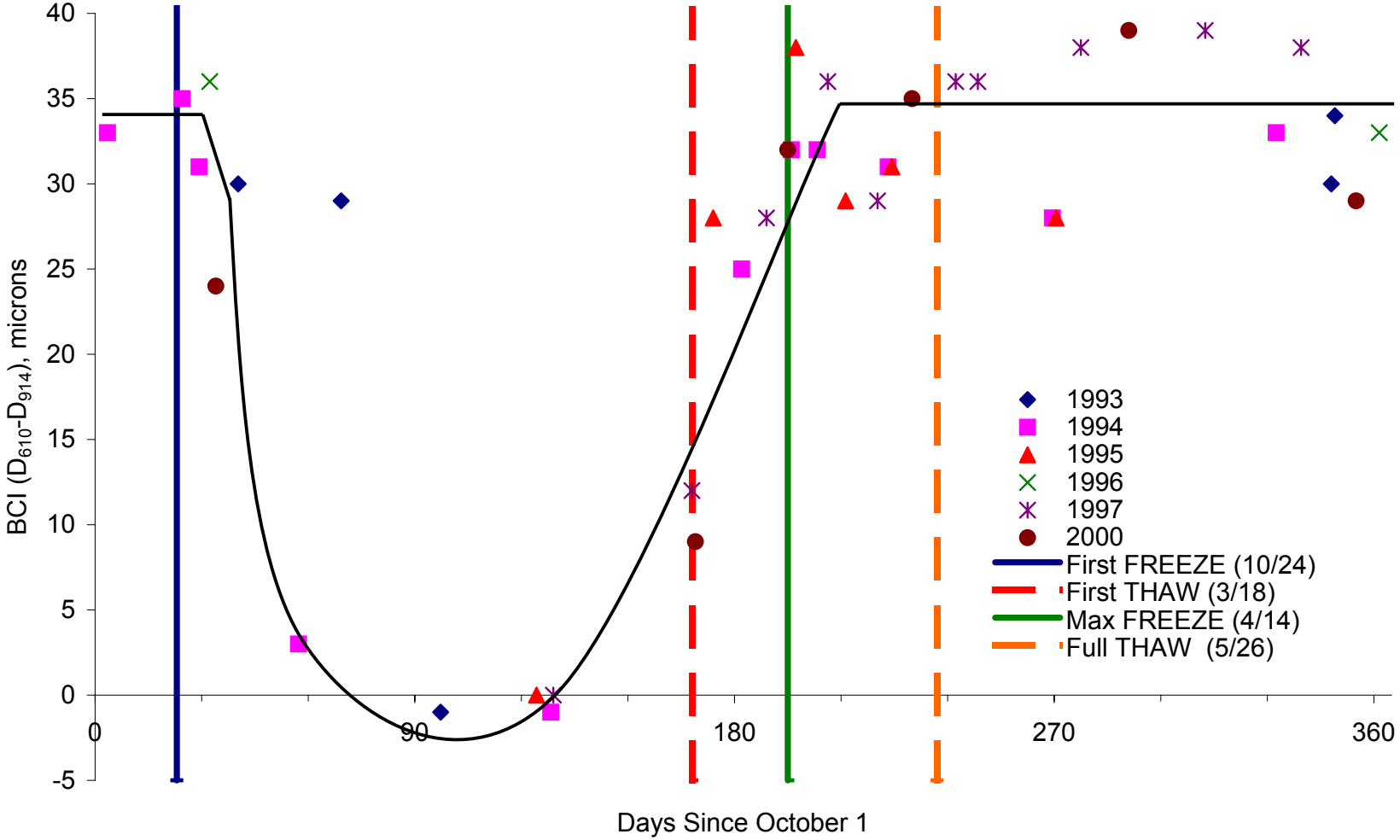

Figure P-9. Index BCI at Site 27-6251 (Poorly Graded Sand with Silt)

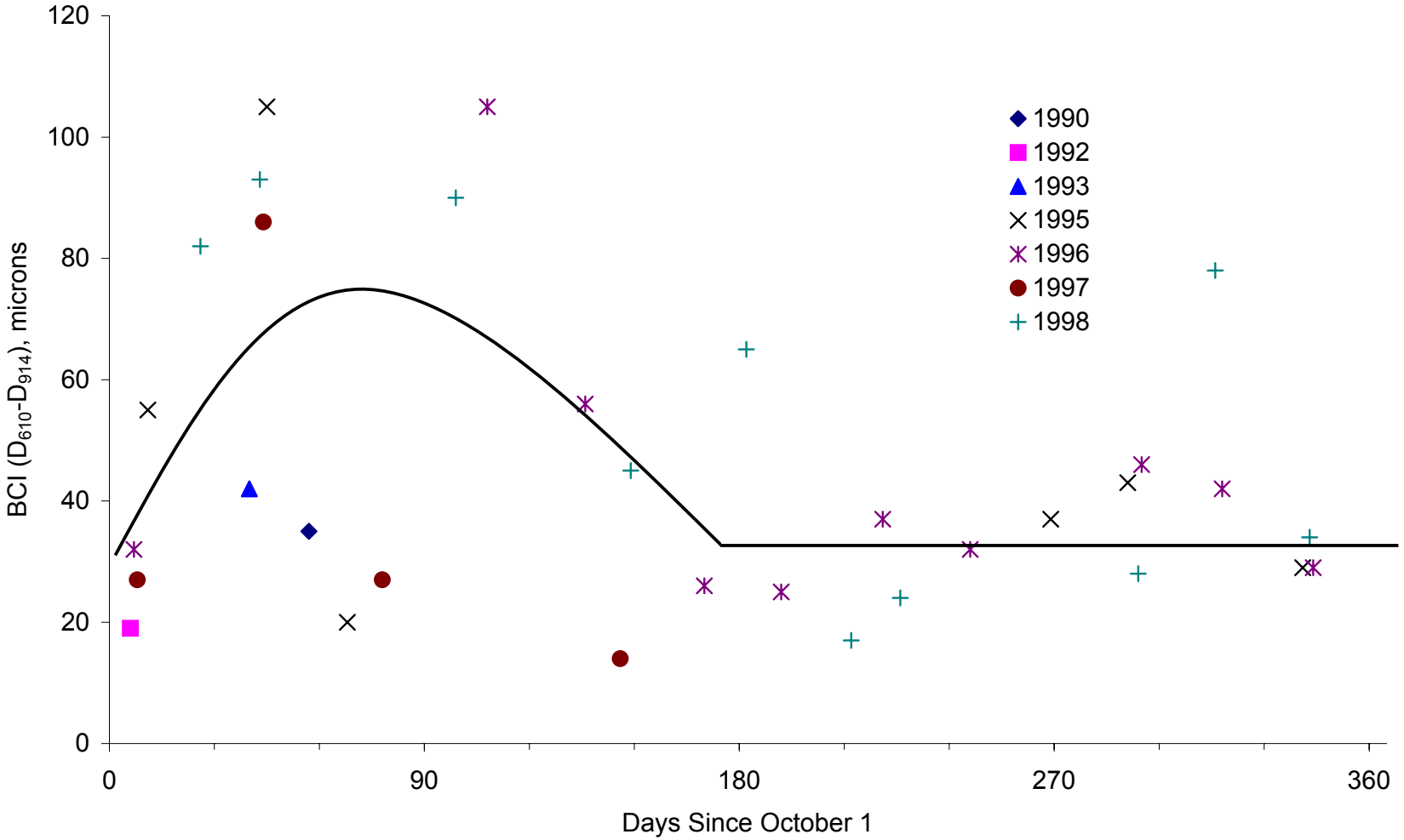

Figure P-10. Index BCI at Site 28-1802 (Poorly Graded Sand)

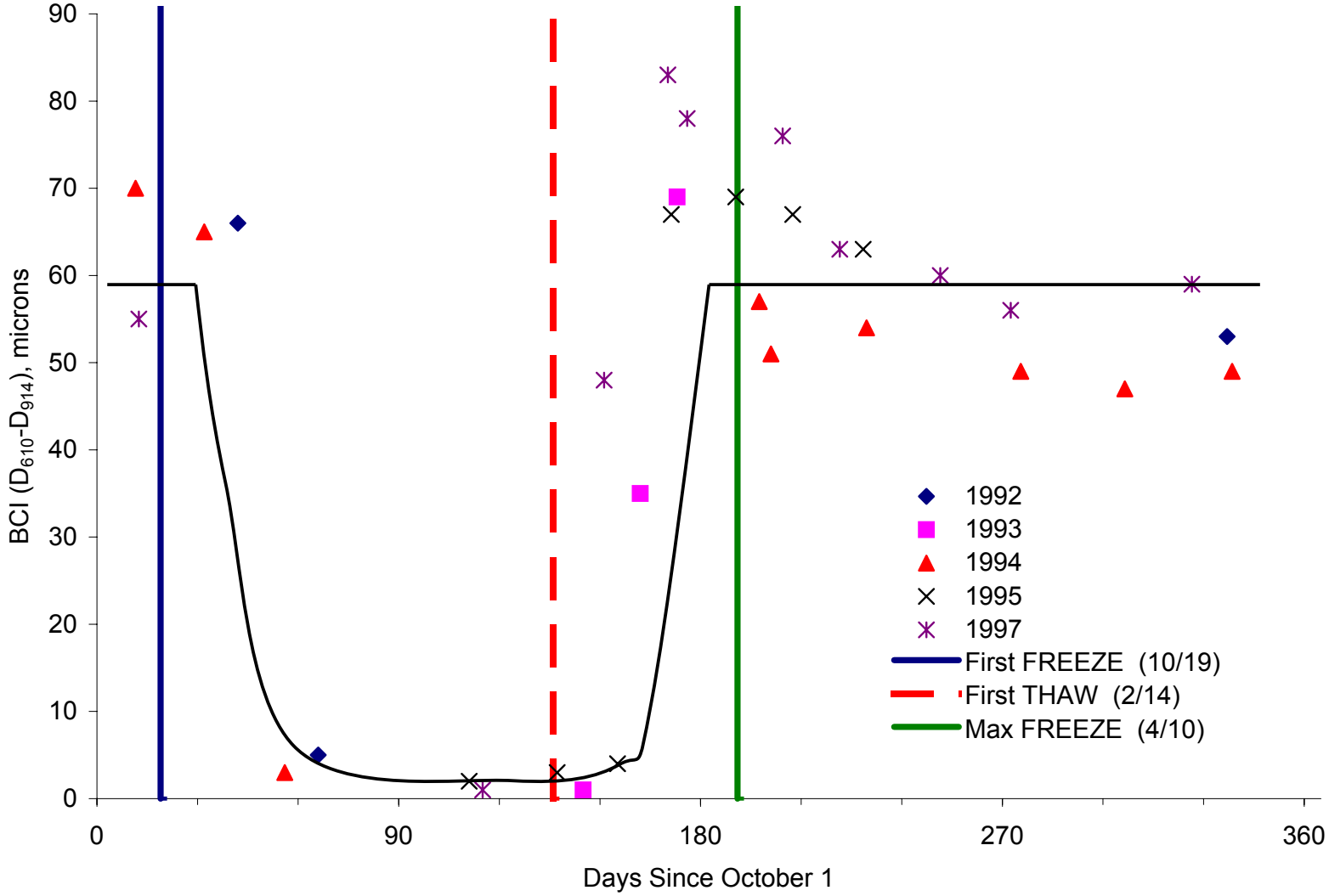

Figure P-11. Index BCI at Site 30-8129 (Poorly Graded Sand with Silt)

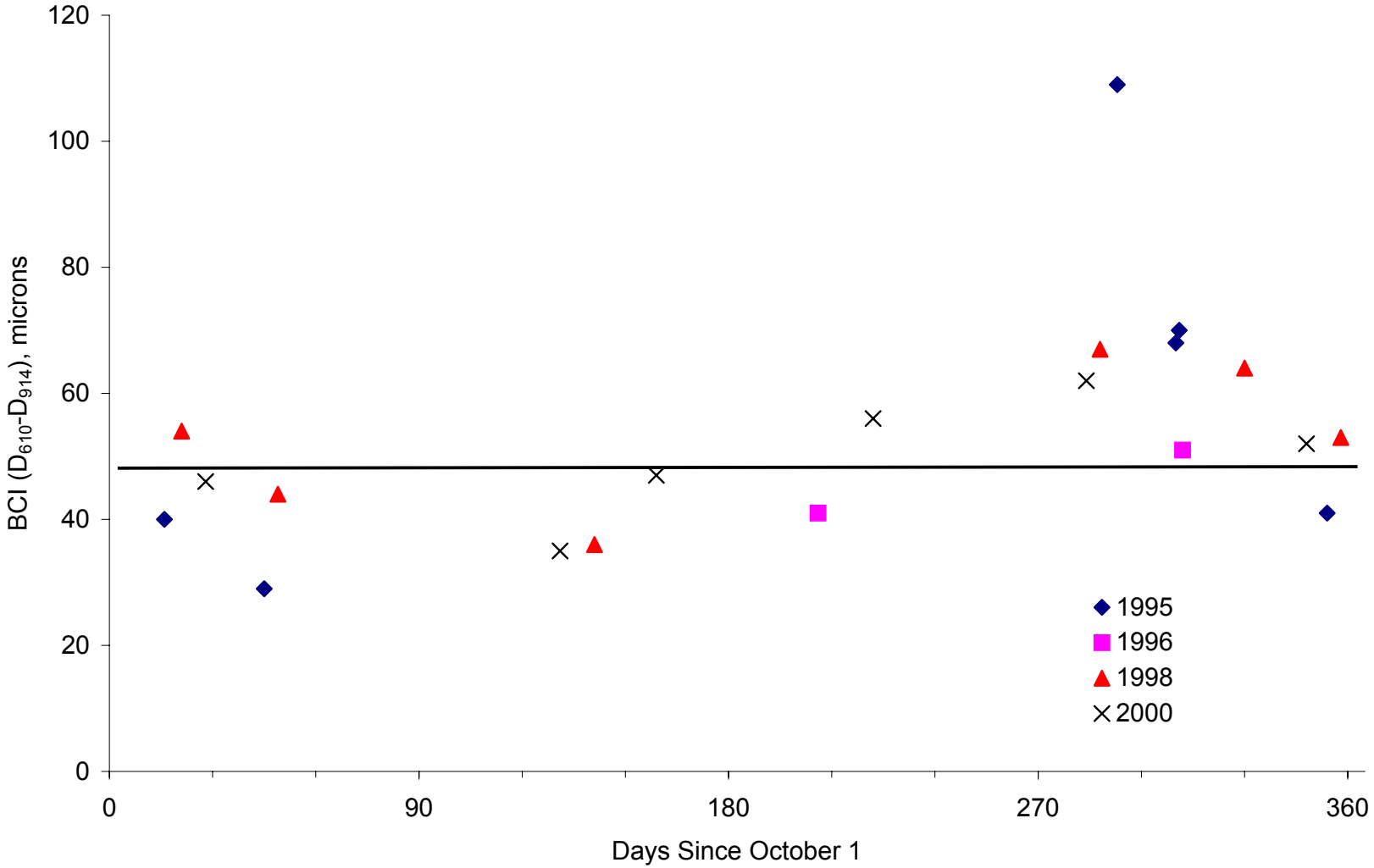

Figure P-12. Index BCI at Site 31-0114 (Silty Clay)

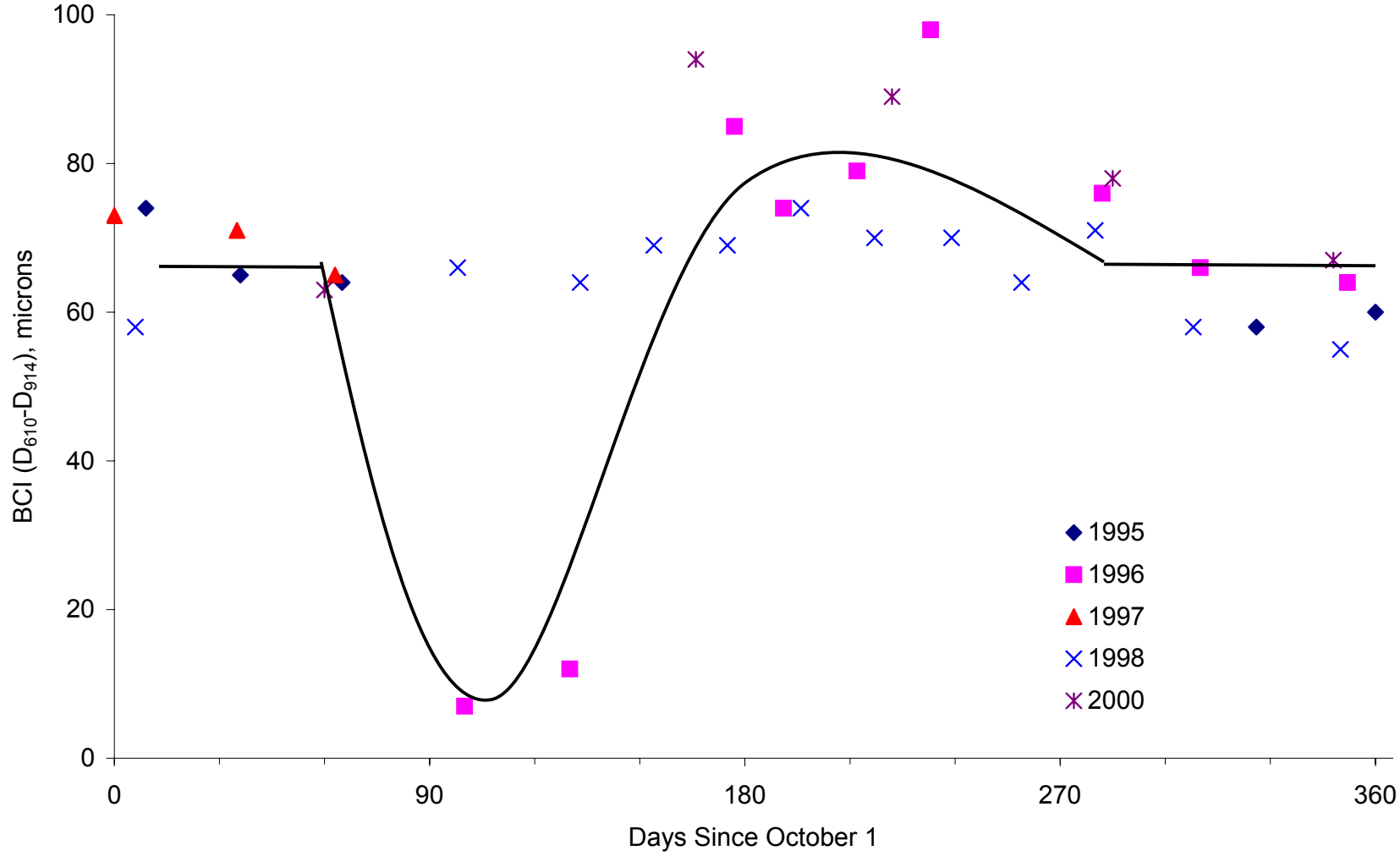

Figure P-13. Index BCI at Site 36-0801 (Silty Sand)

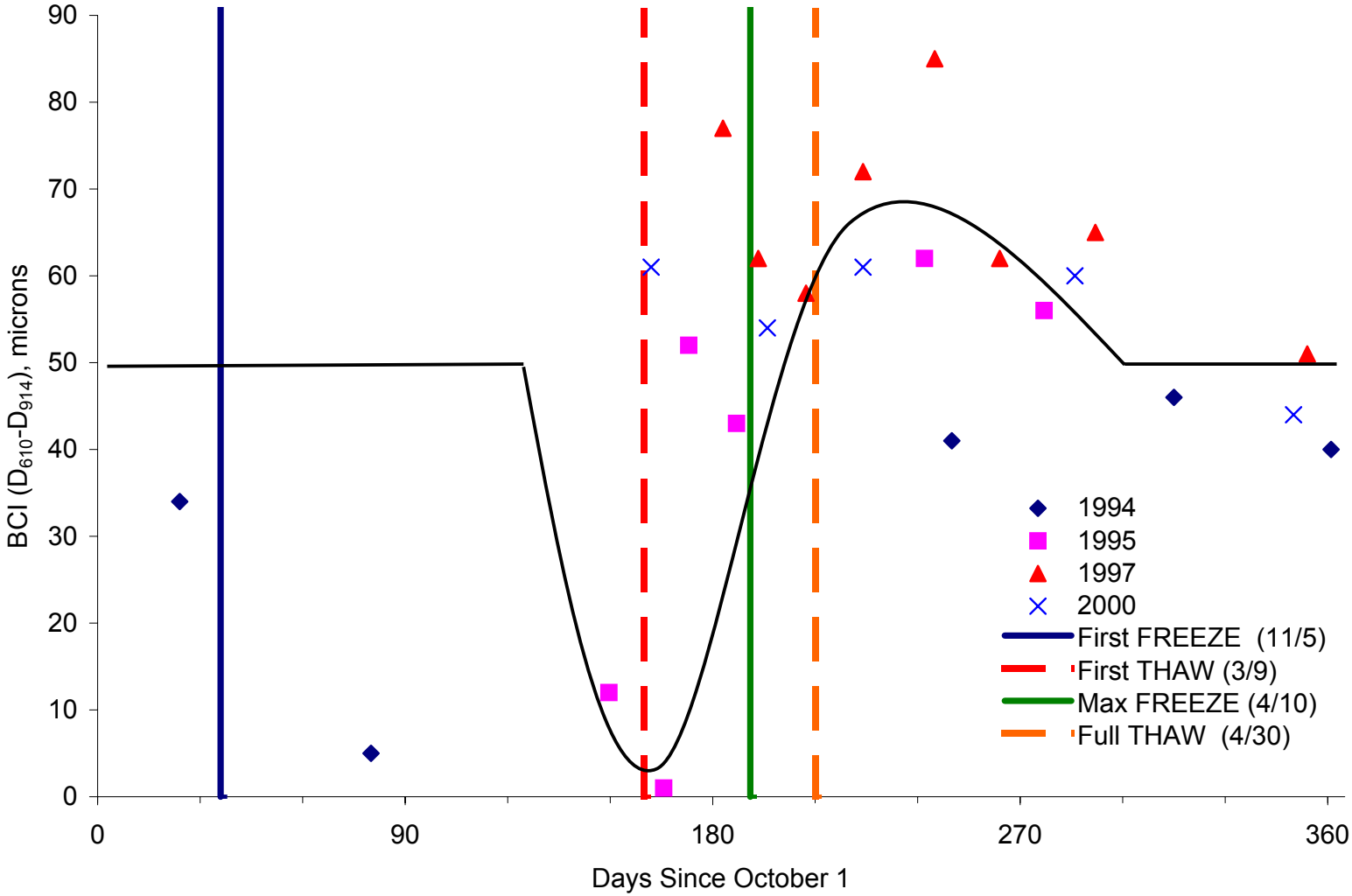

Figure P-14. Index BCI at Site 46-0804 (Silty Clay)

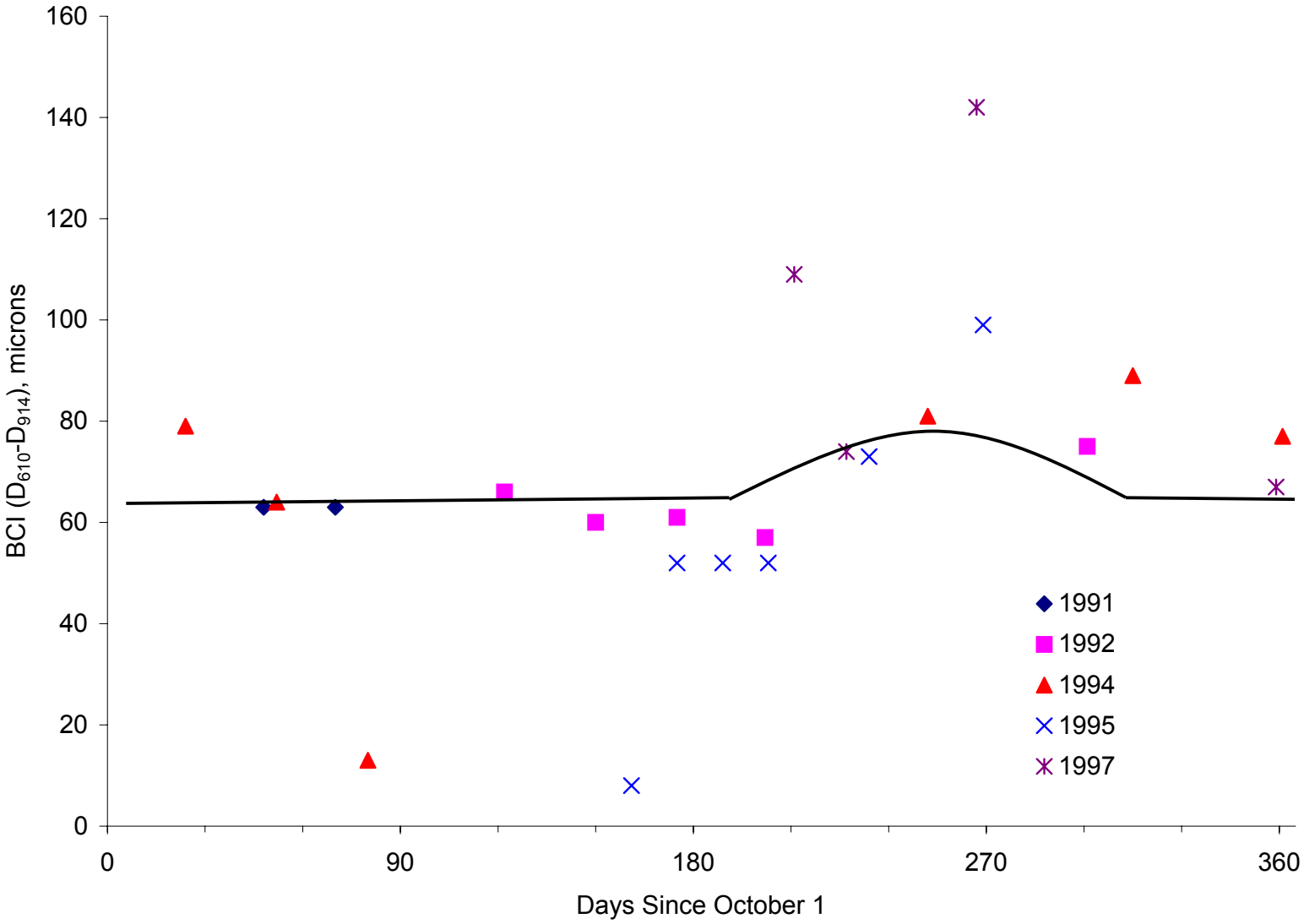

Figure P-15. Index BCI at Site 46-9187 (Lean Inorganic Clay)

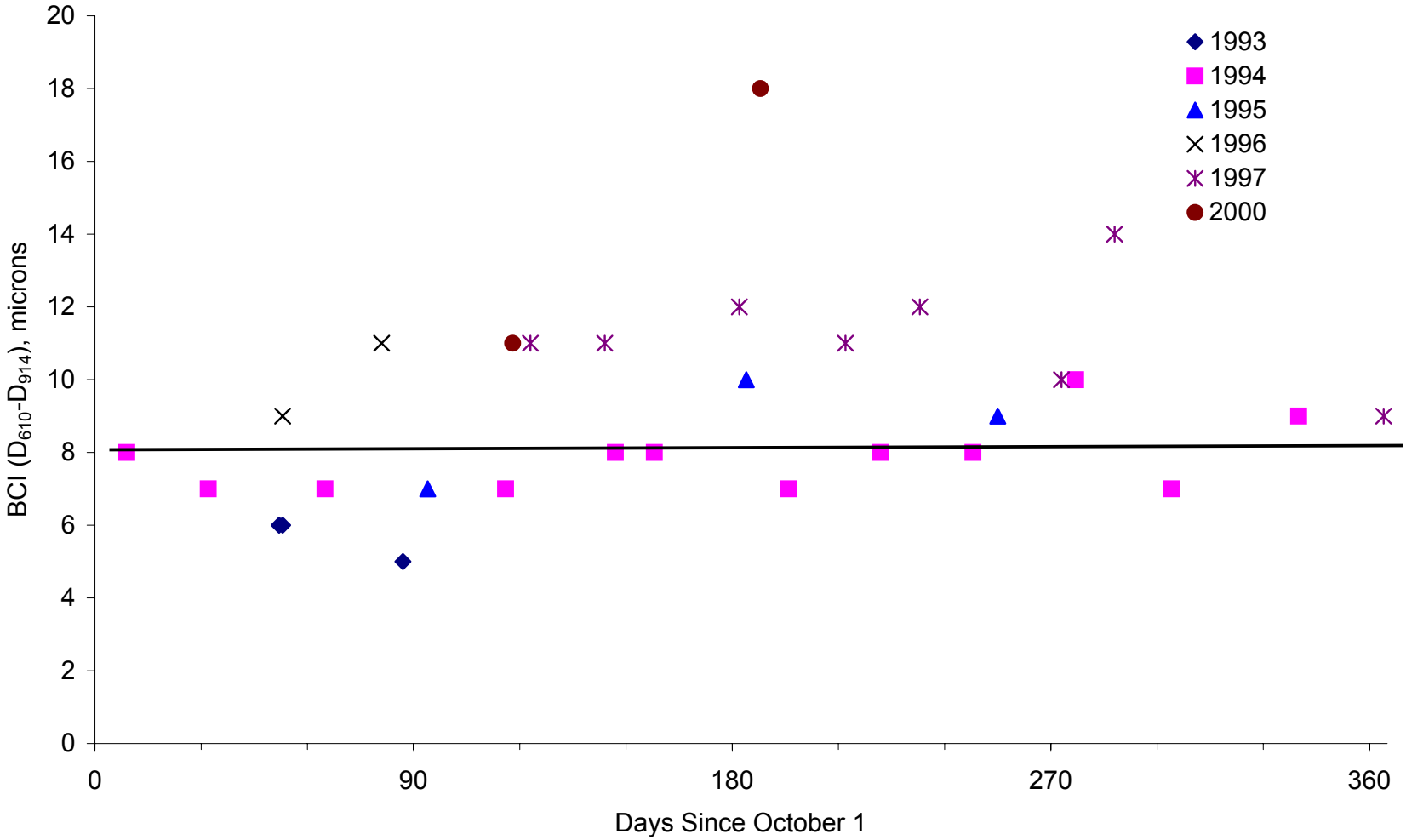

Figure P-16. Index BCI at Site 48-1122 (Clayey Sand)

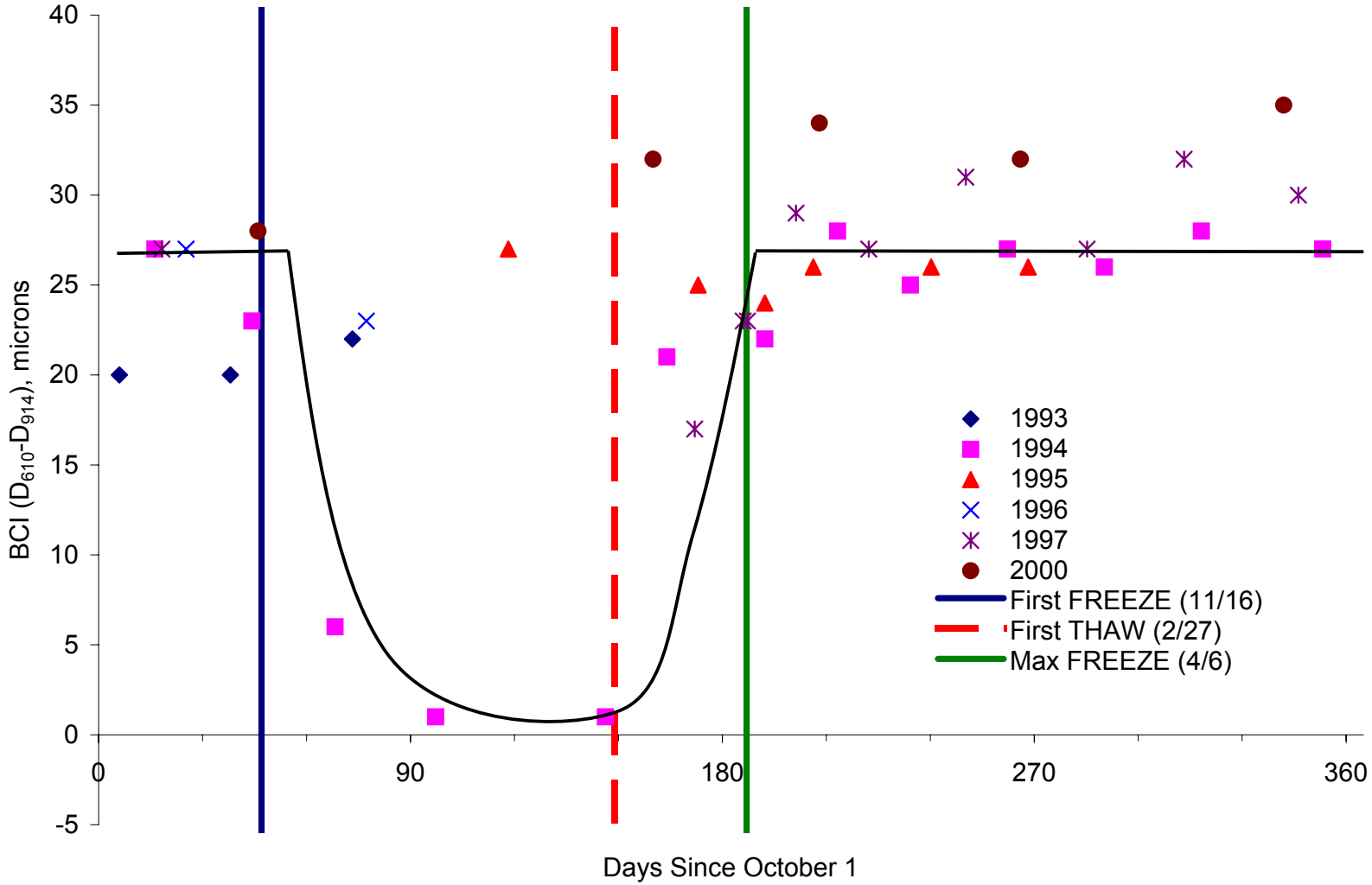

Figure P-17. Index BCI at Site 50-1002 (Poorly Graded Gravel with Silt and Sand)

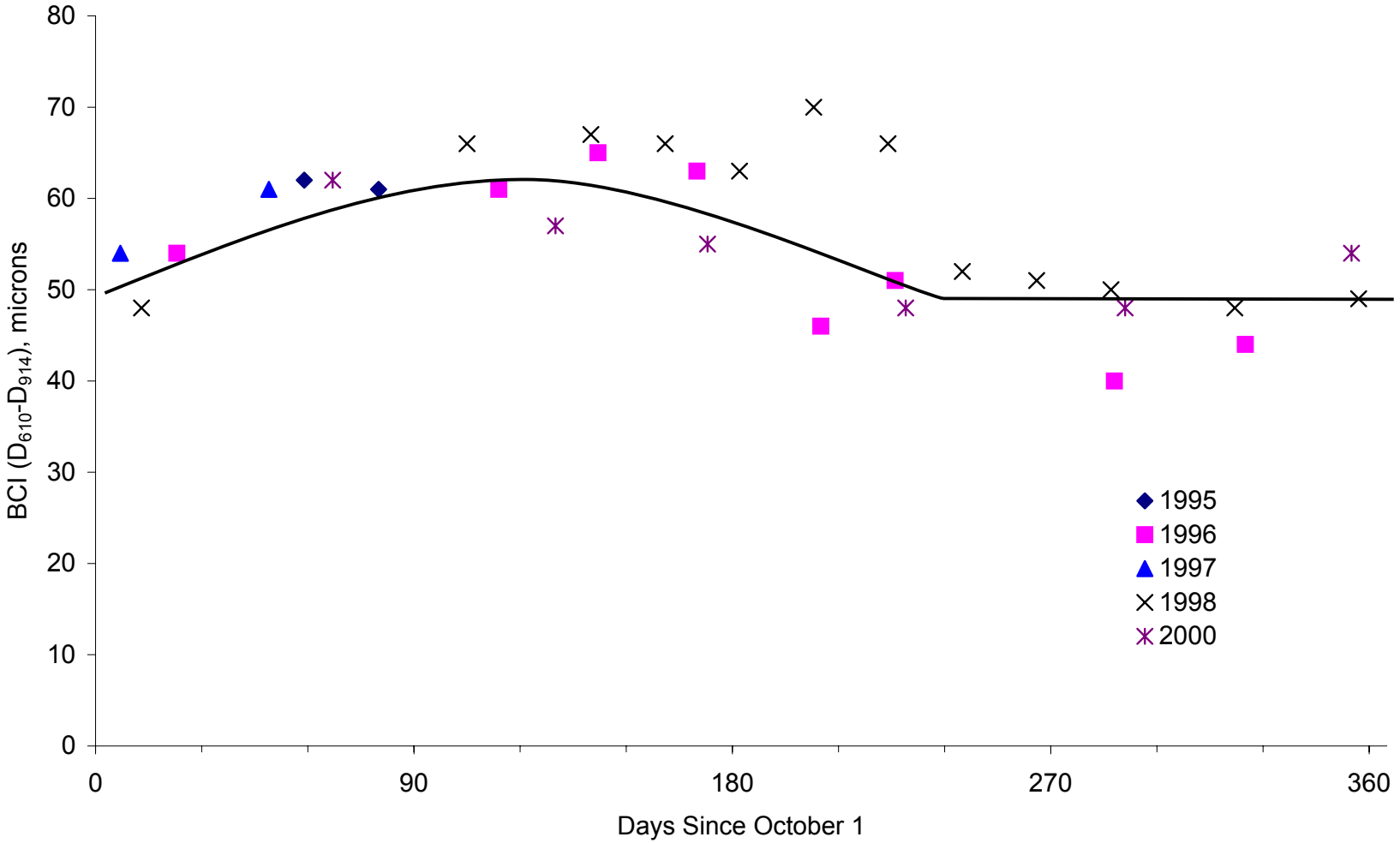

Figure P-18. Index BCI at Site 51-0113 (Silt)

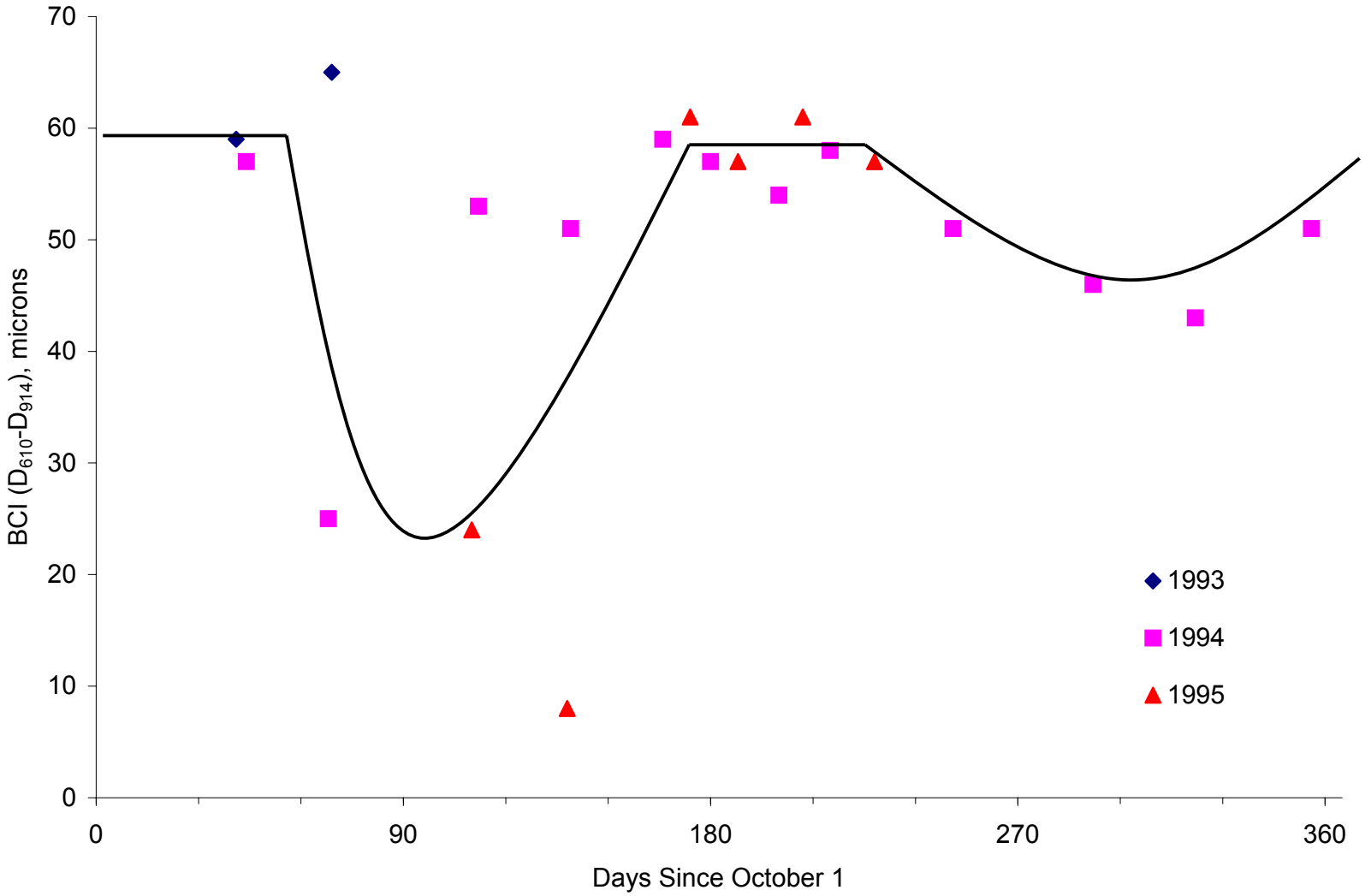

Figure P-19. Index BCI at Site 56-1007 (Silty Sand with Gravel)

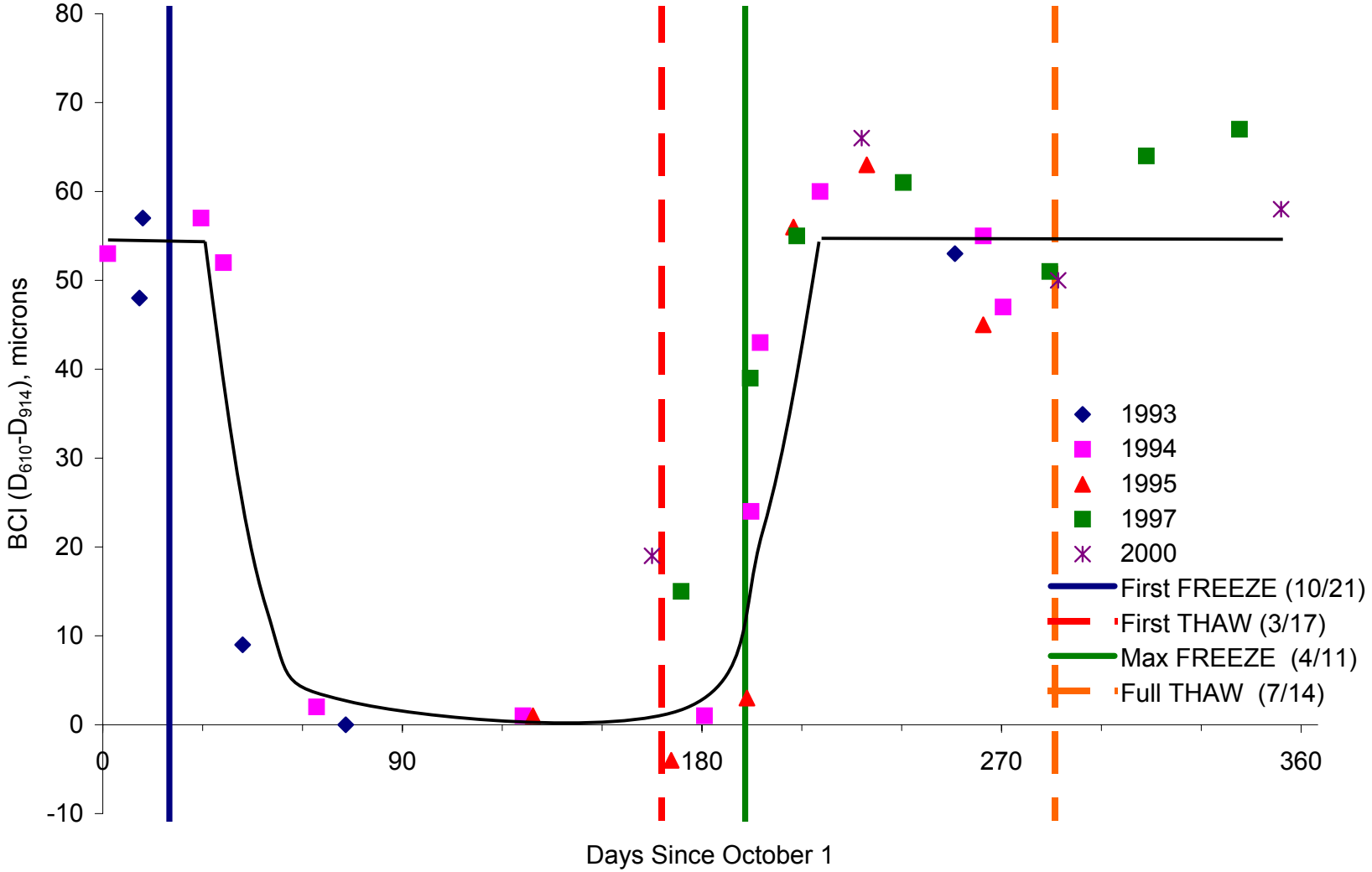

Figure P-20. Index BCI at Site 83-1801 (Silty Sand)

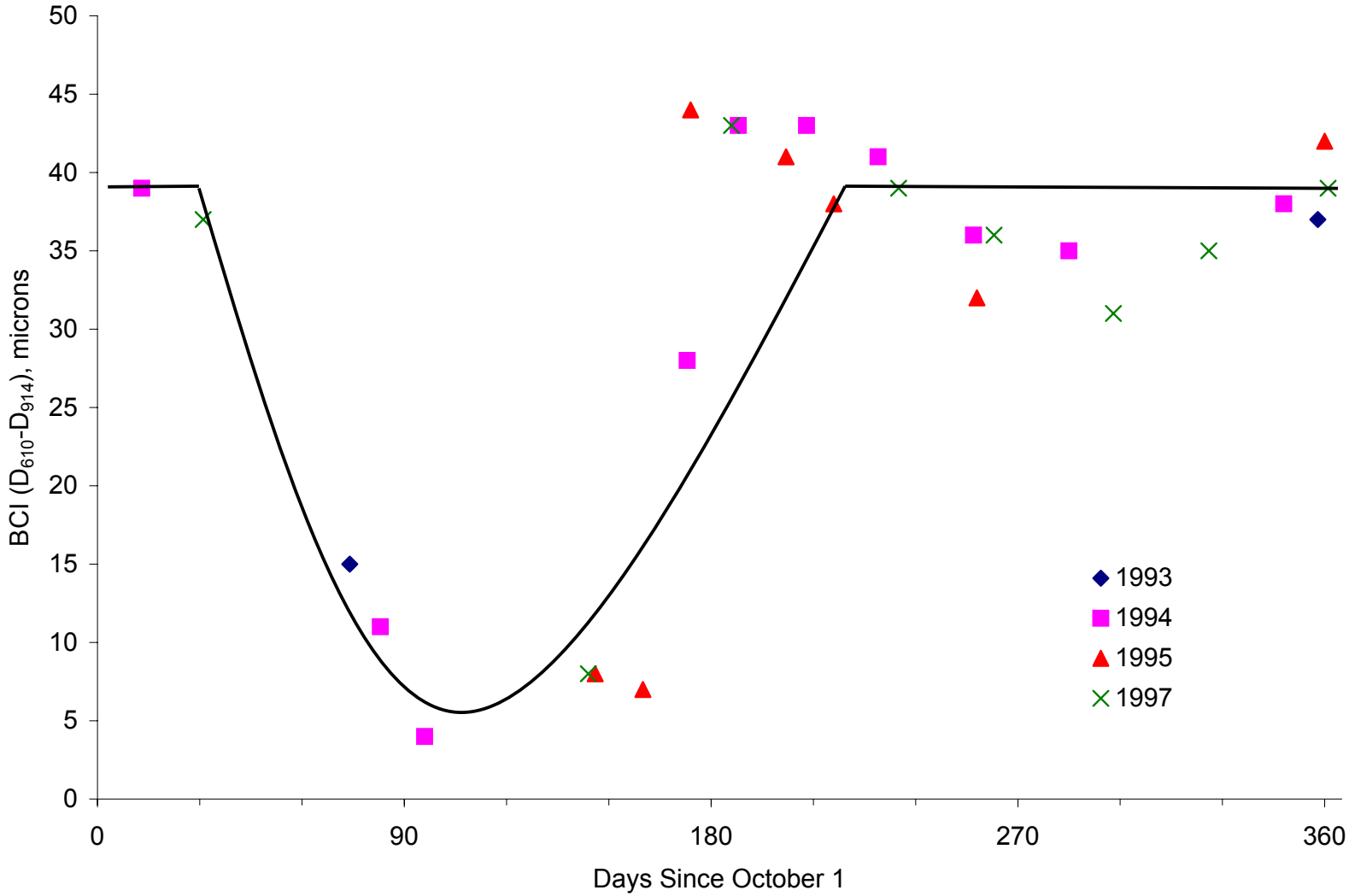

Figure P-21. Index BCI at Site 87-1622 (Sandy Silt)

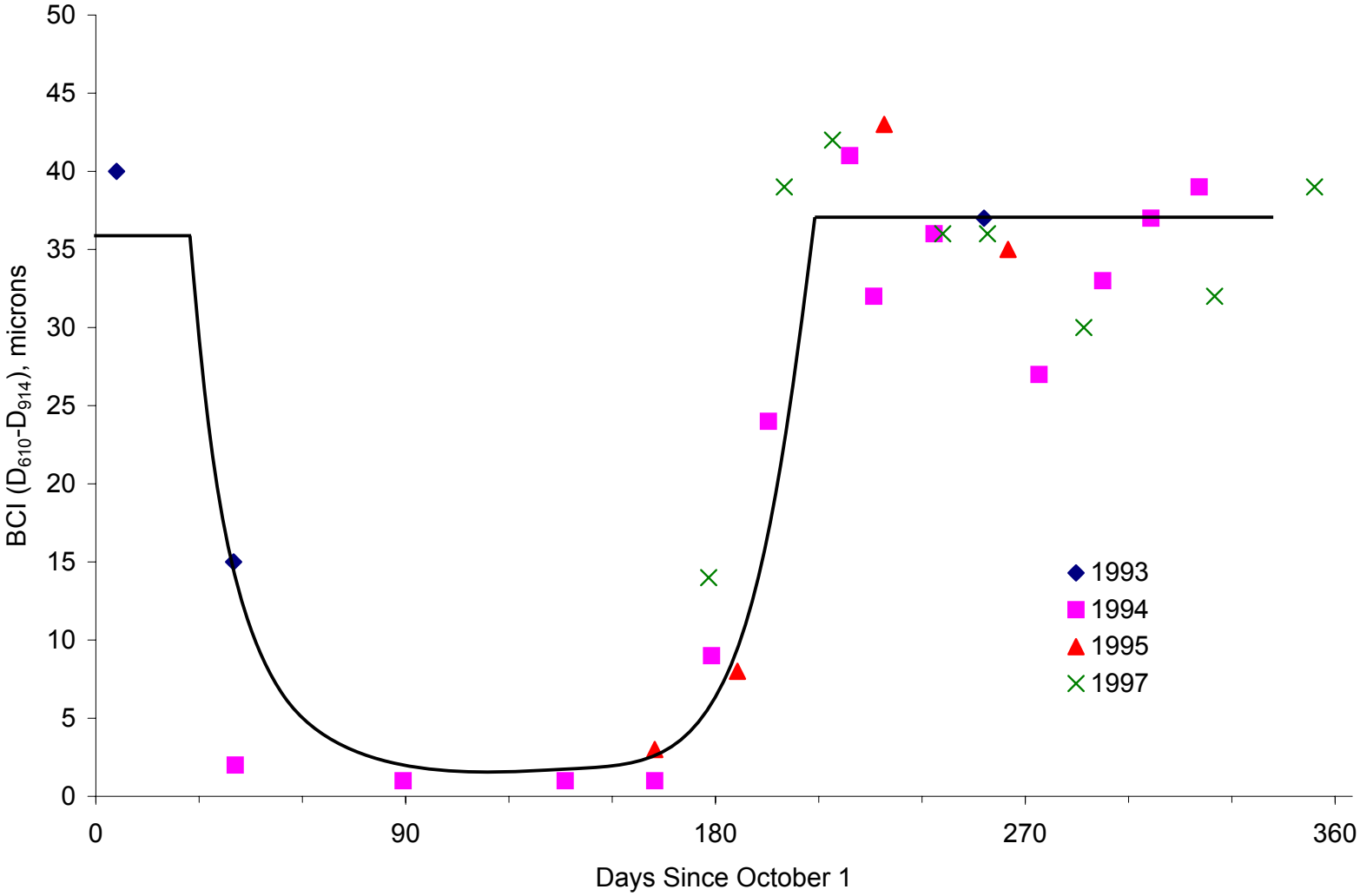

Figure P-22. Index BCI at Site 90-6405 (Silty Sand)

APPENDIX Q

SEASONAL VARIATIONS OF INDEX SDI

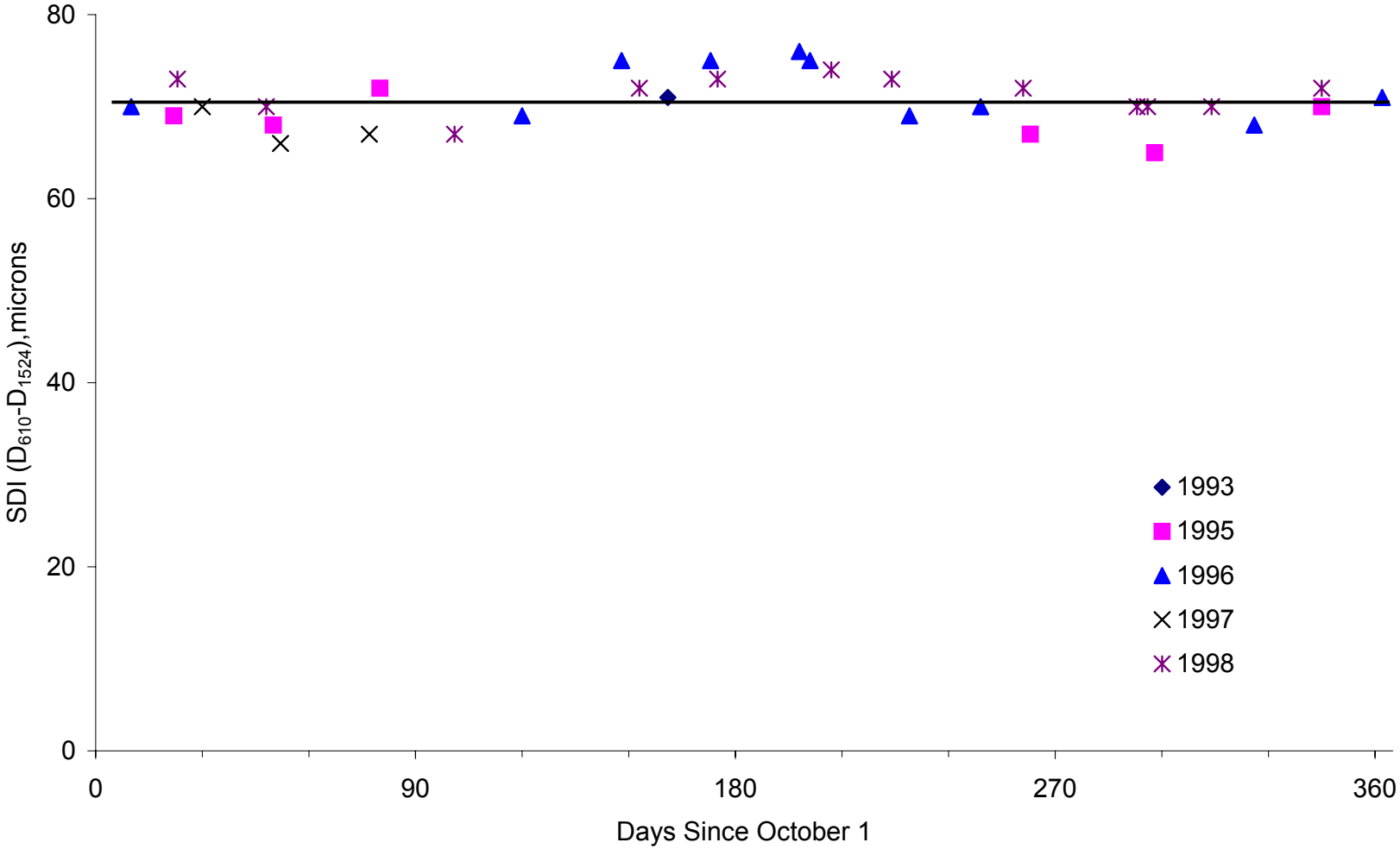

Figure Q-1. Index SDI at Site 01-0101 (Sandy Silt)

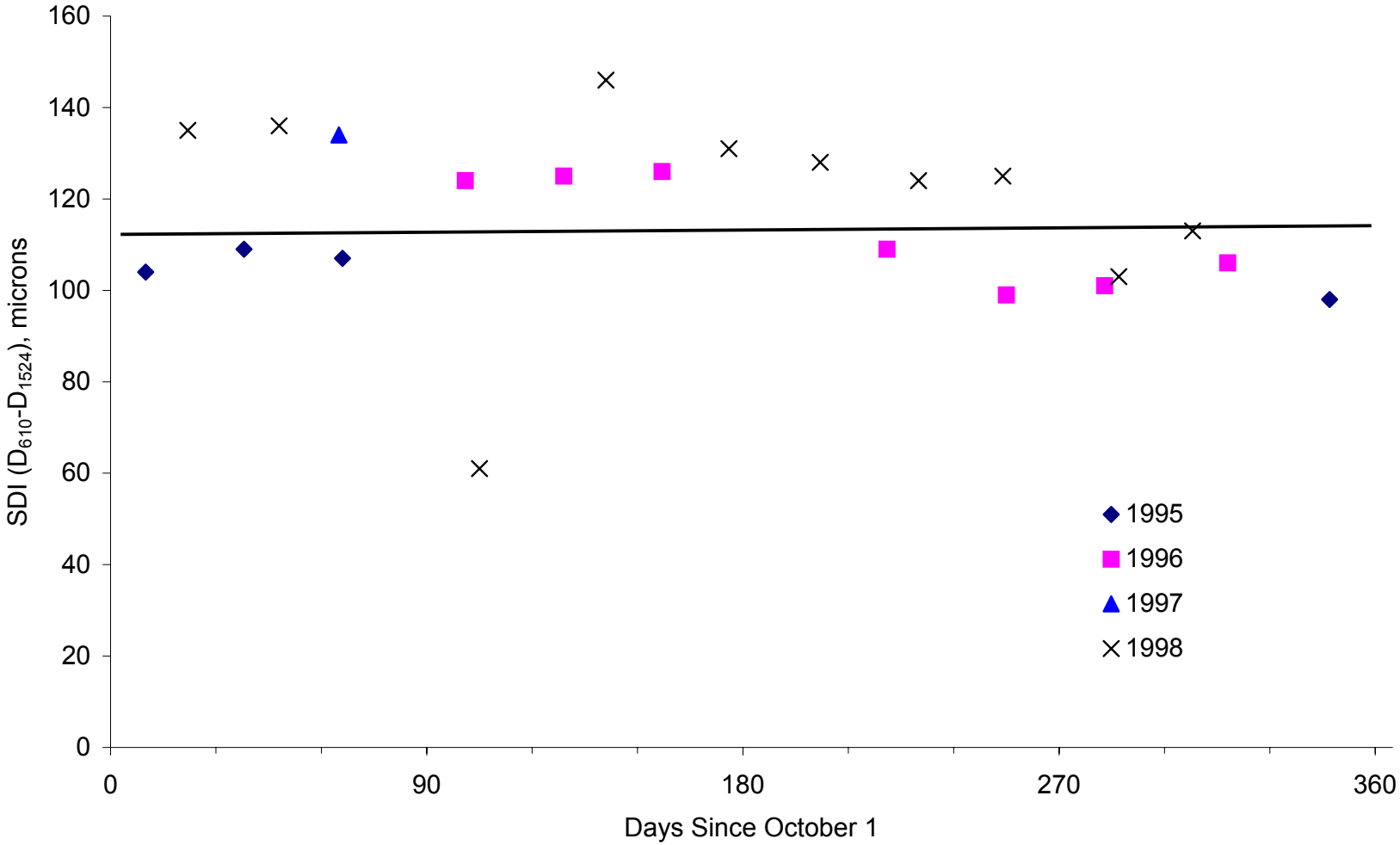

Figure Q-2. Index SDI at Site 04-0113 (Well Graded Sand with Silt and Gravel)

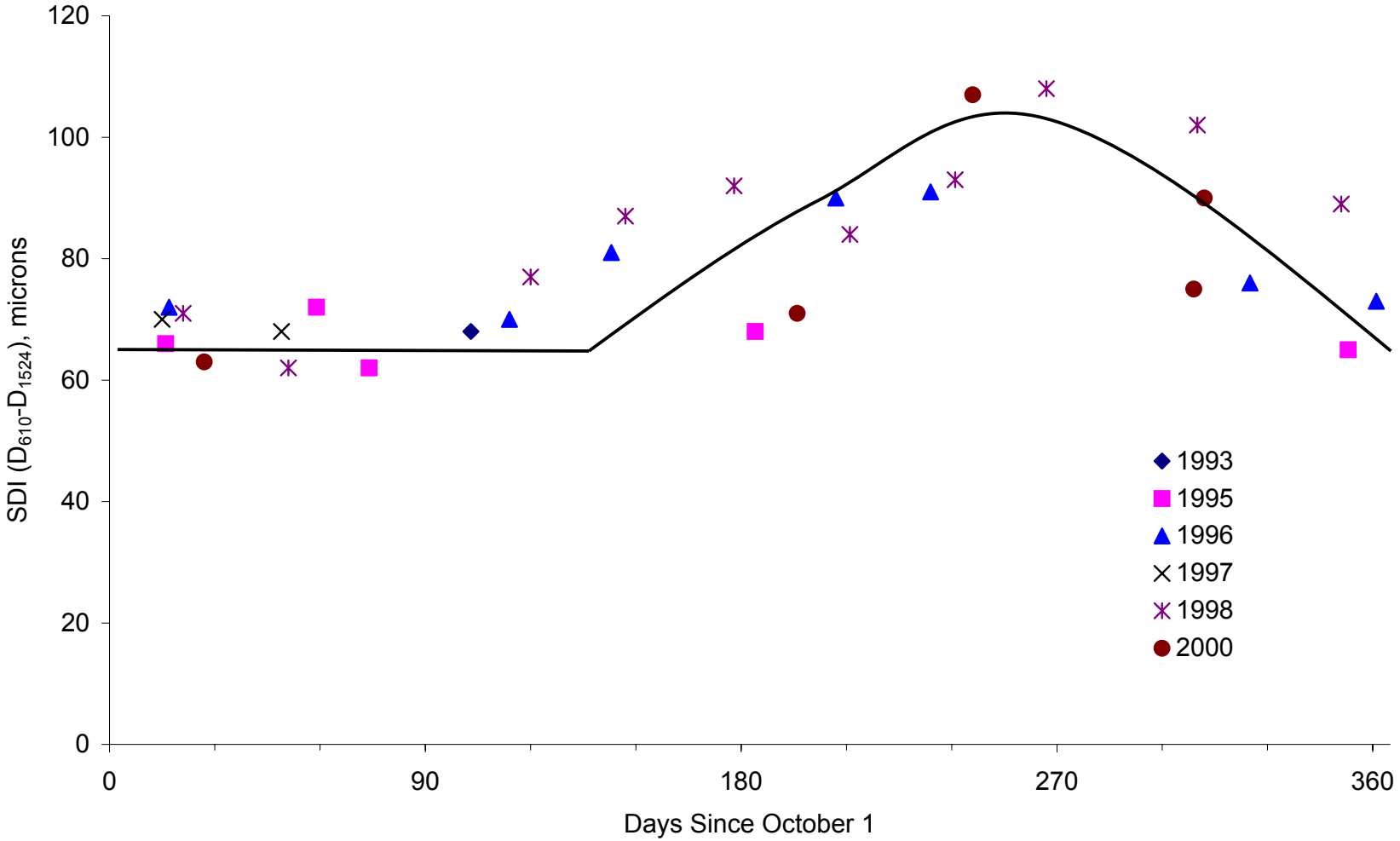

Figure Q-3. Index SDI at Site 13-1031 (Silty Sand)

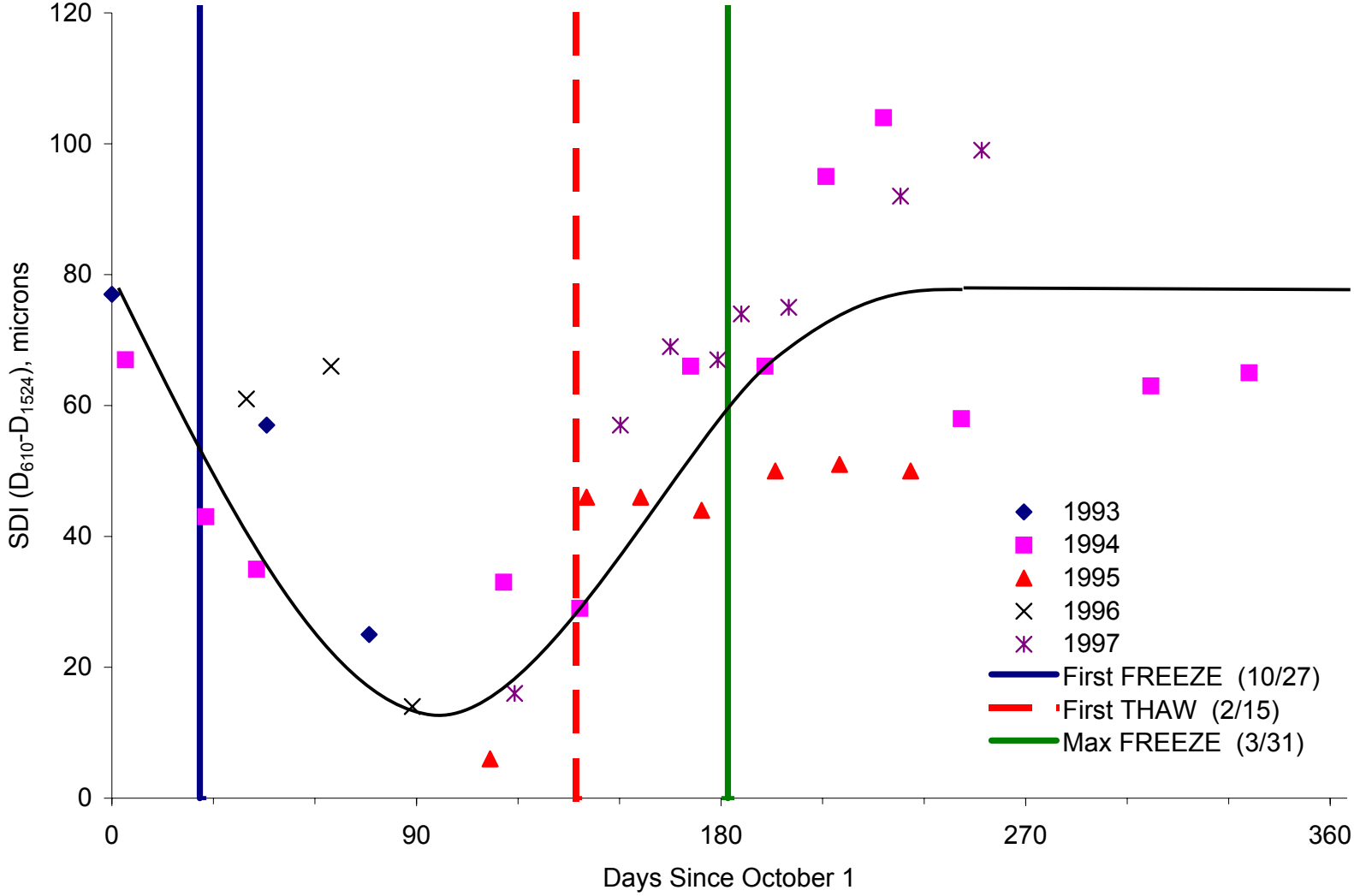

Figure Q-4. Index SDI at Site 16-1010 (Silty Sand)

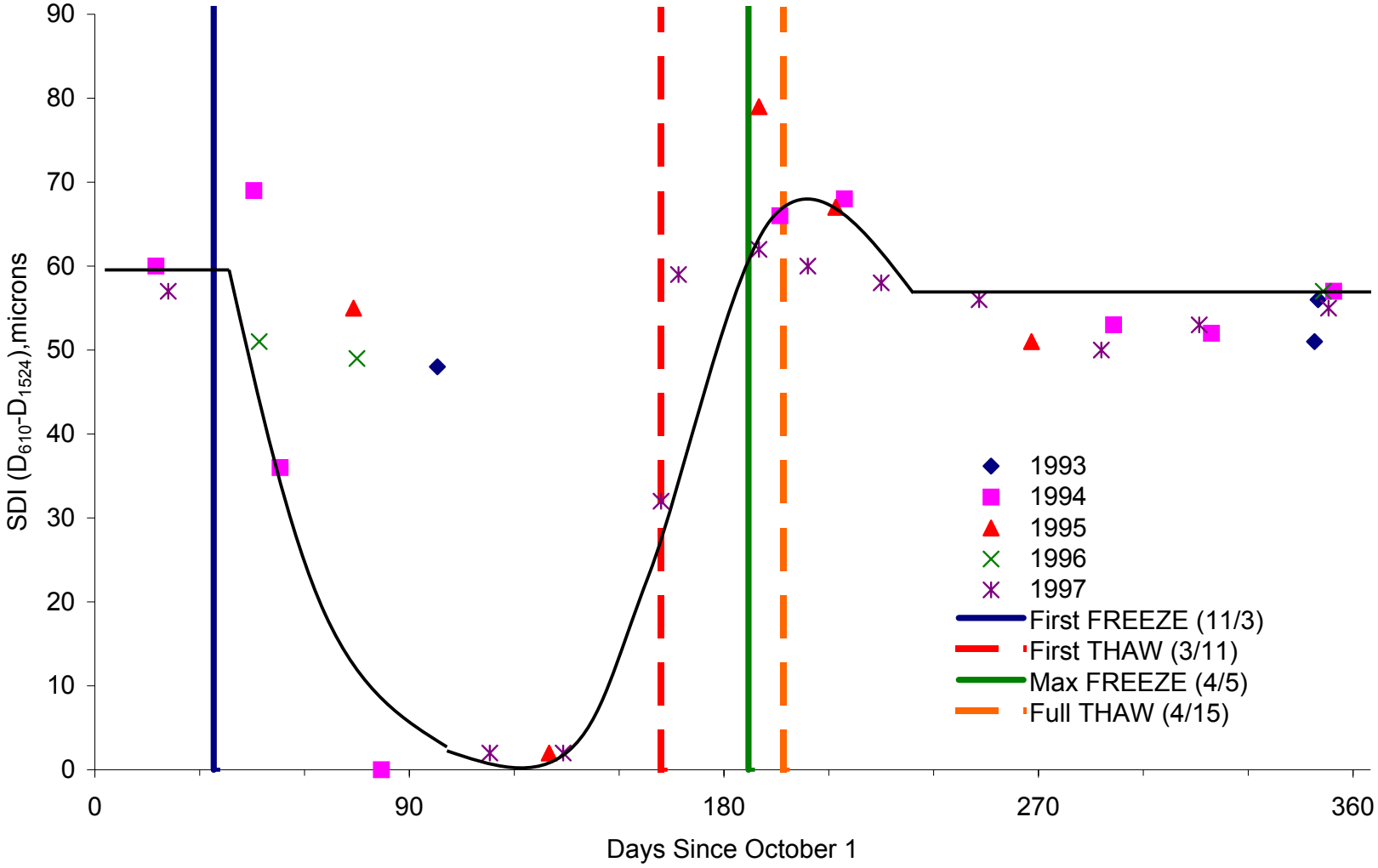

Figure Q-5. Index SDI at Site 23-1026 (Silty Sand with Gravel)

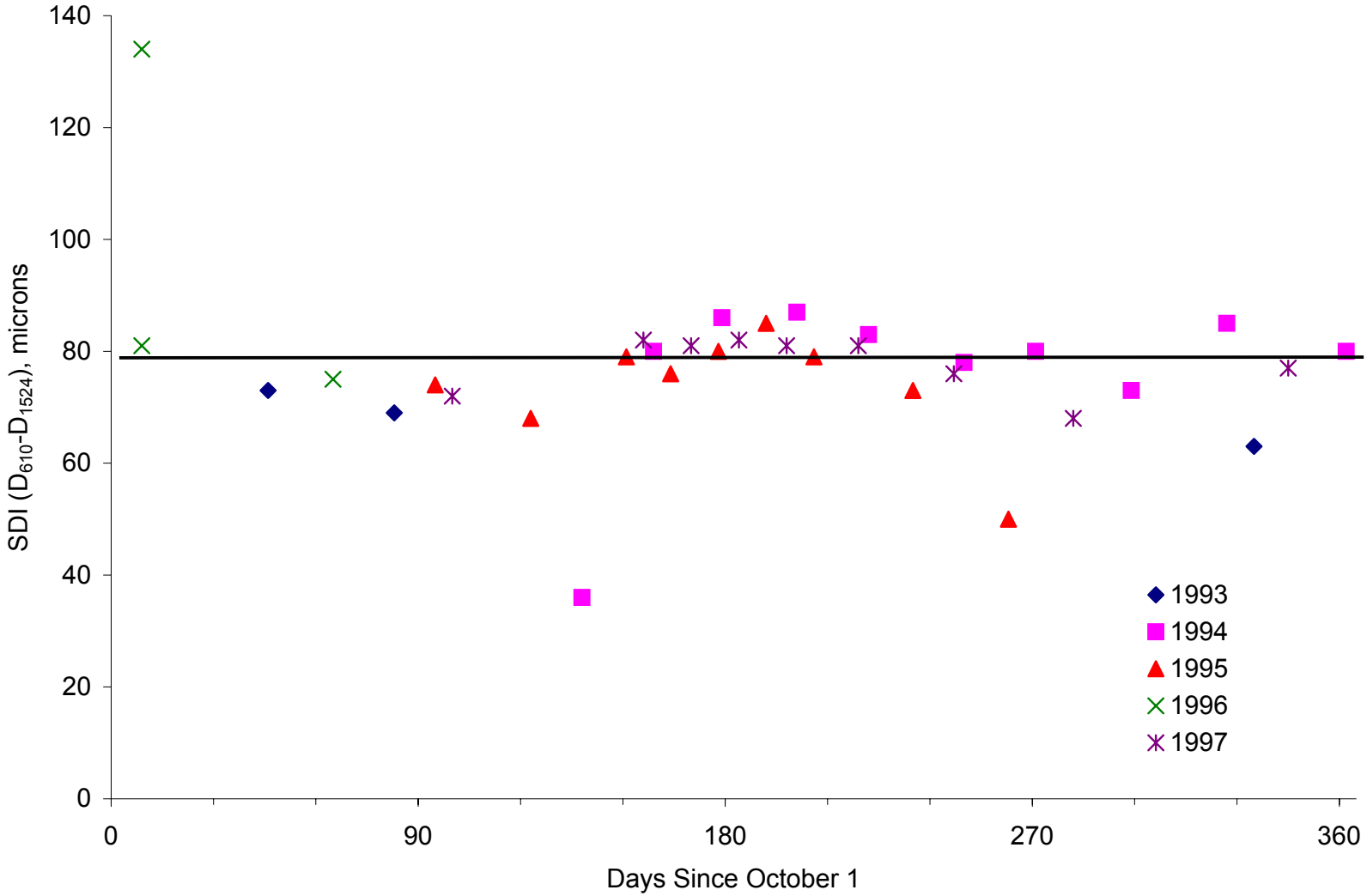

Figure Q-6. Index SDI at Site 25-1002 (Poorly Graded Sand with Silt)

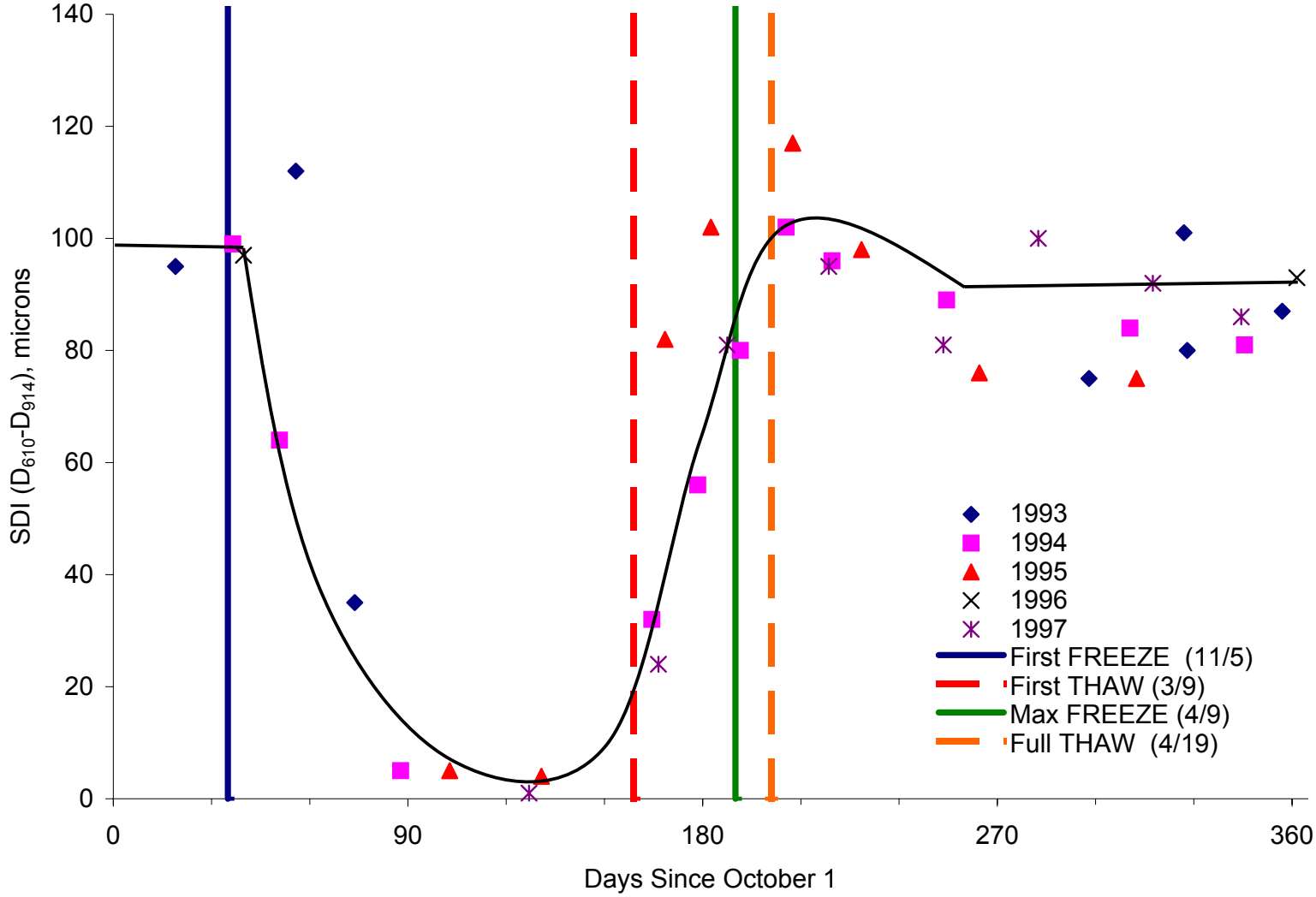

Figure Q-7. Index SDI at Site 27-1018 (Poorly Graded Sand with Silt)

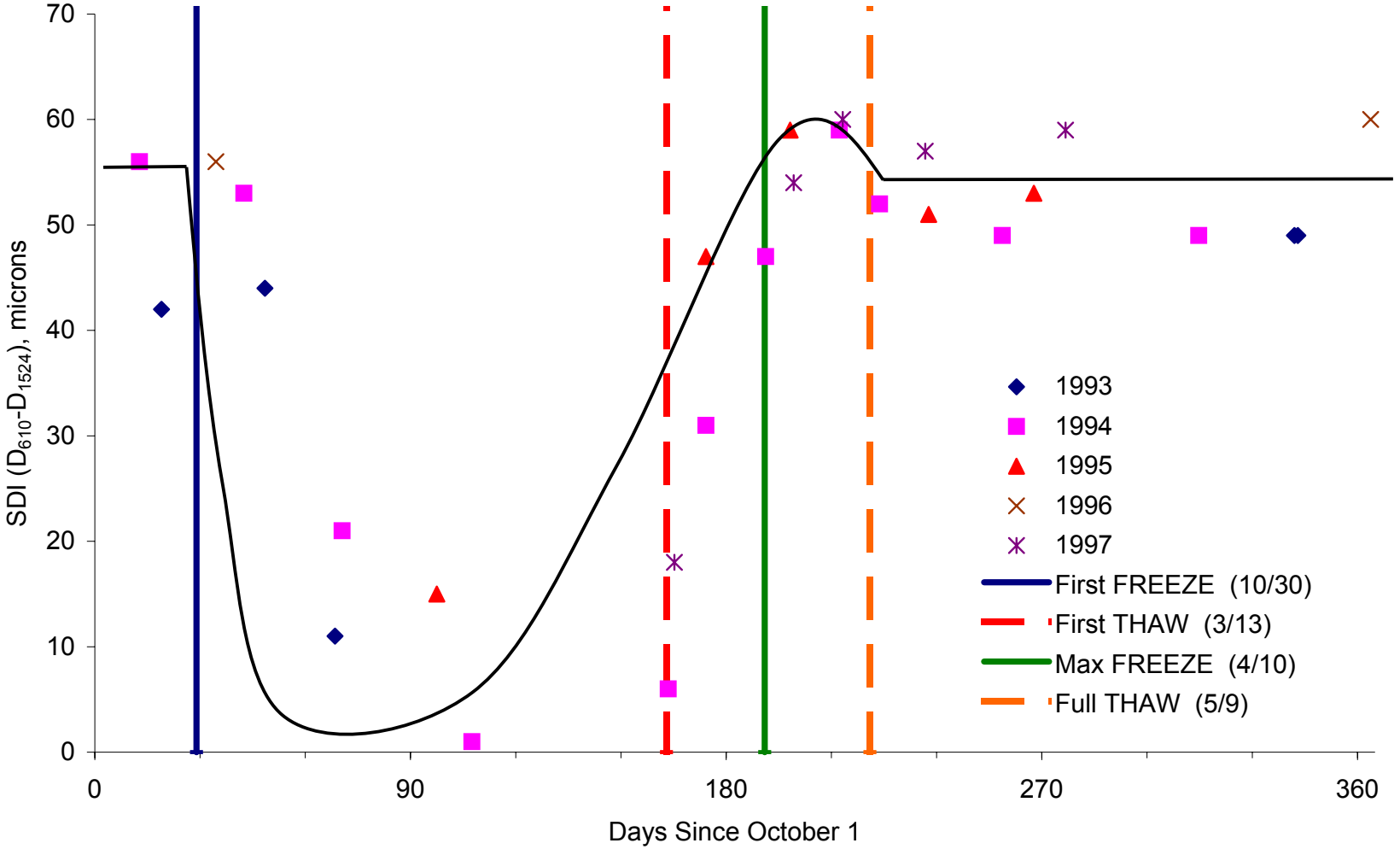

Figure Q-8. Index SDI at Site 27-1028 (Poorly Graded Sand with Silt)

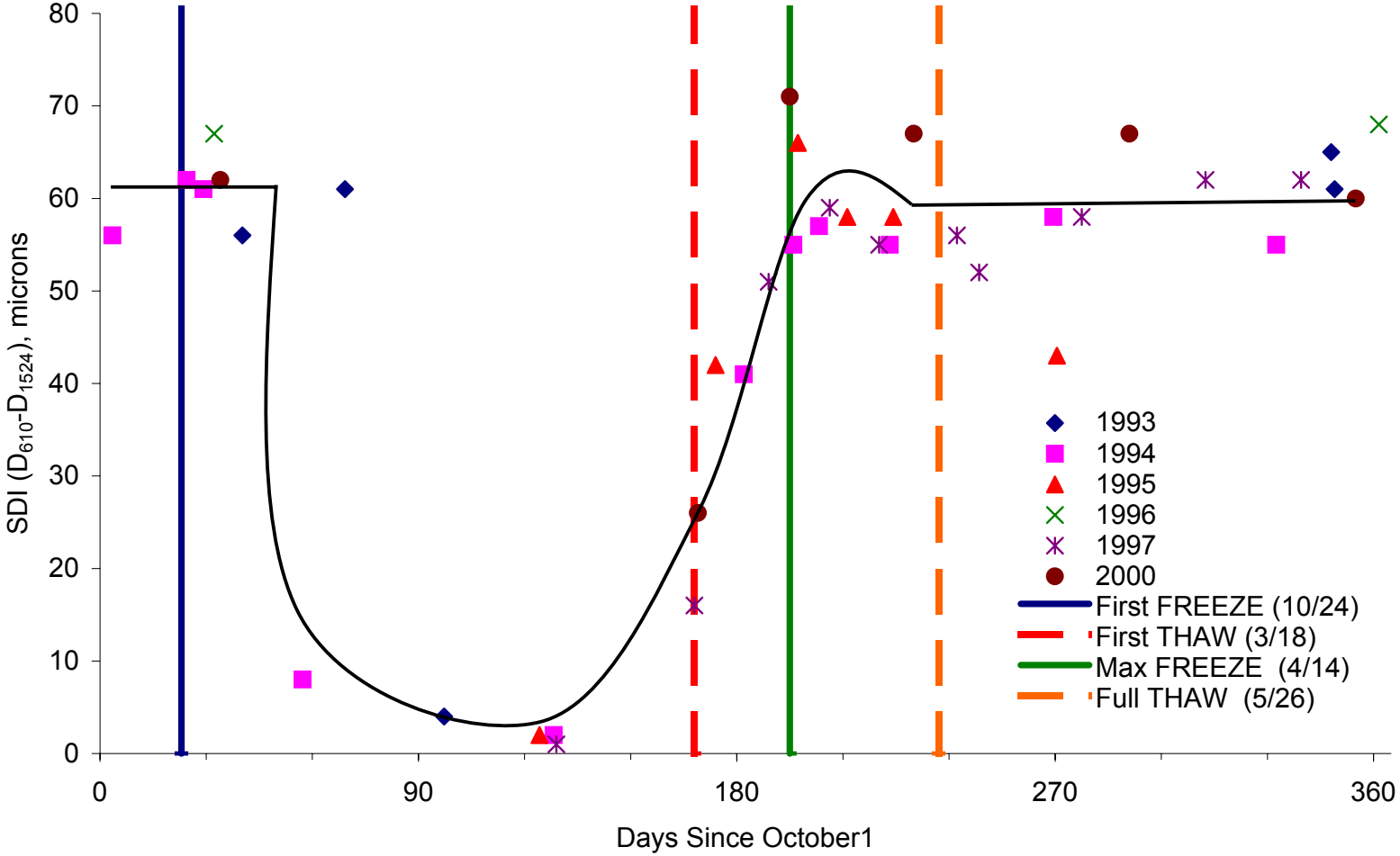

Figure Q-9. Index SDI at Site 27-6251 (Poorly Graded Sand with Silt)

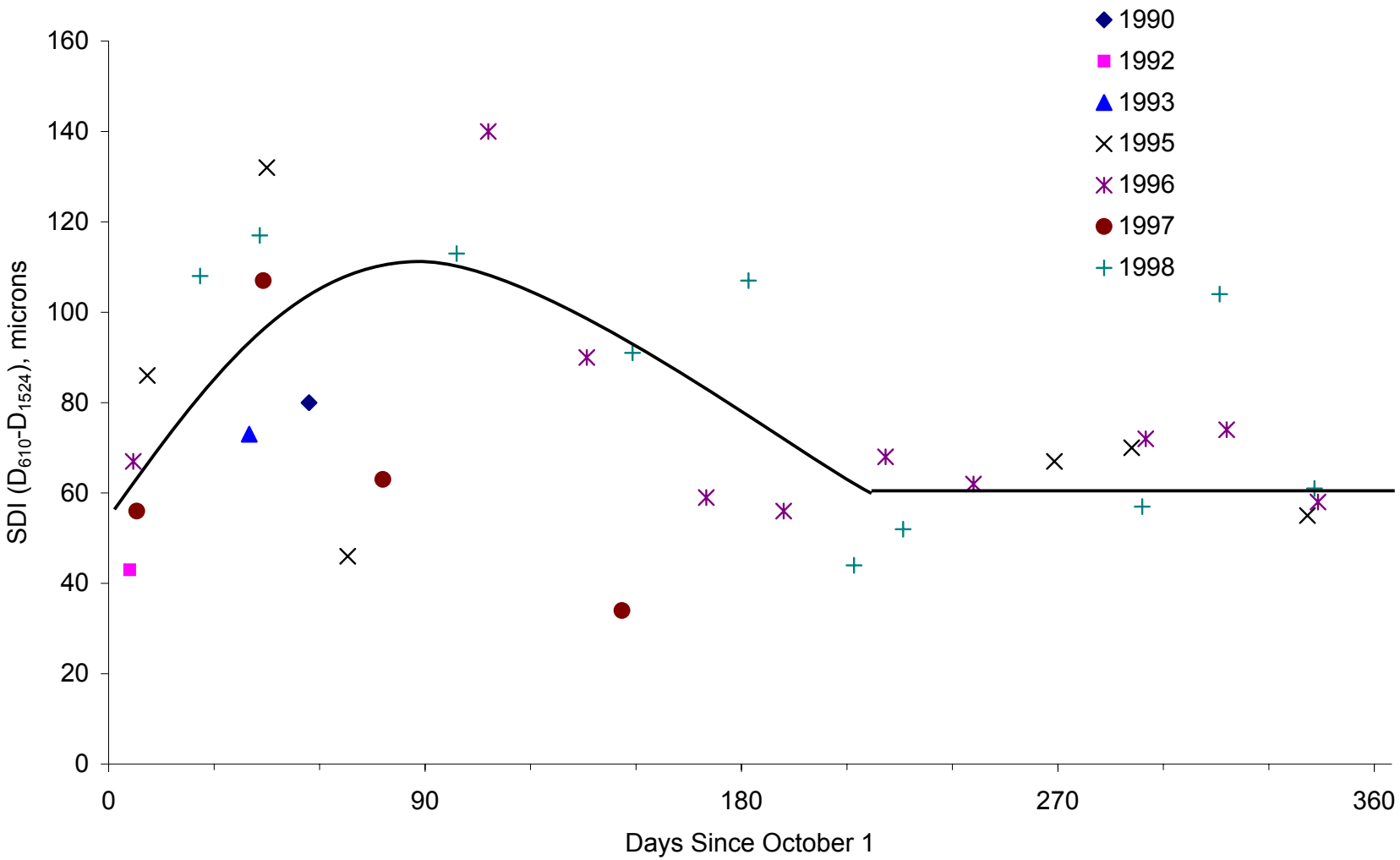

Figure Q-10. Index SDI at Site 28-1802 (Poorly Graded Sand)

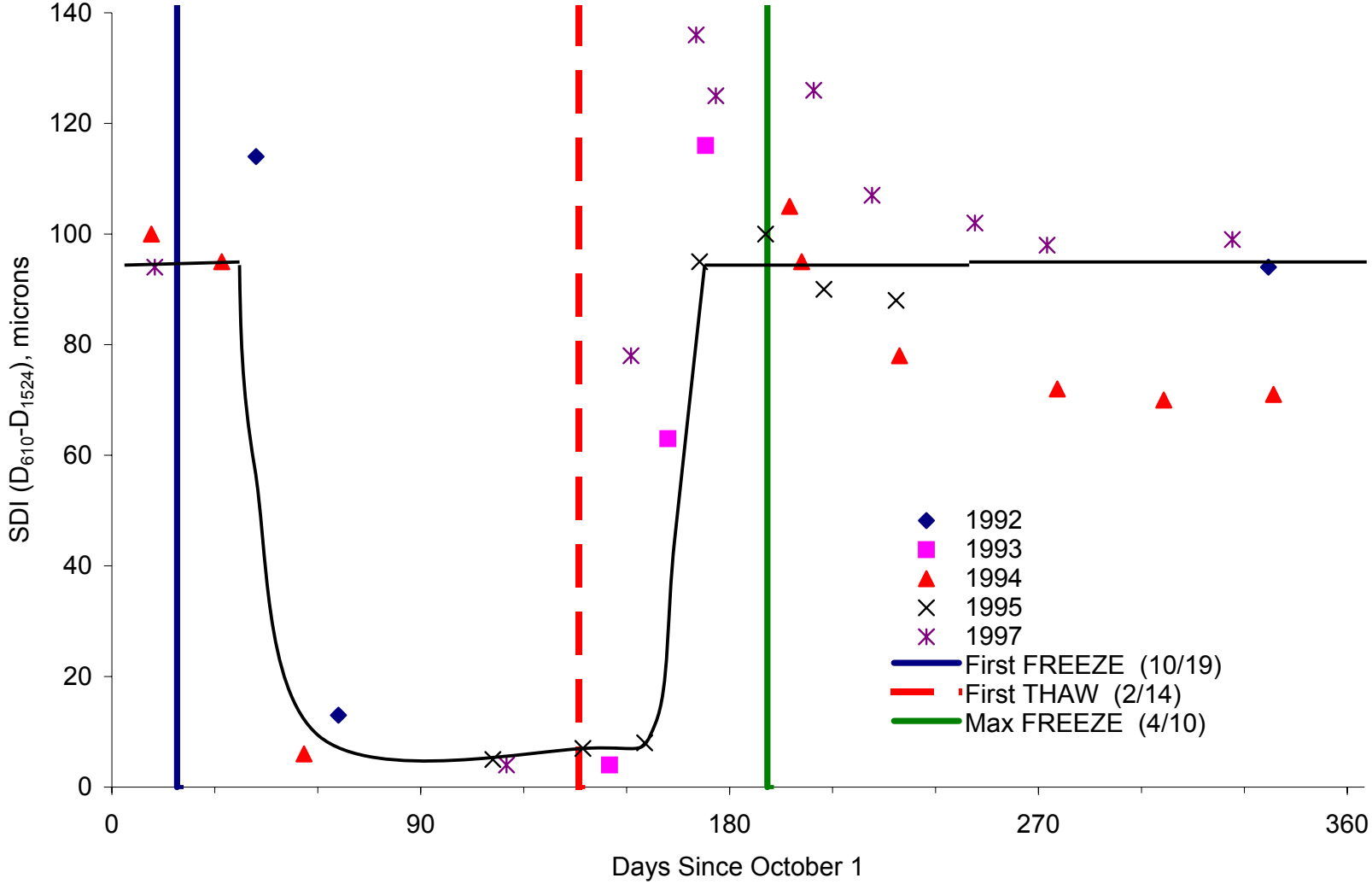

Figure Q-11. Index SDI at Site 30-8129 (Poorly Graded Sand with Silt)

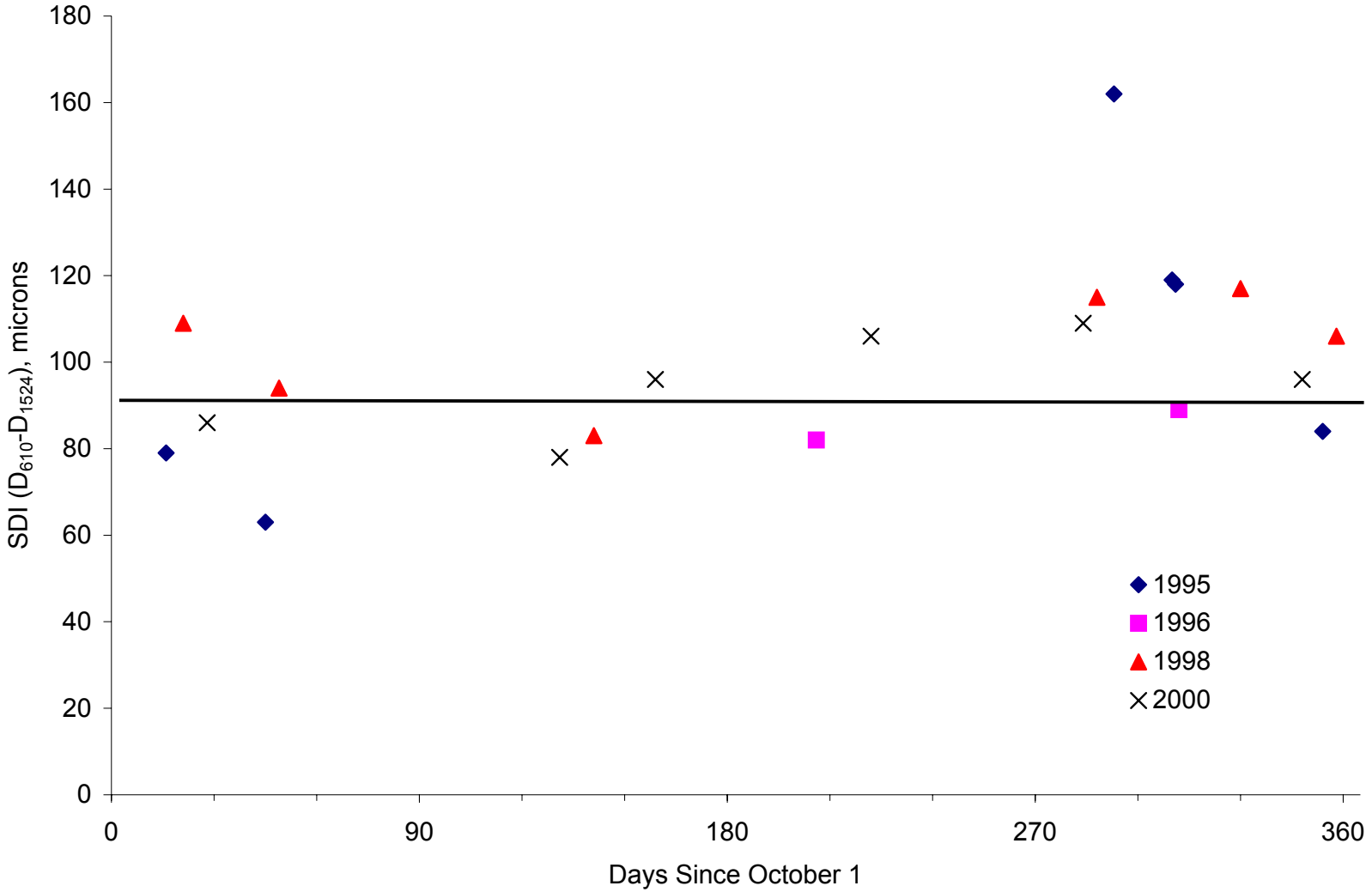

Figure Q-12. Index SDI at Site 31-0114 (Silty Clay)

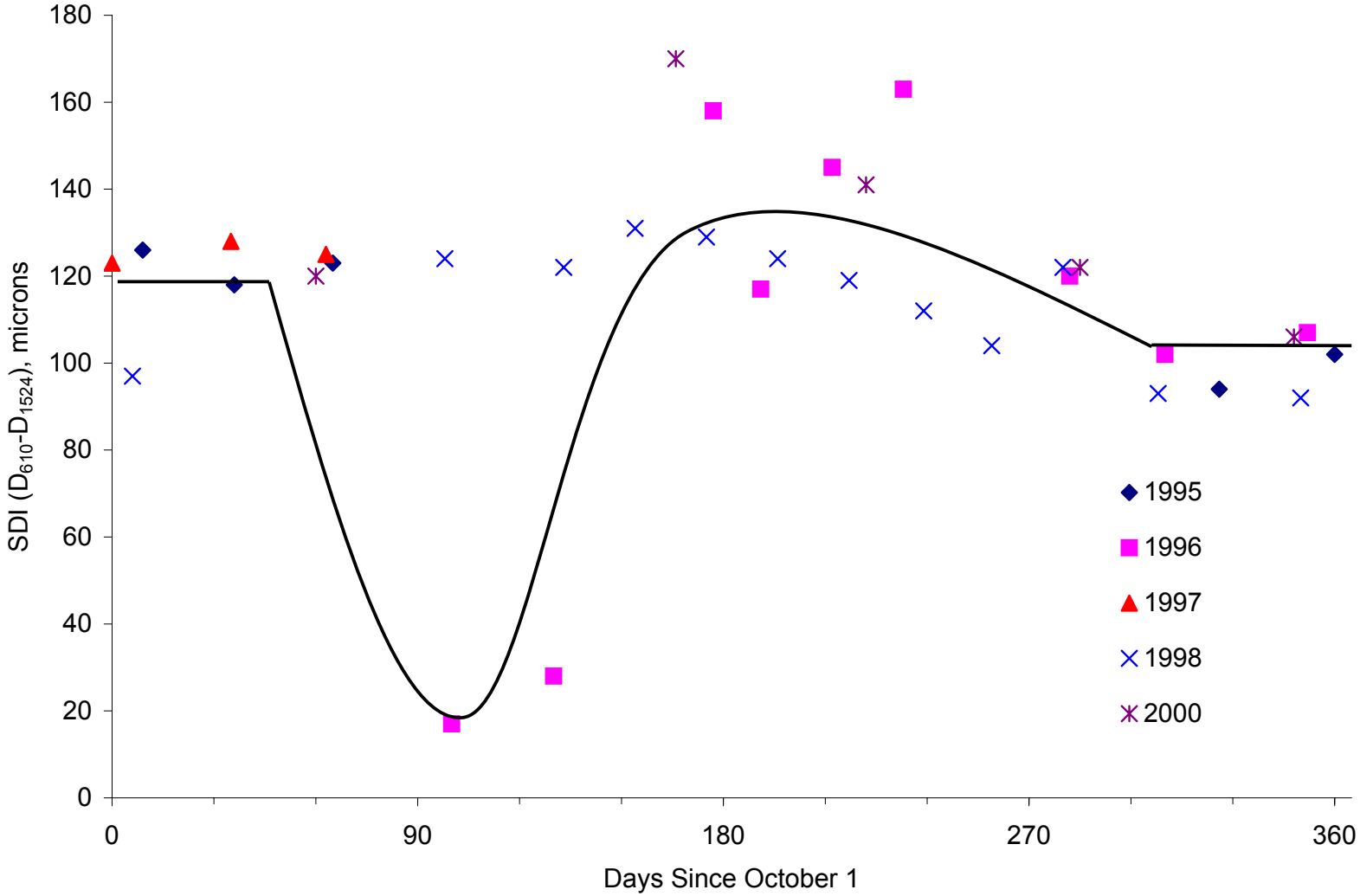

Figure Q-13. Index SDI at Site 36-0801 (Silty Sand)

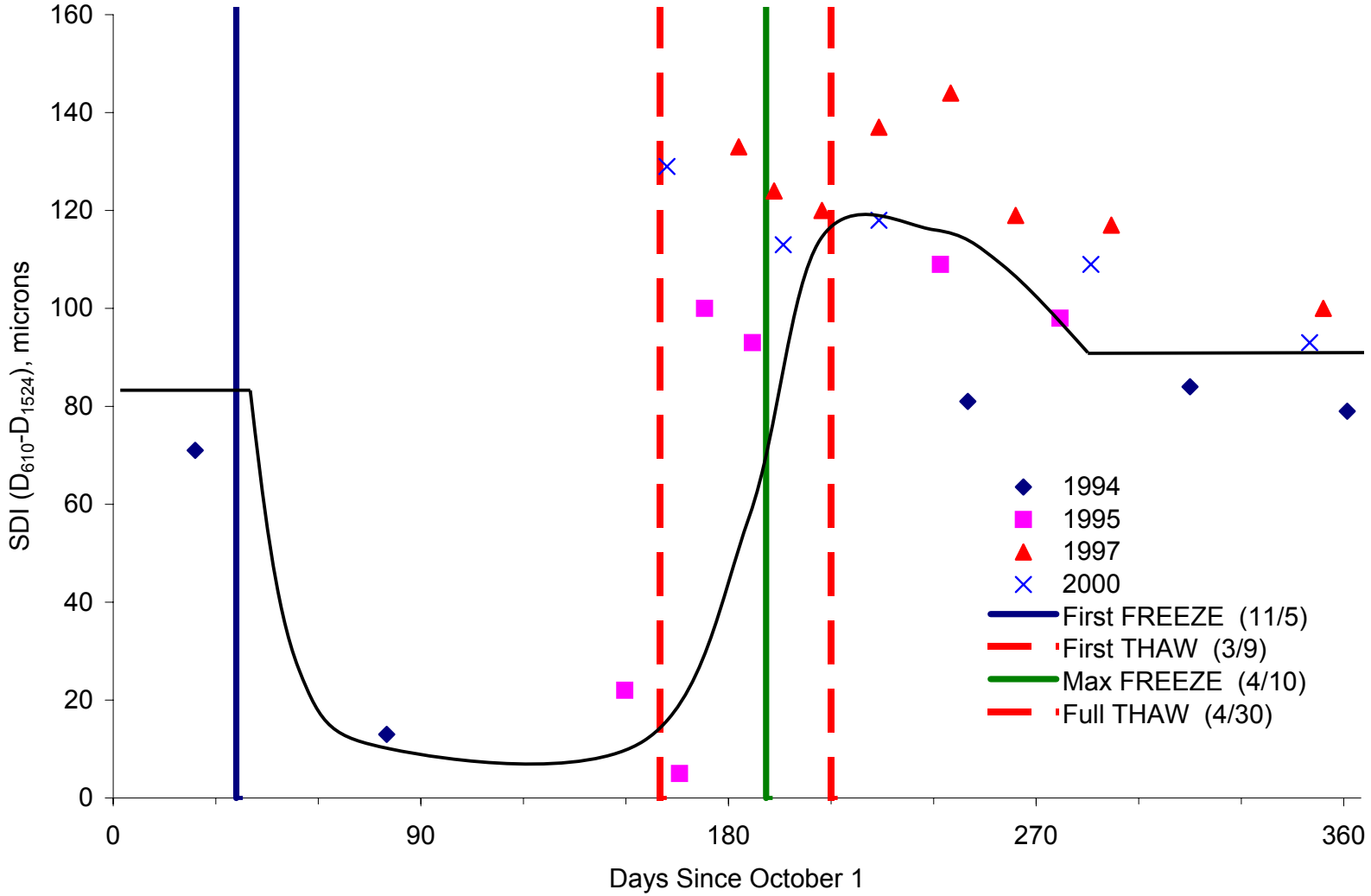

Figure Q-14. Index SDI at Site 46-0804 (Silty Clay)

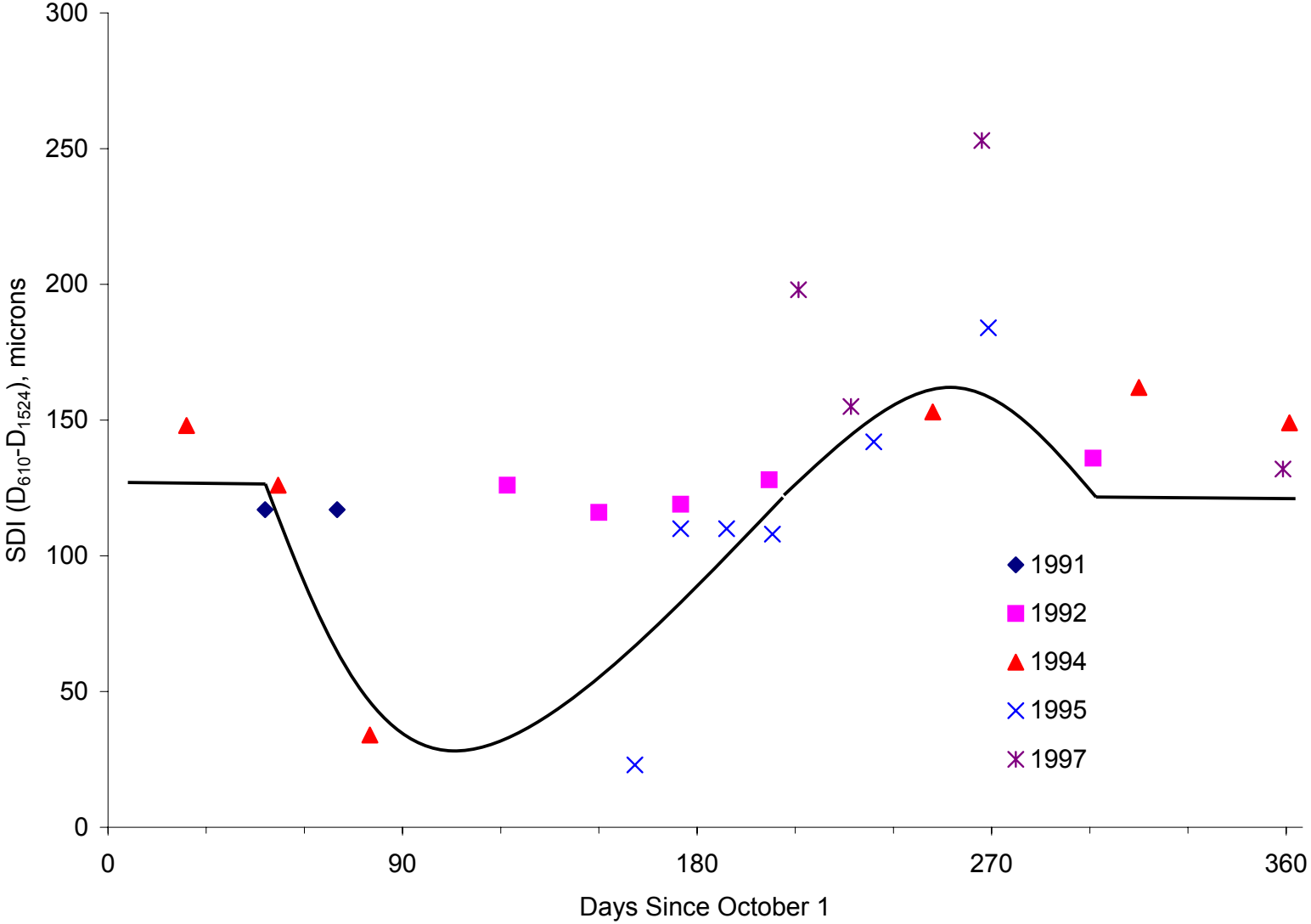

Figure Q-15. Index SDI at Site 46-9187 (Lean Inorganic Clay)

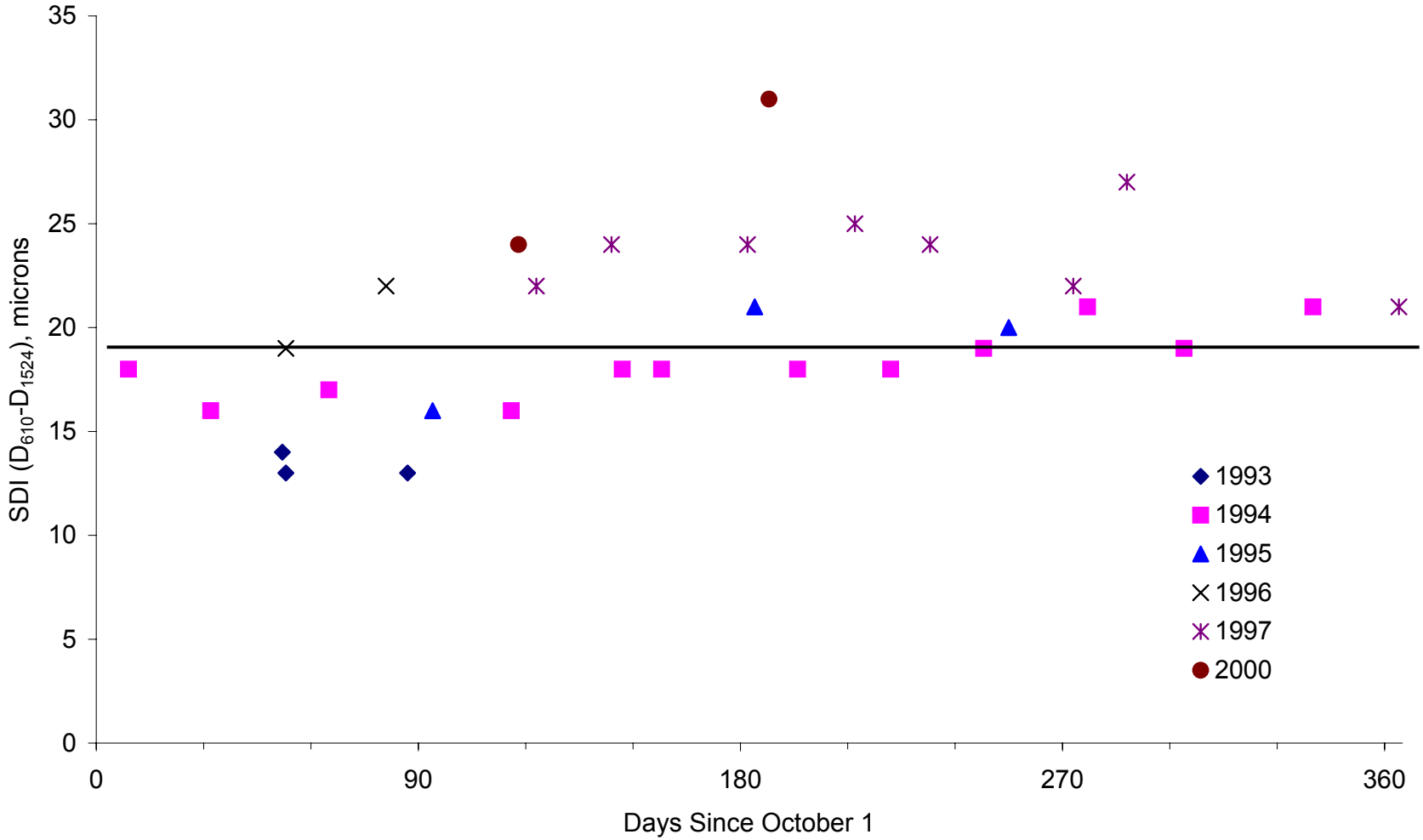

Figure Q-16. Index SDI at Site 48-1122 (Clayey Sand)

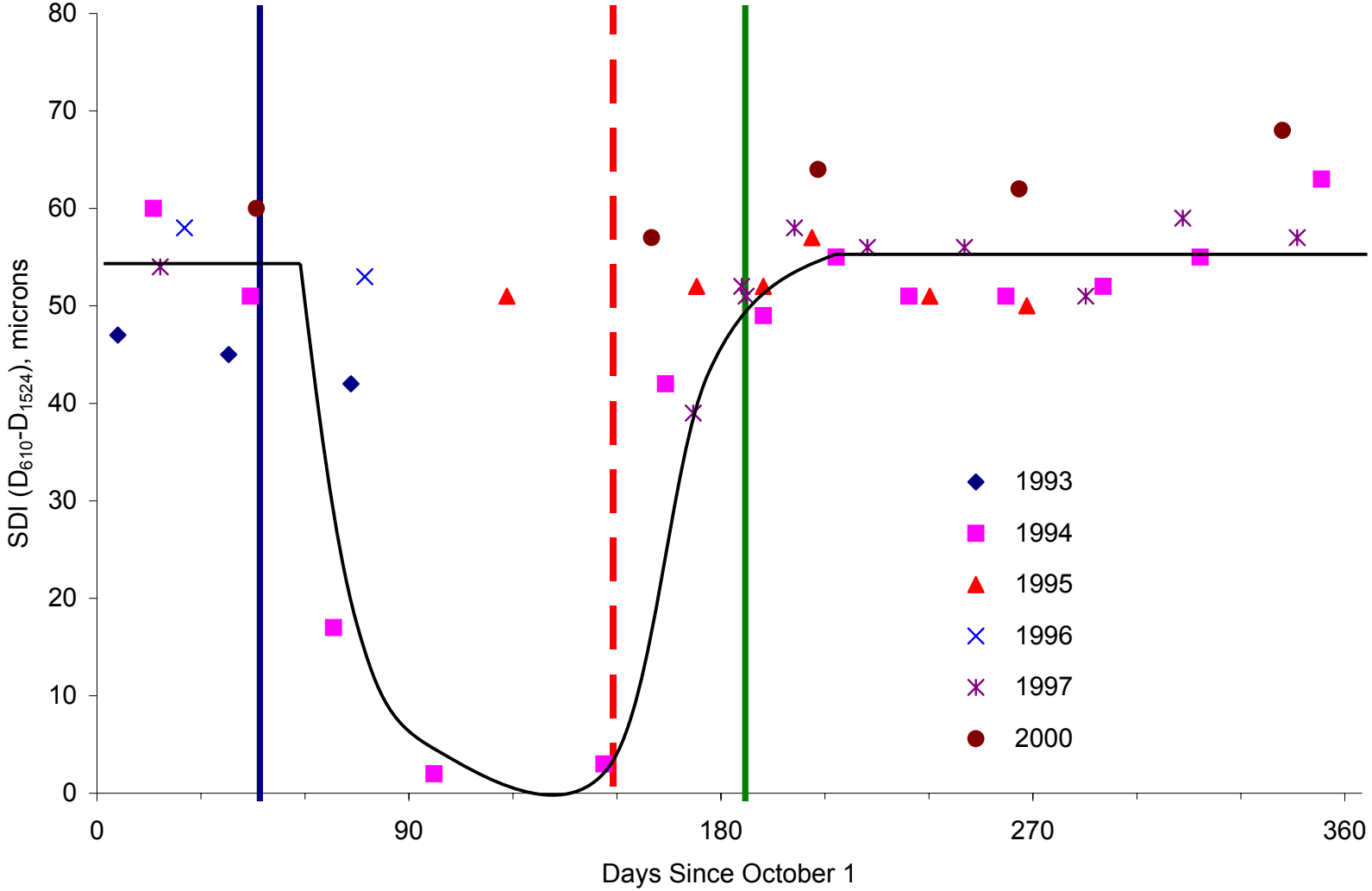

Figure Q-17. Index SDI at Site 50-1002 (Poorly Graded Gravel with Silt and Sand)

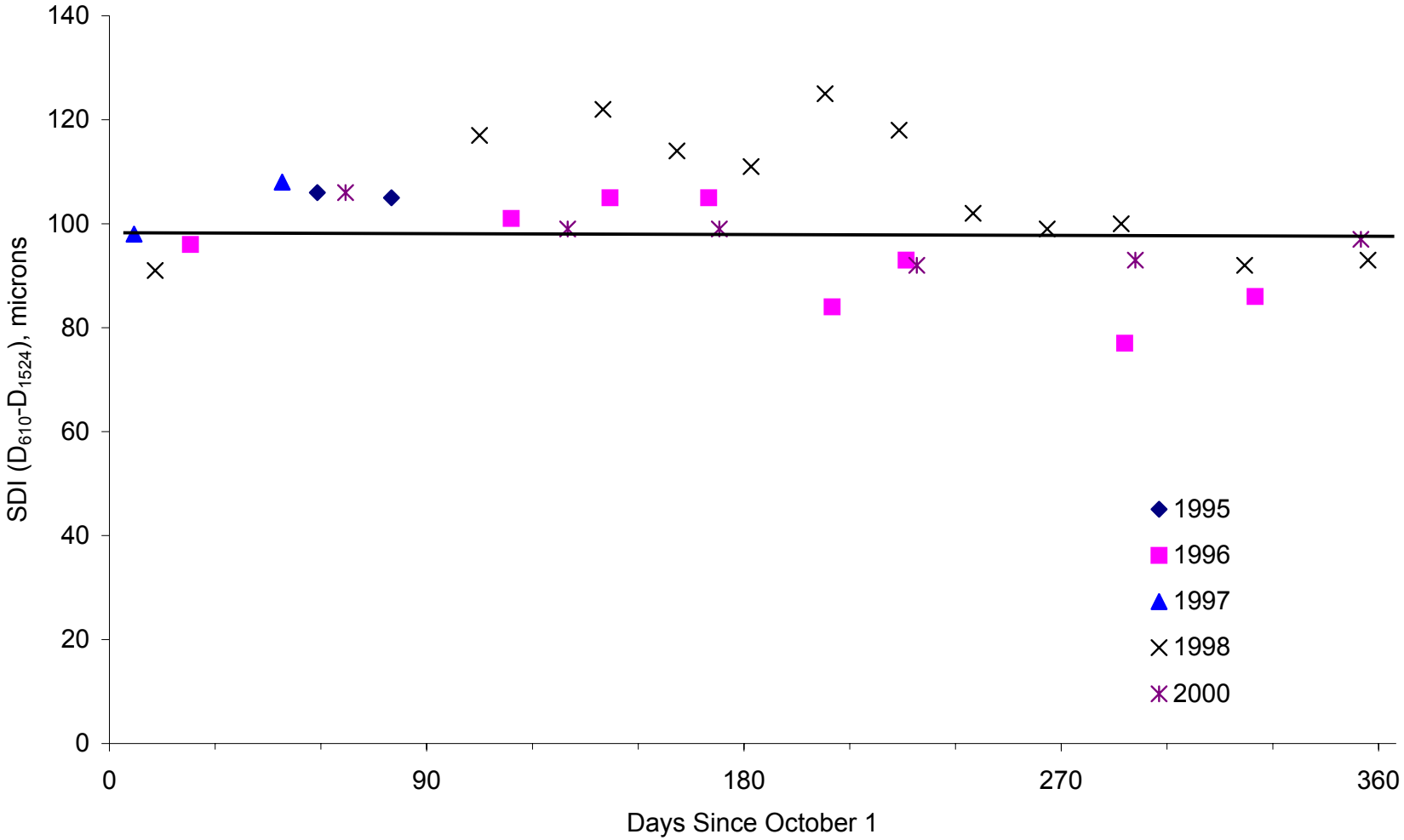

Figure Q-18. Index SDI at Site 51-0113 (Silt)

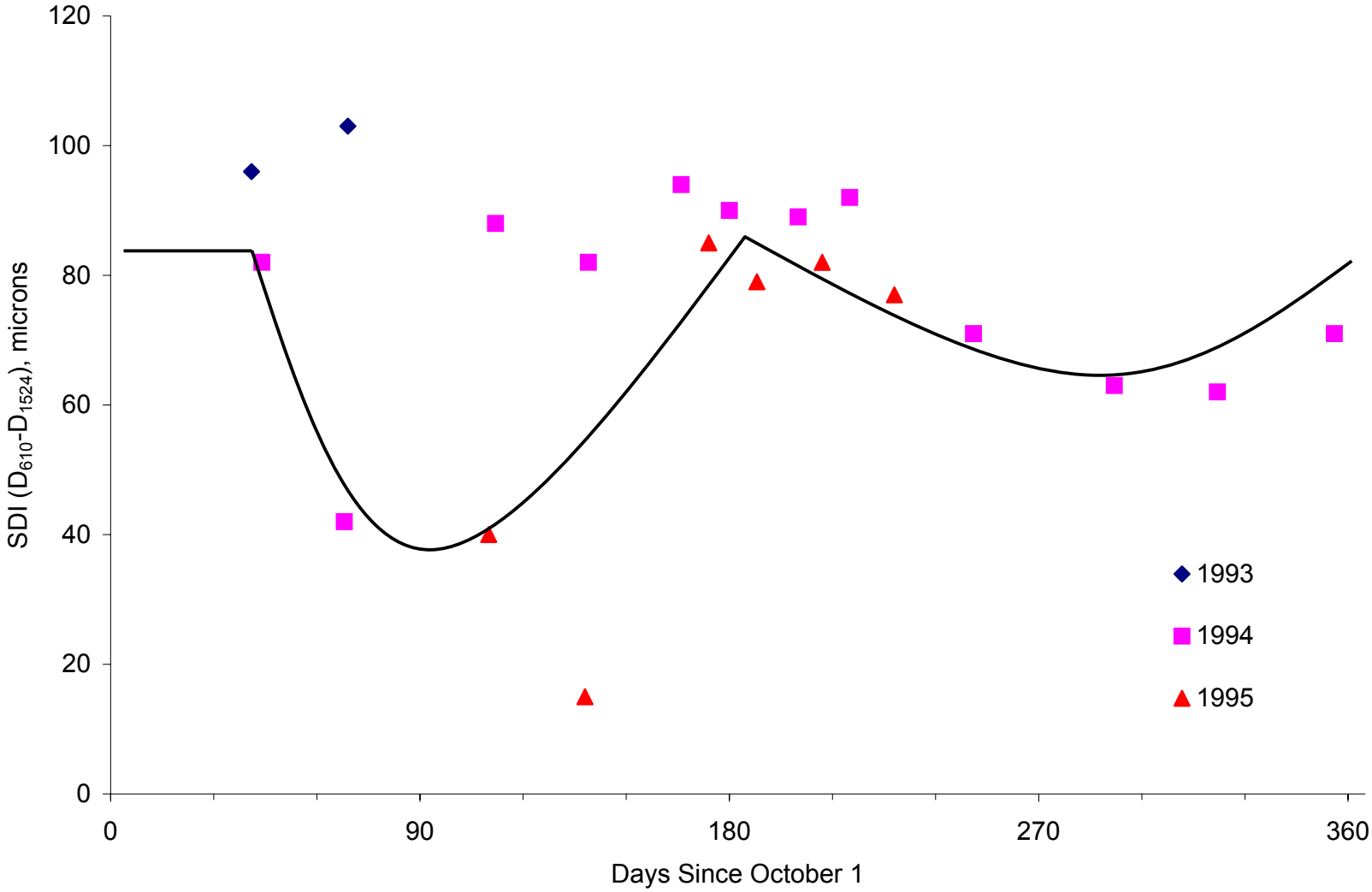

Figure Q-19. Index SDI at Site 56-1007 (Silty Sand with Gravel)

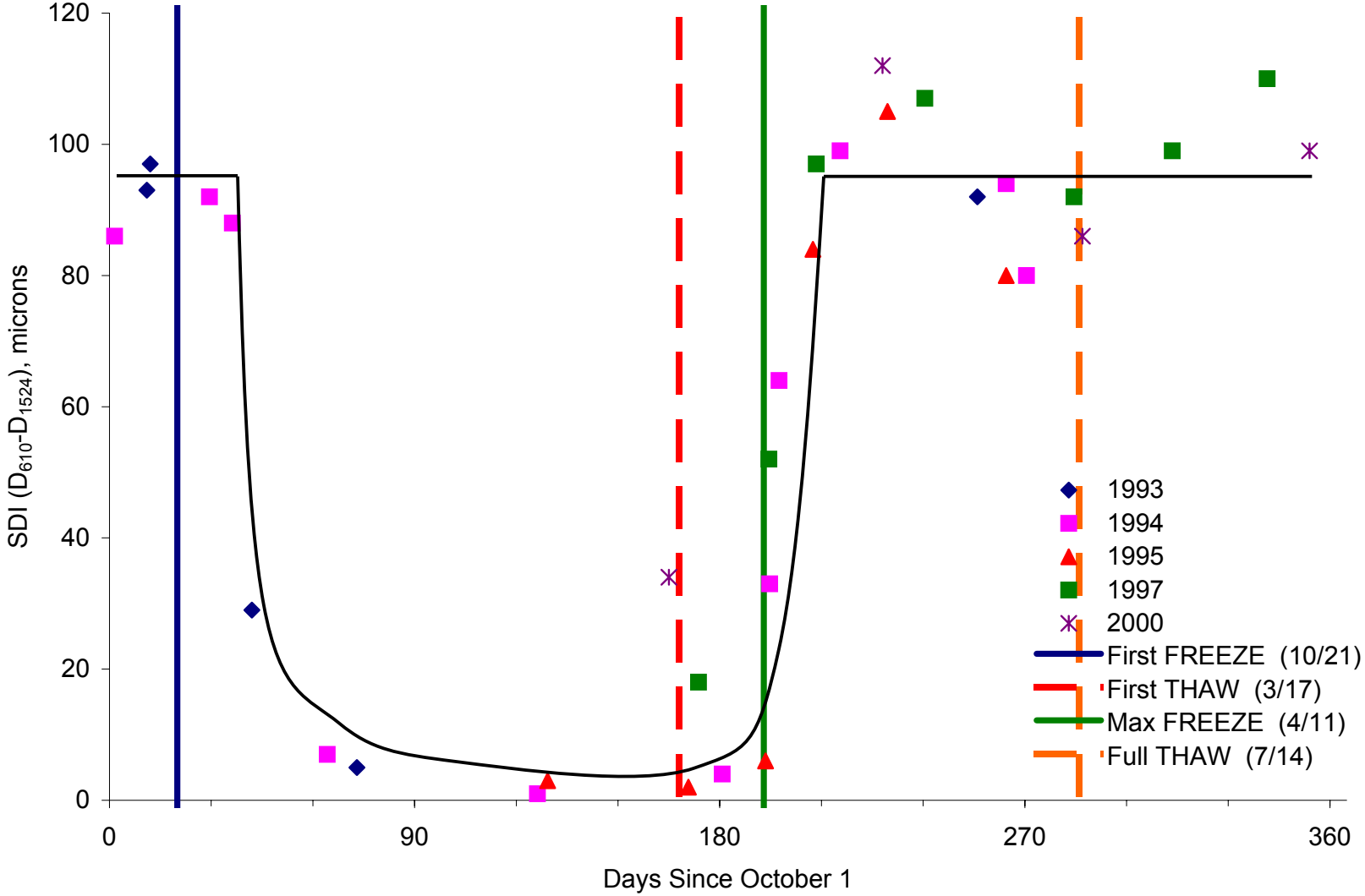

Figure Q-20. Index SDI at Site 83-1801 (Silty Sand)

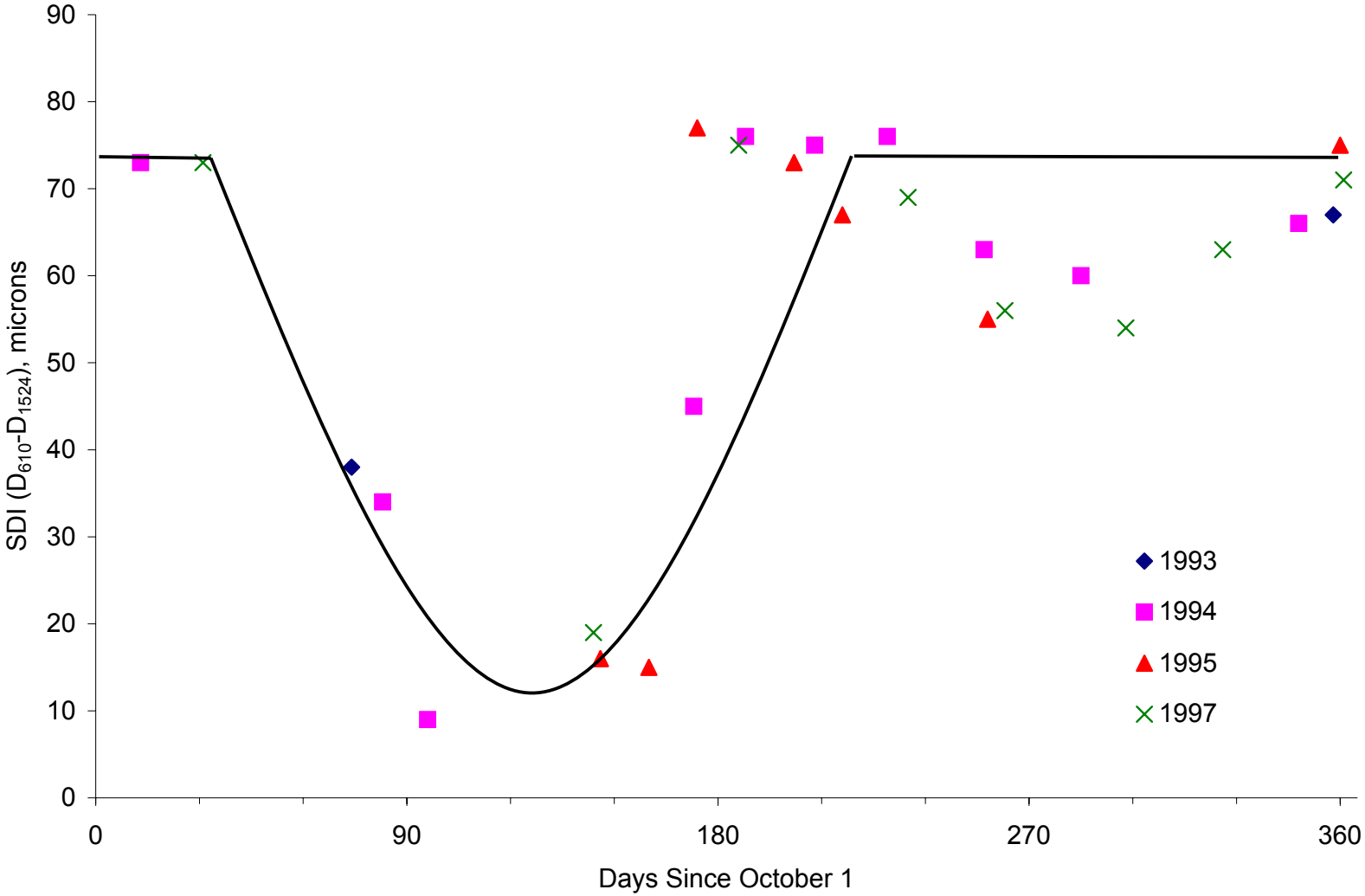

Figure Q-21. Index SDI at Site 87-1622 (Sandy Silt)

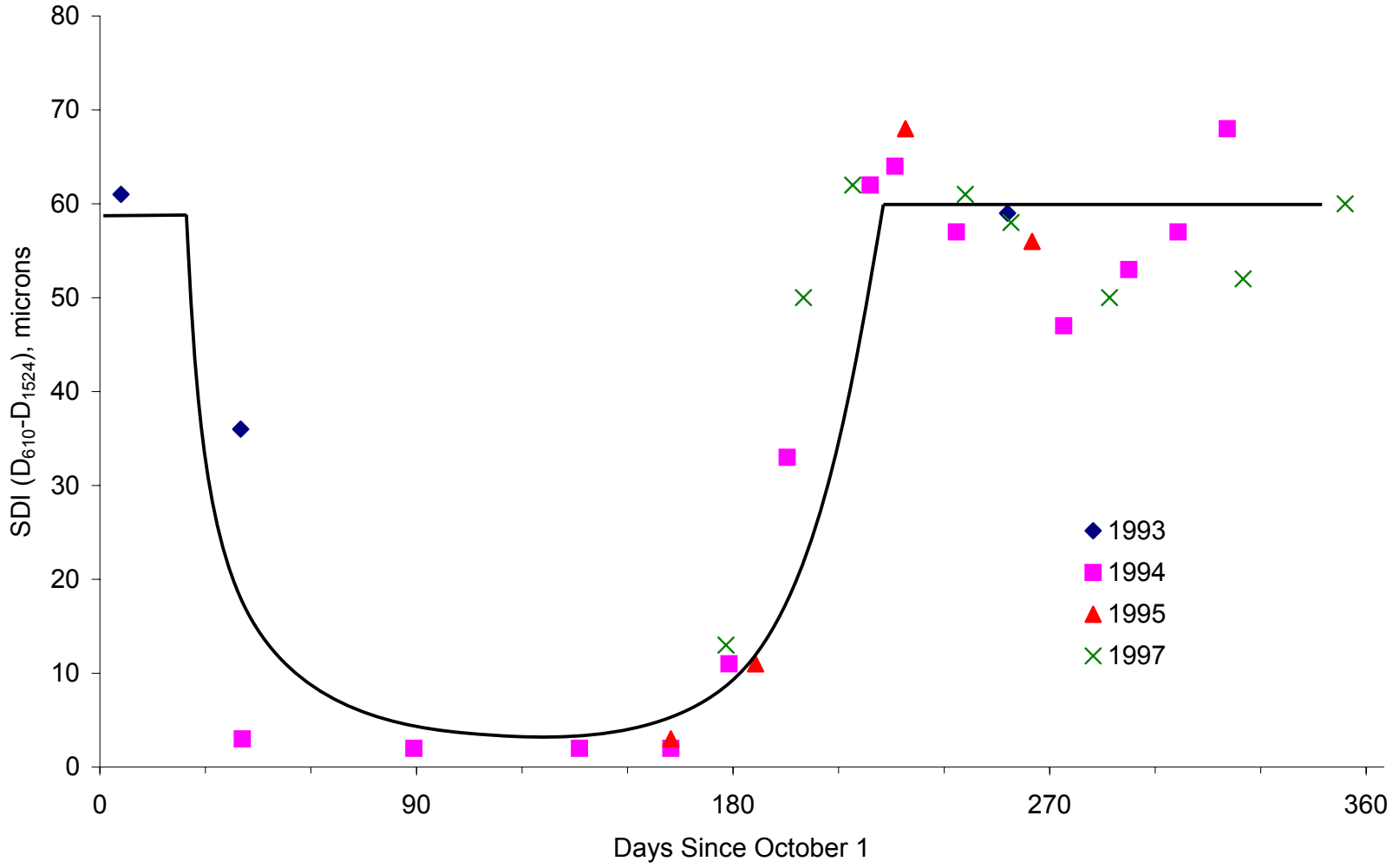

Figure Q-22. Index SDI at Site 90-6405 (Silty Sand)

APPENDIX R

SEASONAL VARIATIONS OF INDEX SI

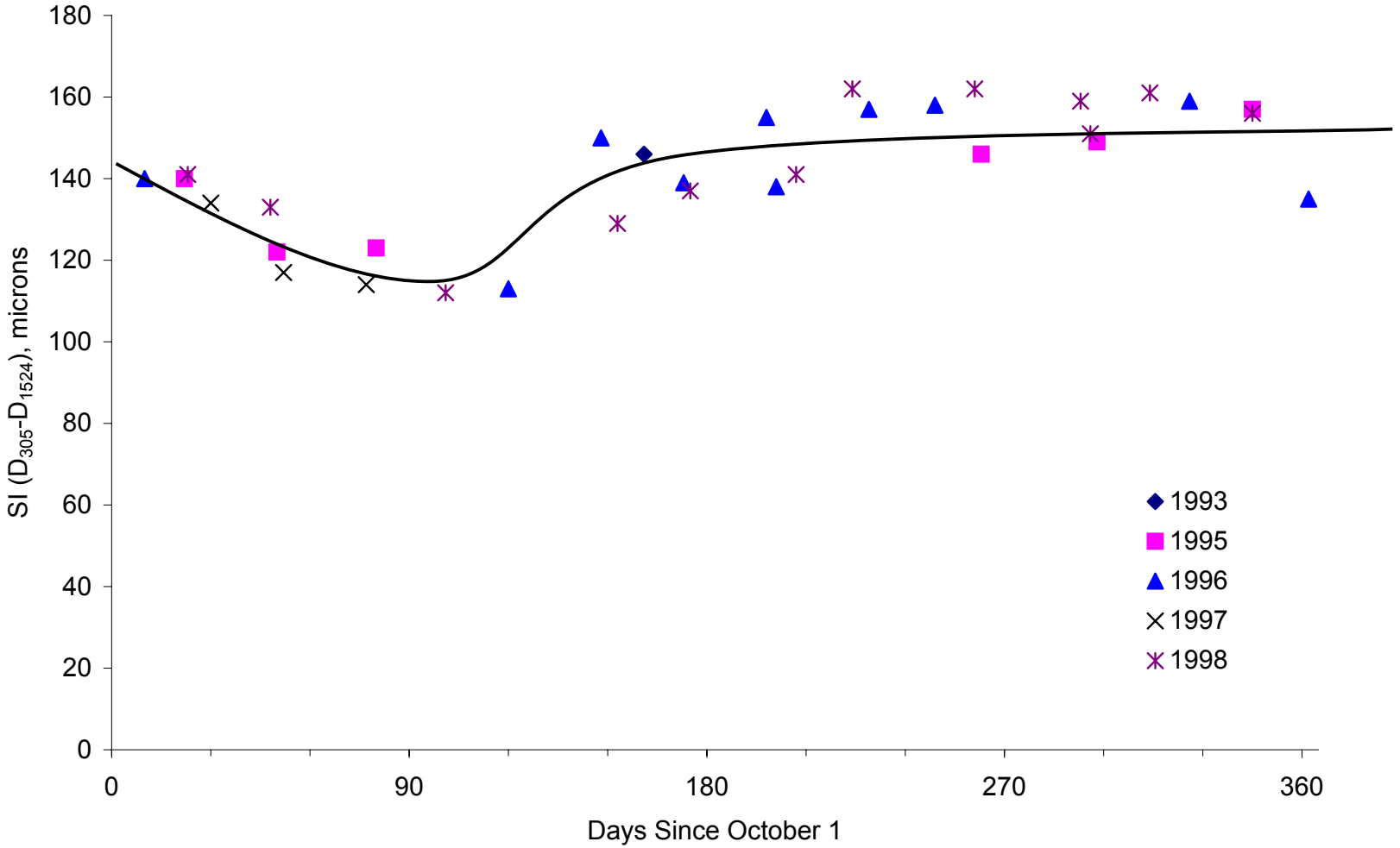

Figure R-1. Index SI at Site 01-0101 (Sandy Silt)

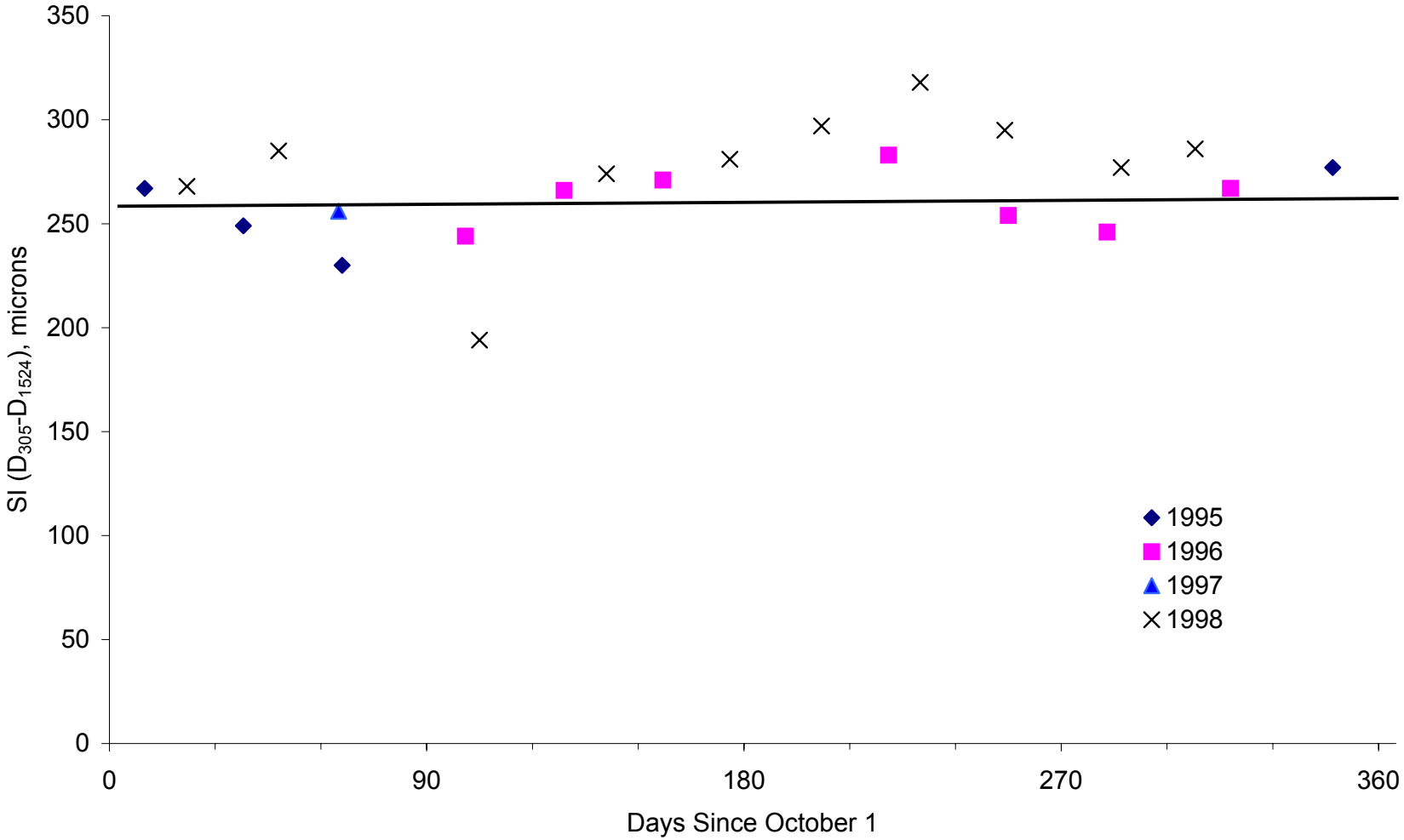

Figure R-2. Index SI at Site 04-0113 (Well Graded Sand with Silt and Gravel)

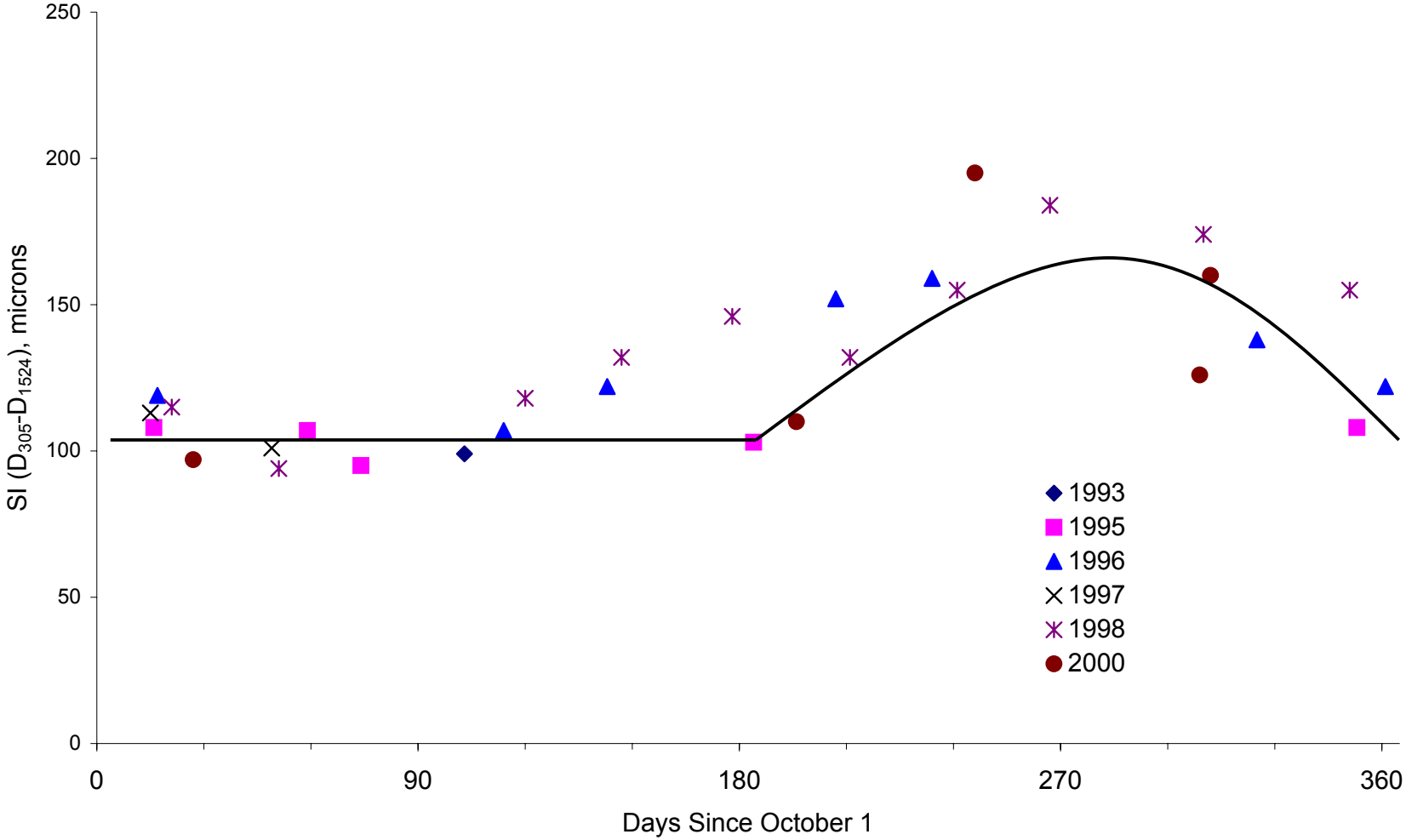

Figure R-3. Index SI at Site 13-1031 (Silty Sand)

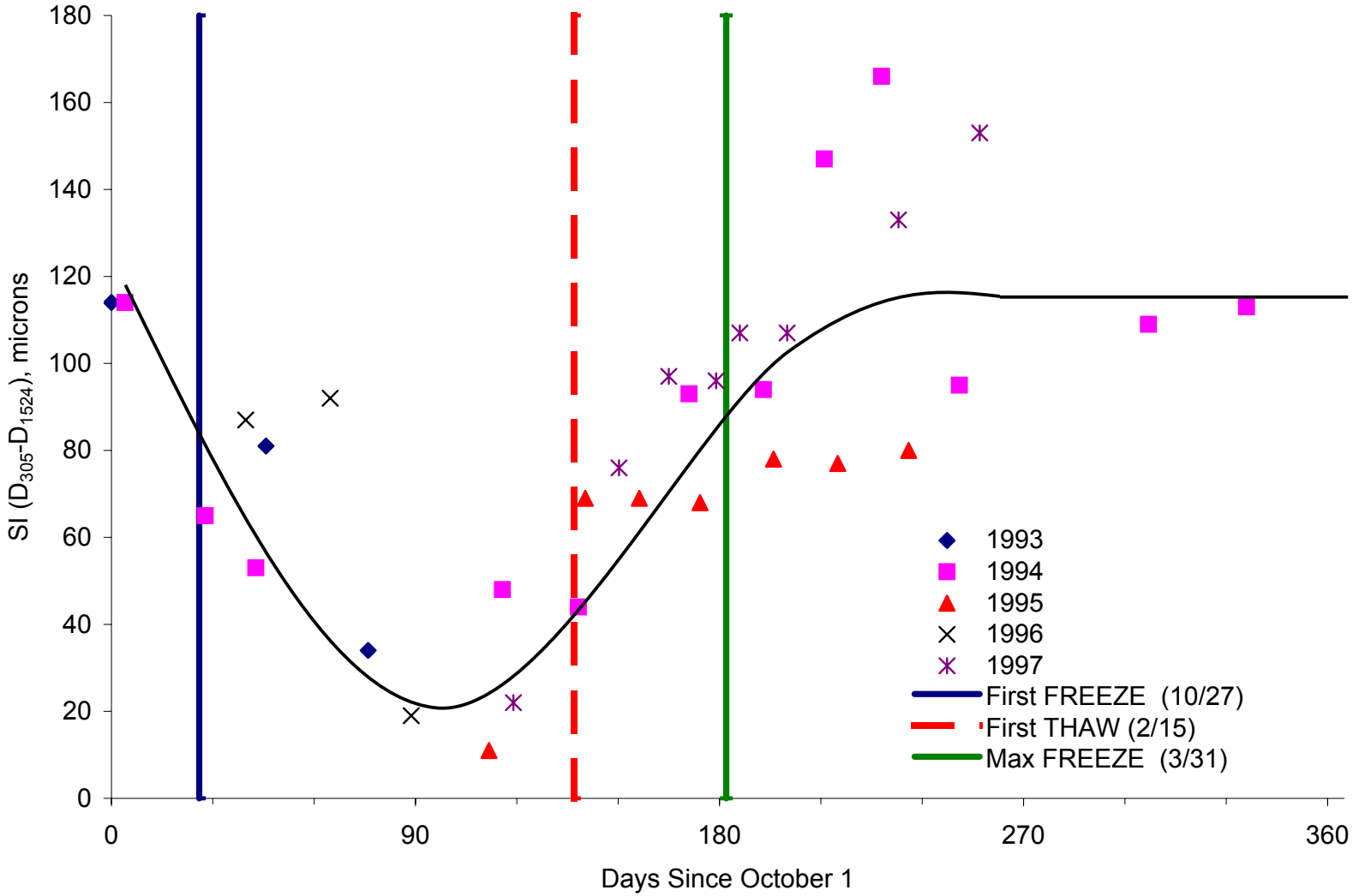

Figure R-4. Index SI at Site 16-1010 (Silty Sand)

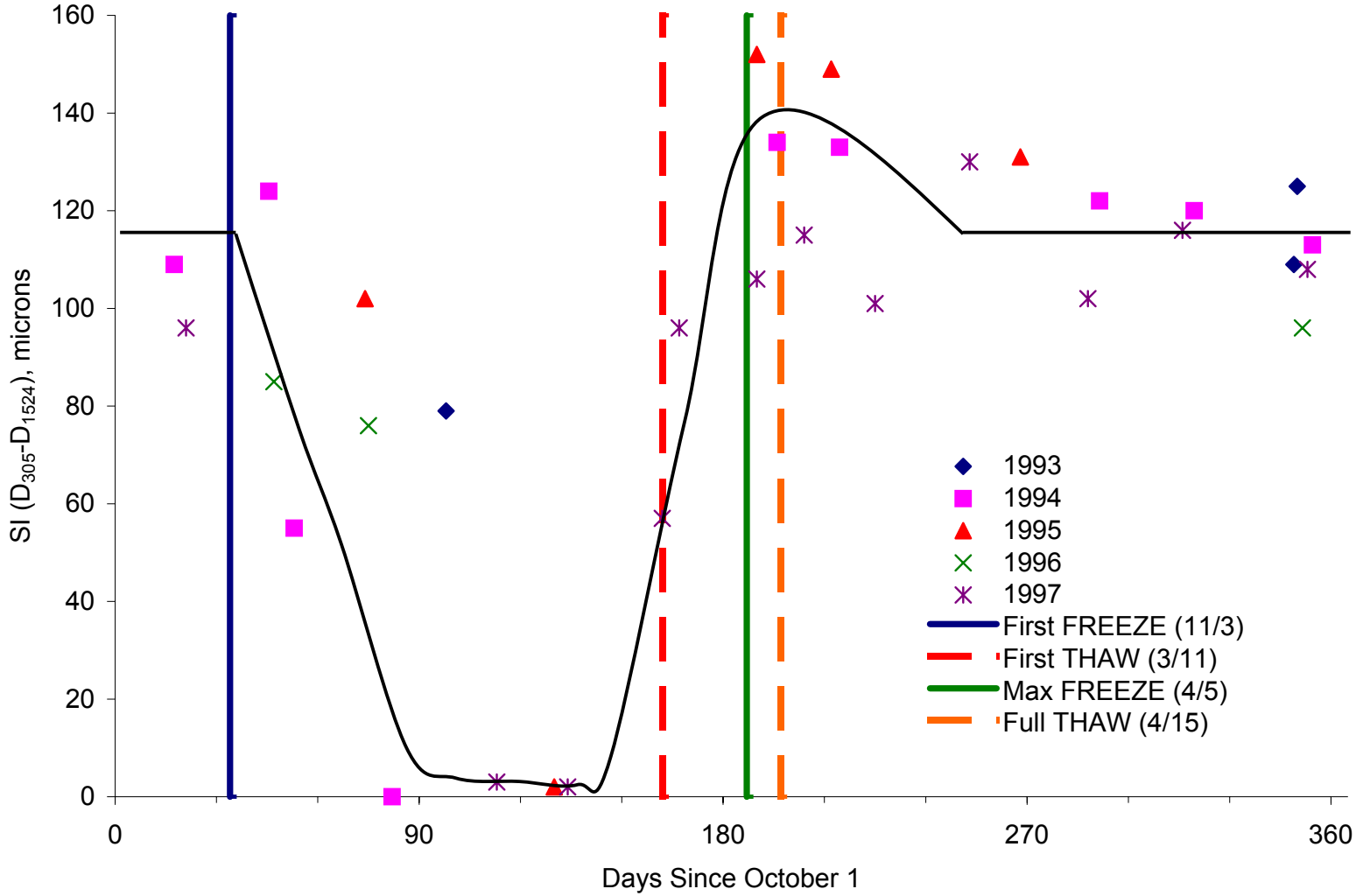

Figure R-5. Index SI at Site 23-1026 (Silty Sand with Gravel)

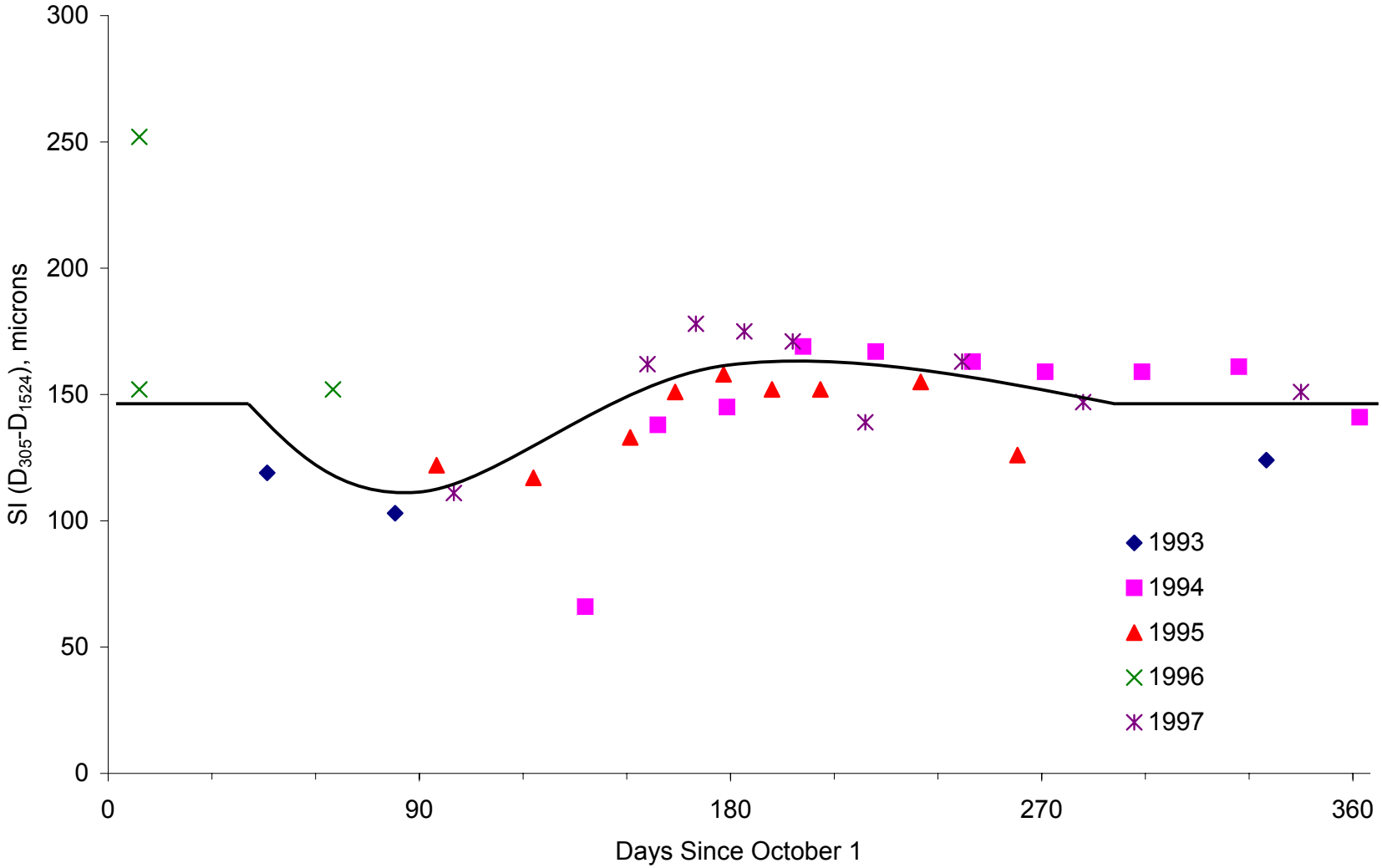

Figure R-6. Index SI at Site 25-1002 (Poorly Graded Sand with Silt)

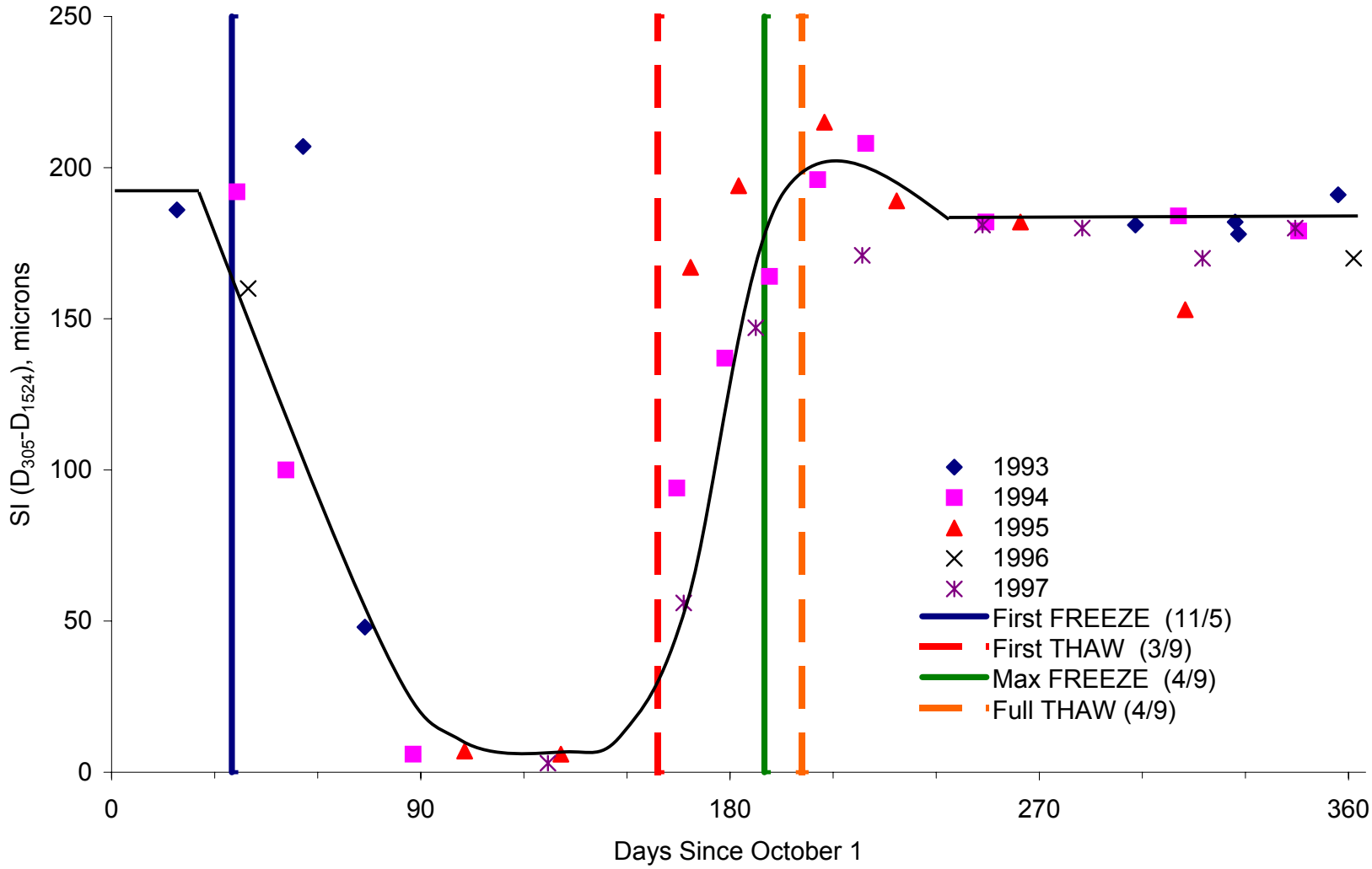

Figure R-7. Index SI at Site 27-1018 (Poorly Graded Sand with Silt)

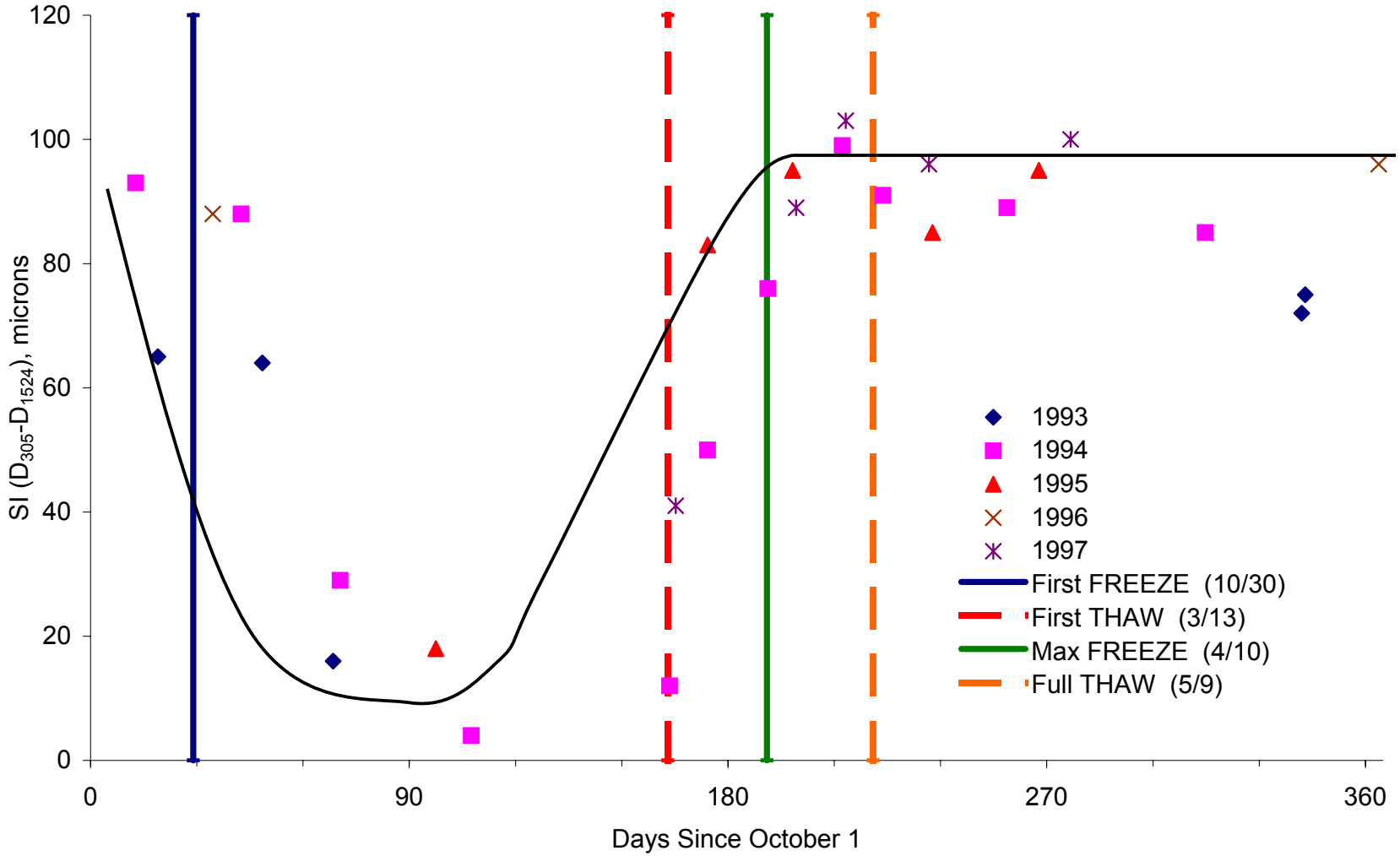

Figure R-8. Index SI at Site 27-1028 (Poorly Graded Sand with Silt)

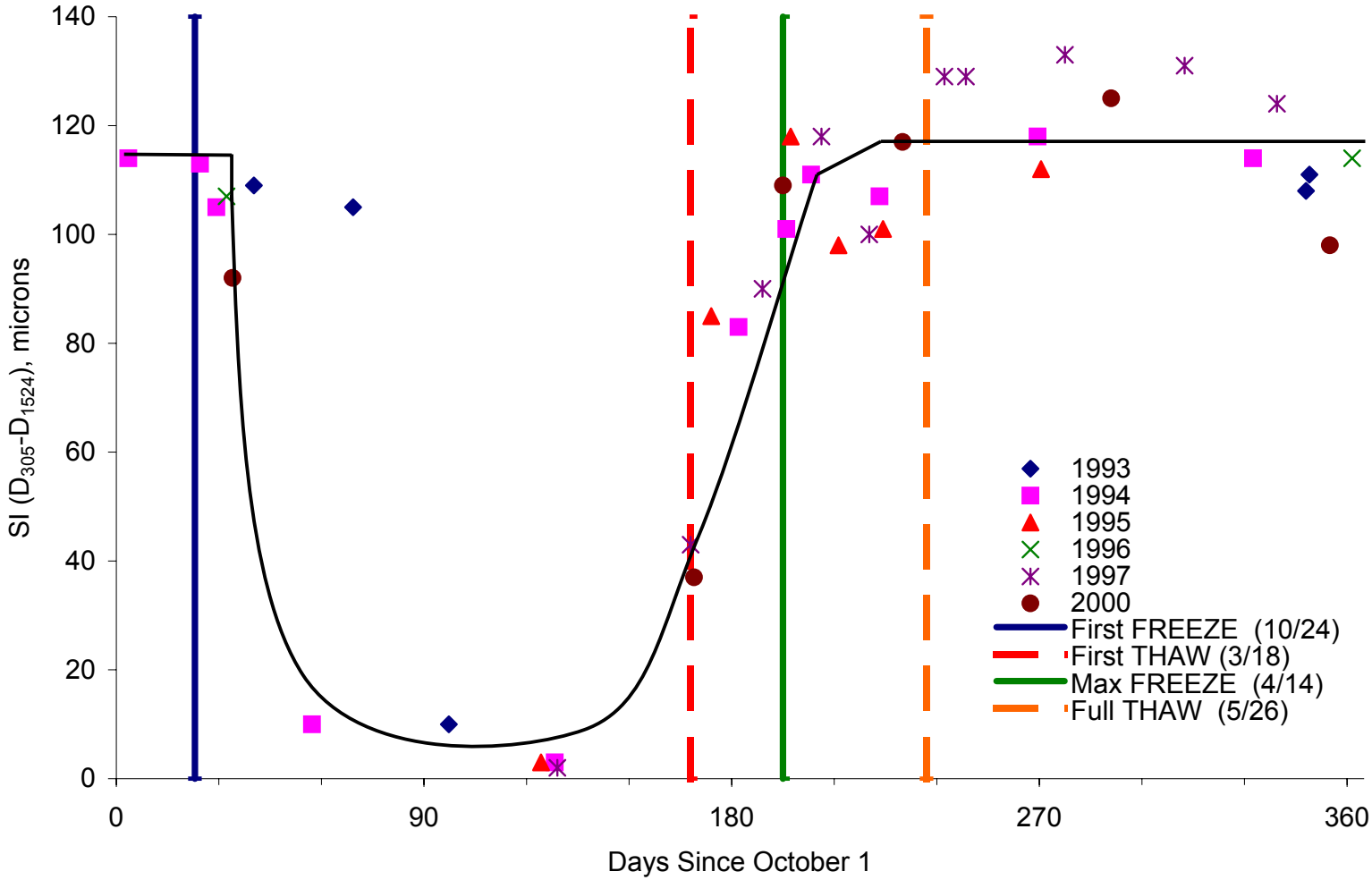

Figure R-9. Index SI at Site 27-6251 (Poorly Graded Sand with Silt)

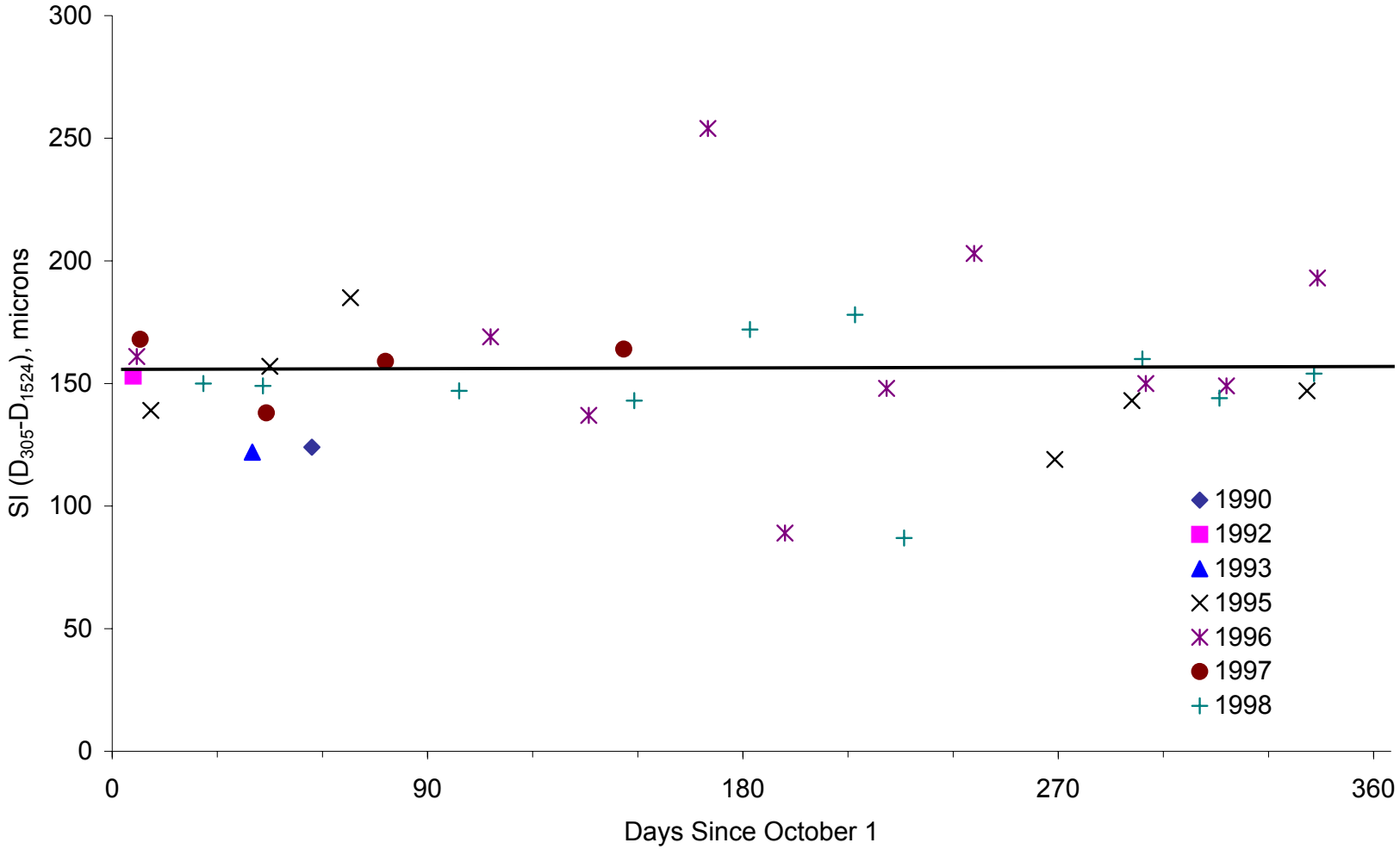

Figure R-10. Index SI at Site 28-1802 (Poorly Graded Sand)

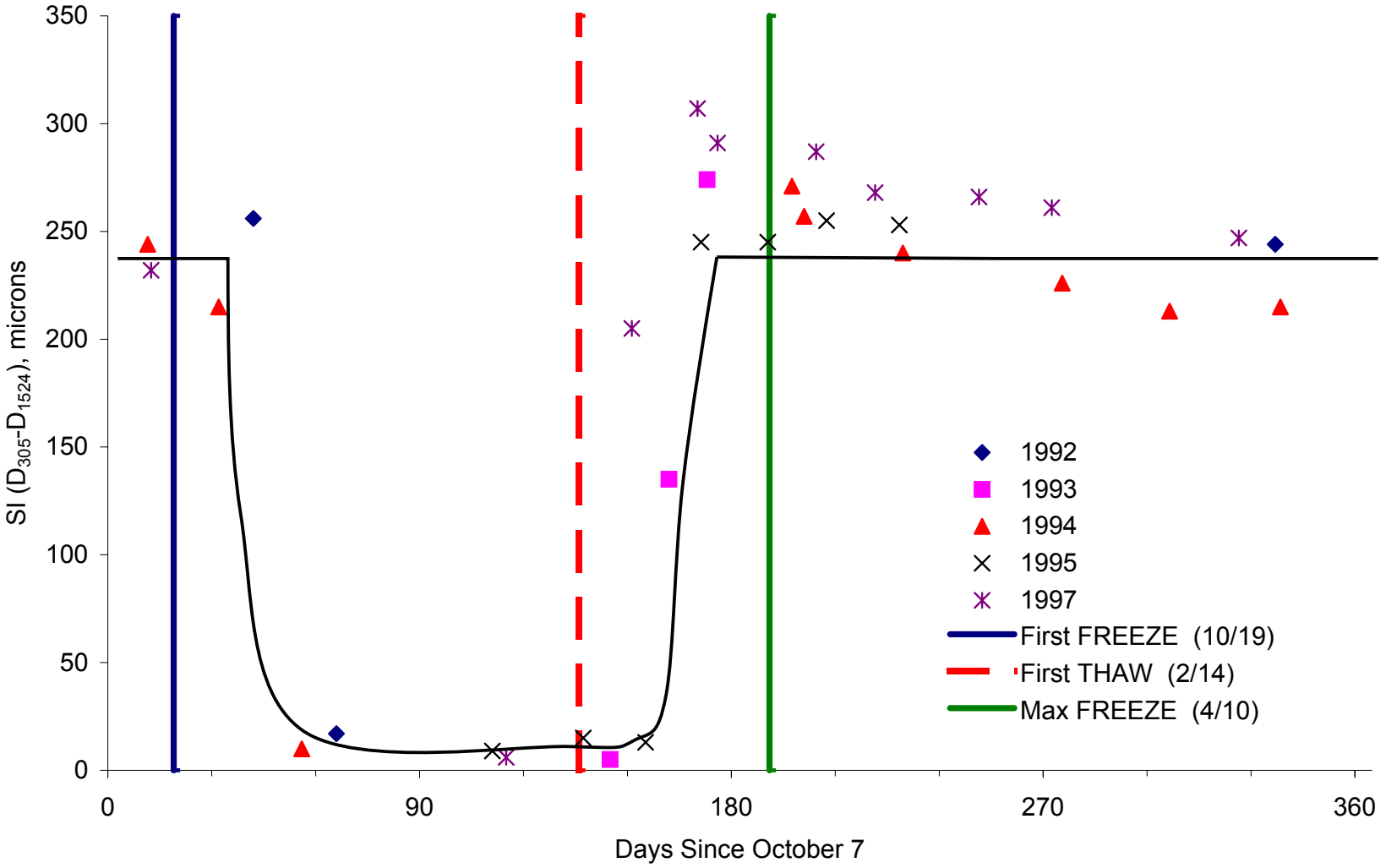

Figure R-11. Index SI at Site 30-8129 (Poorly Graded Sand with Silt)

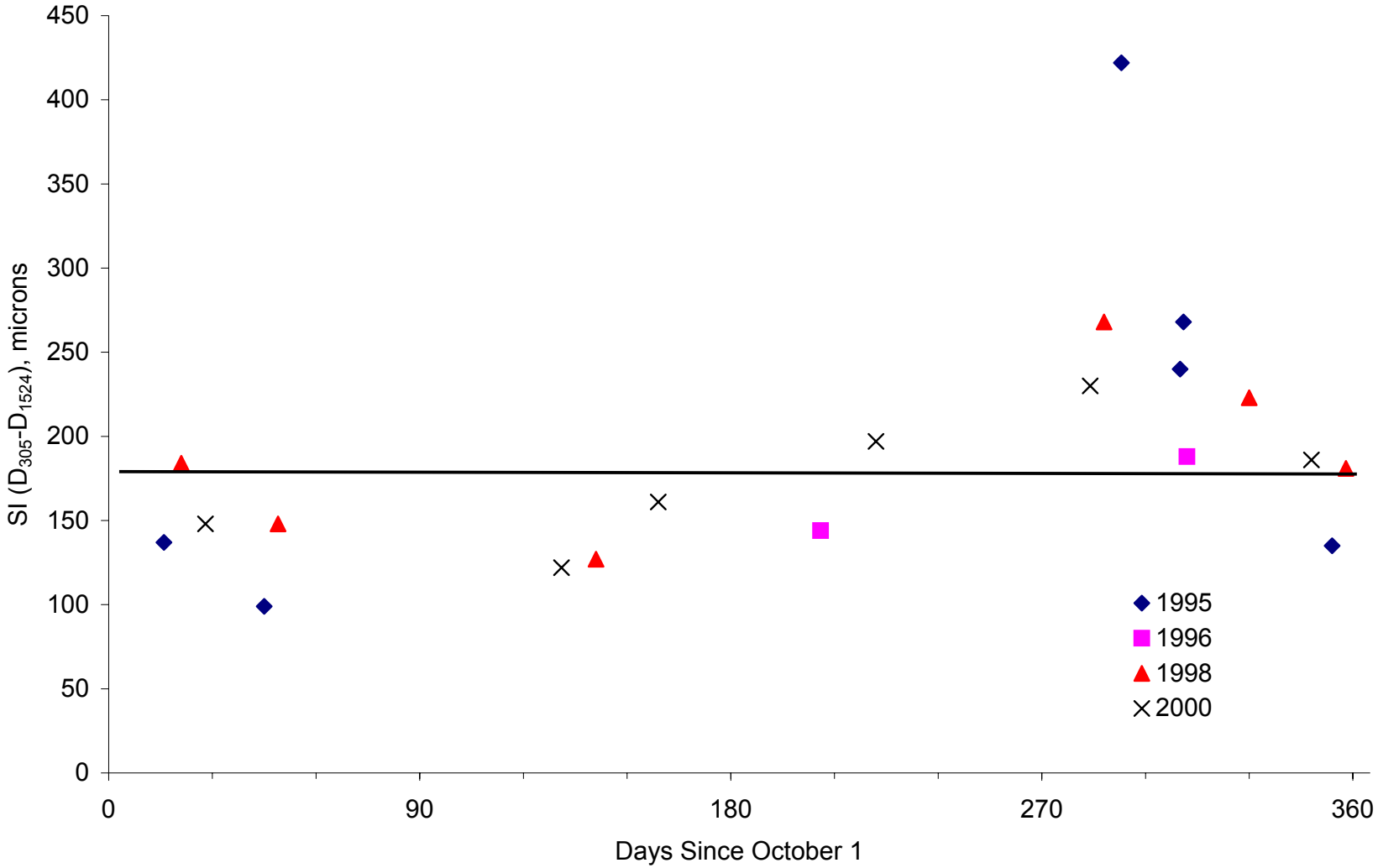

Figure R-12. Index SI at Site 31-0114 (Silty Clay)

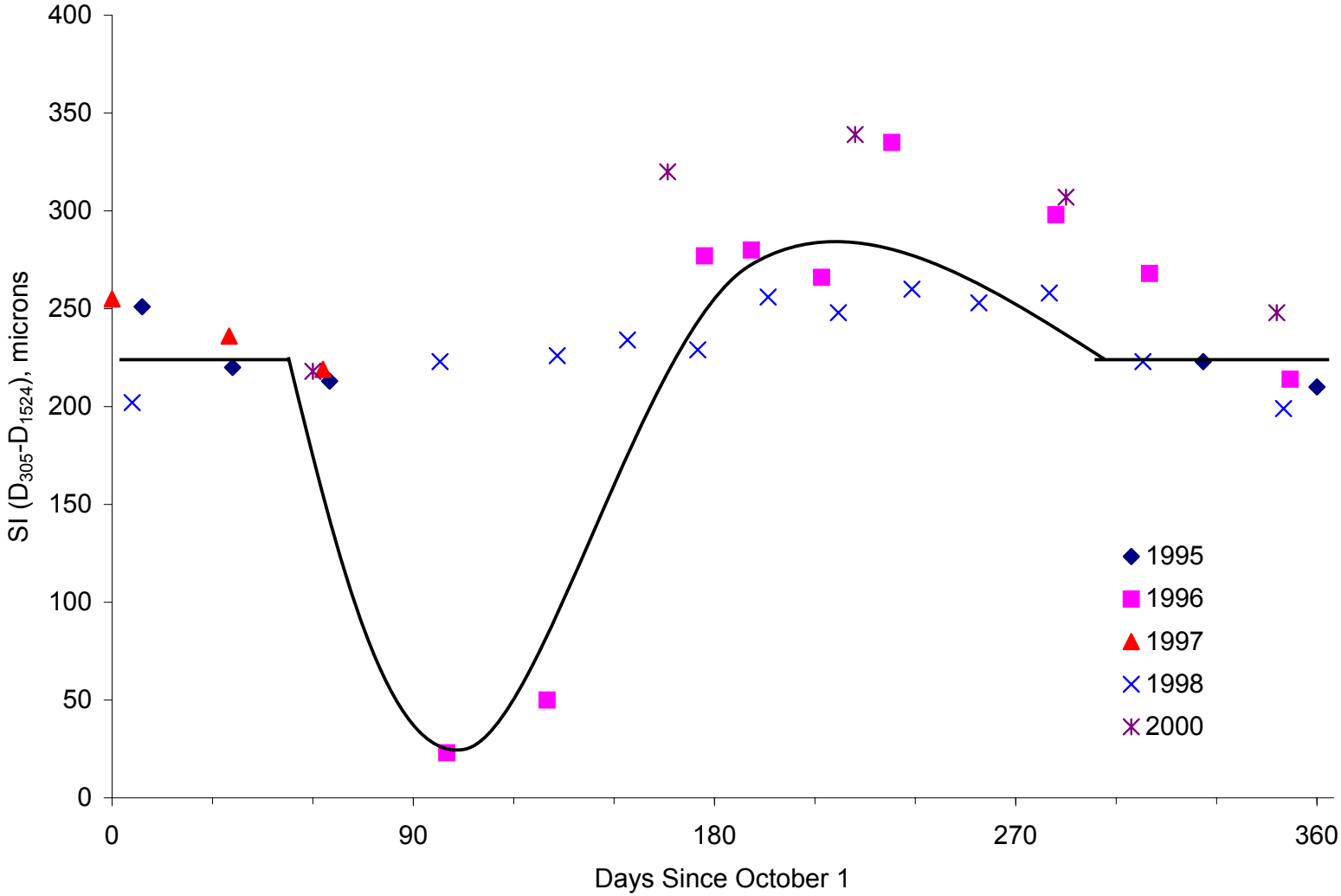

Figure R-13. Index SI at Site 36-0801 (Silty Sand)

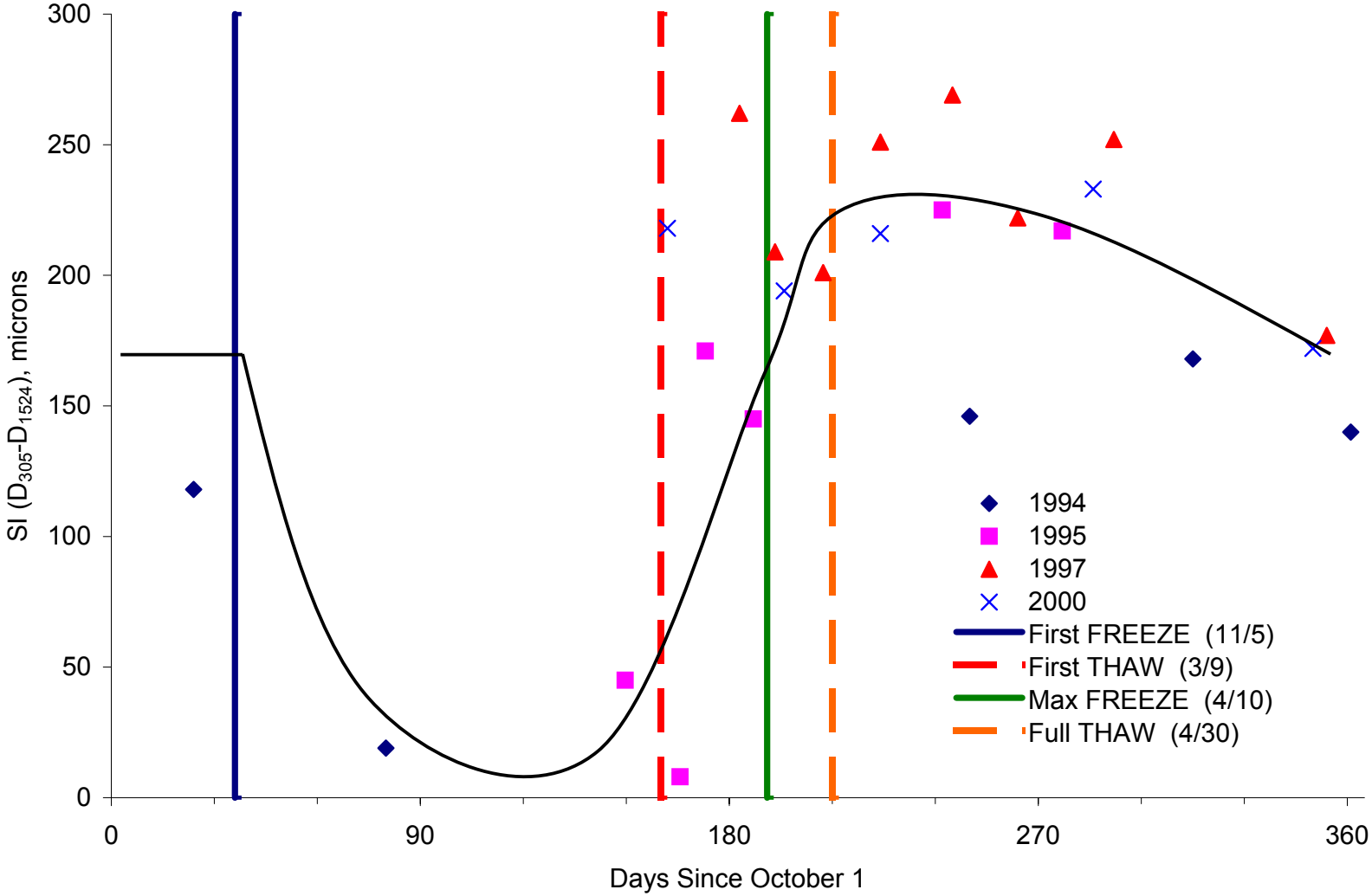

Figure R-14. Index SI at Site 46-0804 (Silty Clay)

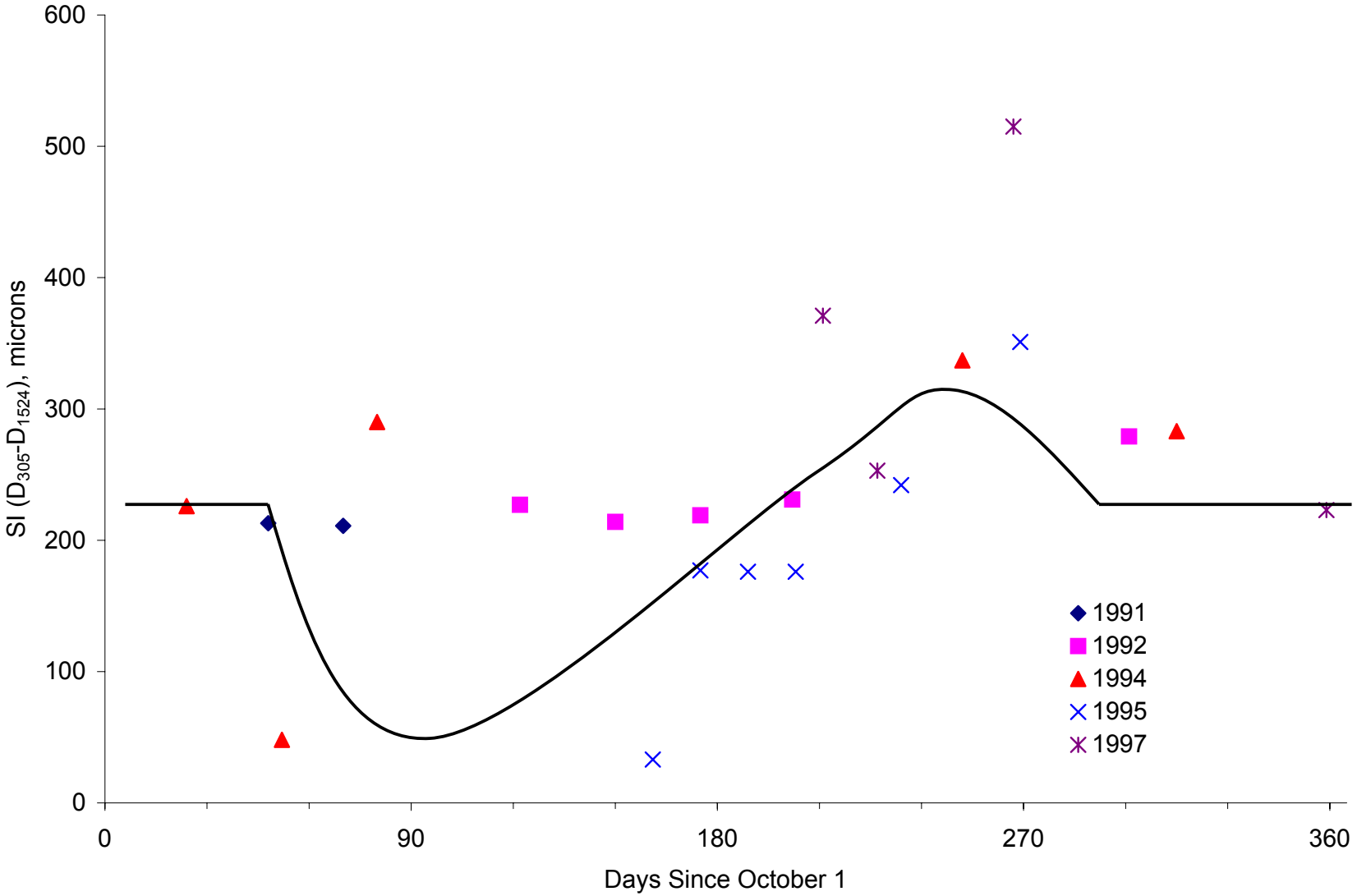

Figure R-15. Index SI at Site 46-9187 (Lean Inorganic Clay)

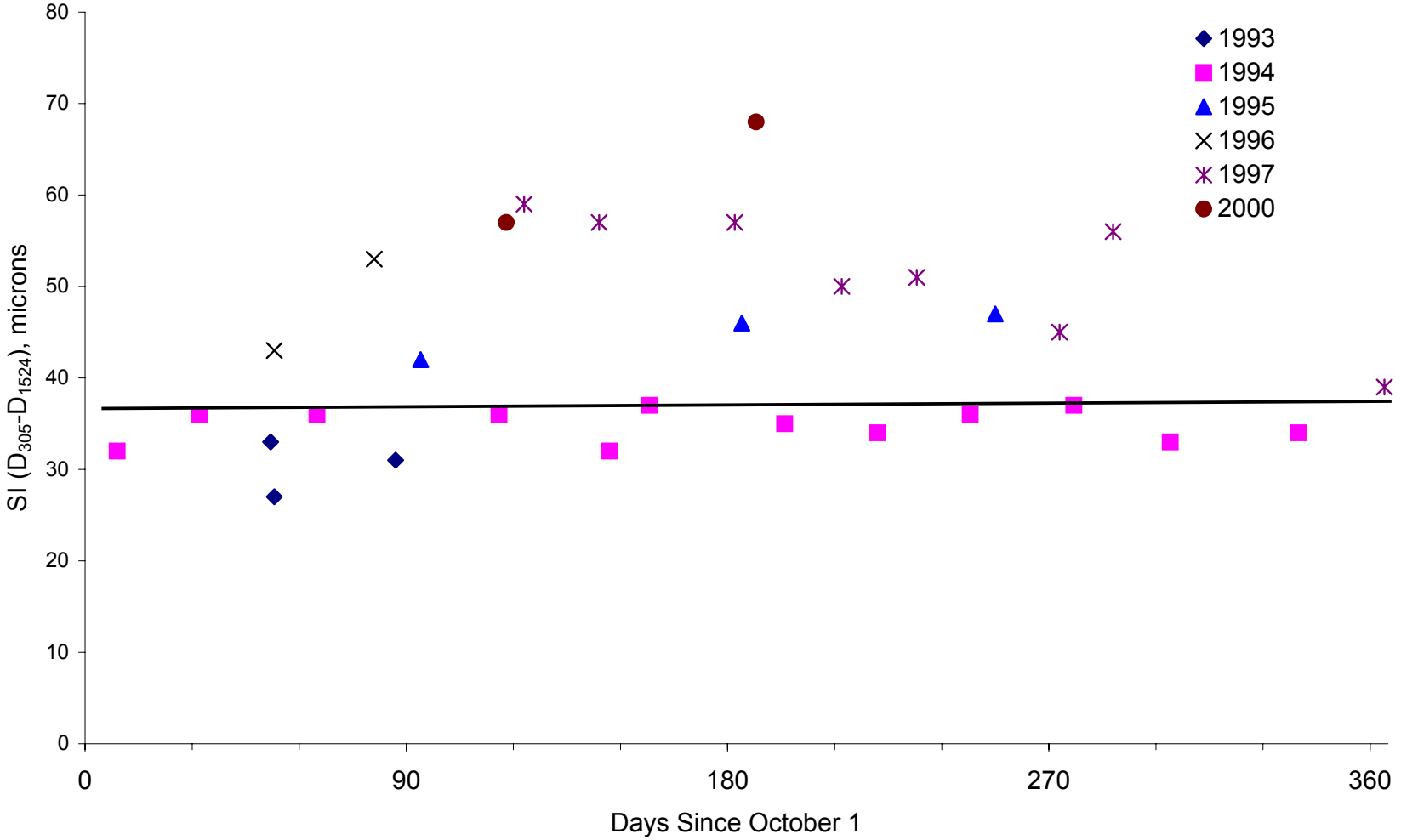

Figure R-16. Index SI at Site 48-1122 (Clayey Sand)

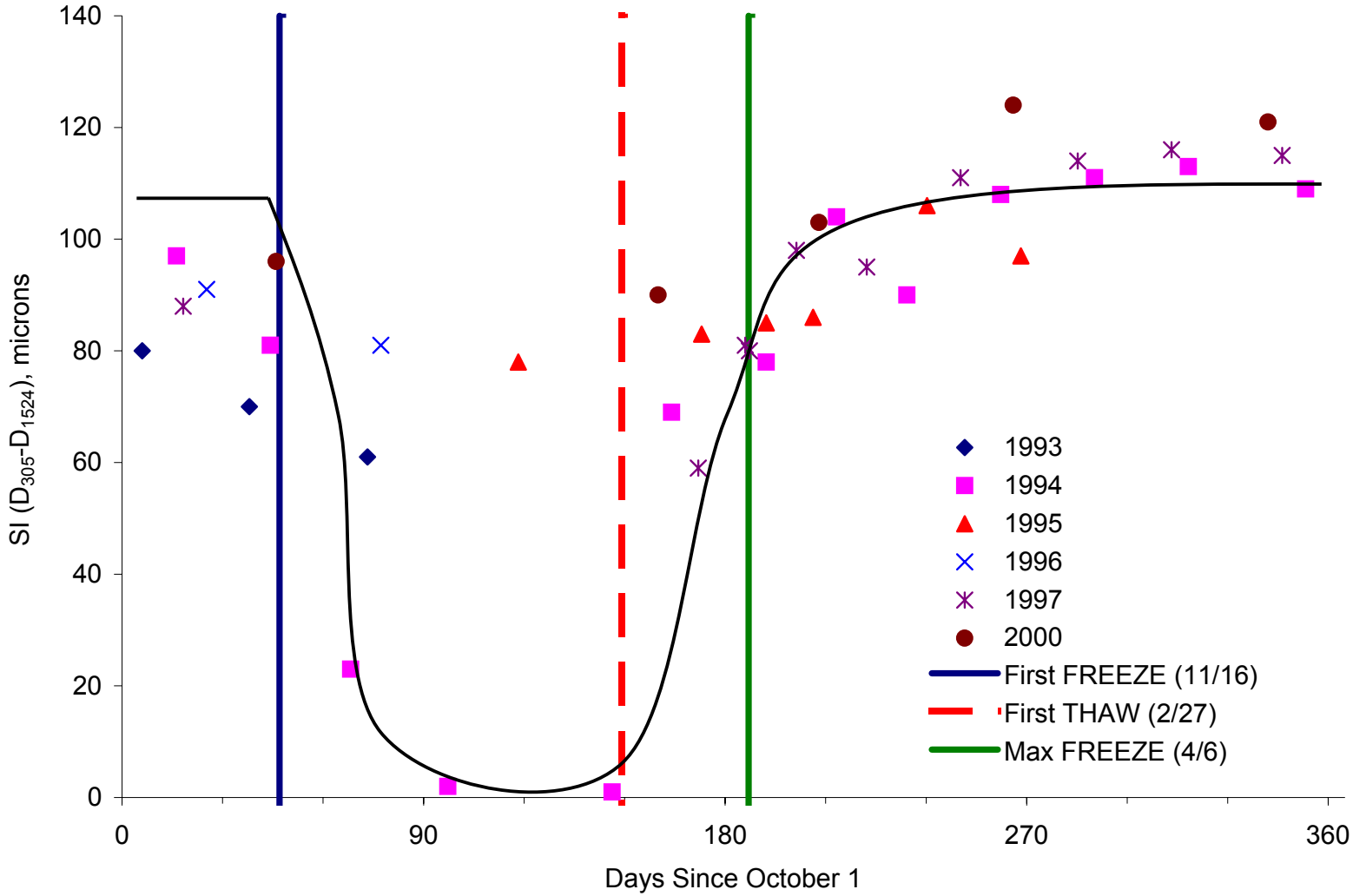

Figure R-17. Index SI at Site 50-1002 (Poorly Graded Gravel with Silty and Sand)

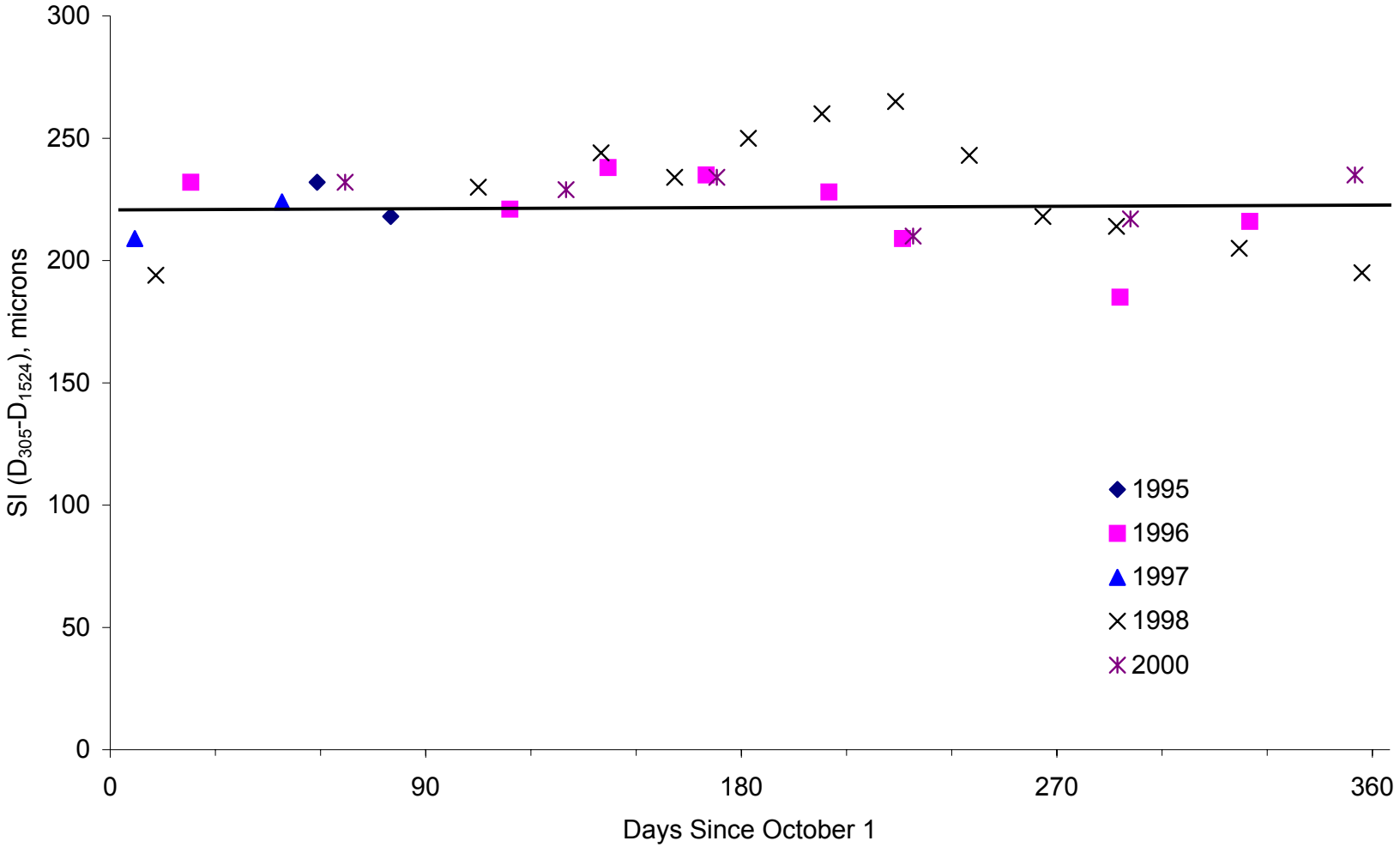

Figure R-18. Index SI at Site 51-0113 (Silt)

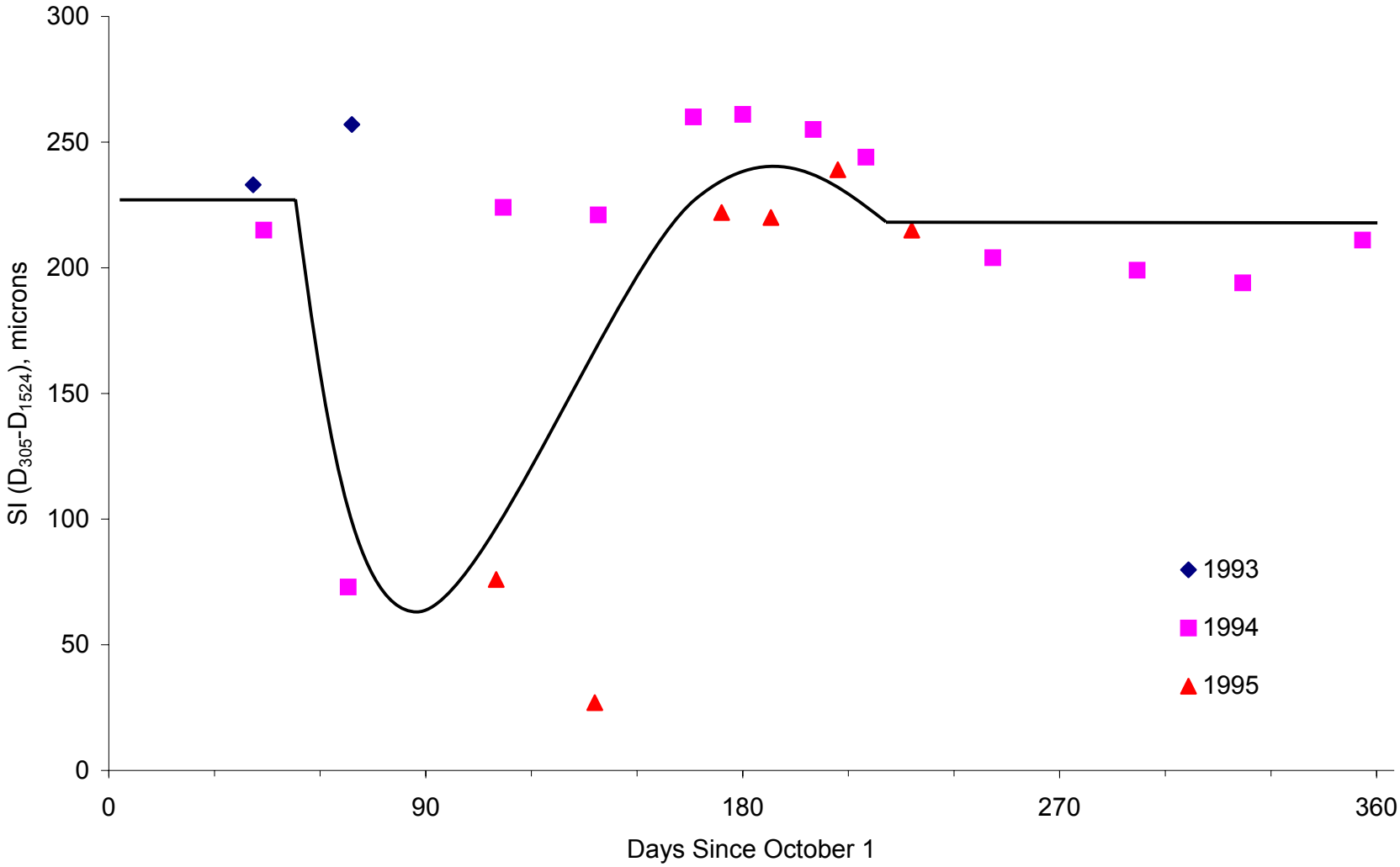

Figure R-19. Index SI at Site 56-1007 (Silty Sand with Gravel)

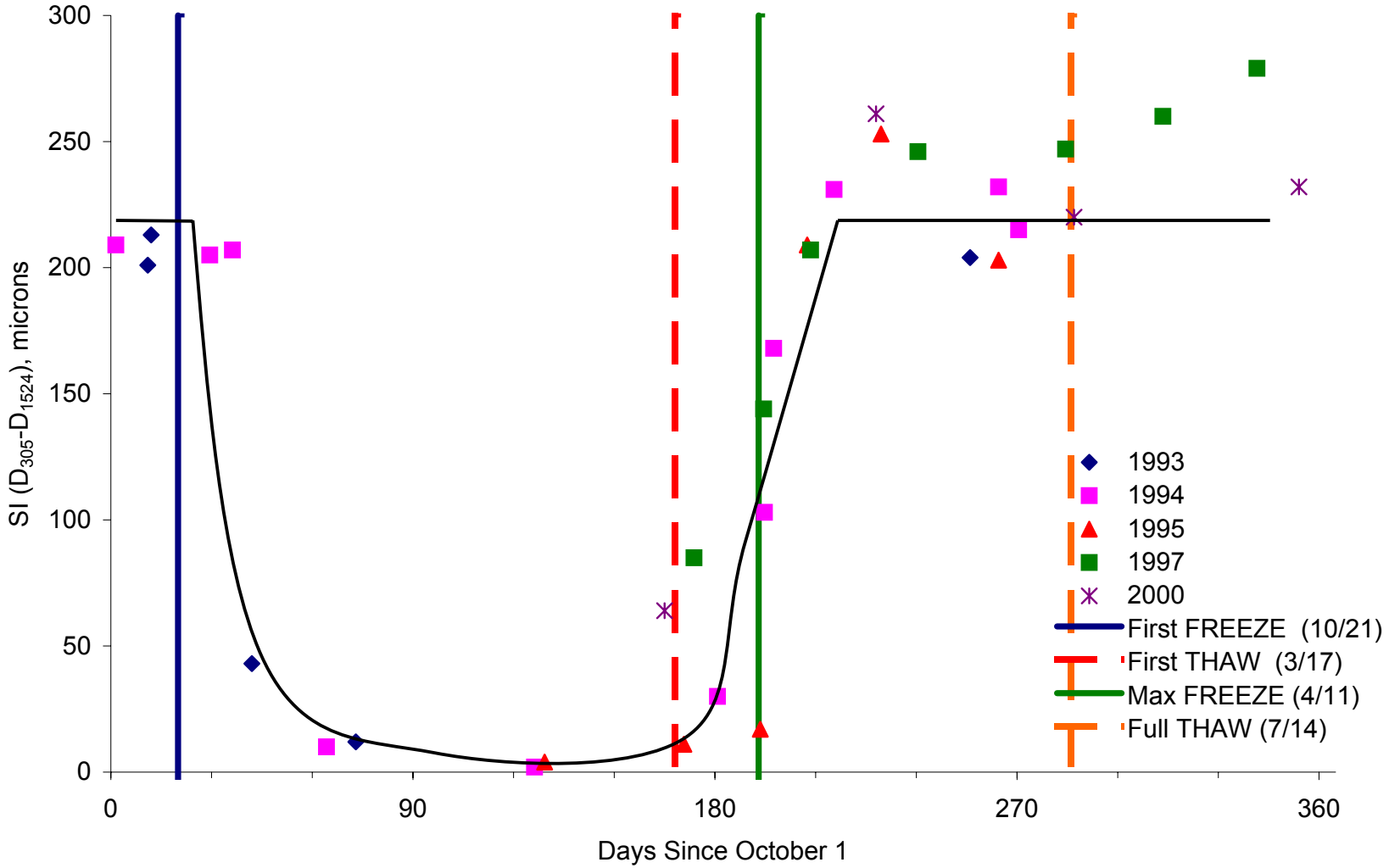

Figure R-20. Index SI at Site 83-1801 (Silty Sand)

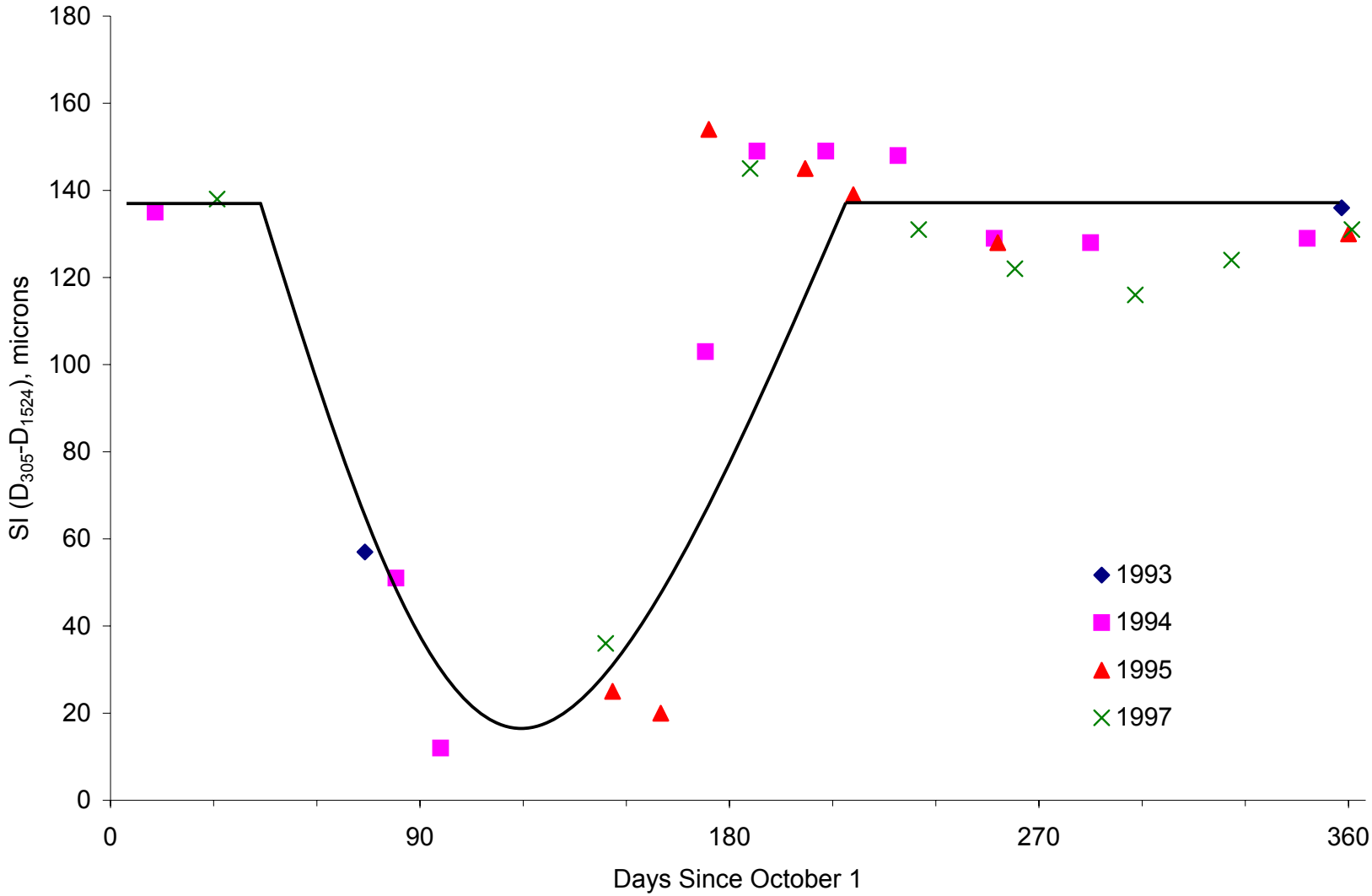

Figure R-21. Index SI at Site 87-1622 (Sandy Silt)

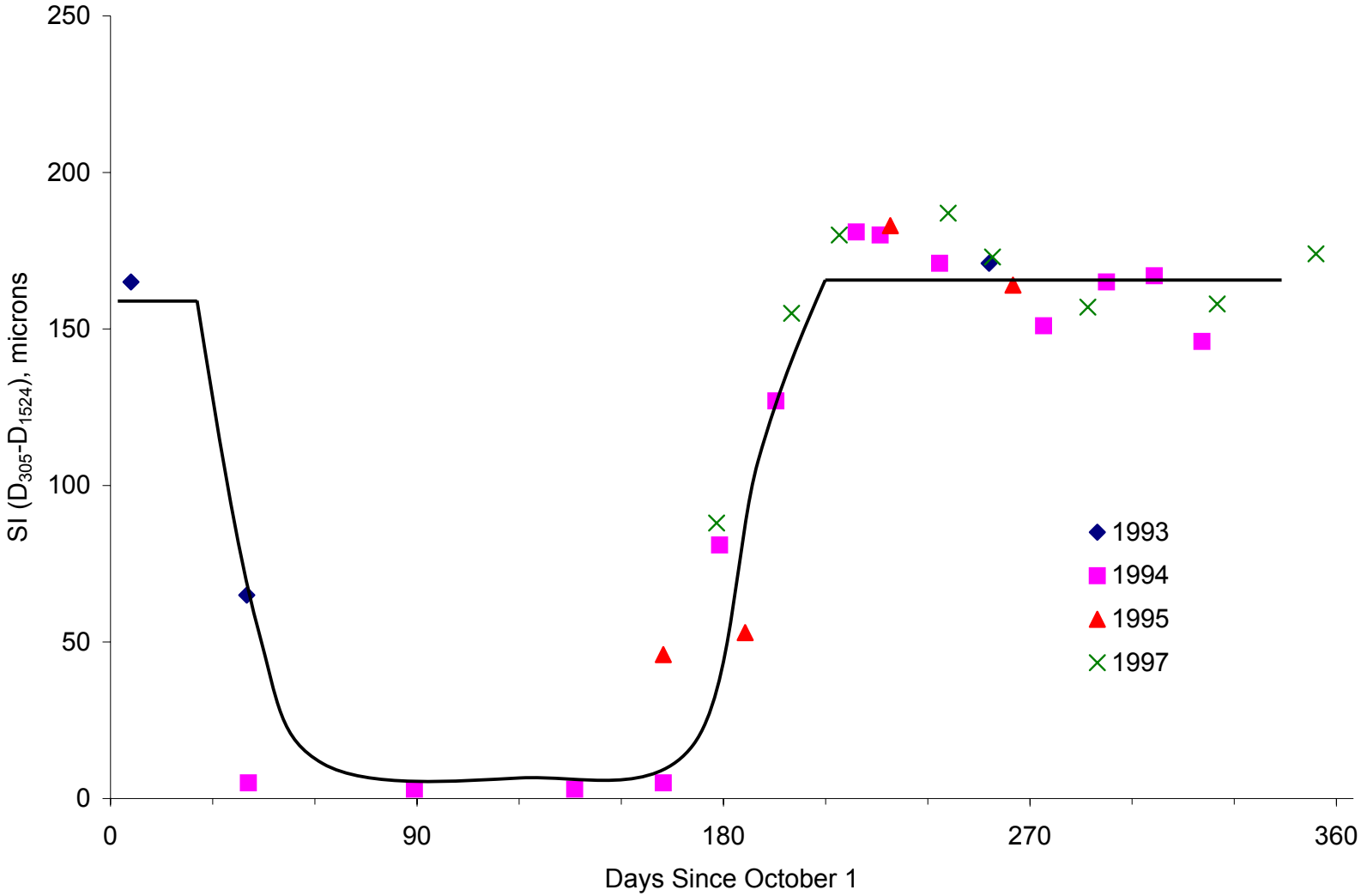

Figure R-22. Index SI at Site 90-6405 (Silty Sand)

APPENDIX S

SEASONAL VARIATIONS OF INDEX PA

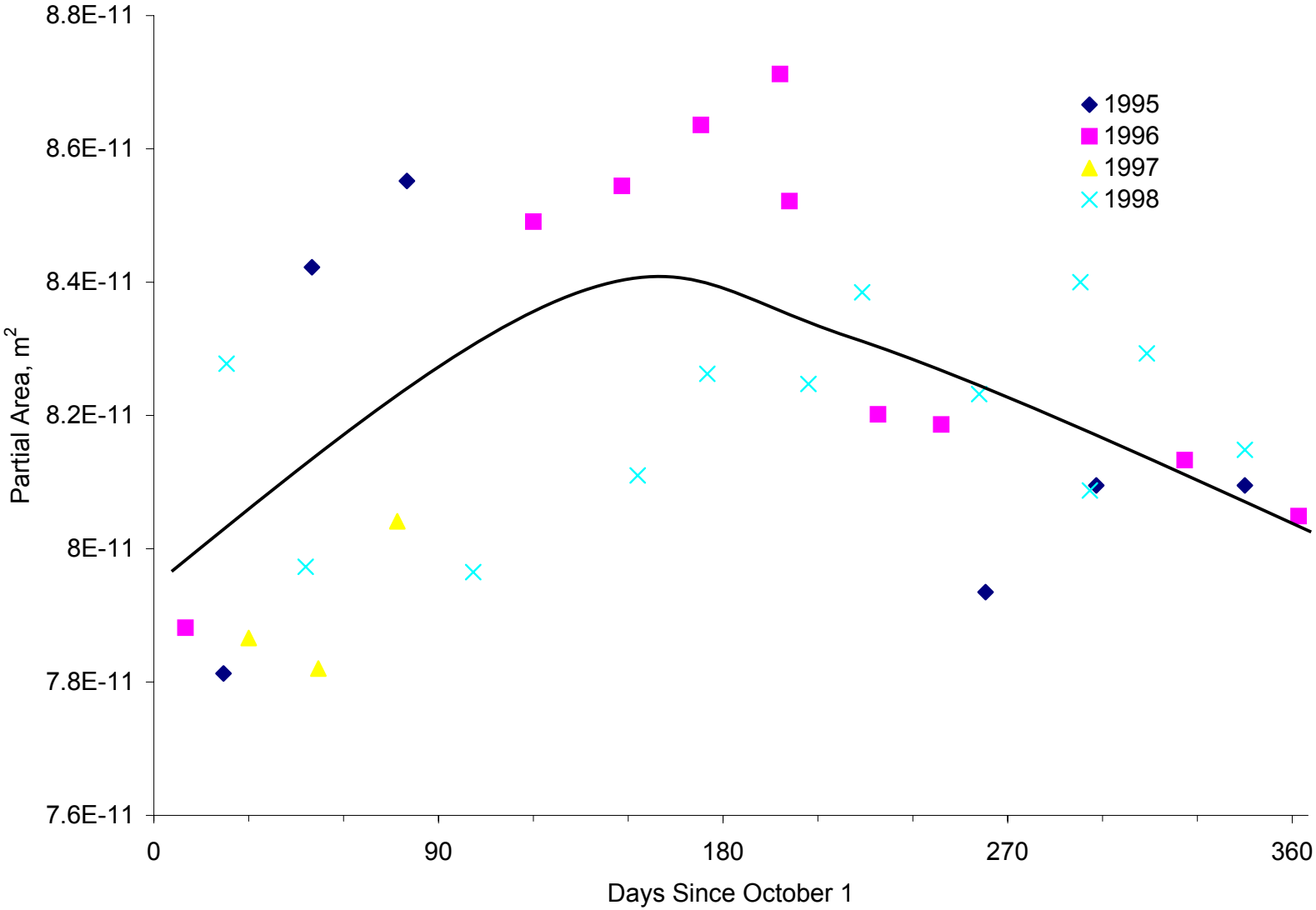

Figure S-1. Index PA at Site 01-0101 (Sandy Silt)

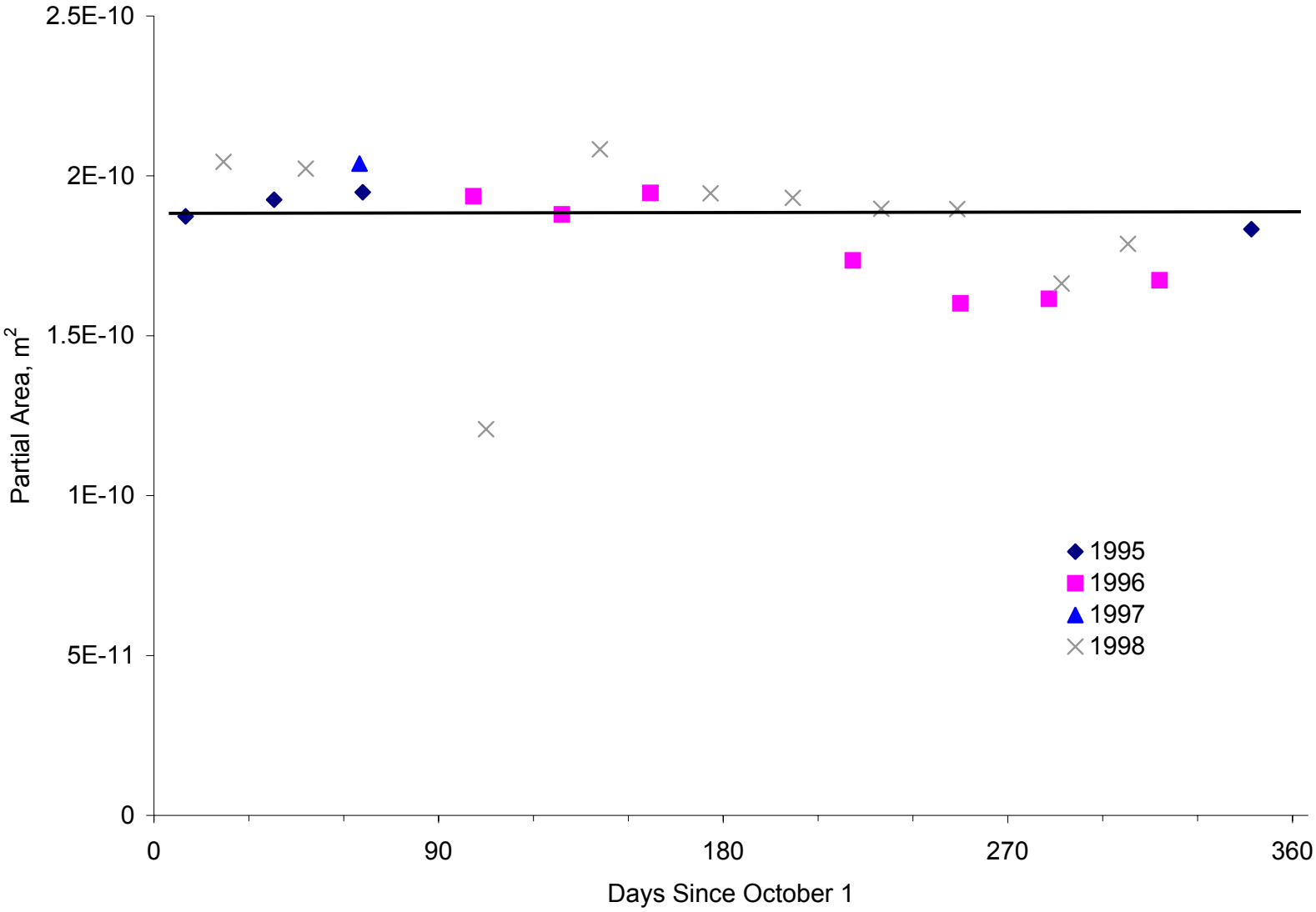

Figure S-2. Index PA at Site 04-0113 (Well Graded Sand with Silt and Gravel)

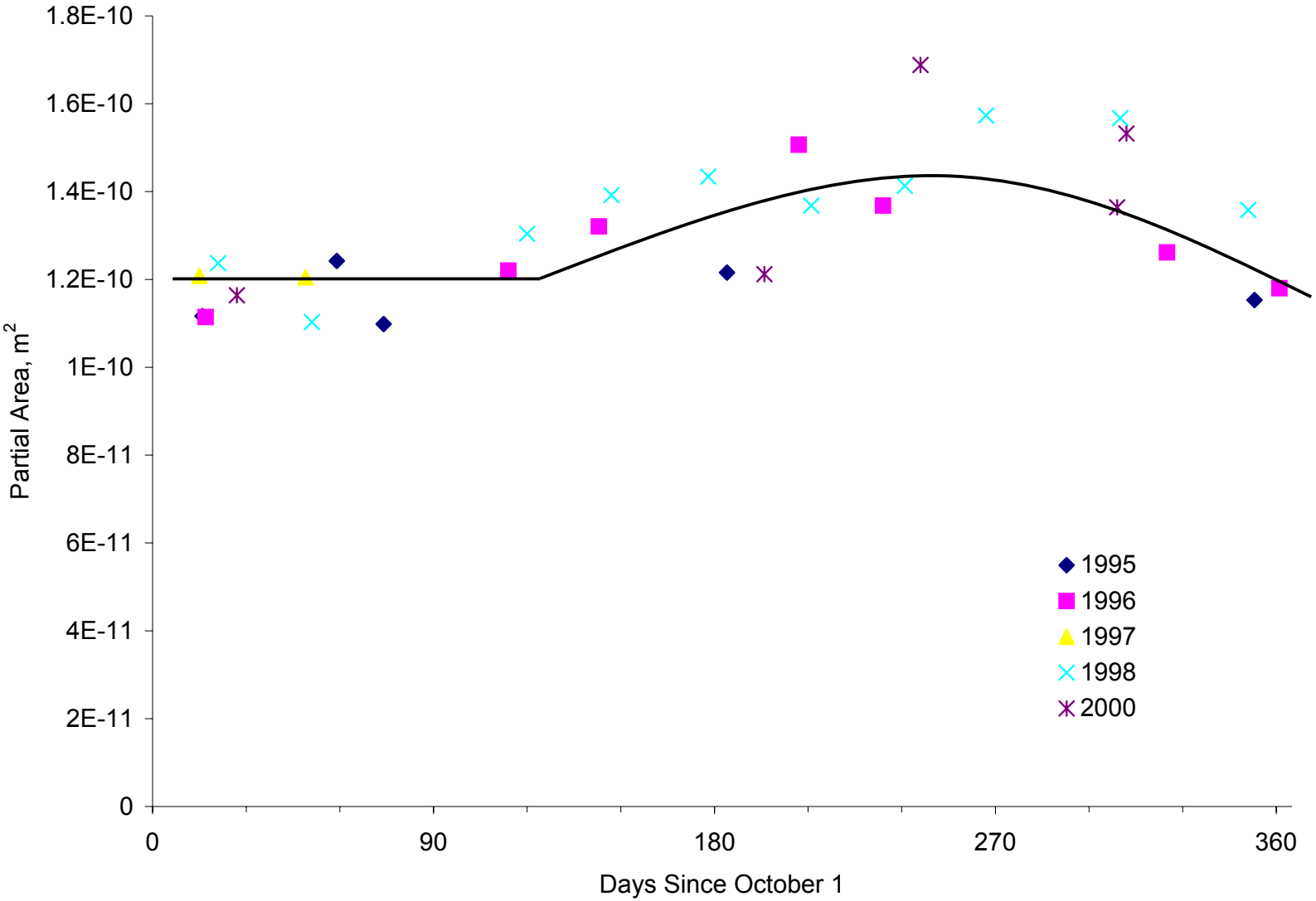

Figure S-3. Index PA at Site 13-1031 (Silty Sand)

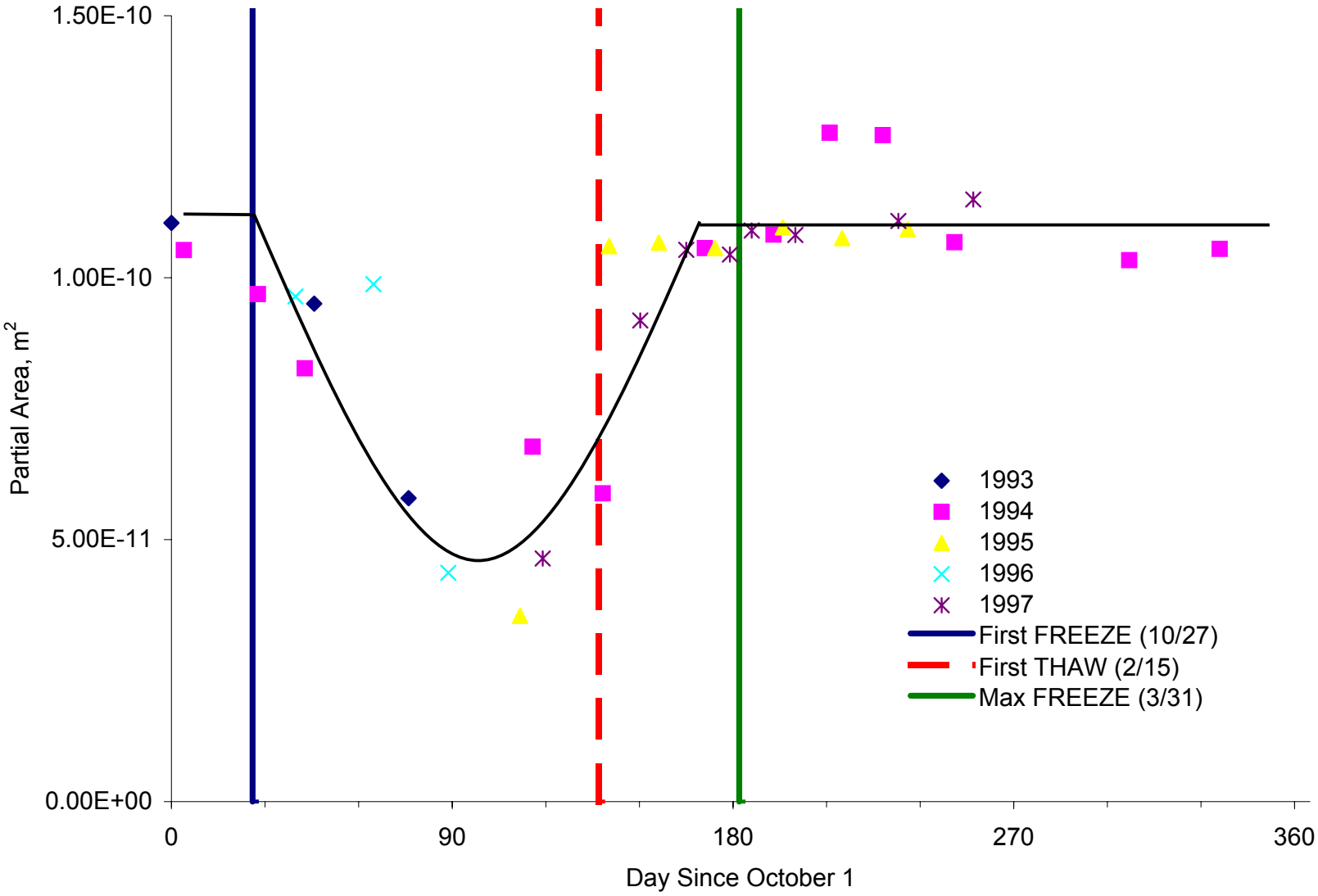

Figure S-4. Index PA at Site 16-1010 (Silty Sand)

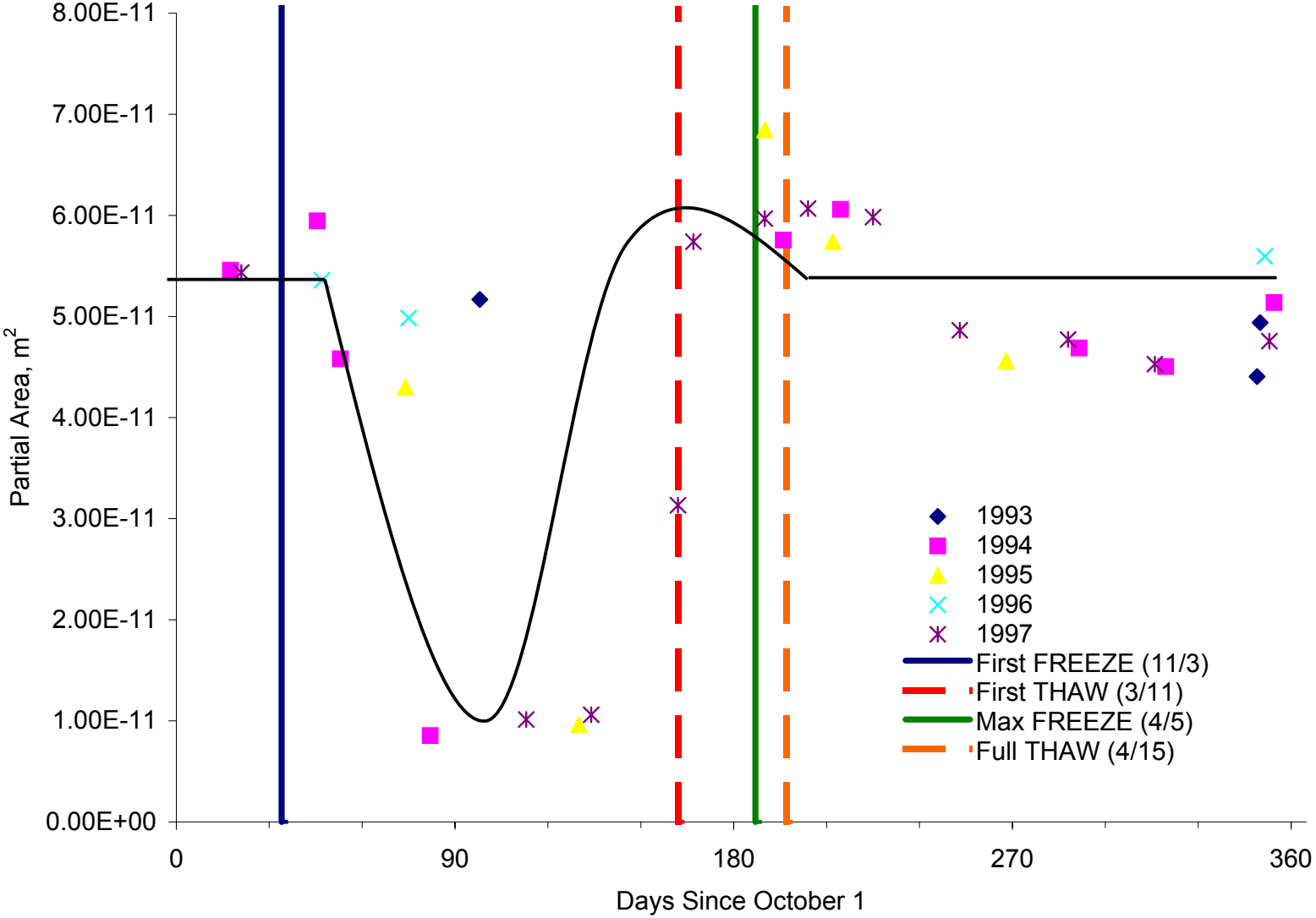

Figure S-5. Index PA at Site 23-1026 (Silt Sand with Gravel)

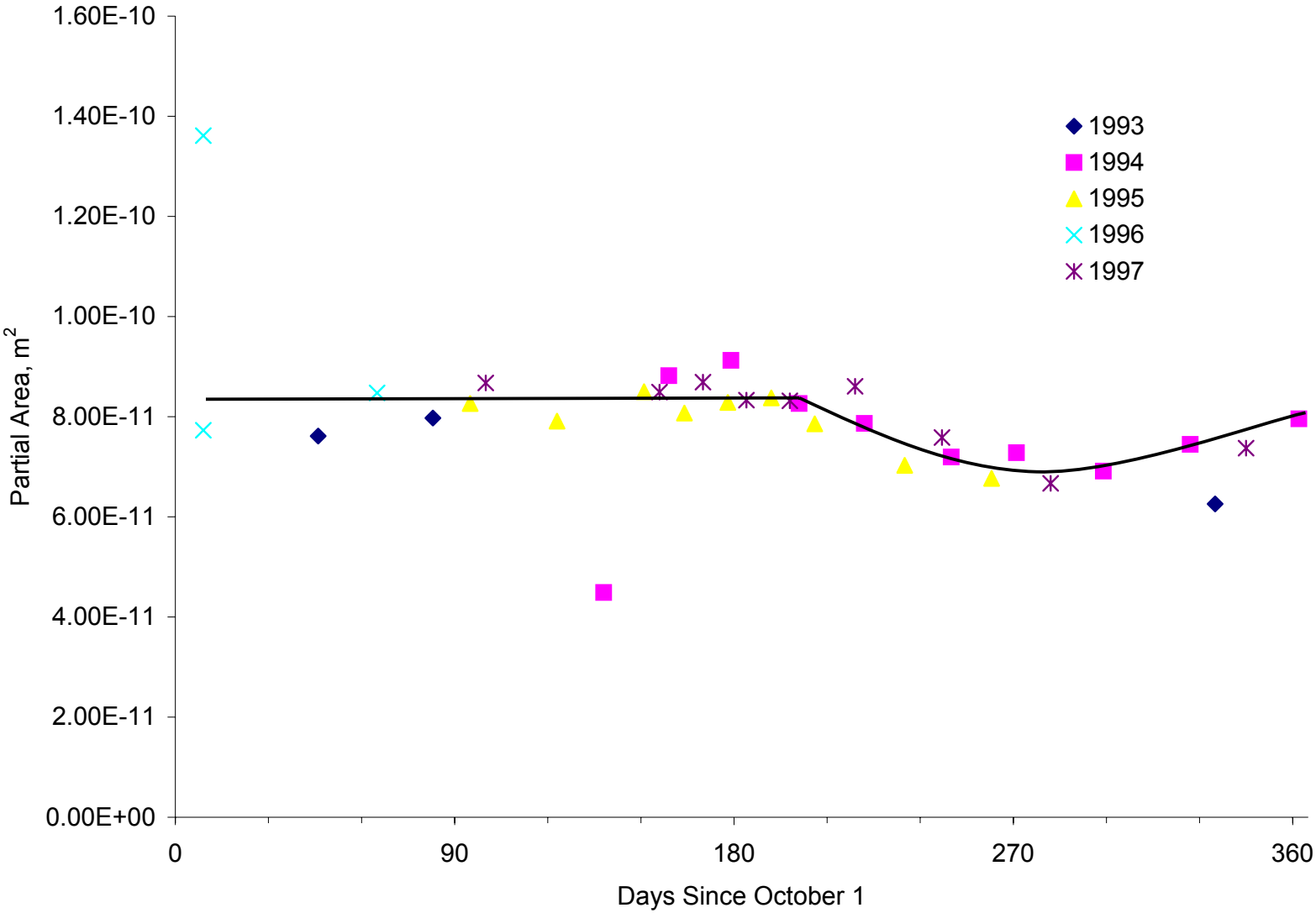

Figure S-6. Index PA at Site 25-1002 (Poorly Graded Sand with Silt)

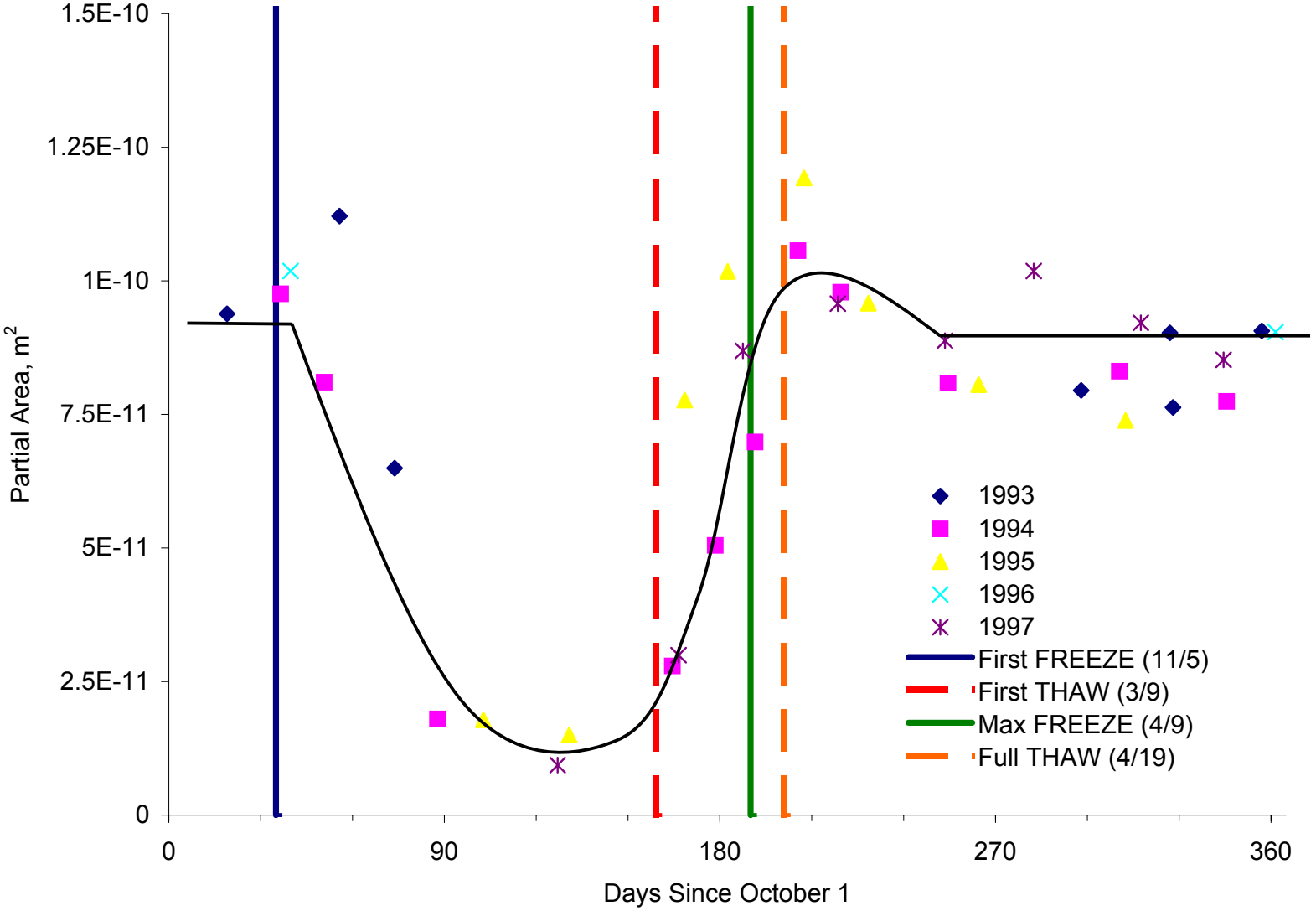

Figure S-7. Index PA at Site 27-1018 (Poorly Graded Sand with Silt)

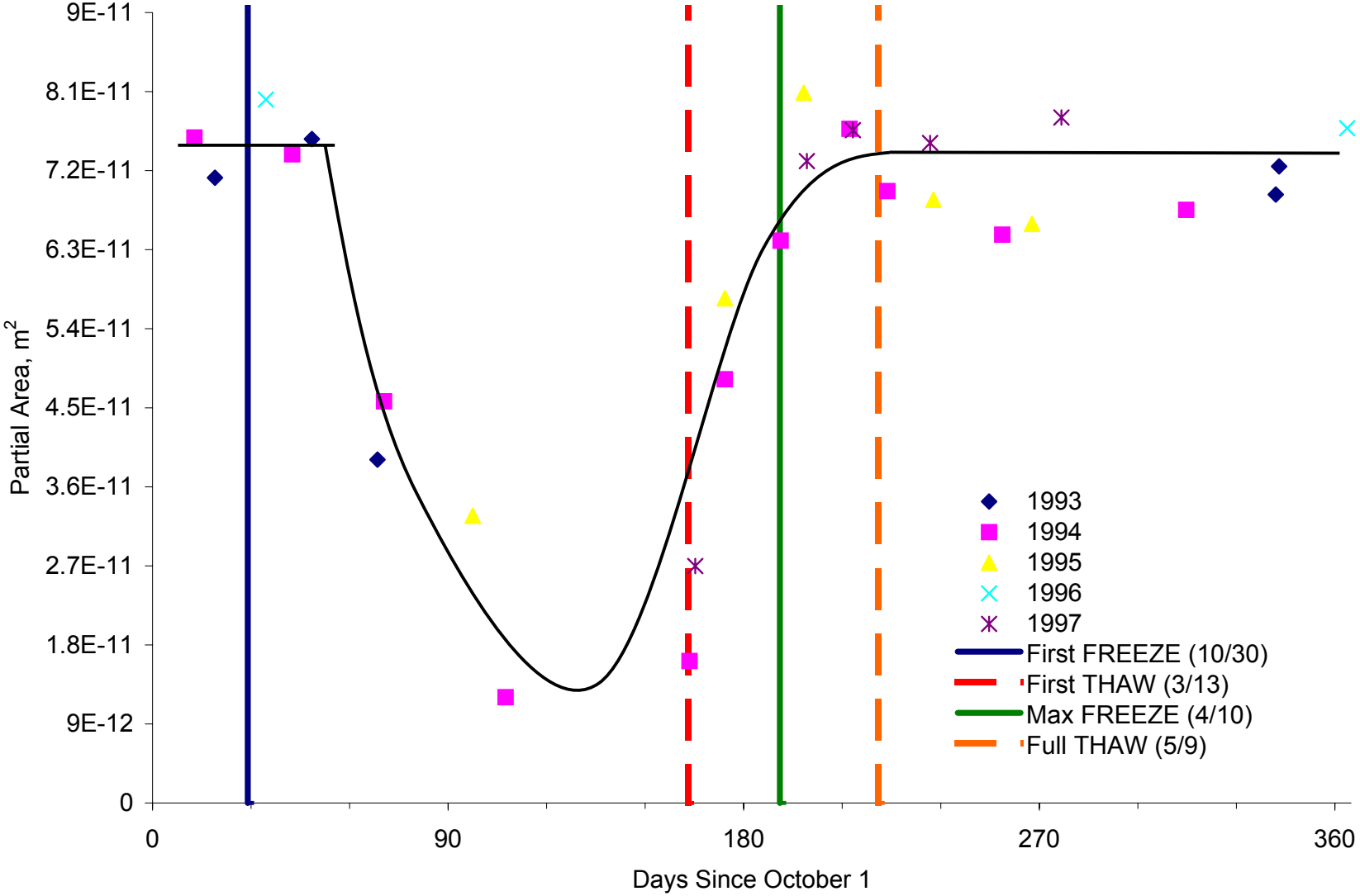

Figure S-8. Index PA at Site 27-1028 (Poorly Graded Sand with Silt)

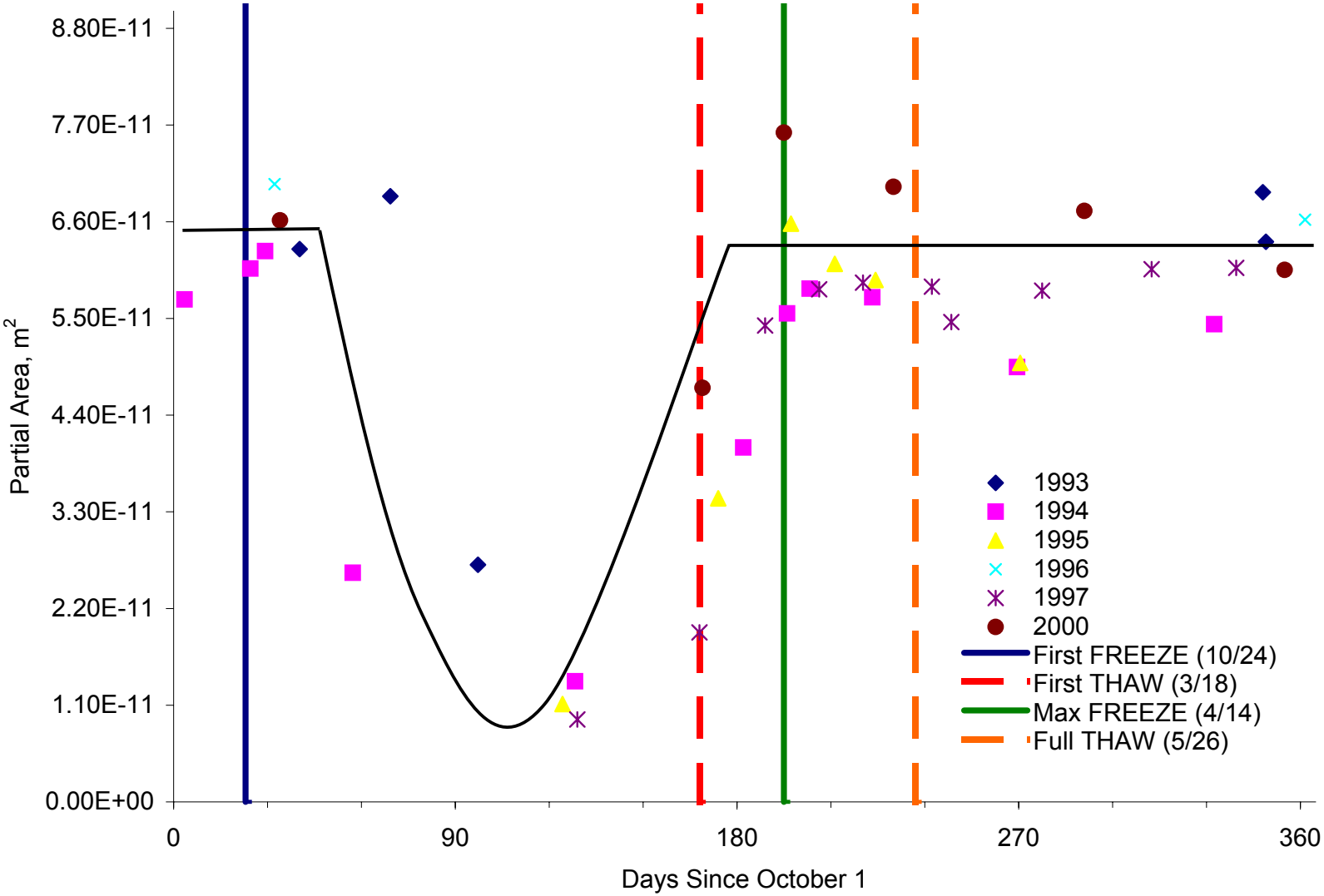

Figure S-9. Index PA at Site 27-6251 (Poorly Graded Sand with Silt)

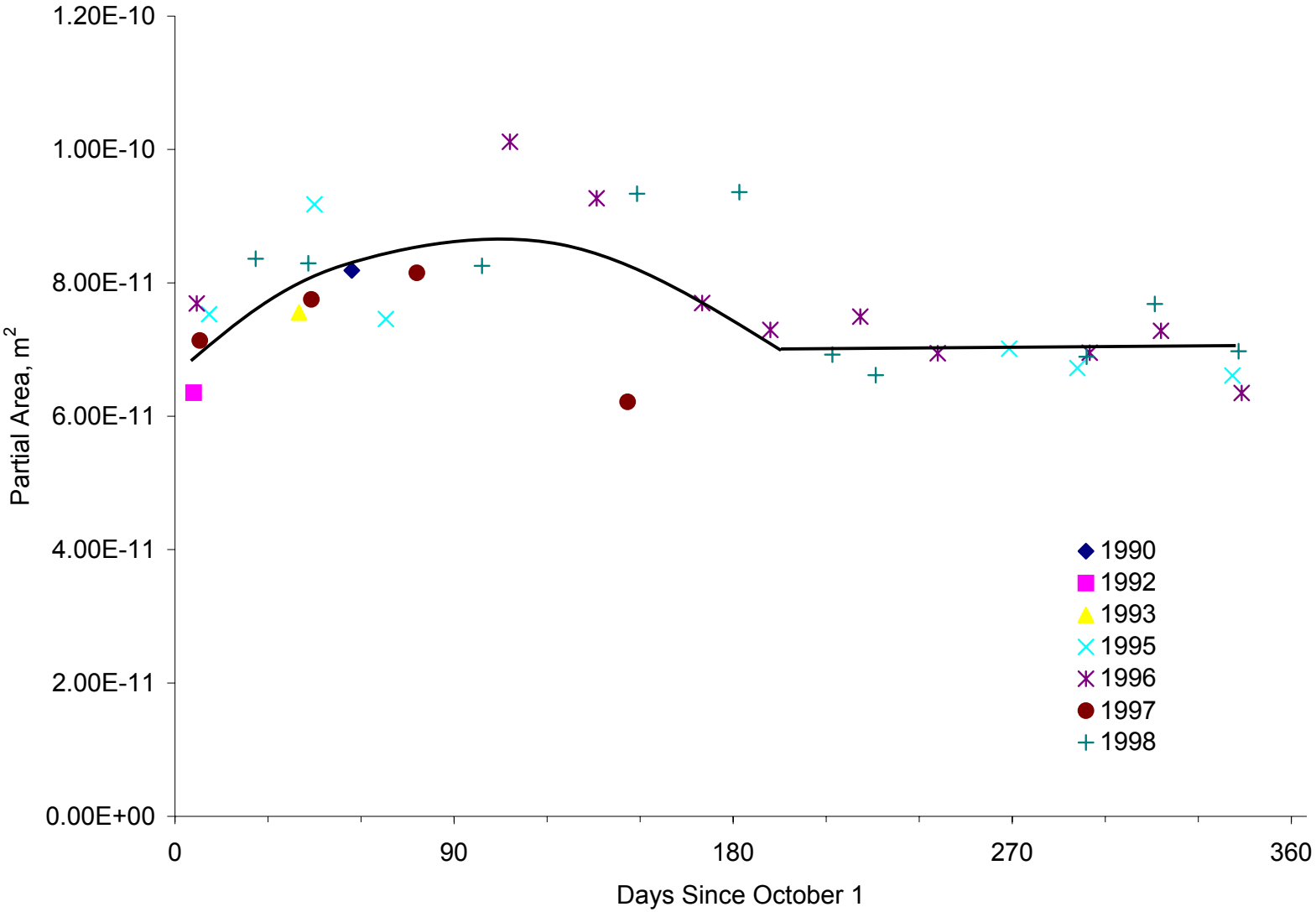

Figure S-10. Index PA at Site 28-1802 (Poorly Graded Sand)

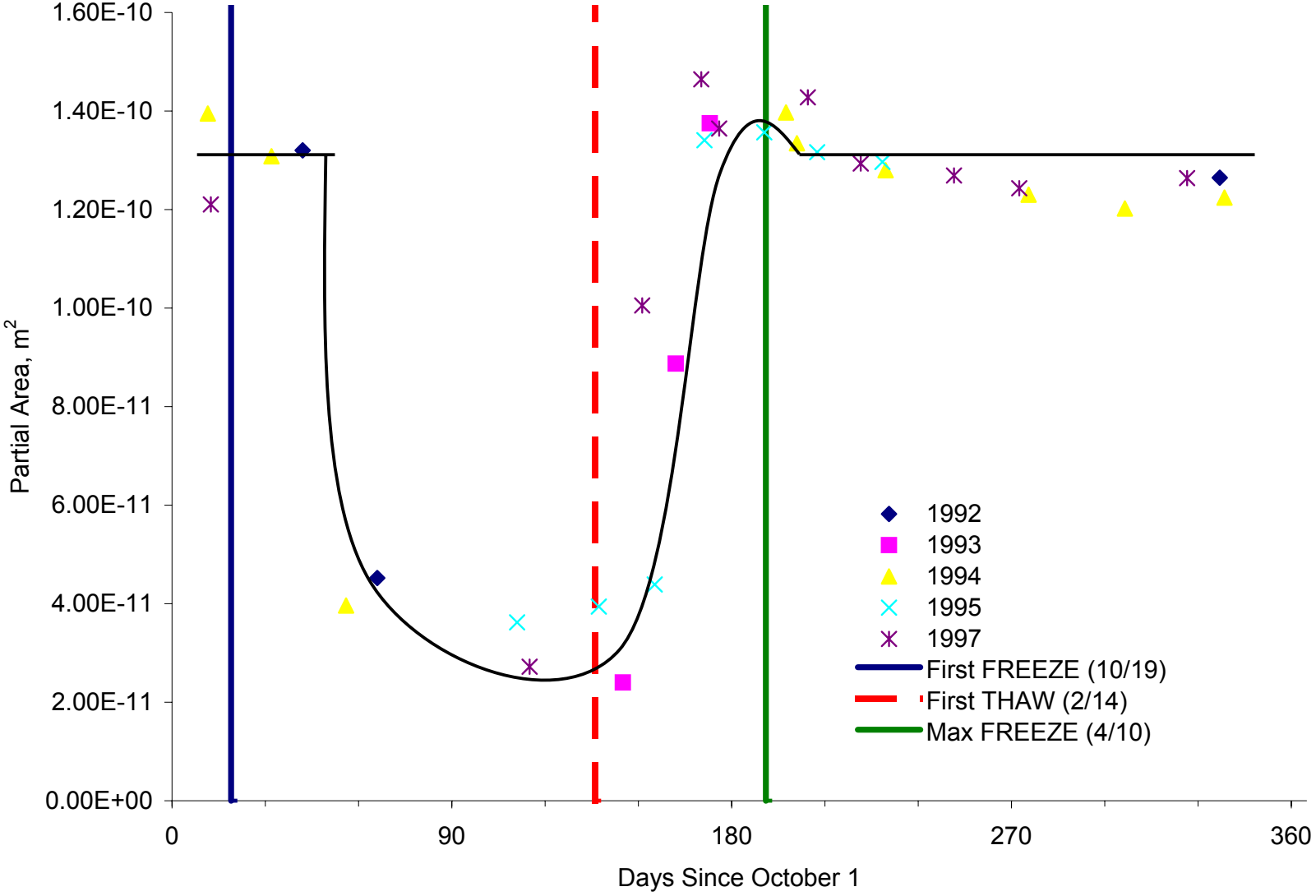

Figure S-11. Index PA at Site 30-8129 (Poorly Graded Sand with Silt)

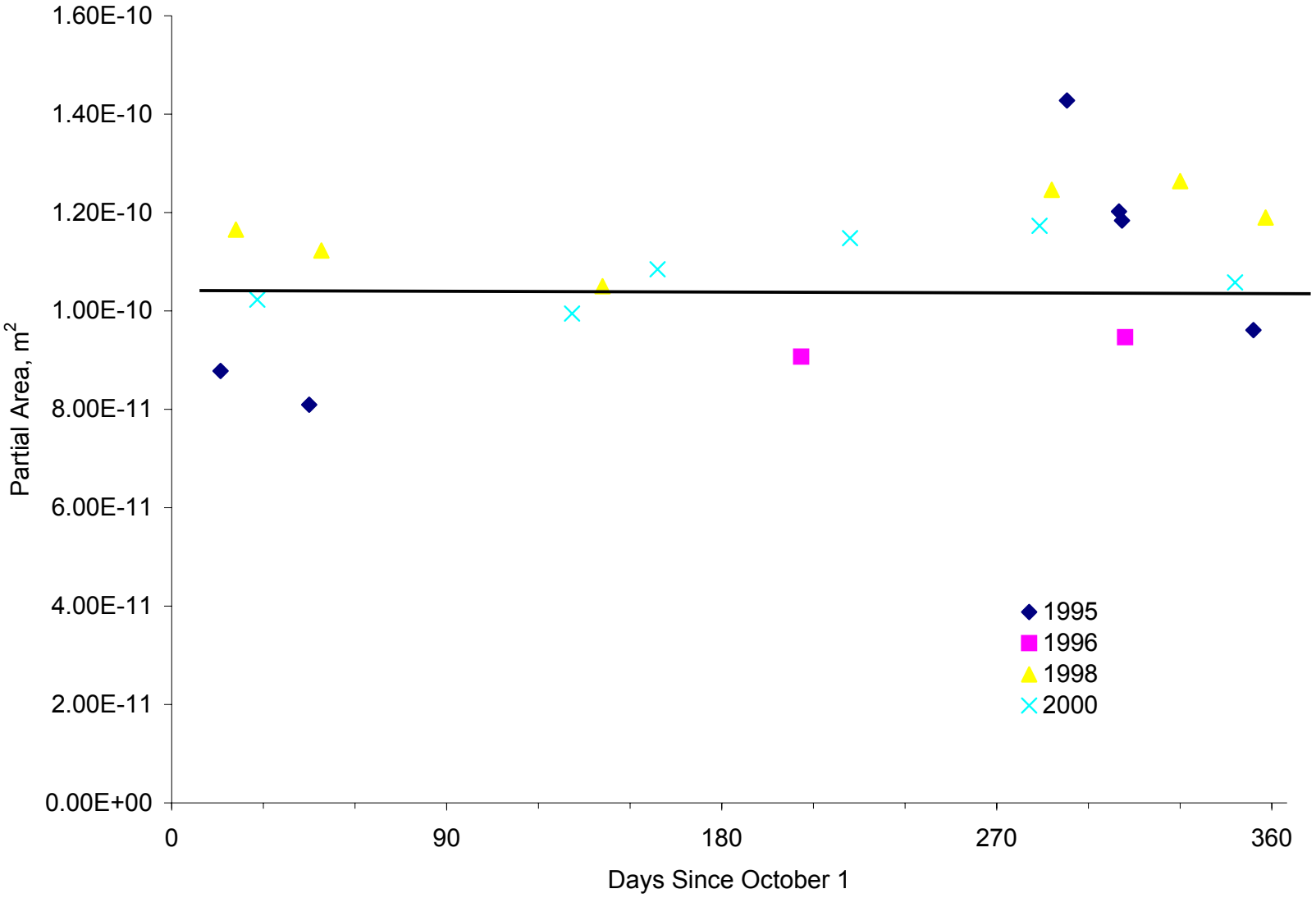

Figure S-12. Index PA at Site 31-0114 (Silty Clay)

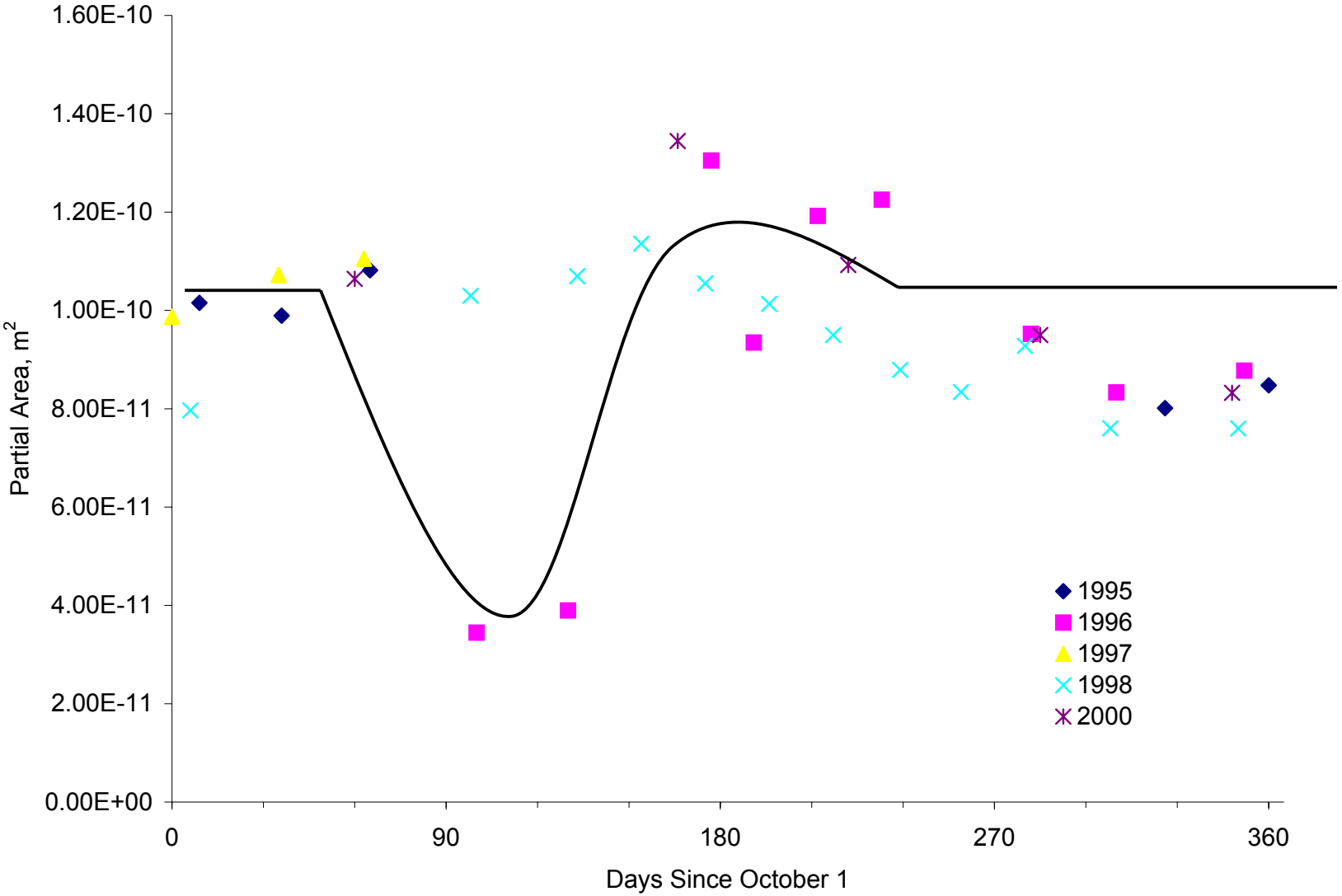

Figure S-13. Index PA at Site 36-0801 (Silty Sand)

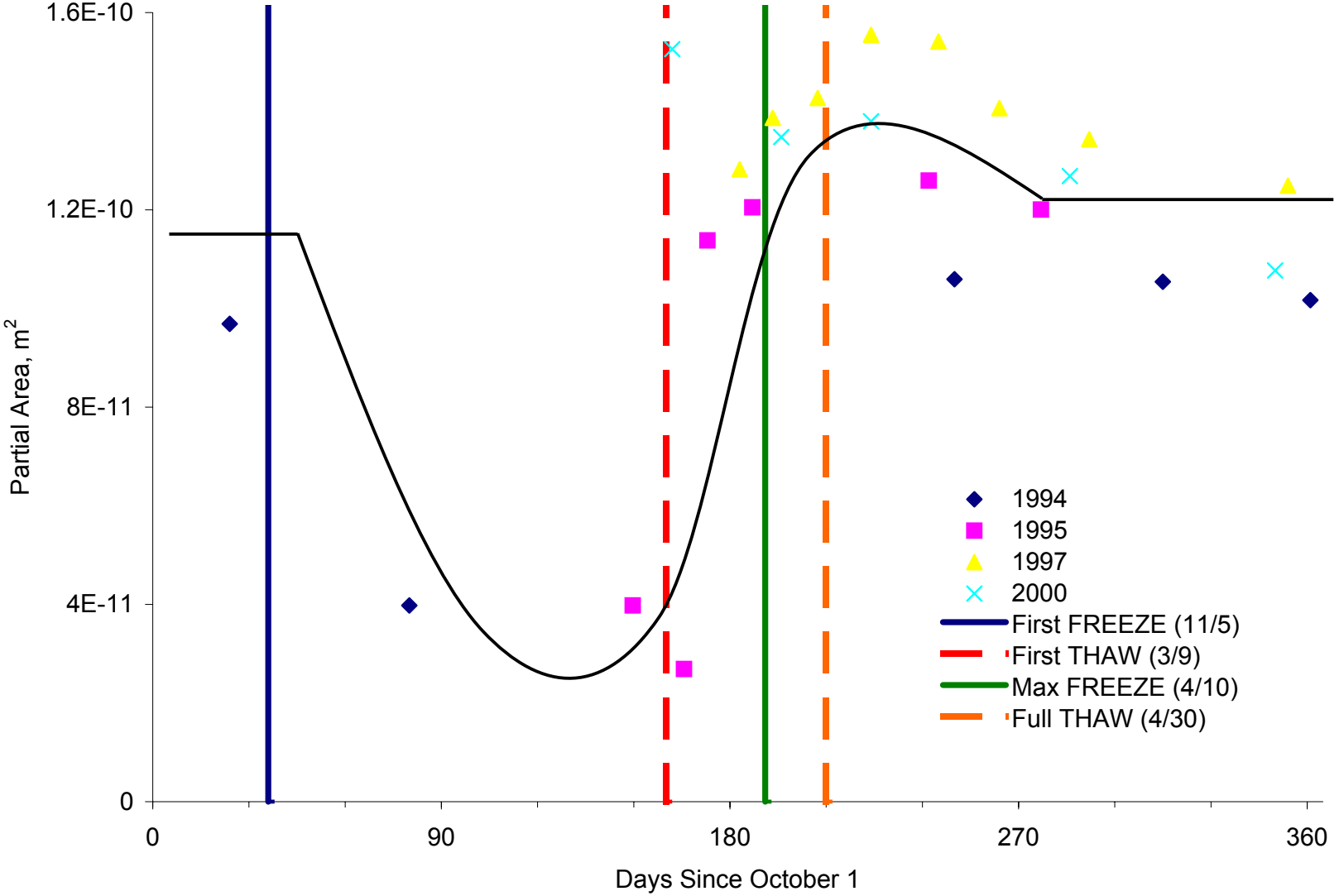

Figure S-14. Index PA at Site 46-0804 (Silty Clay)

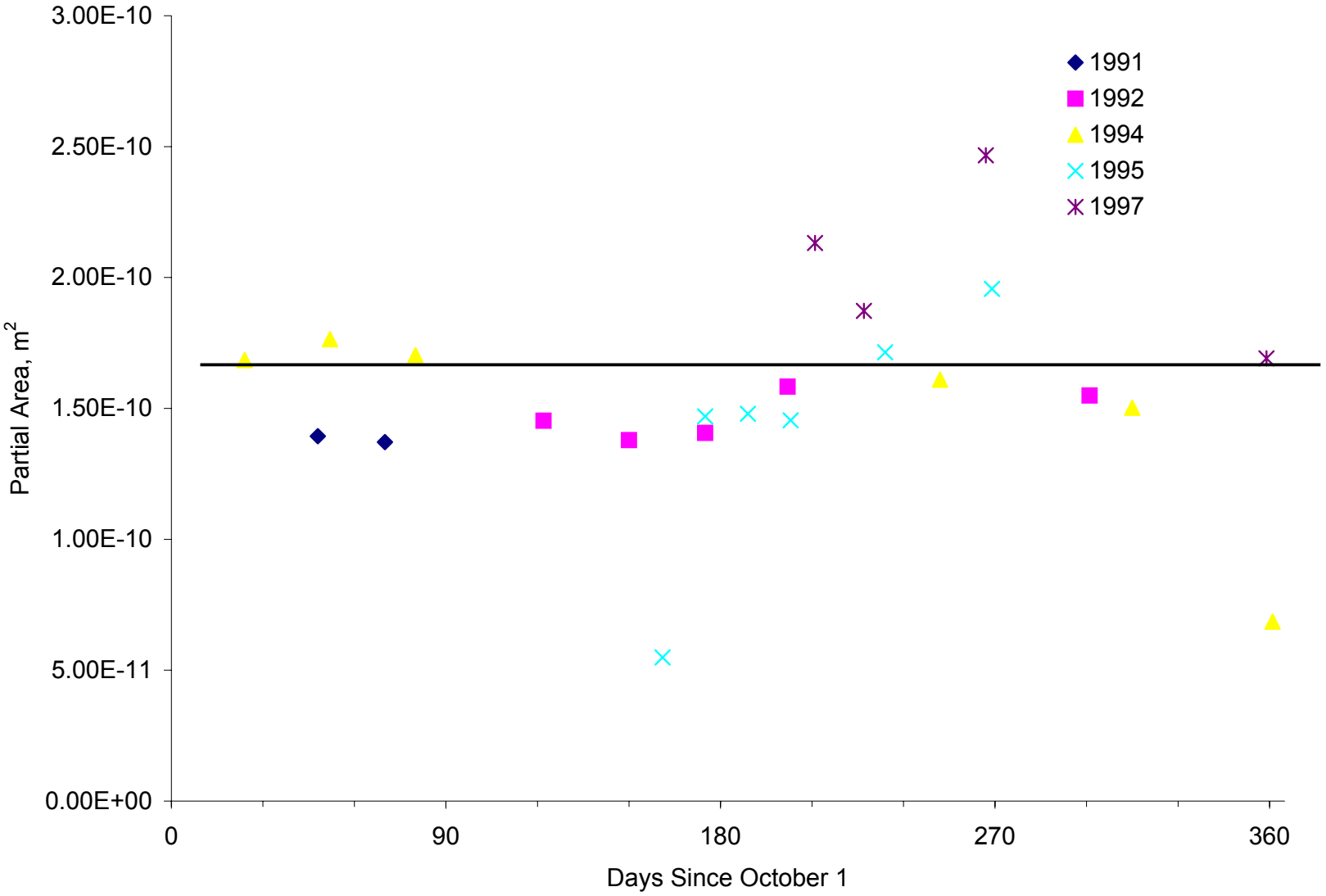

Figure S-15. Index PA at Site 46-9187 (Lean Inorganic Clay)

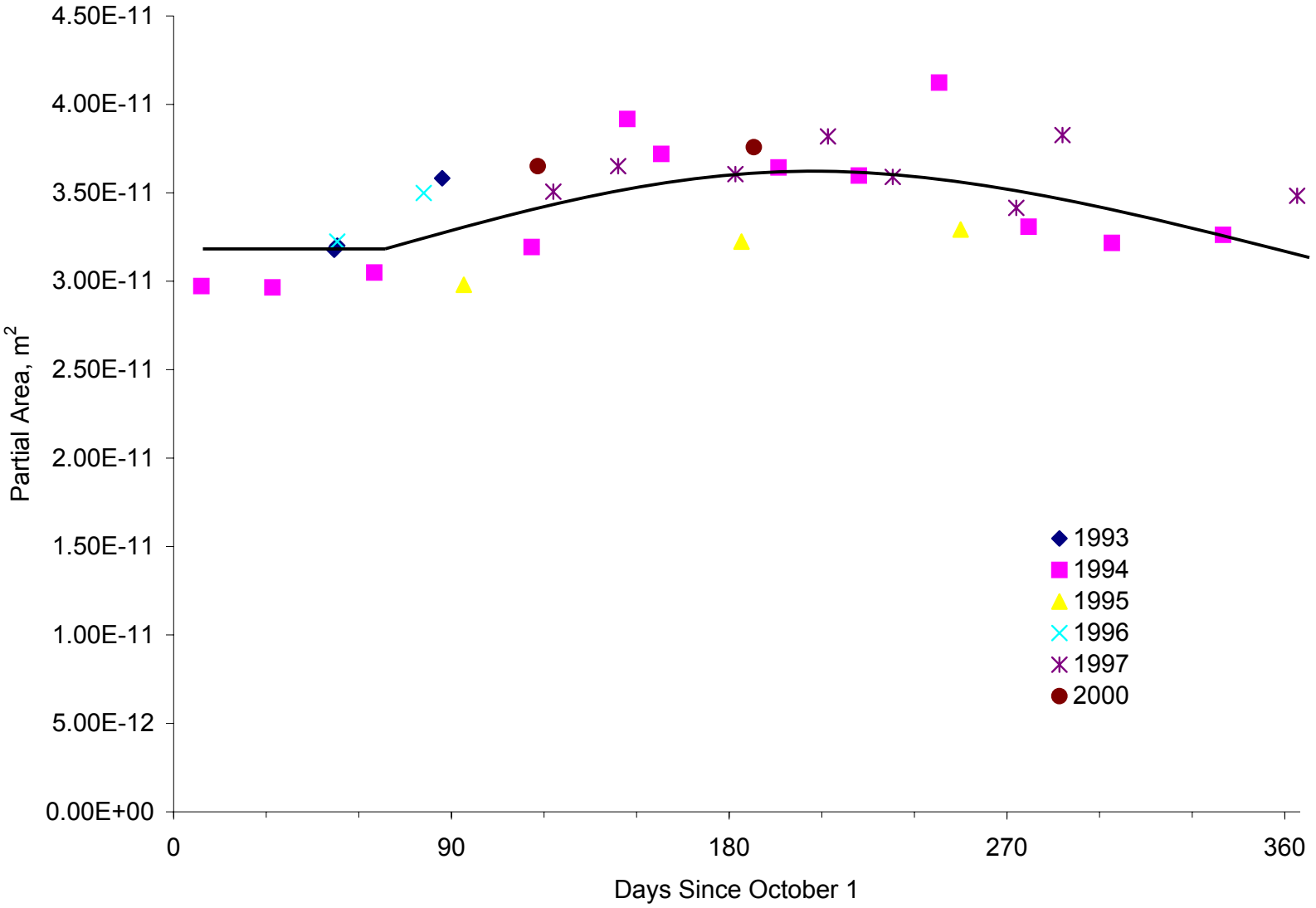

Figure S-16. Index PA at Site 48-1122 (Clayey Sand)

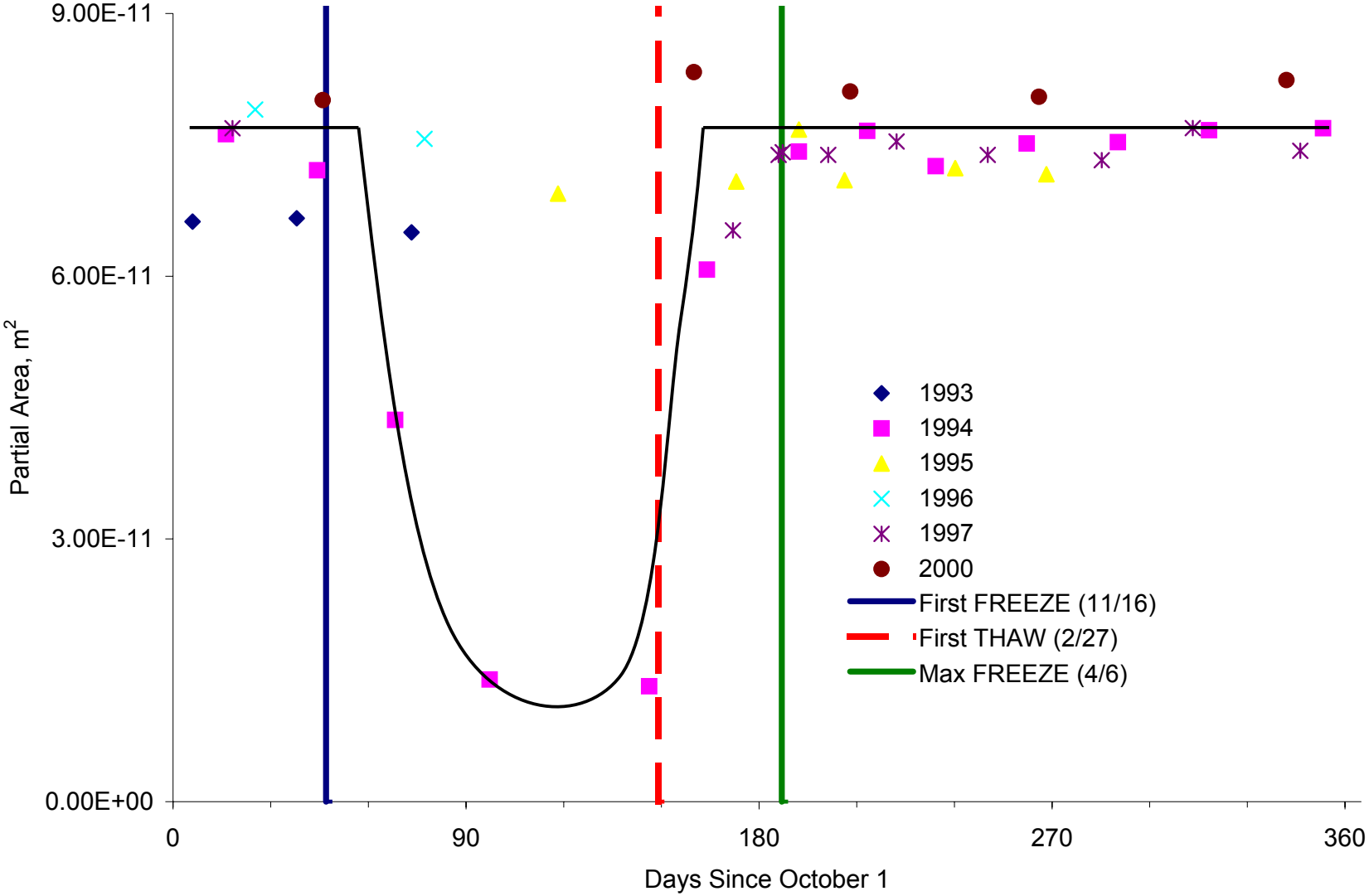

Figure S-17. Index PA at Site 50-1002 (Poorly Graded Gravel with Silt and Sand)

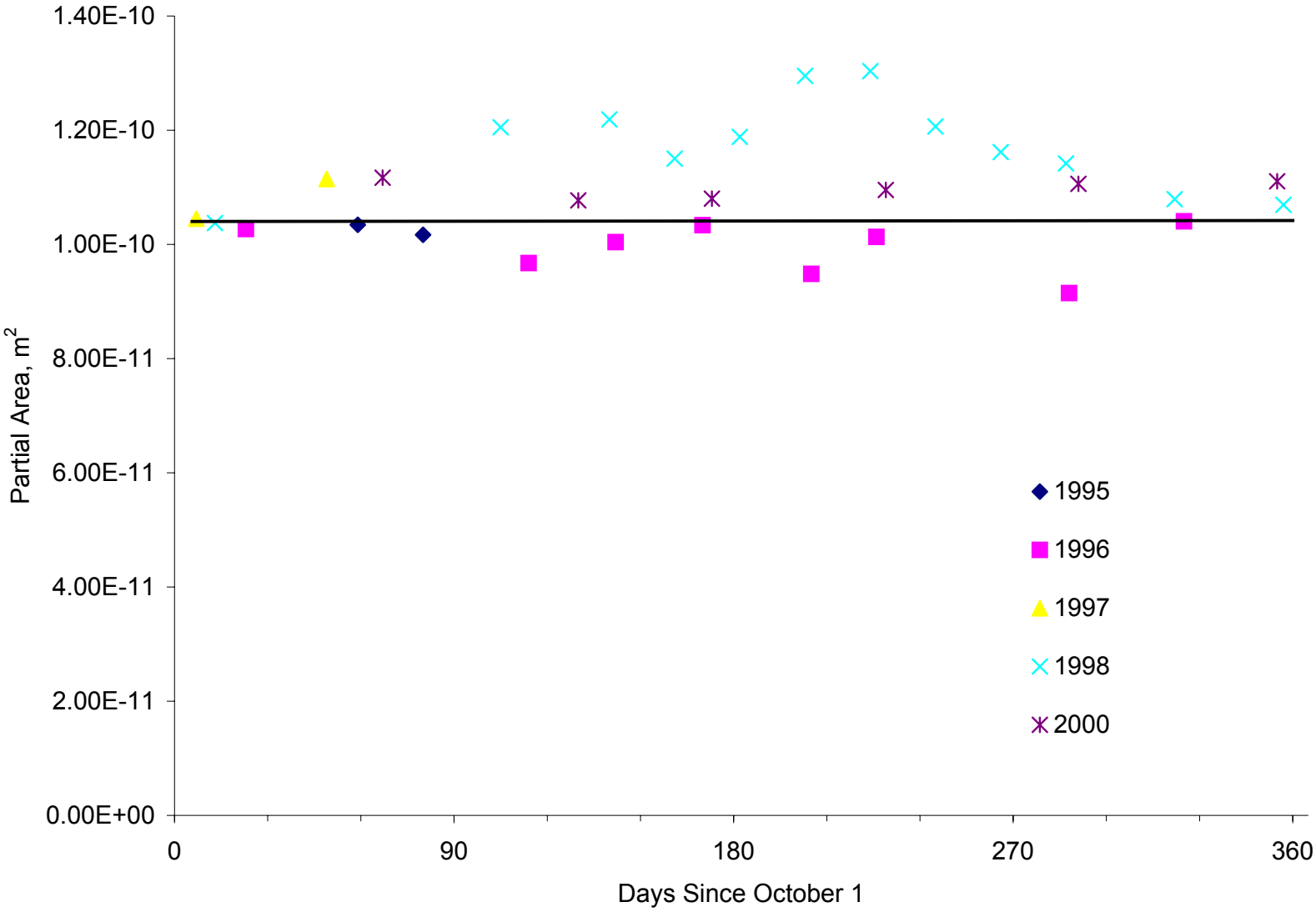

Figure S-18. Index PA at Site 51-0113 (Silt)

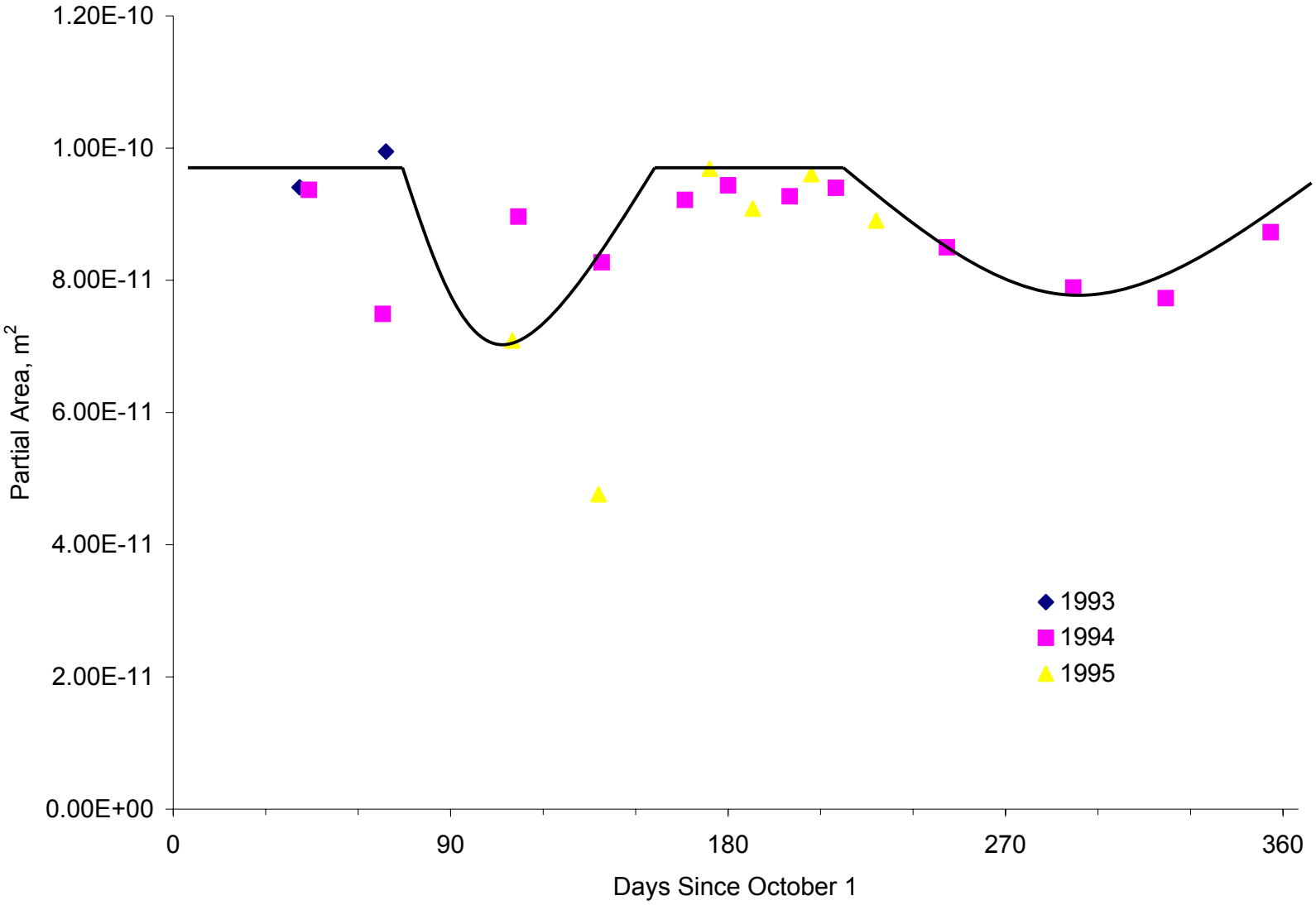

Figure S-19. Index PA at Site 56-1007 (Silt Sand with Gravel)

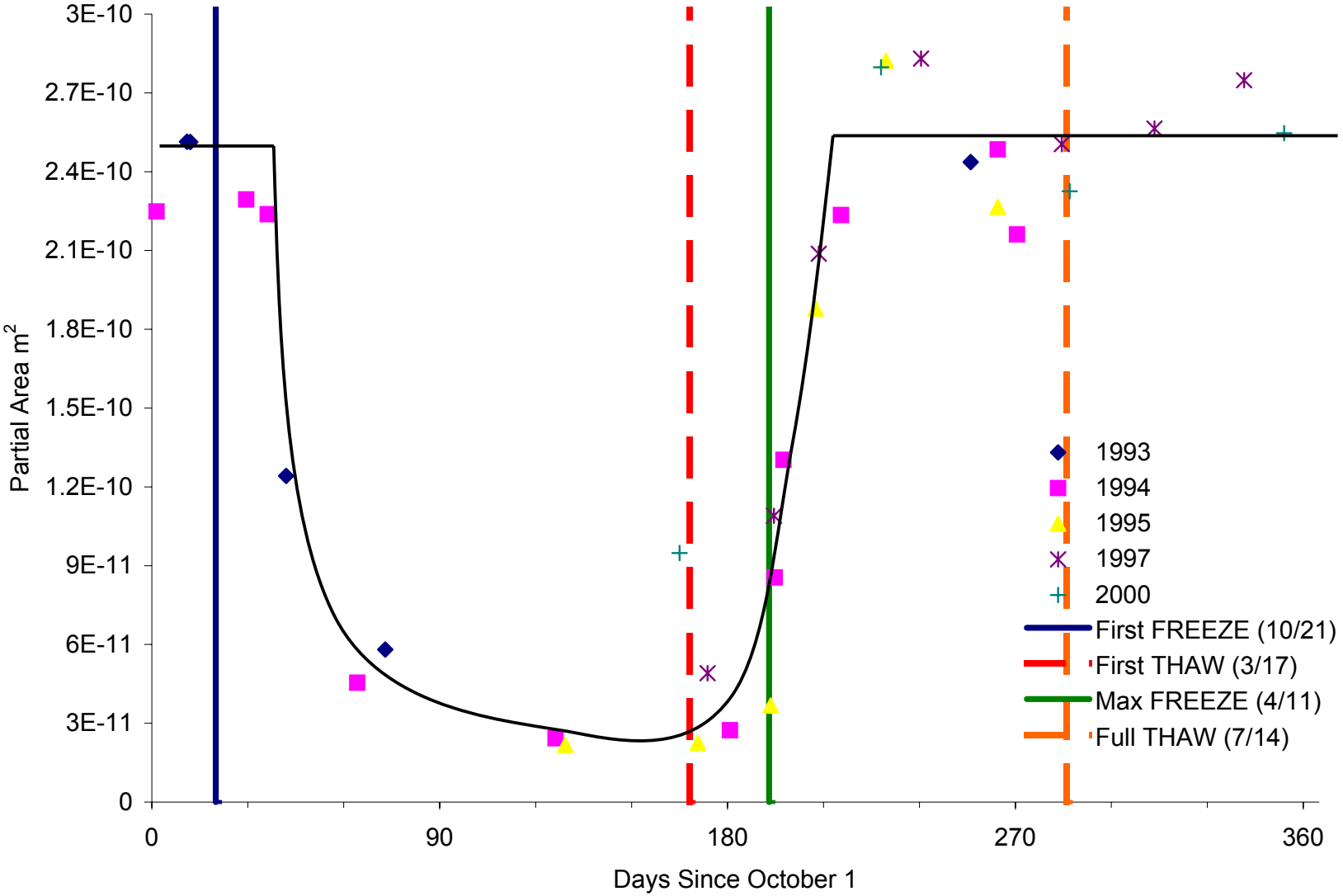

Figure S-20. Index PA at Site 83-1801 (Silty Sand)

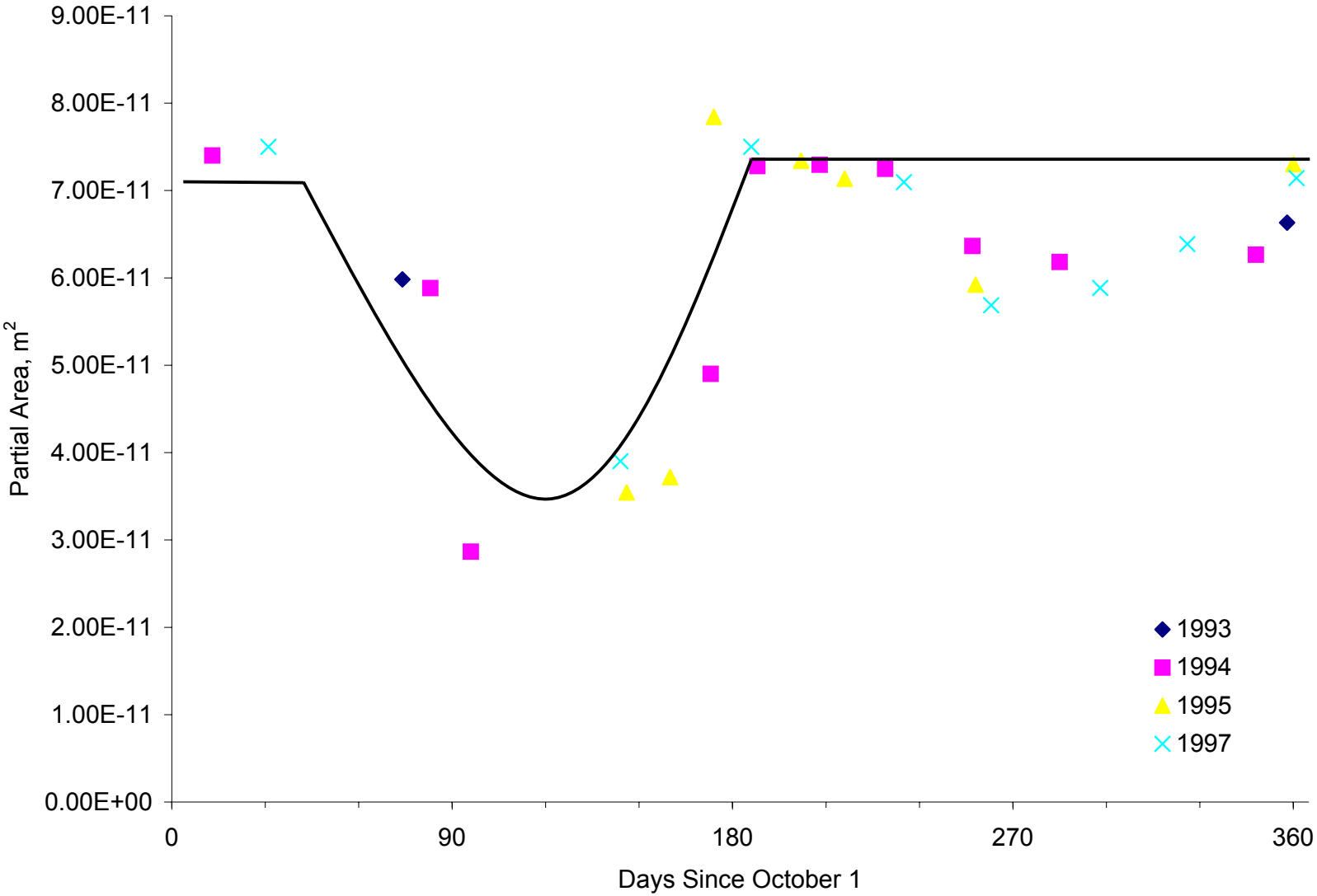

Figure S-21. Index PA at Site 87-1622 (Sandy Silt)

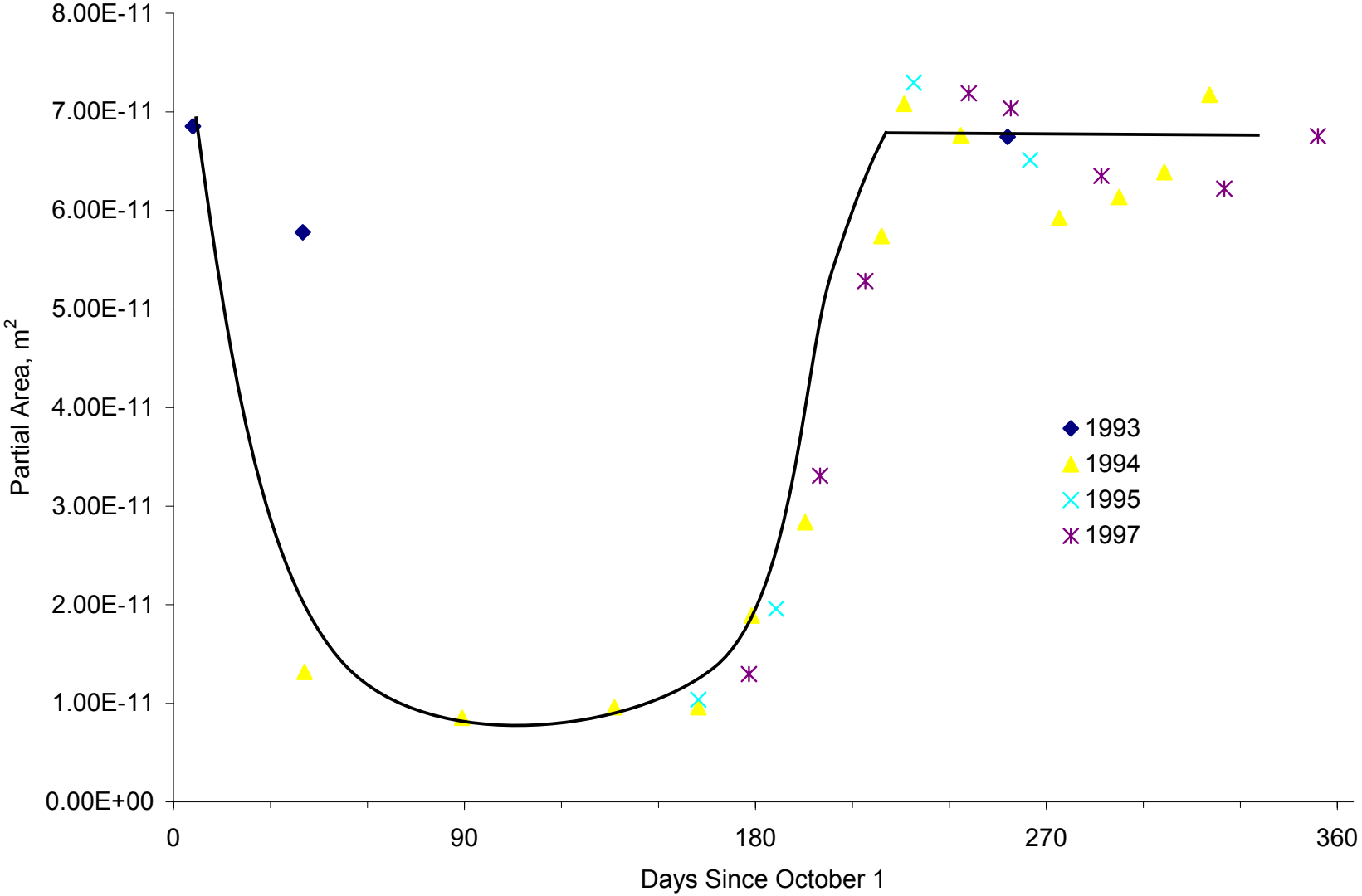

Figure S-22. Index PA at Site 90-6405 (Silty Sand)

APPENDIX T

PREDICTED FWD DEFLECTION BASINS

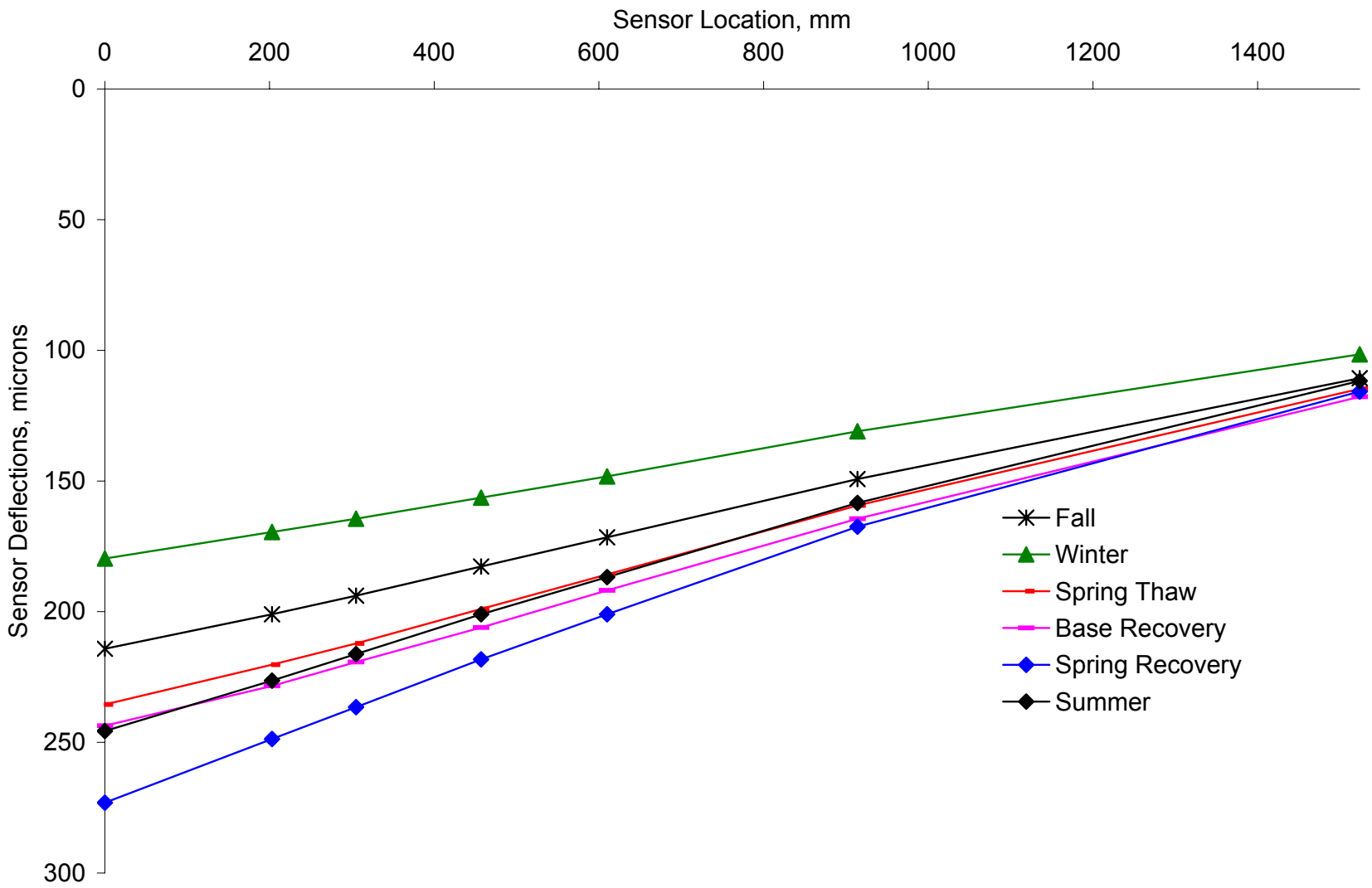

Figure T-1. Deflection Basins at Site 16-1010 (Silty Sand)

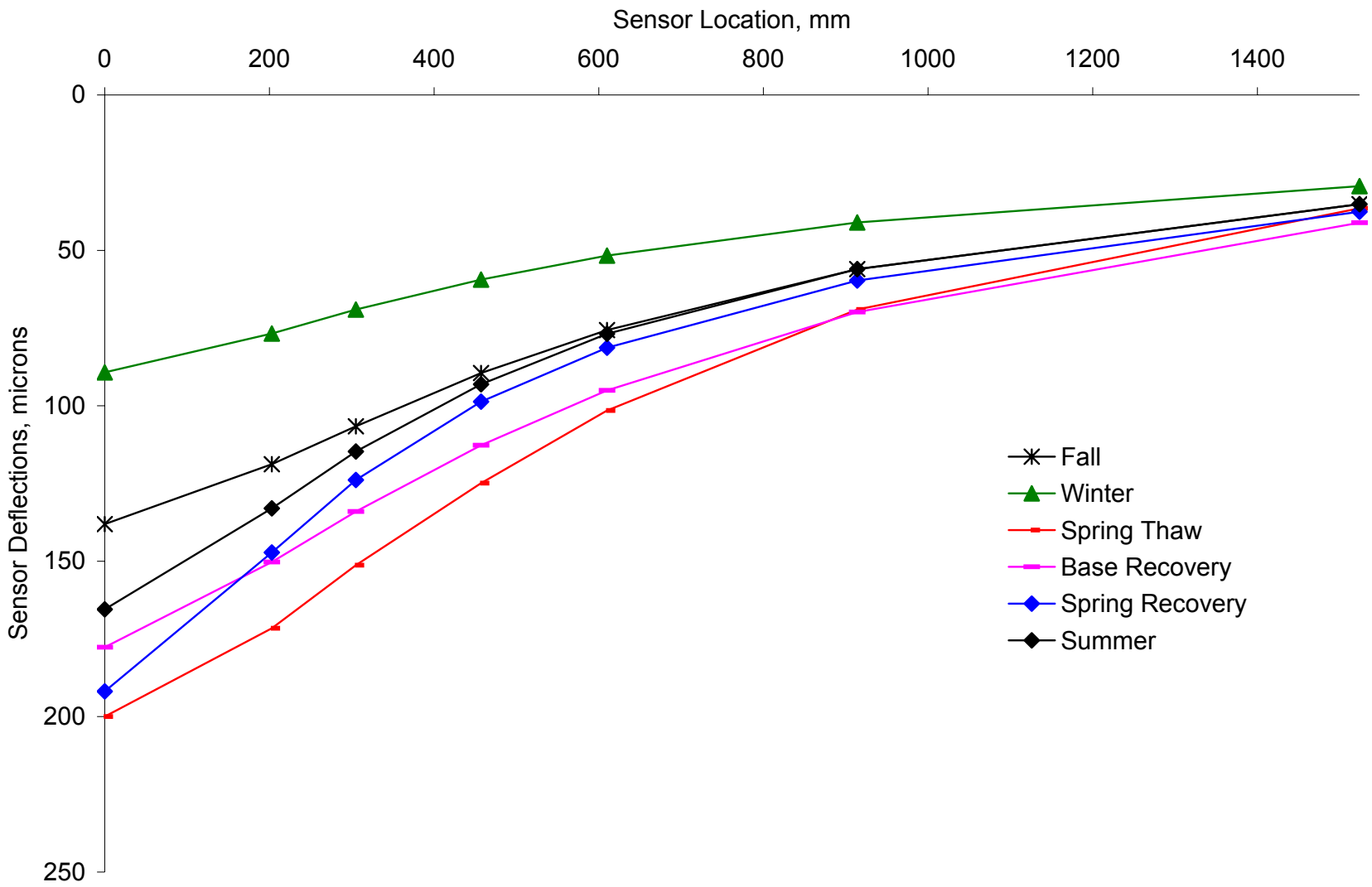

Figure T-2. Deflection Basins at Site 23-1026 (Silty Sand with Gravel)

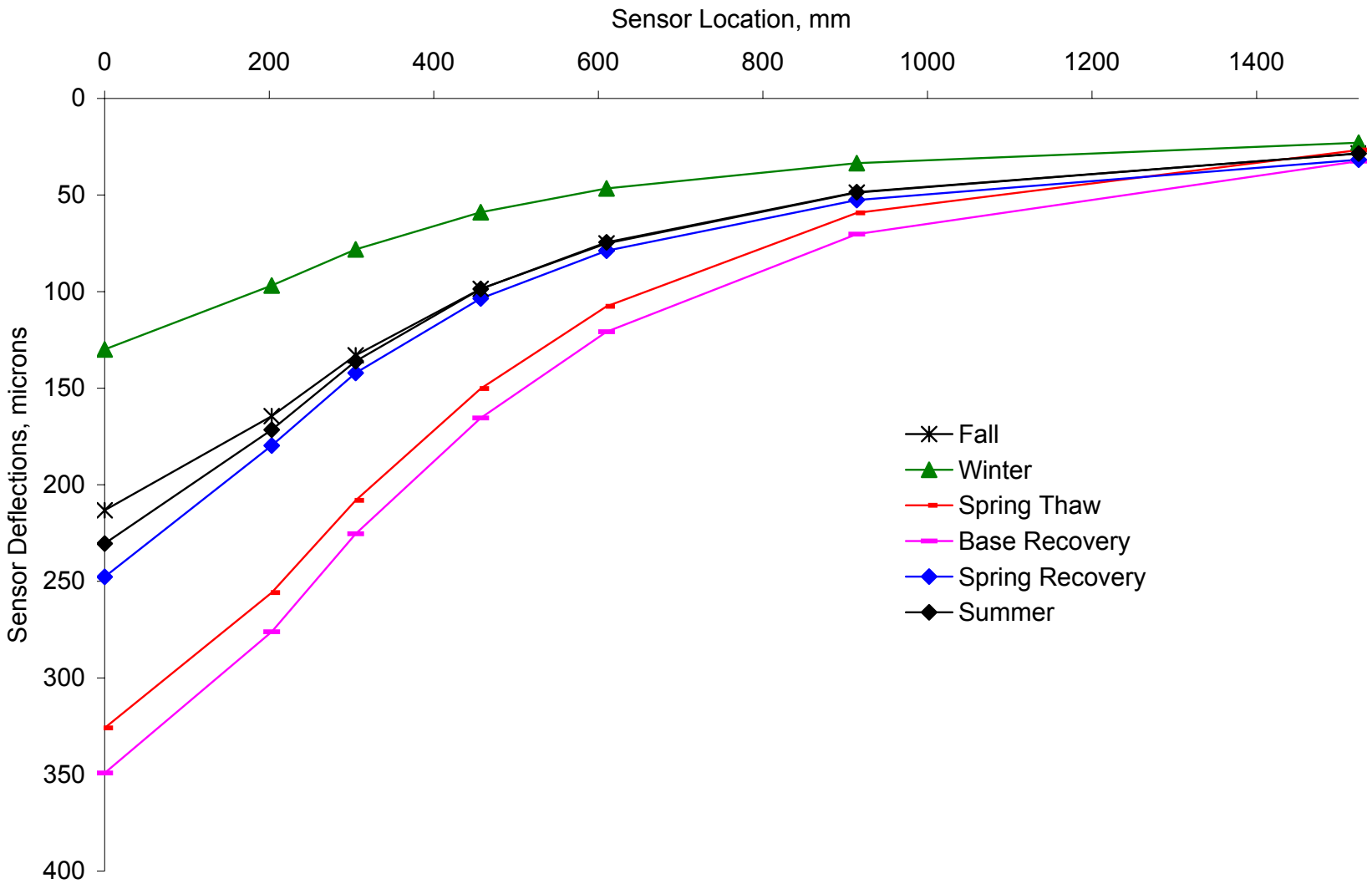

Figure T-3. Deflection Basins at Site 27-1018 (Poorly Graded Sand with Silt)

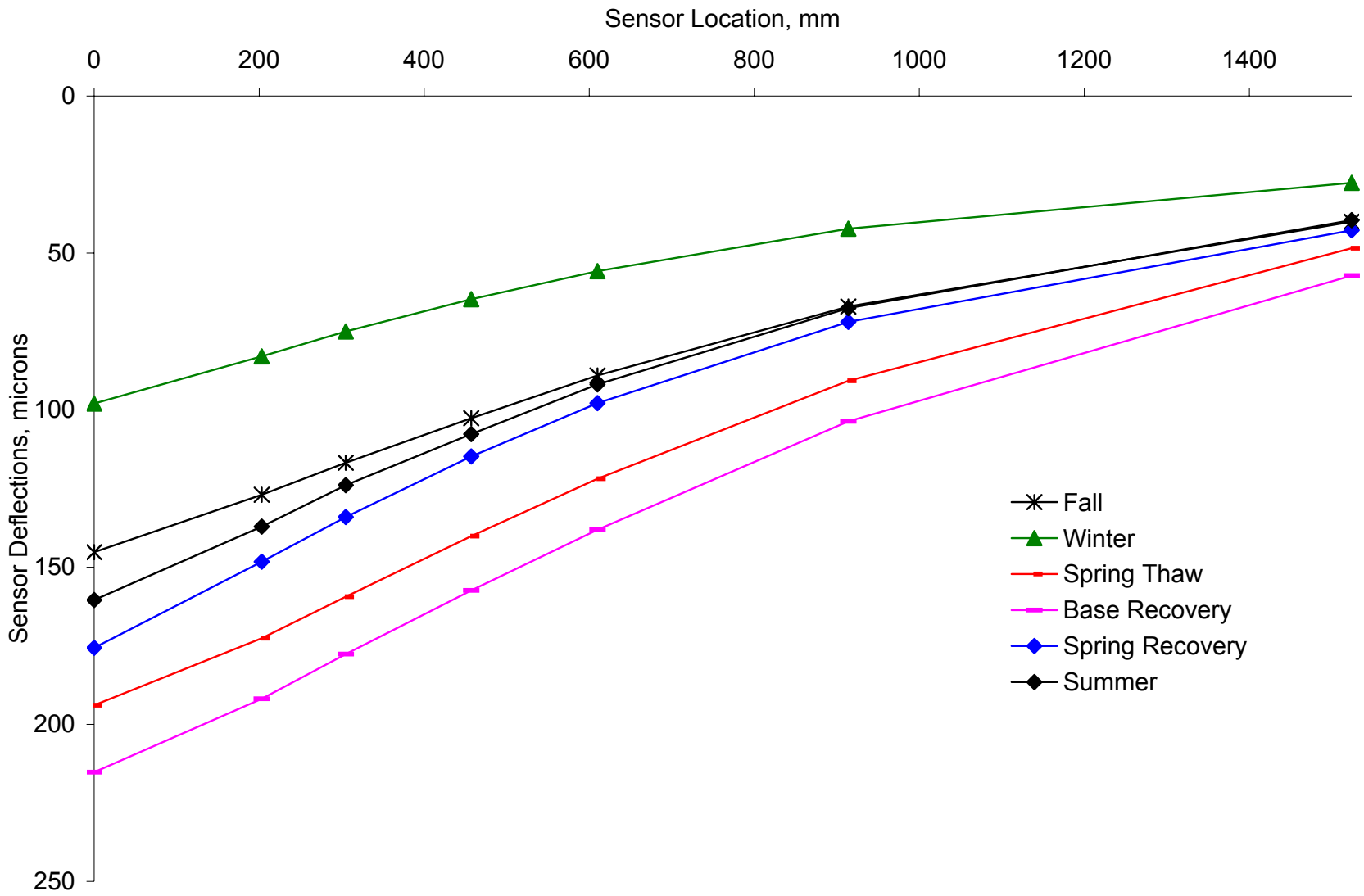

Figure T-4. Deflection Basins at Site 27-1028 (Poorly Graded Sand with Silt)

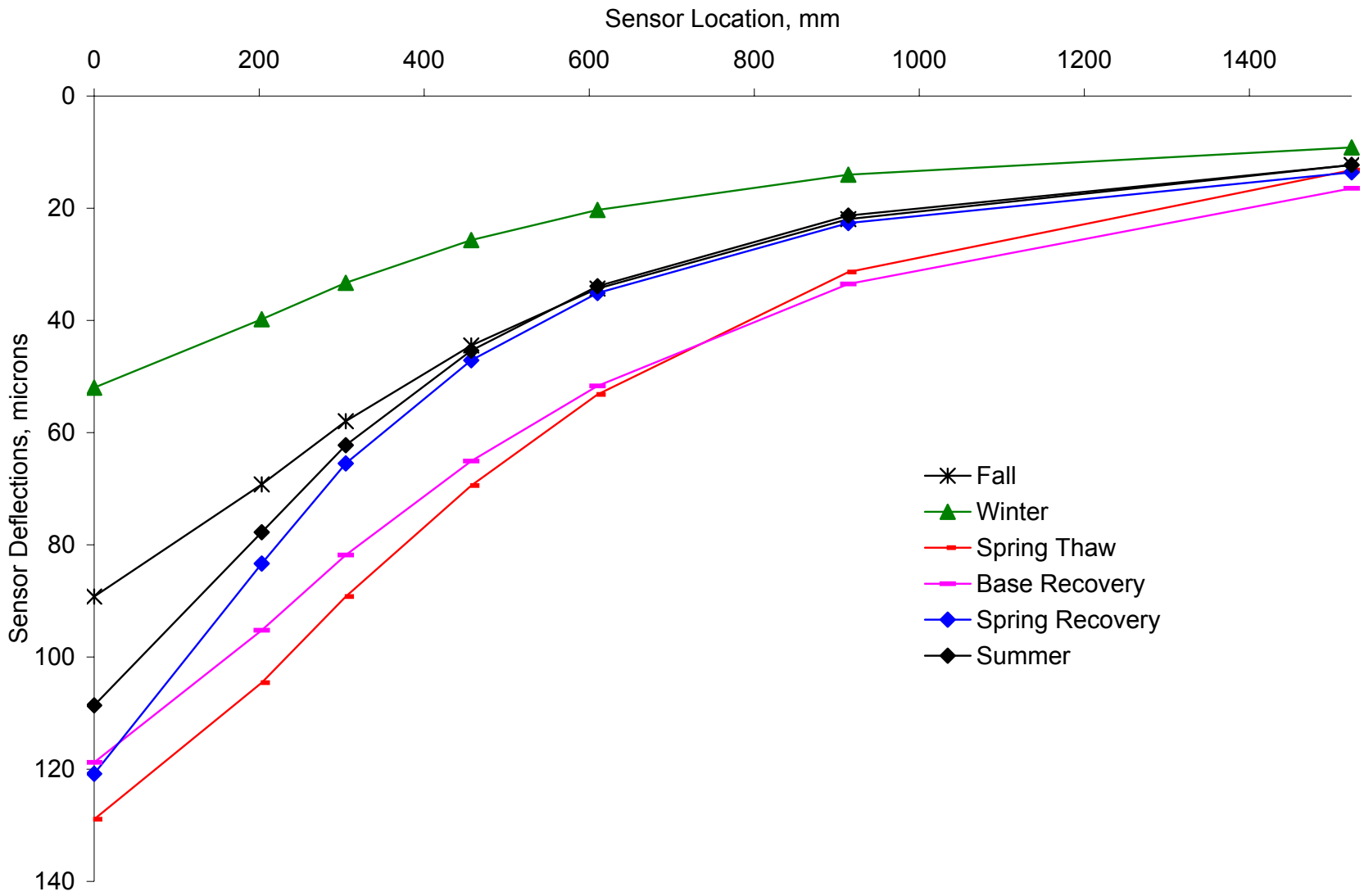

Figure T-5. Deflection Basins at Site 27-6251 (Poorly Graded Sand with Silt)

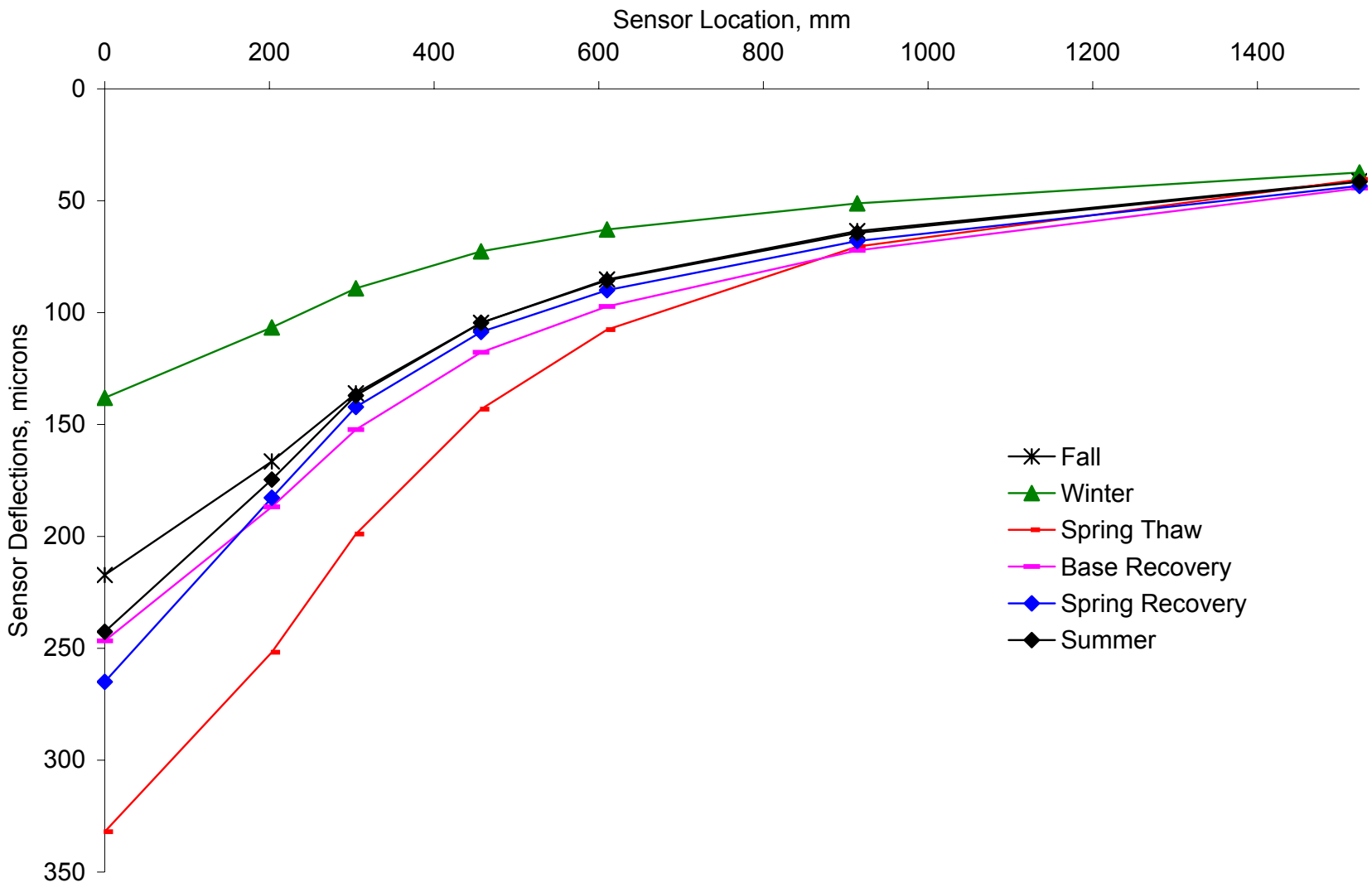

Figure T-6. Deflection Basins at Site 30-8129 (Poorly Graded Sand with Silt)

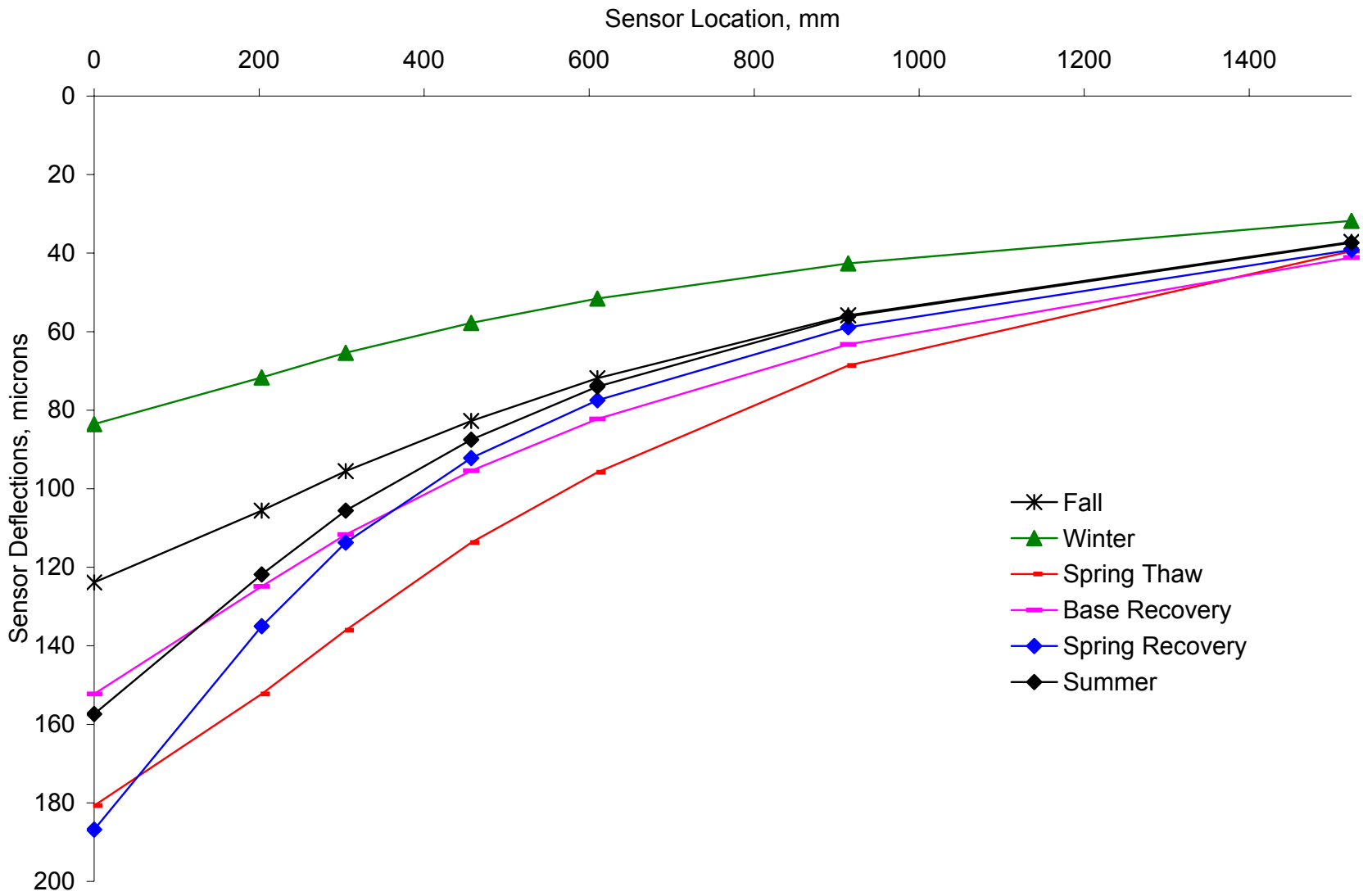

Figure T-7. Deflection Basins at Site 50-1002 (Poorly Graded Gravel with Silt and Sand)

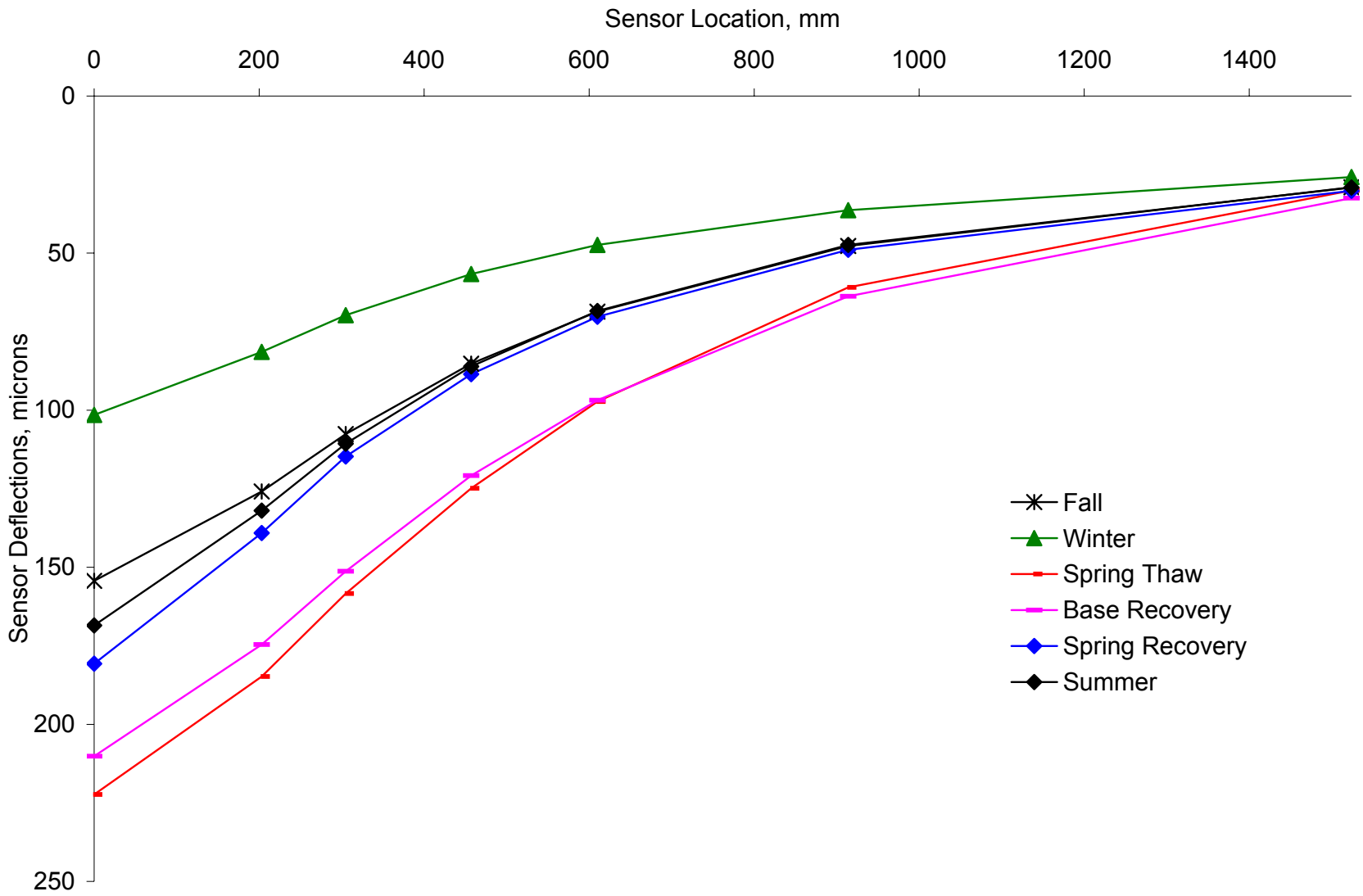

Figure T-8. Deflection Basins at Site 87-1622 (Sandy Silt)

APPENDIX U

SEASONAL VARIATIONS OF PREDICTED INDEX BCI

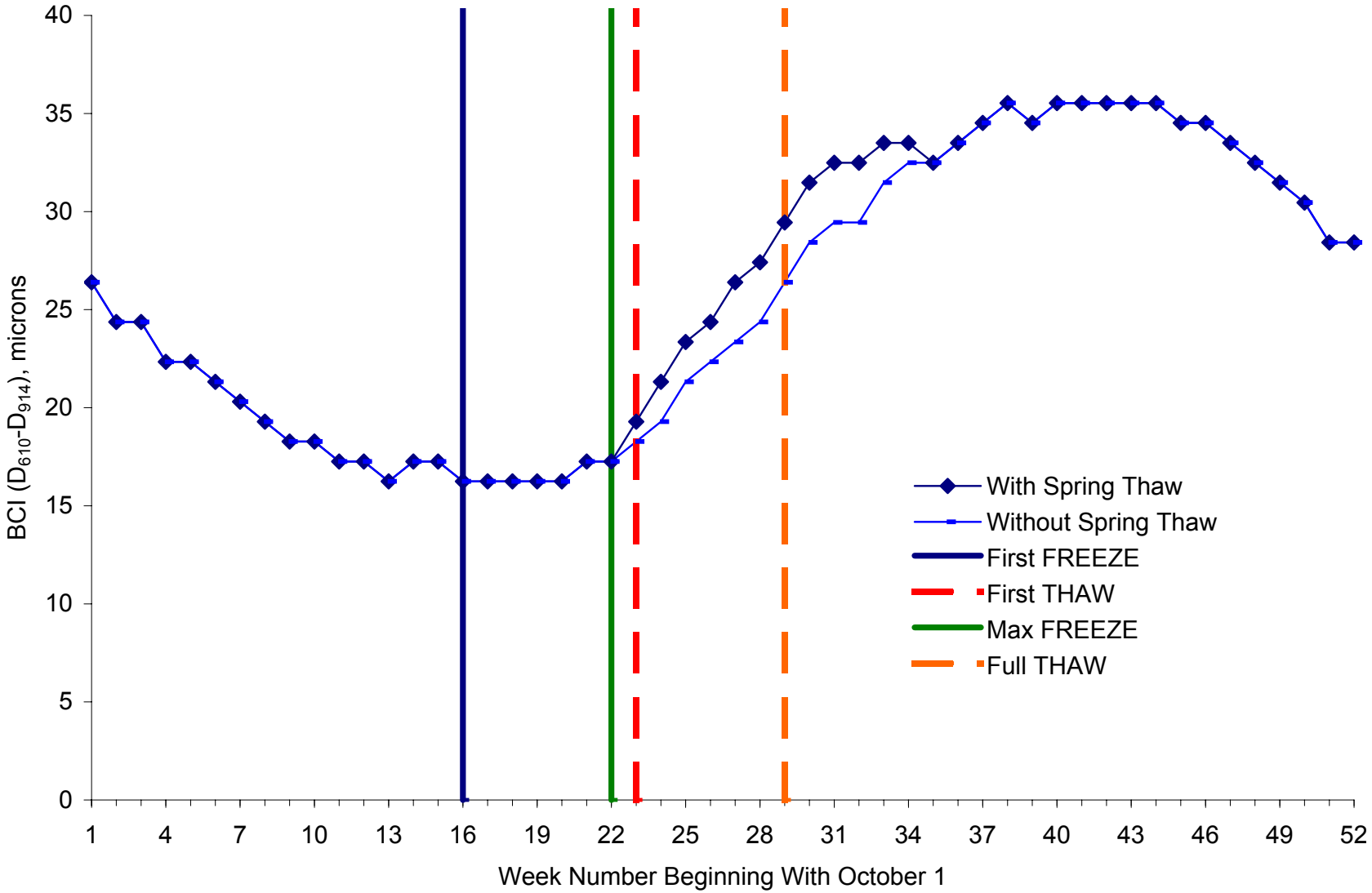

Figure U-1. Index BCI at Site 16-1010 (Silty Sand)

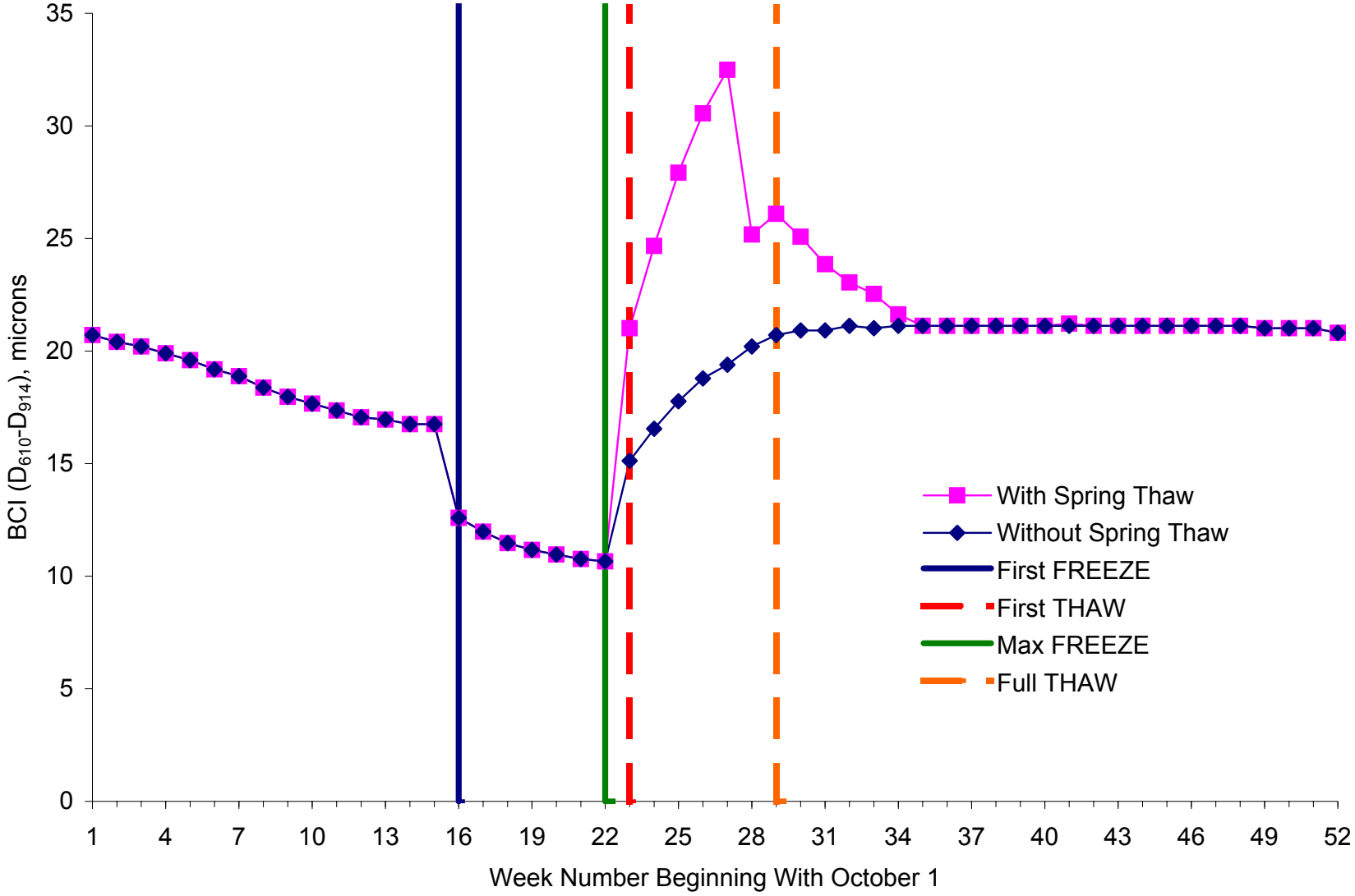

Figure U-2. Index BCI at Site 23-1026 (Silty Sand with Gravel)

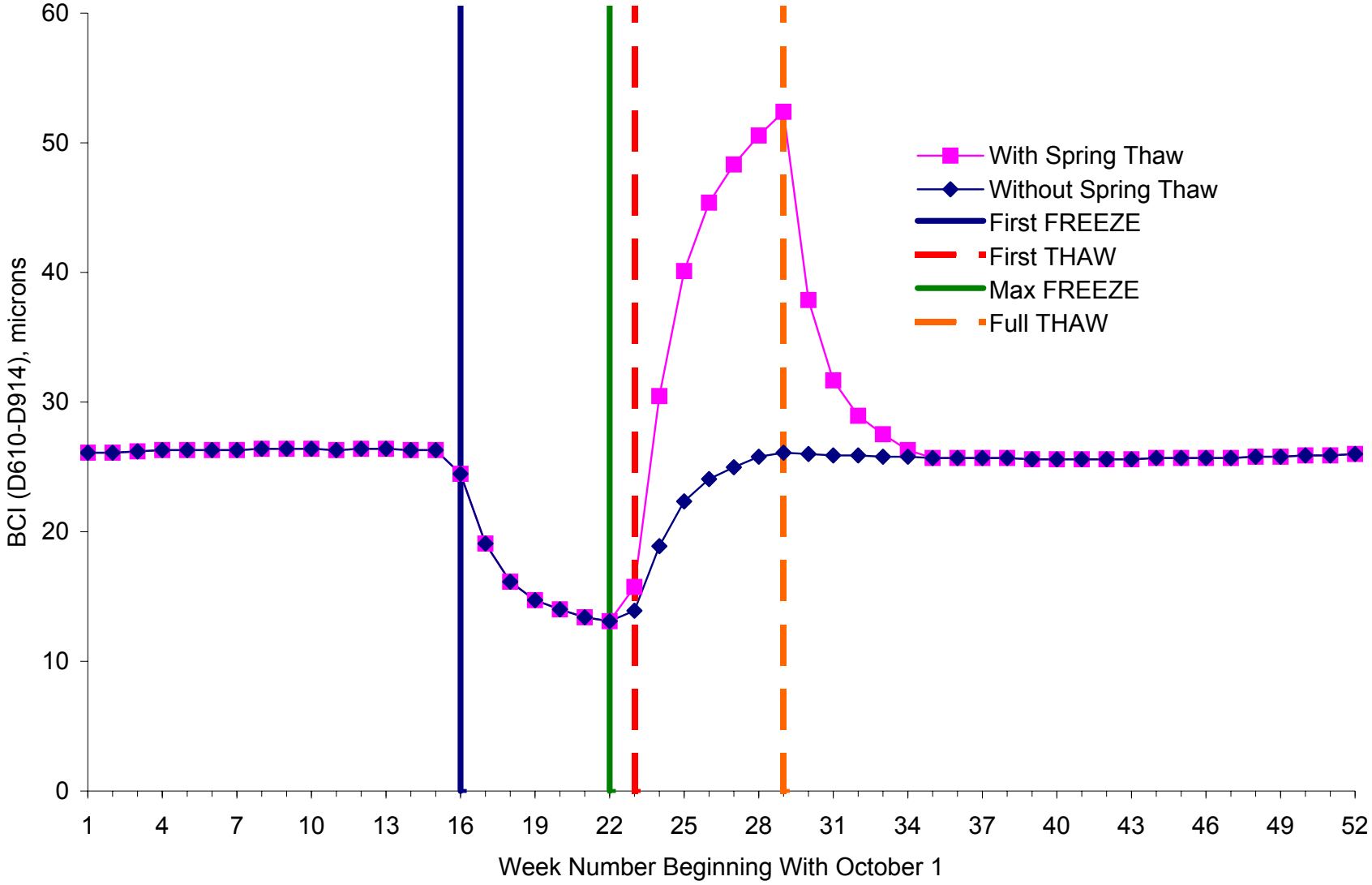

Figure U-3. Index BCI at Site 27-1018 (Poorly Graded Sand with Silt)

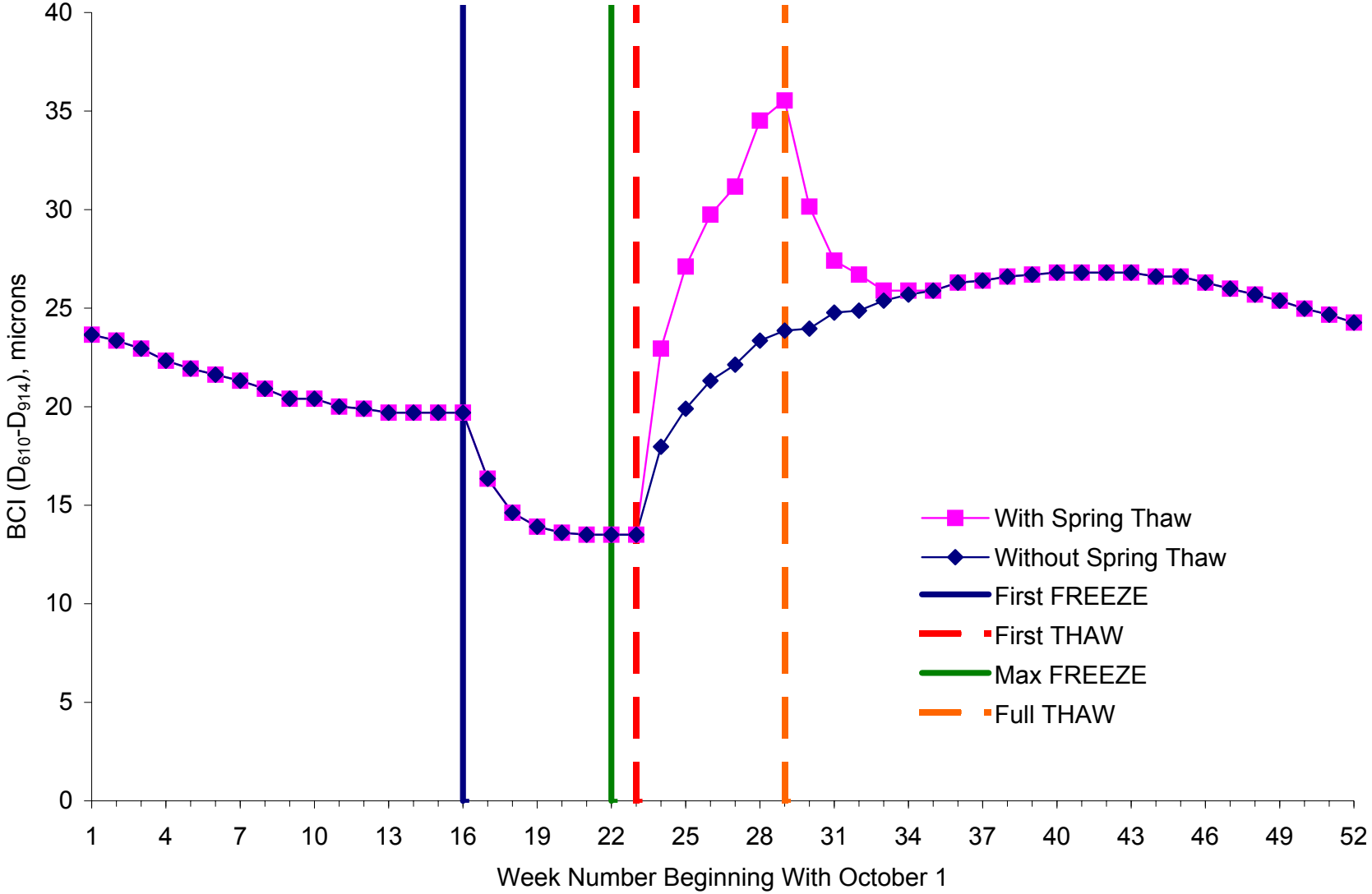

Figure U-4. Index BCI at Site 27-1028 (Poorly Graded Sand with Silt)

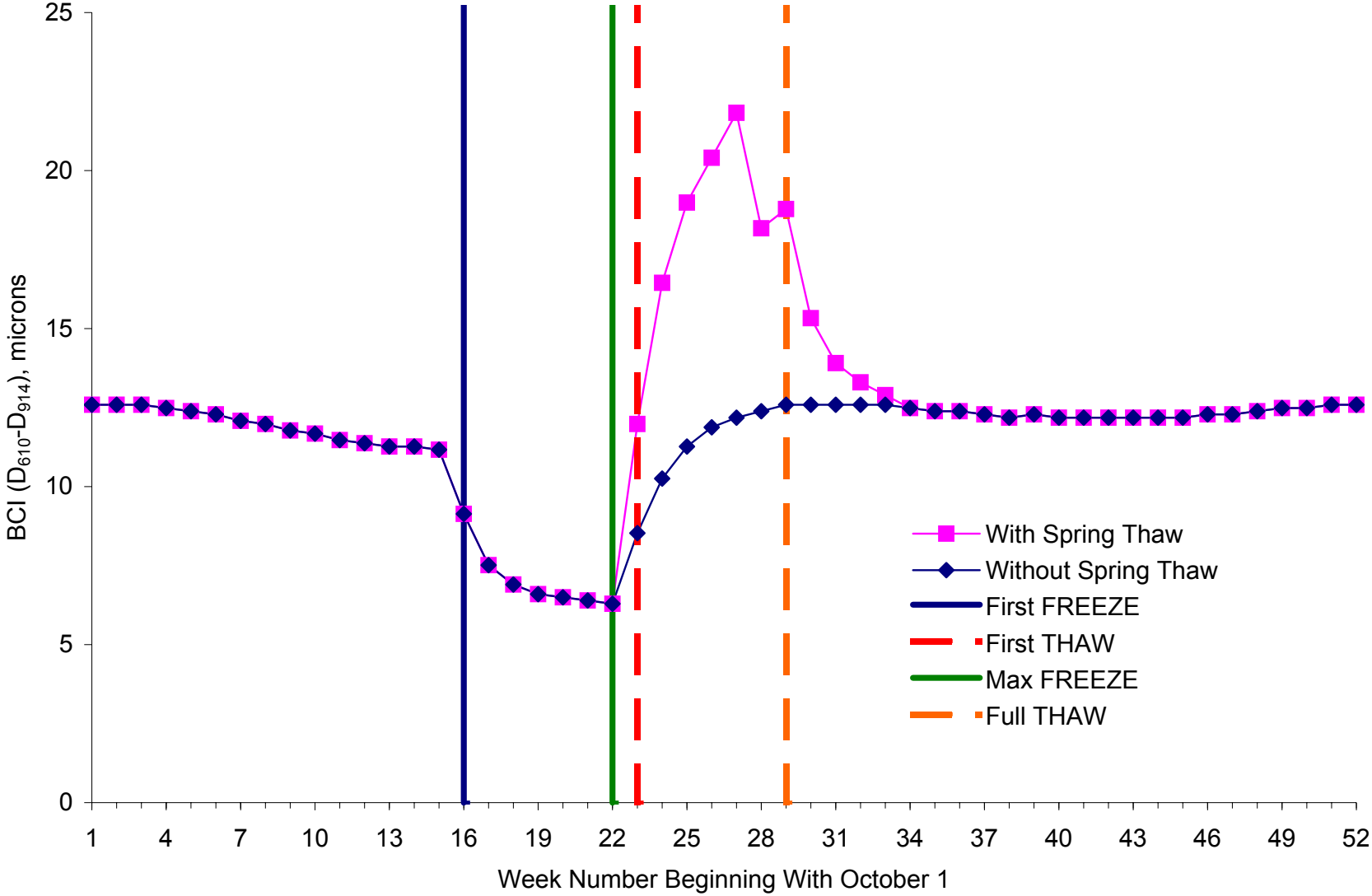

Figure U-5. Index BCI at Site 27-6251 (Poorly Graded Sand with Silt)

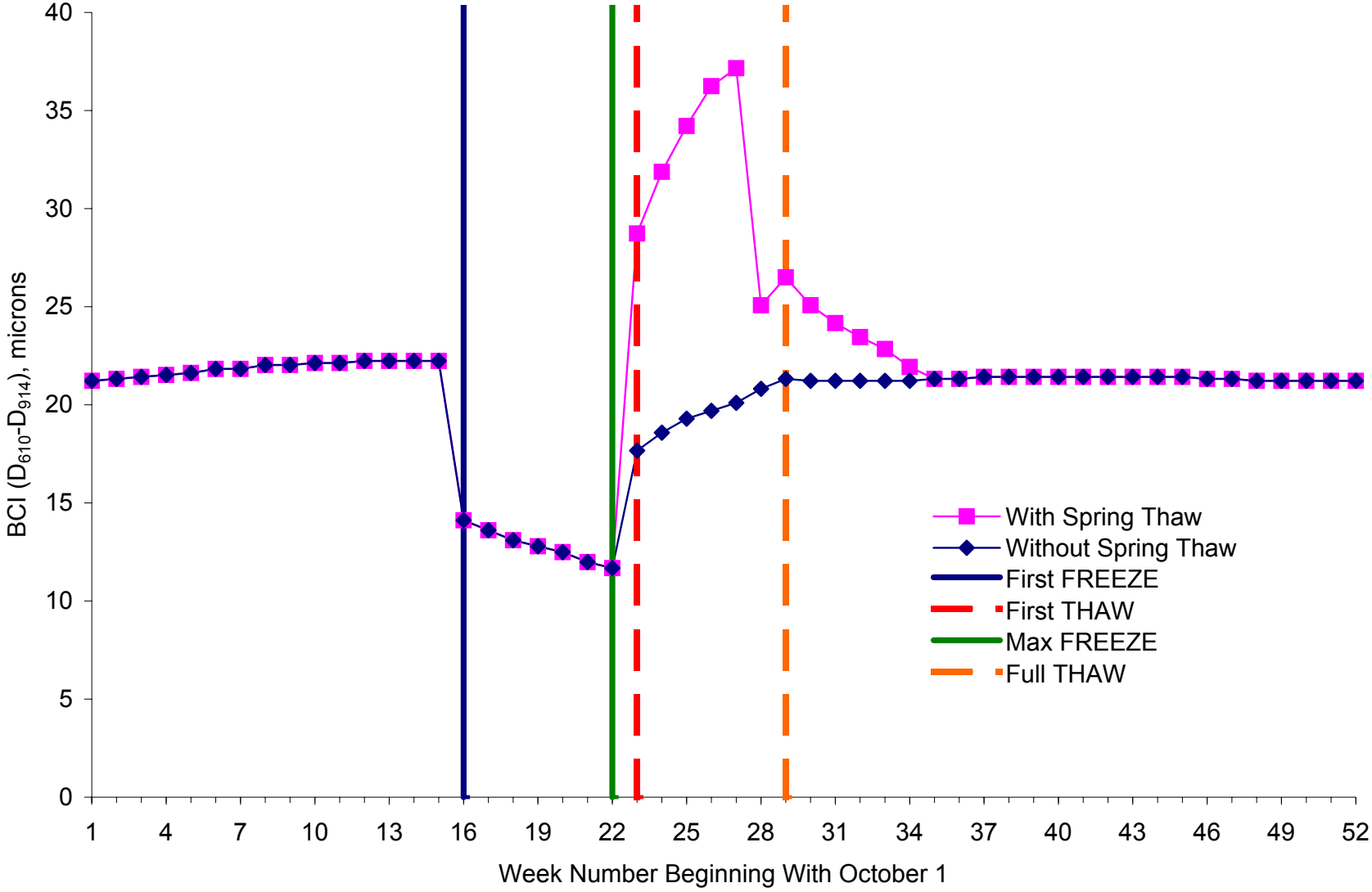

Figure U-6. Index BCI at Site 30-8129 (Poorly Graded Sand with Silt)

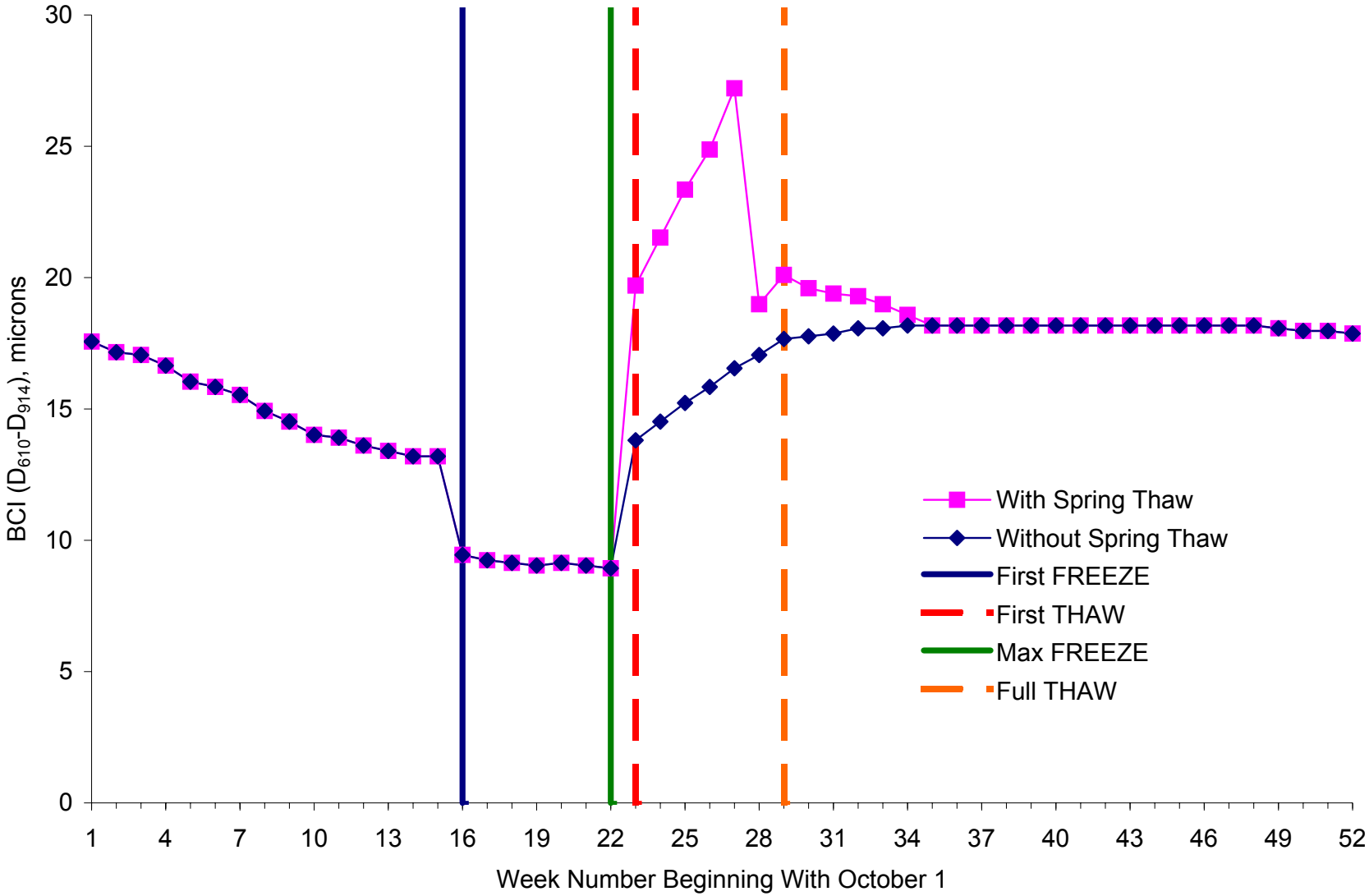

Figure U-7. Index BCI at Site 50-1002 (Poorly Graded Gravel with Silt and Sand)

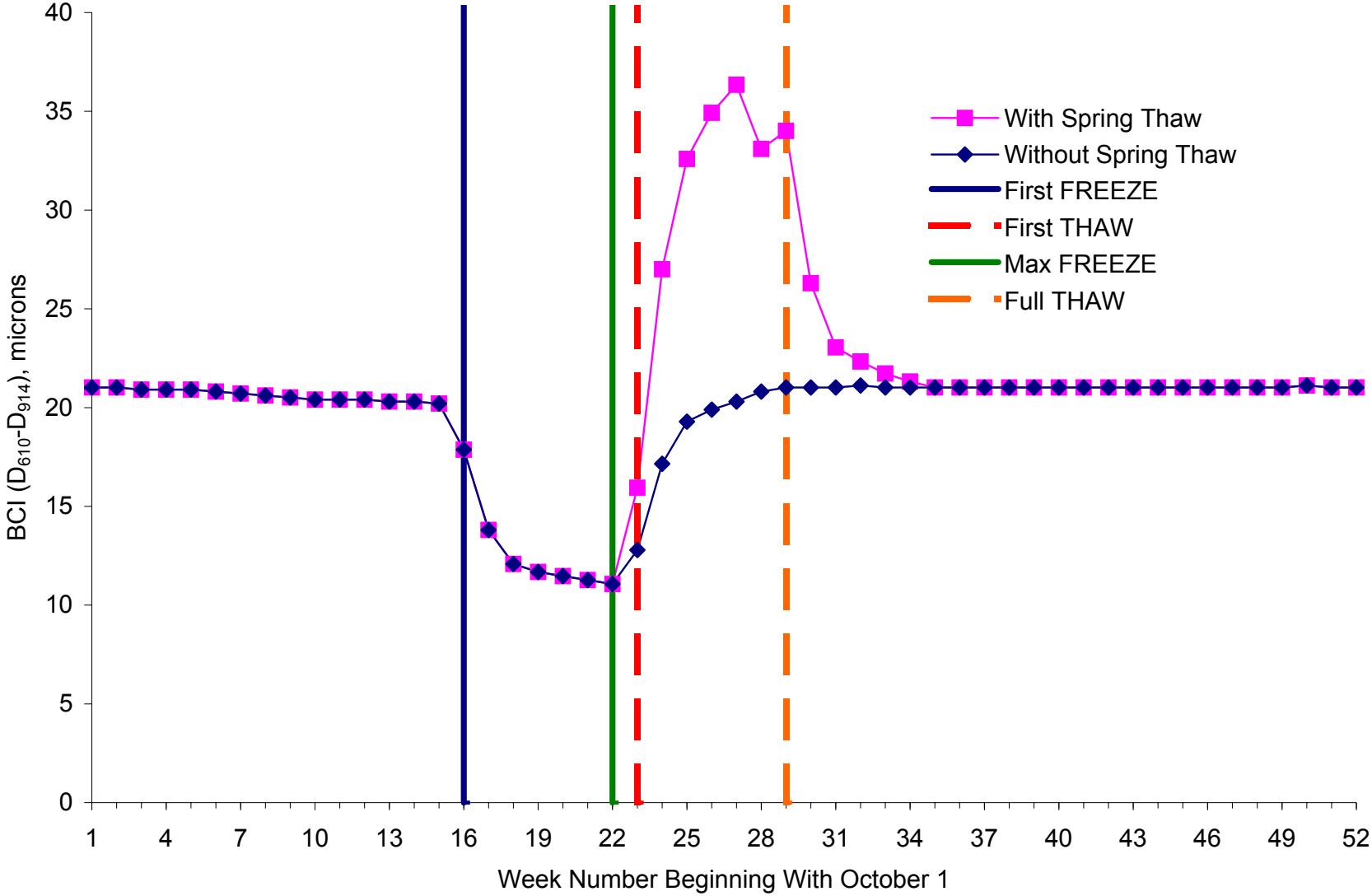

Figure U-8. Index BCI at Site 87-1622 (Sandy Silt)

APPENDIX V

SEASONAL VARIATIONS OF PREDICTED INDEX SDI

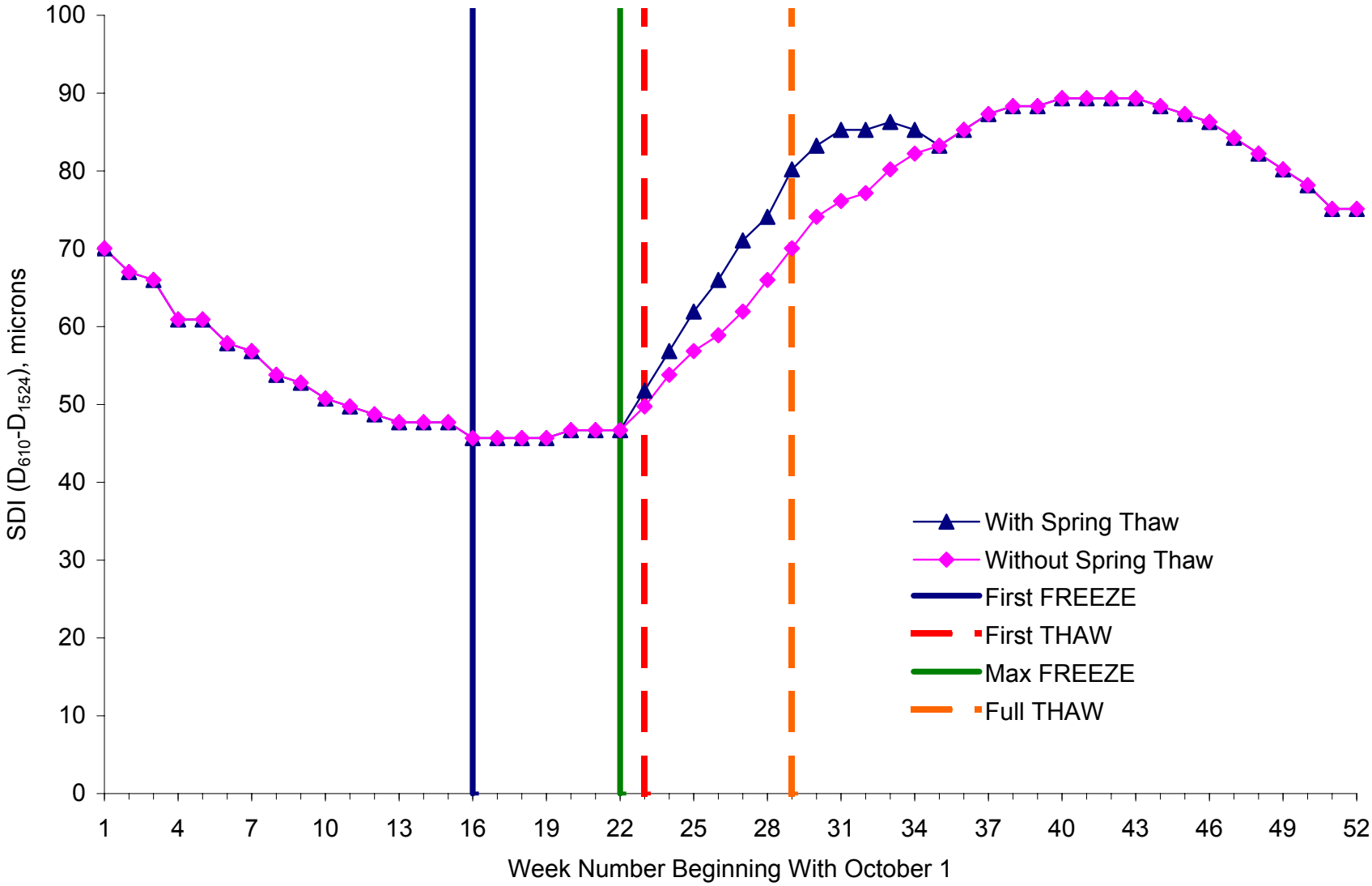

Figure V-1. Index SDI at Site 16-1010 (Silty Sand)

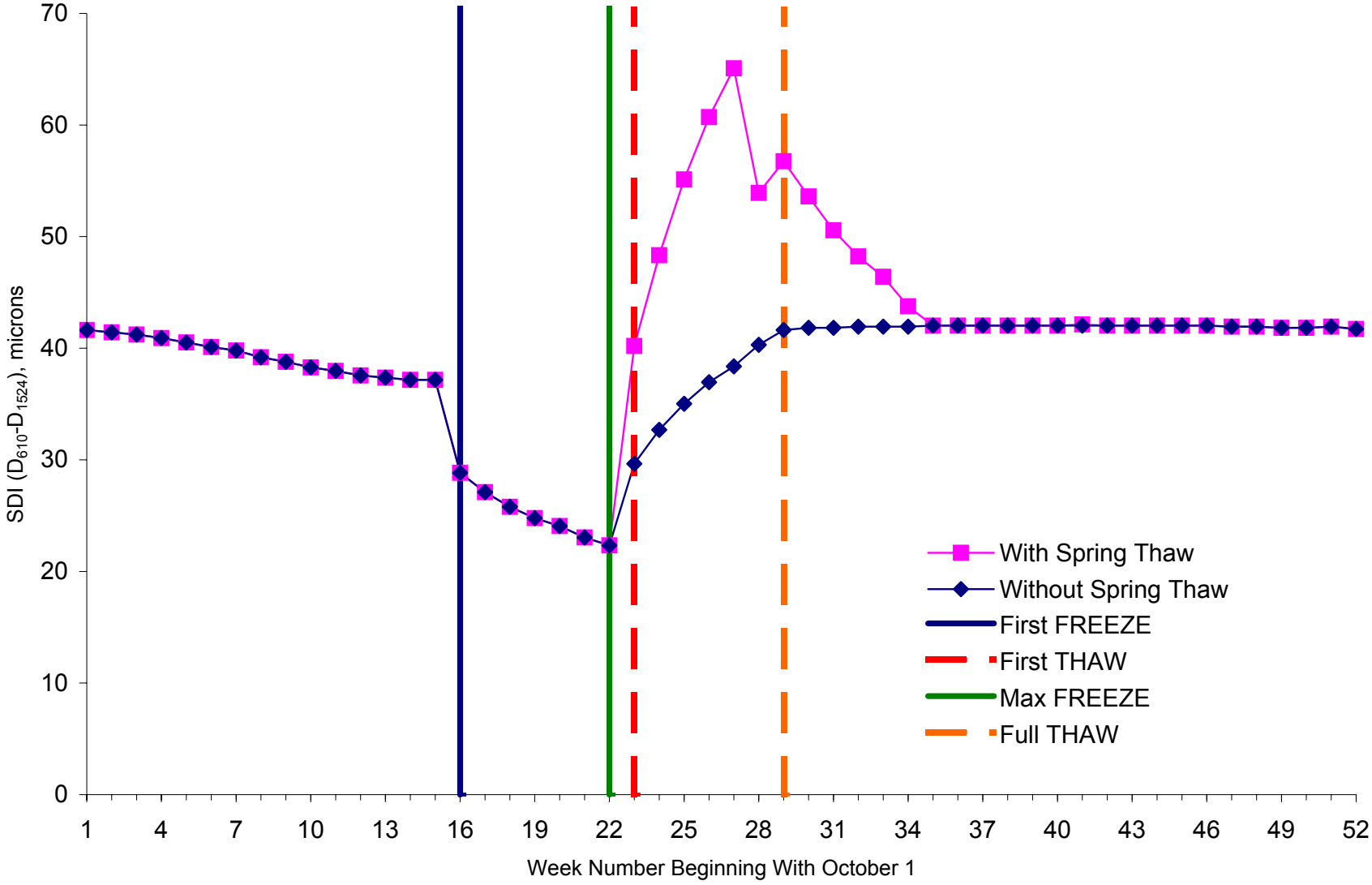

Figure V-2. Index SDI at Site 23-1026 (Silty Sand with Gravel)

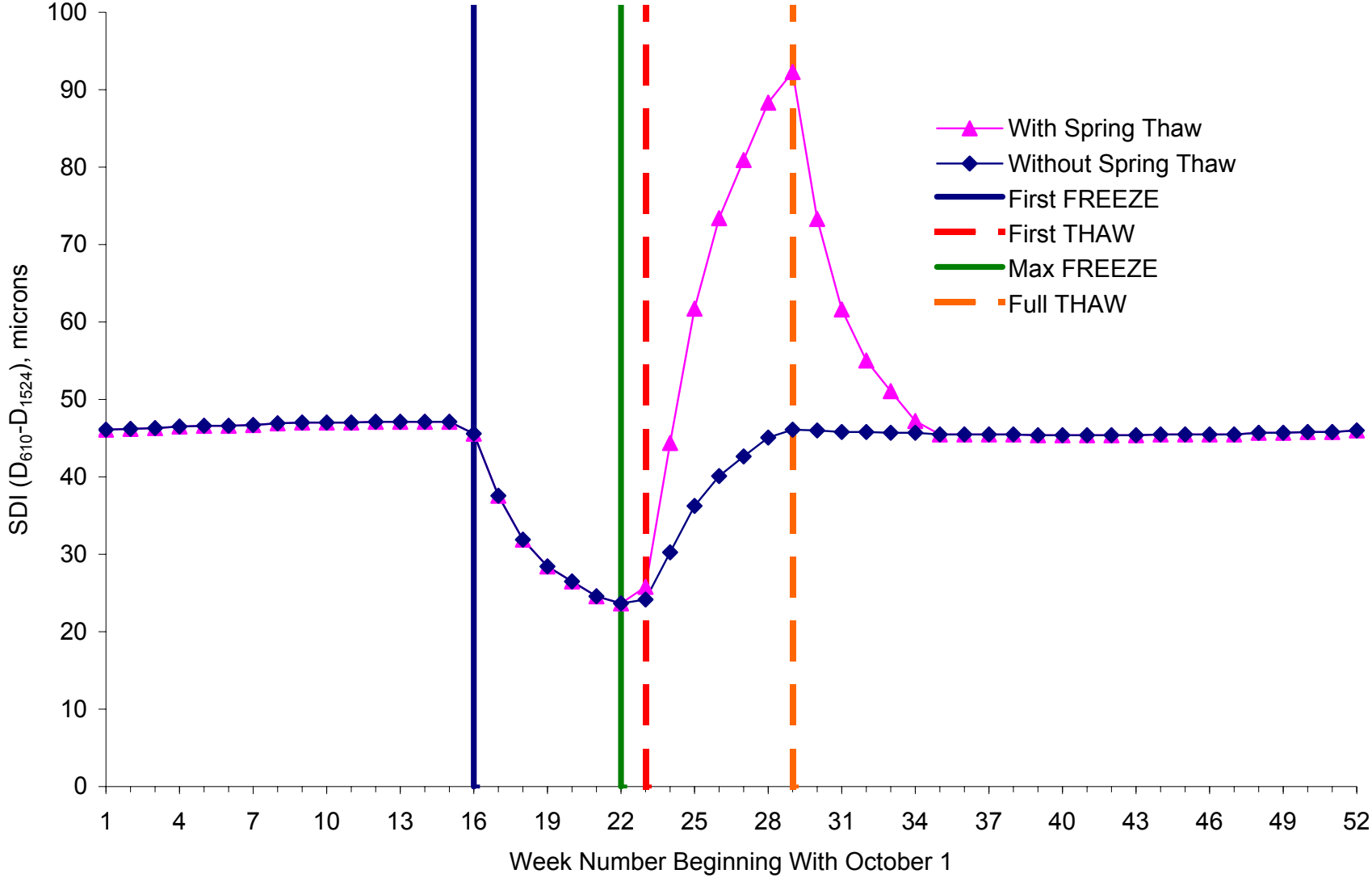

Figure V-3. Index SDI at Site 27-1018 (Poorly Graded Sand with Silt)

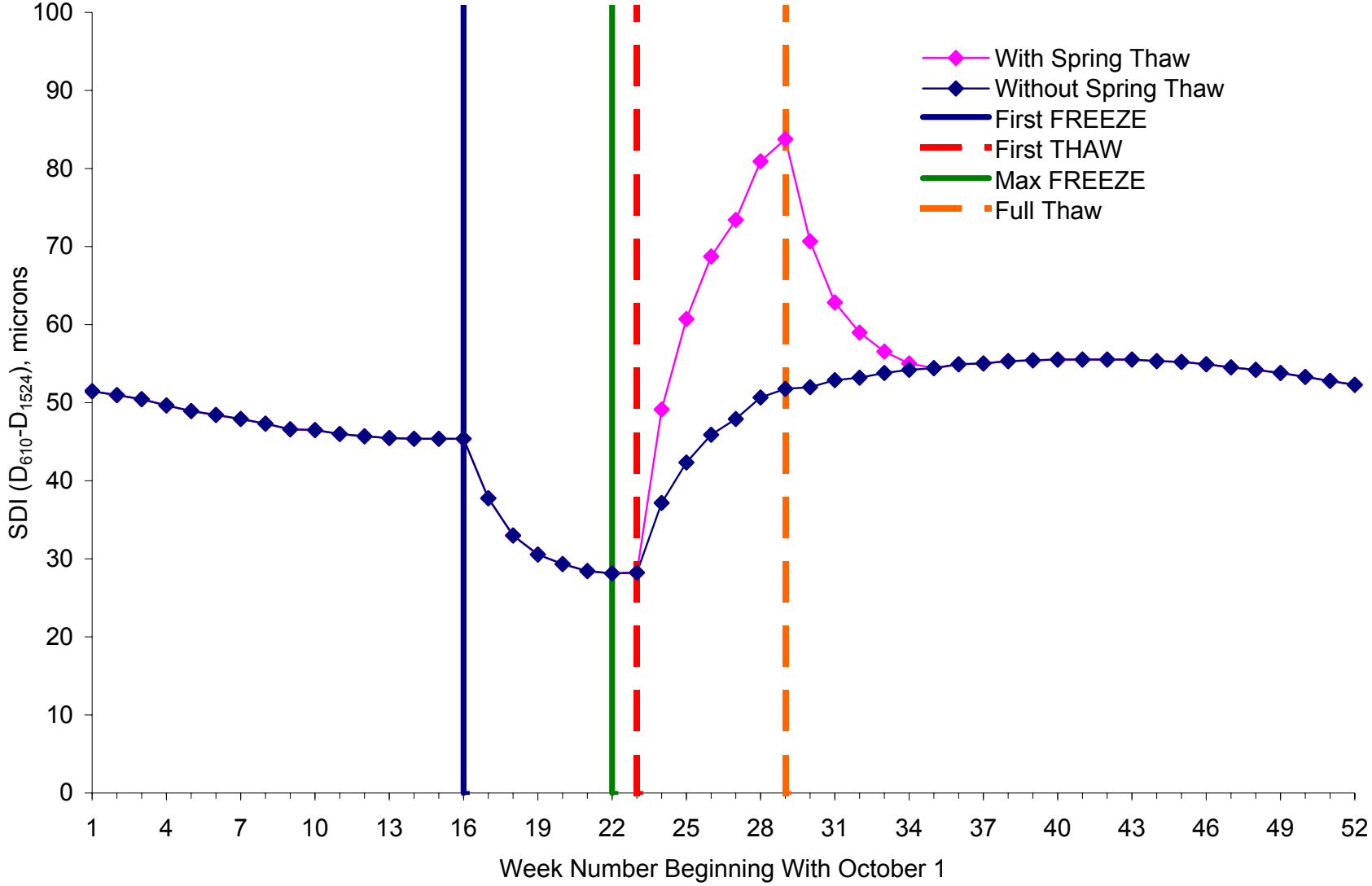

Figure V-4. Index SDI at Site 27-1028 (Poorly Graded Sand with Silt)

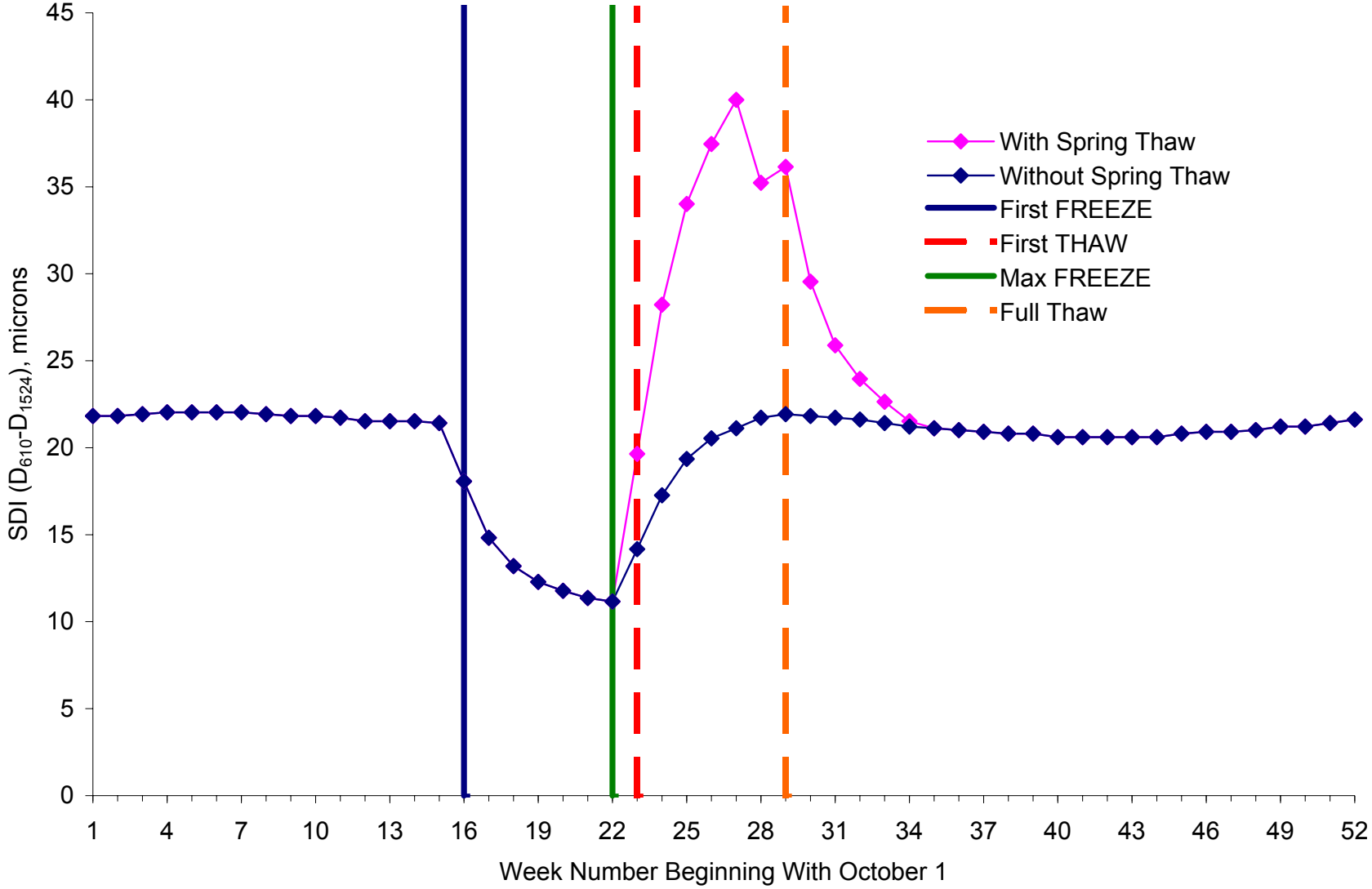

Figure V-5. Index SDI at Site 27-6251 (Poorly Graded Sand with Silt)

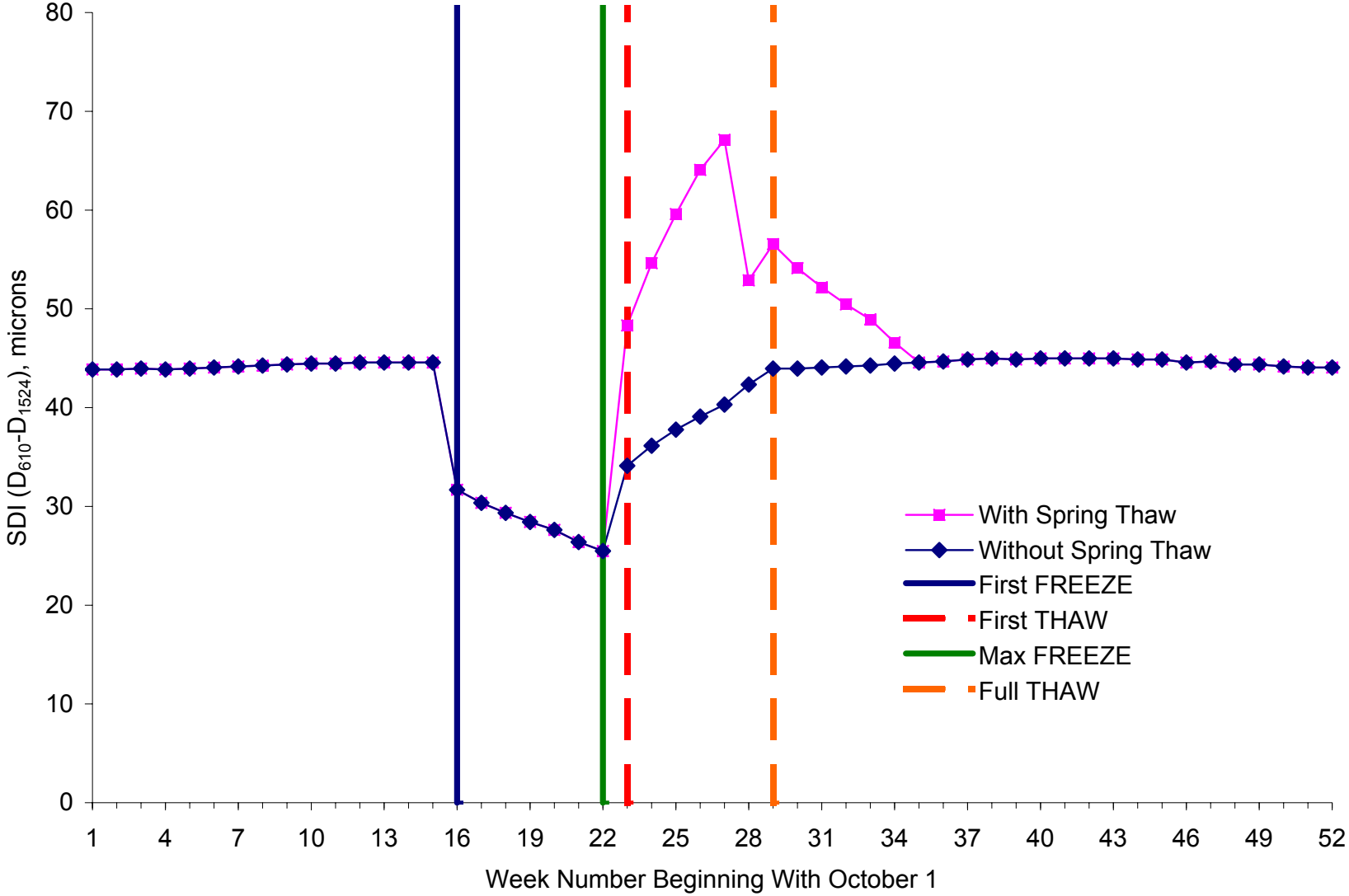

Figure V-6. Index SDI at Site 30-8129 (Poorly Graded Sand with Silt)

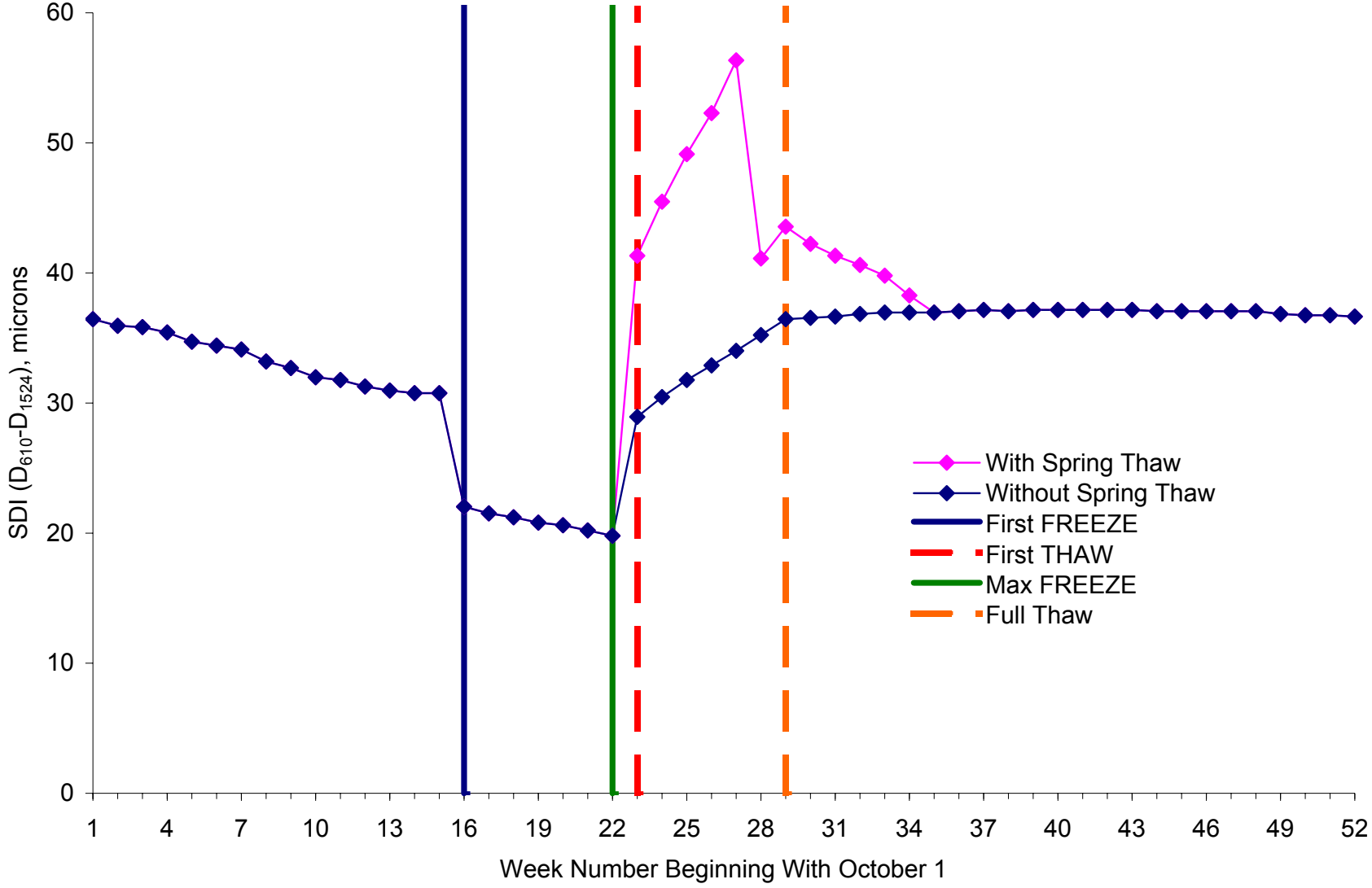

Figure V-7. Index SDI at Site 50-1002 (Poorly Graded Gravel with Silt and Sand)

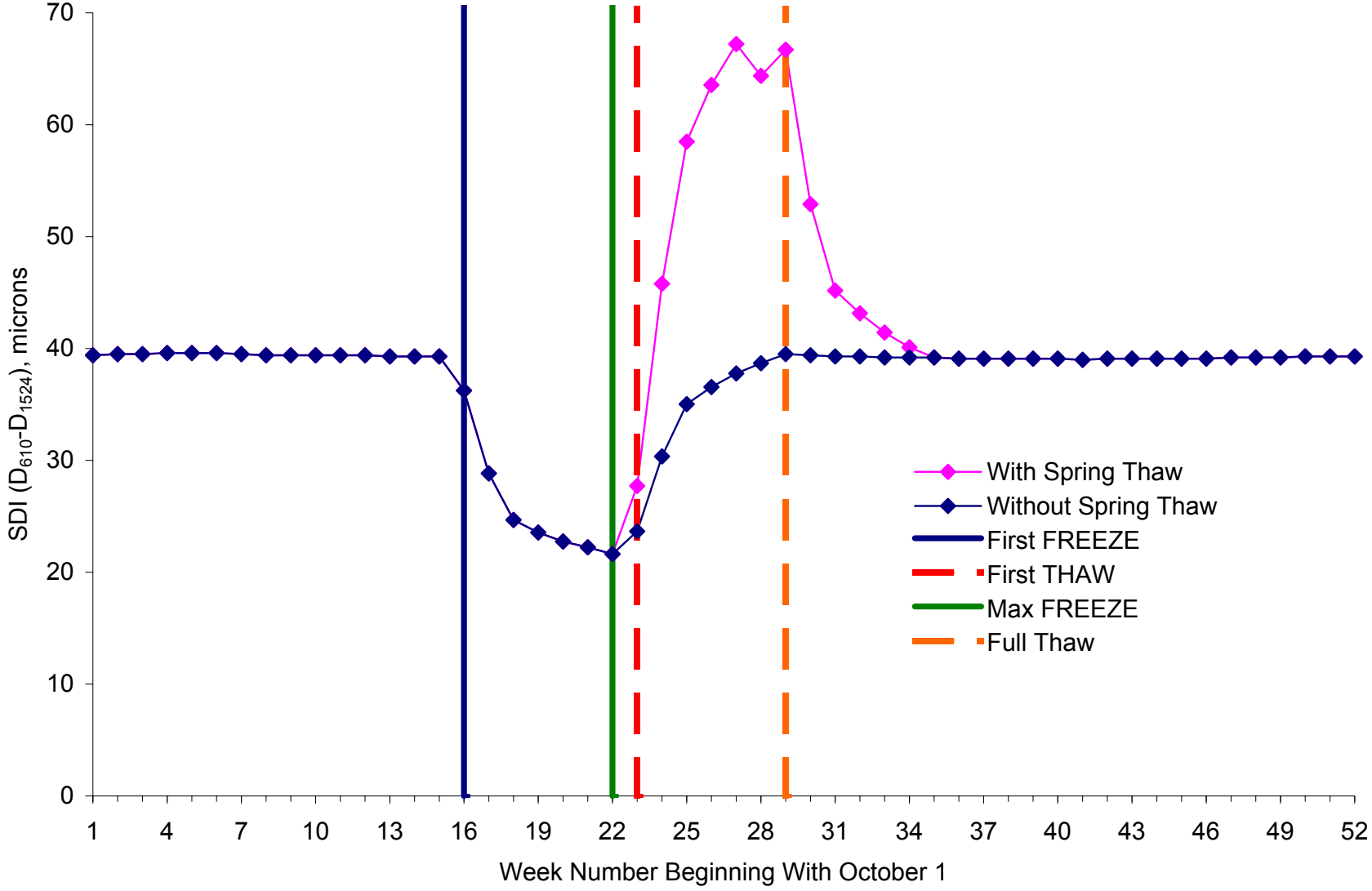

Figure V-8. Index SDI at Site 87-1622 (Sandy Silt)

APPENDIX W

SEASONAL VARIATIONS OF PREDICTED INDEX SI

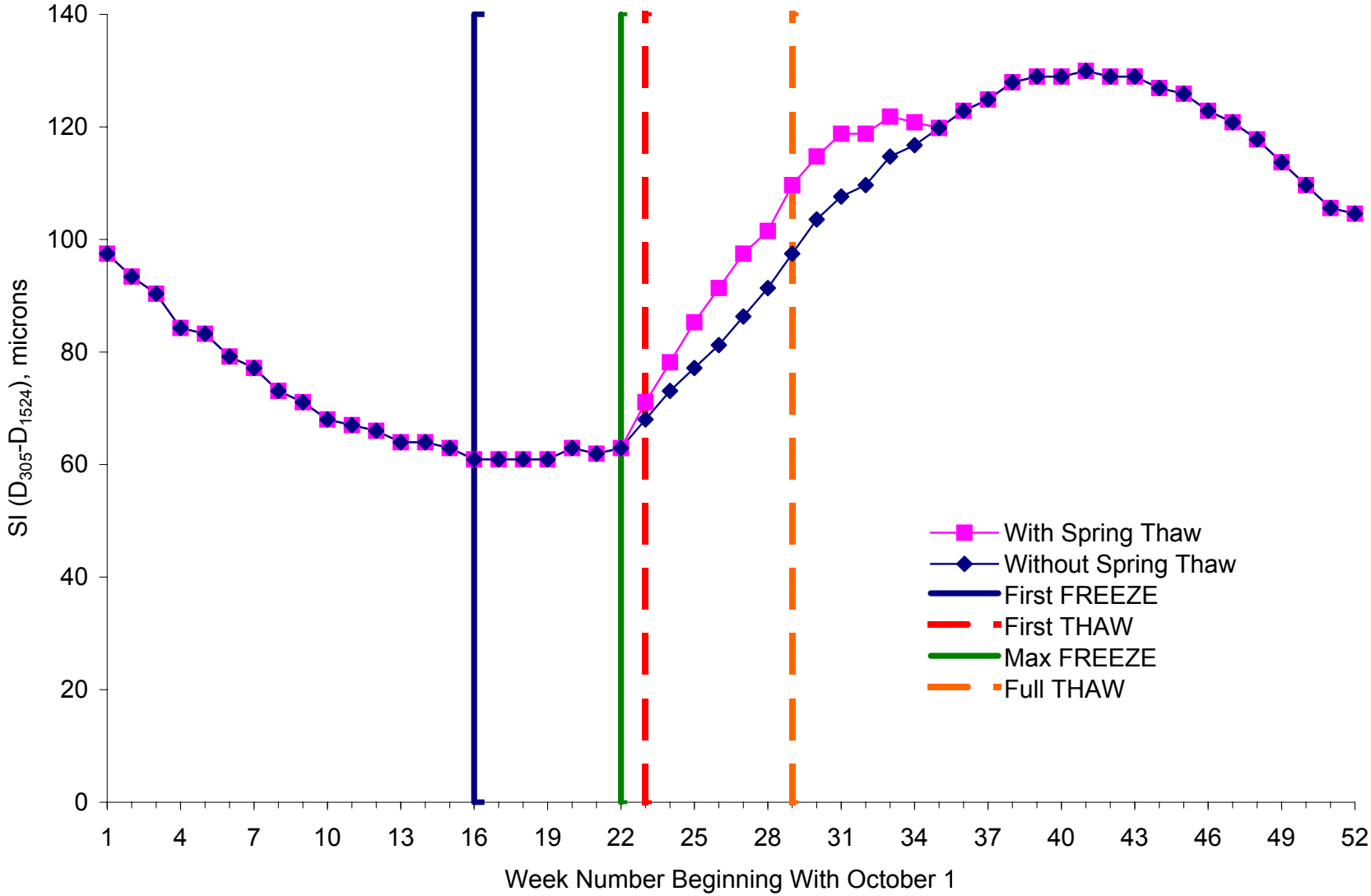

Figure W-1. Index SI at Site 16-1010 (Silty Sand)

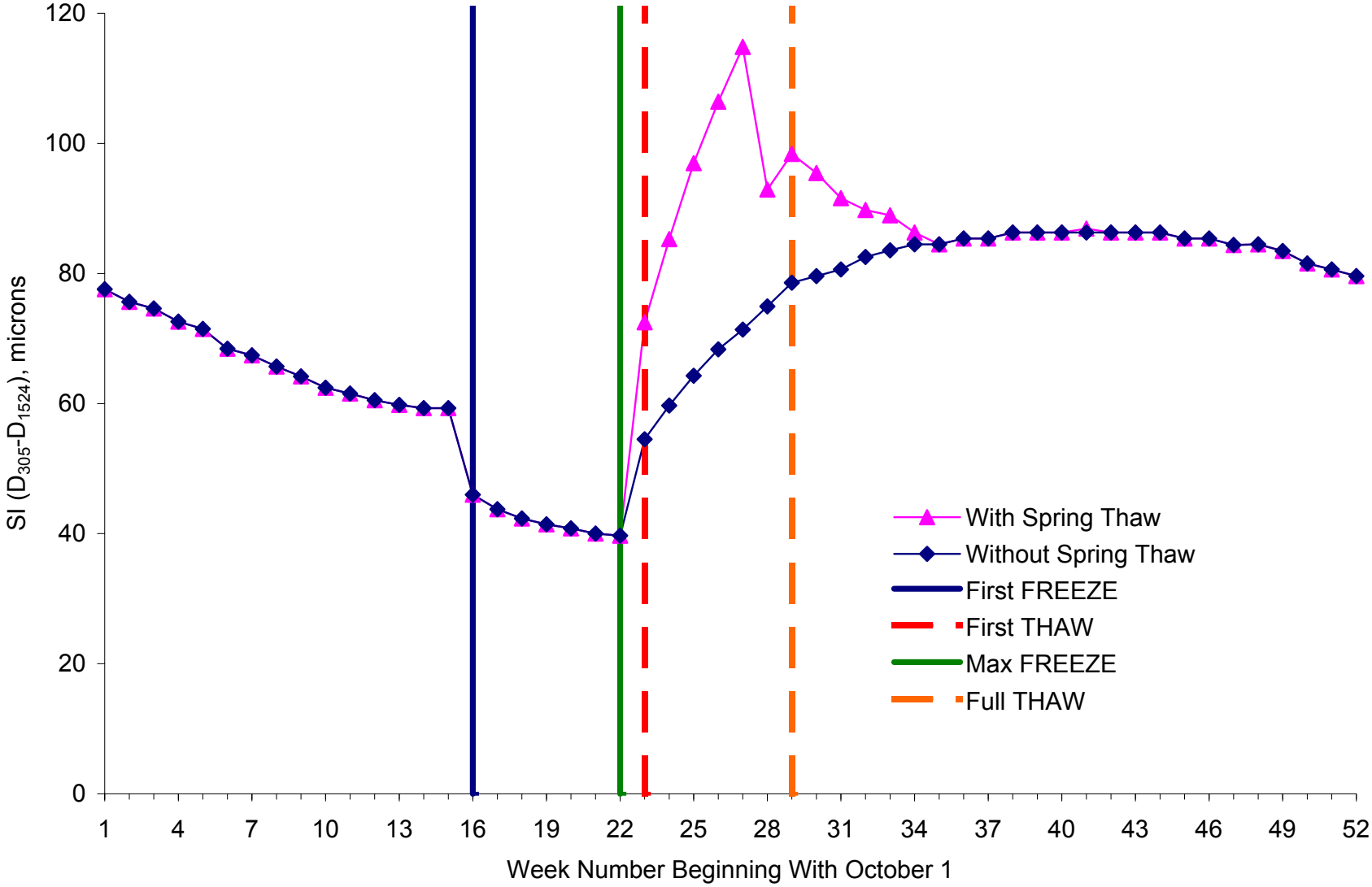

Figure W-2. Index SI at Site 23-1026 (Silty Sand with Gravel)

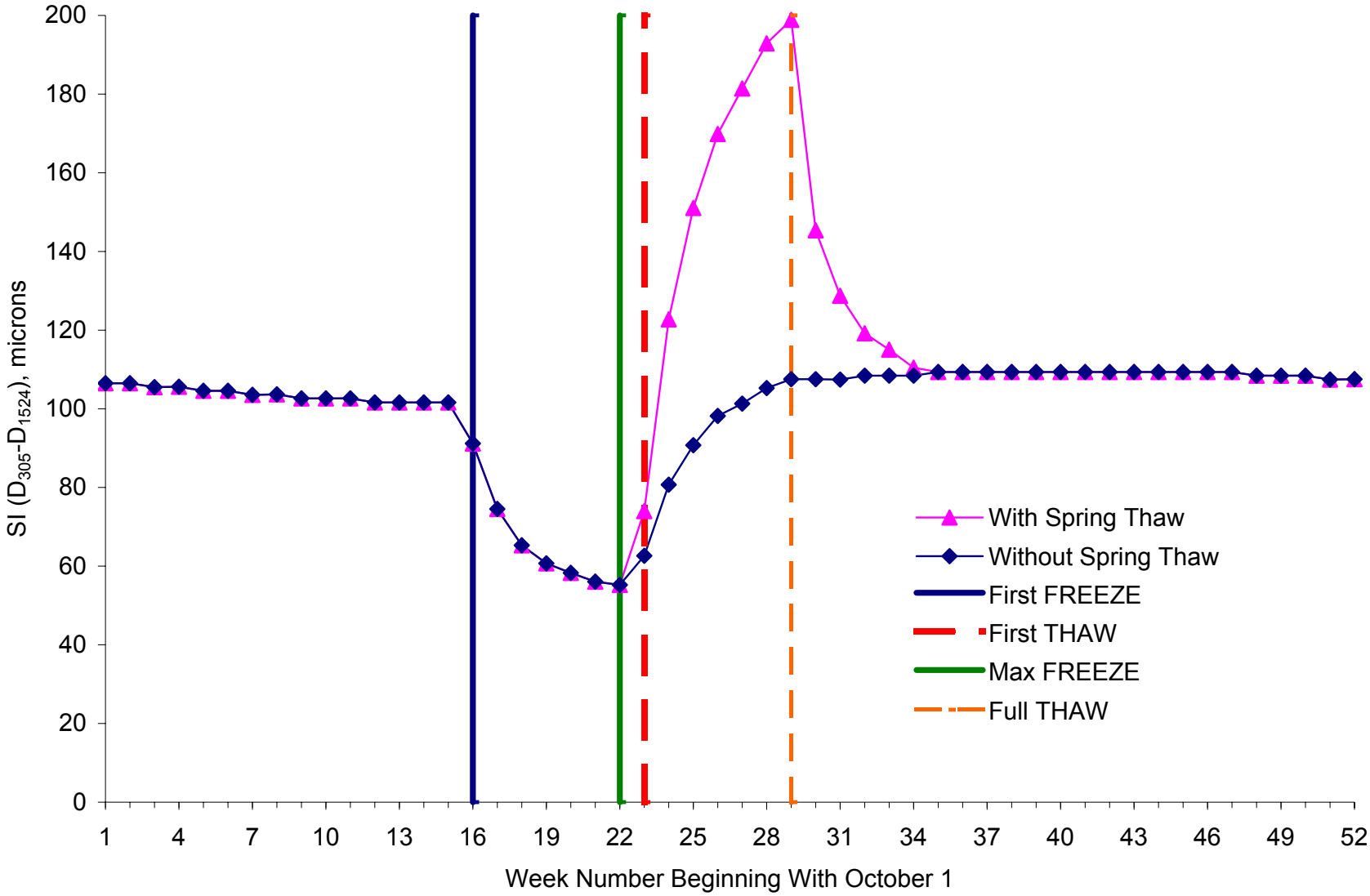

Figure W-3. Index SI at Site 27-1018 (Poorly Graded Sand with Silt)

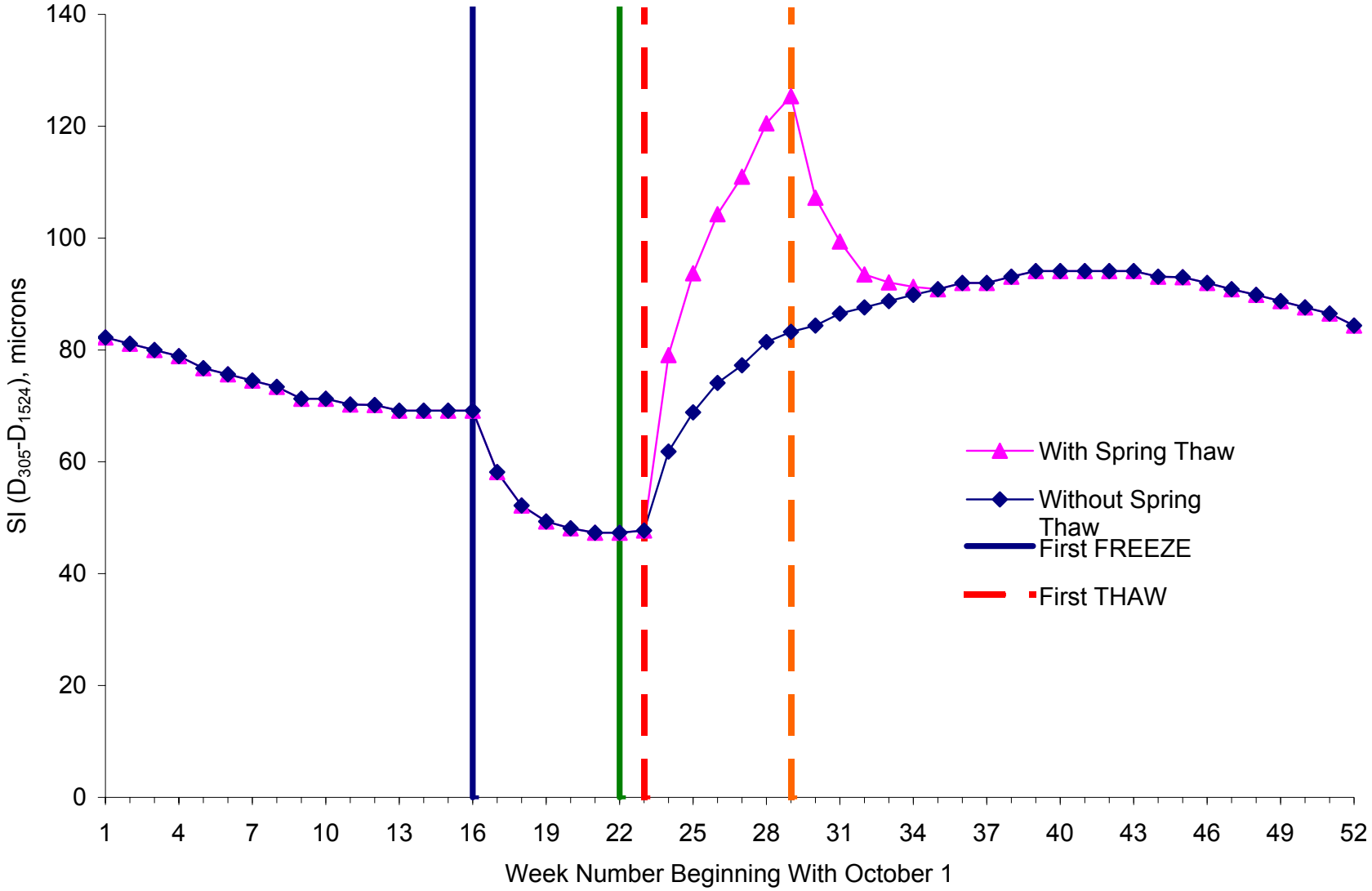

Figure W-4. Index SI at Site 27-1028 (Poorly Graded Sand with Silt)

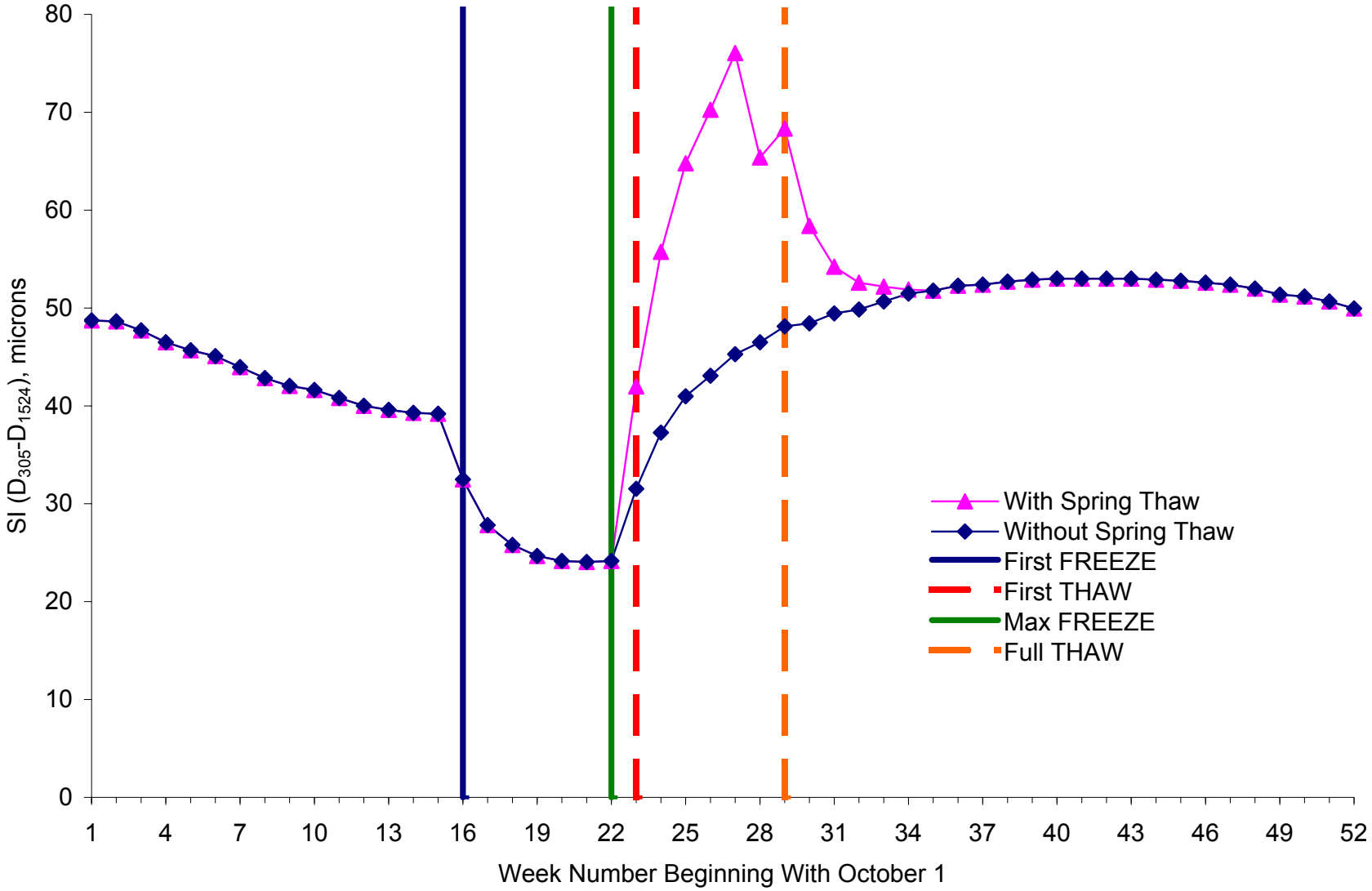

Figure W-5. Index SI at Site 27-6251 (Poorly Graded Sand with Silt)

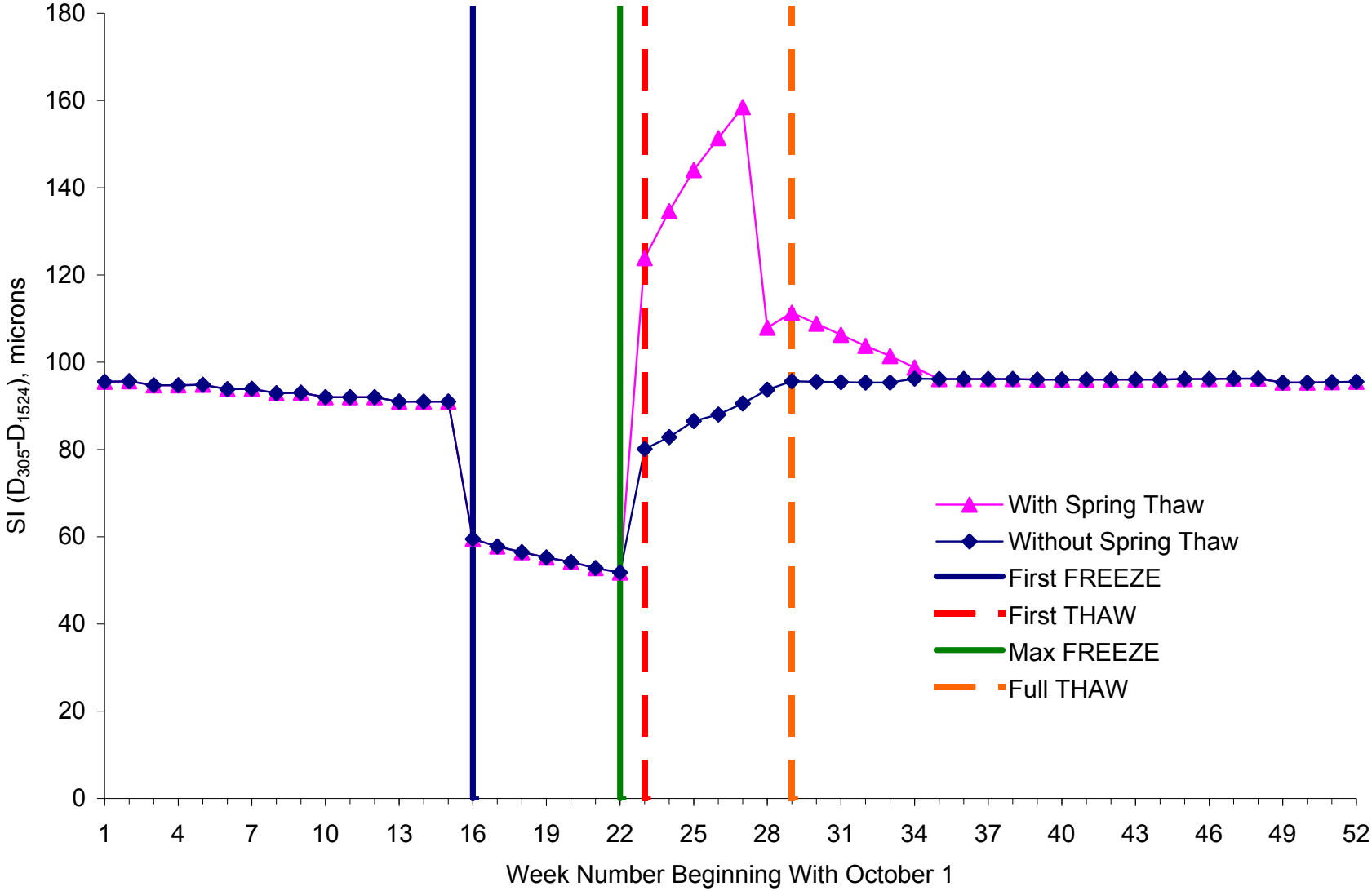

Figure W-6. Index SI at Site 30-8129 (Poorly Graded Sand with Silt)

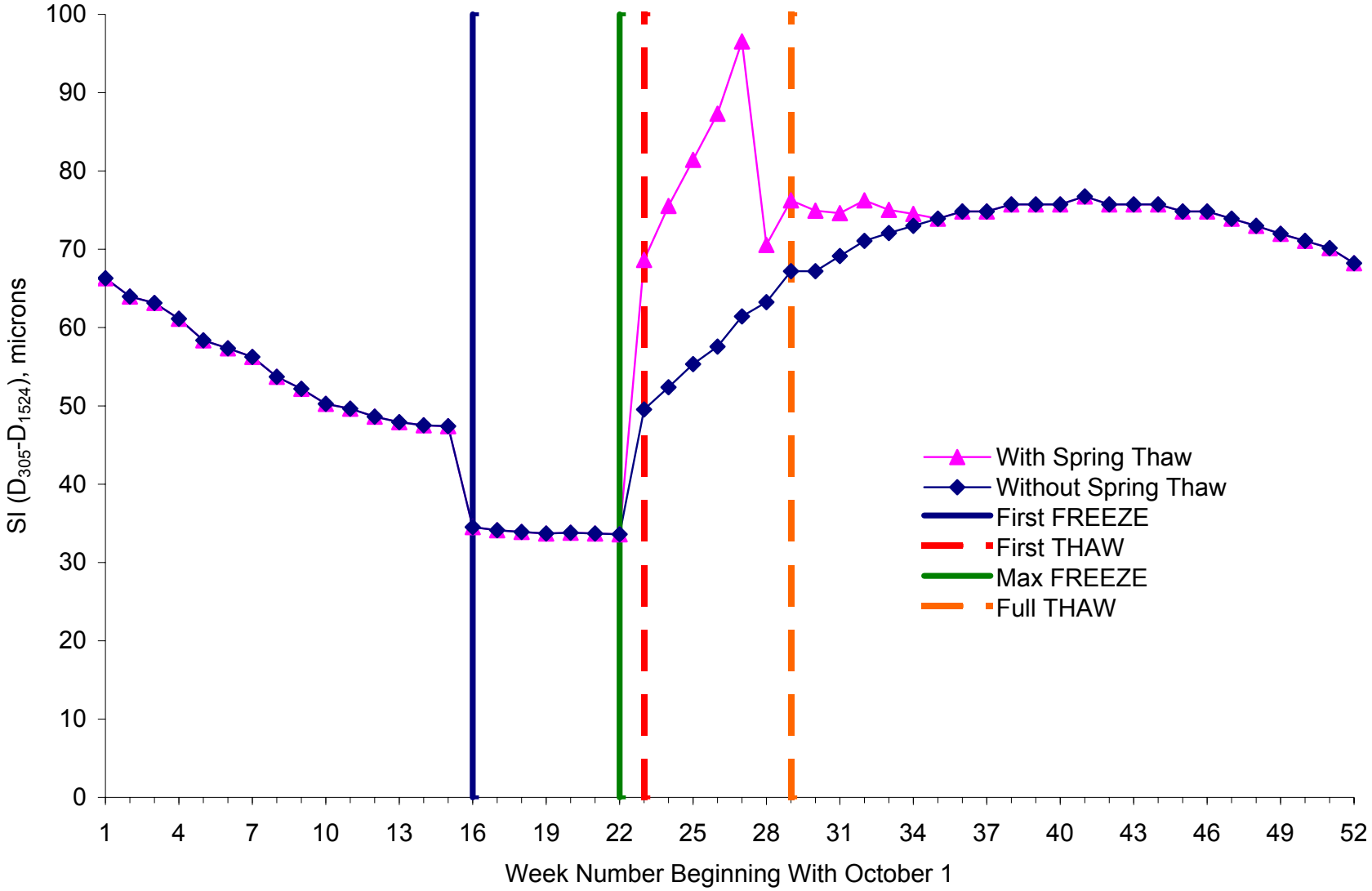

Figure W-7. Index SI at Site 50-1002 (Poorly Graded Gravel with Silt and Sand)

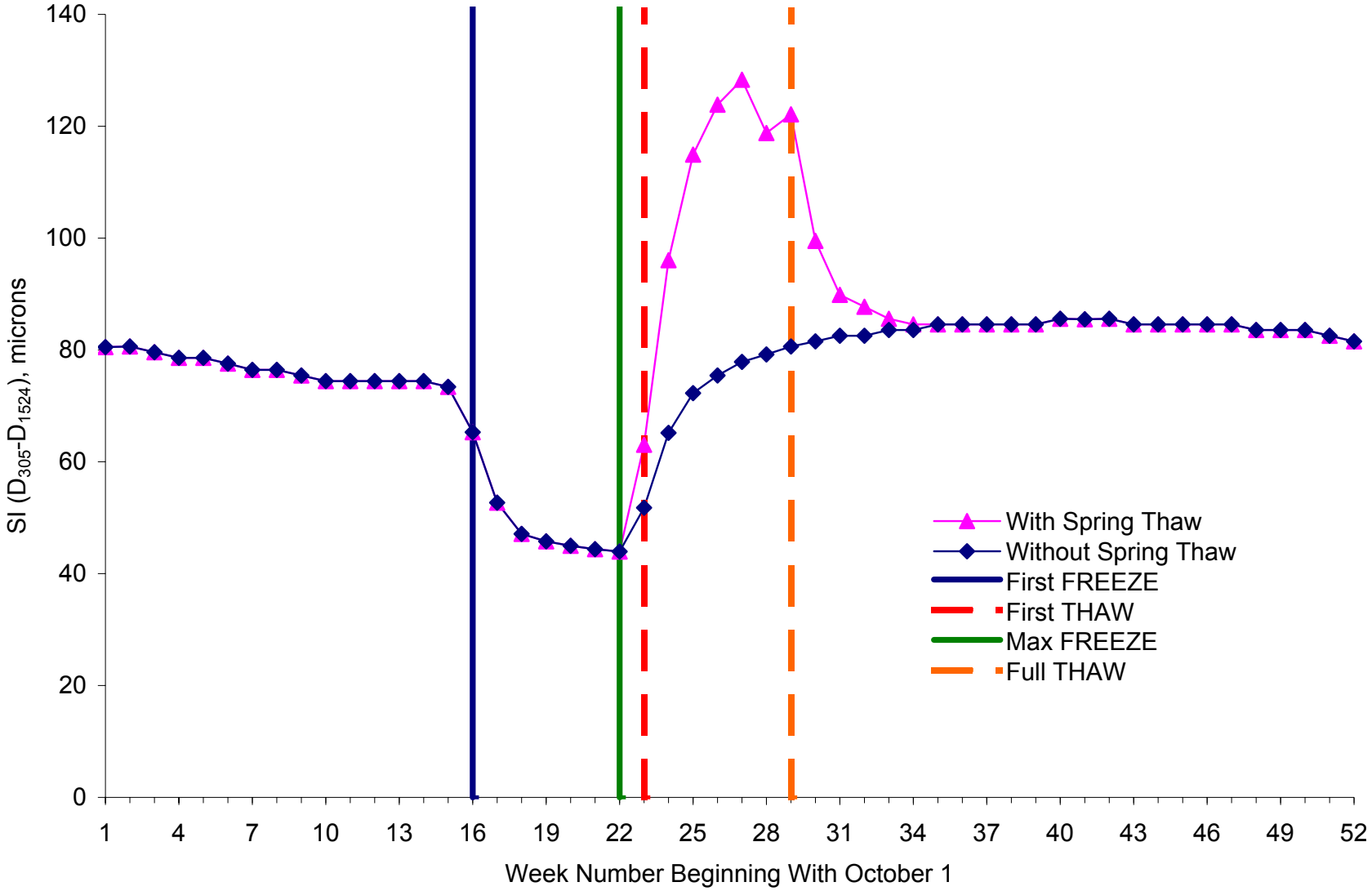

Figure W-8. Index SI at Site 87-1622 (Sandy Silt)

APPENDIX X

SEASONAL VARIATIONS OF PREDICTED INDEX PA

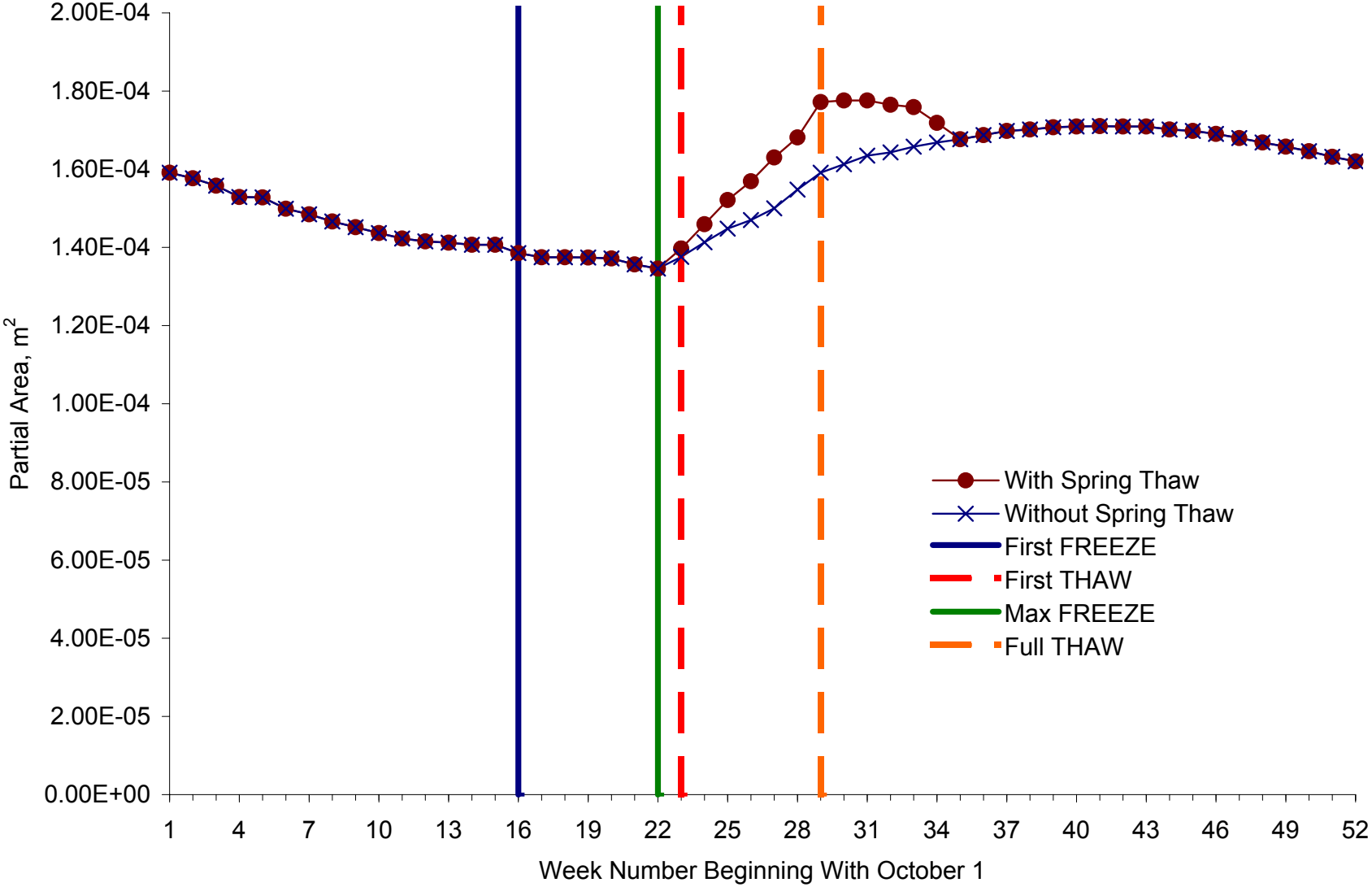

Figure X-1. Index PA at Site 16-1010 (Silty Sand)

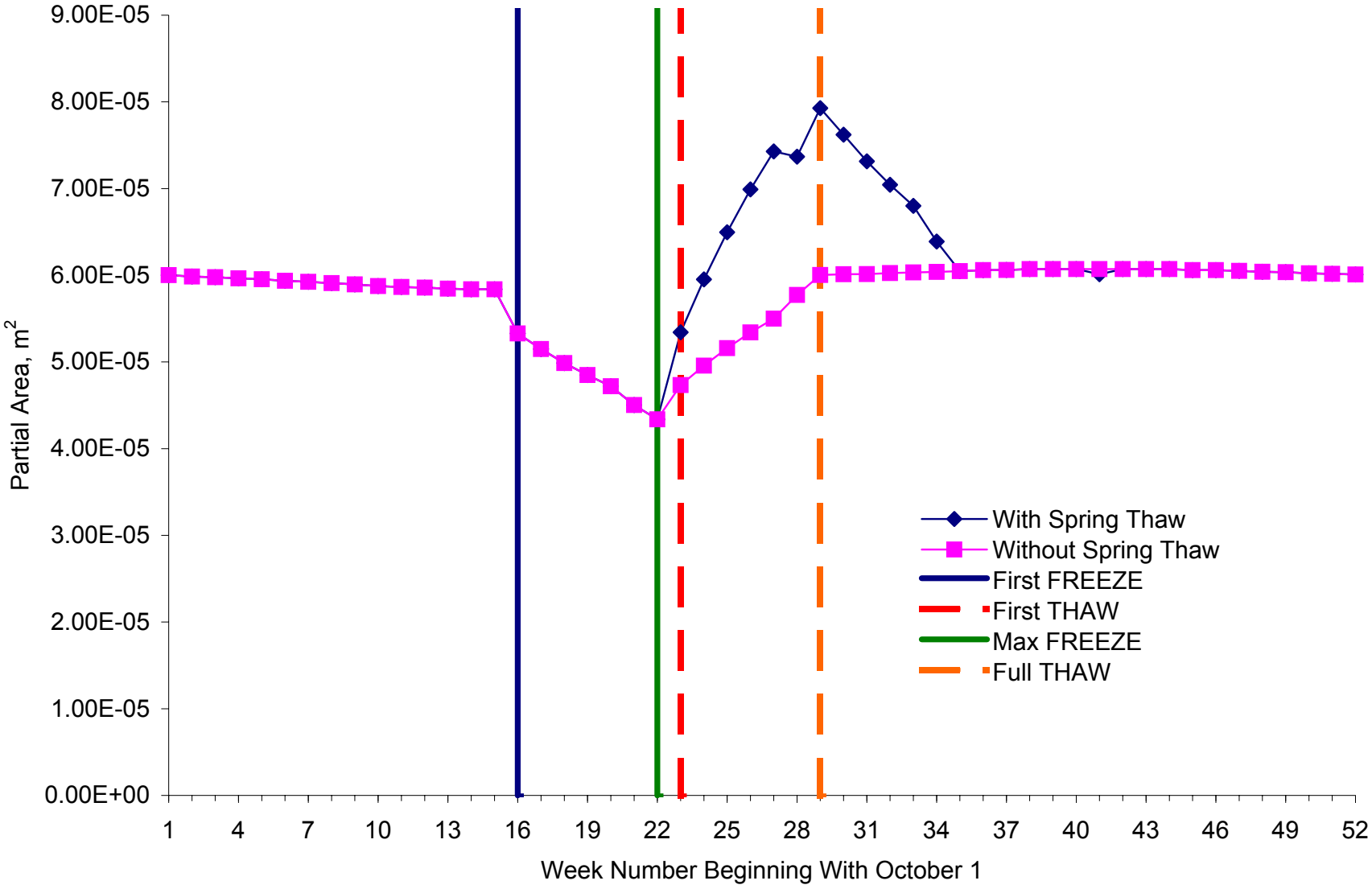

Figure X-2. Index PA at Site 23-1026 (Silty Sand with Gravel)

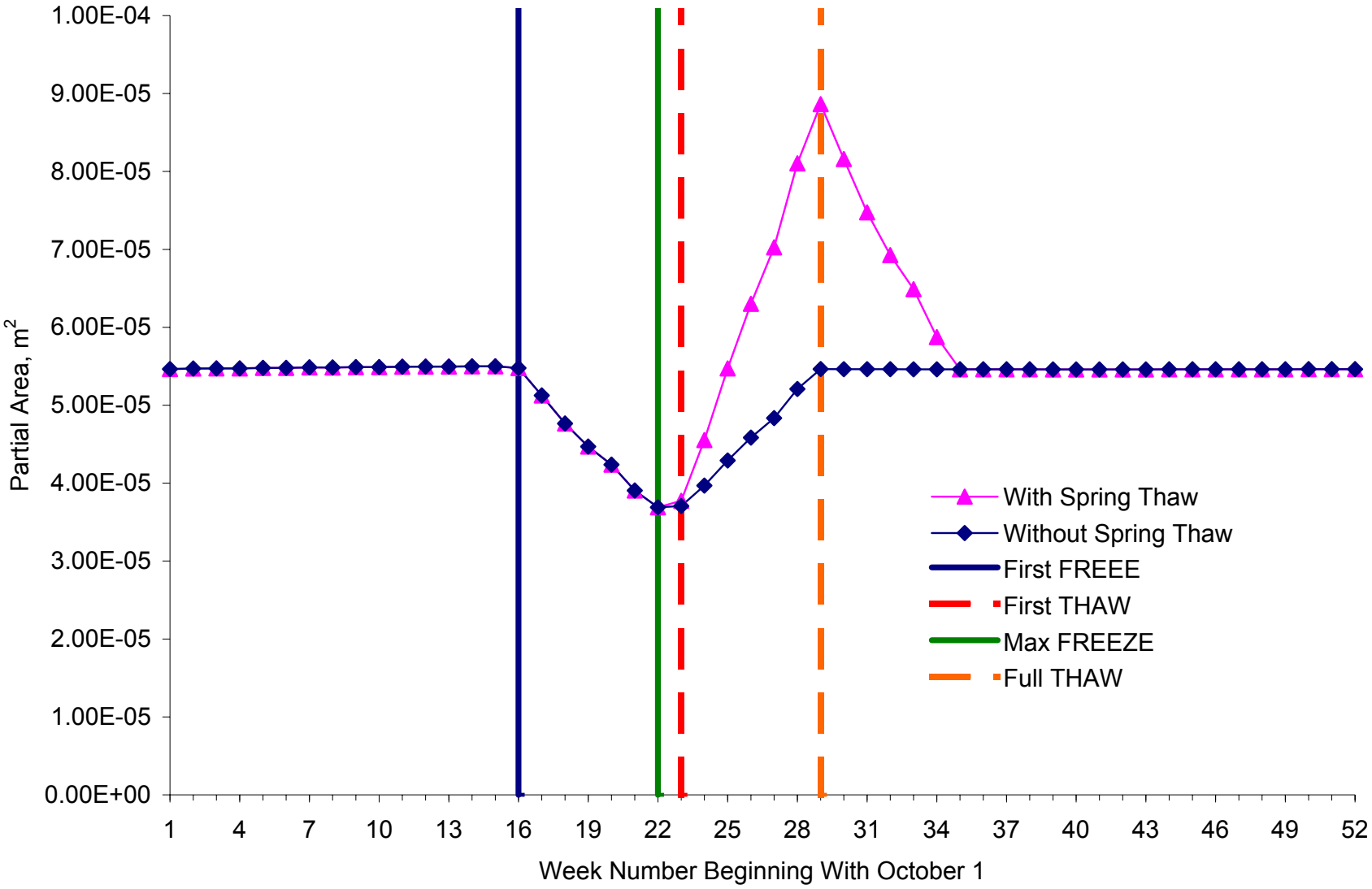

Figure X-3. Index PA at Site 27-1018 (Poorly Graded Sand with Silt)

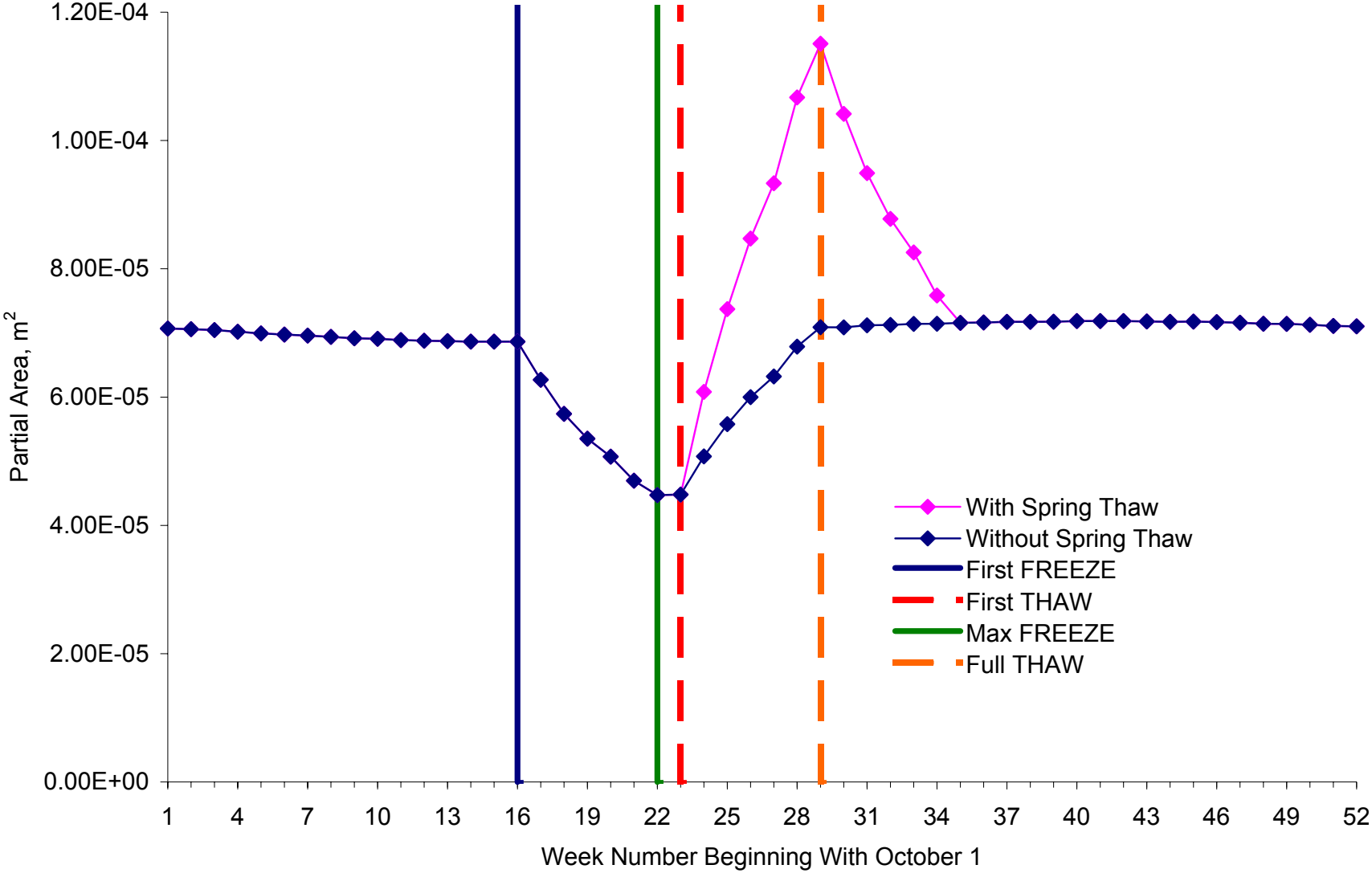

Figure X-4. Index PA at Site 27-1028 (Poorly Graded Sand with Silt)

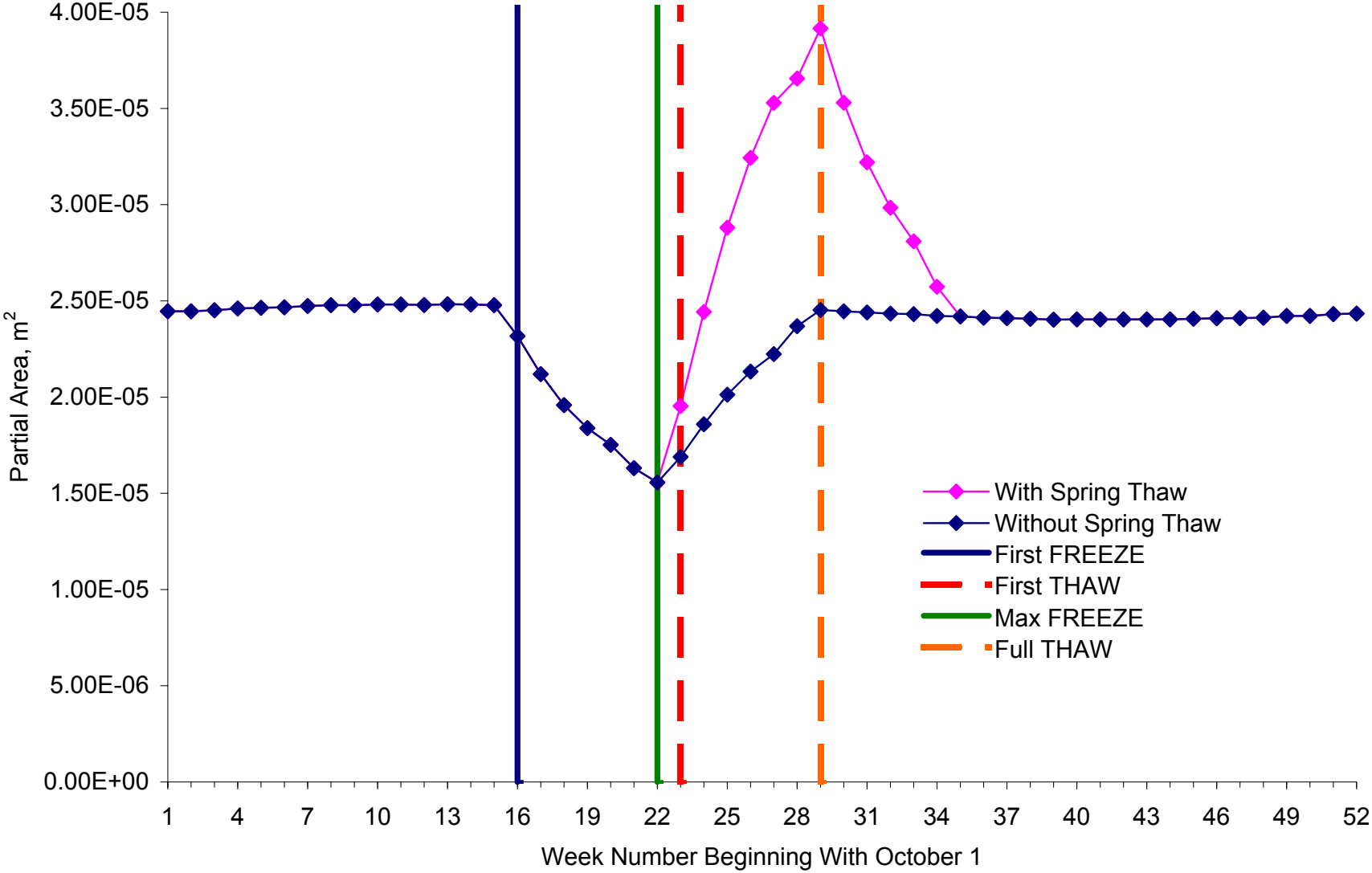

Figure X-5. Index PA at Site 27-6251 (Poorly Graded Sand with Silt)

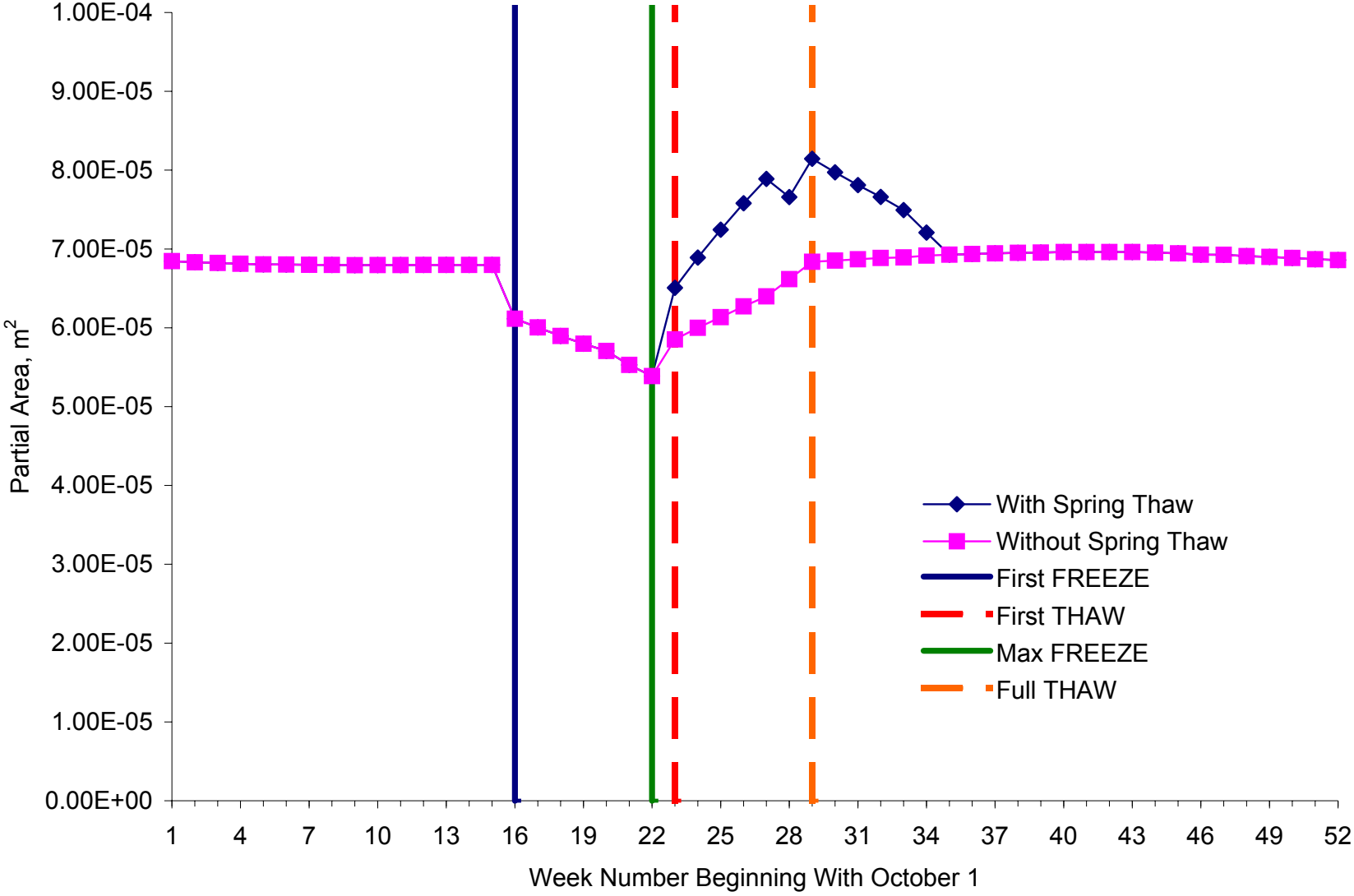

Figure X-6. Index PA at Site 30-8129 (Poorly Graded Sand with Silt)

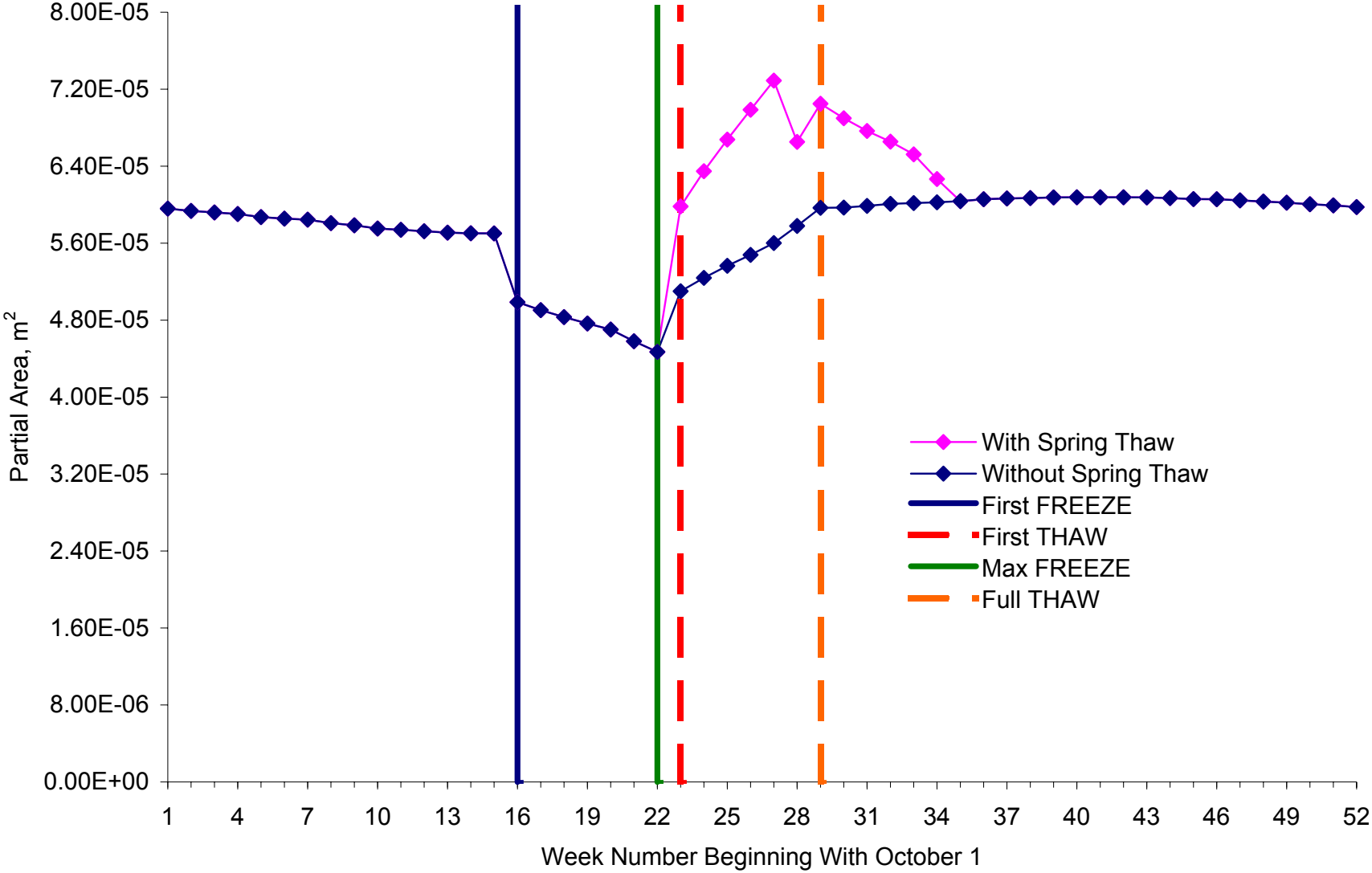

Figure X-7. Index PA at Site 50-1002 (Poorly Graded Gravel with Silt and Sand)

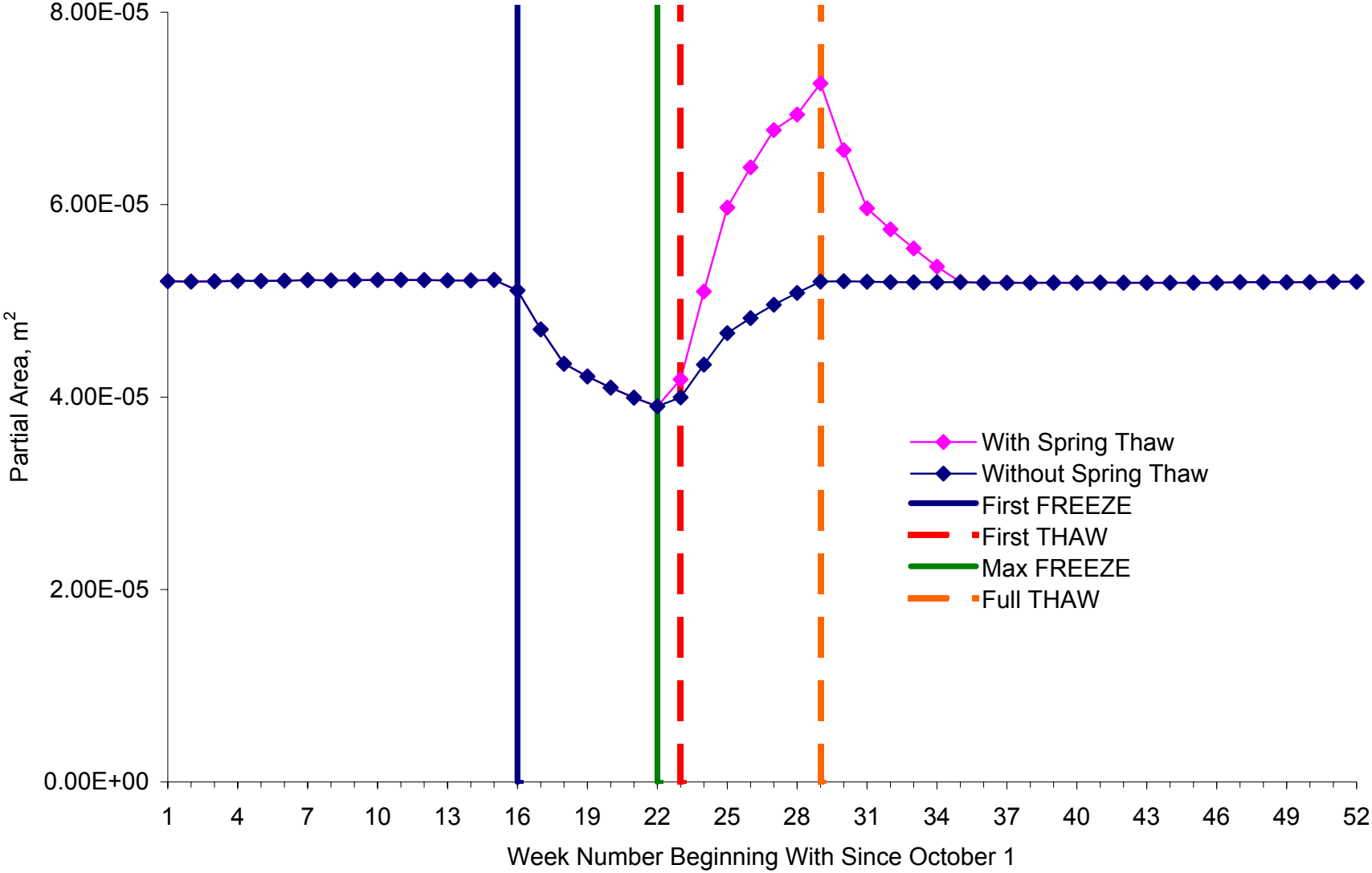

Figure X-8. Index PA at Site 87-1622 (Silty Sand)

APPENDIX Y

SEASONAL VARIATIONS OF PREDICTED NORMALIZED AC STRAIN

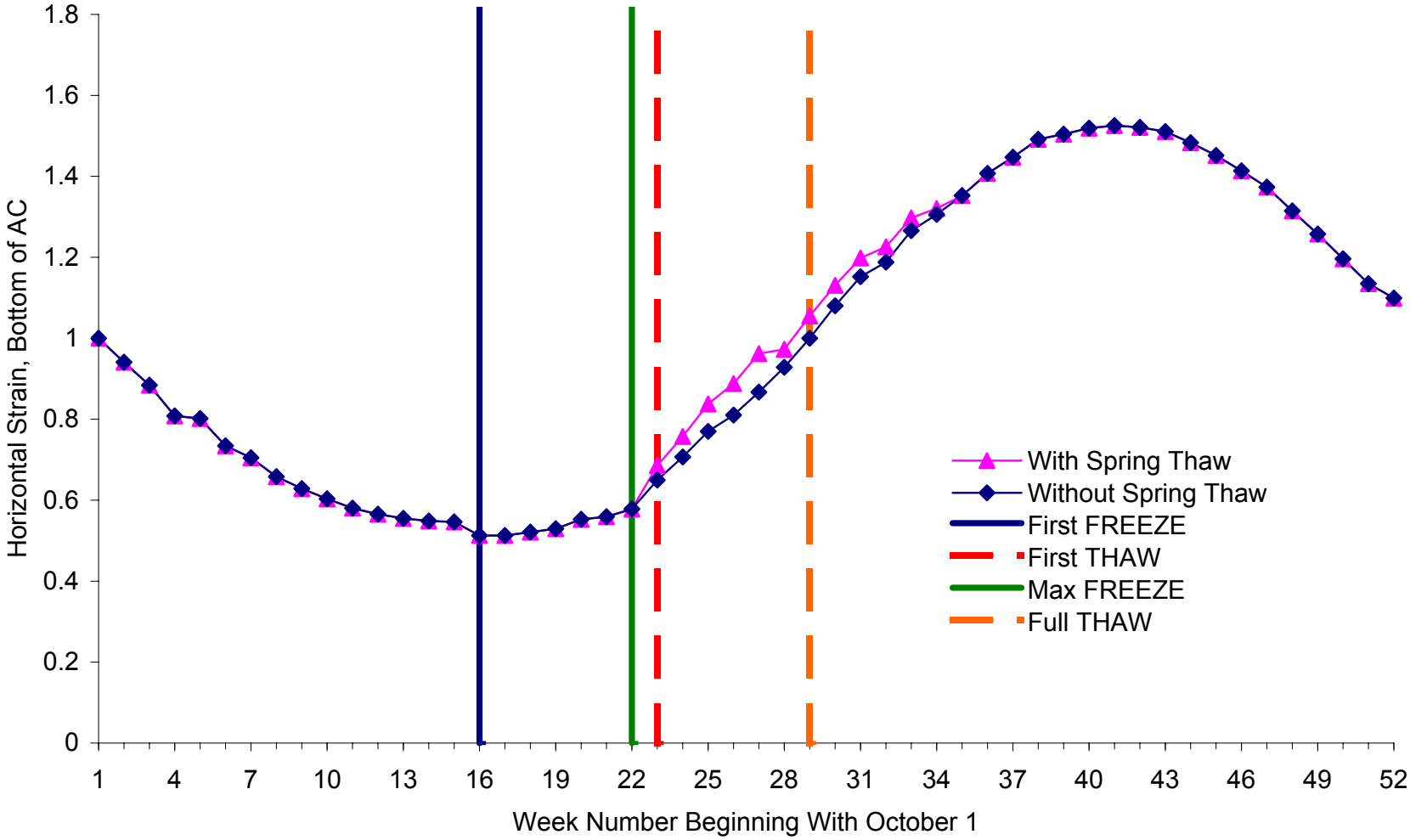

Figure Y-1. Normalized Horizontal AC Strain at Site 16-1010 (Silty Sand)

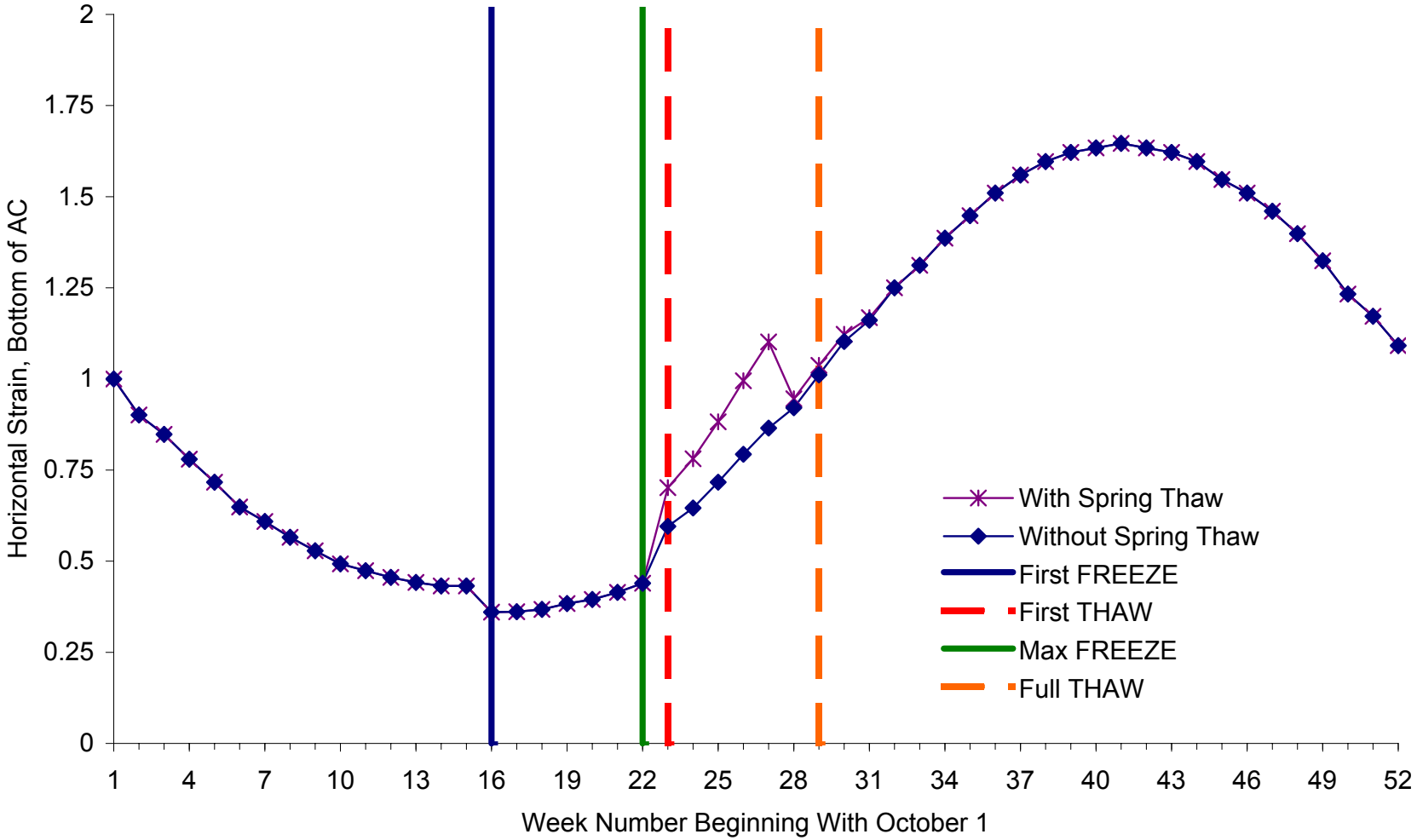

Figure Y-2. Normalized Horizontal AC Strain at Site 23-1026 (Silty Sand with Gravel)

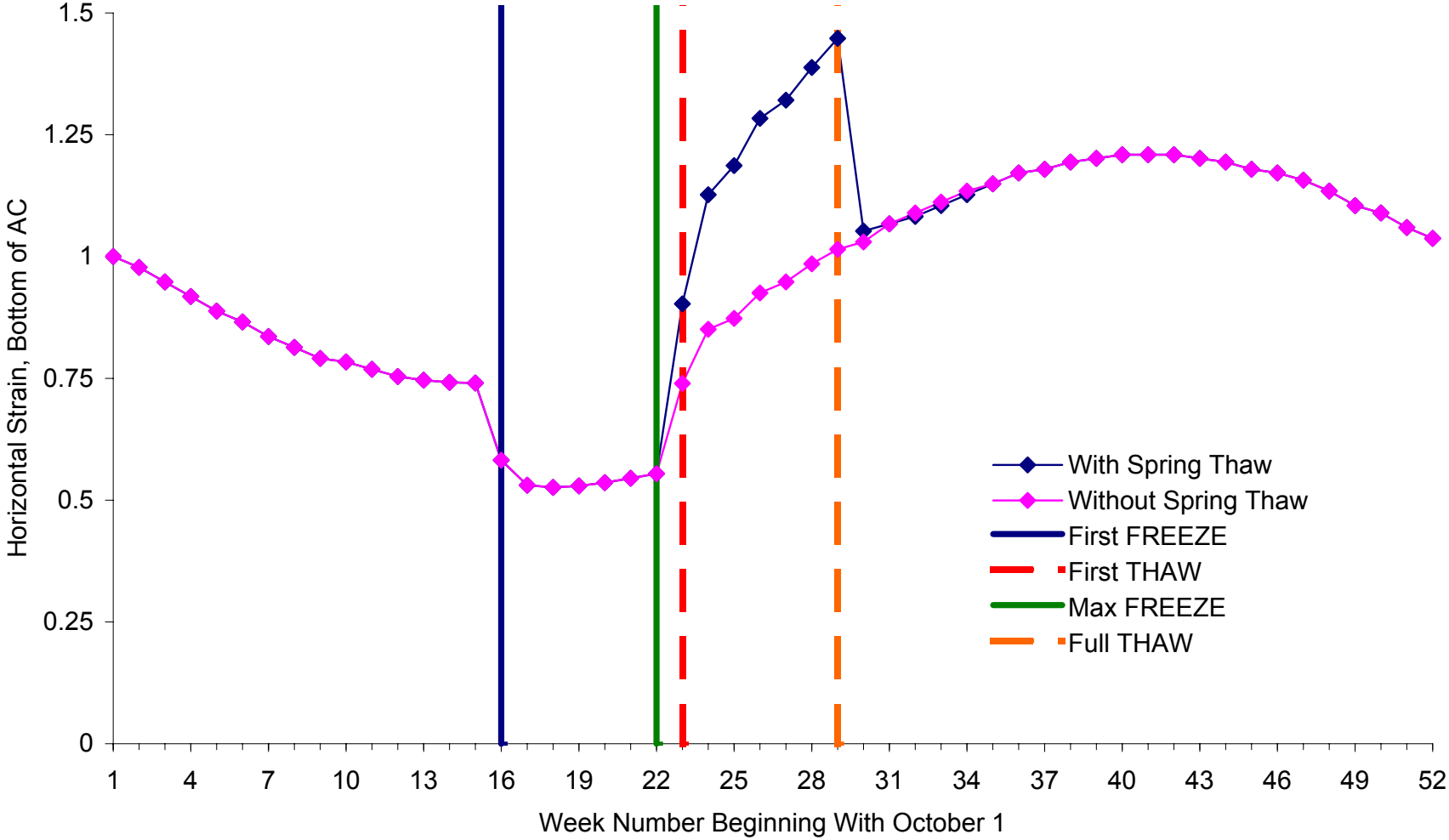

Figure Y-3. Normalized Horizontal AC Strain at Site 27-1018 (Poorly Graded Sand with Silt)

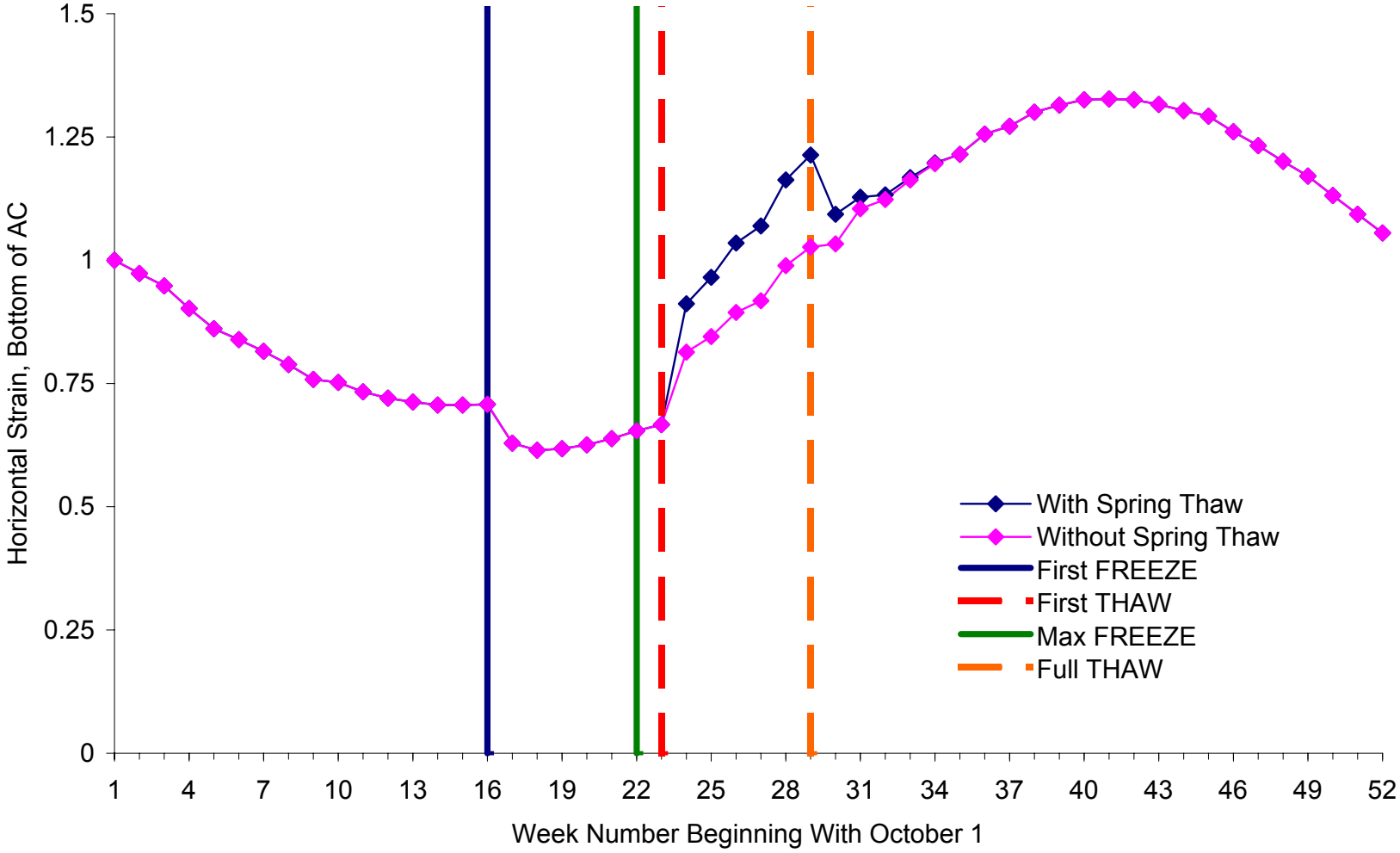

Figure Y-4. Normalized Horizontal AC Strain at Site 27-1028 (Poorly Graded Sand with Silt)

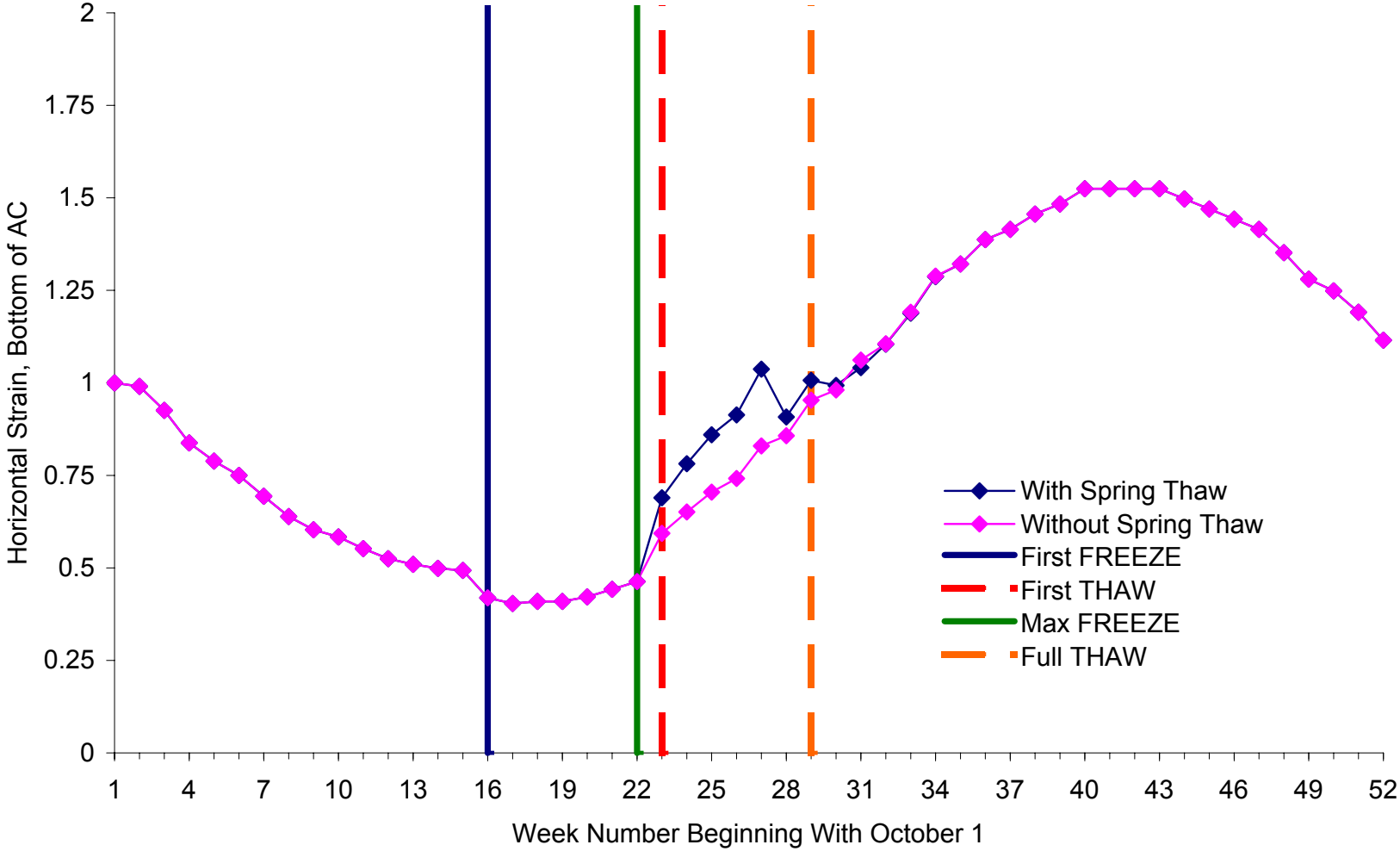

Figure Y-5. Normalized Horizontal AC Strain at Site 27-6251 (Poorly Graded Sand with Silt)

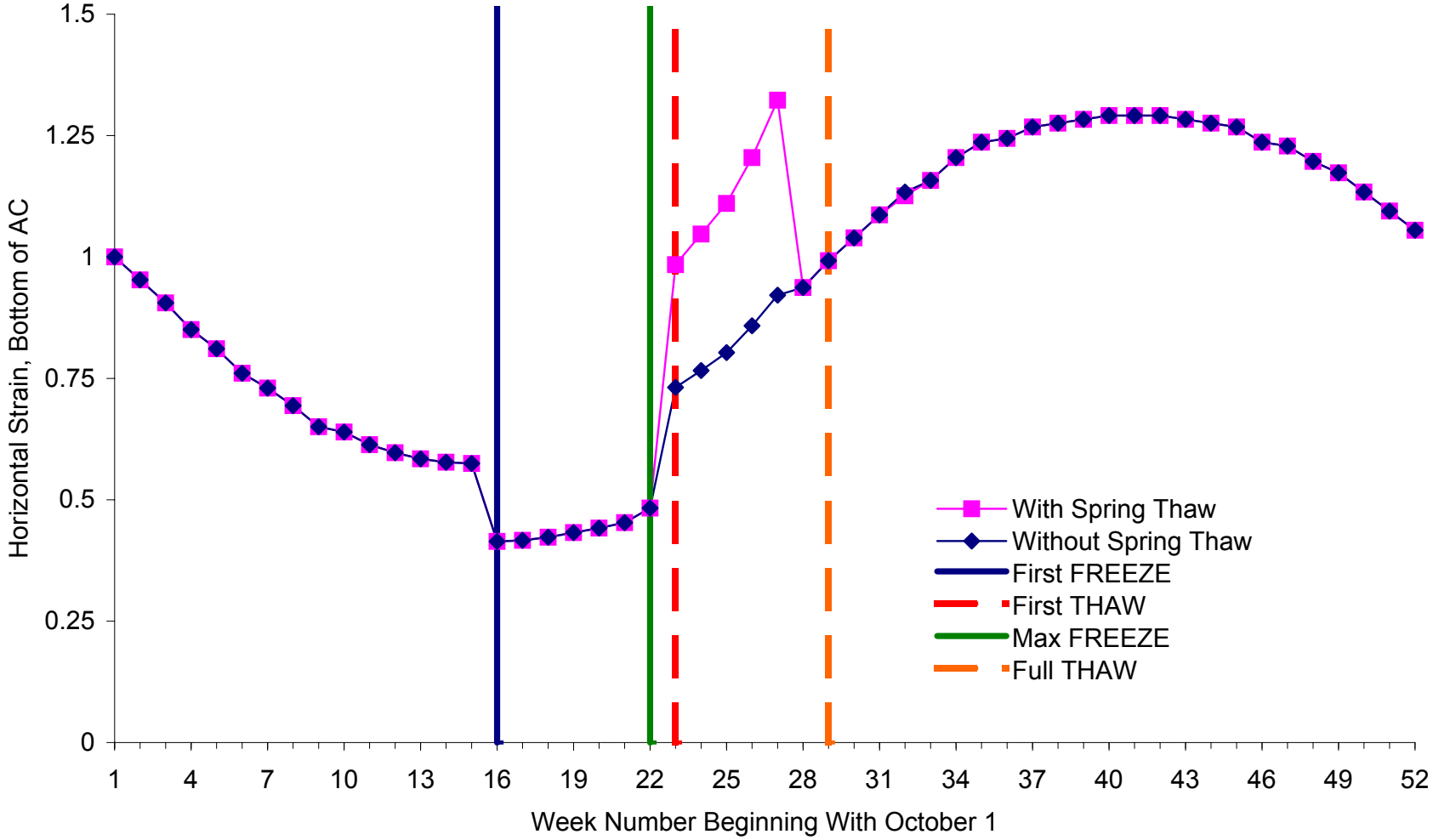

Figure Y-6. Normalized Horizontal AC Strain at Site 30-8129 (Poorly Graded Sand with Silt)

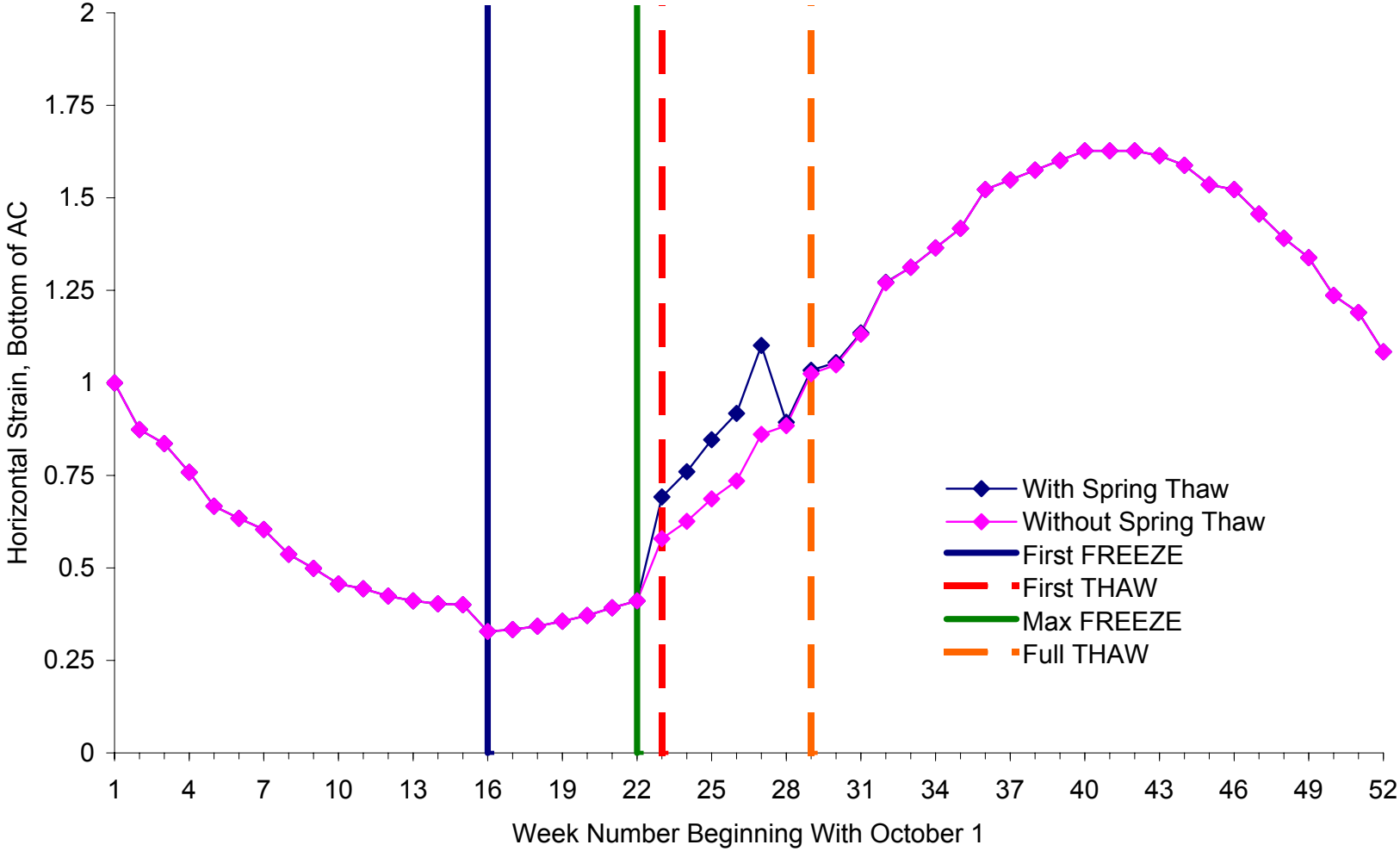

Figure Y-7. Normalized Horizontal AC Strain at Site 50-1002 (Poorly Graded Gravel with Silt and Sand)

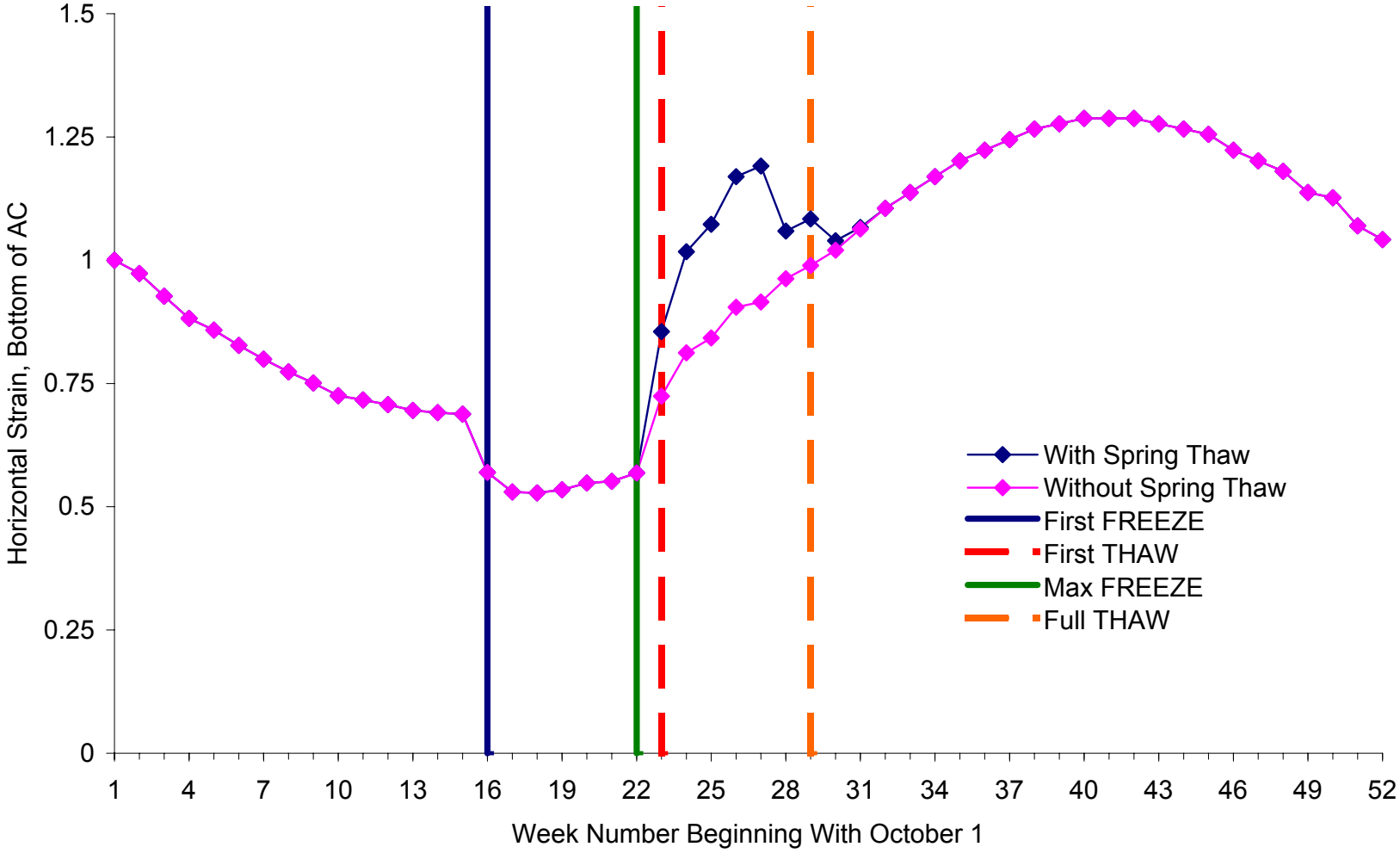

Figure Y-8. Normalized Horizontal AC Strain at Site 87-1622 (Sandy Silt)

APPENDIX Z

SEASONAL VARIATIONS OF PREDICTED NORMALIZED SUBGRADE STRAIN

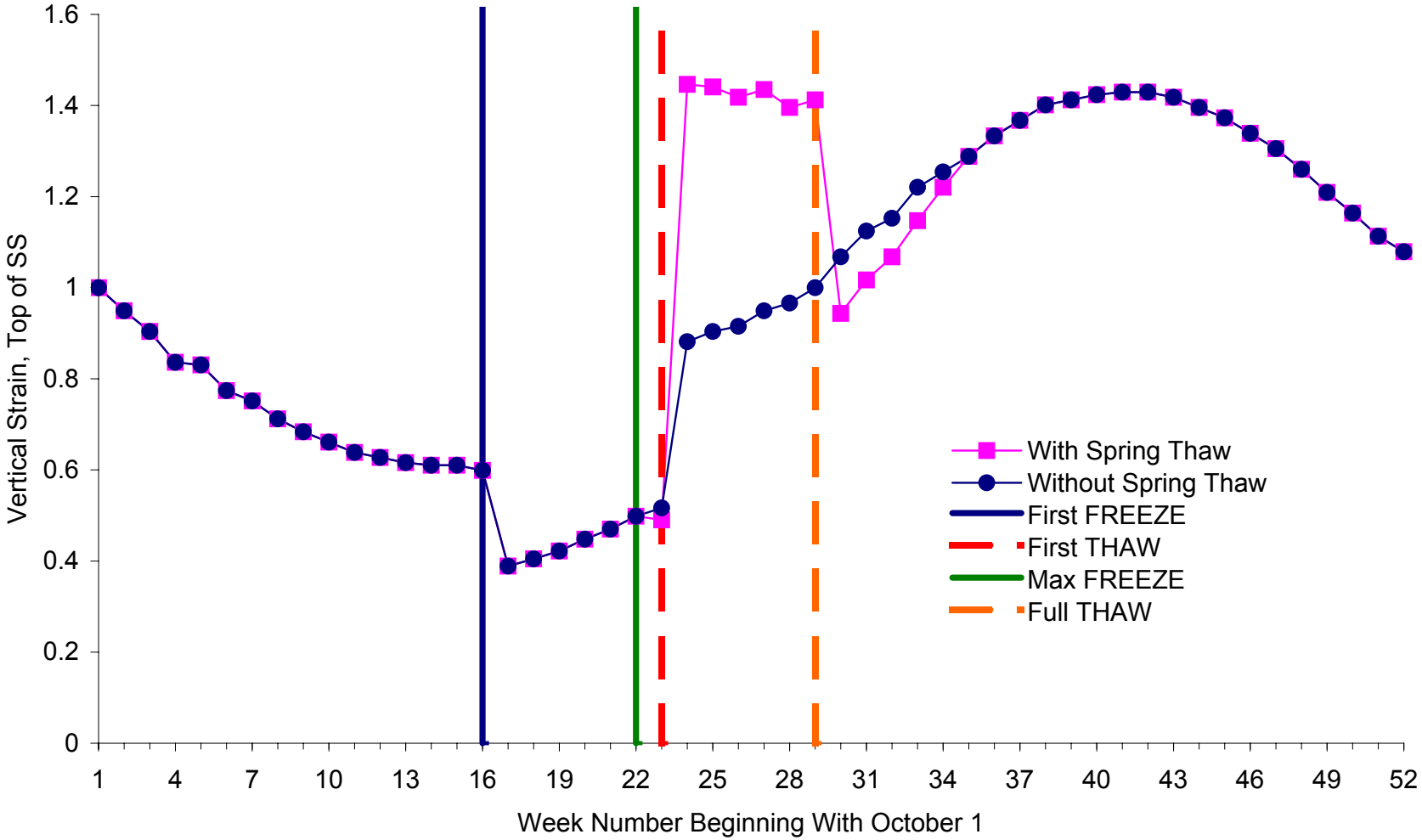

Figure Z-1. Normalized Vertical Subgrade Strain at Site 16-1010 (Silty Sand)

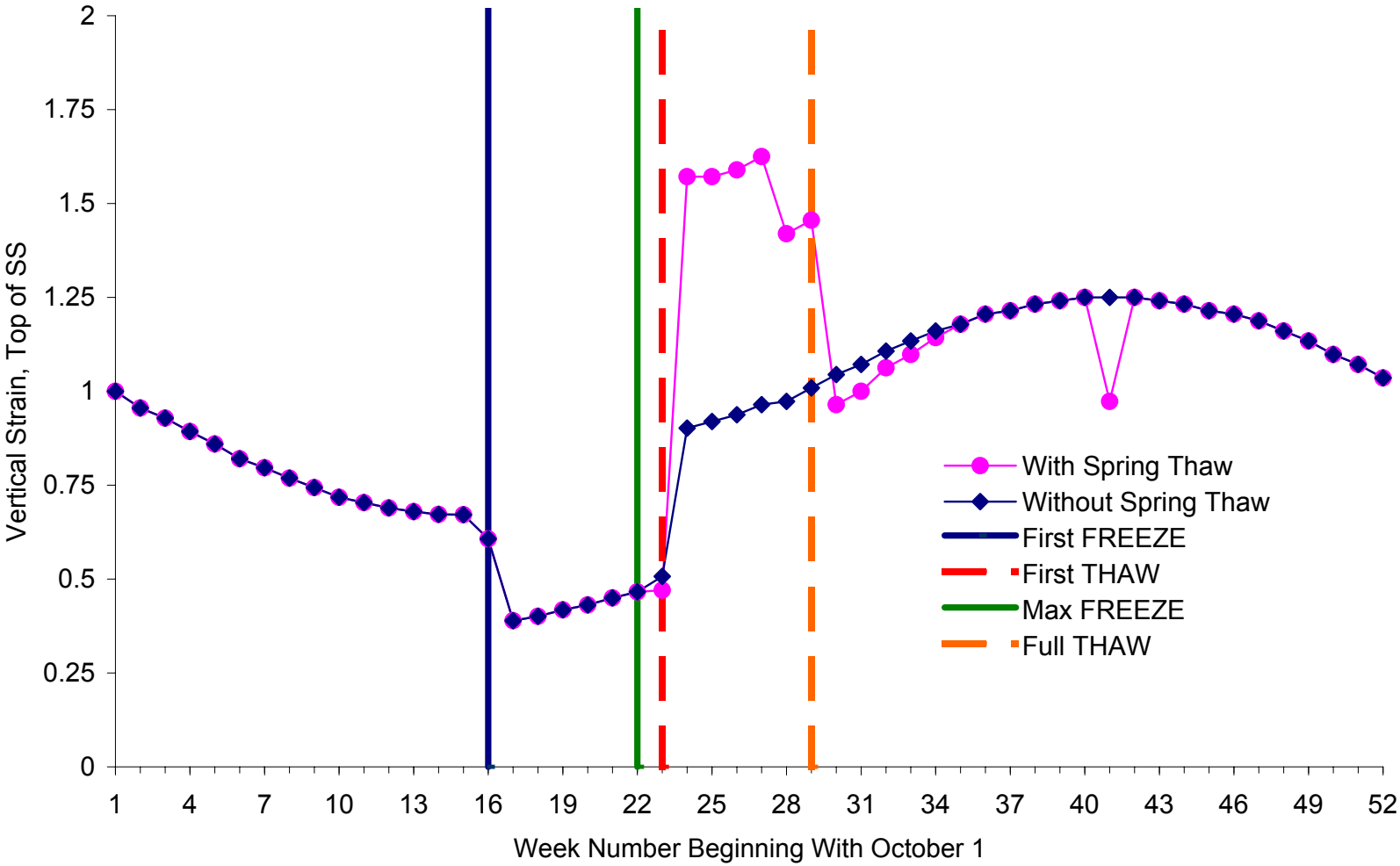

Figure Z-2. Normalized Vertical Subgrade Strain at Site 23-1026 (Silty Sand with Gravel)

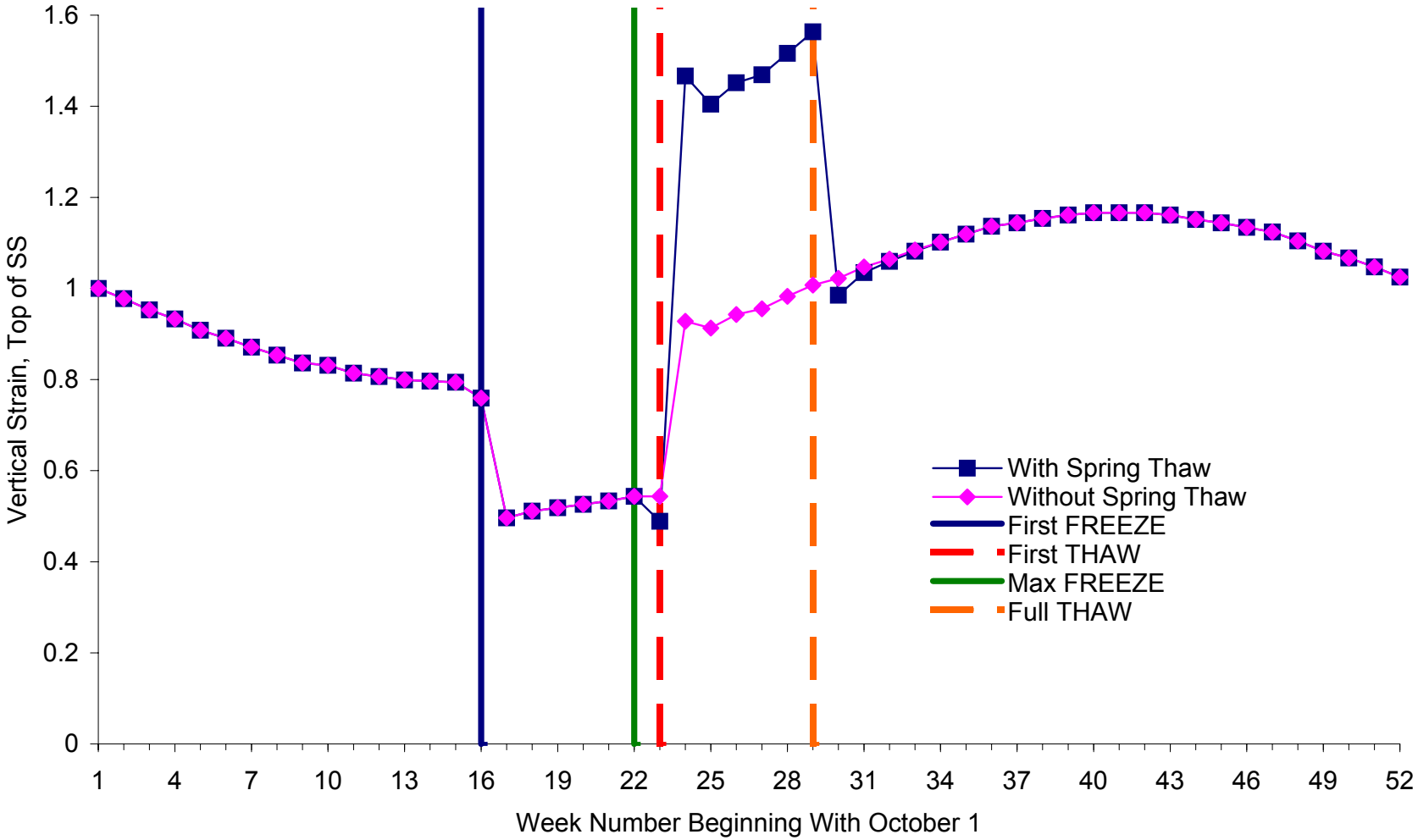

Figure Z-3. Normalized Vertical Subgrade Strain at Site 27-1018 (Poorly Graded Sand with Silt)

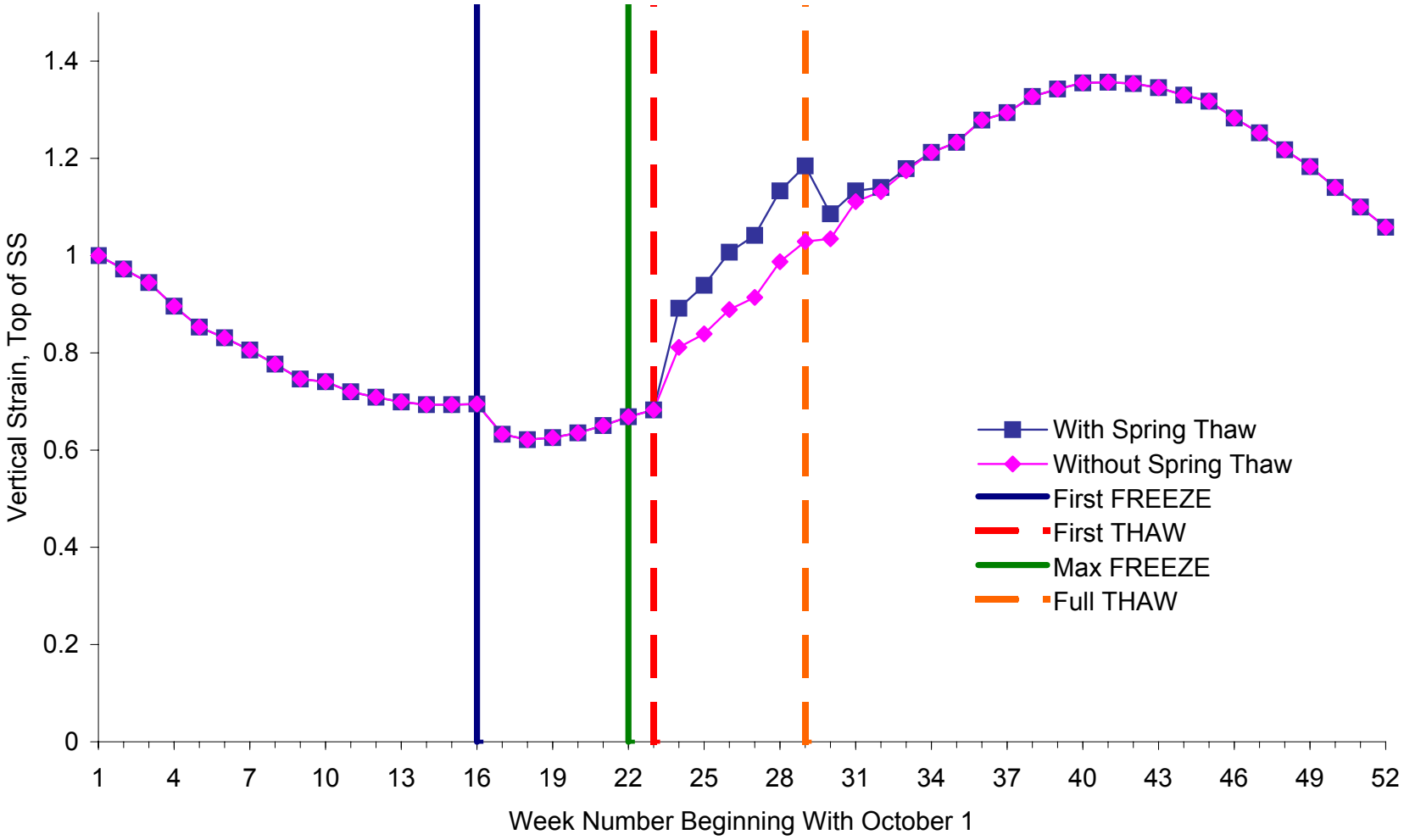

Figure Z-4. Normalized Vertical Subgrade Strain at Site 27-1028 (Poorly Graded Sand with Silt)

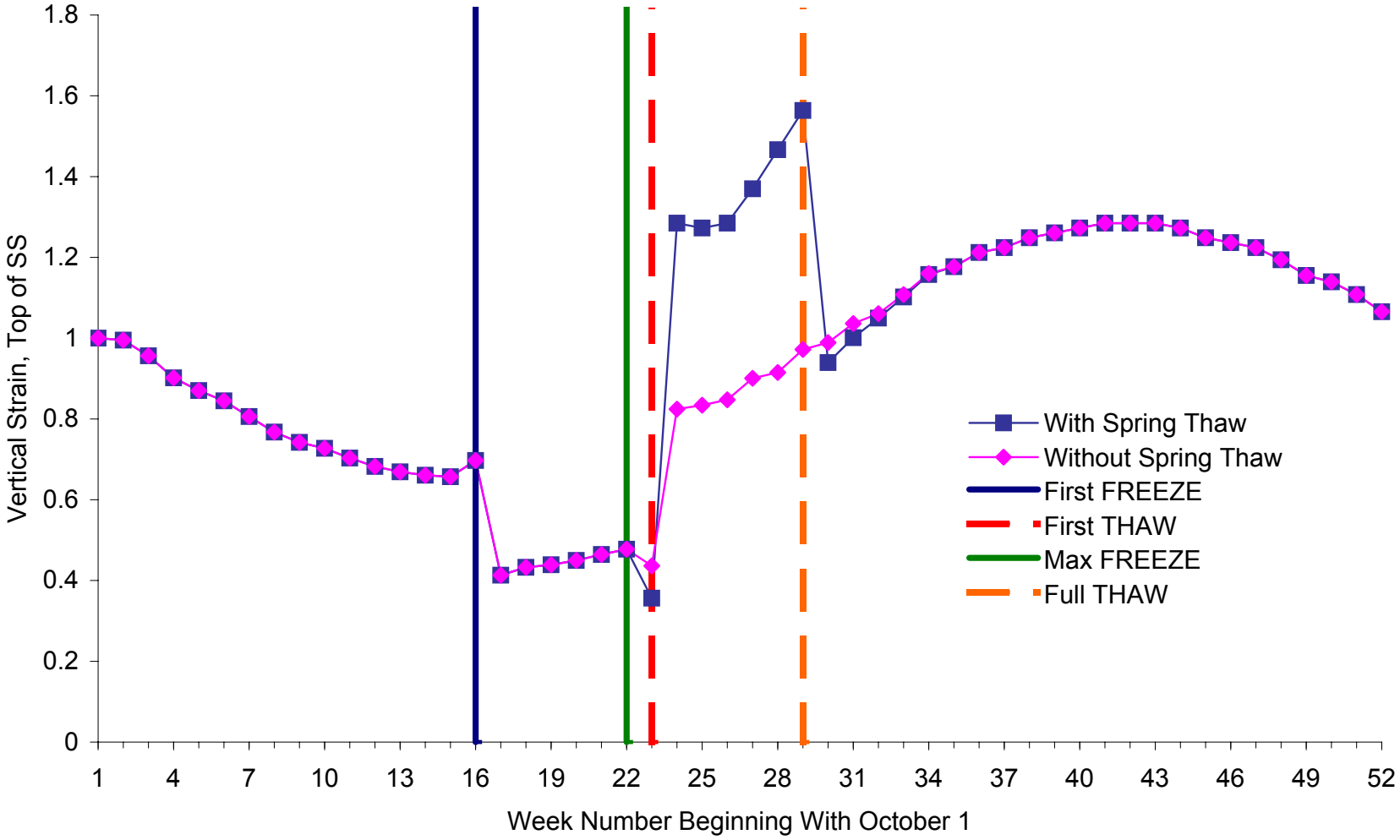

Figure Z-5. Normalized Vertical Subgrade Strain at Site 27-6251 (Poorly Graded Sand with Silt)

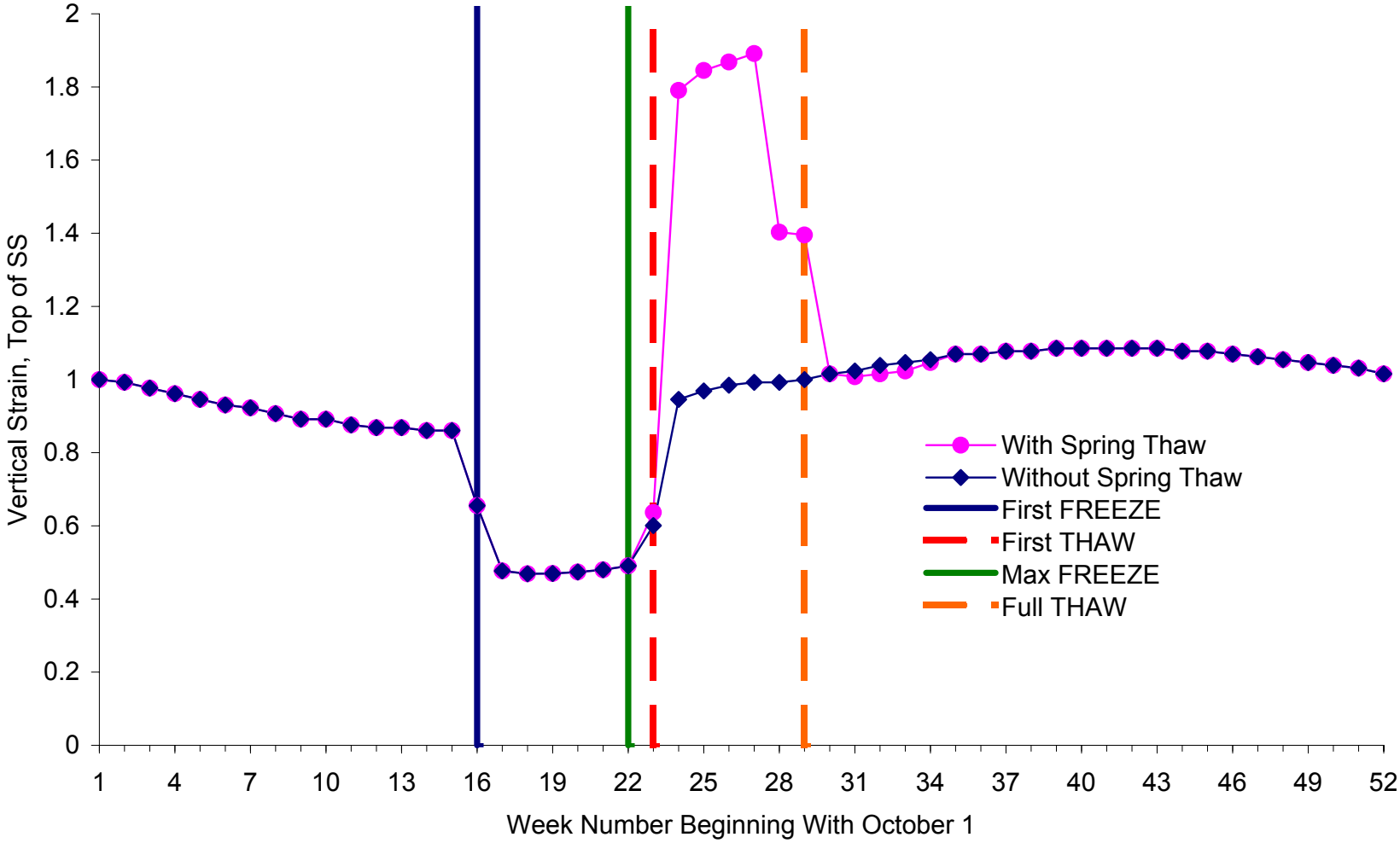

Figure Z-6. Normalized Vertical Subgrade Strain at Site 30-8129 (Poorly Graded Sand with Silt)

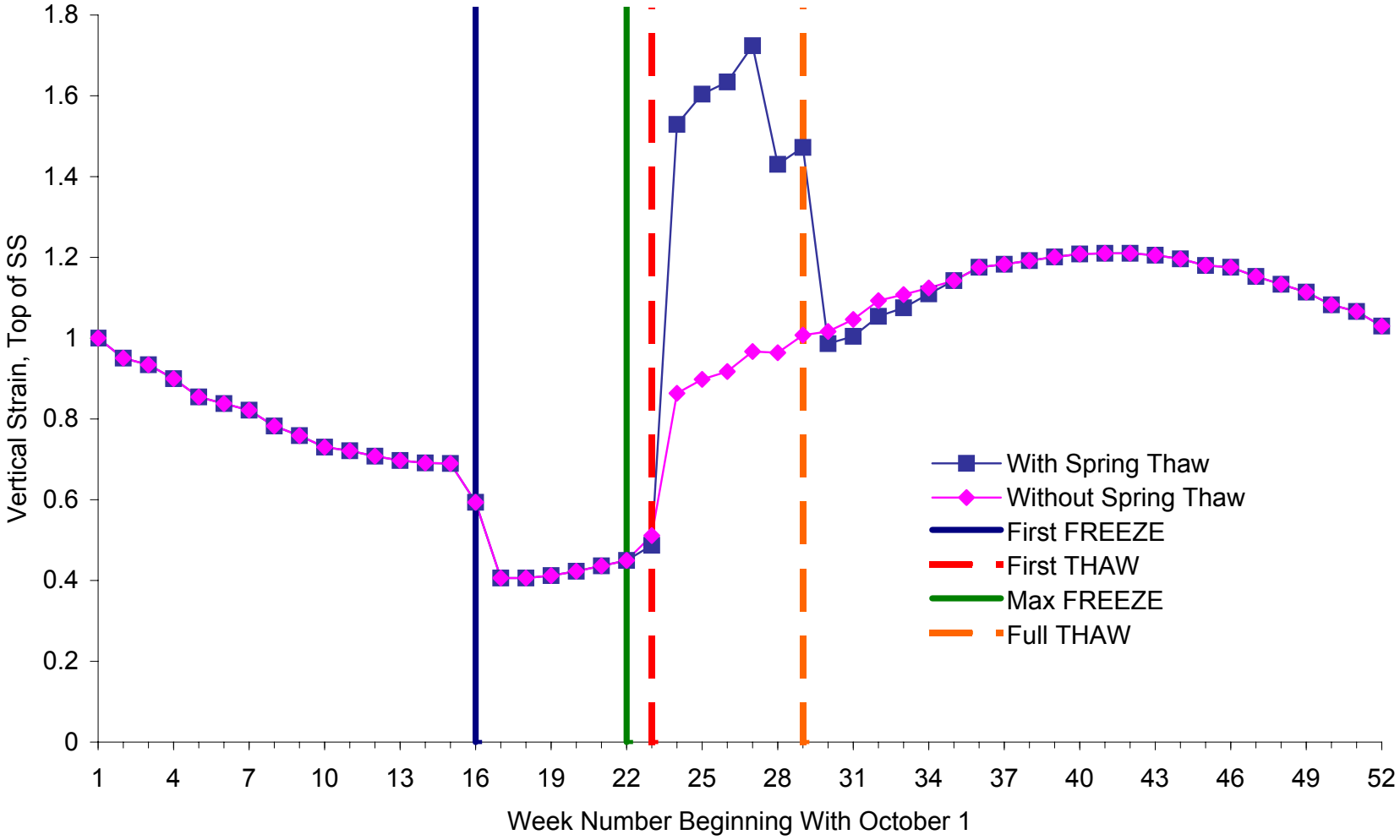

Figure Z-7. Normalized Vertical Subgrade Strain at Site 50-1002 (Poorly Graded Gravel with Silt and Sand)

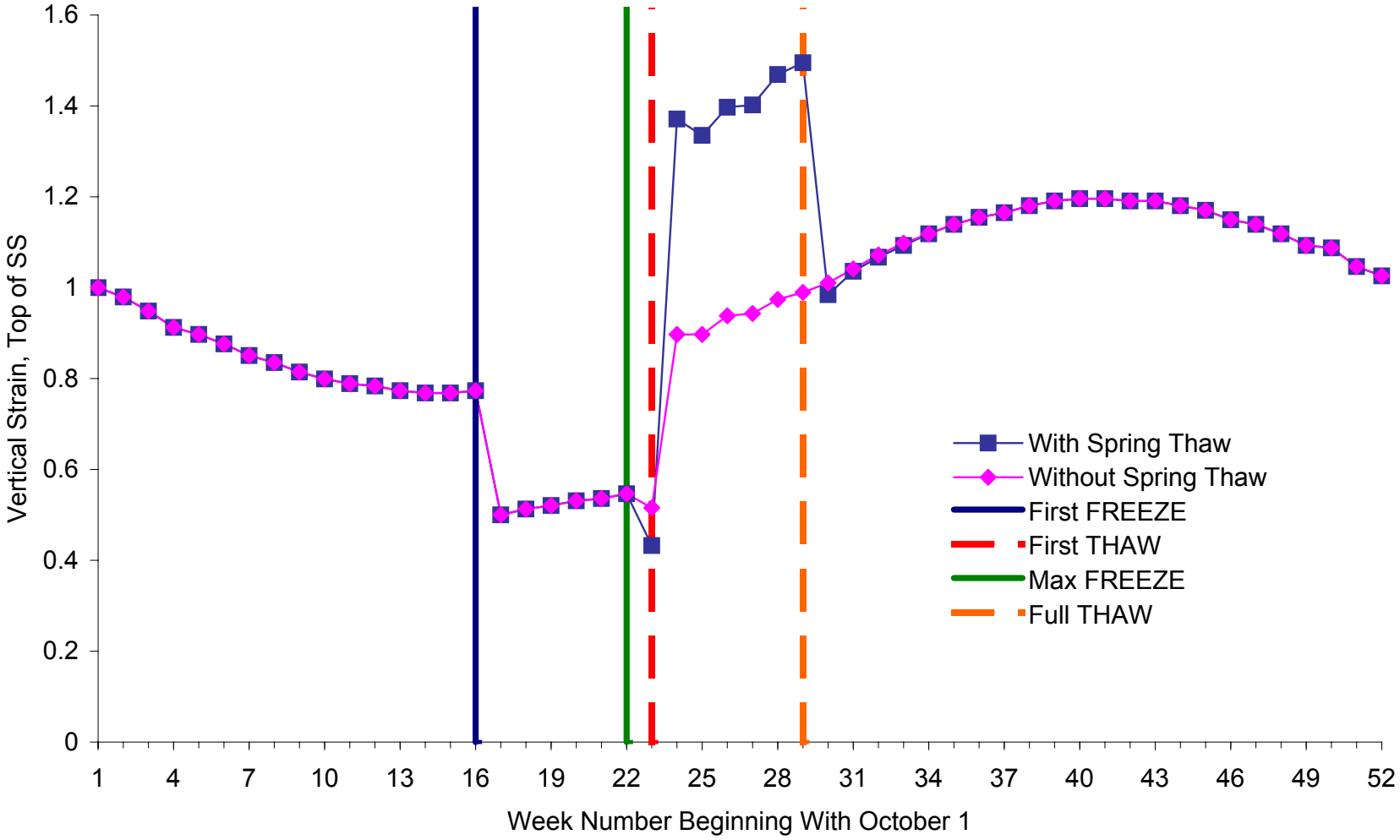

Figure Z-8. Normalized Vertical Subgrade Strain at Site 87-1622 (Sandy Silt)